HAL
open science

# Évolution spatio-temporelle des déformations sismiques tardi-Pleistocènes et Holocènes dans le massif du Gobi-Altaï, Mongolie : approches morphotectonique et paléosismologique

Robin Kurtz

**To cite this version:**

Robin Kurtz. Évolution spatio-temporelle des déformations sismiques tardi-Pleistocènes et Holocènes dans le massif du Gobi-Altaï, Mongolie : approches morphotectonique et paléosismologique. Sciences de la Terre. Université Montpellier, 2017. Français. NNT : 2017MONTT141 . tel-01726714

**HAL Id: tel-01726714**

**https://theses.hal.science/tel-01726714**

Submitted on 8 Mar 2018

**HAL** is a multi-disciplinary open access archive for the deposit and dissemination of scientific research documents, whether they are published or not. The documents may come from teaching and research institutions in France or abroad, or from public or private research centers.

L'archive ouverte pluridisciplinaire **HAL**, est destinée au dépôt et à la diffusion de documents scientifiques de niveau recherche, publiés ou non, émanant des établissements d'enseignement et de recherche français ou étrangers, des laboratoires publics ou privés.

# THÈSE POUR OBTENIR LE GRADE DE DOCTEUR DE L'UNIVERSITÉ DE MONTPELLIER

En Morphotectonique et Paléosismologie

École doctorale GAIA

Unité de recherche Géosciences Montpellier

# Évolution spatio-temporelle des déformations sismiques tardi-Pléistocènes et Holocènes dans le massif du Gobi-Altaï, Mongolie : approches morphotectonique et paléosismologique

Présentée par Robin KURTZ
Le 24 novembre 2017

Sous la direction de Jean-François Ritz
et Yann Klinger

Devant le jury composé de

| | |
|---|---|
| Mme Lucilla Benedetti, DR, CEREGE | Examinatrice |
| M. Jérôme Van der Woerd, CR, IPGS | Rapporteur |
| M. Riccardo Vassallo, MC, ISTerre | Rapporteur |
| M. Richard Walker, PR, University of Oxford | Examinateur |
| M. Matthieu Ferry, MC, Géosciences Montpellier | Co-encadrant |

UNIVERSITÉ DE MONTPELLIER

**Abstract**

Western Mongolia experienced an exceptional intracontinental seismic activity during the first part of the XX$^{th}$ century, with four seismic events with Mw > 7.9, located on large strike-slip faults with a transpressive lateral motion. This historical seismicity has been qualified as a cluster, and paleoseismological studies indicate that this phenomenon might have occurred 3 to 4 ka ago. Although the eastern part of the Gobi-Altai mountain range broke during the eponymous earthquake in 1957 (Mw8) along the Eastern Bogd Fault (EBF), several fault traces affecting Holocene formations and presenting continuous fault length > 100 km have been documented in the western part of the range, while not have been the purpose of quantitative studies.

This thesis first gives an inventory of the seismic activity within the Gobi-Altai, through detailed mapping of the fault scarps, showing evidences of activity during the late-Pleistocene, also with an analyze of the fault segmentation regarding to geometric and kinematic criteria. Secondly, some morphotectonical and paleoseismological surveys have been carried on, along with dating techniques as $^{10}$Be *in situ*, OSL and radiocarbon, which allow quantifying the faults slip-rates since late-Pleistocene, and paleo-ruptures ages during the Holocene period on the two main strike slip faults analyzed : the Valley of Lakes Fault (VOLF), and the Western Bogd Fault (WBF). Preliminary data also allow quantifying the slip rates and the age of the most recent event along the Tsogt Fault (TF) and the Tsagaan Gol fault (TGF), respectively located in the westward continuation of the WBF and the VOLF. Moreover, systematic lateral offset measurements have been carried on along the faults traces, and especially along the 1957 surface rupture, where a statistical approach based on probability density functions has been applied in order to assess the average lateral offsets successively recorded by the landforms, and reveals that the slip distribution along the EBF over 3 seismic cycles. This suggests first that the slip distributions rather even along the rupture, and secondly that the slip related to the 1957 earthquake is of the same amount than previous major ruptures on that fault, for half of the main 1957 surface rupture. This approach of average coseismic slip assessment on several seismic cycles is promising but still presents some inconsistencies, and we propose developments and validation perspectives.

Morphotectonic parameters and ages of paleo-earthquakes reported in this thesis present a strong consistency with former studies along the EBF, with slow slip-rates (0,7 ± 0,2 mm.yr$^{-1}$ on the WBF and 0,5 ± 0,1 mm.yr$^{-1}$ on the VOLF), and significant left lateral coseismic offsets of 1.5 to 4.0 m for most recent events. Our measurements of slip rates indicate furthermore a distribution of the on-fault deformation from the EBF to the WBF and the VOLF, splitting the deformation in two branches, the north one reaching the TGF and the southern one visibly branches on the TF. Assessments of the paleoearthquakes ages show three possible clusters among the studied faults during the Holocene time, and one of them may break the three faults (WBF, EBF and VOLF), and seems as well to correspond to the cluster possibly identified to date 3-4 kyr ago. The fault parameters presented in this thesis allow computing the paleomagnitudes related to last seismic events along the WBF and the VOLF, ranging from Mw7.6 and Mw8, depending of parameters and empirical relations considered. Finally those fundamental data may serve as basic pattern for current seismic hazard assessments in Mongolia.

## Résumé

La Mongolie occidentale a connu une sismicité intracontinentale exceptionnelle au cours de la première moitié du XX$^{e}$ siècle, avec 4 évènements sismiques d'une magnitude supérieure à 7.9, localisés sur des grandes structures décrochantes en régime transpressif. Cette sismicité historique a été qualifiée d'essaim sismique, et des études paléosismologiques indiquent que ce phénomène a déjà pu se produire par le passé (3 à 4 ka). Mais si la partie Est de la chaine du Gobi-Altaï a rompu lors du séisme du même nom en 1957 (Mw8) le long de la faille de Bogd orientale (WBF), plusieurs traces de failles affectant des formations Holocènes et présentant des longueurs > 100 km ont été documentées dans la partie ouest du massif, sans pour autant faire l'objet d'études quantitatives.

Cette thèse apporte un état des lieux de l'activité sismique dans le Gobi-Altaï, au travers d'une cartographie détaillée des escarpements de failles actives au cours du pléistocène supérieur, associée à une analyse de la segmentation au regard de critères géométriques et cinématiques. Parallèlement, des investigations morphotectoniques et paléosismologiques, couplées à des méthodes de datations au 10Be *in situ*, OSL et $^{14}C$, ont permis de quantifier les vitesses de glissement depuis le Pléistocène supérieur, et les âges des paléo-ruptures au cours de l'Holocène sur les deux principaux décrochements analysés : les failles de la Vallée des Lacs (VOLF), et de Bogd occidentale (WBF) ; des données préliminaires permettent également de contraindre l'âge de la dernière rupture et la vitesse de glissement sur les failles de Tsogt (TF) et de Tsagaan Gol (TGF), situées respectivement dans le prolongement occidental de la WBF et de la VOLF. De plus, des mesures systématiques des décalages cosismiques horizontaux enregistrés par la morphologie, notamment le long de la rupture de surface du séisme de 1957, couplés à l'utilisation et le développement d'une approche statistique de détermination des glissements cosismiques moyens au regard de la segmentation, a permis de déterminer la fonction de distribution du glissement le long de l'EBF sur 3 cycles sismiques. Ces résultats suggèrent d'une part une distribution du glissement assez homogène le long de la rupture, et d'autre part que le glissement du séisme généré en 1957 est d'une amplitude comparable de celle des précédents séismes, pour au moins 50 % de la rupture principale. Cette approche de détermination statistique des glissements moyens sur plusieurs cycles sismiques est prometteuse mais présente néanmoins certaines incohérences, et des voies de développement et de validations sont proposées.

Les paramètres morphotectoniques et les âges des paléoséismes documentés dans cette thèse présentent une grande cohérence avec les données précédemment acquises sur l'EBF, avec des vitesses de faille lentes (0,7 ± 0,2 mm.a$^{-1}$ sur la WBF et 0,5 ± 0,2 mm.a$^{-1}$ sur la VOLF), des périodes de retour longues (4,0 ± 1,2 ka pour la WBF), et des décalages cosismiques de 1,5 à 4,0 m pour les derniers évènements. Nos mesures de vitesses de faille indiquent par ailleurs une distribution de la déformation depuis la EBF vers les WBF et VOLF, séparant la déformation en deux faisceaux de failles, l'un se branchant au nord depuis la VOLF sur la TGF, et l'autre se branchant sur la TF au sud. Les déterminations des âges de paléoséismes indiquent une possibilité de cluster entre les différentes failles étudiées, avec trois ruptures potentiellement synchrones au cours de l'Holocène, dont une, rompant l'intégralité des décrochements analysés (WBF, EBF et VOLF), s'avère être temporellement corrélée au précédent cluster potentiellement identifié à 3 – 4 ka. Les paramètres présentés dans cette thèse permettent finalement de calculer des paléomagnitudes associées aux deniers évènements sur les WBF et VOLF, comprises entre Mw7,6 et Mw8 selon les paramètres et les lois considérés. Ces données fondamentales pourront servir de canevas de base pour les actuelles études d'aléas sismique en Mongolie.

À mes parents

*…De la jouergitude des choses…*

# Remerciements

Cette thèse fut une belle aventure, qui n'aurais pas été la même sans l'aide et le soutient d'un grand nombre d'acteurs qui m'ont à leur manière permis de mener à bien ce travail, tout en ne cessant d'y prendre du plaisir. Ces années ont été riches d'enseignements, de découvertes, de voyages et de rencontres, dont je garde un intense souvenir, et que j'ai taché de consigner dans ce manuscrit.

Chaque strate arpentée au cours de ce périple a son importance : la qualité de l'encadrement bien sûr, les riches rencontres avec les mongoles et leur pays, la belle ambiance du labo, mais aussi le soutient à la maison, les collocs, la famille et les amis, qui permettent de se ressourcer avant de replonger dans les tranchées.

Je tiens en premier lieu à remercier le Jury d'avoir accepté d'évaluer ce travail et d'y avoir consacré une grande considération. Merci à Jeff et Yann pour leur confiance, leurs enseignements et leur suivit tout au long de cette thèse. Merci également pour votre patience, et pour m'avoir transmis votre approche et votre rigueur. Un grand merci à Matthieu, pour sa bonne humeur et ses innombrables conseils techniques qui me sont fort utiles. Ces missions en Mongolie resteront gravés, et constituent je l'espère une belle base pour mes futurs travaux.

Un grand merci à tout le labo de GM, pour ces sourires partagés, ces moments de réflexions autours de projets aussi multiples qu'intéressants. Merci en outre à l'équipe risque, pour ces nombreux échanges et pour avoir accepté de partager le budget. Je remercie particulièrement Rodolphe, Laurent, Serge, Cédric et Fred Bouchette pour leur considération et leur attention à mon égard depuis le Master.

J'adresse un grand merci à l'ensemble de l'IAG à Ulan Battor, Demeberel, Ulzii, Odon, ainsi qu'à Nara et aux chauffeurs Tsarana, Puje et Tsolbot, qui ont su nous convoyer en sécurité sur les routes mongoles. Un grand merci au gouverneur de Chandmani pour son aide et sa considération à notre égard au cours des missions, ainsi qu'à l'ensemble des nomades que nous avons rencontré. Je remercie tout particulièrement Toogii pour son amitié et ses innombrables services qu'il nous a rendus en tant que manager, logisticien et interprète. Longue vie et belle carrière à toi Tog's.

Merci à Magali Rizza, Laurent Bollinger et Carole Prentice pour avoir partager leur connaissance du terrain, ainsi qu'à Régis Brocher pour son encadrement et son aide lors des analyses Berylium, ainsi que qu'à Magali et l'ensemble de l'Aster Team du CEREGE et leurs doctorants : Jim, Amandine, Claire et tous les autres.

Je remerci Shannon Mahan et Markus Fluchs pour leur travaux sur les échantillons OSL.

Merci à toute la jouerge clique des doctorants de GM, Alizia, Anaïs, Anitouch, Alexandre, Antoine, Audrey, Barbara, Ben, Carlotta, Cypoutch, Enora, Fabounet, la Gaine, Justine, Laure et ses boucles, Lulu, Manar, Manon, Manoon, Oliv, Romain, Romanus Bouthanus, Séverine, Sven, Théo, Yannick et tous ceux que j'ai oublié ! Spécial big up à Anita, sa bonne humeur, ses sourires et ses conseils Matlab ! Une belle pensée également à tous les membres de l'IPGP et la bande des doctorants associée, tout particulièrement Amandine, Amaury, Marthe et Pierre. Merci pour leur chaleureux accueil.

Un grand merci à ma famille, qui m'a toujours fait confiance et m'a donné son soutient et son intérêt : Maman pour son énergie, Papa pour sa curiosité, ses relectures, ses questionnement perpétuels et son amour du paysage, mais aussi à Martine, Franck, Phil et Marie, Kévin, toute la clique vertaco des Blaches, Maya, les Krutz du sud et les Zbans du Nord.

Un immense merci à Wiwi pour ses infaillibles encouragements, son perpétuel soutient et son enseignement de la volonté et du travail.

Merci à tous les copains pour ces bouffées d'air et ces sessions velues : le Gamin, Simon, Camomille, JB, Max et Lulu, Matis, Brice et la Uts team de St Hil, Loulou, John et Louise, Tony et Zoé, Matthiou et plein d'autres !

Je remercie de tout cœur les habitants et visiteurs de la colloc d'Aiguelongue, havre de jouregitude Montpelliéraine : Guillou, Tutur, Sandra, Alex, Samounet, Cajou, Claudia et Coco. Enfin, la meilleure pour la fin, mille mercis à Fredou, mon rayon de soleil, pour son soutient quotidien, sa tempérance, ses talents de cuisinière mongole et sa tolérance pendant ces deniers mois délicats.

Tout le meilleur !

# Table des matières

Remerciements ..... 5
Introduction générale ..... 10

Chapitre 1. Contexte géologique et sismotectonique du Gobi-Altaï ..... 14
I. Contexte tectonique ..... 14
II. Sismicité historique et instrumentale ..... 15
III. Taux de déformation géodésiques ..... 17
IV. Morphologie et structure du Gobi-Altaï ..... 19
V. Données sismotectoniques sur la faille de Bogd-Est ..... 22
V.1. Description ..... 22
V.2. Vitesses de glissement le long de la faille de Bogd Est ..... 24
V.3. Données paléosismologiques ..... 26
VI. Tectonique récente et active du Gobi-Altaï ..... 28
VII. La chaîne du Gobi-Altaï et son héritage géologique ..... 31
VII.1. Du Précambrien au Mésozoïque : Accrétion des « *terranes* » ..... 32
VII.2. Evolution Cénozoïque ..... 35
VII.3. Du Néogène à l'actuel : réactivations successives ..... 37

Chapitre 2. Approches, matériels et méthodes ..... 39
I. Approche morphotectonique: Caractérisation d'une rupture de surface ..... 39
I.1. Principe ..... 39
I.2. Géométrie de la rupture : Cartographie et Identification de sites ..... 40
I.3. Analyse de la distribution spatiale du glissement ..... 43
I.4. Quantification des vitesses de glissement et de leurs variations au cours du temps ..... 53
II. Approche Paléosismologique ..... 73
II.1. Principe ..... 73
II.2. Travaux en tranchée ..... 74
II.3. Datations ..... 78
II.4. Implications et limites ..... 80

Chapitre 3. Horizontal surface-slip distribution through several seismic cycles: the Eastern Bogd fault, Gobi-Altai, Mongolia ..... 81
I. Introduction ..... 82
II. Setting ..... 83
II.1. Geological setting ..... 83
II.2. Slip rates and past earthquakes along Eastern Bogd Fault ..... 84
II.3. Seismic activity in Mongolia ..... 85

II.4. The 1957 surface rupture ..... 86
III. Orthophotographs ..... 86
IV. Data Analysis ..... 88
IV.1. Surface rupture mapping and fault segmentation ..... 88
IV.2. Offset Measurements ..... 89
V. Results and Discussion ..... 94
V.1. Slip-per-segment ..... 94
V.2. The 1957 Gobi-Altai earthquake ..... 96
V.3. Paleoearthquakes rupture enveloppes ..... 99
V.4. Characteristic slip ..... 100
VI. Summary ..... 103
Acknowledgment ..... 103
References ..... 104
Figures ..... 112

Chapitre 4. Late-Pleistocene - Holocene spatio-temporal distribution of seismic activity within the Western Gobi-Altai ..... 122
I. Introduction ..... 122
II. Tectonic setting ..... 124
III. Material and methods ..... 126
III.1. Mapping ..... 126
III.2. Coseismic offset assessments ..... 128
III.3. Slip rates ..... 131
III.4. Paleoseismology ..... 132
IV. Results ..... 133
IV.1. Main surface ruptures of the Gobi-Altai mountain range ..... 133
IV.2. Earthquake geology of the WBF ..... 145
IV.3. Earthquake geology of the VOLF ..... 231
IV.4. Tsagaan Gol Fault ..... 270
IV.5. Tsogt fault ..... 293
IV.6. South Gichigniy Nuruu faults ..... 313
IV.7. N-Chandmani fault ..... 315
V. Summary of results and paleomagnitude computations ..... 318
V.1. Estimating recurrence intervals and magnitudes of past-earthquakes ..... 318
V.2. EBF ..... 319
V.3. WBF ..... 322
V.4. VOLF ..... 322
V.5. NCVF ..... 323
V.6. TGF ..... 323

V.7. Tsogt fault....324
V.8. NABF....325
VI. Conclusion....327

Chapitre 5. Discussions et perspectives....330
I. Limites et hypothèses de travail....330
I.1. Longueurs des ruptures de surfaces....330
I.2. Vitesses de glissement long-terme....333
I.3. Indentification des paléoséismes et estimation des périodes de retour....337
I.4. Quantification des décalages cosismiques....339
I.5. Question de l'épaisseur crustale dans le calcul des magnitudes....350
II. Corrélations entre les paramètres déterminés....351
II.1. Bilan des vitesses de glissement dans le massif du Gobi-Altaï....352
II.2. Déplacements cosismiques moyens et longueur de ruptures....353
II.3. Périodes de retour et déplacement cosismiques moyens....355
II.4. Corrélation des paléoséismes entre les principales failles du Gobi-Altaï : essaims de sismicité ?....359
III. Perspectives....362
III.1. Cartographie....362
III.2. Modélisation....362
III.3. Segmentation....363
III.4. Paléosismologie et distribution du glissement....365

Conclusion générale....366

Références 368
Annexes 387
I. *Supplementary materials*, Chapitre 3 (papier à Tectonophysics)....387
II. Radiocarbon ages....392
III. OSL ages along the Western Bogd Fault....394
IV. OSL ages along the Valley of Lakes Fault....400
V. Horizontal offset measurements along the Western Bogd Fault....410
VI. Horizontal offset measurements along the Valley of Lakes Fault....411
VII. Horizontal offset measurements along the Eastern Bogd Fault....412

# Introduction générale

L'étude des failles actives est fondamentale pour comprendre l'évolution géodynamique d'une région et caractériser son aléa sismique. La motivation de ce travail de thèse est de caractériser l'activité sismique de la chaine du Gobi-Altaï, en Mongolie, au cours de l'Holocène, et son évolution sur la période tardi-Pléistocène – Holocène.

La Mongolie occidentale est affectée par une déformation tectonique transpressive, essentiellement localisée sur des décrochements d'échelle crustale (e.g. Tapponnier et Molnar, 1979), et a connu une crise sismique majeure au XX$^{e}$ siècle, avec 4 séismes de magnitude Mw>7.9 entre 1905 et 1957 (e.g. Baljinnyam et al., 1993). Cette sismicité a été définie comme exceptionnelle compte tenu du contexte intracontinental, des faibles taux de déformation de l'ordre de $10^{0}$-$10^{1}$ mm.an$^{-1}$ (e.g. Ritz et al., 1995; Calais et al., 2003; Vergnolle et al., 2003; Walker et al., 2006), et des temps de retour importants ($10^{0}$ ka) associés à de tels évènements (Schwartz et al., 1996; Prentice et al., 2002; Ritz et al., 2009; Rizza, PhD, 2010). Chéry et al. (2001) ont suggéré que cette sismicité correspond à un essaim sismique localisé dans le temps, se répétant à intervalles réguliers par un processus de transfert de contraintes viscoélastiques dans la croûte supérieure ou le manteau inférieur. Les données paléosismologiques (i.e. âges des paléoruptures, et analyse combinée de la distribution du glissement cosismique avec les vitesses long terme) récoltées sur deux des failles ayant cassé au XX$^{e}$ siècle (i.e. Bogd orientale et Bolnay) suggèrent effectivement que l'essaim sismique du XX$^{e}$ siècle ait déjà pu se produire auparavant avec une période de récurrence d'environ 3-4 ka (Rizza, PhD, 2010; Rizza et al., 2011, 2015).

La rupture la plus récente au XXe siècle s'est produite le 4 décembre 1957, dans le massif du Gobi-Altaï, au sud-ouest de la Mongolie (Figure 0-1-A), lors du séisme du même nom, de magnitude Mw8. Depuis, la faille de Bogd, située dans la partie orientale de la chaine (Figure 0-1-B), sur laquelle s'est produit ce séisme, a fait l'objet de plusieurs études morphotectoniques et paléosismologiques (e.g. Florensov et Solonenko, 1965; Kurushin et al., 1998; J. F. Ritz et al., 1995, 2003, 2006; Prentice et al, 2002; Vassallo et al., 2007; Rizza et al., 2011; Choi et al., 2012). Par contre, bien que des évidences de ruptures de surface quaternaires supérieures à 100 km de long aient été documentées dans la partie ouest de la chaine (i.e. Florensov et Solonenko, 1965; Baljinnyam et al.,

1993; Cunningham et al., 1996; Schlupp, PhD, 1996), leur étude quantitative, notamment sur le terrain, n'a fait l'objet que d'un seul travail (Mushkin, PhD, 2007).

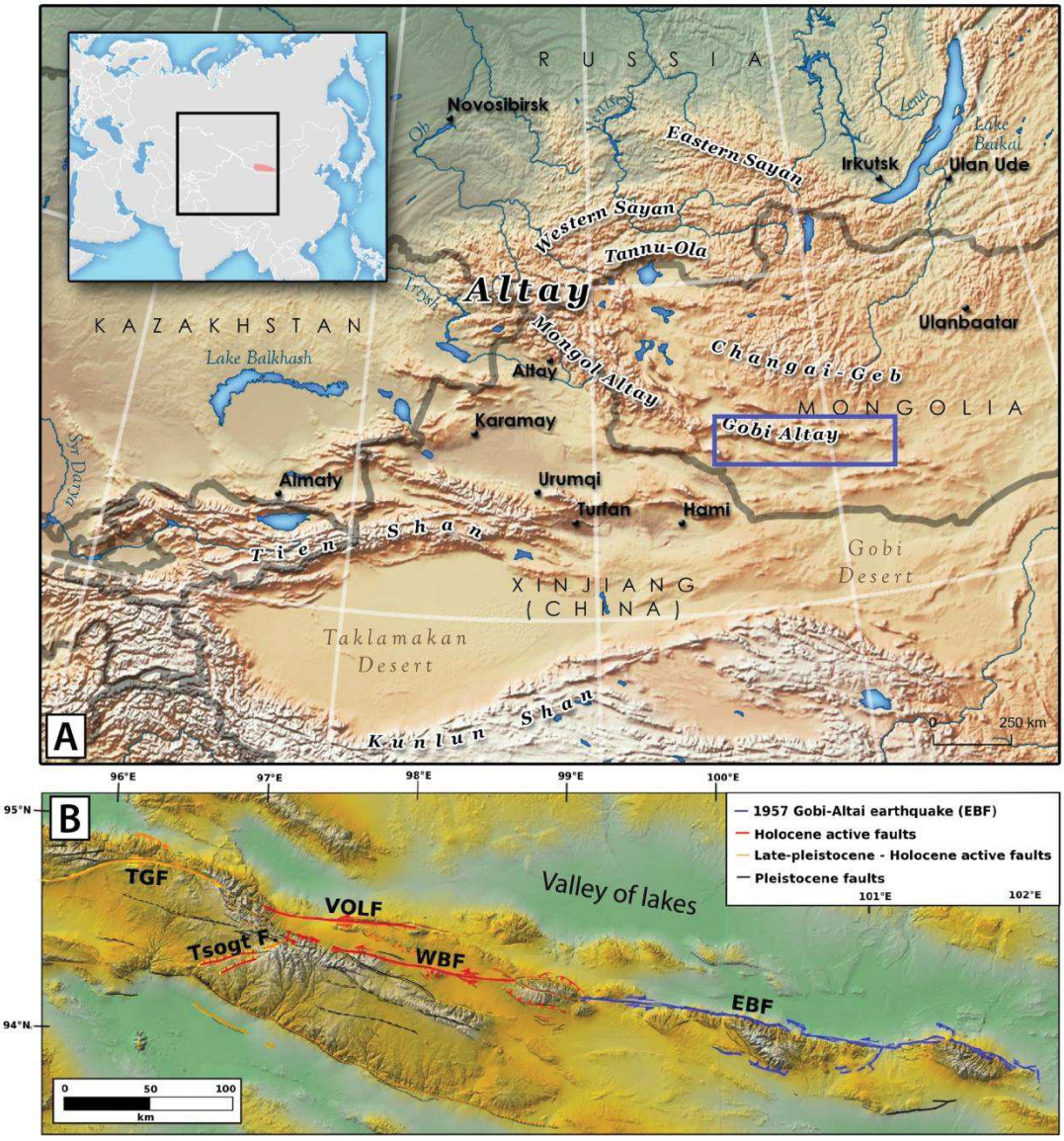


**Figure 0-1 : Contexte de l'étude. A. Carte topographique de l'Asie centrale, le cadre bleu indique la zone d'étude. L'encart localise la carte au sein de l'Asie, et la zone ombrée rouge représente la chaine du Gobi-Altaï. Les traits plein ombrés représentent les frontières politiques (carte modifiée de wikimedia.org/wiki/File:Altai_Mountains). B. Carte topographique du Gobi-Altaï et localisation des principales failles étudiées dans ce travail : TGF, Tsagaan Gol Fault ; VOLF : Valley of Lakes Fault (faille de la Vallée des Lacs) ; Tsogt F. : Tsogt Fault ; WBF : Western Bogd Fault (Faille de Bogd occidentale) ; EBF : Eastern Bogd Fault (faille de Bogd orientale).**

Les questions relatives à la distribution dans l'espace et dans le temps de ces autres grandes ruptures du Gobi-Altaï occidental restent donc posées : Comment s'intercalent-elles dans le temps et dans l'espace avec les failles qui semblent jouer en essaim ? Fonctionnent-elles également en essaim ? Ou bien, est-ce que l'activité de l'ensemble des failles du Gobi-Altaï est plus aléatoire qu'il n'y parait au premier abord ?

Notre objectif a donc été de caractériser la distribution dans l'espace et dans le temps des grandes ruptures sismiques qui se sont succédé dans le Gobi-Altaï au cours de l'Holocène. Cette analyse constitue une étude de cas du comportement sismique d'un système de failles actives en milieu intracontinental, et fournit un canevas de base pour les études d'aléas sismique dans cette région de la Mongolie.

Pour mener à bien cet objectif, nous nous sommes intéressés dans un premier temps à l'identification des principales failles sur l'ensemble de la chaine, et à la cartographie détaillée des ruptures de surface associées (géométrie, cinématique, distribution, segmentation). Dans un second temps, nous avons mené des investigations morphotectoniques et paléosismologiques sur le terrain, avec des levés microtopographiques, des analyses de tranchées paléosismologiques et des échantillonnages en vue de dater l'abandon des marqueurs ($^{10}$Be cosmogénique) ou l'âge des dépôts dans les tranchées (OSL, $^{14}$C). Le traitement et l'interprétation de l'ensemble de ces données, permettent en définitive de déterminer les paramètres des failles cartographiées : longueurs, segmentations, vitesses, décalages cosismiques, paléomagnitudes, âges des paléoséismes et éventuellement leurs périodes de retour. En parallèle, cette thèse présente une analyse de la distribution du glissement le long des failles décrochantes, par une évaluation statistique des décalages cosismiques successifs associés à différentes ruptures sur une section de faille donnée. Ce travail nous a permis d'analyser la question de la variation ou de la stabilité des déplacements le long d'une même faille au cours de cycles sismiques successifs. Dans un troisième temps nous avons analysé la distribution dans l'espace et dans le temps de la déformation sismique dans la chaîne du Gobi-Altaï.

Ces travaux permettent en outre une comparaison entre données paléosismologiques et paramètres morphotectoniques en ce qui concerne le fonctionnement des failles dans le temps : les périodes de retour déterminées sur l'Holocène en tranchées sont-elles cohérentes avec celles déduites des décalages cosismiques et des vitesses de failles ? L'évaluation des décalages cosismiques permet-elle de contraindre la taille (longueur de rupture et magnitude) des paléoséismes sur les grandes failles décrochantes intracontinentales ?

Ce manuscrit de thèse est composé de 5 chapitres :

Le premier chapitre présente le contexte géologique et sismotectonique du Gobi-Altaï, et rappelle les résultats morphotectoniques publiés sur la région. Il présente également une synthèse de l'histoire géologique du Gobi-Altaï et des déformations qui ont affectées les régions voisines.

Un second chapitre décrit les données et méthodes utilisées dans cette étude, en distinguant les approches paléosismologique (datations radiocarbone et OSL des paléoséismes), et morphotectonique (cartographie des failles, mesures et traitement statistique des décalages, analyse de la distribution du glissement, datations $^{10}$Be et OSL des marqueurs morphologiques, quantification des vitesses long terme).

Le chapitre 3 constitue une étude de la distribution du glissement horizontal le long de la rupture associée au séisme de 1957 (faille de Bogd orientale), au travers de plusieurs cycles sismiques. Cette étude est basée sur l'analyse de photos aériennes historiques prises lors d'une mission de l'Union Soviétique en 1958. Nous y exposons l'acquisition d'une base de données de mesures de décalages horizontaux par reconstruction en 3 étapes de marqueurs morphologiques, et son traitement statistique. Cette analyse permet de discuter de notre capacité à identifier les glissements cosismiques associés à des séismes successifs dans un contexte intracontinental, et d'analyser la question du glissement caractéristique le long de la faille de Bogd.

Le chapitre 4 expose les travaux de cartographie effectués sur l'ensemble de la partie occidentale du Gobi-Altaï, ainsi que les résultats acquis pendant trois campagnes de terrain menées durant les étés 2014, 2015 et 2016. Ce chapitre constitue une base de donnée morphotectonique, qui permet une première caractérisation de l'activité sismique des principales failles du Gobi-Altaï occidental (géométrie, segmentation, cinématique, vitesse de déplacement, âges et magnitudes du/des derniers séismes) ainsi qu'un bilan de la déformation sur la période tardi-Pléistocène – Holocène.

Le chapitre 5 discute tout d'abord de l'ensemble des résultats obtenus, notamment au regard des hypothèses de travail initiales, et des limites relatives aux approches utilisées dans cette thèse. Nous y discutons ensuite des corrélations observées ou non, au sein des paramètres de failles mesurés d'une part, et entre les paramètres mesurés et les paramètres théoriques pouvant être estimés par des relations empiriques (e.g. Wells et Coppersmith, 1994) d'autre part. Enfin nous présentons quelques perspectives de ce travail.

# Chapitre 1. Contexte géologique et sismotectonique du Gobi-Altaï

## I. Contexte tectonique

Au XXe siècle, la Mongolie a été le théâtre d'une intense activité tectonique intracontinentale, comme en attestent les 4 ruptures de surface associées aux séismes de magnitude Mw ≥ 7.9 qui se sont produits entre 1905 et 1957 dans sa partie occidentale et sa région frontalière avec la Chine (Baljinniam et al., 1993).

Cette activité tectonique est générée par un régime de compression NNE-SSW issu de la collision Inde-Eurasie, qui s'est propagé progressivement vers le nord (Molnar et Tapponnier, 1975; Tapponnier et Molnar, 1979; Patriat et Achache, 1984). Ainsi, bien que la Mongolie soit distante de plus de 2000 km du front himalayen, une partie des 35 $mm.a^{-1}$ de convergence entre les plaques Indienne et Eurasiatique est absorbée dans les massifs de l'Altaï et du Gobi-Altaï, après avoir généré au sud les reliefs de l'Himalaya, du Tibet, du Qilian Shan, du Kunlun et du Tien Shan, et réactivé en décrochement d'anciennes zones de failles telles que les failles du Fleuve rouge en Chine (e.g. Leloup et al., 1995), de l'Altyn Tagh au Tibet (e.g. Van der Woerd et al., 2000; Chevalier et al., 2005) ou de Talas-Fergana (Campbell et al., 2013; Mackenzie et al., 2015; Saint-Carlier et al., 2016; Abdrakhmatov et al., 2016) (Figure 1-1).

La déformation, qui a débuté au Sud à l'Oligocène-Eocène (Patzelt et al., 1996), s'est propagée progressivement vers le Nord, et bien que la chronologie des déformations au travers l'Asie ne soit pas complètement contrainte, la formation des chaînes du Gobi-Altaï et de l'Altaï apparaît morphologiquement et structuralement postérieure à celle des chaînes plus méridionales d'Asie Centrale (Kunlun Shan, Qilian Shan, Tien Shan) qui sont plus élevées en altitude, plus découpées et plus déformées (Vassallo, PhD, 2006). Au Nord Est du Gobi Altaï, Vassallo et al., (2007) ont estimé le début de la surrection du massif de Ih Bogd au Miocène sup-Pliocène (5 ± 3 Ma) par traces de fission sur apatites, faisant du Gobi-Altaï l'un des plus jeunes reliefs d'Asie Centrale.

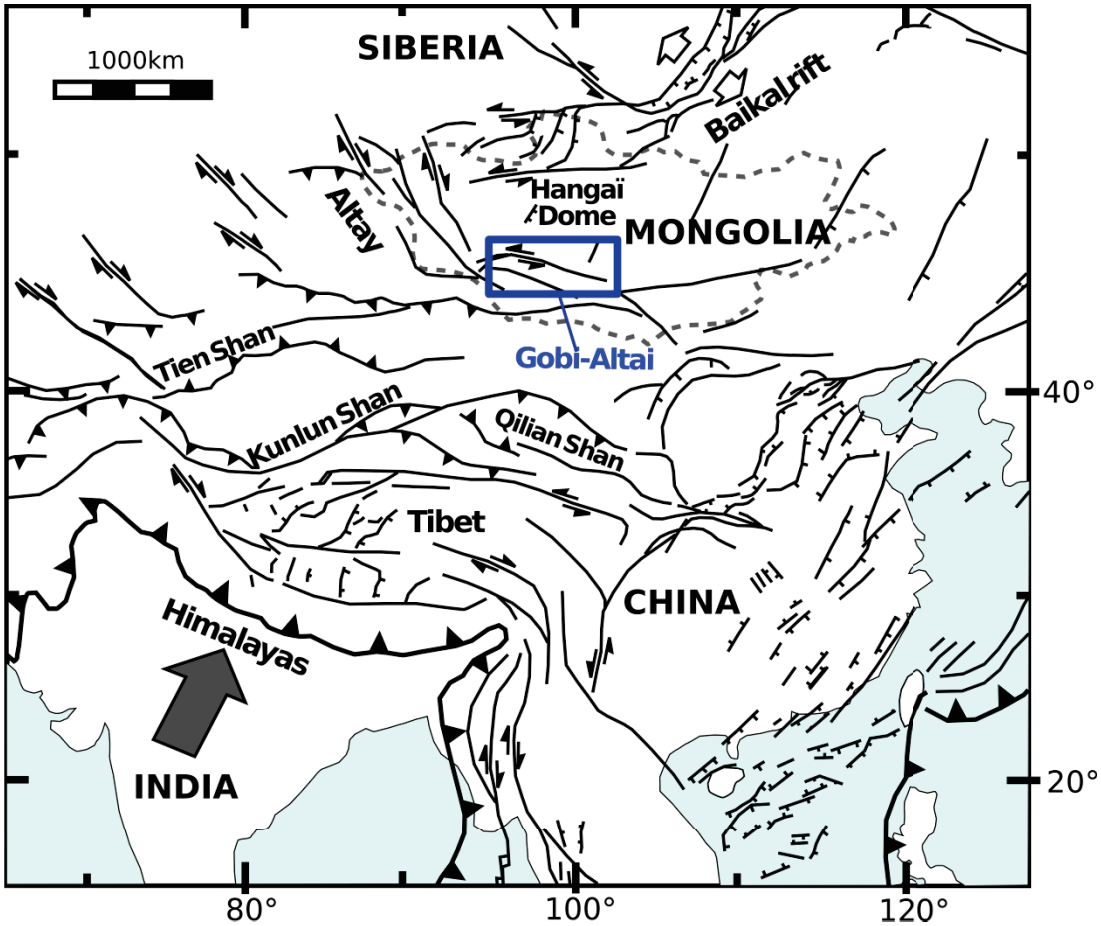


**Figure 1-1 : Schéma structural simplifié à l'échelle de l'Asie. Les noms en noir sont les principales chaînes de montagnes, le cadre bleu indique la zone d'étude et le massif du Gobi-Altaï. La vitesse de convergence entre l'Inde et la Sibérie est donnée par GPS, d'après Bettinelli et al., (2006). Abréviations des principaux grands décochements : AT, Altyn Tagh ; KaF, faille du Karakorum ; KuF, faille de Kunlun ; RR, faille du Fleuve Rouge ; TF, faille de Talas-Fergana.**

## II. Sismicité historique et instrumentale

L'activité sismique de la Mongolie occidentale se distingue par l'occurrence de grandes ruptures sismiques en régime transpressif, dextres dans l'Altaï et senestres dans le Gobi-Altaï (Figure 1-2). Ces ruptures de plus de 100 kilomètres se localisent sur des zones de cisaillement héritées (Cunningham, 2010), et présentent une géométrie complexe et segmentée (Florensov et Solonenko, 1965; Ritz et al., 1995; Klinger, 2010; Rizza et al., 2011, 2015; Choi et al., 2012).

Les mouvements horizontaux le long des segments associés aux grands décrochements sont transférés en mouvements verticaux dans les zones de relais, et les terminaisons des ruptures apparaissent systématiquement changer de direction, vers la droite ou la gauche dans le cas d'une cinématique senestre ou dextre respectivement, avec une composante essentiellement inverse (Bayasgalan et al., 1999).

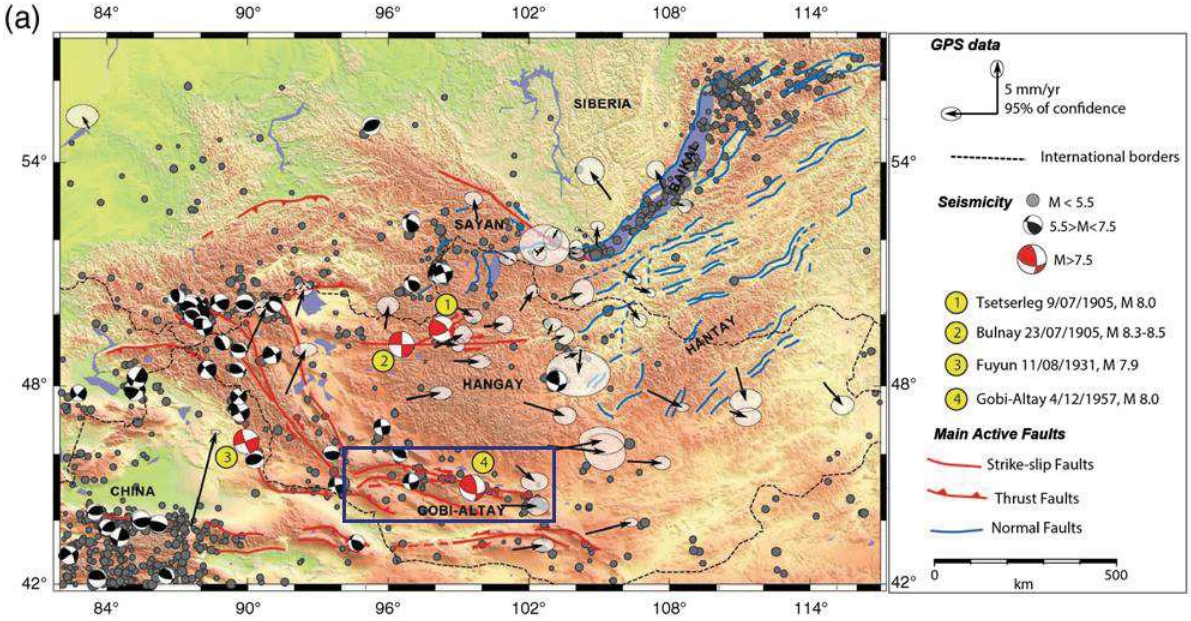


**Figure 1-2 : Carte sismotectonique de la Mongolie, d'après Rizza et al., (2015). Les flèches noires correspondent aux vitesses géodésiques d'après Calais et al., (2003), représentées à 95 % d'intervalles de confiance. Les points gris indiquent les épicentres des séismes entre 1980 et 2008. Les mécanismes au foyer indiqués en noir correspondent aux solutions du *Global Centroid Moment Tensor Catalog*. Les quatre séismes majeurs du XX$^{e}$ siècle sont indiqués avec les mécanismes au foyer rouges, et numérotés de 1 à 4 (d'après (Okal, 1976; Schlupp et Cisternas, 2007). Le cadre bleu représente la zone d'étude.**

La forte activité sismique au XX$^{e}$ siècle de la Mongolie Occidentale (Figure 1-2) débute par les séismes en décrochements senestres de Tsetserleg et de Bolnay (Mw 7,9 et 8,3 respectivement) en 1905 dans la région éponyme, qui se sont produits à 14 jours d'intervalle sur un même système de failles, cumulant une longueur totale de ~676 km sur quatre failles distinctes (Florensov et Solonenko, 1965; Schlupp et Cisternas 2007; Rizza et al., 2015; Choi et al., accepté). Le séisme de Fuyun, Mw 7,9, a eu lieu en 1931 au sud-ouest de l'Altaï, dans la région chinoise du Xinjiang, et est associé à une rupture de surface dextre de 160 km (Tapponnier et Molnar, 1979; Lin et Lin, 1998; Klinger et al., 2011). Le séisme du Gobi-Altaï, Mw ~8, a eu lieu en 1957 dans la partie nord-est du massif du même nom, le long des deux tiers est de la faille de Bogd, pour une rupture de surface totale de 360 km de long (Florensov et Solonenko, 1965; Ritz et al., 1995, 2003, 2006; Kurushin et al., 1998; Rizza et al., 2011; Choi et al., 2012). S'ajoute également la rupture de la faille de Mogod, en 1967, qui a produit deux séismes, de Mw 7,1 et 6,4 (Bayasgalan et Jackson, 1999). Ces évènements sismiques font de la Mongolie l'une des régions intracontinentales les plus actives du monde au cours du XXe siècle, et cette sismicité exceptionnelle a par ailleurs été interprétée comme étant un essaim sismique dû à un transfert des contraintes viscoélastiques entre ces grands décrochements, au niveau de la croûte inférieure (Vergnolle et al., 2003; Pollitz et al., 2003; Chéry et al., 2001).

L'instrumentation sismologique dont dispose aujourd'hui la Mongolie, révèle une activité microsismique intense, principalement localisée au niveau des reliefs en surrection et des bassins sédimentaires associés, et qui pour l'essentiel souligne, au travers des répliques, les grandes ruptures du XX$^{e}$ siècle (Figure 1-3).

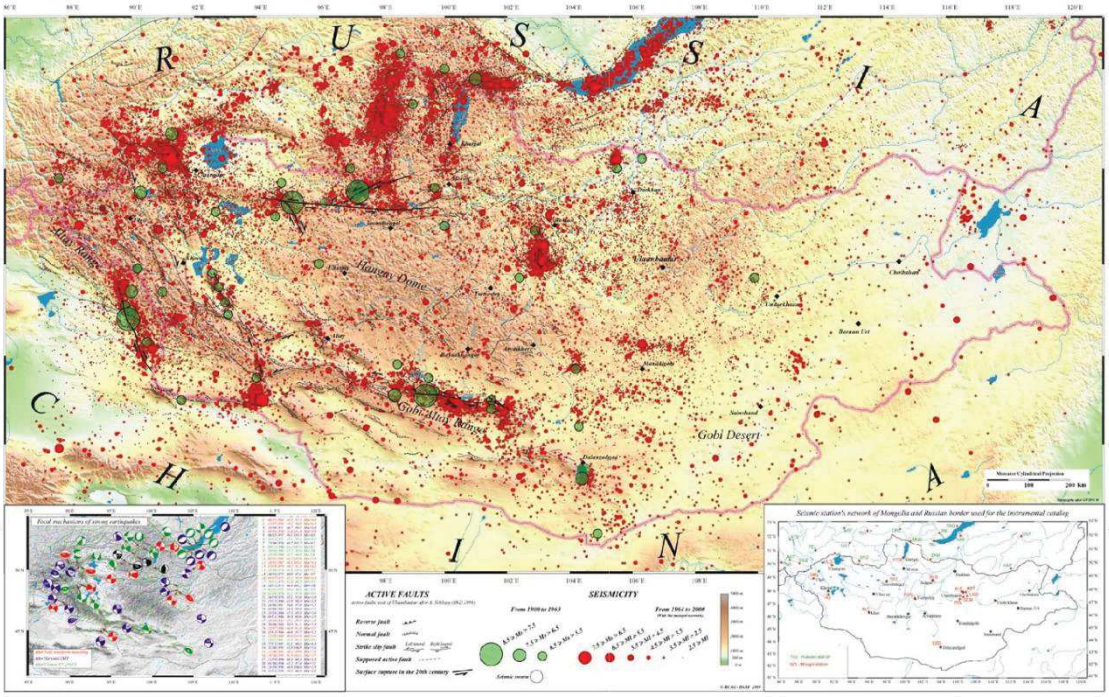


**Figure 1-3 : Carte de la sismicité de la Mongolie au cours du dernier siècle (d'après Adiya et al., 2003).**

## III. Taux de déformation géodésiques

Les études géodésiques de Calais et al. (2003) et Vergnolle et al. (2003), indiquent (Figure 1-4) : i. des vitesses de déformation de 10 mm.a$^{-1}$ en compression N-S réparties au travers des chaînes de l'Altaï et du Sayan, accommodées par un cisaillement dextre et senestre respectivement, distribués sur un réseau de failles transpressives NNO-SSE ; ii. 3 à 6 mm.a$^{-1}$ de cisaillement senestre absorbés au niveau de la Mongolie centrale, incluant le Gobi-Altaï, dôme de Hangay et région de Bolnay ; iii. 4 mm.a$^{-1}$ distribués dans la Mongolie orientale et dans la région du Baïkal.

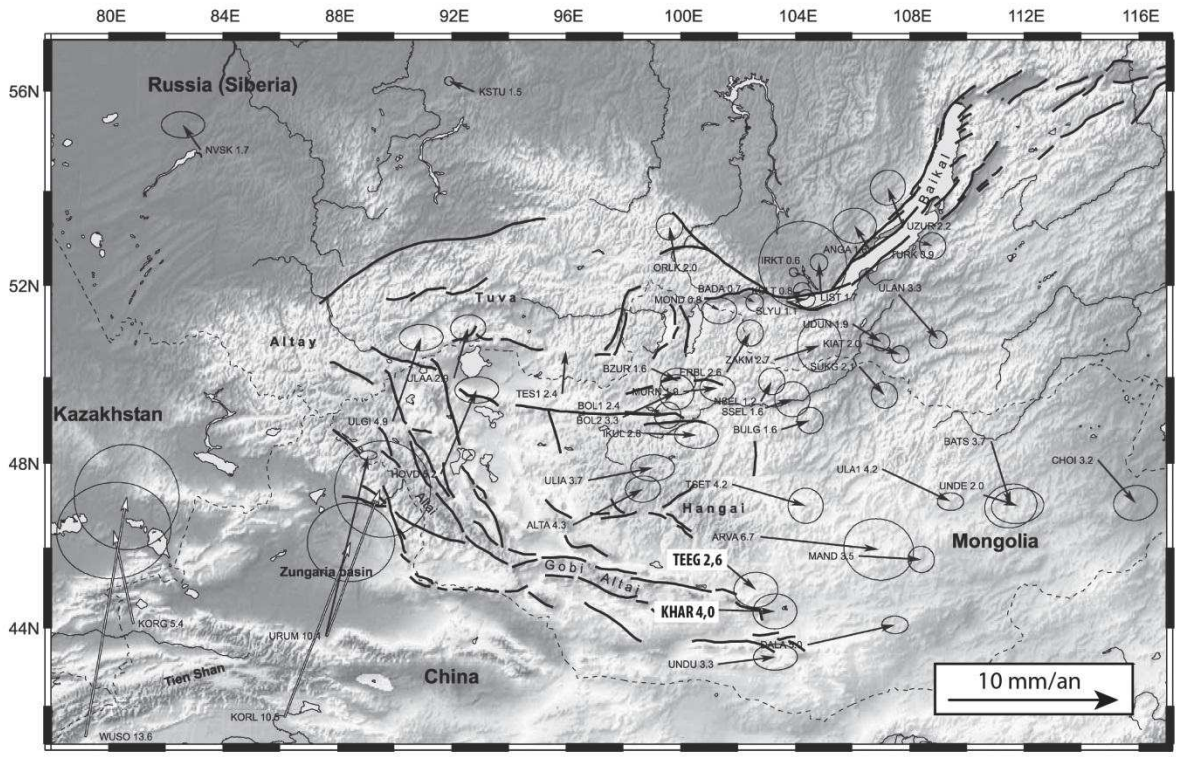


**Figure 1-4 : Vitesses GPS par rapport à Eurasie fixe, à échelle de l'Asie (from Calais et al., 2003). Les vitesses sont données en mm.a$^{-1}$ et les ellipses représentent les intervalles de confiance à 95%.**

Ces données sont cohérentes avec les calculs de vitesses de glissement long terme (Pléistocène supérieur) obtenues à partir d'analyses morphotectoniques sur les grandes failles actives du Gobi-Altaï et de l'Altaï, suggérant des vitesses de glissements millimétriques ( Ritz et al., 1995, 2006; Vassallo et al., 2005, 2007; Walker et al., 2006; Nissen et al., 2009; Rizza et al., 2011, 2015). Rizza et al., (2015) ont par ailleurs déterminé une vitesse de glissement long terme moyenne de 3,1 ± 1,7mm.a$^{-1}$ sur la faille de Bolnay, cohérente avec la vitesse géodésique sur cette faille déterminée par Calais et al., (2003) de 2,6 ± 1,0 mm.a$^{-1}$ (intervalle de confiance à 95 %).

Dans la région du Gobi-Altaï, bien que Calais et al., (2003) ne donnent pas une estimation de la vitesse le long de la faille de Bogd, les champs de déplacements géodésiques sont cohérents avec la tectonique observée sur la faille de Bogd : la différence des vecteurs des stations KHAR et TEEG, situées de part et d'autre de cette faille (Figure 1-4), suggèrent un taux de chargement intersismique de l'ordre de 1 mm.a$^{-1}$, analogue aux vitesses de glissement horizontal long terme mesurées sur la faille de Bogd Orientale (Ritz et al., 1995, 2006; Vassallo et al., 2007; Rizza et al., 2011). Ces données morphotectoniques sont détaillées dans les parties V et VI de ce chapitre.

## IV. Morphologie et structure du Gobi-Altaï

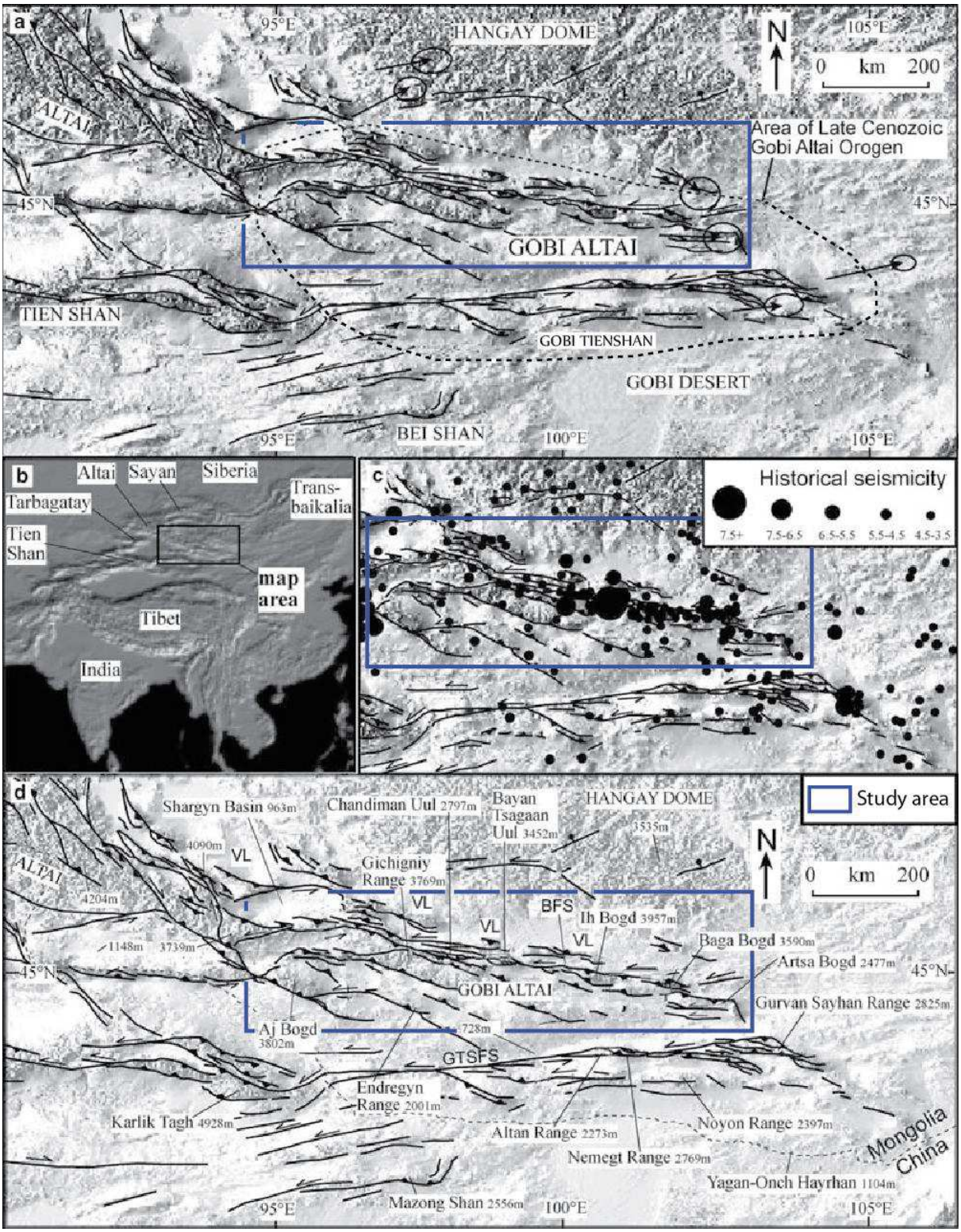


**Figure 1-5 : Cartes du Gobi-Altaï, modifiée d'après Cunningham 2010. (a) Cartographie des failles quaternaires ; (b) Ceintures orogéniques voisines du Gobi-Altaï et localisation de (a), (b), (c), et (d) ; (c) Sismicité historiques du Gobi-Altaï, d'après Adiya et al., 2003 ; (d) Cartographie des sites mentionnés dans le texte. BFS, *Bogd Fault System* ; GTFS, *Gobi Tien Shan Fault System* ; VL, Vallée des Lacs.**

La région du Gobi-Altaï constitue une large ceinture de déformation, d'approximativement 200 km de large sur 600 km de long, localisée au sud-ouest de la Mongolie (Figure 1-5.b, Cunningham, 2013), et liée topographiquement à l'ouest à la partie méridionale de la chaîne de l'Altaï. Au sud du Gobi-Altaï, se trouve le massif du Gobi-Tien Shan, lié à l'ouest à la chaîne du Tien Shan, et caractérisé par un système de faille transpressive de ~700 km de long, le Gobi-Tien Shan Fault System (GTFS, Figure 1-5.a, Cunningham, 2010).

La partie sud du Gobi-Altaï et le GTFS présentent une physiographie de type basin and range, avec des blocs montagneux orientés O-NO, E-O et E-NE (Cunningham, 2013). Bien que le GTFS présente des escarpements de failles quaternaires, aucune sismicité significative n'est reportée, et les rares travaux sismotectoniques dans la région suggèrent que la zone n'a pas présenté de forts séismes depuis le Pléistocène (Cunningham, 2013 ; Mushkin, PhD, 2007).

A l'ouest du Gobi-Altaï, la plaine de la Sharga et sa région sud constituent la jonction avec la chaîne de l'Altaï et sont le lieu d'une activité tectonique quaternaire caractérisée par des décrochements conjugués (Figure 1-5.b, Tapponnier et Molnar, 1979; Schlupp, PhD, 1996; Cunningham et al., 2009). Au sein du Gobi-Altaï, la cinématique transpressive senestre génère des relais compressifs plurikilométriques et des rides transpressives discontinues, alternées de dépressions endoréiques comblées de sédiments alluviaux issus de l'érosion des reliefs. La déformation néogène au sein du Gobi-Altaï est distribuée avec des sections de failles décrochantes localisées sur les structures E-NE à E-W, alors que les segments inverses sont orientés préférentiellement NO-SE (Cunningham 2010).

Les altitudes s'étendent de 1000 m à 3957 m (Ih Bogd), et les principaux sommets correspondent à des reliques d'une pénéplaine Jurassique, attestant d'une surrection cumulée d'au moins 2000 m depuis la réactivation néogène (Jolivet et al., 2007; Vassallo et al., 2007) (Figure 1-6).

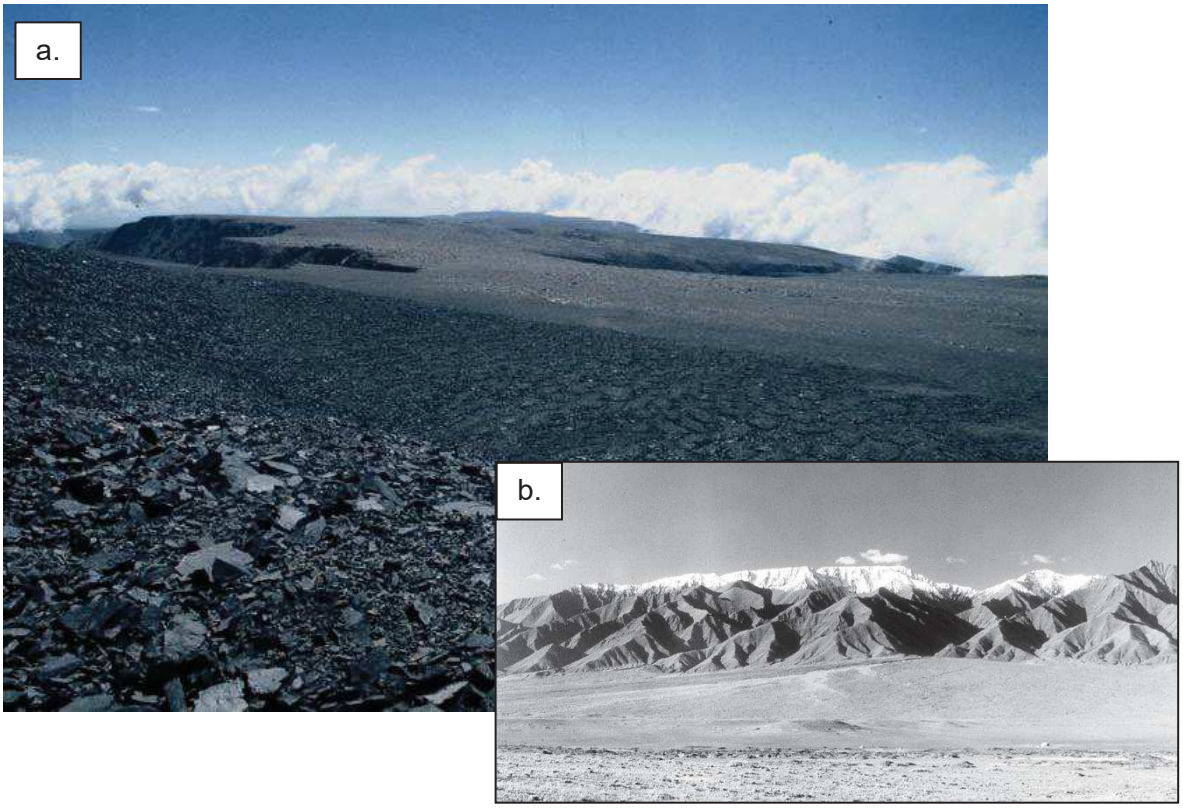


**Figure 1-6 : (a) Photographie vers le SE de la pénéplaine au sommet de Ih Bogd (Vassallo, 2007). (b) Photographie vers le sud de Ih Bogd et son plateau sommital (photographie P. Molnar, d'après Kurushin et al., 1998).**

Une particularité de la région du Gobi-Altaï est l'occurrence de glissements de terrain géants, d'échelle kilométrique, associés à l'activité tectonique et à la croissance des escarpements de failles (Philip et Ritz, 1999; Mushkin et al., 2004). Ainsi, les traces de deux séquences de glissements géants ont été observées, qui sont directement associées à des ruptures sismiques de surface. Leurs géométries en bourrelets frontaux indiquent un niveau de décollement superficiel, certainement composé de lentilles d'évaporites déposées au fond des bassins endoréiques de la Vallée des Lacs (e.g. lacs d'Orog Nur, Tsagan Nur et Biger Nur). Le glissement de Baga Bogd, d'un volume estimé à 50 $km^3$, est situé au nord du massif de Baga Bogd, et présente l'une de ses séquences directement alignée avec le Hetsüü foreberg, qui a rompu lors du séisme de 1957 (Figure 1-7, Philip et Ritz, 1999).

## V. Données sismotectoniques sur la faille de Bogd-Est

### V.1. Description

La faille de Bogd s'étend sur près de 400km avec une orientation N100±10°, et est divisée en deux parties distinctes, est et ouest (Figure 0-1). La partie ouest borde au sud la vallée de Chandman, et la partie est délimite par le nord les massifs de Bayan Tsagaan, Ih Bogd, Baga Bogd et Artz Bogd, 4 relais compressifs d'échelles crustales, i.e. 20 - 30 km de long (Figure 1-5 et Figure 0-1). Seule la partie est a rompu lors du séisme du Gobi-Altaï (Figure 1-7), sur une longueur de 270 km entre les massifs de Bayan Tsagaan et de Artz Bogd, non inclus. Des segments inverses ont également rompu lors de l'évènement de 1957 au sud de Ih Bogd, 25 km au sud de la rupture principale, sur une longueur totale de 90 km. La rupture de surface associée à ce séisme est particulièrement complexe, et fut le principal sujet des études morphotectoniques menées dans la zone (Florensov et Solonenko, 1965; Ritz et al., 1995, 2003; Kurushin et al., 1998; Vassallo et al., 2005; Rizza et al., 2011; Choi et al., 2012). Les complexités géométriques de la faille de Bogd Est sont pour partie associées à des *right-steps* (des échelons ou des changements de directions se produisant vers la droite par rapport à la direction moyenne de la faille), créant des relais compressifs et extensifs, ainsi qu'à un partitionnement superficiel de la déformation. Ces complexités reflètent les variations de cinématiques le long de la rupture, et la segmentation de la faille (Figure 1-7) (Kurushin et al., 1998); Rizza et al., 2011; Klinger et al., 2011; Choi et al., 2012). En particulier, au niveau des principaux massifs de Baga Bogd et de Ih Bogd, la faille, habituellement verticale lorsque la cinématique est décrochante, se branche sur des failles à faible pendage, générant des chevauchements progradant sur les bassins, et formant des linéaments de collines peu élevées, appelés forebergs (Figure 1-7) (Kurushin et al., 1998; Bayasgalan et al., 1999b; Vassallo et al., 2005).

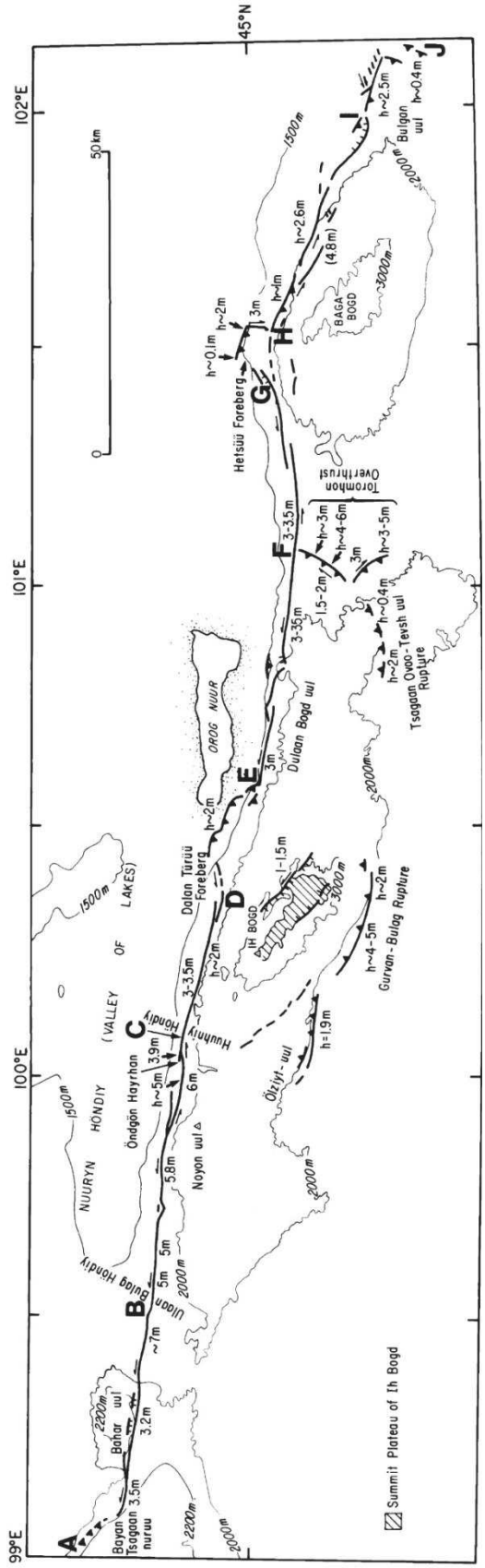


**Figure 1-7 : Cartographie simplifiée de la rupture du séisme du Gobi-Altaï, 1957, d'après Kurushin et al. 1998. Les chiffres indiquent l'amplitude des décalages horizontaux, et les décalages verticaux sont précédés par un 'h'. Les lettres majuscules indiquent la segmentation.**

L'abondance des marqueurs morphotectoniques le long de la rupture de surface de 1957, ainsi que leur disposition et leur préservation, permettent une étude détaillée de la distribution spatiale du glissement sismique de surface (e.g. Rizza et al., 2011; Choi et al., 2012). La nature transpressive senestre de la faille de Bogd génère la surrection de reliefs principalement au sud de la faille, aboutissant à un drainage sub-orthogonal à la faille, et favorisant ainsi l'enregistrement des déformations cosismiques par les marqueurs morphotectoniques (e.g. Kurushin et al., 1998). Des études s'intéressant à la distribution et à l'amplitude des déplacements le long de la rupture de 1957 estiment un déplacement moyen de 3 à 4 m et des amplitudes de glissement allant jusqu'à 7 m (Figure 1-7) (Florensov et Solonenko, 1965; Kurushin et al., 1998; Rizza et al., 2011; Choi et al., 2012). De plus, des mesures de déplacements cumulés (Figure 1-8.A) suggèrent que la distribution du glissement associée au séisme de 1957 pourrait se répéter dans le temps, et serait par conséquent de nature caractéristique (Kurushin et al., 1998; Ritz et al., 2003; Rizza et al., 2011).

### V.2. Vitesses de glissement le long de la faille de Bogd Est

Des études morphotectoniques ont permis d'estimer la vitesse de glissement long terme de la faille de Bogd Est en différents points, et sur différentes échelles de temps. Ritz et al., (1995) estiment une vitesse de faille à 1,2 mm.a$^{-1}$. Notons qu'il s'agit — avec l'étude réalisée sur la faille de Owens Valley par Bierman et al., (1995) —, de la première application de la méthode de datation « $^{10}$Be produit in situ », pour déterminer l'âge d'exposition de surfaces alluviales déplacées le long d'une faille.

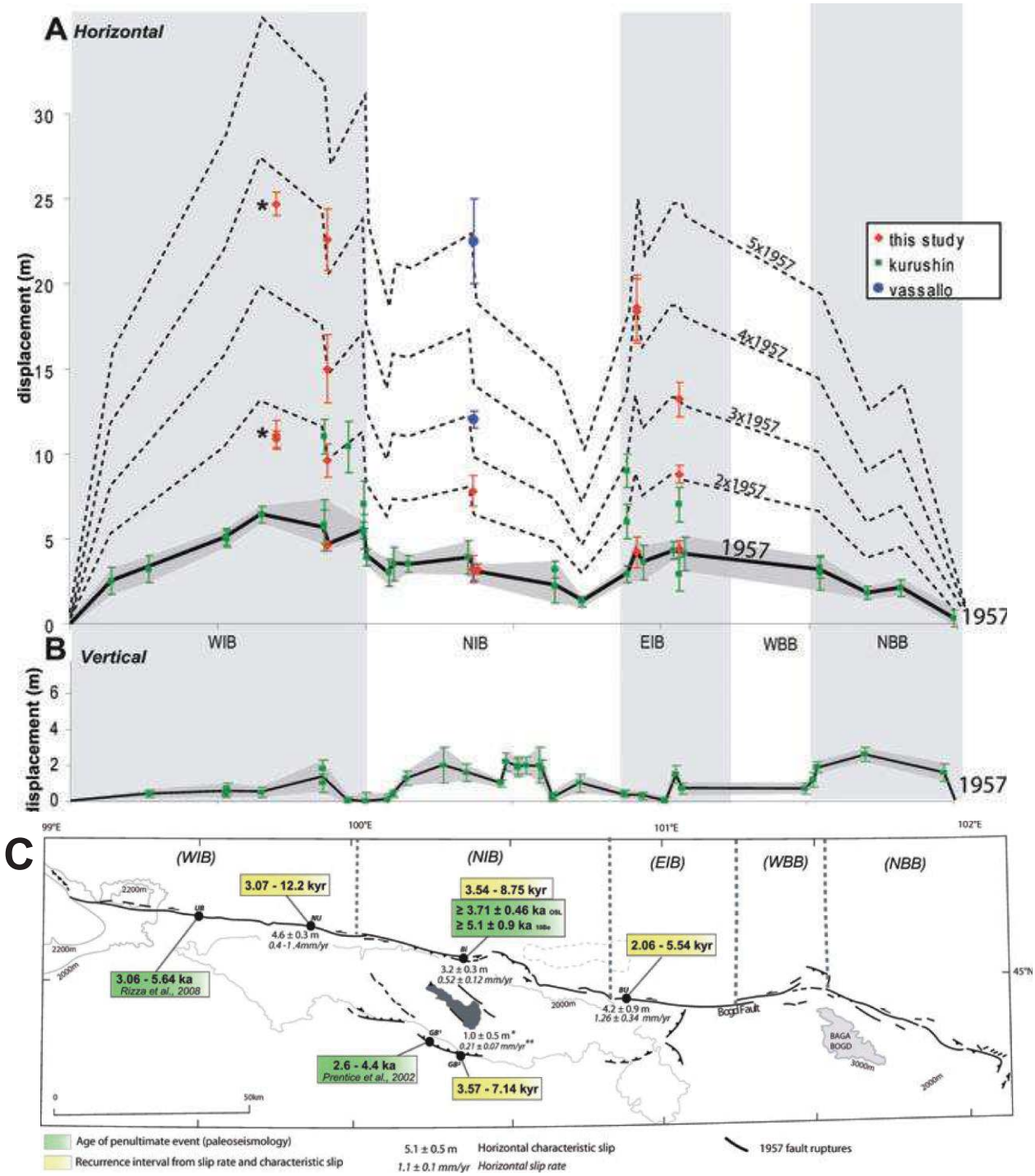


**Figure 1-8 : (A) Distribution spatiale du glissement le long de la faille de Bogd Est et synthèse des données sismotectoniques, d'après Rizza et al. (2011). Les données de déplacement proviennent de Rizza et al. (2011), Vassallo et al. (2007) et Kurushin et al. (1998). Nomenclature des segments : WNU, West Noyon Uul ; NU, Noton Uul ; Bi, Bitut ; BU, Baast Uul ; ZS, Zadgay Sayhr. La ligne noire représente la courbe du glissement de 1957, et la zone grisée les incertitudes correspondantes. Les lignes pointillées représentent les multiples de la distribution de 1957. (B) Distribution verticale du glissement le long de la faille de Bogd Est, d'après les mesures de Kurushin et al. (1998). (C) Intervalles de récurrence et âges des séismes pénultièmes le long de la rupture de 1957, d'après Rizza et al. (2011).**

Des mesures complémentaires, basées sur des décalages de terrasses alluviales indiquent corollairement des vitesses de glissement long terme moyennes de ~1,0 mm.a$^{-1}$ et ~0,2 mm.a$^{-1}$, respectivement horizontale et verticale (Ritz et al., 2006; Vassallo et al., 2007; Rizza et al., 2011) (Figure 1-8.C). Rizza et al., (2011) relèvent qu'il existe des variations de vitesse de glissement entre la partie ouest de la rupture de 1957, orientée N100°, où les vitesses ont été mesurées entre 1,2 et 1,6 mm.a$^{-1}$, et la section de faille située au nord de Ih Bogd, orientée N105°, pour laquelle la vitesse de glissement a été estimée à 0,6 mm.a$^{-1}$. La variation de vitesse peut être associée à des changements d'orientation et de cinématique, la composante verticale étant plus significative au niveau du massif de Ih Bogd (Rizza et al., 2011).

Considérant un glissement caractéristique, une vitesse long terme constante, et combinant les données de vitesses avec la distribution spatiale du glissement le long de la faille de Bogd, l'intervalle de récurrence moyen pour des séismes majeurs est estimé entre 2500 et 5200 ans (Rizza et al., 2011).

### V.3. Données paléosismologiques

Des investigations paléosismologiques ont été menées sur les sections ouest et centrale de la rupture principale du séisme de 1957, ainsi que sur le foreberg de Gurvan Bulag (Figure 1-7) ( Schwartz et al., 1996; Prentice et al., 2002; Ritz et al., 2007; Ritz et al., 2009; Rizza, PhD, 2010). Les résultats indiquent que plusieurs séismes majeurs ont eu lieu sur chacune de ces sections, et suggèrent qu'un évènement analogue au séisme du Gobi-Altaï a eu lieu il y a environ 3 à 4 ka BP, rompant au moins les deux-tiers ouest de la rupture de 1957, ainsi que les sections inverses au sud de Ih Bogd ( Prentice et al., 2002; Rizza, PhD, 2010). Il est à noter que par manque de données, la longueur de cette pénultième rupture n'est pas contrainte sur les sections de Baga Bogd, de Toromhon et de Bayan Tsagaan (Figure 1-7Figure 1-8). Un évènement antérieur a été mis en évidence sur le chevauchement de Gurvan Bulag avant 7,5 ka BP (Prentice et al., 2002), et deux autres séismes ont également été identifiés le long de la rupture principale, amenant à 4 le nombre d'évènements majeurs ayant affectés cette section de faille au cours de l'Holocène (Ritz et al., 2009; Rizza, PhD, 2010).

Par ailleurs, un évènement postérieur à 1200 an BP a été identifié dans deux tranchées sur la section centrale dans la zone de Zadgay Sayhr (évènement E2 sur la Figure 1-9.B), qui n'est pas présent au niveau des autres sections de la faille analysées (Schwartz et al., 2007; Rizza, PhD, 2010). L'hypothèse d'un séisme modéré, ne rompant qu'un segment de 23 km, générerait un séisme de magnitude minimale Mw ~6,5 (d'après Wells et Coppersmith, 1994). Cet évènement a donc été interprété comme mineur,

générant des décalages de l'ordre de 25 à 50 cm, visibles dans les études paléosismologiques, mais non identifiable dans la morphologie (Rizza, PhD, 2010).

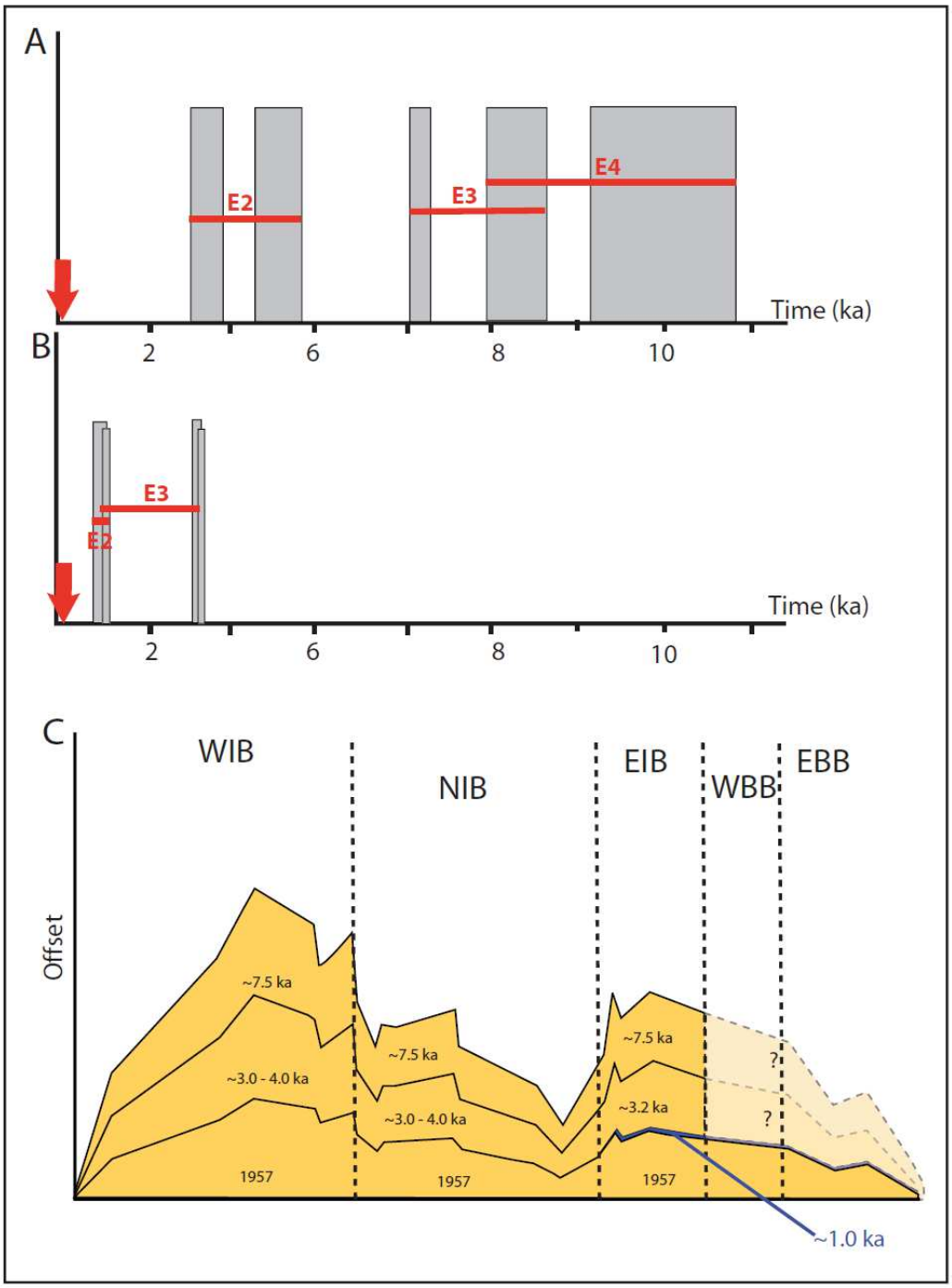


**Figure 1-9 : Synthèse des données paléosismologiques sur la faille de Bogd Est, d'après Rizza (PhD, 2010). Intervalles de temps (barres rouges) où les paléoséismes ont eu lieu à Ulaan Bulag (A) et à Zadgay Sayhr (B). (C) Distribution des glissements horizontaux le long de la faille de Bogd Est et âges de paléoséismes en fonction de la segmentation proposée par Rizza et al., (2011). Le séisme identifié autour de 1000 an BP est représenté en bleu et le déplacement associé est inférieur à 50cm.**

Rizza (PhD, 2010) conclut que les résultats des études paléosismologiques réalisées sur la faille de Bogd indiquent un glissement caractéristique pour les séismes majeurs (Mw >

7,5), et que les intervalles de récurrences sont similaires le long des parties ouest et centrale ainsi que le long des chevauchements sud de la rupture de 1957. Ainsi, certains segments de la faille de Bogd pourraient produire des séismes caractéristiques (Shimazaki et Nakata, 1980; Schwartz et Coppersmith, 1984).

## VI. Tectonique récente et active du Gobi-Altaï

Bien que la rupture du séisme du Gobi-Altaï, située à l'Est de la chaîne du Gobi-Altaï ait concentré une grande partie de l'attention, on note la présence de nombreux escarpements de failles quaternaires sur plusieurs dizaines, voire centaines de kilomètres dans la partie Ouest de la chaîne (Molnar et Tapponnier, 1975; Tapponnier et Molnar 1979; Schlupp, PhD, 1996; Cunningham, 2010). Ces failles sont par ailleurs en partie soulignées par la sismicité du Gobi-Altaï, certainement associée à des répliques car visiblement plus importante dans les zones ayant produit des ruptures durant le siècle dernier (Figure 1-5).

A. Mushkin (PhD, 2007) a réalisé une première reconnaissance morphotectonique et paléosismologique de ces escarpements sur le terrain et a proposé, sur la base des données obtenues, un scénario pour l'évolution spatiale et temporelle de la déformation sismique dans le Gobi-Altaï (Figure 1-10). La section suivante présente une synthèse de ses résultats.

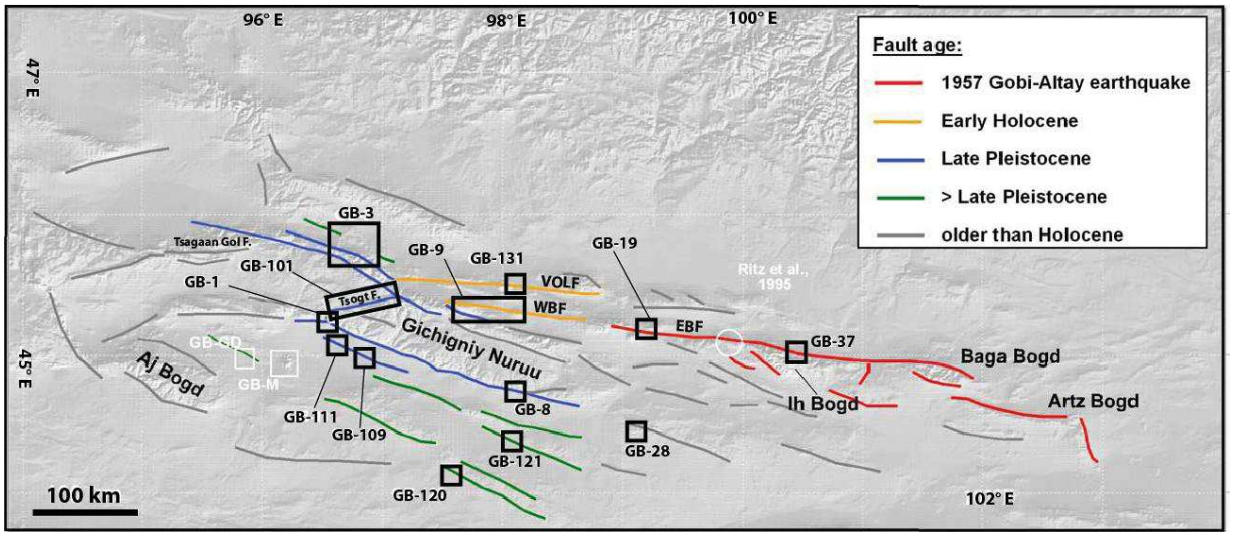


**Figure 1-10 : Bilan spatio-temporel de l'activité des principales failles du Gobi-Altaï, d'après Mushkin (PhD, 2007). VOLF, Valley of Lakes Fault ; WBF, Western Bogd Fault ; EBF, Eastern Bogd Fault.**

A partir de mesures de décalages de cônes alluviaux et de leurs datations OSL, Mushkin (PhD, 2007) estime la vitesse de déplacement horizontale le long de la faille de Bogd Est sur deux sites et obtient 5,8 ± 0,8 mm.a$^{-1}$ et à 6,5 ± 0,6 mm.a$^{-1}$ sur des périodes de 60 ka et 130 ka respectivement (sites GB-37 et GB-19 sur la Figure 1-10). Une autre

estimation de la vitesse de glissement, sur une section de la faille de la Vallée des Lacs, à l'aide de marqueurs issus de l'interprétation de la mise en place du gigantesque glissement de terrain de Namalzah Hills (site GB-3 sur la Figure 1-10) et d'une datation OSL suggère également une vitesse de glissement de 6,3 ±1,4 mm.a$^{-1}$ sur une période de 120 ka.

Ces résultats sont supérieurs aux estimations de Ritz et al., (1995, 2006), Vassallo et al., (2007) et Rizza et al., (2011), d'un facteur 5 à 7. Une telle différence pourrait se discuter en invoquant une répartition du glissement sur différents accidents, des variations de vitesse de glissement au cours du temps, ou encore des changements de géométrie de micro-blocs ; néanmoins, compte tenu des  données géodésiques précédemment citées (cf. Calais et al., 2003) ainsi que du bilan des déformations en Asie centrale, les estimations de vitesse de Mushkin (2007) n'apparaissent pas valides.

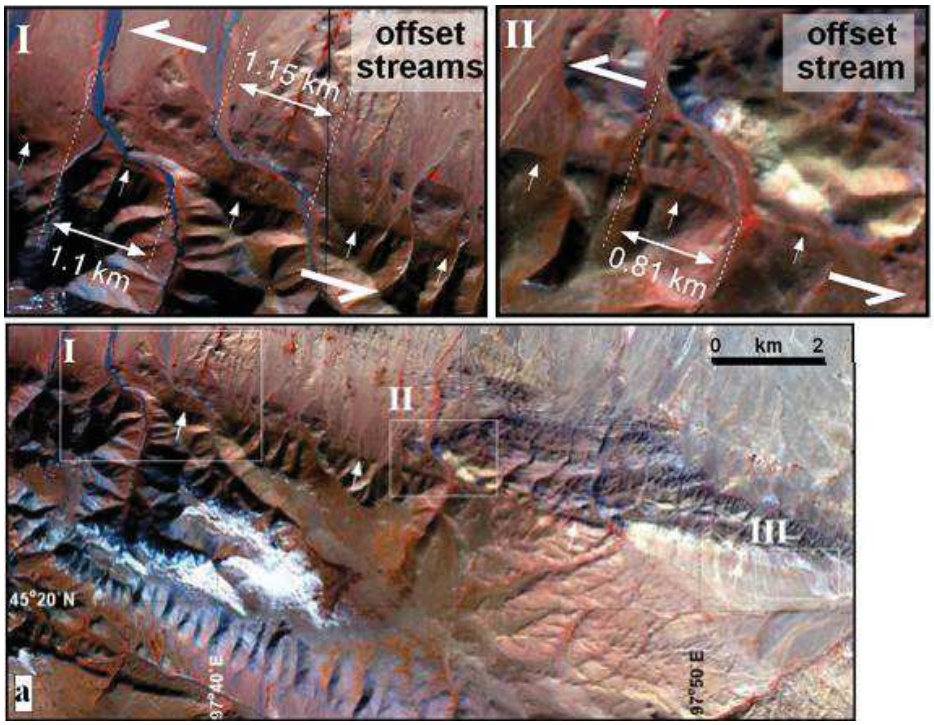


**Figure 1-11 : Evidences morphotectoniques de décrochement senestre le long de la faille de Bogd Ouest, dans la région de Chandman, d'après Mushkin (PhD, 2007). La localisation du site est 20km à l'ouest de la ville de Chandman, à l'ouest du site GB-9 sur la figure 1-10. Les triangles blancs marquent la faille. Les images sont des ATSER à 15m de résolution. (a) Localisation de (I) et (II). (I) Deux incisions fluviales profondes sont décalées de manière senestre sur 1,1-1,15km. (II) Talweg décalé de manière senestre sur 0,81km.**

Un site d'étude paléosismologique (site GB-131 sur la Figure 1-10), se trouvant à l'est le long de la faille de la Vallée des lacs, a permis de dater par thermoluminescence la dernière rupture comme postérieure à 6.8 ± 1,9 ka (Mushkin, PhD, 2007). Les observations morphotectoniques sur la faille de Bogd Ouest, dans la région de Chandman, montrent des décalages horizontaux cumulés allant jusqu'à 1,15 km (site

GB-9 sur la Figure 1-10, et Figure 1-11), associés à une forte composante verticale au sud de la faille (Mushkin, PhD, 2007).

Une reconnaissance le long de la faille de Tsogt (site GB 101 sur la Figure 1-10) suggère une cinématique normale-senestre, avec des déplacements d'au moins 180 m à l'horizontal, et un rejet vertical total d'environ 700 m (Mushkin, PhD, 2007). Aucune contrainte temporelle n'est cependant mentionnée pour l'activité de la faille de Tsogt.

Une activité oblique en chevauchement est reportée au sud et au sud-est des Gichigniy Nuruu (site GB-1 et GB-8 sur la Figure 1-10), et les âges minimums des dernières ruptures sur ces sites sont estimés par des datations OSL à respectivement 91 ± 9 ka et 61 ± 7 ka (Mushkin, PhD, 2007). Le chevauchement situé 20 km au sud de la limite sud des Gichigniy Nuruu (site GB-111 et GB-109 sur la Figure 1-10) apparait présenter une composante senestre, et la dernière rupture sur cette faille est estimée s'être produite entre 150 ± 13 ka et 190 ± 15 ka. Les escarpements de failles quaternaires situées plus au sud (sites GB-28, GB-121, GB-122 et GB-M sur la Figure 1-10) ne présentent pas d'évidences de rupture de surface depuis le Pléistocène. Mushkin (PhD, 2007) propose finalement un modèle d'évolution de l'activité des failles du Gobi-Altaï au Quaternaire, depuis le Sud-Ouest vers le Nord-Est, avec tout d'abord une zone de déformation sud (SDZ), orientée N105°-N110°, qui deviendrait inactive au Pléistocène, puis une zone de déformation centrale (MDZ) orientée N100°-N105°, prendrait alors le relai et arrêterait de fonctionner à la fin du Pléistocène, tandis que l'activité se déplacerait à l'Holocène sur une zone nord (NDZ), orientée N95° - N100° (Figure 1-12).

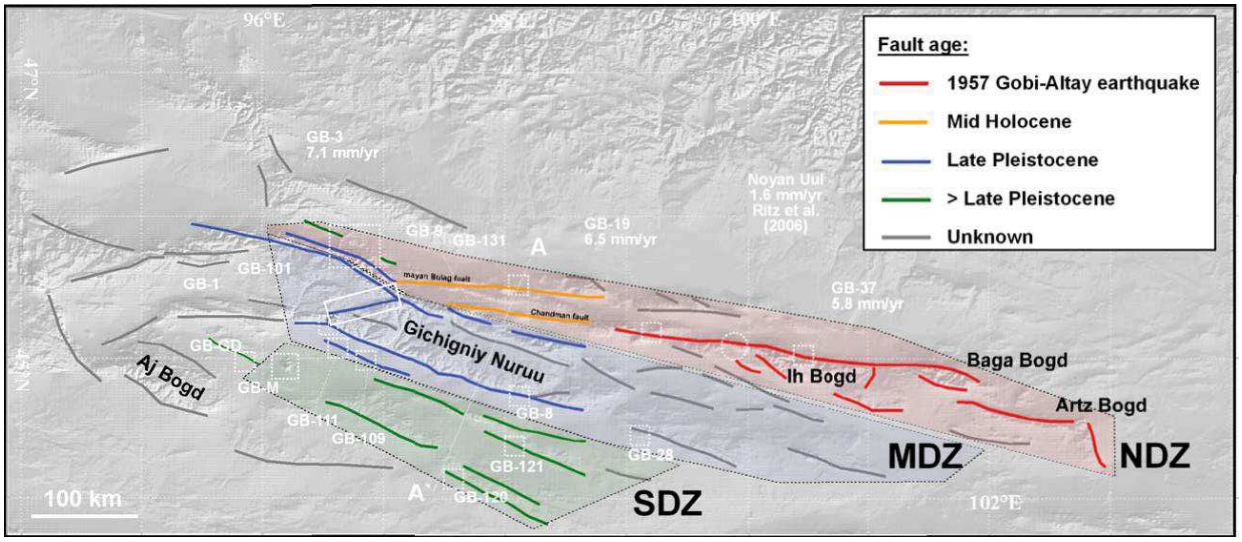


**Figure 1-12 : Zones de déformation du système de faille du Gobi-Altaï, au regard des plus récentes ruptures de surface, d'après Mushkin (PhD, 2007). NDZ, *Northern Deformation Zone*, les failles y sont orientées N95-100° ; MDZ, *Middle Deformation Zone*, les failles y sont orientées N100-105° : SDZ, *Southern Deformation Zone*, les failles y sont orientées N105-110°. Le segment A-A' localise la coupe présentée en figure 1-13.**

Les structures en fleurs décrites par Cunningham et al. (1996), seraient donc indépendantes géométriquement (Figure 1-13), et associées à des mouvements de rotation horizontaux (axes verticaux) de petits blocs d'échelle crustale.

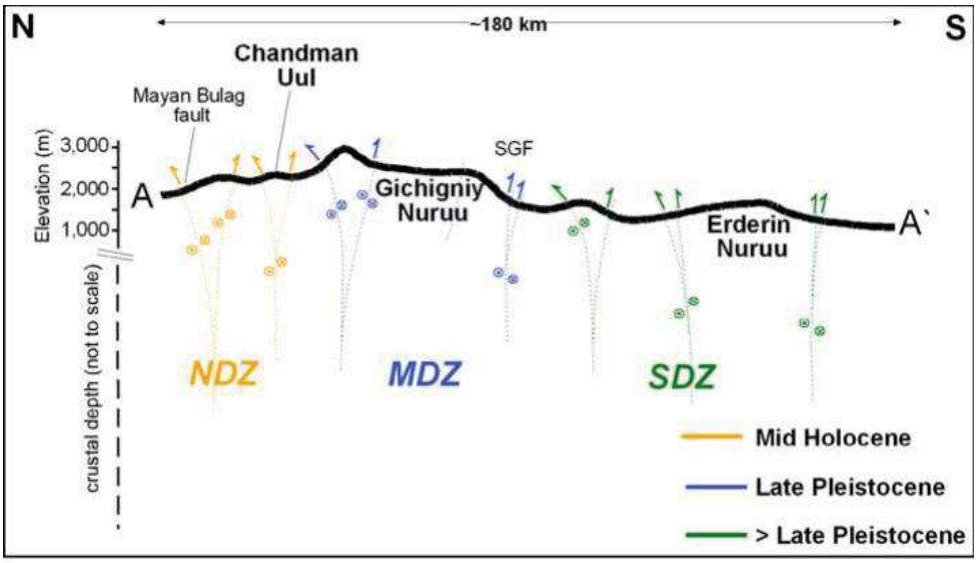


**Figure 1-13 : Coupe schématique N-S du système de faille du Gobi-Altaï, d'après Mushkin (PhD, 2007). La topographie a été extraite du MNT SRTM90, et les profondeurs crustales ne sont pas à l'échelle.**

Dans son étude, Mushkin (PhD, 2007) conclut que la partie nord du Gobi-Altaï semble accommoder un glissement senestre de 5 à 8 mm.a$^{-1}$ depuis le Pléistocène, et que la déformation tardi-Cénozoique s'est concentrée dans une zone de cisaillement de 150 km de large. La tectonique quaternaire a été asynchrone, migrant du sud vers le nord (Figure 1-12), et se propageant vers le nord-est. Ainsi, la tectonique Holocène se concentre principalement dans la partie nord-est du Gobi-Altaï, le long de failles qui semblent avoir subi une rotation antihoraire d'approximativement 5 à 10°, au regard des failles plus anciennes, maintenant inactives (Schlupp et al., 1995; Schlupp, PhD, 1996; Mushkin, PhD, 2007).

## VII. La chaîne du Gobi-Altaï et son héritage géologique

L'héritage géologique jouant un rôle important dans la géométrie et la profondeur des ruptures sismiques actuelles (e.g. Hanks et Kanamori, 1979; Cunningham, 2005), il constitue un prérequis essentiel pour la compréhension de la distribution et de la cinématique des réactivations crustales dans la zone d'étude au cours du Quaternaire. Ceci est particulièrement approprié dans ce contexte intracontinental, dans la mesure où les limites de « terranes » — les « terranes lithostratigraphiques », aussi appelés microcontinents, sont des blocs d'échelle crustale ayant une histoire géologique singulière les unes des autres — , les failles, les fabriques métamorphiques et les axes de plissements préexistants définissent la structuration du socle, ainsi que ses

réactivations en fonction de ses orientations et de ses propriétés rhéologiques (Cunningham, 2013; van Hinsbergen et al., 2015). Les sections suivantes synthétisent l'histoire géodynamique et structurale de la région.

### VII.1. Du Précambrien au Mésozoïque : Accrétion des « *terranes* »

Le Gobi-Altaï est situé dans la partie orientale de la ceinture orogénique centre-asiatique (CAOB, Central Asian Orogenic Belt, aussi appelée Altaïds), orogène majeure d'Asie centrale, ayant subi une évolution polyphasée au Phanérozoïque, notamment lors des orogénèses Calédonienne et Hercynienne (Şengör et al., 1993; van Hinsbergen et al., 2015). Le réseau de failles du Gobi-Altaï est par ailleurs aligné sur le *Main Mongolian Lineament* (MML), qui représente la principale frontière tectonique séparant le domaine Néoprotérozoïque au nord du domaine Paléozoïque au sud (Badarch et al., 2002; Lehmann et al., 2010) (Figure 1-14).

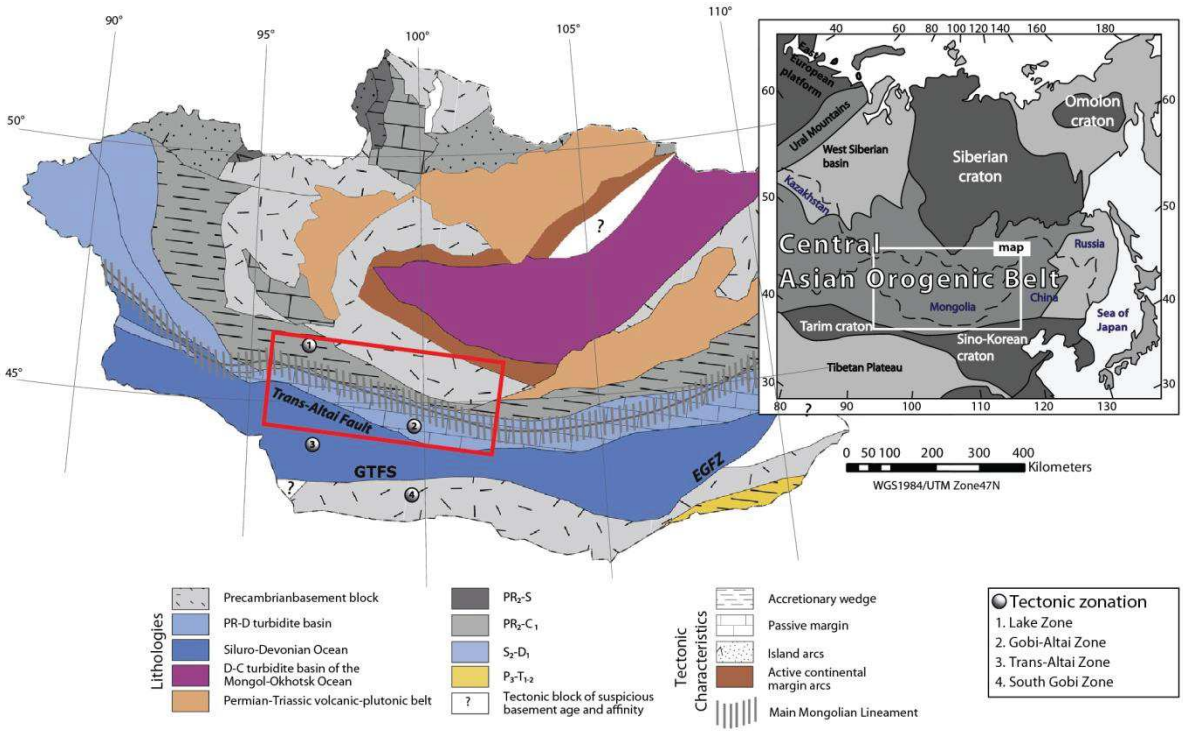


**Figure 1-14 : Principales unités géologiques de la ceinture orogénique centre asiatique (CAOB), modifiée d'après Guy et al. (2014). L'insert présente la localisation de la Mongolie au sein de la CAOB, cernée par les cratons. Le cadre rouge montre la zone d'étude. PR : Protérozoïque ; S : Silurien ; C : Carbonifère ; P : Permien ; T : Trias, J : Jurassique. GTFS : Gobi Tien Shan Fault System ; EGFZ : Eastern Gobi Fault Zone.**

La géologie régionale du Gobi-Altaï est caractérisée par un microcontinent d'origine néo-protérozoïque, constituant aujourd'hui les parties sud et ouest du dôme de Hangay ; microcontinent qui s'est distendu au Silurien et Dévonien pour laisser place au domaine océanique trans-Altaï (Lehmann et al., 2010; Guy et al., 2014). Dès le Carbonifère, des mouvements de convergence E-O aboutissent à la formation d'arcs insulaires et à la

fermeture de ce domaine océanique. Par la suite, toujours au Carbonifère, une rotation antihoraire du système va amener les structures jusqu'à l'orientation E-O qu'elles connaissent aujourd'hui (Şengör et al., 1993). La période Permien-Jurassique est caractérisée par une convergence N-S affectant toute la CAOB, et entraînant un fort épaississement crustal, avec la mise en place des plutons granitiques (Blight et al., 2010; Kozlovsky et al., 2015; Hanžl et al., 2017). La poursuite unidirectionnelle de cette orogène aboutie à un raccourcissement hétérogène du domaine orogénique, avec une accrétion avant-arc, vraisemblablement du nord au sud, d'arcs insulaires, d'ophiolites et de prismes d'accrétion, incluant le microcontinent Néo-Protérozoïque (Xiao et al., 2004). Les formations paléozoïques sédimentaires et volcaniques constituent la moitié sud du Gobi-Ataï, dans les Gichigniy Nuruu, alors que les unités d'arc insulaires et de complexes ophiolitiques se localisent le long du MML (Kozlovsky et al., 2015; Hanžl et al., 2017) (Figure 1-15).

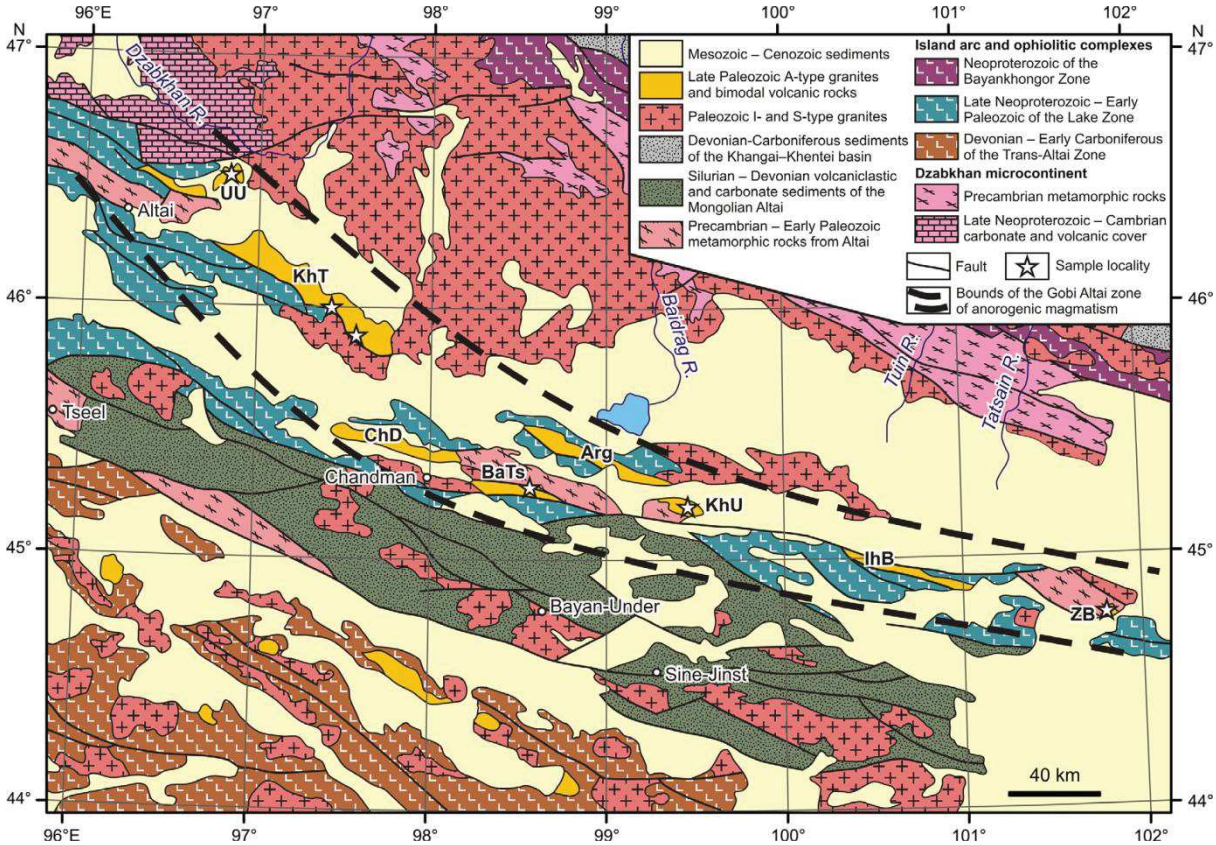


**Figure 1-15 : Carte géologique simplifiée du Gobi-Altaï (modifiée d'après la carte géologique du MPR au 1 : 2 500 000, 1989) d'après Kozolovsky et al. (2015). Les indications abrégées indiquent les unités magmatiques anorogéniques.**

De même, les granites Paléozoïques affleurent actuellement à l'est du massif de Baga Bogd, à l'est de la faille de la Vallée des lacs, autour de la ville de Chandmani et au sud de la faille de Tsagaan Gol (Figure 1-1 et Figure 1-15). Plus particulièrement, les granites triasiques se concentrent au niveau du MML, le long d'une ceinture de

magmatisme anorogénique constituant la moitié nord du Gobi-Altaï (Kozlovsky et al., 2015), et sont actuellement en contact systématique avec les failles de Bogd et de la Vallée des lacs (Figure 1-15).

L'évolution jurassique de ces « *terranes* », (aussi nommées Altaïdes sud), est caractérisée par des plissements E-O, des surrections et exhumations de plus de 2 km (Vassallo et al., 2007), ainsi que par la réactivation en décrochements transpressifs d'anciennes frontières du domaine océanique (Lehmann et al., 2010). A partir de mesures de décalages de bassin sédimentaires et de plutons, Heumann et al., (2014) estiment que la zone de faille Est-Gobi (EGFZ, Eastern Gobi Fault Zone), structure crustale majeure orientée NE-SO et située directement à l'est et au droit du Gobi-Altaï (Figure 1-14), a enregistré 150 à 200 km de décrochement senestre au cours du Trias, accommodant une extrusion continentale associée à la collision N-S des blocs Chine du sud et du nord. Cette même période est également caractérisée par l'ouverture de bassins selon une extension N-S dans le Gobi-Altaï avec des dépôts basaltiques atteignant une épaisseur de 1500m dans la région du massif d'Ih Bogd (van Hinsbergen et al., 2015).

La croissance latérale des Altaïds sud représente un apport massif de matériaux juvéniles à la croûte Paléozoïque (Şengör et al., 1993), dans lesquels la tectonique néogène va se localiser, ou se distribuer. La zone du Gobi-Altaï est ainsi située dans la partie souple ('*Soft core*') de l'Asie centrale, région qui sera un terrain préférentiel pour l'expression de la déformation néogène réactivant, dans le cadre de la collision Inde-Eurasie, ces structures crustales héritées de phénomène d'accrétions plus anciens (Windley et al., 1990; Cunningham, 2013;). Enfin l'absence de lithosphère cratonique rigide s'ajoute à l'histoire structurale complexe, pour faire de la région du Gobi-Altaï une zone tendre de la croûte continentale, pré-conditionnant la localisation et la cinématique de la réactivation néogène. Au premier ordre, le schéma structural de la région était ainsi déjà établi il y a 200 Ma (Badarch et al., 2002; Cunningham, 2013).

Le Crétacé marque l'arrêt des subductions dans la CAOB, et s'accompagne d'un phase de distension très étendue, caractérisée par un rifting diffus, dont l'architecture demeure peu documentée (Cunningham et al., 2009, 2013; van Hinsbergen et al., 2015).

Une brève période de transpression senestre survient au crétacé intermédiaire et supérieur, réactivant les rifts jurassique-crétacé dans la région du Gobi-Altaï (Graham et al., 2001; Johnson et al., 2004; Cunningham, 2013). On retrouve l'une de ces structures au sud-est de Ih Bogd (Figure 1-16), dans un bassin en demi-graben à vergence nord associé au système de faille de Bogd (van Hinsbergen et al., 2015). Il est à noter que,

bien que la géométrie en profondeur de ces failles ne soit pas contrainte (Figure 1-16), les auteurs insistent sur l'importance de prendre en compte l'architecture de ce *rifting* dans la compréhension de la réactivation néogène de ces structures, et dans le développement néotectonique du Gobi-Altaï (Cunningham et al., 2009, 2013; van Hinsbergen et al., 2015).

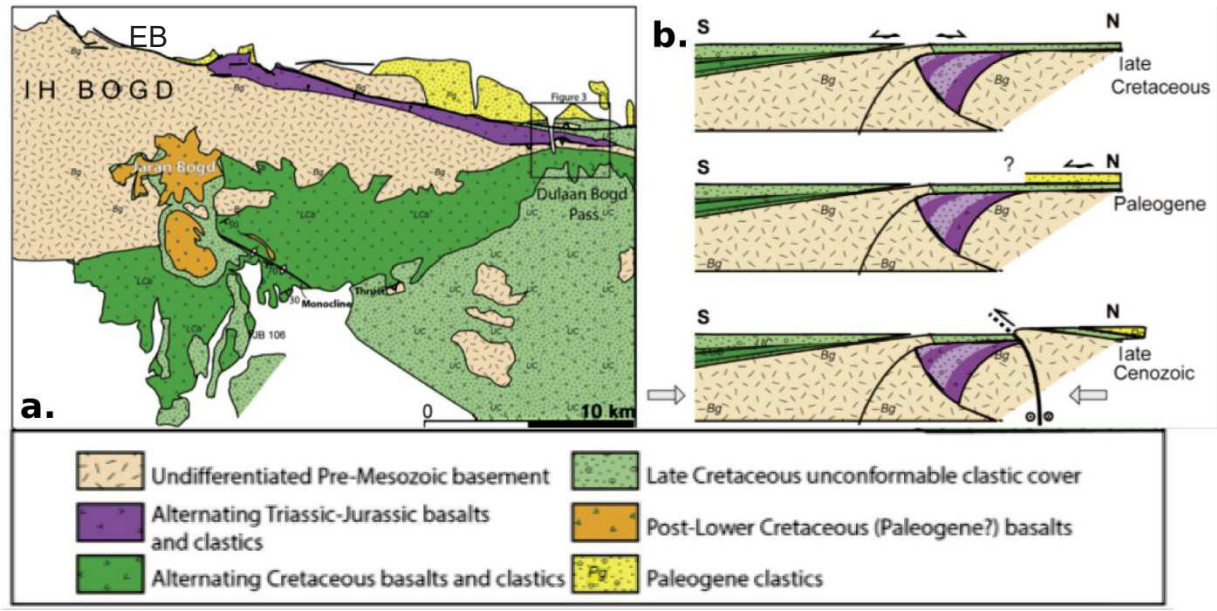


**Figure 1-16 : (a) Carte géologique de la partie est de Ih Bogd, modifiée d'après Zabotkin (1988) et van Hinsbergen et al. (2014). EBF : Eastern Bogd Fault, rupture de surface de 1957. (b) Interprétation de l'évolution tectonique dans la zone au sud de Zadgay Sayhr, ici nommée Dulaan Bogd Pass, d'après van Hinsbergen et al. (2014). La localisation du profil est N-S au centre du rectangle noir en (a). Noter la faible contrainte sur la géométrie des failles en profondeur, et la supposée absence de zone de faille, à la position de l'actuelle faille de Bogd Est.**

### VII.2. Evolution Cénozoïque

Au Paléogène, la région a connu une période de relative quiescence tectonique et d'intense érosion, comme en atteste les surfaces d'abrasions de grande ampleur, et la quasi-absence de dépôts (Cunningham, 2013). Cette période correspond en effet à un épisode de pénéplanation majeur de la CAOB orientale, ayant débuté lors de l'arrêt de la convergence Jurassique, et s'étendant sur près de 100 Ma (Jolivet et al., 2007; Vassallo et al., 2007). On retrouve cette pénéplaine, préservée par les conditions intracontinentales de faible taux d'érosion, du nord de l'Altaï au Gobi-Altaï, perchée à des altitudes similaires de 4000m (Ritz et al., 2003; Jolivet et al., 2007). Cette pénéplaine est particulièrement préservée dans le Gobi-Altaï, notamment aux sommets d'Ih Bogd (Figure 1-6), et d'Eemeltik Uul.

Si la période tardi-Mésozoïque ne présente pas de surrections importantes dans la partie occidentale de la Mongolie, des évènements géodynamiques ont cependant affecté les régions adjacentes au cours de l'Oligocène (Figure 1-17).

La période Eocène-Oligocène est tout d'abord caractérisée par une extension crustale dans la région du lac Baikal, avec la formation du bassin éponyme, associé à l'intrusion de diapirs (Logatchev et Florensov, 1978; Logatchev et Zorin, 1992). La déformation extensive se prolongera dans la région jusqu'au Quaternaire, période au cours de laquelle se produit une inversion de cinématique dans la partie sud-ouest du Baikal, d'un régime transtensif à l'oligocène a un régime transpressif au Plio-Quaternaire (Petit et al., 1996; Delvaux et al., 1997; Larroque et al., 2001; Arjannikova et al., 2004).

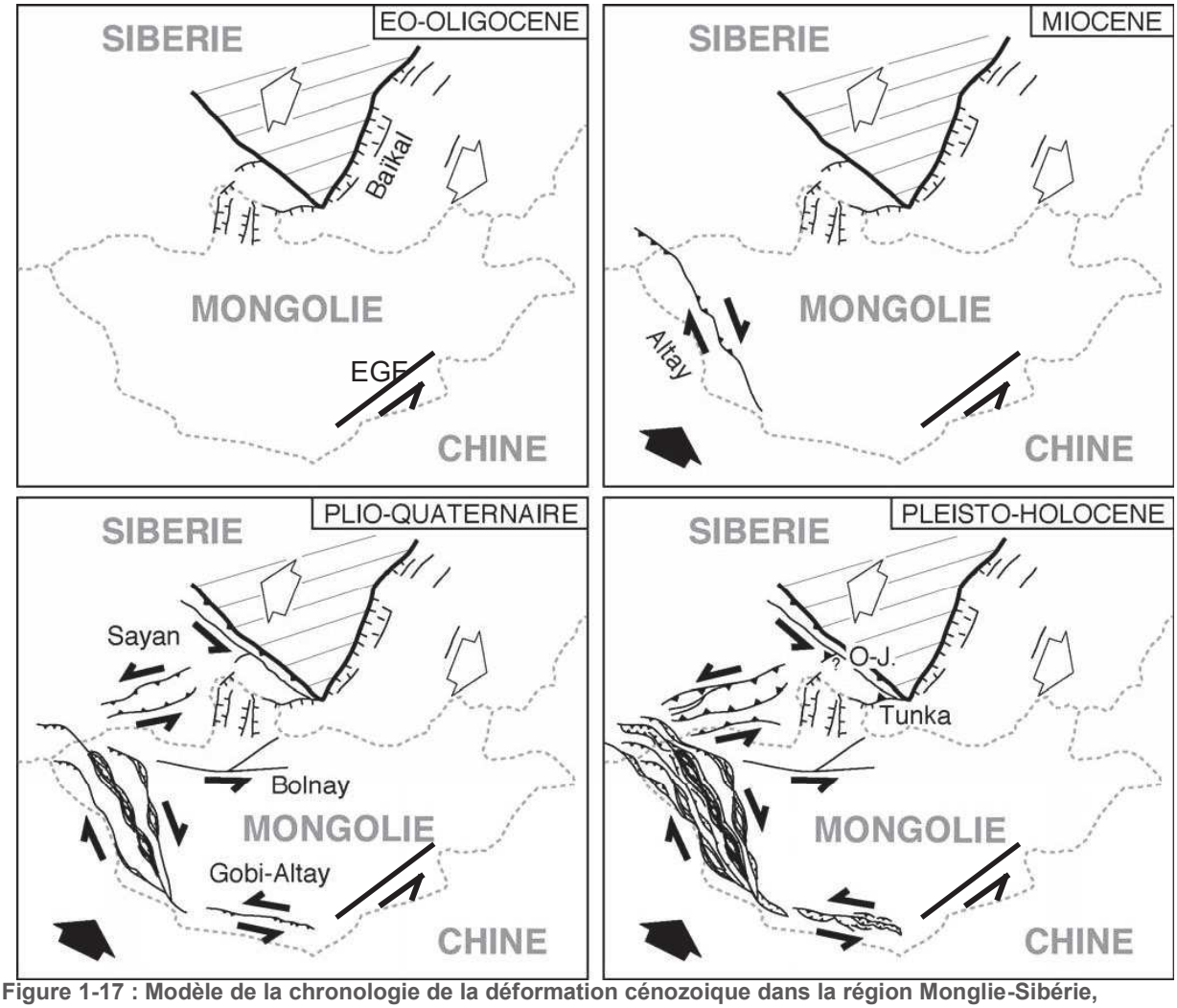


**Figure 1-17 : Modèle de la chronologie de la déformation cénozoique dans la région Monglie-Sibérie, modifié d'après Vassallo, (PhD, 2007). EGF : Eastern Gobi Fault zone ; O-J : faille de Okino-Jombolokskii.**

A l'est du Gobi-Altaï, un déplacement de 90 à 100km de décrochement senestre est également reporté à l'Oligocène supérieur sur la *Eastern Gobi Fault Zone* (EGFZ),

Figure 1-17), potentiellement associé aux conditions dynamiques sur la marge pacifique à cette période, voire à la collision Inde-Eurasie. En effet la EGFZ semble être corrélée cinématiquement à la faille de l'Altyn Tagh, via une zone de faille distribuée dans la région d'Alxa (van Hinsbergen et al., 2015).

Au sud-ouest les analyses thermochronologiques et stratigraphiques montrent que l'orogenèse du Tien Shan s'est initiée à l'Oligocène (Sobel et al., 2006), puis s'est accélérée au Miocène (Métivier et Gaudemer, 1997; Sobel et Dumitru, 1997; Fu et al., 2003). Cette orogenèse se poursuit par ailleurs à l'Holocène, comme en attestent les forts séismes historiques de la zone ; e.g. séisme de Manas, 1906, M8.3 (Avouac et al., 1993).

### VII.3. Du Néogène à l'actuel : réactivations successives

D'après Cunningham (2001), la formation du dôme de Hangay s'est produite au cours de l'Oligocène, mais de récentes études indiquent que la surrection du massif s'est probablement initiée préalablement, durant le Mésozoïque (Meltzer et al., 2012; Ancuta et al., 2013; McDannell et al., 2014). Bien que les processus géodynamiques à l'origine de ce dôme topographique de 700 km de long et 500km de large demeurent mal compris, le dôme de Hangay est décrit comme un '*indenteur*' passif dans la propagation vers le nord de la collision Inde-Eurasie, autour duquel se juxtaposent les chaînes de l'Altaï à l'ouest, et du Gobi-Altaï au sud, avec des cinématiques transpressives dextre et sénestre respectivement (Tapponnier et Molnar, 1979; Patriat et Achache, 1984; Cunningham, 2001, 2013; Petit et al., 2002; Bayasgalan et al., 2005).

Le dôme de Hangay présente toutefois des marques de déformation plio-quaternaire, principalement en extension, avec des escarpements de failles normales cumulant plusieurs centaines de mètres (Baljinnyam, 1993; Cunningham, 2001; Walker et al., 2007). Ces structures représentent un lien structural et cinématique important entre la province du Baïkal, au nord, et les chaînes transpressives de l'Altaï et du Gobi-Altaï à l'ouest et au sud respectivement (e.g. Vassallo, PhD, 2006).

La chaîne de l'Altaï, de direction moyenne NNO-SSE, est marquée par la coalescence de différents massifs, et montre dans sa partie centrale des reliefs plus évolués et plus complexes que ceux observés dans la chaîne du Gobi-Altaï, situés dans des zones de relais compressifs, et isolés le long d'un décrochement principal (Vassallo, PhD 2006). La formation de l'Altaï a donc possiblement commencé plus tôt que le Gobi-Altaï, en même temps que le Tien Shan, à l'Oligocène terminal-Miocène Moyen (Avouac et al., 1993; Métivier et Gaudemer 1997; Sobel et Dumitru 1997; Bullen et al., 2001; Charreau et al., 2005; Sobel et al., 2006). Par ailleurs, les traces de fission sur apatites indiquent

un âge de réactivation de l'Altai plus ancien que le NE-Gobi-Altaï, i.e. 2 - 8 Ma (Vassallo 2006; Vassallo et al., 2007) (Figure 1-17).

Au Miocène, la EGFZ connaît un arrêt de la déformation, probablement associé au changement relatif de déplacement des plaques sur la marge pacifique (van Hinsbergen et al., 2015). Cette même période voit par contre une initiation de la déformation sur le GTFS (Gobi Tien-Shan Fault System), décrochement majeur de 1200 km situé dans la prolongation est du Tien Shan et constituant la moitié sud de la région du Gobi-Altaï (Cunningham et al., 1996; Rippington et al., 2013).

**Summary:**

At first, this chapter gives an overview of the of the Gobi-Altai geomorphology, and of the knowledge of its seismological, morphotectonical and paleoseismological setting. Especially, we recap the quantified data along the Eastern Bogd Fault by presenting the whole fault geometry, slip rates and main paleoearthquakes characterized by former studies. In a second time, we present a synthesis of the investigations done on the western part of the Gobi-Altai, essentially by reviewing the morphotectonical and paleoseismological results of Mushkin (PhD, 2007). In order to highlight the strong lithological and structural inheritance of the Gobi-Altai, this setting is completed by a summary of the Gobi-Altai and surrounding regions geological evolution.

# Chapitre 2. Approches, matériels et méthodes

Ce chapitre vise à décrire brièvement les approches morphotectonique et paléosismologique adoptées, ainsi que les méthodes utilisées pour répondre aux problématiques précédemment énoncées.

L'approche générale débute par l'acquisition de données morphotectoniques, d'abord d'ordre spatial, comme les photos de terrain, les orthophotographies et les MNT, puis d'ordre temporel, au travers de datations. L'obtention de ces données peut se faire par télédétection (cartographie des ruptures de surfaces, caractérisation de leur géométrie et de la cinématique des failles, identification de sites prônes aux observations paléosismologiques), ou lors d'investigation de terrain (tranchées, échantillonnage, levés microtopographiques). De ces informations seront extraits des paramètres propres aux failles comme leurs vitesses long terme, leurs dimensions et les âges des séismes qui s'y produisent, permettant la caractérisation de l'évolution spatio-temporelle de l'activité sismique dans la zone d'étude au regard du contexte sismotectonique et de l'héritage géologique.

## I. Approche morphotectonique: Caractérisation d'une rupture de surface

### I.1. Principe

L'approche morphotectonique mise en œuvre vise à caractériser la déformation sismique de surface enregistrée dans la géomorphologie à diverses échelles spatiales, de la rupture sismique dans son ensemble ($10^4$-$10^5$m), aux détails morphologiques des marqueurs ($10^1$-$10^{-1}$m). La caractérisation de l'activité tectonique passe ainsi nécessairement par l'identification et la description des principales failles actives au sein de la chaîne du Gobi-Altaï. Plus particulièrement, l'attention sera consacrée à l'analyse des ruptures de surfaces, de la cinématique des failles, et de leurs complexités géométriques (e.g. Yeats et al., 1997; Wesnousky, 2008).

La première étape de l'approche morphotectonique est ainsi la cartographie détaillée (échelle 1 : 2000) et systématique des ruptures de surface récentes, et l'identification de sites présentant des marqueurs géomorphologiques clairement affectés par des déformations cosismiques. Dans un second temps, la quantification des décalages enregistrés par ces marqueurs permet de rendre compte de l'amplitude et de la distribution spatiale du glissement associé aux séismes. Enfin, couplées aux datations,

les mesures de décalages cumulés permettent d'estimer les vitesses de glissement long terme (pléistocène-supérieur) sur les failles considérées.

## I.2. Géométrie de la rupture : Cartographie et Identification de sites

### *I.2.1. Données et traitement*

La cartographie des ruptures de surface est réalisée principalement à l'aide photographies satellites en libre accès, d'images Spot 5, 6 et 7 (résolution de 1,5 m à 2 m), ainsi qu'à partir de photos aériennes en ce qui concerne la rupture du séisme du Gobi-Altaï. Le traitement des images aériennes est plus particulièrement effectué par une méthode photogrammétrique de *''structure from motion''* (Koenderink et Doorn, 1991), dont le schéma est illustré en Figure 2-1 ; cette méthode est explicitée plus en détail dans le Chapitre 3.

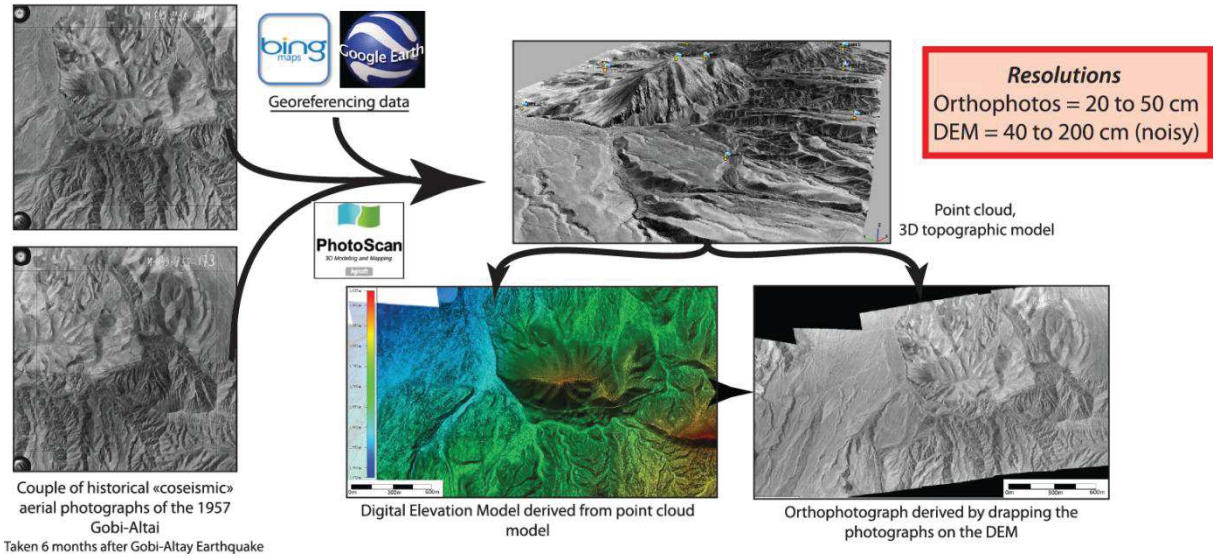


**Figure 2-1 : Processus de traitement par *structure from motion* de photos aériennes historiques (cf. Chapitre 3).**

Les MNT sont ensuite traités à l'aide d'outils d'analyses spatiales, puis exploités pour les travaux de cartographie et d'identification des marqueurs décalés, en vue de mesures directes de décalages (notamment cumulés) et d'identification de sites d'échantillonnages potentiels.

### *I.2.2. Critères de rupture quaternaire et cinématique*

La qualification d'une rupture de surface comme 'récente' demeure une démarche arbitraire, en fonction des critères temporels que les auteurs ont choisi de considérer. Afin de distinguer au premier ordre les escarpements de failles actifs au cours de la période tardi-pléistocène-holocène des failles néogènes, les principaux critères

considérés dans cette étude sont : i. La présence de formations et morphologies quaternaires (essentiellement des surfaces de dépôts alluvionnaires : cônes, terrasses, talus ou talwegs) affectées par la faille ; ii. La présence de figurés de déformation spécifiques dans des formations quaternaires (*sag-ponds*, fentes de tension, petits *pull-apparts*, *mole tracks*, *pressure ridges* ou encore *shutter ridges*) ; iii. L'identification de marqueurs géomorphologiques pérennes (e.g. principaux réseaux hydrographiques, glissement de terrain de grande ampleur) présentant systématiquement des décalages au contact de la faille.

La Figure 2-2 montre d'une part une rupture considérée comme holocène (A), car clairement continue et affectant systématiquement tant les formations pléistocènes que les formations holocènes actives, et d'autre part une rupture discontinue (B), n'affectant que les cônes anciens et abandonnés, dont la préservation est probablement associée à une surrection au nord de la faille, cet escarpement étant associé à la faille sud Gichigniy Nuruu (SGNF) qui est un chevauchement à vergence nord.

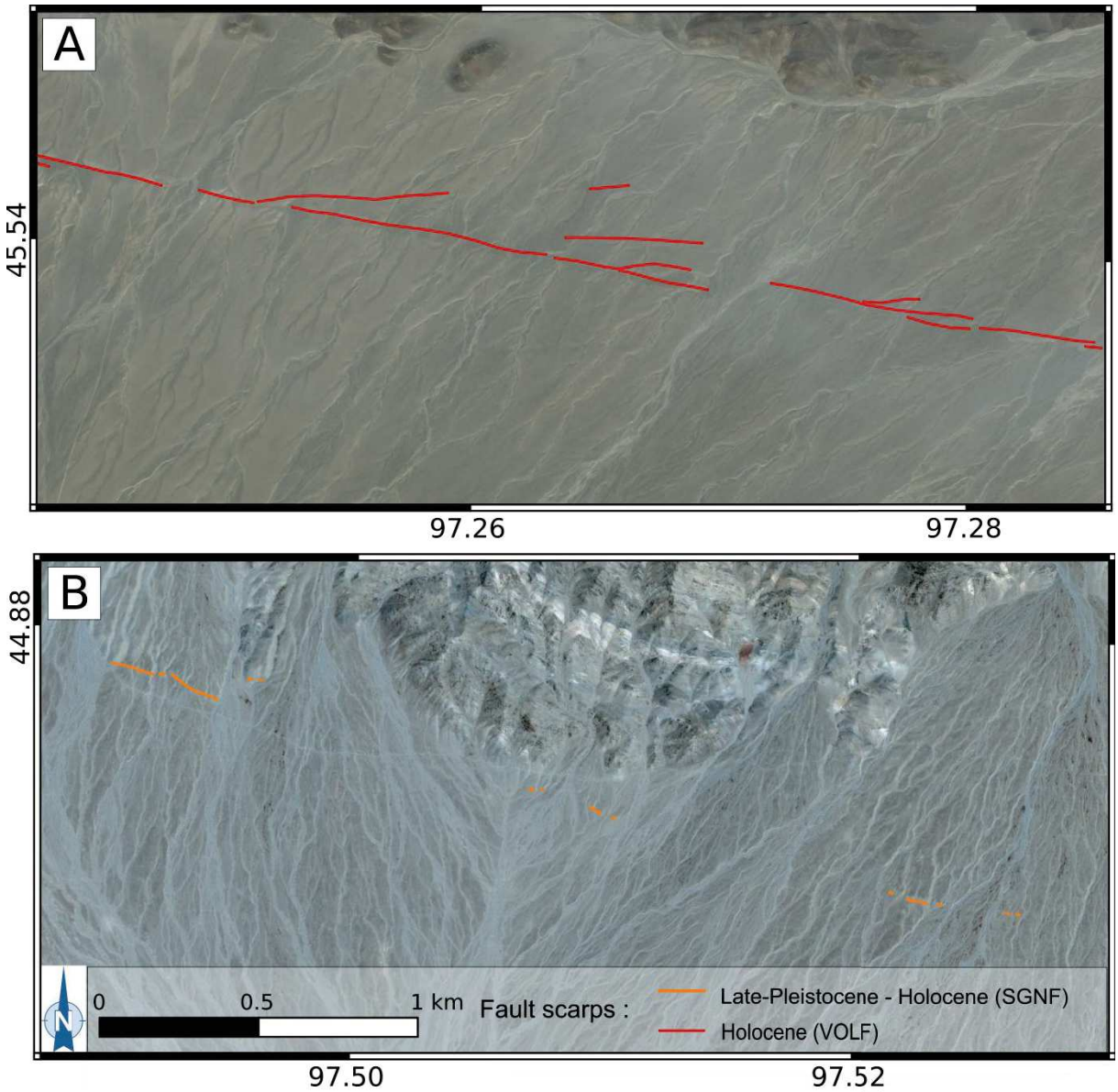


**Figure 2-2 : Exemples de cartographie de traces de failles. A. Rupture de surface holocène le long de la faille de la Vallée des Lacs (VOLF). B. Rupture de surface tardi-pléistocène ou holocène le long de la faille sud Gichigniy Nuruu (SGNF).**

Les décalages cumulés et les figurés de déformation permettent en outre de qualifier la cinématique de la faille sur plusieurs cycles sismiques, ainsi que de révéler la présence de relais et leurs dimensions, observations indispensables pour discuter la segmentation et l'étendue des ruptures de surface (e.g. Wesnousky, 2006, 2008). Il est à noter que la détermination du vecteur glissement par télédétection reste incertaine au vu des modestes résolutions des MNTs en accès libre, entrainant une faible contrainte de la composante verticale.

## I.3. Analyse de la distribution spatiale du glissement

### *I.3.1. Acquisition de données microtopographiques*

Trois principales méthodes ont été mise en œuvre sur le terrain pour effectuer les levés microtopographiques et générer les MNT : scanner au sol (TLS, pour *Terrestrial Laser Scanning*), photogrammétrie aérienne par cerf-volant (KAT, pour *Kite Aerial Topography*), et photogrammétrie aéroportée par drone.

#### I.3.1.1. Scanner 3D

Le scan 3D utilisé est un TLS moyenne portée (330 m en théorie) de la marque Faro®. Le principe est d'effectuer une série de scans à 360° à partir d'un module de scan composé d'une tête rotative, mesurant par impulsions radar à la fois la distance et la réflectance des objets et permettant ainsi une imagerie 3D haute résolution (densité théorique de 2 points par cm² à 20 m). Les différentes acquisitions de nuages de points sont ensuite alignées, filtrées puis assemblées à l'aide de plusieurs logiciels dédiés, brièvement décrits dans les sections suivantes. Le scanner utilisé est également muni de plusieurs capteurs (notamment GPS, clinomètre, boussole, altimètre et appareil photo) permettant d'une part une acquisition correcte des données (horizontalité des stations et estimation de leurs positions relatives), et d'autre part une optimisation du traitement, notamment pour les étapes d'alignement des différents scans.

L'acquisition doit tenir compte des zones d'ombre générées par la topographie et de la faible hauteur de l'appareil, simplement fixé sur un trépied à environ 1,7 m du sol. Un scan depuis le toit d'un véhicule permet de gagner en hauteur, mais la présence de vent peut cependant gêner la mesure en faisant osciller le véhicule, et être ainsi source d'artefact sur les résultats finaux. Le placement des stations est crucial pour une bonne couverture de la zone étudiée, et des schémas de configuration de scan sont systématiquement réalisés avant chaque manipulation. En plus de guider l'acquisition, ces schémas sont d'une grande utilité pour optimiser l'alignement lors du post-traitement des données. L'alignement peut être réalisé selon plusieurs procédés, le plus précis étant l'utilisation de cibles fixes. Ces cibles, constituées de sphères blanches (pour maximiser la réflectance, et donc leur identification) ou de damiers, sont distribuées le plus largement possible autour des stations, de façon à spatialement contraindre au mieux les positions relatives des stations de scan et permettre l'alignement précis des nuages de points. Néanmoins, la distance entre cibles et stations ne doit pas excéder 20 m, distance au-delà de laquelle la densité de points sur une cible n'est plus suffisante pour qu'elle soit identifiée par le scanner. Dans ce cas, l'alignement basé sur cible ne

peut pas être réalisé, et un alignement de ‘nuage à nuage’ est nécessaire, avec un ajustement manuel au premier ordre.

Le traitement des données de scan est effectué par l’utilisation successive des logiciels suivant :

i. Logiciel ‘Scene®’ propre aux scanner Faro® : dépouillement des fichiers, alignement sur cibles, export des fichiers au format nuage de point (.e57).

ii. LAS Tool (Isenburg, 2012) : outils spécialisés dans le traitement de données type ‘nuage de points’. Filtration des éléments de scan ayant une forme de moins de 50cm de diamètre pour une hauteur de plus de 20cm. Les objets ayant une telle morphologie sont, dans le contexte écosystémique et géomorphologique du Gobi-Altaï (végétation exclusivement herbacée et érosion souvent dominée par la déflation), associés à des touffes d’herbes. Cette étape permet ainsi de s’affranchir d’une partie du signal lié à la végétation. Les fichiers sont exportés en format lidar (.las) pour la suite du traitement.

iii. Logiciel Cloud-Compare : alignement si cibles non détectées, optimisation de l’alignement, filtre de point caché (*hidden point removal*) pour partiellement s’affranchir de la végétation restante.

iv. Global Mapper® : rasterisation, interpolation si nécessaire.

Les MNT sont ensuite exportés à des résolutions allant de 5 cm à 20 cm, en fonction de la texture de la zone investiguée, de la surface couverte et de la densité de stations. Les photos permettent finalement de colorer les orthophotos.

L’avantage de cette méthode est la précision des mesures, donnée à 2 mm par le constructeur (cf. « Faro doc. » 2017). Les principales limites sont l’absence de géoréférencement des données de topographie finales, ainsi que le temps de traitement, notamment dans le cas d’un alignement dit ‘de nuage à nuage’, partiellement manuel. Localement, des artefacts peuvent persister dans les zones peu ou pas recoupées par plusieurs stations, principalement associés à la nature radiale de la mesure et à la présence de végétation (en particulier, les hautes herbes entrainent ce type d’artefact). Il est à noter qu’une attention toute particulière est donnée à l’imagerie des *piercing lines*. Ainsi les artefacts n’impactent pas, dans l’ensemble, les mesures de décalages.

#### I.3.1.2. KAT

L'acquisition de photos aériennes à différentes positions et selon différents angles de visée permet de générer des MNT et des orthophotos par traitement photogrammétrique. Le système utilisé est constitué d'un cerf-volant mono-ligne, et d'un appareil photo fixé sur un support mobile dédié à ce type d'acquisition, lui-même suspendu à la ligne du cerf-volant. Le système de fixation de l'appareil photo permet de changer l'incidence et l'azimut des prises de vue entre chaque photo. Les photos sont prises automatiquement à intervalle de temps régulier, à l'aide d'une carte SD spécialement programmée à cet effet. Bien entendu ce système reste tributaire des conditions aérologiques (i.e. force du vent modérée et absence de nébulosité en basses couches).

Le traitement des photographies est effectué selon un protocole de '*structure from motion*', sous le logiciel commercial *Agisoft* P*hotoscan*®. Afin d'assurer le géoréférencement, des mires géolocalisées par GPS différentiel peuvent être placées au sol. Ces points de contrôles permettent d'une part l'optimisation du traitement photogrammétrique, et d'autre part le géoréférencement des MNT et orthophotos produits.

L'avantage certain de cette méthode est l'indépendance énergétique du système aéroporté (des batteries sont tout de même nécessaires pour l'appareil photo et pour le support). L'une des principales limites de cette méthode reste néanmoins le faible contrôle de la distribution spatiale des clichés. En effet, bien que l'azimut et l'incidence des prises de vues soient variables, le cerf-volant mono-ligne n'est pas contrôlable, et les mouvements décrits par le cerf-volant dans une masse d'air turbulente limitent l'exhaustivité de la couverture de la zone investigué par les photos. Ceci entraine des difficultés de traitement (non corrélations de certaines images) et ainsi une couverture parfois partielle de la zone d'étude par les données. Enfin, la nature herbeuse des steppes mongoles du Gobi-Altaï entraine une texture uniforme de la surface du sol, limitant par là même le potentiel de corrélation de différentes photos. Les MNT produits par cette méthode ont des résolutions de 10cm à 30cm selon la qualité et le nombre de prises de vue.

#### I.3.1.3. Photogrammétrie par drone

Une seconde méthode d'acquisition de photographies aériennes fut l'utilisation d'un drone *DJR*® équipé d'un appareil photo 13 Mpx. Les photos ont été réalisées à une hauteur de 200 à 300 m au-dessus du sol, avec un angle d'incidence de 80°. Les prises de vue sont effectuées automatiquement toute les 5 secondes, de manière à ce que

chaque point au sol soit visible au moins 3 fois en un passage – soit au minimum 60 % de recouvrement. Pour une meilleure acquisition, la couverture de la zone doit autant que possible être effectuée selon un quadrillage. En effet, un passage simple ou aller-retour selon une trajectoire rectiligne aura pour conséquence de maximiser l'effet de '*doming'* inhérent au traitement photogrammétrique de photos aériennes (James et Robson, 2014). Le drone étant équipé d'un GPS différentiel entre l'engin et la commande, le géoréférencement des images est automatique, et cette information, prise en compte lors de la modélisation photogrammétrique par '*structure from motion'*, permet un géoréférencement des MNT et orthophotos. Les résolutions obtenues selon cette méthode, fonction de l'altitude d'acquisition, de la résolution de l'appareil photo et du nombre de clichés, sont de 5 à 10 cm pour les orthophotos, et de 10 à 20 cm pour les MNT.

Les principaux avantages que présente cette méthode d'acquisition sont sa rapidité d'exécution et de traitement, sa simplicité de mise en œuvre et la précision des données obtenues (qui reste dépendant de la distribution des photos, de leurs résolutions, et du géoréférencement). Le principal inconvénient réside dans la lourdeur des procédures administratives pour l'utilisation des drones – même si la Mongolie présente à ce jour un certain vide juridique à cet égard.

### *I.3.2. Mesures de décalages*

#### I.3.2.1. Nature des marqueurs morphotectoniques

Les marqueurs géomorphologiques utilisés dans cette étude sont essentiellement des figures de dépôt ou d'érosion d'origine hydrologiques, de préférence faiblement soumis aux phénomènes d'érosion. On utilisera par exemple des talus de terrasses alluviales, des chenaux incisés dans des surfaces colluvionnaires de type cônes alluviaux, ainsi que les différents éléments des talwegs : lignes de crêtes, talus et chenaux actifs. Afin d'optimiser les incertitudes dans la quantification du décalage au niveau d'une rupture de surface, les marqueurs doivent être de préférence linéaires et orientés le plus perpendiculairement possible à la direction de la rupture (Yeats et al., 1997; Salisbury et al., 2015). La dynamique sédimentaire locale (e.g. taille et activité des drains, régimes fluviatiles, affluents…), l'érosion (e.g. sapement de talus, diffusion, mouvements gravitaires...), ainsi que les déformations directement associées à la faille (Figure 2-3) doivent être systématiquement analysées avant interprétation des déplacements et échantillonnages en vue de datation.

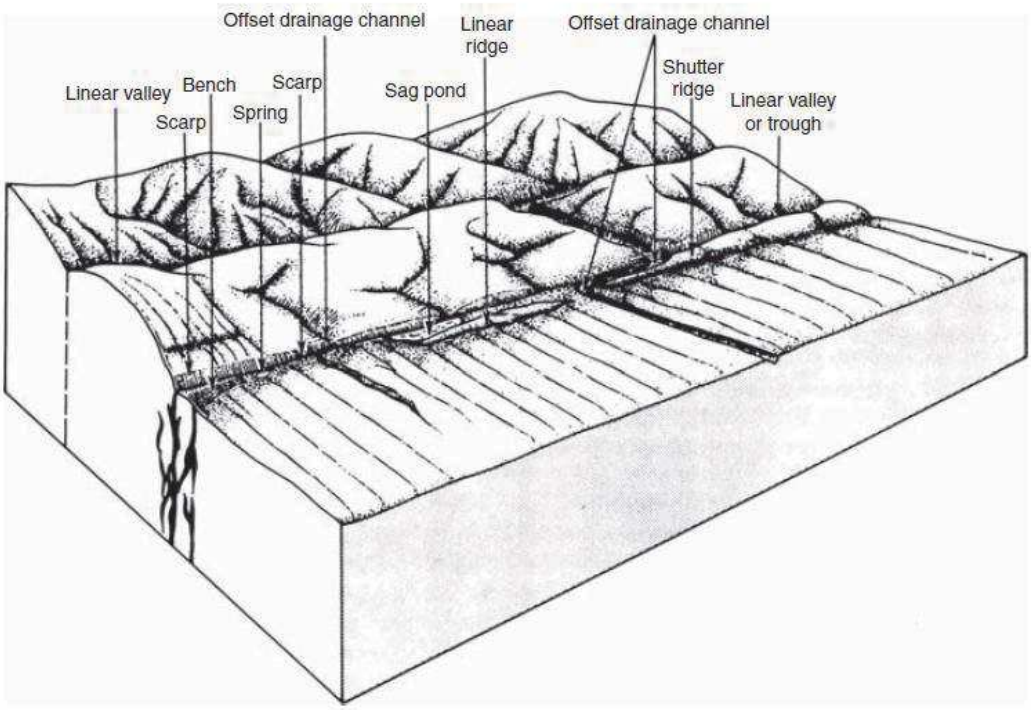


**Figure 2-3 : Exemple de déformations le long des failles décrochantes (d'après Costa et Baker, 1981).**

La mesure de déplacement est obtenue soit en interprétant des *piercing lines* par projection de linéations de marqueurs sur quelques dizaines de mètres de part et d'autre de la faille, soit en mesurant des profils topographiques longitudinaux à la faille. Dans tous les cas, l'objectif est de déterminer l'amplitude et la direction du vecteur glissement d'après ses composantes horizontales et verticales (Figure 2-4).

**Les réseaux de drainage** constituent l'essentiel des marqueurs analysés dans ce travail, principalement de par leur abondance et leurs aspects linéaires. On distingue par exemples les chenaux actifs, les chenaux abandonnées, les axes de talwegs ou encore les rides les délimitant. Bien que de moindre ampleur que les mouvements horizontaux, les failles décrochantes sont souvent associées à des mouvements verticaux, entraînant heureusement un drainage à fort angle par rapports à l'axe de la faille. Les différents marqueurs sont systématiquement décalés latéralement par la faille au cours d'un séisme, et leur analyse les uns au regard des autres permet de contraindre l'orientation et l'amplitude du vecteur glissement (Figure 2-4). Il convient également de prêter une attention particulière à l'angle décrit par le drainage par rapport à la faille ainsi qu'à la pente locale, cette dernière influençant le décalage par phénomène de déflexion des drains.

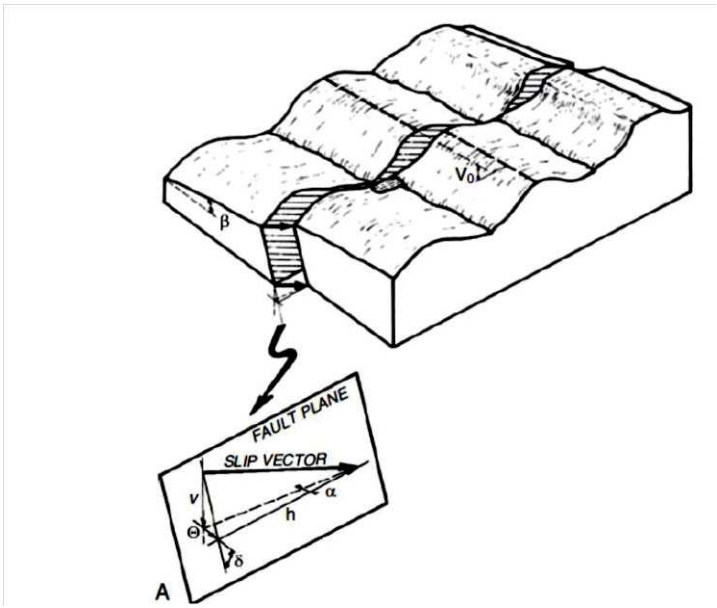


**Figure 2-4 : Bloc diagramme schématique d'un décalage produit par une faille décrochante senestre sur deux talwegs (d'après Peltzer et al., 1988). Le vecteur glissement (encart A) est déterminé en fonction des composantes verticales et horizontales du glissement. Noter l'importance des décalages verticaux apparents (zones grisées). Une bonne estimation du décalage doit dans ce cas être réalisée à l'aide de profils topographiques longitudinaux.**

**Les terrasses alluviales** sont créées par l'incision du chenal actif d'une rivière consécutif à un abaissement du niveau de base, généralement induit par des variations climatiques (e.g. stades glaciaires). Parfois, lorsque des terrasses sont situées au niveau d'une rupture de surface, la croissance verticale des escarpements de faille entraine également l'incision voire le basculement de ces surfaces. Quoi qu'il en soit, la nature tabulaire et étagée de ces formations offre de grandes opportunités d'enregistrement de la déformation lorsqu'elles sont affectées par des ruptures de surface. Les talus de ces terrasses présentent d'une part fréquemment des morphologies linéaires, aisément identifiables, et d'autre part l'étagement de ces terrasses permet d'intégrer la déformation cumulée sur plusieurs cycles sismiques. Ainsi, certains sites permettent de rendre compte de la déformation cumulée, qui corrélée à l'âge d'abandon de cette surface, permet de quantifier la vitesse de la faille au niveau du site à différentes échelles temporelles ($10^4$ à $10^5$ a). Il est à noter néanmoins que l'analyse et l'interprétation de l'effet de l'érosion et de l'évolution de ces talus (préservation) est indispensable pour quantifier les décalages et en tirer des conséquences sur les vitesses de glissement.

**Les cônes alluviaux** se mettent en place dans des zones de pertes de charge, souvent à l'exutoire de drains encaissés dans les reliefs, et s'étendent, dans le contexte aride du Gobi-Altaï, jusqu'au centre des dépressions endoréiques bordant les massifs. De par leur localisation et leur aspect imposant, les cônes de déjection constituent des

marqueurs pérennes de la déformation. Bien que les mesures de décalages présentent des incertitudes importantes du fait de leur morphologie grossière et des régimes d'écoulements radiaux, leur maintien dans le paysage permet de dater des décalages cumulés importants. De plus, leur structuration en '*bar and swales*', et les reprises d'incision qui se développent sur leur surface constituent autant de marqueurs de moindre échelle qui permettent de mieux contraindre leur évolution. Les mesures de déplacements latéraux sont extraites de *piercing lines* dérivées soit directement des principaux drains affectant la surface du cône, soit par l'intégration des éléments radiaux, afin de localiser l'apex du cône. Ces repères sont ensuite alignés sur l'exutoire des talwegs d'où proviennent les matériaux composant le cône. Enfin, la succession de la mise en place des cônes alluviaux à l'exutoire d'un drain majeur, permet, au même titre qu'avec les terrasses alluviales, d'effectuer des mesures de vitesses de glissement à différentes échelles de temps. Dans l'exemple ci-dessous (Figure 2-5), Ritz et al. (1995), ont ainsi déterminé la vitesse de glissement long terme de la fille de Bogd Est à 1,2 mm.a$^{-1}$ depuis le pléistocène-supérieur.

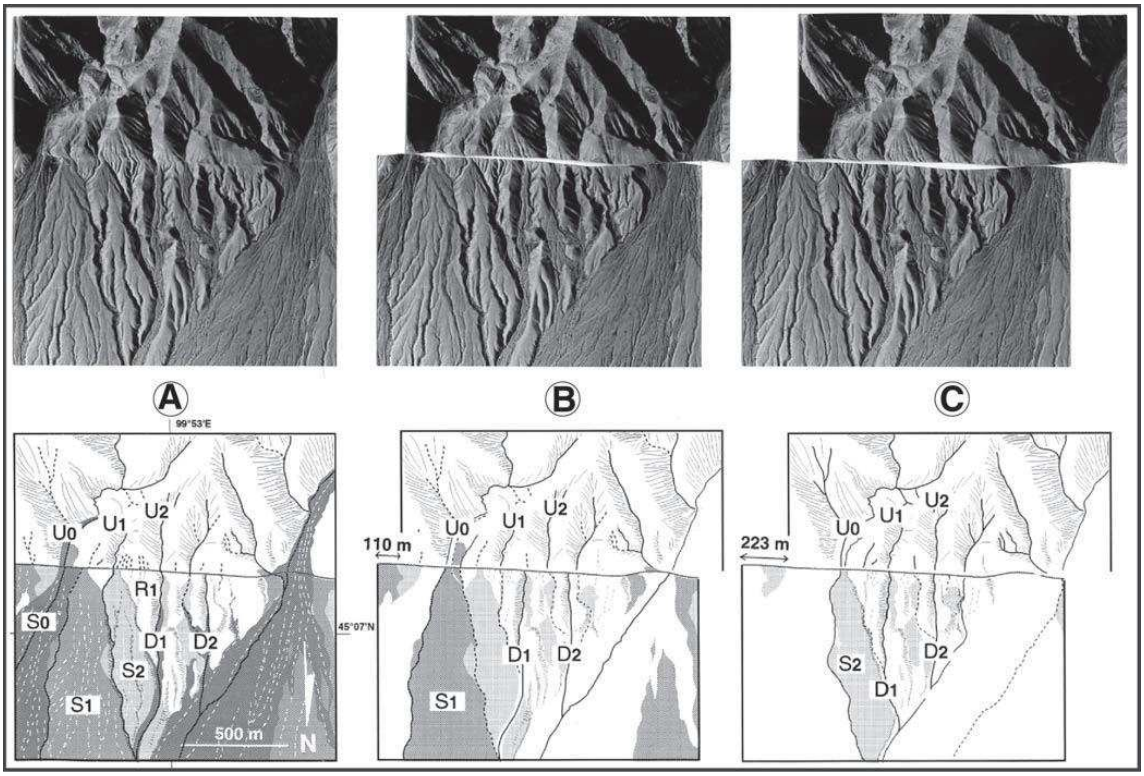


**Figure 2-5 : Reconstitution de l'histoire de dépôt et d'érosion d'un cône alluvial le long de la faille de Bogd Est (d'après Ritz et al., 1995). A : Actuel. B : Reconstruction pour 110 m de déplacement sénestre. C : Reconstruction pour 223 m de déplacement sénestre. Les lignes continues U0, U1 et U2 désignent les axes des chenaux principaux en amont de la faille ; D1 et D2 sont les axes des chenaux principaux en aval de la faille. Les lignes pointillées indiquent des vallées de moindre ampleur. Les ombrages représentent l'âge relatif des surfaces de dépôts (S2, S1 et S0) ; les couleurs plus claires correspondent aux surfaces les plus vieilles. Seules les reliques encore présentes des cônes alluviaux S1 et S2 sont présentées dans B et C.**

### I.3.2.2. Méthode de mesure de décalages

La principale méthode de mesure de décalage utilisée dans cette étude consiste à retrouver la configuration du marqueur morphotectonique considéré, avant le décalage causé par la rupture sismique, par l'identification de *piercing lines* ou de profils topographiques, respectivement orthogonaux et parallèles à la faille.

Plusieurs supports visuels sont utilisés pour la localisation des *piercing lines*. Les supports de base sont les orthophotos et les MNT, mais un traitement de ces derniers selon des outils d'analyses spatiales SIG permet de mettre en exergue les éléments de la morphologie particulièrement intéressants pour les mesures d'offset, comme les ruptures de pente ou les axes de chenaux et talwegs. Sont par exemple utilisées les cartes de pentes, d'orientations de pentes ou de dérivés de pente (Figure 2-6).

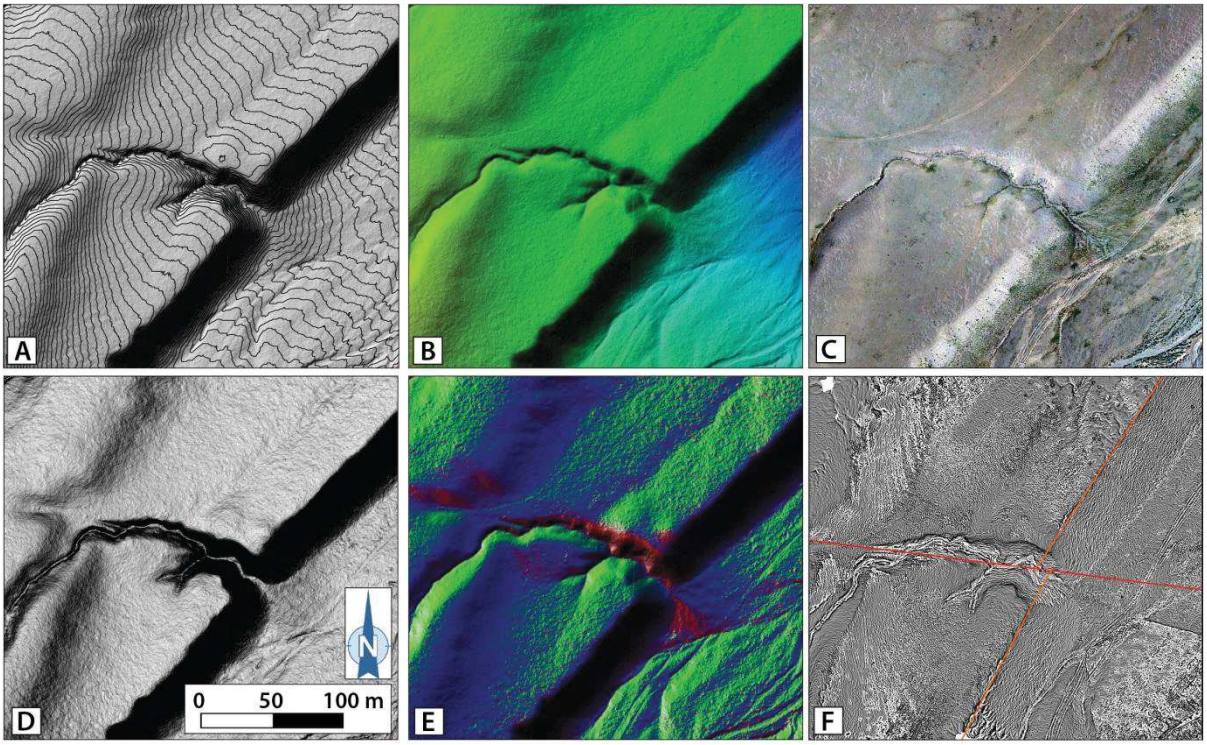


**Figure 2-6 : Illustration des données utilisées pour les mesure des décalages, site de Biger Terraces, rive gauche (ouest), dérivées par traitement photogrammétrique de photographies aériennes acquises par drone. A. Ombrage sur MNT (20 cm de résolution) et courbes de niveau (isoplèthes à 50 cm) ; B. Ombrage sur MNT avec palette de couleur correspondant aux altitudes ; C. Orthophotographie (10 cm de résolution) ; D. Niveaux de gris associés aux pentes (noir pour pentes fortes, blanc pour zones tabulaires) ; E. Carte d'exposition des pentes en palette de couleur : rouge vers le sud, jaune vers l'ouest, vert vers le nord et bleu vers l'est ; F. Courbes de même courbure de pente (*slope curvature*). Le trait rouge indique la faille de la Vallée des Lacs (VOLF) et les traits orange les *piercing lines* associées au sommet du talus de la terrasse principale.**

Dans ce travail, le choix a été fait d'effectuer l'alignement du marqueur manuellement en 3 temps : tout d'abord une mesure dite préférentielle, puis des mesures dites maximale et minimale en explorant les positions 'extrêmes' cohérentes avec l'alignement des *piercing lines* de part et d'autre de la faille. Ces mesures permettent ainsi au premier

ordre de quantifier l'incertitude associée à chaque mesure. Il est à noter qu'un marqueur morphotectonique peut enregistrer des incréments successifs de glissements, en fonction du nombre de séismes l'ayant affecté et de sa conservation dans le paysage, et que cette méthode de mesure ne tient pas a priori compte de la nature simple ou multiple d'un déplacement. Un traitement statistique pourra à cette fin être appliqué, comme détaillé dans le Chapitre 3.

Certains marqueurs, comme les surfaces, ne présentent pas systématiquement de *piercing lines*. Dans ce cas, un alignement à partir de profils longitudinaux permet de mesurer les décalages, moyennant la connaissance du vecteur glissement.

#### I.3.2.3. Qualité des mesures de décalages

La détermination précise des décalages sur le terrain ou par télédétection n'est pas une tache triviale, d'une part parce que la configuration exacte du marqueur avant la mesure n'est pas connue, et d'autre part parce que les modifications du marqueur après décalage ne sont ni connues ni contraintes. De plus, la capacité et la fiabilité de la mesure sont partiellement dépendantes de l'utilisateur (e.g. Salisbury et al., 2015). Il est par conséquent nécessaire de renseigner, pour chaque mesure de décalage, la qualité de la mesure, elle-même dépendante de facteurs morphologiques (e.g. géométrie et préservation du marqueur), morphotectoniques (e.g. géométrie, cinématique et distribution de la déformation) et purement techniques (i.e. nature et résolution des données spatiales, présence d'artefacts).

Ces informations peuvent par la suite être utilisées afin de sélectionner ou de pondérer les mesures, notamment en vue de la détermination de la distribution spatiale du glissement associée à des évènements successifs, et de leur éventuelle modélisation (Chapitre 3).

### *I.3.3. Traitement des distributions spatiales du glissement*

Il est aujourd'hui admis que la distribution de la déformation en surface le long d'une rupture sismique permet de rendre compte des processus sous-jacents, que ce soit en terme de quantité d'énergie relâchée au cours d'un séisme (Wells et Coppersmith, 1994), qu'en terme de dynamique de la rupture elle-même (e.g. Wesnousky, 2008). Les premières distributions de glissement (e.g. Sieh, 1978; McGill et Sieh, 1991) ont entre autre permis d'identifier de possibles régularités dans les amplitudes de glissements au regard de la segmentation de la faille. Schwartz et Coppersmith (1984), ont ainsi proposé 3 modèles de glissement (Figure 2-7).

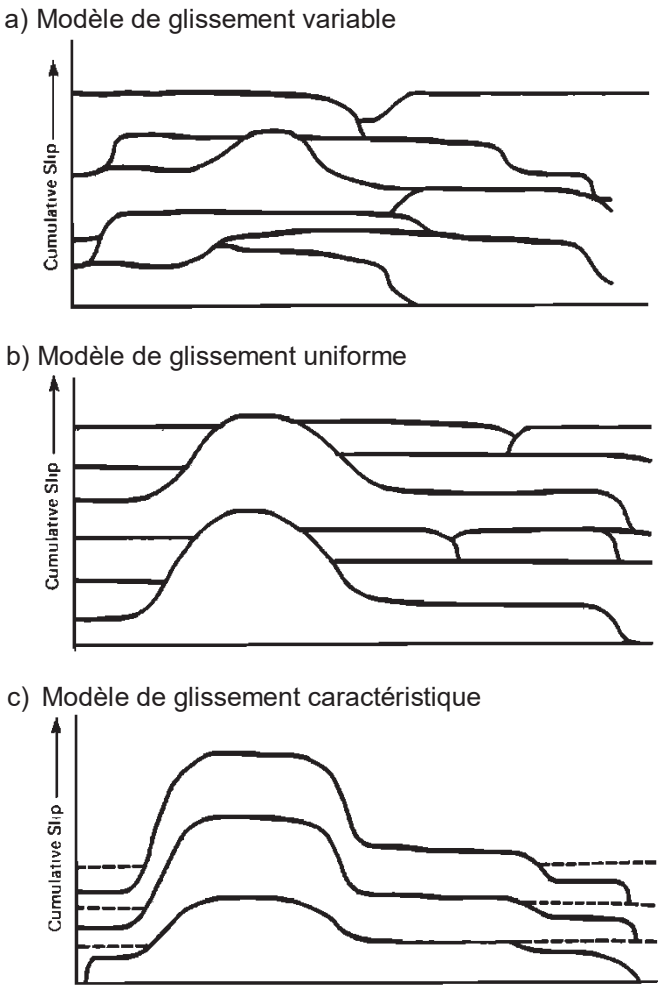


**Figure 2-7 : Modèles de glissement le long d'une faille (d'après Schwartz et Coppersmith, 1984)**

Le modèle de glissement variable Figure 2-7.a) présente des déplacements variables lors de chaque séisme en tous points de la faille. La vitesse de la faille est constante, et les séismes ont une magnitude variable. Le modèle de glissement uniforme (Figure 2-7.b) présente des déplacements similaires en tous points de la faille lors de chaque séisme. La vitesse de faille est constante, avec des séismes majeurs de fréquence similaire, mais une plus forte fréquence des séismes de faibles magnitudes. Enfin dans le modèle de glissement caractéristique (Figure 2-7.c), les déplacements sont similaires en tous points de la faille lors de chaque séisme, mais la vitesse varie alors le long de la faille. Les séismes majeurs ont une magnitude similaire, mais les séismes de plus faibles magnitudes sont plus rares.

Bien que l'une des questions majeures sous-tendues par ces modèles soit la variabilité de la vitesse de faille au cours du temps, il apparait ici que l'inventaire des déplacements le long d'une rupture de surface, et plus particulièrement l'identification de la nature simple vs cumulée de ces déplacements est une démarche essentielle dans la caractérisation de l'activité d'une faille.

L'amélioration des méthodes d'analyse des déformations sismiques, notamment avec l'apport des nouvelles technologies (INSAR, drones, acquisitions microtopographiques, photographie satellitaire à très haute résolution, pixel corrélation, *structure from motion*, etc.), permet une observation toujours plus complète des déformations, des processus qui les entraînent et de leurs temporalités (e.g. *afterslip*, *aseismic-slip*...). L'appréhension de la distribution de la déformation, notamment aux abords des relais dans le cas de failles décrochantes, est ainsi de plus en plus fine, et de récentes études basées sur la *pixel correlation* ont pu montrer par exemple que ce qui était jusque-là considéré comme du déficit de glissement en surface par rapport à la profondeur provenait principalement de l'imprécision des méthodes de mesures de la déformation (Fialko, 2004; Rockwell et Klinger, 2013; Vallage et al., 2015). Cependant, la surface du sol correspondant à une surface libre, la distribution de la déformation est plus distribuée qu'en profondeur (par phénomène de diffraction), et la détermination de décalages d'après une approche morphotectonique doit être interprétée comme une mesure minimale de l'amplitude totale des déformations générées par un séisme lors des calculs de magnitudes et de vitesses de glissement (Gold et al., 2015).

## I.4. Quantification des vitesses de glissement et de leurs variations au cours du temps

### *I.4.1. Mesures de décalages cumulés*

L'estimation de vitesses de glissement horizontales à partir de décalages de marqueurs alluviaux peut présenter des difficultés, notamment sur l'interprétation de l'âge des marqueurs décalés. Lorsque les marqueurs sont étagés, comme des terrasses alluviales par exemple, il peut y avoir une ambiguïté sur la correspondance du décalage avec l'âge de la terrasse supérieure, celui de la terrasse inférieure, ou un âge intermédiaire (Rizza et al., 2011; Van der Woerd et al., 2000; Cowgill 2007; Gold et al., 2009). L'exemple ci-dessous (Figure 2-8) présente la méthodologie pour encadrer la vitesse de glissement sur un site de terrasses alluviales, en considérant des talus de rivières ayant subies des évolutions différentes en étant décalées par la faille (Gold et al., 2009).

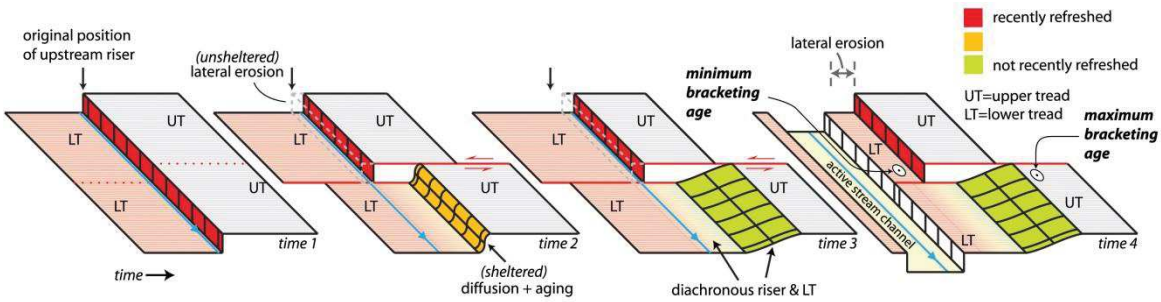


**Figure 2-8 : Modèle conceptuel illustrant l'évolution de talus diachrones de terrasses alluviales, d'après Gold et al. (2009). Au temps 1, un talus est formé alors que l'écoulement est actif sur la terrasse inférieure (LT). Au temps 2, le glissement latéral le long de la faille protège la talus situé en aval de l'érosion du chenal actif, et son profil est principalement affecté par de la diffusion. Le talus supérieur subit quant à lui un sapement par le chenal actif, ce qui entraîne son retrait et l'effacement progressif du décalage cosismique, tout en assurant l'aspect frais de sa morphologie. Au temps 3, la poursuite du décalage au niveau de la faille maintient le recul et la raideur du talus en amont de la faille, alors que le talus en aval, toujours protégé, continue de diffuser, au point que ses *piercing lines* migrent de part et d'autre de la position initiale du talus. Au temps 4, lorsque l'incision du chenal actif induit un abandon de la terrasse inférieure, les talus qui délimitent les terrasses en amont et en aval de la faille n'ont plus le même âge, et les déplacements observés permettent uniquement d'encadrer la valeur réelle du déplacement latéral. Les déplacements des talus en amont et en aval de la faille constituent respectivement les bornes minimale et maximale du déplacement utilisés pour le calcul du slip rate. Dans le cas d'une incertitude trop importante, des critères additionnels comme la présence de marqueurs au sein des surfaces peuvent permettre de contraindre l'amplitude de l'érosion du talus non protégé.**

### *I.4.2. Datations*

Afin d'apporter la composante temporelle dans la détermination de la vitesse de glissement d'une faille, deux méthodes ont été utilisées dans cette étude, permettant d'estimer l'âge de dépôt ou d'abandon des marqueurs morphotectoniques: la datation aux nucléides cosmogéniques, et la datation par luminescence stimulée optiquement (OSL, *Optically Stimulated Luminescence*).

#### I.4.2.1. $^{10}$Be *in situ*

Initialement développée pour l'étude des météorites, la méthode de datation par nucléides cosmogéniques, à la faveur de l'amélioration de la spectrométrie de masse par accélérateur de particule et de la spectrométrie des gaz rares (Lal et Arnold, 1985), est aujourd'hui communément utilisée dans les domaines de la glaciologie, de la pétrologie, ou encore de la géomorphologie.

##### *I.4.2.1.1. Principes généraux*

Le principe est simple : sous l'effet du bombardement de particules de haute énergie, elles-mêmes résultant de l'interaction du rayonnement cosmique avec les atomes de l'atmosphère terrestre, certains atomes constituant les roches vont subir des réactions nucléaires de spallation, aboutissant à la production de nouveaux éléments qui vont se substituer aux atomes cibles et rester dans le maillage minéralogique (Dunai, 2010; Gosse et Phillips, 2001; Stone, 2000).

L'essentiel des interactions entre le rayonnement cosmogénique incident et les matériaux terrestres s'effectue dans l'atmosphère, générant des particules secondaires (protons et neutrons) au cours une succession d'interactions, qui vont à leur tour entraîner de nouvelles spallations. La cascade réactionnelle se propage ainsi jusqu'au sol (Figure 2-9), et interagie finalement avec les matériaux de la surface. Par exemple un atome d'oxygène ($^{16}$O) impacté par un neutron produira du $^{10}$Be, 4 protons et 3 neutrons (Dunai, 2010).

Ces réactions de spallations produisent des éléments plus légers, alors nommés nucléides cosmogéniques ou cosmonucléides, pouvant être stables (e.g. $^{3}$He et $^{21}$Ne) ou radioactifs (e.g. $^{36}$Cl, $^{14}$C, $^{10}$Be), ainsi que des particules plus légères et moins énergétiques (protons et neutrons) qui sont éjectées. L'accumulation de ces nouveaux isotopes dans les dépôts est fonction du temps, de la dénudation et de la profondeur, et la mesure de leur concentration peut être utilisée comme un sablier pour le mesurer.

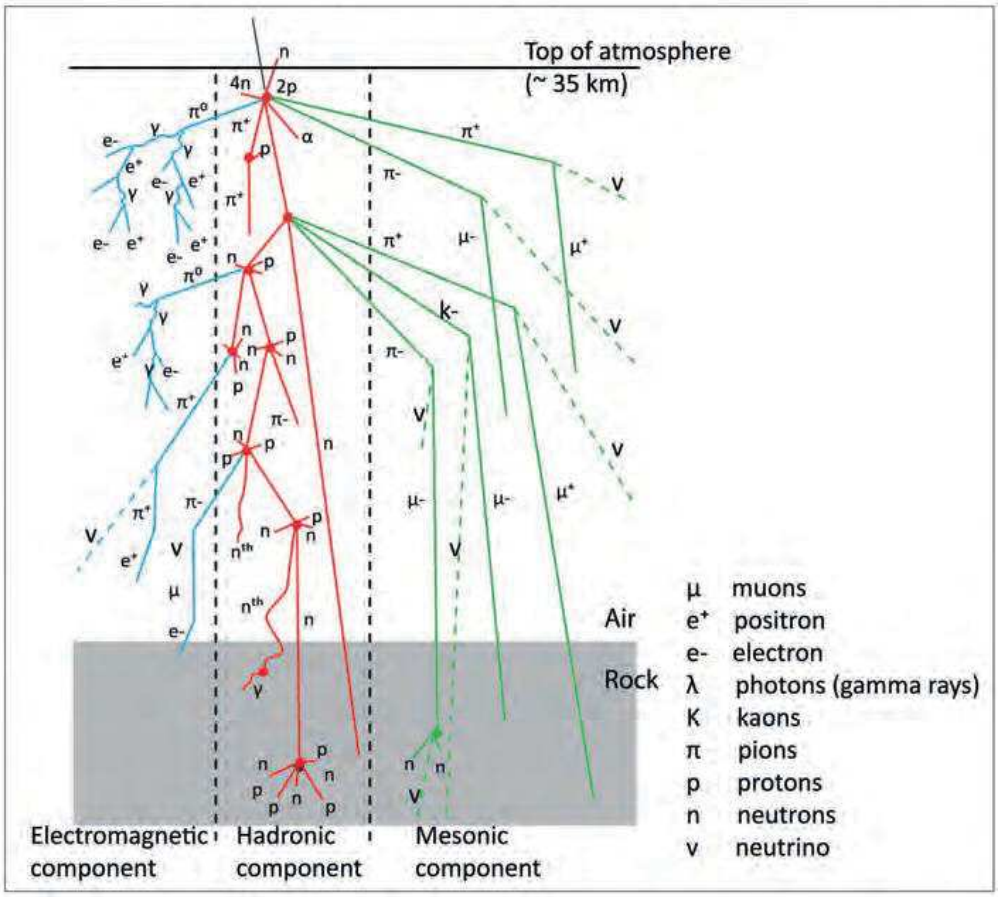


**Figure 2-9: Production de particules dans l'atmosphère et le sol, d'après Gosse et Phillips, 2001. Les réactions de spallation provoquent la formation d'isotopes cosmogéniques dans l'atmosphère et la lithosphère.**

#### *I.4.2.1.2. Taux de production*

L'un des paramètres principaux nécessaire pour utiliser les nucléides cosmogéniques est le taux de production, exprimé en atome $at.g^{-1}.a^{-1}$, correspondant à la vitesse à laquelle un isotope cosmogénique in situ (par opposition à atmosphérique) s'accumule dans un minéral. Le taux de production dépend d'une part du flux et de l'énergie des particules cosmiques qui atteignent le minéral (latitude, altitude et profondeur), et d'autre part de la composition chimique du minéral.

Les particules cosmiques incidentes (protons, particules β ou électrons) étant chargées, elles sont influencées par le champ magnétique terrestre, et dans le contexte géomagnétique dipolaire actuel, le taux de production augmente avec l'augmentation de la latitude.

L'altitude est également un facteur important dans la mesure où l'immense majorité du rayonnement cosmique est intercepté dans l'atmosphère (seul 0,1% du flux de particules cosmique arrive au sol avec suffisamment d'énergie pour générer des réactions de

spallation). L'épaisseur d'atmosphère traversée est donc directement liée au taux de production dans le sol, et le taux de production augmente donc avec l'altitude.

Le taux de production de référence actuel pour le $^{10}Be$ est égal à 4,02 ± 0,02 at.g $^{-1}$.an$^{-1}$ au niveau de la mer (Borchers et al., 2016). Ce taux est ensuite corrigé en fonction de la latitude et de l'altitude du site d'échantillonnage (Stone, 2000). Les reliefs alentours peuvent également agir comme des obstacles à l'arrivée du rayonnement cosmique sur le site de datation, réduisant le taux de production par phénomène d'écrantage. Il convient par conséquent de considérer, pour chaque site, la hauteur des reliefs environnant pouvant faire obstacle aux rayonnements cosmiques incidents, afin de corriger le taux de production d'un éventuel écrantage. L'écrantage est déterminé par la mesure de l'angle constitué par les principaux sommets et points bas environnant le site d'échantillonnage, puis utilisé dans le calcul du taux de production au travers d'un coefficient allant de 0 à 1, ici déterminé à l'aide de l'outil présenté dans Balco et al., (2008) ; 0 étant un écrantage complet (cas d'un dépôt souterrain par exemple), et 1 l'absence d'écrantage par les reliefs avoisinants (cas d'un site au relief tabulaire).

Le sol étant beaucoup plus dense que l'atmosphère (1,2 à 2,6 contre 0,0001 pour l'air), les rayons cosmiques sont donc atténués en fonction de l'épaisseur de matière traversée, et de sa masse volumique. Il en résulte une décroissance exponentielle du taux de production avec la profondeur, qui est caractérisée par un paramètre appelé longueur d'atténuation, exprimé en g.cm$^{-2}$, qui dépend du type de particule et de la densité du milieu. Un échantillonnage pour estimation de la masse volumique du dépôt est donc systématiquement réalisé.

L'atténuation théorique du taux de production en fonction de la profondeur est donnée par la loi :

$$P(x) = P_0\, e^{\left(\frac{\rho x}{\Lambda}\right)} \qquad \text{(I-1)}$$

Où $\mathbf{P_0}$ est le taux de production en surface, $\rho$ est la densité de la roche en g/cm3, $x$ la profondeur en cm, et $\Lambda$ la longueur d'atténuation des particules qui vaut 150 g/cm2 pour les neutrons, 1500 g/cm2 pour les muons lents et 4320 g/cm2 pour les muons rapides (Braucher et al., 2011). Les contributions muoniques, bien que négligeables en surface (~2 % de la production) deviennent prépondérantes en profondeur. La production de nucléides cosmogénique peut donc être observée de la surface à plusieurs dizaines de mètres de profondeurs.

#### *I.4.2.1.3. Datation au $^{10}Be$*

Les isotopes cosmogéniques demeurent, après avoir été produits, piégés dans les mailles minéralogiques de certains minéraux, comme le quartz, qui présente par ailleurs un réseau cristallin qui limite les pertes par diffusion. De plus, le quartz présente une composition bien déterminée ($SiO_2$), et ces deux éléments (oxygène et silicium) sont susceptibles de produire du $^{10}Be$ par spallation. Le quartz étant un matériau à la fois très résistant et abondant, et il est couramment présent dans les dépôts sédimentaires, et constitue un outil primordial pour effectuer des datations de marqueurs morphotectoniques, en vue de mesurer les vitesses de glissement des failles actives.

Le $^{10}Be$ est un isotope radioactif de demi-vie $T_{1/2}{}^{10}Be = 1{,}387.10^6$ a, et une compétition entre production et désintégration va ainsi s'opérer en fonction du temps d'exposition (Figure 2-10), selon l'équation différentielle suivante :

$$\frac{\partial C(x,t)}{\partial t} = \varepsilon \times \frac{\partial C(x,t)}{\partial x} - \lambda C(x,t) + P_0 \times e^{\frac{-\rho x(t)}{\Lambda}} \qquad \text{(I-2)}$$

où $C(x,t)$ est la concentration en $^{10}Be$ en fonction de la profondeur $x$ et du temps $t$, $\lambda$ est la constante de décroissance radioactive du $^{10}Be$ ($4{,}62.10^{-7}$ $a^{-1}$) et $\varepsilon$ le taux d'érosion en $g.cm^{-2}.a^{-1}$.

La différentiation des contributions neuroniques (n) et muoniques (μ1 et μ2) et l'hypothèse d'un taux de production contant permet d'obtenir l'équation suivante :

$$C(x,t) = C(x,0) \times e^{-\lambda t} + \sum_{i=n;\mu1;\mu2} \frac{P_0 \times P_i}{\frac{\varepsilon\rho}{\Lambda_i} + \lambda} \times e^{\frac{-\rho x}{\Lambda_i}} \times \left(1 - e^{-\left(\lambda + \frac{\varepsilon\rho}{\Lambda_i}\right)t}\right) \qquad \text{(I-3)}$$

où C(x,0) est la concentration initiale de l'échantillon en fonction de la profondeur, c'est-à-dire, dans le cas d'un dépôt instantané, l'héritage en $^{10}Be$.

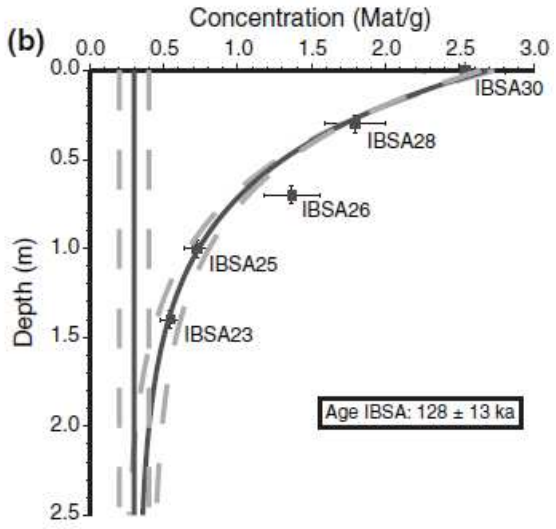


**Figure 2-10 : Exemple de distribution de la concentration en $^{10}$Be selon un profil en profondeur, d'après (Vassallo et al., 2005). A 2,5m de profondeur la concentration en $^{10}$Be est de l'ordre de 0,3 Mat.g$^{-1}$, correspondant à l'héritage des matériaux lors du dépôt. La courbe noire représente le meilleur modèle, pour un âge de 128 ka.**

Au bout d'un certain temps, un équilibre entre le taux de production et le taux de désintégration va se produire, limitant la période couverte par cette méthode de datation à quelques centaines de milliers voire quelques millions d'années, en fonction du taux de production local (altitude, latitude) ; lorsque cet équilibre est atteint, on parle alors d'état stationnaire (Figure 2-11). Le taux de production étant variable avec la profondeur d'enfouissement, des phénomènes d'aggradation ou d'érosion de la surface auront des implications sur la distribution en profondeur des concentrations en $^{10}$Be, et par conséquent l'interprétation d'une datation sera soumise à des hypothèses sur le taux d'érosion et l'histoire géomorphologique du dépot investigué. Le palier d'état stationnaire sera d'autant plus précoce que le taux d'érosion sera important (Brown et al., 1991) (Figure 2-11).

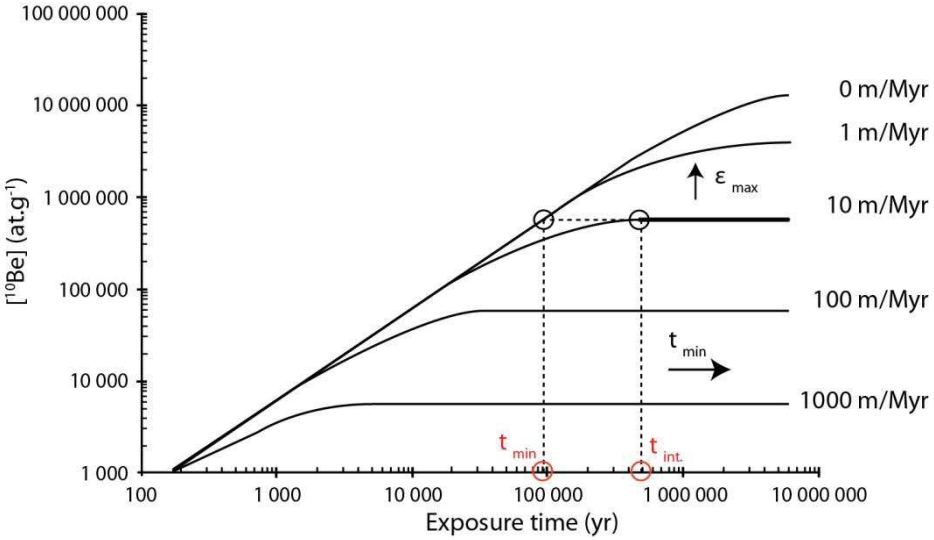


**Figure 2-11 : Evolution théorique des concentrations en 10Be en fonction des temps d'exposition et de différents taux d'érosion, modifié d'après Brown et al., (1991). $t_{min}$ : âge minimum pour un taux d'érosion nule (dans le cas d'une concentration de $6.10^6$ at/g); $t_{int}$ : âge d'intégration, âge minimum pour atteindre l'état stationnaire (dans le cas d'un taux d'érosion de 10 m/Ma).**

La distribution des concentrations en $^{10}$Be avec la profondeur décrit donc théoriquement une décroissance exponentielle, et l'estimation de l'héritage peut se faire de manière graphique, au travers d'une asymptote verticale (Figure 2-10) ; une valeur nulle de cette asymptote indiquant un héritage nul en $^{10}$Be.

Le profil de concentrations en $^{10}$Be avec la profondeur est ensuite modélisé par l'équation (I-3), et un test de chi2 est effectué entre ce modèle et les données mesurées. La valeur recherchée (i.e. l'âge d'abandon du marqueur ou le taux de dénudation) ainsi que l'héritage sont finalement déterminés par la minimisation de la valeur du Chi2.

Néanmoins, la résolution de l'équation (I-3) requiert de faire certaines hypothèses, dans la mesure où elle présente 3 inconnues, l'âge (t), le taux d'érosion (ε) et l'héritage.

Une première approche consiste à considérer un taux de dénudation nul ($\varepsilon = 0$), et ainsi de déterminer un âge d'exposition minimal $t_{min}$ (Figure 2-11).

Une seconde approche consiste à estimer la dénudation  en considérant une surface à l'état stationnaire (i.e. temps d'exposition infini) :

$$\varepsilon = \left(\frac{P_0}{C(0,\infty) - C_0}\right) \times \Lambda \qquad \text{(I-4)}$$

Cette information peut également être apportée par l'échantillonnage d'une surface analogue (contexte de dépôt et localisation), clairement abandonné depuis plus longtemps que la surface que l'on cherche à dater, qui sera ainsi considéré comme à

l'état stationnaire. Le taux d'érosion ainsi déterminé est nécessairement associé à un temps d'intégration ($t_{int}$), qui correspond à la durée minimale nécessaire pour atteindre l'état stationnaire, compte tenu du taux de production et de l'érosion préalablement déterminée (Figure 2-11).

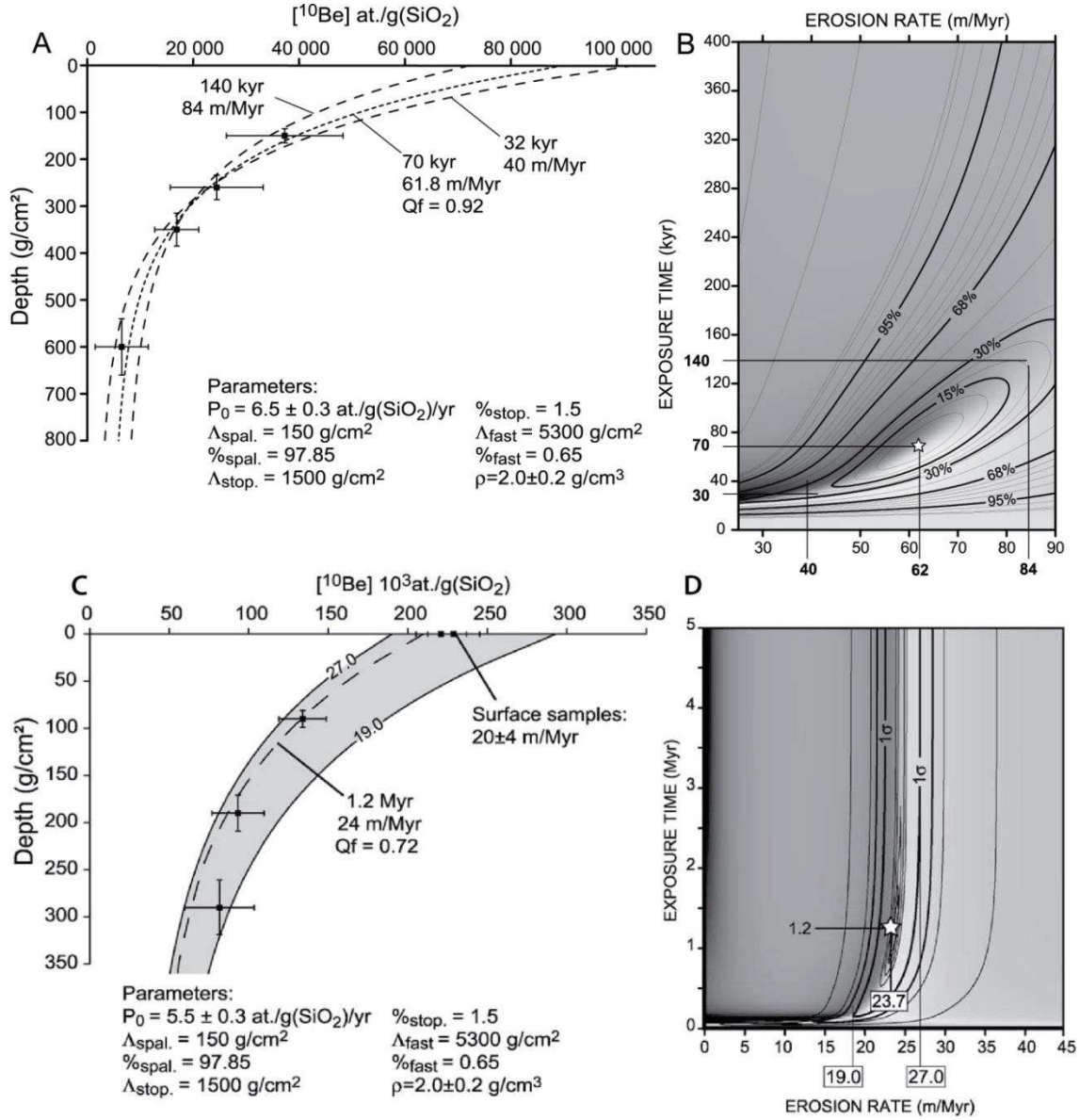


**Figure 2-12: Exemples d'interprétation de profils au $^{10}$Be, d'après Siame et al. (2004). Meilleures corrélations au test du chi² pour les terrasses considérées. A. Profil de concentration au $^{10}$Be en fonction de la profondeur, et incertitudes associées. Les lignes pointillées représentent les décroissances exponentielles modélisées pour différents taux de dénudation déterminés en B. B. Graphique des solutions de l'inversion bayésienne pour des durée d'exposition allant de 0 à 400 ka, et pour des taux de dénudation de 25 à 90 m/Ma. C. Profil de concentration au $^{10}$Be en fonction de la profondeur, et incertitudes associées. La ligne pointillée représente la décroissance exponentielle modélisée, et les paramètres correspondants. Les traits pleins correspondent aux décroissances exponentielles pour une durée d'exposition infinie, avec des taux de dénudation déterminés en D. D. Graphique des solutions de l'inversion bayésienne pour des durée d'exposition allant de 0 à 5 Ma, et pour des taux de dénudations de 0 à 45 m/Ma.**

La Figure 2-12 représente un exemple de deux interprétations de profils au $^{10}$Be par inversion bayésienne, d'après Siame et al. (2004). Le premier profil est associée à une surface alluviale n'ayant pas atteint l'équilibre stationnaire (Figure 2-12-A et B). La figure B, en forme ''de moule'' montre que l'âge d'exposition est bien contraint, contrairement au taux de dénudation. Les différents âges proposés dépendent du taux de dénudation considéré. Le second profil montre par contre un profil considéré comme à l'état stationnaire (Figure 2-12-C et D). La distribution des solutions, en forme de crosse, indique une valeur centrée sur le taux de dénudation, mais l'âge d'abandon de la surface ne peut être contraint que par l'âge d'intégration, correspondant à la durée minimale d'exposition pour atteindre l'état stationnaire.

#### *i. Protocole d'échantillonnage*

La composition d'une surface de dépôt récente n'étant que rarement homogène, et chaque claste étant susceptible d'avoir une histoire qui lui est propre, il convient d'appliquer une approche statistique pour l'échantillonnage. Dans cette thèse, toutes les datations au $^{10}$Be sont effectuées à partir d'échantillonnage à une profondeur donnée d'amalgames d'au moins 50 clastes, de taille et de lithologie analogues. Les échantillonnages de surface doivent être réalisés en sélectionnant des clastes clairement enchâssés dans la surface que l'on cherche à dater, pour s'assurer de ne pas polluer l'amalgame avec des apports plus récents.

Les marqueurs morphotectoniques utilisés dans cette thèse pour l'estimation des vitesses de glissement des failles sont exclusivement constituées de dépôts colluvionnaires ou alluvionnaires (cônes et terrasses), et les matériaux qui les composent, ayant donc été transportés sur des distances plus ou moins importantes présentent nécessairement un héritage en $^{10}$Be relatif à leur exposition au rayonnement cosmique pendant le transport. Pour estimer la part de la concentration en $^{10}$Be associée à l'héritage, il convient d'effectuer un échantillonnage selon un profil vertical (Figure 2-13), mettant en exergue la décroissance de la concentration avec la profondeur. Travailler dans un profil permet à la fois de caractériser l'atténuation, d'estimer l'héritage, et de contraindre les hypothèses de temporalité du dépôt, de taux d'érosion, et d'équilibre stationnaire entre le taux de production du $^{10}$Be et son taux de désintégration.

L'échantillonnage est effectué dans un trou (*soil pit*) d'au moins 1,5 m, creusé à la pelle au sein du marqueur que l'on cherche à dater (Figure 2-13). Un log stratigraphique est systématiquement levé pour discuter de l'homogénéité ou de la nature stratifiée du dépôt. Un dépôt clairement stratifié avec des unités distinctes et des niveaux érosifs, indiquera une temporalité complexe dans la mise en place du marqueur, et sera l'indice

d'un profil de concentration en $^{10}$Be potentiellement non uniforme, réduisant notre capacité à correctement dater le marqueur.

**Figure 2-13 : Photographies d'échantillonnages. A. Ouverture d'un '*soil pit*' dans une surface de cône alluvial, dans l'Altaï. B. Echantillonnage du '*soil pit*' dans une terrasse alluviale affectée par la faille de la Vallée des Lacs (site de *Biger Terraces*). C. Levé du log dans un '*soil pit*' dans l'Altaï. D. Echantillonnage d'un amalgame de sédiment riche en matière organique pour datation $^{14}$C, dans une tranchée sur la faille de Bogd Occidentale (Tranchée 3 du site de *Rain Creek*).**

L'échantillonnage d'amalgames de clastes riches en quartz est ensuite effectué à des profondeurs précises de 0, 25, 50, 75, 100, 150 et 200 cm (Figure 2-13).

Une méthode d'échantillonnage analogue, mais moins coûteuse (une datation sur un profil requiert l'analyse d'au moins 7 amalgames) consiste à mesurer uniquement la concentration en $^{10}$Be à la surface (mesure de l'accumulation + héritage), et soit en profondeur, soit au niveau de l'arrivée des sédiments (apex actif du cône de déjection ou lit actif d'une rivière dans le cas de datation de terrasse) afin de quantifier l'héritage en $^{10}$Be des clastes lors de leur mise en place sur le marqueur. Il est à noter que cette approche présente d'importantes hypothèses, qui ne seront pas contraintes par la modélisation du profil (cf. équations sections I.4.2.1.2 et I.4.2.1.3), comme la stricte homogénéité du dépôt dans le cas d'un échantillonnage en profondeur, et l'actualisme de l'héritage en $^{10}$Be des clastes en cours de transport dans le cas des échantillonnages

de chenaux actifs. Ces points seront systématiquement abordés lors de l'interprétation de vitesses de glissement mesurées selon ce protocole.

### *ii. Extraction des concentrations en $^{10}$Be d'amalgames*

Les travaux de préparation chimique des échantillons ont été réalisés au laboratoire du CEREGE, sous la supervision de Régis Braucher, selon le protocole ASTER (Leanni et ASTER team, 2013), dont les principales étapes sont rappelés ci-dessous :

- Broyage, séchage et tamisage des amalgames entre 0,25-1mm. Tris au séparateur magnétique (Frantz), et récupération de la fraction non magnétique dans des bouteilles de Nalgène®, dont la masse à vide a été mesurée.
- Décarbonatation à l'acide chlorhydrique (HCl), pour nettoyage de la matière organique et des carbonates.
- Elimination des minéraux autres que le quartz par attaques acides successive à l'acide héxafluoridrique ($H_2SiF_6$) et à l'acide chlorhydrique (HCl), 24h d'agitation suivit de rinçage et séchage, jusqu'à l'obtention de grains blancs translucides, alors pesés.
- Elimination du 10Be atmosphérique ayant diffusé dans les imperfections du quartz à partie de la surface. Trois attaques successives à l'acide fluorhydrique (HF) sont ainsi réalisées, dissolvant 10% de la masse de quartz. De nouveau pesée de la masse de quartz restante.
- Ajout de l'entraineur (env. 0,1mL), constitué de $^{9}$Be à 3065 ppm, afin de fixer le rapport isotopique $^{10}$Be/$^{9}$Be.
- Dissolution totale du quartz à l'HF, par ajout d'une quantité d'acide en excès.
- Récupération et nettoyage par formation de précipités successifs et centrifugations.
- Elimination des cations métalliques par fixation sur résines échangeuses d'ions (fer et Manganèse, puis bore et aluminium) et récupération du béryllium et de l'aluminium.
- Dosage à l'ICP des rapports isotopiques en aluminium.
- Récupération du béryllium dans un creuset et oxydation pour obtention d'oxyde de béryllium (BeO).
- Cathodage du BeO en vue des dosages des rapports isotopiques en cosmonucléides au spectromètre de masse à accélérateur de particules (AMS).

Tout au long de ces étapes, un échantillon 'blanc' suit le protocole, afin d'identifier voir corriger les concentrations des éventuelles pollutions générées au cours de la préparation.

### *iii. Discussions*

### *iv. Hypothèses*

L'utilisation des cosmonucléides, et en particulier le $^{10}$Be présuppose certaines hypothèses. La mise en évidence du non-respect de ces hypothèses sera discutée pour l'interprétation de chaque datation.

Une première hypothèse est celle d'un champ magnétique constant depuis le pléistocène (plage de temps investiguée par datation au $^{10}$Be). En effet des variations significatives du champ magnétique vont influencer le taux de production en $^{10}$Be.

L'analyse d'un profil de concentration en $^{10}$Be requiert une seconde hypothèse, qui est que le dépôt étudié est uniforme en composition (lithologie, granulométrie, dynamique de dépôt) sur l'ensemble du profil. En effet si l'on souhaite analyser les concentrations les unes en regard des autres (modélisation), il est indispensable que les échantillons aient la même histoire. L'avantage d'une datation en profil est en outre que si le dépôt n'est pas homogène (i.e. s'il est stratifié), le profil reflète cette variabilité (i.e. il ne décrit pas cette décroissance de la concentration avec la profondeur). Heureusement, la nature uniforme d'un dépôt est cohérente avec des épisodes de pulses climatiques formant les surfaces alluviales (e.g. Ritz et al., 2003).

Enfin une dernière hypothèse qu'il convient de mentionner est l'absence d'écrantage, même temporaire, depuis l'abandon de la surface. Une saison hivernale avec de fortes couches de neige, ou de dépôt d'avalanches, voir la présence de blocs de forte densité au sein du dépôt, peut influer le taux de production, et par conséquent avoir un effet sur la concentration en $^{10}$Be (e.g. Gosse et Phillips, 2001). La présence de blocs au sein des formations est donc systématiquement relevée, mais dans le contexte du Gobi-Altaï (très faibles précipitations), la couverture neigeuse est raisonnablement considérée comme négligeable.

### *v. Mesure de masse volumique*

La masse volumique du dépôt échantillonné contrôle au premier ordre l'atténuation du rayonnement cosmique avec la profondeur, et doit donc être systématiquement mesurée pour chaque site d'échantillonnage. La détermination de la masse volumique n'est pas

aussi triviale qu'il y parait, et nous proposons ici une méthode simple et rapide afin de la quantifier in situ.

Dans un premier temps, installer des marqueurs précisément localisés dans le mur du *soil pit* : les aligner sur un même plan vertical, et mesurer précisément leur localisations relatives (typiquement, un carrée de 20 cm de côté peut être défini par des clous). Prendre ensuite une série de photographies de la zone selon des directions et position variables, en vue d'une modélisation par *structure from motion* de la zone considérée. Echantillonner ensuite un volume d'environ 1 litre de matériaux dans la zone ayant été imagée (entre les marqueurs), sans toucher les marqueurs, et en prenant garde de bien récupérer tout le matériel excavé. Une fois le prélèvement réalisé, réitérer les prises de vues de la zone excavée. De retour au laboratoire, peser la masse de matériaux, puis réaliser une modélisation photogrammétrique de la zone échantillonnée avant, et après prélèvement, en précisant la localisation des marqueurs afin d'orthorectifier le modèle. Exporter les MNT correspondant dans le plan du mur, puis les soustraire pour calculer le volume entre les deux surfaces. Le rapport de la masse pesée par ce volume donne la masse volumique in situ du dépôt.

Cette méthode peut être appliquée à différentes profondeurs au sein d'un *soil pit*, de façon à moyenner d'éventuelles variation de la masse volumique avec la profondeur, ou encore à contraindre l'erreur aléatoire sur la mesure.

Cette méthode n'est bien sûr pas normalisée, et n'a pas encore fait l'objet de tests de validation, mais au vu de la difficulté relative à la mesure précise des masses volumiques in situ, elle apparaît être à la fois simple et efficace.

#### I.4.2.2. Datation par luminescence

##### *I.4.2.2.1. Principes généraux*

La méthode de datation par luminescence stimulée optiquement (OSL pour *Optically Stimulated Luminescence*) est basée sur la rétention d'électrons libres dans les défauts du maillage minéralogiques de certains minéraux. Ces défauts dans le maillage proviennent par exemple d'éléments manquants dans le maillage, de phénomènes de diffusion solides ou de séquelles laissés par les rayonnements à haute énergie. Les électrons libres proviennent des processus radioactifs environnant, associés principalement aux radio-isotopes $^{238}U$, $^{232}Th$, et $^{40}K$, ainsi que du rayonnement cosmique. Le temps de piégeage des électrons dépend de la température et de l'abondance de 'pièges' dans un minéral donné. Néanmoins si ces électrons sont soumis à un stimulus tel qu'une augmentation de la chaleur ou une exposition au soleil, ils

changent de niveau électronique, en émettant un photon : la luminescence. On dit alors que le matériel est blanchi (Figure 2-14), et la quantité de lumière ainsi émise correspond à la dose environnementale ou dose équivalente $D_e$, exprimée en grays (Gy).

La mesure des propriétés de piégeage d'un minéral, et de la radioactivité ambiante à un échantillon, permet d'utiliser ce processus pour dater la dernière exposition du sédiment à la lumière, et ainsi déterminer l'âge de son dépôt et de son enfouissement (Huntley et al., 1985) (Figure 2-14).

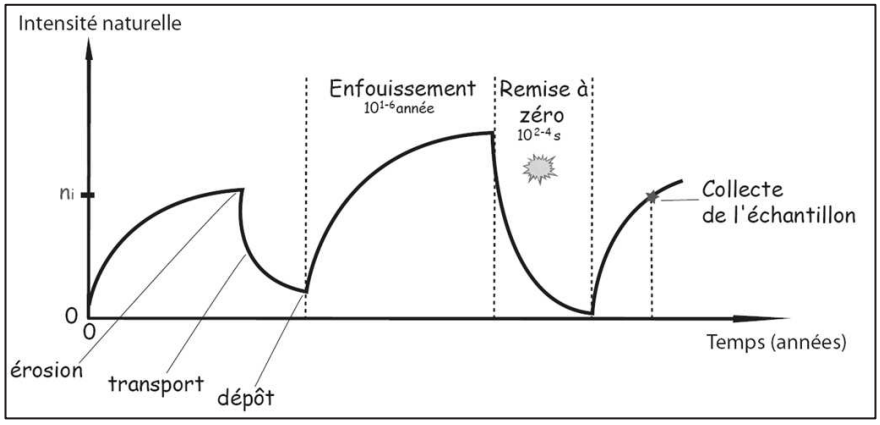


**Figure 2-14 : Principe de variation d'énergie ($n_i$) au cours du temps, stockée dans un sédiment en milieu naturel. Cette intensité est annulée (i.e. blanchissement) lorsque le matériel est soumis à une exposition lumineuse (i.e. soleil) lors de son transport, puis augmente progressivement au cours du temps après son enfouissement (i.e. son dépôt). Selon la nature et la durée du transport, le matériel peut être partiellement blanchi (cas de gauche).**

Le blanchissement du sédiment au cours de son transport et l'absence d'exposition à la lumière ou à de fortes températures (environ 500°C) après son enfouissement sont des prérequis pour l'application de cette technique de datation (Aitken, 1985). Il est donc important d'évaluer les processus de remobilisation ou de contamination, par exemple par bioturbation ou cryoturbation. Cette méthode s'applique sur des matériaux granulaires fins, tels que les silts et les sables fins (≤ 200 microns).

L'intensité de la $D_e$ est mesurée et considérée comme proportionnelle à la quantité d'électrons piégés, elle-même fonction de l'environnement radiatif (radioactivité locale et intensité du rayonnement cosmique). La détermination du taux de radiation est appelée dose annuelle $D_r$ ou *dose rate, exprimée en gray* par unité de temps (classiquement $Gy.ka^{-1}$). La dose rate est déterminée par le dosage au spectromètre de masse des principaux éléments radioactifs habituels ($^{238}U$, $^{232}Th$, et $^{40}K$), et par l'appréciation du rayonnement cosmique incident sur le site considéré (lui-même fonction de l'altitude, la latitude, le taux de production calibré, les effets de masquage et la profondeur de l'échantillon, moyennant des hypothèses sur le taux d'érosion ou d'aggradation, voir

section I.4.2.1.2). L'âge d'enfouissement (***A***) d'un sédiment est déterminé par le rapport entre la dose équivalente (***D***$_e$) et la dose annuelle (***D***$_r$).

$$A\ (ka) = \frac{De\ (Gy)}{Dr\ (Gy.ka^{-1})} \qquad (\mathrm{I}-5)$$

En laboratoire, pour générer la luminescence, les échantillons sont exposés à une stimulation optique selon une longueur d'onde spécifique, et les photons émis par le sédiment sont analysés dans un ''tube-multi-photon''. Il est important que la fréquence à laquelle est stimulé l'échantillon soit significativement plus grande que la fréquence lumineuse à laquelle la réponse en luminescence du sédiment est mesurée (nécessairement plus faible en énergie, donc à une fréquence lumineuse moindre). L'exposition de l'échantillon à une source radioactive permet également de construire la courbe dose-réponse, en jaugeant la réponse du minéral en fonction de la durée d'exposition, ce qui permet la caractérisation statistique (car réalisée sur un grand nombre de grains) du potentiel du minéral à piéger les électrons (et donc à chronométrer le temps). Il est à noter qu'en raison du nombre fini de pièges dans un réseau minéralogique, au bout d'un certain temps le signal arrive à saturation, et le potentiel de datation est par conséquent limité. Ce temps de saturation correspond à une dose, et est fonction de la dose rate et des caractéristiques du minéral (potentiel de piégeage), lui-même fonction de son histoire : nombre de cycles transport (i.e. blanchissement / dépôt, Figure 2-14).

La luminescence donne de bons résultats dans la datation de dépôts, en allant de 0,1 ka jusqu'à environs 350 ka -- modulo les paramètres précédemment énoncés -- (Andrew et al., 2002) avec de nombreuses applications, notamment en morphotectonique pour des estimations de vitesses de glissement de faille ou de l'âge des peléoséismes (e.g. Prentice et al., 2002; Fattahi et al., 2006; Nissen et al., 2009; Rizza et al., 2015).

Les datations OSL utilisées dans cette thèse ont été effectuées sur des quartz et sur des feldspaths potassiques par le protocole SAR (single Aliquot Regeneration), selon deux méthodes : l'IR50 et le post-IR-IRSL-225 (Murray et Wintle, 2003; Buylaert et al., 2009). Ces deux méthodes de stimulations offrent des réponses différentes (***D***$_e$ normalement plus grand avec post-IR-IRSL-225), permettant de mettre en évidence des processus de blanchissement partiel, ou de *fading* (évanouissement progressif de la luminescence). Cependant la méthode post-IR-IRSL est bien plus lourde à mettre en place, et elle ne sera pas systématiquement appliquée aux datations. Ces aspects seront discutés plus en détail pour les différents âges lors de l'interprétation des datations, au regard notamment du contexte géomorphologique.

La méthode de datation par luminescence est particulièrement utile en Mongolie du fait de la faible présence de charbons et de matière organique dans les dépôts, limitant la probabilité de trouver des charbons dans les dépôts, ainsi que du fait de la prépondérance des transports éoliens, favorisant le blanchissement. Ainsi, plusieurs études ont permis la datation de dépôts alluviaux et lacustres dans la région du Gobi-Altaï (Owen et al., 1999; Lehmkuhl et Lang, 2001; Prentice et al., 2002; Rizza et al., 2015).

#### *I.4.2.2.2. Protocole d'échantillonnage*

En raison de l'importance pour les échantillons de ne pas être exposés à la lumière, des protocoles spécifiques d'échantillonnage, de conditionnement et de stockage doivent être strictement suivis. Deux méthodes d'échantillonnage ont été utilisées dans ce travail : l'échantillonnage par bloc, et l'échantillonnage par percussion de tube. Dans tous les cas, une épaisseur d'au moins 10 cm doit être retirée du mûr dans lequel l'échantillonnage va être effectué, de manière à s'assurer que le matériau n'ait pas été exposé à la lumière pendant les travaux de creusement et de levés de log (Figure 2-15).

- Echantillonnage par bloc :

Cette méthode d'échantillonnage consiste à tailler un bloc cubique d'au moins 15 cm de côté directement dans la formation que l'on souhaite échantillonner (Figure 2-15). Cette dimension est nécessaire pour s'assurer que la partie centrale du bloc ne soit pas exposée à la lumière ; les parties externes du bloc, en plus de servir de masque au cours de l'extraction, seront ensuite utilisées afin de déterminer la dose rate $D_r$. La taille est réalisée à l'aide d'un couteau, et il est particulièrement important de procéder délicatement, de manière à ne surtout pas rompre le bloc (son intégrité est une condition *sine qua non* pour la validité de son analyse). Le bloc est ensuite enveloppé dans du film plastique alimentaire étirable pour d'une part lui assurer un conditionnement cloisonné, et d'autre part maintenir son contenu en eau, car l'humidité influence la propagation des radiations, et impacte par conséquent la $\boldsymbol{D_r}$. Le bloc est ensuite enveloppé dans plusieurs couches de papier aluminium pour l'isoler de la lumière, et enfin de ruban adhésif renforcé pour le protéger des chocs inhérents au transport. Les échantillons sont ensuite marqués puis placés dans des boites en plastiques, pour les protéger là encore lors du transport. Les avantages de l'échantillonnage par bloc sont la grande quantité de matériau échantillonné et le fait qu'il peut être réalisé de jour. Une limite à cette méthode est néanmoins la nécessaire cohésion du matériau pour que le bloc reste intègre.

**Figure 2-15 : Echantillonnage par bloc OSL. A. Site de Rain Creek tranchée 2 (WBF), B. Site de Rain Creek Riser (WBF). C. Tranchée de Moskito Creek (WBF). D. Tranchée de Swan Lake (WBF). Noter l'emballage, composée de plusieurs couches, successivement imperméables (film plastique), opaques (feuille aluminium) et protectrices (adhésif toilé).**

- Echantillonnage par percussion de tubes

Lorsque le matériau n'est pas assez cohésif pour tailler des blocs sans que ceux-ci ne se disloquent, il est possible d'effectuer l'échantillonnage en enfonçant par percussion un tube au sein de la formation que l'on souhaite échantillonner. Cette opération est effectuée de préférence de nuit et sans lampe, pour éviter une éventuelle exposition de l'échantillon à la lumière, notamment lors du retrait du tube. Le tube, ainsi que les bouchons à ses extrémités doivent être fait d'un matériau parfaitement opaque (typiquement des tubes en métal avec des bouchons adaptés sont recommandés). Après ablation, par sécurité, d'une couche de mur sur le site d'échantillonnage, le tube est percuté au marteau sur un martyr protégeant le bouchon, puis retiré et immédiatement bouché. Il est ensuite enveloppé dans du ruban adhésif renforcé, puis marqué et stocké dans des boites en plastiques dédiées.

#### *I.4.2.2.3. Discussions*

Trois principaux paramètres relatifs à la nature et à l'histoire du sédiment influencent la datation par luminescence : le blanchissement partiel, le type de dépôt, et la

granulométrie. L'une des hypothèses indispensables dans l'approche de datation par luminescence est le bon blanchissement lors du transport des matériaux constituant l'échantillon (Figure 2-14) (Murray et al., 1995; Olley et al., 1998; Wintle et Murray, 2006). Le phénomène de blanchissement partiel aboutit à une surestimation de l'âge des matériaux (e.g. Wallinga, 2002; Jain et al., 2004; Madsen et Murray, 2009), et peut être mis en évidence en utilisant un protocole dit 'grain par grain', permettant d'estimer la distribution des doses équivalentes dans les grains (une plus forte distribution dans les $\boldsymbol{D_e}$ des grains indiquant au premier ordre la nature partielle du blanchissement). La datation de dépôts éoliens est idéale dans la mesure où le transport offre une forte exposition au rayonnement solaire, assurant ainsi un bon blanchissement de l'échantillon (Frechen et al., 2009). Dans le cas de datation de dépôts alluviaux le contexte du Gobi-Altaï fait que le transport est souvent limité, pouvant aboutir à un blanchissement partiel des échantillons et ainsi à une surestimation de l'âge du dépôt. La nature temporaire des cours d'eau dans le Gobi-Altaï est associée à des écoulements torrentiels sur de faibles distances, limitant l'exposition des grains à la lumière. Les principaux processus permettant aux matériaux d'être exposés en contexte alluvial sont la saltation, la reptation et la suspension, processus limités dans le cas d'écoulement torrentiels, aboutissant à des dépôts plutôt '*clast-supported*'. Il a ainsi été montré que les doses équivalentes sont d'avantage distribuées dans le cas de sédiments alluviaux que dans le cas de dépôts éoliens (Olley et al., 1998), aboutissant également à une surestimation des âges, et à des incertitudes plus importantes. Cette dispersion décroit néanmoins avec l'augmentation de l'âge des sédiments. Les sédiments originaires de processus gravitaires (colluvions) ont un transport très réduit, et sont par conséquent encore peu voire non blanchis. Enfin, les dépôts présentent souvent des fractions différentes de grain pour un même matériel, ce qui va impacter la dose équivalente mesurée en accroissant sa dispersion. Il a ainsi été montré que la matrice la plus grossière du matériel est plus facilement blanchie que les fractions plus fines (Olley et al., 1998; Colls et al., 2001).

La Mongolie, et particulièrement la région du Gobi-Altaï, est réputée pour donner des signaux instables sur le quartz, principalement dus aux faibles distances de transport limitant le blanchissement, et aux multiples sources de quartz – l'histoire héritée des dépôts influant sur la susceptibilité du maillage à piéger des électrons (Mahan S., pers com.).

Le phénomène de percolation des grains dans le sol peut entrainer une contamination d'un horizon par des dépôts situés plus haut dans la stratigraphie. Cette contamination est d'autant plus importante si le dépôt est grossier, et est souvent associée à de la

bioturbation ou de la cryoturbation. Ainsi, si le matériel à l'origine de la contamination est bien blanchi, cela va entrainer une sous-estimation de l'âge de l'enfouissement. Il est à noter que cette relation de causalité ne tient pas compte du contexte du site d'étude, et que la proximité de la zone de faille peut inverser ce phénomène : ainsi dans le cas de rejet de failles chevauchantes, la contamination peut venir d'un dépôt initialement sous-jacent à celui constituant l'échantillon, et la contamination entraînera par conséquent un vieillissement de l'âge déterminé par luminescence. Ce phénomène de contamination a principalement lieu proche de la surface, là où la percolation d'eau et la bioturbation sont les plus importantes. Enfin, des processus de friction sur les failles en elle-même aboutissent à des échauffements très important pouvant blanchir le sédiment. Ce phénomène étant restreint à la faille, il convient simplement de prélever les échantillons OSL hors des fractures associées à un ou des séisme(s).

## II. Approche Paléosismologique

Les données sur les séismes historiques au-delà du XX$^{e}$ siècle sont très limitées dans la région du Gobi-Altaï, et excepté la rupture de 1957 et les répliques associées, l'identification des séismes passés doit donc se faire exclusivement par une approche paléosismologique.

La paléosismologie est une discipline relativement récente des géosciences, initiée par R.E. Wallace au milieu du XX$^{e}$ siècle par l'étude de la faille de San Andreas et des périodes de retour associées aux séismes qui s'y produisent (Wallace, 1946, 1968, 1970; Allen, 1968). Du point de vue du cycle sismique, la paléosismologie s'attache à distinguer des mouvements instantanés au sein de cycles représentant des milliers d'années. Ainsi, le cycle sismique est abordé par l'étude d'un ensemble de séismes passés. Néanmoins, seul les séismes suffisamment importants génèrent des ruptures atteignant la surface (Mw > 5,5 – 6) et sont ainsi accessibles dans l'archivage sédimentaire, sur lequel se base la paléosismologie (e.g. Yeats et al., 1997; McCalpin, 2009).

Après avoir détaillé le principe de l'approche, cette partie propose un aperçu des méthodes employées pour identifier les paléoséismes, tout d'abord par l'implantation de tranchées de paléosismologie, la présentation des principaux critères d'identification des séismes, et ensuite par la présentation des méthodes de datations utilisées dans les tranchées détaillées dans cette thèse.

### II.1. Principe

L'approche paléosismologique a pour objectif l'identification et la caractérisation des séismes historiques et préhistoriques dans le temps et dans l'espace, par la détermination de leur glissement cosismique, de leur périodes de retour, et de leur magnitude (e.g. McCalpin, 2009). Cette approche est complémentaire de l'approche morphotectonique qui vise une compréhension régionale, alors que la paléosismologie se concentre sur l'étude des anciens séismes à l'échelle du site d'étude. De plus, si l'approche morphotectonique permet d'investiguer des périodes temporelles allant jusqu'à quelques centaines de milliers d'années, la paléosismologie se limite aux dernières dizaines de milliers d'années (Sieh, 1978, 1996; Sieh et al., 1993; McCalpin 2009), voir même, dans cette étude, à la période de l'Holocène.

L'estimation de la magnitude se fait principalement via la quantification des décalages cosismiques. Ces décalages peuvent être observés et quantifiés dans les tranchées afin de déterminer la composante verticale des glissements cosismiques, mais dans le cas

des failles décrochantes, la quantification des glissements, dominés par la composante horizontale, se fait plutôt au travers de l'analyse morphotectonique (cf. I.3.2).

## II.2. Travaux en tranchée

### *II.2.1. Implantation de tranchée*

L'objectif de l'approche paléosismologique étant la datation des ruptures de surfaces, les investigations sont menées dans des tranchées le plus souvent creusées perpendiculairement à la trace de faille (McCalpin, 2009) (Figure 2-16). L'implantation de ces tranchées se fait au regard de l'enregistrement sédimentaire, préalablement estimé par l'analyse de photographies aériennes ou satellitaires, couplé à des observations de terrain. Ainsi, les sites de tranchée doivent dans l'idéal faire l'objet d'un enregistrement stratigraphique continu, et d'un minimum (voire d'absence) d'érosion. La présence de développement de sols dans des dépressions associées à la failles (dans le contexte du Gobi-Altaï, des flaques ou marais sont des milieux prompts au développement de sols riches en matière organique), associés à des *sag ponds,* des escarpements de faille à contre pente, des *shutter ridges* ou de fentes de tension, constituent également des prérequis intéressants pour l'implantation d'une tranchée, leur préservation dans la stratigraphie offrant des opportunités de datation au $^{14}C$, et ainsi la possibilité de contraindre les intervalles d'occurrences des paléoséismes.

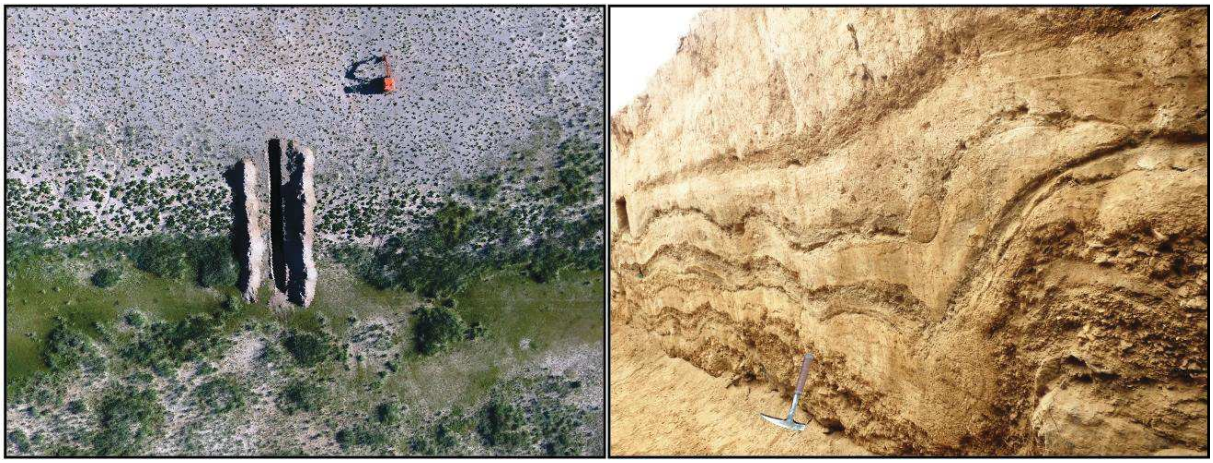

**Figure 2-16 : Photographie de tranchées paléosismologiques sur la faille de Bogd occidentale. Gauche : photographie aérienne d'une tranchée à la pelle mécanique (site de Swan Lake). Droite : Photo vers le sud de la stratification observée dans la tranchée 2 de Rain Creek.**

Les tranchées paléosismologiques peuvent présenter des dimensions variables, de quelques mètres à quelques dizaines de mètres de long, et sont creusées soit à la main, soit à l'aide d'engins mécaniques, si la zone est accessible et que de telles machines sont disponibles –ce qui n'est pas évident dans le Gobi-Altaï. Une attention particulière doit être portée à la stabilité des murs de la tranchée, surtout lorsque celle-ci est assez

profonde (par rapport à la compétence des matériaux), au travers d'une surveillance systématique de l'apparition de fissures en surface, et de la pose d'étais ou le creusement de terrassements dans les murs (bancs) si nécessaires. Ensuite, des grilles horizontales (avec un carroyage typiquement de 1 ou 0,5 m de côté) sont installées sur les murs de la tranchée, afin de les '*logger' (i.e.* cartographier*)* avec précision.

### *II.2.2. Critères de paléoséismes*

Le travail de *logging* des murs de la tranchée consiste à identifier et caractériser les différents horizons composant le dépôt, ainsi que les déformations associées aux séismes. Les unités sont décrites selon la granulométrie du dépôt, le type de matrice et son abondance, la stratification et les figurés associés (pendage, lamines, imbrications des clastes, surfaces d'érosion etc.), la couleur du dépôt, et le granoclassement. Dans le contexte décrochant, certain indicateurs stratigraphiques (par la suite nommés critères) sont généralement rencontrés dans les tranchées transversales à la faille, permettant une reconnaissance des paléoséismes. Ces critères sont détaillés ci-dessous (Figure 2-17) :

#### *II.2.2.1.1. Terminaisons supérieures de failles*

Ce critère est couramment observé dans le contexte décrochant, et consiste en l'identification d'une rupture se propageant vers le haut, et s'interrompant lors d'un changement d'horizon : l'horizon inférieur pré-date l'évènement sismique à l'origine de cette rupture, et l'horizon supérieur le postdate (Figure 2-17-A). Il est à noter que l'identification d'un évènement sur un seul critère de terminaison supérieur de faille est parfois délicat, et il est préférable de se baser sur plusieurs de ces critères pour une même unité, afin d'avoir une vision statistique de la détermination de l'évènement (e.g. Weldon et al., 2002). Par exemple, en milieu semi-aride, l'alternance de périodes humides et sèches, couplées à la présence de dépôt argileux, peut aboutir à l'apparition de fissures par phénomène de retrait-gonflement des agriles, alors purement associées à des variations de teneur en eau et non à des phénomènes sismiques.

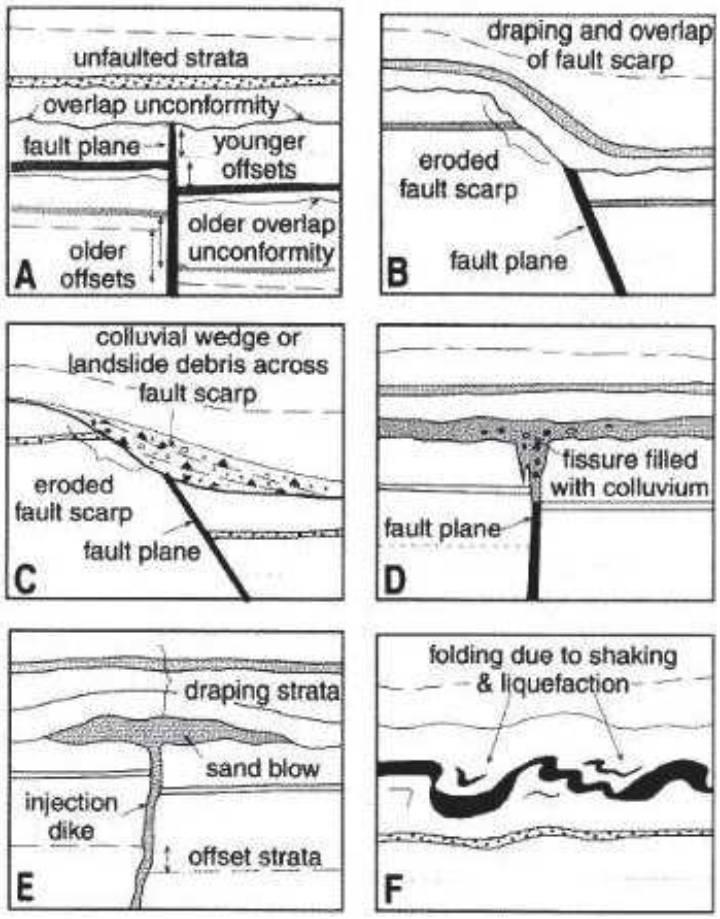


**Figure 2-17 : Diagramme schématique des indicateurs stratigraphiques typiques des paléoséismes, d'après Gurrola et Rockwell (1996) et : A : dépôts horizontaux sur des terminaisons supérieures des failles, B : dépôt sur un escarpement de faille érodé, C : formation d'un coin colluvial sur un escarpement de faille érodé, D : remplissage d'une fissure tectonique, E : déformation en surface d'une couche horizontale, F : figures de liquéfaction.**

#### *II.2.2.1.2. Coins colluviaux*

Les coins colluviaux correspondent à des figures d'effondrement et de dégradation, postérieurs à la formation d'un escarpement raide, par exemple associé au rejet de la faille (vertical ou simplement apparent) ou à l'ouverture d'une fente de tension. Le matériel environnant vient alors soit combler la dépression ainsi formée, soit retrouver un profil topographique diffusif par effondrement gravitaire de l'escarpement (e.g. Dawson et al., 2003) (Figure 2-17-C). Ainsi les coins colluviaux peuvent provenir de processus gravitaires (effondrement et diffusion) ou fluviatiles lorsque la dépression est associée à des captures de drains ; les matériaux les composant sont généralement non granoclassés et relativement pauvres en matrice, bien que ce ne soit pas toujours le cas. Le nombre de coins colluviaux peut parfois être associé au nombre de ruptures, mais certains de ces objets peuvent également provenir de processus d'érosion distinct de l'activité tectonique (e.g. McCalpin et Forman, 1988).

#### *II.2.2.1.3. Décalages d'unités stratigraphiques*

Dans le contexte décrochant, sont observées en tranchée des juxtapositions d'unités stratigraphiques distinctes au niveau des zones de failles (fissures ou zones de cisaillement), indiquant le déplacement horizontal associé au glissement de la faille (Figure 2-17). Cependant, les variations latérales de dépôts (e.g. chenaux, effondrements etc.), peuvent également aboutir à ce type d'observation. A l'inverse, un dépôt tabulaire et uniforme décalé par un mouvement purement horizontal ne présentera pas ce type de critère.

#### *II.2.2.1.4. Fissures et injections de sable*

Les fissures se distinguent des failles par une ouverture en cisaillement pur (contre simple dans le cas des zones de cisaillement), ensuite remplies par le matériel de l'unité qui se dépose après le séisme (Figure 2-17-D). Il est également possible d'observer des figures d'injections de sables, provenant d'unités sous-jacentes, et venant s'étendre soit en surface, soit entre deux unités préexistantes (Figure 2-17-E).

#### *II.2.2.1.5. Figures de liquéfaction*

Les figures de liquéfaction sont associées aux vibrations générées par le séisme et se localisent dans les unités mal consolidées et souvent saturées en eau (Figure 2-17-F), comme des milieux lacustres. Ces types de dépôts sont alors appelés sismites (Figure 2-18), et peuvent être identifié même loin de la faille (McCalpin, 2009). Dans le contexte du Gobi-Altaï, où les températures hivernales sont très rudes, les sismites peuvent potentiellement être confondues avec des figures de cryoturbation (Figure 2-18).

**Figure 2-18 : Photographie de sismites couplées à de la cryoturbation sur la faille de Bogd Occidentale.**

## II.3. Datations

### *II.3.1. $^{14}C$*

La méthode de datation au $^{14}C$, ou radiocarbone, est basée sur la mesure de la concentration en $^{14}C$ dans la matière organique. Le principe repose sur la fait que tout organisme vivant, animal ou végétal, échange du carbone avec son environnement, et le rapport $^{14}C/^{12}C$ est par conséquent à l'équilibre avec l'atmosphère (et a *fotiori* avec la biosphère) (e.g. Bowman, 1990).

Le $^{14}C$ étant un isotope radioactif de demi-vie 5730 ± 40 a, il va se dégrader dans le temps, et sa concentration dans les organismes va décroître après leur mort ou la mort d'une de leur partie. Cette décroissance exponentielle va ainsi permettre de quantifier le temps écoulé depuis la mort de l'organisme considéré. Il est néanmoins nécessaire de calibrer la méthode en fonction des variations de concentration en $^{14}C$ qu'a connu l'atmosphère, et en particulier retrouver ce ratio au moment de la mort de l'organisme, en croisant l'âge déterminé avec une courbe de calibration (Figure 2-19), principalement construite par dendrochronologie (e.g. Reimer et al., 2013). Les calibrations ont été réalisées dans cette thèse à l'aide du logiciel Oxcal (Lienkaemper et Ramsey, 2009).

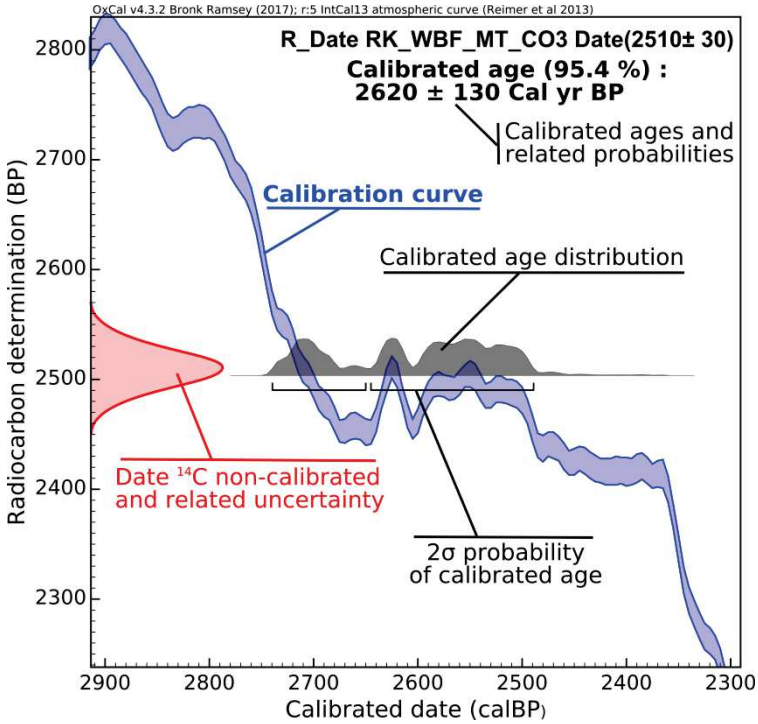


**Figure 2-19 : Calibration d'un âge radiocarbone à partir du logiciel Oxcal. La courbe bleue correspond à la courbe de calibration d'après Reimer et al. (2013) ; la distribution grise représente la gamme d'âges probables correspondant à l'intersection entre : i. la gaussienne rouge, représentant l'âge carbone non-calibrée de l'échantillon et les incertitudes associées, et ii. La courbe de calibration.**

La qualité d'une datation au radiocarbone dépend de l'âge de l'échantillon et de sa teneur en carbone. Ainsi, les limites de cette méthode viennent du temps écoulé et de l'histoire de l'échantillon entre la mort de l'organise (ou l'enfouissement dans le cas de paléosols) et le prélèvement. En effet, dans le cas d'un charbon détritique, il existe des incertitudes relatives au temps écoulé entre la mort de cette partie de l'arbre et son dépôt, d'une part au travers de *l'inbuilt* (âge hérité avant le transport du charbon), et d'autre part provenant du temps de stockage *''in situ"* avant d'être remobilisé, et de la durée du transport. Cet intervalle de temps, inconnu, va induire un âge apparent plus vieux que l'âge réel de la mort de l'organisme, entraînant systématiquement une surestimation de l'âge du dépôt considéré (e.g. Gavin, 2001; Bollinger et al., 2016). Dans le cas d'une datation sur amalgame de sédiments (e.g. paléosol), des phénomènes de contamination de l'échantillon par de la matière organique moderne, essentiellement dûs à des processus de bioturbation, pourra à l'inverse entrainer une sous-estimation de l'âge de l'échantillon.

En conséquence, nous avons dans cette étude tâché autant que possible de coupler plusieurs datations, $^{14}C$ et OSL, afin de déterminer les âges (i.e. les intervalles d'occurrences) des paléoséismes.

### *II.3.2. Datation par luminescence stimulée optiquement (OSL)*

La datation OSL offre dans le contexte du Gobi-Altaï des opportunités de datation intéressantes, étant donné la très faible teneur des dépôts en carbone organique. Ainsi les remplissages par dépôts éoliens ou fluviatiles peuvent être datés, dans la mesure où ils ne sont pas trop proche de la surface et donc sujet à des bioturbations et cryoturbation. La description de cette méthode est présentée dans la partie I.4.2.2.

Quelques précautions d'usage doivent donc être prises lors de la sélection d'un horizon et son échantillonnage pour datation par luminescence :

- Eviter les dépôts ayant eu un très cours transport, comme les coins colluviaux. Ces derniers peuvent d'une part avoir été partiellement blanchis avant le séisme, et d'autre part le blanchissement lors de leur mise en place est très hasardeux.
- Eviter les dépôts trop fins, type argiles et silts fins. La méthode SAR étant basée sur une sélection granulométrique d'une population de grain, les matériaux trop fins dispersent le signal et donnent de moins bons résultats.
- Eviter d'échantillonner sur une fissure associée à la faille, l'échauffement par friction lors du séisme pouvant 'blanchir' les matériaux au contact de la faille.

### II.4. Implications et limites

L'observation de ces critères au sein de la stratigraphie mise en évidence dans une tranchée permet une vision du cycle sismique intégrée sur un ensemble de paléoséismes, et d'en extraire, avec plus ou moins de précision, les temps de récurrence. Néanmoins certains problèmes peuvent être rencontrés, comme la surestimation ou la sous-estimation du nombre d'évènement dans une tranchée. Les sections suivantes détaillent quelques causes pouvant être à l'origine de ces problèmes.

L'interprétation d'un évènement peut être erronée : par exemple si celui-ci n'est observé que sur un seul mur de la tranchée avec peu de critères, ou encore s'il n'est pas présent dans des tranchées implantées à proximité (e.g. Nelson et al., 2000), il peut s'agir simplement de fissure dans les argiles ou de tassement différentiel associé à de gros animaux (vaches, chameaux et chevaux dans notre cas). De plus, lorsque les critères sont constitués exclusivement de terminaisons de failles, il arrive que certaines branches d'une même faille n'atteignent pas la surface, en particulier suite à des phénomènes de diffraction de la faille principale en se rapprochant de la surface. Enfin, en domaine décrochant, la rupture présente parfois un motif en échelons, et la localisation de la tranchée par rapport à ces échelons (ou fentes de tension) peut aboutir à manquer un évènement. Afin de limiter ces problèmes, il est recommandé de creuser plusieurs tranchées, et de comparer les critères, nombres d'évènements et datations effectuées sur chaque mur.

Les lacunes sédimentaires, associées soit à un arrêt de la sédimentation, soit à un épisode érosif, peuvent aboutir à l'absence d'enregistrement d'un (ou plusieurs) évènements dans la stratigraphie.

L'abondance et la précision des méthodes de datation constituent également des facteurs potentiellement limitant la capacité à dater les paléoséismes. En effet, si les temps de retour sont très courts ($10^1$ – $10^2$ a), il ne sera pas possible de distinguer les évènements dans les incertitudes associées aux datations.

La détermination du décalage cosismique en tranchée demeure également un point délicat, surtout si le glissement présente une composante horizontale significative (i.e. cinématique décrochante). Le glissement vertical observé en tranchée est alors uniquement apparent, et si l'on veut mesurer des décalages horizontaux, il convient de faire des tranchées 3D, lourdes de mise en œuvre et d'interprétation, notamment pour déconvoluer la part tectonique dans les décalages latéraux de la part associé à la variabilité latérale naturel de l'objet observé (chenaux, paléo-talus etc.).

# Chapitre 3. Horizontal surface-slip distribution through several seismic cycles: the Eastern Bogd fault, Gobi-Altai, Mongolia

**Ce chapitre fait l'objet d'un article qui a été soumis à Techtonophysics le 11 juillet dernier.**

**R. Kurtz, Y. Klinger, M. Ferry, J-F. Ritz**

Abstract

The 1957, $M_W$ 8.1, Gobi-Altai earthquake, Southern Mongolia, produced a ~360-km-long surface rupture along the Eastern Bogd fault. Cumulative offsets of geomorphic features suggest that the Eastern Bogd fault might produce characteristic slip over the last seismic cycles.

Using orthophotographs derived from a dataset of historical aerial photographs acquired in 1958, we measured horizontal offsets along two thirds (~170 km) of the 1957 left-lateral strike-slip surface rupture. We propose a new empirical methodology to extract the average slip for each past earthquake that could be recognized along successive fault segments, to determine the slip distribution associated with successive past earthquakes.

Our results suggest that the horizontal slip distribution of the 1957 Gobi-Altai earthquake is fairly flat, with an average offset of 3.5 m ± 1.3 m. A combination of our lateral measurements with vertical displacements derived from the literature, allows us to re-assess the magnitude of the Gobi-Altai earthquake to be between $M_W$ 7.8 and $M_W$ 8.2, depending on the depth of the rupture, and related value of the shear modulus. When comparing this magnitude to magnitudes derived from seismic data, it suggests that the rupture may have extended deeper than the 15 km to 20 km usually considered for the seismogenic crust.

We observe that some fault segments are more prone than others to record seismic deformation through several seismic cycles, depending on the local rupture complexity and geomorphology. Hence, our results allows defining the horizontal slip function for the 1957 Gobi-Altai earthquake and for three previous paleoseismic events along 70% of the studied area. Along about 50% of the fault sections where we could recognize three past earthquakes, our results suggest that the slip-per-event was similar for each earthquake.

# I. Introduction

Characterization of surface ruptures and slip distribution for large continental earthquakes is a fundamental step in the understanding of earthquake processes in time and space. It is often assumed that for large continental earthquakes, and for strike-slip earthquakes in particular, the slip distribution at the surface is representative of the pattern of slip at depth (Zielke et al., 2012), and that it contains significant information about earthquake rupture processes.

Previous earthquake studies show that in most cases surface-slip distribution appears to be controlled by rupture segmentation (e.g. Sieh et al., 1993; Haeussler et al., 2004; Klinger et al., 2005; Vallage et al., 2015; Choi et al., 2017, in press), including during complex ruptures involving multiple faults (Wei et al., 2011; Hamling et al., 2017). Earthquake-rupture segmentation is generally associated with major fault discontinuities and geometric asperities in the fault trace (Wesnousky, 2006; Klinger, 2010). These discontinuities correspond to changes in fault azimuth, relay zones, or connecting side faults. Such fault structuration is likely controlled at first order by the thickness of the seismogenic crust (Bilham and Williams 1985; Klinger 2010), although local variability associated with geological structures and preexisting secondary faults are also important (e.g. Vallage et al., 2016).

Measurements of displacement recorded in the morphology by reconstructing landforms geometry, either shortly after an earthquake or for past earthquakes, contribute to our knowledge of how earthquakes generate deformation through earthquake cycles. In the case of strike-slip faulting, co-seismic offsets are usually estimated by restoring piercing lines across the rupture (McGill and Sieh, 1991; Ritz et al., 1995; Klinger et al., 2000, 2005, 2011; Zielke et al., 2010; Salisbury et al., 2015; Manighetti et al., 2015). Along a given fault segment, the variation of co-seismic slip along strike suggests that, at first order, the slip distribution associated with an earthquake is controlled by the interaction of the seismic rupture with geometric asperities, while propagating onward (Sieh et al., 1993; Berberian and Yeats, 1999; Klinger et al., 2006). Within relay zones, slip is distributed on faults with a wide range of azimuth, thus reducing the efficiency of strain release along these parts of the rupture during the earthquake (King and Nabelek, 1985; King, 1986). In addition, comparison of measurements derived from field surveys with measurements based on remote-sensing techniques shows that in most cases data collected in the field represent a minimum value of the total displacement accommodated at the surface (Klinger et al., 2015). Variable amounts of deformation are distributed off-

fault in a wider zone of tens to hundreds of meters around the localized rupture, a process that is difficult to assess from field data or photo interpretation alone (Gold et al., 2015; Vallage et al., 2015). Dense slip measurements along fault surface ruptures have shown that such lateral-slip variability can be as large as 30 % over distances as short as a few tens of meters (Rockwell et al., 2002; Rockwell and Klinger, 2013). Therefore, any individual offset measurement, even one that is very well constrained, may or may not be representative of the slip on the entire fault segment (Gold et al., 2015).

In this study, we revisit the surface rupture associated with the 1957, $M_W$ 8.1, Gobi Altai (Mongolia) earthquake. This earthquake produced a 270 km-long strike-slip rupture (Florensov and Solonenko, 1965) with co-seismic slip between 2 m and 7 m (Kurushin et al., 1998; Rizza et al., 2011; Choi et al., 2012). In addition, ~ 100 km of dip-slip rupture occurred during the same event on several nearby faults (Figure 3-1) (Kurushin et al., 1998). Our study is focused on the strike-slip part of the rupture. Using orthorectified aerial photographs from a low-altitude survey flown in 1958, we mapped the rupture in details and we systematically measured offset landforms along the strike-slip sections. Our measurements include offsets due to the 1957 earthquake, as well as cumulative offsets related to previous earthquakes. We propose a method to statistically differentiate clusters of offset measurements for the different rupture segments. Each cluster is then associated with a specific past earthquake, allowing us to reconstruct the slip distribution for the 1957 event and for several previous earthquakes.

In a first part of this work we introduce the seismotectonic context of the Eastern Bogd Fault. A second part describes the generation of orthophotographs. We then present data analysis, including mapping, offset measurements, and statistical modeling. Finally we discuss the slip distribution results, regarding to the 1957 and other past-earthquake ruptures.

## II. Setting

### II.1. Geological setting

Western Mongolia experienced one of the largest intracontinental earthquake series during the XX$^{th}$ century, with four $M_W$ > 7.9 earthquakes in a period of 52 years (Baljinnyam et al., 1993). This seismic crisis has been interpreted as related to the northernmost effects of the collision between India and Eurasia (Molnar and Tapponnier, 1977), which has reactivated ancient shear zones with a NNE-SSW direction since 3 Ma to 8 Ma (Vassallo et al., 2007). The southern and western regions of the Hangay Dome, in central Mongolia, are formed by Archean-Proterozoic crust. Hence, the Hangay dome

acts as a semi-rigid backstop to the northward propagation of the deformation (Figure 3-1) (Cunningham, 2013). This results in a compressional belt composed of the Altai and Gobi-Altai mountain ranges, which are respectively characterized by large dextral and sinistral transpressive strike-slip faults (Tapponnier and Molnar, 1979; Cunningham, 1998, 2005; Vassallo et al., 2007). Still, part of the deformation occurs north of the Hangay Dome, as attested by large, active, strike-slip faults in the Bulnay and Baikal regions (Baljinnyam et al., 1993).

In the Gobi-Altai, many mapped bedrock faults strike N123 ± 15°E. These faults displace intrusive and metamorphic Paleozoic formations, which are overlain by Mesozoic sediments and volcanic terrains. The transpressive deformation includes several major strike-slip faults in the western part of the Gobi-Altai, while eastward the deformation is more localized along the Eastern Bogd strike-slip fault, which strikes N100 ± 15°E (Figure 3-1) ( Cunningham, 2013).

The Gobi-Altai Mountain Range, bounding to the north the Gobi desert, has a semi-arid climate. It has experienced minimal Quaternary glacial activity (e.g. Lehmkuhl and Lang, 2001), resulting in multiple well preserved geomorphic features that are displaced across active faults (Ritz et al., 1995; Vassallo et al., 2005; Vassallo et al., 2007). When a landform is abandoned following an earthquake, for instance because of stream capture or alluvial terrace uplift, the co-seismic offset may be preserved. However, numerous offset geomorphic markers actually relate to alluvial features that might still be active after the earthquake, leading to potential erosion that mask or destroy the co-seismic offset. Figure 3-2.A illustrates for the same site the differences between a 1958 orthophotograph and a recent satellite image (here, a Bing image acquired on October 2012), and respective geomorphic interpretations. This example highlights the rapid evolution of geomorphic markers: within 55 years, offsets affecting active river channel margins have been significantly smoothed and the bend in the riser has migrated downstream along the river bed for several tens of meters (at least 20 m for the eastern riser in this example), due to fluvial erosion of the channel. Hence, the 1957 offset has locally been erased and is no more visible on recent satellite images. Working with the 1958 orthophotographs rather than recent satellite images, offers therefore better opportunities to accurately quantify the 1957 on-fault deformation.

### II.2. Slip rates and past earthquakes along Eastern Bogd Fault

Due to limited GPS data and unsuitable configuration of the GPS network within the Gobi-Altai area, direct geodetic determination of the slip rate across the Gobi-Altai fault system is not yet possible. Hence, to compare the geodetic strain budget across whole

Mongolia and published slip rates for the major regional strike-slip faults, both Calais et al. (2003) and Vergnolle et al. (2003) directly used the Upper Pleistocene – Holocene rate of 1.2 mm/yr estimated by Ritz et al. (1995) for the left-lateral Bogd Fault System.

Several geologic slip rates have been determined along the main strike-slip fault of the Eastern Bogd Fault, on the basis of geomorphological measurements and $^{10}$Be cosmogenic dating (Ritz et al., 1995; Owen et al., 1999; Ritz et al., 2003; Vassallo et al., 2005; Rizza et al., 2011). Horizontal slip rates cover a time span ranging from 30 kyr to 150 kyr, and range from 0.52 mm/yr ± 0.12 mm/yr to 1.26 mm/yr ± 0.34 mm/yr (Figure 3-1). Along-strike variations have been attributed to variations in fault kinematics, themselves controlled by changes in fault azimuth (Rizza et al., 2011). The vertical slip rate has solely been constrained at the Gurvan Bulag foreberg (Figure 3-1), with an estimation of 0.21 mm/yr ± 0.07 mm/yr during the last 20 kyr (Ritz et al., 2003; Vassallo et al., 2005).

Paleoseismological investigations have been conducted along the Eastern Bogd fault to constrain the timing of the last major ruptures (Schwartz et al., 2007; Ritz et al., 2009; Rizza et al., 2011) (see Figure 3-1 for site locations). Four successive past surface ruptures have thus been identified, but individual rupture extents along strike are not well constrained. Based on available co-seismic offsets measured in the field and paleoseismological data, Rizza et al. (2011) proposed that the average recurrence time for large earthquakes along the Eastern Bogd fault is about 2.5 kyr – 5.2 kyr.

### II.3. Seismic activity in Mongolia

Four major earthquakes occurred in or near western Mongolia during the XX$^{th}$ century: the 1905 $M_W$ 7.6 Tsetserleg and $M_W$ 8.3 Bolnay earthquakes, the 1931 $M_W$ 7.9 Fuyun earthquake, and the 1957 $M_W$ 8.1 Gobi-Altai earthquake (Florensov et al., 1965; Baljinnyam et al., 1993; Schlupp and Cisternas 2007). These four strike-slip earthquakes reactivated pre-Cenozoic faults, and were associated with surface rupture lengths exceeding 100 km (Cunningham, 1998; Lehmkuhl and Lang, 2001; Vassallo et al., 2007; Cunningham, 2010; Klinger et al., 2011; Choi et al., 2017, in press). Similarly to the Bogd fault, the long-term geological slip rates for these faults are about one to three millimeters per year, over periods of $10^4$ yr to $10^5$ yr (Ritz et al., 1995, 2003, 2006; Walker et al., 2006; Vassallo et al., 2007; Nissen et al., 2009; Rizza et al., 2011, 2015). Considering the low slip rates and multi-millennia recurrence times for large earthquakes, the probability of occurrence of four large earthquakes in such a short time period seems low and this sequence is often described as a typical example of temporal

seismic clustering (Molnar and Qidong, 1984; Baljinnyam et al., 1993; Schlupp, 1996; Rizza et al., 2011, 2015).

### II.4. The 1957 surface rupture

The $M_W$ 8.1 Gobi-Altai earthquake occurred on December 4th 1957 along the Eastern part of the Bogd fault. The associated surface rupture was complex; in addition to the 270-km-long strike-slip rupture along the Eastern Bogd Fault, multiple additional faults ruptured adding another 90 km of surface rupture, mostly with a reverse motion (Florensov and Solonenko, 1965; Kurushin et al., 1997). Based on seismological data, the epicenter of the 1957 Gobi-Altai earthquake was located along the western part of the fault (Figure 3-1), suggesting that the rupture propagated mainly eastward (Okal, 1976; Chen and Molnar, 1977; Rukavičková and Hanžl, 2012).

The Bogd fault system includes several restraining bends forming right step-overs along the main oblique strike-slip fault, with five thrust-fault sections, located to the south of the Ikh Bogd restraining bend (Figure 3-1) (Florensov and Solonenko, 1965; Kurushin et al., 1998). The long-term fault trace is geomorphically well expressed, and the overall topographic expression is consistent with repeated co-seismic motion along the Eastern Bogd fault, suggesting that the fault location has not changed significantly during the Holocene period (Bayasgalan et al., 1999; Ritz et al., 2006).

Previous works include several field measurement campaigns along the Eastern Bogd fault using a variety of methods, including tape and compass, total station and real-time-kinematic-GPS (Florensov and Solonenko, 1965; Kurushin et al., 1998; Vassallo et al., 2007; Rizza et al., 2011; Choi et al., 2012). Results show an average horizontal co-seismic slip ranging from 3.0 m to 5.2 m depending on the fault segment, and a maximum slip of 7 m in a restraining jog (Florensov and Solonenko, 1965; Kurushin et al., 1998; Choi et al., 2012). Rizza et al. (2011) and Choi et al. (2012) have shown that the vertical slip and the horizontal slip are anticorrelated, likely due to slip transfer between the strike-slip and the dip-slip components of motion, depending on the local fault strike.

## III. Orthophotographs

We mapped surface ruptures and measured deformation recorded by geomorphic markers using aerial photographs taken by a Soviet mission during the first part of summer 1958, 6 to 7 months after the 1957 Gobi-Altai earthquake (Florensov and Solonenko, 1965). There are two series of photographs, hereafter referred to as S10000

and S25000, thus named for their respective approximate scales. The S10000 series follows linearly the main surface rupture, and the S25000 series fully covers the mountains surrounding the 1957 surface rupture. Such photographs contain distortions due to topography, perspective and variations in relative flight altitude, and therefore they must be orthorectified to be used as a base for measuring horizontal offsets.

The standard photogrammetric approach to aerial photographs orthorectification relies on accurately defined internal and external orientation parameters (e.g. Moffitt, 1959), which are not available in this case (e.g. position of the optical axis relative to the image, photograph position and orientation, lenses distortion, etc.). Hence, we followed a structure-from-motion approach (Koenderink and Doorn, 1991), using the commercial software Agisoft® Photoscan Pro, which allowed us to reconstruct orientation parameters and to generate 3D topographic models and orthophotographs. Specific details about techniques for orthorectifying historical photographs and photogrammetric processes are found in *Supplementary materials*. We generated orthophotographs from S10000 and from S25000 photographs and outputted images at resolutions of 15 cm to 20 cm and 50 cm, respectively. Our orthophotographs cover 150 km of the western part of the main 1957 surface rupture, including the Bhaar Uul, Noyon Uul, Ikh Bogd and Dullan Bogd areas (Figure 3-1). About 120 km are covered with S10000 and 30 km with S25000 (Figure 3-1). On the easternmost part of the 1957 earthquake surface rupture, only 20 km are covered with S10000 (Baga Bogd). Locally, where 1958 aerial photographs were not available to cover the surface rupture, we used recent high-resolution optical satellite images instead.

We used freely-available satellite images (Google Earth and Bing Aerial) and the SRTM30 dataset for topography (Slater et al., 2006) to georeference the aerial photographs, through the selection of common Ground Control Points (GCPs). We selected a minimum of 5 GCPs for each aerial photograph. However, low accuracy for elevation data from SRTM, large uncertainties in GCPs locations, poor preservation for some of the 60 years-old photographs (paper deformation, scratches, etc.), and an unfavorable linear configuration for the S10000 series (James and Robson, 2014) led to noticeable artifacts and barrel effect. In order to minimize the barrel effect, only a small number of aerial photographs (typically 5 to 6) are orthorectified at once. In some places for instance, one may observe artifacts such as distortion, inadequate georeferencing, texture artifacts, or ghosting within the orthophotographs. Where recognized, these artifacts have been accounted for during the quality assessment of measurements extracted from our orthophotographic dataset. Eventually, if any artifact is affecting the geomorphic markers at location of the offset, no measurement has been done.

In order to validate our image orthorectification process and to assess its limitations and uncertainties, we compared the distances between pairs of GCP measured on the orthophotographs to the distances between the same pair of GCP identified in the satellite images used for georeferencing. This test shows that distance measurements derived from orthorectified photographs and from satellite images are consistent, with less than 5% average errors on the length measurements and 1σ standard deviation of 0.17 m, 0.38 m and 1.09 m for measurement classes of 0 m to 5 m, 5 m to 15 m and 15 m to 50 m respectively.

# IV. Data Analysis

## IV.1. Surface rupture mapping and fault segmentation

Using our newly generated orthophotographs, complemented by some optical satellite images, we performed detailed mapping of the 1957 rupture at a scale of 1:1000. In order to reflect the complexity of the 1957 Gobi-Altai earthquake co-seismic surface deformation, we defined three types of surface ruptures (Figure 3-2): i) Main rupture: a continuous surface rupture corresponding to the main fault trace and generating the largest displacements at a given location. ii) Cracks: short discontinuous surface ruptures, mainly tension gashes and gravity-related fractures with length of a few tens of meters. Cracks reveal damage zones and are often associated with the main surface rupture and secondary faults. iii) Secondary faults: surface rupture occurring tens or hundreds of meters away from the main rupture.

Analysis of the surface-rupture geometry and of geomorphic-marker offsets allows us to recognize rupture patterns, to document spatial distribution of faulting, and to assess off-fault deformation (Figure 3-2). For instance, a widely distributed complex surface rupture is likely to yield poorly constrained measurements of co-seismic offsets (Figure 3-2.b). Conversely, a narrow fault zone along a single straight scarp (Figure 3-2.c) will allow for a more accurate measurement of the co-seismic offset (Gold et al., 2015).

The main scarp strikes N85 – N115 and co-seismic displacement is dominantly left-lateral, although some dip-slip motion may be observed locally. In detail, ~ 90 km of the total length of the rupture displays pure left-lateral strike-slip motion, striking N95 – N105. About 100 km of rupture striking mostly N105 – N115 display a reverse component of motion. Finally, 80 km of rupture striking N85 – N95 show partitioning between strike-slip and shallow normal dip-slip displacements (Kurushin et al., 1998). Additionally, secondary thrust-fault scarps form forebergs that bound the Ikh Bogd restraining bend to the South and East for about 90 km (Figure 3-1). Thorough descriptions of the Gobi-Altai

earthquake surface ruptures were published by Florensov and Solonenko (1965) and Kurushin et al. (1998), and are not repeated here.

Using our new 1957 earthquake rupture map, we propose a segmentation model for the Gobi-Altai earthquake main surface rupture. Segments are defined as sections of fault having homogeneous fault pattern, kinematics, and strike, separated from each other by relay zones. These relay zones, also called jogs, are typically characterized by significant vertical motion, and they generally correspond to local changes in the azimuth of the rupture. Figure 3-3 presents an example showing the segment S3, delimited by the two jogs R2 and R3. The surface rupture pattern along S3 is very straight, with only a minor complexity in its central part related to a ~200 m wide landslide. Jogs are characterized by a more complex rupture pattern, including numerous cracks and a wider damage zone, of basically one to three kilometers: the R2 releasing bend, at the western end of S3, is associated with a large pull-apart basin with numerous fault strands presenting a strong dip-slip component (Figure 3-3). Conversely, R3 is a short compressive jog that corresponds to a change of ~ 10° in fault strike. Adjacent segments S4 is characterized by distributed deformation along its entire length. In addition to geometric criteria, segmentation appears to also be influenced by lithological variations. In fact, 10 of the 14 jogs that we mapped are located at, or very close to boundaries between geological units (Figure 3-4.b), suggesting that seismic rupture propagation is influenced by preexisting geological structures (e.g. Vallage et al., 2016).

Overall, we identified 15 fault segments along the 1957 main surface rupture (Figure 3-4.a) as well as five thrust fault segments along secondary faults, south of Ikh Bogd (two west of Gurvan Bulag, the Gurvan Bulag foreberg, and the Toronhovd and Tsagaan Ovoo-Tevsh segments) (Figure 3-1). Surface rupture lengths for the main segments range from 6.7 km to 24.0 km without accounting for the jogs, with an average length of 14 km. Secondary thrust segments are 11.2 km to 24.5 km in length.

## IV.2. Offset Measurements

### *IV.2.1. Data acquisition*

Along most of the 1957 Gobi-Altai earthquake surface rupture, the co-seismic and cumulative deformation are well localized and limited to a narrow fault zone. Numerous geomorphic markers such as terrace risers, talwegs, river channels and alluvial fan bars and swales are offset, allowing us to quantify the co-seismic displacement. We identify each marker by its spatial coordinates and we assess the measurement quality using

criteria we developed and describe below. If consecutive markers are spatially close to each other (less than ~20 m), we consider them as a group that we treat as a single marker, both for quality assessment and for offset measurement.

The criteria we developed to assess our offset measurements are based on the quality of the marker, the number of splays and secondary faults (rupture distribution), and the quality of the orthophotographs (Figure 3-5). The quality of a marker depends on its obliquity relative to the fault zone, its sinuosity and its sharpness (Figure 3-5.a). The obliquity is defined as the angle between the piercing line and the fault trace. Following Salisbury et al. (2015), we consider three obliquity classes: i) < 30° (worst), ii) 30 - 60° and iii) > 60° (best). The sinuosity of a marker reflects its straightness over a few tens of meters on either side of the fault zone. Our assessment of sinuosity is qualitative, and is determined by how many times the marker crosses the piercing line. The sharpness of the marker reflects our ability to define piercing lines associated with a marker accurately, and it depends on the edge curvature of the marker, as well as possible shadows cast over the marker on the imagery. In summary, a smooth and sinuous riser, difficult to locate accurately, will provide a poorer measurement than a straight and sharp break-in-slope marker (Figure 3-5.a). We evaluate rupture distribution by determining the number of splays forming the fault zone at the location of the considered offset, and the number of secondary faults visible outside of the measurement area (Figure 3-5.b). We assume that the number of splays is representative of the width of the surface rupture. Secondary faults or volumetric deformation (Vallage et al., 2015) may also accommodate some part of the deformation and thus reduce the offset along the main fault trace (Klinger et al., 2005; Choi et al., 2017, in press). Such deformation is often difficult to quantify and our measurements, based on discrete offset markers, should be considered as minimal values relative to the total offset. We use piercing lines derived from geomorphic features that extend ~20 m meters on each side of the fault. This allows integrating close-fault damage in offset measurements, and partially averaging out marker sinuosity (Fig 6.b for instance) (Gold et al., 2015; Vallage et al., 2015). Finally, we assess the local quality of the image based on its resolution (mainly depending of the origin of the pictures, i.e. S10000 versus S25000, or satellite images), its clarity and the occurrence of artifacts (Figure 3-5.c).

For each marker, we used these criteria and the following weighting rules listed in Table 3-1 to assign a quality score. In theory, scores may range from -2 to +10; practically, the minimum score attributed is +2, given that doubtful offsets were not measured. Higher scores indicate markers that are well suited for offset measurements, while lower scores point to sites where offset measurements will likely be have larger uncertainty. Figure 3-

6.1 shows examples of geomorphic markers and their scores: Figure 3-6.1.a, Figure 3-6.1.b, and Figure 3-6.1.c show sites with a high-value score, a medium-value score and a low-value score, respectively. This scoring allowed us to sort offsets for further statistical treatment.

We measured horizontal offsets by reconstructing geomorphic markers into a proposed initial position, without any assumption about the number of earthquakes markers had experienced. For each marker, we propose 3 offset reconstructions yielding preferred, maximum, and minimum offset values (Figure 3-6). Our preferred value corresponds to our best reconstruction of the geomorphic features forming the piercing lines, while the maximum and minimum values represent extreme, but still plausible, initial positions of the piercing lines. The final value we used in this study is the preferred value (Figure 3-6.3), with the minimum (Figure 3-6.2) and the maximum (Figure 3-6.4) displacements used as lower and upper bounds for uncertainty. Although our measurements were made individually, markers were considered within the context of the local fault geometry, encompassing a few hundreds of meters around the marker, to assess the local geomorphology and to measure the local fault strike.

No measurement was taken along the eastern third of the main Bogd Fault, north of the Baga Bogd range (Figure 3-1), given that this area is not well covered by S10000 orthophotographs, and is characterized by significant reverse oblique motion and a highly distributed fault pattern.

#### *IV.2.2. Modeling*

Due to the natural variability of the geomorphic record, large datasets of offset measurements present some inherent scattering that can hinder the identification of slip pattern associated to individual earthquakes (Schwartz and Coppersmith, 1984; Sieh et al., 1993; Zielke et al., 2010; Rizza et al., 2011; Klinger et al., 2011; Ansberque et al., 2016). Therefore, we decided for each data point to represent our preferred ($U_{pref}$), maximum ($U_{max}$) and minimum ($U_{min}$) offset values as a Probability Density Function (PDF) centered on our preferred value (McGill and Sieh, 1991; Zielke et al., 2010, 2012; Klinger et al., 2011; Salisbury et al., 2015). PDFs are computed for each offset as asymmetric non-centered normal laws with preferred offset value as mean, and $\sigma$ and $\tau$ the standard deviations reflecting uncertainties derived from minimum and maximum offset measurements, respectively (Fig 7.a):

$$f(x) = \frac{\sqrt{2}}{\sqrt{\pi}(\sigma+\tau)} \times \begin{cases} e^{\frac{-(x-m)^2}{2\sigma^2}} & x \leq m \\ e^{\frac{-(x-m)^2}{2\tau^2}} & x > m \end{cases}$$

with f=PDF, $m=U_{pref}$, $\sigma=U_{min}$, $\tau=U_{max}$.

These PDFs can then be stacked to produce a Cumulative Offset Probability Density function (COPD), for which local maxima are interpreted as average offset values for specific fault sections (McGill and Sieh, 1991; Klinger et al., 2011; Zielke et al., 2010, 2012, 2015; Zielke and Arrowsmith 2012; Madden et al., 2013; Salisbury et al., 2015).

Because each segment of the rupture has its own characteristics (azimuth, style of deformation) that may influence surface displacements, we computed segment-specific COPDs. Following common practice, we assume that for each fault segment the average slip associated with a large seismic event follows a Gaussian distribution: the COPD may then be viewed as the sum of an unknown number of co-seismic Gaussians. Alternatively, a Weibull distribution could also being used to describe our slip measurements. Because we start here from the symmetric, empirically extracted slip signal associated with the most recent earthquake, the fit of this signal with either a two-parameters Gaussian, or a three-parameter Weibull distribution yields to similar slip, confounded in the blue-line width in Figure 3-7. Eventually, the Gaussian fit offers a direct estimation of the slip-per-segment: the mean of the Gaussian function corresponds to the average slip and the standard deviation to the related uncertainty (Madden et al., 2013; Zielke et al., 2015). Hence, we limited our investigation to the Gaussian model in the following

We assume that in our dataset the smallest displacement recorded at each site is co-seismic, and that it was produced by the most recent large surface-rupturing earthquake; in our case the 1957 Gobi-Altai earthquake (E1). Then, we extract empirically the average slip associated with the most recent earthquake rupture from the COPD function by decomposing our COPD into a series of Gaussian functions (Figure 3-7), considering the first maximum peak described by the COPD to be the average slip associated with the most recent earthquake (Klinger et al., 2011; Zielke et al., 2012). Practically, the rising part of the COPD curve is extracted and used to build a symmetric Gaussian function (Figure 3-7.d) that would represent the modeled average slip due to the last earthquake along the considered segment (Figure 3-7.e). This modeled slip signal is then subtracted from the COPD (Figure 3-7.e) to derive a residual COPD that we

assume to correspond to the cumulative tectonic deformation prior to the 1957 earthquake, recorded by the geomorphic markers. In this process, we consider that the misfit between our COPD and the Gaussian distribution, which actually corresponds to the misfit between the rising part of the COPD and the Gaussian function, is not related to a previous rupture, but rather to the Gaussian approximation itself. Therefore, any unrealistic negative residual located ahead of the last average slip is discarded before the next iteration.

The iteration of that protocol (Figure 3-7.f,g) allows us to determine average slip-per-segment for three to six past earthquakes that resulted in a total of 25 meters of cumulative displacement (Figure 3-7.h). Then, depending on the number of offset measurements, their amplitudes and their quality, the residual COPD becomes nearly flat and the Gaussian fit unconstrained (Figure 3-7.h): if the associated amplitude is below 10% of the maximum amplitude of the COPD, we consider estimate to be unreliable and it is then discarded. It is worth noting that the successive surface slip signals that we identified consistently fit local maxima visible *a-priori* in the COPDs: in Figure 3-7.h for example, the 3$^{rd}$ (E3), 4$^{th}$ (E4) and 5$^{th}$ (E5) slip signals correctly fit visible local maxima at 8.6 ± 1.0m, 11.8 ± 1.3m and 13.9 ± 0.7m, respectively. To account for variability in slip signal quality and to produce robust results, we only retain the first four slip estimates for each segment to use in our interpretation of past slip distributions.

For the 1957 earthquake main surface rupture, the cumulative length of the nine major relay zones identified (Figure 3-4a), represents ~10% of the total length. Though our approach is generally restricted to well-defined fault segments, some of the major relay zones are large enough to allow a sufficient number of slip measurements (> 30) to be similarly processed and included in our analyses.

#### *IV.2.3. Validation*

To validate our approach and test the sensitivity of the results to the slip distribution extraction protocol, we performed three tests. First, we defined sub-sets with different score thresholds: scores higher than 2/10, 6/10, 7/10 and 10/10, representing 1700, 1426, 713 and 153 offsets respectively. We estimated an average slip-per-segment value for these different sub-sets and cross-compared them. Variability for the average slip-per-segment does not exceed 30% for the sub-sets considered, meaning that if the lower-score data are ignored, the remaining data are homogeneous. Secondly, we tested our results against two independent datasets. On the one hand we compared our average slip-per-segment values with 10 individual offset values derived from real-time-kinematic-GPS micro-topography (Rizza et al., 2011) and we observed no significant

discrepancy between our results and the independent data, within the uncertainties. On the other hand, we compiled a field dataset from the 84 best offsets (according to each author) measured by Kurushin et al. (1998) and Choi et al. (2012), and we applied our protocol to this dataset. We then compared the resulting COPDs to the COPDs we obtained for each segment: for any sub-set including data with a score better than 6/10 (84% of our measurements), correlation between our sub-set and the field dataset reaches 95 %. Hence, from our 1700 measurements, we retain the best 1426 values (score ≥ 6) for further statistical analysis.

## V. Results and Discussion

This section is divided in four parts: first, we describe our results concerning slip determined for each segment, and discuss their variability, uncertainty, and the significance of slip for each segment, as well as between consecutive segments. Next, we focus more specifically on the 1957 earthquake surface-slip distribution. We compare it to previously published slip distributions along the Eastern Bogd fault and to similar strike-slip earthquake slip distribution along other continental faults. We also use our data to re-assess the magnitude of the 1957 earthquake and discuss our magnitude estimate in comparison with previously published magnitude estimates. Then, we describe slip-distribution models for prehistoric earthquakes and discuss in detail uncertainties and variability for successive past earthquakes. Finally, we discuss our dataset in the framework of various slip distribution models proposed in the literature (Sieh, 1996).

### V.1. Slip-per-segment

Figure 3-8 presents the horizontal offsets we have measured along the western part of the 1957 surface rupture, which range from 0.7 m to 25 m. Although we measured additional larger offsets that demonstrate the longer-term activity of the Eastern Bogd fault (i.e. ~ 25 kyr for 25 m at an average slip rate of ~ 1 mm/yr (Rizza et al., 2011). These larger cumulative values are too sparse to be included in our analyses and are therefore not shown in figure 8.

For our core dataset, measurement sites are satisfactorily evenly distributed along the rupture trace, with the exception of the Dalan Turuu foreberg segment (S7), which is dominated by thrust and therefore is not associated with any significant horizontal offsets, either on the orthophotographs or in the field (Kurushin et al., 1998; Choi et al., 2012). There are several additional, although shorter (<2km), no-data sections where there are neither adequate geomorphic markers nor visible horizontal displacements, or where the fault slip is distributed over a very broad zone of deformation. Large

cumulative offsets are more common along segments where strike-slip motion is dominant (S2, S3, S4, S5, S8, S9 and S10) than along segments with oblique motion (S1, S6 and S11) (Figure 3-8.c).

Individual segment COPDs are asymmetric with: i) a maximum that corresponds to the larger amount of data likely associated with the most recent earthquake, and ii) a long tail that includes secondary maxima related to older events. Applying the protocol described in section IV.2.2 to each segment, we extracted slip signals associated with the 1957 earthquake and with earlier events. Along most segments (S1, S2, S3, S5, S8, S9, S10 and S11) the peaks of each successive Gaussian distribution match local maxima visible on the COPD, except for segments such as S4, where the strike-slip motion is distributed over a wide zone, or S6, where the displacement is oblique.

Whether or not a record of multiple past earthquakes is preserved along a fault segment depends on the number of offset geomorphic markers and on how well they are preserved in the landscape. Segment S1 for instance crosses mostly large active Quaternary alluvial fans (Figure 3-4.b). Hence, the 1957 surface rupture is evenly recorded in the morphology by numerous small gullies and rills. Preserved offsets for earlier ruptures, however, are significantly fewer (Figure 3-8.d) because the active alluvial processes are reshaping fan surfaces at a time scale shorter than the earthquake return time. In such case of limited number of measurements (< 3 measurements within $1\sigma$), our statistical approach is not robust enough and could not be pursued. Consequently, we did not account for the slip assessment for the $4^{th}$ earthquake on S1 in our analysis (Figure 3-8.c). Moreover, the number of offset measurements impacts the reliability of the COPD. For instance, we made 268 measurements along the Ulan Bulag segment (S2) and only 39 along the Ihk Bogd segment (S6) (Figure 3-8.c). We take this variability into consideration in our further analyses of past-slip distributions.

Although consistent along strike, our dataset is characterized by a large standard deviation associated with the average slip for each segment ($\sigma$ is 38 % on average for the 1957 slip distribution). We interpret this scattering of the data as partly resulting from the combination of uncertainties associated with image processing and offset measurements, as previously discussed. Some of this scattering, however, is likely real. In fact, similar high-frequency variations of slip along-strike have been documented for other strike-slip events (e.g. Rockwell and Klinger, 2013; Vallage et al., 2015; Gold et al., 2015). The reason for such variability is not yet fully understood, but it has been recently suggested that part of it might reflect the amount of deformation accommodated off-fault or in geometric complexities, in comparison with the total budget of deformation

produced during an earthquake (Klinger et al., 2006; Klinger, 2010; Vallage et al., 2015; Gold et al., 2015, Choi et al., 2017, in press). Unfortunately, our approach could not yield significant measurements on secondary faults to test further this assumption, as displacements on secondary features are too small (typically < 1m) with respect to image resolution.

Beyond variability, our dataset shows significant differences in slip between the different segments. These differences are partly explained by differences in the style of deformation for each segment, which depends mainly on the azimuth of the segment relative to the regional stress field. Where the segment is too oblique relative to the stress field, some motion is accommodated by dip slip, in this case mostly reverse slip. For instance, we found areas of superficial slip partitioning (King et al., 2005), associated with strain transfer from the N95 – N105 main strike-slip fault (segments S3 and S8) to the two N90 – N100 transtensionnal segments of Bahar Uul half-graben (segments S1 and S2), as well as to the N105 – N110 transpressive segment (S6) north of Ikh Bogd (Vassallo et al., 2007). However, we cannot quantify the dip-slip component accurately, due to widespread noise in our DEM (the ~1m high frequency noise is of the same order of magnitude as the measurements), thus limiting our ability to determine the full budget of deformation along sections of the rupture where the dip-slip is dominant. In fact, we are unable to distinguish apparent offsets from true offsets because we do not know the slip vectors for most locations along the fault.

Due to the intrinsic scattering of the offset data, we cannot rule out the possibility that we might have missed some moderate-magnitude paleoearthquakes in our earthquake interpretation of the offset distributions (Zielke et al., 2010; Klinger et al., 2011). In fact, intermediate seismic events, in the $M_W$ 6-7 range, would generate small surface displacements (≤ 1m) along few fault segments (Wells and Coppersmith, 1994; Rizza et al., 2011). Such sub-metric displacements would be undetectable in our approach, but may contribute to data scattering, and to average-slip uncertainties (Figure 3-8.b).

### V.2. The 1957 Gobi-Altai earthquake

Building on our COPD analysis, we can unambiguously identify offset measurements related to the 1957 earthquake (Figure 3-9). The studied portion of the 1957 surface rupture is statistically defined by 743 offset measurements (including measurements within fault jogs), with a large-enough number of good-quality measurements per segment: from 9 along S6 to 148 along S10.

The average co-seismic slip for the entire study area is 3.5 ± 1.3 m, which is consistent with previous studies (Kurushin et al., 1998; Rizza et al., 2011; Choi et al., 2012). The average co-seismic slip-per-segment varies from 2.7 ± 1.1 m (S2) to 4.3 ± 1.6 m (S4).

The shape of our slip function appears to be flatter than slip distributions previously published (Rizza et al., 2011; Choi et al., 2012). As the air photos were acquired in 1958, about 6 months after the 1957 rupture, it is likely that this survey already captured a significant part of any post-seismic deformation (Gold et al., 2015). Because our analysis is done within the near-field area of the rupture trace, the main post-seismic process that may affect our data is afterslip. However, it has been suggested that for large (M > 7) continental earthquakes, afterslip tends to be less important, about one order of magnitude less, than the co-seismic deformation (Freed, 2007). Hence, the 6 months timespan between the earthquake and the air photographs acquisition is probably sufficient to include more than 50 % of the afterslip, which is likely 1 m or less in total (Fialko, 2004; Perfettini and Avouac, 2007; Bruhat et al., 2011). Therefore, post-seismic processes are unlikely to explain the moderated differences between our dataset and previously published slip distributions.

Instead, we interpret this difference in roughness of the slip distribution as resulting from a better assessment of the uncertainty of the measurements in our case, and of systematic analysis of the dataset using COPD that limits chances to confuse cumulative offsets for 1957 offsets, which would artificially introduce large slip variations over short distances. Conversely, our work might potentially smooth local slip variations, as our analysis is using average slip values.

The apparent flatness of the 1957 earthquake slip distribution in our model is consistent with observations for other large strike-slip earthquakes occurring on slow intracontinental faults, such as the 1931 Fuyun earthquake (Klinger et al., 2011), the 1905 Bolnay earthquake (Choi et al., 2017, in press), or the 1997 Zirkuh earthquake (Berberian et al., 1999) for example. These slip distributions depart significantly from more asymmetric slip distributions typically observed along faster plate-boundary fault systems, such as the $M_W$ 7.7, 1857, Fort Tejon earthquake along the San Andreas fault (Sieh, 1978; Zielke et al., 2012) or the $M_W$ 7.8, 2001, Kokoxili earthquake along the Kunlun fault (Klinger et al., 2006). Although this difference in slip pattern is not yet fully understood, we suggest that it might be due to the fact that along slower faults, long return time for large earthquakes compared to post-seismic relaxation time allows for smoothing of stress heterogeneities along the fault that leads to a more even slip distribution during the next earthquake.

Our 1957 Gobi-Altai earthquake co-seismic offset measurements allow us to re-assess the seismic moment released during that earthquake, based on average surface-slip measurements for each segment and jog we analyzed. The seismic moment $M_O$ (in dyn.cm) is defined as the product of the fault surface ($S$ in cm², defined as $S = L * W$, with L-length of the fault in cm, and W-fault width, in cm), by the earthquake co-seismic displacement (D in cm), and the shear modulus (μ in dyn/cm²): MO = μ.S.D (Kanamori and Anderson, 1975).

At some sites we had to complement our dataset with data from the literature: horizontal displacement in the Baga Bogd area (segments S12 to S15) was taken from Kurushin et al., (1998) and Choi et al., (2012); slip along secondary thrusts, South of Ikh Bogd, was taken from Kurushin et al., (1998) and Prentice et al., (2002). In addition, Kurushin et al., (1998) indicate 2 m of average vertical displacement along the Dalan Turuu foreberg segment (S7), and ~1 m of average vertical displacement for the remaining fault. The width of the rupture is poorly constrained: seismologic studies in western Mongolia suggest that large earthquakes of the XX$^{th}$ century, like the Bolnay or the Gobi-Altai earthquakes, may have affected the whole thickness of the crust (50 km thick seismogenic zone), or may even have extended into the lithospheric mantle (Schlupp and Cisternas 2007). The crust has been estimated to be ~ 48 km thick for western Mongolia from thermobarometric and petrologic analyses of xenoliths (Ionov et al., 1998), to be 50 to 60 km thick from seismic tomography (Villaseñor et al., 2001), and to be 48 km thick from forward modeling of gravity data (Petit et al., 2002). We therefore computed the seismic moment using rupture thicknesses of 20 km and 60 km, corresponding to the upper crust and the entire crust, respectively. The shear modulus is typically taken as 3.2 x $10^{11}$ N.m-2 for average crustal rocks, although Vergnolle et al., (2003) suggested that assuming uniform slip, a shear modulus can be taken as the weighted average of rigidity values according to the elastic stratification, and therefore that for earthquake rupture deeper than 20 km, the shear modulus could be taken as 4.15 x $10^{11}$ N.m$^{-2}$.

Our seismic moment $M_O$ estimates range between 5.22 x$10^{27}$ and 2.11x$10^{28}$ dyn.cm, considering: i) for lower $M_O$ value: the 270 km-long main strike-slip fault, a 20 km-thick seismogenic zone and the shear modulus for average crustal rocks, ii) for the upper $M_O$ value: the total 359 km-long surface rupture, with a 60 km-thick seismogenic zone and a shear modulus for average lithospheric rocks for the main strike-slip fault (270 km) and a 20 km thick crust and a shear modulus for average crustal rocks for the 89 km of secondary thrusts, according to the flower structure geometry suggested by Vassallo et

al., (2007). The moment magnitude for the 1957 Gobi-Altai earthquake is determined by relation from Hanks and Kanamori, (1979): $M_W = 2/3 \log M_O - 10.7$. Our computation of moment magnitude yields $M_W$ = 7.8 - 8.2, considering the different combinations of parameters listed above. This magnitude is consistent with values derived by Kurushin et al. (1998) and Rizza et al. (2011) who used measured offsets and a 20 km rupture depth to get magnitudes, ranging between7.8 and 7.9, and between 7.78 and 7.95). Our range of magnitude is also consistent with the magnitude $M_W$ ~ 8.1 proposed by Chen and Molnar (1977) and Molnar and Qidong (1984), on the basis of a 270-km-long by 20-km-wide rupture and an overestimated average slip of 8 m. Finally, our magnitude is consistent with seismological estimates of $M_W$ 8.0-8.3 (Okal, 1976; Chen and Molnar, 1977; Pacheco and Sykes, 1992; Schlupp, 1996), provided a 50 to 60-km-wide rupture area, regardless of the chosen surface rupture length.

Some of the moderate discrepancies between the magnitude we derive from surface observations with a 20 km-fault-width and the magnitude derived from seismological observations could be due to one or a combination of several possibilities. First, the rupture associated with the 1957 earthquake may have involved the lower crust, as it has been suggested for very large earthquakes that have long surface rupture and large magnitude (e.g. Lapusta and Rice, 2003). Secondly, some slip was reported on secondary faults (Florensov and Solonenko, 1965; Kurushin et al., 1998), that are now difficult to recognize and to quantify, even in the field. Furthermore, several kilometric-scale blind thrusts are reported between Ikh Bogd and Baga Bogd, which may have been activated during the 1957 earthquake (Florensov et Solonenko. 1965; Baljinnyam et al., 1993; Kurushin et al., 1998). However, those thrust faults did not break the surface, and potential co-seismic slip cannot be assessed (Kurushin et al., 1998; Carretier et al., 2002). In the case of the 1905 Bulnay earthquake, Choi et al., (2017, in press) have shown that in some places, slip on secondary ruptures can account for as much as 25% of the total surface slip, which could also be possible here.

### V.3. Paleoearthquakes rupture enveloppes

Using our COPD analysis, we have first extracted offset measurements associated with the 1957 earthquake (E1) from our dataset. Following the same procedure, we have also concluded that larger offsets correspond to cumulative slip associated with two, three or four past earthquakes (E2 to E4 in Figure 3-9). Accordingly, for each fault segment, each data point that falls within 1$\sigma$ of the average slip-per-segment determined from COPD analyses is color coded according to the earthquake it may represent. Although the number of data points for each earthquake and for each segment is not the same

everywhere along the rupture, we identified 3 successive surface ruptures along the Eastern Bogd fault (Figure 3-9), and a potential fourth one on 9 segments out of the 10 strike-slip segments that we analyzed. The penultimate earthquake (E2), shown in orange, the third event back in time (E3), shown in green, and the fourth event back in time (E4), shown in purple, are statistically defined by 270, 132 and 62 measurements respectively.

Prehistoric earthquakes along the western end of the rupture (S1) are not well defined, because this segment crosses a zone of active alluvial fans, and we could not recognize cumulative offsets related to the 4$^{th}$ past earthquake (E4) (see section V.1). Slip distributions for past earthquakes along fault segments< with relatively few data points, such as S4 and S6, are likely more uncertain. The lack of data points along these fault segments is due to greater rupture complexity associated with oblique slip and wide zones of surface rupture. The colored lines of Figure 3-9 show the average slip function for each earthquake along each fault segment, color-coded symbols indicate the corresponding average slip values for each segment, and black symbols are measurements related to average slip on jogs. We note that the measurements on the jogs are consistent with the average slip measured on adjacent segments (Figure 3-9).

When correlation of the average slip between adjacent segments is ambiguous, either due to the limited number of available data to compute the average slip, or large lateral variations of average slip, the color line is dashed. For example, along segment S6 average slip associated with the 3$^{rd}$ past earthquake (E3) is poorly constrained, being determined only from three measurements, and correlation with the average slip from adjacent segments remains uncertain. We note that the uncertain determination of the average slip for the 3$^{rd}$ past earthquake (E3) propagates to the estimate of the average slip for the 4$^{th}$ past earthquake (E4), which therefore has large standard deviation. A similar situation applies to the 4$^{th}$ past earthquake (E4) along segment S4, where the average slip is defined by only 4 measurements. Along the northern side of Ikh Bogd (segment S6), where the motion is reverse oblique and where the S10000 photos do not include the fault scarp, our interpretation of the cumulative slip function related to adjacent segments must be limited to the 2$^{nd}$ past earthquake (E2).

### V.4. Characteristic slip

A given fault section generates characteristic slip when the local amount of co-seismic slip during each earthquake is similar.

The preservation of offset geomorphic features over tens of thousands of years along the Eastern Bogd fault allows analyzing the deformation through several seismic cycles (e.g.

Ritz et al., 1995; Vassallo et al., 2007). Hence, building on our large dataset we can further test if the Bogd fault system, and more specifically the section that ruptured in 1957, behaves following a characteristic-slip fashion, as suggested by Rizza et al. (2011).

In figure 3-9 we use the slip distribution that we determined for the 1957 earthquake as a template to predict the cumulative slip for one to three past earthquakes, assuming a characteristic-slip behavior. Multiples of the 1957 surface-slip distribution are presented by dashed black lines on Figure 3-9. The slip distribution associated with the 2$^{nd}$ past earthquake (E2), in orange, is about twice the 1957 slip distribution anywhere the rupture trace is simple, which represents 70% of the segments analyzed and 50% of the whole main surface rupture. Where the fault trace is more complex, similarity between 1957 and E2 slip distributions is less straightforward. For the third earthquake back in time (E3), the discrepancy between the 1957 rupture template and the actual slip distribution increases significantly in the areas where the fault pattern is complex. However, for the sections where the fault is simple (about 50% of the whole main strike-slip rupture length), the agreement between the data and the predicted slip distribution still holds. One should keep in mind that when predicting slip distribution for multiple 1957-like earthquakes by multiplying the 1957 slip values, we also multiply associated uncertainties. This could lead to overestimate uncertainties as they do not necessarily increase linearly with cumulative slip, and is might result in an artificial emphasizing of the mismatch between predicted slip distribution and actual data.

Hence, for the part of the 1957 rupture that we have documented (about 70% of the total main strike-slip rupture), we propose that anywhere where the fault pattern is simple, the fault has behaved following a characteristic-slip pattern, at least during the last three earthquake cycles.

Eventually, at first order, if one assumes that the fault behaves in a characteristic-slip fashion and that the slip rate is steady over time, one could estimate the return time for 1957-like earthquakes. If we use an average slip rate along pure strike-slip sections of 0.9 ± 0.5 mm/yr for the Eastern Bogd fault (average value of Rizza et al., 2011) and an average slip of 3.5 ± 1.3 m (this study), we estimate a return period of 3.9 ± 3.60 kyr, which, notwithstanding the uncertainty, is consistent with the return time of 4500 ± 1400 years derived from paleoseismological evidence suggested by Ritz et al. (2009) and Rizza (PhD, 2010).

Our results suggest that at least half of the Eastern Bogd fault has generated characteristic slip, producing the same amount of slip during successive major

earthquakes on a given fault segment. However, in order to discuss the potential for proper characteristic earthquake, similar extent in addition to local co-seismic slip (Schwartz and Coppersmith, 1984), we need to consider the lateral extent of the surface rupture as well. Fault scarps have been mapped within the region located south-eastward of the Bogd Fault System (Figure 3-10), especially westward and northward of Artz Bogd Mountains (Kurushin et al., 1998; Cunningham et al., 1997; Bayasgalan et al., 1999; Vassallo et al., 2005). No surface rupture occurred along the forebergs located south of Baga Bogd during the 1957 event (Kurushin et al., 1998; Vassallo et al., 2005), but these faults are directly linked to the thrust north of Artz Bogd (Owen et al., 1999; Vassallo et al., 2005), which is the main structure creating this 80-km-long monocline (Figure 3-10), standing easternmost of the Gobi-Altai Mountains (Cunningham, 2010) (Figure 3-10). This reverse fault deforms Quaternary fans, and is well expressed only in the western part of the range where field observations and OSL dating indicate that it produced at least one surface-rupturing earthquake in the last 37.7 ± 6,1 kyr (Owen et al., 1999). Further east along Artz Bogd, the fault trace is unclear on satellite images. Although drainages that cross Quaternary fans are vertically displaced, no major surface rupture has been mapped in the area (Figure 3-10).

At the western end of the 1957 Gobi-Altai surface rupture, the rupture stopped near the eastern part of the Bayan Tsagaan Nuruu restraining bend (Figure 3-1), rupturing both its North-Eastern and South-Eastern edges with reverse foreberg and horse-tail patterns, respectively (Kurushin et al., 1998). An aftershock of the 1957 event, the Bayan Tsagaan earthquake, M6.9, 7 April 1958 produced a 7 km to 15 km long surface rupture South of the Bayaan Tsagaan range (Florensov and Solonenko, 1965; Khilko et al., 1985; Baljinnyam 1993; Kurushin et al., 1998). The 1957 rupture, however, did not propagate farther west, and it has been suggested that this large bend acted as a barrier during the Gobi-Altai earthquake rupture propagation (Florensov and Solonenko, 1965). West of the Bayan Tsagaan range, however, Holocene faulting continues for at least 100 km along two left-lateral transpressive fault strands and it displays two large surface ruptures with a similar transpressive left-lateral fault pattern (Baljinnyam et al., 1993): the Chandmani surface rupture, directly prolonging the Bogd Fault over at least 50 km (Khilko et al., 1985), and 20 km further north-west the 80 km long Valley of Lakes Fault scarp (Figure 3-10).

Consequently, if large seismic activity is uncertain, but limited eastward of the Bogd fault system, the western part of this fault system clearly shows evidence of Holocene cumulative fault scarps, providing evidence of large past-seismic events. Our assessment of the possibility for characteristic earthquakes along the Eastern Bogd fault

is limited by the lack of paleoseismic data along the Holocene faults west of the 1957 earthquake surface rupture within the central part of the Gobi-Altai mountain range.

## VI. Summary

We orthorectified aerial photographs taken along the Western Bogd Fault surface rupture shortly after the 1957 Gobi-Altai earthquake, and we used them to systematically measure offsets along 170 km of the main strike-slip fault, scoring each offset measurement depending on marker quality, fault distribution, and image quality. We then developed a method to extract the average slip-per-segment associated with successive past earthquakes from our dataset. We use these data to: i) revisit the lateral slip distribution of the 1957 Gobi-Altai earthquake, which displays a fairly flat shape with an average horizontal offset of 3.5 m ± 1.3m, ii) define individual slip distributions associated with 3 paleoearthquakes along the main strike slip segments (70 % of the studied area), and iii) suggest that at least 50% of the 1957 earthquake main strike-slip surface rupture produced characteristic slip during the last three seismic cycles.

## Acknowledgment

This work has been supported by the ANR program Geosmec (ANR-12-BS06-0016) and by INSU Tellus-Aleas 2017. Aerial images were bought thanks to the program INSU Tectoscope 1993. We thank our Mongol colleagues Todbileg, Demberel Sodnomsambuu, Ulzii Munhuu and Odonbaatar Chimedtseren for fruitful discussions, and the Institute of Astronomy and Geophysics of Mongolia for their logistical support. We are grateful to O. Zielke, an anonymous reviewer and the editor for their constructive comments and their help to improve the manuscript.

## References

Ansberque, C., O. Bellier, V. Godard, C. Lasserre, M. Wang, R. Braucher, B. Talon, J. de Sigoyer, X. Xu, and D. L. Bourlès. 2016. « The Longriqu Fault Zone, Eastern Tibetan Plateau: Segmentation and Holocene Behavior: the longriqu fault ». Tectonics 35 (3): 565‑85. doi:10.1002/2015TC004070.

Baljinnyam, I., éd. 1993. Ruptures of major earthquakes and active deformation in Mongolia and its surroundings. Memoir 181. Boulder: Geological Society of America.

Baljinnyam, I., A. Bayasgalan, B. A. Borisov. 1993. Ruptures of major earthquakes and active deformation in Mongolia and its surroundings. Boulder, Etats-Unis: The Geological Society of America.

Bayasgalan, A., J. Jackson, J-F. Ritz, and S. Carretier. 1999. « Field Examples of Strike-Slip Fault Terminations in Mongolia and Their Tectonic Significance ». Tectonics 18 (3): 394‑411. doi:10.1029/1999TC900007.

Berberian, M., J. A. Jackson, M. Qorashi, M. M. Khatib, K. Priestley, M. Talebian, and M. Ghafuri-Ashtiani. 1999. « The 1997 May 10 Zirkuh (Qa'enat) earthquake (Mw 7.2): faulting along the Sistan suture zone of eastern Iran ». Geophysical Journal International 136 (3): 671‑94. doi:10.1046/j.1365-246x.1999.00762.x.

Berberian, M., and R. S. Yeats. 1999. « Patterns of Historical Earthquake Rupture in the Iranian Plateau ». Bulletin of the Seismological Society of America 89 (1): 120‑39.

Bilham, R., and P. Williams. 1985. « Sawtooth segmentation and deformation processes on the southern San Andreas fault, California ». Geophysical Research Letters 12 (9): 557–560.

Bruhat, Lucile, Sylvain Barbot, and Jean-Philippe Avouac. 2011. « Evidence for Postseismic Deformation of the Lower Crust Following the 2004 Mw6.0 Parkfield Earthquake ». Journal of Geophysical Research 116 (B8). doi:10.1029/2010JB008073.

Calais, E., M. Vergnolle, V. San'kov, A. Lukhnev, A. Miroshnitchenko, S. Amarjargal, and J. Déverchère. 2003. « GPS Measurements of Crustal Deformation in the Baikal-Mongolia Area (1994-2002): Implications for Current Kinematics of Asia: gps measurements in mongolia ». Journal of Geophysical Research: Solid Earth 108 (B10). doi:10.1029/2002JB002373.

Chen, Wang-Ping, and Peter Molnar. 1977. « Seismic Moments of Major Earthquakes and the Average Rate of Slip in Central Asia ». Journal of Geophysical Research 82 (20): 2945‑69. doi:10.1029/JB082i020p02945.

Choi, J., Kwangmin J., Dandar E., Battogtokh D., A. Bayasgalan, and Y. Kim. 2012. « Rupture Propagation Inferred from Damage Patterns, Slip Distribution, and Segmentation of the 1957 M W 8.1 Gobi-Altay Earthquake Rupture along the Bogd Fault, Mongolia ». Journal of Geophysical Research 117 (B12). doi:10.1029/2011JB008676.

Cunningham, D. 2005. « Active Intracontinental Transpressional Mountain Building in the Mongolian Altai: Defining a New Class of Orogen ». Earth and Planetary Science Letters 240 (2): 436‑44. doi:10.1016/j.epsl.2005.09.013.

Cunningham, D. 2010. « Tectonic Setting and Structural Evolution of the Late Cenozoic Gobi Altai Orogen ». Geological Society, London, Special Publications 338 (1): 361‑87. doi:10.1144/SP338.17.

Cunningham, D. 2013. « Mountain Building Processes in Intracontinental Oblique Deformation Belts: Lessons from the Gobi Corridor, Central Asia ». Journal of Structural Geology 46 (janvier): 255‑82. doi:10.1016/j.jsg.2012.08.010.

Cunningham, D. 1998. « Lithospheric Controls on Late Cenozoic Construction of the Mongolian Altai ». Tectonics 17 (6): 891‑902. doi:10.1029/1998TC900001.

Cunningham, D., B. Windley, L. Owen, T. Barry, D. Dorjnamjaa, and J. Badamgarav. 1997. « Geometry and style of partitioned deformation within a late Cenozoic transpressional zone in the eastern Gobi Altai Mountains, Mongolia ». Tectonophysics 277 (4): 285‑306. doi:10.1016/S0040-1951(97)00034-6.

Fialko, Y. 2004. « Evidence of Fluid-Filled Upper Crust from Observations of Postseismic Deformation Due to the 1992 Mw7.3 Landers Earthquake ». Journal of Geophysical Research: Solid Earth 109 (B8): B08401. doi:10.1029/2004JB002985.

Florensov, N. A., V. P. Solonenko, 1958- Sovetsko-mongolśkaia Gobi-Altaĭskaia ekspeditsiia, Akademiia nauk SSSR. Sibirskoe otdelenie. Vostochno-Sibirskiĭ geologiches ki institut, et Mongolia. Committee for Sciences and Higher Education. 1965. The Gobi-Altai earthquake (Gobi-Altaiskoe zemletryasenie). Jerusalem, Israël: Israel Program for Scientific Translations.

Freed, A. M. 2007. « Afterslip (and Only Afterslip) Following the 2004 Parkfield, California, Earthquake ». Geophysical Research Letters 34 (6): L06312. doi:10.1029/2006GL029155.

Gold, R., N. Reitman, R. Briggs, W. Barnhart, G. Hayes, and E. Wilson. 2015. « On- and off-Fault Deformation Associated with the September 2013 Mw 7.7 Balochistan Earthquake: Implications for Geologic Slip Rate Measurements ». Tectonophysics 660 (octobre): 65‑78. doi:10.1016/j.tecto.2015.08.019.

Haeussler, P., D. Schwartz, T. Dawson, H. Stenner, J. Lienkaemper, B. Sherrod, F. Cinti. 2004. « Surface Rupture and Slip Distribution of the Denali and Totschunda Faults in the 3 November 2002 M 7.9 Earthquake, Alaska ». Bulletin of the Seismological Society of America 94 (6B): S23‑52. doi:10.1785/0120040626.

Hamling, I., S. Hreinsdóttir, K. Clark, J. Elliott, C. Liang, E. Fielding, N. Litchfield. 2017. « Complex Multifault Rupture during the 2016 Mw 7.8 Kaikura Earthquake, New Zealand ». Science 356 (6334): eaam7194. doi:10.1126/science.aam7194.

Ionov, D., S. O'Reilly, and W. Griffin. 1998. « A Geotherm and Lithospheric Section for Central Mongolia (Tariat Region) ». In Mantle Dynamics and Plate Interactions in East Asia, édité par rtin F. J. Flower, Sun-Lin Chung, Ching-Hua Lo, and Tung-Yi Lee, 127‑53. American Geophysical Union. doi:10.1029/GD027p0127.

James, Mike R., and Stuart Robson. 2014. « Mitigating Systematic Error in Topographic Models Derived from UAV and Ground-Based Image Networks: mitigating systematic error in topographic models ». Earth Surface Processes and Landforms 39 (10): 1413‑20. doi:10.1002/esp.3609.

Kanamori, H., and D. Anderson. 1975. « Theoretical Basis of Some Empirical Relations in Seismology ». Bulletin of the Seismological Society of America 65 (5): 1073‑95.

Khilko, S. D., R. A. Kurushin, V. M. Kotchetkov, L. A. Misharina, V. I. Melnikova, N. A. Gileva, S. V. Lastochkin, I. Baljinnyam, and D. Monhoo. 1985. « Strong earthquakes, paleoseismogeological and macroseismic data ». Earthquakes and the Base for Seismic Zoning of Mongolia, 19–83.

King, G. C. P. 1986. « Speculations on the Geometry of the Initiation and Termination Processes of Earthquake Rupture and Its Relation to Morphology and Geological Structure ». In Friction and Faulting, édité par Terry E. Tullis, 567‑85. Birkhäuser Basel. doi:10.1007/978-3-0348-6601-9_9.

King, G., and John Nabelek. 1985. « Role of Fault Bends in the Initiation and Termination of Earthquake Rupture ». Science 228 (mai): 984‑88.

Klinger, Y. 2005. « High-Resolution Satellite Imagery Mapping of the Surface Rupture and Slip Distribution of the Mw 7.8, 14 November 2001 Kokoxili Earthquake, Kunlun Fault, Northern Tibet, China ». Bulletin of the Seismological Society of America 95 (5): 1970‑87. doi:10.1785/0120040233.

Klinger, Y., J. P. Avouac, N. Abou Karaki, L. Dorbath, D. Bourles, and J. L. Reyss. 2000. « Slip rate on the Dead Sea transform fault in northern Araba valley (Jordan) ». Geophysical Journal International 142 (3): 755–768.

Klinger, Y., M. Etchebes, P. Tapponnier, and C. Narteau. 2011. « Characteristic slip for five great earthquakes along the Fuyun fault in China ». Nature Geoscience 4 (6): 389‑92. doi:10.1038/ngeo1158.

Klinger, Y, R Michel, and G King. 2006. « Evidence for an Earthquake Barrier Model from Mw~7.8 Kokoxili (Tibet) Earthquake Slip-Distribution ». Earth and Planetary Science Letters 242 (3‑4): 354‑64. doi:10.1016/j.epsl.2005.12.003.

Klinger, Y. 2010. « Relation between Continental Strike-Slip Earthquake Segmentation and Thickness of the Crust ». Journal of Geophysical Research 115 (B7). doi:10.1029/2009JB006550.

Koenderink, J., and A. van Doorn. 1991. « Affine Structure from Motion ». JOSA A 8 (2): 377‑85. doi:10.1364/JOSAA.8.000377.

Kurushin, R. A., A. Bayasgalan, M. Ölziybat, B. Enhtuvshin, Peter Molnar, Ch. Bayarsayhan, Kenneth W. Hudnut, and Jian Lin. 1998. « The Surface Rupture of the 1957 Gobi-Altay, Mongolia, Earthquake ». In Special Paper 320: The Surface Rupture of the 1957 Gobi-Altay, Mongolia, Earthquake, 320:1‑144. Geological Society of America. doi:10.1130/0-8137-2320-5.1.

Lapusta, N., and J. Rice. 2003. « Nucleation and Early Seismic Propagation of Small and Large Events in a Crustal Earthquake Model ». Journal of Geophysical Research: Solid Earth 108 (B4): 2205. doi:10.1029/2001JB000793.

Lehmkuhl, F. and A. Lang. 2001. « Geomorphological Investigations and Luminescence Dating in the Southern Part of the Khangay and the Valley of the Gobi Lakes (Central Mongolia) ». Journal of Quaternary Science 16 (1): 69‑87. doi:10.1002/1099-1417(200101)16:1<69::AID-JQS583>3.0.CO;2-O.

Madden, C., D. Haddad, B. Salisbury, O. Zielke, R. Arrowsmith, R. Weldon, and J. Colunga. 2013. « Appendix R—Compilation of slip-in-the-last-event data and analysis of last event, repeated slip, and average displacement for recent and prehistoric ruptures ». US Geological Survey Open-File Report 1165: 65.

Manighetti, I., C. Perrin, S. Dominguez, S. Garambois, Y. Gaudemer, J. Malavieille, L. Matteo, E. Delor, C. Vitard, and S. Beauprêtre. 2015. « Recovering Paleoearthquake Slip Record in a Highly Dynamic Alluvial and Tectonic Region (Hope Fault, New Zealand) from Airborne Lidar: earthquake slip record in lidar data ». Journal of Geophysical Research: Solid Earth 120 (6): 4484‑4509. doi:10.1002/2014JB011787.

McGill, S., and K. Sieh. 1991. « Surficial Offsets on the Central and Eastern Garlock Fault Associated with Prehistoric Earthquakes ». Journal of Geophysical Research: Solid Earth 96 (B13): 21597‑621. doi:10.1029/91JB02030.

Moffitt, F. H. 1959. « Photogrammetry ». https://trid.trb.org/view.aspx?id=91359.

Molnar, P., and D. Qidong. 1984. « Faulting associated with large earthquakes and the average rate of deformation in central and eastern Asia ». Journal of Geophysical Research: Solid Earth 89 (B7): 6203–6227.

Molnar, P., and P. Tapponnier. 1977. « Relation of the Tectonics of Eastern China to the India-Eurasia Collision: Application of Slip-Line Field Theory to Large-Scale Continental Tectonics ». Geology 5 (4): 212‑16. doi:10.1130/0091-7613(1977)5<212:ROTTOE>2.0.CO;2.

Nissen, E., R. Walker, A. Bayasgalan, A. Carter, M. Fattahi, E. Molor, C. Schnabel, J. West, and S. Xu. 2009. « The late Quaternary slip-rate of the Har-Us-Nuur fault (Mongolian Altai) from cosmogenic 10Be and luminescence dating ». Earth and Planetary Science Letters 286 (3–4): 467‑78. doi:10.1016/j.epsl.2009.06.048.

Okal, E. 1976. « A surface-wave investigation of the rupture mechanism of the Gobi-Altai (December 4, 1957) earthquake ». Physics of the Earth and Planetary Interiors 12 (4): 319–328.

Owen, L., D. Cunningham, B. W. M. Richards, E. Rhodes, B. Windley, D. Dorjnamjaa, and J. Badamgarav. 1999. « Timing of Formation of Forebergs in the Northeastern Gobi Altai, Mongolia: Implications for Estimating Mountain Uplift Rates and Earthquake Recurrence Intervals ». Journal of the Geological Society 156 (3): 457‑64. doi:10.1144/gsjgs.156.3.0457.

Pacheco, J., and L. Sykes. 1992. « Seismic Moment Catalog of Large Shallow Earthquakes, 1900 to 1989 ». Bulletin of the Seismological Society of America 82 (3): 1306‑49.

Perfettini, H., and J.-P. Avouac. 2007. « Modeling Afterslip and Aftershocks Following the 1992 Landers Earthquake ». Journal of Geophysical Research: Solid Earth 112 (B7): B07409. doi:10.1029/2006JB004399.

Petit, C., J. Déverchère, E. Calais, V. San'kov, and D. Fairhead. 2002. « Deep structure and mechanical behavior of the lithosphere in the Hangai–Hövsgöl region, Mongolia: new constraints from gravity modeling ». Earth and Planetary Science Letters 197 (3): 133–149.

Pollitz, F., M. Vergnolle, and E. Calais. 2003. « Fault Interaction and Stress Triggering of Twentieth Century Earthquakes in Mongolia: stress triggering of earthquakes in mongolia ». Journal of Geophysical Research: Solid Earth 108 (B10). doi:10.1029/2002JB002375.

Prentice, C., K. Kendrick, Kelvin Berryman, A. Bayasgalan, J.-F. Ritz, and J. Spencer; 2002. « Prehistoric Ruptures of the Gurvan Bulag Fault, Gobi Altay, Mongolia ». Journal of Geophysical Research 107 (B12). doi:10.1029/2001JB000803.

Ritz, J. F., E. T. Brown, D. L. Bourles, H. Philip, A. Schlupp, G. M. Raisbeck, F. Yiou, and B. Enkhtuvshin. 1995. « Slip rates along active faults estimated with cosmic-ray–exposure dates: Application to the Bogd fault, Gobi-Altaï, Mongolia ». Geology 23 (11): 1019–1022.

Ritz, J.-F., M. Rizza, C. Prentice, and D. Schwartz. 2009. « Détermination de l'aléa sismique: l'approche paléosismologique ». Géochronique 110 (Néotectonique): 25–26.

Ritz, J.-F., D. Bourles, E. T. Brown, S. Carretier, J. Chéry, B. Enhtuvshin, P. Galsan, R. C. Finkel, T. C. Hanks, K. J. Kendrick, H. Philip, G. Raisbeck, A. Schlupp, D. P. Schwartz, and F. Yiou « Late Pleistocene to Holocene Slip Rates for the Gurvan Bulag Thrust Fault (Gobi-Altay, Mongolia) Estimated with 10Be Dates ». Journal of Geophysical Research 108 (B3). doi:10.1029/2001JB000553.

Ritz, J.-F., R. Vassallo, R. Braucher, E.T. Brown, S. Carretier, and D.L. Bourlès. 2006. « Using in Situ–produced 10Be to Quantify Active Tectonics in the Gurvan Bogd Mountain Range (Gobi-Altay, Mongolia) ». In Special Paper 415: In Situ-Produced Cosmogenic Nuclides and Quantification of Geological Processes, 415:87‑110. Geological Society of America. http://specialpapers.gsapubs.org/cgi/doi/10.1130/2006.2415(06).

Rizza, M., J.- F. Ritz, C. Prentice, R. Vassallo, R. Braucher, C. Larroque, A. Arzhannikova. 2015. « Earthquake Geology of the Bulnay Fault (Mongolia) ». Bulletin of the Seismological Society of America 105 (1): 72‑93. doi:10.1785/0120140119.

Rizza, M., J.-F. Ritz, R. Braucher, R. Vassallo, C. Prentice, S. Mahan, S. McGill, et al., 2011. « Slip Rate and Slip Magnitudes of Past Earthquakes along the Bogd Left-Lateral Strike-Slip Fault (Mongolia): Slip Rate and Slip Value along the Bogd Fault ». Geophysical Journal International 186 (3): 897‑927. doi:10.1111/j.1365-246X.2011.05075.x.

Rizza, M. 2010. « Analyses des vitesses et des déplacements cosismiques sur des failles décrochantes en Mongolie et en Iran: approche morphotectonique et paléosismologique ». Thèse de doctorat, Montpellier, France: Géosciences.

Rockwell, T. K., and Y. Klinger. 2013. « Surface Rupture and Slip Distribution of the 1940 Imperial Valley Earthquake, Imperial Fault, Southern California: Implications for Rupture Segmentation and Dynamics ». Bulletin of the Seismological Society of America 103 (2A): 629‑40. doi:10.1785/0120120192.

Rockwell, T., S. Lindvall, T. Dawson, R. Langridge, W. Lettis, and Y. Klinger. 2002. « Lateral offsets on surveyed cultural features resulting from the 1999 Izmit and Düzce earthquakes, Turkey ». Bulletin of the Seismological Society of America 92 (1): 79–94.

Rukavicková, L., et P. Hanžl. 2012. « Mud Volcanoes in the Khar Argalantyn Nuruu, NW Gobi Altay, Mongolia as Manifestation of Recent Seismic Activity ». Journal of GEOsciences, juillet, 181‑91. doi:10.3190/jgeosci.024.

Salisbury, J. Barrett, D.E. Haddad, T. Rockwell, J R. Arrowsmith, C. Madugo, O. Zielke, and K. Scharer. 2015. « Validation of Meter-Scale Surface Faulting Offset Measurements from High-Resolution Topographic Data ». Geosphere, octobre, GES01197.1. doi:10.1130/GES01197.1.

Schlupp, A. 1996. « Neotectonic of western Mongolia analysed using field, seismological and remote sensing data ». Theses, Université Louis Pasteur - Strasbourg I. https://tel.archives-ouvertes.fr/tel-00155858.

Schlupp, A., et A. Cisternas. 2007. « Source History of the 1905 Great Mongolian Earthquakes (Tsetserleg, Bolnay) ». Geophysical Journal International 169 (3): 1115‑31. doi:10.1111/j.1365-246X.2007.03323.x.

Schwartz, D. P., A. Bayasgalan, T. C. Hanks, K. Hanson, W. Lund, C. S. Prentice, J. F. Ritz, T. K. Rockwell, et K. Rockwell. 2007. « Paleoseismic investigations of the 1957 Gobi-Altay surface ruptures ». In 50th Anniversary Earthquake Conference Commemorating the 1957 Gobi-Altay Earthquake.

Schwartz, D. P., T. C. Hanks, C. S. Prentice, A. Bayasgalan, J. F. Dolan, T. K. Rockwell, P. Molnar, et R. B. Hermann. 1996. « The 1957 Gobi-Altay earthquake (M= 8.1); complex: long recurrence (?) interval faulting in the middle of a continent ». Seismol. Res. Lett 67: 54.

Schwartz, D. P., and K. Coppersmith. 1984. « Fault Behavior and Characteristic Earthquakes: Examples from the Wasatch and San Andreas Fault Zones ». Journal of Geophysical Research: Solid Earth 89 (B7): 5681‑98. doi:10.1029/JB089iB07p05681.

Sieh, K. E. 1978. « Slip along the San Andreas Fault Associated with the Great 1857 Earthquake ». Bulletin of the Seismological Society of America 68 (5): 1421‑48.

Sieh, K., L. Jones, E. Hauksson, K. Hudnut, D. Eberhart-Phillips, T. Heaton, S. Hough. 1993. « Near-Field Investigations of the Landers Earthquake Sequence, April to July 1992 ». Science 260 (5105): 171‑76.

Sieh, Kerry. 1996. « The repetition of large-earthquake ruptures ». *Proceedings of the National Academy of Sciences* 93 (9):3764–3771.

Slater, J., Graham G., C. Johnston, J. Haase, B. Heady, G. Kroenung, et J. Little. 2006. « The SRTM Data “Finishing” Process and Products ». Photogrammetric Engineering & Remote Sensing 72 (3): 237‑47. doi:10.14358/PERS.72.3.237.

Tapponnier, P., and P. Molnar. 1979. « Active faulting and Cenozoic tectonics of the Tien Shan, Mongolia, and Baykal regions ». Journal of Geophysical Research: Solid Earth (1978–2012) 84 (B7): 3425–3459.

Vallage, A., Y. Klinger, R. Grandin, H. S. Bhat, and M. Pierrot-Deseilligny. 2015. « Inelastic Surface Deformation during the 2013 Mw 7.7 Balochistan, Pakistan, Earthquake ». Geology 43 (12): 1079‑82. doi:10.1130/G37290.1.

Vallage, A., Y. Klinger, R. Lacassin, A. Delorme, and M. Pierrot-Deseilligny. 2016. « Geological Structures Control on Earthquake Ruptures: The Mw7.7, 2013,

Balochistan Earthquake, Pakistan ». Geophysical Research Letters 43 (19): 2016GL070418. doi:10.1002/2016GL070418.

Vassallo, R., M. Jolivet, J.-F. Ritz, R. Braucher, C. Larroque, C. Sue, M. Todbileg, and D. Javkhlanbold. 2007. « Uplift Age and Rates of the Gurvan Bogd System (Gobi-Altay) by Apatite Fission Track Analysis ». Earth and Planetary Science Letters 259 (3‑4): 333‑46. doi:10.1016/j.epsl.2007.04.047.

Vassallo, R., J.-F. Ritz, R. Braucher, M. Jolivet, S. Carretier, C. Larroque, A. Chauvet, et al., 2007. « Transpressional Tectonics and Stream Terraces of the Gobi-Altay, Mongolia: FLUVIAL INCISION VS UPLIFT IN GOBI-ALTAY ». Tectonics 26 (5): n/a-n/a. doi:10.1029/2006TC002081.

Vassallo, R., J.-F. Ritz, R. Braucher, et S. Carretier. 2005. « Dating Faulted Alluvial Fans with Cosmogenic 10Be in the Gurvan Bogd Mountain Range (Gobi-Altay, Mongolia): Climatic and Tectonic Implications ». Terra Nova 17 (3): 278‑85. doi:10.1111/j.1365-3121.2005.00612.x.

Vergnolle, M., F. Pollitz, et E. Calais. 2003. « Constraints on the Viscosity of the Continental Crust and Mantle from GPS Measurements and Postseismic Deformation Models in Western Mongolia: CRUST AND MANTLE VISCOSITY IN MONGOLIA ». Journal of Geophysical Research: Solid Earth 108 (B10). doi:10.1029/2002JB002374.

Villaseñor, A., M. H. Ritzwoller, A. L. Levshin, M. P. Barmin, E. R. Engdahl, W. Spakman, et J. Trampert. 2001. « Shear velocity structure of central Eurasia from inversion of surface wave velocities ». Physics of the Earth and Planetary Interiors, Tomographic Imagining of 3-D Velocity Structure and Accurate Earthquake Location, 123 (2): 169‑84. doi:10.1016/S0031-9201(00)00208-9.

Walker, R. T., A. Bayasgalan, R. Carson, R. Hazlett, L. McCarthy, J. Mischler, E. Molor, et al., 2006. « Geomorphology and structure of the Jid right-lateral strike-slip fault in the Mongolian Altay mountains ». Journal of Structural Geology 28 (9): 1607‑22. doi:10.1016/j.jsg.2006.04.007.

Wei, S., E. Fielding, S. Leprince, A. Sladen, J.-P. Avouac, D. Helmberger, E. Hauksson. 2011. « Superficial Simplicity of the 2010 El Mayor-Cucapah Earthquake of Baja California in Mexico ». Nature Geoscience 4 (9): 615‑18. doi:10.1038/ngeo1213.

Wells, D., et K. Coppersmith. 1994. « New empirical relationships among magnitude, rupture length, rupture width, rupture area, and surface displacement ». Bulletin of the seismological Society of America 84 (4): 974–1002.

Wesnousky, S. 2006. « Predicting the Endpoints of Earthquake Ruptures ». Nature 444 (7117): 358‑60. doi:10.1038/nature05275.

Zielke, O., J. R. Arrowsmith, L. Grant Ludwig, et S. O. Akciz. 2012. « High-Resolution Topography-Derived Offsets along the 1857 Fort Tejon Earthquake Rupture Trace, San Andreas Fault ». Bulletin of the Seismological Society of America 102 (3): 1135‑54. doi:10.1785/0120110230.

Zielke, O., J R. Arrowsmith, L. G. Ludwig, et S. O. Akciz. 2010. « Slip in the 1857 and Earlier Large Earthquakes Along the Carrizo Plain, San Andreas Fault ». Science 327 (5969): 1119‑22. doi:10.1126/science.1182781.

Zielke, O., and J. R. Arrowsmith. 2012. « LaDiCaoz and LiDARimager—MATLAB GUIs for LiDAR data handling and lateral displacement measurement ». Geosphere 8 (1): 206–221.

Zielke, O., Y. Klinger, and R. Arrowsmith. 2015. « Fault Slip and Earthquake Recurrence along Strike-Slip Faults — Contributions of High-Resolution Geomorphic Data ». Tectonophysics 638 (janvier): 43‑62. doi:10.1016/j.tecto.2014.11.004.

## Figures

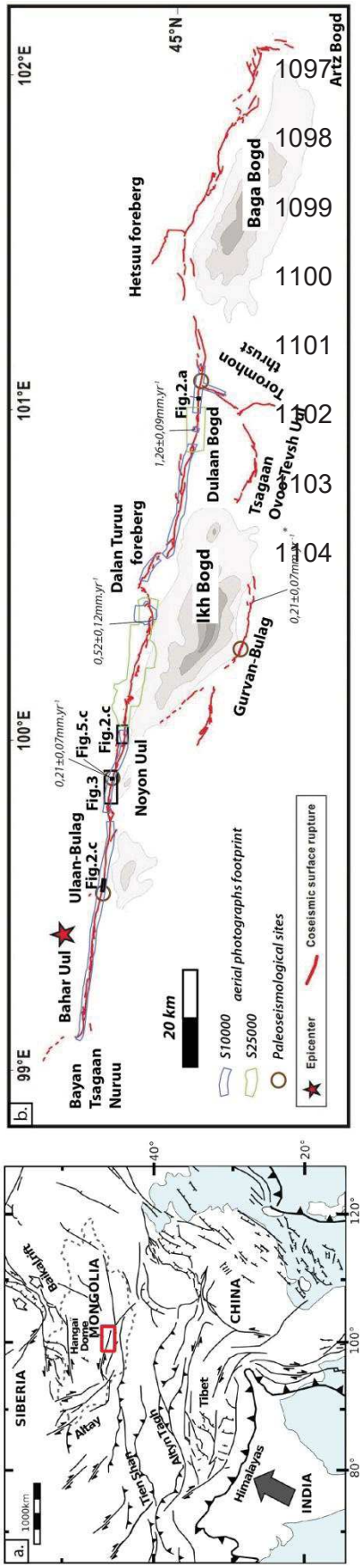


**Figure 3-1: General tectonic context, modified from Choi et al., (2012), Rizza et al., (2011) and Kurushin et al., (1997). a. Schematic map of the main active faults in central Asia. The red box shows the eastern part of the Bogd fault system. b. Surface ruptures associated with the December 4, 1957 M8 Gobi-Altai earthquake. Red star marks the epicenter (*USGS, M 8.1 – Central Mongolia, http://earthquake.usgs.gov/earthquakes/eventpage/iscgem887636#region-info*).**

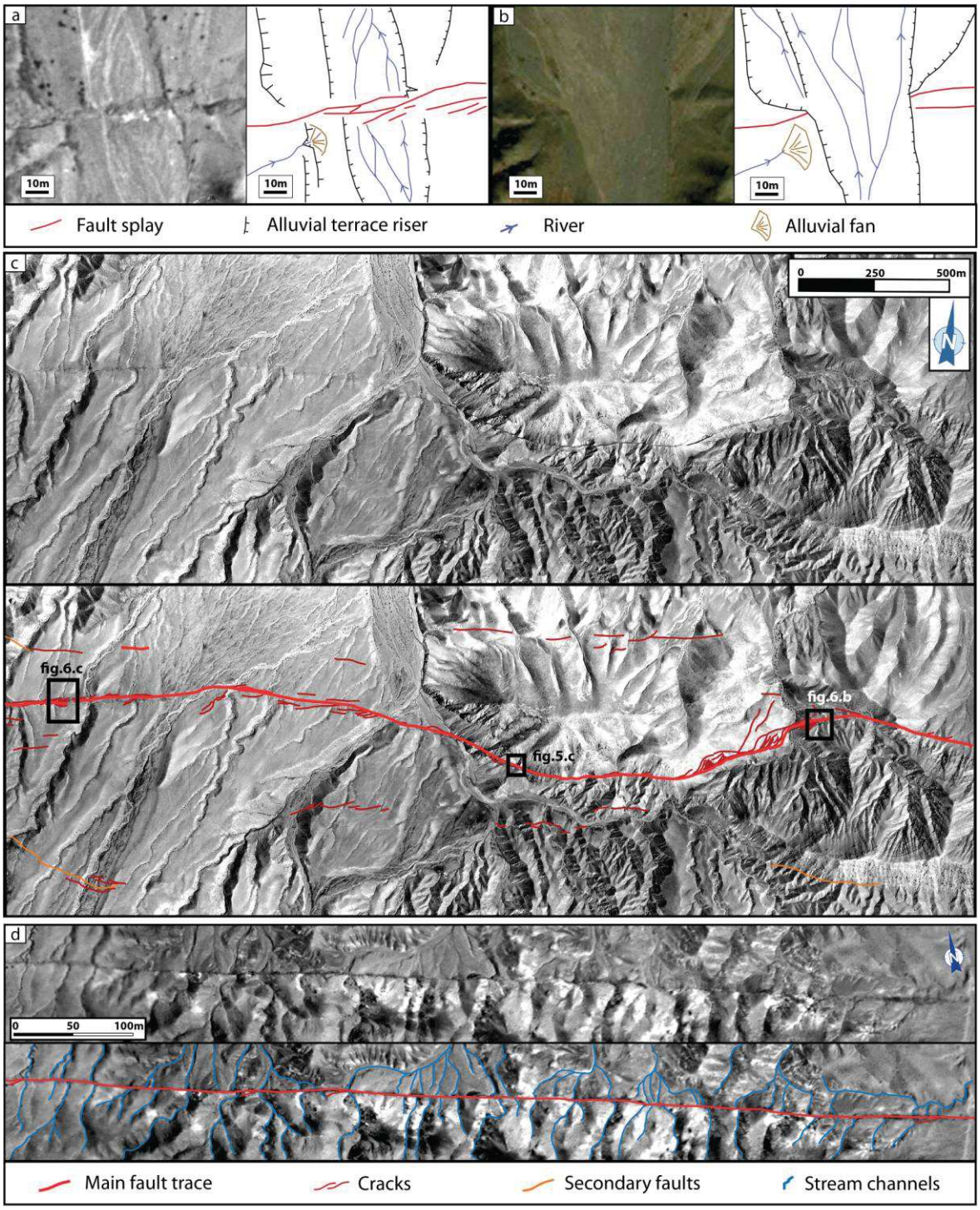


**Figure 3-2: Examples of the Gobi-Altai surface rupture observed on high-resolution aerial photographs and Bing satellite images (2013). a. Orthophotos derived from 1958 aerial photographs, (ground resolution 20 cm) and interpretation (Dulaan Bogd, segment (S10) N44.940°; E101.009°). b. Bing satellite images (70 cm resolution) and interpretation; same site as (a.). c. 1957 surface rupture within complex and distributed section (Egg Mountain, segment (S4), N45.102°; E100.000°). d. 1957 surface rupture within a straight, narrow fault section and morphotectonic interpretation (Ulan Bulag, segment (S2), N45.152°; E99.506).**

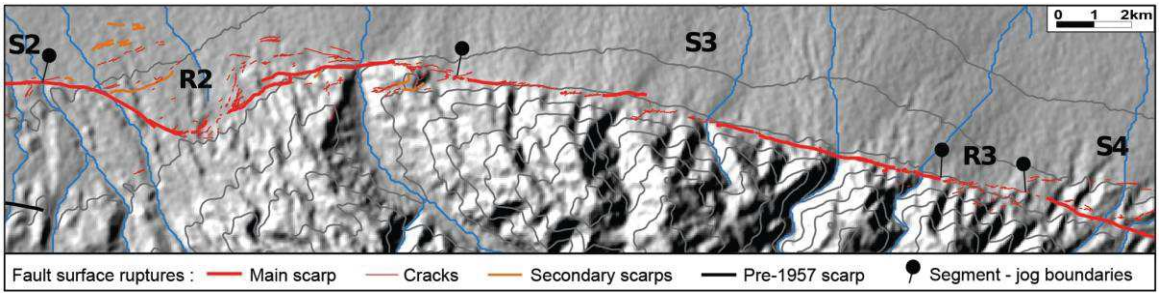


**Figure 3-3: Detailed mapping of the surface rupture along the segment S3 and relay zones R2 and R3 joining S3 with S2 and S4, respectively. Black pins are segment - jog boundaries, and solid grey lines are 100 m contour lines, Background is shaded-DEM from SRTM30.**

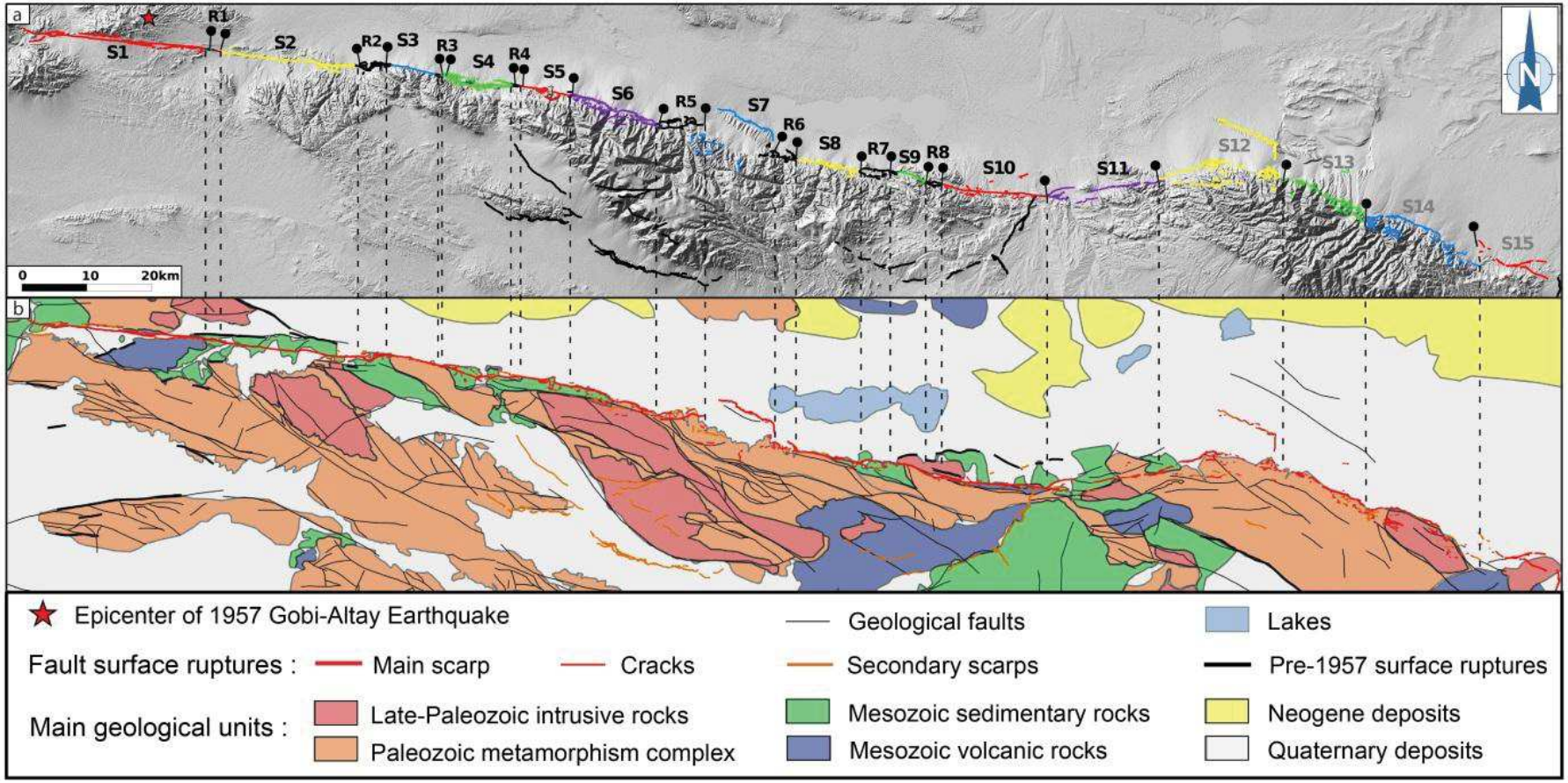


**Figure 3-4: Fault segmentation. a) Segmentation of the 1957 Gobi-Altai earthquake surface rupture. Colored lines are segments, black lines are jogs and secondary fault surface rupture. Topographic data are from SRTM30. b) Simplified geological map of the eastern Gobi-Altai modified from the Geological Map of Mongolia at scale of 1:200,000 (Institute of Geology and Mineral Resources, Academy of Sciences, 1998).**

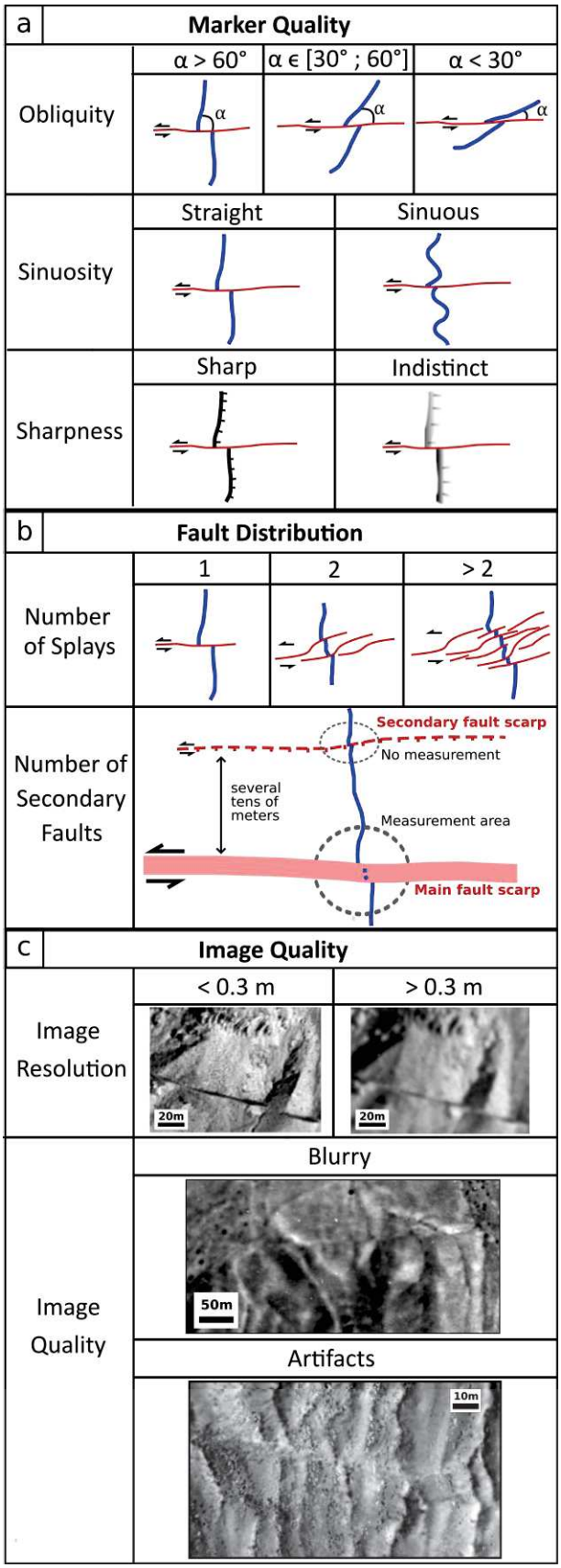


**Table 3-1: Weighting of offset measurements for evaluation. Best score is 10.**

| Sinuosity | Sharpness | α < 30° | α ϵ [30° ; 60°] | α > 60° | |
|---|---|---|---|---|---|
| Sinuous | Smouth | 0 | 1 | 3 | Total /5 |
| Sinuous | Sharp | 1 | 2 | 4 | |
| Straight | Smouth | 1 | 2 | 4 | |
| Straight | Sharp | 2 | 3 | 5 | |

| Fault distribution | Number of secondary faults | | | | |
|---|---|---|---|---|---|
| Number of fault splay | 0 | 1 | 2 | 3 | |
| >2 | 1 | 0 | -1 | -2 | Total /3 |
| 2 | 2 | 1 | 0 | -1 | |
| 1 | 3 | 2 | 1 | 0 | |

| Image quality | | Resolution | | |
|---|---|---|---|---|
| Neatness | Artifacts | < 30 cm | > 30 cm | |
| Neat | No | 2 | 1 | Total /2 |
| Neat | Yes | 1 | 0,5 | |
| Blurry | No | 1 | 0,5 | |
| Blurry | Yes | 0 | 0 | |

**Figure 3-5: Offset measurement evaluation criteria. 8 criteria for 3 main aspects of the fault measurements: a. Marker quality, b. Fault distribution and c. Image quality, see Figure 3-2c for location of "Image resolution" picture.**

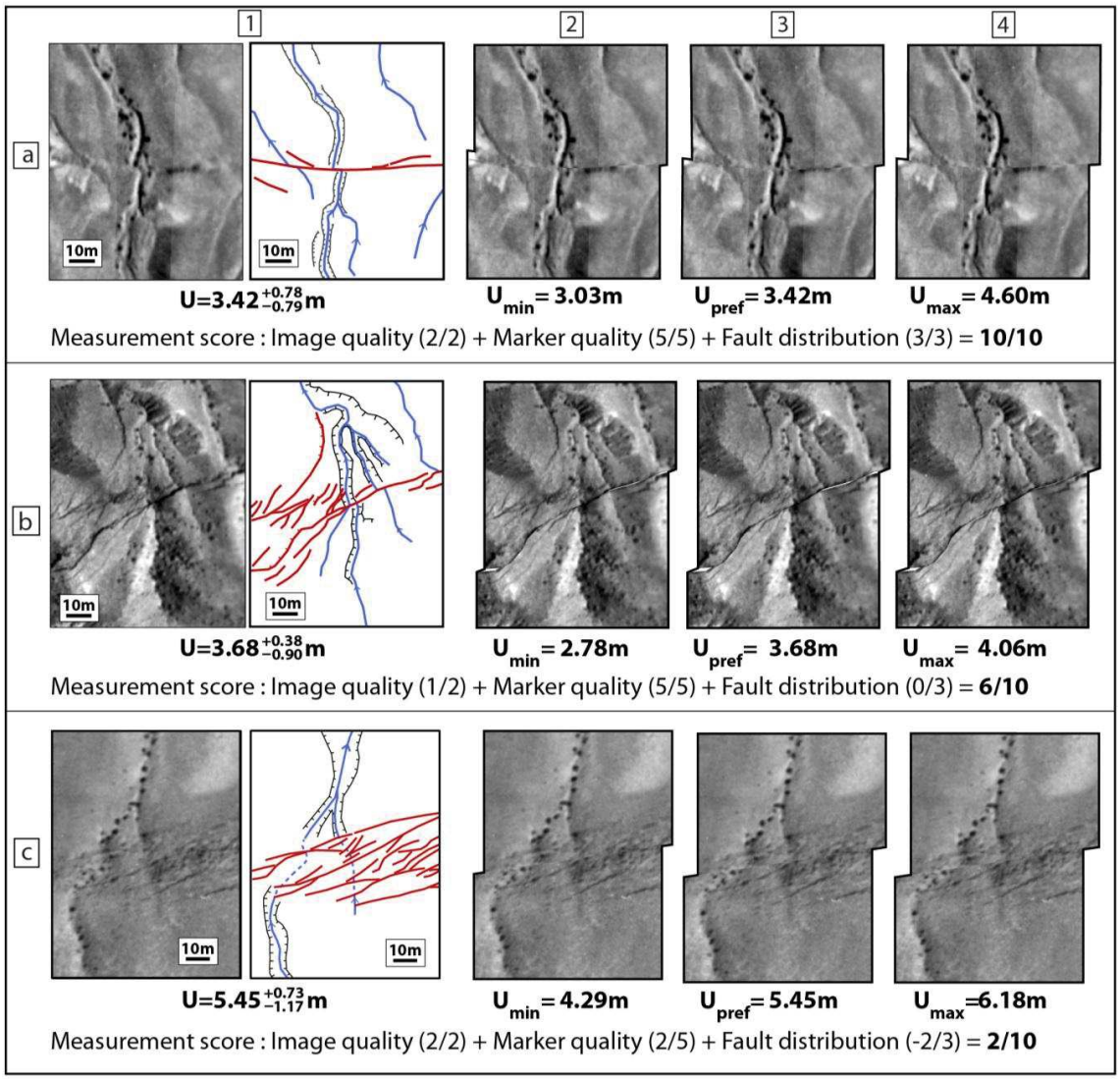


**Figure 3-6: Examples illustrating our methods of measuring and ranking horizontal offset geomorphic markers. Lines a, b and c correspond to good, average and poor quality measurements, respectively. Column 1 shows the marker in orthophotographs before retro-deformation and corresponding geomorphologic interpretation. Columns 2, 3 and 4 correspond to minimum, preferred and maximum offset values, respectively.**

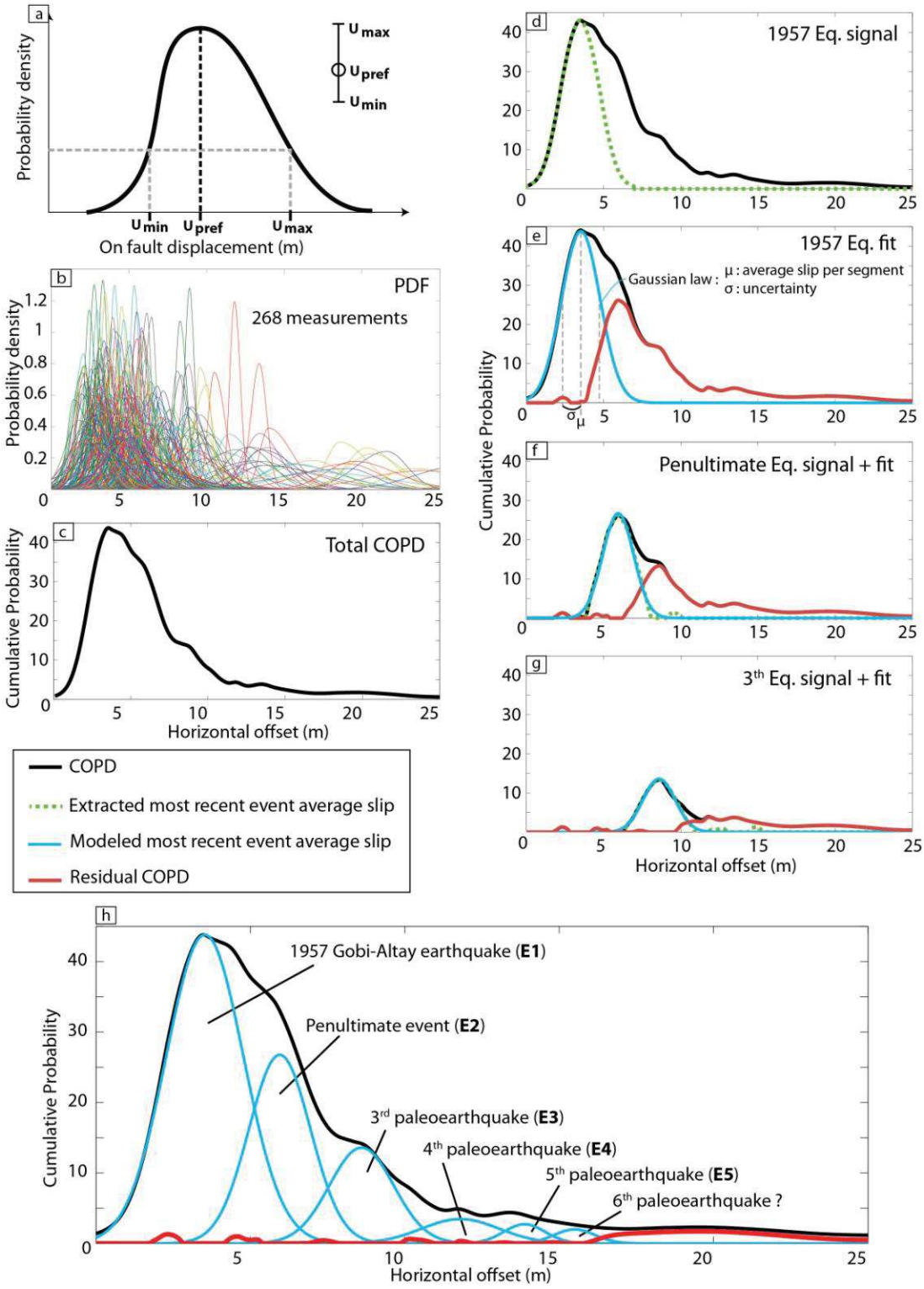


**Figure 3-7: Steps of the statistical analysis for one segment. a) Probability density function (PDF) corresponding to one offset measurement. Upper and lower uncertainties ($U_{max}$ and $U_{min}$ respectively) are used as standard deviations in an asymmetric normal law. b) Example of PDFs for one segment (S2). c) Corresponding cumulative offset probability density (COPD). d) Extraction of the 1957 surface rupture signal (green line), corresponding to the increasing of the COPD until its first maximum, and its symmetric decreasing. e) Modeling of the 1957 surface rupture by fitting the signal with a Gaussian curve (blue line). Red line is the residue of the COPD after subtracting 1957 slip model from the full segment COPD. f) Same process as c, d and e for the penultimate event, starting from the residual COPD. g) Idem for the pre-penultimate event. h) S2 full COPD and modeled slip for the 6 last surface ruptures. Red line is the final residue after 6 iterations.**

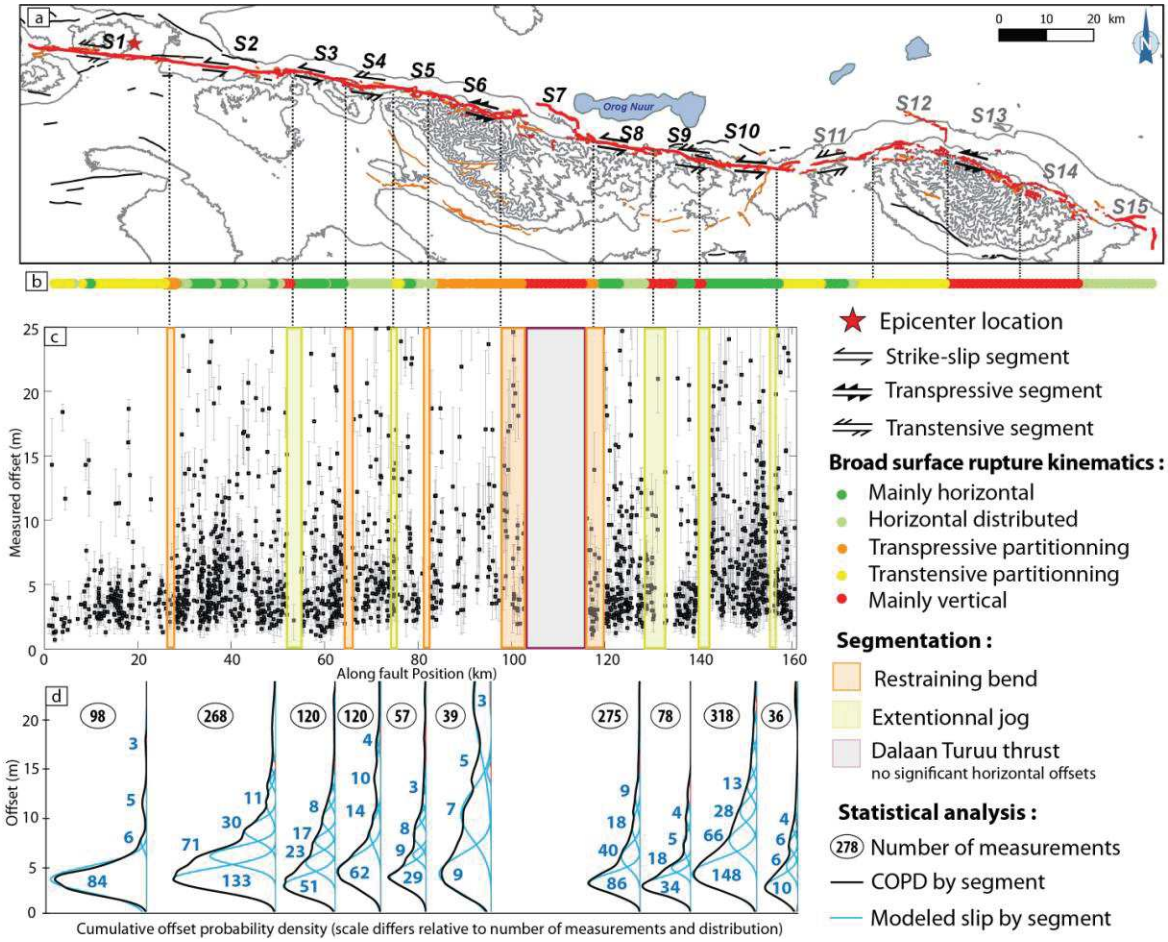


**Figure 3-8: Mapping, measurements and statistical results. a) Map of the 1957 Gobi-Altai earthquake's surface rupture and our proposed segmentation of the Eastern Bogd Fault. Main rupture strands in red. Secondary surface ruptures are in orange. Star shows epicenter location (*USGS, M 8.1 – Central Mongolia, http://earthquake.usgs.gov/earthquakes/eventpage/iscgem887636#region-info*). Contour lines are every 500 m. b) Main kinematics observed along the surface rupture. c) Horizontal slip distribution along the main fault. Color bars correspond to the relay zones. d) Cumulative offset density probability per segment (black lines) and modeled average slip (blues lines). Blue numbersindicate the number of measurements ranging to a maximum of 1σ from the mean of the Gaussian function for each derived slip. X-axis is normalized for for each individual COPD according to its maximum number of observation. Offsets and analysis on jogs are not shown.**

**Table 3-2: Computed offsets associated with the 1957 Gobi-Altai earthquake and cumulative offsets associated with three paleoearthquakes, according to our model. These values are shown graphically in figure 3-9. Uncertainties are 1 σ. ND: number of measurements within 1σ is less than 4 so the computed offset value is not shown. Discarded: discarded because of no distinction of paleoearthquakes average slips within errors.**

| Segment | $U_{mean}$ 1957 (E1) | $U_{cum}$ (E2) | $U_{cum}$ (E3) | $U_{cum}$ (E4) |
|---|---|---|---|---|
| S1 | 3.5 ± 1.3 | 7.5 ± 0.8 | 11.5 ± 1.3 | ND |
| S2 | 3.5 ± 1.2 | 6.0 ± 1.0 | 8.6 ± 1.0 | 11.8 ± 1.3 |
| S3 | 2.8 ± 1.1 | 5.2 ± 1.0 | 7.5 ± 0.8 | 9.8 ± 1.0 |
| S4 | 4.3 ± 1.6 | 8.4 ± 1.5 | 14.2 ± 2.3 | ND |
| S5 | 3.7 ± 1.2 | 6.1 ± 0.7 | 8.2 ± 1.0 | 10.1 ± 0.7 |
| S6 | 4.1 ± 1.9 | 10.4 ± 1.9 | ND | Discarded |
| S8 | 3.0 ± 1.0 | 5.9 ± 1.2 | 9.1 ± 1.4 | 12.4 ± 1.3 |
| S9 | 2.8 ± 0.9 | 4.7 ± 0.7 | 7.1 ± 1.2 | 10.0 ± 0.8 |
| S10 | 4.0 ± 1.6 | 7.6 ± 1.5 | 10.7 ± 1.2 | 13.4 ± 1.0 |
| S11 | 2.6 ± 1.1 | 4.9 ± 0.9 | 7.2 ± 0.8 | 9.0 ± 0.8 |

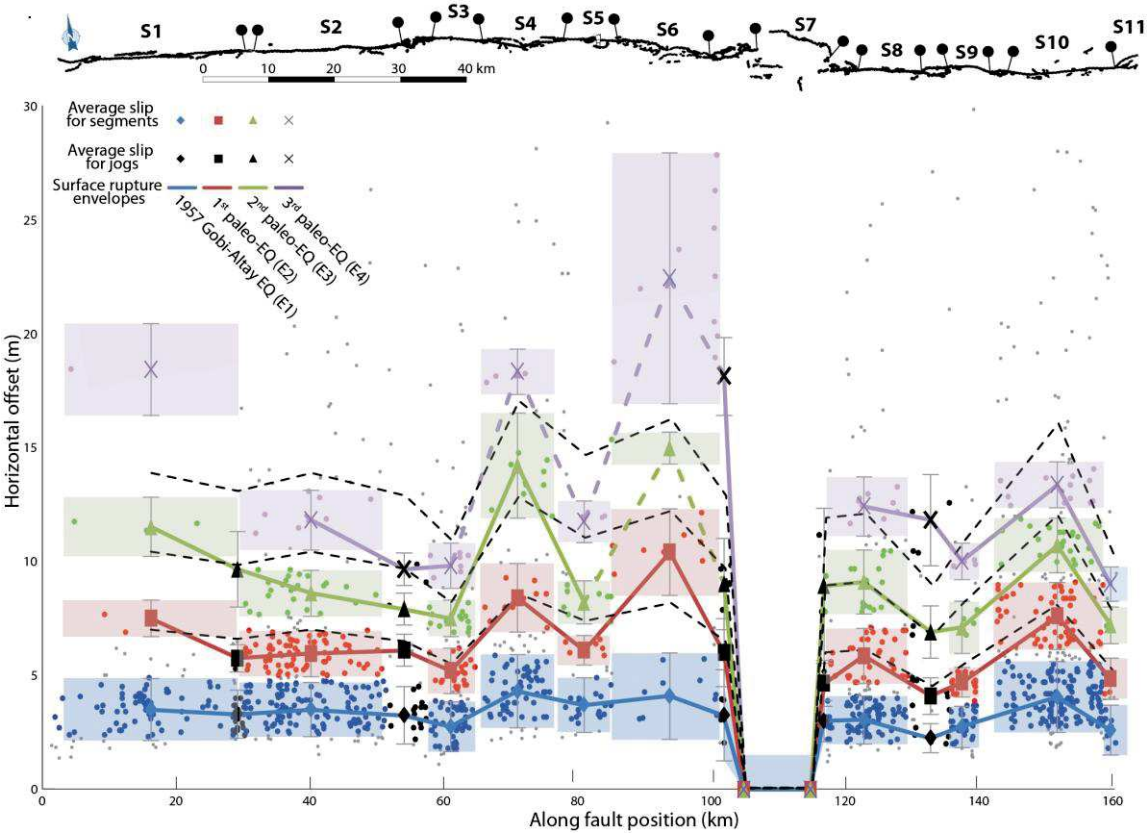


**Figure 3-9: Along fault horizontal slip functions, for lateral offset measurements with quality ranking ≥ 6/10, regarding to fault segmentation. Colored squares are average slip-per-segment, and color-shaded areas indicate the related uncertainties. Area length scales with segments length. Black symbols indicate the average slip on jogs. Colored lines link average slips on segments and jogs, and are dashed when ambiguous (see text for details). Colored dots correspond to lateral displacements associated with successive earthquake-slip functions within 1 σ of the average slip-per-segment. Grey dots are measurements out of 1σ from the average slip-per-segment. Black dashed lines are multiples of the 1957 earthquake horizontal slip distribution.**

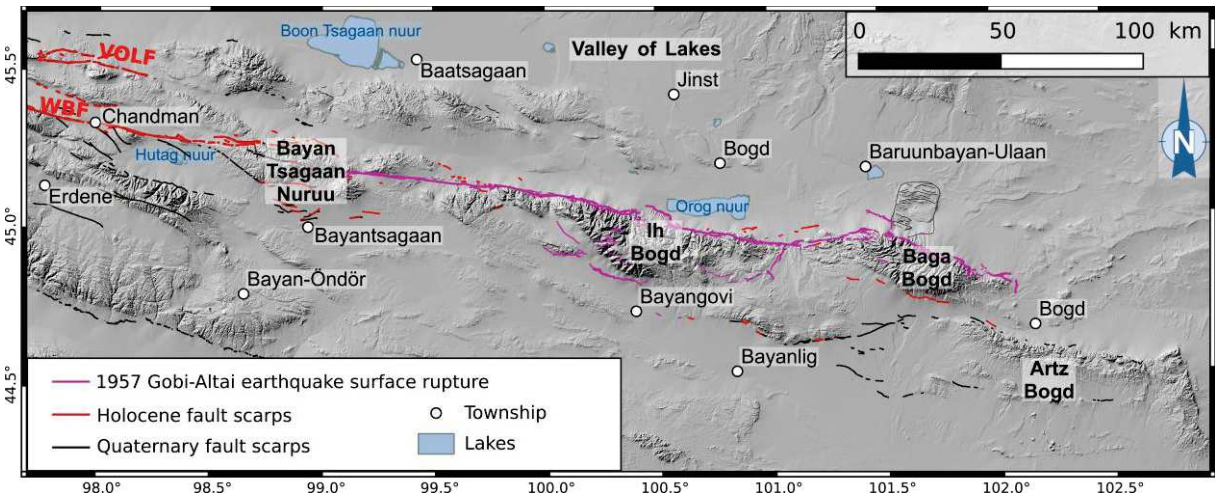


**Figure 3-10: Map of main fault scarps surrounding the Gobi-Altai surface rupture area, and main mountain ranges. VOLF Valley of Lake Fault ; WBF: Western Bogd fault. Background is shaded-DEM from SRTM30.**

# Chapitre 4. Late-Pleistocene - Holocene spatio-temporal distribution of seismic activity within the Western Gobi-Altai

This chapter constitutes an extensive draft for future publications of the morphotectonics and paleoseismological field survey and dating done in the Gobi-Altai area during this thesis. Consequently it is written in English and it briefly recalls the geological and active tectonics contexts of the area.

## I. Introduction

Identifying and characterizing active faults and their related surface-rupturing events is fundamental for understanding earthquake cycles and assessing seismic hazards.

Western Mongolia experienced an exceptional intraplate seismicity during the XXth century, with four Mw ≥ 7.9 earthquakes generated along several hundred kilometers long strike-slip faults associated to a transpressive kinematics (Khilko et al., 1985; Baljinnyam et al., 1993) : the Mw 7.9 and 8.3 Tsetserleg and Bolnay earthquakes, 14 days apart in July 1905, located in the Bolnay region (Schlupp and Cisternas, 2007; M. Rizza et al., 2015); the Mw 7.9 Fuyun earthquake, in August 1931, located in the Chinese Altai (Klinger et al., 2011); and the Mw 8.0 Gobi-Altai earthquake, in December 1957, along the eastern part of the Bogd Fault System, north-eastern Gobi-Altai (Florensov and Solonenko, 1965; Kurushin et al., 1998; Rizza et al., 2011) (Figure 0-1).

These large strike-slip faults are segmented and systematically associated to secondary reverse faults, which define restraining bends along which crustal uplift is driven (Bayasgalan et al., 1999b; Vassallo et al., 2007, 2007b). Morphotectonics surveys along these faults allowed characterizing them as slow slip rate faults with millimeter slip rates over periods of $10^4$ - $10^5$ yr (Ritz et al., 1995, 2003, 2006; Vassallo et al., 2007; Rizza et al., 2011, 2015), displaying several meters horizontal coseismic offsets that range from 2 to 5 m. (Vassallo et al., 2007; Ritz et al., 2006; Rizza et al., 2011, 2015; Klinger et al., 2011; Choi et al., 2012). Note that the these characteristics (low slip rate, characteristic slip distribution were also described or suggested along other strike-slip faults of Altai (eg Walker et al., 2006; Nissen et al., 2009; Klinger et al., 2011). Along the eastern Gobi-Altai (Bogd fault) and along the Bolnay fault, they are in agreement with paleoseismic

investigations showing that previous surface-rupturing events occurred with millennial return periods (Prentice et al., 2002; Ritz et al., 2009; Rizza et al., 2011, 2015).

The results altogether suggest that the four M8 events that occurred during the XXth century in western Mongolia was an exceptional crisis (e.g. Baljinnyam et al., 1993). This actually corresponds to a seismic cluster that repeats itself over time (Rizza et al., 2015). Mechanical coupling between main strike slip faults, involving stress loading through visco-elastic stress transfer in the upper crust has been proposed to explain these clustering phenomena (Chéry et al., 2001; Pollitz, et al., 2003; Vergnolle et al., 2003).

However, the four faults that ruptured during the XX century are not the only active faults in western Mongolia, and numerous others faults with quaternary fault scarp features have been documented in Mongolie (e.g. Khilko et al., 1985; Baljinnyam et al., 1993; Schlupp, PhD, 1996; Cunningham, 1998; Cunningham, 2013; Frankel et al., 2010; Gregory et al., 2014). In the Gobi-Altai, if numerous studies were carried out along the Bogd fault that ruptured in 1957 in the eastern Gobi-Altai (Figure 0-1) and several Holocene fault traces have been identified on the western Gobi-Altai (Baljinnyam et al., 1993; Schlupp, PhD, 1996) Nevertheless, only one field study (Mushkin, PhD, 2007) quantified fault scarp features associated with the active faults in the western Gobi-Altai.

In this study, using both morphotectonics and paleoseismology, we aim to characterize in time and space the seismic deformations that occurred in the western Gobi-Altai during the late-Pleistocene and the Holocene periods. We followed three axes (Figure 4-1):

1. Identifying the main fault traces, mapping and describing their geometry, distribution, kinematics and segmentation.
2. Determining the morphotectonical parameters of the identified faults: lengths, amount of coseismic offsets associated with major seismic events, long term fault slip rates.
3. Determining the ages of paleoearthquakes, their recurrence intervals and their magnitudes.

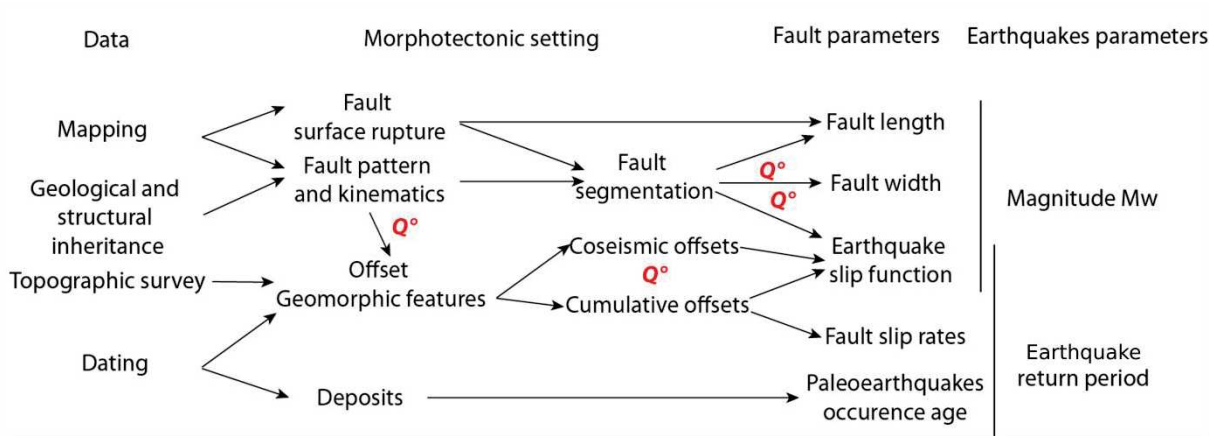


**Figure 4-1: Schematic approach carried in this study. Red questions are specific points discussed in this thesis.**

## II. Tectonic setting

Western Mongolia is experiencing intracontinental tectonics due to the northward propagation of the deformation related to the Indo-Eurasian collision (Tapponnier and Molnar 1979). This collision, initiated within the Himalayan front during the Eocene, successively generated orogenesis in central Asia in the Kunlun Shan, then Tien Shan, and finally the Altai and Gobi-Altai mountain ranges since the Late-Miocene-Pleistocene (Tapponnier et al., 2001). These late Cenozoic deformations reactivated ancient shear zones, distributing the deformation on large transpressive strike slip faults (Vassallo et al., 2007; Cunningham, 2013). Apatite fission tracks analysis on the main Gobi-Altai reliefs suggest that the uplift started 5 ± 3 Ma ago (Vassallo et al., 2007).

The Gobi-Altai area has undergone a multi-stage geological history, punctuated by: i. Cambrian to Permian amalgamation of Neoproterozoic Altaids terrane collage, evolving several ocean closure events with both north and south dipping subduction zones, widespread accretionary arcs and magmatism (e.g. Sengör, et al., 1993; Badarch et al., 2002; Lehmann et al., 2010); ii. tectonic quiescent period in Triassic to early-Jurassic, associated with granitic plutonism and foreland sedimentation (e.g. Traynor and Sladen, 1995; Lamb et al., 1999; Kozlovsky et al., 2015); iii. Late-Mesozoic alternations of erosional and intracontinental deformation, contractional during early--mid-Jurassic (e.g. Traynor and Sladen, 1995; Zorin et al., 1999; Lamb et al., 2008) and extensional during late-Jurassic to Cretaceous (Graham et al., 2001; Johnson 2004; Cunningham et al., 2009; van Hinsbergen et al., 2015); iv. quiescent period during Paleogene (e.g. Traynor and Sladen, 1995; Jolivet et al., 2007; Cunningham 2010); v. intraplate crustal reactivation in sinistral transpressional mode, with limited volcanism and mountain building (Tapponnier et Molnar 1979; Baljinnyam et al., 1993; W. D. Cunningham 1998; Calais et al., 2003; Vassallo et al., 2007).

Seismicity across Mongolia during the last century highlights the major ruptures of the XXth century (Figure 1-3), especially in the Gobi-Altai (Figure 4-2) where microseismicity mostly locates around the 1957 Gobi-Altai fault surface rupture (Adiya et al., 2003; Cunningham 2010; Radziminovich et al., 2016). During the period between 1964 and 2010, small to moderate earthquakes can still be noticed in the western Gobi-Altai, especially on the westernmost part of the Chandmani Valley (between WBF and VOLF in Figure 0-1 ; Figure 4-2), where few moderate earthquakes of magnitude Mw 5.0 – 5.9 occurred in 1996, followed by two events with magnitudes Mw 6.0 and 6.9 on June 15th 2006, and one Mw 4.9 on the April 14th 2007 (Cunningham, 2013; Radziminovich et al., 2016). A minor cluster might be also identified in the Khaliun region (Figure 4-2), on central part of the Tsagann Gol Fault (TGF). Another seismic cluster can be identified on the southernmost junction with the Altai Mountains. Instead, seismicity within the southern part of the Gobi-Altai – out of the Bogd Fault System – displays little and sporadic seismicity (Figure 4-2).

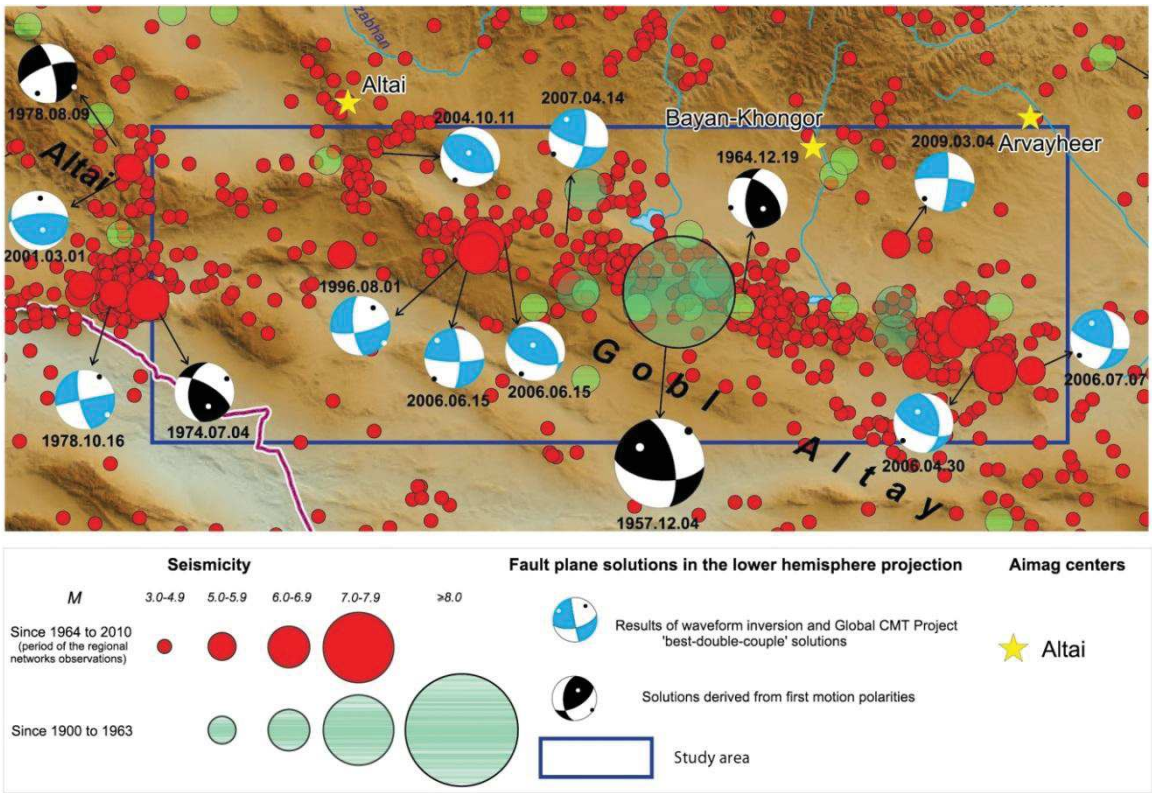


**Figure 4-2: Seismicity of the Gobi-Altai, modified from (Radziminovich et al., 2016).**

Only few geodesic data are available in the literature to constrain the deformation rates in the Gobi-Altai (i.e. Calais et al., 2003; Vergnolle et al., 2003), and although vector directions are consistent with observed fault kinematics (i.e. transpressive left-lateral), there is no estimate of the geodetic- slip rate across the Bogd Fault System (BFS).

The two main strike slip faults described to produce Holocene surfaces ruptures in the Western Gobi-Altai (Baljinnyam et al., 1993; Schlupp, PhD, 1996) are: i. the Myangain rupture, named Valley of Lakes fault (VOLF) in this study, and ii. the Chandmani fault, named here the Western Bogd fault (WBF). Concerning the eastern Gobi-Altai, a review of the morphotectonics setting along the Easter Bogd Fault (EBF) is detailed in chapters 1 and 3 of this thesis.

As detailed in Chapitre 1, Mushkin (PhD, 2007) carried out an extensive field survey of the Gobi-Altai and suggested that the seismic deformation migrated from south to north since the Late-Pleistocene. Chronologically, three areas were defined: a southern one that was active before the Late-Pleistocene, a central one that was active during the early Pleistocene, and an eastern one where the deformation is presently fully localized: the Bogd Fault System, on the northern bound of the mountain range.

## III. Material and methods

### III.1. Mapping

#### *III.1.1. Data*

In order to identify and characterize the Pleistocene and Holocene fault surface ruptures, we carried detailed mapping (1: 2000) using high resolution satellite images covering the whole Gobi-Altai mountain range. Mapping was done using freely available satellite images (Google Maps and Bing dataset), as well as panchromatic SPOT 5, 6 and 7 satellite images. Resolution of free dataset is variable, from 0.7 m to 2.5 m when well resolved, up to 15 m when no new images have been uploaded recently. During mapping, we switched the source of images (i.e. from Google Maps to Bing and *vice versa*), in order to optimize our mapping depending of the images resolution and quality (e.g. light, nebulosity, sun orientation, season, etc.). This approach allows mapping of almost all parts of the Gobi-Altai. If locally, within few hundreds of meters, there was no high resolution satellite image available, mapping was done only if the fault scarp was obvious; conversely we did not map it. Resolutions of SPOT images are 2.5 m for SPOT 5, and 1.5 m for SPOT 6 and 7.

Additionally, we carried out field surveys on selected sites for detailed surface rupture mapping, and acquisition of topographic and UVA aerial photographs DEMs (see Chapitre 2).

### *III.1.2. Surface rupture criteria*

Identifying recent surface ruptures is obvious when fault traces are cutting through modern alluvial fans. This is trickier when the surface rupture is located within bedrock in mountainous terrains. In order to have a systematic approach for identifying surface ruptures, we defined ahead some criteria. Firstly, the surface rupture must clearly affect some late-Pleistocene alluvial deposits in the area. Secondly, in the case of strike-slip fault and in particular when the fault is running into bedrock devoid of late Pleistocene deposits, the fault trace must be associated to systematic offsets of alluvial features. We particularly cared to take in account geomorphic processes like channel capturing, stream deflection or presence of seismic-related landforms, such as pressure ridges, sag ponds or mole track fault patterns, which may affect the hydrological network and enhance our ability to assess the fault location and motion. In the case of dip-slip motion, we considered especially the resumption of incisions by differential erosions between both sides of the fault. Thirdly, we paid particular attention to the cumulative deformation along the fault, like offsets of main drainages in the case of strike slip sections, or uplifted and subsided surfaces in the case of oblique and dip-slip fault sections (Figure 2-2).

From these criteria and field investigations, we consider three classes of fault surface ruptures:

1. The Holocene surface ruptures, red on maps, which present either an instrumental seismic activity, or some field geomorphic evidences concluding to an Holocene activity.
2. The late-Pleistocene to Holocene surface ruptures, orange on maps, which display on satellites images evidences of recent activity, either affecting various stages of late-Pleistocene formations, or displaying a strong continuity in the landscape.
3. The Pleistocene surface ruptures, yellow on maps, which although presenting a continuity at large scale (1 : 20 000) and offsets in remnants of major Pleistocene fans, do not present systematic offsets in landforms (neither in late-Pleistocene nor in bedrock outcrops), or are strongly related to geological heterogeneities, for instance dikes or bedding. Hence, some segments might be shown with various colors, if several fault traces show different criteria.

A specific attention is devoted for not confusing fault traces with not seismic-related features in the landform, such as lithological heterogeneities or anthropic features (roads of walls). In fact, some dikes produce lineaments in the landscape, often associated to hydrological network disturbances, which may look as lateral or vertical offsets. In

several places, dikes or lithological lineated features (e.g. very elongated outcrops, often obviously related to faulting, but not necessary to quaternary one) are associated to fault surface rupture, which makes the discrimination between lithological and seismological features arguable. At first order, roads are easy to identify, but looking carefully, some of them, and especially in locations bordering main reliefs, could be confused with fault traces associated with reverse faulting (Figure 2-2). This makes sense if we consider that Mongolian drivers are looking for ramps in order to come down and go up from the uncountable talwegs they have to cross when following alluvial fans: fault scarps are places of stronger erosion due to fracturing, often leading to smoother risers of the talwegs. Eventually when there is some confusion of fault traces with lithological or anthropological features, fault scarps are mapped discontinuously, only where they are directly linked to unambiguous evidences of faulting within late-quaternary features.

#### *III.1.3. Segmentation criteria*

For each main surface rupture that we identified, we describe its segmentation from geometric and kinematic criteria. A segment is defined by homogeneous surface rupture pattern, fault motion and distribution within its whole length. It is delimited by the occurrence of discontinuities, which could be kilometer-scale relay zones (as well named jogs and bends), changes in the fault strike, or (and) important branching. Identification of fault patterns, relays and branches is carried out through analysis of previously detailed mapping, assuming that relays present a stronger distributed surface rupture pattern (e.g. restraining bends, pull apart basins, conjugated faulting) than segments, and are typically shorter. Finally, the faults Tip Zones (TZ) are defined as sub-segment describing specific fault pattern (i.e. in our case of left-lateral faulting: right shifts with reverse faulting, or horsetail patterns associated with left shifts of the fault trace), terminating main strike slip fault traces.

### III.2. Coseismic offset assessments

In order to estimate the coseismic offsets related to past earthquakes, we carried out high resolution topographic surveys of fault sections presenting abundant laterally offset geomorphic features, and systematic measurements of both single and cumulative displacements recorded by the offset landforms. Additionally, we applied a statistical treatment (using the '*COPD approach'*) described in Chapitre 3.IV.2 to identify and quantify the coseismic displacements generated by successive surface rupturing earthquakes on a unique fault segment or section.

Microtopographic surveys were carried out using Terrestrial Laser Scanning (TSL) when appropriate and available, Kite Aerial Topography (KAT), or UVA survey. Data were then

post-processed and georeferenced. In addition to orthophotographs and DEMs, we generated hill-shaded-, slope-, slope direction- and profile curvature-maps, which allowed us better defining the geomorphic features lineaments used in offset measurements (Figure 2-6).

The offset measurements were done following the 3-steps retrofit method developed in the previous chapter (Chapitre 3.IV.2), which consists first to identify the piercing lines corresponding to the offset geomorphic features and to derive the along fault corresponding piercing points, and secondly to make three retrofitting measurements: one is the preferred marker reconstruction according to the piercing marks, a second corresponds to the maximum retrofit that the marker could reasonably fit, and the third one corresponds to the minimum. In order to minimize the close-fault geomorphic disturbances (e.g. fault distribution, marker sinuosity, post-deformation stream deflection, etc.), piercing lines related to the landforms were defined considering at least a distance of 20 meters on both sides of the fault. We considered that this approach allowed assessing the uncertainties inherent to the offset measurements with relevance, by defining the end-members positions that the marker could fit.

Additionally, we evaluated the quality of the offset marker with respect to its proneness for offset measurement, regarding to the fault distribution, the marker geometry, and the image quality. Following the approach detailed in Chapitre 3.IV.2.1, we defined weighted quality criteria, in order to provide a scoring of the offset measurements quality: the marker sinuosity (vs straightness, arbitrary defined as sinuous or straight), its sharpness (ability to identify landform lineaments), its obliquity regarding to the fault, the fault distribution (number of fault splays within the measurement area and presence of secondary faults out of the measurement zone), the occurrence of artefacts or missing data in the microtopographic dataset, and finally our ability to relevantly fit the geomorphic lineament composing the marker. Total scoring is rated on 10 points (Figure 3-6), and weighted as follow: sinuosity and sharpness are rated on 2 points ; obliquity regarding to the fault strike is defied by three classes following Salisbury et al. (2015): < 30°, 30° - 60°, >60°, rated respectively to 1, 2 and 3 points ; fault distribution is rated on 2 points, accounting for fault cracks and secondary traces ; finally artefact presence and ability to relevantly retrofit the geomorphic marker is rated on 3 points.

Alike in Chapter 3, when datasets are sufficiently consistent along a fault section (> 4 offset measurements), we computed the Cumulative Offset Probability Density (COPD) and applied an empirical model to extract average slips related to successive past earthquakes as briefly reminded ahead (Figure 3-7). Firstly, each offset measurement

and related uncertainties were converted in a Probability Density Function (PDF, i.e. an asymmetric normal law centered on the preferred value, accounting for asymmetric uncertainties (minimum and maximum offset values) with a 2σ standard deviation. We chose here, unlike in the EBF study (Chapter 3), to consider the offset estimates in their 2σ standard deviation, given the higher resolution dataset used to carry out the measurements (i.e. at least 10 cm resolution orthophotographs and 20 cm resolution DEMs, versus 20 cm resolution orthophotographs associated to noisy DEMs in Chapter 3). Secondly, for a given fault section, all PDFs were stacked in order to compute the COPD. Thirdly, the average slip related to the most recent surface rupturing seismic event was extracted, assuming that: i. it corresponds to the higher cumulative probability exhibited by the COPD (its maximum), ii. all cumulative probability of smaller offsets are exclusively related to it (i.e. the portion of the COPD inferior to is maximum), and iii. its signal follows a Gaussian shape function. Hence, we extracted this last-cited slip function using the maximum of the COPD as a mean, and the increasing part of the COPD (left part from maximum) as representative of the 1σ average slip assessment uncertainty. Afterward, we subtracted the slip signal related to the most recent surface rupturing earthquake to the whole COPD, to generate a residual COPD that we assumed to be representative of the slip recorded in the landform before the most recent event. Starting from the residual COPD, we perpetuated iterations of the process, which allowed us, depending on the consistency of the dataset and on slip amplitudes, to assess the average slip per event through three to four seismic cycles.

Results are analyzed along each fault section for both the whole dataset and two subsets defined by selection of best-rated offset measurements, in order to discuss the variability of the signal and the robustness of the computed average slips.

Note that this approach is propagating large uncertainties, and that results consequently yield a first order statistical assessment of the number and amount of successive coseismic displacements, produced in surface on a fault, and recorded by the landforms. Especially, due to rather large uncertainties in estimating average slips, we didn't expect to identify moderate seismic events (typically generating < 1 m lateral offsets).

Eventually, high resolution topographic data allowed estimating some vertical offsets. Although vertical offset measurement was systematically done along the Gobi-Altai active faults, we documented them when appropriate. Vertical offset measurements are done on fault-transverse profiles, projecting surface topography through the fault zone, and taking care to image the topography on several tens of meters on both sides of the fault. Measurement are assessed with respect to the vertical axis, on both upper and

lower extreme positions the fault might stand. We used the average value as the offset measurement, and extreme values as uncertainties.

### III.3. Slip rates

In order to determine the slip rates along the main surface ruptures of the western Gobi-Altai, we looked for cumulative offset geomorphic features prone to be dated by $^{10}$Be or OSL techniques. The approach consisted firstly to carry out a microtopographic survey in order to assess the offset, and then to sample the most preserved part of the geomorphic feature, for estimating its abandonment (with $^{10}$Be) or depositional age (with OSL). The ratio between offset and age yielded the slip-rate.

#### *III.3.1. Cumulative offset measurements*

A high resolution topographic survey (5 cm to 20 cm resolution) has been done for each site where we aimed to determine the fault slip rates. Measurement of offset for slip rate computation was done by 3-steps retrofit of the landforms, from high resolution orthophotographs, coupled to topographic dataset and derived analysis, such as for instance DEMs hill-shade, terrain curvature, and slope direction (Figure 2-6). Then, for the slip rate estimate, we used the preferred alignment value and an average value of both upper and lower uncertainties.

The geomorphic context of the deposition and abandonment of the offset landform regarding to the fault motion has to be assessed in order to determine whether the measured slip was post-dating or predating the age of abandonment of the feature. For instance, the offset recorded by a terrace riser situated downwards a dated terrace corresponds to a minimum offset since the abandonment of the terrace. This is because we do not have constraints of the time-span between the abandon of the terrace and the beginning of the offset within the riser. On the other hand, following the same line of reasoning, the offset recorded by the riser situated upwards a dated terrace corresponds to a maximum offset since the abandonment of the terrace (some displacements may have affected the upwards riser while the river bed was still running along it) (cf. Chapitre 2.I.4.1 for details). Consequently, the resulting slip rates have to be considered as minimum and maximum values, respectively.

#### *III.3.2. Dating of geomorphic features*

To date the geomorphic features, we used cosmogenic $^{10}$Be (see details in Chapitre 2.I.4.2.1). $^{10}$Be analyses have been carried in CEREGE, in collaboration with Régis Braucher, who supervised the chemical process, and attended to the data modeling using Hidy et al. (2010) software.

Chi-square inversions of $^{10}Be$ profiles have been done using the parameters (disintegration time and effective attenuations) presented in Table 3:

**Table 3: Decay constant and effective attenuations used for $^{10}Be$ dating (Braucher et al., 2011; Borchers et al., 2016).**

| | |
|---|---|
| $^{10}Be$ Half life (yr) | 1,39E+06 |
| Lambda $^{10}Be$ | 4,997E-07 |
| $L_n$ (g.cm$^{-2}$) | 160 |
| $L_{\mu 1}$ (g.cm$^{-2}$) | 1500 |
| $L_{\mu 2}$ (g.cm$^{-2}$) | 4320 |
| $P_{0\ SLHL}$ (at.$^{-1}$g.yr$^{-1}$) | 4.02 |

Lambda : $^{10}Be$ radioactive decay constant.

L: effective attenuations for n, neutrons; $\mu_1$, slow muons; $\mu_2$, fast muons.

$P_{0\ SLHL}$: sea-level, high-altitude (SLHL) production rate.

### III.4. Paleoseismology

Paleoseismic investigations have been carried out in fault-transverse trenches, following the approach described in Chapitre 2.II.2.

We used radiocarbon dating of charcoal and organic materials from sediment (bulk sample), analyzed in the LMC14 lab, as well as optically stimulated luminescence (OSL) for dating units (see details in Chapitre 2.II.3). Whole 14C ages are summarized in Annexe II.

The OSL dating have been realized either by Shanon Mahan (samples from Valley of Lakes Fault), USGS (Annexe IV), or by Markus Fuchs and Suzann Zielker (samples from the Western Bogd Fault), University of Gießen (Annexe III).

# IV. Results

In this section, we first present the main fault traces that we identified within the western Gobi-Altai, and give an overview of their location, and kinematics (sense of motion). This overview is mainly based on high resolution satellite images. Then, for each active fault identified, we give a detailed description of the surface rupture, and its segmentation. For more detailed viewing, '*kml'* files of fault traces are given in supplementary materials. In a third step, based on field survey, we analyze the slip distribution, the slip rate, and the paleoseismicity.

## IV.1. Main surface ruptures of the Gobi-Altai mountain range

Based on the mapping survey, six main Late-Pleistocene - Holocene surface ruptures have been identified within the Western Bogd fault system (Figure 4-3). Three of them are major left-lateral strike-slip faults more than 100-km long: the *Western Bogd Fault* (WBF), the *Valley Of Lakes Fault* (VOLF), and the *Tsagaan Gol Fault* (TGF). Two other faults are dip-slip faults,~30 km-long: the North-Chandmani Valley thrust Fault (NCVF), and the Tsogt normal fault. The 6$^{th}$ active fault we identified is the South Gichighiy Nuruu Fault (SGNF), which corresponds to a couple of discontinuous thrusts, totalizing ~150 km in length (Figure 4-3).

The WBF corresponds to the direct prolongation to the west of the Eastern Bogd Fault (EBF). The connecting region between these two faults shows a complex distributed surface ruptures pattern, defining a classical flower structure geometry (e.g. Cunningham et al., 2003; Vassallo et al., 2007), around the ~40 km wide Bayan Tsagaan range restraining bend. (Figure 4-3).

The VOLF is situated ~20 km north of the WBF and both faults strike N095°E, with azimuth variations of ± 15° at kilometer scale. The area located between these faults is composed of two distinct geomorphic regions: 1) to the NE set reliefs that are composed of mostly Néoproterozoic metamorphic rocks and late Paleozoic granites; 2) to the SE sets the Chandmani Valley that is filled out by quaternary fanglomerates (Figure 4-5). The N110 ± 5°E trending NCVF is a rather continuous north-dipping reverse fault precisely located on the boundary between these geomorphic domains, standing 5 km north of the Chandmani town and likely connecting at depth the VOLF strike-slip fault.

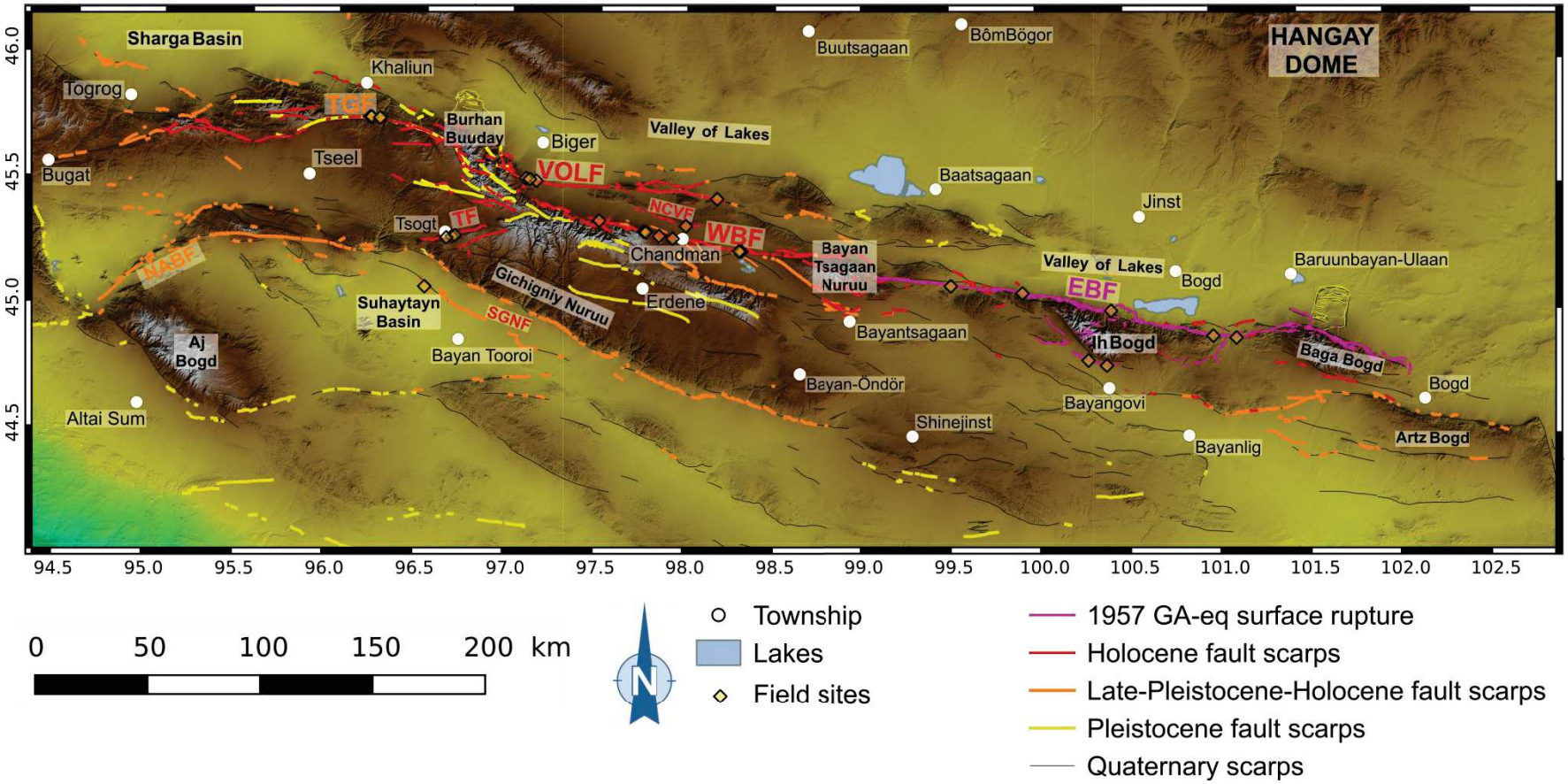


**Figure 4-3: Active faults of the Gobi-Altai. EBF, Eastern Bogd fault; WBF, Western Bogd Fault; VOLF, Valley Of Lakes Fault; TGF, Tsagaan Gol Fault; NCVF: North Chandmani Valley Fault; TF, Tsogt Fault; SGNF, South Ginigniy Nuruu Fault; SCF, South Chandmani Fault. Background: color panel of SRTM Topographic dataset.**

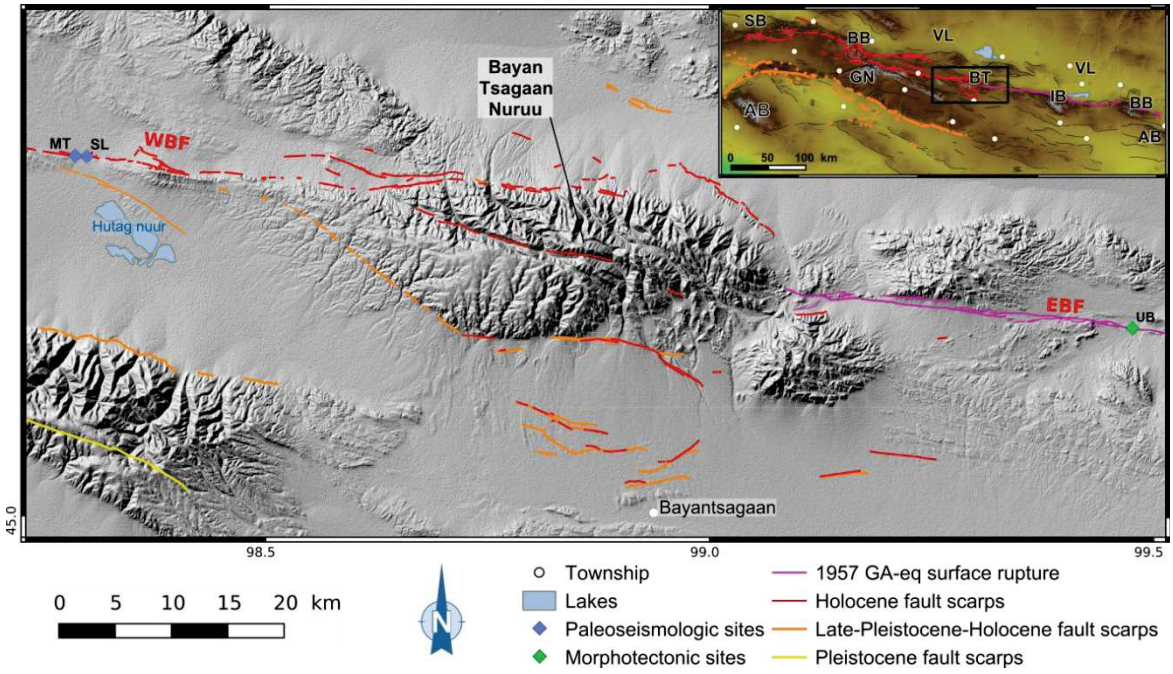


**Figure 4-4: Active faults map of the Bayan Tsagaan Nuruu area. Faults Abbreviations: EBF, Eastern Bogd fault; WBF, Western Bogd Fault. Field sites abbreviations: MT: Moskito Trench; SL: Swan Lake trench; UB: Ulaan Bulag. Background is a hill-shading of the SRTM Topographic dataset. Insert abbreviations: SB: Sharga Basin, BB: Burhan Buuday; VL: Valley of Lakes; GN: Gichigniy Nuruu; BT: Bayan Tsagaan; IB: Ih Bogd; AB: Artz Bogd.**

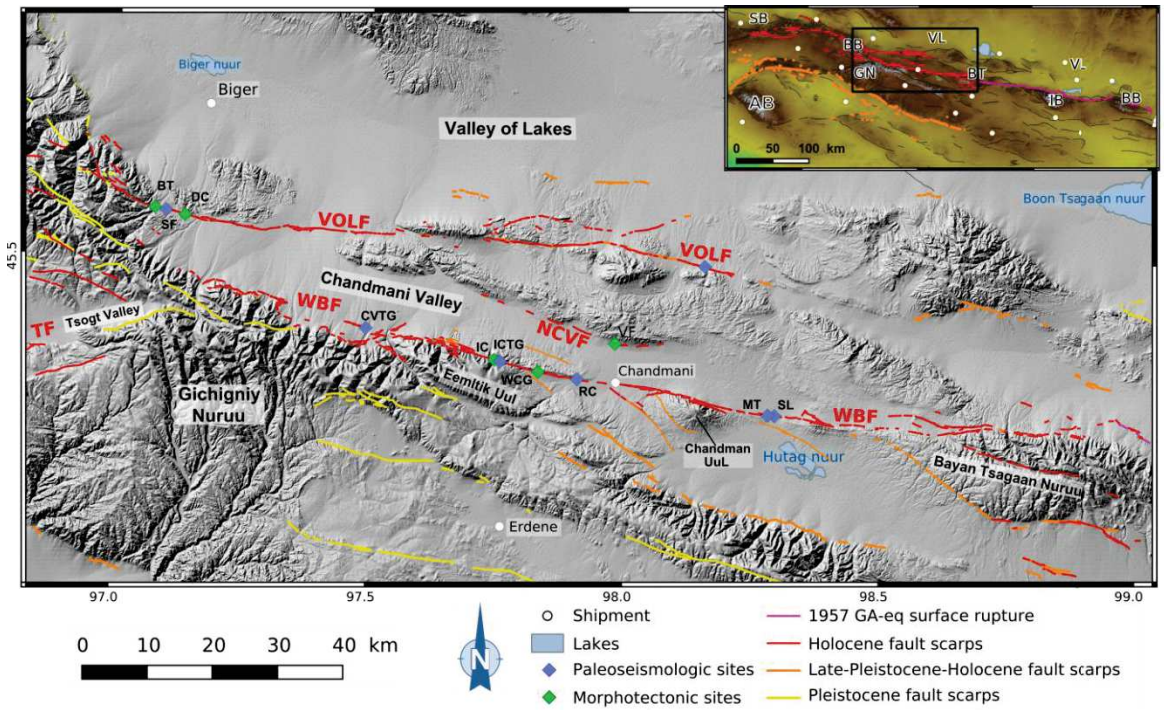


**Figure 4-5: Active faults of the Chandmani Valley region, bounded by the WBF and the VOLF. Faults abbreviations: VOLF: Eastern Bogd fault; WBF: Western Bogd Fault; TF: Tsogt fault; NCVF: North Chandmani Valley fault. Field sites abbreviations: BT: Biger Terraces; SF: Storm Creek; DC: Dark Creek; CVTG: Chandmani Valley Tension Gash; IC: Ice Creek; ICTG: Ice Creek Tension Gash; RC: Rain Creek; MT: Moskito Trench; SL: Swan Lake trench. Background is a hill-shading of the SRTM Topographic dataset. Insert abbreviations: SB: Sharga Basin; BB: Burhan Buuday; VL: Valley of Lakes; GN: Gichigniy Nuruu; BT: Bayan Tsagaan; IB: Ih Bogd; AB: Artz Bogd.**

The Tsogt fault is an intra-mountainous normal fault, striking N075 ± 15°E, and located south-west of the WBF western tip-zone (Figure 4-6). Preserved peneplain allows estimating a minimum quaternary cumulative scarp of 400 to 700 m along the Tsogt fault according to Mushkin (PhD, 2007), without accounting the sedimentary infill that accumulated at the base of the fault. This fault is, consequently associated to an intra-mountainous asymmetric valley, oriented N072°E. Surface ruptures are observed within the two southwestern thirds of the valley, while no clear evidences of Late-Quaternary surface faulting are observed along the northeastern part. A second fault, with a surface rupture almost-parallel to the main Tsogt fault trace, is located 3 to 6 km eastward, and presents a smaller vertical cumulative offset, regarding to the peneplain. Further details about the Tsogt faults are presented in section IV.5 of this chapter.

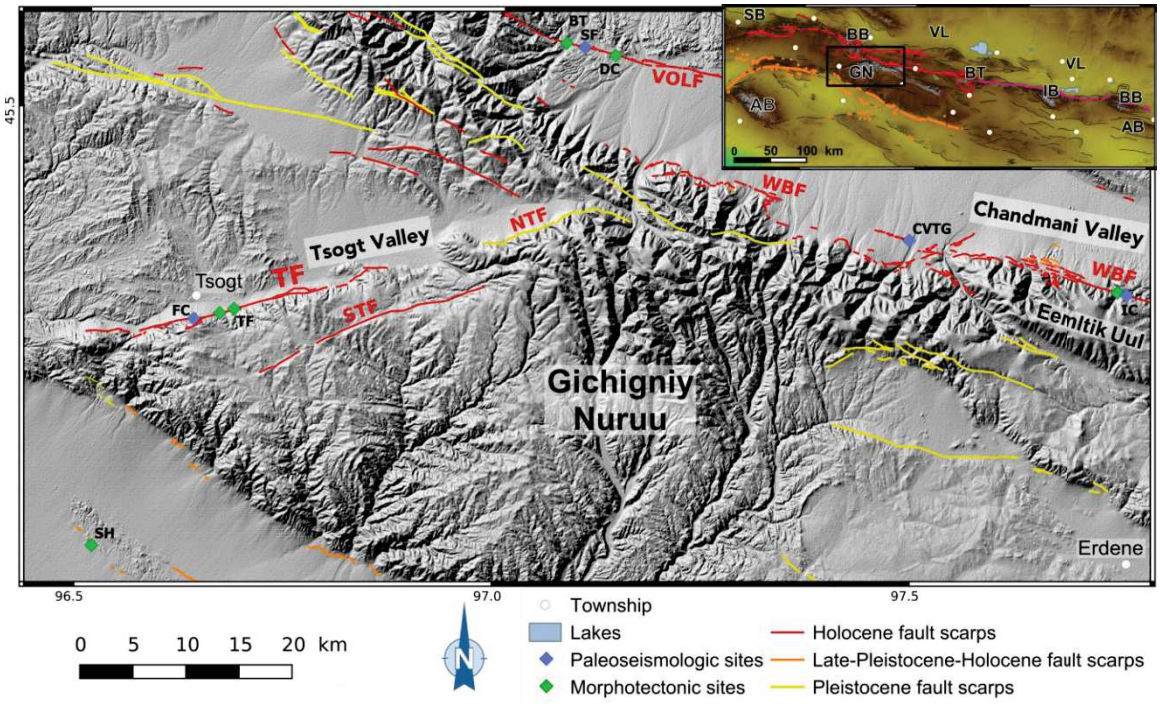


**Figure 4-6: Active faults map in the Tsogt region. Faults abbreviations: VOLF: Eastern Bogd fault; WBF: Western Bogd Fault; TF: Tsogt fault. Field sites abbreviations: BT: Biger Terraces; SF: Storm Creek; DC: Dark Creek; SH: Shuhaytayn Hills; FC: Fox Creek; TF: Tsogt Fan; CVTG: Chandmani Valley Tension Gash; IC: Ice Creek. Background is a hill-shading of the SRTM Topographic dataset. Insert abbreviations: SB: Sharga Basin; BB: Burhan Buuday; VL: Valley of Lakes; GN: Gichigniy Nuruu; BT: Bayan Tsagaan; IB: Ih Bogd; AB: Artz Bogd.**

As the Chandmani Valley, the WBF stops westward at a location matching with the NE continuation of the Tsogt Valley, while the VOLF western tip zone locates against the northernmost part of the Gichigniy range: the Burhan Buudai area (Figure 4-7).

The Tsagaan Gol Fault (TGF) corresponds to the westward continuation of the VOLF. It defines a curved structure to the North starting with a N110°E trend along its eastern part and end with a N070°E trend along its western part. The VOLF and the TGF are

separated by the ~40 km wide Burhan Buudai restraining bend (Figure 4-7). Within this area, the fault cut exclusively through bedrock and it is therefore difficult to distinguish active fault scarps from inherited lineaments. However, cumulative deformation displays clear deflections of the drainage network, attesting of the recent activity of the fault (Figure 4-8). The Burhan Buudai restraining bend displays a strong distributed deformation, on a 20 km wide zone, mainly concentrated within its central and southern parts. Bounding the northern foothills of the restraining bend, and cutting through the 18 km wide Namalzah Hills landslide (Mushkin et al., 2004), an ancient (Early – mid-Pleistocene ?) fault scarp is visible, but does not seems to exhibit offsets of upper-Pleistiocene – Holocene features (Figure 4-7). To the West, the TGF joins the Har Azagyn range, located on the southern edge of the Sharga Basin (Figure 4-10). The termination of the TGF trace, located eastward of the pull apart basin where is located the Togrog town, corresponds to a highly distributed deformation zone, with numerous fault branches (Figure 4-10).

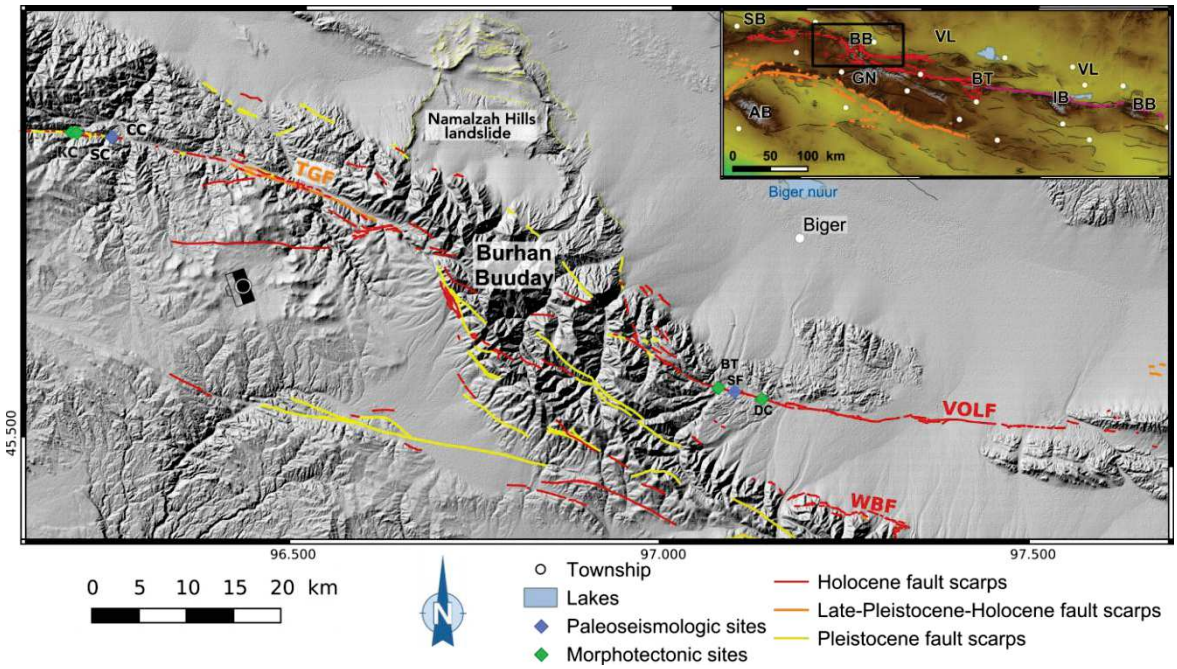


**Figure 4-7: Active faults of the Burhan Buuday Nuruu area. Camera is location of Figure 4-8. Faults abbreviations: VOLF: Eastern Bogd fault; WBF: Western Bogd Fault; TFG: Tsagaan Gol fault. Field sites abbreviations: KC: Kurilik Creek; CC: Camel Creeks; BT: Biger Terraces; SF: Storm Creek; DC: Dark Creek. Background is a hill-shading of the SRTM Topographic dataset. Insert abbreviations: SB: Sharga Basin; BB: Burhan Buuday; VL: Valley of Lakes; GN: Gichigniy Nuruu; BT: Bayan Tsagaan; IB: Ih Bogd; AB: Artz Bogd.**

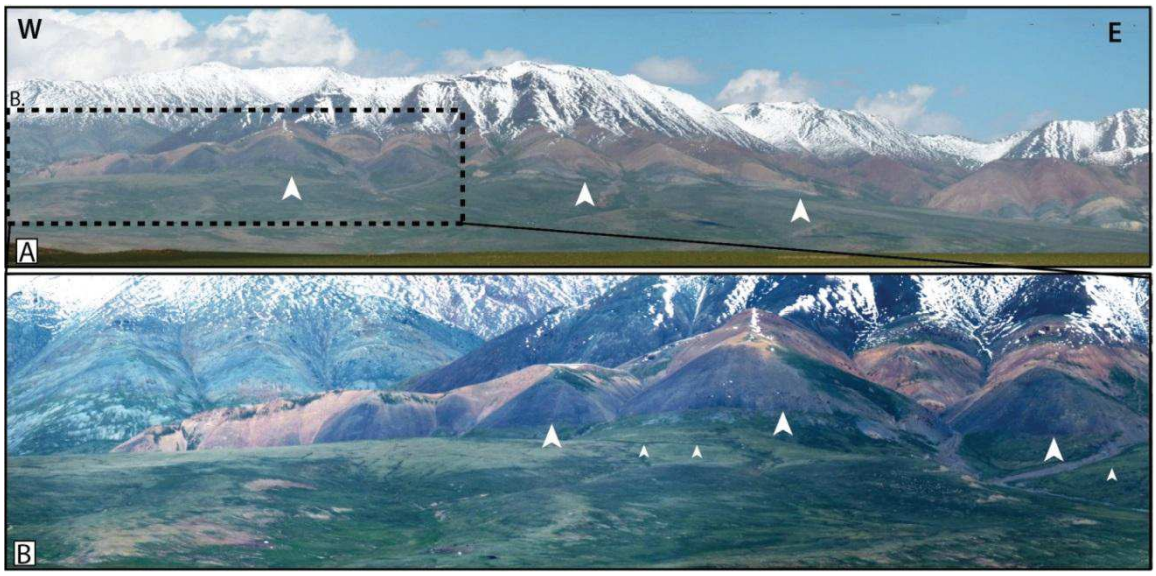


**Figure 4-8 : Panoramic view of the southern front of the Burhan Buuday. Mountain front is 600 m-high. Location of the picture is in Figure 4-7. White arrows indicate fault traces. Black dashed box is location of zoom B.**

The Gichigniy Nuruu (also referred as the '*Trans-Altai belt*'; e.g. Ruzhentsev et al., 1985) has been described by Cunningham (1998, 2010, 2013), as an uplifted block of thrust-dominated structural domain, sandwiched between the left-lateral Bogd and Gobi Tien-Shan deforming belts. The southern boundary of this range constitutes a continuous major thrust front of ~400 km-long, affecting quaternary alluvium (Figure 4-3). In this study, the fault scarps associated to this preeminent mountain front (Figure 4-9) will be furtherly describe regarding to their location within the Gobi-Altai range; from west to east: i. the Aj Bogd region (North Aj Bogd fault), ii. the South Gichiniy Nuruu Fault (SGNF), and the southwestern Gichighiy Nuruu region (Figure 4-3).

**Figure 4-9 : Photograph to the north of the South-Gichigniy Nuruu mountain front (background). On the foreground are the Suhaytayn Hills.**

The SGNF bounds the Gichigniy Nuruu to the South. It is composed by two parallel thrust faults, easily identified within their western part. One sets at the foothills of the relief, while the second is cutting through the southwards alluvial plain, along the Suhaytayn Hills (Figure 4-9 and Figure 4-11). The eastern section of the SGNF displays a discontinuous scarp, only visible within the oldest fans, which suggest the absence of Holocene activity along this part of the fault.

Next sections present mapped active faults in areas of the western Gobi-Altai which were not studied on the field. Subsequently, after the following overview, they will not be furtherly detailed in this study.

The westernmost Gobi-Altai mountain range corresponds to the junction region with the Altai mountain range, and shows a complex fault network. To the North sets the Sharga Basin, and to the South is the Aj Bogd region. The Sharga Basin defines a wide flat area bounded by active strike-slip/reverse oblique faults. The basin is 150 km long in an E-W direction and 70 km long in a N-S direction. The strike-slip faults bounding northwestward the Sharga basin (the Sharga fault, according to Baljinnyam et al., 1993) have been described as conjugate faults, related to the relay zone between right lateral kinematics of the Altai range and left-lateral motion of the Gobi-Altai range (e.g. Tapponnier and Molnar, 1979; Baljinnyam et al., 1993; Schlupp, PhD, 1996). Southwestward, the N070°E trending oblique-normal Tögrög fault, prolonging southwesterly the TGF, extends over a distance of ~60 km until Bugat town (Figure 4-10). Although the fault is underlined in the morphology by a linear valley, it does not show evidences of Holocene surface faulting.

East of the Sharga basin, right south of the town of Khaliun, is the Khaliun fault (Figure 4-10). It displays a discontinuous thrust trace, visible over length of ~ 30 km, fairly well expressed in a large range of late-Pleistocene fans, which might suggest it was active during Holocene time. The Khaliun fault is oriented N100 ± 20°E, related to a steep and rather straight mountain front, and is prolonged eastward over more 30 km, with some apparently older fault traces. Also, it seems to be involved in its eastern part with the Pleistocene Namalzah hills landslide (Mushkin, PhD. 2007, Figure 4-7). The Khaliun fault was not studied on the field, but a morphotectonics survey would be suitable along the western part of this fault, especially in order to assess its vertical slip rate and the age of the last surface rupturing earthquakes which occurred on this fault. Also, the Khaliun thrust could be involved in an earthquake sequence along the TGF, alike the Bayan Bulag foreberg that broke 15 km south of the main EBF surface rupture during the 1957 Gobi-Altai earthquake (Figure 3-1.b). Particularly, a comparison of the timing of the

paleoearthquakes occurring along the Khaliun fault and the TGF might allow constraining this presumed fault connection.

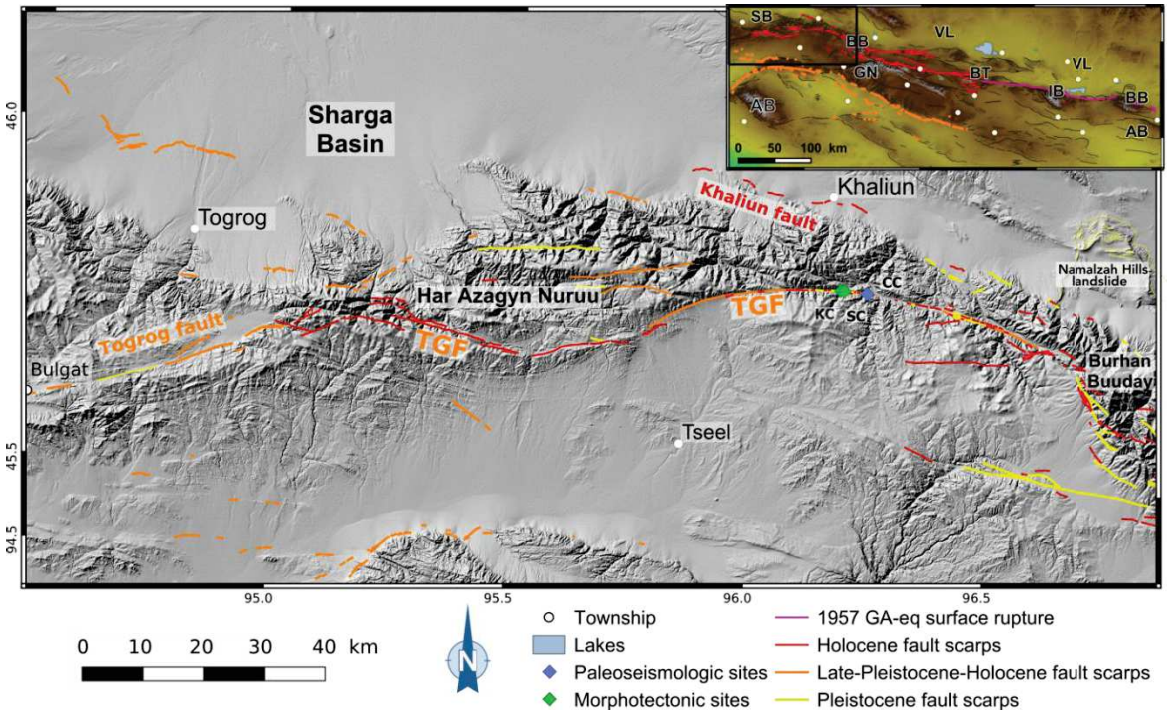


**Figure 4-10: Tsagaan Gol Fault and active faults of the surrounding area. TFG: Tsagaan Gol fault. Field sites abbreviations: KC: Kurilik Creek; CC: Camel Creeks. Background is a hill-shading of the SRTM Topographic dataset. Insert abbreviations: SB: Sharga Basin; BB: Burhan Buuday; VL: Valley of Lakes; GN: Gichigniy Nuruu; BT: Bayan Tsagaan; IB: Ih Bogd; AB: Aj Bogd.**

To the South of the junction zone between Gobi-Altai and Altai sets the Aj Bogd mountain range (Figure 4-11). To the SW, the massif is bounded by a thrust fault, which was described as active during the Quaternary by Cunningham (2013). However, we could not find clear and obvious evidences of faulting affecting late-Pleistocene deposits. Also, these scarps are systematically associated to bedrock outcrops within the alluvial fans they are standing on. Although the main range does not display significant active faulting, the surrounding region does exhibit three clear active fault scarps which are associated with left-lateral displacements, as detailed in next sections.

A first fault is located ~70 km eastwards of the Altai town (44.300°N, 97.417°E), partly following the Chinese border, and trends N080 ± 5°E (Figure 4-11). This ~40 km-long surface rupture is composed of two segments, both displaying evidence of cumulative oblique-left-lateral offsets, and visibly dipping North as they are generating an uplift on the northern side of the fault, and basins south of the fault. Discontinued thrust fault scarps stand ~10 km southwards from the main rupture and may correspond to foreberg structures (See Bayasgalan et al., 1999b), defining with the main fault a transpressive partitioned system. This structure is continuing discontinuously to the East until

Longitude E97.117. The fault scarps are well visible, but does not produce important displacements of the late-quaternary alluvial network.

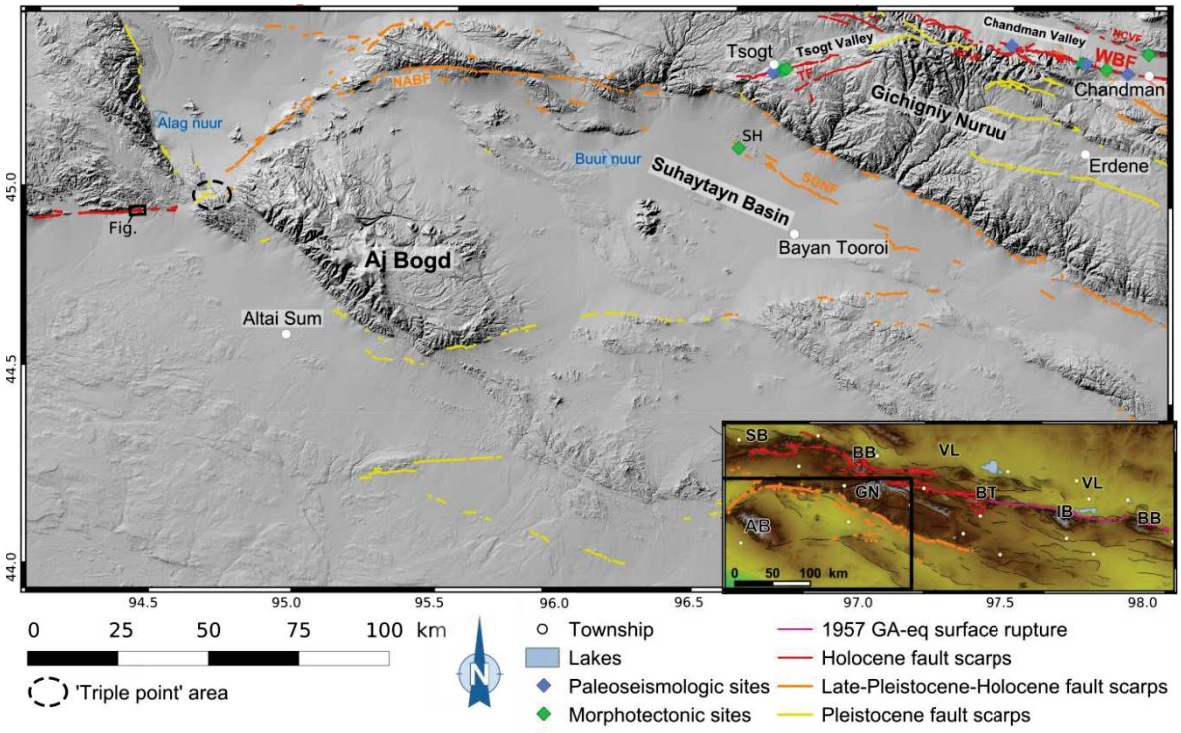


**Figure 4-11: Fault surface ruptures in the Aj Bogd region. Black solid box is location of Figure 4-12 and dashed ellipse is the ''triple point area''. Faults abbreviations: NABF: North Aj Bogd Fault. WBF: Western Bogd Fault. NCVF: North Chandmani Valley Fault. TF: Tsogt Fault. SGNF: South Gichigniy Nuruu Fault. Field site abbreviation: SH: Shuhaytayn Hills. Background is a hill-shading of the SRTM Topographic dataset. Insert abbreviations: SB: Sharga Basin; BB: Burhan Buuday; VL: Valley of Lakes; GN: Gichigniy Nuruu; BT: Bayan Tsagaan; IB: Ih Bogd; AB: Artz Bogd.**

A second surface rupture is located ~65 km North-West from Altai town (Figure 4-11). This fault used to produce historical seismicity (Figure 4-2), and its eastern end is located within a 'triple point area' (44.967°N, 94.617°E). This 60 km-long surface rupture strikes N090 ± 10°E, and displays numerous evidence of left-lateral and reverse oblique faulting. Two major canyons are offset by 240 ± 40 m and 360 ± 80 m respectively, and a larger offset on both canyon yield about 700 ± 200 m (Figure 4-12). This fault, which certainly experienced the Mw7.0 Tahiynshar earthquake in July 1974 (Tapponnier and Molnar 1979; Khilko et al., 1985; Huang and Chen 1986; Baljinnyam et al., 1993), is located on the Altai domain, but propagates easterly to connect with the third active strike-slip fault of the Aj Bogd region, the '*North Aj Bogd Fault*' (NABF), located only 20 km to the NE, 10 km north of the triple point area.

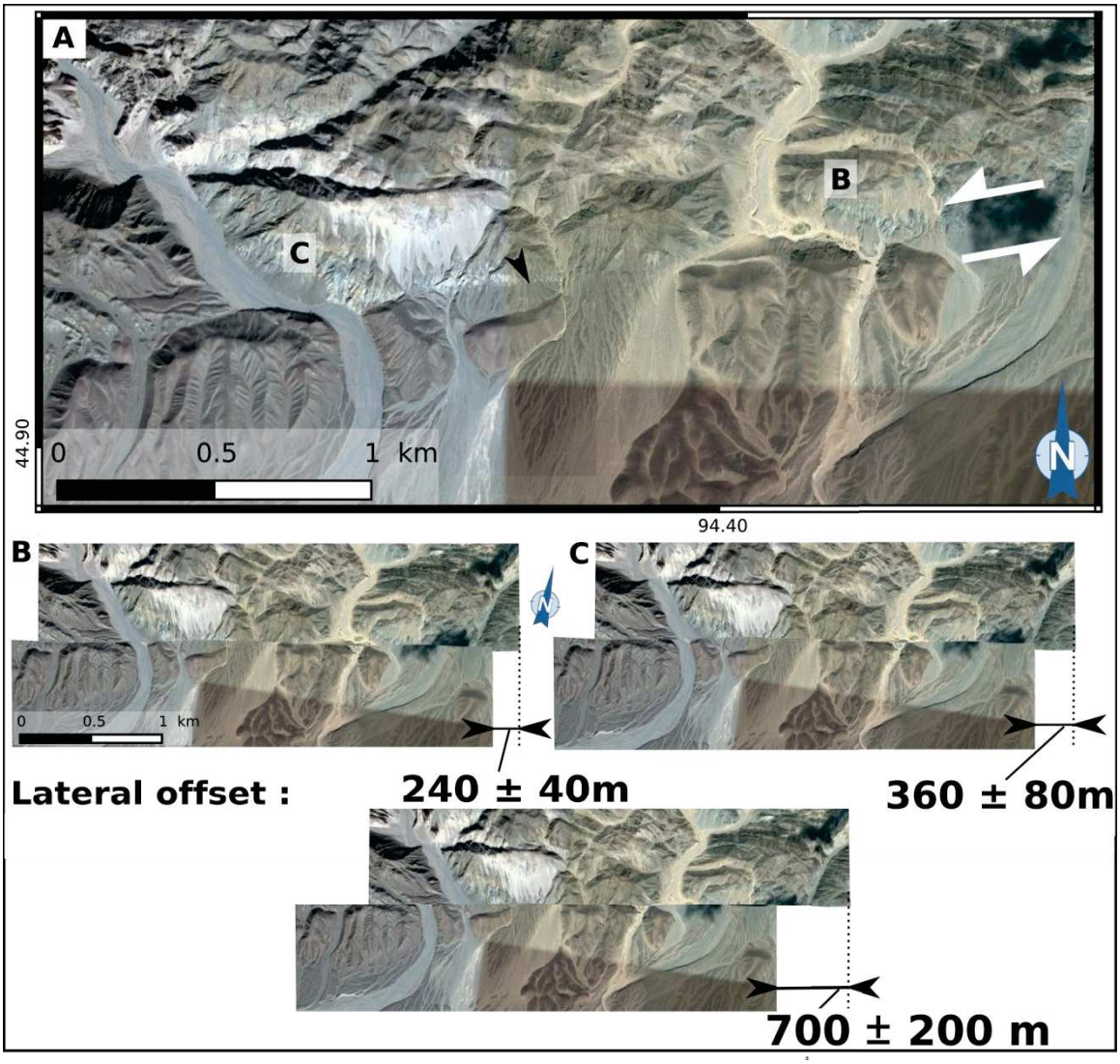


**Figure 4-12 : Cumulative offset measurements of major canyons along the southernmost fault of the Altai mountain range, 15 km west of the 'triple point area'. A. Google earth view, images are from February 2013. Black arrow indicates the fault, and white arrows the left-lateral motion. Letters B and C indicate the main canyons reconstructed in respective insets. B. Reconstruction of the eastern canyon, offset is assessed to 240 ± 40 m by 3-steps landform retrofit. C. Reconstruction of the western canyon, offset is assessed to 360 ± 80 m by 3-steps landform retrofit.**

The triple point area between these faults (Figure 4-11) is undergoing distributed deformation related to fault branching, connecting three faults: 1) to the south-west to the aforementioned oblique N090°E left-lateral fault; 2) to the north-west a N140 ± 15E° oblique right-lateral fault within Altai range, out of the study area, which displays few clear scarps in late-quaternary fans, while the main fault traces are partly confused with the bedrock's structure; 3) to the north-east is the third fault, which displays a fairly continuous scarp, oriented N045 ± 5E°, affecting left-laterally late-quaternary deposits. One may note that a fourth fault is branching 10 km to the south, which is the aforementioned thrust on south of Aj Bogd, likely inactive during Holocene time.

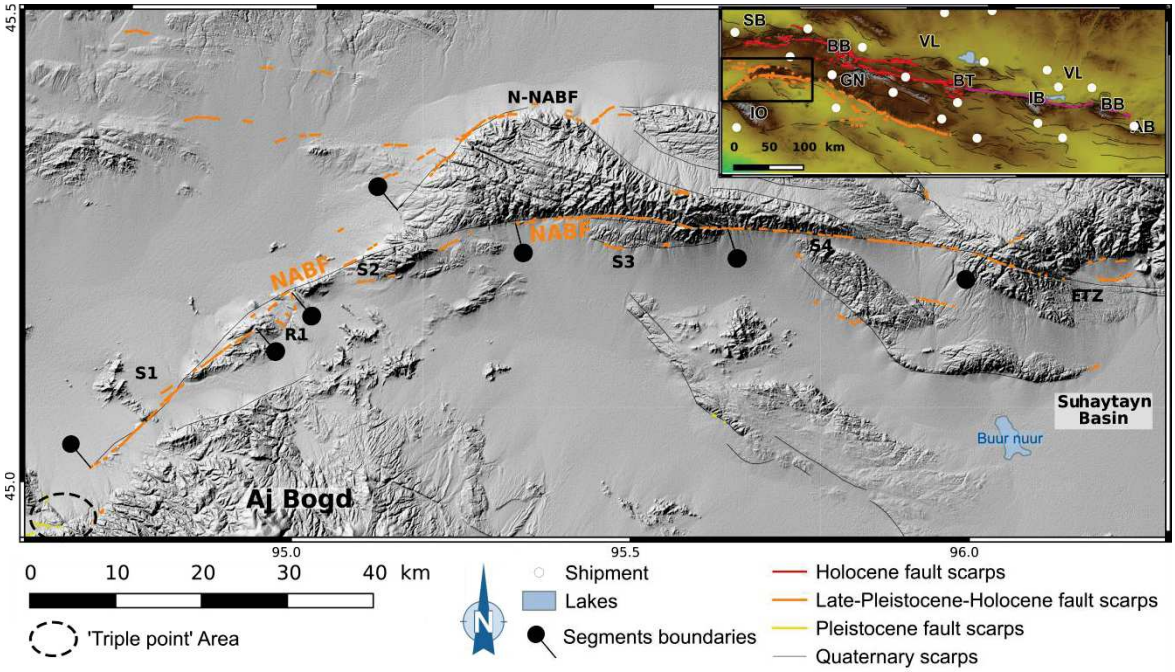


**Figure 4-13: Map of the North Aj Bogd Fault (NABF) surface rupture and segmentation. Insert abbreviations: SB: Sharga Basin; BB: Burhan Buuday; VL: Valley of Lakes; GN: Gichigniy Nuruu; BT: Bayan Tsagaan; IB: Ih Bogd; AB: Artz Bogd.**

The NABF presents a major but complex surface rupture (Figure 4-13), which can be followed over a distance of ~130 km. Its southwestern part trends N045°E and then curve progressively easterly to the North, to finally trend N105°E within its north-eastern part. The whole fault can be divided into 4 segments, to which is associated another 30 km-long northern section (here named the NABF northern branch): The first N045°E trending south-westernmost segment is 27 km-long and mostly left-lateral, without related topography. Its separation with the third next segments define a small 3 km-long jog, composed of 4 surface ruptures displaying clear vertical displacements.

The second segment is made of two discontinuous fault scarps, bounding an uplifted area. The eastern fault scarp trends N070 ± 10°E and is ~20 km long, while the western trends N065 ± 5°E and is 15 km long. This western scarp is followed by another thrust fault scarp located to the west, which affects Quaternary deposits and distributes itself on to branches, one continuing the main fault, and a second initiates the northern branch, 5 km northward. This northern branch is strongly oblique and displays a sinuous trace (at kilometer scale) trending from N040°E to N095°E, which attests of a strong reverse component associated to the left-lateral motion. The area between the main NABF fault and the northern branch displays a piggy-back basin bounded by straight mountain fronts, although few evidences of quaternary faulting have been found.

The 23 km-long third segment of NABF trends N090 ± 10°E and curves progressively toward the south. The left-lateral movement seems to be associated to shallow reverse faulting on both north and south reverse faults located 3 to 4 km from the main strike-slip trace, attesting of surficial slip-partitioning process.

The fourth segment is mainly cutting through the bedrock, and displays localized deformation, with several cumulative left-lateral offsets observed within the talwegs incising the mountain front (Figure 4-13). This N092 ± 5°E trending, ~25 km-long segment is very straight, and at 5 to 10 km to the south is a pressure ridge, bounded by active faults, showing reverse movement along the southern front and left-lateral movement along the northern front (Figure 4-13).

The eastern end of the NABF is actually made of several discontinuous surface ruptures trending from N060°E to N105°E. Deformations are distributed along the eastern part within an intra-mountainous basin (45.267°N, 96.183°E), bounded by active thrust scarps both on its NW and SE borders (piggy-back). This tip zone is located 30 km west from the Suhaytayn Hills (SH on figure IV-7).

On the eastern part of the of the Suhaytayn basin, southeastward of the Gichignyi Nuruu, the fault traces are more discontinuous, although some significant quaternary scarps can be identified (Figure 4-11). The uplift of late-quaternary surfaces appears sporadic along the straight southern face of the Gichigniy Nuruu, which overthrust southwards over the quaternary fanglomerates (e.g. Mushkin, PhD, 2007). The region seems to have undergone significant faulting during the Pleistocene, however despite careful mapping no evidence of late-Pleistocene faulting has been found, suggesting that the fault of the area might not have been active during Holocene.

South-east of the Gichigniy Nuruu, 20 km south of Shinejinst town (Figure 4-3), fault traces can be identified only on few remnants of fan surfaces, nearby main outlets. Those sporadic fragments of late quaternary deposits obviously do not belong to Holocene time, and although the landforms of the area display abundant younger fans surfaces, none of them are visibly affected by surface faulting. This observation is by the way in good agreements with field reconnaissance done by Mushkin (PhD, 2007).

## IV.2. Earthquake geology of the WBF

### *IV.2.1. Western Bogd Fault surface ruptures mapping*

We describe arbitrarily the fault trace from west to east regarding to its segmentation, starting at the western tip zone of the WBF. Five distinct segments named S1 to S5 have been defined, following the segmentation criteria presented in section III.1.3.

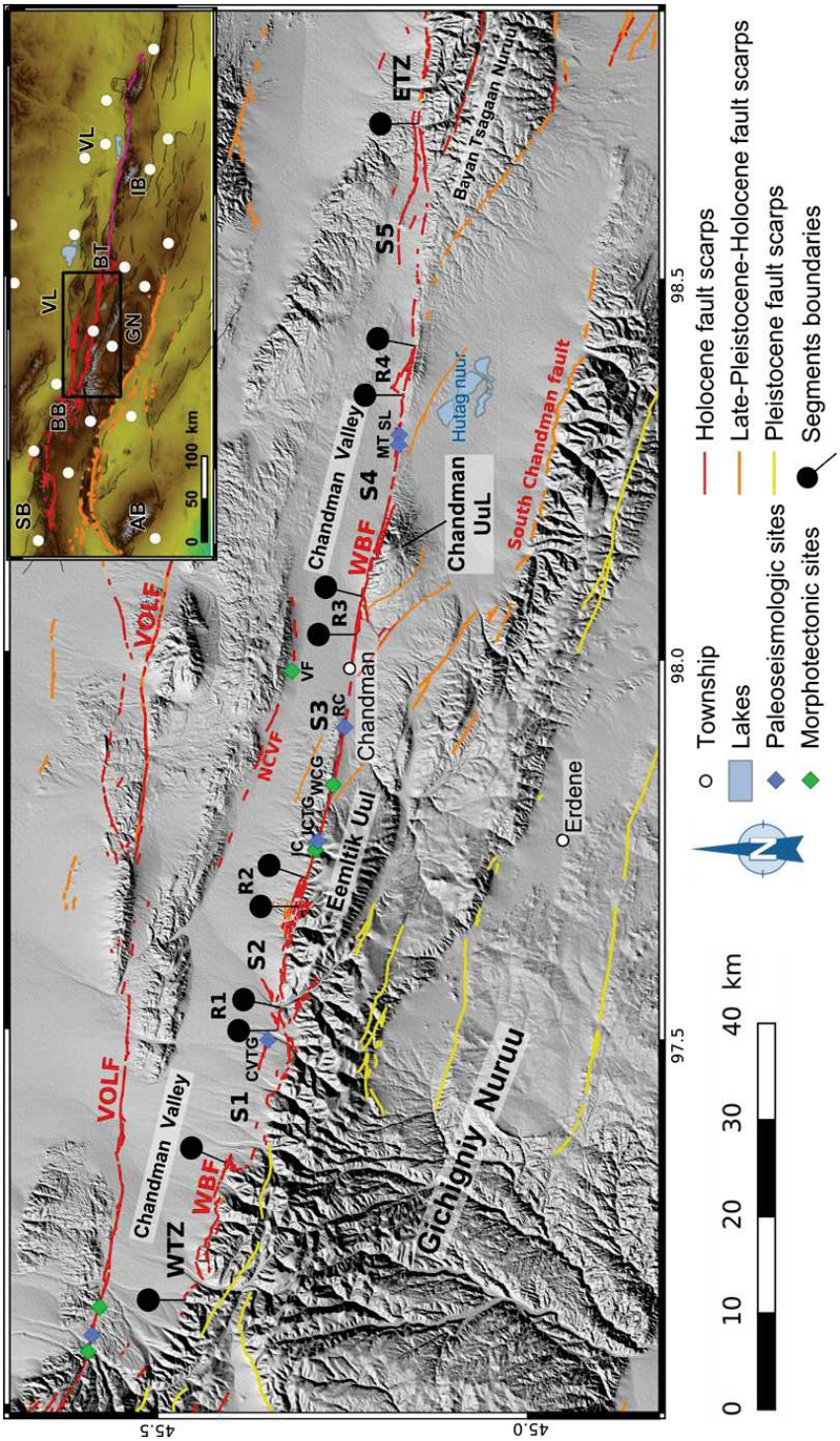


**Figure 4-14: Segmentation of the Western Bogd Fault. Faults abbreviations: VOLF: Eastern Bogd fault; WBF: Western Bogd Fault; NCF: North Chandmani Valley fault. Field sites abbreviations: CVTG: Chandmani Valley Tension Gash; IC: Ice Creek; ICTG: Ice Creek Tension Gash; RC: Rain Creek; MT: Moskito Trench; SL: Swan Lake trench. Background is a hill-shading of the SRTM Topographic dataset. Insert abbreviations: SB: Sharga Basin; BB: Burhan Buuday; VL: Valley of Lakes; GN: Gichigniy Nuruu; BT: Bayan Tsagaan; IB: Ih Bogd; AB: Artz Bogd.**

The probable western end of the fault surface rupture is located around the coordinates 45.477°N, 97.150°E, 25 km south of Biger town. Further west, the fault trace might continue, as the mountain front is very sharp (Figure 4-14). Visible significant gravity processes however (slides and slows, according to categories of Varnes, 1978), may hide the fault scarp, but only few noticeable surface traces related to cumulative deformation of late-quaternary geomorphic features have been identified.

The Western Tip Zone of the WBF is 14 km-long (WTZ on Figure 4-15), and displays mainly reverse motion, with a distributed fault-pattern ~ 1 km-wide, likely associated to shallow slip-partitioning with reverse motion on the southern branch (Figure 4-16-A). The fault is mainly located at the mountain front where bedrock is outcropping, and trends N106°E in average, varying from N080°E to N116°E. We observe a strong uplift on the southern part of the fault, as attested by abandoned uplifted surfaces along the main drainages (Figure 4-16-B). The area corresponds also to the northeastern end of the Tsogt Valley, tectonically controlled by the North Tsogt fault, which stands out only 10 km southwestwards from the WBF tip zone (Figure 4-5).

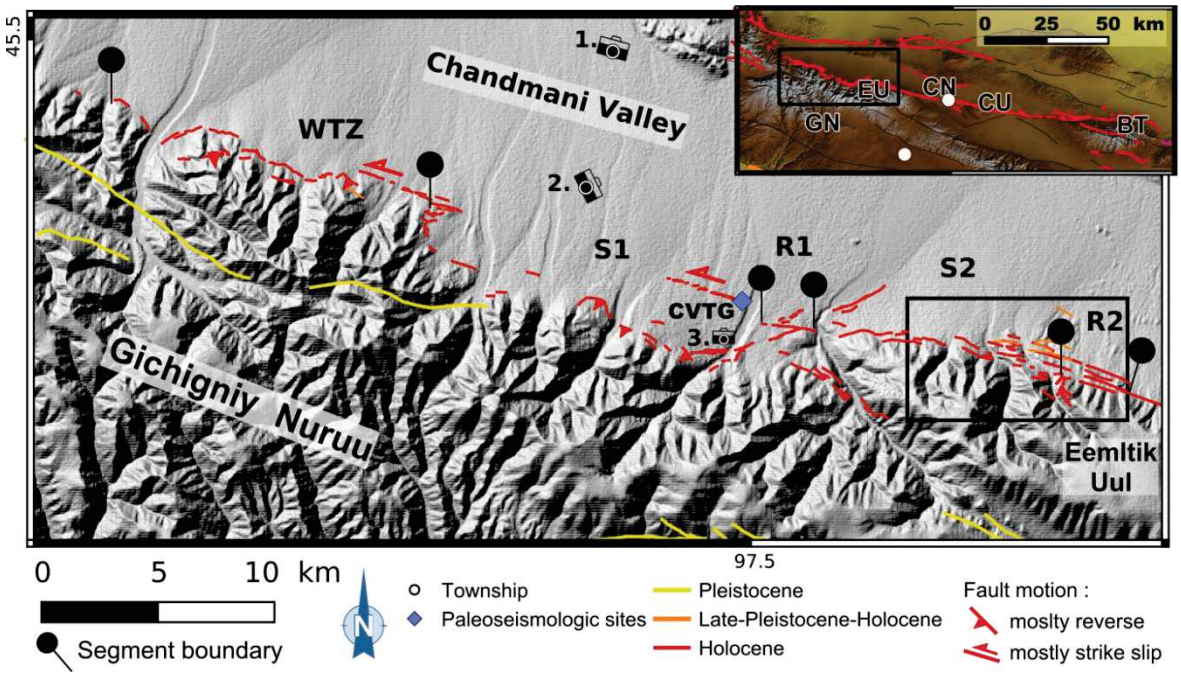


**Figure 4-15: Fault surface ruptures and segmentation along the western part of the WBF. Black solid box is location of Figure 4-19. CVTG: Chandmani Valley tension gash field site. Cameras correspond to locations of: 1. Figure 4-16-A; 2. Figure 4-16-B; 3. Figure 4-16-C. Insert footprint is same as Figure 4-14. GN: Gichigniy Nuruu; EU: Eemltik Uul; CN: Chandmani Nuruu, CU: Chandmani Uul; BT: Bayan Tsagaan.**

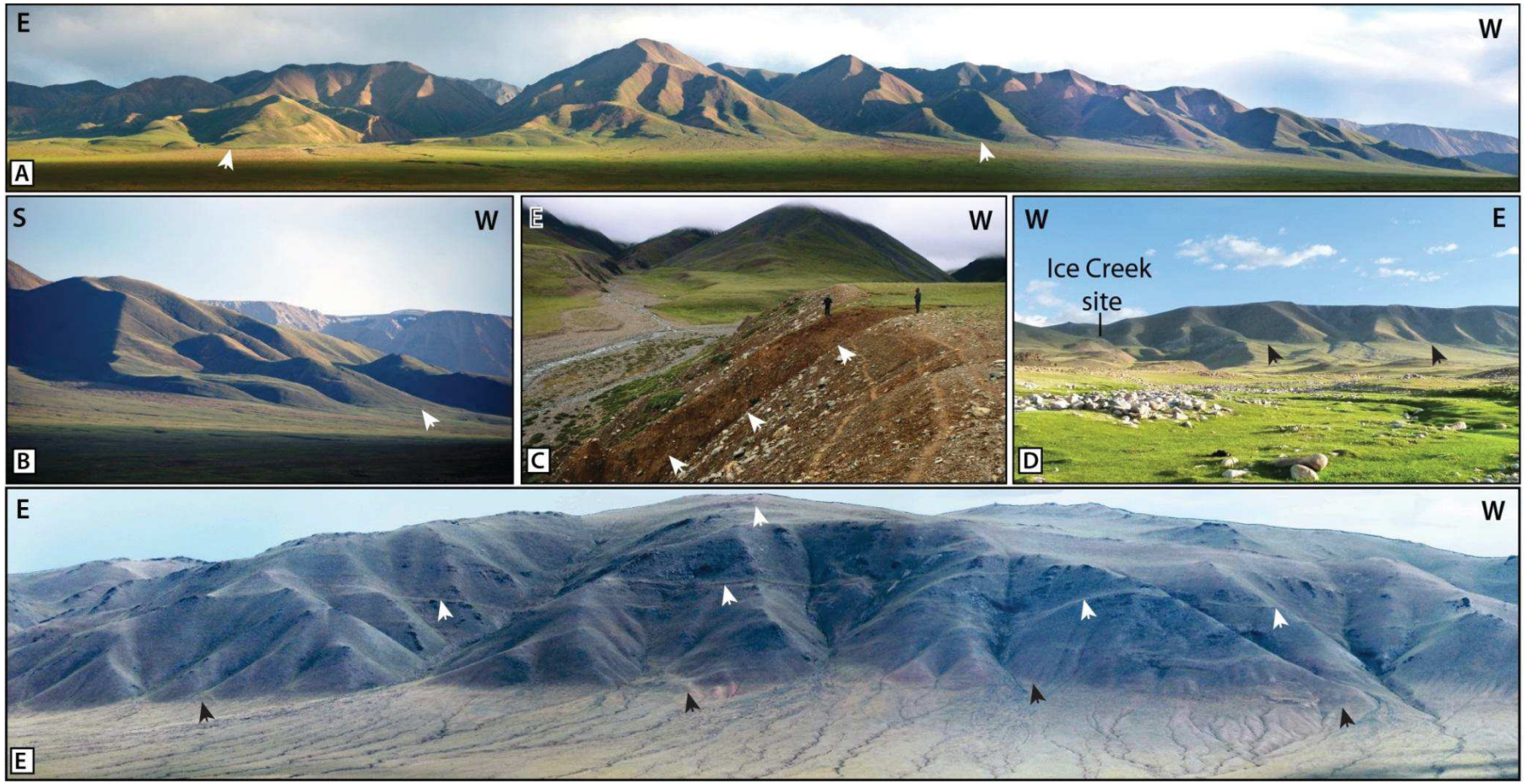


**Figure 4-16 : Photographs of the WBF surface rupture. Pictures locations are in Figure 4-15 and Figure 4-20. Arrows indicate the fault traces. A. Panorama to the south of the Western Tip Zone (on rigth of the picture) of the WBF ; central part is the WBF-R1 relay zone, and left part is the WBF-S1 segment. Montain front is 1000 m high. B. Photograph to the SW showing uplifted terraces along the WBF-R1 relay zone. Note the flat suummit plateau of Gichingiy Nuruu on background, corresponding to a relict of the paneplain. Montain front is 500 m high. C. Photograph to the south of a left-lareral offset on a riser of a terrace belonging to a major drainage, on ''Chandmani Valley Tension Gash'' site. D. Photograph to the south of the western part of the WBF-S3 segment, on Ice Creek Site (main valley). Mountain front is 1000 m high. E. Panorama to the south of the northern face of the Chandmani Uul restraining bend. Black arrows show the main strike-slip fault traces, and white arrows show intramountainous associated faults. Mountain front is 400 m high.**

Eastwards of the western tip zone (WTZ), is a branching zone associated to uplifted surfaces south of the fault (Figure 4-16-A), and then the first fault segment of the WBF: WBF-S1 (S1 on Figure 4-15). This 14 km-long segment shows distributed deformation: first is a straight left-lateral strike-slip fault trace (especially visible on the eastern part of the segment, made of large tension gashes, 30 to 250 m-long) that trends N106°E and cut through the quaternary fans, and a N070°E to N160°E discontinuous fault trace; secondly is a sinuous south-dipping reverse fault, situated 2-3 km southwards the strike-slip fault, which bounds the reliefs and makes the bedrock thrusting over the quaternary deposits (Figure 4-15). One of the tension gashes of the strike slip branch has been investigated (CVTG on Figure 4-15), for which results are presented in part IV.2.4.1.

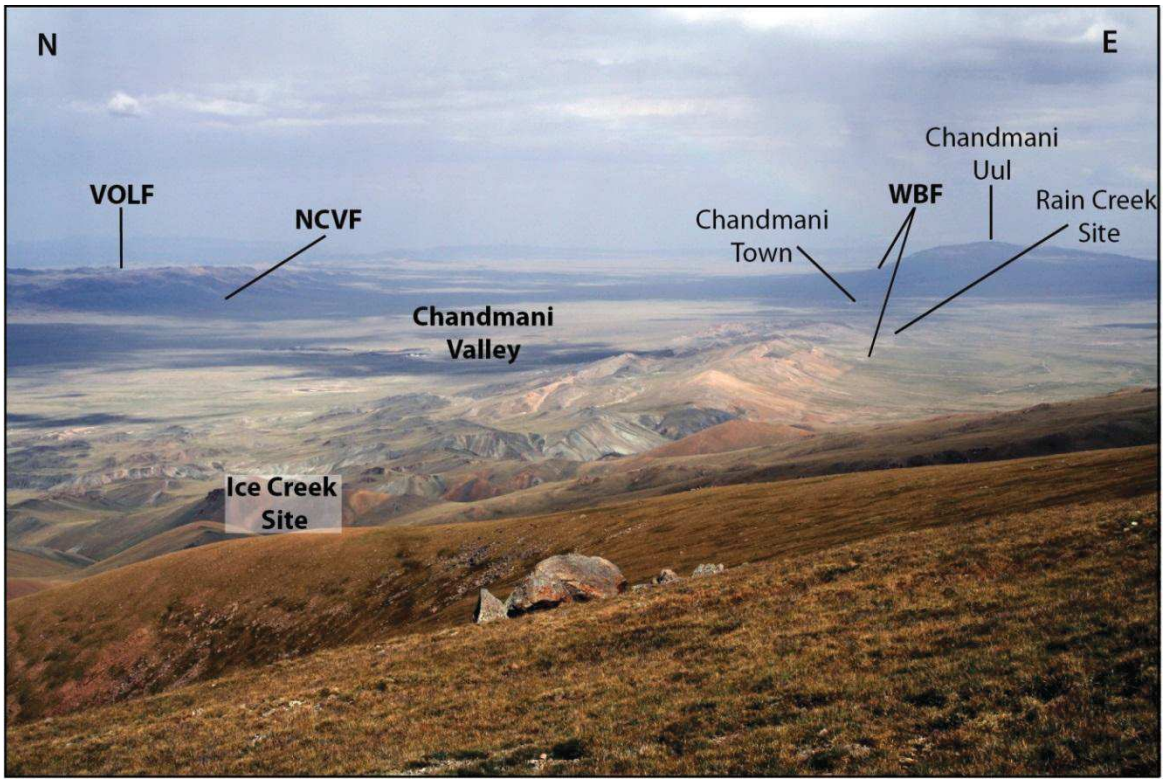


**Figure 4-17 : Photograph to the NE of the Chandmani Valley, from the top of Eemltik Uul.**

Eastward, around coordinates 45.392°N, 97.515°E is a 2 km-wide relay area (R1 on Figure 4-15) showing very distributed deformations and conjugate faulting, characterized by the branching between five faults. The two western ones correspond to the 2 WBF-S1 branches previously described; the one to the NE is a minor 4 km-long-branch trending N065 ± 5°E, and the fourth to the east corresponds to the WBF-S2 segment, detailed ahead. To the south-east is a major branching, trending N130 ± 20°E, with the ~100 km-long South-Chandman-Fault (Figure 4-14), a quaternary fault well expressed in the morphology, but which does not show evidences of late-Pleistocene activity along its western part (Figure 4-14). The whole geometry of the South Chandmani Fault is

regularly curved to the north, striking N120°E on its western part to N100°E along its eastern active part (Figure 4-14). The continuation of this fault is associated to a deep 40 km-long axial valley incised into the bedrock southwards the Eemltik Uul (Figure 4-14). The eastern part, however, located 30 km SE of Chandmani town, is associated to an 800 m-high mountain front which corresponds to the northern face of the Gichigniy Nuruu (Figure 4-14), and displays discontinuous evidences of Pleistocene activity, with mostly reverse motion (Figure 4-18). The preserved peneplain on top (see flat summit in Figure 4-18) of the range allows estimating a total uplift of at least 800 m, without counting the sediments that accumulated in the basin on the northern side of the fault (foreground in Figure 4-18).

**Figure 4-18: Panorama to the south of the South Chandmani fault. White arrows indicate the main oblique fault trace. Note the preserved peneplain on top of the relief. The whole relief is 800 m-high.**

The deformation associated with the mountain range potentially presents slip partitioning: additionally to this northern thrust fault scarp, a strike slip fault trace is located 8 to 10 km to the south, bounding the mountain range southward (in yellow in Figure 4-14). However, evidences of deformations along this scarp are located into bedrock, following a clear pre-existing tectonic contact. Hence it is difficult to tell for sure whether this contact is still active during Quaternary. Eventually the central part of this fault, 12 km south of Chandmani town, is located into bedrock terrains, devoid of quaternary geomorphic features.

The WBF-S2 segment is 14 km-long, slightly curved to the south, trending N100 ± 10°E in average, and displaying an oblique-reverse-left-lateral kinematic (Figure 4-15). The southern side of the fault is uplifted, and the fault trace displays distributed deformations on two main collinear traces. The eastern part of the WBF-S2 segment seems to correspond to a relay zone, given the abrupt change of the lithological units on both sides of the fault, and the strong distribution of surface ruptures. As pointed out by Mushkin (PhD, 2007), this WBF-S2 segment shows two major cumulative offsets within 2 main drainages that we re-estimated at 870 ± 200 m and 1020 ± 200 m (Figure 4-19).

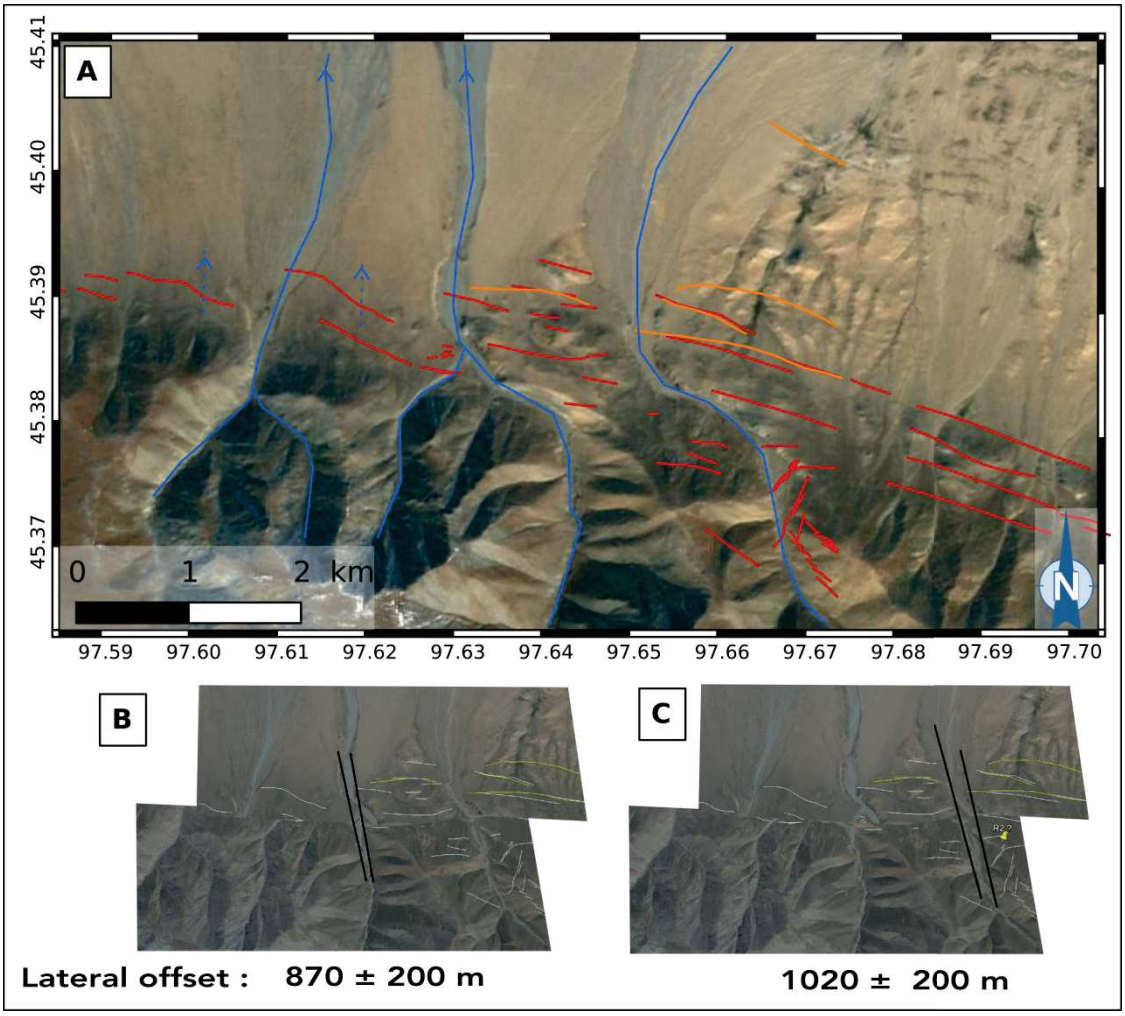


**Figure 4-19 : Cumulative offset measurements of major canyons flooding to the Chandmani Valley along the Western Bogd Fault (WBF-R2 relay zone). A. Google earth view, images are from 2013. Solid red lines indicate Holocene fault traces, and orange solid lines older fault scarps. Blue lines are main drain, and dashed blue lines are abandoned channels. B. Reconstruction of the western canyon. C. Reconstruction of the western canyon. Black solid lines are piercing lines related to main canyons, used to derive the offsets associated with these features, here very similar. The uncertainties are given from 3-steps retrofit of the landforms.**

The WBF-R2 relay zone, around coordinates 45.375°N, 97.685°E, coincides with an abrupt lithological change from metamorphosed to plutonic rocks (cf. « Russian Geological 1:200 000 maps of Mongolia » 1987). This ~2 km-long relay zone takes place exclusively in the bedrock and in spite of the limited quality of the satellite images for the area, we can observe a large distribution of surface ruptures where some fault traces seems to connect to a structural lineament to the SE (Figure 4-19). On the eastern part there are 4 parallel fault traces, which coalesce eastward on the WBF-S3 segment (Figure 4-20).

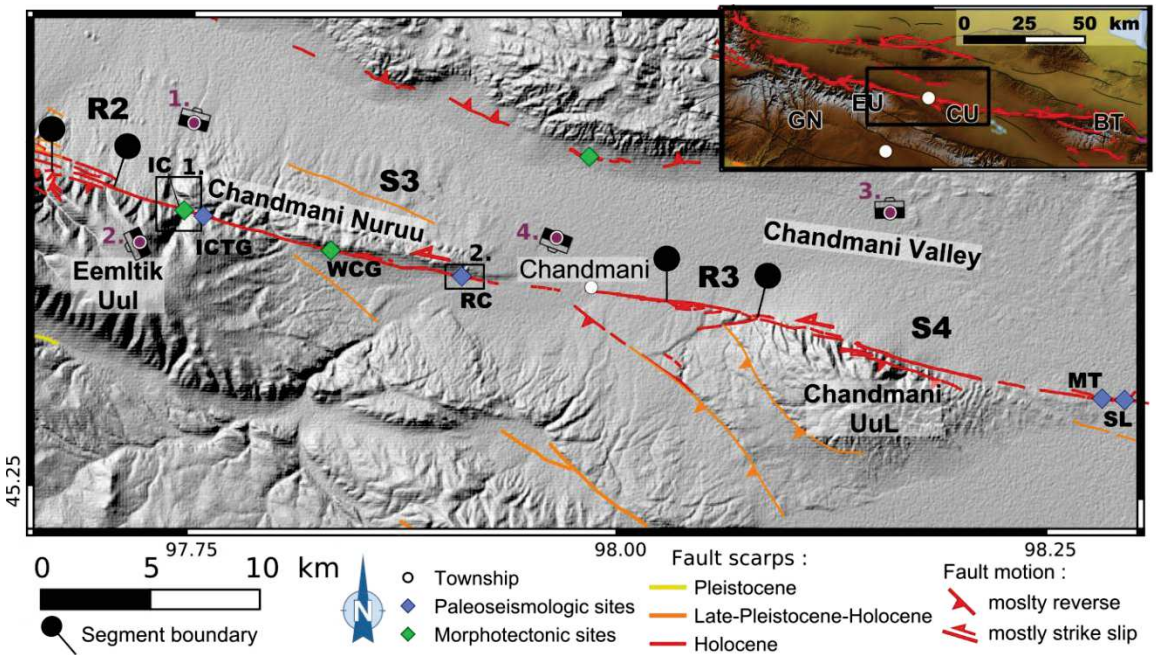


**Figure 4-20: Fault surface ruptures and segmentation along the central part of the WBF. Cameras correspond to location of: 1. Figure 4-16-D; 2. Figure 4-17; 3. Figure 4-16-E; 4. Figure 4-136-A. Abbreviations of field sites: IC: Ice Creek; ICTG: Ice Creek tension gash; WCG: West Chandmani Gullies; RC: Rain Creek; MT Moskito Trench; SL Swan Lake Trench. Insert footprint is same as Figure 4-14. GN: Gichigniy Nuruu; EU: Eemltik Uul; CN: Chandmani Nuruu, CU: Chandmani Uul; BT: Bayan Tsagaan.**

The WBF-S3 segment is continuous, straight and slightly curved to the north. Its average trend is N100°E, from N095°E along its western part, to N105°E along its eastern part. The deformation is localized (see straight fault trace in Figure 4-17), with a mostly left-lateral motion, as attested by observation of systematic left-lateral offsets and numerous right-stepping tension gashes. Reliefs located south and north of the fault segment within its western and central part, respectively, suggest that long-term cumulative uplifting processes are associated with the fault motion. Uplifts are located on the southern side of the fault for the western quarter and on the northern side of the fault for the two central quarters. Instead, the eastern quarter of the segment does not display significant vertical deformation. Mushkin (PhD, 2007) proposed that these long-term kinematic variations are related to the changes of the fault orientation. Two important sites were investigated along this fault segment: “Ice Creek” and “Rain Creek” sites, which are detailed in parts IV.2.4.2 and IV.2.4.3 , respectively (Figure 4-16-D). In the same time, surveys of offsets (simple and cumulative) observed on preserved landforms have been carried out to analyze the slip distribution and to constrain the average coseismic lateral slip component associated with large surface-rupturing events along this segment.

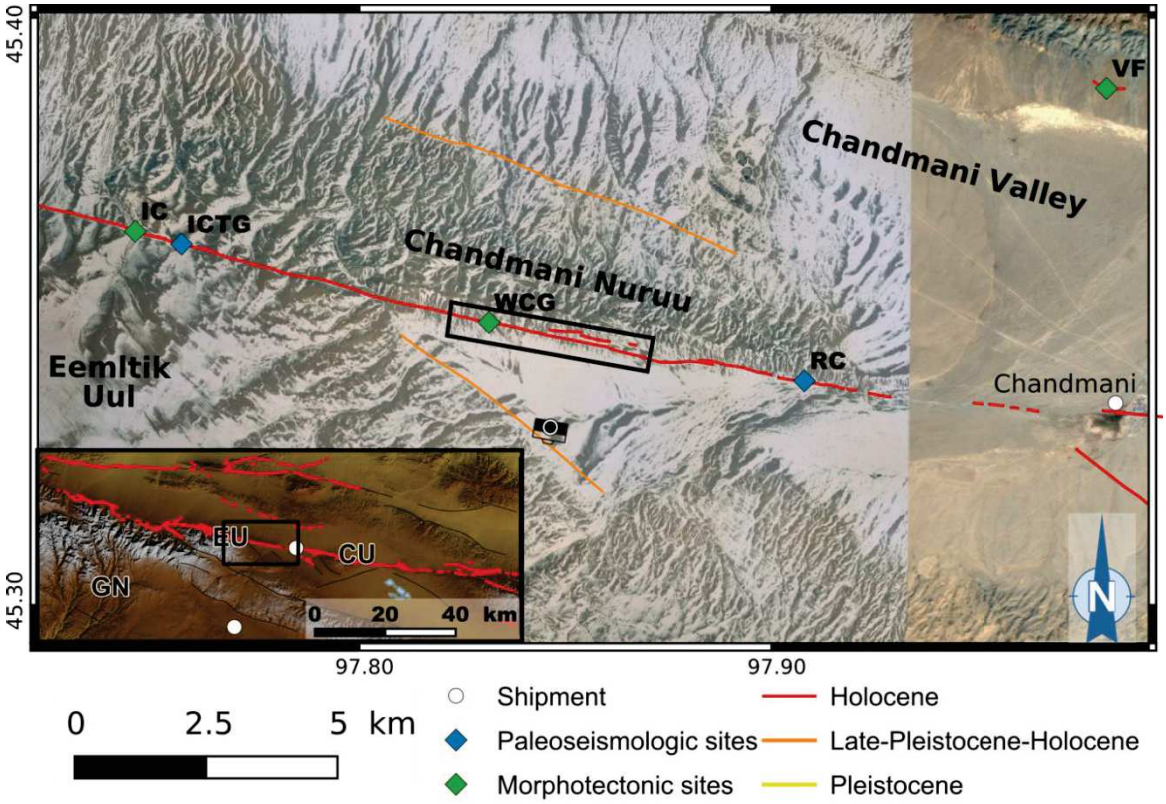


**Figure 4-21 : Map of fault traces and field sites west of Chandmani. Camera is location of picture in Figure 4-24, and black solid box is footprint of the UVA survey detailed in section IV.2.2 and Figure 4-25. Abbreviations of field sites: IC: Ice Creek; ICTG: Ice Creek tension gash; WCG: West Chandmani Gullies; RC: Rain Creek.**

Two secondary faults were identified (Figure 4-20 and Figure 4-21). The first one is situated 5 km northwards, and trends N110 ± 5°E parallel to the main WBF fault trace. It bounds the Chandmani ridge to the North and shows a left-lateral-reverse kinematics. The second one is oblique to the main WBF trace and trends N140°E. It displays displacements with a normal motion, with a possible right lateral strike-slip component as suggested by Mushkin (PhD, 2007). Few offset features can be identified in the bedrock's morphology, but no clear evidence of deformation associated to these secondary faults where found affecting late-Pleistocene deposits. Further East, 1 km south of the Chandmani town, a 15 km-long N125°E trending fault branch shows evidences of quaternary faulting with a mostly left-lateral kinematics. This fault branch bends southwards after 6 km, to N140 ± 5°E. This azimuth change is correlated to a change in lithological units (from quaternary sediments to granitic bedrock), and also to change in fault kinematics, from strike-slip to reverse-oblique motion. This reverse faulting process is controlling the growth of the Chandmani Uul restraining bend, for which the northern flank is bounded by the, WBF-S4 segment.

The WBF-R3 relay zone is a 3 km-long pull-apart basin, trending N100 ± 20°E and situated around coordinates 45.325°N, 98.050°E. Its northern edge corresponds to the

straight main strike-slip WBF, while 3 oblique-normal faults, 1 to 3 km-long develop southward. An 8 km-long sinuous N140°E branch, is also starting from this small extensional jog, and displays mostly a reverse motion; it is parallel to the aforementioned N140°E branch that starts from Chandman, and is clearly related to the Chandmani Uul restraining bend.

The next segment, WBF-S4, bounds to the North the ~500 m high, 15 km-long (E-W) and 5 km-wide (N-S) Chandmani Uul restraining bend (Figure 4-16-E and Figure 4-20). The segment is slightly curved to the north, and shows partitioned deformation between left-lateral and reverse movements within its N105° ± 5°E western part. The segment becomes mostly strike-slip along its N095° ± 5°E eastern part, and run through a NS drained basin. We carried out paleoseismological investigations along this eastern part of WBF-S4, within the swampy area related to the drained basin, (sites MT and SL on Figure 4-22). Results are detailed in section IV.2.4.4.

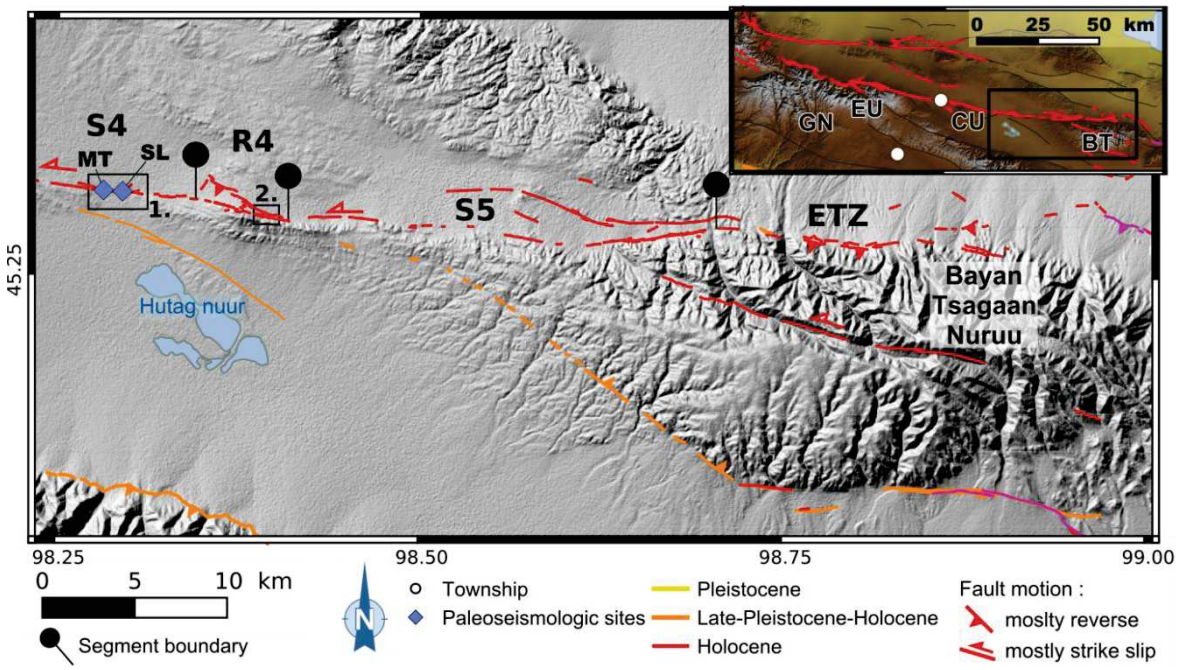


**Figure 4-22: Fault surface ruptures and segmentation along the eastern part of the WBF. Black boxes indicate location of: 1. Figure 4-51, 2. Figure 4-23. Abbreviations of field sites: MT: Moskito Trench; SL: Swan Lake trench. Insert footprint is same as Figure 4-14. GN: Gichigniy Nuruu; EU: Eemltik Uul; CN: Chandmani Nuruu, CU: Chandmani Uul; BT: Bayan Tsag**

The WBF-R4 relay zone is a 5 km-long asymmetric piggy back basin (Figure 4-22), bounded to the South by the N103 ± 5°E trending WBF strike-slip-reverse fault, and to the North by a sinuous N120 ± 10°E reverse fault strongly related to bedrock outcrops (uplift and incisions). This restraining jog displays numerous evidences of recent surface ruptures, along which channels are systematically displaced with a left-lateral movement, and channel incisions within the thrusting hanging-walls (Figure 4-23).

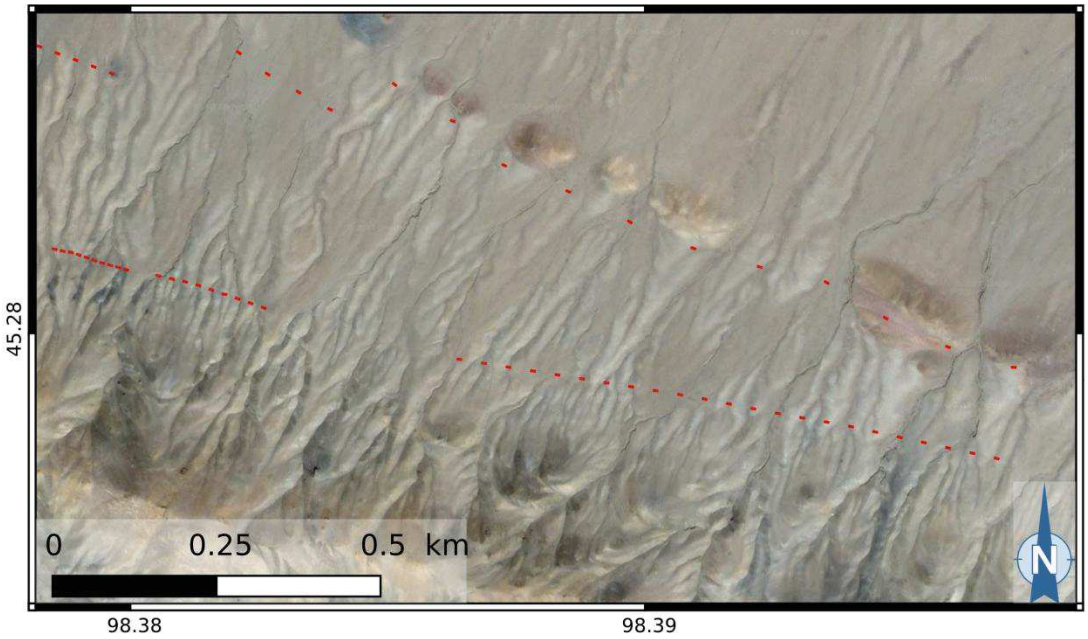


**Figure 4-23 : Detailed view of the WBF-R4 relay zone. Fault scarp are dashed to allow the observation of landforms.**

The next segment WBF-S5, shows a distributed deformation associated with transtensional deformations. The segment is average trending N090 ± 15°E, discontinuous and shows a general curve to the south (Figure 4-22). The segment depicts a sigmoid shape, which is consistent with the general left-lateral motion along the WBF, with a subsided area between two sinuous branches, 1 to 2 km away from each. The sedimentary bedrock seems to have had a strong influence on the geometry of faults given that the ruptures systematically locate into stratification lineaments. This sinuosity of the fault is also consistent with the left-lateral-reverse deformation observed along the northwestern side of the Bayan Tsagaan restraining bend.

Further East, the WBF tip zone is difficult to define, and corresponds to the branching with the faults associated with the main Bayan Tsagaan restraining bend that makes the link with the Eastern Bogd fault (EBF). The deformation is very distributed, notably to the North, within several sinuous thrusts faults associated with forebergs.

According to our satellite images mapping, the whole WBF surface rupture displays an almost continuous fault trace that affects Holocene geomorphic features on a length of at least 150 km (Figure 4-14).

### *IV.2.2. Coseismic offset measurements*

In order to determine the amounts of left-lateral offsets along the WBF, we carried out an analysis of offset geomorphic features by a three steps landform reconstruction along the Chandmani Gullies site, a 4 km-long section (Figure 4-24) of the WBF-S3 segment located 8 to 12 km west of Chandmani town (Figure 4-20). Landform reconstructions are done from Digital Elevation Models (DEM) and orthophotographs of 20 and 10 cm resolutions, respectively, acquired by an UVA photogrammetric survey (Figure 4-25.A-B-C). Additionally, complementary microtopographic TSL survey have been done on 4 offset channels, situated out of the UVA survey footprint, 1 to 3 km eastward.

The studied fault-section of Chandmani Gullies is located immediately to the West of the Rain Creek site, and is parallel to the Chandmani Nuruu, a ~10 km long E-W ridge oriented N100°E. The main WBF fault trace is located on the southern flank of the Chandmani Nuruu, into alluvial fan surfaces displaying systematic left-lateral offsets at their intersections with the fault (Figure 4-24). As mentioned in the previous section, 2 secondary faults can be identified (Figure 4-20 and Figure 4-21).

The main offset geomorphic features are alluvial fan surfaces incised by shallow gullies (Figure 4-25). Minor secondary scarps may be noticed, few tens of meters northward of the main fault trace, but do not display significant coseismic offset (Figure 4-24). Three main fan surfaces may be identified: the F3 surface is exclusively located north of the fault, and regularly cut by small gullies, whereas F2 and F1 surfaces are situated southward of the fault, with the smaller and younger F1 surfaces being deposited over F2 surfaces or incising them (Figure 4-25). Remaining surfaces (not shaded on the Figure 4-25) are active drains and modern fans furtherly named F0. The fault motion along this section is mostly left-lateral, with a minor uplift component, with north side of the fault up. This minor vertical component might be perennial as suggested by the occurrence of the ~100 m uplifted Chandmani Nuruu north of the main fault (Figure 4-21). The fan surface F3 cannot be identified to the south of the fault, but measurements of the cumulative vertical displacement between identified fan surfaces along two profiles transverse to the fault show scarp heights of: 3.0 ± 0.3 m between F3 and either F1 or F0 , and 3.7 ± 0,2 m between F3 and F2 (Figure 4-26).

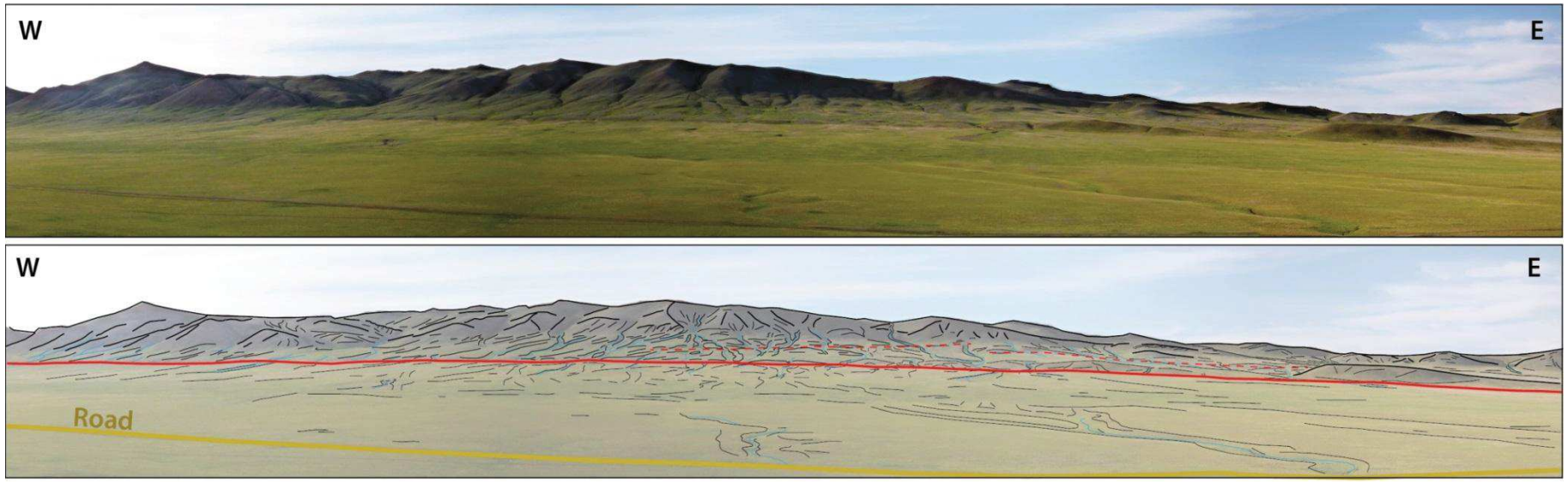


**Figure 4-24: Panoramic view to the north of the Chandmani Gullies site, and photointerpretation. The area covered by this picture corresponds to the UVA survey. See location of photograph in Figure 4-21.**

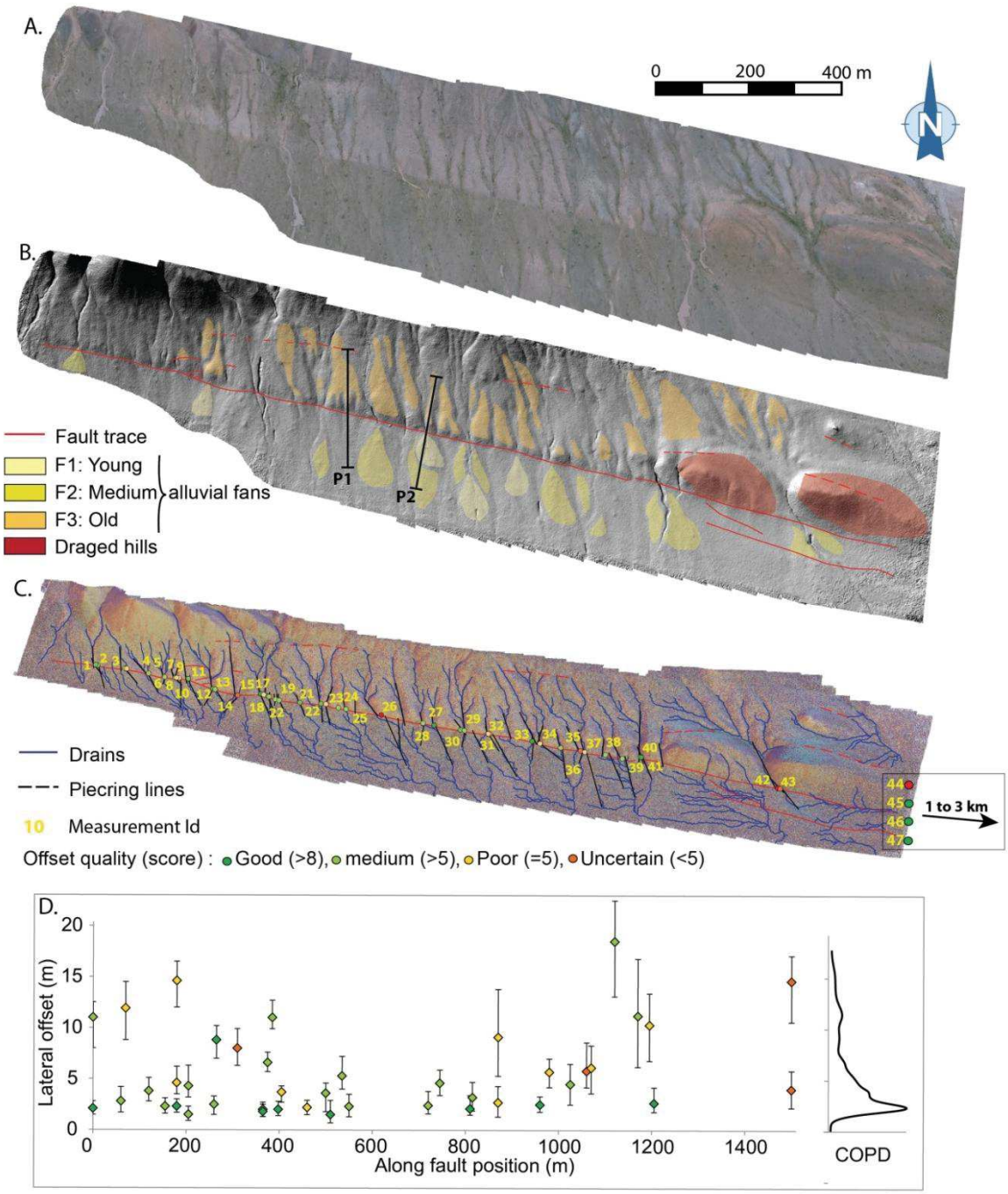


**Figure 4-25: Morphotectonic survey of the Chandmani Gullies site. Microtopographic data are derived from UVA survey and photogrammetric modeling. A. Orhtophotograph. B. Hill-shaded DEM with mapping of the fault traces and main alluvial fan surfaces. Black segments are location of profiles P1 and P2, presented in Figure 4-26. C. Slope direction shading, blue lines are DEM-derived drainage and dots are location of the offset measurements. Yellow numbers are measurement id and color scale on dots is based on offsets quality. D. Horizontal slip distribution of the offset measurements regarding to the on-fault position on C., and related uncertainties. Color scale on dots as in C. Black curve on right of the figure is computed COPD, as detailed in Figure 4-27.**

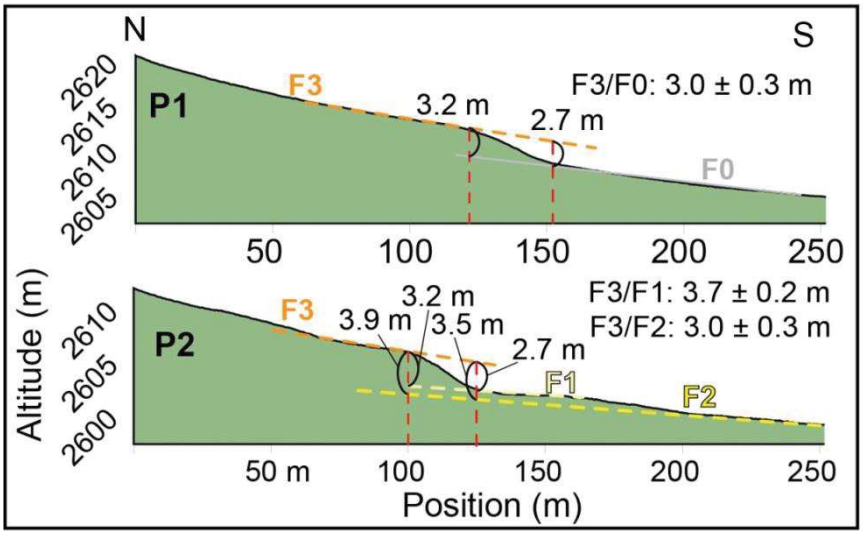


**Figure 4-26: Apparent cumulative vertical offset measurements on Chandmani Gullies site, on transverse topographic profiles derived from photogrammetric modeling of UVA-acquired air-photos. Location of P1 and P2 are figured in Figure IV 15. F0, F1, F2 and F3 are same f an surfaces as in Figure 4-25.B.**

The slightly oblique drainage to the east may impact our lateral offset measurements, generating some channel deflection. Altough the slip vector cannot be accurately determined despite of sufficiently preserved geomorphic markers (F3 has not been identified south of the fault), the fault motion is visibly mostly left-lateral and we assume that the landform likely correctly recorded the fault-related lateral deformation.

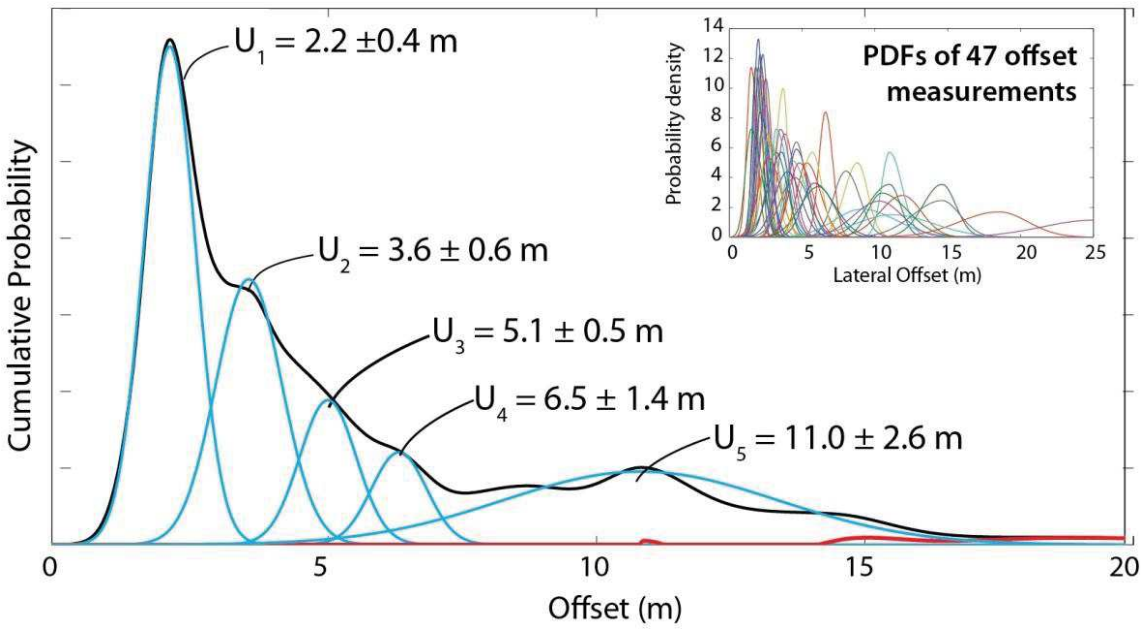


**Figure 4-27: Figure 4-28: Statistical modeling of lateral offset measurements on Chandmani Gullies. Inset represents the Probability Density Functions (PDF) for the whole offset dataset, assuming 2σ uncertainties. Main graph represents the identification of successive cumulative slips related to past earth quakes. Black line is the Cumulative Offset Probability Density (COPD), and Blue lines are extracted Gaussian slip signal of past earthquakes, for which the average slips are indicated in black numbers, associated to 1σ standard deviation.**

We performed 47 offset measurements, ranging from 1.5 to 25 m, 80% of them being inferior to 10 m (Figure 4-25.D), and we assessed the quality of each measurement regarding to criteria described in part III.2 of this chapter. Measurements table is presented in Annexe V. To analyze the distribution, three subsets were defined: i. whole dataset; ii. 35 best results, with measurement quality scores > 3/10, representing 75 % of the dataset; iii. 30 best measurements, with measurement quality scores > 6/10, representing 63 % of the dataset. Comparison of statistical analysis (Figure 4-27) carried out on each of these subsets yields consistent results about both the number of seismic events and their related average slip (Figure 4-29). The results thus show 5 successive slip increments cumulating 11 m of displacement, each of them generating a coseismic offset > 1.0 m. We however notice that assessments of cumulative offsets visibly fit with inflexions of the COPD, but are not associated to distinct peaks.

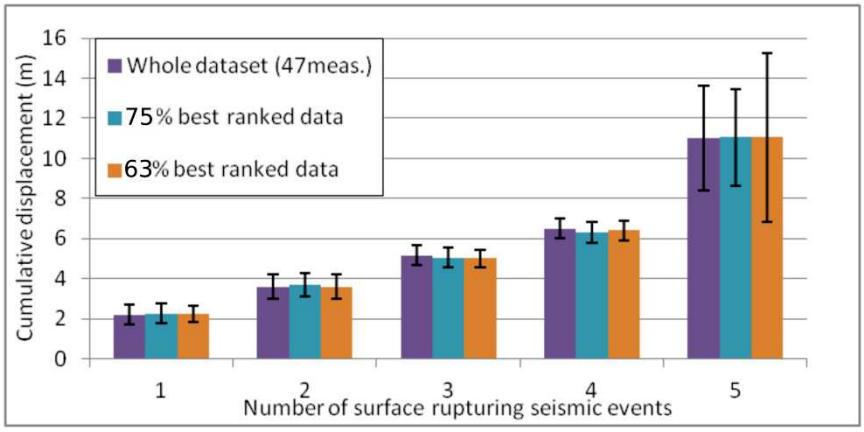


**Figure 4-29: Comparison of statistical cumulative slip related to past earthquake for whole dataset (47 measurements) and for the two subsets of best-ranked measurements. Error bars are 1σ standard deviation.**

According to our analysis (Figure 4-25, Figure 4-27 and Figure 4-29), the most recent large seismic event (E1) produced an average slip of 2.2 ± 0.4 m. The coseismic slips related to previous earthquakes fit with the variations of the COPD, although the COPD signal does not display well-separated peaks (Figure 4-27). Cumulative displacements related to previous earthquakes identified in the statistical distribution are 3.6 ± 0.6 m, 5.1 ± 0.5 m, 6.5 ± 0.4 m and 11.0 ± 2.6 m (Figure 4-27). Individual coseismic slip estimation may be derived from these cumulative slips, subtracting each signal to the previous one, and propagating the uncertainties, which yields values of 1.4 ± 1.1 m, 1.5 ± 1.1 m, 1.4 ± 1.0 m and 4.5 ± 3.0 m for events E2, E3, E4 and E5, respectively. These results suggest that E2, E3 and E4 had similar amount of slip, while E5 produced an offset three times larger. This observation must be nuanced given that the identification of E5 is rather weak, as it presents strong uncertainties. Looking at the local extrema of the COPD higher than 7 m, it seems that the slip related to an earthquake has been

missed by the model, given that the local extremum at 11 m has a stronger representation. This observation is not consistent with the fact that the larger the recorded displacement, the older the geomorphic feature, given that it has been likely less preserved in the landscape due to larger timespan. This relation can however be influenced by climatic pulses and base level variation – either related to local hydrological perturbations or regional tectonic processes – which generate time-uneven depositions, incisions and abandonments of geomorphic features. Accordingly, we suggest that the calculation of the coseismic slip related to event E5 is probably not correct, but is rather cumulating the displacements associated with two events. Consequently, the 4.5 ± 3.0 m observed on our dataset is potentially related to a cumulative offset rather to a coseismic slip related to one single event.

We notice that the assessments of cumulative offset from that dataset have to be considered with care, as although the coseismic offset associated to the most recent event is fairly well resolved, cumulative values only generate inflexions of the COPD, and not distinct peaks.

**Figure 4-30: Photograph to the E-NE of the WBF surface rupture, along the Chandman Gullies site. Black arrow indicates the WBF main surface rupture, and red arrow indicates the WBF trace, at Chandmani town. Location is gully n°40 on Figure 4-25-C.**

Assuming that the cumulative displacement of 11 m observed within the COPD represents the total left-lateral offset corresponding to the 3.7 m cumulative vertical offset, and that the surface T3 correspond at first order to T0 (which is arguable), may

allow determining the kinematic characteristics (e.g. Nazari et al., 2009) of the left-lateral-reverse WBF fault, westwards Chandmani village. After our calculation, its strike and pitch are N°100E and 17°E respectively. Also, the fault dip has been observed on the field as almost vertical (Figure 4-30).

We conclude from our assessment of coseismic slip recorded by the landforms along the WBF-S3, that this fault involves unitary coseismic offsets of at least 1.5 m, which correspond to Mw6 to Mw7 earthquakes, according to the empirical regression functions of Wells and Coppersmith (1994).

### *IV.2.3. Determining slip rates along the WBF*

The geomorphological slip rate along the WBF has been quantified at the Ice Creek Valley site (45.405°N, 97.492°E). This site is located at an altitude of 2650 m, on a north-facing valley, incised within the north face of the Eemltik Uul mountain range, bounding the Chandmani Valley to the south (Figure 4-20). The Ice Creek valley is covered by quaternary fan deposits in its center and has been affected by minor glacial activity as shown by glacial slickensides observed on *in situ* bedrock outcrops and by remnants of a few moraine deposits on the central part, ~300 m downstream from the fault (Figure 4-31-A). The valley defines a narrow U-shaped profile with a bar-and-swale morphology in its axial part, corresponding to the post-glacial debris fan (Figure 4-32). The fault trends N105°E and cuts perpendicularly through the valley with a pure left-lateral strike-slip motion (Figure 4-32). At a larger scale the whole valley describes a large bayonet that recorded a total cumulative left-lateral offset of 900 ± 60 m, after landform reconstruction (Figure 4-31-B).

On the western bank of the valley, two main levels of terraces can be identified (Figure 4-33): T1 is a recent stream terrace, and T3 is a wide surface continuing westward at the foothills of the relief. Further west, a well-preserved terrace (surface *S',* Figure 4-34) was mapped as contemporaneous of T3, given that both surfaces have similar morphology and are found at the same altitude (Figure 4-31-A). This T3 surface is also visibly associated with the analogue (altitude, texture and morphology) continuous surface constituting the eastern bank of the valley, furtherly describes as the surface *S* (Figure 4-35).

Additionally, on south of the fault, a remnant of an intermediate terrace (*T2*) is located on the central part of the valley (Figure 4-33), inset in another fan surface (*F*) showing a bar and swale morphology, and especially three fan-related bars of aligned boulders, furtherly named from west to east B1, B2 and B3. The T2 tread is not present downstream of the fault, most likely because of its offset along the fault and its subsequent erosion by the active stream. The eastern flank of the valley presents a west-facing gentle slope, the surface S*,* which is left-laterally shuttered by the fault showing a south-facing counter-slope fault scarp, corresponding to a purely apparent vertical offset (Figure 4-33).

200 m downstream of the fault, two terraces can be identified on the western bank, named T1' and F' as they seem to belong from corresponding surfaces (respectively T1 and F) close to the fault (Figure 4-34). Especially, the F' terrace corresponds to a triangular strath terrace incised into the surface S, given that it is aligned with main

drainage direction and display large rolled cobbles deposited on the bedrock (Figure 4-34-B).

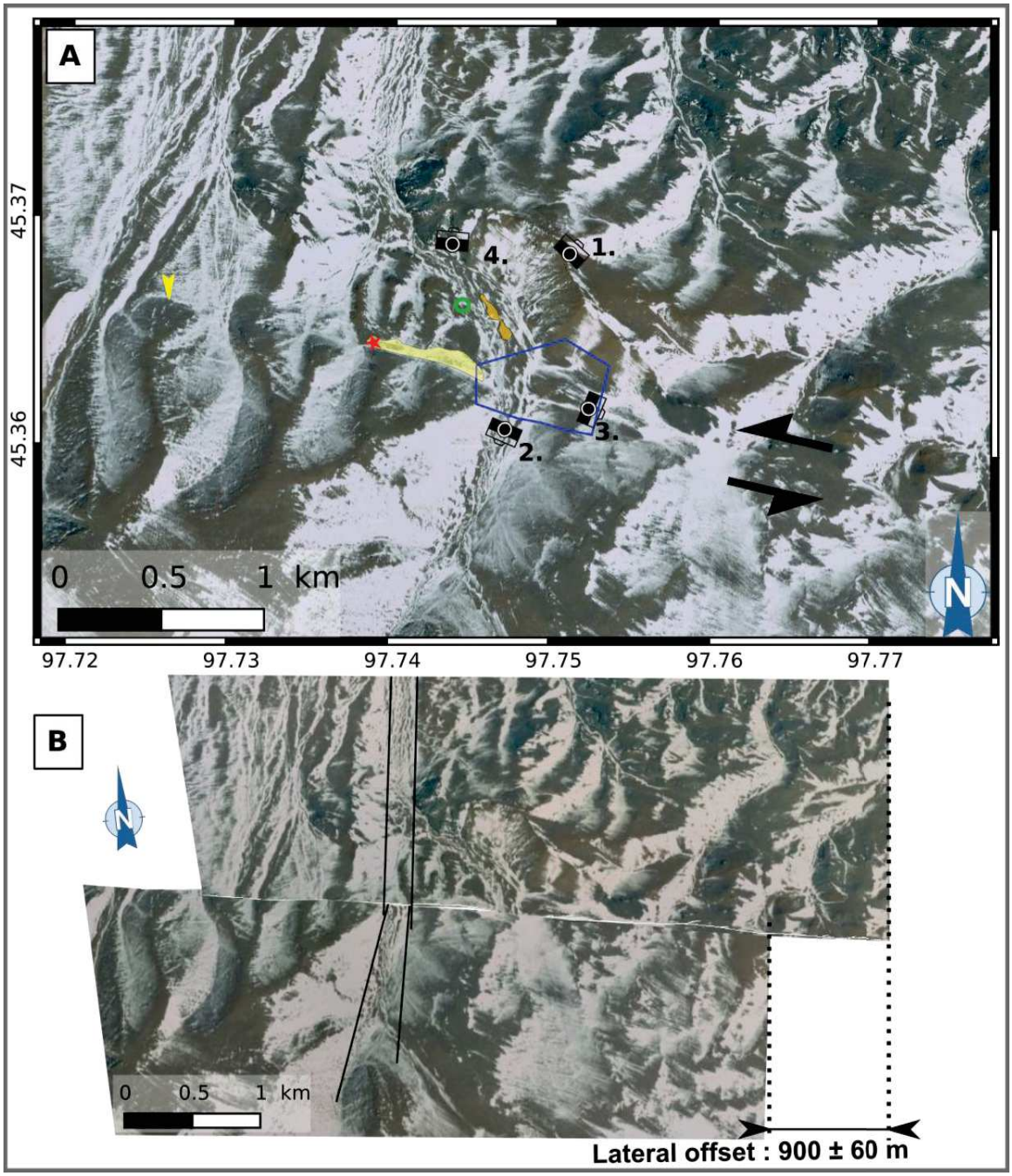


**Figure 4-31: A. Satellite photograph of the Ice Creek Site. The river is flowing to the north. Yellow arrow points out the main fault trace and black arrows show the left-lateral fault kinematics. Green circle corresponds to the location where glacial slickensides on bedrock were observed (N45° 22.02', E97°44.60'). Yellow shaded area is surface S' and orange shaded area shows the location of the remnants of moraine deposits. Red star indicates the location of sample ICT4S. Cameras are locations of: Figure 4-32 (1), Figure 4-33 (2), Figure 4-34-A (3) and Figure 4-34-B (4). B. Restoring the largest cumulative offset associated with the Ice creek valley allows estimating a left-lateral offset of 900 ± 60 m. Black dashed lines are piercing-lines on both sides of the main drainage.**

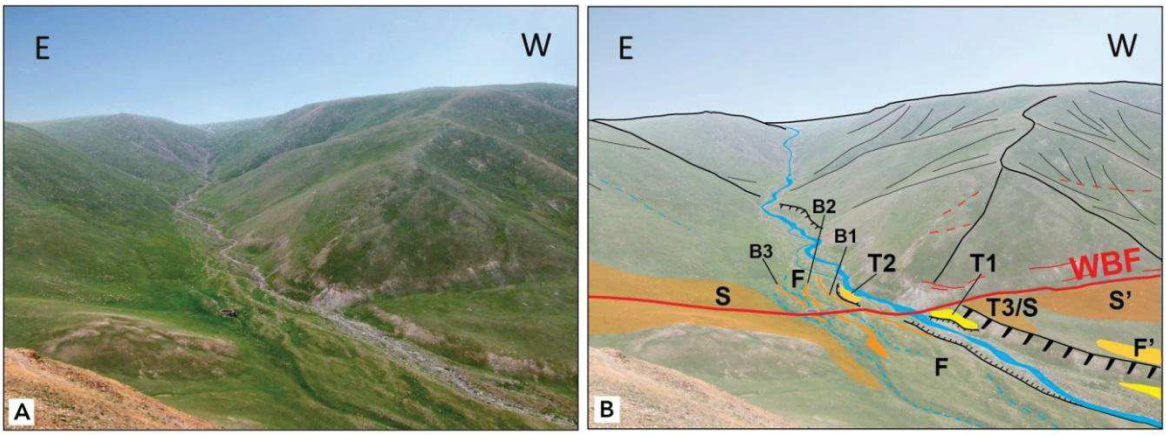


**Figure 4-32: Panoramic view to the south of the Ice Creek site. A. Photomosaic. B. Photointerpretation with main geomorphic features used for offset measurements (see text for details).**

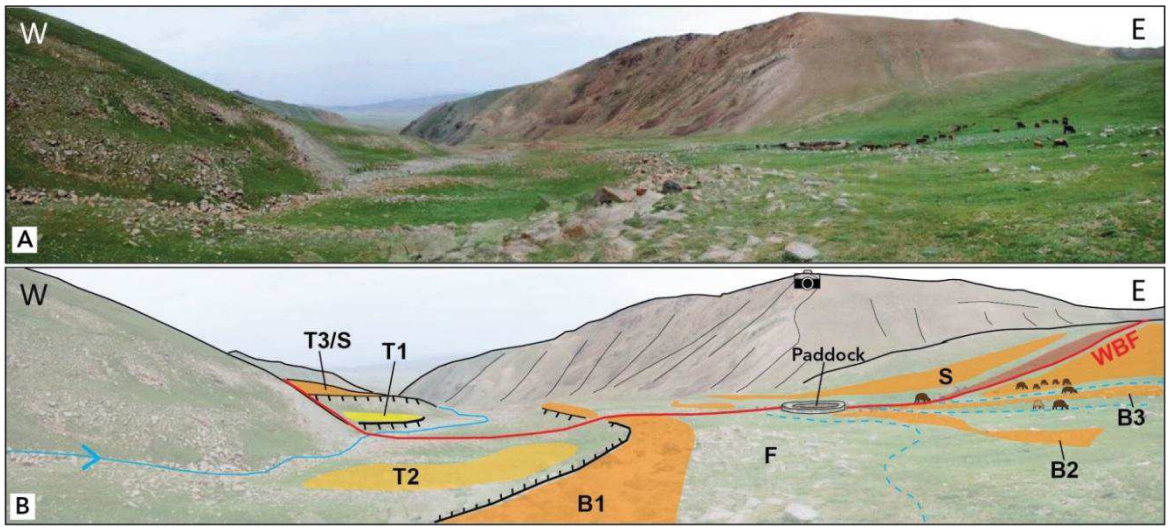


**Figure 4-33: Panoramic view to the north of the Ice Creek site. A. Photomosaic. B. Photointerpretation with main geomorphic features used for offset measurements (see text for details). The south-facing counter slope scarp offsetting the eastern flank of the valley (surface S) is highlighted in red. The camera on top of the mountain indicates the location of the picture presented in Figure 4-32.**

Accounting only for geomorphic observations, the ice Creek landforms probably established as follow: In first time the alluvial surface S (and belonging T3) and S' were deposited; in a second time the fan surface F have been deposited, with belonging bars (B1, B2 and B3) upstream of the fault and the F' strath terrace downstream; in a third time the rivers incised into the fan surface F, and generated the terrace T2, then T1 and T1'.

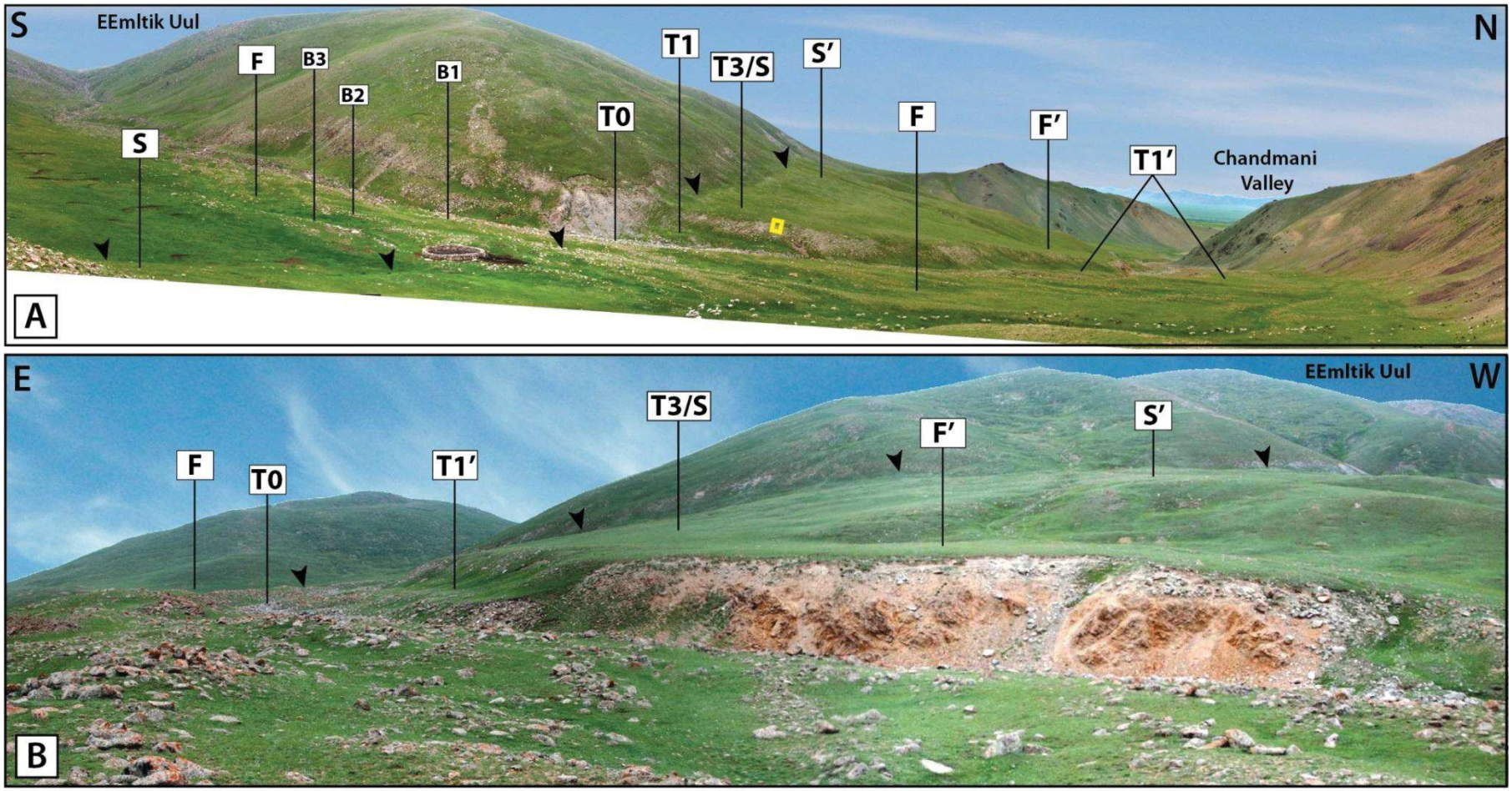


**Figure 4-34: Panoramic views of Ice Creek site, and label of main geomorphic features. Black arrows indicate the main WBF scarp, and yellow box locates the soil pit location. See location of pictures in figure. A. Panorama to the west. For scale, the paddock on the foreground is ~10 m-wide. B. Panorama to the south. For scale, the reddish bedrock riser in foreground is ~15 m-high.**

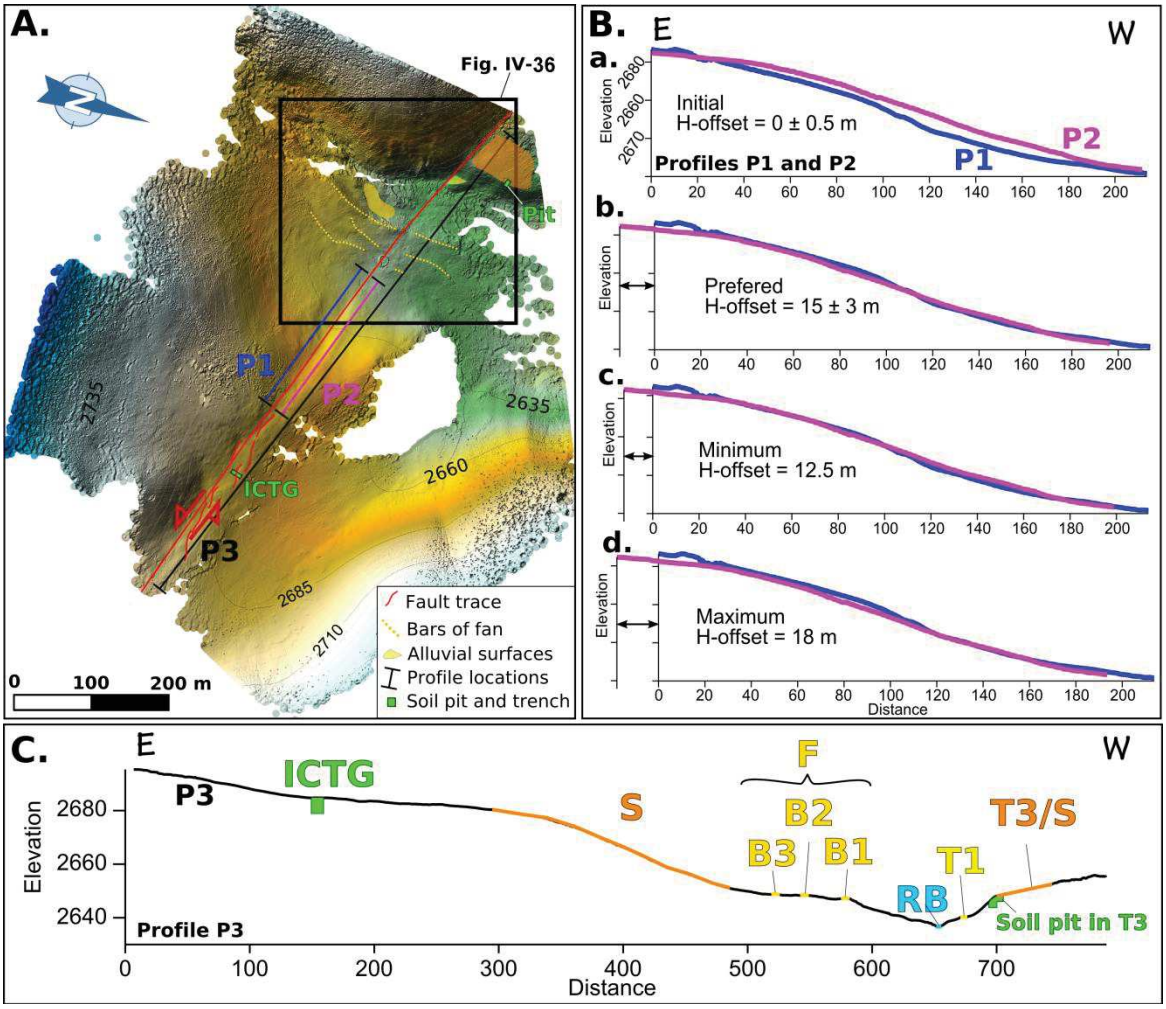


**Figure 4-35: A. DEM from TLS survey on whole Ice Creek Site, with center located 45.350°N; 97.735°E. Color panel shows altitudes, contours are 25 m, and white parts are no data area. Shaded areas are identified surfaces: yellow is T1, light orange is T2 and dark orange is T3. Segments are location of along-fault profiles: Blue is P1, pink is P2 and black is P3. Green squares are location of the Ice Creek Tension Gash trench (ICTG) and of soil pit in T3 for $^{10}$Be profile sampling. Black square is location of the Figure 4-36. B. Offset measurements of the lateral displacement recorded by the surface S, by three steps reconstruction of along fault profiles: a. Initial positions of the profiles, uncertainty relative to profile position; b. Preferred offset value, uncertainty derived from maximum and minimum offset values; c. Minimum offset value; d. Maximum offset value. C. Along fault topographic profile across Ice Creek site, labelling the main studied geomorphic features. Note the consistent correlation between S and T3 surfaces.**

In order to determine the fault slip-rate on Ice Creek site, we carried a microtopographic TLS survey (see footprint in Figure 4-35) and collected samples for $^{10}$Be cosmogenic dating (Figure 4-35.A and Figure 4-36).

On several hundred meters wide areas such as the Ice Creek site, the TLS survey must be done by a sequence of scans, and due to sharp and hummocky landforms related to presence of blocs and little hills, the obtained DEM presents some shadow areas, obscuring the full area (white areas in Figure 4-35.A). However, the geomorphic features used to determine the offsets have been satisfactorily covered.

Amount of offsets are assessed by 3-steps retrofits of the landforms, using the DEM and DEM-derived slope direction and slope curvature data (Figure 4-36):

1. We first analyze the fan surface F with the bar-and-swale morphology, using the 3 central bars (B1, B2 and B3) as piercing lines, as they display systematic left-lateral offsets. Because the western bar (B1) is located just at the edge of the surface, it is affected by moderate rock fall close to the fault, limiting the accuracy of left-lateral offsets measurements. The contact between the fault and the two other bars B2 and B3 is partly masked by a paddock, and we therefore extrapolated the piercing lines by extending them ~10 m straight until the fault line. Using a 3-step marker reconstruction we determine offsets of $8.8^{+1.5}_{-1.3}$ m, $9.3^{+1.8}_{-1.7}$ m and $7.4^{+2.1}_{-1.6}$ m for B1, B2 and B3, respectively. Those three measurements agree within errors, and we calculated an average offset value of 8.5 ± 1.7 m using these landforms.
2. We also attempt to use the riser between T1 and T3 terraces to assess the recorded offset: the riser is well defined downstream the fault, (Figure 4-36), and despite it appears very steep and devoid of vegetation, it has not been affected by no landslide processes. However it is likely that the riser retreated since the abandon of T3, increasing its apparent offset. Upstream the fault, we do not observe the equivalent T1-T3 riser. Instead, we observe a riser within the outcropping bedrock curving to the West. The riser presents evidence of erosion, but visibly more related to cryoclastic processes and chemical weathering than recent fluvial erosion, even though the active stream is located at the bottom of it. The riser probably undergone a retreat, but potentially less pronounced than the T3-T1 downstream riser, considering that bedrock is less prone to erosion than terrace deposits. Consequently, we consider that the offset between the two markers corresponds to a maximum value of the coseismic displacement experienced by the landforms. To assess the offset, we use the following piercing lines: southward of the fault, we use the base of the riser, while northward the fault, we use the base of the T3-T1 riser (Figure 4-36). This yields a maximum offset of $12.9^{+3.2}_{-2.5}$ m. We however notice that the piercing lines here defined are uncertain and that although this offset measurement constitutes an estimation of the cumulative offset experienced by the T3/S surface, we will not furtherly use this measurement for slip rate computation.
3. Eventually, we assessed the offset affecting the surface S on the eastern flank of the valley (Figure 4-32, Figure 4-35-A and Figure 4-37). The matching of fault-longitudinal profiles (Figure 4-38), which cover the whole surface S until the

surface F on both sides of the fault, yields to an horizontal offset of 15 ± 3 m (Figure 4-35.B). This is consistent with the offset estimated within the west bank risers and also coherent with the interpretation we propose for the geomorphological establishment of late-quaternary landforms in both sides of the Ice-Creek valley (i.e. T3 contemporaneous with surface S).

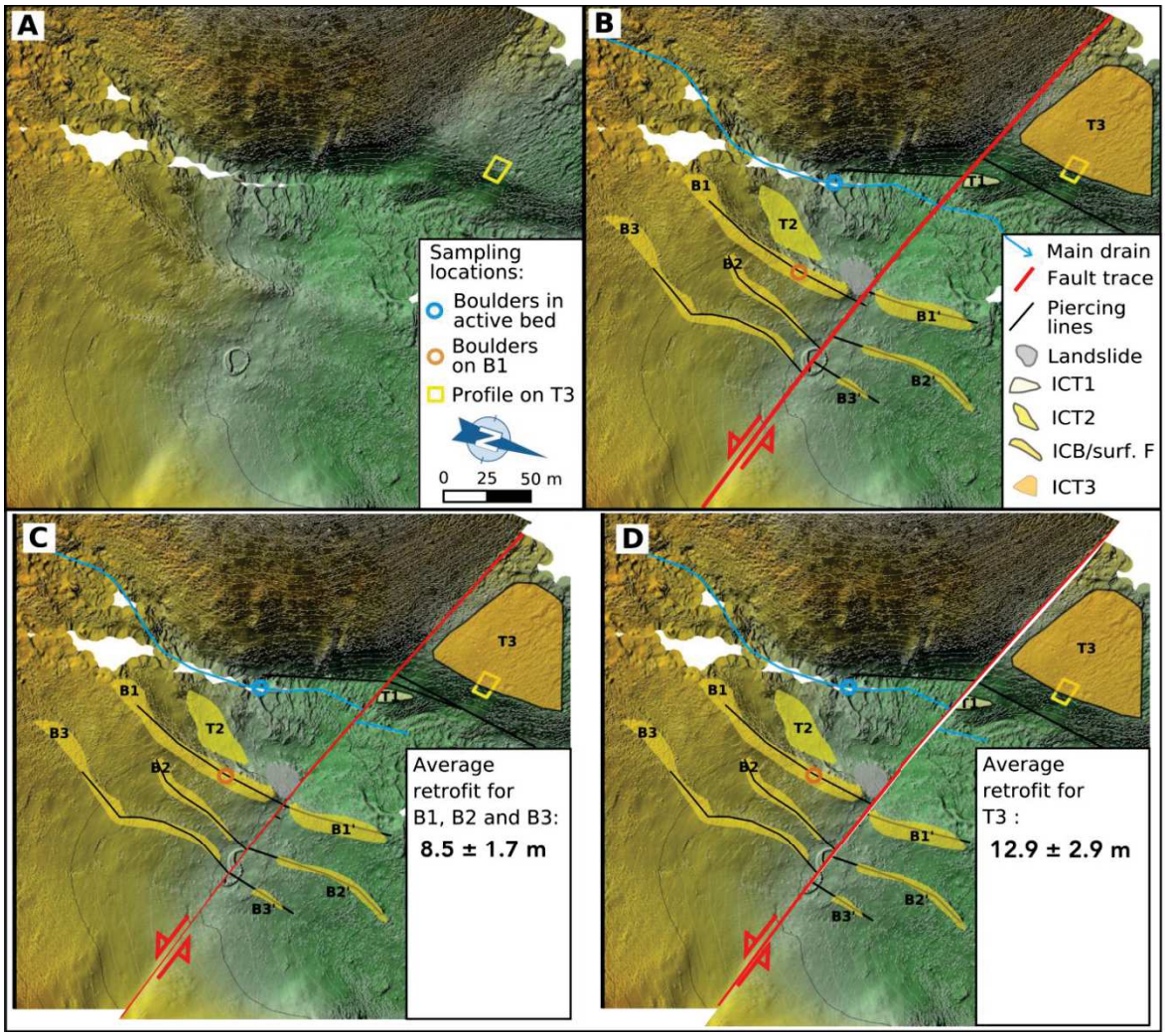


**Figure 4-36: Offset measurements and sampling locations on fan-related bars and terrace riser in Ice Creek Valley. See location on Figure 4-35. A. DEM from TLS survey; yellow square is location of the Soil Pit in T3 for $^{10}$Be profile. The round shape, close-center of the picture is a paddock. B. Mapping of the main geomorphic features used in offset measurements, with related piercing lines shown as black solid lines. ICT1: Ice Creek terrace 1 (T1); ICT2: Ice Creek terrace 2 (T2); ICT3: Ice Creek terrace 3 (T3); ICB: Ice Creek bars of the central fan (B1, B2 and B3 south of the fault, and corresponding B1', B2' and B3' north of the fault) C. Average offset measurement by retrofit for the central bars of the fan, B1, B2 and B3. D. Average offset measurement by retrofit for the riser of T3 terrace.**

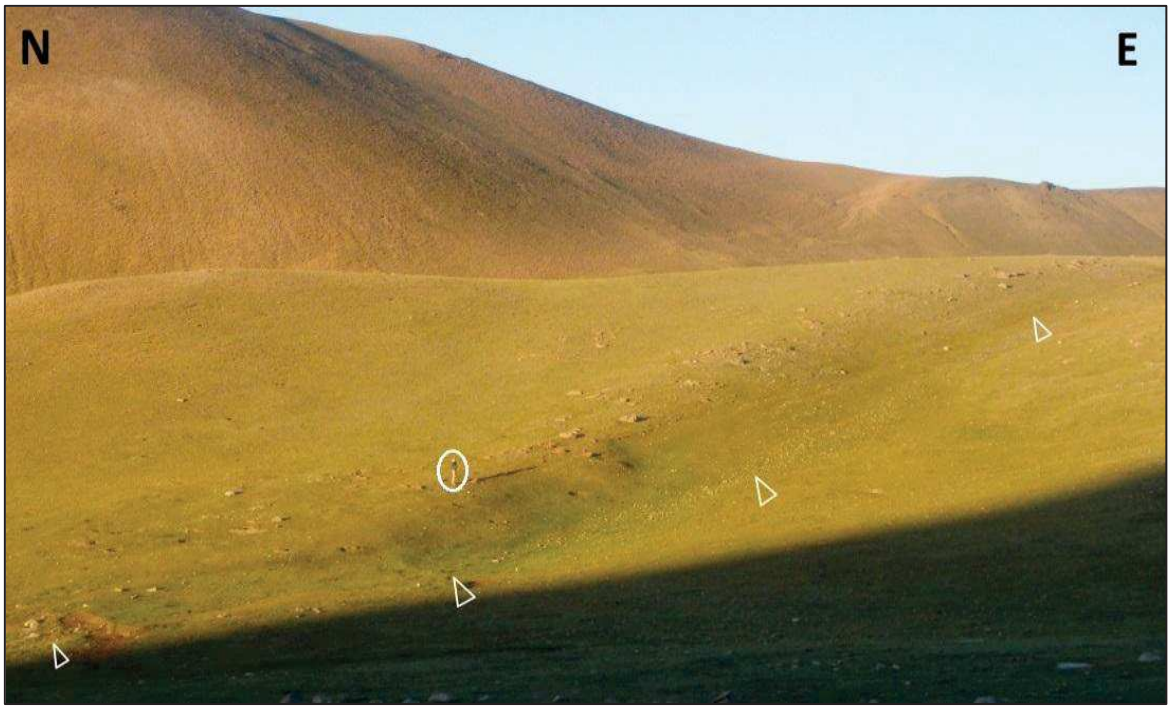


**Figure 4-37: Photograph of the shuttered eastern flank of the Ice Creek valley (surface S), along the WBF. White circle on character for scale, and arrows point out the base of the counter-slope scarp.**

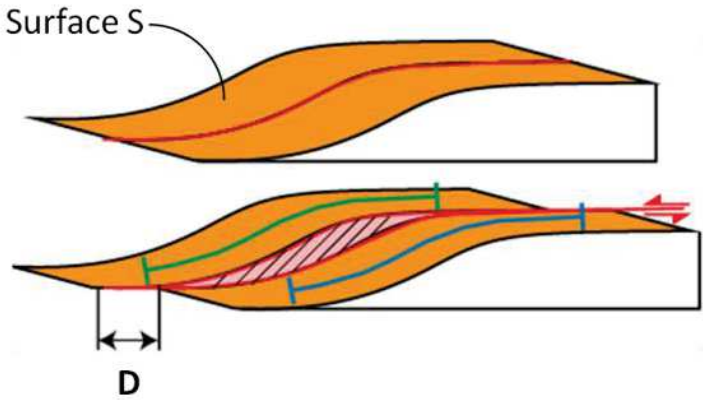


**Figure 4-38: Bloc diagram of the cumulative lateral offset measurement (D) recorded by the surface S, from alignment of longitudinal profiles, for a pure left-lateral coseismic displacement.**

To date the markers, we sampled T3 on the western side of the valley and the bar B1 on center of the valley (Figure 4-36). The abandon age of T3 has been determined by sampling amalgams of 50 quartz-rich granitic cobbles along a 2 m depth profile in a 2-bench-soil-pit dug within highest-part of the T3 riser assuming active refreshment of the riser slope as it is devoid of vegetation. No stratification was observed, neither within the soil pit nor on T3 riser (Figure 4-32 and Figure 4-39) and seven samples have been collected along the depth profile (Table 4).

To determine the ages of B1, B2 and B3 bars, we collected clast amalgams from tops of ~1 m diameter granitic boulders within B1 bar where it was the best preserved. Being unable to dig a soil pit in the surface, we collected an amalgam from boulders located into the active stream, assuming that their content in $^{10}$Be corresponds to the mean-pre-existing concentration (i.e. the inheritance) that we would found at depth bellow the bars.

The distribution in depth of the soil pit samples ICT3-1 to ICT3-7 shows a steep profile, fitting rather well with a model profile of $^{10}$Be produced in situ, as presented in Chapitre 1. The steepness of the profile indicates a strong $^{10}$Be inheritance > $5x10^5$ at.gr$^{-1}$.

Only the topmost samples (ICT3-6 and ICT3-7) present a low concentration regarding the model. This low content in $^{10}$Be of the surface could be explained by recent colluvial input within the surface, originated from the ~45 %-steep slope situated 20 m right upslope from the sampled site. One may argue that such infill in the surface could occurred all along the history of the T3 surface, potentially affecting the significance of the $^{10}$Be profile; however, looking to the T3 surface geomorphology, it is fairly flat, significantly dipping north, and it only displays sporadic un-enchased pebbles, visibly coming from colluviation along the aforementioned slope. No distinction in deposit natures (i.e. colluvial or alluvial) has been noticed in the soil pit during the sampling. These observations let think that this surface is truly abandoned, while it possibly involves rejuvenation due to moderate colluviation. Eventually, we notice that another surface sample (ICT4S), collected on S' 200 m west at same elevation, is richer in $^{10}$Be (Figure 4-39). At this site, the surface S' is wider, and the input of colluviums from neighboring slopes among surface terrace material is weak.

Consequently, we considered that the topmost samples of the pit (ICT-6 and ICT3-7) were outliers, and we therefore did not took it into account in the model to calculate the abandon age of the surface (Figure 4-39-A).

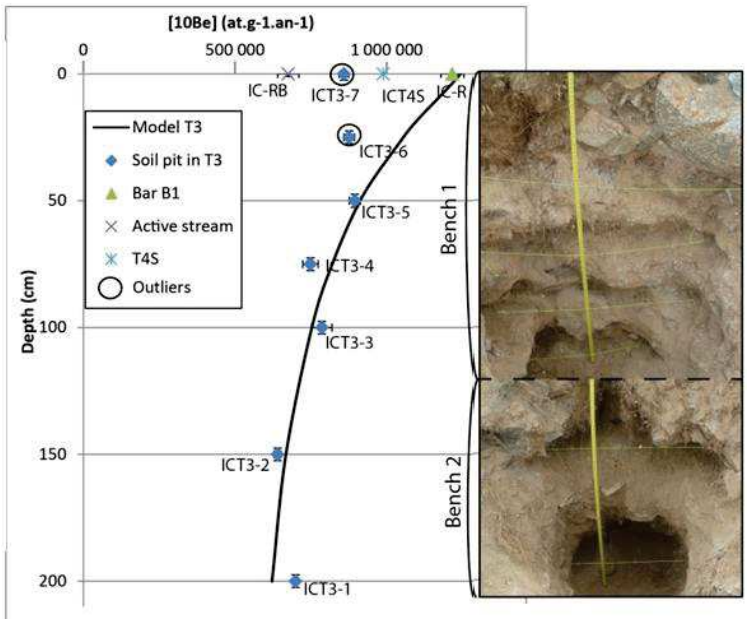


**Figure 4-39: $^{10}$Be analysis on Ice Creek site. A. Concentration in $^{10}$Be: ICT3 is the profile in depth of $^{10}$Be within the T3 terrace; IC-R is the sampling of the top boulders of B1, and IC-RB corresponds to the sampling of boulders in the active stream. B. Log of the 2-bench soil pit within the riser of T3.**

In order to assess if this $^{10}$Be profile already reaches the steady state or not, and to better constrain the modeled profile, we carried a modeling (Hidy et al., 2010). Results of the age vs erosion rate show that the abandon age is best constrained to 20.7 ± 0.2 ka (shape of the Figure 4-40-B), but yield an uncertain erosion rate of 25 ± 8 m.Myr$^{-1}$. This age is consistent with the last glacial maximum (e.g. Clark et al., 2009), consistent with fluvio-glacial control of the geomorphology of the Ice Creek site.

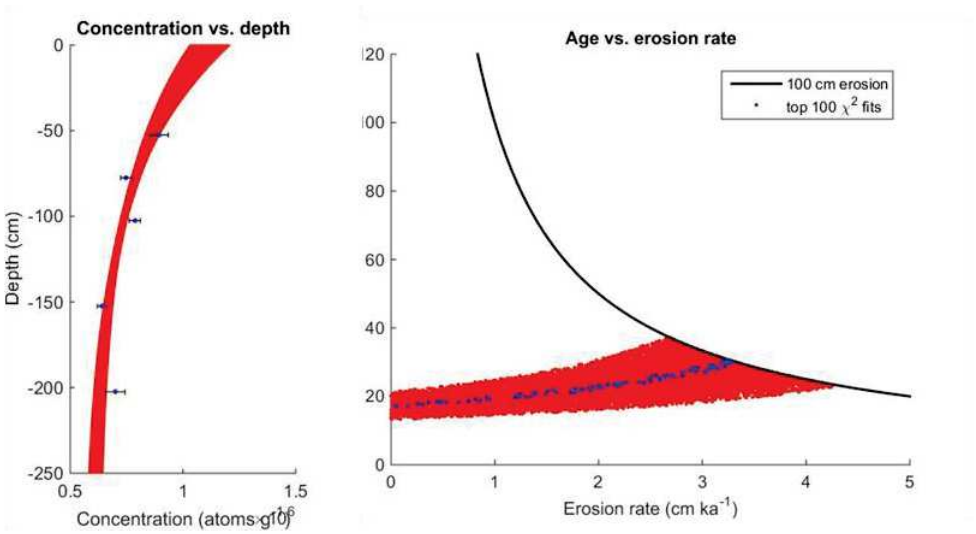


**Figure 4-40: Bayesian modeling of the $^{10}$Be profile in T3. A. Modeled profile. B. Age vs erosion modeling.**

Assuming the geomorphological analysis of the surfaces on both banks of the Ice Creek Valley with a contemporaneity of T3 and S surfaces (indicated by the topographic profile on Figure 4-35.C), this age can also be attributed to abandon age of surface S.

Regarding to the assessment of the abandon age of the bars B1, B2 and B3 from the two samples took on top of the B1 bar and within the active stream, we derive two ages depending on assumptions of erosion and inheritance: First, assuming a negligible erosion rate, and taking the difference in $^{10}$Be content of those two amalgam samples, we calculate a deposition age of 17.6 ± 1.0 ka. Secondly, assuming a steady state and a nil-inheritance, we derive an erosion rate of 16.1 ± 1.0 m.Myr$^{-1}$, associated to an integrative age of 39.0 ± 2.3 ka. Those values are consistent with the older abandon age measured for the terrace T3. We hence conclude from geomorphic interpretation that the abandon age of the Bars B1, B2 and B3 is 17.6 ± 1.0 ka.

We notice that these dates assume no snow cover, which can influence the production rate: a smaller production under snow cover engendering a younger age (e.g. Gosse and Phillips, 2001). We do not have constrain on this parameter, except that we know that there is systematically snow during winter, with moderate thickness given that there are few precipitation in southern Mongolia (e.g. Climatedata.org). Moreover, ice sheets may be involved in the geomorphic evolution of this site, in spite of minor glacial activity and reduced precipitation in southern Mongolia (e.g. Lehmkuhl, 1998).

Looking the $^{10}$Be content of the boulders sampled within the active stream Ice Creek Valley (sample IC-RB on Figure 4-39), it appears that, despite of the difference of size of the samples (10 to 20 cm pebbles in T3 and ~1 m boulder within the central fan), there is a fair correlation between the inheritance in $^{10}$Be quantified into the soil pit, and the inheritance assessed 10 m westward in the active stream bed, with a high value of ~6.7x10$^{5}$ at.g$^{-1}$. Despite the difference of clast sizes, the similarity of the assessment of the inheritance can likely be explained by the torrential and glacial processes involved in the establishment of the Ice Creek morphology. In fact, those processes carry both fine and very coarse sediments, which may deposited with similar inheritance in $^{10}$Be. These observations indicate first a relevant measurement of the inheritance on the materials deposited in Ice Creek site, and secondly that the principle of uniformitarianism – i.e. that the inheritance in $^{10}$Be content in currently stream-carried sediment is representative of the inheritance of the clasts composing the alluvial geomorphic features formerly deposited by the same stream –, evocated to assess the $^{10}$Be inheritance appears relevant on that site.

**Table 4: The $^{10}$Be nucleide concentrations and modeled ages for samples at Ice Creek site.**

| Sample | Lat (dec°) | Lon (dec°) | Alt (masl) | [$^{10}$Be] (at.g$^{-1}$) | err. [$^{10}$Be] 1σ (at.g$^{-1}$) | Shield. Cor. | Density | Depth (cm) | $^{10}$Be age $t_{min}$ (ka) | $^{10}$Be age $t_{int}$ (ka) | Erosion rate (m.Ma$^{-1}$) |
|---|---|---|---|---|---|---|---|---|---|---|---|
| ICT3_1 | 45,364 | 98,745 | 2640 | 7,00E+05 | 4,36E+04 | 0,983 | 2,0 | 200 | | | |
| ICT3_2 | 45,364 | 98,745 | 2640 | 6,40E+05 | 2,00E+04 | 0,983 | 2,0 | 150 | | | |
| ICT3_3 | 45,364 | 98,745 | 2640 | 7,86E+05 | 2,45E+04 | 0,983 | 2,0 | 100 | | | |
| ICT3_4 | 45,364 | 98,745 | 2640 | 7,49E+05 | 2,46E+04 | 0,983 | 2,0 | 75 | | 12,6 ± 0,8 | 63,0 ± 3,8 |
| ICT3_5 | 45,364 | 98,745 | 2640 | 8,95E+05 | 3,92E+04 | 0,983 | 2,0 | 50 | | | |
| ICT3_6 | 45,364 | 98,745 | 2640 | 8,77E+05 | 3,05E+04 | 0,983 | 2,0 | 25 | | | |
| ICT3_7 | 45,364 | 98,745 | 2640 | 8,59E+05 | 2,98E+04 | 0,983 | 2,0 | 0 | | | |
| ICR_S | 45,364 | 98,746 | 2640 | 1,22E+06 | 6,78E+04 | 0,983 | 2,0 | 0 | 17,6 ± 1,0 | 39,0 ± 2,3 | 16,1 ± 1,0 |
| ICR_RB | 45,364 | 98,746 | 2640 | 6,76E+05 | 5,97E+04 | 0,983 | 2,0 | 0 | | | |
| IC_T4S | 45,364 | 98,746 | 2640 | 9,88E+05 | 3,07E+04 | 0,983 | 3,0 | 0 | 13,9 ± 0,8 | | |

To conclude on the geomorphic analysis of the Ice Creek site, those two dating are consistent, giver that the abandon age of the surface in which the river bed is incised is older than the deposition age of the fan deposits into that valley. We notice that the surface S does not describe significant topographic change when joining the surface of the fan (Figure 4-35), and that the climatic pulses undergoing the evolution of such mountainous landscape involve quick developments of both incision and deposition, combining torrential and glacial processes. Also dates are consistent whether the dating method used for those age determination is distinct (given that although both dating approaches are based on amalgams, the dating of T3 is done by a profile sampling of decimeter clasts within a preserved surface, while the age of the fan-related bars is determined from two samples from top of boulders, on top of the bars and in the active river bed).

Hence a combination of obtained ages, measured offsets and geomorphic interpretations allow assessing two horizontal slip rates along the WBF at Ice-Creek site:

- from the fan-related bars, considering a mean offset of 8.5 ± 1.7 m, and an abandon age of 17.6 ± 1.0 yr, the computed slip rate is 0.48 ± 0.12 mm.yr$^{-1}$.
- From the T3 surface on the east bank, considering an offset of 15 ± 3 m and a abandon age of 20.7 ± 2.2 ka, we computed a maximum slip rate of 0.72 ± 0.22 mm.yr$^{-1}$.

Averaging those slip rate estimations (although the second is a maximum) yields 0.62 ± 0.19 $mm.yr^{-1}$.

The moderate discrepancies between the slip rates computed on T3 and on the fan-related bars, might be partly explained by the reduced number of seismic cycles the bars experienced. In fact, assuming coseismic offsets of 1.5 m to 3 m (assessed along the same segment in part IV.2.2), offset measurements of 9 m might encompass three to six seismic cycles, leading to a slip rate uncertainty relative to the current position in the earthquake cycle (i.e. close or far from the age of the most recent event ?) of 10 to 15%.

### *IV.2.4. Ages Paleoearthquakes along the WBF*

#### IV.2.4.1. Chandmani Valley tension gashes

A field prospection has been done within a 45 m-long tension gash located 45.405°N; 97.490°E, by digging a small trench, 2 m-long and 1.2 m-deep (Figure 4-41). Sampling of organic matter in soil-rich horizon (considered as paleosoil), allows post-dating the rupture-related opening of the tension gash. Two samples have been collected for radiocarbon dating at 90 and 100 cm depth (table), and yielded ages of 730 ± 26 CalyrBP and 1340 ± 23 CalyrBP, respectively. These ages are consistent with the stratigraphic distribution of the samples, and allow post-dating the last surface rupturing event at 1340 ± 23 CalyrBP.

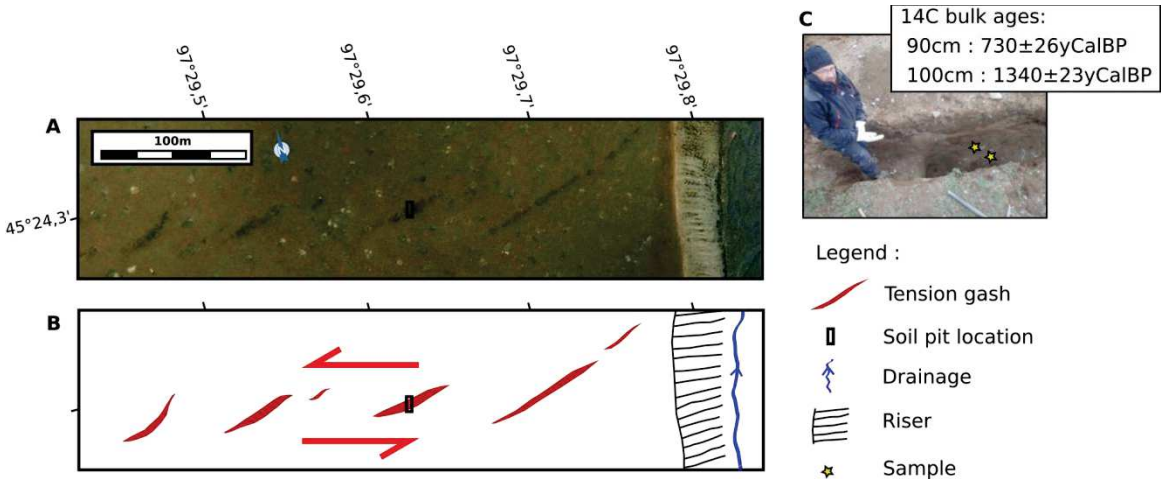


**Figure 4-41: Chandmani Valley Tension Gash. A. Satellite image of the tension gashes; B. Interpretation of A; C. photograph of the small soil pit and approximate location of radiocarbon samples.**

**Table 5: Radiocarbon ages of samples collected in South Chandmani Valley Tension Gashes.**

| Site | Sample | Nature | Depth (cm) | Masse C (mg) | Age yr BP | Err age yr BP | Age CalyrBP | Err age CalyrBP | 68% range CalyrBP | |
|---|---|---|---|---|---|---|---|---|---|---|
| Chandmani Tension Gash | M15-TG-5 | bulk | 90 | 1,41 | 815 | 30 | 730 | 26 | 703 | 756 |
| Chandmani Tension Gash | M15-TG-6 | bulk | 100 | 1,20 | 1440 | 30 | 1340 | 23 | 1316 | 1363 |

#### IV.2.4.2. Ice Creek Tension Gashes site

At Ice-creek site, 360 m east from the ice creek stream, is an alignment of right-stepping 10 to 30 m long tension gashes. Drainage is flowing northwards according to the major hillslope right south of the trench site, with a westward component due to the proximity of the Ice Creek valley. Along the fault, the pure left-lateral cumulative offset (see section

IV.2.3), combined with tension gashes and local channels, produce a smooth counter-slope scarp. This feature generates locally westwards drainage, punctured by smooth water sinks related to the tension gashes (Figure 4-42).

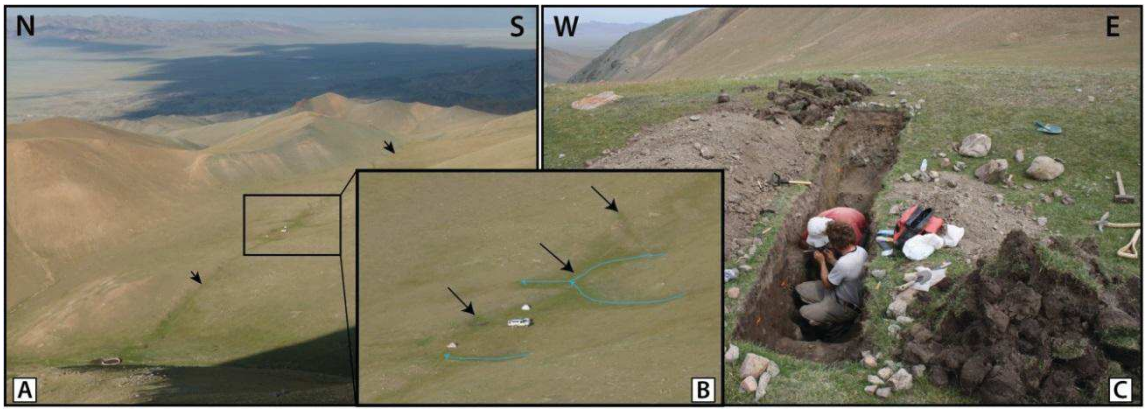


**Figure 4-42: Photographs of the Ice Creek Tension Gashes along the WBF. A. Panoramic view towards the East of the tension gashes, situated within the western flank of the Ice Creek Valley (see the 10 m-large paddock for scale). Black arrows indicate the main trace of the WBF. B. Studied area showing the trench opened within one of the tension gashes. The trench is immediately left of the car. C. Photograph of the trench towards the North.**

We dug a small trench, 5 m-long and 1.4 m-deep, located at N45°21.74', E97°45.16'. The trench is transverse to one of the tension gashes, crossing the northern side of the gash, through a fault contact between a grassy and soft ground and the surrounding surface (Figure 4-42). Both trench walls expose similar faulted Holocene colluvial deposits and paleosoils (Figure 4-42).

#### *IV.2.4.2.1. Trench description*

Figure 4-43 depicts stratigraphic horizons and the ruptures that were exposed in the trench. Because the trench is only 50 cm wide and the observations are very consistent between the two walls, we propose to describe them at once. The tension gash infill is dark, rather stratified, with some pebbles and cobbles. The uppermost part, composed of U10 and U10b, corresponds to the current soil layer and is characterized by an organic-rich horizon with lots of living roots. On the central part of the trench, U10b is more clayey and clearer colored than U10. Below U10, U11 is a very dark and well stratified gravelly to pebbly unit, with clear lenses of paleosoils. Radiocarbon dating of organic material found in U11 (i.e. some well-preserved peat chunks, and two charcoals in paleosoil) yields three ages: 2254 ± 64 CalyrBP (peat IC-C04), 2534 ± 128 CalyrBP (Charcoal and peat IC-C09) and 2942 ± 44 CalyrBP (charcoal and peat IC-C06). On the southern part of the trench, unit U11 shows decimeter scale folds, likely due to local cryoturbation, in which a charcoal (IC-C08) yielded an age of 3146 ± 55 CalyrBP. The ages of the sampled charcoals appear older than the age on the peat (IC-C04), which

can be explained by *inherited* components. We conclude that the depositional age of U11 is 2254 ± 64 CalyrBP.

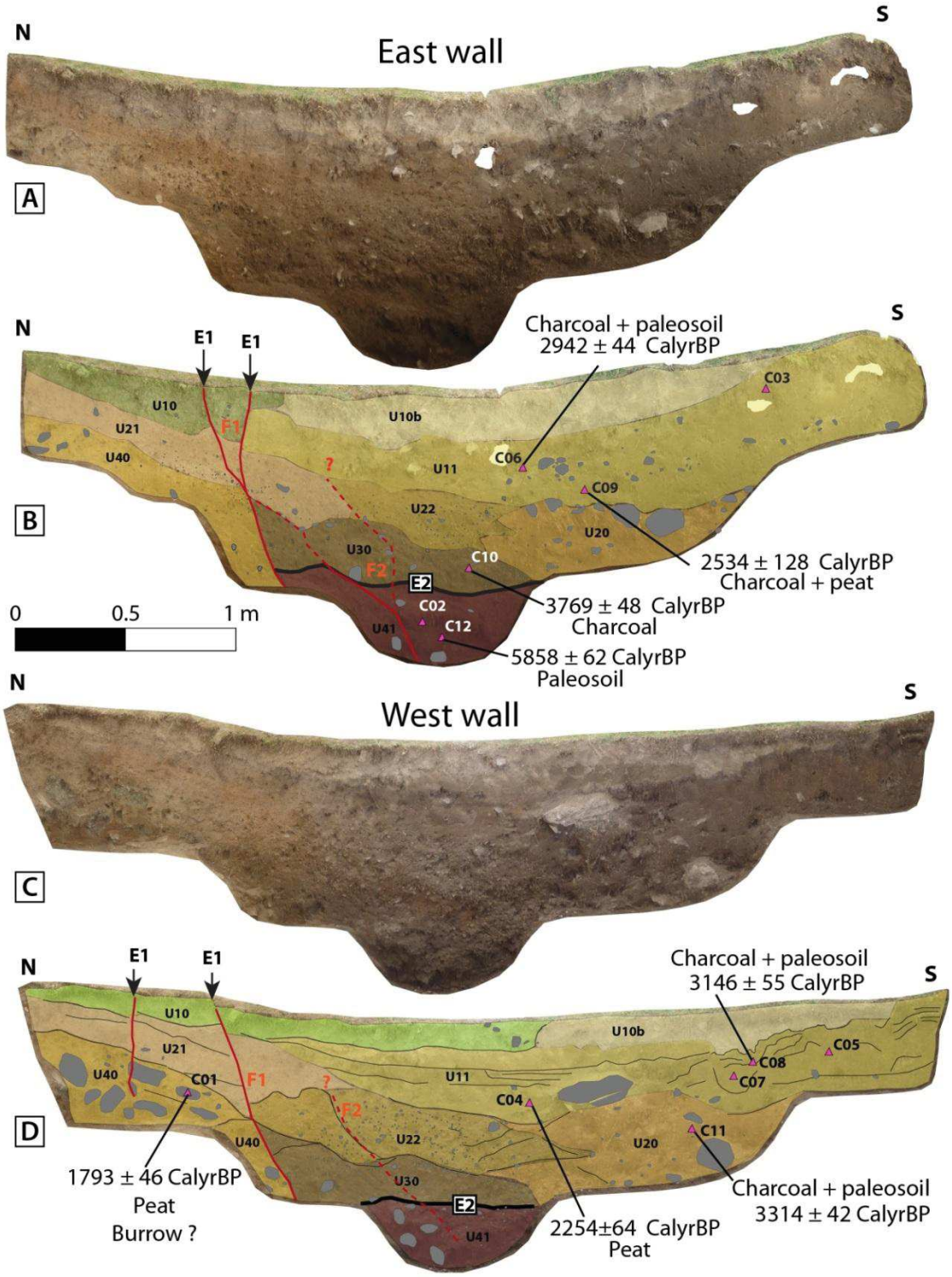


**Figure 4-43: Pictures and logs of the trench opened in Ice Creek Tension Gashes site. See legend of units below. A. and C. are photomozaics of the eatern and the western walls, respectively. B. and D. Corresponding trench logs with radiocarbon ages (pink triangles), black solid line corresponds to event horizon E2.**

U10 : Soil horizon, bioturbated (roots), wet, organic matter rich
U10b : Clayey horizon, dry, stratified, orange patches
U11 : Very dark, stratified, gravel to pebbles with paleosoil layers
U20 : Coarse sand to pebbles few cobbles, angular, unsorted.
U21 : Sandy to silty, clear beige, stratified, few pebbles.
U22 : Darker than U20. No stratification identified.
U30 : Gravel to pebbles with some cobbles, silty matrix supported, angular, unsorted.
U40 : Very coarse unit, beige, granitic pebbles to cobbles, some altered.
U41 : Coarse dark unit, clast-supported, angular, some organic matter.

U20, U21 and U22 are coarse sandy, poorly stratified units, and seem to have a normal contact with upper layers; they have however a limited lateral extensions within the trench. North of the trench, the beige sandy to silty stratified unit U21 is slightly dipping south. On the southern part, U20 is dark brown, suggesting enrichment in organic material. It is composed of stratified, coarse sands and elongated angular pebbles, with few centimeter cobbles. A charcoal collected in unit U20 yields an age of 3314 ± 42 CalyrBP (IC-C11). On the central part of the trench, the sandy-gravelly unit U22 looks clearer, moister and richer in roots than U20. However, units U20 and U22 seem to be synchronous, displaying interfingering features. The variation in the composition between the two units may be explained by the different origins of infilling materials. In fact, the central part is drained from the East, in parallel to the tension gash, whereas the southern part is prone to be filled by material coming from the hillslope, immediately south of the trench (Figure 4-42-B).

**Table 6: Radiocarbon ages of samples collected in Ice Creek Trench.**

| Site | Sample | Nature | Depth (cm) | Weight C (mg) | Age BP | Err age BP | Age CalyrBP | Err age CalyrBP |
|---|---|---|---|---|---|---|---|---|
| Ice Creek Tension Gashes Trench | M15-IC-C01 | MO | 45 | 0,94 | 1855 | 30 | 1793 | 46 |
| | M15-IC-C04 | Peat | 45 | 1,50 | 2240 | 30 | 2254 | 64 |
| | M15-IC-C06 | Charcoal + sediment | 42 | 1,15 | 2835 | 30 | 2942 | 44 |
| | M15-IC-C08 | Charcoal | 45 | 1,77 | 2965 | 30 | 3146 | 55 |
| | M15-IC-C09 | Org. Mat. + Charcoal | 53 | 1,07 | 2445 | 30 | 2534 | 128 |
| | M15-IC-C10 | Charcoal | 91 | 1,52 | 3485 | 30 | 3769 | 48 |
| | M15-IC-C11 | Charcoal + sediment | 77 | 1,28 | 3090 | 35 | 3314 | 42 |
| | M15-IC-C12 | Sediment | 130 | 1,46 | 5135 | 30 | 5858 | 65 |

Unit U30, located beneath U22, is dark-grey colored with yellowish patches, matrix supported and composed of unsorted angular gravel to pebble clasts. The unit can be interpreted as a colluvial wedge, given that it is rich in unsorted and altered granitic clasts. After the radiocarbon dating of one charcoal (IC-C10) found on top of U30, this colluvial wedge unit has a maximum age of 3769 ± 48 CalyrBP. Although the coarse composition of this unit limits identifying internal structures (fractures or stratigraphy), the unit is clearly delimited in its northern side by a fault splay.

Unit U40 is visible only on the northern side of the trench, and corresponds to a very coarse beige unit, unstratified, with decimeter granitic cobbles, some of them showing strong alteration (very crumbly). We interpret this unit as a detrital unit, composing the surface (composed of colluvial materials coming from surrounding granitic reliefs) in which the tension gash opened. The radiocarbon dating of organic material found in the unit yields an age of 1793 ± 46 CalyrBP. This age appears too young regarding to the ages obtained within the tension gash. We therefore supposed that this sample has been contaminated by recent bioturbations processes (burrow, roots...).

Unit U41 is a dark, coarse sand layer, clasts-supported visible at the bottom of the trench. The unit contains some cobbles and organic material, and does not show a clear stratification. The unit is bounded on north by the south-dipping fault F1, along which a normal component is observed. An organic-rich lens, sampled at 1.3 m deep, yields an age of 5858 ± 62 CalyrBP (sample IC-12).

Surface ruptures are only visible on the northern part of the tension gash (F1 and F2), and are mainly materialized by contacts between units and offsets. Affected units are U41, U40, U30 and U11. We also observed few oriented pebbles, but no obvious shear zone or systematic clasts alignment.

U40 is the unit the most affected by faults. It displays a vertical offset of ~40 cm, while upper units show offsets of less than 10 cm (fault F1).

The difference of offset between U40 and upper units, suggests that the U40 has been affected by more than one event. This is consistent with the occurrence of the colluvial wedge unit U30 covering U40. These features suggest that an event (E2) (presumably the penultimate one), occurred between 5858 ± 65 CalyrBP (IC-12) and 3769 ± 42 CalyrBP (IC-10).

Thus, the analysis of relationships between fault and stratigraphic units allow interpreting 2 events: The most recent event (E1) is observed along faults F1 on both walls that cut through the all units, including the soil unit U10, and reached the ground surface. Within the western wall, the ground surface shows a small scarp associated with F1. After radiocarbon ages obtained in unit U11, this first event occurred after 2254 ± 64 CalyrBP (sample IC-C04). A penultimate event (E2), is characterized on both walls the colluvial wedge unit U30 postdating the offset of U41. Its age is bracketed between 5858 ± 62 and 3769 ± 42 CalyrBP (samples IC-12 in U41 and IC-11 in U20, respectively).

#### *IV.2.4.2.2. Summary of the Evidence for Paleoseismic Events on ICTG site*

As a preliminary synthesis, paleoseismological investigations of the Ice Creek tension gash suggest that the most recent event along the WBF occurred after 2254 ± 64 CalyrBP, which is consistent with the observation made within the Chandmani Valley tension gash, 15 km eastward on a different segment (cf. section IV.2.4.1). A probable penultimate surface rupturing event occurred between 5858 ± 62 and 3769 ± 42 CalyrBP (Figure 4-44).

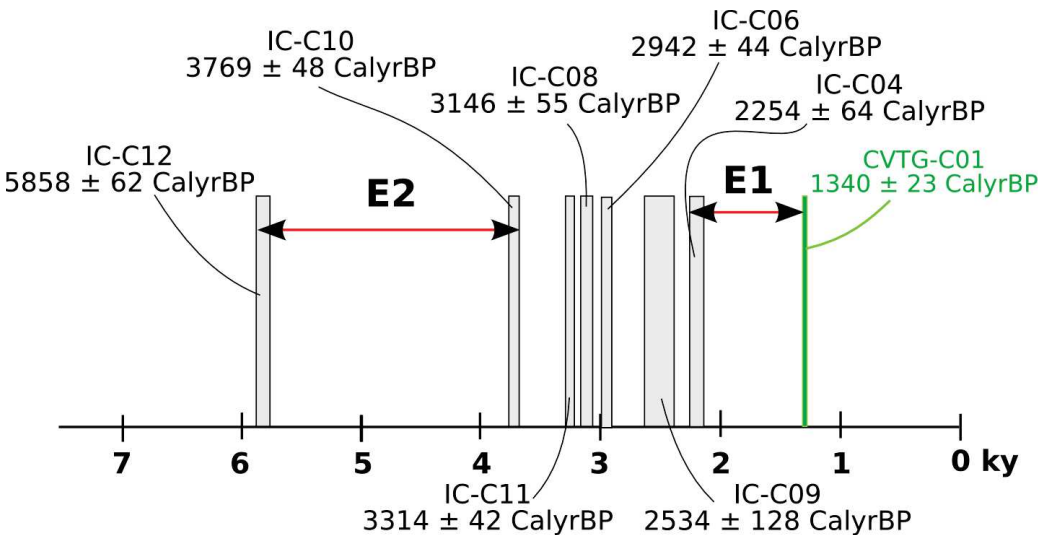


**Figure 4-44: Synthesis of age constraints for paleoseismic events observed in Ice Creek trench (in black) and of the Chandmani Valley tension gash (in green).**

### IV.2.4.3. Rain Creek site

The Rain creek site is located 6 km west of Chandmani town, on the left bank of one of the Chandmani Gol meander (45.335°N; 97.915°E) (Figure 4-45 and Figure 4-46-A). There, the fault is cutting through alluvial fans to the west and river deposits to the east. Three sections allow analyzing paleoseismology: One natural riser (RCR), along the Chandmani Gol stream, and two 8 m-long, 2 m-deep hand-dug trenches (RCT2 and RCT3), located 100 and 140 m west of the riser (Figure 4-45 ).

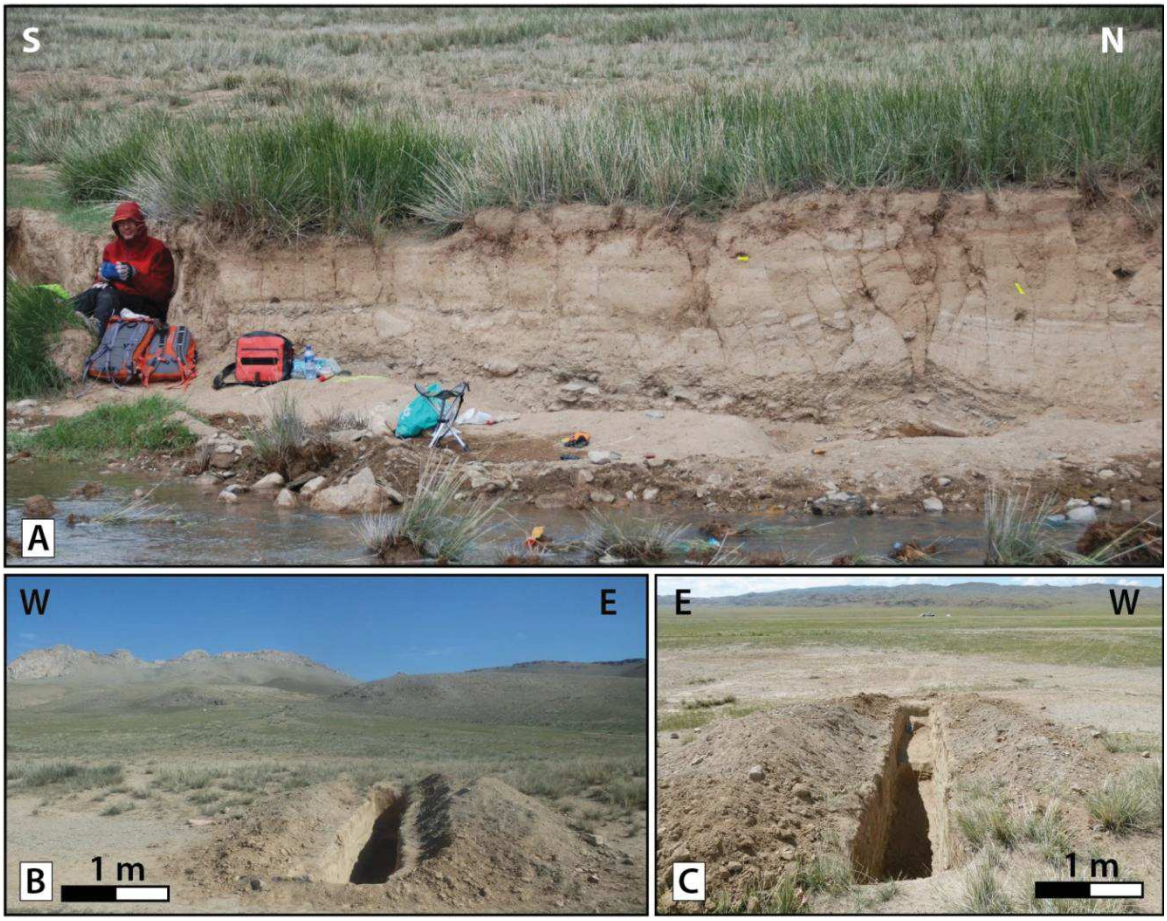


**Figure 4-45: Photographs of the Rain Creek site. A. Photograph to the West of the Rain Creek riser (RCR). B. Photograph to the north of the Rain Creek Trench 2 (RCT2). Note the low-relief dune in which the trenches have been dug, and the alluvial fan on the background. C. Photograph to the south of the Rain Creek Trench 3 (RCT3).**

### *IV.2.4.3.1. Rain Creek riser*

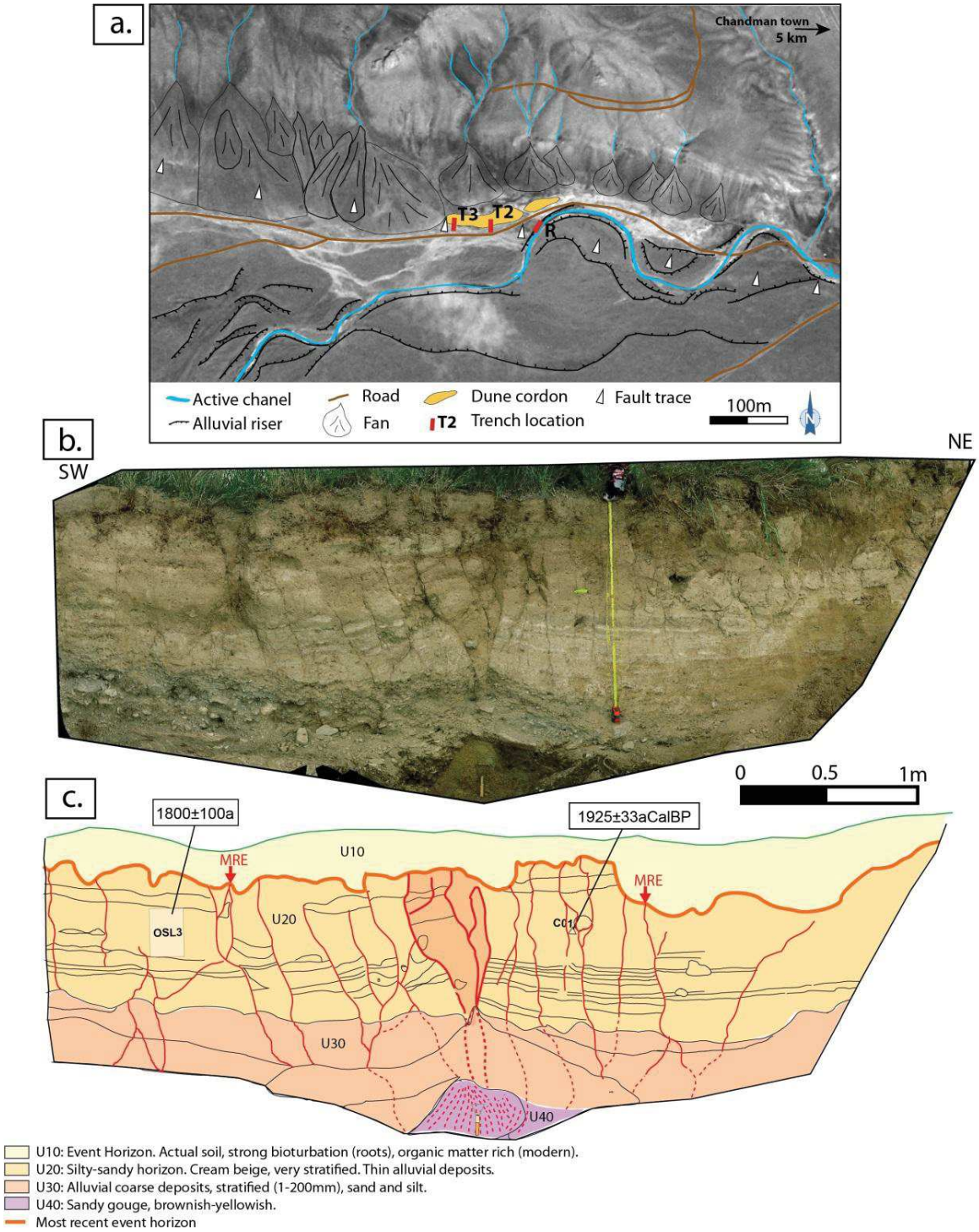


**Figure 4-46: A. Morphotectonic map of the Rain Creek Site; B. Ortho-mosaic of the Rain Creek Riser; C. Log of the Rain Creek Riser and samples locations.**

The riser (RCR, N45°20.25', E97°54.81') displays a nicely stratified fine-grained silty-clayey unit (U20), covering a pebbly unit (U30) affected by several ruptures depicting a flower structure. U30 is a coarse unit, stratified, composed of round shaped coarse sand to cobbles (≤ 200 mm diameter). U20 as U30 are interpreted as alluvial deposits relative

to the Chandmani Gol River; U30 suggests nevertheless a stronger energy than U20, as it is coarser. A clayey reddish gouge unit (U40), is outcropping 1 m under the surface at the center of the flower structure, which displays a couple of tens of fault splays, sub-vertical, dipping north southward of the fault, and south northward of the fault. Slight normal dip-slip components, generating vertical bloc rotations (10 cm) are well visible in U20. All fault splays end on top of U20, attesting that the limit between U20 and U10 corresponds to the most recent event horizon. Above the event horizon, the very shallow U10 presents strong soil development, and hence does not allow us finding samples in order to post-date this earthquake. On the other hand, two samples have been collected within U20: a charcoal, 50 cm deep, yielded an age of 1925 ± 33 CalyrBP and an OSL bloc, 40 cm deep, yielded an age of 1800 ± 200 yr (2σ). OSL analysis are presented in Annexe III. One may note that the OSL sample displays partial bleaching (problematic behavior with respect to recycling ratios with pIRIR225 signals), and that the equivalent dose is here determined from the IR50, making the OSL age weaker and less constrained (see method section: Chapitre 2.I.4.2.2), reflected by consequent uncertainty. Although, the two ages are obtained from different technics, they are consistent within errors, especially considering the reworked detrital nature of the charcoal, which therefore contains some inherited age component.

This analyze of the RCR, allow then pre-dating the most recent event at 1925 ± 33 CalyrBP (Table 7).

**Table 7: Radiocarbon ages of samples collected in Rain Creek Trenches (RCR, RCT2 and RCT3).**

| Site | Sample | Nature | Depth (cm) | Masse C (mg) | Age (yr BP) | Err age (yr) | Age CalyrBP | Err age CalyrBP | 68% range CalyrBP | |
|---|---|---|---|---|---|---|---|---|---|---|
| Rain Creek Riser | M15-RC-CO1 | Charcoal | 50 | 0,65 | 1965 | 30 | 1925 | 33 | 1891 | 1958 |
| Rain Creek T2 | M15-RC-54 | bulk | 170 | 1,07 | 7135 | 35 | 7970 | 23 | 7947 | 7993 |
| Rain Creek T3 | M15-RCT3-C01 | Charcoal | 40 | 1,58 | 9435 | 50 | 10668 | 61 | 10607 | 10729 |
| Rain Creek T3 | M15-RCT3-C02 | MO | 110 | 1,78 | 9160 | 45 | 10330 | 64 | 10266 | 10394 |
| Rain Creek T3 | M15-RCT3-C05 | Charcoal | 48 | 1,67 | 9445 | 45 | 10675 | 59 | 10615 | 10734 |
| Rain Creek T3 | M15-RCT3-C06 | Charcoal | 40 | 1,03 | 8785 | 45 | 9809 | 89 | 9718 | 9897 |

#### *IV.2.4.3.2. Rain Creek trench 2*

The Rain Creek trench 2 (RCT2, 45.338°N; 97.912°E) has been dug within a ~100 m-long and ~20 m-wide vegetated dune cordon, aligned on the fault scarp. The geometry and location of this landform relative to the fault suggests that the fault trace may be partly responsible for its establishment, by producing a push-up or a pressure ridge, with an analog geometry as observed on RCR, 100 m eastward. This dune cordon is positioned downstream of three fans located northward, while southward is an alluvial terrace associated with the Chandmani Gol river (Figure 4-46). Eastward, the dune is prolonged by 30 m as main winds are blowing from the west, hence propagating the dune eastward. This easternmost portion of the dune appears without link with the seismic deformation, given that it is out of the fault trace. Possibility of a secondary scarp could not be ruled up, but the main scarp is definitely standing 40 m to the south, at RCR.

##### *i. Trench description and sampling*

The trench has been dug transversely to the fault, also to the dune cordon, cutting it from north to south. Figure 4-47 shows the west section, from the top to the bottom of the aeolian feature, which may allow us to both see the dune's deposits, infilling materials trapped downstream by active runoff, and composition of the apparently underlying alluvial terrace. Additionally, some post-seismic materials might be deposited on the southern foot of the dune. The occurrence of a northern fault branch on northern side of the dune, few meters north of the trench is probable (Figure 4-46), and we choose the southern side of the dune because it is sharp and straight. The trench walls display clear stratified units, faulted in two locations, furtherly named central (F1) and northern fault zones (F2, F3, F4). The first one is located on the central part of the trench, and seems to correspond to the southern edge of the pop-up (flower structure) from which the dune aggregated. The second one is located on the northern part of the trench and is close to the axis of the dune.

Figure 4-47 depicts the strata and faults that were exposed in trench 2. The trench deposits can be divided in four main units from top to bottom: U10 to U40. Those main units are divided in sub-units, regarding to their internal structure and composition.

U10 is the topmost unit, and corresponds to modern soil. It is composed of silts and sands with dark clay organic-rich, ~7 cm-thick lenses. The unit presents soil development and is affected by few bioturbation. U10 is stratified with one lower sub-unit, U11, coarser than U10 (sandy to silty), and with very little clay. We interpreted U10 and U11 as eolian deposits, Unit U11 is very homogeneous, rich in quartz and feldspar grains,

sub-angular to rolled, likely aeolian. An OSL dating using the IR-IRSL-255 protocol on feldspar, has been carried on a small block sampled within U11 (OSL1), and yielded a deposit age of 0.25 ± 0.02 ka (1σ). No faulting has is observed in U10 and U11 that are consequently post-dating the most recent event.

The underlying unit, U20, is a massive silty to clayey deposit, yellowish to light brown, which displays numerous burrows, especially on the central fault zone. Except some thin horizontal clay-rich dark lenses aligned on a level located on the lower quarter of the unit, no stratification is distinguishable in the unit, which suggests that it corresponds to eolian deposits, related to the dune. The lower part, U21, is coarser, matrix supported, with scattered rounded gravel to sand and few pebbles, attesting of its alluvial nature. U21 shows a vertical offset of 25 to 32 cm, along the fault F1, considering top and bottom of the layer respectively. At two places on the southern part of the fault, U21 is interrupted with circularly shape, and filled with U20. Both U20 and U21 show gentle folding features that seem mainly related to fault zones.

U20 is thicker (130 cm) on the northern part than on the southern (40 cm) part of the trench. Moreover, the central part seems pinched between the two fault zones F1 and F2, where it is only 10 cm-thick. Instead, U11 seems to be slightly thicker on central part of the trench. While the erosion surface is not obvious looking at the contact between U20 and U11, this thickness variability may suggest that U20 underwent significant erosion. Moreover, the unit was capping a former relief, as U20 is aeolian and U21 is mostly alluvial.

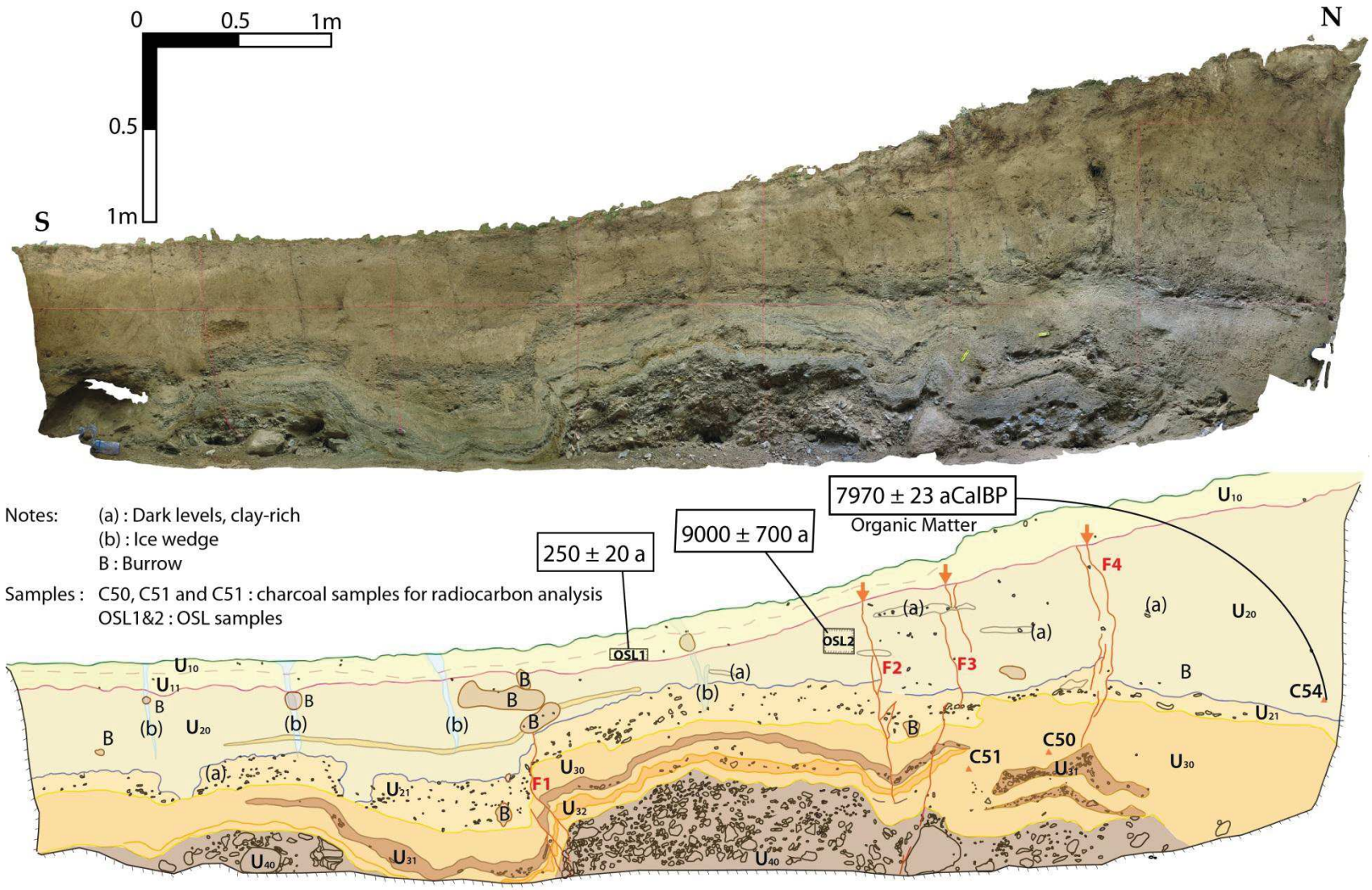


**Figure 4-47: Orto-mosaic and detailed log of the Rain Creek Trench 2. Red arrows indicate the surface rupturing event identified in that trench. See legend on next page.**

U10 : Sand and silt with soil development, dark, bioturbation
U11 : Sand and silty, very few clay

U20 : Clayey silt , light brown
U21 : Gravel and sand, scattered gravels, matrix-supported

U30 : Silt-clay, yellowish
U31 : Gravel level, grey, clast-supported
U32 : Oxidized coarse sand unit, matrix-supported

U40 : Grey alluvial deposits with Pebbles to boulders(5-50 cm), silty clayed matrix, cryoturbation features

Two samples have been dated within U20. An OSL block sample (OSL2), taken on the center of the unit, between the two fault zones, yields an age of 9.0 ± 0.7 ka (1σ). OSL results are presented in Annexe III. An organic-rich lens (C54), taken on northernmost part of the trench, 10 cm upward from the bottom of the unit, yields an age of 7970 ± 23 CalyrBP. These ages are consistent considering 2σ errors.

U30 corresponds to a mainly silty, yellowish clay-rich unit with a significant content of gravel. It is composed of 5 well stratified, isopach alluvial layers. The whole aspect of this unit is folded, visibly more than U20, and sub-units of U30 are systematically affected by the fault. Sub-units in U30 differ from global aspect: color, granulometry, composition. For instance, U31 is a clast-supported gravel layer, while U32 is an oxidized coarse sandy unit, matrix supported. All those layers are clearly offset in the central fault zone, by a 10 cm wide shear zone (F1). Vertical offset component are 24 to 30 cm for U31 or U32, respectively. Note that this corresponds to the same amount of offset registered by U21. The northern fault zone is affecting the sub-units in U30 by small vertical offsets and thickness variations, but it seems that the motion was mainly left-lateral.

Unit U40 is composed of coarse to very coarse (≤ 50 cm) alluvial deposits, rounded, unsorted, unconsolidated and poorly stratified. Its folding, also visible in upper layers, seems to be related with abundance of coarse material, and especially to boulders. If some part of the observed folding seem to be associated to faulting processes, one can wonder if some of it could not be associated or reinforced by cryoturbation processes given that folding is also observed away from the fault zones. Cryoturbation processes are common within porous and permeable pocket of pebbles and boulders. Moreover, cryoturbation is present in the upper part of the trench, where several ~ 50 cm-long ice wedges are starting from the surface and propagating downward until unit U21 are observed.

#### *ii. Fault zones description*

The central fault zone is composed of a sub-vertical 10 cm-wide anastomosed shear zone (F1) within the lower part of the trench, offsetting vertically U30 and corresponding to clasts alignments in U40. Its upwards prolongation is more localized and vertical within U21, but is unfortunately not visible within the clayey unit U20 where it is difficult to distinguish fault splays. Note as well that three burrows located on the probable fault splay within the western wall have limited our observations.

The northern fault zone is composed of three discontinuous fault splays, ~10 cm-wide, which display upward fault terminations on the bottom of U11 (F2 and F3), or U10 (F4) if U11 is not present.

Either on the central and the northern fault zone, and for both trench walls, the trench exhibits deformation within lower part, and systematical fault termination on the bottom of U11, which therefore correspond to the event horizon of the last earthquake recorded in that trench. Whether the lower part of this trench (U30 and U40) seems to be more deformed than the upper part (U20), no unambiguous criteria were found as evidence of previous earthquake in that trench.

#### *iii. Summary of RCT2*

To summarize, at least one event is observed in the trench, on both walls and within both the central and the northern fault zones, with fault terminations criteria stopping at the bottom of U11. After age's constraints, this event is post 7970 ± 20 CalyrBP (C54), and pre 250 ± 20 yr (OSL1).

More events are suspected given the hiatus of stratigraphic records between 9000 ± 200 yr and 250± 20 yr, and the observations made within the nearby riser (see IV.2.4.3.1).

### *IV.2.4.3.3. Rain Creek trench 3*

The Rain Creek trench 3 (RCT3, 45.338°N; 97.911°E) was hand-dug 40 m west of RCT2, following the same strategy: crossing the southern flank of the dune cordon, from top to the bottom. Compared to RCT2 trench, this third trench presents the advantage to be partially draped downstream (on south of the trench) by the toe of an alluvial fan flooding from NW and circumventing the western edge of the dune (Figure 4-46).

Figure 4-48 and Figure 4-49 depict the strata and faults that were exposed in RCT3, for eastern and western walls, respectively.

As for RCT2, deposits are well stratified and affected by two main fault zones: the first within the center of the trench (F1, to F4), and the second within the northern part (F5 to F7, index ‘e’ or ‘w’ to fault labels indicate the wall: ‘east’ of ‘west’). Four main units have been recognized, U10 to U40, which correspond, at first order, to those identified in RCT2, as well as sub-units representing the stratigraphy and structural complexities. Both walls of the trench display consistent stratigraphy and locations of fault zones. Note however that the ruptures in unit U20, within the upper part of the trench, are more visible and localized in the western wall than on the eastern wall.

### *i. Trench description and sampling*

The uppermost unit, U10, is composed of two sub-units U11 and U12, and corresponds to gray coarse sand and gravel deposits, associated to the NW fan. U10 is only visible on the southern part of the western wall of RCT3, and corresponds to a small depression forming a pool during storm events southwest of the trench, and indicating a deposition area. No ruptures were observed in it.

The underlying unit U20 is similar to unit U20 in RCT2. It is a massive creamy to yellowish clayey silts unit, likely eolian, in which identification of deformation is difficult due to absence of stratigraphy. Where U10 is not present, in the northern part of the trench, the topmost part of U20 presents soil development, with a lot a roots, and bioturbation processes. The unit is perforated with many burrows, and affected by a ten of ice wedges (accounting for both trench walls) in contact with the surface; the three deepest of them (~1 m-deep) stop downward just at the contact with U22. On the west wall, as in RCT2 trench, U20 is thicker on the northern part of the trench than on the southern part, even though this observation is less remarkable on the east wall. On both walls, U20 is thinner within the central faulted zone. Three charcoals sampled within the lower part of U20, yield calibrated ages of 10675 ± 59 CalyrBP (CO5), 10668 ± 61 CalyrBP (C01) and 9809 ± 89 CalyrBP (C06). The two first ages are consistent, while the third one is younger. However, these results, when compared to those obtained in the same unit (U20) in trench RCT2 (i.e. 7970±20 CalyrBP for a radiocarbon age of the bulk sample C54, and 9000±200a for an OSL2 sample; see Fig. IV-5), suggest inherited ages of charcoals, compared to younger ages obtained on sediment.

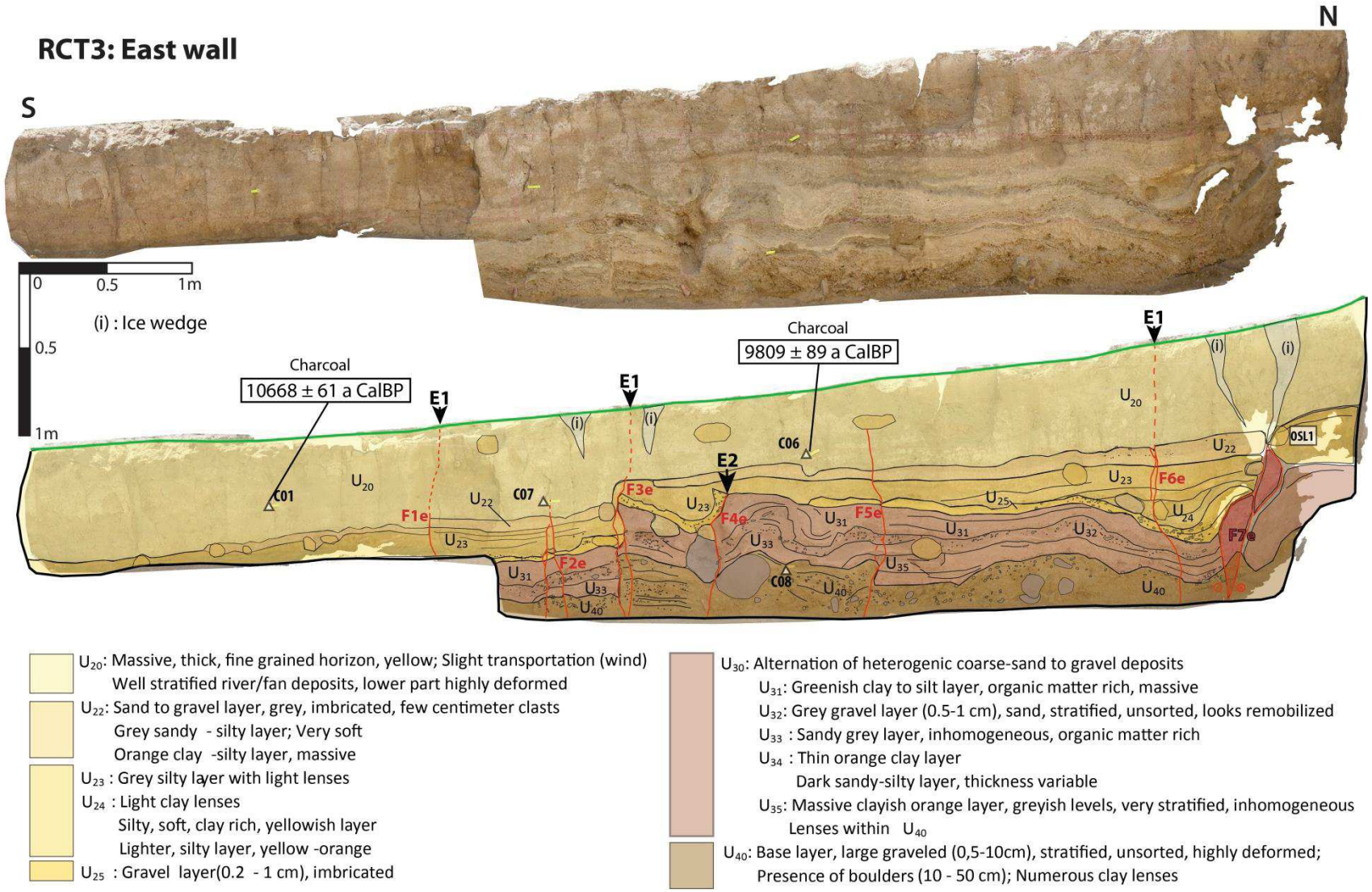


**Figure 4-48: Orto-mosaic and detailed log of the east well of Rain Creek Trench 3. Black arrow indicates the event horizons of the two surface-rupturing event identified in that trench. White triangles are locations of radiocarbon samples, and solid box of the OSL sample.**

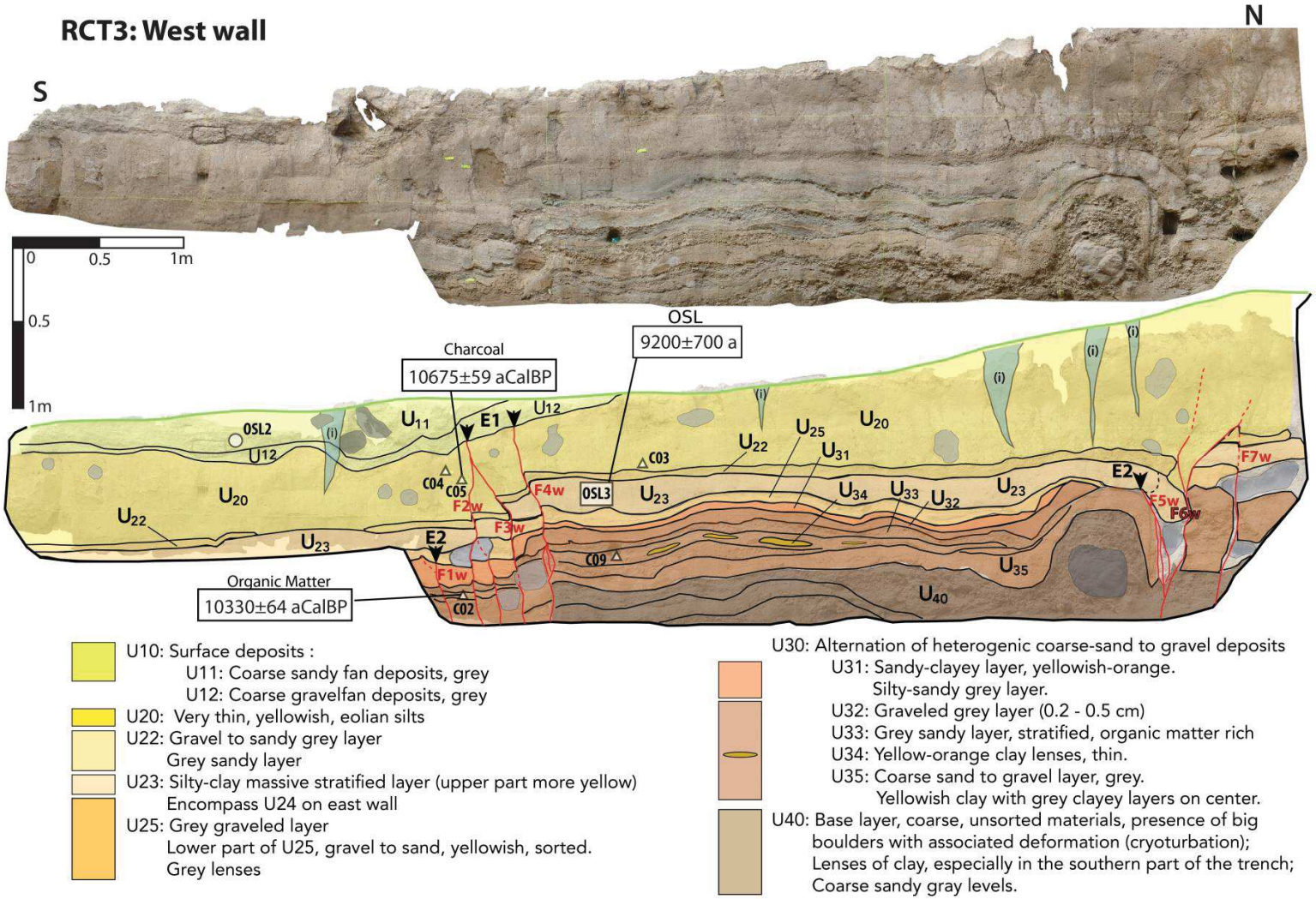


**Figure 4-49: Orto-mosaic and detailed log of west wall of the Rain Creek Trench 3. Black arrow indicates the event horizons of the two surface-rupturing event identified in that trench. White triangles are locations of radiocarbon samples, and solid boxes are locations of OSL sample.**

U22 is a gravelly to sandy unit with a silty matrix. U22 seems to increase in thickness northward, from 5 cm on south of the trench to 15 cm on north, but appears also discontinuous, especially close to the fault zones where it is offset or pinched (F1e, F3e, F6e, F7e F2w, F3w, F4w, F6w and F7w).

U23 is a silty-clayey massive layer, with a yellowish upper part and a grey lower part. It is clearly vertical offset along three fault splays within the central fault zone on the west wall (F2w, F3w and F4w), and two on the east wall (F1e and F3e). Using the top and bottom of the unit as piercing lines, offset measurements of these apparent dip-slip offsets through the central fault zone yield a total vertical offset across the fault zone (cumulating offsets on different faults) comprised between 23 and 32 cm within the west wall, and between 20 to 27 cm within the east wall, using each time top and bottom of the layer, respectively. Along the northern fault zone, on both walls, U23 also appears clearly affected (F5e, F7e and F7w). Note that on the east wall, deciphering units beyond the northern fault zone is very uncertain, given the ambiguous correlation between units on both sides of the faults. On the west wall, unit U23 describes a antiform associated to the occurrence of a 70 cm-wide boulder within the underlying U30, and is affected by two fault splays: one (F5w) seems to end at the bottom as we observe no evidence of any displacements; a second one (F6w) clearly affects U23 with a vertical displacement of 30 to 35 cm. The antiform seems to be mostly correlated to the presence of the boulder, given that it is not observed in the opposite wall (Figure 4-48). Instead, we observe a stratified synform, with thickening of U23 composed of yellowish clay and silt deposits. These sub-units in U23 are clearly faulted along the northernmost fault splays (F6w, F7w and F7e) and show also a rupture within the southern part of the synform (F6e). On west wall an OSL bloc-sample, collected in the unit, within the central part of the trench (between the two fault zones) yields, using the IR-IRSL-225 protocol on feldspar grains, an age of 9.2 ± 0.7 ka for the deposition of this alluvial layer.

U25 is a stratified alluvial unit, composed of rounded gravel with few interbedded pebbles. The unit looks folded and is eroded by unit 23 within the northern part of the trench. The aforementioned antiform is visible in stratified units bellow U25 (U30 and U40) on west wall, which is associated to the underlying boulder in U30, as no antiform can be observed on east wall. At three places, some fault splays appear to terminate on the bottom of unit U25: on central fault zone for both walls (F1w and F4e), and a clearly third time in the northern fault zone on west wall (Fw5). That observation of fault terminations may indicate that bottom of the U25 is an event horizon.

The 50 cm thick unit U30 (U31 to U34) is an alternation of heterogenic coarse-sand to gravel deposits (e.g. U32) with clay layers, sometimes lenticular with yellowish to orange oxidized levels (U34). The stratification, as well as rounded shape of these materials and the presence of few imbricated pebbles, may indicate moderate energy alluvial deposits. A bulk sample (C02) collected in a clayey organic-rich lens in unit (U33), yield an age of 10330 ± 89 CalyrBP, consistent with age constraints obtained within the western wall of trench RCT2. This sequence is fairly continuous along the trench, while layers are systematically offset by fault splays. Measurements of the apparent vertical offset of U30 sequence through the central fault zone are comprised between 20 and 26 cm on the east wall, and yield 26 cm on the west wall (measurement was carried out only on top of the sequence, its bottom being not outcropping south of the fault zone). To the north, on the east wall, the U30 sequence stops abruptly against the main northern fault zone (F7), while on the west wall, its thickness diminishes, to form a thin regular antiform around the aforementioned boulder. Contact with the shear zone, north of the boulder, displays sub-vertical stratification and internal shear with oriented gravel and small gouge.

Northward of the shear zone, a chunk of U35 might be recognizable by its orange clay lenses, and is capped by really coarse alluvial deposits; it is however conceivable that this chunk in a clay-to-sand lens which belong to the furtherly described heterogeneous structure of U40.

As in RCT2, the unit U40 is composed of very coarse heterogeneous alluvial deposits in a silty matrix, with clasts heterogenic, sub-angular to rounded, sizing from gravel to boulders (≤ 70 cm). U40 unit is clast-supported, unsorted, poorly stratified, and inserted with lenses of sand to clay with traces of oxidation. Biggest boulders are systematically associated with antiform on overlying units (U35 to U23). Identification of fault splay within this very coarse material is rather tough, but significant offsets are identifiable within the central fault zone on both walls, as previously measured with the top of U30. On the northern fault zone, U40 does not describe clear vertical offset, but seems to be vertically pinched and hence involved within the shear zone; more especially on the west wall, where faulting appears to be linked with a the 70 cm-wide boulder. Last mentioned boulder actually looks to be ‘raised’ by at least half a meter in contact south with the main shear zone, while no such significant offset is identified in the deformed overlaying layers (for instance U23 or U30 sequence). Northward of the north shear zone, it is challenging to identify the contact between U30 and U40, as a rough outcrop of U30 seems to overtop some U40 deposits. We cannot rule out that what we identified here as a chunk of U30 could actually be a clay-to-sand lens within U40, which was offset by the fault.

### *ii. Description of fault zones*

On the west wall, the central fault zone is composed by three main fault splays (F2w, F3w and F4w) which clearly vertically offset, as previously measured U30 and U20 units (by ~25 cm), northern side of the fault uplifted. These fault splays join in two traces within U20, to noticeably stop upward on bottom of U12. This criterion of fault termination is considered as indicating an earthquake, with bottom of U12 being an event horizon. A fourth fault splays has been identified 20 cm south (F1w), and seems to stop upward in U24; the fault termination in not sharp, and it is unclear if U24 is affected or not by the faulting. On the east wall, the central fault zone is more complex and composed of one main shear zone (F3e) generating significant offsets previously documented (also ~25 cm), and three other fault splays (F2e and F4e), about 1 to 2 m away from the main shear zone. The southernmost fault splay (F1e) is only visible on U20 and U22, offsetting this last-cited unit by ~ 5 cm, north side of the fault uplifted, and prolonging upward until the surface, given that U10 is absent on this wall. 40 cm south of the main shear zone, a couple of fault splays F2e slightly offset U30 sub-units, as well as U23, and seems to extend upward within U23 to finally join on U22. U20 is likely affected, but the trace of the fault splay has been identified only on the bottom of the unit, and upward extending could only be inferred. 50 cm north of the central shear zone is the fault splay F4e bordering two rolled boulders, ~ 40 cm diameter each, on the bottom of the trench (U40 and U30). This fault splay location corresponds to the norther part of a small synform described by U25. In that place U25 is clearly entrained and offset by faulting, as attested by folding and aligned gravel and pebbles. Furthermore, this fault splay describes fault termination as it encounter U23; at that location U25 is sub-vertical, instead the overlying U23 is sub-tabular. The unconformity of the erosive contact, together with differential folding may be interpreted as a criterion for an earthquake, with an event horizon defined either by the bottom or the top of U25. Finally, 1 m north of the main central shear zone, the F5e splay is propagating upward, creating a clear offset mainly in U40, while U30, U23 and U22 layers appear slightly affected, without significant offset. This fault splays propagated upward through half of the U20 thickness, and terminates in a burrow; no continuation of this fault splay has been found upward.

The northern fault zone is characterized on both trench walls by a main shear zone and a couple of secondary splays, as well as strong presence of burrows, limiting correlation of units in both sides of the fault zone. On the east wall, the main northern shear zone F7e is well developed, and presents some sigmoid-shaped, sheared chunks of silt to clay materials, which present gouge development and are bounded by aligned clasts. The second splay F6e is visibly affecting U40, U30 and U24, with tight apparent vertical

offsets of few centimeters, south side of the fault uplifted. It is the opposite upward for the offset displayed by the contact between U22 and U20. As in RCT2, we interpret this discrepancy in apparent vertical offsets, as the result of the dominant left-lateral motion on this fault zone. Observed vertical offsets are hence purely apparent, and could be variable depending of the dipping and thickness variability of each horizon. The F6e fault splay however, cannot be clearly identified within U20, but we consider that this may mostly be due to our inability to identify faulting within U20, than related to a real fault termination. On the west wall, as previously detailed, the main shear zone F6w is associated to a 70 cm-wide boulder, which was probably involved in fault motion, as it seems uplifted. Consequently, we observe the pinching of U24 and the upper part of U30 (U31, U32 and U33), and including with it an antiform of U35 and U40. As observed in RCT2, deformations associated to this boulder are certainly partly relative to cryoturbation, which locates within the permeable and porous U40 unit, but the promiscuity of the main shear zone may not be a coincidence. Unable to quantify the contributions of each process, we conclude that this antiform may be due to both faulting and cryoturbation processes. The second splay of the northern fault zone, F7w, is located 20 cm to the north of the main shear zone, and appears to reach the main fault zone on top of U22. This splay seems to generate some offsets which cannot be quantified, as layers are delimited by burrows. Both the shear zone and the F7w splay are difficult to identify within U20. Eventually, another fault splay (F5w) is rising from the main shear zone, and connects with the northern side of the anticline described by U30. As previously detailed, in this unit, the fault splay generated fairly strong shear criteria, with aligned clasts and gouge formation, but it ends in contact with the bottom of U23. This fault termination can be interpreted as a criterion for an earthquake with U30 sequence as event horizon. This observation is consistent with the fault termination observed of bottom of U25 on central fault zone in east wall, as U25 is here pinched by the boulder-related antiform.

#### *iii. Summary of RCT3*

To summarize, the RCT3 displays deformations related to both faulting and cryoturbation processes. However, noticeable evidences of fault displacements are shown in the central fault zone, with fault terminations criteria on U12 unit, for which the bottom constitute the event horizon relative to the last earthquake recorded in that trench. A second event has been identified, from criteria of fault termination on bottom of U25, and differential folding between U20 and U30. One may however note that the differential folding could as well be due to cryoturbation processes, and is not itself the determining criterion for this second event. Dating within RCT3 does not allows better constrain the

age of the most recent event along the WBF, but suggest that an earthquake occurred between 10330 ± 89 CalyrBP and 9.2 ± 0.7 ka (1σ) considering respectively the radiocarbon dating of U28b and the OSL dating of U23.

#### *IV.2.4.3.4. Summary of the Evidence for Paleoseismic Events on rain creek site*

Paleoseismic investigations at the Rain Creek site allow recognizing the main geomorphic features characterizing the site, which are the dune cordon along the fault, the active fan on the north, and the Chandmani gol alluvial terraces to the south. Combining the analysis and the dating of the three trenches, two earthquakes have been identified and partially constrained in time: i. the most recent event occurred between 1925 ± 33 CalyrBP and 250 ± 20 yr; ii. a previous event is aged of 10330 ± 89 CalyrBP to 9.2 ± 0.7 ka. This second age is assessed considering respectively the ages of a clayey lens rich in organic matter, and of the OSL-deposit age of a silty-clay stratum, according to differential folding and fault termination criteria. This last result might be put in perspective, as it assumes strong inbuilt (up to 500 yr) in at least 2 charcoals (which appears nonetheless older than OSL-deposit age and radiocarbon dating of organic matter within same characteristic aeolian formation but different trench), and by cryoturbation processes involved in folding.

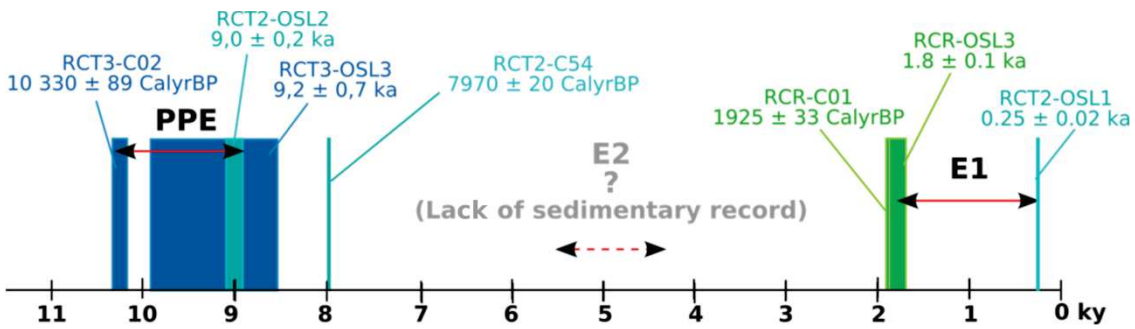


**Figure 4-50: Synthesis of paleoseismic interpretation of the Rain Creek trenches: RCR in green, RCT2 in light blue, and RCT3 in dark blue.**

Eventually, these results may suggest that we do not have good sedimentary records of the period between 8000 and 2000 yrBP. However, paleoseismic survey at Ice Creek tension gash suggests the occurrence of a surface rupturing event during that time-span. We conclude here that we probably missed an event, which likely occurred between the two earthquakes that we identified in the Rain Creek trenches.

.

### IV.2.4.4. Swan Lake site

The swan lake site is located 45.288°N; 98.288°E, 25 km east of the Chandmani town, in a place which corresponds to the main outlet of the eastern Chandmani Valley, 7 km northwest of the endorheic Hutag Nuur Lake (Figure 4-22). The site is a flat swamp, in a valley bounded westward by the Chandmani restraining bend, and eastward by the western end of the Bayan Tsagaan Nuruu (Figure 4-15). The main fault trace is trending N93°E, and it crosses orthogonally the 1.6 km-wide swamp, characterized by temporary active channels, which dissect low-relief alluvial surfaces, scarcely remaining at various low-range elevations.

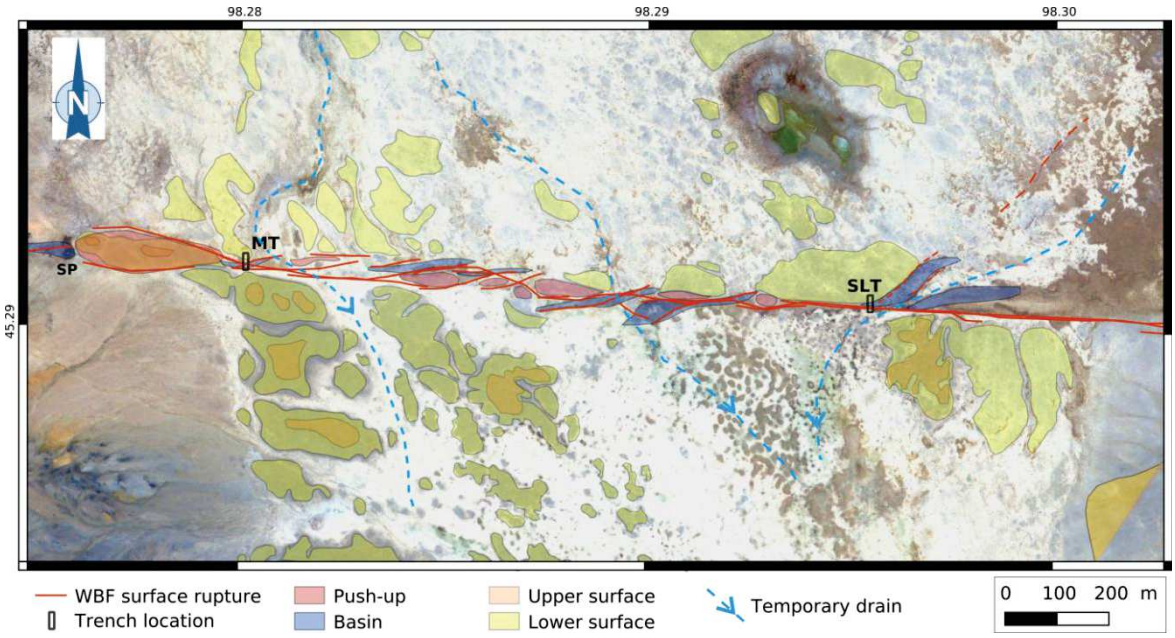


**Figure 4-51: Morphotectonic map of the Swan Lake Site. MT: Moskito Trench; SLT: Swan Lake Trench; SP Sag Pond.**

The alluvial surfaces (likely a smoothed bars and swale landform) are alternatively more visible on southern side of the fault along the western third of the site, then north of the fault on the central third, and are finally more pronounced south of the fault on the eastern third (Figure 4-51). Hence, no significant vertical offset can be identified within these landforms relative to the fault trace. Two cumulative left-lateral offsets of 36 ± 18 m and 170 ± 30 m can be measured by reconstruction of rises delimiting the surfaces (Figure 4-52). Accounting for such large cumulative offset, one can infer that those surfaces are likely late-Pleistocene, and experienced numerous seismic cycles. The main fault trace displays few meters tension gashes and pressure ridges, resulting in a discontinuous mole track pattern, consistent with a mostly strike-slip fault motion (Figure 4-51). One may note that 1.5 to 2 km south of the main fault trace, a southern secondary branch strikes N110°E and seems to affect late quaternary alluvial deposits. It also

bounds northward the Khutug Lake (Figure 4-22). This secondary fault trace appears to be connected to the WBF within the Chandmani restraining bend 1.5 km west of the site, but presents a limited development of 12 km to the south east, bounding southward the western end of the Bayan Tsagaan Nuruu.

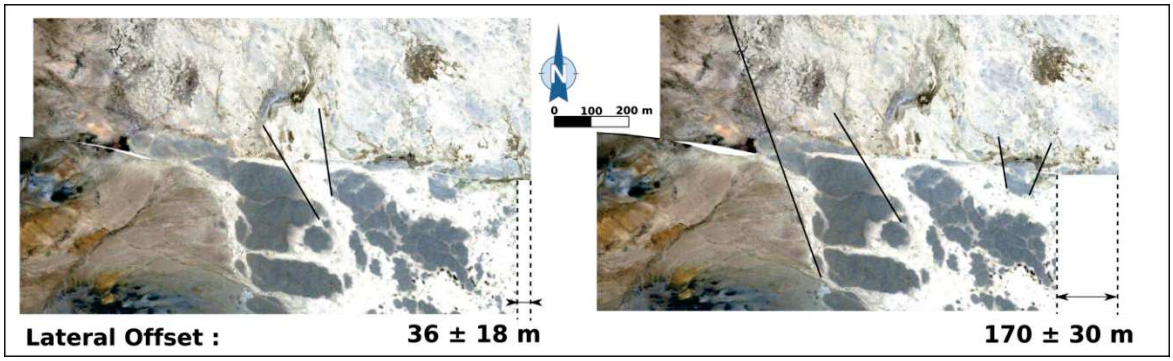


**Figure 4-52: Cumulative offset measurement by retrofit of the landforms, on western part of Swan Lake Site (left part of Figure 4-51). Black solid lines are piercing lines used to derive the offset values. Left: Risers of the alluvial surfaces on south of the fault are used to fit the active bed on north of the fault, and yield an offset of 36 ± 18 m. Right: Risers of alluvial terraces on south of the fault are used to fit a strass terrace on north of the fault.**

Along the main scarp and on eastern side of the valley is a deeper swamp, situated north of the fault (on right of Figure 4-51), and possibly related to normal dip-slip along a ~600 m-long secondary branch, striking N50°E. A first trench, the Swan Lake trench (SLT), has been dug westward of the junction of this branching with the main trace (Figure 4-51, Figure 4-53), in order to optimize the appreciation of the fault-related deformation into the trench and to have a sedimentary record by sediment contributions from the swamp (Figure 4-53). Westward of the valley, two sag-ponds can be documented: the first (SP on Figure 4-51) is round, rather deep as it is currently filled by water and visibly related to tension gashes. A second pond (MT on Figure 4-51) is located on a minor branching, constituted by a 6 m-wide and 30 m-long clayish depression, relatively moist, aligned with the fault and located close to a major temporary channel, 50 m to the northeast (Figure 4-51). The branching is with a 120 m-long branch, which strikes N107°E to the northwest, and noticeably corresponds to eastern end of the Chandmani Uul restraining bend.

**Figure 4-53: Photograph to the East of the Swan Lake Trench. Shaded area is the section of the trench in Figure 4-55. Black arrows indicate the WBF. Note the change of materials when crossing the fault trace.**

The Moskito Trench (MT) has been dug through this second pond, in order to maximize the appreciation of the deformation while having several fault splays, and to obtain a transect of the whole pond and its related sedimentary records (Figure 4-54). Both trenches are oriented N-S, perpendicularly to the fault. They have been dug using an excavator. Additionally, a drone survey of the full site has been done at 200 m altitude relative to ground, in order to derive orthophotographs and DEM, with resolutions of 8 cm and 15 cm respectively.

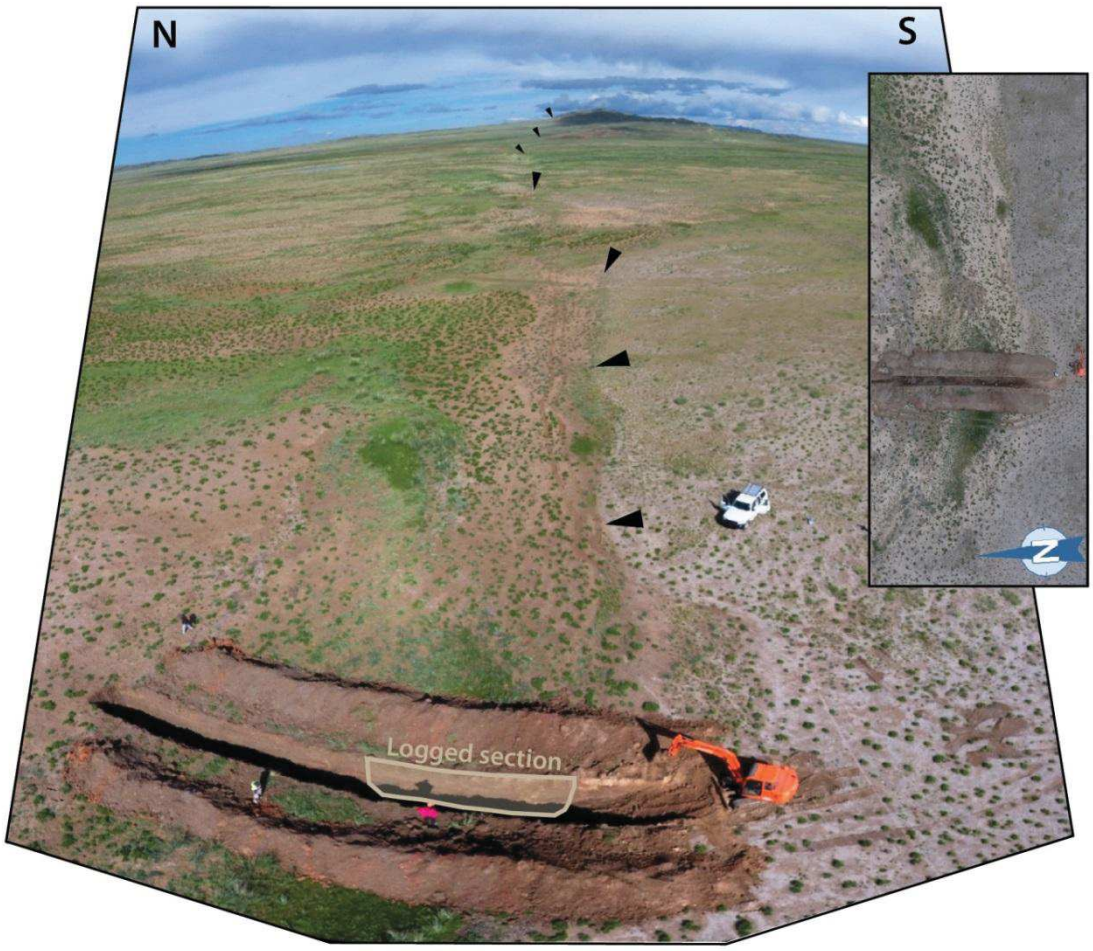


**Figure 4-54: Photograph to the East of the Moskito Trench. Shaded area is the section of the trench in figure. Black arrows indicate the WBF. The Inset is an aerial photograph of the Moskito Trench sag pond. Fault is N-S on center of the picture.**

#### *IV.2.4.4.1. Swan Lake Trench*

The SLT is located 45.290°N; 98.295°E. It is 25 m-long, 2.2 m-wide and ~2 m-deep, as this depth corresponds to the water-table encountered during the digging process. In surface, the northern part of the trench is located into a low-level terrace, formed by heterogenic gravel to pebble clasts, angular to sub-angular (Figure 4-56). The central part of the trench corresponds to the riser of the terrace, which is collinear with the fault and displays a shallow vegetated dune formation, likely situated here as the relief related to the terrace riser constitutes a trap for eolian deposits – main winds coming from northwest. The southern part of the trench corresponds to the bottom of the riser. It displays a flat, clayey, and grassy surface, corresponding to the western prolongation of the previously mentioned deep swamp (Figure 4-53), easternmost of Swan Lake site (Figure 4-51). Southwestward, the swamp shows evidences of recent flooding and desiccation cracks. Because the northern part of the trench is mostly composed of stratified gravel to pebble alluvial sediments which does not display significant fault deformation, only the southernmost 15 m of the trench are furtherly detailed.

##### *i. Trench description*

Figure 4-55 depicts the strata and fault zone that were exposed in SLT. The trench is mostly composed of coarse gravel to pebbles, unsorted. Horizons are massive, coarsely stratified in the 4 southern meters and on the northern half of the trench, but more disturbed in the 10 m-wide central part. This central part corresponds to a complex faulted zone, containing the main north dipping shear zones, furtherly named ‘central fault zone’. Ruptures are labeled Fe and Fw (1 to 9) for respectively the East and West walls. The northern half of the fault (out of the log) shows well stratified gravel layers, where few additional splays are also identifiable. Due to its highly deformed appearance and coarse material composition in the faulted central part, it is tough to identify the different units and ruptures; moreover, correlation of units between northern and southern parts of the central shear zone appears ambiguous, which is probably attributable to the mostly strike-slip fault motion, as described from surface observations. The two walls of the trench display rather consistent deposits and fault-related deformation, and three main units can be identified, U10 to U30, furtherly detailed in sub-units on the log. U10 is the uppermost unit of the trench and presents soil development; unit U20 corresponds of a patchwork of coarse alluvial deposits, dry and heterogeneous within the whole trench, and U30, which represents the most deformed unit of the trench, is a clay-rich, sandy to gravel deposit, wet, with evidences of alluvial source.

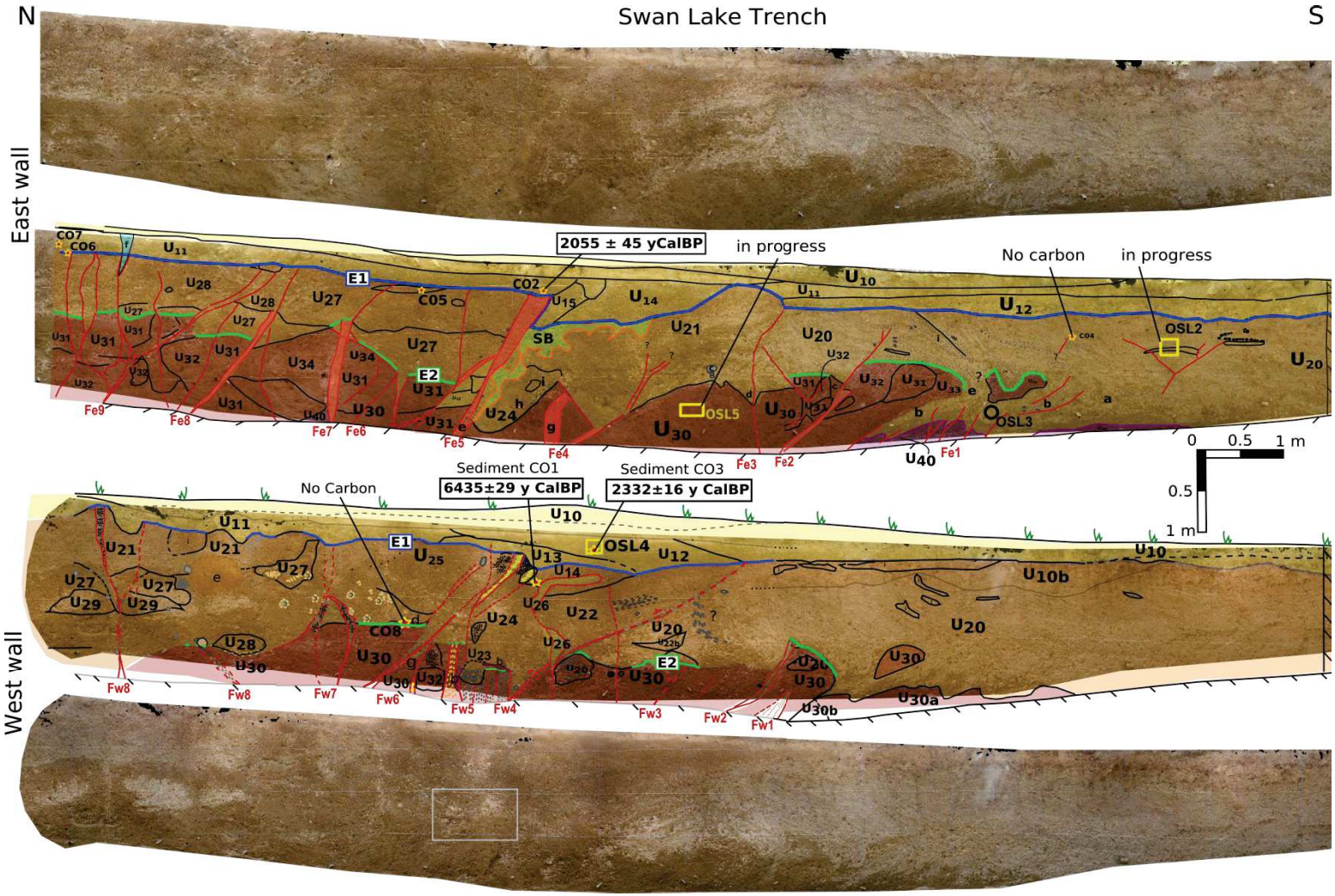


**Figure 4-55 : Log of the Swan Lake trench. Orthomozaics are shown (uppermost and lowermost figures) regarding the logging (centrals figures). East wall is on top and west wall is on bottom of the figure. Blue and green solid lines are the event horizons of surface rupturing paleo-events E1 and E2. Stars are locations of the radiocarbon samples and yellow solid boxes the OSL samples. Grey solid box is location of picture in Figure 4-56. Detailed legends are presented in next pages.**

## Legend Swan Lake Trench, East Wall

**Units :**

**U10**: Soil unit, silty to fine sand, dark beige, lot of roots, probably eolian deposit.
U11: Silty unit, yellowish, roots, eolian deposit: loess.
U12: Silty matrix lot of gravels, been size, matrix supported, lot of roots, red brown.
U14: Unit localized in the Fault zone. Matrix supported, very fine sand, quite consolidated, dark brown. Saltpeter (sulfurs).
U15: Like U14 but more lightly, more consolidated, lot of saltpeter.
U16: Sandy layer, discontinuous, affected by faulting.

**U20**: Main Unit of south part, Coarse sand and gravel, stratified alluvial layer, alternating clast and sand, clast supported, gravel dominant, large and more indurated sandy layer, slightly south dipping
Nota: following U20 sub-units are different from U20, attesting of strong left-lateral fault motion.
U21: Clast supported gravel layer, stratified, some sandy matrix-supported layers, more indurated. Light grey.
U24: Clast-supported unit, sandy matrix, clast mm to cm, unsorted, slightly stratified on lower part. Roots rich.
U25: same as U24 but much rich in clay, moist. Some confusions with U30.
U26: Clast rich unit, mm to cm, matrix supported, fine sand, channel shaped, moist.
U27: Orange massive unit, fine sand, matrix supported, not loose, powder.
U28 : Coarse, grey, gravel, clast supported, massive unit.

**U30** : Wet, clayey layer with lot of gravels. Matrix supported Stratified but unsorted. Few pebbles. Brownish to dark brown. Fine-sand to clay matrix.
U31 : Clay, hard to scrap, moist, dark brown, cm to mm gravels. Looks like U30.
U32 : Clast supported, cm gravel, grey, unsorted, slightly stratified, not so wet. Sandy matrix, slightly reddish. Some part matrix dominant. Looks like U30.
U33 : Same as U32 but in the other side of U31, separated from U31 by sandy layer. Clearer than U32. Few pebbles.
U34 : Gravels to pebbles, rounded, unsorted, stratified, heterogenic, clast-supported, sandy matrix

**U40** : Bottom layer, coarse sand, wet, grey but with varied sand colors.

**Notes :**

a: Pocket of gravels, distributed in a deformed layer.
b: Cm gravels on top of more little ones, oriented. It could be during deposition but due to orientation of that structure it could be consistent with drag folding of that unit: Shear band.
c: Pebbles with stage 3 calcrete development on its present lower part.
d: Little wedge, unsorted gravels, light grey.
e: Sandy clay shear zone
f: Fault propagation through U14 could be associated to ice wedge, but finally considered as a significant shear zone.
g: Shear zone, 2 bands : 1. 3 cm, 1 cm-wide, left light brown, yellowish clay rich and right dark brown, more sandy ; 2. 10cm large sandy band on the left: shear zone.
h: Lens of paleosoil.
i: Indurated sandy layers
SB (Sand Blow): Thin sand, dark yellowish, moist, sand blow coming from under unit (not visible in the trench). Clearly associated with shear zones.

## Legend Swan Lake Trench West Wall

**Units :**

**U10**: Soil unit. Loess: Silty (eolian) layer, yellowish, roots rich. Higher part dark beige, lower more clayey

U10b: Sandy with a lot of little gravel (0,5cm), located in channels under U10. Matrix supported. Roots rich, Yellowish to light beige (paleosoil). Correspond to U 12 on eastern wall.

U11: Sand + gravels + lot of roots

U12: Sandy silty, light brown, some clay.

U13: Yellowish-beige level, silty-sandy, altered pebbles with white powder (saltpeter)

U14: Paleosoil, 70% cacao chocolate brown, dark, wet white powder.

U15: Same U14, under the soil

**U20**: Coarse, massive cast supported, sand to gravel, light grey deposits. Stratified, loose, dry alluvial, unsorted, slightly south dipping. Some sandy levels (dots).

U21: Coarse sand and gravels with some folds on gravels (deformed), unsorted, brown grey, poorly consolidated.

U22: Coarse sand with gravels, bedding northward with alternations loose/indurated banks.

U23: Massive, matrix supported, wet, brownish, gravel to pebble imbricated.

U24: Whitish, loose, not super-loose, matrix supported, dry, gravel to pebble imbricated.

U25: Sandy-gravel whitish, very indurated, saltpeter (desegregated graves, alternations gravel-sand).

U26: Sandy unit, bowed from below, interposed just above the paleosoil.

U27: Matrix supported unit, sandy, light brownish with cm gravels, hard to describe orientation. Gravel pocket, cm, unsorted, not oriented. Few pebbles.

U28: Clast supported with cm gravels, some sand, dray, light grey.

U29: Coarse unit, gravel to pebble with sandy matrix, light grey.

**U30**: Clay deposits with a lot of gravels (0, to 1,5cm), matrix supported.

U30a: Coarse sandy- (gravel to 1,5cm), matrix supported. Quite wet, probably due to underground water table or to a content more clay rich). Correspond to U40 on eastern wall.

U30b: Coarse to medium sand, sorted, really wet.

U31: Vertical alternations coarse sand / fine sand.

U32: Coarse sand with gravels in a silty matrix, no bedding, and clast dominated.

U33: Coarse sand with gravels, very loose (pockets)

U40: Coarse sand, unsorted, varied colors, grey unit, few types of gravel.

**Notes:**

a: Sand filled crack. Clear orientation parallel to faulting. Central part thinner than borders on whole crack length. Lower part composed only by thin sand (Shear zone).

b: Sandy pocket, thin sand with left part really dark. Paleosoil? The sand seems to come from under layers.

c: Altered pebbles, saltpeter (white powder, crunchy, no taste) The saltpeter seems not associated to units but to a specific depth. Hence it may originate by hydro-pedological phenomena.

d: Dark reddish lens, does not smear, not organic matter.

e: Big borrow? Really loose, roots.

f: Sub-vertical stratigraphy, not well understood, correspond to a transfer zone with U20 to the right and U21 on the left, which are totally distinct.

g: Shear zone, very clayey. Slight boudinage.

i: Indurated levels

Unit U10 corresponds to the top unit of the trench, and it presents soil with development and a sandy to silty matrix, likely aeolian. Important bioturbation could be reported within U10, as well as a rather clear stratification. Lower sub-units are lighter and present paleosoils lenses and horizontal concretions of white powdery (possibly saltpeter) which seems to diffuse through the silty matrix and to crystalize on the trench walls, given that they dry during the few hours following the wall cleaning. Few coarser lenses of gravel to pebbles are interspersed between sub-units of U10, and the sandy uppermost sub-unit, in central part, is probably related to the small dune we observed on surface, capping the terrace riser. In the underlying sub-unit U11, 40 to 50 cm under the surface, some clayey lenses display a noticeable light brown color, indicating the presence of paleosoil. Two bulk samples have been sampled within this sub-unit of U10, one from each wall, which allows, using radiocarbon dating AMS protocol, estimating the paleosoils ages at 2055 ± 45 CalyrBP for U11 and 2332 ± 16 CalyrBP for U12, on east and west wall respectively. No faulting has been reported within the U10 soil unit and the underlying U11 sub-unit, but the lower part of U10, the dark-brown sub-units U14 and U15, seem to be involved in the faulting, and especially by the fault Fe5. Consequently, this age obtained in U11 may post-date the most recent event recorded in that trench.

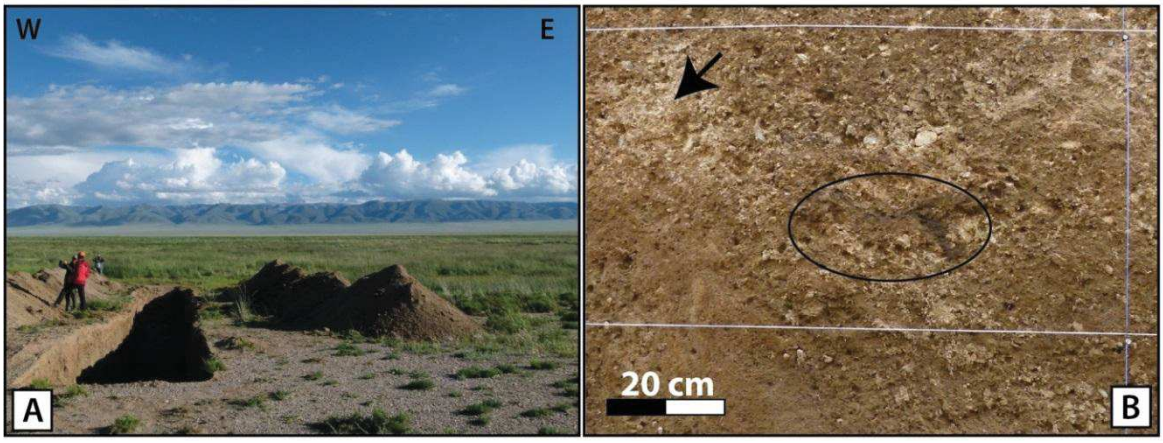


**Figure 4-56: A. Photograph to the south of the Swan Lake trench. Note on the background the Gichigniy Nuruu, with the South Chandmani Fault on bottom of the relief (see Figure 4-18) and the preserved peneplain on top. B. Photograph of details of the Swan Lake trench, west wall. Back arrow indicates a fragmented pebble, associated with white powdery concretion (likely saltpeter). Black ellipse indicates a manganese dark reddish level.**

The units U20 and its sub-units present a complex geometry. They are composed of coarse alluvial materials, gravel to pebbles, sub-angular, grey colored, and are roughly stratified while laterally discontinuous, given that they are significantly deformed. Two domains can be identified in U20, separated by the complex central fault zone:

1. On the southern part of the trench, U20 is clast-supported, dry, very loose, unsorted and well stratified, slightly dipping south (U20 to U25). Its lower part

appears to be faulted with a reverse motion located on north-dipping fault splays. This unit presents some indurated sandy levels, which highlight the fault-related deformation, while some cryoturbation is also suspected. However, due to the coarse and very loose aspects of the deposits, fault terminations within U20 cannot be accurately identified in that part of the trench. Some fault-bonded, deformed, matrix supported patches of wetter materials, likely related to significant content in clay, appear analogous to U30, although they are included into U20. By the same, some dry, clast supported patches of U20 appear to be included in the matrix-supported unit U30. Such observation is interpreted as related to left-lateral faulting and penetrative deformation or liquefaction processes, which mixes U30 and U20, and causes the observed patches. Close to the fault zone, U20 describes a synform drag fold, perceptibly related to the lowest-dipping fault branch Fw3, south of the main shear zone. The faulting observed in the lower half-part of these southern sub-units of U20 is mostly dipping north, with few conjugated fault splays dipping south. An OSL-tube has been sampled within the middle part of U20 (~70 cm from the surface), in order to estimate its abandon age, and eventually to both post-date the penultimate and pre-date the most recent surface rupturing events along this section of the WBF. The analysis of this sample is in progress.

2. On the northern part of the trench, U20 displays a patchwork of clastic sub-units, alternatively matrix- and clast-supported, globally loose to very loose with, however, few indurated sandy layers (U26 to U28). Clasts are sub-angular, and some imbricated levels attest of the alluvial nature of those deposits, hence certainly related to the low-relief alluvial terrace in which the northern part of the trench has been dug. The apparently complex structuration of those deposits appears to be both linked to stratification and faulting. Presence of large burrows and very weathered cobbles (fragmented clay-rich limp-pebbles), is visibly related to presence of saltpeter (Figure 4-56). Eventually, the sub-units of U20 are significantly more faulted on northern side of the main shear zone than on southern one.
3. Within the central fault zone, the west wall displays a light sandy shear zone (Fw6), north dipping by ~45°, and which affects the uppermost part of U20, as well as a dark sandy pocket, rich in organic matter, for which a radiocarbon dating on bulk, based on the AMS analysis protocol, gives an age of 6435 ± 29 CalyrBP. The sandy shear zone describes fault termination just 15 cm upward, on bottom of U10, and hence this age seems to pre-date at least the most recent event

recorded in that trench. At same position, the east wall presents a complex and really sharp sub-unit of thin sand, dark-yellow, rather moist, unsorted and un-stratified, which is clearly linked on its bottom to one of the major shear zone in U30 (Fe5). We interpret this feature (SB on Figure 4-55) as a sand blow, probably related to the most recent seismic event recorded in that trench, as it seems to blow within the contact between U20 and U10. On the top of the sand-blow, the contact with U10 is rather flat, instead downward the contact with U20 is uneven, describing 10 cm-large shark-tooth shapes.

On both walls, on the central shear zone, contacts between U20 and U30 display clear apparent vertical offsets of few centimeters (e.g. Fe2, Fe7, Fw2 or Fw6). Instead, upper limit of U20, in contact with U10, does not exhibit significant offset related to faulting, but systematic fault terminations, especially concerning fault splays north of the central fault zone (e.g. Fe9, Fe8 or Fw8). Hence, accounting of this dissimilarity of deformation and for the fault terminations criteria, we interpret that the contact between U20 and U10 corresponds to the event horizon related to the most recent event recorded in the trench's stratigraphy. Moreover, on both walls, the contact between U30 and U20 corresponds to the interruptions of ~15 cm-wide shear zones (Fe2, Fe4, Fe7, Fw2, Fw5 and Fw8). On west wall, this fault termination is frank, without evidence of upward faulting (Fw2, Fw5 and Fw8), while on east wall some fault splays (Fw2 and Fw7) are prolonging upward, with nonetheless a rupture pattern fairly dissimilar, as there is no significantly wide shear zone, but rather a really thin fault splay, systematically offsetting or interrupting U20 strata.

Unit U30 constitutes the lower part of the trench on both walls, and is composed of sands to gravel materials supported in a clayey matrix, with few pebbles. Like for U20, U30 sub-units are more heterogeneous northward than southward of the central shear zone. U30 is laterally discontinuous, with alternations of sorted stratified sandy units, and loose gravel pockets. Lateral deposit variations appear to be correlated to faulting, as contacts are systematically associated to apparent vertical offsets, with some aligned clasts. The overall stratigraphy of U30 and sub-units seems to be irregularly dipping north, and locally the faulting displays a minor reverse component, as in four places where U30 visibly thrust on U20 (Fe1, Fe5, Fw4, Fw6). Apparent offsets range from 20 to 120 cm, regarding solely to the bottom of U20, as the bottom of U30 is not visible in the trench. Within the central fault zone, U30 displays on both walls clear shear zones (e.g. Fe4, Fw5, Fw4, Fw1), characterized by aligned clasts, apparent vertical offsets, slight socking and small gouge formation sub-vertically oriented. On west wall, a shear zone (Fw4) is 65 cm-wide, with a clayey gouge on its northern part (Fw5), clearer than

the sandy southern part of the gouge, marked by grain lineations. Those shear zones describe net fault terminations against the bottom of U20, and appear related, especially on the west wall, to ~20 cm dark-reddish lenses, sometime vertically shifted, as involved within the gouge. An attempt of radiocarbon dating of those lenses shows they are devoid of organic carbon. Hence they probably correspond to manganese precipitation, coupled to oxidation. We interpret the multiple shear zone terminations as an earthquake criterion, and propose that the limit between U30 and U20 is an event horizon related to at least a second surface-rupturing earthquake occurred on the WBF. An OSL-bloc sample has been taken within U30, in order to estimate its abandon age and eventually to pre-date the at least penultimate surface rupturing event along this section of the WBF – analyze of this sample is currently in progress.

A wet sub-unit (U40), which may be related to U30, is outcropping on the bottom of the east wall, south of the central shear zone. U40 is composed of unsorted stratified coarse sand, mostly grey but also yellowish to orange, probably indicating oxidized deposits, and therefore presence of fluids. This distinctive formation seems to underneath other sub-units of U30, given that a chunk of U40 is visible on bottom of the central shear zone, but on south of the central fault zone, in direct contact upward with U20. This may suggest an erosion of the upper parts of U30 south of the main fault, which appears consistent with surface drainage observation on south of the fault, potentially generating erosional processes. Clear evidence of reverse north-dipping faulting can be observed within U40, for which the fault splays seem to go on upward within at least the lower part of U20, and visibly offset (by 2 to 10 cm) the contact between those units (Fe1, possibly Fw1).

#### *ii. Fault description*

Faulting is mainly located within the southern half of the SLT, and is distributed on a ~10 m-wide deformation zone, for which the central part represents the central fault zone, containing the main shear zones and a high density of fault cracks. On the east wall, we count six shear zones with significant thickness (arbitrary ≥ ~5 cm) within U30, with two of them prolonging into U20 with a similar pattern (Fe5, Fe8), and two others prolonging upward with a less pronounced shear pattern (Fe2 and Fe7), given that they are fault splays. On the west wall, eight significantly wide shear zones are counted, with here again four fault cracks reaching bottom of U10 (Fw4, Fw6, Fw7 and Fw8). Noticeably, the southernmost shear zone (Fw1) appears to stop within U30, and may be related to a former seismic event.

Main fault termination are identified in one hand on the U20/U30 horizon for the major shear zones, and in the other hand on the bottom of U10, associated to a sand blow.

We note that although the identification individual event is not obvious regarding to the distributed deformation in the coarse materials composing the central fault zone, the deeper are shear zones the more pronounced. For instance the shear zones observed on U20 are maximum 15 cm-wide (Fe5). Instead, in U30 some are 40 cm-wide (Fw4). This may constitute an additional argument to 2 or more events recorded in that trench.

Considering the fault kinematics, the difference of the various sub-units among each sides of the main shear zone is interpreted as reflecting the dominant left-lateral motion of the main WBF. The global kinematics of vertical apparent faulting within the trench is nonetheless consistent with surface topographic observations, as for instance the southernmost thrust identified seems to correspond to the topographic scarp on surface, norther side of the fault uplifted. Eventually, we documented that the deformation within U20 and U30 is systematically more pronounced on northern part of the central fault zone than on southern one. This observation makes sense with a slight thrust component of last earthquakes, generating more damages in the hanging wall on north of the fault.

#### *iii. Synthesis of paleoseismic evidences in SLT*

Paleoseismic investigations of the SLT allow identifying at least two surface-rupturing seismic events, based on criteria of fault terminations.

The most recent event in that trench is defined by the blue event horizon on Figure 4-55, as the bottom of U10 and sub-units corresponds to systematic fault splay terminations. Radiocarbon dating of paleosoils located within the sub-units located above and under this event horizon allow post-dating the most recent event in the SLT at 2055 ± 45 CalyrBP (SLT-C02) to 2332 ± 16 CalyrBP (SLT-C03), and pre-dating it to 6435 ± 29 CalyrBP (SLT-C03). Those ages are consistent with each other regarding to their relative stratigraphic position, given that the older post-dating age is 10 cm deeper that the younger one, while located on the opposite wall, and the pre-dating age is again 15 cm deeper, in a distinct sub-unit.

In turn, considering the ages of paleoearthquakes previously determined along the WBF (sections IV.2.4.1, IV.2.4.2 and IV.2.4.3) and the hypothesis of a unique event rupturing the whole WBF, these post-dating results of 2055 ± 45 CalyrBP and 2332 ± 16 CalyrBP appear too old by respectively 130 ± 78 and 407 ± 49 yr compared to the post-dating MRE ages found in the RCR, and by 199 ± 109 yr and 78 ± 80 yr compared to the post-

dating MRE age found in ICTG. Those discrepancies might be moderated, as the radiocarbon dating of sediment may involve remobilization processes.

**Table 8: Radiocarbon ages of samples collected in Swan Lake and Moskito Trenches.**

| Site | Reference sample | Nature | Prof. (cm) | mg C | Age yrBP | Err age yrBP | Age CalyrBP | Err age CayrlBP | 68% range CalyrBP | |
|---|---|---|---|---|---|---|---|---|---|---|
| Swan Lake Trench | MO16_SLT_C01 | Bulk paleosol | 65 | 0,65 | 5645 | 30 | 6435 | 29 | 6406 | 6464 |
| Swan Lake Trench | MO16_SLT_C02 | Bulk paleosol | | 1,14 | 2075 | 30 | 2055 | 45 | 2010 | 2100 |
| Swan Lake Trench | MO16_SLT_C03 | Bulk | 40 | 1,11 | 2305 | 30 | 2332 | 16 | 2316 | 2348 |
| Moskito Trench | MO16_MT_C02 | Paleosol | 100 | 0,92 | 3355 | 30 | 3601 | 37 | 3564 | 3622 |
| Moskito Trench | MO16_MT_C03 | Sediment | 60 | 0,69 | 2510 | 30 | 2614 | 87 | 2527 | 2701 |
| Moskito Trench | MO16_MT_C04 | Bulk | 75 | 0,84 | 5495 | 30 | 6299 | 13 | 6286 | 6312 |
| Moskito Trench | MO16_MT_C06 | Bulk | 110 | 1,03 | 4510 | 30 | 5179 | 88 | 5091 | 5267 |
| Moskito Trench | MO16_MT_C07 | Charcoal | 125 | 1,04 | 7420 | 45 | 8260 | 54 | 8206 | 8314 |
| Moskito Trench | MO16_MT_C08 | Sediment | 215 | 0,46 | 4350 | 30 | 4917 | 42 | 4875 | 4959 |
| Moskito Trench | MO16_MT_C09 | Bulk | 90 | 0,98 | 3470 | 30 | 3760 | 52 | 3708 | 3812 |
| Moskito Trench | MO16_MT_C12 | Charcoal | 125 | 0,95 | 4310 | 30 | 4892 | 37 | 4855 | 4929 |
| Moskito Trench | MO16_MT_C13 | Charcoal | 300 | 0,46 | 4000 | 30 | 4476 | 35 | 4441 | 4511 |

The pre-dating age of 6435 ± 29 CalyrBP found in SLT does not agree with the proposed interval for penultimate event determined in ICTG (i.e. 3272 to 3816 CalyrBP). The three possibilities to explain that observation are: i. this bulk sample has been remobilized and content inherited organic matter formerly developed; ii. as supposed in RCT2 and RCT3, the SLT deposits did not recorded, due to erosion, the evidences of the penultimate event and hence this age corresponds to pre-dating age of the pre-penultimate seismic event or; iii. the age in Ice-creek may be associated to a minor event that did not break the fault along the Swan Lake section (segment WBF-S4).

The potential penultimate event in SLT is identified by the green event horizon in Figure 4-55, which corresponds to terminations of the major shear zones identified in that trench

(Fe2, Fe4, Fe7, Fw2, Fw4, Fw5, and Fw8). This event is clearly post-dated by the paleosoil development, at 6435 ± 29 CalyrBP. This age is, in that case, in agreement with observations done within ICTG, RTC2 and RCT3, which suggest a former event in early-Holocene.

Additional earthquakes are possibly visible in that trench because the stratigraphy displays a complex fault cracks network, with a stronger deformation observed within U30 than in U20 and some shear zones seem to end on central part of U20. However, no clear additional event horizon with convincing earthquake criteria has been identified in SLT. OSL dating of these units (U20 and U30) are currently in progress, which may help to constrain the deposition history and the paleoseismicity recorded in that trench: first by defining the age of the second earthquake we identified, and secondly by highlighting the time-laps between the two events and potentially pointing out that we missed some events.

#### *IV.2.4.4.2. Moskito Trench*

The MT is located 45.290°N; 98.280°E and oriented~N10, orthogonally to the fault trace. It is 30 m-long, 2.2 m-wide and~2 m-deep in average (Figure 4-54 and Figure 4-57). The main deformed zone, south of the trench, has been extended to 3 m-deep until the depth of the water table. In surface, the northern part of the trench is seated within an alluvial surface, visibly abandoned while it is elevated by only 40 to 50 cm centimeters from active channels. The southern part of the trench shows a transversal transect through a clayey grassy-vegetated sag-pond. 50 m to the east, it connects to the main drain from where likely come the infilling deposits of the pond by an along-fault channel. Southward of the trench is a low-relief alluvial terrace, which is clearly affected by faulting as attested by the presence of the pond and given that it displays little pressure ridges causing the mole track morphology of the fault trace (Figure 4-51). Just south of the pond, a N-S shallow channel is visible in the terrace and may correspond to a temporary outlet of the MT pond. It is clearly not active often, given that there is no evidence of flooding or related deposits on the surface. Consequently, it seems that for moderate flooding, this pond acts as a minor/local sink and we can infer that the current deposition regime is of low energy. Looking at the trench walls, the northern part is composed by coarse gravel to cobbles alluvial deposits, stratified, with a noticeable underlying massive red clay unit in a depth of 1.5 m (Figure 4-57-B). There are few splays cutting that stratification, but we concentrate our analysis on the main deformed zone, located on southern part of the trench, where it cuts the pond. Thus, only the clearly deformed southern part of the trench is detailed in this study (Figure 4-54).

The whole structure of the trench is well stratified, and presents on its southern part an obvious deformed zone, furtherly named ‘central fault zone’, which corresponds to the sedimentary filling of a > 3 m deep depression, bounded by two steep combined normal faults. Those faults are furtherly named main northern (F1) and southern (F2) faults depending of their relative position into the pond. They are dipping 70° to 80°, and match in surface with the borders of the pond. The logged part of the trench can be divided in five main units, U10 to U50, furtherly detailed in order to describe and interpret the deformation recorded in that trench, and to constrain the occurrence of related earthquakes.

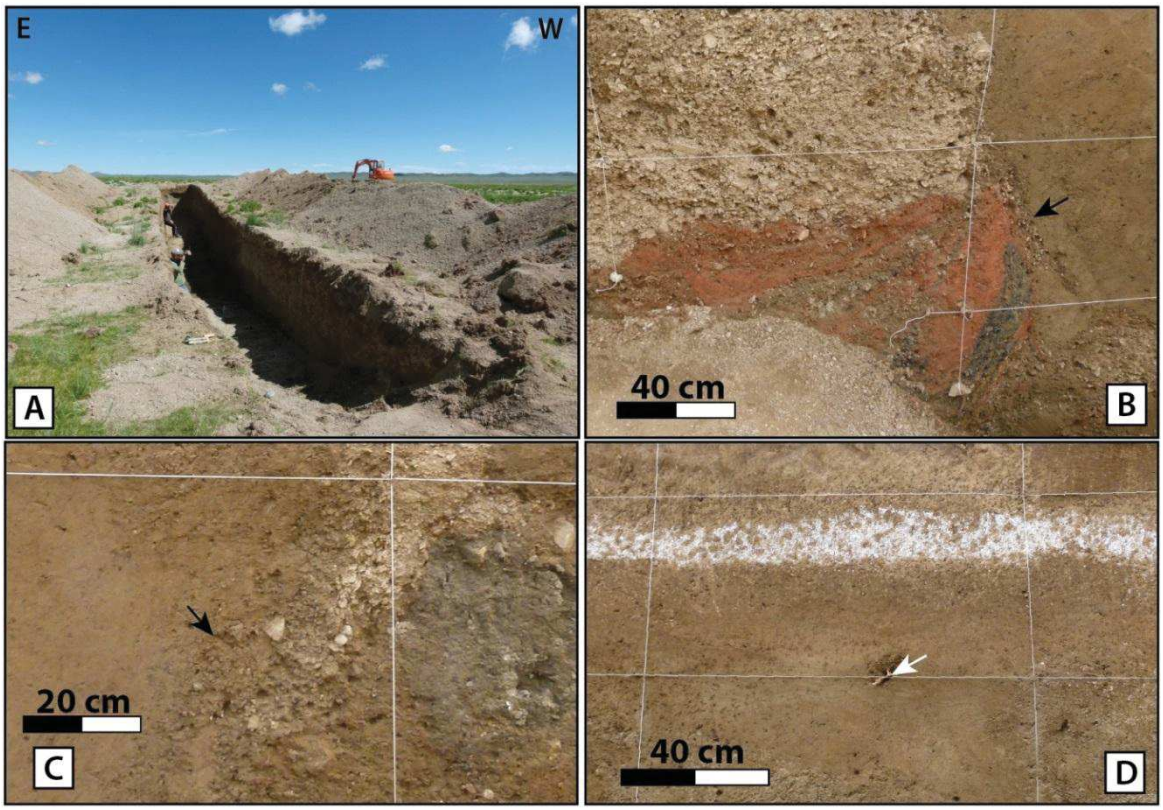


**Figure 4-57: Photographs of the Moskito Trench. A. Context photograph of the Moskito Trench. B. Photograph of the bottom of F1 on west wall, showing the deformed reddish clay deposits (U50). Black arrow indicats aligned clasts within F1. C. Details of the east wall, with deformed gravel pockets (U30). The arrow shows shearing criteria with aligned clast along the F2 fault. On the right of the picture, the grey unit is U50b. D. Photograph of the west wall, with the white concretion band. White arrow indicates the location of a bone.**

### *i. Description of units and sampling*

Unit U10 corresponds to a capping of lower units by a massive clear colored, clay to silt deposits, with few sub-angular to rounded pebbles, probably of alluvial origin as observed on surface. This ~ 50 cm-thick unit presents bioturbation and is rich in roots, given that its upper part constitutes the current soil. The massive, thin and un-stratified nature of this unit makes hard the identification of fault splays and U10 does not seem to exhibit significant deformation or evidence of faulting – although looking to the surface morphology, it is likely that the cracks related to most recent event reach the surface. The contact between U10 and underlying deposits U20 is unclear and mostly based on color and moisture variation than on grain size. The contact seems to be irregular despite of the flatness of the topography. U10 thickness ranges from 20 to 60 cm.

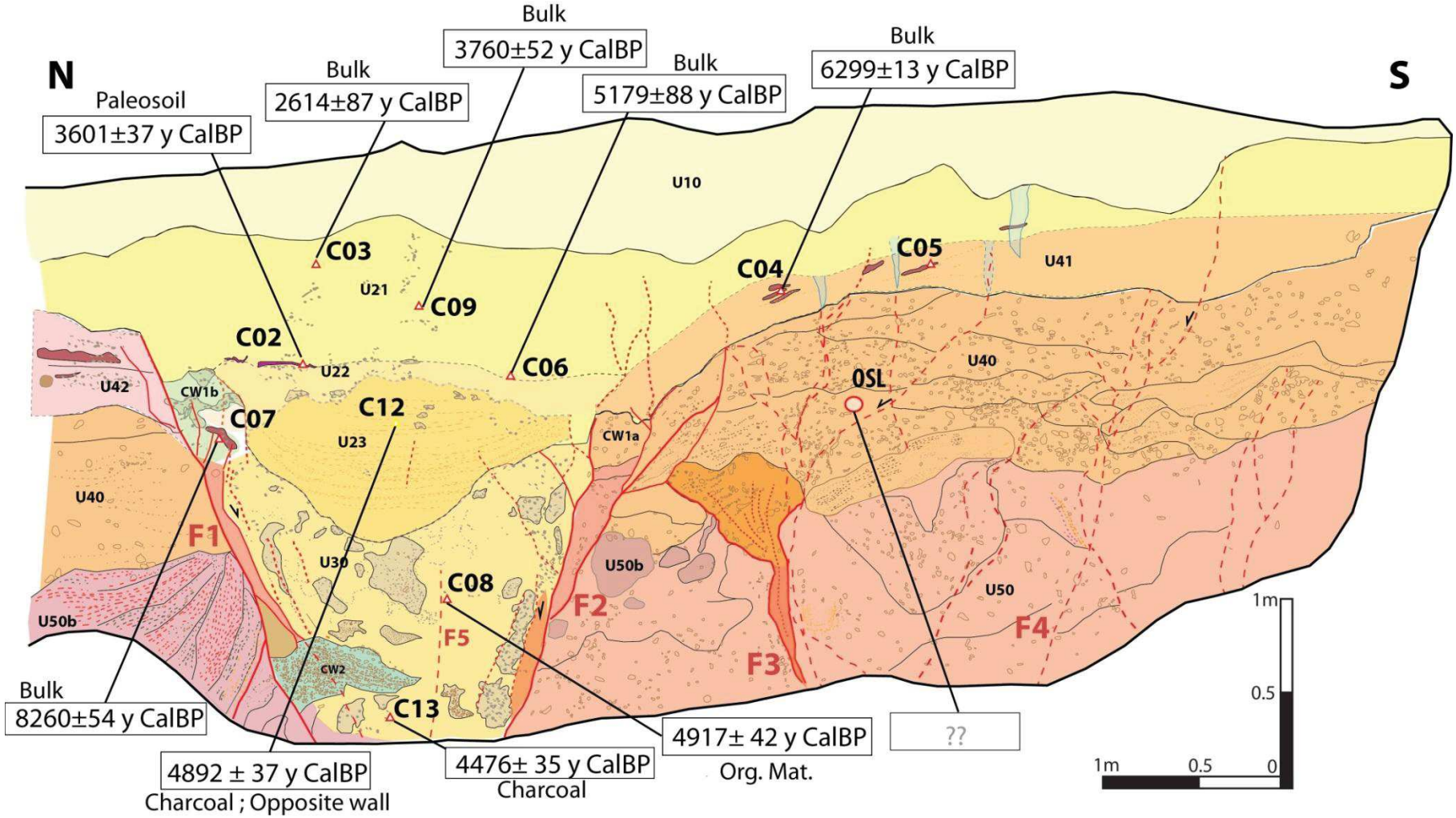


**Figure 4-58: Log of the eastern wall of the Moskito Trench. F1 to F5 are labels of main faults. red triangles are radiocarbon samples, with age and nature given out of the log, and red circle is OSL sample, in progress. See orthomozaic and legend of units on next pages.**

**Figure 4-59: Orthomozaic of the eastern wall of the Moskito Trench.**

**Legend Moskito Trench, both walls**

- U10: Soil unit. Massive, clear colored clay to silt deposit. Angular to sub-angular pebbles, alluvial.
- U20: Clay to sot deposit, clear brown, pockets of sand to gravel, unsorted, angular clasts. Matrix-supported, clayey
  - U21: Clayey, massive and un-stratified. Beige to yellowish.
  - U22: Clayey, massive and un-stratified, darker that U31. Paleosoil on the bottom.
  - U23: Clayey, massive, yellowish, stratified.
- U30: Massive, un-stratified clay to silt deposits. Sandy pockets supported in clay matrix.
- U40: Coarse-sand to cobble deposit, sub-angular, heterogeneous, clast-supported in a sandy matrix.
  - U42: Stratified deposit, brown, clay to silt matrix-supported. Rich in organic matter.
  - U41: Stratified, yellowish silt to thin sand. Rich in organic matter.
- U50: Alluvial basement, stratified and highly deformed. Patchy.
  - U50a: Stratified clay deposit with some gravels to pebbles, light red in its upper part, and very dark on the lower part
  - U50b: Coarse sand to cobble, supported in a silt-to-clay matrix, very dark.
- CW1a: Faulted slice of U41, with a normal motion. Stratified.
- CW1b: Disturbed and faulted chunk of U42, sheared, rich in organic matter.
- CW2: Colluvial wedge, unsorted, unstratified, faulted on central part, associated to fault F1, same composition as U40.

Half a meter under U10, appeared in the few hours following the cleaning of the trench walls a very clear horizontal band of abundant white powdery concretions, chemically unidentified but possibly saltpeter (Figure 4-57-D). This band, preferentially located on clayey horizons, visibly does not follow the stratification but is limited to depth of 1 to 1.5 m and hence might be more related either to hydrological or biological processes than to structural setting of the trench.

Unit U20 is composed of clay to silt deposits, clear brown, with some sinuous, irregular, sand to gravel pockets filled with unsorted angular clasts, supported in a clayey matrix. At mid-height, we observe a noticeable dark brown discontinuous paleosoil with red bottom, separating the lower from the upper part of U20. This 1 to 6 cm-thick paleosoil, potentially resulting from a fire, has been sampled as bulk for radiocarbon dating (MT-C02). Analyze of this sample yields an age of 3601 ± 37 CalyrBP. Unit U20 is massive, and can be divided in three sub-units: over the paleosoil is U21, clayey, massive and un-stratified, in which identification of deformation is difficult because it is devoid of stratigraphic markers. Few fault cracks are however suspected in that sub-unit, especially above the main southern fault (F2). The upper part of U20, U21, extends laterally beyond the pond: on north of the pond, it does not appear to be affected by faulting, given that one some of the major faults (F1 and F3) seem to stop on its bottom. On south of the central fault zone, it is prolonged on 3 m, and is progressively pinched between the overlying U10 and the underlying U41. A discreet fault splay, F5, may affect U21. Two bulk samples of darker clay have been sampled within U21 for radiocarbon dating. The intermediary part of U20, U22, is bounded upward by the paleosoil, and displays massive clay with few horizontally elongated gravel pockets; the thickness of

U22 is variable, ranging from 5 to 20 cm, which could be related either to erosional processes, cryoturbation or to fault-related deformation. U22 is constrained to the pond limits, as it seems de be laterally delimited by fault cracks F1 and F2 – while absence of stratigraphic markers prevent offset assessments. Additionally to the sampling of the paleosoil (MT-C02), a second bulk sample has been collected within U22 for radiocarbon dating (MT-C06). Analyze of this sample yields an age of 5179 ± 37 CalyrBP, clearly older than MT-C02.

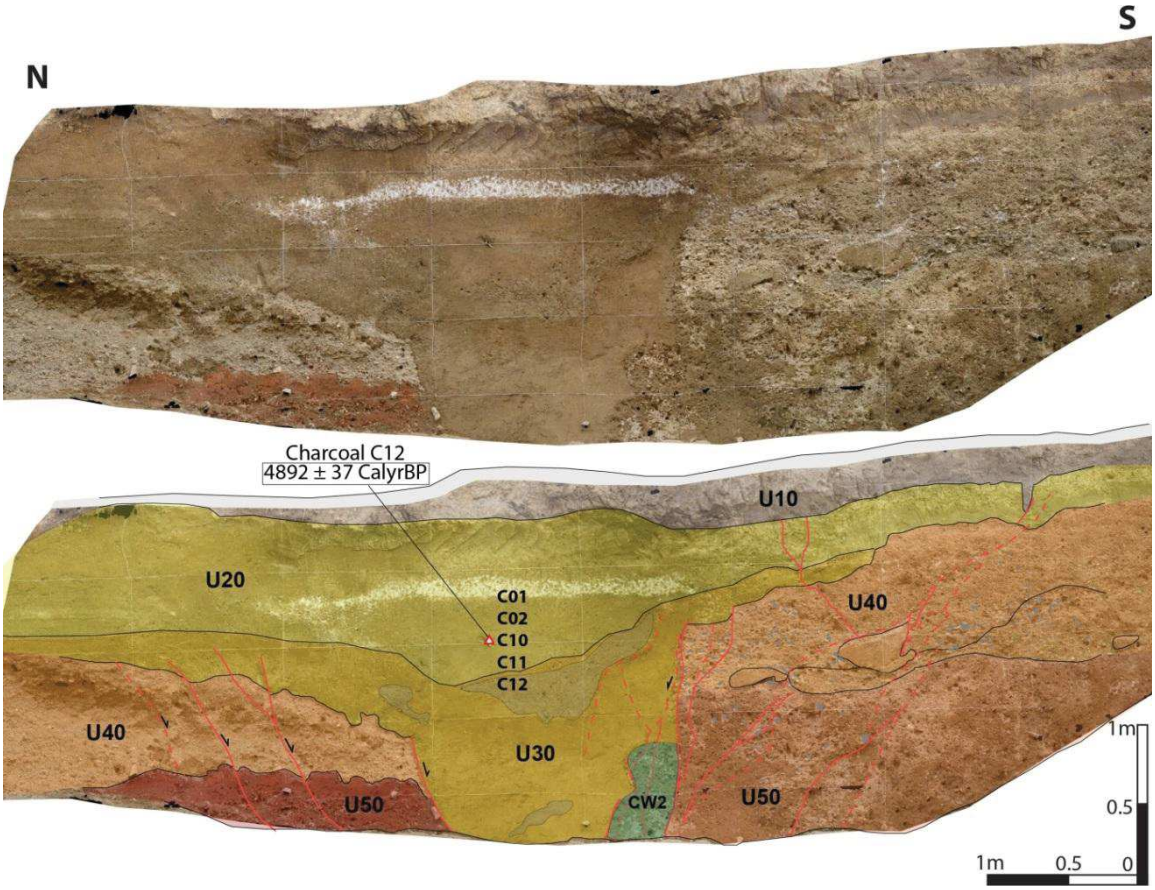


**Figure 4-60: Log of the wetsern wall of the Moskito Trench. On top is the orthomozaic. On bottom is the log and location of samples (red triangle).**

Instead of the un-stratified upper part of U20, under the paleosoil, the lower part U23 displays a clear stratification, almost un-deformed while slight fault cracks may be identifiable. U23 is composed of yellowish to dark-orange laminations, alternating ~5 cm thick silt layers and clearer beige clay layers. The stratified lower part of U20 is mostly visible between the faults, and seems to be pinched both on north and south of the depression. On the central part of the central fault zone, those strata describe a soft antiform, symmetrically situated regarding to the main conjugated faults F1 and F2. Underlying this feature, the contact between U23 and the coarser unit U30 appears channel shaped whether it is not evenly identifiable. It displays, on the lowermost part of

U23, systematic evidences of an angular discordance, involving probable alluvial erosion during the time-span between deposition of U30 and U23. The uppermost layers of U23 however, are collinear to the contact, and then stop southward against a loose chunk of stratified coarse sand to cobbles (CW1a), bounded by fault splays of F2.

Also, two reverse fault-splays, conjugated with the main southern fault, can be observed within the synform clay bedding, which seems to be variably vertically offset by few centimeters (junction between F2 and F3). To the north, the contact between lower part of U23 and U30 is verticalized, alike the U23 inner strata, and does not display contact with the main fault F1. While instead, is may be a chunk of U30 or a colluvial wedge from U42 (CW1b), associated to some faulted sand to gravel pockets.

Five bulks for radiocarbon dating have been sampled within U20, and the ages then derived using AMS protocol. Firstly, the dating of the well-localized dark paleosoil lens (C02), in U22 within the central fault zone yields an age of 3601 ± 37 CalyrBP. In turn, in the same layer and symmetrically regarding to the axis of the central fault zone, the radiocarbon dating of an organic-matter-rich clayey lens, rich in small roots (C06) gives an age of 5179 ± 88 CalyrBP. One may note that while the samples seem to be in the same stratigraphic layer and only 1 m from each other, this second sample C06 has a really different nature than C02, especially regarding to the aspect and concentration of the organic matter. Such strong discrepancy is hard to explain, because whether this unit is slightly deformed, the paleosoil bedding is sub-tabular. The older sample is only 10 cm under the paleosoil compared to the surface, and located at visibly the same level regarding to the bedding. Easiest explanation is that this sample is an outlier, but it is tricky to argue the possible inbuilt of a bulk sample: one may propose that the sediment constituting this un-stratified massive upper part of U20 has been formerly remobilized from an older adjacent horizon – for instance U41 as this sub-unit presents significant content in organic matter. On the other hand, the organic matter analyzed may partly originate from leaching of overlying soils. Another sample (C09) has been taken between C02 and C06, 30 cm upward, in U21, and yielded an age of 3760 ± 52 CalyrBP. This sample is older by 159 ± 89 yr than the paleosoil, although it is located higher in the stratigraphy. While this difference is not large, this result is incoherent regarding to the stratigraphic order. This moderate discrepancy could be explained either by: i. some slight contamination of the paleosoil by modern roots of other biological activity, making potentially younger the paleosoil, ii. by some remobilization of the C06 materials from a former deposition, iii. by inexact calibration of the sample, especially regarding to the parameter relative to the $\delta^{13}C$ (here defined the IntCal13 curve in OxCal). Nevertheless, we consider that the paleosoil dating MT-C02 remain the strongest dating within U20,

because its outcrop is sharp and clearly defined compared to the other bulks we sampled. Moreover, other radiocarbon dating in U30, due to their visible poorer content in organic matter (from color at first order), enhanced a stronger contamination by biological and hydrological processes, or even a remobilization by erosional processes. Next bulk sampling has been done on topmost part of U21 (C03), and gives an age of 2614 ± 87 CalyrBP, stratigraphically consistent with previously documented ages, as this is both the uppermost and the youngest sample analyzed in this trench. Finally, on the opposite wall (west wall), a charcoal has been found within the clay laminations of U23, and gives an age of 4892 ± 37 CalyrBP, which appears to be logical, regarding to its position, with the other samples dated in U20.

Unit U30 constitutes the lower part of the filling of the pond, and is composed of massive, un-stratified clay to silt deposits, with numerous pockets of sand to gravel clasts, supported in a silty matrix. These pockets are of irregular shapes and sizes, up to 50 cm in diameter. U30 is exclusively located within the pond, between the two main faults F1 and F2, with which it is systematically in contact. The more the pockets are close to the main faults, the more they appear elongated collinearly to the faults with a normal motion (strike slip motion is certainly involved, but not quantifiable in this fault-transverse trench). Pockets also display few shear criteria, as aligned clasts (Figure 4-57-C). On northern bound of the pound (F1), set on the lower part of U30 and at 2.5 to 3 m-deep, is a clear colluvial wedge of whitish, unsorted, clast-supported, angular pebbles (CW2), for which the composition is similar to unit U40. This likely indicates that the materials falls from this unit, located 90 to 150 cm above following the F1 fault trend considering respectively bottom and top of U40. This colluvial wedge is interpreted as resulting from a former earthquake which used to partly open the pond. However, considering the previous observation that faulting is affecting uppermost units, the next earthquake likely generated as well some offset along the main norther fault F1. Following that reasoning and regarding exclusively to vertical offset (as the horizontal component cannot be determined here), the displacement measured between the colluvial wedges and its original unit may involve several offsets. Consequently the relative height of the wedge compared to its supposed original unit cannot be correlated to a single apparent vertical displacement. Three distinctive types of fault splays can be identified within U30, all extending above the colluvial wedge: i. as previously mentioned, some fault splays are related to the lateral elongated gravel pockets, on both sides of the unit (F1 and F2), ii. a unique fault splay, hardly distinguishable, in the central part of the central fault zone (F5), which does not seems to extend on the upper part of U30, nor in U20, while no fault termination criteria has been found, iii. On the southern side of the central fault zone

(F2), two clear fault splays appear to extend upward until the clayey strata of U20. The uneven discordant contact between U20 and U30 looks reasonably simple in the central part of the fault zone, but is more complex on the edges, close to the main faults F1 and F2. On southern part of the central fault zone, U30 is confounded with the gravel shear zone related to the main southern fault F2, and ends upward on the same U40 preserved chunk than U20 (CW1a). On the northern side (F1), the material remains same nature of U30, with in upper part, however, a wedge of sharp and sinuous sand to gravel levels (CW1b), visibly deformed and involved in the shearing related to the main fault. One of these features has been sampled as a bulk for radiocarbon dating (MT-C07).

Two radiocarbon samples have been found within U30. A first one is a charcoal (MT-C13), collected on the bottom of the trench, 3 m-deep from the surface, just below the colluvial wedge, and is gives an age of 4476 ± 35 CalyrBP. We interpret this age as pre-dating at least the two last earthquakes recorded in MT. We note that this age is younger by 416 ± 72 yr compared to the radiocarbon age derived from radiocarbon dating on the MT-C12 charcoal found in the overlying unit U23 in the western wall. A significant inbuilt in MT-C12, or a remobilization (after a previous deposition) may explain this discrepancy. A second sample is a bulk (MT-C08), sampled on the central part of U30, close to the central fault splay, and gives an age of 4917 ± 42 CalyrBP. This second sample C08 is 441 ± 77 yr older than C13, while located more than 50 cm above in the stratigraphy, and visibly in the same unit. Here again, we have a charcoal younger than a bulk, although lower in the stratigraphy. This observation is rather hard to explain, because charcoal are supposed to be older than their buried age, due to inbuilt related to tree lifespan and inheritance of transportation or former deposition. Instead, the bulk is supposed to be theoretically younger than the buried age, due to potential post-buried contamination by bioturbation of percolation processes. Eventually, we sampled a bulk within the sheared zone or colluvial wedge CW1b for which analysis using AMS protocol allows deriving an age of 8260 ± 54 CalyrBP. This age is ~4 ka older than radiocarbon dating done 1.5 m in U30 (i.e. MT-C12). This large discrepancy likely confirms that the CW1b is not belonging to U30, but to a sheared part (or a collapsed part) of U42, describe ahead.

Unit U42 is a stratified sub-unit, composed of alternated brown, clay to silt, matrix-supported layers with grey clast-supported coarse sand to gravel layers, and is identifiable only on the northern side of the central fault zone. Some organic matter rich lenses can be identified by their dark color and loose consistency. This unit is clearly faulted in contact with the main northern fault F1, and appears correlated, geometrically and by its composition, to the CW1b located in the southern side of the central fault zone

and sheared by F2. Apparent vertical offset could be quantified to 20 to 25 cm, with a normal dip-slip motion. Assuming that CW1b belong to U42, its deposition age can be estimated to 8260 ± 54 CalyrBP according to MT-C07 dating.

The unit U41 is a stratified sub-unit, composed of yellowish silt to thin-sand, in which is intercalated a dark horizon rich in organic matter that we sampled for radiocarbon dating (MT-C04). In the bedding, we identified three to four vertical features, interpreted as ice wedges, which connect downward with discreet fault splays. No vertical stratification, (potentially related to ice wedge growth) has been observed within the ice wedges, possibly suggesting a mostly tectonic origin. The nature of these features (i.e. cracks or cryoturbation) remains ambiguous.

The sample location for dating of U41 (MT-C04) is situated just southward of the central fault zone, within a dark horizon previously mentioned, probably related to a paleosoil, and gives an age of 6299 ± 13 CalyrBP. This age provides a temporal upper bound for the deposition of the alluvial bedrock in MT. Moreover, looking at the proximity of the C06 sample, this rather old age may suggest that some remobilization of upper part of U41 into U22, which could explain the strong discrepancy observed for C06 age with other radiocarbon ages done in the same layer (i.e. other dating of U20 and U30). We hence propose that part of U22 is coming from remobilization of organic matter rich U41, which explain the outlier nature of dating of C06.

Unit U40 is a coarse-sand to cobble deposit, sub-angular, heterogeneous, and clast-supported with a sandy matrix. Coarse materials, few crosscut stratifications and imbricated clasts indicate the alluvial nature of these deposits, likely related to the low-relief alluvial terraces documented in surface. U40 is composed of a patchwork of coarsely stratified and sheared sub-units, which represent the upper part of the alluvial MT ‘bedrock’.

On north of the central fault zone (F1), this gravel unit appears massive, less disturbed than in southern part, and is clearly delimited to the south by the main northern fault F1, along which some clasts are dragged and aligned, showing normal dip-slip motion (Figure 4-57-B).

On southern part, the laterally discontinuous alluvial sub-units of U40 describe sinuous and irregular contacts, and are slightly dipping north by 5° to 20°. On the lower part of U40, a noticeable well stratified clay unit is affected by faulting (F3), although it does not display significant vertical offset. In fact, it is cut by a sub-unit of unsorted coarse gravel, which seems to be injected from an underneath shear zone located in U50, into the

above clearer sub-unit, which is composed of sorted coarse sand to pebbles with a rough stratification and some bedding of imbricated clasts. Numerous other sinuous fault splays (F3, F4 and related splays) are identified within U40, mostly related to lateral limits of the sub-units, and materialized by few centimeter-wide shear zones and aligned clasts (F3 and F4). However, fault terminations criteria remain ambiguous due to the coarse nature of these deposits and to cryoturbation processes documented within U41 (ice wedges). Because no significant offset are identified within the sub-units, we suggest that motion on these fault-splays is mostly strike-slip. An OSL-tube sample has been collected on central part of the unit (MT-OSL), southward from the central fault zone, in order to assess the deposit age of this unit, and to pre-date the opening of the pond – the analysis are in progress.

Unit U50 constitutes the lowermost part of the alluvial bedrock visible on MT. U50 presents rather different characteristics between northern and southern part of the central fault zone, and is hence furtherly distinguished as U50a and U50b respectively. North of the fault zone, U50a is composed of a stratified clay deposit with some gravel to pebbles, light red in its upper part, and very dark on the lower part. This sequence describes clear folding, with the black lower part verticalized on the contact with the fault, and furthermore involved in the fault shear zone, as a clear 3 cm-wide red clay band is dragged downward along the fault, highlighting the normal dip-slip fault motion. The folding in turn seems to be a drag fold related to fault motion. However, the synclinal nature of the fold is not compatible with a normal motion of the fault. Hence we interpret that folding as a structural inheritance of that deposit from former fault-related deformation, mostly strike slip with a potential shallow reverse component, preceding the opening of the pond. South of the central fault zone (F2), U50b is deformed, with a rather different composition: instead of colored clay deposits, clasts are here coarse sand to cobble, supported in a silt-to-clay matrix, unsorted, and without obvious stratification. Close to the main southern fault, some sheared and folded chunks of U50a can be clearly identified, included in U50b. This observation, whether limited to a deformation occurred formerly to the pond aperture, can be interpreted in one hand to a larger shear zone in U50 than the one materialized by the main conjugated faults defining the pond (i.e. F1 and F2), and in the other hand by some penetrative deformation in the coarse U50b material. The shear zone F3 is visible right south of the patchy sub-unit containing chunk of U50a, and is related to the gravel-to-sand-blow identified upward within U40. Right of this shear zone is a tight synclinal fold, attesting of the strongly deformed nature, as in U50a, of these deposits.

### *ii. Description of faults*

Three main faults have been identified within MT; two of them, the main northern fault (F1) and the main southern fault (F2), are delimiting the pond. A third one, limited to U50 and U40, is a shear zone related to a gravel-to-sand-blow (F3). More cracks have been documented (e.g. F4 and F5), but are not associated to unambiguous earthquake criteria.

The main northern fault F1 dips ~80° to the south, is rather straight and related to a shear zone limiting U30 and materialized by elongated and deformed gravel pockets (Figure 4-57-C). On the bottom of the trench, the CW2 is related to this F2 fault, and appears affected by the faulting after its deposition. Under the CW2, the fault F2 seems to distribute, with a branch straight prolonging to the pond border and one splay at least branching on the U50a structuration. On top, the main northern fault F1 is associated to a ~30 cm-wide deformed band, also called CW1b as it could be interpreted as a colluvial wedge, probably involving some U42 materials. The fault F1 is moreover delimiting to the south the U42 sub-unit. Eventually, the main northern fault F1 describes a fault termination on top of U42, which remain partly uncertain due to the inability of massive clayish U21 to clearly register fault-related deformation.

The main southern fault F2 dips 70° to 80° to the north, and is more localized on its lower than on its upper part. Close to the bottom of the trench, F2 is steep and associated to a collinear secondary fault, shearing an elongated gravel pocket. The main F2 fault is separated from the gravel pocket by a yellowish fat clayey shear zone (on orange on figure), bounded by vertically oriented clasts (Figure 4-57-C). On its upper part, the main southern fault F2 splays in two main traces, one straight, dipping 80°, delimitates upward the pond, and the second one flatten to 70° and generates displacements within U40. Some reverse cracks affecting U30 and partly U20 can also be identified within the filling of the pond. Between the two main branches is a ~1 m-long slice, composed of similar materials than U40 but more disturbed, with an uppermost part composed of a chunk of a of U41, in which the stratification is preserved, allowing to assess the apparent vertical offset of 30 to 50 cm, with a normal motion. The main northern fault F2 seems to propagate into U20 by three fault splays, whether these cracks are hardly distinguishable and no fault termination has been identified.

Eventually, the shear zone F3 located in U50 is vertical, highlighted by oriented clasts and rather localized on its lower part. It is related to a gravel-blow in U40 and splays upward in several branches: some join the main southern fault F1 and some propagate sinuously until reaching U23/U32 – without significant vertical offsets. Although this

structure represents a major deformation in MT, clear criteria for identifying earthquake haven't been found, due to coarse and very loose materials composing U40 and U50.

### *iii. Synthesis of paleoseismic evidences in MT*

Paleoseismic investigations of the Moskito Trench allow identifying at least two surface rupturing events based on colluvial wedge, fault terminations and faulting criteria.

No clear evidence of faulting within U10 has been identified and hence this unit is interpreted as post-dating the most recent event within the MT. Upper part of unit U20, U21, displays few discreet cracks, potentially confused with cryoturbation, but visibly linked in depth with major fault splays. It seems from folding and discreet fault splays that the whole unit has been affected by the most recent event recorded in that trench. The deformation is more visible in the lower part, but considering the absence of stratigraphic marker and the apparent faulting of the upper, we assume that the whole unit has been deposited prior to the occurrence of the most recent surface-rupturing event on this section of the WBF.

We also associate to this most recent earthquake the sheared zone bordering U42, which generate an apparent vertical offset of 20 to 25 cm on F1, as well as a tilt of the U23 clay lamination associated to few cracks on the central and southern part of this sub-unit. This most recent earthquake also generated some displacements on the main southern fault F2, which laterally cut the southern edge of U23 and sheared the gravel pockets within U30. Identified fault terminations, associated to probable ice wedges within topmost part of U41 are however considered as prolonging upward in U20, although little visible due to massive and thin nature of U21. Hence, we suggest that the most recent event in MT is pre-dated by 2614 ± 87 CalyrBP.

According to our field observations, U30 has experienced at least two earthquakes: one resulting in the colluvial wedge on the lower part of the unit (CW2), and a second one revealed by faults (F1 and F2) propagating within upper part of U30, and in U20. Hence, we interpret that an earthquake, identified by the CW2, occurred during the deposition of U30, whether no inner stratification allows clear subdivision of U30.

The penultimate surface rupturing seismic event within MT is hence materialized by the collapse of a part of U40 to form the CW2, and by normal faulting of the slice of U40 by F2 in southern part of the central fault zone (and possibly to offset of the CW1). This penultimate event can be temporally constrained by samples MT-C09 and C13 between 3750 CalyrBP and 4480 CalyrBP. This result, however, requires considering the bulk sample MT-C08 as an outlier due to remobilization of the clay sediment on which organic

matter is adsorbed. It also requires considering that charcoal MT-C12, located in U23, presents an inbuilt age (and/or remobilization) superior to 700 hundred year, given that this is the discrepancy with charcoal MT-C13 age.

Another interpretation of the successive earthquakes recorded by this trench is that there are three events: two of them correspond to those previously described, and a third one might be associated to the deposition of the colluvial wedges CW1a and CW1b. The presence of those potential wedges with which both U20 and U30 are in lateral contact, might indicates an intermediate third event, furtherly sheared by E1, involving propagation of the fault splays within whole U20. However, the natures of the colluvial wedges appear disputable: the southern one (CW1a) is stratified, clearly bonded by faults on both sides, and seems to have the same structuration than the uppermost sub-unit of U40. The northern colluvial wedge (CW1b) is clayey, same composition as U30 but, as well as the older U42, is deformed as attested by sinuous and faulted sand-to-gravel pockets.

We conclude from our observations and dating that at least two surface ruptures occurred within the central sag pond of Moskito Trench during the last 6 ka, although possibility of a third event cannot be rulled out.

##### *IV.2.4.4.3. Summary of the Evidence for Paleoseismic Events in Swan Lake site*

Paleoseismological analysis of two fault-transverse trenches in Swan Lake site allow determining the ages of two surface rupturing paleo-events during the last 5 ka (Figure 4-61). Because trenches are located 1.2 lm from each other, we consider here that they experienced same surface rupturing events during the Holocene period.

The most recent event identified is constrained between 2700 CalyrBP and 2310 CalyrBP. This age is slightly older (<100 yr) that the one determined in other sites along the WBF (sections IV.2.4.1, IV.2.4.2, IV.2.4.3). The second event identified here is constrained between 4510 CalyrBP and 3570 CalyrBP, and might correspond to the E2 identified in the Ice Creek Tension Gash Trench.

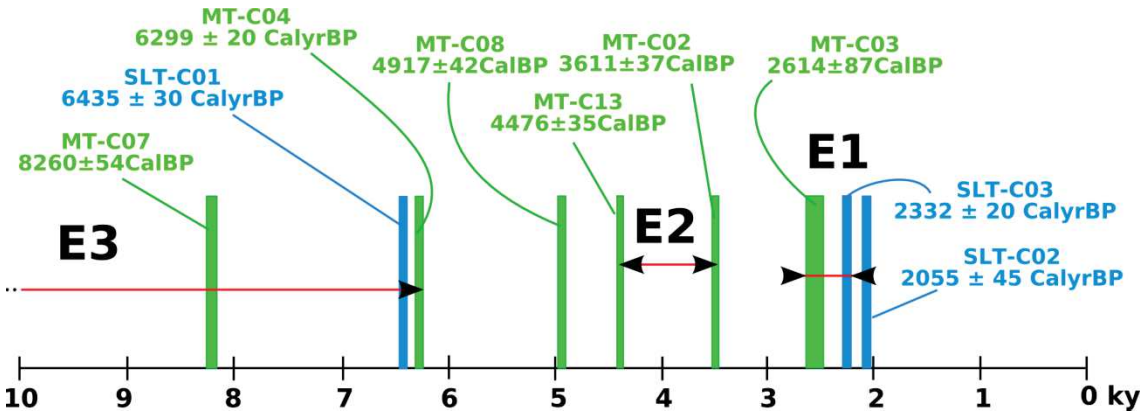


**Figure 4-61: Synthesis of age constraints for paleoseismic events observed in Swan lake (in blue) and Moskito trenches (in green).**

A comparison between paleoseimic results documented along the WBF is proposed in next section.

### *IV.2.5. Summary of paleoseismic survey along the WBF*

The Figure 4-62 synthetize the ages the paleoearthquakes estimated in this study along the WBF, regarding to their along-fault position. The trenches are distributed on three fault segments: CVTG site is located on the segment WBF-S2; ICTG and RC sites along the WBF-S3, and MT and SLT along the WBF-S4.

Almost all trenches yield an age for most recent event between 1980 CalyrBP and 1360 CalyrBP, except the SLT which yield an age slightly older (by 30 to 350 yr depending on the sample). Thus at first order, the observations on SLT mismatch those in other trenches. However, we note that although the age obtained in the RCR (charcoal C01, consistent with OSL age OSL3) is fairly strong, the radiocarbon ages in SLT are based on sediment, and that such ages have to be considered with care, as the processes of remobilization and contamination are not known while possibly significant. Three explanations might be proposed for this observation: i. Two seismic events succeeded in a reduce time laps (< 650 yr); ii. Radiocarbon ages on sediment present moderate biases (e.g. from calibration), and all trenches give same age; iii. The most recent event has been missed in the SLT. Anyway, supplementary paleoseismic analyses are needed to better constrain the age of most recent event along the fault (especially the post-dating), and if it broke the whole fault at once, or by a cluster of smaller events.

All the trenches with available mid-Holocene sedimentary records (i.e. except RC) agree with a penultimate event which occurred between 3720 CalyrBP and 4930 CalyrBP.

Only the Rain Creek trenches recorded the early Holocene post-penultimate earthquake, for which the age is constrained between 10330 ± 89 CalyrBP to 9.2 ± 0.7 ka.

Assuming the three paleoearthquakes documented along the WBF, we can propose a return period of major seismic event (or cluster along the fault) of 4.0 ± 1.1 ka.

Assuming that radiocarbon ages on sediment in SLT present a biases (proposition ii. in interpretation of the most recent event), we propose to compute an Oxcal modeling (Lienkaemper et Ramsey, 2009) of these results, presented in Table 9 and Figure 4-63.

Although those paleoseismic data are not sufficiently precise to rule on the simultaneity of the surface rupturing events, we observe a good correlation between the ages of the paleo-events in the different segments of the fault. Hence those observations indicate the occurrence of large earthquakes, with long return times and prone to break the whole fault. Those large events, here observed within paleoseismic trenches, are furthermore consistent with the continuous and rather homogeneous surface fault trace > 100 km.

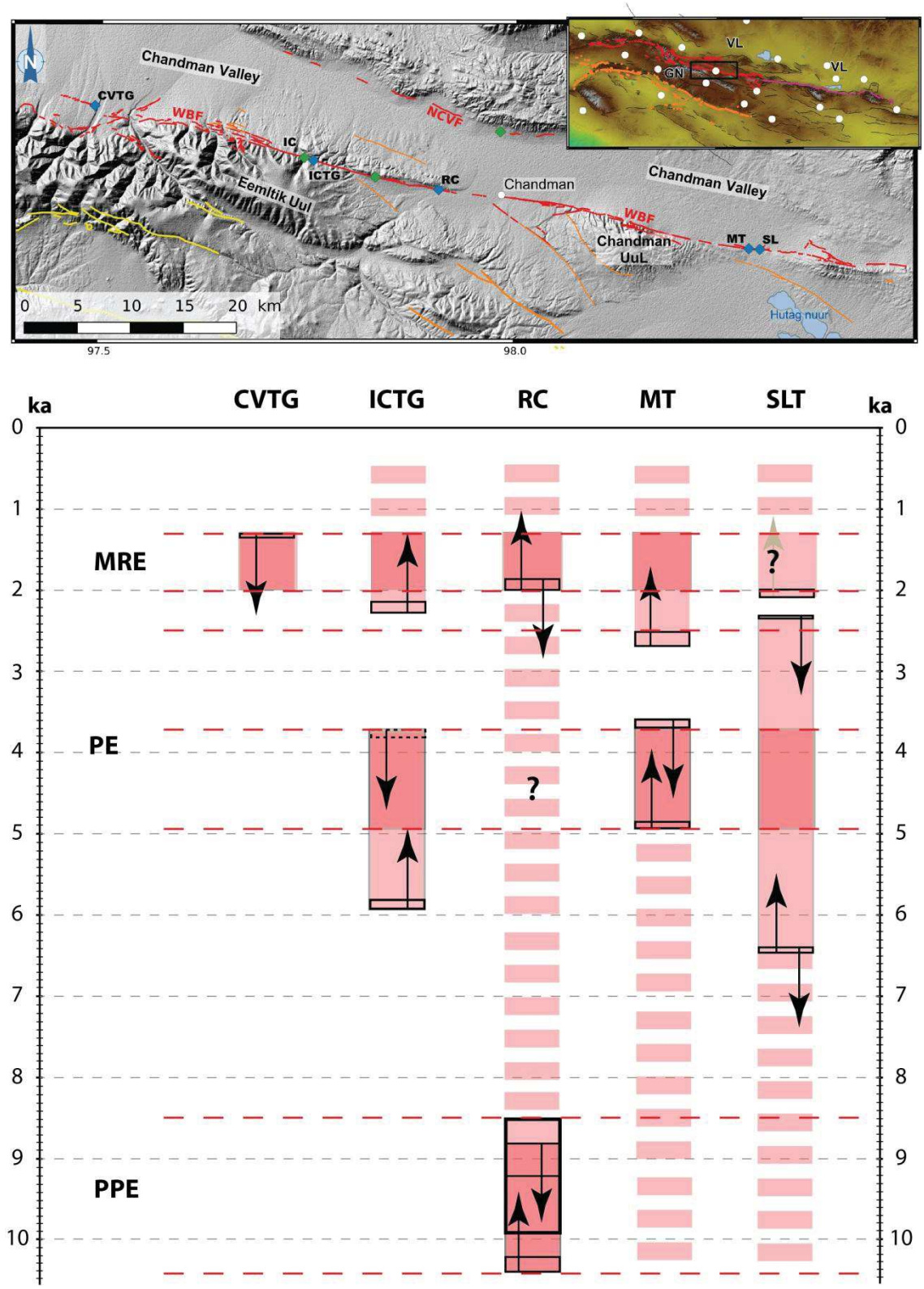


**Figure 4-62: Summary of identified paleoearthquakes along the WBF. Map: central part of the Valley of Lakes fault. Blue dots are paleoseismic sites green dots are morphotectonics sites. White circle are townships. Graph: vertical axis is time, in ka. Red areas are estimated ages of paleoearthquakes on each paleoseismic site. Dashed pink areas are time span without sedimentary records. Black arrows indicate the position of the samples regarding to earthquake criteria in the trench.**

**Table 9: Parameters and results of the Oxcal modeling for whole WBF, without the two younger radiocarbon ages on SLT.**

| Name<br>Show all<br>Show structure | Unmodelled (BP) | | | Modelled (BP) | | | Indices<br>$A_{model}$=101.6<br>$A_{overall}$=101.6 | | | | | Select<br>All<br>Visible | Page break |
|---|---|---|---|---|---|---|---|---|---|---|---|---|---|
| | from | to | % | from | to | % | $A_{comb}$ | A | L | P | C | | |
| ▼ WBF_full Sequence | | | | | | | | | | | | 2 | |
| Base Boundary | | | | 12350 | 10240 | 95.4 | | | | | 95.5 | 3 | |
| ▼ Inf_PPE Phase | | | | | | | | | | | | 4 | |
| RCT3_C02 R_Date(9160,45) | 10490 | 10230 | 95.4 | 10490 | 10230 | 95.4 | | 100.9 | | | 99.9 | 5 | |
| PPE | | | | 10370 | 9010 | 95.4 | | | | | 99.7 | 6 | |
| ▼ Post_PPE Phase | | | | | | | | | | | | 7 | |
| RCT3-OSL3 N(-7185,700) | 10540 | 7730 | 95.4 | 9850 | 8240 | 95.4 | | 118 | | | 100 | 8 | |
| RCT2-OSL3 N(-6985,200) | 9340 | 8530 | 95.4 | 9320 | 8520 | 95.4 | | 100.7 | | | 99.9 | 9 | |
| ▼ PE_PPE Phase | | | | | | | | | | | | 10 | |
| MT_C07 R_Date(7420,45) | 8360 | 8160 | 95.4 | 8360 | 8160 | 95.4 | | 99.9 | | | 99.9 | 11 | |
| SLT_C01 R_Date(5645,30) | 6500 | 6320 | 95.4 | 6500 | 6320 | 95.4 | | 99.7 | | | 99.9 | 12 | |
| MT_C04 R_Date(5495,30) | 6400 | 6210 | 95.3 | 6400 | 6210 | 95.4 | | 99.5 | | | 99.9 | 13 | |
| ▼ Inf_PE Phase | | | | | | | | | | | | 14 | |
| MT_C13 R_Date(4000,30) | 4530 | 4410 | 95.4 | 4530 | 4410 | 95.4 | | 99.7 | | | 99.8 | 15 | |
| ICTG_C10 R_Date(3485,30) | 3840 | 3640 | 95.4 | 3860 | 3710 | 95.4 | | 100.4 | | | 99.9 | 16 | |
| PE | | | | 3830 | 3660 | 95.4 | | | | | 100 | 17 | |
| ▼ Sup_PE Phase | | | | | | | | | | | | 18 | |
| MT_C09 R_Date(3470,30) | 3840 | 3640 | 95.4 | 3800 | 3630 | 95.4 | | 90.4 | | | 99.8 | 19 | |
| MT_C02 R_Date(3355,30) | 3690 | 3480 | 95.4 | 3690 | 3480 | 95.4 | | 100.3 | | | 99.9 | 20 | |
| ▼ Inf_MRE Phase | | | | | | | | | | | | 21 | |
| MT_C03 R_Date(2510,30) | 2740 | 2480 | 95.4 | 2740 | 2480 | 95.4 | | 99.7 | | | 99.9 | 22 | |
| ICTG_C04 R_Date(2240,30) | 2340 | 2150 | 95.4 | 2340 | 2150 | 95.4 | | 99.6 | | | 99.9 | 23 | |
| RCR_C01 R_Date(1965,30) | 2000 | 1830 | 95.4 | 2000 | 1860 | 95.4 | | 99.4 | | | 99.9 | 24 | |
| MRE | | | | 1920 | 1330 | 95.4 | | | | | 99.9 | 25 | |
| ▼ Post_MRE Phase | | | | | | | | | | | | 26 | |
| TG-5 R_Date(815,30) | 790 | 680 | 95.4 | 790 | 680 | 95.4 | | 99.7 | | | 99.8 | 27 | |
| TG-6 R_Date(1440,30) | 1390 | 1290 | 95.4 | 1390 | 1290 | 95.4 | | 100.6 | | | 99.9 | 28 | |
| ▼ Top Boundary(1900) | 60 | 50 | 95.4 | 60 | 50 | 95.4 | | 100 | | | 100 | 29 | |
| 1900 | | | | | | | | | | | | 30 | |

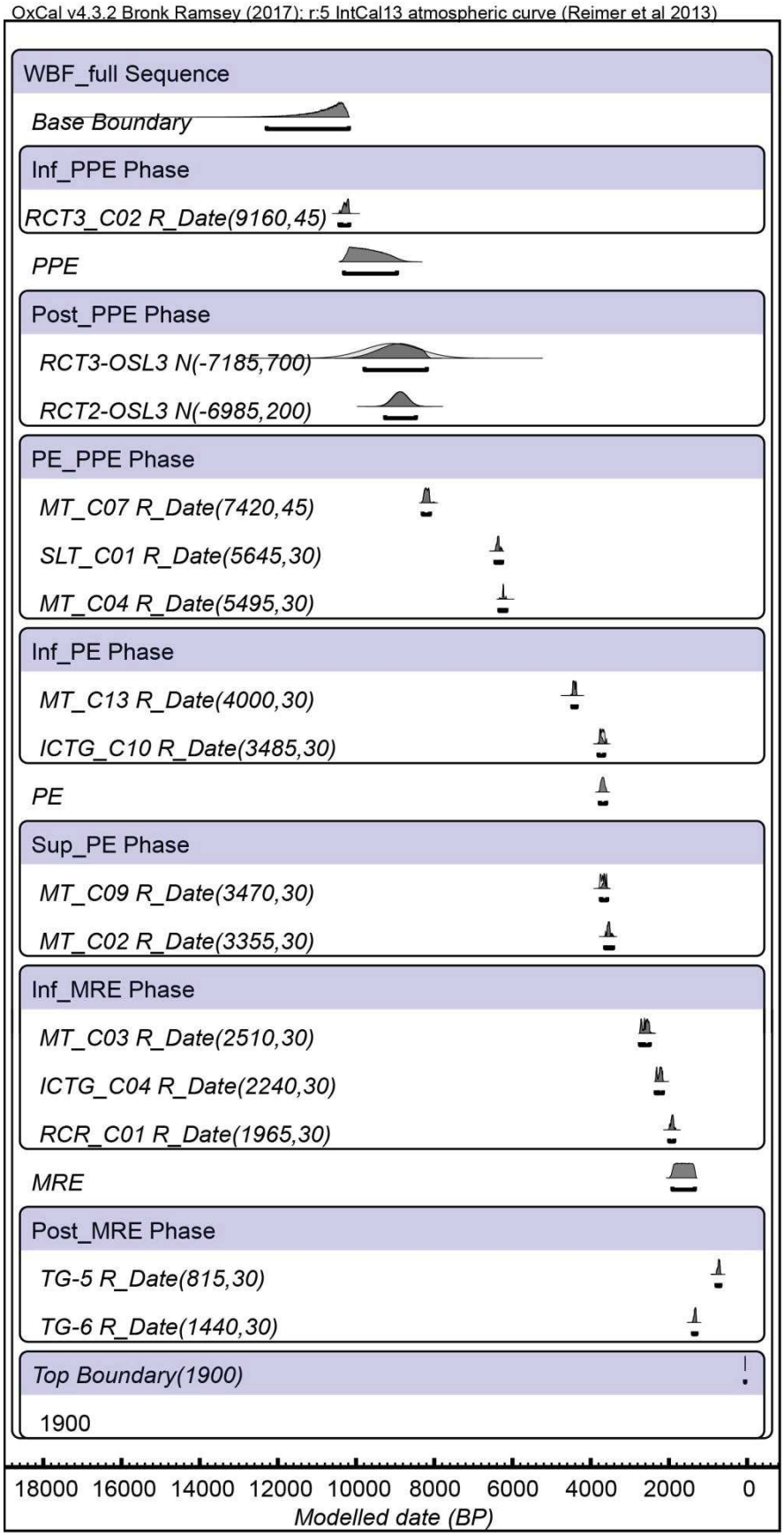


**Figure 4-63: Multiplot of Oxcal modeling on whole WBF. Radiocarbon ages are given for 94.5 % uncertainties.**

## IV.3. Earthquake geology of the VOLF

### *IV.3.1. Valley of Lakes Fault surface ruptures mapping*

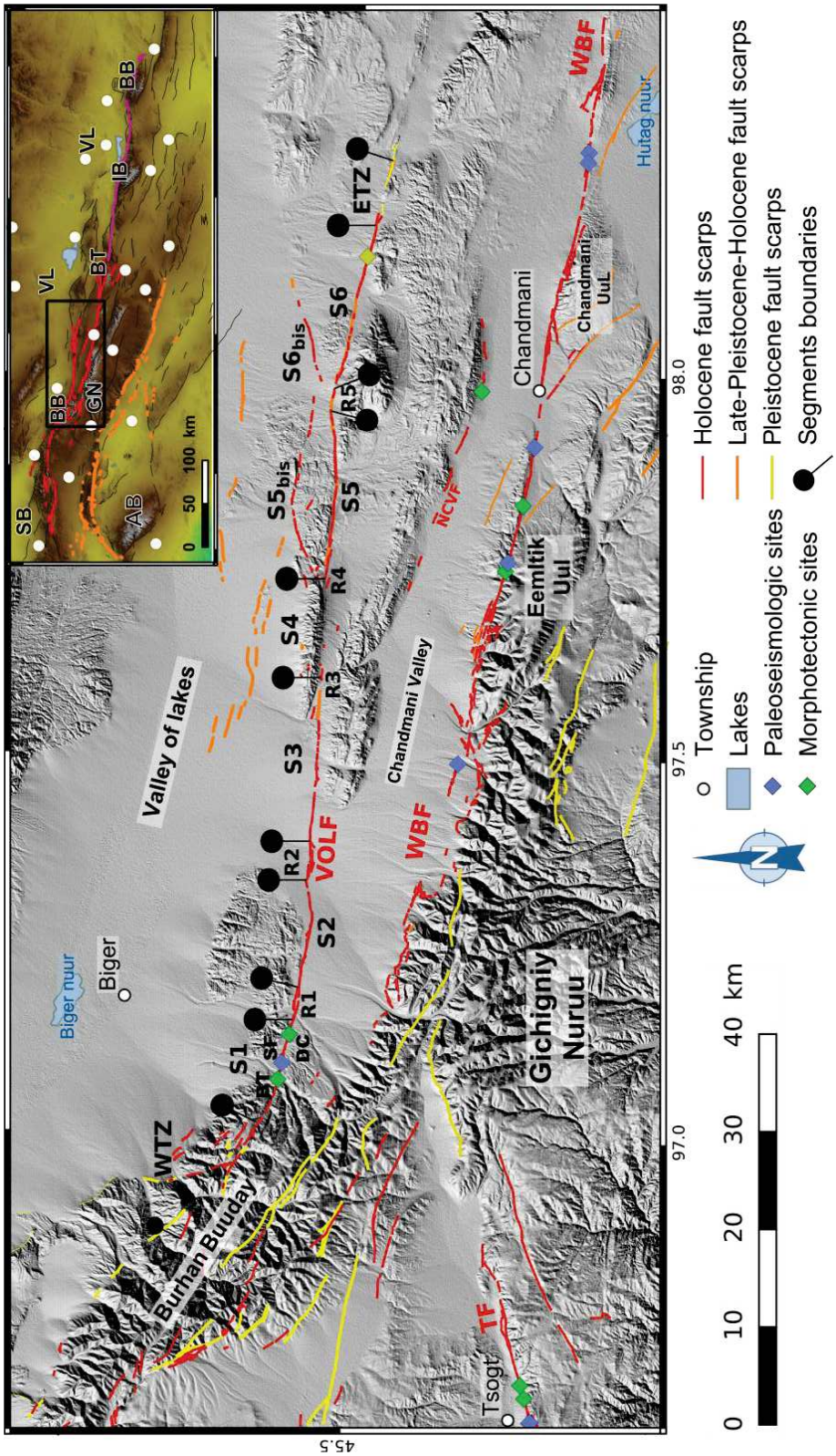


**Figure 4-64: Segmentation of the Valley of Lakes Fault. Fault abbreviations: VOLF: Eastern Bogd fault; WBF: Western Bogd Fault; NCF: North Chandmani Valley fault; TF: Tsogt Fault. Field sites abbreviations: BT: Biger Terraces; SF: Storm Fan; DC: Dark Creek. Background is a hill-shading of the SRTM Topographic dataset. Insert abbreviations: SB: Sharga Basin; BB: Burhan Buuday; VL: Valley of Lakes; GN: Gichigniy Nuruu; BT: Bayan Tsagaan; IB: Ih Bogd; AB: Artz Bogd.**

The VOLF trace is described in the following sections from west to east, starting by its western tip zone. Six distinct main segments, two tip zones and two secondary segments have been defined (Figure 4-64), following the segmentation criteria presented in section III.1.3.

The western tip zone of the VOLF, located 45.610°N; 96.930°E in bedrock, is 11 km-long and shows distributed fault pattern. The main strike slip fault trace trending N115 ± 5°E, and two thrust branches are shifted to the north-west with a N150°E to N160°E trending.

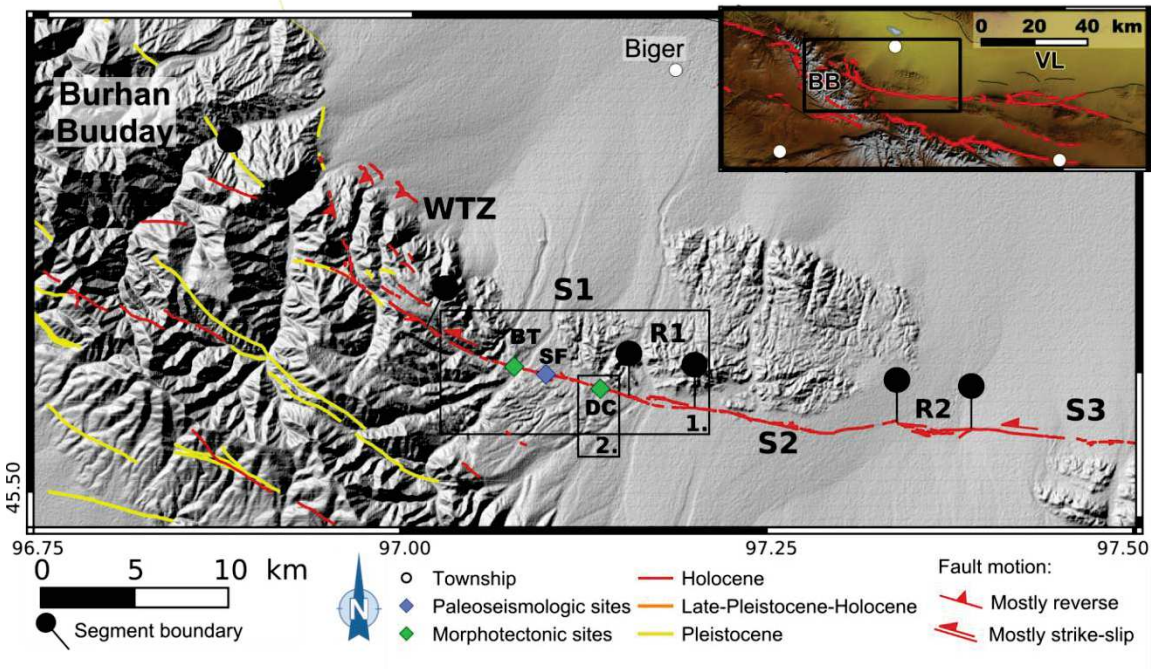


**Figure 4-65: Fault surface ruptures and segmentation along the western part of the VOLF. BT: Biger Terraces; SF: Storm Fan; DC: Dark Creek. Insert footprint is same as Figure 4-64. BB: Burhan Buuday; VL: Valley of Lakes.**

The westernmost segment, VOLF-S1, is 11 km-long, curved to the north on its western part, by trending N120°E instead to N100°E along its straight eastern part (Figure 4-65). Deformation is localized along one main trace is mostly left-lateral (Figure 4-66). The central and eastern parts of the segment display numerous offsets on late-quaternary alluvial geomorphic features, offering opportunity to characterize the seismic activity of this fault. In fact, a UVA survey of the whole eastern half of the segment has been done, and three sites have been investigated: Biger Terraces site (Figure 4-66-A and C), Storm Fan site and Dark Creek site (Figure 4-65). These sites are detailed in parts IV.3.3.2, IV.3.4 and IV.3.3.1, respectively.

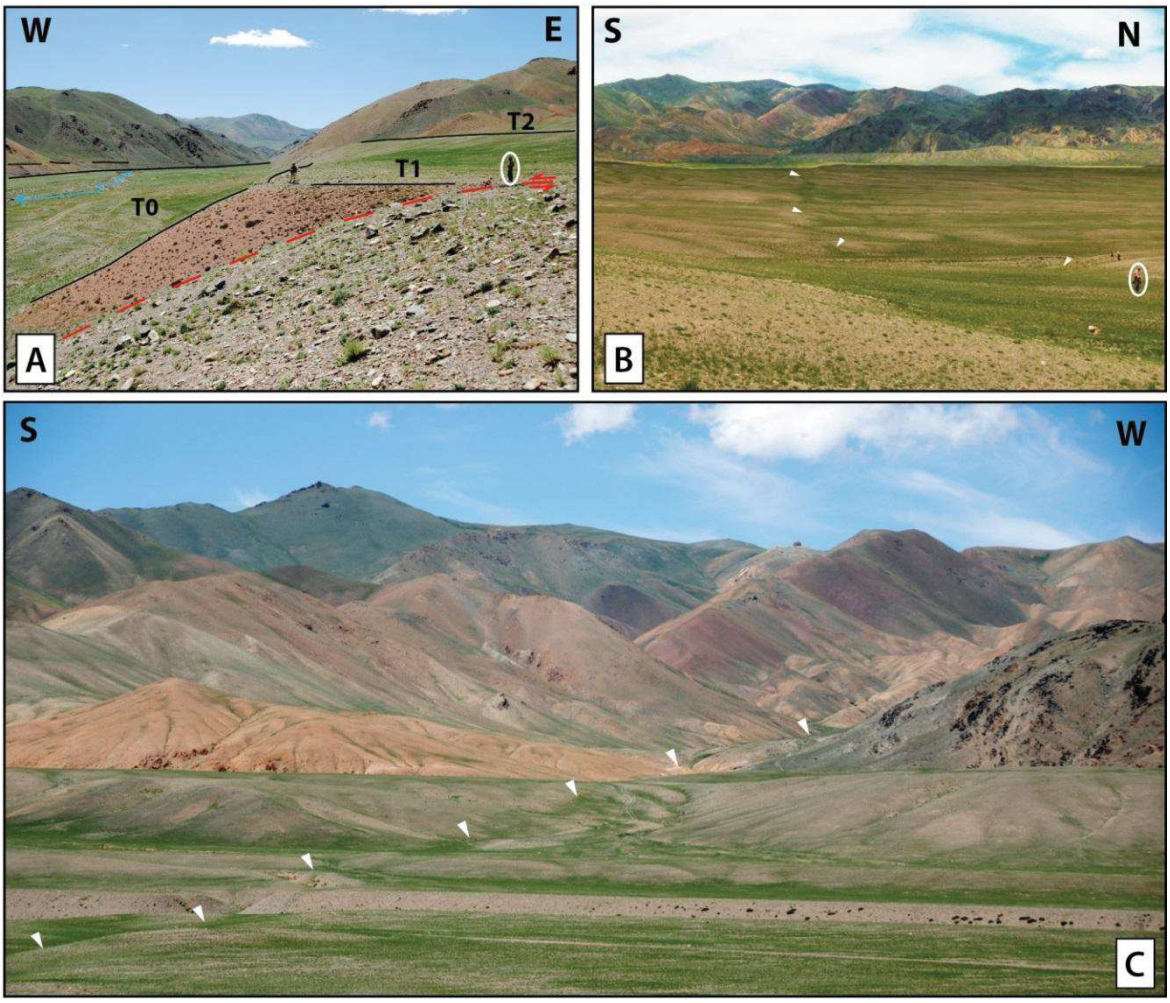


**Figure 4-66: Photographs of the VOLF surface rupture. White arrows indicate the fault location. A. Photograph to the south of the offset alluvial terrace T1 riser in Biger Terrace site (location BT on Figure 4-65). Red dashed line in the main VOLF trace, blue solid line is drainage within the river bed T0. Terrace risers are highlighted by black solid lines. Red shaded area corresponds to the apparent vertical offset of T1 riser. B. VOLF trace in late-Pleistocene alluvial terraces, east of Dark Creek Site (DC on Figure 4-65). C. VOLF trace on Biger Terrace site. Note the left-lateral offset of large alluvial terraces.**

The VOLF-R1 relay zone is composed of a 3.5 km-long pull apart basin, elongated following fault strike and located 45.550°N; 97.175°E (Figure 4-65). This 400 m-wide transtensive jog trends N098 ± 10°E, and displays shallow slip partitioning with the normal dip-slip scarp located on north and the strike-slip trace on south.

The VOLF-S2 segment is 10.5 km-long, curving from N103°E on the eastern part to N80°E within the eastern part (Figure 4-65). The fault trace is located in late-Pleistocene fans, and is continuous but sinuous. The fault motion is mostly left-lateral, with a minor vertical motion on the western part of the segment and the north side of the fault uplifted. The fault pattern is distributed with several hundred meter long branches trending N085°E, likely steered by structural inheritance of the bedrock, cropping out a few tens to

hundreds of meters from the fault trace. The eastern part of this segment keeps this trend until the next relay zone: VOLF-R2.

The VOLF-R2 relay zone is a 4.3 km-long pull-apart basin, with an average trend of N093°E but the fault directions of the secondary branches defining the basin range from N056°E to N114°E (Figure 4-67). The southern edge of this transtensive jog dips to the north, and offsets late-quaternary fans with a normal motion, as it is associated with one of the major springs on the region. Instead, the northern trace of the jog displays left-lateral motion, with several tension gashes and a pressure ridge.

The VOLF-S3 segment (Figure 4-67) is trending N092 ± 5°E, and displays pure left-lateral motion, as attested by a typical strike-slip fault pattern with tension gashes and mole track, and by the absence of cumulative vertical displacements. This 16.7 km-long segment is comparatively straight and continuous, and is more visible on the western part where many late-quaternary alluvial features are offset, instead of along its eastern part, where it is in bedrock (Figure 4-67).

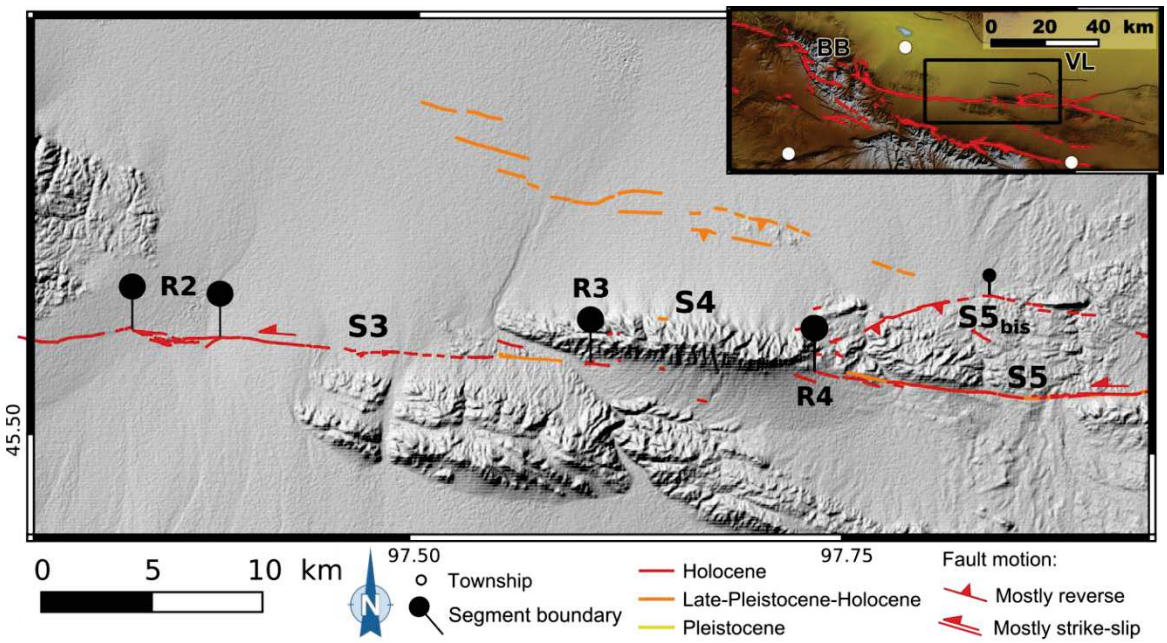


**Figure 4-67: Fault surface ruptures and segmentation along the central part of the VOLF. Insert footprint is similar to Figure IV 32. BB: Burhan Buuday; VL: Valley of Lakes.**

At 45.535°N; 97.600°E, the VOLF trace seems to stop abruptly: WBF-R3 is then more an interruption of the main fault trace than a jog (Figure 4-67). A careful look along the next apparently fully distributed VOLF-S4 segment allows identifying few probable surface ruptures, hundreds of meters-long in a deformed sedimentary basin to the south and in basaltic relief to the north, but no major fault trace has been identified along the next 10 km east until the next jog. The asymmetric morphology along this segment, with higher

relief north of the fault and a straight mountain front (in spite of a significant river) suggests that the north-side of the fault is uplifted. No obvious branching occurs along this segment, but two structures may explain the interruption of the fault trace. Firstly, the NCVF stands 12 km southwest of the VOLF-R3 location but is likely closer given that a potential fault trace may have been eroded by the active river (Figure 4-64). Some part of the deformation could potentially be transferred to this fault. Secondly, what might be an asymmetric, discontinuous blind thrust is located 7 km north of the main scarp, and visibly affects quaternary fans with a fault pattern describing three kilometer-scale right-steps, with an average trend of N105 ± 10°E (Figure 4-67). No clear surface rupture has been identified along this 15 km-long structure related to metamorphic bedrock outcrops, where the relief is increasing to the east. Nevertheless late quaternary fans seem to systematically show disturbance of stream incisions. The eastward prolongation of this segment shows discontinuous but clear stream disturbances related to reverse cumulative offset, and may join the secondary segment of VOLF-S5bis (Figure 4-67), described ahead. Because no field survey has been done on that potential scarp, and due to the absence of DEM data at a suited resolution, we cannot statute on the activity of this potential thrust branch, and on its relation to the VOLF main trace. It even seems that this secondary structure might be an active – and potentially blind as no precise fault trace has been identified – thrust. When looking at the structural inheritance, we note a main sedimentary unit south of the fault, which displays a structure collinear to the fault trend, and volcanic rocks north of the fault, displaying strong structural inheritance with a neat axial valley related to visible geological contacts. To summarize about VOLF-S4, we thus suggest that the absence of a clear fault scarp along this segment could be explained by distributed deformation, either on secondary faults (like the NCVF for instance, Figure 4-64) and the northern secondary blind thrust, or within inherited rock structures. Note that very poor satellite image quality in the area limits our ability to precisely describe such distributed fault pattern.

The VOLF-R4 area, located 45.535°N; 97.735°E, displays distributed deformation on a 2 km-wide area, and corresponds to both a new start of the main fault trace, trending N100 ± 5°E, and to a branch with a thrust fault to the NE, the VLF-S5bis (Figure 4-67).

This secondary branch (VOLF-S5bis) is reverse-oblique, discontinuous, south curved, and strikes NO60°E on its western part (Figure 4-68). It also describes a strong azimuth change after 8 km, when encountering the eastern prolongation of the northern potential blind thrust on 45.562°N; 97.825°E. The second part of this branch is 10 km-long, relatively straight, with an average trend of N100 ± 10°E, and seems to be associated with oblique reverse motion. In fact, although only a few places exhibit late-quaternary

geomorphic features affected by this fault, some of them are clearly affected by cumulative oblique offset. Instead, the main drainages do not display important cumulative displacement. The eastern end of this branch is at the same level as the next jog (VOLF-R5), but keeps a N100°E trend to reach the next secondary branch, VOLF-S6bis (Figure 4-68).

The VOLF-S5 segment is 18 km-long, continuous, slightly curved to the north and trends N100°E along its western part, and N080°E along the eastern part (Figure 4-67 and Figure 4-68). The main motion is strike-slip, and the small dip-slip component shows a minor uplift on the northern part of the fault. The central part of this segment presents a curious 1.5 km-long shutter ridge, likely produced by apparent vertical offset of an axial valley collinear to the fault trace (Figure 4-69).

The next relay zone, VOLF-R5 is located at 45.530°N; 97.960°E, and is composed of a Neogene volcano, situated on the exact location of a major branching between the N103°E main fault trace of the VOLF and a N070°E branch: the VOLF-S6bis (Figure 4-68). The eastern end of the VOLF-S5bis is only 1.7 km north, and considering a 2 km radius circular area around the volcano, this branching encompasses four branches (Figure 4-68).

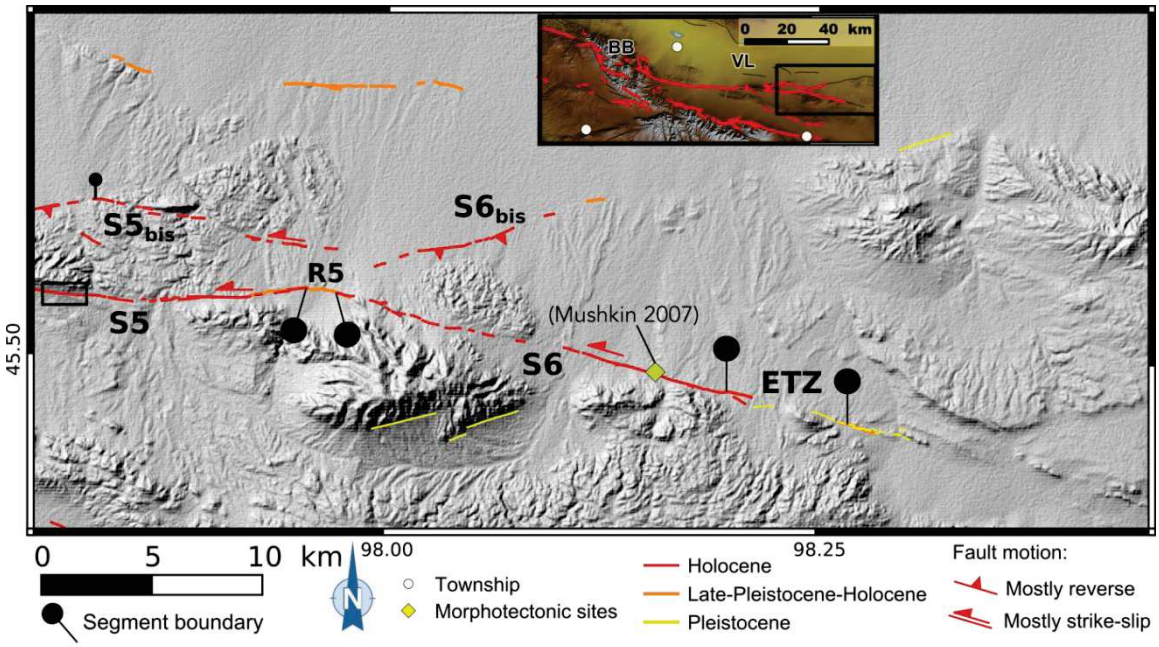


**Figure 4-68: Fault surface ruptures and segmentation along the eastern part of the VOLF. Black solid box is location of Figure 4-69 Field site is documented by Mushkin (PhD, 2007). Insert footprint is same as Figure IV 32. BB: Burhan Buuday; VL: Valley of Lakes.**

The VOLF-S6bis branch presents a N072 ± 8°E sinuous discontinuous scarp, which ends by joining a major quaternary thrust that displays a clear cumulative reverse scarp,

associated to bedrock exhumation (Figure 4-64 and Figure 4-68). This thrust is prolonged northeastward, but does not display clear fresh surface rupture after 13 km NE from VOLF-R5.

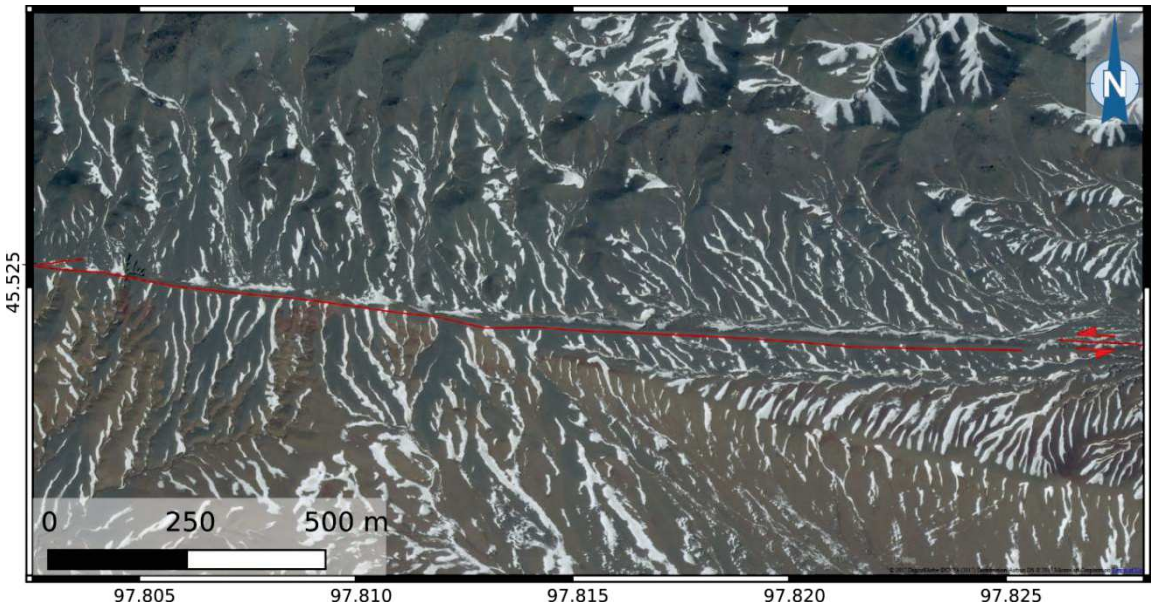


**Figure 4-69: Detailed map of the VOLF main trace (red solid line) along the central part of the segment VOLF-S5. The western half of the figure shows offset alluvial fans, and the eastern part shows a 1.5 km-long shutter ridge (along the mapped fault trace).**

The 18.3 km-long VOLF-S6 segment is mostly located in late-quaternary fans, in which geomorphic features are systematically offset. The fault trace is rather discontinuous and sinuous along the western part, but fairly straight and continuous on the eastern part (Figure 4-68). The average trend of this segment is N104 ± 5°E and its motion is mostly left-lateral, with a small vertical component uplifting the north side of the fault. Sedimentary terrains crop out north of the main trace and south of the VOLF-S6bis, as this northern branch seems to be an active south-dipping thrust. The uplift of the sedimentary units situated between VOLF-S6bis and VOLF-S6 appears to be clearly related to seismic motion on both segments (Figure 4-68). The site documented by Mushkin (PhD, 2007), showing a most recent surface rupturing seismic event post 6.8 ± 1,9 ky is located on the eastern part of this segment (see chapter 1, section ).

Eastward of 45.485°N; 97.200°E is the ETZ, a 6 km-long jog which displays a distributed fault pattern, likely related to lithological complexities, as the bedrock is composed of a mix of Mesozoic sedimentary and basaltic terrains, as well as Neogene volcanism (« Russian Geological 1:200 000 maps of Mongolia » 1987). These are deformed by numerous faults, highlighting the local topography. This area could be described as the eastern tip zone of the VOLF, given that no more evidence of recent surface rupture faulting has been identified eastward. We still identified a very discontinuous and

apparently old scarp (as no modern deposits are offset by the fault), 20 to 40 km eastward and 20 km north of the Bayan Tsagaan range, but its connection to the active VOLF remains uncertain. The VOLF ETZ does not present a specific fault pattern as usually encountered on fault terminations (Bayasgalan et al., 1999a), but a steep and straight mountain front is found on the south-west, surrounding asymmetric quaternary basins. Accordingly, while the active fault trace seems to finish on ETZ, the VOLF structure definitely continues to the east and southeast, until reaching the Bayan Tsagaan structures, 25 km to the south-east.

The total length of the almost continuous – except along VOLF-S4, where the fault is distributed – and a homogeneous fault surface rupture of the VOLF is 114 km, in addition to 30 km of secondary branches.

### *IV.3.2. Coseismic offset measurements*

In order to assess the coseismic slip related to major seismic events along the VOLF, an UVA survey has been done along a 12.5 km-long section, within the VOLF-S1 segment and VOLF-R1 relay zone. This microtopographic survey enable us producing 20 cm resolution DEMs and an 8 cm resolution orthophotographs by structure from motion photogrammetric modeling (see footprint of the survey in Figure 4-70). This fault section displays numerous alluvial geomorphic features crossing the perpendicularly the fault. Its topographic survey allows efficient imaging of the numerous left-lateral displacements recorded by geomorphic features, resulting from both simple and cumulative on-fault coseismic offsets.

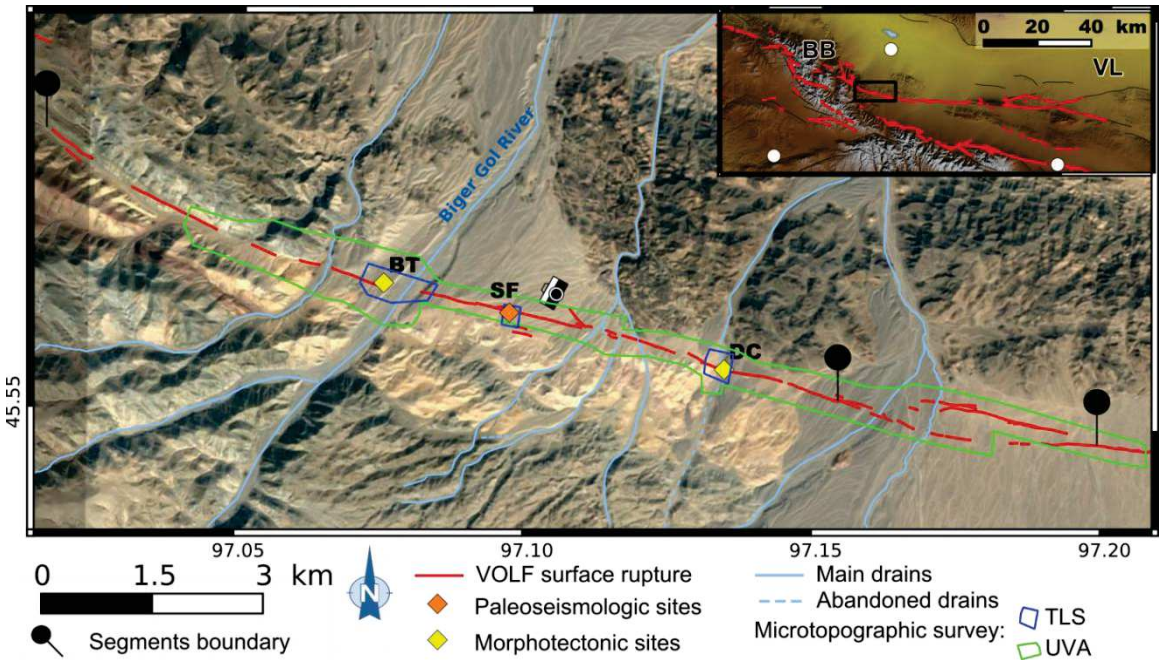


**Figure 4-70: Map of the area covered by UVA and TLS microtopographic surveys along the WBF-S1 segment and WBF-R1 jog of the VOLF. Camera is the location of Figure 4-71. Background is free access satellite images from *2017 Digital globe*®. Field sites abbreviations: BT: Biger Terraces; SF: Storm Fan; DC: Dark Creek. Insert footprint is same as Figure 4-64. BB: Burhan Buuday; VL: Valley of Lakes.**

As described in section IV.3.1, the VOLF-S1 displays here a fairly continuous fault trace, bordering to the south a quaternary basin filled with an alluvial fan complex (Figure 4-70). Here, alluvial landforms such as channel incisions or terrace risers flooding to NNE, are systematically offset when crossing the fault (see for instance Figure 4-71). No significant secondary fault trace has been identified along this segment. Moreover, the fault motion appears mostly horizontal, although a small vertical component (north side of the fault uplifted) may unevenly offset late-quaternary alluvial surfaces, vertical offsets ranging from 0 m up to ~4 m (Figure 4-71).

**Figure 4-71: Photograph of the VOLF trace, looking to the east. White triangles highlight the cumulative fault scarp. See characters for scale. Location of this picture is on Figure 4-70.**

The westernmost part of the VOLF-S1 is located in the bedrock outcrops of the Burhan Buuday range, within a longitudinal valley collinear to the fault, until the prominent alluvial terraces of Biger Terrace site (Figure 4-66-A and C). These are related to the Biger Gol River (Figure 4-70), and correspond to the western edge of the intra-mountainous quaternary basin (Figure 4-65 and Figure 4-70). The central part of the segment is fairly straight, and the fault pattern seems to be localized (Figure 4-71).

The VOLF-R1 relay zone constitutes the eastern quarter of our survey, and displays a transtensive fault pattern, as the fault trace splits into two branches defining a 3.6 km-long by 0.4 km-wide elongated pull-apart basin (Figure 4-70).

Average along-fault slope is ~8 % along the western intra-mountainous part of VOLF-S1, 3 % on the eastern part of the VOLF-S1 in the quaternary basin, while the along fault topographic profile is instead tabular along the VOLF-R1 relay zone.

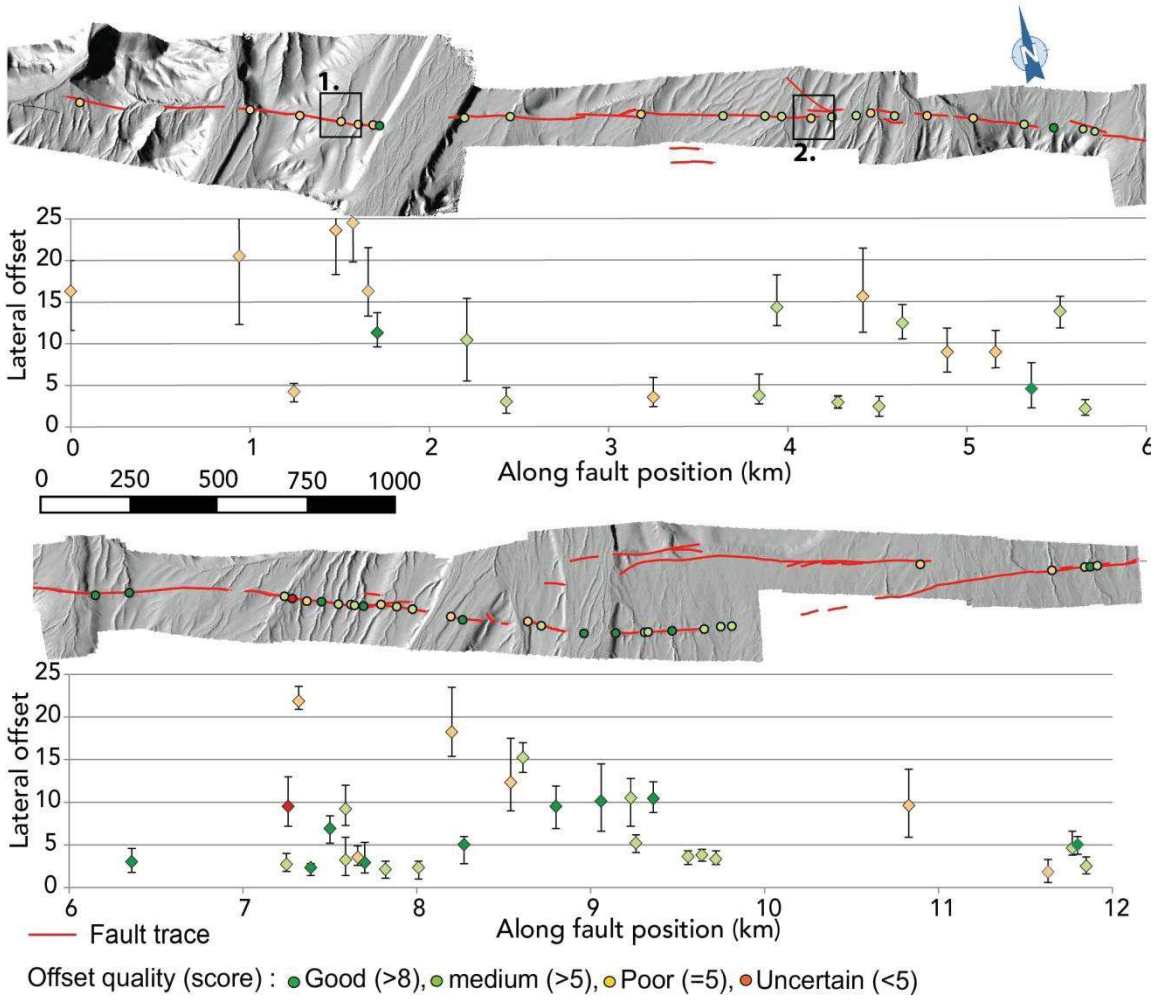


**Figure 4-72: Horizontal slip distribution along the studied section of the VOLF. Maps are hill-shaded DEM of the UVA survey, and graphs show the offset measurement values and uncertainties regarding the along-fault position. Red solid lines are the VOLF trace, and dots are measurements locations, color coded regarding their respective quality. Black solid boxes are location of offset measurements presented in Figure 4-73. 4 offset measurements are > 25 m and are consequently not displayed on this figure.**

53 lateral offset measurements have been done using the 3-steps landform reconstruction (Figure 4-73), along with assessment of the offset measurement quality as presented in section III.2.

Our measurements range from 1.8 m to 61 m (65 % of which are inferior to 10 m), and two data subsets have been then defined, by selecting the best measurements, ranking better than 7/10 and 8/10 – which correspond respectively to 63 % and 40 % of the whole dataset (see measurements table in Annexe VI).

We apply to the dataset the statistical process presented in section III.2, in order to assess the coseismic slips related to successive faulting. Given our high-resolved geomorphic dataset associated to an almost non-vegetated study area, we assume that

the measured asymmetric uncertainties can be used as 2σ standard deviations. Modeling results are presented in Figure 4-74.

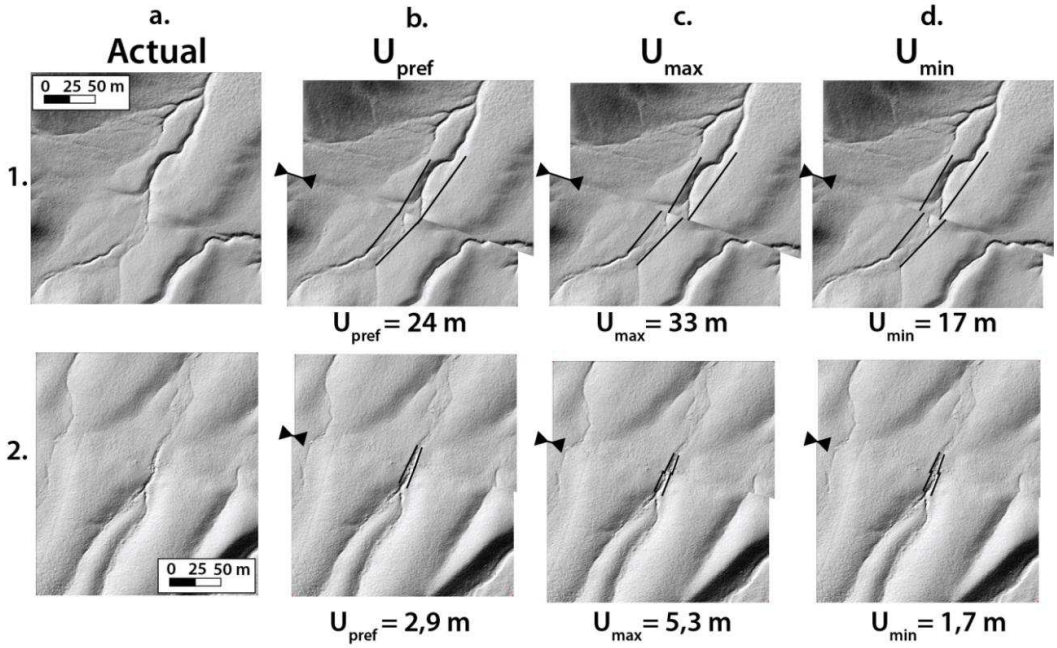


**Figure 4-73: Offset measurements by three-step retrofit of the landforms, based on UVA microtopographic survey. See locations on Figure 4-72. Background is 20 cm hill shaded DEM. Black lines are piercing lines used to derive the measurements, and black arrows are location and amount of displacement. 1. Cumulative offset on a gully on western part of Biger Terrace site (N45.5860°; E97.0730°). 2. Offset gully, 1 km East of Storm Fan site (N45.5610°; E97.1089°). a. Original data. b. Preferred retrofit value. c. Maximum retrofit value. d. Minimum retrofit value.**

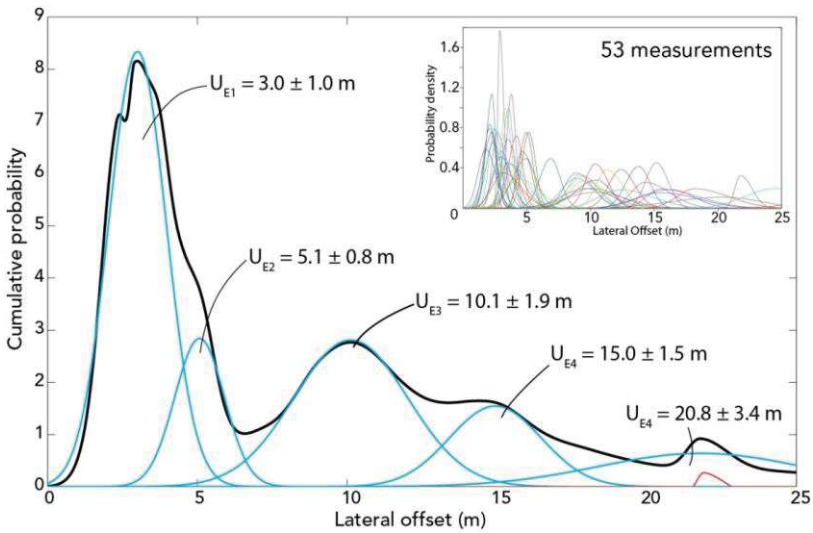


**Figure 4-74: Statistical modeling of the whole dataset of lateral offset measurements along the studied section along the VOLF-S1 segment and VOLF-R1 relay zone. Insert represents the Probability Density Functions (PDF) for the whole offset dataset, assuming 2σ uncertainties. Main graph represents the identification of successive cumulative slips related to past earthquakes. Black line is the Cumulative Offset Probability Density (COPD), and Blue lines are extracted Gaussian slip signal of past earthquakes, for which the average slips are indicated in black numbers, associated to 1σ standard deviation.**

Comparison of statistical analysis done on each of the subsets lead to consistent assessment of both the number of seismic events and the related average slips (Figure 4-75), indicating 5 distinct successive slip increments within 25 m of displacement, which we interpret as 5 successive large seismic events, generating unitary coseismic offsets ≥ 2.0 m. Due to the consistency between the subsets and the whole dataset, we elect to present the results obtained by the whole dataset of 53 offset measurements.

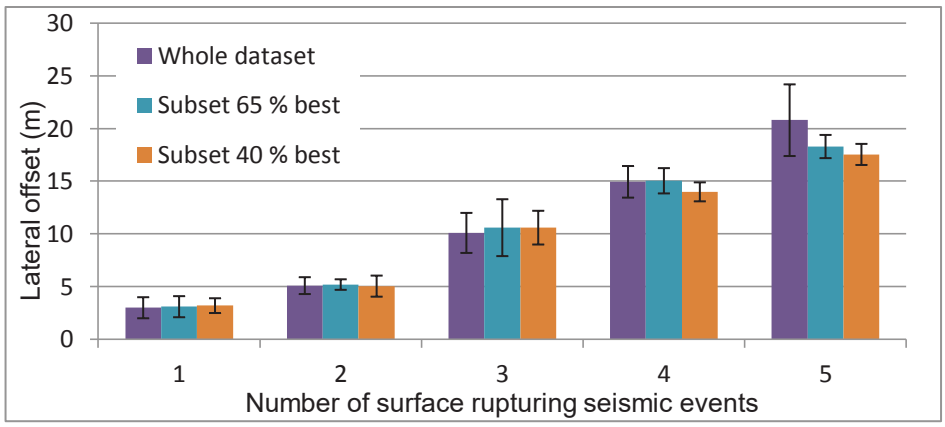


**Figure 4-75: Comparison of statistical cumulative slip related to past earthquake for whole dataset (53 measurements) and for the two subsets of best-ranked measurements. Error bars are 1σ standard deviation.**

Considering our offset measurement dataset and modeling (Figure 4-72 and Figure 4-74), the most recent large seismic event (E1) along the VOLF-S1 segment produced an average slip coseismic slip of 3.0 ± 1.0 m, well visible on the COPD although not perfectly smooth, with a sharp minor peak on the left part of the supposed-Gaussian slip signal (Figure 4-74). Furthermore, the peak corresponding to the penultimate slip (E2) appears instead minor on the COPD, with weak amplitude, as it is partly diluted with the prominent signal of E1. Nevertheless, accounting for the distinct inflexion the COPD shows on E2 position, it is unambiguous that there is a slip signal related to E2, with an average offset value of 5.1 ± 0.9 m. These observations, of a poor distinction between E1 and E2, could be interpreted as the result of our limited ability to measure the offset and to distinguish the E2 slip signal from the distributed (i.e. wideness of the modeled slip per event, in blue lines in Figure 4-74) E1 signal – leading potentially to both an overestimation of the E1 coseismic slip, and an underestimation of the cumulative slip related to E2. An alternative interpretation could be that the first event produced significantly more displacement than the second, and hence that both earthquake slip signals are mixed in our dataset.

The rest of the COPD signal displays three well-separated peaks, at 10.1 ± 1.9 m, 15.0 ± 1.5 m and 20.8 ± 3.4 m for events E3, E4 and E5 respectively. Identified slip signals

related to E3 and E4 appear fairly strong, which is highlighted by relatively small uncertainty; whereas E5, which is less resolved, involves a larger uncertainty. This last cited identified earthquake (E5) is possibly overestimated, as the two subsets give significantly lower assessment of the cumulative slip. However, the signal relative to E5 is more defined using the whole dataset, and we suggest that the presented result is trustworthy. We notice that the assessment of such amount of displacement remains a first order estimation, and the conclusion involving E5 has to be considered with caution, as this measurement remains uncertain.

Assuming these average cumulative slips identified in the statistical distribution, one can attempt to derive the successive slips related to previous earthquakes. Individual coseismic slip estimations can, for instance, be derived from those individual cumulative slips by subtracting each signal from the previous one, and summing the uncertainties, giving 2.1 ± 1.9 m, 5.0 ± 2.8 m, 4.9 ± 3.4 m and 5.8 ± 4.9 m for respectively E2, E3, E4 and E5.

We stress that these results have to be considered as some first order estimations, as reflected by the related consequent uncertainties. Those results are based on a short 12.5 km-section of the VOLF, which is not necessary of the slip per event involved in other parts of the fault. Last, our dataset is based on on-fault horizontal offset measurements. Because the fault geometry is pretty localized along this fault-section, we most-likely record the main part of the slip, but our dataset definitely does not account for off-fault deformation.

Considering the central values, the assessment of individual coseismic slips on four to five earthquake cycles along this section of the VOLF indicates variable amount of slip, basically from 2 to 5 meters. This suggests, assuming a constant slip rate, significant variations of earthquake magnitudes and recurrence times. However, considering the large uncertainties associated to these average-slip assessments, the hypothesis of a characteristic slip (i.e. same amount of slip generated by successive earthquakes) along the VOLF cannot be discussed.

We conclude that the VOLF is susceptible to produce lateral coseismic slip of 2 m to 5 m, which correspond to potential Mw7 to Mw8 earthquakes, according to empirical relations between coseismic offsets and earthquake magnitude for strike slip faults of Wells and Coppersmith (1994). This conclusion might be mitigated as those empirical laws have not been designed for Mw>8 strike-slip earthquake, and as we do not account for along fault slip variations.

### *IV.3.3. Determining slip rates along the VOLF*

Determinations of geomorphological long term fault slip rate have been done on two sites along the VOLF-S1 segment, using TLS and UVA micro-topographic survey and $^{10}$Be cosmogenic dating: the Dark Creek and the Biger Terraces sites (locations on Figure 4-70).

#### IV.3.3.1. Dark Creek site

The Dark Creek site (45.555°N; 97.135°E) is composed of a north-flooding medium-size temporary stream, incised into a late-Pleistocene fan, which displays a rather dark color: the Dark Creek fan (Figure 4-76). This fan has been deposited over granitic bedrock, as attested by upstream strath terraces associated with this surface within the bedrock, on both banks of the Dark Creek River (Figure 4-76).

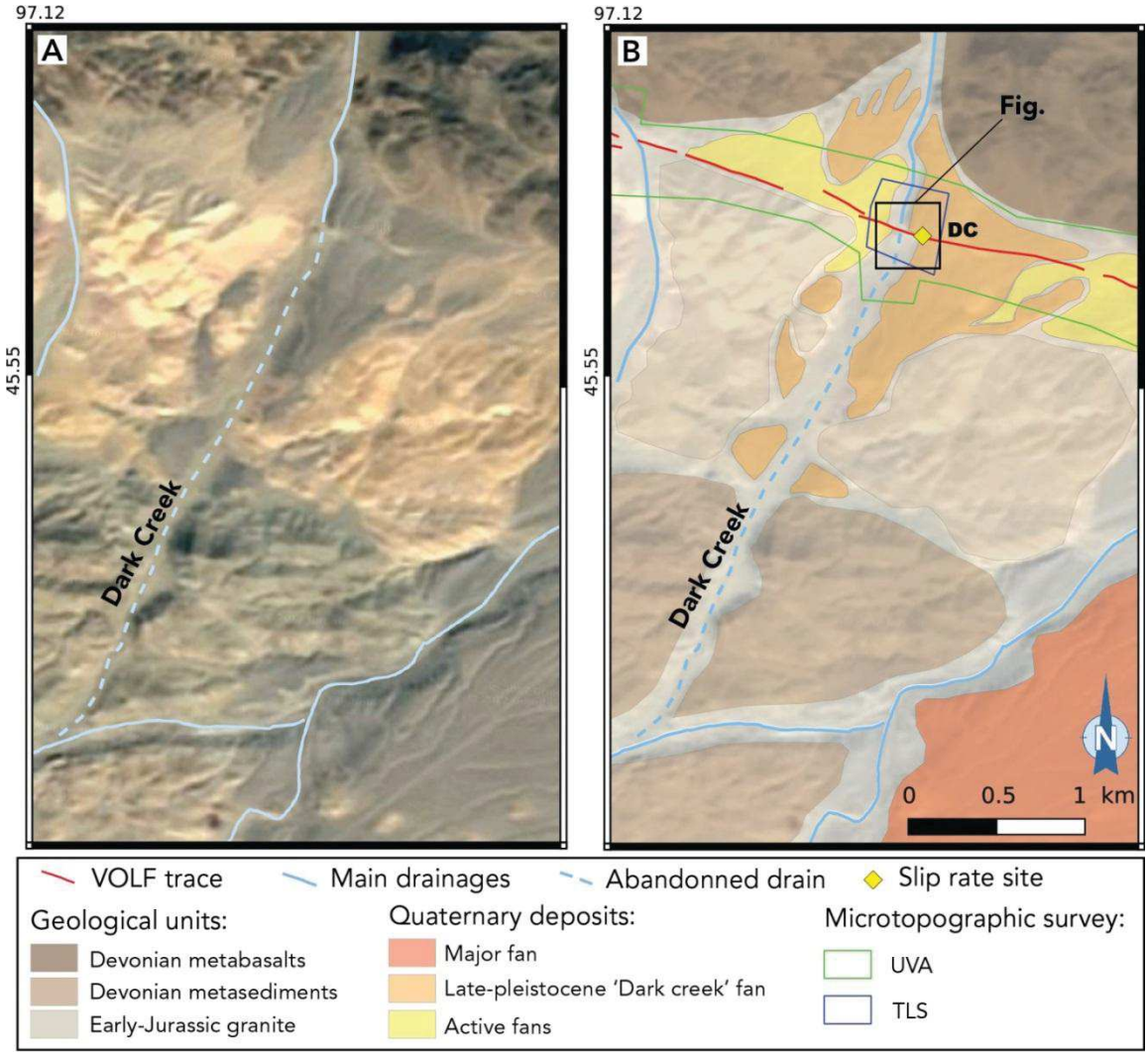


**Figure 4-76: Context map of the Dark Creek site. A. Satellite image of the Dark Creek site and upstream area, with main drains. Flooding is northward. Note the stream capture on SW edge of the map. B. Geological interpretation of the satellite map on A., with location of the dark creek fan offset and footprint of microtopographic surveys. Nature of geological units from Russian geological maps (ref. L47-XX).**

The right bank of the Dark Creek river displays a continuous riser that develops straight and smooth upstream, south of the fault, and appears sharper although more sinuous on north of the fault (Figure 4-77). Noticeably, the riser related to the Dark Creek fan describes a clear left-lateral cumulative offset when crossing the fault, which will be used later on to calculate the fault slip rate (Figure 4-77). An intermediate terrace is identified upstream, on south of the fault trace, and a gully is located on bottom of the riser between the Dark Creek Terrace and the intermediate terrace (Figure 4-77). Although this terrace is not figured downstream, one can consider that the upstream gully was aligned with the current active channel, and that this feature can be used to constrain a minimum offset recorded by the Dark Creek fan. Eastward, within the Dark Creek fan surface, is another gully, more pronounced, and although it is sinuous, it is visibly offset given that a beheaded gully of same incision depth is well visible on south of the fault (Figure 4-77). Hence, we propose to use those three piercing lines (the gully in the intermediate terrace, the Dark Creek fan riser, and the gully within the dark creek fan) to assess the offset experienced by the Dark Creek fan surface (Figure 4-77).

On the left bank of the Dark Creek River, there is a 10 m-long pressure ridge which is associated with a 3 m apparent right-lateral offset of the main stream channel. We interpret this observation as related to the growth of the pressure ridge during the Holocene activity of the fault (Figure 4-77). One may notice that the dark creek stream used to be stronger in the past, as it has been visibly captured 2.51 km upstream from the fault (Figure 4-76), and the main river is now flooding two kilometers eastward, across the transtensive VOLF-R1 jog (Figure 4-70). We may presume that either the subsidence of the VOLF-R1 releasing jog, 2 km eastward caught the stream as it flows there at present, or that the uplift of the Devonian terrain (figure) could make more difficult the river to go through. We actually do not have further evidence or temporal constrains for this stream capture.

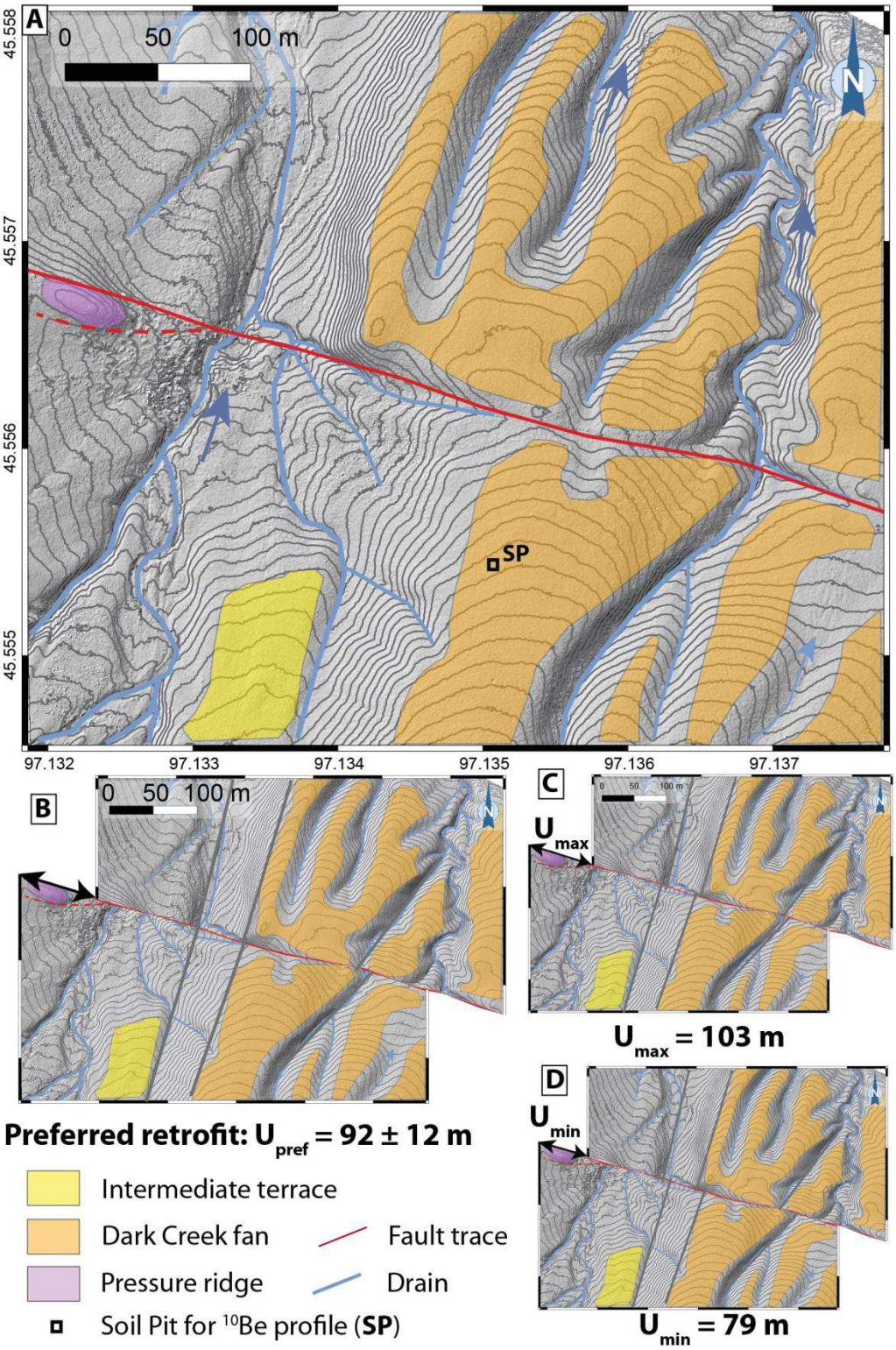


**Figure 4-77: Lateral offset measurement on Dark Creek site. A. Morphotectonic map of the Dark Creek site. Background is UVA-derived DEM, and Contours are 0.5 m. B. Preferred retrofit value of the riser of Dark Creek fan, uncertainties from measurements presented in (C) and (D). Grey lines are piercing lines used to retrofit the markers. C. Maximum retrofit value, given by the eastern gully. D. Minimum retrofit value of the riser, given by the gully in the intermediate terrace.**

A 3-step retrofit of the riser, using the 20 cm resolution DEM acquired by UVA, allows estimating the cumulative left-lateral offset recorded by the fan surface riser at 92 ± 12 m, according to previously describe piercing lines (Figure 4-77). Alignment of the three piercing lines (i. intermediate terrace gully, ii. Dark Creek Terrace riser and iii. Eastern gully incised into Dark Creek surface, see Figure 4-77) are consistent with each other, given that all three lines fit to their relatives downstream. Considering the north-flooding dark creek, the left-lateral fault motion exposes the riser to the undermining of the active stream – which although being captured, displays an active channel currently being incised. Moreover, the riser slope is significantly steeper downstream than upstream of the fault, and the minimum offset recorded by the riser, assessed with the gully in the intermediate terrace (displayed dashed on figure, given that the downstream marker is not incised in the same surface that the upstream gully). Contrarily, the eastern gully did not experienced significant retreat, and is slightly larger than the offset defined by the main riser. These observations suggest that the riser evolution involves a retreat. We can consider this retreat as minor given that the offset recorded by the eastern gully within Dark Creek surface yields an offset consistent with the one on the riser (Figure 4-77). No significant vertical cumulative offset (<1.0 m) has been identified within the surface of the Dark Creek fan.

The $^{10}$Be cosmogenic dating has been performed in a soil-pit implanted ~100 m uphill from the fault, within a preserved part of the fan surface in a place evidently devoid of recent incision or deposit processes (Figure 4-77). A 2 m deep soil-pit has been dug, and amalgam samples of 50 quartz-rich clasts were collected at 200, 150, 100, 75, 50, 25 and 0 cm-deep from the soil-pit walls, plus one on the surface itself (Figure 4-78).

The resulting profile displays (Figure 4-78 and Table 10) a consistent exponential decrease of $^{10}$Be concentrations with depth, correctly modeled by a Chi2 inversion. At first order, considering a zero-erosion, a strong inheritance can be assessed, which leads to a minimum abandon age of 120 ka (Figure 4-78.A). However, the application of Bayesian modeling (Hidy et al., 2010) shows that the profile already reaches the steady state (Figure 4-78.F), as the distribution in depth of erosion rates and integration ages is well centered, with a corresponding erosion rate of 6 to 8 m.Myr$^{-1}$(Figure 4-79), and an integration time of 111.8 ± 4.7 ka. We notice that this modeled profile displays a steady state, given that the results are strongly dispersed in age, but correctly constrain the erosion rate (Figure 4-79). This age is further used as a minimum abandon age of the Dark Creek fan.

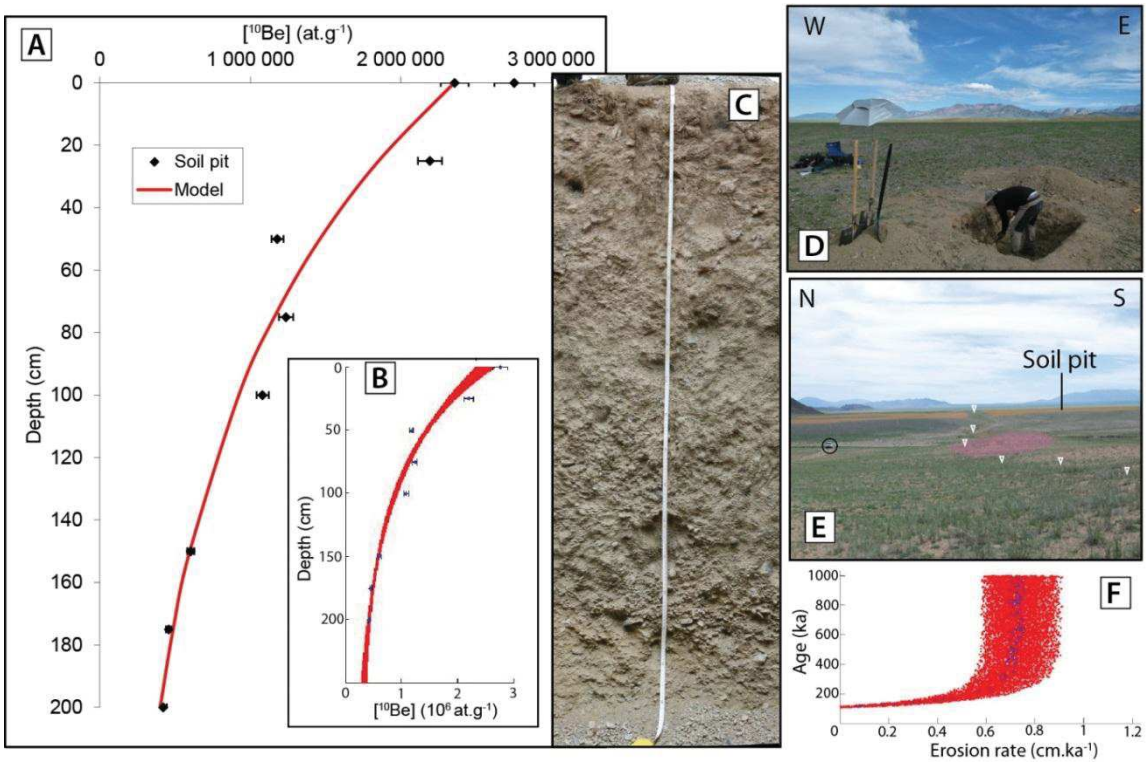


**Figure 4-78: 10Be dating of the Dark Creek fan surface. A.$^{10}$Be profile and model. B. $^{10}$Be modeled profile from Bayesian modeling. C. Photomosaic of the log of the soil pit, full picture is 2 m high. D. Photograph to the south-east of the soil pit digging, within preserved part of the Dark Creek fan surface. On the background are the Gichigniy Nuruu Mountains, with preserved peneplain on top. E. View to the east of the Dark Creek fan, shaded in orange, and location of the soil pit. The car in the black solid circle is for scale. The pressure ridge is shaded in purple and white triangle highlight the VOLF trace. F. Age vs Erosion rates derived from the Bayesian modeling. The shape is here characteristic of a steady state profile and gives integration age and assessment of the erosion rate.**

We can see on the field a good preservation of the landform, increased by the abandoned nature of the Dark Creek stream. The $^{10}$Be profile indicates a clear steady state, which yields to a significant erosion (8 m.Ma$^{-1}$), consistent with values found along the Bogd fault (Ritz et al., 2006). Also, the age of this surface is consistent with other fan surfaces dated by cosmogenic $^{10}$Be approach in Ih Bogd region (eastern Gobi-Altai, e.g. Vassallo PhD, 2006; Ritz et al., (2006), which suggest that such surfaces has been deposited subsequently to climatic pulses, leading to large emplacement of alluvial terraces in the region.

**Table 10: The $^{10}$Be nucleide concentrations and modeled ages for samples at Dark Creek site.**

| Sample | Lat (dec°) | Lon (dec°) | Alt (masl) | 10Be Conc (at/g) | 10Be err. 1σ (at/g) | Shield. Corr | Density | depth (cm) | 10Be age tint (yr) | Erosion rate (m.Ma-1) |
|---|---|---|---|---|---|---|---|---|---|---|
| VOL14_P1 | 45,555 | 97,135 | 2096 | 4,220E+05 | 2,286E+04 | 0,9999 | 2,0 | 200 | 116224 | 8,1 |
| VOL14_P2 | 45,555 | 97,135 | 2096 | 4,591E+05 | 1,956E+04 | 0,9999 | 2,0 | 175 | 101724 | 9,3 |
| VOL14_P3 | 45,555 | 97,135 | 2096 | 6,038E+05 | 2,381E+04 | 0,9999 | 2,0 | 150 | 108791 | 8,7 |
| VOL14_P4 | 45,555 | 97,135 | 2096 | 1,081E+06 | 4,122E+04 | 0,9999 | 2,0 | 100 | 125745 | 7,5 |
| VOL14_P5 | 45,555 | 97,135 | 2096 | 1,237E+06 | 4,756E+04 | 0,9999 | 2,0 | 75 | 113476 | 8,3 |
| VOL14_P6 | 45,555 | 97,135 | 2096 | 1,181E+06 | 3,952E+04 | 0,9999 | 2,0 | 50 | 84765 | 11,3 |
| VOL14_P7 | 45,555 | 97,135 | 2096 | 2,194E+06 | 8,049E+04 | 0,9999 | 2,0 | 25 | 125612 | 7,5 |
| VOL14_P8 | 45,555 | 97,135 | 2096 | 2,755E+06 | 1,327E+05 | 0,9999 | 2,0 | 2 | 123823 | 7,6 |
| VOL14_S | 45,555 | 97,135 | 2096 | 2,359E+06 | 9,296E+04 | 0,9999 | 2,0 | 0 | 105615 | 9,0 |
| | | | | | | | | Mean: | 111752 ± 4730 | 8,2 ± 0,7 |

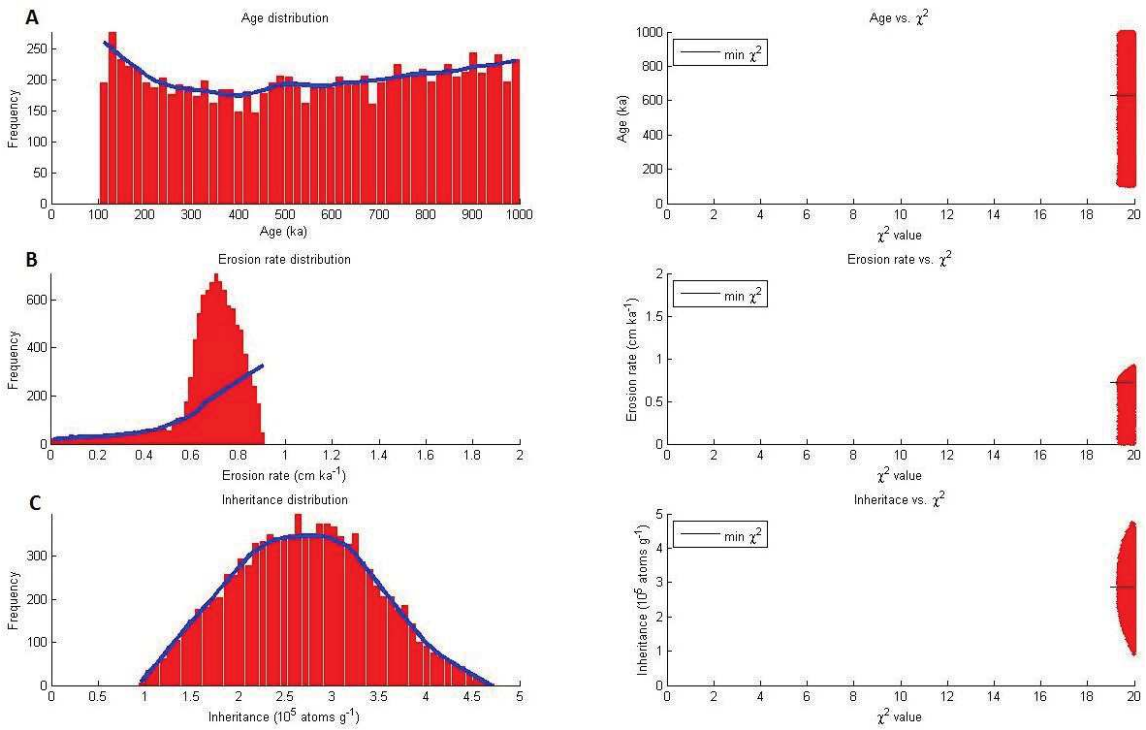


**Figure 4-79: Bayesian modeling of the Dark Creek 10Be profile. A. Distribution of integration ages. B. Distribution of erosion rates. C. Distribution of inheritances.**

Therefore on the basis of careful geomorphic surveying, we suggest that although the uncertainty of the slip rate cannot be strictly constrained (given that we have no maximum offset), the maximum left-lateral slip rate can be assessed along the westernmost section of the VOLF to 0.82 ± 0.14 mm.yr$^{-1}$ during the late-Pleistocene period (120 ka). This takes into account a minimum abandon age of 111.8 ± 4.7 ka and a left-lateral offset of 92 ± 12 m.

### IV.3.3.2. Biger Terrace Site

The Biger Terrace site (45.565°N; 97.075°E) is located 20 km south of Biger town and 4.5 km west of Dark creek site (Figure 4-65). The VOLF crosses here a major drainage, the Biger Gol River, with an obliquity angle of ~ 60°, and generates systematic left-lateral offset of large alluvial terraces. We carried out microtopographic TSL and UVA surveys on this site in order to assess the fault-related cumulative displacements recorded by the landforms (Figure 4-80).

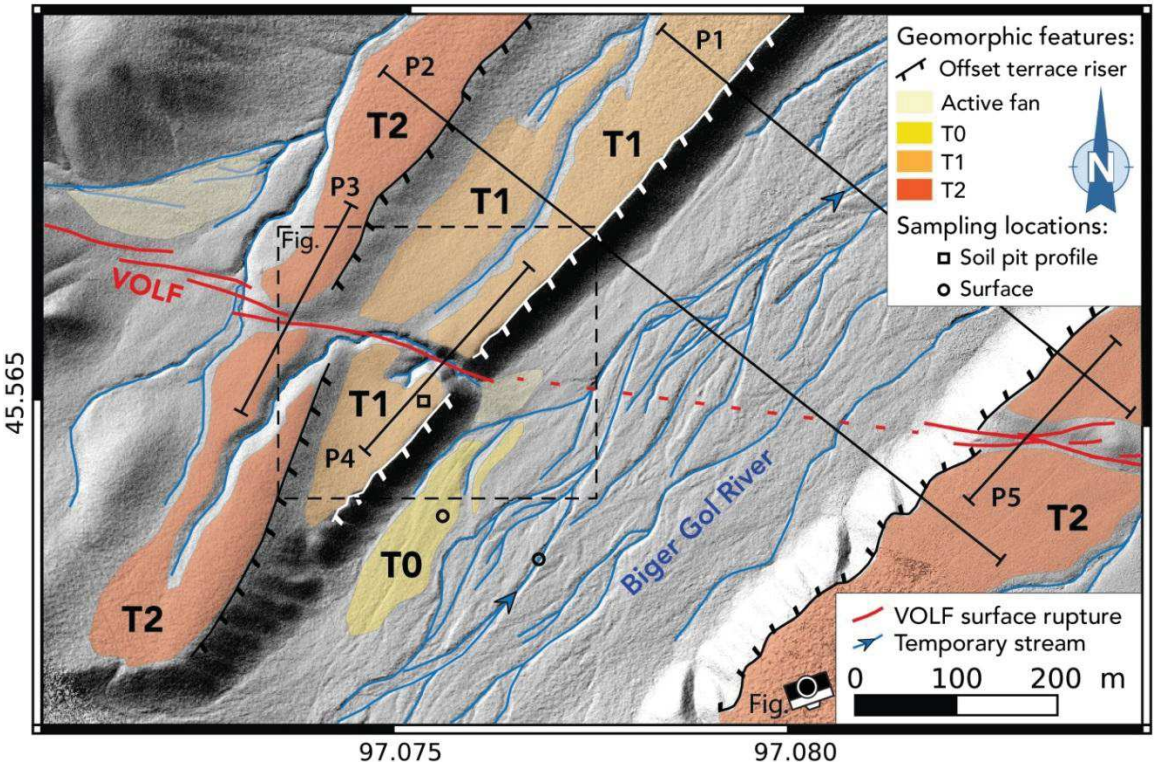


**Figure 4-80: Morphotectonic map of Biger Terraces site. Background is hill-shaded DEM from UVA survey. Solid red line is the VOLF fault trace. Black segments are location of vertical profiles P1 to P5 presented in Figure 4-83. Camera is location of Figure 4-81 shooting place.**

Two main levels of terraces, T1 and T2, are visible on the western bank (Figure 4-81 and Figure 4-82). In addition some remnant pieces of a possibly abandoned terrace (T0) bounds by the south-east the temporary but nevertheless active ~400 m-wide central anastomosed river bed of the Biger Gol River (Figure 4-80). T1 is separated from T0 and the active stream by a prominent ~15 m-high sharp riser; conversely, the riser between T1 and T2 is smooth and slightly curved. Only one terrace level can be identified on the eastern bank (Figure 4-81).

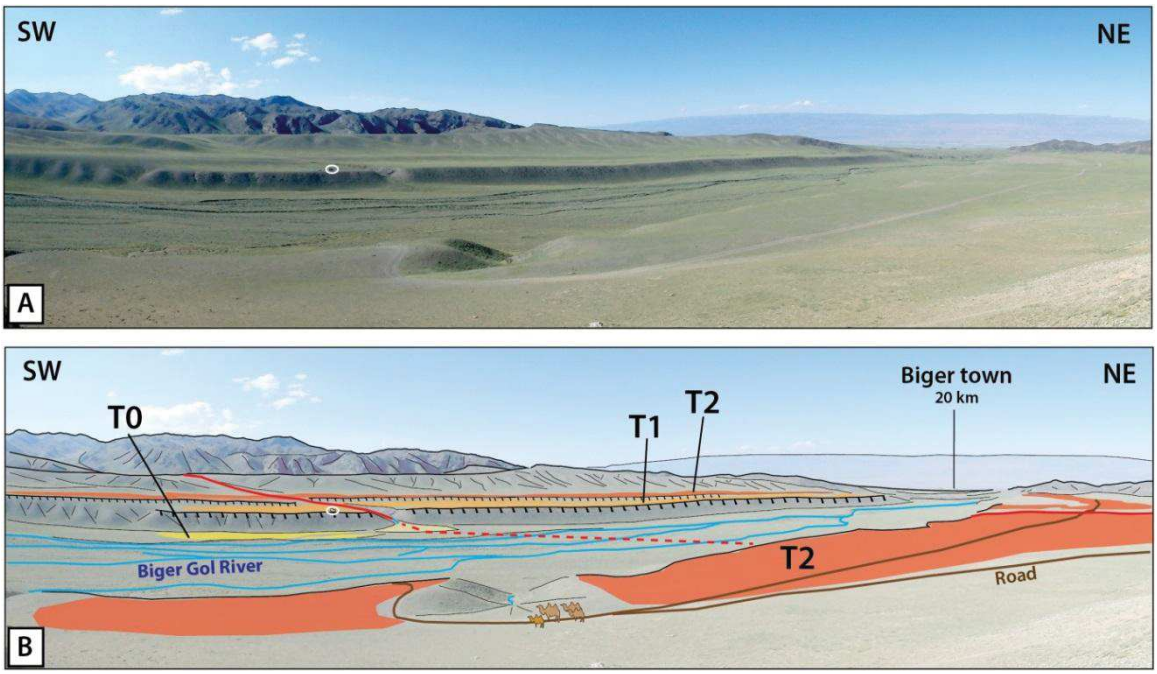


**Figure 4-81: Panoramic view to the north-west of Biger Terraces site. A. Photomosaic. For scale, the white circle surrounds a car. On the background, to the right of the picture is Biger town, in the Valley of Lakes. B. Photo-interpretation of the picture in (A). VOLF surface rupture is the red line, dashed when inferred in the active bed of the stream. Main temporary drains of the Biger Gol River are shown in blue, and reads in brown. White circle and camels are for scale. Shaded areas are same as in Figure 4-80.**

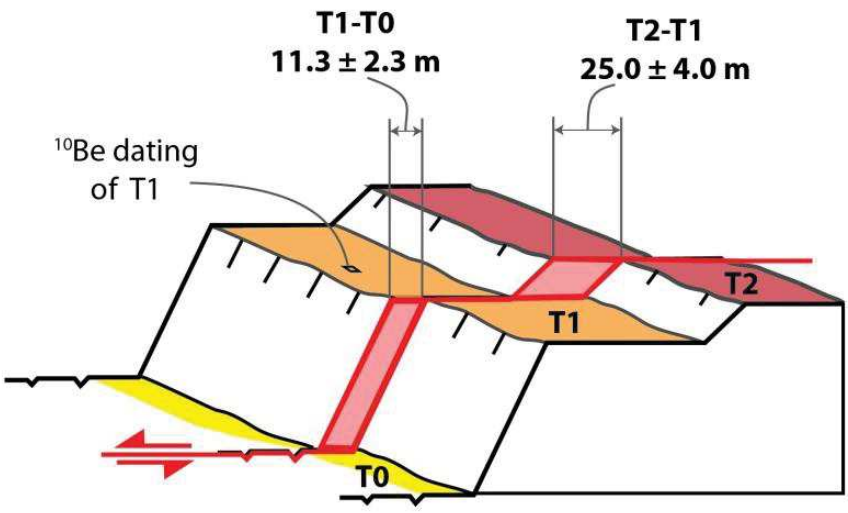


**Figure 4-82: Bloc diagram of the western bank of the Biger Gol River, at Biger Terraces site, view to the south.**

According to river-transverse topographic profiles P1 and P2 extracted orthogonally of the river (Figure 4-80), the terrace visible on the eastern bank of the Biger Gol River is associated with the T2 level on the western bank (Figure 4-83). The P1 profile, located on the northern part of the trench, actually displays a misfit of ~10 m between the altitudes of the terraces related to the main treads on both side of the Biger Gol River

(Figure 4-83). The same amount of elevation difference can be identified on the P2 profile, although it crosses the fault. Hence the fault motion likely involves unsignificant coseismic vertical displacements. Cross-fault profiles P2, P3 and P4 (Figure 4-83) display apparent vertical offsets of 2.1± 0.2 m for T1, 1.3 ± 0.3 for T2 on western bank, and 2.0 ± 0.2 m for T2 on the eastern bank. We suggest that those vertical offsets correspond to cumulative displacements, and are merely partials offsets, due to the discrepancy between the offset recorded by younger T1, and the smaller offset recorded by older T2. Along stream slope of both terraces T1 and T2 is very consistent (4,0 ± 0,5 % from Figure 4-83-C and D). There is headward erosion of the T2 surface by talwegs visibly related to the fault zone for the southern gully (Figure 4-80). Instead, the northern gully has been retrofit as figured in Figure 4-73-1. Eventually, those measurements of the vertical component of cumulate coseismic slips indicate a mostly horizontal fault-motion, because the horizontal offset recorded by these structures are one order of magnitude higher, as previously described.

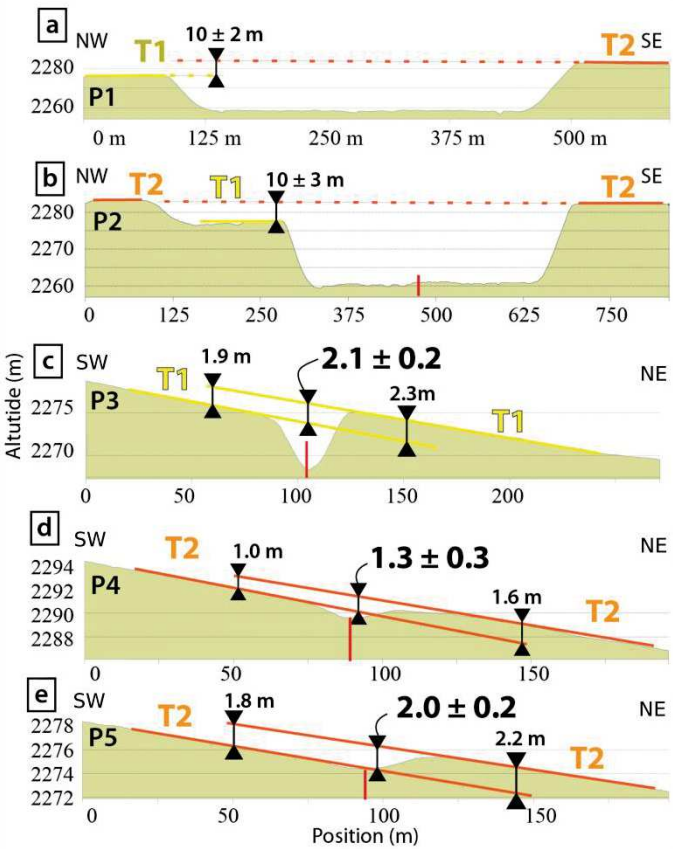


**Figure 4-83: Topographic profiles of Biger Terraces, locations on Figure 4-80. Solid color lines are Biger Terraces, dashed when interpolated. Red vertical solid line is approximate VOLF location. Black arrows are vertical offset measurements, specified with uncertainties. a. P1, cross-river profile, north of the fault. b. P2, cross-river profile, crossing the fault. c. P3, cross-fault profile of T1, western bank. d. P5 cross-fault profile of T2, western bank. e. Cross-fault profile of T2, eastern bank.**

We propose, using four remarkable horizontal offsets of the terraces T1 and T2, to assess the long-term slip rate on the Biger Terrace site. Measurements are done on orthophotographs and DEMs-derived geomorphic data, by three steps landform reconstructions (Figure 4-84).

Firstly, the main riser describes two consistent offsets on both riverbanks, of 11.3 ± 2.3 m between T0 and T1 on the western bank (Figure 4-84), and of 10.4 ± 4.9 m between T2 and the mainstream channel (on right of Figure 4-80). Those measurements are consistent although not related to the same level of terrace, and we interpret this observation as probably indicating a partial erasing of the offset registered by the eastern riser. This is especially because in this context of eastern bank of a north-flooding river, the lateral motion directly exposes the riser to erosion by the active stream. Nevertheless the measurement made on the riser on the western bank appears relevant, as the riser is very straight, sharp, and has a downstream part protected from flooding erosion by the presence of an active fan, eastward along the fault. Furthermore, we notice that we obtain strictly the same offset value using either piercing lines derived from the upper edge of the main T1 tread, or from the lower edge (Figure 4-84.B.). Nevertheless, partial erosion of the upstream riser cannot be ruled out, and the measured offset between T0 and T1 have to be considered as a minimum value of the fault-related displacements recorded by the T1 terrace.

Secondly, a smooth and straight channel is well visible north of the fault within the preserved surface of T1, and is probably related south of the fault to a steep tributary of the obviously fault-related talweg, well pronounced despite of significant watershed (Figure 4-84.A.). Restoration of this landform gives a left-lateral offset of 16.5 ± 4.1 (Figure 4-84.C.). We suggest that this incision took place specifically here due to the former existence of a swale, and that this landform can be used to derive a relevant cumulative offset of the VOLF coseismic deformation since the abandonment of T1, as the incision within T1 is necessarily subsequent to the surface abandonment.

Thirdly, although the gentle risers between T1 and T2 are slightly oblique to each other on both sides of the fault, we estimate a cumulative displacement of 25 ± 4 m (Figure 4-84.D), consistent with measurement on the northern gully, displayed in Figure 4-73-1 (which corresponds to the westernmost gully in Figure 4-80). Considering that the offset of this feature has been attributed formerly to the abandonment of T1, the measured displacement corresponds to a maximum cumulative offset since the abandonment of T1.

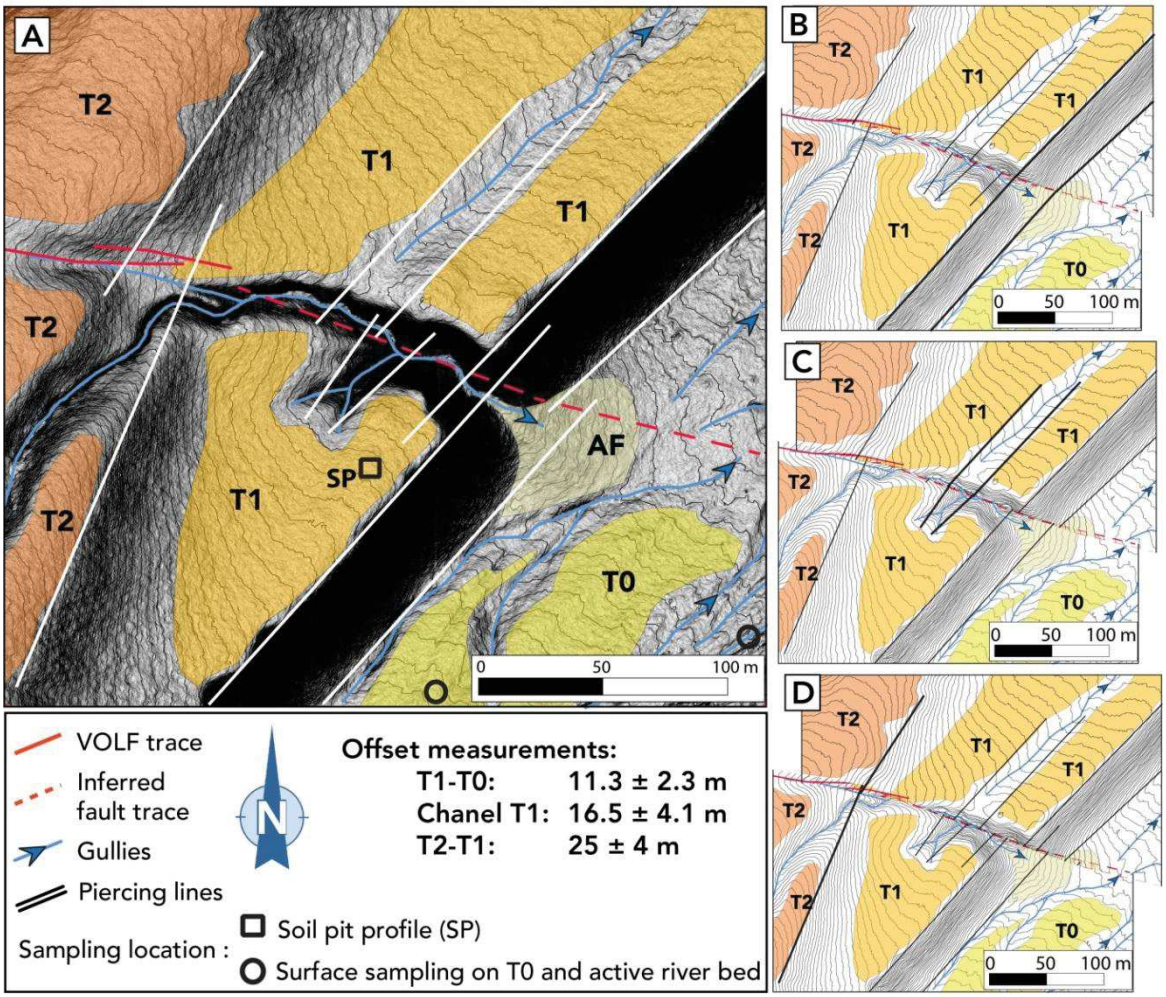


**Figure 4-84: Offset measurements of the Biger Terraces. Shaded areas are Biger Terraces delimitations, and contours are 50 cm. A. Morphotectonic map of the offset Biger Terraces. Solid white lines are piercing lines. Background is slope gradient shade. Surface samplings are done on a wide area, and not restricted to black circles. B. Preferred retrofit for the T1-T0 riser. C. Preferred retrofit for the channel in T1. D. Preferred retrofit for the T2-T1 riser.**

Eventually, we may associate the vertical offset recorded by T1 (2.1± 0.2 m) to the minimum and maximum horizontal offsets (respectively 11.3 ± 2.3 m and 25 ± 4 m), to derive the dip of the average slip vector, which ranges from 5° to 10° (10 to 20 %). Hence, this defined a slip vector of (N100°E, 7°E).

In order to use the previously described offsets to derive fault slip rates, we sampled for $^{10}$Be cosmogenic dating of the abandon age of the T1 and T0 terraces, using in situ produced $^{10}$Be. The dating of the T1 terrace has been done by sampling amalgams of quartz-rich clasts in a 1.5 m-deep profile, dug out from a well preserved part of the surface (Figure 4-84.A and Figure 4-85.C.D). We sampled at depths of 150, 100, 75, 50, 25 cm, up to the surface itself. When checking the soil pit log, we see that the fan deposits present a crude stratification of clast-supported materials, from sand to pebbles, with a silty matrix, indurated by pronounced calcretisation (Figure 4-85.B). No evidence

of soil development or bioturbation has been identified. We also attempted to date the T0 terrace by amalgam-sampling from the active bed to assess the inheritance of the incoming clast in $^{10}$Be, but also from the T0 surface (Figure 4-84 and Figure 4-85.A).

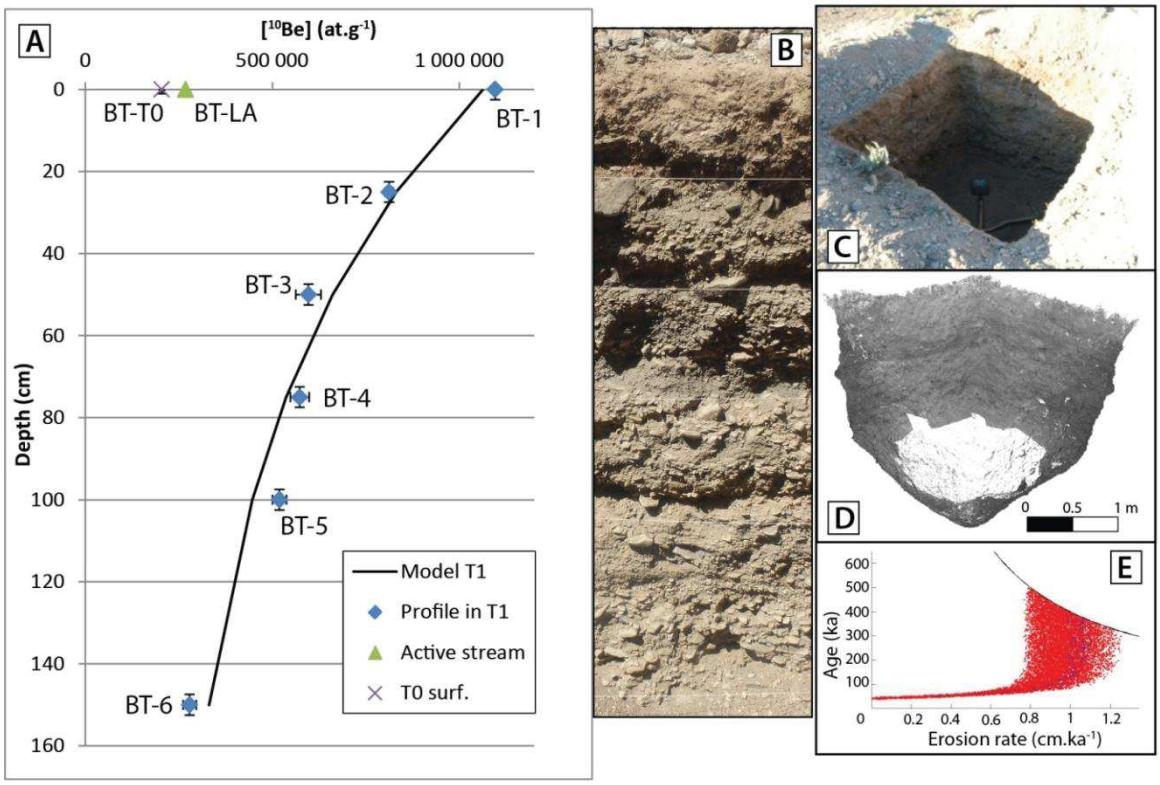


**Figure 4-85: $^{10}$Be dating of the Biger Terraces site. A. $^{10}$Be profile. B. Photomosaic of the log of the soil pit, full picture is 1.5 m high and corresponds to the profile in (A). C. Photograph of the soil pit, side of the pit is two meters-long. D. This 3D model of the soil pit has been done by structure from motion modeling, and allows orthomosaics of the trench walls, as well as density calculation (cf. Chap.2.I.4.2.1.6.iii). E. Age vs Erosion rates derived from the Bayesian modeling. Here the shape is characteristic of a steady state profile, and gives integration age and assessment of the erosion rate.**

Results of $^{10}$Be concentration are in Table 11. Figure 4-85.A. shows the well-defined $^{10}$Be profile obtained in the soil pit in T1, which has an acceptable fit with the model. Despite good constraints on the inheritance and assuming nil-erosion, we can assess a minimum abandon age of 38 ± 1 ky. However, the application of Bayesian modeling (Hidy et al., 2010), shows in Figure 4-85.E and Figure 4-86 that the T1 surface very likely already reaches the steady state, given that we have a rather poor assessment of the age – with a still stronger occurrence close to the integration time –, while instead a good constraint of the erosion rate to 21.0 ± 1.3 m.Myr$^{-1}$ (Figure 4-86-B). This erosion rate is corresponding to an integration time of 37.4 ± 2.2 ka, which must be considered as a minimum abandon age of the T1 Biger Terrace for further slip rate computation.

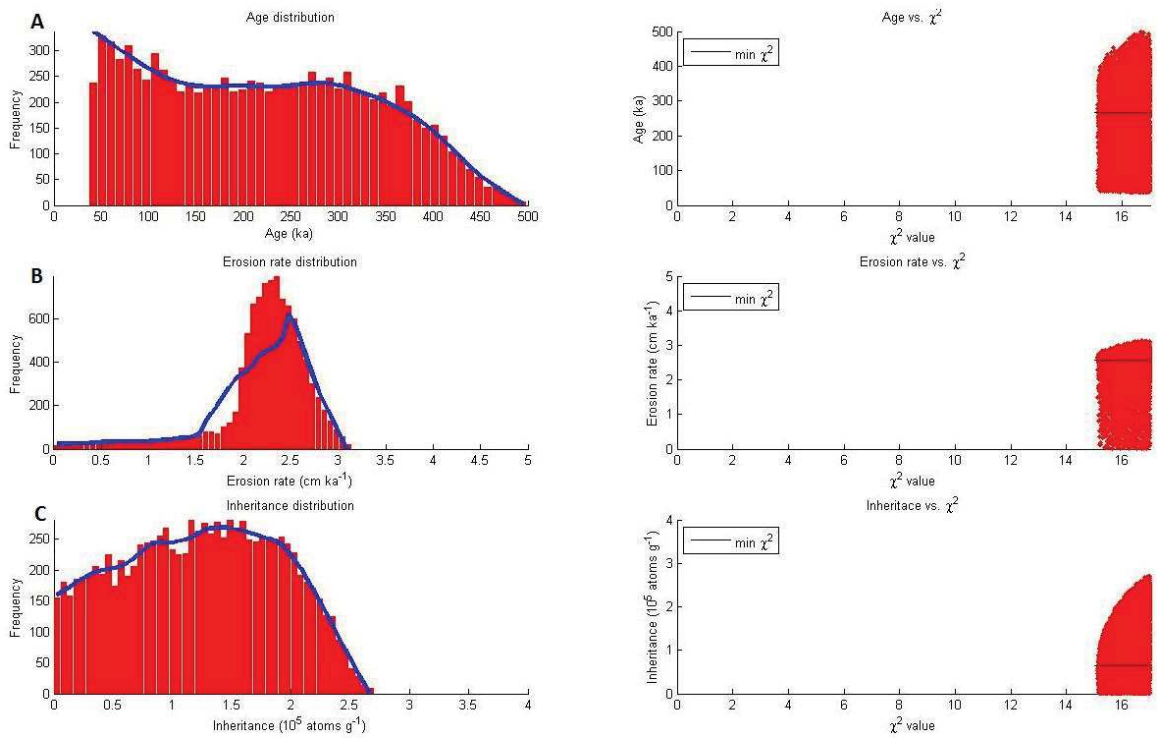


**Figure 4-86: Bayesian modeling of the Bigger Terraces $^{10}$Be profile. A. Distribution of integration ages. B. Distribution of erosion rates. C. Distribution of inheritances.**

Interestingly, the $^{10}$Be concentration in the river (sample BT-LA on Figure 4-85.A) is fairly close to the inheritance determined from the profile in T1 (Figure 4-85-A), which suggests a good consistency of the proposed uniformitarianism of the inheritance in $^{10}$Be of Biger Gol River sedimentary load.

**Table 11: The $^{10}$Be nucleide concentrations and modeled ages for samples at Biger Terraces site.**

| Sample | Lat (dec°) | Lon (dec°) | Alt (masl) | [10Be] (at.g-1) | err. [10Be] 1σ (at/g) | Shield. Cor. | Density | Depth (cm) | 10Be age tmin (ka) | 10Be age tint (ka) | Erosion rate (m.Ma-1) |
|---|---|---|---|---|---|---|---|---|---|---|---|
| BT1 | 45,565 | 97,075 | 2178 | 1,10E+06 | 3,37E+04 | 0,999 | 2 | 5 | | | |
| BT2 | 45,565 | 97,075 | 2178 | 8,13E+05 | 2,52E+04 | 0,999 | 2 | 25 | | | |
| BT3 | 45,565 | 97,075 | 2178 | 5,97E+05 | 1,85E+04 | 0,999 | 2 | 50 | 38 ± 1 | 37,4 ± 2,2 | 21,0 ± 1,3 |
| BT4 | 45,565 | 97,075 | 2178 | 5,73E+05 | 1,78E+04 | 0,999 | 2 | 75 | | | |
| BT5 | 45,565 | 97,075 | 2178 | 5,19E+05 | 1,62E+04 | 0,999 | 2 | 100 | | | |
| BT6 | 45,565 | 97,075 | 2178 | 2,79E+05 | 1,61E+04 | 0,999 | 2 | 150 | | | |
| BTL0 | 45,565 | 97,075 | 2170 | 2,04E+05 | 6,33E+03 | 0,999 | 2 | 0 | | | |
| BTLA | 45,565 | 97,075 | 2170 | 2,68E+05 | 1,09E+04 | 0,999 | 2 | 0 | | | |

Regarding the assessment of the abandonment age of the T0 terrace, the concentration found on the surface (BT-T0) is slightly lower than the inheritance assessed with BT-LA sample, which is improbable although the difference is moderate. A possible explanation

for this discrepancy might be that the T0 terrace is not actually abandoned, or at least not definitely. Hence in both cases, these measurements would lead to an assessment of the inheritance, which when combined, provide an estimate consistent with the one derived from the profile on T1. Consequently, we can neither propose an abandonment age for the T0 surface, nor argue that the major riser between T0 and T1 was protected by the abandoned T0 from the undercutting of the active stream.

Regarding previously detailed field observations, and the minimum abandon age of the T1 terrace, we may propose the following slip rates along the western section the VOLF during the last 40 ka:

1. The horizontal offset of the riser between T0 and T1 leads to a lateral slip rate of 0.30 ± 0.08 $mm.yr^{-1}$.
2. The horizontal offset of the channel within T1 leads to a lateral slip rate of 0.44 ± 0.14 $mm.yr^{-1}$.
3. The horizontal offset of the riser between T1 and T2 leads to a maximum lateral slip rate of 0.67 ± 0.15 $mm.yr^{-1}$.
4. The vertical offset of T1 on western bank leads to a vertical slip rate of 0.06 ± 0.01 $mm.yr^{-1}$, with the north side of the fault uplift.

Because the geomorphic features related to terrace T1 (i.e. risers and channels) necessarily post-date the abandonment of the terrace, and because the assessment of the abandon age of T1 is a minimum value, it remains undetermined whether the slip rates thus derived are maximum or minimum assessment values. The same observation can be done for the vertical slip rate on T1. Nevertheless, accounting for the assessed young age of the Bigger Terraces, and from the maximum-slip rate assessment, we propose that the most-probable slip rate recorded along the Biger Terraces ranges from 0.3 to 0.7, which leads to an average value of 0.5 ± 0.2 $mm.yr^{-1}$. This result is fairly consistent with the slip rate determined on the Dark Creek fan.

### IV.3.3.3. Summary of slip rate assessments along the VOLF

A total of four slip rates have been assessed along the VOLF (Figure 4-87). Although these measurements do not allow an assessment of the slip rate variations during the late-Pleistocene period, they do lead to a confident value of slip rate, which ranges between 0.30 ± 0.08 mm.yr$^{-1}$ and 0.82 ± 0.14 mm.yr$^{-1}$ (Figure 4-87), with a most-probable slip rate of 0.5 ± 0.2 mm.yr$^{-1}$, as the upper bound is a maximum slip rate value.

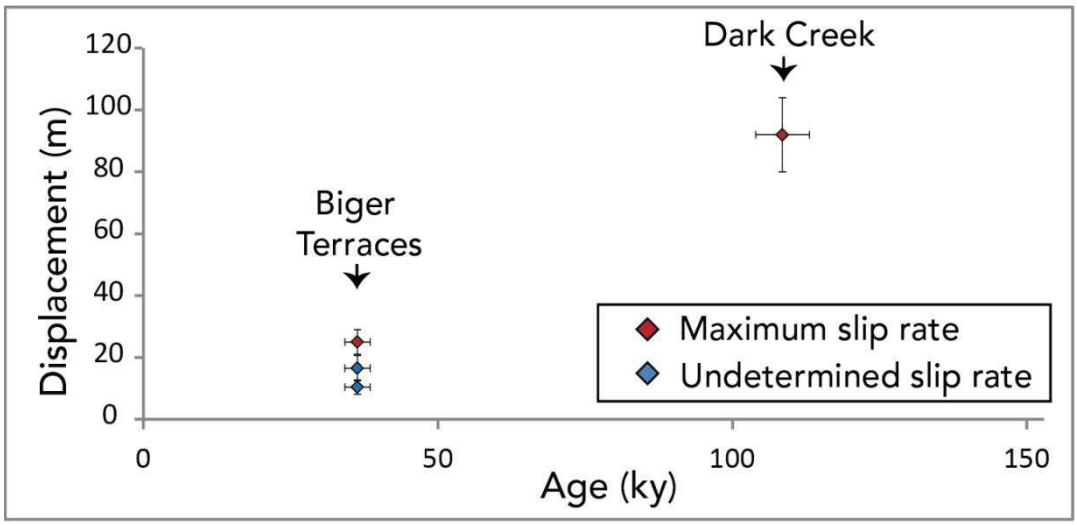


**Figure 4-87: Slip rates along the VOLF**

We note a strong discrepancy between the erosion rates and integration times calculated in Dark Creek and Biger Terraces sites. This observation makes sense considering that differences in erosion rates necessary involves different integration times. Additionally, one may wonder why erosion rates are so different (factor 2 to 3) while both sites are located in the same area (<5 km from each other)? This question might find reasons on the geomorphic context, given that the watershed on the Biger Gol River is significantly larger and located in a more mountainous area (Figure 4-88).

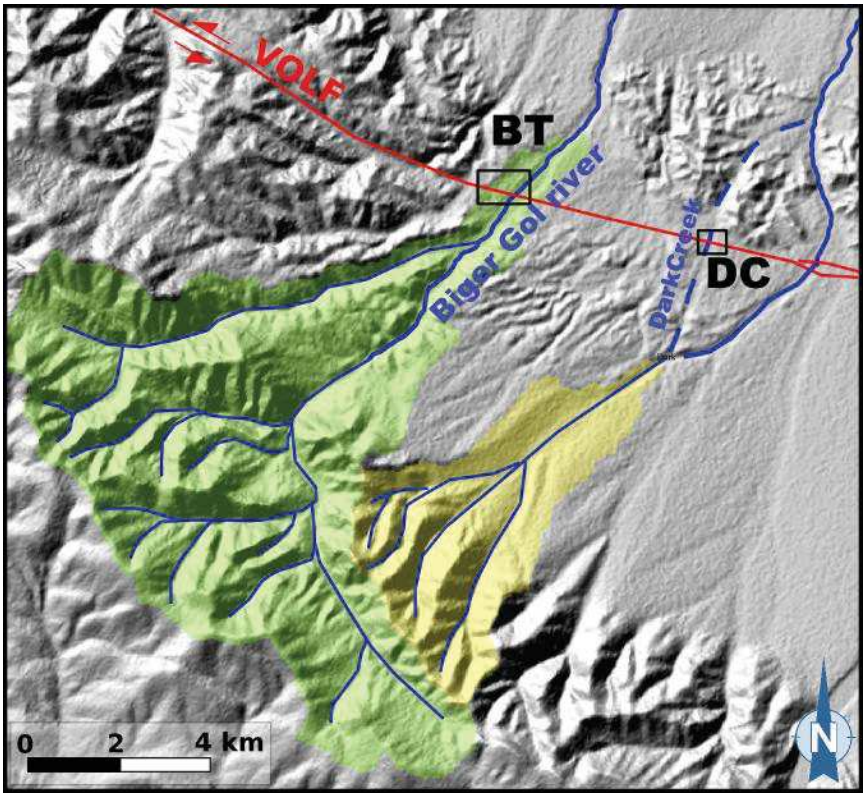


**Figure 4-88: Watershed of the Biger Gol River (green shaded area) and the Dark Creek stream (yellow shaded are). Blue solid lines are main drains associated with the watersheds. Red solid line is the VOLF. Black solid boxes are Biger Terraces (BT) and Dark Creek (DC) sites.**

The inheritances observed at both sites are same order of magnitude ($10^5$ at.$g^{-1}$), in spite of the different terrain composing each watershed. In fact the watershed of the Biger Gol River is mostly located in the Lake zone (Figure 1-15), composed of Late-Neoproterozoic terrains (cf. « Russian Geological 1:200 000 maps of Mongolia » 1987), instead the Dark Creek river (and tributaries) is exclusively located into Devonian volcanoclastic terrains (« Russian Geological 1:200 000 maps of Mongolia » 1987). This observation here refers to the figure of Kozlovsky et al., 2015, Figure 1-15), but is actually done from 1:200 000 « Russian Geological maps of Mongolia », (1987).

.

### *IV.3.4. Ages of paleoearthquakes along the VOLF*

In order to assess the ages of last surface rupturing earthquakes on the VOLF, two trenches has been dug at the Storm Fan site: the first during the 2014 field campaign, then re-occupied in 2016. The Storm Fan site is located 45.563°N; 97.098°E, 3 km west of Dark Creek site, and 1 km east or Biger Terrace site (Figure 4-89). Here the fault presents mostly left-lateral motion, but it seems to also produce a slight uplift on north side of the fault. In fact, the drainage is flowing mainly northward, from granitic hills to a small quaternary basin presumably associated to the presence of the VOLF (Figure 4-70). At the outlet, an alluvial fan forms, where the river gets out of the bedrock hills, ~100 m on south of the fault (Figure 4-90). This fan abuts against the fault scarp that it buried (Figure 4-91), yielding to accumulation of recent deposits within a paleo-channel, East of the fan (Figure 4-89). The fault trace does not display visible vertical offset across the active fan and the active stream is now flowing to another channel, along the western part of the fan (Figure 4-89). However, recent small overflow deposits can be seen atop the trench location (Figure 4-90-A). The two trenches are 4 m-long by 1.5 m-deep, and located almost at the same location, ~1 m apart.

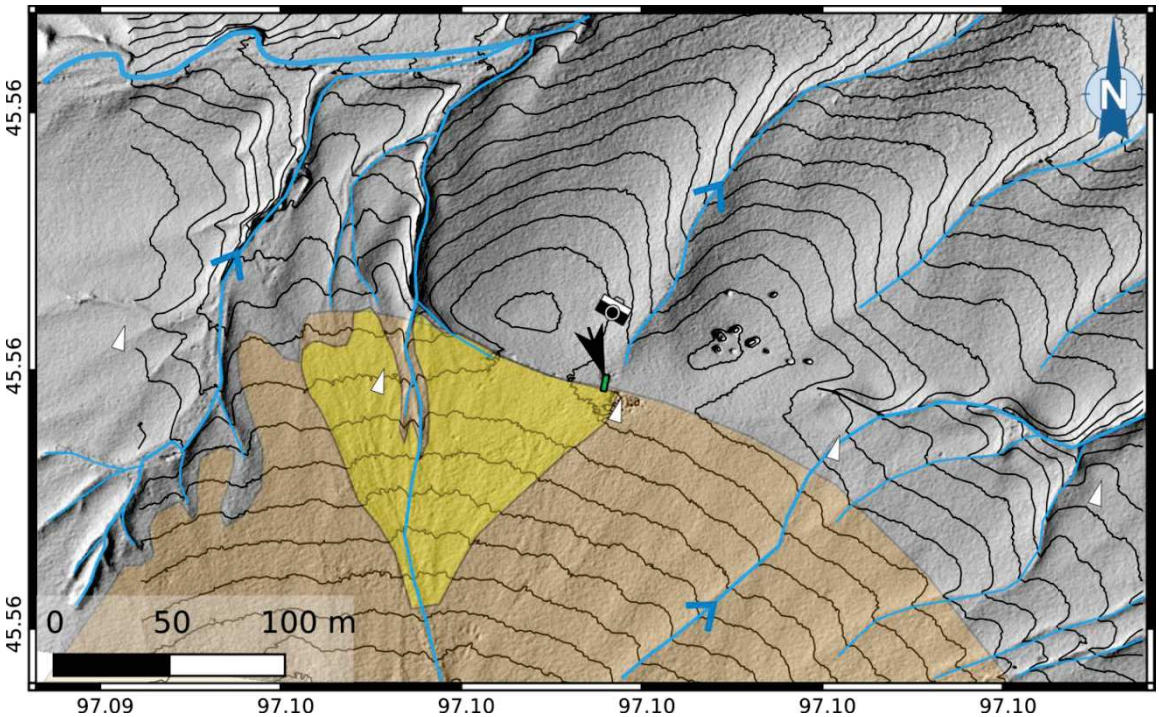


**Figure 4-89: Morphotectonic map of the Storm Fan site. The Storm Fan trenches correspond to the green box, indicated by a black arrow. White arrows indicate the VOLF trace. Background is 20 cm resolution DEM from UVA survey, and contours are 1 m. The fan surfaces are shaded, with the orange older than the yellow one. Blue solid lines are temporary active drains. The camera indicates the location of Figure 4-90-A.**

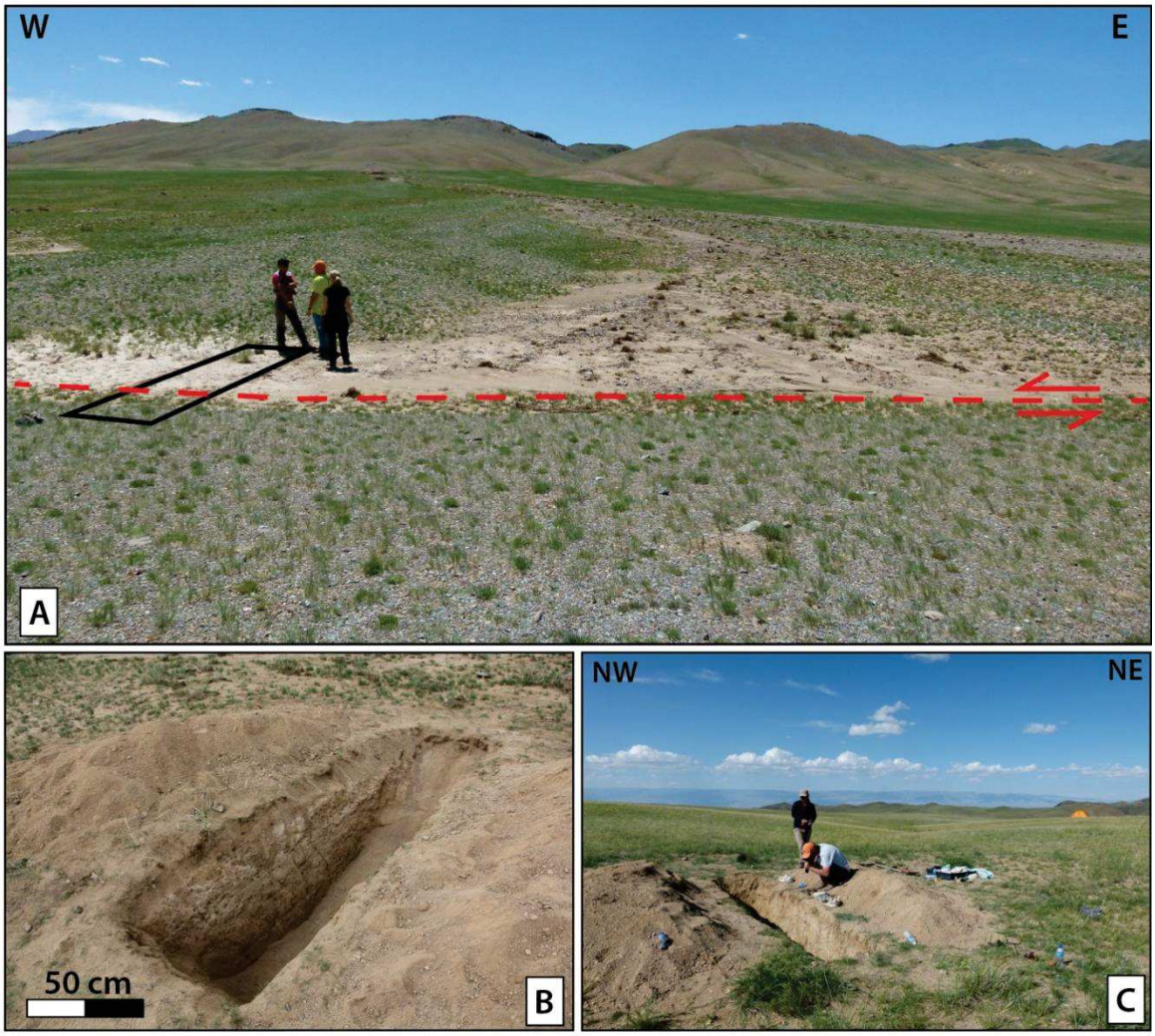


**Figure 4-90: Photographs of the Storm Fan site and trenches. A. Photograph to the south of the Storm Fan. See location of Figure 4-89. Black solid box is location of the 2014 trench. Red dashed line is the VOLF main trace. B. Photograph to the south-west of the Storm Fan Trench 2014. C. Photograph to the north of the Storm Fan Trench 2106.**

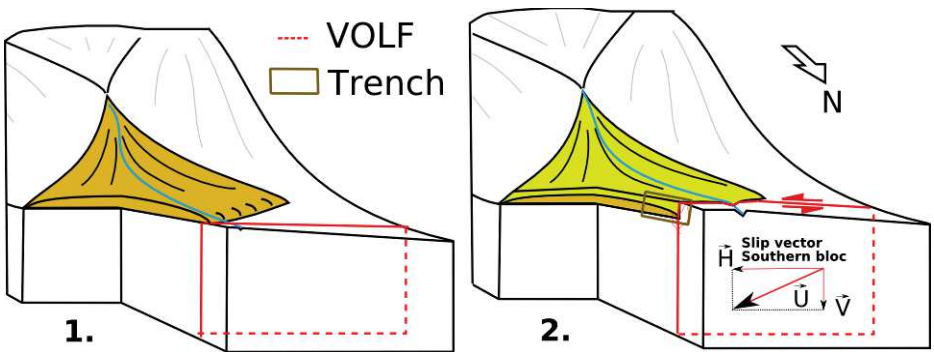


**Figure 4-91: Scheme of the Storm Fan site. 1. Before surface rupture, a fan (orange) is deposited over the fault trace. 2. After the earthquake, a second fan (yellow), not faulted, overlaps the former fan. The slip vector is qualitative, and corresponds to the displacement of the southern bloc. Trench description 2014**

### IV.3.4.1. Trench description 2015

Figure 4-92 depicts the strata and the structures displayed within the Storm Creek Trench 2016. The overall structure of the trench is horizontally stratified and faulted by six visible fault cracks on the central part of the trench, and one crack on the northern part of the trench. Four main units can be identified within the trench, U10 to U40, further described and detailed in subunits when appropriate. The stratigraphy in the trench is sand-dominant with a lot of pebbles and a silty matrix, and the trench is devoid of charcoal or organic matter, hindering radiocarbon dating.

The capping unit, U10, is sandy-silty with few clasts, beige, and corresponds to the current soil, affected by many roots, but no significant deformation can be identified. Hence, this unit is considered to be deposited after the most recent surface rupturing seismic event on this section of the VOLF. Unit U10 has been sampled with an OSL bloc (Figure 4-93-B), for which the analysis, using IRSL simple aliquot analysis, indicates an imperfect bleaching, but still allows determining (accounting for the lowest equivalent dose presented by the grain population) a deposition age of 3400 ± 140 yr (Mo14-OSL1). This post-dates the most recent event along this section of the VOLF.

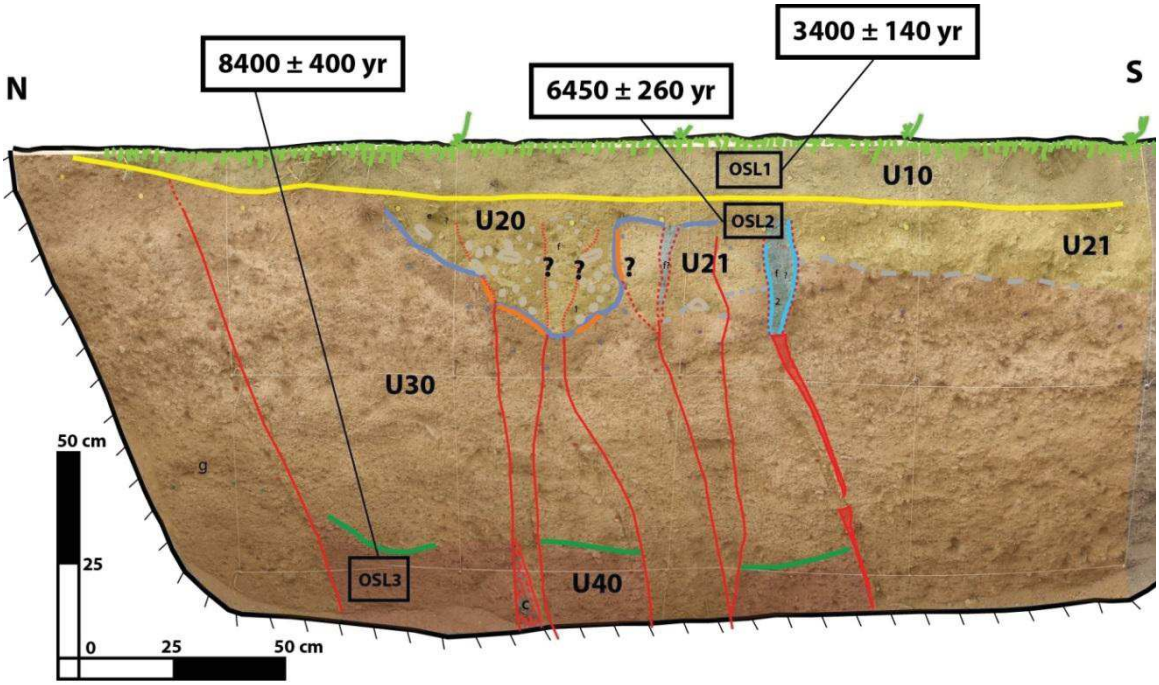


U10: Silty-sandy capping unit with few clasts (cm), beige, many roots. Post-MRE
U20: Loose sand to gravels-sand channel; unclear whether faulted or not. in center. Few pebbles up to 4 cm, most < 1cm.
U21: Fine moist (silt cap over few gravels) slightly sandy with few gravels; strong CaCO3 (white to beige in appearance). Pre-MRE.
U30: sandy pebble gravel, crude horizontal bedding, pebbles sub-angular up to 5cm, unsorted, clast-supported – few gravels.

**Figure 4-92: Log of the west wall of the Storm Fan Trench 2014. Background is orthomozaic. Ages are OSL datings. Yellow solid line is the event horizon associated with the most recent event. Green solid line is the event horizon associated to a former event. Blue solid line corresponds to a possible event horizon on the bottom of U20; question marks are related to questionning about the faulting of U20.**

Below, in the central part of the trench lies unit U20, which corresponds to a channel, filled with loose coarse sand to gravel, with a few pebbles < 4 cm-diameter. It is unclear if this unit is affected or not by faulting. While U20 is restricted to the central part of the trench, it is underlay by unit U21, a fine wet silty unit, slightly sandy with some gravel. U21 is also consolidated by calcrete precipitation, and extends to the south with a constant thickness of ~20 cm. In the central part of the trench where U21 lies beneath U20, there is internal faulting which is highlighted by a darker band, tilted to the north by at least four cracks. Some of these, however, might be associated with cryoturbation processes (ice wedges). Furthermore, the contact with U20 channel is either a fissure or erosive. Hence, we assume that this U21 horizon is pre-dating the most recent event recorded in that trench. The uppermost part of the faulted U21 has been sampled with an OSL bloc and analyzed using IRSL simple aliquot analysis (see results in Annexe III). The analysis indicates imperfect bleaching, but still allows (accounting for the lowest equivalent dose) determining a deposition age of 6450 ± 260 yr (Mo14-OSL2), pre-dating the most recent event along this section of the VOLF.

**Figure 4-93: Photographs of the Storm Fan Trench 2014. A. Zoom on the gouge identified within U40. Red dots are nail heads for scale (5 mm diameter). B OSL sampling (OSL-1).**

The underlying unit U30 is the most represented unit in this trench. It is composed of clast-supported sub-angular sand to pebbles, unsorted, which display crude horizontal bedding. This unit is faulted on its whole thickness by clear fault cracks, although no evident fault terminations criteria have been identified.

At the bottom of the trench, there is a discontinuous contact with the underlying U40 unit, coarse sand to pebble, clast supported and unsorted, in which there is a distinct shear zone (or a tilted stratified block) (Figure 4-93-A), which ends on contact with the bottom of U30. We propose that this fault termination corresponds to an earthquake horizon,

and that U40 is pre-dating the penultimate event in the trench. An OSL bloc has been sampled in this U40 unit, and analyzed using IRSL simple aliquot analysis. The analysis indicates here again imperfect bleaching, but still allows determining a deposition age of 8400 ± 400 yr (Mo14-OSL3), pre-dating the penultimate surface rupturing seismic event along this section of the VOLF.

To summarize, the observations within the Storm Creek trench 2014 allow identifying at least two surface rupturing seismic events: the most recent one occurred between 6.45 ± 0.26 ky and 3.40 ± 0.14 ky, according to OSL dating of U21 and U10 respectively, and a previous one (possibly the penultimate), between 8.40 ± 0.40 ky and 6.45 ± 0.26 ky, according to OSL dating of U40 and U21, respectively.

The following questions remain: is channel U21 affected by faulting or not? And what is the exact nature of its contact with underlying U21 (i.e. fissure of erosive)? Consequently, is there a third event recorded in the trench for which the age would rages between deposit ages of U21 and U10 (i.e. 6.45 ± 0.26 – 3.40 ± 0.14 ky)?

To attempt to answer these questions, we dug a second trench one meter away, as described in the following section.

#### IV.3.4.2. Trench description 2016

Figure 4-94 depicts the strata and the structures displayed in the Storm Creek Trench 2016. In general, the strata are tabular, faulted but only slightly deformed, and three main units can be identified, U10 to U30, further detailed in sub-units where appropriate. The overall structure of the trench is stratified, but does not exhibit clear channels or gouge, and the trench is devoid of charcoal and organic matter, ruling out radiocarbon dating. A central fault zone can be identified, better expressed in the lower part of the trench, along with four clear continuous fault cracks. The next sections describe the main stratigraphy of the trench, interactions between these structures, as well as interpretation and sampling.

The uppermost unit, U10, corresponds to the current soil, beige, silt matrix supported with some gravel, pebbles and numerous roots. This ~ 20 cm-thick unit is massive and does not display significant fault criteria. However, it shows several ice wedges, sometimes branched to the underlying fault cracks.

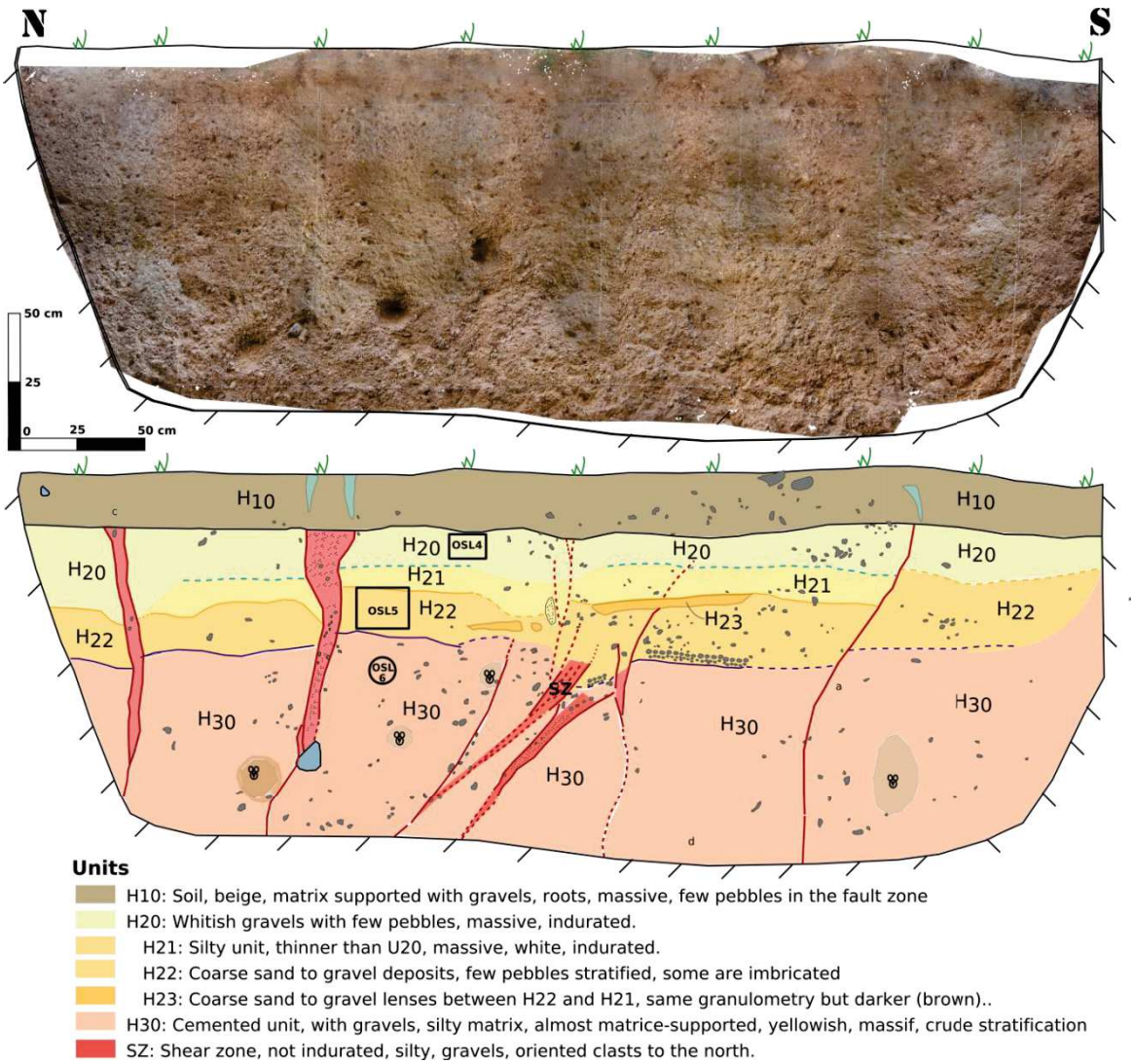


**Figure 4-94: Orthomozaic and detailed log of the west wall of the Storm Fan Trench 2016. Black solid boxes are OSL-bloc sample locations, and round one is for OSL-tube. Blue wedges close to the surface are ice wedges.**

The underlying U20 is massive and indurated, composed of rocky banks of coarse gravel to pebbles, supported by a silty matrix. The intermediate part of this unit is only visible in the central part of the trench, and displays thinner silty deposits, which are whitish, massive and indurated. Southward, U21 abuts against a fault crack, extending until the bottom of U10. Both U20 and U21 are affected by significantly wide cracks, likely related to shearing. This shearing is diffuse on the central part, although highlighted by induration and thickness variations. On the northern part of the fault the shearing is more obvious. Here, U21 is offset, south side uplifted, by two ~10 cm-wide shear zones, widening upward and visibly stopping on the bottom of U10. This widening seems partly associated to cryoturbation processes, but oriented clasts within the shear zones and systematic apparent offset of the horizons, south side uplifted, confirm the fault-related origin of these structures. Hence U20 can be interpreted as the event horizon related to

the most recent surface rupturing earthquake produced on this fault. An OSL bloc has been sampled within U20 (Mo16-OSL4) in order to pre-date the age of the most-recent event; the dating is in progress.

The bottom of U21 displays a sinuous basal contact with a stratified, clast supported subunit U22. Bedding can be identified in its lower part, south of the central shear zone, where it shows distinct bedding of pebbles which are somewhat imbricated. This bedding can still be used as a marker of apparent vertical offset, as it is vertically displaced by ~10 cm, south side uplifted. Additionally, in the central part of the trench, U22 displays some brown lenses (U23) of coarse sand to gravel, supported in a matrix of clay to silt, yellowish and indurated. We note that south of the central fault zone, U23 lenses are located on the uppermost part of U22. Instead, north of the fault zone, lenses are situated on middle of the unit. Furthermore, in the central part of the trench, it is hard to distinguish both horizon boundary and fault terminations on the lower part of U22, as the coarse material is disturbed, unlike out of the fault zone. Also the deformation related to this central fault zone is much more pronounced under the U23 silty lenses compared to above. On the eastern wall especially, four cracks visibly stop upward when joining the U23 lens (unique on this wall). We interpret these fault terminations and strong difference of disturbance as earthquake criteria. The lower part of U22 (under U23 lenses) may correspond to the event horizon related to the penultimate event along this section of the VOLF. An OSL bloc has been sampled within the upper part of U22, north of the fault zone and overlying U23 (Mo16-OSL5), in order to post-date the age of this penultimate event; the dating is in progress.

The lowermost unit of the trench, U30, is a brown, massive and well cemented gravel layer, with some pebbles, supported in an abundant yellowish silty matrix. U30 displays horizontal lineaments, discontinuous, clast-to-matrix-supported deposits and clay zones, but is not actually bedded on its whole. U30 is distinctively more massive and consolidated southward than northward of the central shear zone, which is well expressed in the whole unit (very loose with oriented gravel in a silty matrix). An OSL tube sampling has been done within U30 (Mo16-OSL6) on north of the fault zone, in order to pre-date the age of the penultimate event; the dating is in progress.

The mostly left-lateral fault motion is visible within the trench, through: i. little and varied amounts of apparent vertical offsets of contacts between units and subunits, and ii. systematic discrepancies in deposits induration (except for U10) between the northern and the southern part of the shear zone.

Two surface rupturing seismic events have been identified in the trench on the basis of fault termination and shearing criteria. The most recent event is visible on the central part of the trench with cracks splaying over the central fault zone, as well as on the few cracks out of the fault zone. Corresponding event horizon is uppermost U20. The penultimate event is indicated by the strong deformation involved in the central fault zone within units U30 and U22, and by fault terminations on the bottom of the U23 lenses. The corresponding event horizon is the uppermost U22. We note that the deformation is much more expressed within the lower units, although only cracks are associated with the most recent event; this observation might suggest that the last event was smaller than the penultimate one. Another way to interpret this observation is that the lower part experienced two events, and displays hence a stronger cumulative deformation.

The current vertical apparent motion we identified in the trench, with the southern side uplifted, is not consistent with the fault motion visible in the morphology, given that the cumulative fault scarp displays a northern side uplifted motion (Figure 4-91). We explain this discrepancy by the dominant left-lateral motion affecting the stratification, as those alluvial deposits certainly involve lateral variability (for instance channel deposits, or debris-flow levees and toes). This hampers us to report the true vertical displacement component in such a strike slip context.

#### IV.3.4.3. Synthesis of paleoseismic evidences along the VOLF

Because the two storm creek trenches are very close to each other and their composition and structure are analogous (unsorted stratified clast-dominant fan deposits, faulted by cracks and little expressed shear zones), we can attempt a direct correlation of both trench units and faulting criteria.

At first order, Units U10 and U30 appear equivalent in both trenches, being respectively the capping soil unit, and the prominent massive, clast-dominant, crudely bedded deposit of the trenches. The intermediary horizon, U20, is in both cases formed of similar subunits with stratified sandy to gravel layers. Nevertheless, U20 in the 2014 trench likely exhibits an erosional surface, unlike in the 2016 trench. Additionally, the lowermost unit of the 2014 trench, U40, was not found in the 2016 trench.

Regarding the correlation of identified seismic events within trenches, two events have been identified in the 2016 trench, both related to event horizons within U20 and subunits. However, in the 2014 trench, the older event is confidently related to an event horizon in U40, apparently not visible in the 2016 trench. Furthermore, some questions remain on the interpretation of the 2014 trench about the possibility of a second earthquake recorded by subunits of U20. Consequently, it seems that two events have

been recorded in the 2016 trench, and possibly three in the 2014 trench, and that these three earthquakes occurred during the last 8.40 ± 0.40 ky.

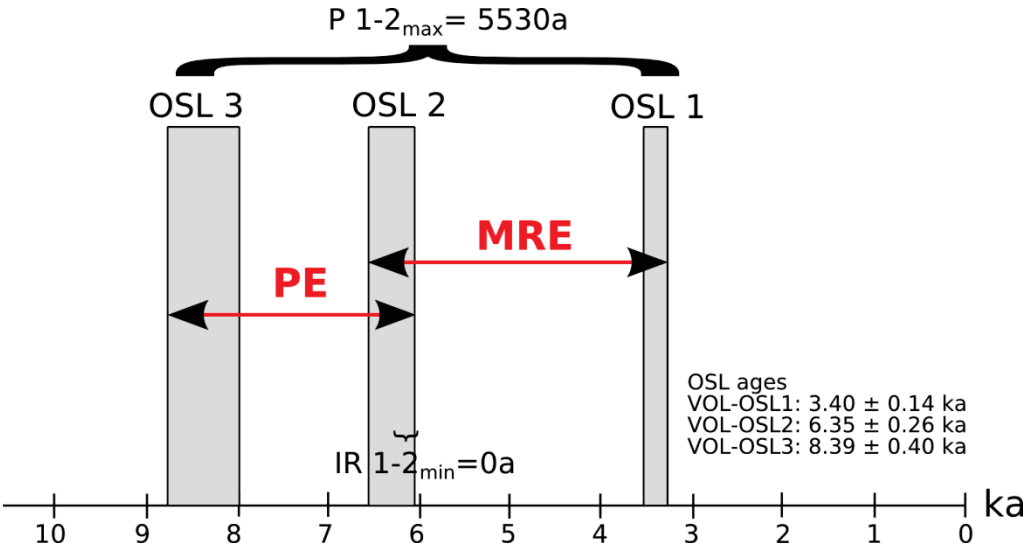


**Figure 4-95: Synthesis of age constraints for paleoseismic events observed in Storm Fan Trench 2014, assuming 2 events. MRE: most recent event. PE: Penultimate event. Assuming 3 events, the extra event is mixed with the MRE.**

Further understanding regarding those observations will be provided by the results of the 2016 OSL samples analyses, which are expected in the coming months.

## IV.4. Tsagaan Gol Fault

### *IV.4.1. Tsagaan Gol Fault surface ruptures*

The Tsagaan Gol fault (TGF) corresponds to the western prolongation of the VOLF, beyond the Burhan Buudai restraining bend (Figure 4-7). The fault is clearly controlled by an ancient fabrics associated to inherited faults or main lithological contacts, and can be subdivided into 5 main segments, all along a succession of deep axial valleys (Figure 4-96).

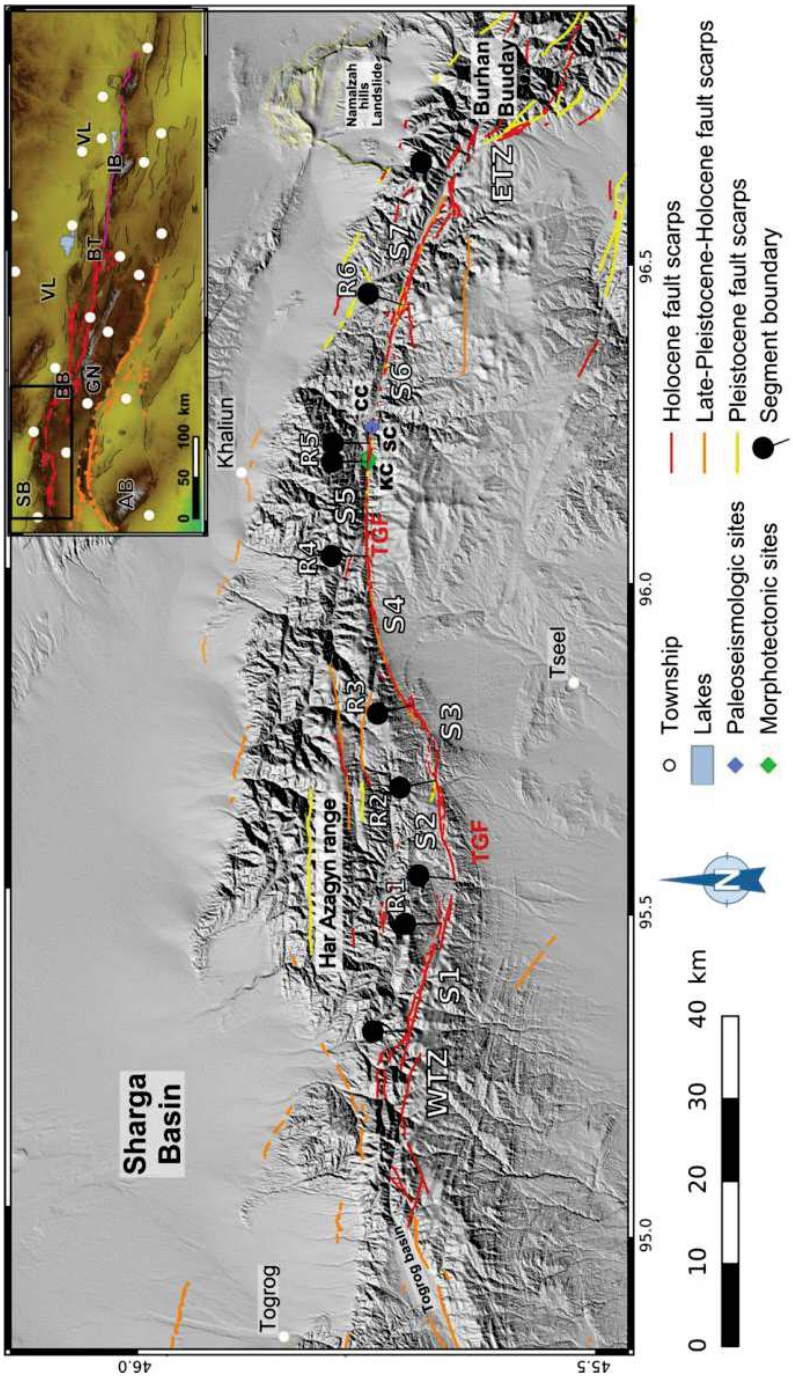


**Figure 4-96: Segmentation of the Tsagaan Gol Fault (TGF). Sites abbreviations: KC: Kurilik Creek, SC: Schist Creek; CC: Camel Creek. Background is a hill-shading of the SRTM Topographic dataset. Insert abbreviations: SB: Sharga Basin; BB: Burhan Buuday; VL: Valley of Lakes; GN: Gichigniy Nuruu; BT: Bayan Tsagaan; IB: Ih Bogd; AB: Aj Bogd.**

As for main surface ruptures previously described, the TGF is detailed from west to east, following the segmentation (Figure 4-96). The TGF western tip zone is located immediately west of coordinates 45.720°N; 95.305°E, and corresponds to the north-westernmost part of the Gobi-Altai mountain range, in the Har Azagyn range area, which links the southernmost edge of the Sharga Basin, the easternmost part of the Togrog pull apart basin, and to the end of the Tsagaan Gol fault (Figure 4-97). This area displays a complex fault network, with faults of various kinematics, notably two sets of oblique left-lateral faults: a main one trending N102 ± 5°E is associated to a reverse component, and a second one, trending N060 ± 5°E, is associated to a normal motion. Those faults join on the southernmost edge of the Sharga basin to the Togrog basin (Figure 4-97). Additionally, some reverse fault scarps trending N120 ± 20°E are visible in the southernmost part of the Sharga Basin. Northwestwards, 30 km northwest from the TGF western tip zone, others active thrust fault scarps have been documented within the southern part of the Sharga Basin (i.e. Cunningham, 2013).

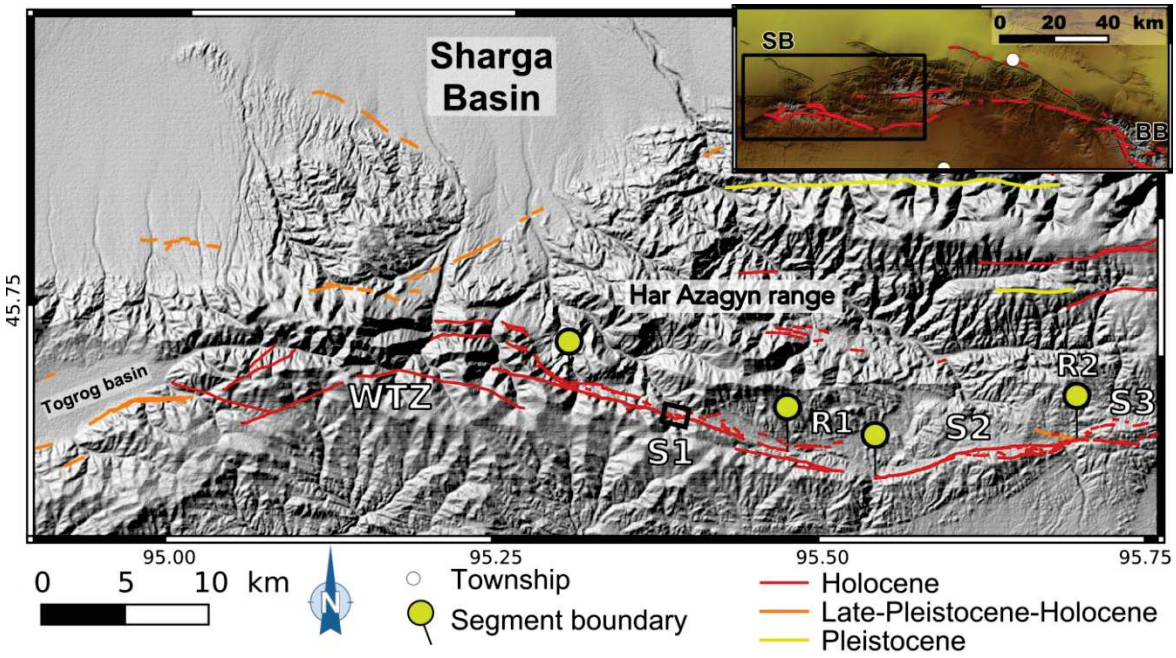


**Figure 4-97: Fault surface ruptures and segmentation along the western part of the TGF. Black solid box indicates the location of Figure 4-98. Insert abbreviations: BB: Burhan Buuday; VL: Valley of Lakes. WTZ: proposed Western Top Zone of the TGF.**

TGF-S1 segment trends N103 ± 5°E and displays a rather distributed fault pattern. It displays two collinear scarps, distant of 200 m to 1 km from each other, standing along the axial valley (Figure 4-97). The southern scarp is a very continuous oblique thrust, and is bounds by the north the mountain flank, in which few cracks can be distinguished as well as 100 m high triangular facets. Those facets are likely related to the uplift of the hanging wall, south of the fault, as we estimate the dipping of the thrust to ~30° to the

south on the intersection with a major drain on 45.705°N; 95.390°E (Figure 4-98). Instead, the northern scarp is more discontinuous, displays numerous tension cracks, and is strongly associated to lithological structuration.

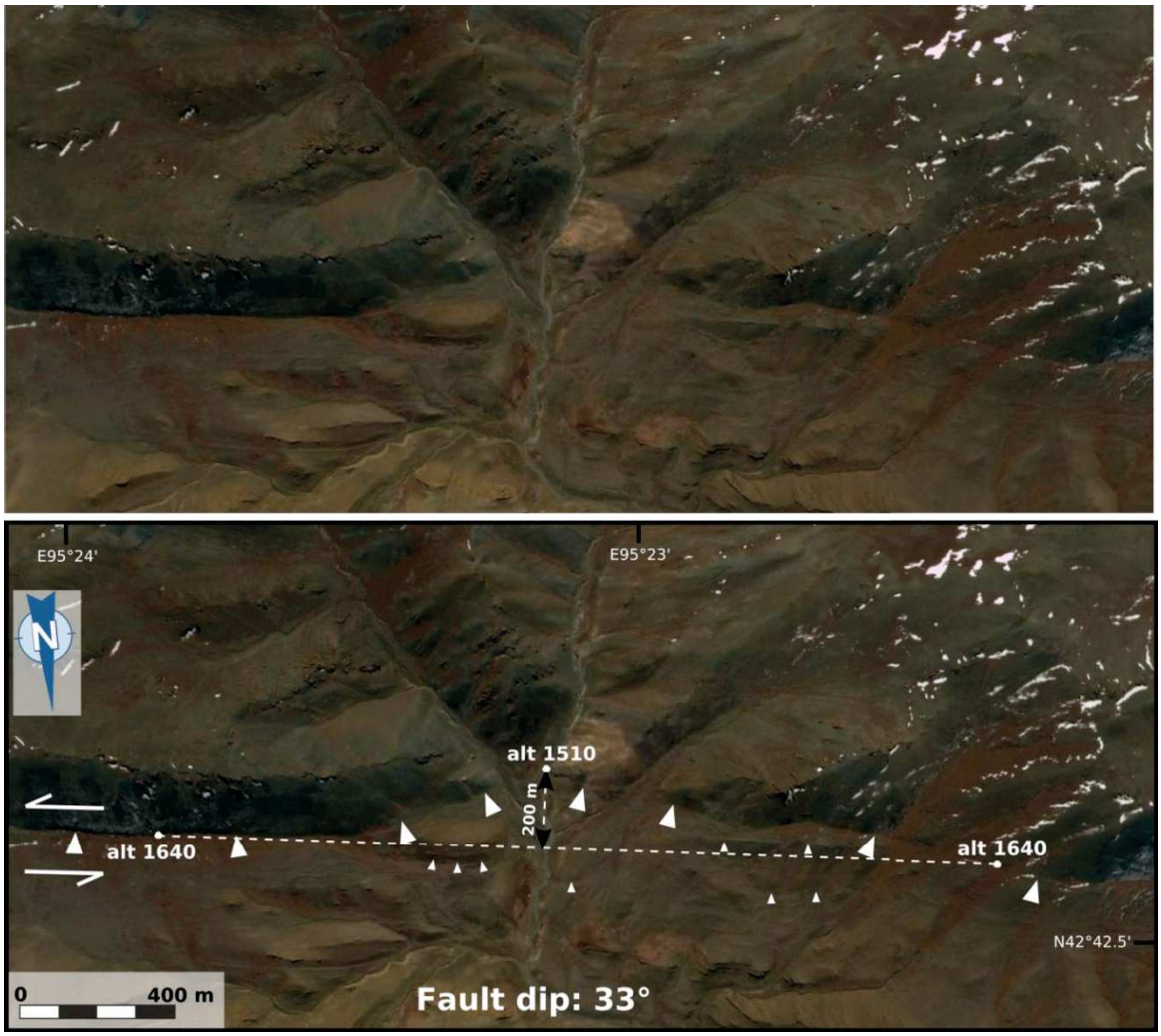


**Figure 4-98: Dipping measurement along a section of the TGF. See location on Figure 4-97. White arrows indicate the TGF traces. Fault dip is calculated from the ratio distance to elevation on the central part of the figure.**

The 5 km-long TGF-R1 relay zone starts on 45.692°N; 95.473°E, which is both the place of a strongly distributed deformation in bedrock on a 1 km wide band and of a branching with a 3 km-long secondary scarp, trending N090 ± 5°E (Figure 4-97). Note that 7 km northward is a minor 5 km-long intra-mountainous basin (Figure 4-97), oriented E-W and bounded by active fault scarps, which have been documented by Baljinnyam et al. (1993), as minor Holocene-active scarps: the Hujirtyn rupture. Eastward, the TGF-R1 stops on 45.678°N; 95.542°E, where the fault shifts to the north, from the N100 ± 5°E average trend along the main scarps composing TGF-R1, to N080 ± 5°E on the western part of TGF-S2 (Figure 4-97).

The TGF-S2 is a 12 km-long segment, trending N075°E in average, with its western half curved to the north from N080°E to N070°E, and a straighter eastern part, oriented N084°E (Figure 4-97). The fault trace along TGF-S2 is discontinuous, located into bedrock (Figure 4-97), and on the central part, when the azimuth changes, it splits into two branches ~ 500 m apart. Those two branches seem to fit with contours of a lens of yellowish magmatic bedrock, sheared between metasedimentary terrains.

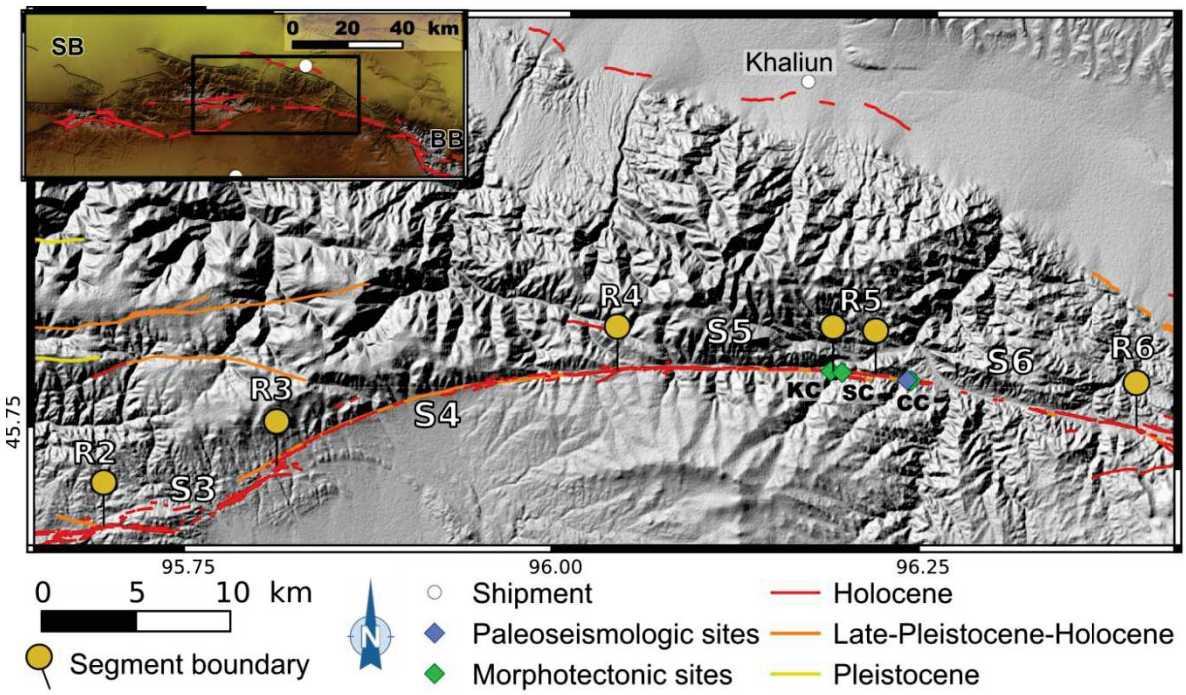


**Figure 4-99: Fault surface ruptures and segmentation along the central part of the TGF. Field sites abbreviations: Insert abbreviations: KC: Kurilik Creek, SC: Schist Creek; CC: Camel Creek. Insert abbreviation: BB: Burhan Buuday; VL: Valley of Lakes.**

The TGF-R2 junction with TGF-S3 is situated on 45.700°N; 95.695°E, which is the place of conjugated faulting between 5 branches: to the west, the main one corresponds to the northern branch of the eastern part of TGF-S2, trending N084°E; a second branch is the southern branch of TGF-S2, oriented N065°E with a discontinuous tension gashes fault pattern; a third branch comes from N-NW, about 2.5 km-long and trending N100 ± 5°E; to the East, the main fault trace trends N090 ± 5°E, and a last curved branch strikes N060 ± 15°E (Figure 4-97). These branches, distant by ~ 1 km, compose the 10 km-long TGF-S3, which is sigmoid shaped, fitting a sheared portion of metamorphosed rocks. Given its blue color on satellite images, it recalls the terrains outcropping north of the TGF, and probably to the Tseel terrane located south of the TGF (Figure 1-15). Two noticeable other faults may be identified within the bedrock, 10 km north of this segment (Figure 4-99); they are respectively 10 and 20 km-long, trend N080 ± 20°E, and despite of quaternary deposits, the fault traces appear well expressed in the morphology, due to

differential erosion and lots of talwegs left-laterally offset. However, no obvious large cumulative offset can be identified along those secondary fault traces, and we cannot exclude the possibility that they might be inherited structures. Eventually, one may notice that they are situated on the fault zone constituting the contact between Gobi-Altai terrane to the South, and the ‘’*Lake domain*’’ north of the fault (Hanžl et al., 2017), and that some relicts of the peneplain can be found just north of those structures.

The next relay zone TGF-R3 (45.737°N; 95.812°E) consists of a ~500 m-wide, ~4 km-long deformation band, located into bedrock as attested by a central sigmoid-shaped yellowish outcrop, which is sheared by fault cracks and dragged into the fault (Figure 4-99). North-east of the jog, the presence of shallow quaternary deposits affected by the fault is likely related to significant vertical fault motion within the relay zone.

Along the 19 km-long TGF-S4 segment, the TGF describes a regular south-curved shape, from N060°E on its western part to N084°E on its eastern part (Figure 4-99). The fault pattern appears discontinuous, with a fault trace located within the bedrock on the western part of the segment, and then bounding the axial valley and affecting alluvial terraces on the eastern part. After the geological map (Hanžl et al., 2017), the central part of this segment corresponds to a strong change in the lithology southwards of the fault, from the metasedimentary Tseel Terrane, to the Gobi-Altai terrane.

The TGF-R4 relay zone (45.787°N; 96.040°E) corresponds both to a branching with a short N060°E, ~1 km-long fault south of the main trace, and to an interruption of the curvy shape of the fault, as the next segment TGF-S5 is rather straight, 11 km-long, and trends N088 ± 5°E (Figure 4-99). The fault trace is discontinuous along this segment, following either the foothills of the north-facing mountains and hidden bellow thick alluvial and colluvial deposits, or following alluvial terraces risers related to the Tsagaan Gol River, which runs in the axial valley. Because of the snow cover on satellite images, only a partial mapping has been performed along this segment.

Further East, the TGF-R5 relay zone is 2.4 km-long, and displays two fault scarps that branch westernmost of the jog, on 45.790°N; 96.190°N: the main scarp, to the North, is discontinuous and trends N090 ± 10°E; the second one toward the south, trends N100 ± 10°E along the mountain flank, and shows a right stepping rupture pattern (Figure 4-99). This point corresponds also to a northward shift of the Tsgaan Gol River that leaves the axial valley to join the Valley of Lakes. Eastward, although there is no active drainage, the axial valley remains visible, attesting of its structural origin. On the western part of the TGF-R5 relay, two levels of alluvial surfaces are incised by sinuous gullies, which

present systematic left-lateral offsets at the intersection with the fault trace (Figure 4-100–B and D. We investigated two sites (i.e. the Kurulik site and the Schist Creek site, Figure 4-99, Figure 4-100), in order to both estimate the coseismic displacements produce on the TGF, and to constrain its long term slip-rate. These analyses are detailed in the next two sections of this chapter (IV.4.2.1 and IV.4.2.3). The fault here exhibits strong cataclastic processes and gouge along the main fault trace, where offsets are observed Figure 4-100–D, E and F). One may eventually note that this relay zone in located only 15 km south of Khaliun town, and by the way to the namesake fault, which display recent faulting in fans (Figure 4-99).

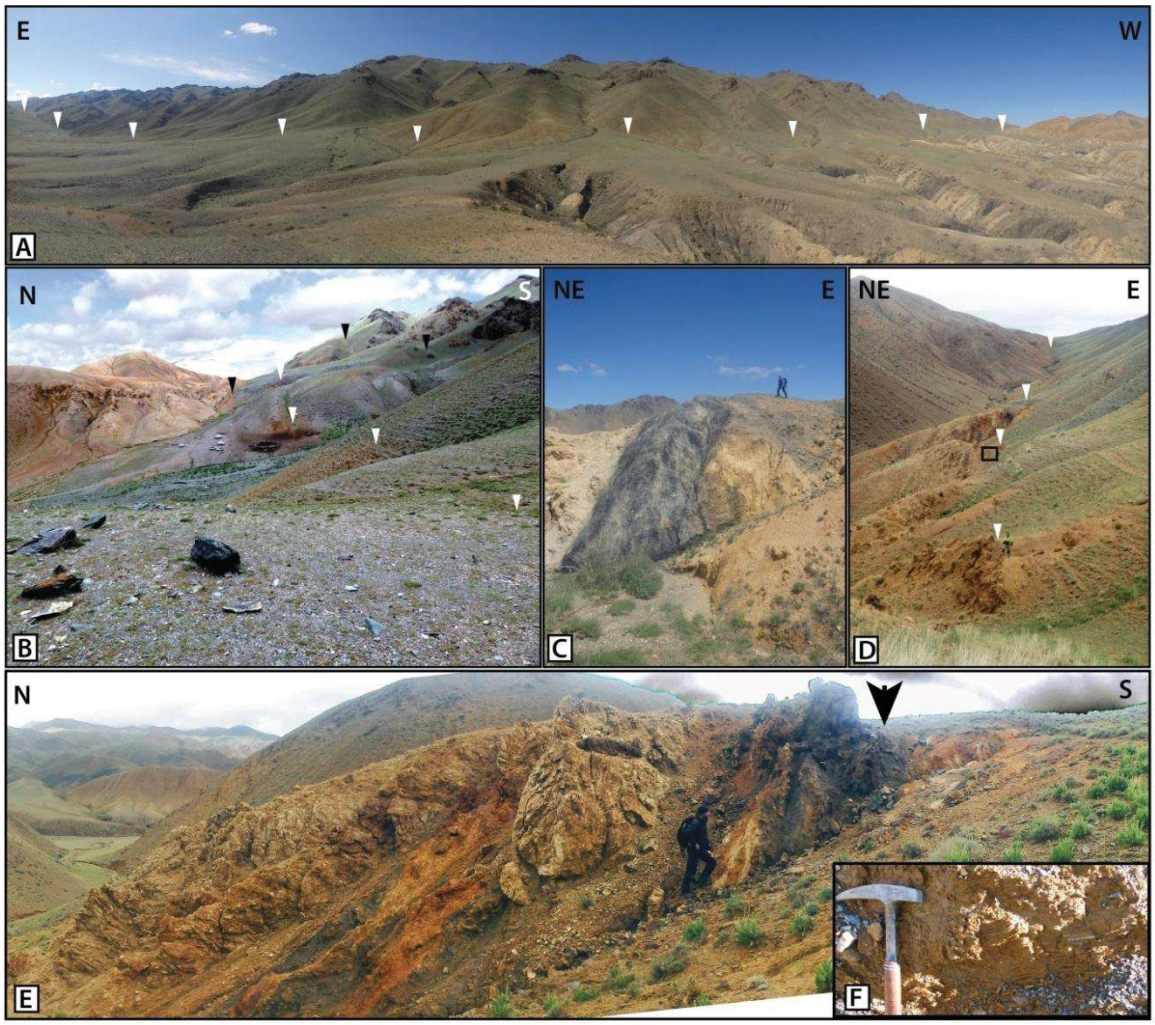


**Figure 4-100: Photographs of fault surfaces ruptures along the TGF (segments TGF-S5 and TGF-S6). White arrows indicate the fault traces. A. Panorama to the South of the TGF, west of the Camel Creek site. The fault here systematically offsets alluvial fans with a mostly left-lateral motion. Mountain front is ~300 m-high. B. Photograph to the East of the TGF trace. The terrace on the background is the Schist Creel terrace. See yurts and cars for scale. Black arrows indicate secondary faults, less expressed in the morphology than the main fault trace indicated by white arrows. See picture location on Figure 4-104. C. Photograph to the south of the damage zone related to the TGF, east of Camel Creek site. D. Photograph to the East of the TGF trace West of Schist Creek site. See character on the foreground for scale. Black solid box is location of photograph *F*. E. Photograph to the east of the TGF damage zone West of Schist Creek site. Black arrow indicates the location of the TGF main trace. F. Photograph of detail of reddish gouge. See location in D.**

The TGF-S6 segment trends N100 ± 3°E and appears rather straight. Along its central part, the segment follows the 200 m-deep axial valley (Figure 4-102), where the fault trace corresponds to the active river bed. Only the extremities of this segment were mapped, where evidences of faulted late Pleistocene alluvial features with numerous left-lateral offset talwegs are observed (Figure 4-100–A). The fault is here again associated with a large damage band, characterized by cataclastic processes, and dark and reddish strong gouges development (Figure 4-100–C). We carried out, a morphotectonics analysis within the westernmost section of this segment, in Camel Creeks site, in order to assess the long term horizontal slip rate along the TGF (Figure 4-102). Results of this analysis are detailed in the next parts of this chapter (IV.4.2.1).

At a larger scale, three major rivers are flooding northward, orthogonally to the TGF fault (Figure 4-101-A). A reconstruction of landforms allows estimating a cumulative left-lateral offset of 1.9 ± 0.2 km (Figure 4-101-B). Given the $mm.yr^{-1}$ slip rates determined along the faults in the Gobi-Altai and Altai mountain ranges, these kilometer scale cumulative offsets attest of the long-term activity of the TGF, during Quaternary time.

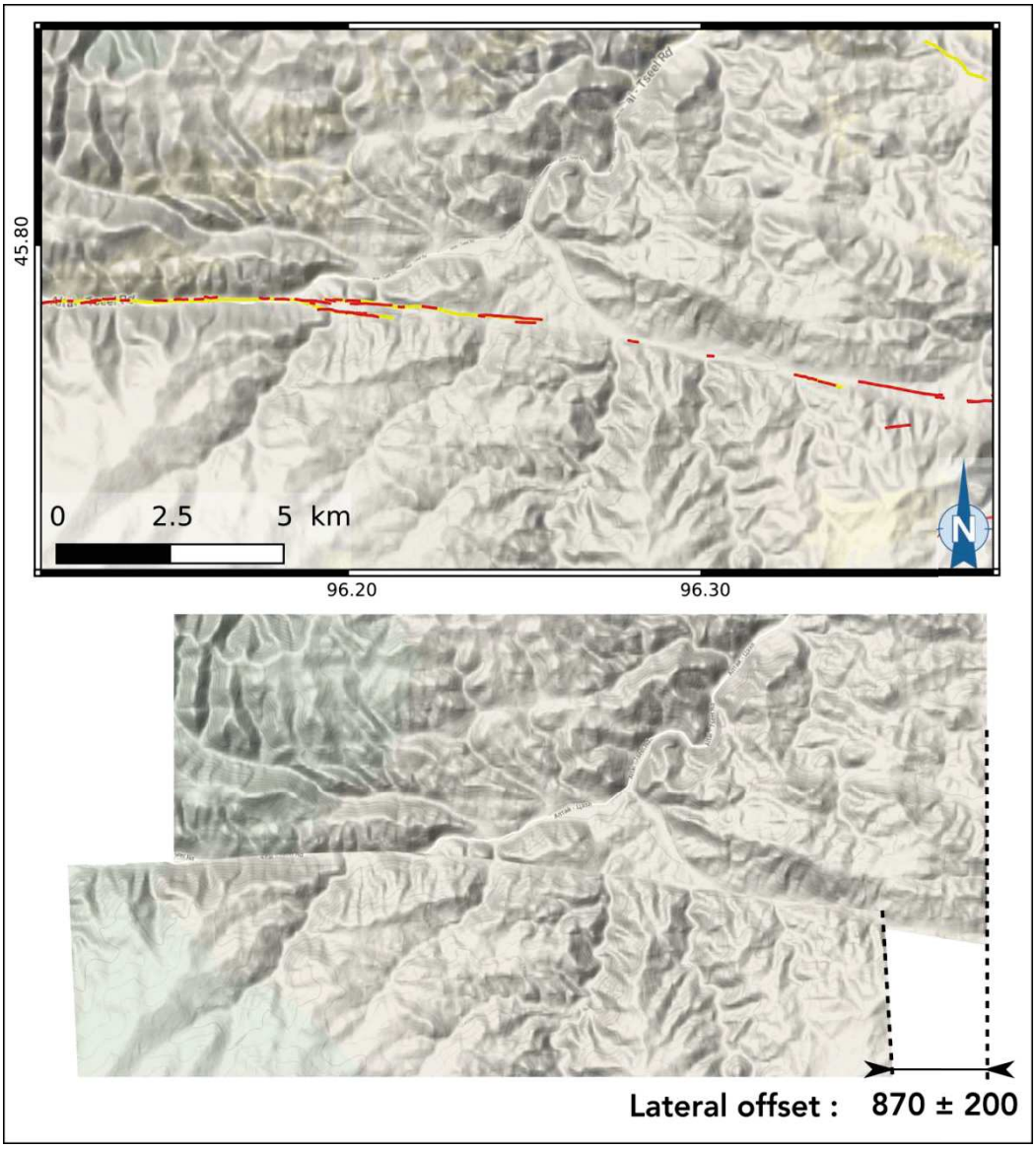


**Figure 4-101: A. Topographic map of a central section of the TGF (segments TGF-S5 and TGF-S6). Red solid lines are fault trace affecting Holocene deposits, and yellow lines fault traces. Background is Google-maps relief data. B. Cumulative offset measurement, by lateral retrofit of the main drainages, yields a displacement of 870 ± 200 m.**

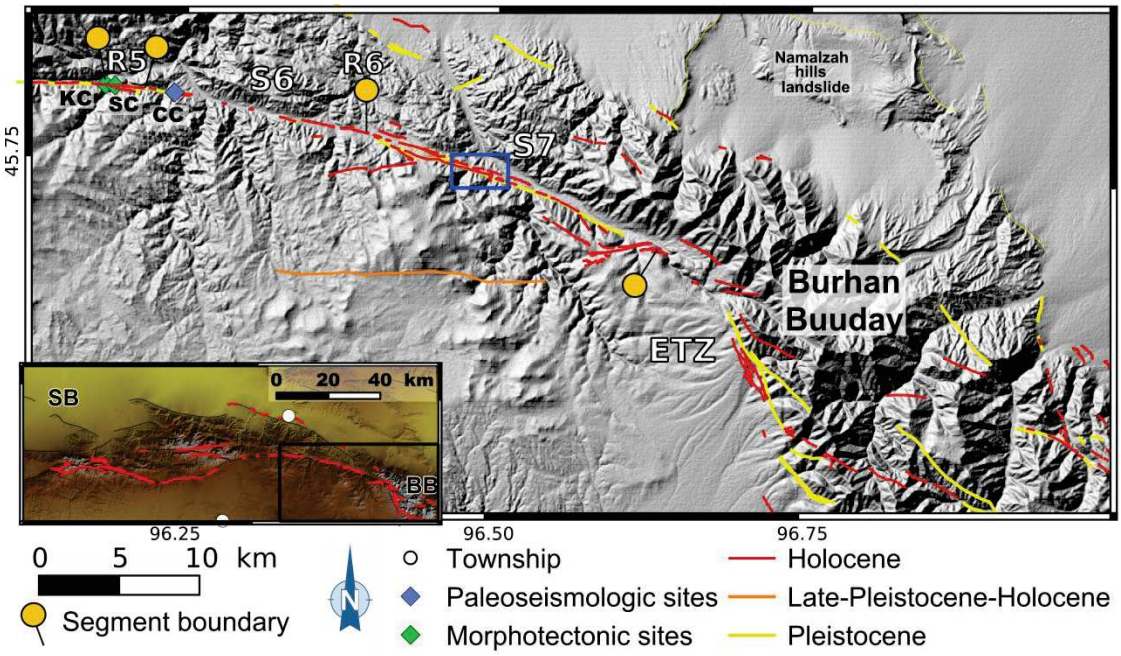


**Figure 4-102: Fault surface ruptures and segmentation along the eastern part of the TGF. Blue box is location of Figure 4-103. Field sites abbreviations: Insert abbreviations: KC: Kurilik Creek, SC: Schist Creek; CC: Camel Creek. Insert abbreviation: BB: Burhan Buuday; VL: Valley of Lakes. ETZ: proposed Eastern Tip Zone of the TGF.**

The next relay zone, TGF-R6, located at 45.770°N; 96.400°E, is related to a significant change in the strike and fault pattern, with localized deformations westwards along TGF-S6, and in the contrary distributed deformations eastwards along the 10 km-long TGF-S7. This last segment runs on a 500 m to 1 km-wide elongated Quaternary depression, oriented N110°E and sloping to the north (Figure 4-102). Two continuous fault scarps are bonding the basin, and display systematic lateral offsets along the northern branch, while the southern looks related to a north-dipping fault, showing normal dip-slip motion as attested by stream incisions within the southern footwall compartment (Figure 4-103).

East of 45.735°N; 96.539°E, we find the eastern tip zone of the TGF, characterized by a very distributed fault pattern (Figure 4-102) and variable kinematics: i. normal motion south of the axial valley in the 8 first kilometers, associated to a kilometer scale landslide as attested by crown scarps on top of the southern flank of the valley; ii. strike slip motion north of the axial valley, as the TGF branches to the Burkhan Buudai structures on the next 5 kilometers, and finally shifts toward the south, bounding southwestward the Burkhan Buudai. The fault are here dipping north with a clear thrust motion on a complex surface rupture, which visibly affect late-quaternary alluvial surfaces, for instance on 45.640°N; 96.710°E.

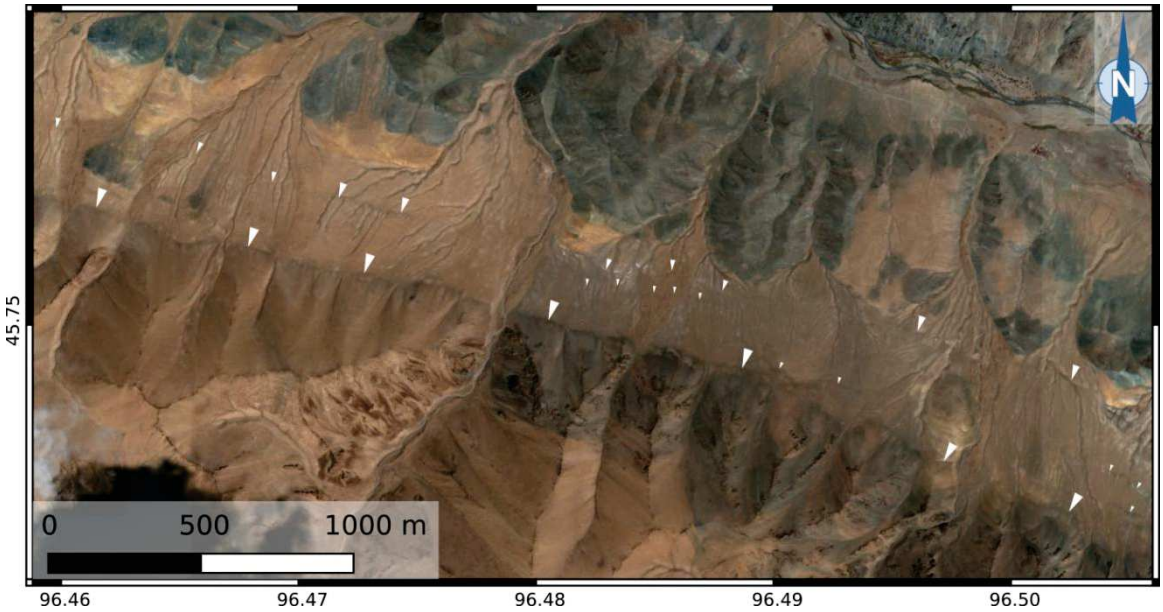


**Figure 4-103: Detailed map of the quaternary basin along segment TGF-S6. Note the shallow slip partitioning, with normal scarp on south and strike slip scarp on center of the basin. See location on Figure 4-102.**

The whole TGF surface rupture appears rather homogeneous, displaying an almost continuous fault trace which visibly affects Holocene geomorphic features. According to our mapping, the total fault length is at least 125 km (Figure 4-96).

### *IV.4.2. Morphotectonic field reconnaissance along the TGF*

#### IV.4.2.1. Kurilik Creek site

The Kurilik Creek site is located at 45.790°N; 96.185°E, within the easternmost section of the TGF-S5 segment. It corresponds to a small 300 m-long watershed southwards the TGF fault, flooding northward (on West of Figure 4-104). The lower part corresponds to a talweg (the '*southern talweg'*) that interrupts on the fault, while its beheaded part is found a few tens of meters westwards along the fault trace (Figure 4-105). At the contact between the southern talweg and the fault scarp, a little offset (meter scale) is materialized within the risers of the active channel (Figure 4-104). Three fan surfaces may be identified on this site: F0, F1 and F2. F2 is the uppermost surface, and correspond to the top of the hill situated to the northeast. F1 is the main mid-slope surface in which the offset talweg is observed (Figure 4-105). A small fan, F0, is associated with the southern talweg (figure).

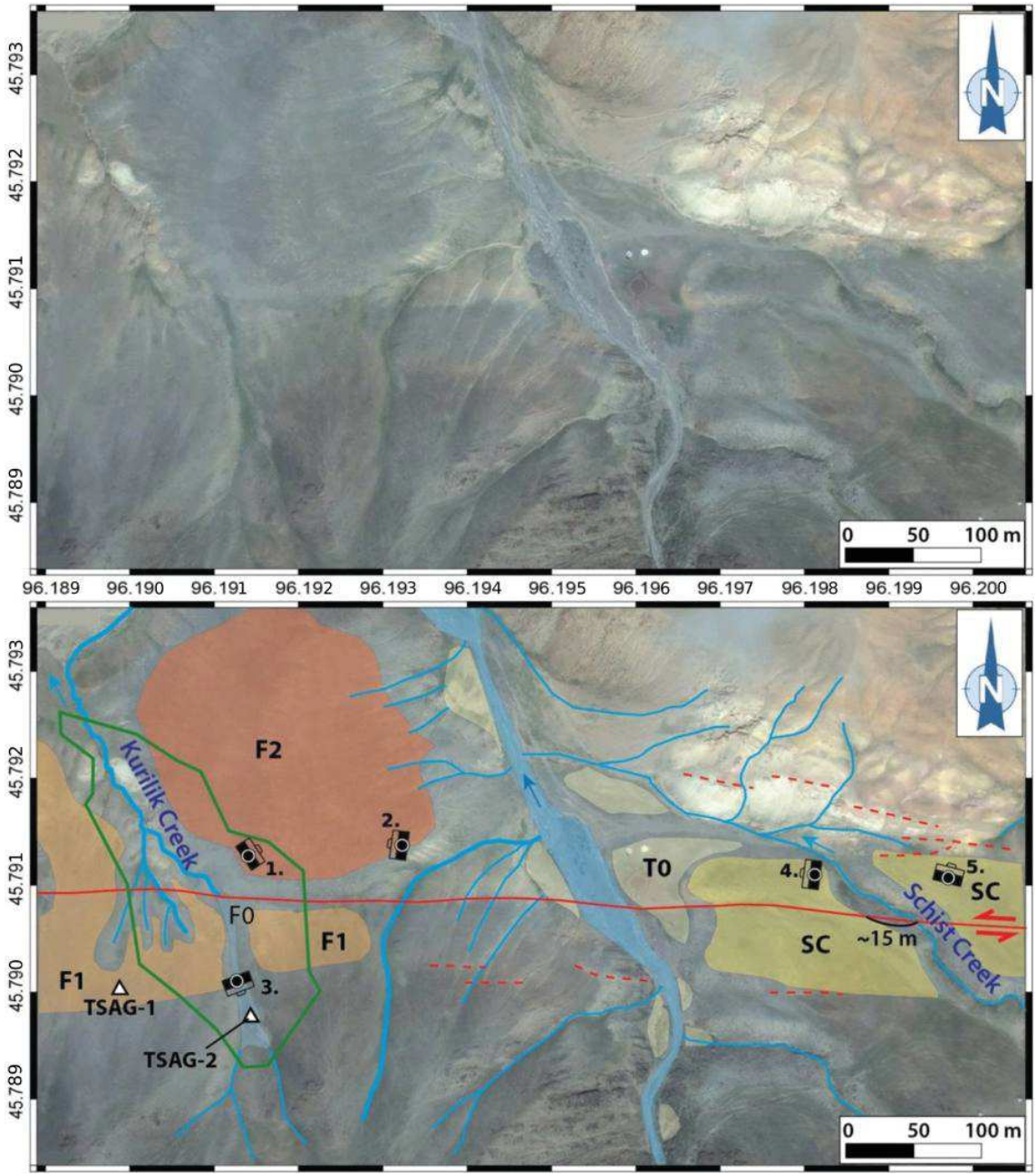


**Figure 4-104: Context map of the Kurilik and Schist Creeks sites. Background is Bing satellite image (July 2011). Shaded areas are identified geomorphic surfaces, and blue solid lines are temporary drainages. Green solid line indicates the location of the microtopographic survey. White triangles are locations of $^{10}$Be sampling. Cameras are locations of figures: 1. Figure 4-105-A, 2. Figure 4-100-B, 3. Figure 4-105-B, 4. and 5. Figure 4-114-A and B respectively.**

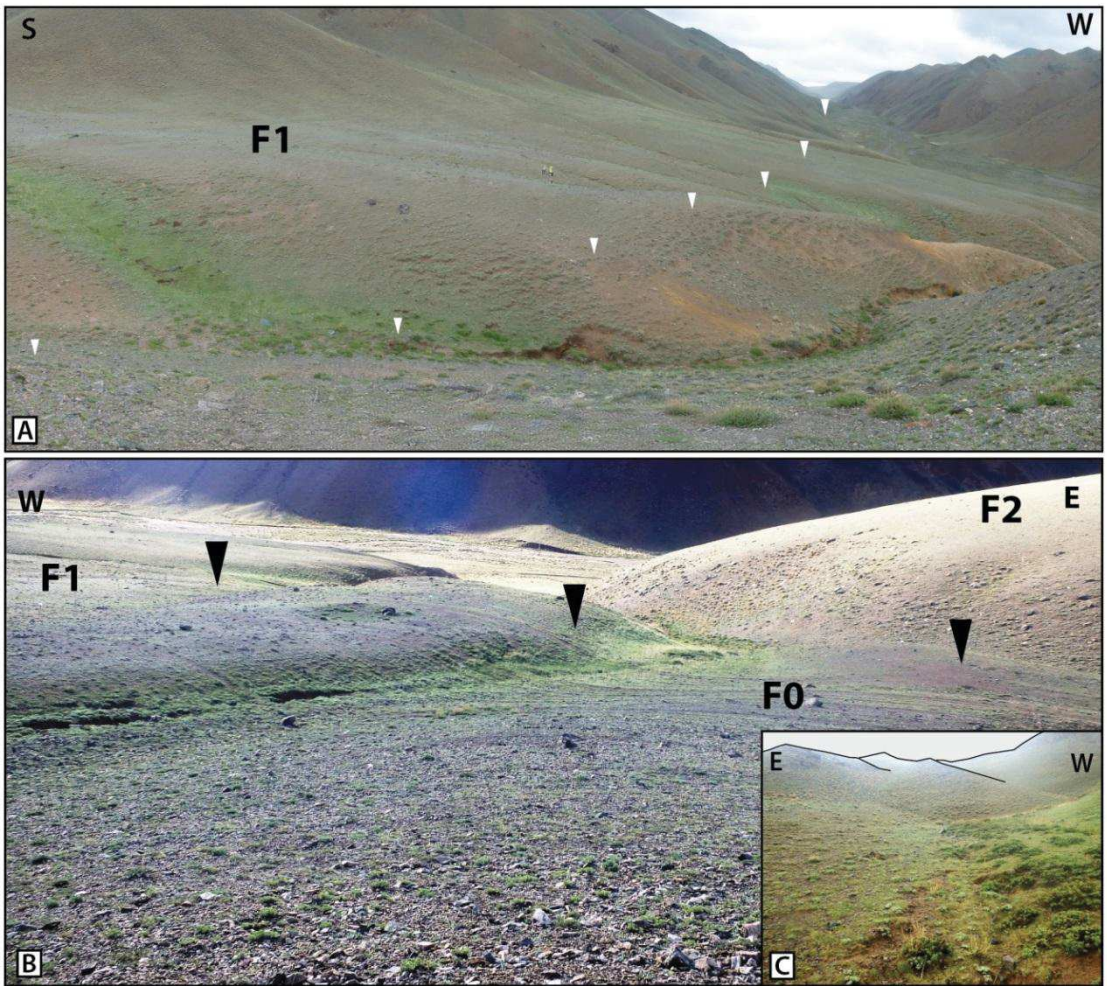


**Figure 4-105: Photographs of the Kurilik Creek site. See location of pictures in Figure 4-104. A. Panorama to the West showing the northern part of the active Kurilik Creek (foreground), and the F1 surface. White arrows indicate the fault trace. See person for scale. B. Photograph to the North of the Southern Talweg crossing the surface F1, with a more recent fan F0 close to the fault. Black arrows indicate the fault trace. C. Photograph to the South of the Southern Talweg. The sampling of TSAG-2 has been done in the active channel on foreground. Location of the picture is shown in Figure 4-106.**

In order to determine the slip rate along the TGF, we carried out a microtopographic survey using TLS to measure the displacement associated with the beheaded talweg, and we sampled F1 surface to estimate its abandon age (Figure 4-105–A). Figure 4-106 depicts the offset measurement by 3-step retrofit of the southern talweg, to fit with the eastern part of the beheaded channel, as this section of the northern talweg is the steepest of the landform, and hence it visibly corresponds to the past-outlet of the southern talweg. Measurements lead to a cumulative left-lateral offset of 61 ± 5 m. We note that two other channels, located few hundred meters west of the Kurilik creek, display the same amount of displacement (Figure 4.107).

We also collected an amalgam (TSAG-1) of analog-size clasts from quartz-rich cobbles embedded in F1 surface (for estimating the accumulated surface $^{10}$Be concentration

corresponding to the sum of the $^{10}$Be that was already contained in the surface cobbles due to inheritance processes, and the $^{10}$Be that was produced since the abandonment of the surface). Another amalgam (TSAG-2) of same size clasts also sampled from quartz-rich cobbles, was collected in the southern talweg present stream bed, see Figure 4-105-C (for estimating the mean $^{10}$Be inherited concentration associated with drainage transport and pre-exposure within the studied site) (Figure 4-104).

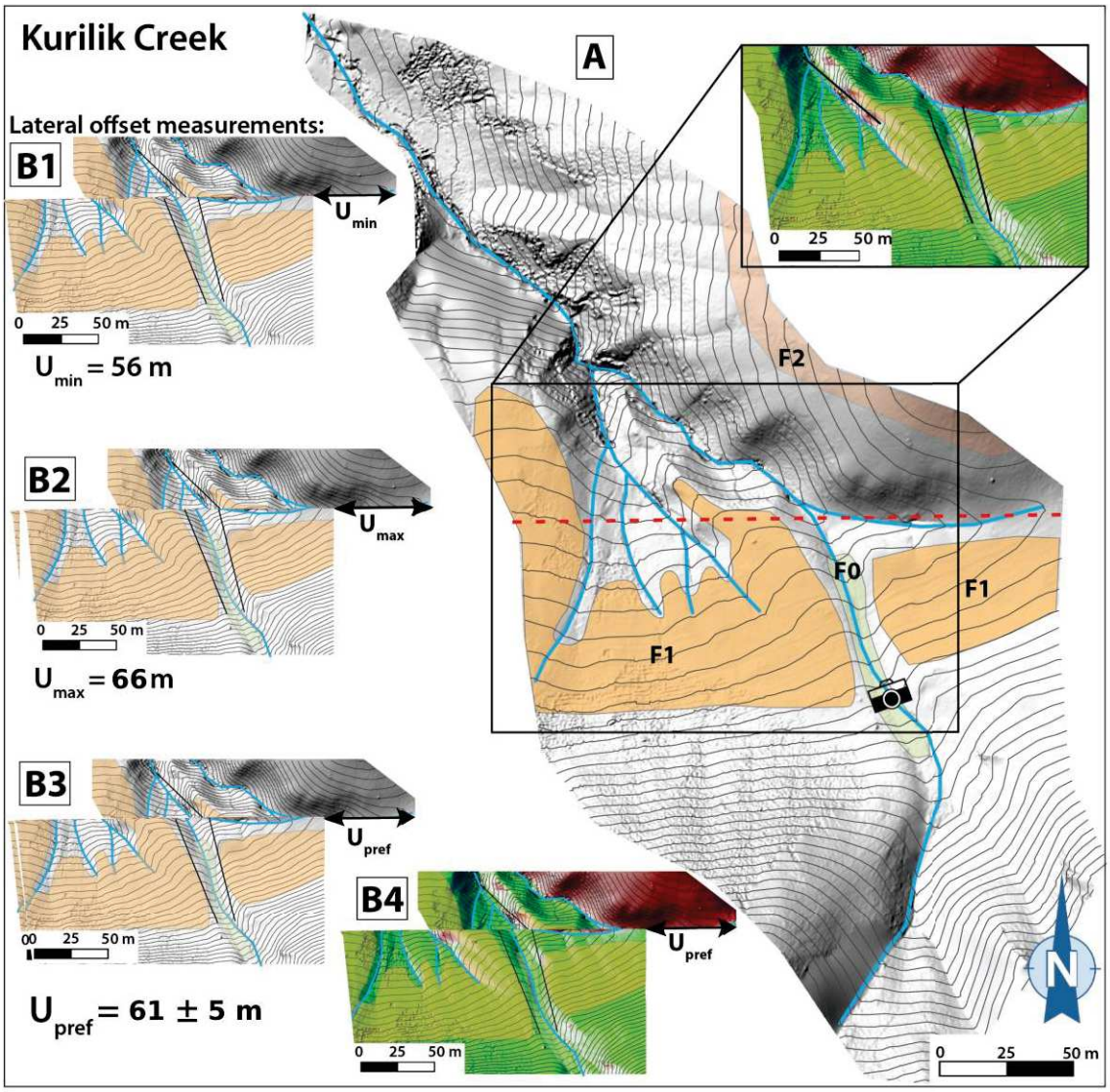


**Figure 4-106: DEM from TSL microtopographic survey in Kurilik Creek site. A. Whole survey of the Kurilik Creek. Shaded areas are identified surfaces and blue solid lines are temporary drainage. Inset in slope direction shader, which allows good definitions of the piercing lines, represented by black solid lines. Camera is location of the Figure 4-105-C. B. Lateral offset measurement of the Kurilik Creek by 3-steps retrofit of the talweg: B1. Maximum offset value; B2: Minimum offset value; B3: preferred offset value on DEM; B4: Preferred offset value on slope direction shader.**

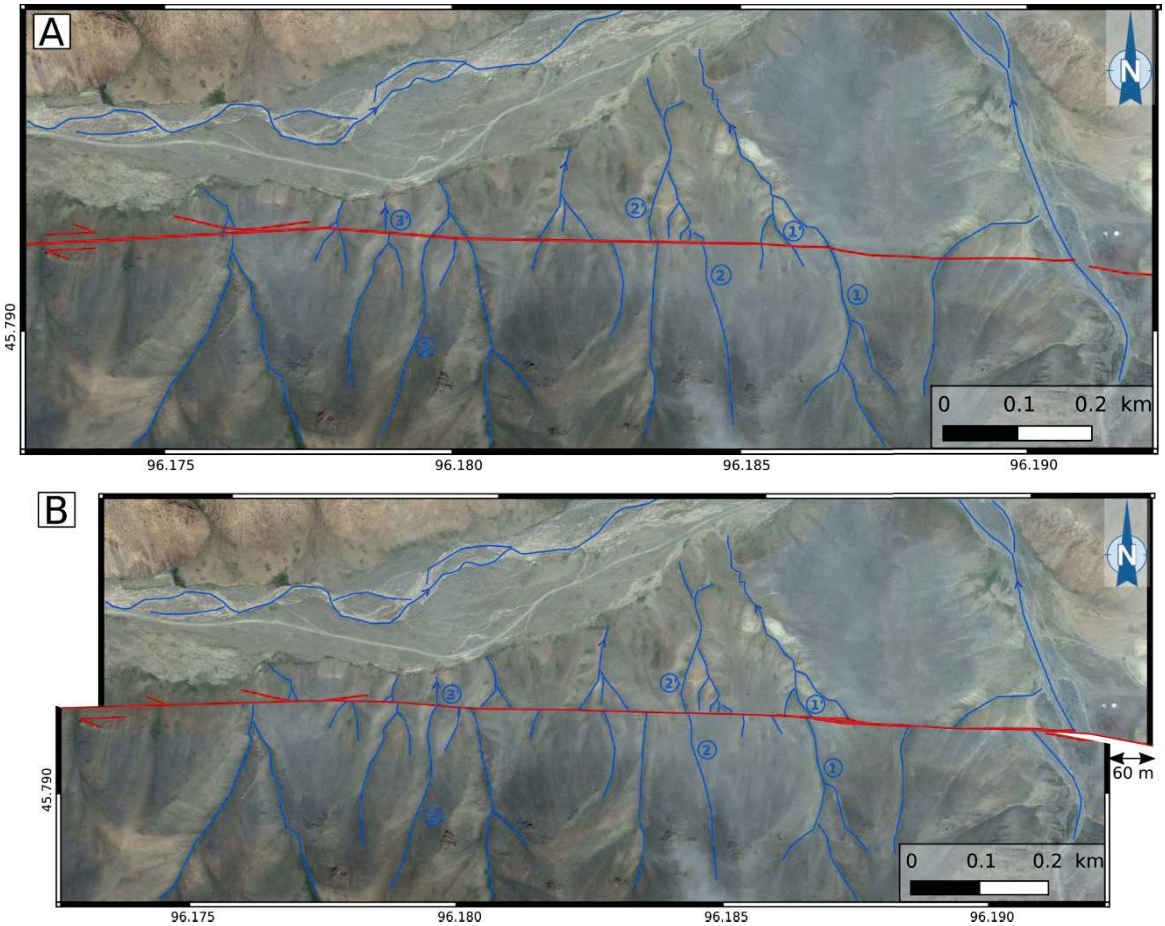


**Figure 4.107: A. Map of the TGF, west of Kurilik Creek (here marked as drain number 1). Blue lines are main drains, and red line is the TGF. Number in blue indicate the channel witch match for an offset of 60 m. B. Reconstruction for an left lateral offset of 60 m.**

Analysis of the $^{10}$Be samples yield the concentrations presented in Table 12, and allow proposing the following ages for the abandonment of F1: i. assuming a zero-erosion and the inheritance given by the *TSAG-2* amalgam sample, a minimum abandon age of 14.4 ± 0.9 ka; ii. assuming a steady state, an erosion rate of 17.4 ± 2.5 m.Myr-$^{1}$, associated to an integration age of 36.1 ± 1.1 ka; iii. assuming the most conservative calculation, by neglecting both the erosion rate and the inheritance, a maximal abandon age of 47.9 ± 1.5 ka.

**Table 12: The $^{10}$Be nucleide concentrations and modeled ages for samples at Kurilik and Creek sites, along the TGF. The sample TSAG-6, in grey, has been discarded due to high 10Be content (see text).**

| Sample | Lat (dec°) | Lon (dec°) | Alt (m) | [10Be] (at.g$^{-1}$) | err. [10Be] 1σ (at.g$^{-1}$) | Shield Cor. | Density | Depth (cm) | 10Be age tmin (ka) | 10Be age tint (ka) | Erosion rate (m.Ma$^{-1}$) | 10Be age tmax (ka) |
|---|---|---|---|---|---|---|---|---|---|---|---|---|
| TSAG-1 | 45.790 | 96.185 | 2140 | 1.07E+06 | 3.32E+04 | 0.997 | 2.0 | 0 | 14.4 ± 0.9 | 36.1 ± 1.1 | 17.4 ± 1.0 | 47.9 ± 1.5 |
| TSAG-2 | 45.790 | 96.185 | 2140 | 7.50E+05 | 2.44E+04 | 0.997 | 2.0 | 0 | | | | |
| TSAG-3 | 45.787 | 96.242 | 2110 | 1.01E+06 | 3.13E+04 | 0.997 | 2.0 | 0 | 18.3 ± 1.1 | 34.6 ± 1.0 | 18.2 ± 1.1 | 46.0 ± 2.7 |
| TSAG-4 | 45.787 | 96.242 | 2110 | 6.09E+05 | 3.12E+04 | 0.997 | 2.0 | 0 | | | | |
| TSAG-6 | 45.787 | 96.242 | 2110 | 1.11E+06 | 3.46E+04 | 0.997 | 2.0 | 0 | | | | |

Those ages appear rather distributed, and once again the assumption of zero-inheritance is necessary untrue. This age however give an upper bound for the abandon age of the F1, and hence yield a minimum value of the slip rate.

According to those dating, this reconnaissance on Kurilik site allows us constraining the slip-rate along the TGF between at least 1.3 ± 0.2 mm.yr$^{-1}$, 1.7 ± 0.2 mm.yr$^{-1}$ and at most 4.2 ± 1.0 mm.yr$^{-1}$ on the Holocene to the late-Pleistocene (15, 20 and 50 ka, respectively).

Those estimations of the slip rate in Kurilik Creek site have low constrains, because of large uncertainties both on the offset and on the abandon age of the geomorphic surface. Those values might be overestimated, because although the lower end-number (1.1 mm.yr$^{-1}$) is same order of magnitude that the slip rates along the EBF, the higher end-number (5.68 mm.yr$^{-1}$) is visibly erroneous, as it is largely over the slip rates determined along the Bogd Fault System (e.g. Ritz et al., 1995, 2006; Vassallo et al., 2007; Rizza et al., 2011). This result (which assures a zero-erosion) may therefore be discarded in spite of coherence with other slip rates estimated in the Gobi-Altai.

### IV.4.2.2. Camel Creek site

#### *IV.4.2.2.1. Fault slip rate*

The Camel Creek site, located at 45.788°N; 96.243°E, corresponds to N-NE flooding gullies and talwegs, incising late-Pleistocene alluvial terraces, and showing left-lateral offsets at their intersections with the TGF (Figure 4-108 and Figure 4-109). At this site, the surface rupture is well localized and presence of systematically offset features attest of a mostly left-lateral displacement. A minor vertical component is observed, through an uplift of the compartment situated north of the fault (Figure 4-109). This minor uplift of the northern block might however be significant as it remains visible while the drainage is slightly oriented to the northeast –and hence potentially generating apparent uplift south of the fault in the case of pure strike slip motion.

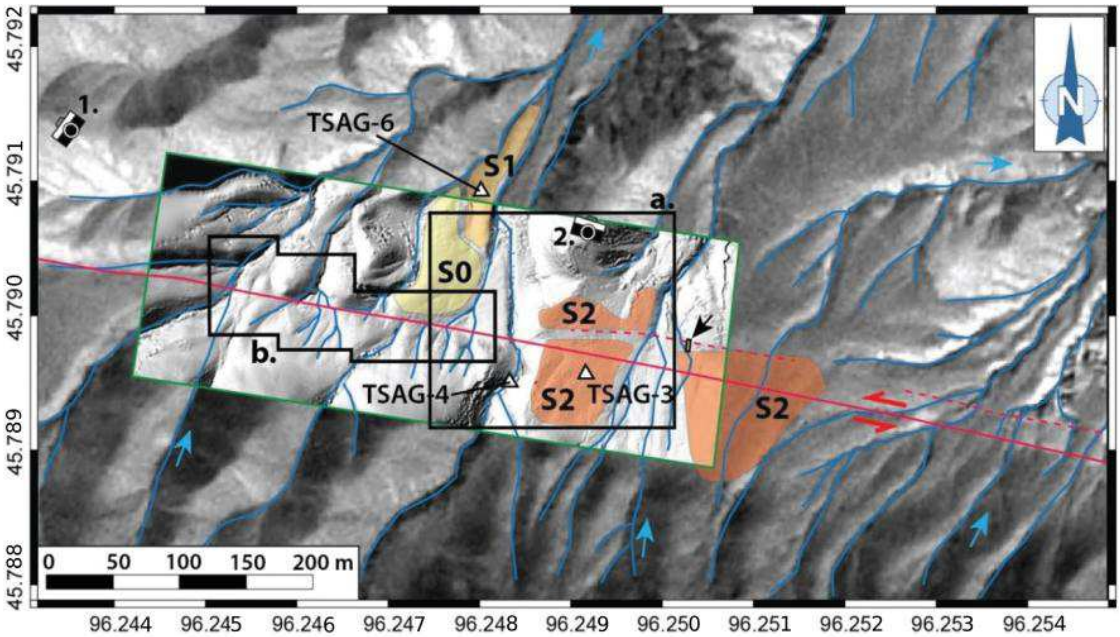


**Figure 4-108: Morphotectonic map of the Camel Creek site. Background is SPOT 6 satellite image. Shaded areas are identified geomorphic surfaces, and blue solid lines are temporary drainages. Green box is TLS-derived hill-shaded DEM. White triangles are locations of $^{10}$Be sampling. Black solid boxes are location of: a. Figure 4-111, b. Figure 4-112.Cameras are locations of pictures in: 1. Figure 4-109-A and 2. Figure 4-110-C.**

Two main fan surfaces can be identified: S1 and S2. The higher S2 terrace is the older and shows an offset riser (Figure 4-109 and Figure 4-110-C), which displays a cumulative left-lateral offset, detailed ahead. This surface display significant denudation, mostly related to deflation, which is highlighted by a strong difference surficial weathering, on lower parts of the boulders enchased in the surface (see Figure 4-110-A). The S1 surface is a remnant fan surface, located north of the fault, and bordered eastward by active channels.

We propose to assess the slip rate on that site using the displacement recorded by the S2 riser, and on the one hand the abandon age of S1, and in the other hand the abandon age of S2 surface, by carrying a microtopographic TSL survey of the area (Figure 4-108), and by sampling the surfaces for $^{10}$Be dating).

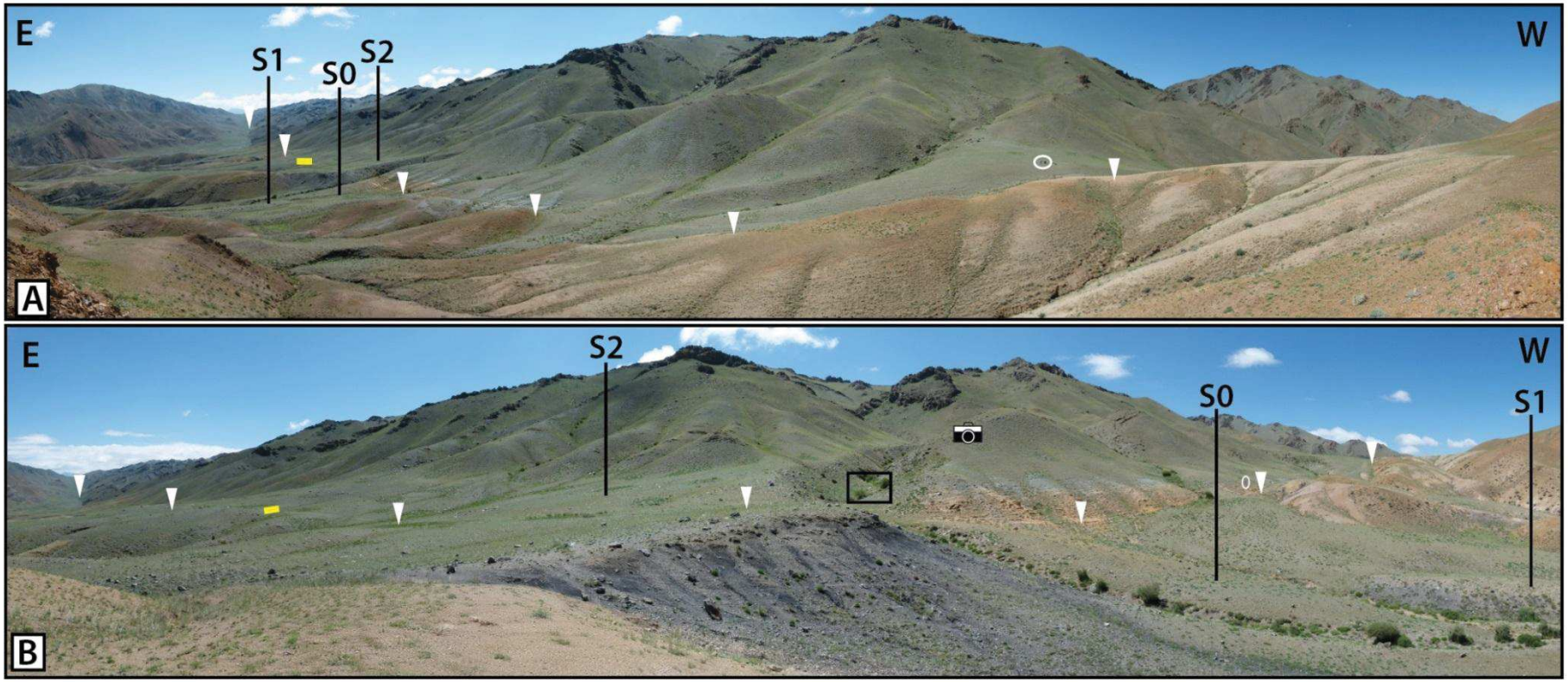


**Figure 4-109: Panoramic views to the South of the Camel Creek Site, and labels of the main studied surfaces. The area covered by the pictures corresponds to the TLS survey. White triangles indicate the TGF trace, yellow box is the location of the Camel Trench and white ellipses indicate characters for scale. Mountain front is ~300 m-high. Pictures locations are given in Figure 4-108. On B., black solid box is the location of Figure 4-110-B, and camera indicates the location of Figure 4-110-C.**

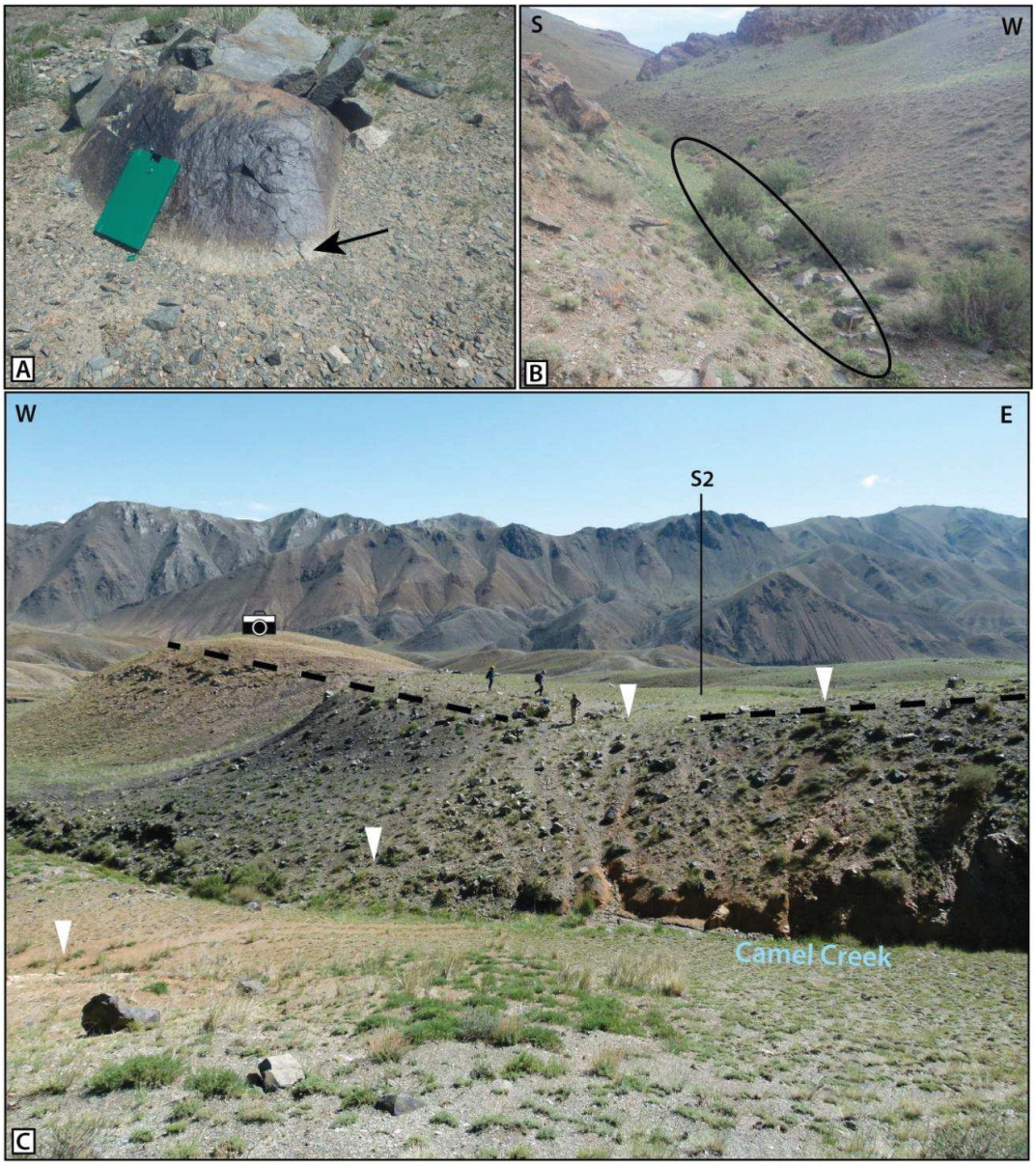


**Figure 4-110: Photographs of the Camel Creek site. A. Evidence of deflation on a boulder enchased in S2: the black arrow indicates the less weathered crown on the bottom of the boulder. B. Temporary active channel of the Came Creek. Ellipse is location of sampling TSAG-4 (see picture location on Figure 4-108 and Figure 4-109). C. Photograph to the North of the offset riser of S2. White arrows indicate the fault trace, black dashed lines are piercing lines used to derive the offset and camera indicates the location of figure-A.**

Figure 4-111 depicts the offset measurement by 3-step retrofit of the S2 riser. Because the riser located north of the fault is discontinuous (potentially due to moderate landslide on to differential erosion, as the fault zone is here associated with strong geological contacts, see Figure 4-100-C), the piercing line on north of the fault is defined from both top of the riser on S1 and from the prolongation of this riser, 50 m to the North (Figure 4-110-C and Figure 4-111). Measurements yield a cumulative left-lateral offset of 8.7 ± 4.2 m.

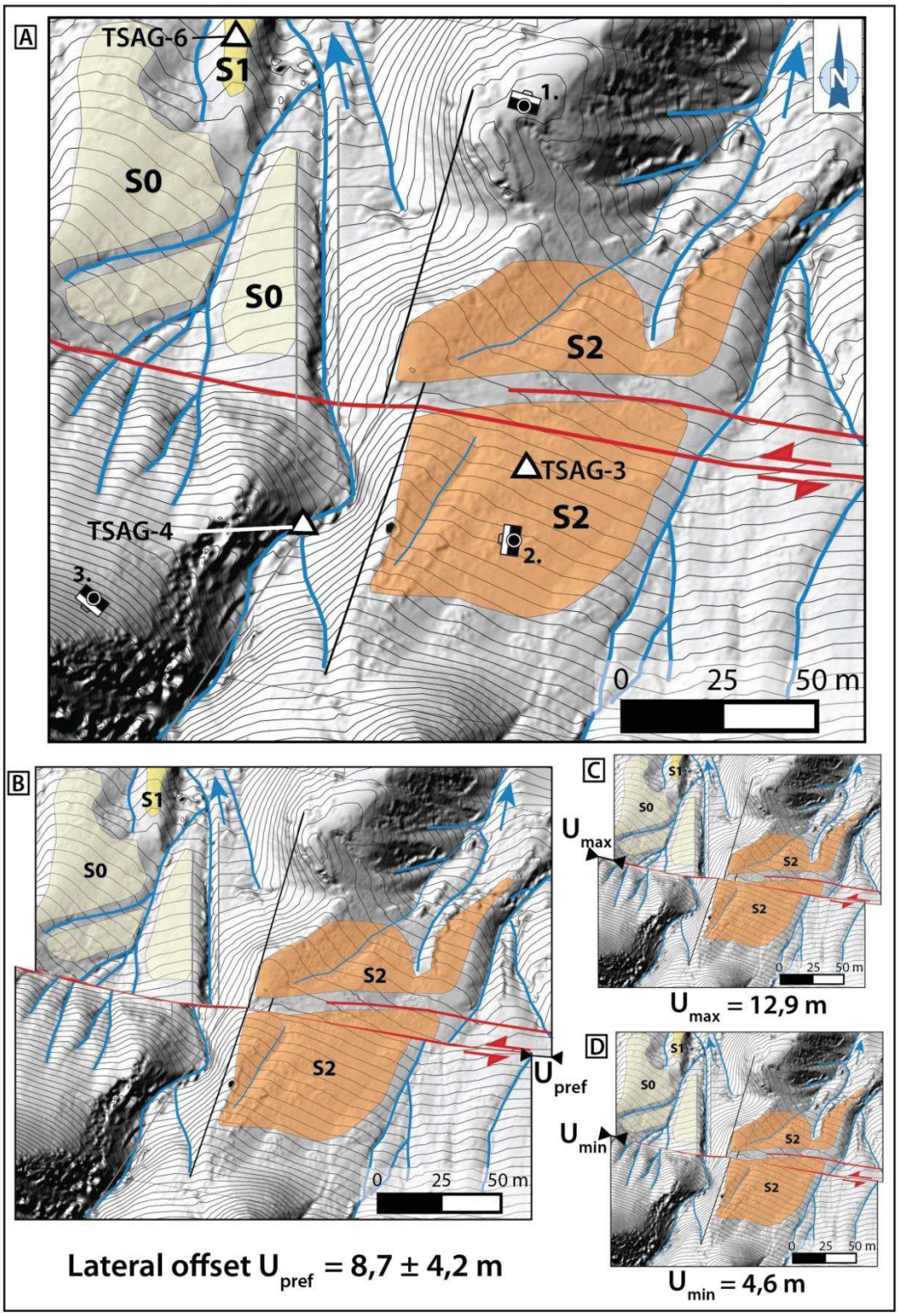


**Figure 4-111: Offset measurement from TSL-derived 20 cm resolution DEM in Camel Creek site. See location in Figure 4-108. A. Detailed morphotectonics map. Red solid line is the TGF trace, shaded areas are identified geomorphic surfaces, and blue solid lines are temporary drainage. Black solid lines are piercing lines related to the top of the S2 riser, from which the preferred offset is derived. Grey solid lines are piercing lines related to the active channel. Black triangles are location of $^{10}$Be surface sampling. Cameras are location of picture on: 1. Figure 4-109-A, 2. and 3. Figure 4-110-A and C respectively. B., C. and D. 3-steps retrofit lateral offset measurement of the Camel Creek, preferred, maximum and minimum offset values, respectively.**

In terms of sampling, we applied the same protocol than described above about the Kurilik site: to estimate the abandon age of S2 and S1, we sampled amalgam samples of same granulometry quartz-rich clasts primarily from each surface to measure the amount of $^{10}$Be accumulated on these surface, and later one from the active channel (Figure 4-110-B) on south of the fault to constrain the inheritance in $^{10}$Be.

Analysis of the $^{10}$Be samples yield the concentrations presented in Table 12, and allow proposing the following ages for the abandonment of S2: i. assuming a zero-erosion and the inheritance given by the *TSAG-4* amalgam sample, a minimum abandon age of 18.3 ± 1.1 ka; ii. assuming a steady state, an erosion rate of 18.2 ± 1.1 m.Myr-$^{1}$ associated to a integration age of 34.5 ± 1.0 ka; iii. assuming the most conservative calculation, by neglecting both the erosion rate and the inheritance, a maximal abandon age of 46.0 ± 2.7 ka.

Those ages appear rather distributed. The assessment of the S1 abandon age presents a strong discrepancy, as the concentration of this surface is stronger than the concentration of the S2 terrace, yet older from geomorphic observations. Hence we consider either: i. the sample TSAG-6 is an outlier, as the surface might be polluted by incomes of older rocks, or ii. our geomorphic interpretation is erroneous, and that the surface S1 is older than S2 –which appear very hard to explain, looking to the morphology of this site. Eventually, this approach of a surface abandon dating based on only two samples (instead of a soil pit), does not allow better understanding the deposition history of the S1 and S2 surfaces and stratification.

To conclude on slip rate determination is Camel Creek site, we can propose slip rates dividing the displacement (8.7 ± 4.2 m) measured within S2 riser by the age of S2 (18.3 ± 1.1 ka to 46.0 ± 2.7 ka) yields a slip rate ranging from of 0.19 ± 0.10 mm.yr$^{-1}$ to 0.48 ± 0.26 mm.yr$^{-1}$. However, the 10be dating performed in this site possibly involves biases we are not able to figure out here, and these results have to be considered as first order estimation.

Nevertheless, the obtained slip rates are same order of magnitude than the slip rates determined along the westernmost segment of the VOLF (i.e. 0.5 mm.yr$^{-1}$), and are more consistent with slip rates around the Chandmani Valley (i.e. sections IV.2.3 and IV.3.3) that those obtained in Kurilik Creek (previous section).

#### *IV.4.2.2.2. Coseismic offset measurement*

Based on the TSL microtopographic survey we carried out in Camel Creek site, we propose three offset measurements (Figure 4-112) which may be related to the most recent large surface rupturing event along this section of the TGF (TGF-S6 segment).

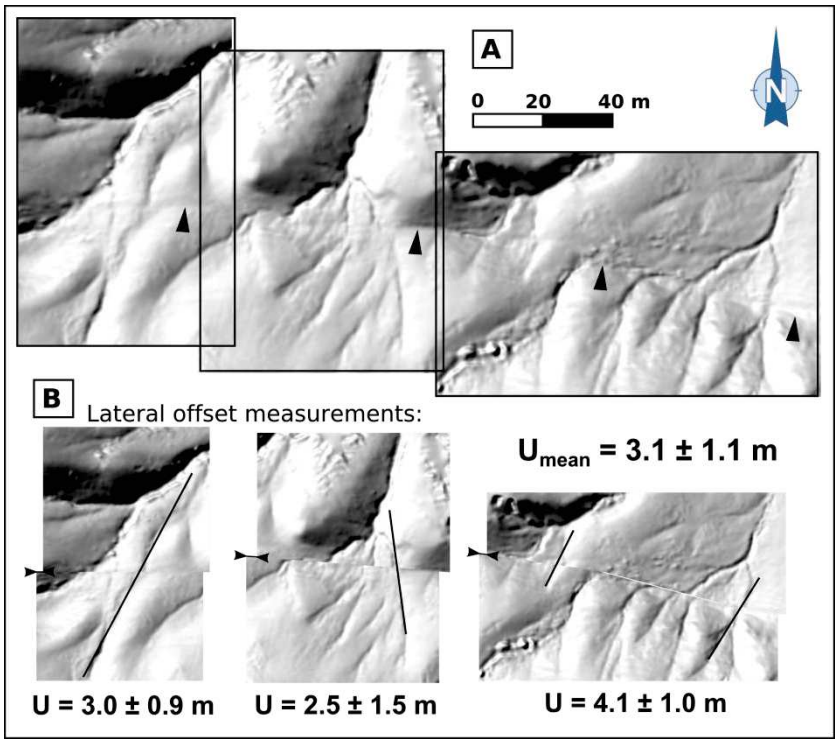


**Figure 4-112: Offset measurement smaller displacement observed within the Camel Creek site. See footprint in Figure 4-108. A. Central part of the TSL survey presented in figure. Black boxes are location of areas used for measurements by 3-steps retrofit displayed in B. B. Preferred retrofit for 3 offset gullies. Uncertainties are derived from maximum and minimum offset values, given in Table 13.**

Offset measurement have been done by three-steps landform retrofit (Figure 4-112), are presented in Table 13, and yield to a mean offset of: 3.2 ± 1.1 m.

**Table 13: Left-lateral offset measurements of smallest offsets observed in Camel Creek site.**

| Unit : m | $U_{pref}$ | $U_{max}$ | $U_{min}$ | Δ+ | Δ- | $Δ_{mean}$ |
|---|---|---|---|---|---|---|
| Offset 1 | 3 | 4,3 | 2,6 | 1,3 | 0,4 | 0,85 |
| Offset 2 | 2,5 | 4,3 | 1,4 | 1,8 | 1,1 | 1,45 |
| Offset 3 | 4,1 | 5 | 2,9 | 0,9 | 1,2 | 1,05 |
| Mean | 3,2 | | | | | 1,1 |

$U_{pref}$ : preferred offset value (m)

$U_{min}$ : minimum offset value (m)

$U_{max}$: Maximum offset value (m)

Δ+ : Upper uncertainty ($U_{max}$-$U_{pref}$) (m)

Δ- : Lower uncertainty ($U_{pref}$-$U_{max}$) (m)

$Δ_{mean}$ : mean uncertainty (m)

We point out that due to the poor number of measurements available along the TGF, no COPD analysis have been performed, but only an average of measured values and uncertainties.

#### *IV.4.2.2.3. Post-dating the most recent event along the TGF*

A small trench has been dug on the western part of the Camel Creek site (see location of Figure 4-108), through an abandoned channel, in order to date its filling, which may be related to the most recent surface rupturing seismic event. In fact, the active channel is now flooding 2 m eastward (Figure 4-113–A), as it is progressively captured by the beheaded downstream talweg.

The trench displays actually a coarse stratification, dominated by sub-angular gravel deposits, in which are paleo-channels, filled by clear beige silty deposits (Figure 4-113-B). Two OSL block-samples have been collected is the paleo-channels (at depths of 55 cm and 85 cm), in order to post-date the most recent event, assuming it generated the abandon of the Channel. Analyses are in progress.

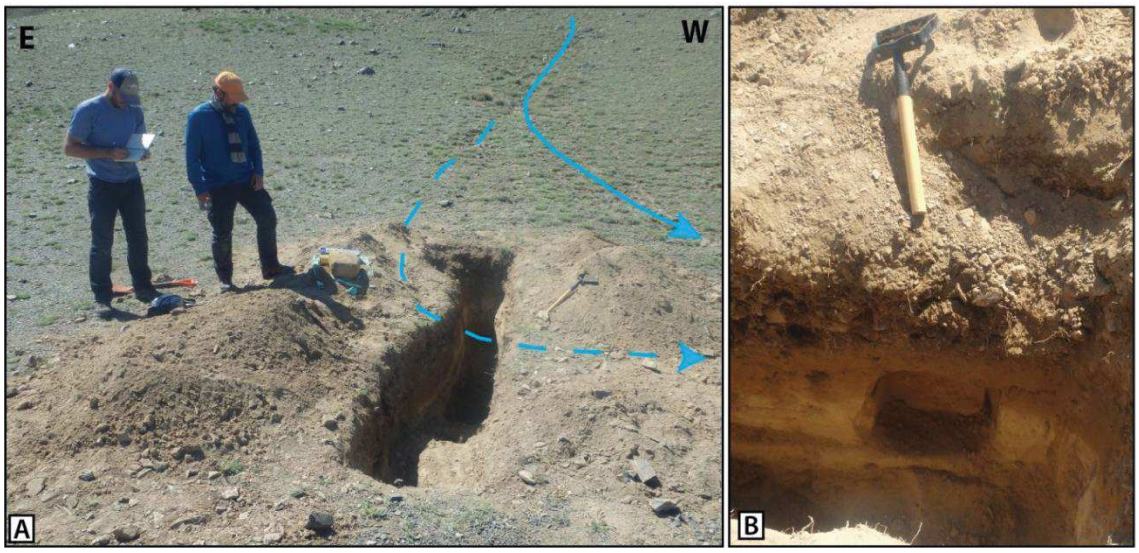


**Figure 4-113: Photographs of the Camel trench. A. Photograph to the south showing the small Camel Trench. Blue solid line shows the active temporary drain, instead dashed blue line displays the abandoned channel observed in the trench. B. OSL bloc-sample of a paleo-channel filled by eolian deposits.**

### IV.4.2.3. Schist creek

The Schist Creek site is located at 45.790°N; 96.195°E within a northwestwards flooding talweg, which crosses obliquely the TGF fault, and displays a left-lateral offset of ~15 m (Figure 4-104). The talweg incises into a late-Pleistocene fan surface (SC on Figure 4-104), characterized by a ~1 m thick shield of schist boulders, originating from the mountain flank, right South of the fault (Figure 4-114-A). A granitic bedrock outcrop can

be identified 4 to 5 m under the surface SC, in contact with the fault at the bottom of the talweg (Figure 4-114-A and B). Gouge development is observed on contact with the bedrock (Figure 4-114- D). We collected samples at following a vertical profile in order to estimate the exposure age of the bedrock (i.e. the incision of the Schist Creek talweg) using the ratio between $^{10}$Be and $^{26}$Al cosmogenic nuclides produced in situ (Figure 4-114-C). Dividing the offset by the age of the talweg incision would yield in turn a minimum slip rate along the TGF, as the displacement recorded by the talweg is a minimum value of the displacement experienced by the SC terrace.

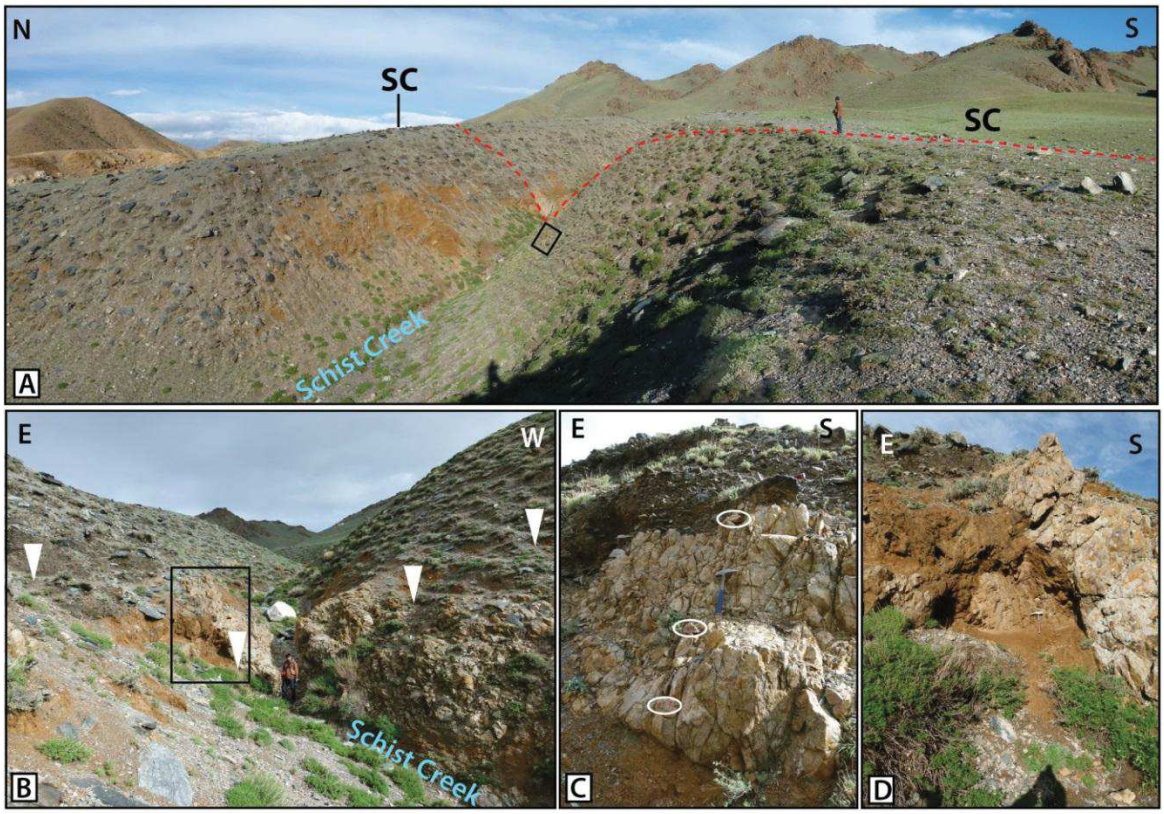


**Figure 4-114: Photographs of the Schist Creek site. A. Panoramic view to the East of the Schist Creek Talweg and the SC surface. Dashed red line is the TGF main trace, and black solid box is the location of picture C. See character for scale. B Photograph to the South of the bedrock outcrop on center of the talweg. White arrows indicate the TGF main trace, and black solid box is the location of picture D. See character for scale. C. Vertical profile sampling within the bedrock, to assess its exposure time. D. Fault-related gouge development in contact with the Bedrock. Note the hammer in center of the picture for scale.**

One may note that the fault surface rupture pattern in that area is rather complex (as this site is located within the TGF-R5 relay zone), and that there are two secondary fault traces located respectively 65 m to the north and 140 m to the South from the main fault trace. These secondary faults may potentially influence the offset measurement, although the geomorphic expression of these scarps is less pronounced than the studied main one.

## IV.5. Tsogt fault

### *IV.5.1. Tsogt Fault surface ruptures mapping*

The Tsogt region corresponds to an elongated intra-mountainous half-graben basin, the Tsogt Valley, trending N070°E and bounded on south-east by a major north dipping normal fault. This basin is obliquely cutting the Gichighiy Nuruu on their central part, and three faults can be perceptibly distinguished in the region: i. the –main– Tsogt fault (TF on Figure 4-115), located on southwestern half of the Tsogt Valley scarp, ii. the north Tsogt fault, located on the northeastern half of the Tsogt Valley, and iii. the south Tsogt fault, located in the footwall of the Tsogt fault, and almost collinear to the Tsogt Valley (Figure 4-6 ).

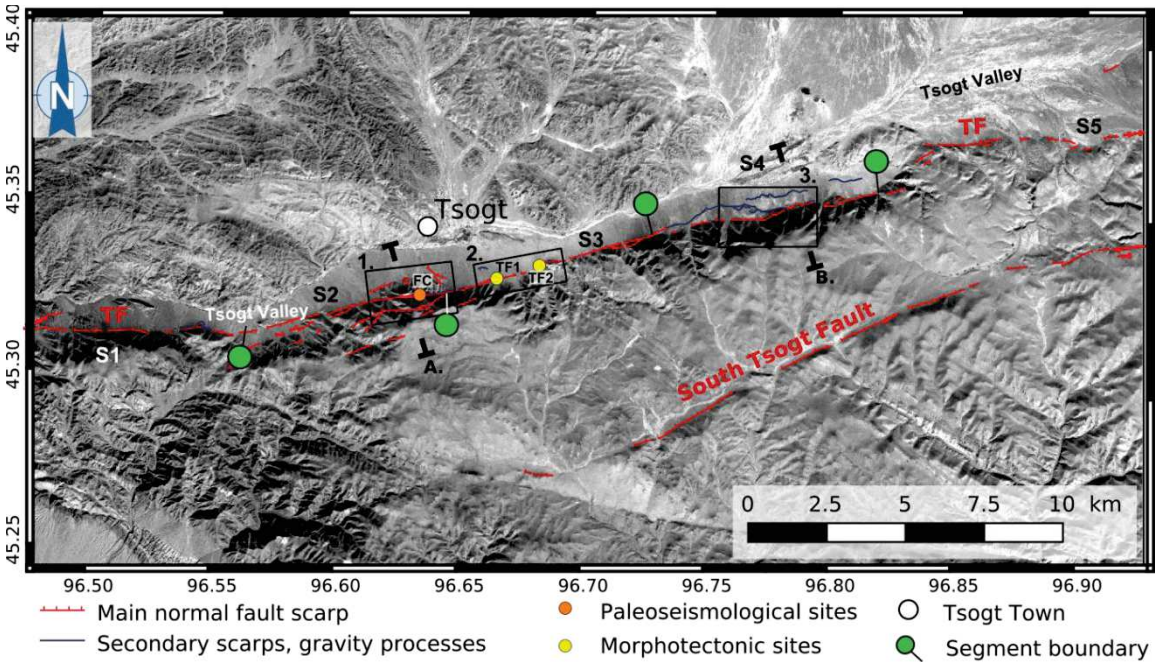


**Figure 4-115: Surface rupture and segmentation of the Tsogt Fault (TF). Field sites abbreviations: FC: Fox Creek; TF: Tsogt Fans 1 and 2. Background is orthorectified SPOT6 satellite image. Black segments A and B correspond to topographic profiles in Figure 4-118–A and B, respectively.**

#### IV.5.1.1. Tsogt Fault surface rupture

The main Tsogt fault is associated with a 32 km-long surface rupture, average trending N75, and appears segmented in five segments, separated by branching, azimuth change and distinct fault patterns (Figure 4-115). The south-westernmost segment, TF-S1, is 4.2 km-long, sinuous, trending N90 ± 15°, and is located on the northern foot of ~350 m-high mountain face (Figure 4-116). This segment displays a clear fault surface rupture (Figure 4-117.A) and two distinct families of triangular facets: the larger one corresponds to the whole mountain face, and the smaller class of facets are 50 to 80 m-high and defined between the shallow talwegs incised within the mountain front. Hence, we suggest that

the mountain front is a relic of the fault plane, which consequently indicates a minimum total cumulative vertical offset of 350 m. The TF-R1 relay zone is located 45.310°N; 96.562°E, and corresponds to a discontinuous small graben 1.5 km-long and ~500 m wide, crossed by several active drainage and filled with faulted late-Pleistocene alluvial deposits.

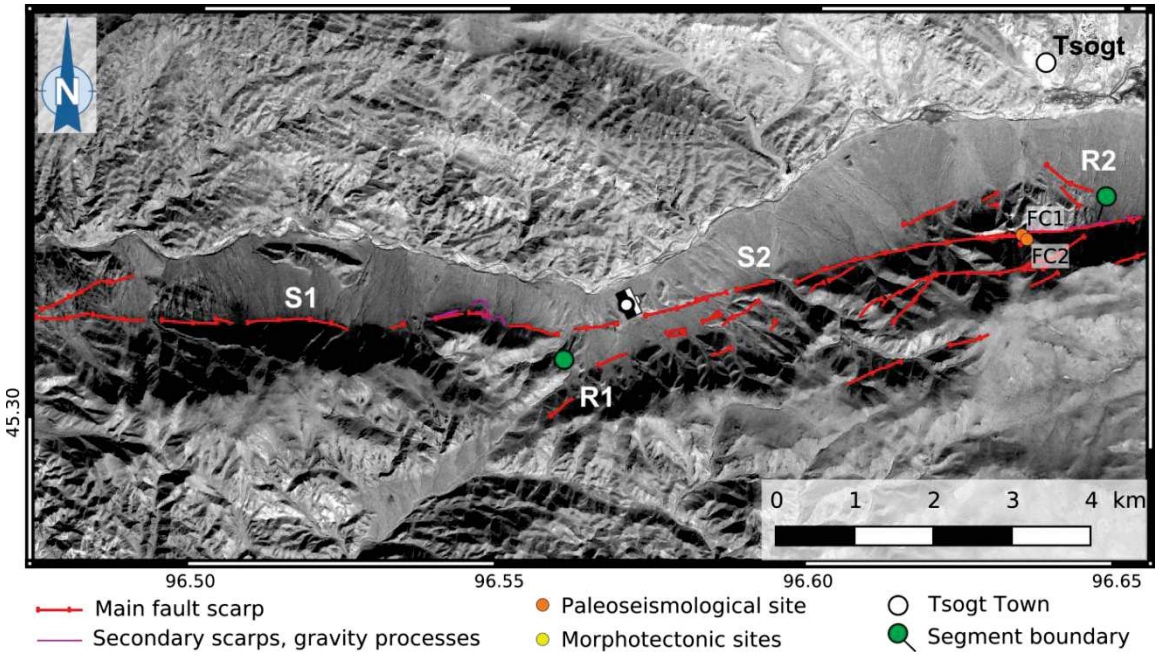


**Figure 4-116: Surface rupture of the western part of the Tsogt Fault. FC: Fox Creek field sites 1 and 2. Camera is location of the Figure 4-117.A. Background is orthorectified SPOT6 satellite image.**

The next segment, TF-S2, is 5 km-long, its western half on bottom of the mountain front, trends N075°E, and its eastern part trends N080°E into the relief, being associated to small scale surficial gravity processes and to two secondary fault scarps on north and south of the main trace, which branch on the next relay zone: TF-R2 (Figure 4-116). The northern secondary scarp is discontinuous, 1.2 km-long, dipping north, trending N115°E and branches with the main fault trace on 45.325°N; 96.650°E, while the northern secondary scarp is continuous, ~ 2 km-long, dipping south regarding to the V-shape displayed when crossing talwegs and branches with the main fault trace on 45.327°N; 96.645°E. One may notice that this very secondary branch is actually composed of two fault scarps distant by 200 m, joining southwestward (Figure 4-116). The total cumulative vertical uplift of the footwall regarding the peneplain relic located on top of the fault-related triangular facets is 200 m along the western part of the segment, and 500 to 600 m along the eastern part (Figure 4-118). Paleoseismological field investigations and sampling have been done along the eastern part of the TF-S2 segment, on two sites along the Fox Creek talweg (Figure 4-119), which exhibit some secondary fault outcrops, and are detailed in part IV.5.3.

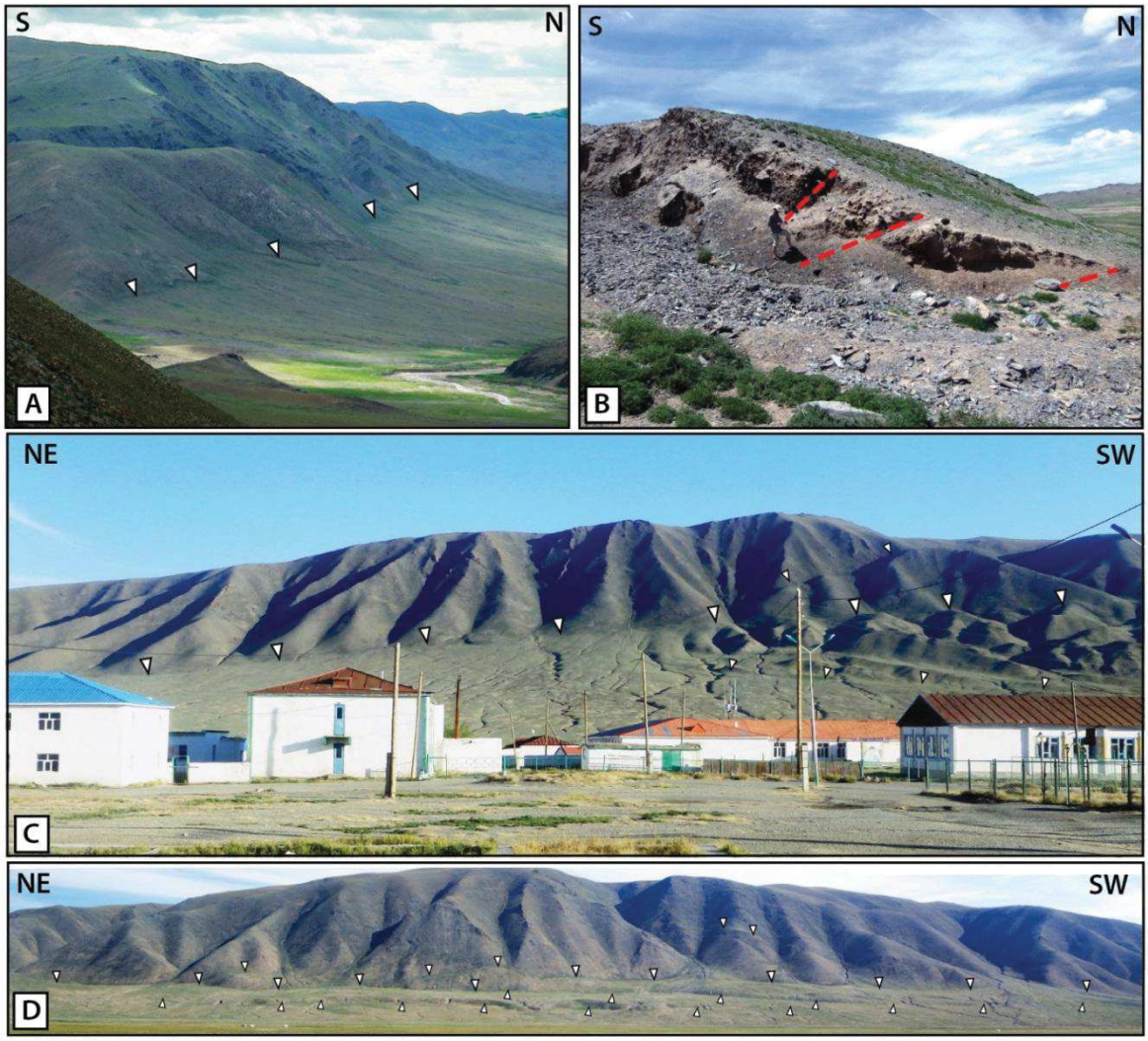


**Figure 4-117: Field views of the Tsogt Fault surface rupture. Fault traces are highlighted by white arrows. A. Photograph to the east of the normal Tsogt Fault scarp, along the TF-S1 segment. Note the two generations of triangular facets on the hanging wall. See location of the picture on Figure 4-116. B. Topographic scarp of a fault-related gravity process located on the hanging wall. See location in Figure 4-120. Several reverse shear zones can be identified on the toe of the structure, visibly prograding on the basin, and related to a tilt to the south. Location of the picture is on Figure 4-120. C. Panoramic view of the Tsogt fault segment TF-S3, south of the Tsogt town. Location of the picture is on Figure 4-119. D. Panoramic view of the western part of the TF-S3 segment. Note the gravity process on the foreground, related to the fault scarp. See location of the picture on Figure 4-119.**

The third segment of the Tsogt fault, TF-S3, is 6.6 km-long, slightly sinuous and trending N72 ± 10°E (Figure 4-119). South of the Tsogt town, the fault is associated to the mountain front (Figure 4-117.C), while instead the central part of this segment is standing into late-Pleistocene alluvial fans, systematically offset on contact with the fault, for which the deformation pattern is continuous and localized. Noticeably, two major fans display interesting and well expressed cumulative vertical displacements, Tsoft-fan1 and Tsogt-fan2 (TF1 and TF2 on Figure 4-119), and have been investigated in order to assess the vertical slip rate involved along the active Tsogt fault. This morphotectonics survey is detailed in part IV.5.2.

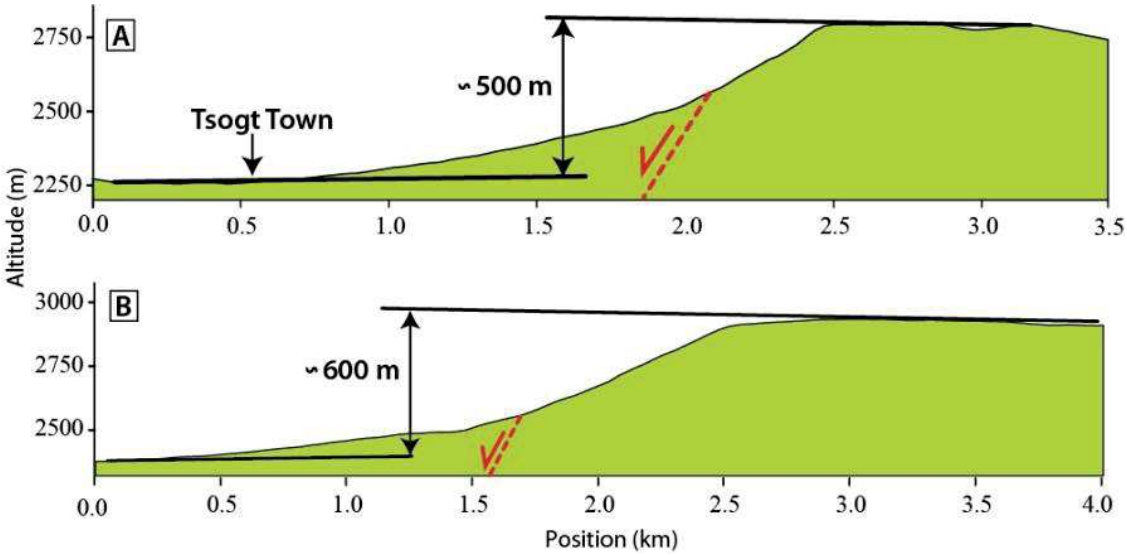


**Figure 4-118: Topographic profiles through the Tsogt Fault yield cumulative offsets between 500 to 600 m. See location of profiles in Figure 4-115. Elevation matches to position. Faults dips are inferred.**

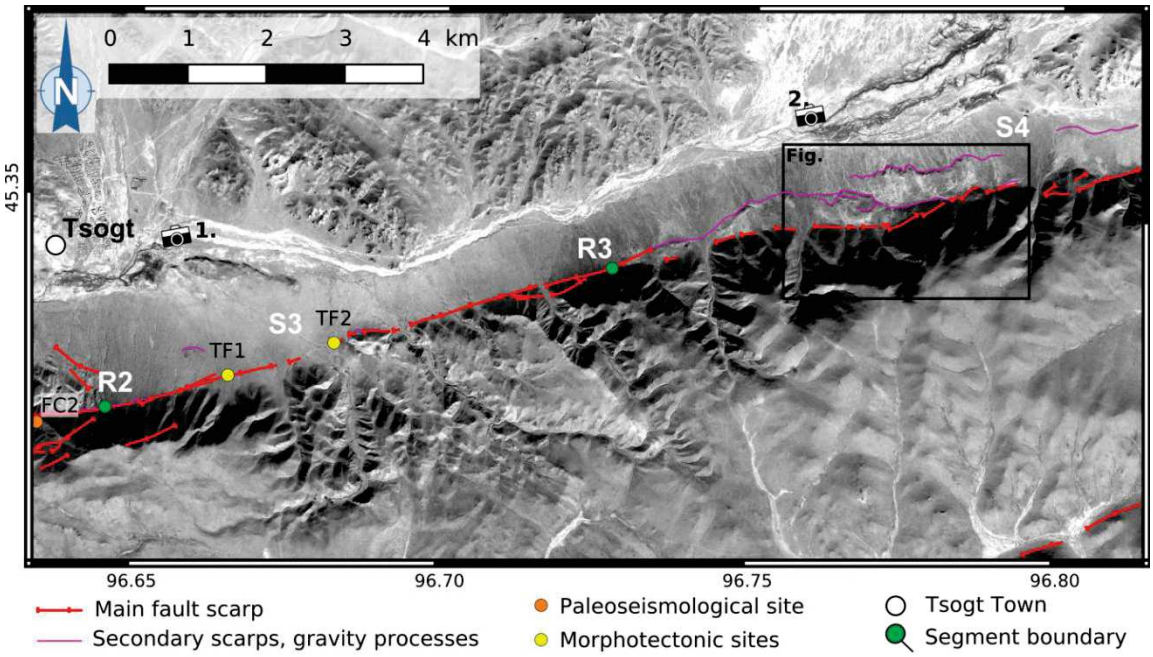


**Figure 4-119: Surface rupture of the central part of the Tsogt Fault. Black rectangle is location of Figure 4-120. Camera 1 and 2 are respectively Figure 4-117.C and D. Field sites: FC: Fox Creek; TF: Tsogt Fan 1 and 2. Background is orthorectified SPOT6 satellite image.**

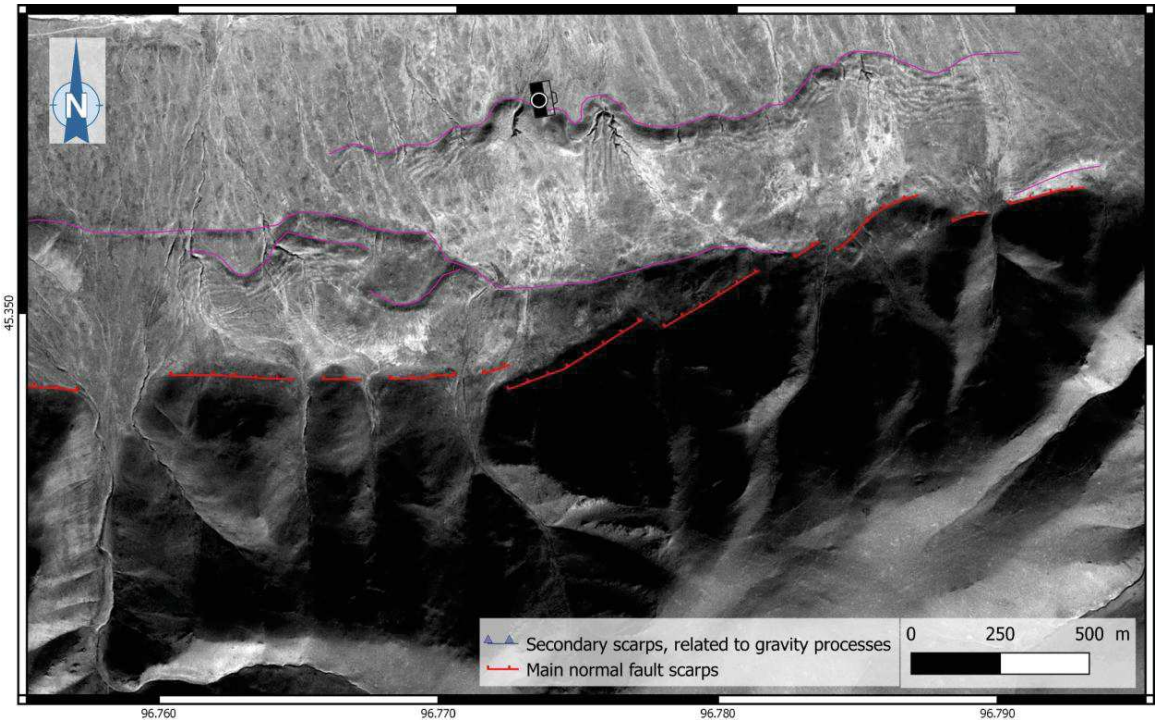


**Figure 4-120: Detailed mapping of secondary shallow thrust, prograding northward on the hanging wall. See footprint in Figure 4-115. Camera is location of the Figure 4-117-B.Frontal thrust fault scarps are 10 to 30 m-high. Note the singular triangular facets on the footwall. Background is orthorectified SPOT6 satellite image.**

The next segment, TF-S4, is defined by a very different fault surface rupture pattern, as the main fault, located on bottom of the mountain slope, is associated with a complex and sinuous network of shallow thrusts, ranging 500 m south of the main trace (Figure 4-120). Total vertical offset on those surficial thrust is only few tens of meters, and we suggest that the deformation of these thrusts is constrained to the sedimentary basin, and does not involve any crustal processes. The length of TF-S4 is 7.5 km, and the main trace, not evenly visible, strikes N077 ± 10°E (Figure 4-119 and Figure 4-121). This segment presents numerous large triangular facets, some of them up to 400 m-high, bounded on top by a peneplain relict, which suggests that this height may correspond to the total uplift encompassed by the footwall.

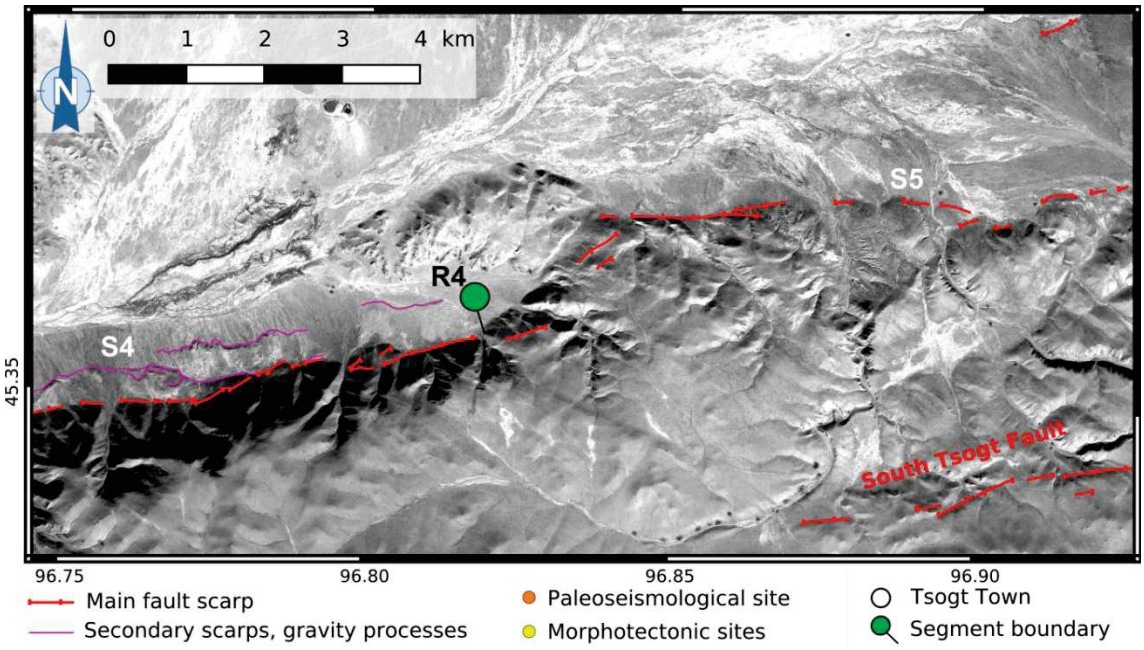


**Figure 4-121: Surface rupture of the eastern part of the Tsogt Fault. Background is orthorectified SPOT6 satellite image.**

The fault pattern visibly changes for the next segment, as the last TF-S5 segment is very sinuous, 6.7 km-long, with its western third oriented N050°E and the next two eastward third remaining on a N085 ± 5°E trend (Figure 4-121). Cumulative displacement along this segment, regarding the whole relief to the south appears smaller than previously documented (200 m instead of 400 m) and the apparent vertical scarp significantly diminishes eastward. Eventually, a minor normal fault scarp may be identified 1.5 km southward of the end of this segment, half way from the south Tsogt fault scarp.

### IV.5.1.2. South Tsogt fault surface rupture

The south Tsogt fault is located 3 to 6 km to the east from the main Tsogt fault, with a length of 24 km, average trend N067°E, slightly oblique compared to the orientation of the main Tsogt fault trace (Figure 4-115). The fault is slightly curved toward the south, as its orientation ranges from N055°E on its westernmost part to N072°E on its easternmost part. The fault trace is apparently less recent than the main Tsogt fault, as it is not systematically expressed in the morphology, and presents smaller offsets, either within late-quaternary geomorphic markers or when considering cumulative vertical offset recorded in the long-term morphology (e.g. peneplain). Figure 4-122 gives a preview of the preservation of the fault scarp. The peneplain is less preserved south of this fault than it is on the footwall of the main Tsogt Fault, but total cumulative vertical displacement of the south Tsogt Fault regarding the peneplain range from 80 m south-westernmost of the fault, to 130 m on the central part, and finally it is almost nil on the northeastern part of the fault.

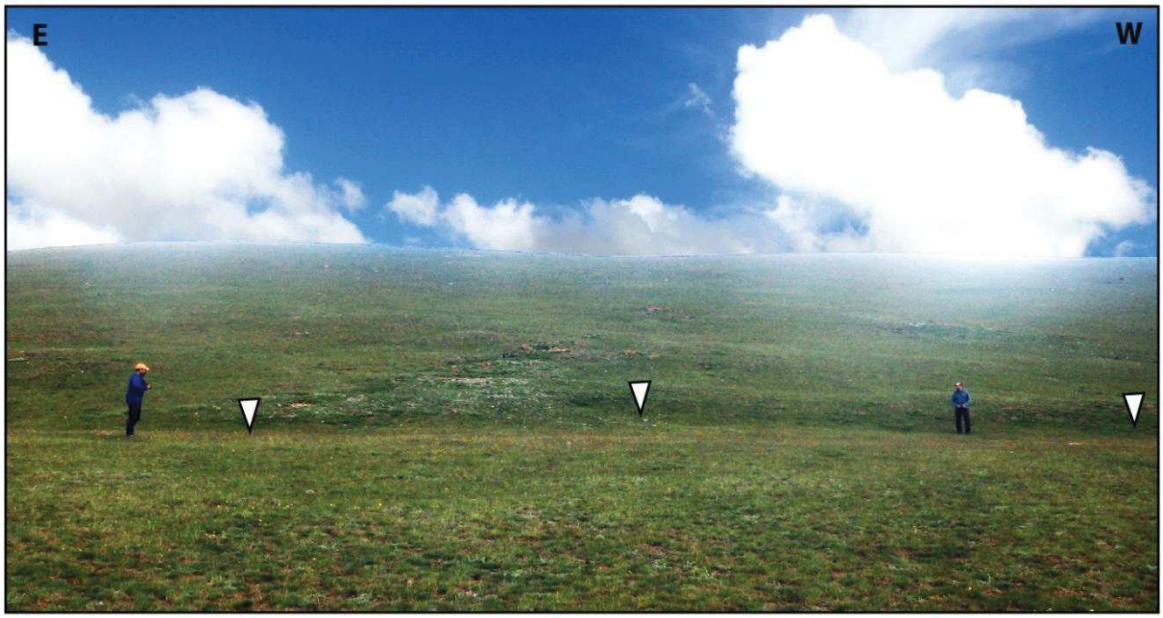


**Figure 4-122: Surface fault scarp of the South Tsogt fault. Duel to the fault of senior paleoseismilogists under the Mongolian Ih Bogd Khan Shinny cloudy eyes. Picture location: 45.320°N; 96.817°E.**

A field reconnaissance along a ~N100°E fault, well visible in the satellite images and SRTM dataset (southernmost of Figure 4-115), associated to an axial valley, and on which the south Tsogt fault branches to the south, shows that no recent tectonic activity occurred on this fault, and that the rather strong morphological expression of this fault is more related to lithological heterogeneities, leading to differential erosion, than to recent tectonic activity.

#### IV.5.1.3. North Tsogt fault

The North Tsogt fault is located on the northeastern half of the Tsogt Valley and constitutes the northeastern prolongation of the main Tsogt fault (Figure 4-6). The North Tsogt fault is 15 km-long, average trend N070°E, with a singular short 2 km-long segment westernmost of the fault, encroaching northward by 2 km on the valley. The main portion of the fault does not display clear surface rupture within late-Pleistocene deposits, but the mountain front displays sharp 500 m-high triangular facets, capped by the fairly preserved peneplain (Figure 4-123). Some fan deposits may display some deformation related to fault motion, but are systematically confused with slope process, preventing by the way offset quantification; only on 45.410°N; 96.05°E, a fan surface is visibly uplifted, but no quantification of this offset has been done. To conclude with the north Tsogt fault, although no Holocene activity has been identified and no quantified time constrain done, the fault displays important cumulative uplift, even larger than on the main Tsogt Fault, and was very probably active during at least the Pleistocene time.

**Figure 4-123: Panoramic view to the east of the northern part of the North Tsogt fault. Mountain front is 700 m-high. Note how linear the mountain front is, the abundant gravity process and the triangular facets. Location of picture is 45.430°N; 96.050°E.**

### *IV.5.2. Slip rates along the Tsogt Fault*

In order to assess the long term slip rate along the main Tsogt fault on two different time-scales, two faulted alluvial fan surfaces (the Tsogt-Fan1 and the Tsogt-Fan2 sites) have been investigated (Figure 4-124), through a TLS microtopographic survey coupled to amalgam sampling for surface abandon age measurements by $^{10}$Be produced in situ method.

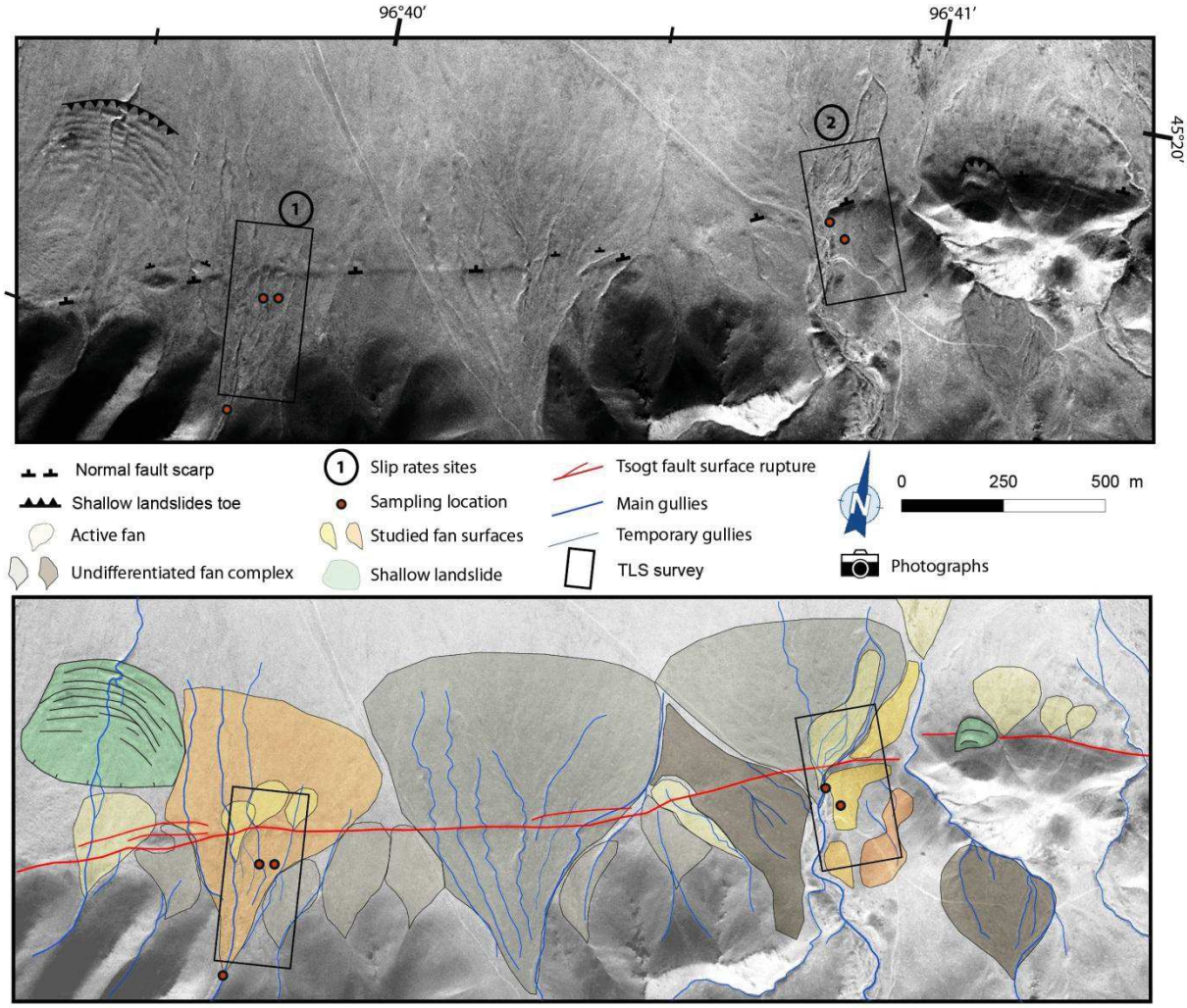


**Figure 4-124: Morphotectonic map of a central section of the Tsogt Fault, and location of the Tsogt Fan sites (1) and (2), investigated for slip rate measurements. TSL survey areas correspond to location of Figure 4-125Figure 4-127 A. Orthorectified SPOT 6 satellite image. B. Geomorphic map of the fan complex analyzed for slip rate assessment. We distinguish the active fans from those assessed for slip rate, and from undifferentiated ones. Color panel is darker as the fan is relatively old compared to others.**

#### IV.5.2.1. Tsogt-fan1 site

The Tsogt-fan1 site is located 45.328°N; 96.665°E, and is composed of an alluvial fan flooding northward, faulted by the main Tsogt Fault and incised by active temporary gullies (Figure 4-124). Additionally, a small fan has been deposited right south of the fault scarp, as the slope slightly changes, from 20% upstream, to 16% downstream of the fault (measurement from SRTM dataset). We carried on a TSL survey on N-S 400 m section, to derive the cross-fault topographic profiles, and to measure the cumulative vertical offset related to the fault scarp (Figure 4-125). 4 measurements have been done (presented in Figure 4-125.B. to E.), which give an average vertical offset value of 3.5 ± 0.7 m.

The $^{10}$Be sampling have been done by taking amalgams of 50 quartz-rich clasts of analog size, first from the fan1 surface to measure the amount of $^{10}$Be produced by cosmic rays and accumulated in the quartz on surface (Figure 4-126.A), secondly from the inlet of the surface (corresponding to the outlet of the upstream talweg) in order to estimate the inheritance in $^{10}$Be contained by the surface clasts (Figure 4-126.E) and thirdly at a two meters depth within the surface, in a spot where an active channel is currently incising the surface, allowing us sampling at that depth (Figure 4-126.F). This natural riser also enable us to see a log of the fan, which appears stratified, with coarse to very coarse levels of pebbles to cobbles, alternated with sandy lenses (Figure 4-126.D). Results of $^{10}$Be analysis are given in Table 14.

**Table 14: The 10Be nucleide concentrations and computed ages for samples at Tsogt fans sites (1 and 2). Grey line indicates a sample which has been discarded (see text for details).**

| Sample | Lat (dec°) | Lon (dec°) | Alt (m) | [$^{10}$Be] (at.g$^{-1}$) | err. [$^{10}$Be] 1σ (at.g$^{-1}$) | Shield. Cor. | Density | Depth (cm) | $^{10}$Be age tmin (ka) | 10Be age tint (ka) | Erosion rate (m.Ma-1) | $^{10}$Be age tmax (ka) |
|---|---|---|---|---|---|---|---|---|---|---|---|---|
| TF1S | 45,329 | 96,665 | 2440 | 5,39E+05 | 1,71E+04 | 0,997 | 2,0 | 0 | 4,9 ± 0,3 | 14,9 ± 0,5 | 42,5 ± 2,5 | 19,8 ± 0,6 |
| TF1W | 45,329 | 96,665 | 2440 | 4,06E+05 | 1,29E+04 | 0,997 | 2,0 | 0 | | | | |
| TF1-2m | 45,329 | 96,665 | 2440 | 1,27E+06 | 4,16E+04 | 0,997 | 2,0 | 200 | | | | |
| TF2S | 45,333 | 96,683 | 2400 | 2,21E+06 | 6,91E+04 | 0,999 | 2,0 | 0 | 63,5 ± 3,7 | 72,5 ± 2,1 | 8,5 ± 0,5 | 85,1 ± 5,0 |
| TF2H | 45,333 | 96,683 | 2400 | 5,63E+05 | 1,74E+04 | 0,999 | 2,0 | 300 | | | | |

The measurements of the contents in $^{10}$Be of the fan1 surface (sample *fan1-S*) and of the inheritance on the outlet (sample fan1-H) show concentrations coherent with the geomorphic setting with an inheritance sample less concentrated than on the surface, while instead the $^{10}$Be content of the sample taken 2 m-deep under the surface (sample *fan1-2m*) is much higher (more than twice) than the $^{10}$Be content of the surface. This likely indicates than, according to the strongly stratified structure of the fan previously

documented, the deposition history of the fan1 does not match with the basis hypothesis that a geomorphic feature has to be deposited in one event, or at least within a short period. We therefore consider that the sample *fan1-2m* is an outlier, useless in our first order approach of assessment of the vertical slip rate on the Tsogt Fault.

Nevertheless, the two surface amalgam samples allow deriving the following results: i. assuming a zero-erosion and the inheritance given by the *fan1-H* amalgam sample, a minimum abandon age of 4.9 ± 0.3 ka; ii. assuming a steady state, an erosion rate of 42.5 ± 2.5 m.Myr-$^{1}$, associated to a integration age of 14.9 ± 0.5 ka; iii. assuming the most conservative calculation, by neglecting both the erosion rate and the inheritance, a maximal abandon age of 19.8 ± 0.6 ka.

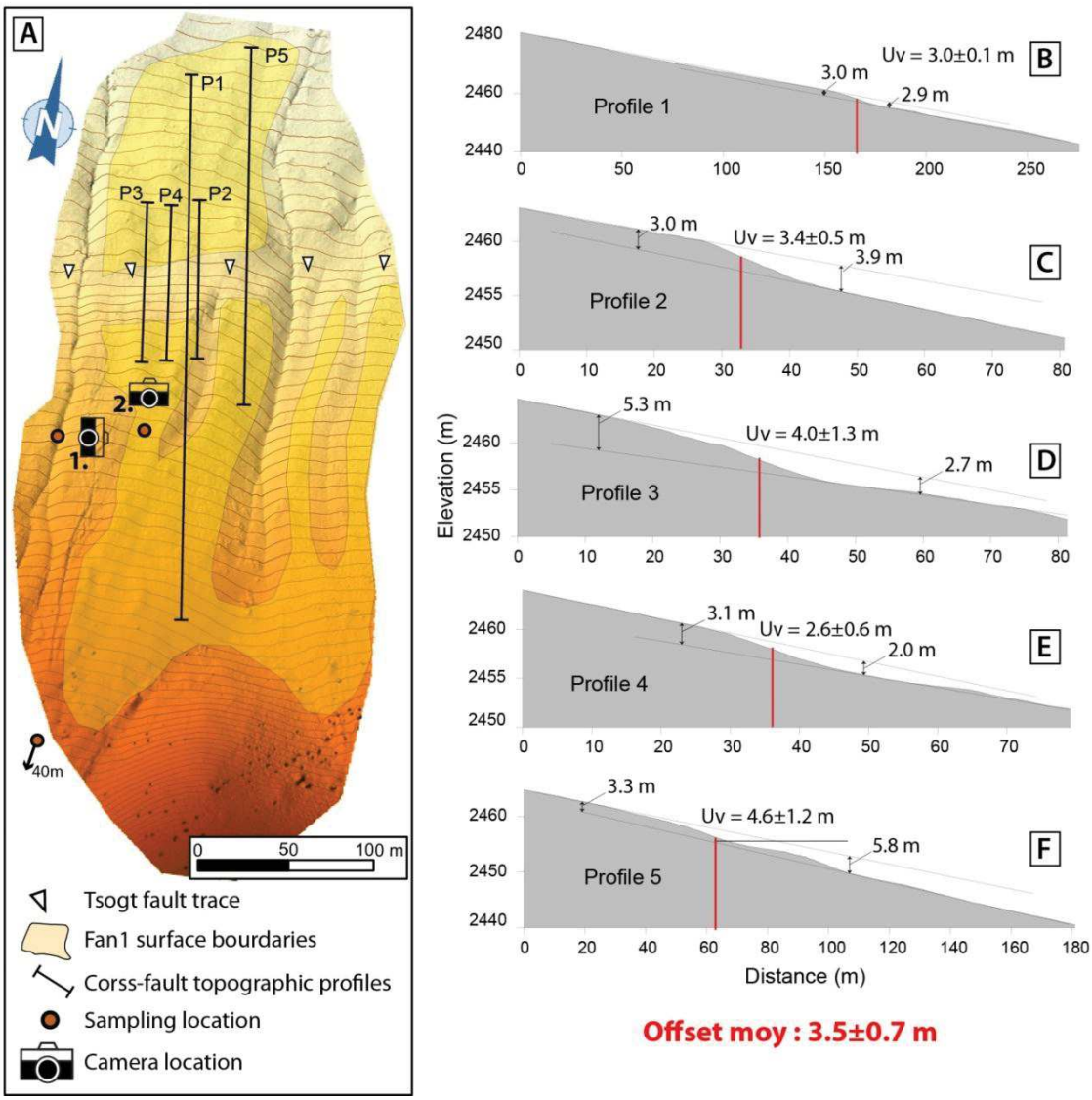


**Figure 4-125: Vertical offset measurement on Tsogt Fan1. A. Hill-shaded DEM from TLS survey, color panel for altitude, and locations of cross-fault profiles. Contour lines are 1 m. Cameras are location of pictures of Figure 4-126: 1. for (*A*) and 2. for *(F)*. Location is on Figure 4-115. B. to F. Cross-fault profiles, respectively P1 to P5 on (A), vertically exaggerated.**

The a-priori hypothesis we assumed for those three slip rate computations are meant to explore the possible ages this dating may provide, knowing the low-constrained approach we carried on. However those hypotheses may be discussed on the basis of geomorphic observations, and additional samples. For instance, the possibility that this surface already reached the steady state appears unrealistic. Actually, the underneath sample *fan1-2m* shows a clearly richer content in $^{10}$Be than the current surface, which means that the equilibrium, necessarily associated to maximum contents close to the surface, in not reached yet. The hypothesis of an insignificant inheritance is moreover very surprising in the climatic context of the Gobi-Altai, which involves slow transportation processes. Finally, considering a nil-erosion – while being on an abandoned alluvial fan located on bottom of a 500 m high relief –, still exposed to the dominant west winds (and then to related orogenic precipitations), appears unconceivable. Hence, we propose to compute two slip rates on the Tsogt fan1, one with the minimum age, and the other with the maximum conservative age. This allows us constraining the vertical slip-rate along the Tsogt fault between at least 0.18 ± 0.05 mm.yr$^{-1}$ and at most 0.71 ± 0.19 mm.yr$^{-1}$ on the Holocene to the late-Pleistocene (5 to 40 ka).

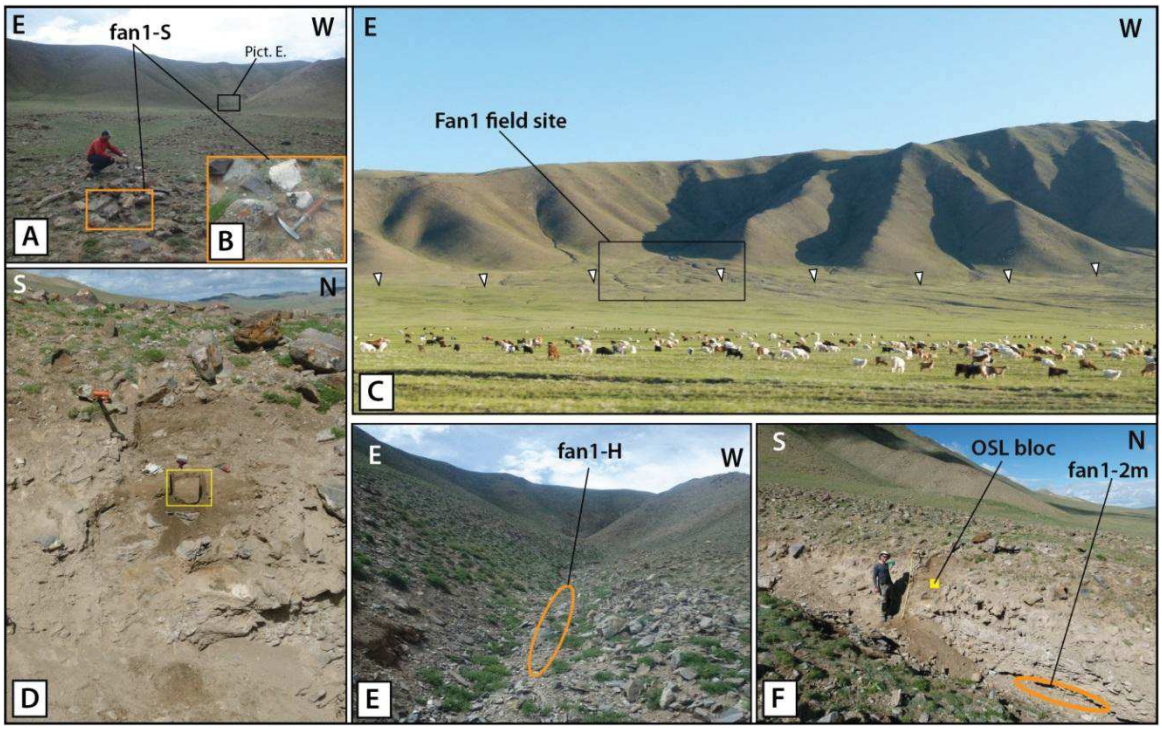


**Figure 4-126: Photographs of the Fan1 site and related sampling. A. Photograph to the south of the bar and swale fan surface. Orange box shows the location of (B). B. Photograph of one of the 50 boulders sampled for amalgam sample *fan1-S*. C. Photograph to the south of the Tsogt fault surface rupture on Fan1 site. D. Photograph to the west of the riser of a gully within fan1, and location of the OSL bloc sample. Orange shovel is for scale, location of the picture is in (*F*). E. Photograph to the south of the fan1-related talweg outlet, sampled for amalgam sample *fan1-H*. F. Photograph to the**

**west of the riser sample for OSL bloc (yellow box) and for 2 m-deep $^{10}$Be amalgam sample *fan-2m* (orange ellipse).**

Additionally, an OSL bloc sample has been extracted from one of the sandy lenses, at a depth of 80 cm, in order to crosscut the deposit age obtained by $^{10}$Be technics to an OSL-based dating. This sample is currently being analyzed, and logically, this OSL age should be slightly older than the abandon age of the surface derived from $^{10}$Be dating, given that its deep location suggests it has been previously deposited.

#### IV.5.2.2. Tsogt-fan2 site

The Tsogt Fan2 site is located 45.333°N; 96.683°E, and corresponds to a faulted alluvial fan surface related to a major drain, flooding northward (Figure 4-124). Two levels of abandoned fan surfaces, F2 and F3 may be identified south of the fault, separated by a smooth and sinuous riser oriented NE-SW (see Figure 4-127.A, although F3 has not been covered on the TLS survey, and thereafter not represented in the figure). West of these surfaces lies the major drain and the related hummocky active bed, F0, which displays an anastomosed network of debris-flow channels, highlighted by sharp lateral levees (Figure 4-125.A). North of the fault, the active bed spreads out in an active alluvial fan F0, and to the east is another small smooth fan, F1, fed by a gully cutting F2 (Figure 4-127.A). One may note that the fan surface F1, as the F0 surface, are active landforms, and that we differentiate them from texture dissimilarities more than topographic changes, as they are sensibly at same altitude (Figure 4-127.A). The F2 western bound is composed of a 3 m-high vertical riser, clearly undermined by active channels of F0 (Figure 4-128.A).

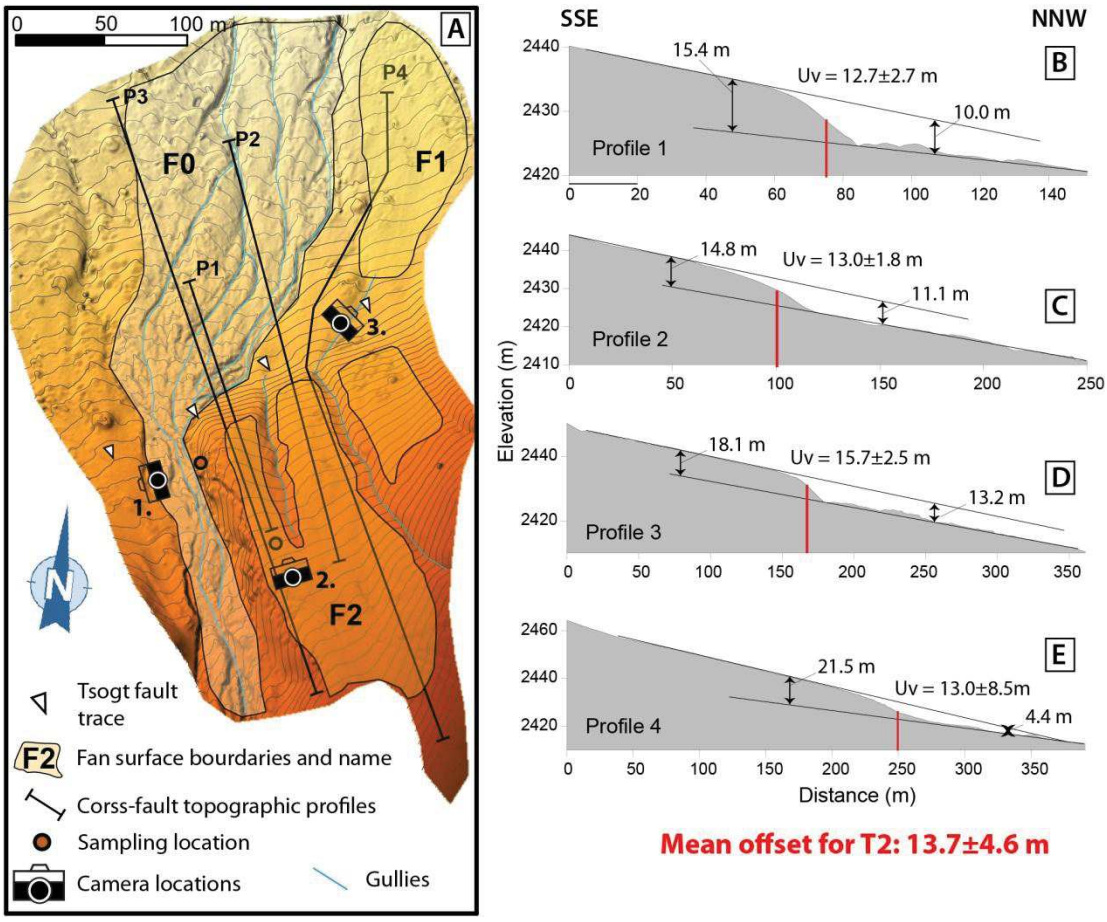


**Figure 4-127: Vertical offset measurement on Tsogt Fan2. A. Hill-shaded DEM from TLS survey, and locations of cross-fault profiles and sampling locations. Contour lines are 1 m. Location is on Figure IV 50, and color panel is related to altitude. Cameras are positions of pictures of Figure 4-128.: 1. for (*A*), 2. for (*C*) and 3. for (*B*). B. P1 cross-fault profile, vertically exaggerated. C. P2 cross-fault profile, vertically exaggerated. D. P3 cross-fault profile, vertically exaggerated. E. P4 cross-fault profile, vertically exaggerated.**

We aim to assess the vertical slip rate along the Tsogt fault by measuring F2 vertical offset compared to the active main fan F0, and by assessing the F2 abandon age using in situ produced $^{10}$Be dating technics.

To do so, we first carried on a TLS microtopographic survey on a 300 m section, orthogonal to the fault and encompassing F2, F1, F0 and the fault scarp where it is the best preserved (Figure 4-127.A). Four profiles are thus derived, three covering F2 and F0 (P1 to P3), and one overlapping F2 and F1 (Figure 4-127.B. to E), in order to identify if there is a meaningful offset difference with that secondary active fan surface. Actually, no significant offset variation has been highlighted but the offset measurement appears more inaccurate in the case of P4, with an uncertainty of 65 %, against a maximum 20 % uncertainty on the 3 other measurements. We may conclude that, the four measurements are consistent with each other, and give an average vertical cumulative offset of 13.7 ± 4.6 m (Figure 4-127). With this measurement, we may assume that the

actual F0 level corresponds to the surface F2 on the hanging wall; this assumption appears reasonable because of no significant topographic changes between F0 and surrounding Pleistocene fans downstream, as we make distinction between each surface from textural criteria.

Two amalgams of granitic clasts have been sampled on Tsogt Fan2 site: one (*Fan2-S*) on the F2 surface, where it is best preserved (Figure 4-128.C) to assess the amount of $^{10}$Be produced by cosmic ray within the surface since its abandon, and one (Fan2-H) taken from the riser between F2 and F0, 3 to 4 m deep, to measure the statistical inheritance in $^{10}$Be presented by the clasts when they were deposited (Figure 4-128.D). We notice here that this very assumption requires neglecting the muons contribution in the $^{10}$Be in situ production, while they are the main contributor at that depth. Hence, the inheritance derived from the *fan2-H* sample may be considered as a maximum value of the inheritance in that site. The fan log is naturally exhibited here (Figure 4-128.D), and presents loose, un-stratified, clast-supported deposits, composed of angular elements of various size, from gravel to boulders (dominantly). The poorly abundant matrix is silty, and no significant horizons were observed.

The measurements of the $^{10}$Be concentrations (Table 14) in both samples allow at first order – as those ages are not derived from a profile – to derive the following results: i. assuming the minimum inheritance and a zero-erosion rate, an abandon age of 63.5 ± 3.7 ka; ii. assuming that the F2 surface already reaches the steady state, an erosion rate of 8.5 ± 0.5 m.My$^{-1}$, associated to an integration time of 72.5 ± 2.1 ka; iii. assuming the most conservative calculation, by neglecting both the erosion rate and the inheritance, a maximum abandonment age of 85.1 ± 5.0 ka.

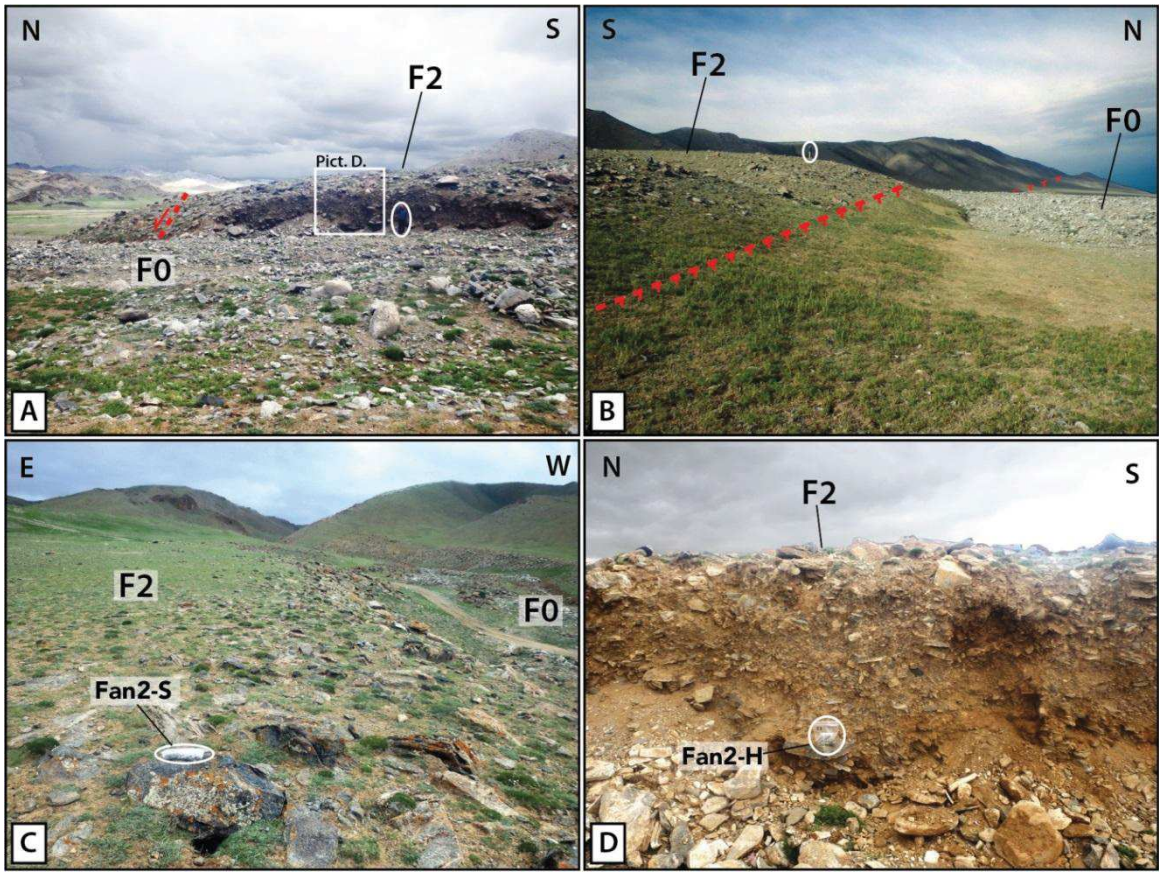


**Figure 4-128: Photographs of the Fan2 site and related samplings. A. Photograph to the east of apparent vertical fault scarp, with vertically offset F2 surface. Red dashed line is the inferred location of the fault scarp, white ellipse indicates a character for scale, and white box is the location of picture in (D). B. Photograph to the west of apparent vertical fault scarp, with vertically offset F2 surface. Red dashed line is the inferred location of the fault scarp, and white ellipse indicates a character for scale. C. Photograph to the south of the F2 fan surface. White ellipse indicate the sample bag (~20 cm for scale) of the *Fan2-S* amalgam surface sampling. D. Photograph to the east of the steep riser between the F2 and F0 fan surfaces. White ellipse indicates the sample bag (~20 cm for scale) of the *Fan2-H* amalgam sampling, 3 m-deep for assessment of the inheritance in $^{10}$Be undergone by the materials composing the Tsogt Fan2.**

Thus, three slip-rates have been computed from those ages and the measured vertical cumulative offset: i. 0.22 ± 0.09 mm.yr$^{-1}$, assuming the minimum age; ii. 0.19 ± 0.07 mm.yr$^{-1}$, assuming the integration time necessary to reach the steady state; and iii. 0.16 ± 0.06 mm.yr$^{-1}$, assuming the conservative maximum abandon age of the surface.

Consequently, accounting for the one significant digit result we use to synthetize our slip-rates results, whatever is the assumption about the dating, we obtain a vertical slip rate along the Tsogt fault of 0.2 ± 0.1 mm.yr$^{-1}$ on the late-Pleistocene – Holocene period (80 ka). This result is coherent with the slip rate defined on the Holocene period in Tsogt Fan1 site.

### *IV.5.3. Ages PaleoEQ*

The Fox Creek site is located 2.8 km south of the Chandmani town, and displays two outcrops where distinct secondary faults can be clearly identified (Figure 4-129): Fox creek 1 (N45°19.45', E96°38.03') and Fox creek 2 (N45°19.43', E96°38.06').

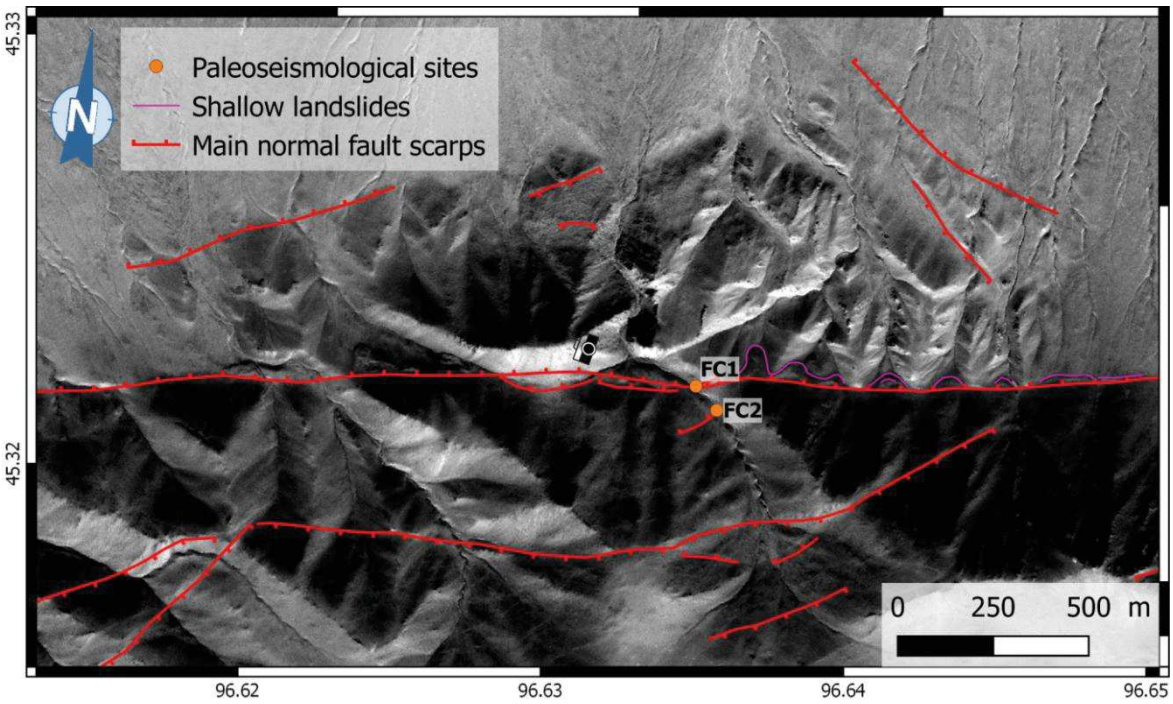


**Figure 4-129: Detailed map of the Fox Creek area. Location is on Figure 4-115. Camera indicates location of Figure 4-130.**

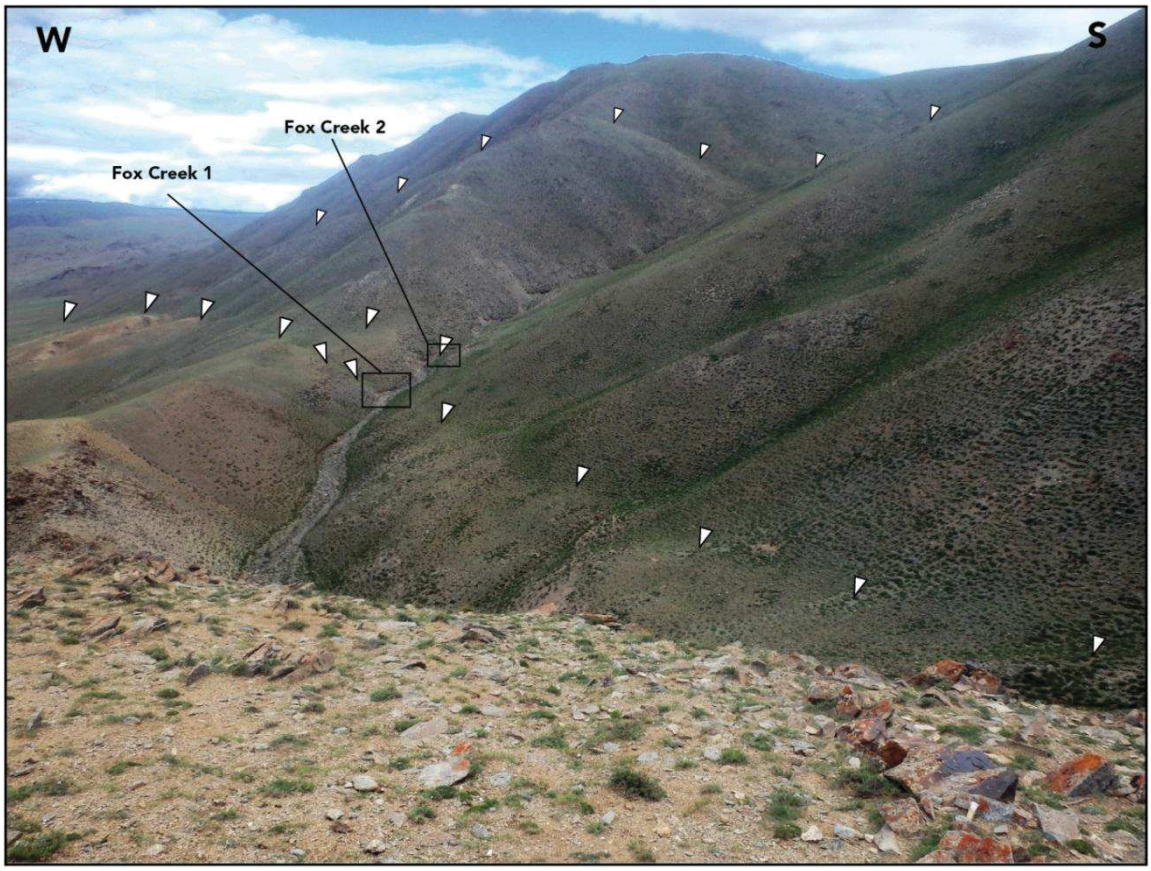


**Figure 4-130: Photograph to the east of the Fox Creek. White arrows indicate the fault traces and field sites are indicated by black boxes.**

The Fox creek 1 site is located at 45.324°N; 96.633°E, on an antithetic fault dipping south, well-marked by a fault trace on eastern flank of the Fox creek talweg, outcropping in a ~1 m-high natural riser capped by slope cobble size colluvium (Figure 4-131). The fault is offsetting Holocene deposits with a normal motion. South of the fault, on the footwall, is a near-horizontal horizon of undisturbed greenish sand to silt, slightly consolidated.

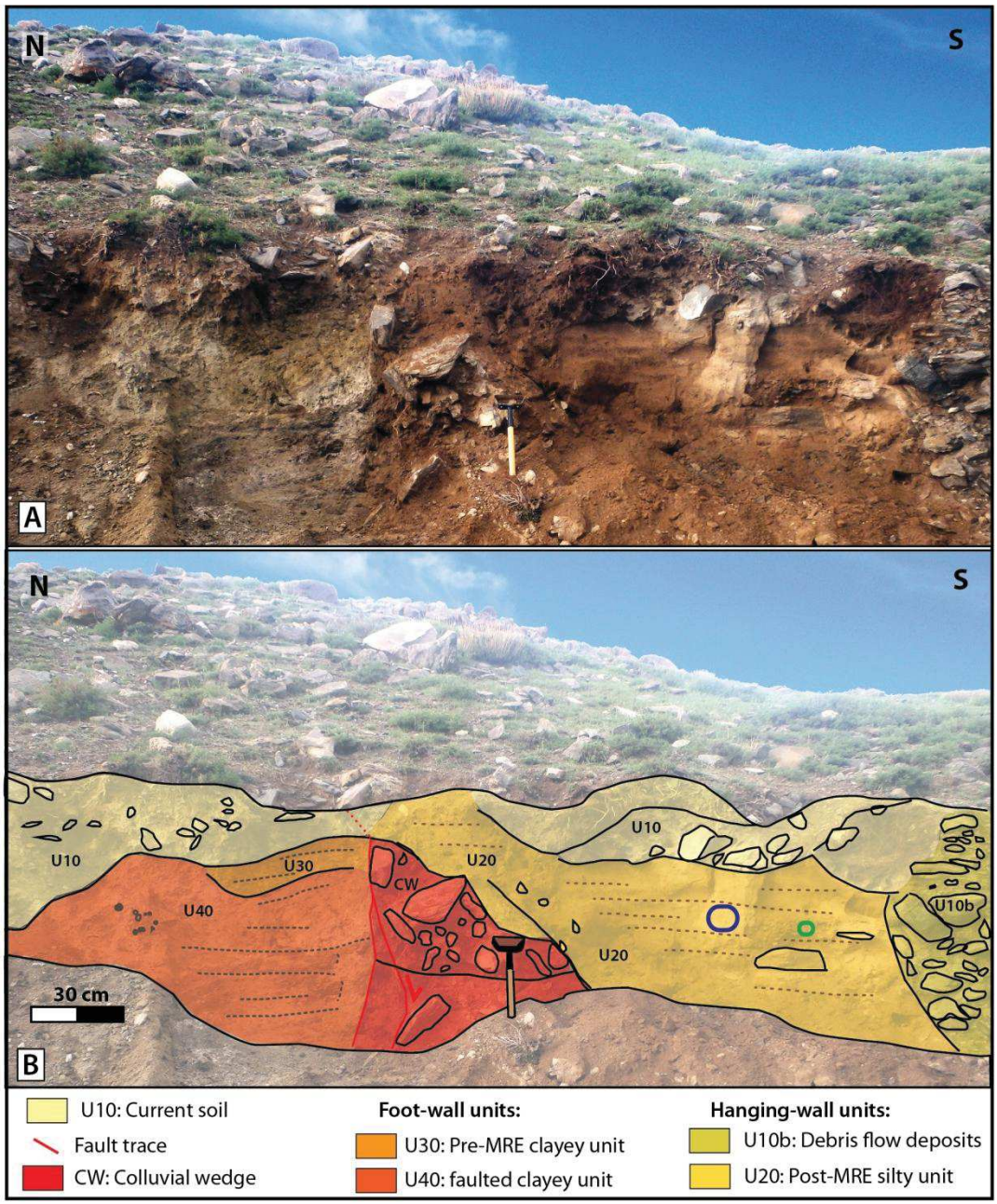


**Figure 4-131: Paleoseismic reconnaissance on Tsogt Fox Creek site 1. A. Photograph to the east of the natural riser where the fault outcrops. B. Photointerpretation of (*A*). Blue ellipse is location of the OSL-bloc sample and green circle is location of radiocarbon sample (Tsogt-C4).**

North of the fault trace, is a colluvial wedge of coarse materials, associated to an on-lapping infill of yellowish sandy-silty deposit, moist and rather loose, in which a fragment of bark has been sampled and analyzed for radiocarbon dating, leading to an age of 616 ± 60 CalyrBP (Tsogt-Fox-C4). We interpret that the colluvial wedge is associated to the most recent event along the Tsogt fault, and consequently this overlying deposit may post-date the most-recent event along the Tsogt fault. This observation assumes that this secondary fault broke during the most recent event, which is objectively possible as the fault trace in surface is marked by the vegetation and generates a visible vertical

offset, unquantified in spite of topographic survey. Additionally, an OSL-bloc has been sampled, in order to constrain the age of this supposed post-faulting infill, and to constrain by a second dating approach the occurrence of the most recent surface-rupturing event along the Tsogt fault (Figure 4-131). This sample analyses are in progress.

The Fox creek 2 site is located ~50 m upstream Fox creek 1, on a north dipping fault scarp collinear to the main one, but visibly located into the footwall, as it does not fit with the fault-related mountain slope. The fault, however, generates a normal metric offset in the bedrock, visible by a clear nick-point in the active channel of Fox creek. On the western flank of the talweg, is a natural riser, where the fault is well visible, as well as the composition of both sides of the fault, on a 2 m-long by 1.5 m-high vertical outcrop, sub-orthogonal to the fault and capped by few cobbles of slope colluvium (Figure 4-132). The fault is here directly affecting the plutonic bedrock, visible on the footwall, fractured with cataclastic process increasing toward the fault. The hanging wall, to the north, displays a colluvial wedge at a depth of ~1m, and an underlying disturbed paleosoil in contact with the fault, in which we sampled an amalgam for radiocarbon dating, which yields an age of 2395 ± 70 CalyrBP (Fox-B2). Overlying the colluvial wedge is an alluvial coarse sand-to-pebble deposits, slightly sorted, in which is a ~1 m-long burrow, characterized by few voids, organic infill of animal dejections of various sizes (from ~0.2 cm to ~5 cm), and horizontally disposed blades of grass, certainly belonging to a rodent nest. Radiocarbon dating of one of the biggest animal dejection leads to a modern age, suggesting that the burrow might have been abandoned for only a few years to decades.

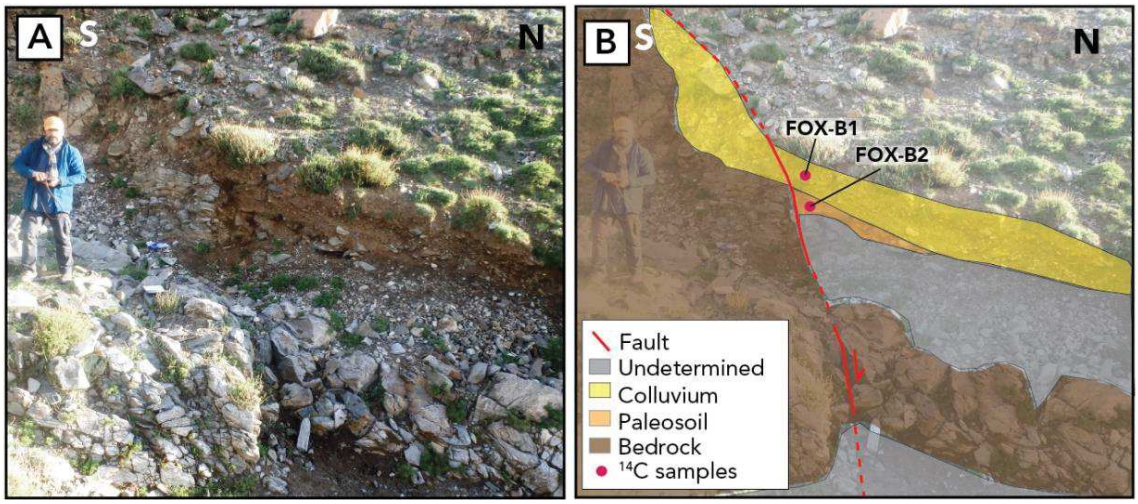


**Figure 4-132: Fox Creek 2 site. A. Photograph to the west of the fault outcrop. Location of the picture is in Figure 4-129. B. Photointerpretation of (A) and location of the radiocarbon samples.**

Assuming that this fault broke during the most recent event along the Tsogt fault, which appears relevant accounting for the distinct nick-point in the active water channel, we interpret the colluvial wedge as associated to the most recent event, and the underneath paleosoil (Fox-B2) age as pre-dating the seismic event.

Hence, we conclude from this paleoseismic reconnaissance on Fox creek sites that the most recent event along the Tsogt fault occurred between 2395 ± 70 CalyrBP and 616 ± 60 CalyrBP.

### IV.6. South Gichigniy Nuruu faults

The northern branch of the SGNF displays a sinuous, very discontinuous thrust fault trace, located mostly within the alluvial fans complex flooding from the Gichigniy Nuruu, and occasionally within the mountain front (Figure 4-133). The consequent variety of alluvial fans reveals that the younger fans systematically do not display fault traces, while some can be found in former deposits. The fault displays here a mostly reverse motion, and metasedimentary terrains thrust on quaternary alluvial deposits (Figure 4-133-B and C).

The southern Branch of the SGNF is located on a large, 20 km-long alluvial fan, associated to the drainage of the Gichigniy Nuruu range to the south, until the endorheic Buur Nuur lake, situated along the central depression of the Suhaytayn Basin (Figure 4-11). The scarp is associated to the Suhaytayn Hills, a 30 km-long low altitude ridge of Devonian meta-basalts, faulted on its southern bound by late quaternary fault trace, which are still well visible in alluvial fan when prolonging eastward, on 30 km. Here, according to Mushkin (PhD, 2007), the fault describes thrust faulting and tilting of Pleistocene lacustrine deposits. Further east, the scarp is still identifiable for 30 km, by distinct segments on central part of the Suhaytayn Basin.

**Figure 4-133: Photographs of the South Gichigniy Nuruu Fault (SGNF). A. Panoramic view to the north of the southern face of the Gichigniy Nuruu. On bottom of the relief is a major thrust. Note the Suhaytayn hills on the foreground. B. Photograph of offset alluvial fan on southern face of the Gichigniy Nuruu. White arrows indicate the thrust fault. C. Photograph to the East of the reverse fault bounding the southern face of the Gichigniy Nuruu. Metasedimentary rocks are thrusted over quaternary alluvial deposits. Location: 45.250°N; 95.518°E. D. Photograph to the North of the southern branch of the SGNF, on southern face of the Suhaytayn hills 545.130°N; 95.518°E°. White arrows show probable location of the fault trace, and characters are for scale. Cumulative vertical offset is ~3 m. E. Photograph of the paved surface offset by the SGNF on south of the Suhaytayn hills (same location as picture D).**

A field reconnaissance done along the Suhaytayn hills (45.130°N; 96.518°E) indicates a couple of paved fan surfaces, uplifted by 1 m to 3 m (Figure 4-133-D and E), attesting of a late-Pleistocene uplift of the ridge. Nonetheless, the paved nature of the fan surfaces certainly suggests a long term abandon, likely ≥ $10^5$ yr. Accordingly, we suggest that the fault south-bounding the Suhaytayn hills, was probably not active during Holocene time.

### IV.7. N-Chandmani fault

The N-Chandmani thrust fault is bounding to the north the central part of the Chandmani Valley. The fault is related to the mountain front, and is well visible within late-Pleistocene alluvial fans, with geometry consistent with a gentle north-deeding fault (Figure 4-134). Total mapped fault trace length is discontinuous and 29.5 km-long. The two western thirds of the surface rupture are trending N100°E, while the eastern part is N089°E.

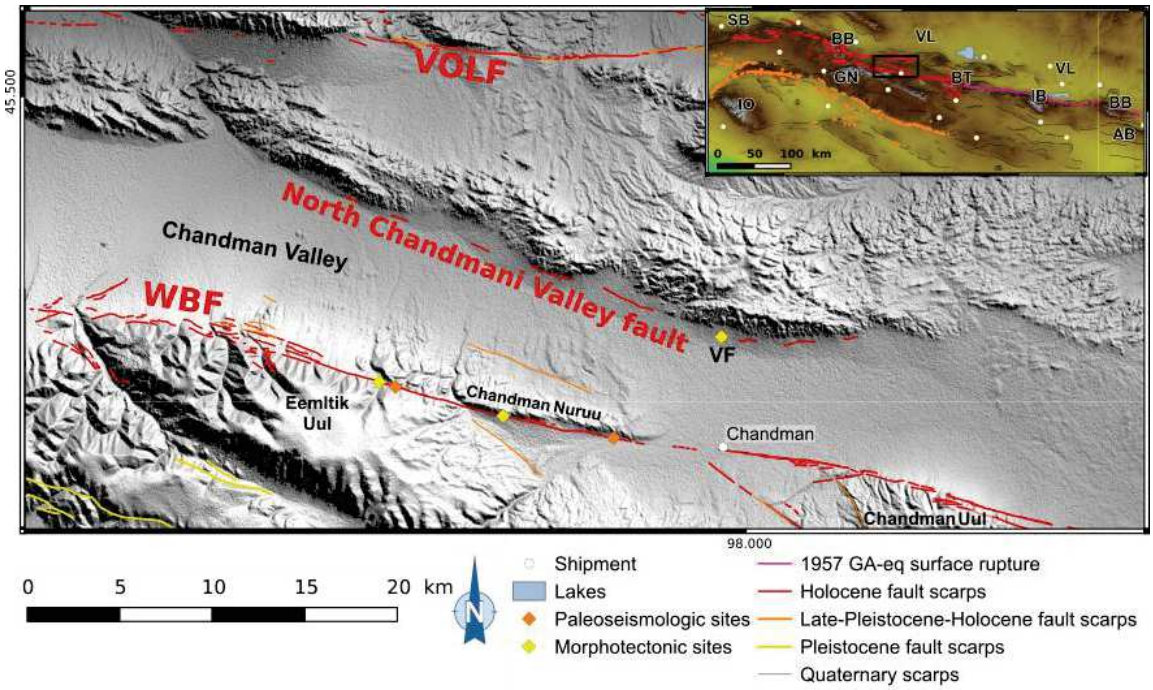


**Figure 4-134: Surface rupture of the North Chandmani Valley Fault and surrounding fault traces. Faults abbreviations: VOLF: Eastern Bogd fault; WBF: Western Bogd Fault; VF: Vulture Fan field site.**

Although the southernmost point of the NCVF is located only 5 km north of the WBF, the north dipping geometry of the fault clearly suggests that it is linked at depth to the VOLF, located 10 to 15 km to the north and that major surface rupturing event on the VOLF very likely involve NCVF.

We carried a field geomorphic survey on Vulture Fan site (45.388°N; 97.582°E), situated on the southernmost point of the fault, on the junction of these faults sections, which is standing only 5.8 km north of the WBF nearby Chandmani town. Vulture fan is a notable alluvial fan, 600 m-wide, in which the fault trace is distinct and, displays continuous cumulative vertical offsets (Figure 4-135.A). The whole fan is visibly abandoned as its surface is fairly flat, and carved by an uneven headward incision, localized on gullies (Figure 4-135.A) where the risers show the surface composition, dominated by pebbles cemented by calcrete on their bottom (Figure 4-136.B).

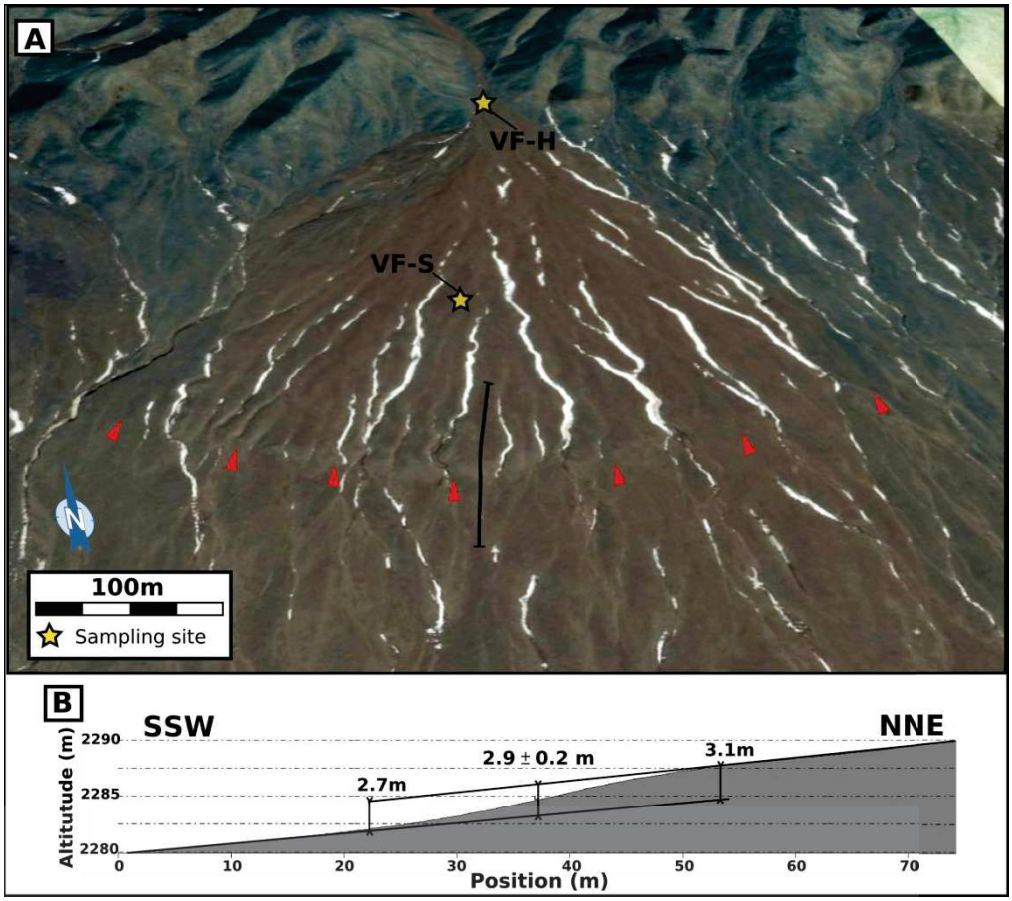


**Figure 4-135: Offset measurement and sample location of Vulture fan site along the North Chandmani Valley Fault. A. Perspective view of the Vulture fan. Red arrows indicate the NCVF scarp, yellow stars the positions of the samples and solid black segment is the location of the profile in (*B*). B. Topographic profile of the NCVF scarp on the Vulture Fan, extracted from TSL microtopographic survey.**

In order to assess the fault slip rate along the NCVF, we carried on a TLS microtopographic survey of an along-slope profile transverse to the fault scarp where it is the best preserved, and a sampling for $^{10}$Be dating of the fan surface exposition age (Figure 4-135.B). The sampling for $^{10}$Be dating has been done from amalgams of 50 quartz-rich clasts of analog granulometry, picked on the one hand on the fan surface (VF-S) and on the other hand in the active channel, nearby the feeding-valley outlet (VF-H), flooding ~700 m north of the fault scarp (location of samples an Figure 4-135.A).

**Figure 4-136: Photograph of Vulture fan site. A. Panoramic view to the north of the NCVF from Chadmani town. Central fan is Vulture Fan. B. Evidences of calcretisation are especially visible on bottom of clasts. C. Photograph of a 50 cm-deep log of vulture fan surface.**

Assessment of the cumulative vertical offset from the 100 m-long profile across the fault scarp leads to a cumulative displacement of 2.9 ± 0.2 m (Figure 4-135.B).

The abandon age of the surface is assessed depending on both concentrations on preserved surface and within the active bed, assuming first a negligible erosion of the fan surface, and secondly that the inheritance in $^{10}$Be of the bedload of the temporary channel is representative of the one related to fan deposits. Analytical results of $^{10}$Be dating lead to a minimum abandon age of vulture fan of 42.8 ± 2.6 ky (Table 15). Conservative computation of the abandon age, assuming a nil-denudation and a nil-inheritance, lead to a maximum abandon age for vulture fan of 81.8 ± 4.8 ky.

Combination of the vertical cumulative offset of the fan, with the surface abandon ages therefore leads to a maximum late-Pleistocene – Holocene vertical slip rate along the NCVF, ranging from 0.04 ± 0.01 to 0.07 ± 0.01 mm.yr$^{-1}$.

**Table 15: The $^{10}$Be nucleide concentrations and computed ages for samples at Vulture Fan site.**

| Sample | Lat (dec°) | Lon (dec°) | Alt (m) | [$^{10}$Be] (at.g$^{-1}$) | err. [$^{10}$Be] 1σ (at.g$^{-1}$) | Shield Cor. | Density | Depth (cm) | $^{10}$Be age tmin (ka) | $^{10}$Be age tint (ka) | Erosion rate (m.Ma$^{-1}$) | $^{10}$Be age tmax (ka) |
|---|---|---|---|---|---|---|---|---|---|---|---|---|
| VFS | 45,389 | 97,892 | 2290 | 1,84E+06 | 6,30E+04 | 0,999 | 2,0 | 0 | 42,8 ± 2,6 | 48,0 ± 2,7 | 10,3 ± 0,6 | 81,8 ± 4,8 |
| VFLA | 45,389 | 97,892 | 2290 | 8,89E+05 | 3,09E+04 | 0,999 | 2,0 | 0 | | | | |

# V. Summary of results and paleomagnitude computations

## V.1. Estimating recurrence intervals and magnitudes of past-earthquakes

Our main results are summarized in Table 16, which presents a synthesis of the fault parameters determined for the main faults in the Gobi-Altai. When appropriate, we also calculate recurrence intervals according to our paleoseimic investigations, and estimated magnitudes of past earthquakes from:

i. The empirical laws of Wells and Coppersmith (1994), which first relate the magnitude and fault surface rupture length :

$$M_w = 5.08 + 1.16 \times \text{Log}(L) \qquad \text{(IV.1)}$$

with $M_w$, the moment magnitude and $L$, the surface rupture *Length*. This allows computing magnitudes for all main surface ruptures of the Gobi-Altai, including the TGF, the NABF, the SCNF, the Khaliun fault, end the North Artz Bogd fault (Figure 4-3). Secondly, regarding the coseismic offset associated with the most recent surface-rupturing event determined fom the 'COPD approach' (given it is the best defined on COPDs) (Chapitre 3.IV.2):

$$M = 6.93 + 0.82 \times \log(U_{mean}) \qquad \text{(IV.2)}$$

with $U_{mean}$, the average displacement.

ii. The moment magnitude scale defined by Hanks and Kanamori, (1979):

$$M_w = \frac{2}{3} \times \text{Log}(M_0) - 10.7 \qquad \text{(IV.3)}$$

with $M_0$ the seismic moment, defined as $M_0 = L.W.U.\mu$, with μ the shear modulus used $3.20 \times 10^{11}$ dyn.cm$^{-2}$ for W ≤ 20 km, and at $4.02 \times 10^{11}$ dyn.cm$^{-2}$ for W > 20 km (Schlupp and Cisternas, 2007; Villaseñor et al., 2001; Petit et al., 2002; Ionov, 2002, see also Chapitre 3.V.2), with W being the fault width (i.e. the seismological thickness). Note that L, W and U are in centimeters, the fault length (L) defined from our mapping, and the coseismic offsets ($U_{mean}$) related to the most recent surface rupturing event is derived from the 'COPD approach' (Chapitre 3.IV.2.2 Kurtz et al., submitted). Because the seismogenic thickness in the Gobi-Altai region in not well constrained (see discussion in Chapitre 3.V.2), magnitudes are estimated from 3 fault widths: 20 km, considering that only the upper continental crust breaks, 50 km for the entire continental crust, and finally 60 km if we consider that the rupture might

propagates into the lithospheric mantle (Schlupp and Cisternas, 2007; Villaseñor et al., 2001; Petit et al., 2002; Ionov, 2002).

Additionally, Figure 4-137 shows in map view the long term slip rates, identified paleoseimic events and coseismic offsets related to the most recent event (MRE) along the main faults: EBF, WBF, VOLF, TGF, NCVF and Tsogt faults.

We acknowledge that in next sections, we consider the fault parameters (ages of past-earthquakes, coseismic offsets and slip rates) as representative of the whole faults, while they were determined in limited fault sections or even, for paleoseismological investigations, at unique sites – even though we know that such transpressive faults involve along fault slip variations (cf. Chap3) and potentially partial rupturing.

### V.2. EBF

The Eastern Bogd Fault (EBF) surface rupture (Chapitre 3.IV.1) is composed of a 260 km-long main strike-slip fault scarp plus 90 km of associated reverse scarps, that ruptured during the 1957 Gobi-Altai earthquake, producing an average horizontal slip of 3.5 ± 1.4 m along the main strike-slip fault trace (Chapitre 3.V.2). The long term slip rate was determined to be ~1,0 mm.yr$^{-1}$ (Ritz et al., 1995, 2006; Rizza et al., 2011). The 1957 surface rupture is larger than any other strike-slip faults identified and analyzed in this study within the western Gobi-Altai (e.g. WBF, VOLF, TGF). Consequently the mean coseismic offset and the estimated magnitudes are also larger. In Chapitre 3.V.2, the magnitude of the Gobi-Altai earthquake has been quantified to Mw8.1, accounting for a 50 km fault width, and integrating mean slips on each segment (main and secondary). Note that for the secondary segments, the fault width was taken at 20 km, based on the geometry of structures criteria suggesting that they joined the main strike-slip fault at the base of the upper crust (e.g. Cunningham et al., 2003; R. Vassallo et al., 2007). Comparatively, the magnitudes for the Gobi-Altai earthquake computed from the fault length and the mean coseismic offset (equations (IV.2) and (IV.2) from W&C94) lead to Mw8.0 and Mw7.5, respectively. The first of these results is consistent with the magnitude estimated from the analysis of the slip distribution along the EBF, while the second result estimated from the average coseismic offset is significantly lower.

| Structure[1] (fautl) | Main Motion[2] (LL - N - R) | Fault length[3] (L. second. F.) (km) | Segmentation[4] (Nb + TZ) (Nb second. F.) | Coseismic offsets[5] Nb. Eq. | Coseismic offsets[5] (m ± 1 σ) | Slip rate[6] SR + Δ SR (mm/yr) | Slip rate[6] Period Covered | Slip rate[6] Nature (min/max) | Paleo-EQ[7] Age min. (yr or CalyrBP) | Paleo-EQ[7] Age Max. (yr or CalyrBP) | Return period[8] P (kyr) | Return period[8] ΔP | Paleomagnitudes[9] (MRE) W & C 94 L_fault | W & C 94 Umean | W & C 94 M | H & K 79 Fault Width | H & K 79 Mw |
|---|---|---|---|---|---|---|---|---|---|---|---|---|---|---|---|---|---|
| Eastern | | 260 | 15 seg. | MRE | 3.5 ± 1.4 | 1.0 ± 0.2 | 200 ky | Most prob. | 1957 | | 4,4 | 1,3 | 350 | - | 8,0 | 20 | 7,9 |
| Bogd Fault | LL - R | (90) | 5 second. Seg. | - | 3.0 ± 2.4 | 0.52 ± 0.12 | 200 ky | Min. | 3070 | 5640 | 5,3 | 3,0 | - | 3,5 | 7,5 | 50 | 8,2 |
| (EBF) | | | 2TZ | - | 2.5 ± 2.1 | 1.12 ± 0.34 | 200 ky | Max. | 7950 | 11310 | | | - | - | - | 60 | 8,3 |
| Western | | 150 | 5 seg. | MRE | **2.2 ± 0.4** | **0.7 ± 0.2** | **20 ky** | **Mean** | 1330 | 1920 | 3,2 | 1,4 | 175 | - | 7,7 | 20 | 7,6 |
| Bogd Fault | LL | (25) | 1 seconds eg. | PEq.2 | 1.4 ± 1.1 | 0,48 ± 0.21 | 13 ky | - | 3720 | 5920 | 4,9 | 1,8 | - | 2,2 | 7,3 | 50 | 7,9 |
| (WBF) | | | 2 TZ | | | 1.2 ± 0.5 | 13 ky | Max. | 8980 | 10370 | Mean. (ka) | | | | | 60 | 8,0 |
| | | | | | | | | | | | 4,0 | 1,6 | | | | | |
| | | 114 | 6 seg. | MRE | **3.0 ± 1.0** | **0.5 ± 0.2** | **40 ky** | **Mean** | 3260 | 6610 | 2,5 | 3,0 | 144 | - | 7,6 | 20 | 7,6 |
| Valley of | LL | (30) | 2 second. seg. | PEq.2 | 2.1 ± 1.8 | 0.82 ± 0.14 | 110 ky | Max. | 6090 | 8790 | | | - | 3,0 | 7,5 | 50 | 7,9 |
| Lakes Fault | | | 2 TZ | PEq.3 | 5.0 ± 2.9 | 0.67 ± 0,15 | 40 ky | | | | | | - | - | - | 60 | 8,0 |
| (VOLF) | | | | PEq.4 | 4.9 ± 3.5 | 0.3 ± 0.08 | 40 ky | | | | | | - | - | - | | |
| | | | | PEq.5 | 5.8 ± 4.10 | 0.06 ± 0.01 | 40 ky | Vertical | | | | | - | - | - | | |
| Tsagaan Gol | | 125 | 5 seg. | - | | 0,19 ± 0.10 | 50 ky | Min | | | | | 145 | - | 7,6 | 20 | 7,6 |
| Fault | LL | (20) | 2 TZ | - | 3.2 ± 1.1 | **1.83 ± 0.39** | 40 ky | - | | | | | - | 3 | 7,5 | 50 | 7,9 |
| (TGF) | | | | - | | | | | | | | | - | - | - | 60 | 8,0 |
| North | | 30 | | - | | 0.04 ± 0,01 | 80ky | Min. Vert. | | | | | 30 | - | 6,8 | | |
| Chandman | R | | - | - | | 0,07 ± 0.01 | 40ky | Max. Vert. | | - | | | - | - | - | | |
| Valley Fault | | | | - | | | | | | | | | - | - | - | | |
| | | 32 | 5 seg. | - | | 0,18 ± 0,05 | 20ky | Min. Vert. | | - | | | 32 | - | 6,8 | | |
| Tsogt Fault | N | (20) STF | | - | | 0,71 ± 0,19 | 20ky | Max. Vert. | 616 ± 60 | 2395 ± 70 | | | 52 | - | 7,1 | | |
| | | (10) NTF | | - | | **0,2 ± 0,1** | **80ky** | **Most Prob.** | | - | | | 62 | - | 7,2 | | |
| SGNF | R | > 150 | | - | | | | | late-Pleistocene ? | | | | 190 | - | 7,7 | | |
| NIO | LL - R | 130 (30) | 4 seg. 1 sec. br. | - | 3,2 | | | | late-Pleistocene ? | | | | 160 | - | 7,6 | | |
| Khaliun | R | 20 | | - | (W & Co) | | | | Holocene ? | | | | 30 | - | 6,8 | | |
| N-Artz Bogd<br>S Baga Bogd | R - LL | 75 | | - | | | | | Holocene ? | | | | 75 | - | 7,3 | | |

**Table 16: Synthetic table of the morphotectonic and paleoseismic results detailed in this study. 1. Fault name; 2. Main motion displayed by the fault; 3. Fault surface rupture length, in bracket are surface rupture lengths of the secondary segments; 4. Number of segments ('seg.'), number of secondary segments ('second. seg.', i.e. associated faults) and number of identified tip zone (TZ); 5. Coseismic offsets assessed by the COPD approach (cf.** Chapitre 3.IV.2.2**), 'MRE' is most recent event, and 'Peq 2 to 5' are paleoearthquakes 2 to 5 (the 2nd being younger than the 5th), uncertainties are 1 standard deviation; 6. Long-term fault horizontal sip rates are given with the corresponding computation time and with the nature of the slip rate assessment (i.e. maximum, minimum or most probable), Min./Max. values are slip rate assessments on one offset, and are given with two significant digits, while instead most probable values are averaged slip rates on field sites, given with one significant digit. Vert.: vertical slip rate; 7. Age of identified paleoearthquakes ('MRE' is most recent event, and 'Peq 2 and 3' are paleoearthquakes 2 and (the 2nd being younger than the 3rd); 8. Return period, computed from data on (7.); 9. Paleomagnitudes, computed regarding on the one hand to (Wells and Coppersmith, 1994) empirical regressions, either from the fault length or from average coseismic offset (3 left columns), and on the other hand from (Hanks and Kanamori, 1979)moment magnitude scale, for various hypothesis of the fault width (i.e. seismogenic thickness) of 20 km, 50 km and 60 km (2 right columns, see text for details).**

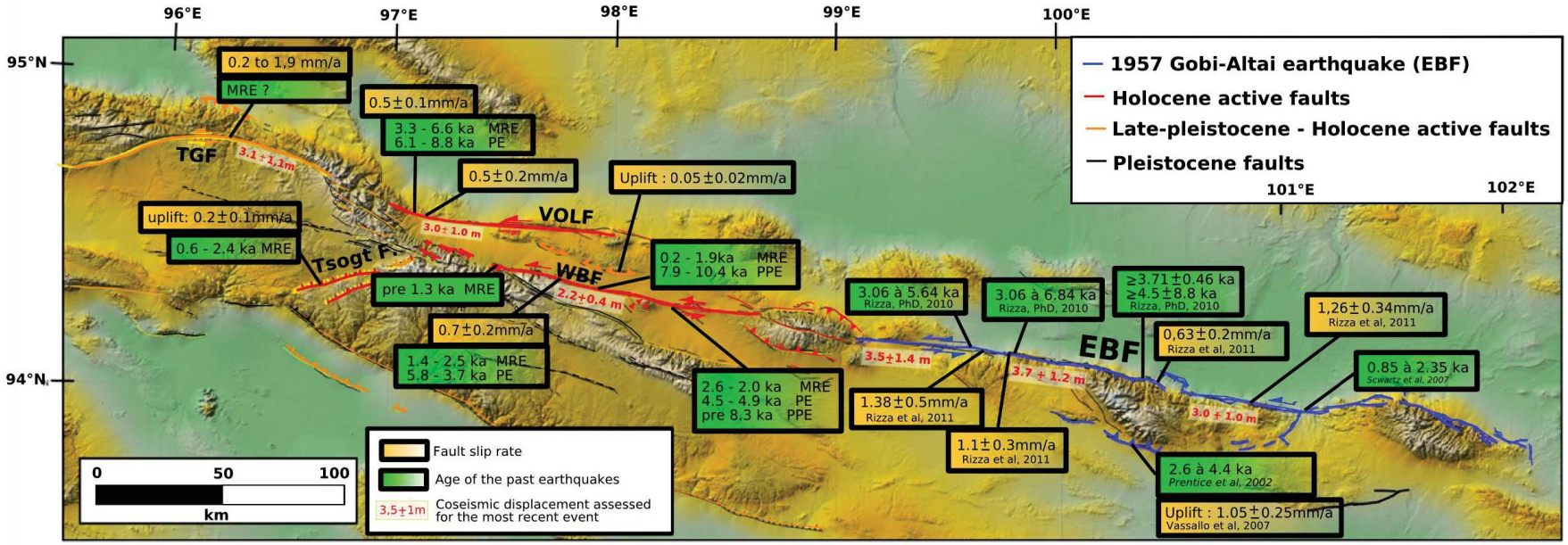


**Figure 4-137: Synthetic map of the morphotectonic and paleoseismic results detailed in this study. MRE: most recent event. PE: penultimate event. PPE: pre-penultimate event.**

### V.3. WBF

The Western Bogd Fault (WBF) is characterized by an almost continuous ~175 km-long long term fault scarp (given that the main scarp is 150 km-long, and we identified 25 km of secondary faults), displaying mostly left-lateral motion. Systematical offset measurements along a 4 km-long section in the central part of the fault enabled us to constrain the coseismic offset related to the most recent surface-rupturing event at 2.2 ± 0.4 m. The penultimate horizontal offset was estimated at 1.4 ± 1.1 m. These results allow estimating moment magnitudes of Mw 7.6 and 8.0 depending on the considered fault width, ranging from 20 to 60 km (see equation (IV.3). These estimates are coherent with the magnitude Mw 7.7 estimated from the fault length with equation (IV.1). However, the magnitude calculated considering the coseismic offset (equation IV.2) is lower with a value of Mw 7.3. Determining the slip rate along the WBF on Ice Creek site yields a mean slip rate of 0.7 ± 0.2 $mm.yr^{-1}$ over the last 20 ka (note that the maximum slip rates were also estimated 1.2 ± 0.2 $mm.yr^{-1}$ for the same time span). Finally, paleoseismic investigations within six trenches dug across the fault allow identifying at-least three paleo-events for the Holocene period (most recent event E1 ϵ [1 920 ; 1 330] CalyrBP, penultimate event E2 ϵ [5 920 ; 3 720] CalyrBP, and prepenultimate event E3 ϵ [10 430 ; 8 800] CalyrBP). This in turn, allows estimating recurrence intervals of 3.2 ± 1.4 ka and 4.9 ± 1.8 ka, separating the last 3 surface-rupturing events that occurred along the WBF. Although we could investigate only two seismic cycles, these results allow proposing an average return time period for major earthquakes along the WBF of 4.0 ± 1.6 ka, which is – notwithstanding large uncertainties – consistent with return times estimated along the EBF (Ritz et al., 2009; Rizza, PhD, 2010).

### V.4. VOLF

The Valley of Lakes fault (VOLF) is associated with an almost continuous, 144 km-long long term fault scarp (the main scarp is 114 km-long, and 30 km of secondary faults have been identified). The VOLF displays a mostly left-lateral motion, and we systematically measured lateral displacements along a 12.5 km-long section within the western part of the fault (where paleoseismic trenches were dug). This yielded a mean coseismic offset of 3.0 ± 1.0 m for the most recent surface-rupturing event, and to an offset of 2.1 ± 1.8 m for the penultimate event. Assuming the different values for the fault width (20 or 60 km), these parameters allow estimating the moment magnitude (Hanks and Kanamori, 1979) at Mw7.6 and Mw8.0 (equation IV.3). Calculating the moment magnitudes from Well and Coppersmith empirical laws from the fault surface rupture length (equation IV-1) and the average coseismic slip (equation IV-2) yield Mw7.7 and Mw7.3, respectively. We note, here again, the consistency between moment magnitudes derived from the fault surface

rupture length and the moment magnitude derived from the seismic moment (Hanks and Kanamori, 1979). On the other hand, there is a significant difference when comparing the magnitude estimated from the average coseismic offset with the magnitude derived from the seismic moment. Determining the slip rate along the VOLF within Dark Creek and Biger Terraces sites yielded to consistent results, with a slip-rate of 0.5 ± 0.2 $mm.yr^{-1}$ over the last 20 ka. Paleoseismic investigations within 2 cross-fault trenches allow identifying at least two events during the Holocene period (the most recent event E1 ϵ [6.61 ; 3.26] ka, and the penultimate event E2 ϵ [8.79 ; 6.09] ka). These are based only on 3 OSL ages, and hence do not allow us to constrain a significant return time period (as it can only be estimated to 2.5 ± 3.0 ka, considering the low constrain of return time between both events) for surface rupturing events along the VOLF. Note that 3 other OSL samples analyses are is progress, and should help us better constrain these preliminary results.

### V.5. NCVF

The North Chandmani Valley Fault is a north-dipping thrust, at least 30 km-long, which although being very close to the WBF (~ 5 km at closest point), is certainly linked at depth to the Valley of Lakes fault, that stands 10-15 km to the north (Figure 4-138). We propose to estimate the magnitude related to potential surface-rupturing event along the NCVF fault using Wells and Coppersmith (1994) empirical relations between Mw and the length of reverse faults (adapting the coefficients of the equation (IV-1) for reverse fault, i.e. $M_w = 5.00 + 1.22 \times \text{Log}(L)$). This yields Mw6.7, keeping in mind that Wells and Coppersmith (1994) empirical relations for thrust faults have moderate correlation ($R^2$=0.89). Note that this estimate considers the NCVF on its own, but a scenario in which the thrust fault would rupture contemporaneously with the VOLF is not excluded (cf. the contemporaneous rupture of the Gurvan Bulag thrust fault with the EBF during the Gobi-Altai 1957 event). The vertical slip rate along the NCVF has been estimated to be 0.07 ± 0.01 $mm.yr^{-1}$, during the last 40 ka. This low slip rate does not allow us to conclude on the Holocene activity of the NCVF fault; further paleoseismic investigations are needed to constrain the age of recent surface rupturing events, and discuss the fault activity during the Holocene.

### V.6. TGF

Our investigations of The Tsagaan Gol Fault (TGF), compared to the others main strike-slip faults in the central and eastern Gobi-Altai, is based on poor satellite images (orographic effects being associated with an important nebulosity), and on field reconnaissance (3 days). However, our investigations allow us to gather preliminary results concerning its main sismotectonic characteristics. The fault is associated with an

almost continuous, 145 km-long cumulative fault scarp (the main fault trace is 125 km-long, and 20 km of secondary faults have been identified) and shows mostly left-lateral motion. Within its central part, the TGF seems to be associated with the south-dipping Khaliun thrust fault, which is located only 15 km northwards. Although no field investigations were carried out along this fault we interpreted it as a foreberg structure joining the TGF at depth (Figure 4-99). 3 offset measurements yielded a mean estimate of 3.2 ± 1.1 m for the coseismic offset related to the most recent event along the TGF. It is delicate to use this result to estimate a magnitude, given that we do not have any insight in slip variability along that section (e.g. Rockwell and Klinger, 2013, Chapitre 3.V.1), or even about total the slip distribution (e.g. Vallage et al., 2016). Nevertheless, we note that it is consistent with the 3.0 m average slip deduced from Wells and Coppersmith (1994) empirical relation that links surface rupture length (L) to average slip ($U_{mean}$) for strike-slip faults (in that case L would be 125 km):

$$\text{Log}\ (U_{mean}) = -1.70 + 1.04 \times \log\ (L) \qquad \text{(IV-4)}$$

Accordingly, we used our coseismic offset estimation (3.2 ± 1.1 m) as an average value to calculate the magnitudes of a potential earthquake breaking the whole TGF using either: i. the Hanks and Kanamori (1979), moment magnitude equation (equation IV.3), which yields magnitudes of Mw7.6 to Mw8.0 depending on the considered fault width; or ii. the Wells and Coppersmith (1994), empirical relations, which yield magnitudes of Mw7.6 using the mapped surface rupture length (equation IV.1), and Mw7.5 using the average coseismic offset (equation IV.2). The horizontal slip rate estimated along the TGF ranges from 0.2 ± 0.1 $mm.yr^{-1}$ to 1.8 ± 0.4 $mm.yr^{-1}$.

### V.7. Tsogt fault

The Tsogt Fault is associated with a continuous 32 km-long surface rupture, here named the ‘main Tsogt fault’. The main Tsogt fault is dominated by normal motion. Considering the uplifted abandoned Jurassic peneplain (Jolivet et al., 2007; Vassallo et al., 2007) as a the main displaced geomorphic marker across the fault, we estimated total cumulative offset comprised between 400 and 700 m,. We estimated the magnitude related to potential surface-rupturing seismic events along the Tsogt fault using the Wells and Coppersmith (1994), empirical relations between the magnitude and the length of normal fault (adapting the coefficients of the equation (IV-1) for normal faults: $M_w = 4.86 + 1.32 \times \text{Log}\ (L)$). This yields a moment magnitude of Mw6.8. The Tsogt fault is associated with: i. the Northern Tsogt Valley fault, 10 km-long, for which surface rupture is hard to distinguish, and hence probably does not represent Holocene activity, and ii. the South Tsogt Fault, 20 km-long, which displays an almost continuous fault scarp, but with a

smaller vertical offset, <1 m. Holocene activity of the South Tsogt Fault has not been estimated in this study, but looking at the good preservation of the surface rupture, we cannot exclude that this fault produced earthquakes during Holocene time. The vertical slip rate has been quantified along the main Tsogt Fault using two vertically offset fan surfaces, Tsogt-fan1 and Tsogt-fan2 (Figure 4-125 and Figure 4-127 respectively). This yielded slip rates ranging from 0.18 ± 0.05 mm.yr$^{-1}$ to 0.71 ± 0.19 mm.yr$^{-1}$ respectively, with a preferred estimate at 0.2 ± 0.1 mm.yr$^{-1}$. A preliminary paleoseismic study along the fault allow estimating that the last event occurred between 2395 ± 70 CalyrBP and 616 ± 60 CalyrBP.

### V.8. NABF

The North Aj Bogd Fault is associated with an almost continuous, 160 km-long cumulative fault scarp (the main fault trace is 130 km-long, and is associated with a 30 km-long secondary north branch). The fault shows a transpressive kinematics, dominated by left-lateral motion. Neither field survey nor systematic offset measurements were conducted along this major structure, and we may only propose hypothetical magnitude and average offset derived from scaling relationship (Wells and Coppersmith, 1994) to be Mw7.6, and $U_{mean}$ = 3.2 m, derived respectively from equations IV-1 and IV-4.

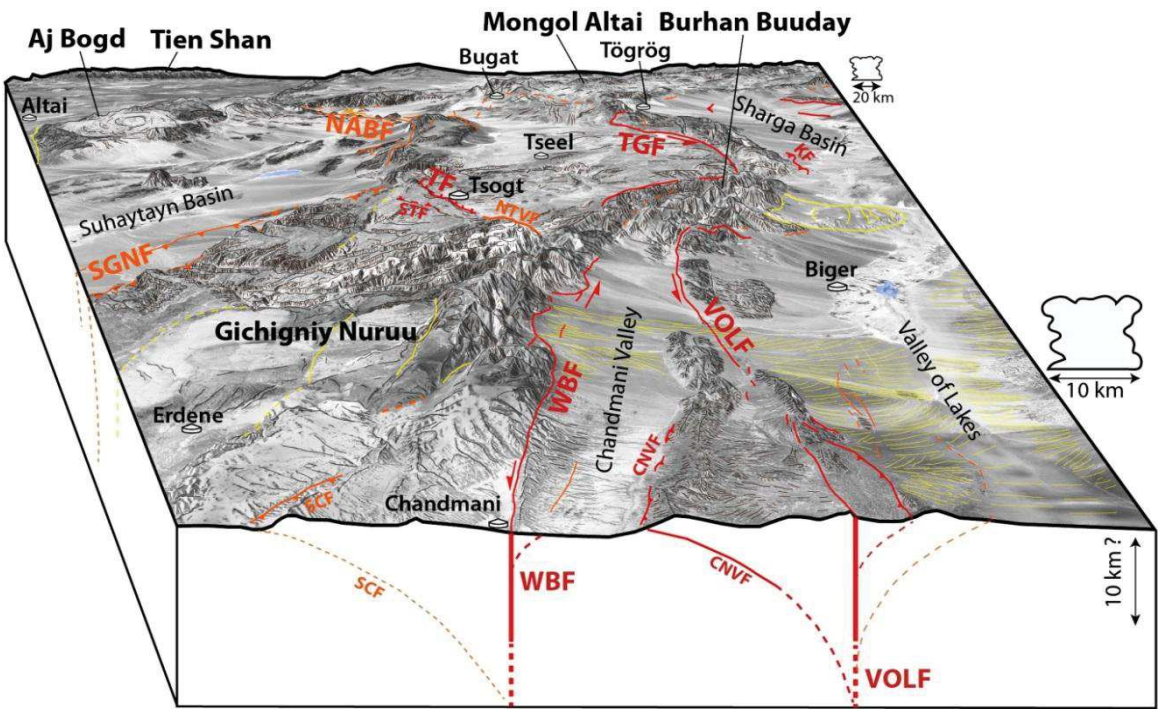


**Figure 4-138: Block diagram of the main active faults of the western Gobi-Altai. Color lines are faults, dashed when inferred. NABF, North Aj Bogd fault; SGNF, South Gichigniy Nuruu fault; SCF, South Chandmani fault; TF, Tsogt fault STF, South Tsogt fault; NTVF, North Tsogt Valley fault; TGF, Tsagaan Gol fault; KF, Khaliun fault; VOLF, Valley of Lakes fault; NCVF, North Chandmani Valley fault.**

### *Remark on the application of empirical laws*

We can see from Figure 4-139, that the moment magnitudes derived from the average offset using empirical relations are systematically lower than the magnitudes computed from fault dimensions. This observation seems to indicate that for large seismic events, the whole crust breaks and consequently, larger earthquakes would not necessary yield a larger offset, but only to a longer fault plane (e.g. Klinger, 2010). We can, for instance, propose the opposite exercise: taking the 260 km-long main EBF surface rupture associated with the 1957 earthquake, Mw7.8 to Mw 8.2, for which we determine an average offset ranging from 5.5 m to 11.5 m using the empirical law, instead systematic analysis of offset geomorphic features yield an average offset of 3.5 m (**Chapitre 3.V.1**, Kurushin et al., 1998; Rizza et al., 2011; Choi et al., 2012). This show again discrepancies between the magnitudes computed from the empirical relation linking the magnitude to the coseismic offset in the Gobi-Altai context. Conversely, the empirical moment magnitude computed from the surface rupture length is systematically close to the moment magnitude derived using the Hanks and Kanamori (1979) logarithmic scale, and more specifically for a fault width of 20 km.

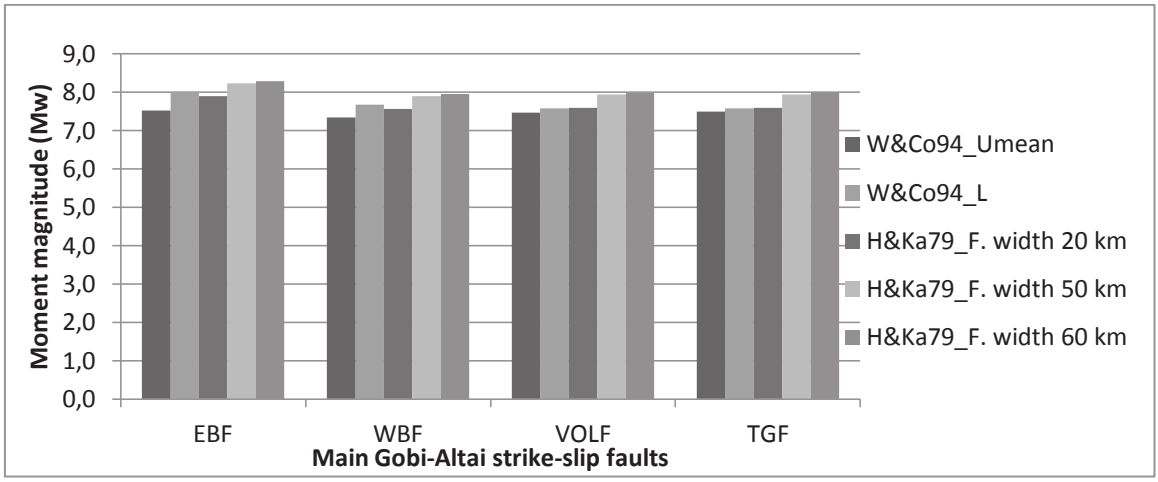


**Figure 4-139 : Paleomagnitudes computed for main Gobi-Altai strike-slip faults, with the following relations: W&Co94_Umean, equation IV-2 ; W&Co94_L, equation IV-1 ; H&Ka79, equation IV-3 for various fault widths (F.width).**

One may also question the quality of the data that were used to build the empirical relationship. It is actually at first order easier to get a good value for the fault length than for the average slip, especially when dealing with old earthquakes.

## VI. Conclusion

To conclude this extensive survey of fault surface ruptures within the western Gobi-Altai, systematic detailed mapping allows identifying the main active faults in the area and discussing the fault activity during the late-Pleistocene period. Morphotectonic field investigations enable us to quantify the fault-related deformation using microtopographic surveys and systematic offset reconstruction. These data, associated with: i. statistical modeling, allow us to quantify successive coseismic offsets recorded by the landforms, and ii. $^{10}$Be dating, lead to assessments of fault slip rates on timescales varying from late-Pleistocene to Holocene. Furthermore, paleoseismic investigations done within cross-fault trenches, allow us to constrain the age of Holocene surface-rupturing seismic events on the WBF, the VOLF and somewhat on the Tsogt fault.

On the basis of these fundamental fault parameters, we propose a computation of earthquake return periods and magnitudes related to the most recent surface rupturing event, using empirical laws of Wells and Coppersmith (1994), as well as the moment magnitude scale of Hanks and Kanamori (1979) for various values of seismogenic thicknesses. We conclude of the Holocene activity of the WBF, the VOLF and the main Tsogt fault, with potential magnitudes up to Mw8, and return time ranging from 2 to 5 ka. Holocene seismic activity along the TGF and the NCVF during the Holocene is probable, but it cannot be appreciated in spite of paleoseismological results. The Khaliun fault, the SGNF and the NIOF present extensive evidence of surface faulting, and certainly require further investigation in order to assess their activity, return period, and potential earthquakes magnitudes.

When looking at the spatial distribution of the seismic deformation through the horizontal slip rates (Figure 4-137), it appears that the rate of ~1 mm.yr$^{-1}$ measured along the Bogd fault (e.g. Rizza et al., 2011) is distributed on the WBF and the VOLF with horizontal slip rates of 0.7 ± 0.2 mm.yr$^{-1}$ and 0.5 ± 0.2 mm.yr$^{-1}$, respectively (Figure 4-140). Westward, two distinct active fault bundles can be defined: the first to the north, composed of the western-VOLF and the TGF, which partly joins the Sharga basin structures and partly prolonges along the Bugat valley until the Altai range. The second bundle, to the south, is composed of the NABF, linked to the WBF by the Tsogt fault. A transfer of the deformation from the WBF to the TGF along the southern bound of the Burhan Buuday restraining bend is also suspected. Unfortunately, the slip rate along the TGF is poorly constrained (between 0.2 ± 0.1 mm.yr$^{-1}$ to 1.8 ± 0.4 mm.yr$^{-1}$) and although it ranges within coherent slip rate values with regard to the rates involved in the region, no conclusions can be drawn on the distribution of the seismic deformation along either the

TGF branch or the NABF branch, via the Tsogt and Burhan Buuday structures. We note that slip rates discussed in this study are constrained by a maximum of two sites along each fault, while along-fault variations of the slip rate are certainly involved.

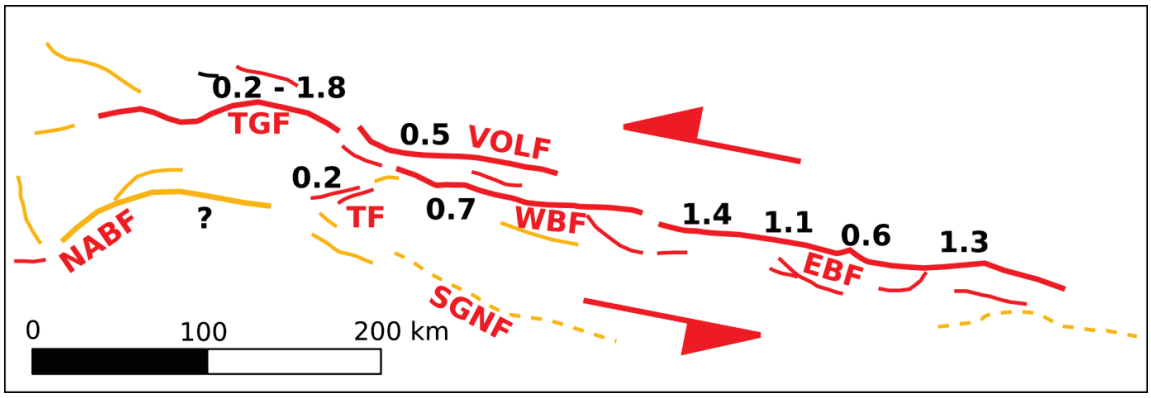


**Figure 4-140: Scheme of the spatial distribution of the horizontal slip rates along the main faults of the Gobi Altai, centered on central values (black numbers). Note that the Tsogt Fault (TF) slip rate is a vertical rate, that we propose here as a horizontal rate, assuming a fault dip of 45°. NABF, North Aj Bogd fault ; SGNF, South Gichigniy Nuruu fault; SCF, South Chandmani fault; TF, Tsogt fault; TGF, Tsagaan Gol fault; VOLF, Valley of Lakes fault.**

These observations are consistent with conclusions suggested by Mushkin (PhD, 2007), by subdividing the Gobi-Altai from south to north, with a southern part which used to be active during early Pleistocene, a central part which was active in the late-Pleistocene but does not show clear evidence of Holocene activity, and a northern active part composed of the Bogd strike-slip Fault System (EBF + WBF + VOLF + TGF). This conclusion is also coherent with the global migration of the deformation through Asia, here observed at regional scale, with northward migration of the deformation within the Gobi-Altai, also associated with a clockwise rotation of the geological blocks constituting the Gobi-Altai range (Schlupp, PhD, 1996). Another observation that can be made about the evolution of the deformation is the migration of vertical deformations (thrusts, see Figure 4-138): first ‘in sequence’ out of the mountain range (for instance the southern branch of the SGNF), secondly ‘out of the sequence’, into the mountain range (for instance the SCVF). Such evolution of thrusts might be related to the increasing lithostatic stress associated to reliefs growing, leading to a progradation of the reverse structures, also resulting in forebergs formations (e.g. Cunningham et al., 2003; Vassallo et al., 2007). For instance the Khaliun fault is visibly prograding northward on the basin; or to the east of Biger, secondary blind thrusts are possibly related to the VOLF, as bedrock outcrops are visible at the center of the basin. Structural characterization of the in-depth geometry of those structures constitutes a notable perspective in the understanding of the evolution of the seismic activity within the Gobi-Altai.

The seismic cycle has been analyzed with a paleoseismic approach, focusing on the occurrence of major events. At first order, this appears relevant regarding large historical earthquakes and relative abundance of large (>100 km) Holocene fault surface ruptures in the Gobi-Altai context. However, the determination of these fault parameters has been made by tools and methods either not capable or not properly designed to reveal the occurrence of moderate seismic events, which do not break the surface – or do so partially with small offsets (< 1m). Assuming that what we see – and describe here – is only what the tools and approaches we carried out allow us to see, we cannot rule out that this region might also produce more moderate seismic activity. Nevertheless the seismic activity during the second half of the XXth century (Figure 4-2) has been described as post-seismic readjustments following the 4 major ruptures. The main faults identified in this study seem to be locked at first order, like the central WBF, Eastern TGF, Eastern VOLF, Tsogt fault, SGNF and NABF.

As a conclusion, according to our data, seismic hazard in western Gobi-Altai is characterized by large earthquakes (Mw > 7.5) of millennial return time (4 ± 2 ka). These are located on crustal strike-slip faults, linked to each other through large transpressive and transtensive structures. The occurrence of earthquakes along these faults is consequently rare, but the potential damages related to such events needs to be taken into account in the Mongolian policy.

Finally, these fault parameters may be compared to each other, in order primarily to test their reliability, and secondly to assess the clustering potential these major structures undergo, as discussed in the next chapter.

# Chapitre 5. Discussions et perspectives

Ce chapitre de discussions rappelle dans une première partie certaines hypothèses de travail relatives à la quantification des différents paramètres avec lesquels nous avons caractérisé les failles dans cette étude (longueur, décalages, vitesse de glissement, intervalle de récurrence, épaisseur sismogénique), et tire un bilan sur les limites que peuvent présenter les approches employées, ainsi que quelques perspectives. Ces limites devront être gardées à l'esprit pour la seconde partie de cette discussion, qui vise à explorer les corrélations, tant spatiales que temporelles, existantes entre les paramètres de failles déterminés. Nous terminons ce chapitre en dégageant les principales perspectives de ce travail.

## I. Limites et hypothèses de travail

### I.1. Longueurs des ruptures de surfaces

Avant de discuter l'estimation de la longueur des ruptures de surface, il apparait nécessaire de rappeler que nos observations morphotectoniques (i.e. cartographie, estimation des offsets cosismiques et détermination des vitesses de glissement) sont restreintes aux évènements sismiques majeurs, ayant rompu la surface de manière significative (i.e. généré des déplacements ≥ 1 m). Bien que le travail de paléosismologie en tranchée permette de déceler des ruptures de surface n'affectant pas de manière significative les marqueurs géomorphologiques (déplacements <1 m), notre attention – en ce qui concerne l'analyse morphotectonique est focalisée sur l'identification et la caractérisation des forts tremblements de terre, i.e. pour des magnitudes Mw > 7,0.

L'une des questions principales dans la caractérisation des paléoséismes générés par des failles décrochantes et l'évaluation des paléomagnitudes associées, est l'estimation de la longueur des ruptures de surface associées aux évènements sismiques (i.e. EBF, WBF, VOLF, TGF, and NIOF).

La cartographie systématique des ruptures de surface permet au premier ordre d'identifier les structures majeures, et d'évaluer leurs dimensions, moyennant la définition de zones de terminaisons de faille, selon des critères géométriques (e.g. Bayasgalan et al., 1999; Wesnousky, 2006).

Dans cette étude, la définition des terminaisons de failles décrochantes (i.e. *tip zones*, '*TZ*' dans le Chapitre 3.I) est ainsi basée sur ces critères (i.e. essentiellement sur une

augmentation relative du glissement vertical, une rotation vers la droite de l'azimut de la rupture - dans le cas d'une cinématique senestre comme dans le Gobi-Altaï - et une distribution de la déformation plus importante, pouvant conduire à la disparition de l'escarpement de faille principal), mais reste le plus souvent arbitraire, et corrélée à la présence de relais compressifs d'échelle déca-kilométriques (e.g. massifs de Bayan Tsagaan et Burkhan Buudai). L'homogénéité des ruptures cartographiées et leurs continuités, sont également des critères intuitifs dans l'estimation de la longueur des ruptures de surface. Ainsi, bien qu'il ne soit pas possible par cette approche d'identifier distinctement si la faille rompt intégralement ou non lors d'un même événement, la continuité, la cinématique et l'homogénéité de la rupture de surface en indiquent la potentialité.

Par exemple, la VOLF présente des segments moins exprimés car associés à des failles secondaires (e.g. VOLF-S5), voir totalement distribués (e.g. VOLF-S4), qui pourraient correspondre à des obstacles lors de la propagation de la rupture, et par conséquent 'limiter' la taille d'un séisme. Cependant, la VOLF présente des décalages cosismiques horizontaux de l'ordre de 3 m dans sa partie ouest. Un tel décalage est potentiellement associé à une rupture de surface de l'ordre d'au moins 100 km de long, si l'on se réfère aux lois empiriques de Wells et Coppersmith (1994) (équation IV.1). Or, si l'on prend par exemple le séisme du Gobi-Altaï, certains segments, comme le segment EBF-S11 (Chapitre 3.IV.1), ne présentent pas de rupture de surface continue, alors que la rupture s'est propagée sur au moins 50 km au-delà de ce segment. Ainsi, on peut se demander par exemple si le segment VOLF-S4 (entièrement distribué) constitue ou non une zone de terminaison de faille. Par conséquent, du point de vue de l'analyse morphotectonique, on ne peut conclure à la possibilité ou non d'une rupture intégrale de la VOLF. Pourtant toutes les mesures (amplitude des décalages cosismiques, vitesses de glissements, période de retour) indiquent la possibilité soit de ruptures intégrales de la failles, soit de ruptures en cascade (e.g. faille Nord Anatolienne).

Ainsi, nous proposons dans cette étude « une découpe » au premier ordre des principales failles actives dans le Gobi-Altaï, en suggérant les zones probables ayant pu constituer des terminaisons de failles ; cependant, la possibilité de ruptures partielles de ces failles lors de paléoséismes ne peut pas être écartée.

La question de la longueur des ruptures sismiques unitaires est de premier ordre, non seulement pour l'estimation des paléomagnitudes, mais également dans l'interprétation des âges des paléoséismes identifiés – la détection des séismes en décrochement dans des tranchées transverses à la faille ne permettant pas d'évaluer la taille de l'évènement,

faute de quantifier le décalage cosismique –, et l'interprétation des paramètres de failles pouvant être déterminés sur le terrain (décalages cosismiques et vitesses). En effet, la détection de ruptures de surface longues (typiquement > 100 km) et continues, implique des décalages cosismiques importants, et donc, en supposant au premier ordre une vitesse de glissement constante et un cycle sismique établi – i.e. succession plus ou moins régulière de forts séismes –, avec des périodes de retour plus importantes. La question de la quantification des longueurs des ruptures de surface soulève également des interrogations relatives aux seuils de décomposition des grandes failles décrochantes : la division de failles en segments, en relais (km), en relais compressifs majeurs ($10^1$ km), l'influence de l'héritage géologique via une structuration prononcée du substratum (e.g. failles héritées, contacts normaux majeures entre unités géologiques, stratifications sédimentaires et volcaniques, foliations et schistosités), ou la présence d'aspérités de dimension crustale (e.g. plutons) sont autant de facteurs à prendre en compte dans la caractérisation d'une faille. Toutefois des questionnements demeurent : quelles sont les natures et dimensions des hétérogénéités géologiques pouvant influer sur la propagation ou non des ruptures sismiques, et comment mesurer leurs incidences sur les séismes ?

Il est également possible de proposer le raisonnement inverse, et d'utiliser notre évaluation des décalages cosismiques associés aux anciens séismes (Chapitre 3.V.3), nos appréciations des périodes de retour ou encore nos estimations de paléomagnitudes, pour discuter des longueurs de ruptures de surface potentielles associées à ces évènements, grâce à la relation empirique liant le décalage moyen à la longueur de faille (Wells et Coppersmith, 1994). Cet exercice est détaillé et discuté en section (II) de ce chapitre.

Rappelons que les magnitudes obtenues sur les EBF, WBF et VOLF, à partir de la longueur de la faille (équation IV-1), sont bien corrélées aux magnitudes dérivées des moments sismiques (équation IV-3), calculées pour les décalages moyens estimés par '*COPD*' sur une section restreinte de la faille et une profondeur sismogénique de 20 km. Cette observation suggère que, lors du dernier évènement majeur (Mw > ~7), chacune de ces failles a probablement rompu sur toute sa longueur.

Notons également la possibilité d'un essaim sismique, incluant la rupture consécutive de plusieurs de ces décrochements majeurs au cours d'une succession d'évènements rapprochés dans le temps, à l'instar de l'activité sismique exceptionnelle de la Mongolie occidentale au XX$^{e}$ (Florensov et Solonenko, 1965; Baljinnyam et al., 1993). L'analyse de la possibilité d'un tel phénomène peut également être abordée au travers d'une

modélisation mécanique du transfert de contraintes, induit sur les structures environnantes par la rupture de l'une des failles (e.g. Chéry et al., 2001), en utilisant les paramètres issus entre autre des travaux de cartographie de ces structures, comme leur cinématique et leur géométrie. Une telle approche devra être menée à échelle régionale, et une couverture exhaustive des structures potentiellement actives apparait fondamentale pour considérer l'ensemble de l'architecture du Gobi-Altaï, et plus spécifiquement celle du '*Bogd Fault System'*.

## I.2. Vitesses de glissement long-terme

### *I.2.1. Qualité des datations*

Une première limite dans les estimations de vitesses de glissement que documente cette étude, est que les vitesses sont attribuées à une faille, alors que les estimations ne proviennent au mieux que de deux sites sur cette même faille, souvent distants de seulement quelques kilomètres. En raison de l'emplacement choisi de ces sites, sur des segments ne présentant pas de distribution significative de la déformation et où la composante décrochante est clairement dominante, il est considéré que cette vitesse est représentative de la vitesse long terme à l'échelle de toute la faille. Néanmoins faute d'une analyse plus exhaustive, on ne peut écarter la possibilité d'une variation de la vitesse le long des failles ce qui modifierait le bilan de distribution de la déformation au niveau de la chaine du Gobi-Altaï.

Afin de déterminer l'âge d'abandon des surfaces alluviales étudiées, deux approches de datations par « $^{10}$Be cosmogénique » ont été adoptées, toutes deux basées sur l'échantillonnage d'amalgames (i.e. 50 clastes prélevés en surface ou en profondeur sur des blocs ou galets de même nature et de taille similaire), mais offrant des avantages et des inconvénients distincts. Une première approche, classique, en profil de concentration avec la profondeur, est rigoureuse et permet d'une part de connaitre l'héritage associé à la surface, et d'autre part, soit la détermination de l'âge si le profil n'est pas à l'état stationnaire, soit dans le cas contraire la détermination du taux de dénudation (e.g. dans la région Ritz et al., 2003, 2006; Vassallo et al., 2007; Niessen et al., 2009; Rizza et al., 2011). Une seconde approche, moins rigoureuse mais offrant l'avantage d'être moins couteuse, vise uniquement la quantification de : i. la concentration en $^{10}$Be hérité, produit lors de l'exposition antérieure au dépôt, au travers de l'échantillonnage d'un amalgame, soit en profondeur – en négligeant la production muonique pourtant dominante à plus de 2 m de profondeur –, soit directement dans la charge sédimentaire du drain actif associé au bassin versant qui a produit la surface en question (i.e. le lit de rivière ou le lit temporaire à l'apex du cône considéré). ii. la quantité

de $^{10}$Be accumulé sur la surface depuis son abandon (qui combine production de surface, dénudation de celle-ci au cours du temps, et décroissance radioactive) au travers de l'échantillonnage d'un amalgame de clastes collectés sur les blocs enchâssés et exposés sur ladite surface (e.g. Seong et al., 2011).

Il est nécessaire de noter que cette seconde approche suggère de déterminer l'âge d'abandon sans contraintes sur l'histoire du marqueur – e.g. sa stratigraphie, la présence d'éventuelles périodes de préexpositions, d'érosion, ou de changement significatif de type de dépôt ; données qui sont normalement documentées pour l'interprétation de l'âge d'abandon. De plus, cette approche suppose directement que l'héritage déterminé au sein du lit actif est représentatif de l'héritage des alluvions lors de leur dépôt.

Afin de limiter la surinterprétation de ces âges, il a été choisi d'apporter les résultats de la manière la plus conservatrice, en proposant 3 âges : l'un minimum, le plus probable si la terrasse ne présente pas d'indice d'équilibre (e.g. en Mongolie, une surface abandonnée depuis ~$10^2$ ka est souvent très plate, affectée par des figurés d'incision régressive, avec des évidences de calcrétisation dans le premier mètre de dépôts, Ritz et al., 2003, 2006) ; le second âge proposé est minimum également au regard de l'abandon de la surface, car il correspond au temps d'intégration nécessaire pour atteindre l'état stationnaire ; enfin un troisième âge, le plus conservateur [illegible], consiste à ne considérer ni héritage, ni érosion, ce qui conduit à l'âge maximum pour l'abandon de la surface. Cette troisième hypothèse n'est cependant pas toujours réaliste (les observations de terrain indiquant par exemple clairement des processus d'érosion, e.g. Figure 4-110-A, ou un héritage significatif, i.e. tous les sites mesurés), et est donné ici afin de balayer toutes les possibilités qu'incombe la méthode de datation utilisée. Nous estimons que si chaque datation est présentée avec les valeurs maximales et minimales, cette approche, combinée avec une analyse morphotectonique de la zone considérée, offre la possibilité d'encadrer l'âge d'abandon du marqueur.

Notons que pour les trois profils analysant la distribution de la concentration en 10Be en profondeur réalisés dans cette étude (sites de *Biger Terrace* et *Dark Creek* le long de la VOLF, ainsi que le site de Ice Creek le long de la WBF), la détermination des âges, et en particulier la distribution des solutions du modèle bayésien de Hidy et al. (2010), indiquait au travers d'une bonne contrainte sur les taux de dénudation et à l'inverse une mauvaise contrainte sur la distribution des âges, que l'état stationnaire était atteint. Ainsi seuls des taux de dénudation ont pu être dérivés de ces profils, accompagnés des

temps d'intégration correspondants (i.e. période minimum nécessaire pour atteindre l'état stationnaire).

Relevons également que pour chacun des profils réalisés (Figure 4-39, Figure 4-78 et Figure 4-85), nous mesurons des taux de dénudation allant de 8,6 à 21 $m.Ma^{-1}$, ainsi que des valeurs d'héritage de l'ordre de 3 à $5.10^6$ $at.g^{-1}$, pour des concentrations en surface de ~$10^6$ $at.g^{-1}$. Ces données sont du même ordre de grandeur que celles publiées précédemment dans le Gobi-Altaï (cf. Ritz et al., 2006). Ces grandeurs reflètent les faibles taux de sédimentations dans le contexte aride du Gobi-Altaï, conduisant à une forte accumulation en $^{10}Be$ avant dépôt. Ces mesures ne sont pas exploitées dans ce travail, mais sont renseignées à des fins éventuels d'analyses de géomorphologie quantitative dans la région – par exemple calcul des taux de dénudation, de déflation, de surrection, ou encore l'estimation de temps de résidence des sédiments dans les réseaux hydrographiques –, hors du champ de cette étude.

### *I.2.2. Détermination des vitesses de faille*

Nous avons vu que l'estimation du décalage cumulé enregistré sur le long terme par un marqueur géomorphologique, aboutit en général à une estimation minimale ou maximale de la valeur réelle du décalage. Par exemple le décalage mesuré en rive droite (coté est) sur le site de Biger Terraces (voir Figure 4-80), entre la terrasse T2 et T0 (qui ici s'est avéré correspondre au lit actif) est mesurée à 10,4 ± 4,9 m. Le rejet senestre amène directement le talus de la terrasse au contact du lit actif, ce qui, par sapement basal du talus de la terrasse T2 par la rivière lors de crues, assure le rafraichissement du talus au détriment de la préservation du décalage. L'utilisation de ce décalage doit alors se faire comme une valeur minimale du décalage associé à l'âge d'abandon du marqueur. Cet exemple montre par ailleurs le bienfondé de ce raisonnement, dans la mesure où l'étagement des terrasses alluviales en rive gauche (coté ouest), mieux préservé, indique en fait que cette valeur est un décalage minimum associé à l'abandon de la terrasse T1, et que le décalage enregistré par la terrasse T2 depuis son abandon, est d'au moins 25 ± 4 m – autrement dit une valeur maximale du décalage enregistré depuis l'abandon de T1.

Considérant que nos datations de l'abandon des surfaces alluviales ne mène qu'à des âges d'abandon minimums (temps d'intégration associés à leurs états stationnaires), et que les mesures de décalages mènent également parfois à des évaluations bornées, il apparait que dans certain cas la détermination de nature (i.e. minimum ou maximum) de la vitesse de glissement que l'on calcul n'est pas déterminée. Néanmoins, cela ne retire pas l'intérêt de telles mesures, au sens où la connaissance du fonctionnement des failles

décrochantes d'échelle lithosphérique en domaine intracontinental, passe certainement par la multiplicité des mesures de vitesse long terme, et des périodes temporelles investiguées. Enfin, notons que ces mesures de vitesses de glissement, bien qu'indéterminées, présentent une grande cohérence au regard du bilan des vitesses de glissement sur les principaux décrochements au travers du Gobi-Altaï.

#### *I.2.3. Implications des vitesses de glissement sur l'activité des failles*

L'une des interrogations qui s'est posée lors de l'interprétation de vitesses de faille très faibles, comme c'est le cas par exemple le long de la NCVF (IV.7), est la possibilité d'utiliser la vitesse de glissement afin de contraindre l'activité de la faille au cours de l'Holocène. En effet, la vitesse verticale est estimée sur le site de Vulture Fan entre 0,04 ± 0,01 mm.a$^{-1}$ et 0,07 ± 0,01 mm.a$^{-1}$ sur les derniers 40 à 80 ka, alors que le décalage accumulé le long de l'escarpement sur cette même période n'est que de 3 m. Se peut-il que ce chevauchement ai été récemment réactivé – au sens ou l'activité pléistocène de ce chevauchement ne fait pas de doutes au regard de la surrection des reliefs situés au nord de la faille –, ou observons-nous un escarpement particulièrement préservé de l'érosion ? Nos observations ne permettent pas de trancher sur ces questions (Chapitre 4-V), mais néanmoins de préciser que l'existence, la géométrie et la cinématique de la NCVF sont vraisemblablement liées à la VOLF, et qu'à l'instar des forebergs de Gurvan Bulag ou de Dalaan Turru qui ont rejoué lors du séisme du Gobi-Altaï en 1957 (Figure 3-1), ce chevauchement est lui aussi capable de rompre de manière synchrone avec le décrochement principal auquel il se rattache. Cependant, si la connaissance des vitesses de faille à diverses échelles de temps (i.e. $10^4$ – $10^6$ ans) et de leurs variations sont des informations importantes pour évaluer l'activité d'une faille (Rizza, 2010), nous disposons ici d'un nombre de mesures trop restreint pour discuter des variations de vitesses de glissement des principales failles du Gobi-Altaï occidental.

Lorsque les périodes ou les déplacements considérés pour le calcul des vitesses de glissement sont du même ordre de grandeur que les périodes de retour ou décalages cosismiques attendus, la position 'actuelle' dans le cycle sismique (i.e. 'proche' du dernier évènement de Mw > 7) peut induire une incertitude sur la vitesse de glissement. En effet, comme proposé en conclusion des évaluations de vitesse sur les sites de Vulture fan (NCVF, avec un décalage cumulé de 3 m) et d'Ice Creek (WBF, avec un décalage cumulé de 9 m), si l'on considère les décalages cosismiques évalués par l'approche '*COPD*' (sur les mêmes segments) et un glissement caractéristique, il apparait que l'on ne mesure la vitesse que sur 3 à 6 cycles sismiques, ce qui induit une erreur de 10 à 15 % ; erreur qui demeure au second ordre vu les vitesses mesurées et

les incertitudes, mais qui peut devenir conséquente sur des vitesses de faille plus importantes.

### I.3. Indentification des paléoséismes et estimation des périodes de retour

L'une des difficultés qui a été rencontrée lors de l'interprétation des tranchées paléosismologiques, fut le constat d'incohérences évidentes entre les positions stratigraphiques des échantillons prélevés et certaines datations radiocarbones, tout particulièrement sur les datations en bloc (« bulk ») de sédiments dans la tranchée de Moskito Trench – par exemple l'âge de MT-C06 est significativement plus vieux (de 200 à 1500 ans) que les dates obtenues d'une part sur le paléosol MT-CO2 situé au même niveau stratigraphique, et d'autre part sur 3 échantillons (2 charbons et 1 amalgame sur sédiment) situés clairement plus bas dans la stratigraphie.

Il est connu que les datations radiocarbones basées sur des charbons, incluent une part d'héritage associées d'une part à la durée entre la mort de la partie de l'arbre en question et la mise en circulation du charbon (*inbuilt*), et d'autre part à d'éventuels enfouissements préalables, suivis de remobilisations (*inherited*) (e.g. Bollinger et al., 2016). Cet effet groupé d'héritage induit systématiquement une surestimation de l'âge de dépôt de l'unité stratigraphique en question, et peut avoir des implications fortes sur les conclusions en ce qui concerne l'activité sismique (e.g. Hossler et al., 2016). L'estimation de l'héritage en $^{14}C$ des charbons analysés dans cette étude n'a pas fait l'objet d'une attention particulière, faute de moyens pour la contraindre. Il est envisageable de discuter cet effet au regard de l'espérance de vie et de la vitesse de croissance de la végétation ligneuse dans le Gobi-Altaï. En effet, la vitesse de développement des arbres et leur espérance de vie intra-spécifique est proportionnelle à la température (e.g. Went, 1953; Pessarakli, 1999), et aux conditions climatiques de la région, avec des hivers longs et rigoureux et des étés courts, et généralement secs (la température moyenne est inférieure à 0°C plus de 6 mois par an dans le Gobi-Altaï, e.g. Climatedata.org ), la croissance des arbres apparait lente, et il est donc probable que l'héritage des charbons de la région soit conséquent. Par analogie, l'observation d'arbres affectés par la rupture de surface associée au séisme de Bolnay, 1905 (Figure 5-1 et Figure 1-2), dont certain ayant été fraichement coupés (dans les quelques dernières années), indique d'une part que le traumatisme du séisme est systématiquement visible dans les cernes de croissance de l'arbre (Figure 5-1-B), et d'autre part le décompte de ces cernes sur 3 arbres entre le traumatisme et la coupe de l'arbre mène à 100 ± 20 ans, âge qui se situe entre la date du séisme et l'été 2015. On montre ici, au travers de cet exemple succinct de dendrochronologie, d'une part l'intérêt de cette approche (e.g. Goldfinger et al., 2003), et d'autre part la vitesse modérée de croissance des arbres en

Mongolie, bien que le contexte climatique de la région de Bolnay (froid et humide) soit très différent de celui du Gobi-Altaï (froid et sec en hiver, tempéré en été). S'ajoute à cette réflexion l'idée que les valeurs d'héritage systématiquement importantes dans les datations de surfaces au $^{10}$Be indiquent un temps de transport long, et bien que cette durée –propre aux matériaux étudiés –, ne soit pas directement assimilable au transport d'éléments comme des charbons, cela laisse supposer, ici encore, un héritage probablement fort en $^{14}$C – notons qu'il ne s'agit ici que de spéculations, basées sur un raisonnement qualitatif et des analogies de premier ordre.

**Figure 5-1: Arbres affectés par la rupture de 1905 le long de la faille de Bolnay (localisation : N49,335 ; E. 97,897. A. Photographie vers l'est d'arbres basculés de part et d'autre d'une fente de tension le long de la faille de Bolnay. Le mouvement des arbres est cohérent avec une cinématique normale des failles bordant la fente de tension. B. Arbre coupé montrant un traumatisme (flèche blanche). Le dénombrement des cernes entre le traumatisme et la coupe de l'arbre (bord de l'arbre) indique 100 ± 20 ans (moyenné sur 3 arbres), cohérent avec la date du séisme en 1905.**

Les datations sur sédiments sont quant à elles plus incertaines, dans la mesure où : i. des processus de contamination post-dépôt par de la matière organique plus jeune – causés notamment par de la bioturbation –, entrainant une surestimation de l'âge par effet réservoir, et ii. des processus de remobilisation du sédiment peuvent entrainer une contamination du sédiment par de la matière organique plus ancienne, conduisant à une sous-estimation de l'âge (e.g. Bowman 1990; Gavin 2001; Reimer et al., 2013).

Les investigations paléosismologiques dans les tranchées creusées perpendiculairement aux ruptures de surface ont néanmoins permis d'encadrer l'âge de 3 paléoséismes ayant rompu la surface sur la WBF, de deux paléoséismes sur la VOLF, et du dernier évènement ayant rompu la surface sur la faille de Tsogt. Notons que sur la faille de Tsogt et la VOLF, nous ne pouvons pas donner de périodes de retour pertinentes, dans la mesure où nous n'avons respectivement que 2 et 3 dates. Dans le premier cas (Tsogt)

ces âges ne donnent que l'intervalle d'occurrence du dernier évènement, et dans le second cas (VOLF) ils encadrent deux évènements avec 3 dates ne permettent pas de proposer qu'un unique intervalle de récurrence, compris entre 0 (car il n'existe qu'un seul échantillon entre les deux évènements) et 5,0 ka. Des datations OSL supplémentaires sur la tranchée de Storm Fan 2016 (VOLF) sont en cours et devraient permettre d'affiner cette estimation. Des temps de retour peuvent néanmoins être déterminés entre les 3 évènements identifiés le long de la WBF, qui sont de 2,1 ± 1,5 ka et 5,9 ± 3,0 ka. Il est ainsi possible de proposer une période de retour moyenne le long de la WBF, de 4,0 ± 1,8 ka. Nous précisons que cette valeur n'est calculée que sur 2 cycles sismiques, et qu'il s'agit ainsi d'une estimation préliminaire. La question de la taille des séismes identifiés est discutée au regard des évaluations de décalages latéraux cosismiques et des vitesses de glissement long terme en partie II de ce chapitre.

De plus amples analyses paléosismologiques sont donc nécessaires afin d'affiner l'estimation des périodes de retour sur la faille de Bogd-ouest, de même que sur l'ensemble des grands décrochements du Gobi-Altaï (notamment par la complétude des investigations sur la VOLF, sur la TGF, par une étude de terrain de la NIOF, etc..), ainsi qu'au travers de la publication des diverses précédentes analyses de tranchées qui ont été effectuées sur la faille de Bogd Est (i.e. sur la rupture du séisme du Gobi-Altaï, 1957, cf. Schwartz et al., 2007; Ritz et al., 2009; Rizza, PhD, 2010; Prentice, Ritz et al, en préparation).

## I.4. Quantification des décalages cosismiques

### *I.4.1. Principes et hypothèses*

#### I.4.1.1. *Travail au regard de la segmentation*

La quantification des décalages cosismiques, tant ceux associés au dernier séisme rompant la surface que ceux représentant un cumul de plusieurs déplacement générés par des ruptures successives, est effectuée dans cette étude par rapport à la segmentation de la rupture. Ce choix a été fait d'une part parce que la segmentation représente une certaine homogénéité du motif de la déformation et de sa cinématique pour une section de faille donnée (Wesnousky, 2006; 2008). D'autre part, les variations d'amplitude du glissement cosismique sont corrélés aux phénomènes de distribution de la déformation en champ proche de la faille (de l'ordre $10^1$ à $10^3$ m, e.g. Gold et al., 2015), pouvant eux-mêmes être influencés par l'orientation de la faille vis-à-vis de l'héritage structural et géologique (e.g. Vallage et al., 2016). Travailler au regard de la

segmentation permet ainsi de rendre compte de la déformation le long de la faille au regard du contexte géologique et structural. De plus, observer la distribution du glissement sur les longueurs < $10^2$ m, entraine une incertitude dominée par la mesure, alors que caractériser les variations du glissement à des échelles ≥ 200 m, revient à analyser les phénomènes physiques réellement associés à la variabilité du glissement (Gold et al., 2013). Enfin, ce choix de décrire les glissements horizontaux moyens au regard de la segmentation, permet d'inclure un nombre significatif de mesures dans chaque détermination de glissement moyen, renforçant par là même la qualité de ces mesures (e.g. Zielke et al., 2010). L'une des hypothèses considérée dans cette approche est donc la représentativité du décalage moyen pour quantifier le glissement – et donc au premier ordre, pour le contexte décrochant, l'énergie ainsi libérée lors du séisme – le long d'un segment donné.

Une autre limite associé à l'analyse des décalages par segment, est que l'ont perd également la notion de décalage minimum et maximum, et les estimations de magnitudes associées (i.e. Wells and Coppersmith, 1994).

#### I.4.1.2. Analyse des décalages sur plusieurs cycles sismiques

Le cycle sismique a été abordé dans cette étude notamment au travers de la quantification de décalages associés à plusieurs séismes successifs, ou encore par l'identification de ruptures de surface successives observées dans des tranchées.

Son emploi dans ce texte ne sous-entend pas une répétition stricte et systématique d'un même phénomène dans des conditions identiques. Néanmoins, dans ce contexte intracontinental, nous observons : des faibles vitesses de déformations (≤ 1 $mm.yr^{-1}$), l'occurrence d'évènements majeurs – à l'instar la forte sismicité au XX$^{è}$ siècle, dont le séisme de 1957 –, des indices d'évènements antérieurs de magnitude analogue et une relative abondance de traces de ruptures affectant des dépôts tardi-pléistocène à holocènes au sein de la chaine. Il semble donc bien que les mesures de décalages étudiées ne découlent pas d'une multitude de petits incréments, mais plutôt de la survenue de grands évènements sismiques, avec des intervalles de retour longs ($10^3$ a).

Cette section remémore le principe de l'approche, ainsi que les principales hypothèses considérées. Notre capacité à identifier des décalages cosismiques moyens sur une section de faille donnée dépend d'une part de l'abondance et de la préservation des marqueurs dans la zone considérée, et d'autre part de la localisation de la déformation – ou à l'inverse de sa distribution. Ces facteurs vont ainsi influencer le signal de glissement, qui sera mesuré puis modélisé sous forme de fonctions densités de probabilités, ensuite additionnées dans un histogramme : la fonction COPD. Etant

donnée l'effacement continu par l'érosion des déplacements enregistrés par la morphologie, une des hypothèses dans cette approche est que le signal maximum décrit par cette fonction correspond au décalage moyen associé au dernier évènement majeur (i.e. générant des décalages > ~1m). Les décalages générés par les précédents séismes sont supposés nécessairement moins nombreux, car partiellement ou totalement effacés par l'érosion. Ce raisonnement peut être adopté afin d'analyser les déplacements enregistrés dans la morphologie au travers de plusieurs cycles sismiques. Cette approche avait déjà été proposé (e.g. Sieh et al., 1993 ; Zielke et al., 2010) en corrélant les pics significatifs présentés par la fonction COPD. Nous avons appliqué cette méthode sur la base de données de mesures abondantes de décalages le long de la rupture principale du séisme de 1957 (> 1400 mesures), et nous proposons d'exploiter d'avantage le signal des fonctions COPD, en venant dans un premier temps soustraire le signal de glissement propre au dernier évènement (supposé suivre une distribution gaussienne), et en poursuivant dans un second temps l'analyse du reliquat de la fonction COPD ainsi obtenue en la considérant représentative de la déformation enregistrée par la morphologie, avant la survenue du dernier évènement. La nature gaussienne du signal de glissement associé à un séisme est une autre hypothèse assumée dans cette approche ; hypothèse qui semble cependant raisonnable, comme le montrent d'autres mesures systématiques – tant par reconstruction de marqueurs que par pixel-corrélation – de la distribution du glissement (e.g. Gold et al., 2013; Rockwell et Klinger, 2013; Milliner et al., 2015).

L'application systématique de cette approche a cependant révélé des limites, et nous avons pu constater qu'il est souvent séduisant de sur-interpréter les résultats obtenus à l'aide de cette approche de « déconvolution » directe des COPD.

Une question qui reste à contraindre est donc : jusqu'où peut-on aller ? Autrement dit, sur quels critères évaluer la significativité des glissements obtenus ? Nous avons ici proposé de soustraire les glissements identifiés afin d'estimer les offsets cosismiques propres aux séismes successifs, approche qu'il serait intéressante de comparer à d'autres jeux de données, ainsi qu'à d'autres méthodes d'évaluation des décalages cumulés (e.g. Zielke et Arrowsmith, 2012; Billant et al., 2016).

Les sections suivantes se proposent de rappeler brièvement les résultats obtenus par cette approche, de discuter des relations pouvant exister entre l'amplitude des décalages moyens par segment et la cinématique ou encore l'orientation de ces segments, et enfin de décrire les principales limites de ce modèle, en détaillant des incohérences manifestes, et en proposant des voies d'amélioration.

### *I.4.2. Décalages cosismiques*

#### I.4.2.1. Synthèse

L'application de ce procédé à 11 segments de la rupture principale du séisme de 1957 sur la EBF a ainsi permis d'identifier au moins 4 glissements consécutifs sur chacun des segments analysés, pouvant être interprétés comme associés à des séismes successifs. De même, ce procédé a été appliqué sur une section de 12,5 km (correspondant à un segment et un relais) le long de la VOLF, et sur une section de 4 km le long de la WBF, aboutissant à la détermination du glissement cosismique associé aux deux derniers évènements sur ces failles, et dans une moindre mesure à un signal de décalage cumulé autour de 10 m.

L'interprétation de ces résultats montre que cette approche permet de quantifier convenablement le glissement cosismique associé au dernier évènement majeur (i.e. le séisme de 1957 sur l'EBF, et les évènements les plus récents sur les VOLF et WBF), avec un signal bien définit – forte amplitude du premier pic de la COPD –, et des incertitudes de 20 à 50 %, alors que la détermination des glissements précédents demeure plus confuse, notamment lorsque les pics de la COPD sont moins prononcés, voir inidentifiables.

Afin de contraindre au premier ordre nos évaluations de décalages cumulés, nous avons recensé le nombre de mesures associées à chaque décalage cumulés identifiées (dans l'intervalle de 1σ), et proposé un seuil minimum de 4 mesures pour que cette évaluation du glissement cumulé soit considérée. De plus, les offsets ainsi déterminés sont présentés au regard de la cinématique dominante sur chaque segment – cette cinématique étant par définition représentative de la proportion des composantes horizontales et verticales (ratio H/V) des glissements moyens considérés. La relation entre l'amplitude des décalages horizontaux et la cinématique ainsi que l'orientation des segments est explorée en section II de ce chapitre.

Nous avons constaté que sur la rupture de Bogd Est, les résultats obtenus sont cohérents avec les mesures de terrain, bien que l'analyse statistique révèle une possible confusion sur certaines mesures de terrain (les plus fortes indiquant le double du décalage moyen), avec des décalages estimés comme cosismiques du séisme de 1957, alors que statistiquement cette valeur de décalage correspond à un cumulé incluant le décalage associé au précédent évènement. Nous précisons que cette assertion ne sous-entend pas que les mesures par télédétections sont meilleures que celles effectuées sur le terrain (au contraire, nous insistons sur leurs limites de qualité d'un point de vue unitaire), mais que statistiquement, nos données ne permettent pas une variation du

glissement horizontal du simple au double au sein d'un même segment. Enfin, notons les décalages mesurés sur le terrain supérieurs à 5 m sont peu nombreux (< 10 pour les études de Rizza et al., 2011 et Choi et al., 2012). Cette observation est à mitiger dans la mesure où il a été démontré que à l'échelle de toute la faille, l'amplitude maximale du glissement de surface associée à un séisme, peut aller jusqu'au double du glissement moyen sur la faille considérée (e.g. Wells et Coppersmith, 1994; Haeussler et al., 2004).

La grande majorité des glissements déterminés par cette approche correspondent aux pics – maximum locaux – décrits par la fonction COPD. Cependant, l'interprétation des résultats n'est pas évidente dans les cas où les glissements modélisés ne se combinent pas à des maximums locaux de la fonction COPD.

Ainsi, nous concluons que cette étude exploratoire de la détermination des décalages cosismiques associés aux séismes majeurs successifs produits sur les grands décrochements intracontinentaux, doit se limiter au premier ordre sur la forme de la fonction : si les maximums locaux ne sont pas distincts ou au moins associés à une inflexion de la fonction COPD, l'estimation du glissement est potentiellement erronée, et n'est en conséquence pas incluse dans les résultats.

#### I.4.2.2. Implications sur le glissement caractéristique

L'analyse de la distribution horizontale du glissement le long de la rupture du séisme du Gobi-Altaï (1957), au regard de la segmentation et au travers de plusieurs cycles sismiques, a permis de conclure que pour au moins 50 % de la rupture principale, cette faille semble produire des glissements caractéristiques sur les 3 derniers cycles sismiques. L'élargissement de cette conclusion à la nature caractéristique des séismes produits par l'EBF requière cependant de contraindre d'une part l'étendue de chacune de ces ruptures (i.e. longueur de la rupture) d'un point de vue paléosismologique (même âges des évènements dans des tranchées creusées sur différents segments), et d'autre part de supposer des vitesses de glissement constantes sur le court terme (i.e. à l'échelle du cycle sismique). Ces deux hypothèses ne pouvant être contraintes à partir des données documentées dans le cas du Gobi-Altaï, il ne nous est pas possible de proposer de conclusion sur la nature caractéristique ou non des séismes produits sur l'EBF (Rizza et al., 2011).

De plus, les analyses de glissements successifs sur les failles de VOLF et de WBF, ont permis l'évaluation des glissements moyens sur une section de faille pour les deux derniers séismes, dont les incertitudes, importantes (20 à 30 % pour les évènements les plus récents, et ~80 % pour les évènements pénultièmes), ne permettent pas de discuter

rigoureusement de la répétition du glissement, et de tirer des conclusions sur la nature caractéristique des glissements sur ces failles.

Cette approche constitue néanmoins un point de départ intéressant pour évaluer les glissements cosismiques associés aux paléoséismes, et ainsi améliorer la connaissance de leurs caractéristiques propres, des cyclicités qui semblent accompagner ces processus, et de l'aléa sismique de la région considérée.

#### I.4.2.3. Incertitudes sur les décalages

Notoirement, les incertitudes associées au glissement du dernier évènement évalué sur des sections des WBF et VOLF, apparaissent inférieures à celles associées aux segments de l'EBF : ~20 et 30 % pour respectivement la VOLF et la WBF, contre 30 à 45 % pour les segments de l'EBF (Table 16).

Cette observation s'explique par le fait que les décalages ont été évalués sur les WBF et VOLF en considérant les positions extrêmes extraites de la construction des marqueurs en trois temps comme des valeurs d'incertitudes à 1σ, alors que les mesures à partir des photos aériennes de 1958 orthorectifiées sont considérées comme des incertitudes à 2σ. Ce choix arbitraire est justifié par la différence de qualité entre les données : les données obtenues par drone étant bien plus précises – de par le géoréférencement des photographies et la faible altitude de vol ; pour rappel, un survol à 300 m avec des photos à 14 Mpx, aboutit à des résolutions d'environ 10 cm pour les orthophotos et 20 cm pour les MNT –, que pour les données dérivées de scans de photos aériennes historiques – de par la méconnaissance des paramètres internes normalement nécessaires pour contraindre une orthorectification par photogrammétrie, et la qualité médiocre des clichés en raison de leur âge –, géoréférencés à partir des bases de données d'images satellites et de MNT proposés gratuitement en ligne (i.e. *Bing maps® et Google maps®, et SRTM30*). De plus, les mesures sur la WBF sont basées exclusivement sur les orthophotos (résolutions de 20 à 40 cm, principalement selon l'altitude d'acquisition des photographies aériennes).

Cette différence dans les incertitudes extraites du modèle est également à rapprocher de la variabilité spatiale du glissement : l'utilisation des décalages ainsi déterminés afin de calculer des magnitudes par exemple, devant systématiquement être modérée par le fait qu'une mesure sur un segment n'est pas nécessairement représentative du glissement sur l'ensemble de la faille. Cette hypothèse est cependant considérée dans la discussion des décalages moyens obtenus, d'une part parce que nos mesures sont nombreuses et intégrées sur une section de faille (par opposition à une conclusion sur les décalages à

partir de mesures en nombre limité), et d'autre part parce que les évaluations du glissement associé au séisme de 1957 sont confondues dans les barres d'erreurs pour tous les segments analysés – i.e. les mesures de déplacement moyen sur chaque segments sont compris dans l'intervalle de glissement moyen sur toute la failles de 3,5 ± 1,4 m.

#### I.4.2.4. Relations déplacements moyens, cinématique, orientation de la faille

La relation entre l'amplitude du glissement horizontal et l'amplitude du glissement vertical est décrite comme anti-corrélée, pour cause de transfert de la déformation depuis la composante horizontale vers la composante verticale (e.g. Rizza et al., 2011; Choi et al., 2012; Zielke et al., 2012; Vallage et al., 2015). Afin d'explorer le possible lien entre la cinématique de la faille à l'échelle des segments et l'amplitude des décalages cosismiques produit par un séisme, nous avons comparé les mesures de décalages cosismiques horizontaux moyens obtenus par application de l'approche '*COPD*' sur la base de donnée de décalages le long de 11 segments de la rupture de surface principale du séisme de 1957 (Chapitre 3), à la cinématique dominante sur chacun de ces segments (Figure 5-2). Au premier ordre, trois classes de cinématiques sont distinguées pour les segments : les segments senestres purs, les segments obliques à composante verticale normale, et les segments senestres à composante verticale inverse. Les résultats obtenus (Figure 5-2) montrent que d'après nos données, il ne semble pas y avoir de corrélation évidente entre l'amplitude du glissement et la cinématique de la faille, souligné ici par l'incohérence des régressions linéaire et polynomiale ($R^2 < 0,3$). Cette observation est surprenante (voir incohérente) à l'échelle du segment, et cette corrélation devrait peut-être être explorée à une échelle inférieure, avec des sections de failles plus courtes, et des orientations de ruptures plus précises que sur un segment complet.

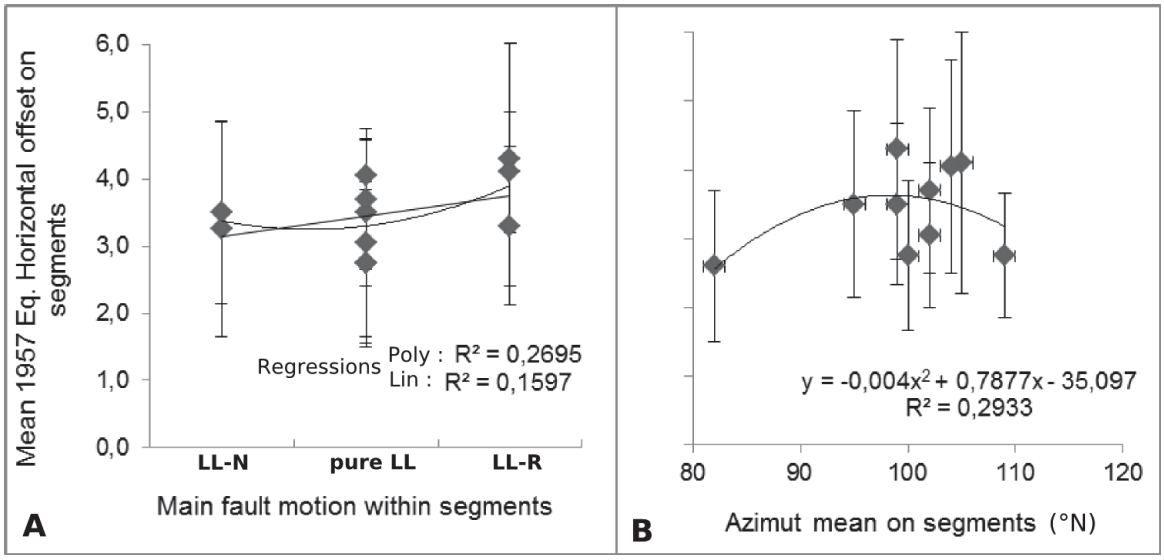


**Figure 5-2 : Corrélation des décalages moyens par segments avec les données de cartographie. A. Relations entre décalages cosismiques moyens par segment et la cinématique globale des segments. B. Relations entre décalages cosismiques moyens par segment et l'orientation des segments.**

Un même exercice peut être proposé, afin d'explorer la distribution entre nos données de décalages moyens par segment et l'orientation moyenne de la faille le long de ces mêmes segments – ici encore, une anti-corrélation entre l'écart à l'azimut moyen de la rupture et l'amplitude des décalages horizontaux est attendue (e.g. Haeussler et al., 2004; M. Rizza et al., 2011; Choi et al., 2012). La Figure 5-2-B montre qu'une interpolation polynomiale de cette distribution, bien que très mal contrainte, est centrée sur un maximum de N99°, correspondant à l'azimut de la faille ; cependant, un coefficient de corrélation de seulement 0,29 indique que cette observation est certainement une coïncidence.

### *I.4.3. Limites de l'approche*

Un certain nombre de limites relatives à cette approche d'analyse systématique des décalages cosismiques et leur modélisation par fonctions COPDs ont été identifiées et discutées dans cette thèse ; cette section vise à décrire plus particulièrement des incohérences observées lors de son application.

Nous avons vu que les déterminations de glissements cumulés par un signal gaussien ne doivent être considérées que si elles sont corrélées à une inflexion de la COPD, et si elles englobent un minimum de 4 mesures dans un intervalle de 1σ autour de la valeur du décalage moyen déterminé. La valeur de l'incertitude inclut : i. La distribution de la déformation (signal gaussien réellement associé à la déformation sismique), et ii. L'incertitude associée aux mesures de décalages.

#### I.4.3.1. Incohérences

Une première incohérence est que l'incertitude sur l'offset déterminé ne croit pas entre chaque itération ; en effet les incertitudes associées aux décalages cumulés ne sont pas nécessairement plus importantes que pour le dernier évènement (Figure 3-8), alors qu'il serait logique que ce soit le cas. Si l'on considère l'hypothèse selon laquelle le signal de glissement associé à un séisme suit une distribution gaussienne, ce signal de déplacement s'applique également aux décalages préalablement enregistrés –avec un signal gaussien– par la morphologie. Ainsi, il faudrait propager la distribution en amplitude du glissement associé au dernier évènement aux glissements précédents lors de leur modélisation. Cependant, le signal comprend également une part de la distribution associée aux incertitudes sur nos mesures et aux erreurs d'orthorectification des images. Une addition directe amène alors simplement à perdre le signal dès le pénultième évènement. Il semble que cette incohérence relève ici d'un problème de normalisation des signaux associés à chaque évènement ; cette piste est développée dans la section I.4.3.2.

Une seconde incohérence peut être observée dans les incertitudes, au travers de l'influence du signal associé au dernier évènement (E1) : s'il est très bien résolu, les décalages suivants seront plus petits (e.g. Figure 3-8). A l'inverse, si le signal de glissement associé au dernier évènement est peu résolu, cela va décaler en conséquence les décalages précédents, en les rendant plus grands. Bien que cette observation ne soit pas systématique – dans l'ensemble, les signaux modélisés et les variations de la COPD sont bien corrélés –, cette observation confirme que seuls les pics au premier ordre décrits par la fonction indiquent un offset cumulé significatif.

Enfin, une troisième incohérence observée est que les amplitudes des déplacements moyens modélisés ne décrivent pas toujours une décroissance exponentielle (i.e. Sieh et al., 1978 ; Zielke et al., 2012), ce qui est au premier ordre incohérent avec l'hypothèse qui suppose que la déformation associée au dernier évènement est prépondérante dans la COPD. En particulier, les avant-derniers évènements sont souvent pour partie 'dilués' dans le signal du glissement moyen associé au dernier évènement. La présence d'un second évènement ne fait pas de doutes au voir de la nette inflexion de la décroissance de la fonction COPD vers les offsets plus importants, alors que cette dernière ne marque cependant pas d'extremum local (e.g. Figure 4-72). Ainsi, lorsque le signal associé au dernier évènement (E1) – systématiquement prépondérant relativement au reste de la COPD – est soustrait de la fonction COPD, la trainée de cette fonction gaussienne vient significativement réduire le signal associée au pénultième évènement (E2), et non le signal de l'antépénultième (E3) – la trainée étant devenue négligeable –, entrainant par

conséquent une prépondérance de ce troisième événement par rapport au second (Figure 4-72).

Il est à considérer que le modèle d'investigation des glissements cosismiques au travers de plusieurs cycles sismiques est pour le moment un modèle initial, et la section suivante indique quelques voies d'améliorations et les perspectives qu'un tel outil pourrait apporter.

#### I.4.3.2. Perspectives du modèle

Une première voie d'amélioration du modèle, par ailleurs proposée par Zielke et al., (2012), serait de pondérer les PDFs en fonction de leur qualité (i.e. les pondérer par des notations déterminées en fonction de la qualité des images, de la qualité du marqueur vis-à-vis de sa reconstruction, et de l'estimation de la distribution de la déformation (cf. Chapitre 3.

Une perspective serait d'approfondir l'analyse des fonctions COPD, et leur déconvolution. Nous proposons à cet égard deux idées :

Une première idée serait de normaliser la fonction COPD en fonction de la décroissance que décrivent les maximums locaux (ou simplement la COPD si elle est très lisse), en assumant que cette décroissance soit représentative de l'effacement des marqueurs au cours du temps, ici matérialisé par le nombre de cycles sismiques ayant généré les glissements mesurés (e.g. Zielke et al., 2015). La procédure suivante peut être proposée: 1. Déterminer le taux de décroissance des décalages, à partir de la COPD dans son ensemble; 2. Extraire le signal associé au premier évènement ; 3. le normaliser ; 4. le soustraire à la COPD normalisée.

Une seconde idée serait d'appliquer une approche bayésienne aux COPDs, afin de les déconvoluer en une série de fonctions gaussiennes. Une première tentative a été développée (non figurée dans cette thèse), en proposant d'imposer une décroissance de l'amplitude associée à chaque glissement, mais la corrélation reste incertaine entre les inflexions visibles sur les fonctions COPDs et le nombre d'évènements. La prochaine série de tests d'inversion envisagée est de proposer soit des valeurs prédéfinies de glissement moyen (par exemple par la méthode de soustraction-reliquat développée dans cette étude), soit un nombre de glissements successifs recherchés, afin d'explorer la meilleure manière de décomposer le signal de déplacements mesuré par une succession de glissements cosismiques sur la section de faille considérée. Une attention particulière sera apportée pour s'assurer que l'on modélise un bon budget de déformation. Une perspective intéressante pourrait être l'identification de glissements de

moindre amplitudes, comme par exemple des glissements de ~1 m, si les incertitudes le permettent.

L'amélioration des données spatiales, notamment avec les images satellitaires de haute résolution et l'usage de drones, devrait permettre une caractérisation encore plus précise des marqueurs de la déformation (e.g. Zielke et al., 2012). Il n'apparait pas illusoire de gagner en qualité sur les mesures de décalages et sur la cartographie, afin de mieux définir les fonctions COPDs – il est à noter que les COPDs obtenues à partie de données LIDAR présentent des pics plus distincts (e.g. Zielke et al., 2010; Klinger et al., 2011; Gold et al., 2013) – et d'envisager non seulement une estimation plus précise des décalages moyens, mais également d'identifier des séismes plus petits. A cet égard, la possibilité de mettre en évidence des sous-sections de faille pouvant rompre indépendamment est un objectif intéressant.

L'application de cette approche sur une rupture de surface aussi bien préservée et riche en marqueurs géomorphologiques que l'EBF a permis de valider cette méthode au regard des études de terrains (validation des mesures de décalages) et des observations sismologiques précédentes (calcul d'une magnitude équivalente), mais l'une des suites que nécessite ce modèle est une application dans un contexte instrumental différent.

Une autre approche, qui peut également être mise en œuvre pour valider la méthode, est de faire un cas d'étude en bac-à-sable. Connaissant les valeurs de glissements, retrouvent-on ces glissements par reconstruction des marqueurs et modélisation par fonction COPD ? Bien que la question des lois d'échelle complexifient l'analogie des mesures faites en bac avec les déplacements cosismiques à l'échelle d'une faille, cela permettrait de tester notre capacité à : i. retrouver les glissements sur plusieurs cycles sismiques, et ii. identifier des petits évènements. Une telle démarche analogique est d'autant plus engageante qu'il serait possible d'y ajouter une campagne de mesure de décalages comparatifs à différentes distances de la faille (avec contrôle par corrélation d'images), et d'en mesurer l'impact sur les fonctions COPDs.

Un deuxième test d'application de cette méthode consisterait à l'appliquer sur un décrochement déjà connu, pour lequel non seulement les bases de données de décalages ont été acquises, mais aussi pour lequel il existe une bonne connaissance de la vitesse moyenne de la faille et de sa paleosismicité (par exemple sur la faille du Levant, la faille Nord Anatolienne, ou encore la faille Alpine). Ce point permettrait de

discuter de la corrélation entre les amplitudes de glissement mesurées, et les intervalles de retour associés.

### I.5. Question de l'épaisseur crustale dans le calcul des magnitudes

L'un des paramètres cruciaux dans le calcul des magnitudes, est l'épaisseur sismogénique, ou largeur du plan de faille (*fault width*).

Cette section propose d'utiliser le séisme du Gobi-Altaï comme proxy pour contraindre l'épaisseur sismogénique : d'après le calcul détaillé en Chapitre 3.V.2, la meilleure solution d'épaisseur sismogénique serait 50 km pour que les observations de terrain satisfassent les observations sismologiques (Okal, 1976; Chen et Molnar, 1977; Pacheco et Sykes, 1992; Schlupp, PhD, 1996) – à savoir 260 km de rupture le long d'une faille décrochante principale (EBF) d'échelle crustale d'après les données de cartographie des formations et structure géologiques à grande échelle, et 90 km de ruptures secondaires essentiellement en failles inverses (Florensov et Solonenko, 1965; Kurushin et al., 1998; Vassallo et al., 2007), que l'on peut supposer n'affecter que la croûte supérieure. Ainsi, nous avons suggéré de ces observations que la profondeur de la rupture de 1957 est potentiellement plus proche de 50 km que de 20 km d'épaisseur (Chapitre 3.V), puis proposé de calculer les moments sismiques en utilisant une épaisseur sismogénique de 50 km pour la rupture principale et de 20 kilomètres pour les ruptures secondaires. Notons que les modules de cisaillement utilisés pour le calcul du moment sismique doivent correspondre aux épaisseurs sismogéniques considérées (cf. Chapitre 3.V.2).

Cependant les comparaisons de paléomagnitudes avec des approches différentes (i.e. calcul du moment sismique ou utilisation des relations empiriques) semblent montrer que si une valeur de 20 km est certainement sous-estimée, les magnitudes extraites pour une épaisseur de 60 km sont quant à elle surestimées.

## II. Corrélations entre les paramètres déterminés

Cette partie vise à analyser les corrélations entre les paramètres de failles déterminés dans cette thèse. Une première section amène une série de questions, qui seront ensuite discutées successivement, sur la base de la Table 17.

Les vitesses de glissement sur les principales failles du Gobi-Altaï sont-elles logiques entre-elles, ainsi qu'avec les précédentes études ? Selon les loi empiriques de Wells et Coppersmith (1994), les décalages cosismiques évalués sont-ils proportionnels à la longueur des failles extraites de la cartographie détaillée ? Auquel cas, les décalages mesurés pour les séismes passés peuvent-ils servir de critères dans l'estimation de la longueur des ruptures de surface associées à ces séismes ? En faisant l'hypothèse d'une vitesse de faille constante, quelles sont les périodes de retour associées aux décalages identifiés ? Sont-elles cohérentes avec les paléoséismes documentés ? Peut-on associer les évènements observés dans les tranchées à ceux déduit de la distribution des décalages ? Enfin, comment se distribuent les ruptures dans le Gobi-Altaï au cours de l'Holocène ? Les paléoséismes identifiés mettent ils en évidence des essaims de sismicité, rompant toutes ou parties des failles du Gobi-Altaï dans une courte période ($10^{-1}$ ka) ?

| A | SR meas. (mm/a) | Δ_SR | L_mapping (km) | Umean meas. (m) | Δ_Umean | P Trenches (ka) | Δ_P |
|---|---|---|---|---|---|---|---|
| EBF | 1,0 | 0,2 | 260 | 3,5 | 1,4 | 4,4 | 1,3 |
| | | | | 3,0 | 2,4 | 5,3 | 3,0 |
| | | | | 2,5 | 2,1 | | |
| WBF | 0,7 | 0,2 | 150 | 2,2 | 0,4 | 3,2 | 2,4 |
| | | | | 1,4 | 1,1 | 4,9 | 1,8 |
| VOLF | 0,5 | 0,2 | 114 | 3,0 | 1 | 2,5 | 3,0 |
| | | | | 2,1 | 1,8 | | |

| B | Uth (L) W&C94 | Lth(U) W&C94 | Uth (L) W&C94 | Uth (P) from P | Δ_Uth (P) SR cst. (m) | Δ_Uth (P) err_Uth (%) | Pth (U) from U | Δ_Pth (U) SR cst. (ka) | Δ_Pth (U) err_Uth (%) |
|---|---|---|---|---|---|---|---|---|---|
| EBF | 6,5 | 108 | 6,5 | 4,4 | 2,2 | 50% | 3,5 | 2,1 | 60% |
| | | | | 5,3 | 4,0 | 76% | 3,0 | 1,8 | 60% |
| | | | | | | | 2,5 | 2,3 | 92% |
| WBF | 3,7 | 80 | 3,7 | 1,5 | 1,4 | 96% | 3,1 | 1,5 | 48% |
| | | | | 4,1 | 3,6 | 86% | 2,0 | 2,1 | 105% |
| VOLF | 2,7 | 98 | 2,7 | 1,3 | 7,1 | 563% | 6,0 | 3,2 | 53% |
| | | | | | | | 4,2 | 4,4 | 105% |

**Table 17 : A. Paramètres de faille déterminés dans le Chapitre 4, et utilisés pour la comparaison. B. Paramètres de faille théoriques, dérivés des paramètres présentés en A. Abréviations : *mean*, moyen ; *th*, théorique ; Δ, incertitude ; SR, vitesse moyenne (*slip rate*) ; L, longueur de faille ; U, décalage cosismique ; P, intervalle de retour. Exemple : Uth (U), déplacement cosismique théorique (Wells et Coppersmith, 1994) en fonction de L mesurée.**

### II.1. Bilan des vitesses de glissement dans le massif du Gobi-Altaï

Nous avons vu que les vitesses de glissement présentent une grande complémentarité, mettant en évidence un transfert de la déformation (ici décrit d'est en ouest) : d'une part de la faille Bogd Est (~1 mm.a$^{-1}$), vers la WBF à l'ouest (0,7 ± 0,2 mm.a$^{-1}$), et vers la VOLF au nord-ouest (0,5 ± 0,1 mm.a$^{-1}$). Ensuite, cette distribution de la déformation entre deux branches principales se prolonge de manière plus prononcée vers l'ouest. Une branche sud (i.e. la faille de Tsogt) franchi le massif de Gichigniy Nuruu (vitesse verticale : 0,2 ± 0,1 mm.a$^{-1}$) pour se brancher visiblement sur la faille de NABF puis sur l'Altaï méridional, et une branche nord franchit le relais compressif de Burhan Buuday et se poursuit vers l'ouest sur la TGF (avec une vitesse entre 0,2 et 2 mm.a$^{-1}$), jusqu'au bassin de Sharga, à la frontière du domaine de l'Altaï (Figure 4-138 et Figure 4-139). Rappelons que ces vitesses de glissement ont été mesurées sur seulement 1 à 2 sites sur chaque faille (1 pour la WBF, 2 pour la VOLF, TGF et Tsogt), et que ces mesures ne sont pas forcément représentatives sur l'ensemble de la faille.

Nos observations morphotectoniques, et notamment les amplitudes des décalages et vitesses de glissement long terme, semblent conduire aux mêmes conclusions que celles proposées le long de l'EBF : une sismicité rare, mais forte, avec des décalages cosismiques de 1,4 à 4 m (possiblement plus) sur les principaux décrochements de la WBF, VOLF, et dans une moindre contrainte sur la TGF. Néanmoins la longueur de ces paléo-ruptures de surface demeure non déterminée.

De même que les vitesses long terme sont évaluées sur des sites ponctuels, les évaluations de décalages cosismiques associés aux deux derniers évènements ne sont déterminées que sur des sections de faille limitées. Même si les sections étudiées sont assez bien préservées et que la déformation y est visiblement peu distribuée, il ne faut pas occulter le fait que l'amplitude du glissement varie le long de la faille, et que si notre approche COPD permet dans une certaine mesure de s'affranchir des variations haute fréquence de la distribution du glissement ($10^1$ – $10^2$ m), ces valeurs de déplacement ne doivent pas être sur-interprétées dans la caractérisation de l'ensemble des ruptures de surfaces identifiées. Ainsi, l'exercice que nous proposons ci-dessous (qui suppose que les glissements moyens sont représentatifs de l'ensemble de la faille), visant à comparer ces valeurs de décalages aux autres paramètres de failles (longueurs, périodes de retour, vitesses de glissement long terme), est une recherche de corrélations au premier ordre entre ces paramètres, afin de discuter de leur robustesse.

### II.2. Déplacements cosismiques moyens et longueur de ruptures

Les longueurs de faille (équation V-1) et les décalages cosismiques (équation IV-4) théoriques ont été estimés d'après les relations empiriques de Wells et Coppersmith (1994) pour comparaisons (Table **17**, Figure 5-3) :

$$\text{Log}\ (L_{th}) = -1{,}68 + 0{,}65 \times \log\ (AD) \qquad \text{(V-1)}$$

Il est observé que pour la VOLF, qui est la plus courte des trois failles comparées ici (WBF, EBF, VOLF), il semble y avoir une bonne corrélation entre le glissement mesuré pour le dernier évènement (3,0 ± 1 m) et la longueur théorique de la faille pour ce même offset : ~100 km (à comparer aux 114 km déterminés par la cartographie). Par contre, dans les cas de l'EBF et de la WBF, les glissements mesurés donnent des longueurs théoriques nettement plus faibles (d'un facteur 2) que la longueur de la rupture de 1957 (EBF), ou celle de la WBF déterminées par des critères cartographiques (Figure 5-3-B).

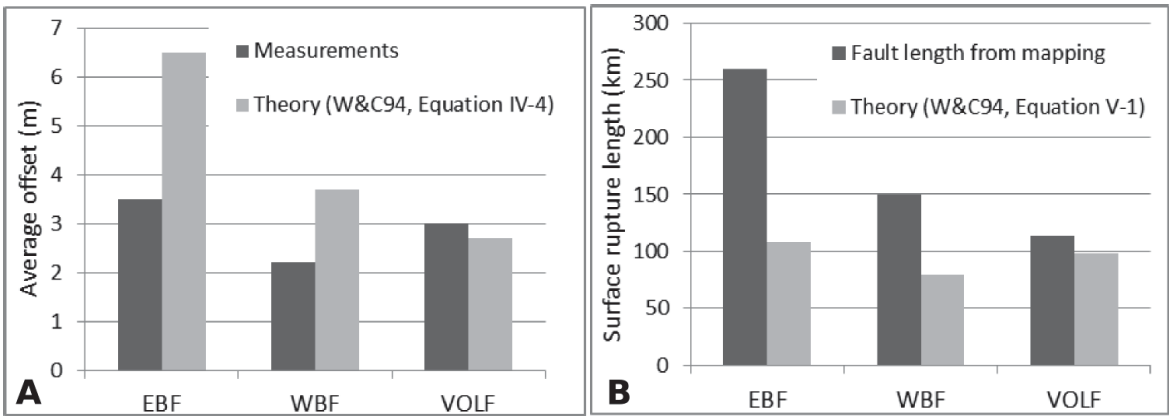


**Figure 5-3: Comparaison des paramètres mesurés avec les paramètres déduits des relations empiriques de (Wells et Coppersmith, 1994). A. Décalages moyens déterminés à partir de la longueur cartographiée des failles. B. Longueurs théorique déterminées d'après les décalages associés au dernier évènement pour chaque faille.**

La même approche en sens inverse consiste à évaluer les décalages moyens théoriques pour des longueurs de failles données (équation IV-4, Table 17, Figure 5-3-A). Les longueurs ainsi extraites des travaux de cartographie amènent à des décalages de 6,5 m pour l'EBF, de 3,7 m pour la WBF, et de 2,7 m pour la VOLF. Ici encore, seule la mesure sur la VOLF apparait cohérente avec les observations de terrain, les décalages théoriques sur les WBF et EBF étant non seulement hors des intervalles de confiance, mais de l'ordre du double de ceux mesurés – observation évidente, vu que les régressions correspondant aux lois empiriques sont issues du même jeu de données.

Il est possible de discuter plus en avant ; par exemple le long de la WBF, le relativement faible décalage cosismique (2,2 ± 0,4 m pour le dernier évènement, amène à une longueur théorique de 80 km, cf. Table 17 et Chapitre 4.V.3) pourrait suggérer

potentiellement que cette faille ne casserait pas d'un seul tenant. Par exemple le relais compressif déca-kilométrique de Bayan Tsagaan (Figure 4-4) a rompu de manière autonome lors d'une réplique du séisme de Bogd en 1958 (séisme de Bayan Tsagaan, 1958, Mw6.9 en accord avec Khilko et al., 1985). Si l'on retranche la région de Bayan Tsagaan de la WBF, sa longueur tombe à 100 km, et en utilisant la relation empirique de Wells et Coppersmith (1994), reliant l'offset moyen à la longueur de la faille (équation IV-4), on obtient un décalage moyen de 2.4 m, similaire à la valeur du décalage moyen mesuré sur la section à l'ouest de la ville de Chandmani (Chapitre 4.IV.2.2). Un autre exemple avec la VOLF montre une meilleure corrélation entre décalage moyen mesuré, décalage moyen théorique, longueur mesurée et longueur théorique (98 km, Figure 5-3-B). Cette observation pourrait être interprétée comme indiquant que la VOLF a rompu en intégralité lors du dernier évènement. Néanmoins, l'EBF, dont le dernier évènement est le séisme du Gobi-Altaï en 1957, nous apporte des contre-exemples des raisonnements proposés ci-dessus. En effet, tant la taille de la rupture de surface que l'amplitude moyenne des décalages cosismiques produits sont dans ce cas bien connus, et cet exercice de comparaison des paramètres de failles montre ici d'importantes incohérences, avec une longueur de rupture théorique de 108 km (contre 260 km pour la rupture principale), et un décalage moyen cosismique théorique de 6,5 m (contre 3,5 ± 1,4 m).

Ces observations sont à mettre au regard des valeurs de magnitudes systématiquement plus faibles obtenues par le calcul empirique à partir du décalage (cf. Chapitre 4.V et Table **17**), les grandeurs U, L et Mw étant naturellement couplées dans les équations de Wells et Coppersmith (1994). Une part de cette différence observée entre la longueur des ruptures par rapport aux décalages moyens peut provenir du fait que nous travaillons ici avec des évaluations de décalages horizontaux, alors qu'il existe souvent une composante mineure verticale. Cette approximation n'explique cependant pas les discordances observées entre ces longueurs et leurs relations empiriques dans la mesure où la composante décrochante est nettement dominante sur l'ensemble des failles, exceptées le long des segments secondaires, dans les zones de relais et les terminaisons de failles.

Deux interprétations semblent possibles pour expliquer ces observations : i. il existe dans le contexte du Gobi-Altaï un seuil sur la longueur de la faille (vers 130 km), au-delà duquel les déplacements cosismiques n'augmentent plus, et on observe une divergence de la relation qui lie le déplacement cosismique à la longueur de la faille –par exemple être proportionnel à la taille requise pour rompre l'ensemble de l'épaisseur sismogénique (e.g. Klinger, 2010). ii. Ces décalages indiquent des ruptures partielles de la faille ; cette

dernière rompant partiellement, elle génère des décalages plus modérés que si elle rompait dans son ensemble. Cette seconde idée dois ici être écartée car le déplacement moyen sur l'EBF est bien contraint, de même que sa rupture de surface principale.

De cette comparaison, il semble que l'on puisse conclure qu'au premier ordre les décalages mesurés ne permettent pas de déduire directement la longueur de la faille. De plus, cette question des relations entre ce que nous mesurons sur le terrain et ce que prédisent les lois empiriques est à approfondir dans le contexte du Gobi-Altaï, mais surtout au regard de d'études comparables, dans des contextes analogues (e.g. Ansberque et al., 2016).

### II.3. Périodes de retour et déplacement cosismiques moyens

Toujours en admettant que i. nos vitesses de déplacement le long des failles, déterminées sur la période tardi-Pléistocène-Holocène, sont représentatives de toute la faille et n'évoluent pas au cours de l'Holocène, et ii. les glissements mesurés sont représentatifs du glissement moyen sur l'ensemble de la faille, il est possible de proposer d'une part des temps de retour pour les séismes à l'origine des décalages cosismiques mesurés ($t_{th} = \frac{U_{mean}}{V}$ , avec $t_{th}$, temps de retour théorique, V, vitesse long terme et $U_{mean}$, décalage moyen). D'autre part des décalages cosismiques associés aux périodes de retour déduites des données paléosismologiques ($U_{th} = V * P$, avec $U_{th}$ décalage moyen théorique et P période de retour déduite des âges des paléoséismes). Les résultats ainsi calculés sont présentés Table 17 et Figure 5-4.

La Figure 5-4 montre que bien que les temps de retour déterminés d'après les âges des séismes en tranchées ne coïncident pas parfaitement avec les temps de retour calculés à partir des vitesses de faille et des glissements cosismiques. Ces valeurs sont confondues dans leurs incertitudes de manière systématique pour les derniers évènements (EBF-1957, WBF-E1 et VOLF-E1, sur la Figure 5-4-A). Il est néanmoins observé que pour les évènements pénultièmes, sur les failles EBF et WBF, où les données paléosismologiques sont suffisantes pour permettre une comparaison, seul le déplacement pour l'EBF (EBF-E2) affiche une cohérence des temps de retour (Figure 5-4.B). En effet la corrélation ne tient pas pour l'évènement pénultième sur la WBF (WBF-E2), dont l'offset mesuré pour ce second évènement était relativement faible (1,4 ± 0,6 m). Cela soulève éventuellement la question de la bonne estimation de l'amplitude du déplacement moyen associé à cet évènement pénultième, identifié à partir d'un signal faible dans la COPD. Ce point repose la question de savoir dans quelle mesure l'approche COPD permet ou non d'identifier et/ou de quantifier des évènements rompant partiellement les décrochements étudiés (un déplacement de 1,4 m étant associé à une

longueur de rupture de surface de ~ 60 km, et à une magnitude Mw ~7,2 d'après Wells et Coppersmith, (1994), équation IV-1 et V-1) ?

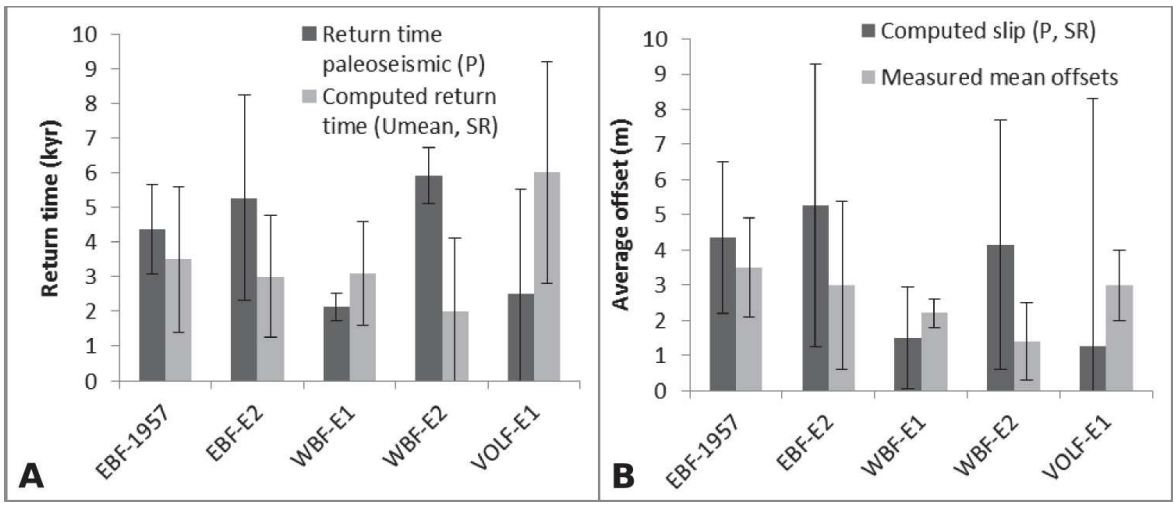


**Figure 5-4 : Comparaison des paramètres de faille mesurés et calculés pour une vitesse de glissement constante sur l'Holocène. Le second évènement sur la VOLF n'est pas représenté faute de disposer du temps de retour associé. A. Temps de retour pour chaque décrochement majeur mesuré. B. Glissement cosismique moyen pour chaque décrochement majeur.**

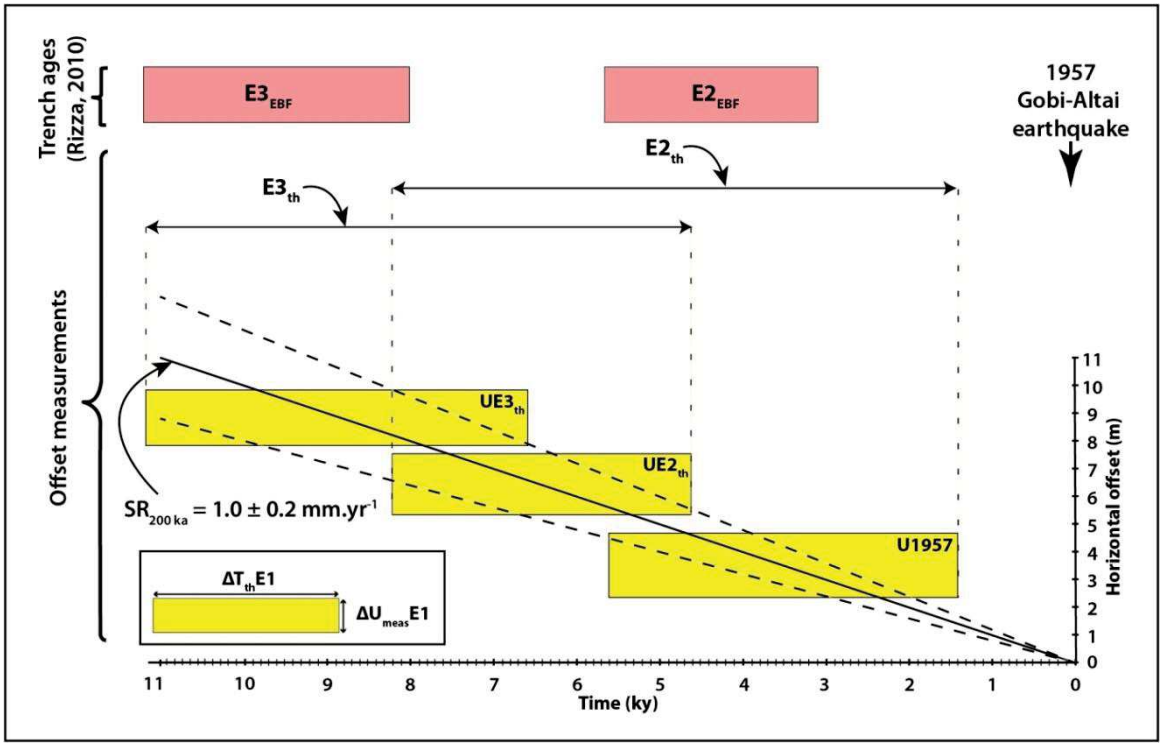


**Figure 5-5 : Représentation graphique de la comparaison des âges dérivés des mesures de décalages moyens à vitesse de faille constante (boites jaunes), par rapports aux âges dérivées des tranchées de paléosismologie (boites rouges, d'après Rizza, PhD, 2010b), sur la faille de Bogd est (EBF).**

Il est à noter que la contrainte du temps de retour sur la VOLF n'est pas déterminée ; cela explique pourquoi les incertitudes associées à cette période de retour sont supérieures à 100% – néanmoins, la contrainte de l'âge des paléoséismes le long de la VOLF par les analyses OSL en cours devrait permettre de préciser ce point.

La comparaison inverse (i.e. des glissements mesurés avec les glissements théoriques obtenus à vitesse de glissement constante) pour les intervalles de retour déterminés à partir de l'âge des séismes observés en tranchée, n'indique pas d'incohérence dans les incertitudes. Cette comparaison n'apparait cependant que peu pertinente dans la mesure où les contraintes sur les décalages théoriques sont faibles, en raison principalement des fortes incertitudes sur les intervalles de retour.

Les Figure 5-5 et Figure 5-6 proposent pour chaque faille une approche graphique de la comparaison entre âges calculés à partir des données morphotectoniques et données paléosismologiques. Les boites jaunes représentent les décalages identifiés par l'approche COPD (UE, E signifiant évènement). Leurs hauteurs correspondent aux incertitudes sur l'évaluation des décalages. Leurs largeurs correspondent aux incertitudes associées d'une part à la détermination du temps de retour à vitesse constante, et d'autre part à l'incertitude sur l'estimation des déplacements. Les flèches noires correspondantes indiquent l'intervalle d'âges théoriques ($E_{th}$, calculés d'après les décalages cosismiques mesurés et une vitesse long terme constante) au cours desquels ont eu lieu les paléoséismes. Les boites rouges représentent les âges déterminés en tranchée (Rizza, PhD 2010 et Ritz et al., 2009 pour la EBF, Chapitre 4 pour les WBF et VOLF), leur largeur définissant l'intervalle d'âge de chaque paléoséisme. Les vitesses de glissement et les périodes de retour utilisées sont présentées en Table **17**. Dans ces représentations, le décalage mesuré sur les failles est représentatif – via la connaissance de la vitesse de glissement – du temps écoulé entre le dernier et le pénultième évènement. Ainsi, cette description ne tient pas compte de la ''position'' actuelle de la faille dans le cycle sismique : d'un point de vue morphotectonique, le décalage associé au dernier évènement peut être 'frais ' (cas 1957), ou 'vieux' (cas du dernier évènement sur la WBF, vraisemblablement autour de 2 ka). Cette observation se traduit par le fait que la vitesse de glissement (trait plein noir sur les Figure 5-5 et Figure 5-6) est toujours fixée à zéro, quel que soit l'âge du dernier évènement.

Il est constaté que pour les trois failles, tant le nombre que l'âge des séismes identifiés par les deux approches (i.e. morphotectonique et paléosismologique) ne présentent pas d'incohérences. De plus, bien que les contraintes sur les âges des paléoséismes et sur les décalages moyens ne soient pas très robustes (voir franchement faibles pour

l'évaluation du temps de retour sur la VOLF et l'identification morphotectonique de l'antépénultième évènement sur la WBF, suggéré en tirets), la cohérence globale des paramètres mesurés est un constat engageant pour la poursuite du développement de l'approche COPD, et de sa corrélation à d'autres bases de données de paléosismologie.

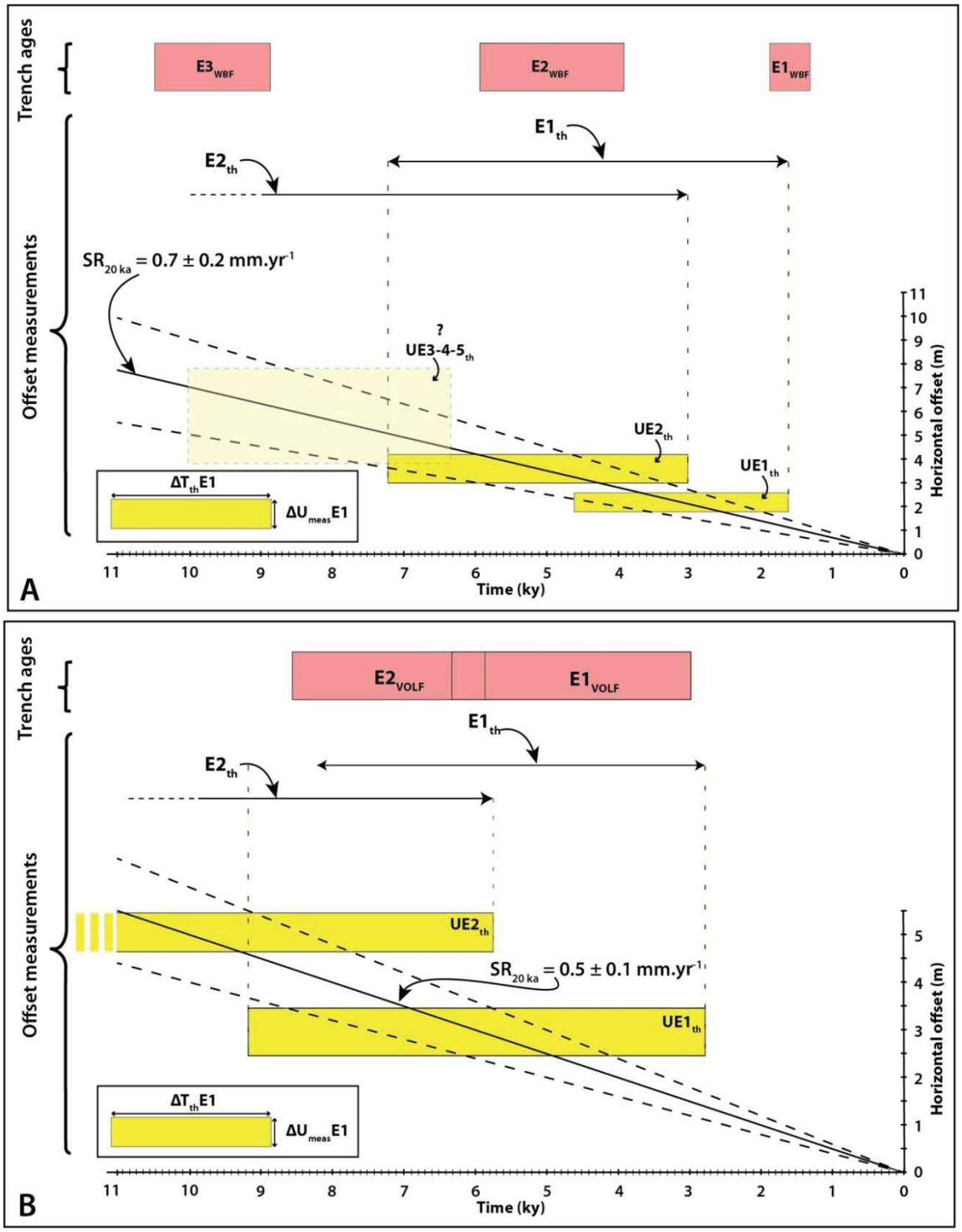


**Figure 5-6 : Représentation graphique de la comparaison des âges dérivés des mesures de décalages moyens à vitesse de faille constante (boites jaunes), par rapports aux âges dérivées des tranchées de paléosismologie (boites rouges). A. Pour la faille de Bogd ouest (WBF). B Pour la faille de la Vallée des Lacs.**

Pour conclure cette comparaison, bien que l'utilisation des offsets pour contraindre l'âge des paléoséismes semble encore imparfaite, il apparait à partir de cette corrélation sur les trois décrochements étudiés dans cette thèse qu'il est possible d'associer l'identification d'une rupture dans la morphologie à des séismes observés en tranchée de paléosismologie, à condition de connaître la vitesse de glissement de la faille à l'Holocène et de la considérer constante. Cette observation est d'autant plus pertinente que l'un des questionnements récurent dans l'analyse comparée morphotectonique et paléosismologie de décrochements est la taille des évènements identifiés dans les tranchées, les rejets horizontaux étant spécifiquement plus délicats à estimer que les rejets verticaux dans des tranchées transverses à la faille – un travail en tranchée 3D offre des opportunités de quantifier les décalages horizontaux, mais demeure délicat à entreprendre, notamment en termes de coût humain et de destruction de l'escarpement (McCalpin 2009). Cette approche apparait bien fonctionner sur l'Holocène à partir des données morphotectoniques et paléosismologiques du Gobi-Altaï, et il est prometteur qu'une amélioration des déterminations des offsets cosismiques (cf Chapitre. 5.I.4.3.2) permette d'étendre la période investiguée au Pléistocène supérieur.

### II.4. Corrélation des paléoséismes entre les principales failles du Gobi-Altaï : essaims de sismicité ?

L'une des questions centrales dans le fonctionnement de ces grands décrochements, est la potentialité que le transfert de contraintes généré par la rupture de l'une des failles déclenche un ou plusieurs évènements sur une ou plusieurs autres failles alentour. De même que pour l'identification des paléoséismes, notre analyse de potentiels essaims de sismicité se limite aux forts séismes (Mw>7,5). Afin d'analyser si les données acquises dans cette étude permettent de mettre en évidence d'éventuels essaims sismiques au cours de l'Holocène au sein même de la chaine du Gobi-Altaï, la Figure 5-7 met en parallèle les évènements sismiques identifiés dans les tranchées. Les données paléosismologiques sur l'EBF proviennent de Ritz et al., (2009), et Rizza (PhD, 2010).

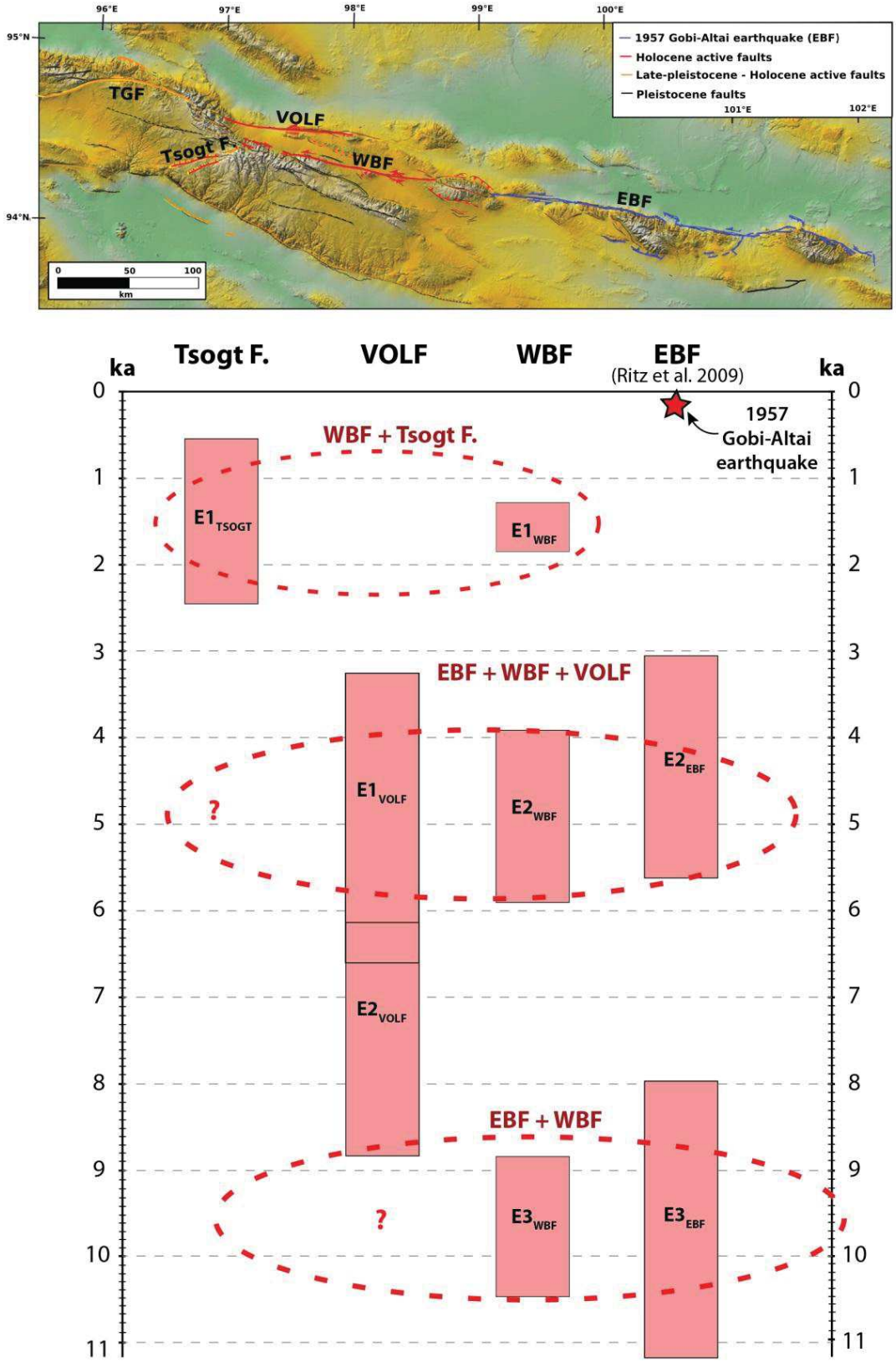


**Figure 5-7 : A. Localisation des principales failles actives du Gobi-Altaï étudiées dans cette thèse. B. Comparaison des âges des paléoséismes sur les failles de Tsogt, VOLF, WBF et EBF au cours de l'Holocène. Les ellipses rouges pointillées indiquent les possibles clusters révélés par ces données.**

Bien que les données paléosismologiques sur la VOLF soient limitées, la Figure 5-7 met en évidence trois possibles essaims répartis sur les 4 failles considérées au cours de l'Holocène. Les contraintes d'âge sur les évènements demeurent faibles (incertitude ~$10^3$ ans), mais de manière intéressante, il est possible de distinguer :

*i. Un premier essaim a pu avoir lieu vers 1,5 ka entre la WBF et la faille de Tsogt, située dans son prolongement, avec une cinématique cohérente à la géométrie de la WBF (le branchement sur la faille de Tsogt s'effectue avec un net changement d'orientation vers la gauche, cohérent avec une cinématique normale sur le branchement).*

*ii. Un second essaim a pu se produire également autour de 4,5 ka entre les 3 décrochements principaux étudiés dans cette thèse : les failles de EBF, WBF et VOLF. Notons que cet essaim, selon les données dont nous disposons, serait contemporain de l'évènement pénultième sur les EBF et WBF. Bien qu'un évènement se soit sans doute produit le long de la WBF depuis, l'identification d'un tel potentiel essaim de sismicité mérite d'être d'avantage étudié, d'autant que l'EBF a rompu au siècle dernier.*

*iii. Un troisième essaim a pu se produite autour de 10 ka, avec rupture de l'ensemble de la faille de Bogd (EBF et WBF) dans un laps de temps modéré (1 ka).*

Deux de ces essaims de sismicité affectent l'ensemble de la faille de Bogd, ce qui représente une longueur de faille principale de ~450 km, et son interaction avec la VOLF pourrait rappeler le contexte de la faille de Bolnay, associée à celle de Tsetserleg, qui ont rompu à 14 jours d'intervalle en 1905. L'une des conclusions qui émane de telle crise sismique, est que les offsets associés sont probablement importants (> 3 m).

Par ailleurs cela amène également la question de possibles essaims de sismicité à plus grande échelle, et notamment à l'échelle de la Mongolie occidentale, à l'instar de la crise sismique du XX$^{ème}$ du siècle. Ainsi, non seulement il serait judicieux de poursuivre la caractérisation des failles du Gobi-Altaï, mais aussi d'appliquer cette comparaison des données paléosismologique de clusters dans les massifs de l'Altaï, de Bolnay, et de Sayan (e.g. Ferry et al., 2015; Choi et al., submitted).

# III. Perspectives

## III.1. Cartographie

La cartographie systématique des ruptures de surface décrochantes associées à des séismes majeurs montre la complexité et la distribution de la déformation à l'échelle régionale, ainsi que dans le détail. En particulier, l'identification de branchements ou de déformation distribuée comme dans les zones de relais permet d'accéder à la caractérisation de la rupture sismique et de sa segmentation.

L'acquisition des MNTs à haute résolution (≤ 1 m), par exemple dérivés d'images Pléiades ou de couverture Lidar, et leur couplage avec la cartographie des failles actives, permettraient l'extraction de la distribution spatiale des rejets verticaux en plus des rejets horizontaux, et ainsi de mieux caractériser la cinématique de la faille et sa géométrie (mesures de plongements, branchements et interactions avec les structures géologiques héritées). Ces informations permettraient de déterminer l'orientation et l'amplitude du vecteur glissement, et ainsi d'améliorer l'analyse de la distribution du glissement le long d'une même faille sur plusieurs cycles. Ces informations pourront par la suite être interprétées vis-à-vis de la géométrie du système de failles dans son ensemble – et en profondeur –, afin de mieux caractériser l'évolution spatiale de la déformation sismique, par exemple dans le cadre d'une modélisation numérique.

## III.2. Modélisation

L'une des perspectives de cette étude est d'utiliser ces données morphotectoniques et paléosismologiques (géométrie des ruptures de surfaces et des failles associées, contraintes paleosismologiques sur l'âge des paléoséismes, détermination des vitesses de glissement long terme) et les paramètres qui en découlent (périodes de retour, paléomagnitudes, localisation des terminaisons de failles), afin de mener une modélisation mécanique des champs de contraintes associés à ces paléo-évènements – en plus du séisme de 1957 (Chéry et al., 2001). Une telle approche permettrait notamment d'explorer le potentiel de couplage des potentiels essaims sismiques d'une part au sein du massif du Gobi-Altaï, et d'autre part avec les principales structures environnantes (failles et réseaux de failles), e.g. *Altai range, Bolnay region, Altai-city region, Bayankhongor*.

Les données produites dans cette étude pourront également compléter les paramètres de modèle d'aléa sismique basé sur la caractérisation des failles actives (e.g. Bender et Perkins, 1982; Pace et al., 2016).

### III.3. Segmentation

La notion de segmentation des failles décrochantes a été utilisée dans cette étude à partir de critères géométriques et cinématiques associés aux ruptures de surface (Chapitre 3.III.1), chaque segment étant ensuite interprété comme une section de faille homogène, afin de déterminer un décalage moyen ou de discuter la longueur des ruptures (e.g. Wesnousky, 2006; Klinger, 2010).

La Figure 5-8 montre les longueurs moyennes des segments identifiés sur les principaux décrochements étudiés.

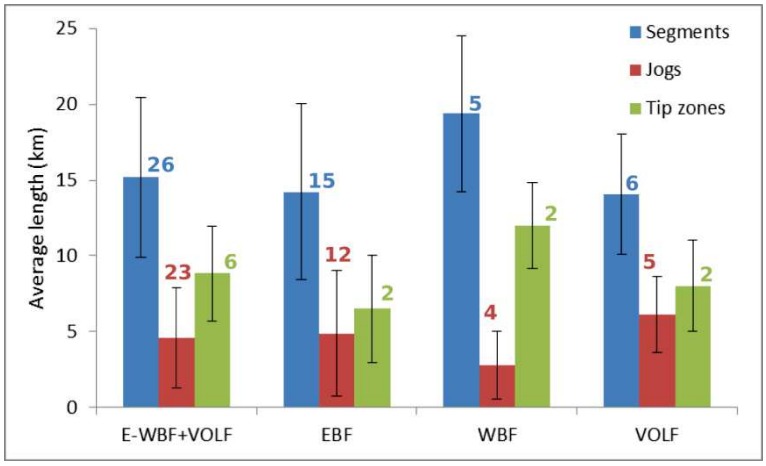


**Figure 5-8 : Longueur moyenne des segments (bleu), des relais (rouge) et des zones de terminaison (vert) pour les trois décrochements majeurs étudiés (EBF, WBF et VOLF), ainsi que pour l'ensemble de ces trois failles (E-WBF+VOLF). Les numéros correspondant indiquent le nombre de d'entités.**

Sur les 26 segments identifés sur les 3 décrochements majeures étudiés, la longueur moyenne des segments est de 15 km, et il apparait que la longueur des relais représente ~20% de la longueur totale des failles.

Une perspective intéressante d'exploitation des travaux de cartographie présentée dans cette étude est l'analyse des relations entre la segmentation et l'héritage structural et lithologique. On peut ainsi se demander quelles sont les natures et dimensions des hétérogénéités géologiques pouvant contrôler la localisation et la géométrie des failles, ainsi que leur évolution (abandon, réactivation) ? Cette perspective nécessite par ailleurs de caractériser les structures aveugles (e.g. failles, plis de propagation).

Bien que cette problématique n'ait pas été étudiée en profondeur au cours de cette thèse, notamment au travers d'une bibliographie appropriée, l'étude détaillée de la rupture de surface du séisme de 1957 constitue un point de départ intéressant. En effet, dans le milieu aride et dépourvu de couverture arborée du Gobi-Altaï, la cartographie détaillée des ruptures de surface, permet d'analyser plusieurs cycles sismiques sur une

période couvrant au moins l'Holocène. De plus, l'absence de végétation dans la région offre une bonne exposition des affleurements à la couverture satellitaire, qui représente une base de données facilement accessible pour l'analyse des fabriques métamorphiques à grande échelle, et des domaines géologiques impliqués dans le modelé de déformation –essentiellement sismique – affectant le système de faille du Gobi-Altaï.

Une comparaison préliminaire est proposée à partir de la segmentation de la rupture de surface associée à l'EBF, qui faute de présenter une corrélation systématique, apparait partiellement associée au changement de domaines lithologiques (Vassallo et al., 2007). Bien que la segmentation de l'EBF ait été définie à partir de critères géométriques et cinématiques extraits de la cartographie de la rupture, il semble qu'il y ait également une corrélation entre la segmentation ainsi obtenue et les principales unités géologiques. En effet, 10 des 14 relais entre les segments correspondent à un changement d'unité géologique au travers de laquelle la faille se propage, et 10 des 15 segments sont localisés au sein d'une même unité (Figure 3-7-b).

De plus, nous remarquons que les sections transpressives (segments S1, S2, S4, S11), et plus particulièrement les deux principaux relais R2 et R6, sont localisés au sein de dépôt continentaux jurassiques. Ces formations ont certainement été impliquées dans la structuration de la zone en demi-graben, avec des failles normales à vergence nord (van Hinsbergen et al., 2015). La géométrie de ces structures, et en particulier leurs relations géométriques avec le décrochement principal demeurent inconnus, mais l'héritage géologique est ici fortement susceptible d'influencer la segmentation de la faille. Cette observation souligne l'importance de l'héritage géologique, aussi bien au cours de la propagation de la faille, que dans son modelé en général (Vassallo et al., 2007; Vallage et al., 2016 ; Choi et al., submitted)).

Nous suggérons ici que l'héritage géologique et structural est à l'origine d'hétérogénéités dans la croûte supérieure, agissant comme des aspérités au cours de la propagation de la faille, en créant des motifs spécifiques dans la rupture de surface, comme du partitionnement superficiel ou des zones d'endommagement ; le motif ainsi produit reflétant partiellement la segmentation de la faille. Pour conclure, la signification de la segmentation des failles décrochantes apparait à de multiples égards un terrain d'étude intéressant pour la compréhension du fonctionnement et de l'évolution des failles, comme dans la caractérisation de l'épaisseur sismogénique maximale (e.g. Bilham et Williams, 1985; Klinger, 2010) ou la détermination de la longueur des ruptures (e.g.

Wesnousky, 2008). Il semblerait d'après nos observations que l'héritage géologique constitue également un paramètre de premier ordre dans la segmentation des failles.

### III.4. Paléosismologie et distribution du glissement

Nous avons pu proposer des comparaisons des mesures de décalages moyens au regard des paléoséismes identifiés en tranchée, et constater qu'avec la résolution et la quantité actuelle des données sur le Gobi-Altaï, l'utilisation des décalages comme critères de tailles de ruptures ne permet pas de discerner la proportion de faille qui a rompu. Nous avons également vu que l'évaluation des décalages sur plusieurs cycles sismiques présente une cohérence avec une succession de grandes ruptures, permettant éventuellement de les identifier les unes des autres – avec l'hypothèse d'une vitesse de glissement constante.

Pour aller plus loin, il est envisageable de poursuivre ce rapprochement des données paléosismologiques – et son acquisition – avec la distribution du glissement le long de la faille, en intégrant ces diagrammes (Figure 5-5 et 4) le long de la rupture, au regard de la segmentation. Cela permettrait, en outre, d'inclure de possibles variations de vitesses de glissement le long de la faille (long termes comme géodésiques), des complexités géométriques (structures héritées, branchement sur failles actives), et des variations latérales de milieu de propagation (unités géologiques, zones d'endommagements, e .g. McGrath et Davison 1995; Kim, et al., 2004; Kim et Sanderson, 2005), afin d'affiner la déterminations de critères pour la rupture de chaque segment.

# Conclusion générale

Cette étude apporte de nouvelles données morphotectoniques et paléosismologiques sur les failles qui affectent la chaine du Gobi-Altaï, en Mongolie, permettant de décrire son activité sismique au cours de l'Holocène.

Les déterminations de vitesses de glissement long terme, grâce à la datation « 10Be *in situ* » de marqueurs morphologiques décalés ont pu être réalisées sur 3 décrochements majeurs : la faille de Bogd occidentale (WBF), la faille de la Vallée des lacs (VOLF), et la faille de Tsagaan Gol (TGF), ainsi que sur une faille normale d'échelle crustale : la faille de Tsogt. La distribution des vitesses ainsi obtenues est cohérente avec la vitesse de déplacement de ~1 $mm.a^{-1}$ déterminée le long de la faille de Bogd orientale (EBF) (e.g. Rizza et al., 2011), avec une vitesse de 0,7 ± 0,2 $mm.a^{-1}$ le long de WBF et de 0,5 ± 0,2 $mm.a^{-1}$ le long de VOLF. Dans la partie la plus occidentale du Gobi-Altaï, la déformation est distribuée sur deux branches : au nord la TGF (vitesse estimée entre 0,2 et 2 $mm.a^{-1}$) qui correspond à la prolongation de la VOLF et au sud la faille de Tsogt (vitesse verticale de 0,2 ± 0,1 $mm.a^{-1}$), faille normale majeure qui recoupe toute la partie médiane du Gobi-Altaï et qui se connecte à la WBF.

Les analyses paléosismologiques ont permis d'identifier les principaux séismes s'étant produits sur les failles de la Vallée des Lacs (VOLF) et de Bogd occidentale (WBF), avec respectivement 2 et 3 évènements au cours de l'Holocène, ainsi que sur la faille de Tsogt (TF), où un denier évènement s'est produit il y a ~1,5 ± 1 ka. La période de retour pour un évènement majeur sur la faille de Bogd Occidentale est estimée à 4,0 ± 1,2 ka. Parallèlement, ces données montrent la possibilité que des essaims sismiques aient pu se produire au sein du Gobi-Altaï, à environ 1,5 ka, 4,5 ka et 10 ka, impliquant respectivement les failles WBF + TF, EBF + WBF + VOLF et WBF + EBF. Ces âges sont ici donnés à titre indicatif dans la mesure où, bien que ces évènements soient soupçonnés d'être majeurs (Mw ≥ 8), la détermination de leurs âges sur les failles VOLF et TF est limitée à un seul site. Ainsi, dans une perspective de caractérisation de ces essaims sismiques en domaine intracontinental, ces résultats demandent d'avantage d'investigations.

D'un point de vue méthodologique, nous avons proposé dans cette étude une décomposition statistique de bases de données de mesures systématiques de décalages cosismiques, afin de déterminer, en fonction de la segmentation, les décalages cosismiques moyens associés aux paléo-évènements enregistrés dans la

morphologie. Cette approche, élaborée sur la distribution du glissement horizontal le long de la faille de Bogd orientale, a permis de reconstituer les glissements successifs de la faille au cours des 3 derniers cycles sismiques, et de suggérer que la distribution du glissement du séisme de 1957 est plus plate que décrite précédemment. Nos résultats semblent également confirmer que les séismes majeurs le long de la faille de Bogd orientale produisent des glissements caractéristiques sur ces trois cycles, pour au moins 50 % de la rupture principale. Bien que cette transcription de l'analyse dite de 'densité de probabilité cumulée' (COPD), présente encore des incohérences et nécessite d'être perfectionnée, elle présente une perspective intéressante, notamment en vue d'attribuer des décalages cosismiques moyens aux paléoséismes identifiés en tranchées. En effet, si l'utilisation des relations empiriques afin de contraindre la longueur des ruptures à partir des décalages cosismiques ne donne pas des résultats cohérents avec nos données, il apparait qu'au premier ordre, en supposant une vitesse de glissement constante de la faille au cours de l'Holocène, les décalages puissent être corrélés avec les ruptures identifiées dans les tranchées.

# Références


Abdrakhmatov, K. E., R. T. Walker, G. E. Campbell, Andrew S. Carr, A. Elliott, C. Hillemann, J. Hollingsworth, et al. 2016. « Multisegment rupture in the 11 July 1889 Chilik earthquake (Mw 8.0–8.3), Kazakh Tien Shan, interpreted from remote sensing, field survey, and paleoseismic trenching ». *Journal of Geophysical Research: Solid Earth* 121 (6):4615–4640.

Adiya et al. 2003. « One century of seismicity in Mongolia ».

Aitken, Martin Jim. 1985. *Thermoluminescence Dating*. Academic press. http://www.bcin.ca/Interface/openbcin.cgi?submit=submit&Chinkey=81864.

Allen, Clarence R. 1968. « The tectonic environments of seismically active and inactive areas along the San Andreas fault system ». *Stanford University Publications. Geological Sciences* 11:70–80.

AMC Şengör, BA Natal'In, VS Burtman. 1993. « Evolution of the Altaid tectonic collage and Palaeozoic crustal growth in Eurasia ». *Nature*, 1993.

Ancuta, L. D., R. W. Carlson, B. D. Idleman, et P. K. Zeitler. 2013. « Geochemistry and geochronology of Hangay Dome volcanic rocks: exploring the source of high topography and volcanism in an intracontinental setting ». In *AGU Fall Meeting Abstracts*. http://adsabs.harvard.edu/abs/2013AGUFM.T42B..08A.

Ansberque, Claire, Olivier Bellier, Vincent Godard, Cécile Lasserre, Mingming Wang, Régis Braucher, Brigitte Talon, Julia de Sigoyer, Xiwei Xu, et Didier L. Bourlès. 2016. « The Longriqu Fault Zone, Eastern Tibetan Plateau: Segmentation and Holocene Behavior: The Longriqu Fault ». *Tectonics* 35 (3):565‑85. https://doi.org/10.1002/2015TC004070.

Arjannikova, A., C. Larroque, J. -F. Ritz, J. Déverchère, J. F. Stéphan, S. Arjannikov, et V. San'kov. 2004. « Geometry and Kinematics of Recent Deformation in the Mondy–Tunka Area (South-Westernmost Baikal Rift Zone, Mongolia–Siberia) ». *Terra Nova* 16 (5):265‑72. https://doi.org/10.1111/j.1365-3121.2004.00565.x.

Avouac, J. P., P. Tapponnier, M. Bai, H. You, et G. Wang. 1993. « Active Thrusting and Folding along the Northern Tien Shan and Late Cenozoic Rotation of the Tarim Relative to Dzungaria and Kazakhstan ». *Journal of Geophysical Research: Solid Earth* 98 (B4):6755‑6804. https://doi.org/10.1029/92JB01963.

Badarch, Gombosuren, W Dickson Cunningham, et Brian F Windley. 2002. « A new terrane subdivision for Mongolia: implications for the Phanerozoic crustal growth of Central Asia ». *Journal of Asian Earth Sciences* 21 (1):87‑110. https://doi.org/10.1016/S1367-9120(02)00017-2.

Balco, Greg, John O. Stone, Nathaniel A. Lifton, et Tibor J. Dunai. 2008. « A Complete and Easily Accessible Means of Calculating Surface Exposure Ages or Erosion Rates from 10Be and 26Al Measurements ». *Quaternary Geochronology* 3 (3):174‑95. https://doi.org/10.1016/j.quageo.2007.12.001.

Baljinnyam, I., éd. 1993. *Ruptures of major earthquakes and active deformation in Mongolia and its surroundings*. Memoir 181. Boulder: Geological Society of America.

Baljinnyam, I., A. Bayasgalan, B. A. Borisov, et et. al. 1993. *Ruptures of major earthquakes and active deformation in Mongolia and its surroundings*. Boulder, Etats-Unis: The Geological Society of America.

Bayasgalan, A., et J. A. Jackson. 1999. « A re-assessment of the faulting in the 1967 Mogod earthquakes in Mongolia ». *Geophysical Journal International* 138 (3):784–800.

Bayasgalan, Amgalan, James Jackson, et Dan McKenzie. 2005. « Lithosphere Rheology and Active Tectonics in Mongolia: Relations between Earthquake Source Parameters, Gravity and GPS Measurements ». *Geophysical Journal International* 163 (3):1151‑79. https://doi.org/10.1111/j.1365-246X.2005.02764.x.

Bayasgalan, Amgalan, James Jackson, Jean-François Ritz, et Sebastien Carretier. 1999a. « Field Examples of Strike-Slip Fault Terminations in Mongolia and Their Tectonic Significance ». *Tectonics* 18 (3):394‑411. https://doi.org/10.1029/1999TC900007.

Bayasgalan. 1999b. « Forebergs', flower structures, and the development of large intra-continental strike-slip faults: the Gurvan Bogd fault system in Mongolia ». *Journal of Structural Geology* 21 (10):1285–1302.

Bender, Bernice, et David M. Perkins. 1982. « SEISRISK II; a computer program for seismic hazard estimation ». US Geological Survey,. https://pubs.er.usgs.gov/publication/ofr82293.

Berberian, M., J. A. Jackson, M. Qorashi, M. M. Khatib, K. Priestley, M. Talebian, et M. Ghafuri-Ashtiani. 1999. « The 1997 May 10 Zirkuh (Qa'enat) earthquake (Mw 7.2): faulting along the Sistan suture zone of eastern Iran ». *Geophysical Journal International* 136 (3):671‑94. https://doi.org/10.1046/j.1365-246x.1999.00762.x.

Berberian, Manuel, et Robert S. Yeats. 1999. « Patterns of Historical Earthquake Rupture in the Iranian Plateau ». *Bulletin of the Seismological Society of America* 89 (1):120‑39.

Bettinelli, Pierre, Jean-Philippe Avouac, Mireille Flouzat, François Jouanne, Laurent Bollinger, Pascal Willis, et Gyani Raja Chitrakar. 2006. « Plate Motion of India and Interseismic Strain in the Nepal Himalaya from GPS and DORIS Measurements ». *Journal of Geodesy* 80 (8‑11):567‑89. https://doi.org/10.1007/s00190-006-0030-3.

Bierman, Paul R., Alan R. Gillespie, et Marc W. Caffee. 1995. « Cosmogenic Ages for Earthquake Recurrence Intervals and Debris Flow Fan Deposition, Owens Valley, California ». *Science* 270 (5235):447‑50.

Bilham, Roger, et Patrick Williams. 1985. « Sawtooth segmentation and deformation processes on the southern San Andreas fault, California ». *Geophysical Research Letters* 12 (9):557–560.

Billant, Jérémy, Olivier Bellier, Vincent Godard, et Jean-Claude Hippolyte. 2016. « Constraining Recent Fault Offsets with Statistical and Geometrical Methods: Example from the Jasneuf Fault (Western Alps, France) ». *Tectonophysics* 693 (décembre):1‑21. https://doi.org/10.1016/j.tecto.2016.09.031.

Blight, James H.S., Quentin G. Crowley, Michael G. Petterson, et Dickson Cunningham. 2010. « Granites of the Southern Mongolia Carboniferous Arc: New Geochronological and Geochemical Constraints ». *Lithos* 116 (1‑2):35‑52. https://doi.org/10.1016/j.lithos.2010.01.001.

Bollinger, L., P. Tapponnier, S. N. Sapkota, et Y. Klinger. 2016. « Slip deficit in central Nepal: omen for a repeat of the 1344 AD earthquake? » *Earth, Planets and Space* 68 (janvier):12. https://doi.org/10.1186/s40623-016-0389-1.

Borchers, Brian, Shasta Marrero, Greg Balco, Marc Caffee, Brent Goehring, Nathaniel Lifton, Kunihiko Nishiizumi, Fred Phillips, Joerg Schaefer, et John Stone. 2016. « Geological Calibration of Spallation Production Rates in the CRONUS-Earth Project ». *Quaternary Geochronology* 31 (février):188‑98. https://doi.org/10.1016/j.quageo.2015.01.009.

Bowman, Sheridan. 1990. *Radiocarbon Dating*. University of California Press.

Braucher, R., S. Merchel, J. Borgomano, et D.L. Bourlès. 2011. « Production of Cosmogenic Radionuclides at Great Depth: A Multi Element Approach ». *Earth and Planetary Science Letters* 309 (1‑2):1‑9. https://doi.org/10.1016/j.epsl.2011.06.036.

Brown, Erik Thorson, John M Edmond, Grant M Raisbeck, Françoise Yiou, Mark D Kurz, et Edward J Brook. 1991. « Examination of surface exposure ages of Antarctic moraines using in situ produced 10Be and 26Al ». *Geochimica et Cosmochimica Acta* 55 (8):2269‑83. https://doi.org/10.1016/0016-7037(91)90103-C.

Bruhat, Lucile, Sylvain Barbot, et Jean-Philippe Avouac. 2011. « Evidence for Postseismic Deformation of the Lower Crust Following the 2004 Mw6.0 Parkfield Earthquake ». *Journal of Geophysical Research* 116 (B8). https://doi.org/10.1029/2010JB008073.

Bullen, M. E., D. W. Burbank, J. I. Garver, et K. Ye Abdrakhmatov. 2001. « Late Cenozoic Tectonic Evolution of the Northwestern Tien Shan: New Age Estimates for the Initiation of Mountain Building ». *Geological Society of America Bulletin* 113 (12):1544‑59. https://doi.org/10.1130/0016-7606(2001)113<1544:LCTEOT>2.0.CO;2.

Buylaert, J. P., A. S. Murray, K. J. Thomsen, et M. Jain. 2009. « Testing the potential of an elevated temperature IRSL signal from K-feldspar ». *Radiation Measurements*, Proceedings of the 12th International Conference on Luminescence and Electron Spin Resonance Dating (LED 2008), 44 (5–6):560‑65. https://doi.org/10.1016/j.radmeas.2009.02.007.

Calais, Eric, Mathilde Vergnolle, Vladimir San'kov, Andrei Lukhnev, Andrei Miroshnitchenko, Sharavyn Amarjargal, et Jacques Déverchère. 2003. « GPS Measurements of Crustal Deformation in the Baikal-Mongolia Area (1994-2002): Implications for Current Kinematics of Asia: GPS MEASUREMENTS IN MONGOLIA ». *Journal of Geophysical Research: Solid Earth* 108 (B10). https://doi.org/10.1029/2002JB002373.

Campbell, G. E., R. T. Walker, K. Abdrakhmatov, J. L. Schwenninger, J. Jackson, J. R. Elliott, et Alex Copley. 2013. « The Dzhungarian fault: Late Quaternary tectonics and slip rate of a major right-lateral strike-slip fault in the northern Tien Shan region ». *Journal of Geophysical Research: Solid Earth* 118 (10):5681–5698.

Charreau, Julien, Yan Chen, Stuart Gilder, Stéphane Dominguez, Jean-Philippe Avouac, Sevket Sen, Dongjiang Sun, Yongan Li, et Wei-Ming Wang. 2005. « Magnetostratigraphy and rock magnetism of the Neogene Kuitun He section (northwest China): implications for Late Cenozoic uplift of the Tianshan mountains ». *Earth and Planetary Science Letters* 230 (1–2):177‑92. https://doi.org/10.1016/j.epsl.2004.11.002.

Chen, Wang-Ping, et Peter Molnar. 1977. « Seismic Moments of Major Earthquakes and the Average Rate of Slip in Central Asia ». *Journal of Geophysical Research* 82 (20):2945‑69. https://doi.org/10.1029/JB082i020p02945.

Chéry, Jean, Sëbastien Carretier, et Jean-Francois Ritz. 2001. « Postseismic stress transfer explains time clustering of large earthquakes in Mongolia ». *Earth and Planetary Science Letters* 194 (1):277–286.

Chevalier, M.-L., F. J. Ryerson, P. Tapponnier, R. C. Finkel, J. Van Der Woerd, Li Haibing, et Liu Qing. 2005. « Slip-Rate Measurements on the Karakorum Fault May Imply Secular Variations in Fault Motion ». *Science* 307 (5708):411‑14. https://doi.org/10.1126/science.1105466.

Choi, J, klinger, Y., Ferry, J-F. Ritz, R. Kurtz, Magali Rizza, Laurent Bollinger, Davaasambuu, Tsend-Ayush, et Demberel. submitted. « Geologic inheritance and earthquake rupture processes: the 1905 M ≥ 8 Tsetserleg-Bulnay strike-slip earthquake sequence, Mongolia », submitted.

Choi, Jin-Hyuck, Kwangmin Jin, Dandar Enkhbayar, Battogtokh Davvasambuu, Amgalan Bayasgalan, et Young-Seog Kim. 2012. « Rupture Propagation Inferred from Damage Patterns, Slip Distribution, and Segmentation of the 1957 $M_W$ 8.1 Gobi-Altay Earthquake Rupture along the Bogd Fault, Mongolia ». *Journal of Geophysical Research* 117 (B12). https://doi.org/10.1029/2011JB008676.

*Clark, P.U., A.S. Dyke, J D. Shakun, A E. Carlson, J. Clark, B. Wohlfarth, J.X. Mitrovica, S.W. Hostetler, A M. McCabe. Science07 Aug 2009 : 710-714*

Climatedata.org. s. d. « Climat Altai: Diagramme climatique, Courbe de température, Table climatique pour Altai - Climate-Data.org ». Consulté le 14 octobre 2017. https://fr.climate-data.org/location/29835/.

Colls, A. E, S Stokes, M. D Blum, et E Straffin. 2001. « Age limits on the Late Quaternary evolution of the upper Loire River ». *Quaternary Science Reviews*, TL/ESR Special, 20 (5):743‑50. https://doi.org/10.1016/S0277-3791(00)00048-2.

Costa, John E., et Victor R. Baker. 1981. *Surficial geology: building with the earth*. John Wiley & Sons.

Cowgill, Eric. 2007. « Impact of riser reconstructions on estimation of secular variation in rates of strike–slip faulting: Revisiting the Cherchen River site along the Altyn Tagh Fault, NW China ». *Earth and Planetary Science Letters* 254 (3–4):239‑55. https://doi.org/10.1016/j.epsl.2006.09.015.

Cunningham, D. 2005. « Active Intracontinental Transpressional Mountain Building in the Mongolian Altai: Defining a New Class of Orogen ». *Earth and Planetary Science Letters* 240 (2):436‑44. https://doi.org/10.1016/j.epsl.2005.09.013.

Cunningham, Dickson. 2010. « Tectonic Setting and Structural Evolution of the Late Cenozoic Gobi Altai Orogen ». *Geological Society, London, Special Publications* 338 (1):361‑87. https://doi.org/10.1144/SP338.17.

Cunningham, Dickson. 2013. « Mountain Building Processes in Intracontinental Oblique Deformation Belts: Lessons from the Gobi Corridor, Central Asia ». *Journal of Structural Geology* 46 (janvier):255‑82. https://doi.org/10.1016/j.jsg.2012.08.010.

Cunningham, Dickson, Sarah Davies, et Gombosuren Badarch. 2003. « Crustal Architecture and Active Growth of the Sutai Range, Western Mongolia: A Major Intracontinental, Intraplate Restraining Bend ». *Journal of Geodynamics* 36 (1‑2):169‑91. https://doi.org/10.1016/S0264-3707(03)00046-2.

Cunningham, Dickson, Sarah Davies, et Duncan McLean. 2009. « Exhumation of a Cretaceous Rift Complex within a Late Cenozoic Restraining Bend, Southern Mongolia: Implications for the Crustal Evolution of the Gobi Altai Region ». *Journal of the Geological Society* 166 (2):321‑33. https://doi.org/10.1144/0016-76492008-082.

Cunningham, W. D. 2001. « Cenozoic normal faulting and regional doming in the southern Hangay region, Central Mongolia: implications for the origin of the Baikal rift province ». *Tectonophysics* 331 (4):389–411.

Cunningham, W. Dickson. 1998. « Lithospheric Controls on Late Cenozoic Construction of the Mongolian Altai ». *Tectonics* 17 (6):891‑902. https://doi.org/10.1029/1998TC900001.

Cunningham, W. Dickson, Brian F. Windley, D. Dorjnamjaa, J. Badamgarov, et M. Saandar. 1996. « Late Cenozoic transpression in southwestern Mongolia and the Gobi Altai-Tien Shan connection ». *Earth and Planetary Science Letters* 140 (1–4):67‑81. https://doi.org/10.1016/0012-821X(96)00048-9.

Cunningham, W. Dickson, Brian F. Windley, Lewis A. Owen, Tiffany Barry, D. Dorjnamjaa, et J. Badamgarav. 1997. « Geometry and style of partitioned deformation within a late Cenozoic transpressional zone in the eastern Gobi Altai Mountains, Mongolia ». *Tectonophysics* 277 (4):285‑306. https://doi.org/10.1016/S0040-1951(97)00034-6.

Dawson, Timothy E., S. F. McGill, et T. K. Rockwell. 2003. « Irregular Recurrence of Paleoearthquakes along the Central Garlock Fault near El Paso Peaks, California ». *Journal of Geophysical Research: Solid Earth* 108 (B7):2356. https://doi.org/10.1029/2001JB001744.

Delvaux, Damien, Rikkert Moeys, Gerco Stapel, Carole Petit, Kirill Levi, Andrei Miroshnichenko, Valery Ruzhich, et Volodia San'kov. 1997. « Paleostress reconstructions and geodynamics of the Baikal region, Central Asia, Part 2. Cenozoic rifting ». *Tectonophysics*, Structural Controls on Sedimentary Basin Formation, 282 (1):1‑38. https://doi.org/10.1016/S0040-1951(97)00210-2.

Dunai, T. J. 2010. *Cosmogenic Nuclides: Principles, Concepts and Applications in the Earth Surface Sciences*. Cambridge; New York: Cambridge University Press. http://dx.doi.org/10.1017/CBO9780511804519.

« Faro doc. » s. d. Consulté le 26 septembre 2017. http://www.faro.com/fr-fr/resources/fiches-techniques/.

Fattahi, Morteza, Richard Walker, James Hollingsworth, Abbas Bahroudi, Hamid Nazari, Morteza Talebian, Simon Armitage, et Stephen Stokes. 2006. « Holocene slip-rate on the Sabzevar thrust fault, NE Iran, determined using optically stimulated luminescence (OSL) ». *Earth and Planetary Science Letters* 245 (3–4):673‑84. https://doi.org/10.1016/j.epsl.2006.03.027.

Ferry, M. A., D. Battogtokh, J. F. Ritz, R. Kurtz, R. Braucher, Y. Klinger, M. Ulzibat, O. Chimed, et S. Demberel. 2015. « Late Pleistocene to Historical Activity of the Hovd Fault (Mongolian Altay) from Tectonic Geomorphology and Paleoseismology ». *AGU Fall Meeting Abstracts* 31 (décembre). http://adsabs.harvard.edu/abs/2015AGUFM.T31A2845F.

Fialko, Yuri. 2004a. « Probing the Mechanical Properties of Seismically Active Crust with Space Geodesy: Study of the Coseismic Deformation Due to the 1992 Mw7.3 Landers (Southern California) Earthquake ». *Journal of Geophysical Research: Solid Earth* 109 (B3):B03307. https://doi.org/10.1029/2003JB002756.

Fialko, Yuri. 2004b. « Evidence of Fluid-Filled Upper Crust from Observations of Postseismic Deformation Due to the 1992 Mw7.3 Landers Earthquake ». *Journal of Geophysical Research: Solid Earth* 109 (B8):B08401. https://doi.org/10.1029/2004JB002985.

Florensov, N. A., V. P. Solonenko, 1958- Sovetsko-mongolśkaía͡ Gobi-Altaĭskaía͡ ekspeditsiía͡, Akademiía͡ nauk SSSR. Sibirskoe otdelenie. Vostochno-Sibirskiĭ geologiches kiĭ institut, et Mongolia. Committee for Sciences and Higher Education. 1965. *The Gobi-Altai earthquake (Gobi-Altaiskoe zemletryasenie)*. Jerusalem, Israël: Israel Program for Scientific Translations.

Frankel, Kurt L., Karl W. Wegmann, Amgalan Bayasgalan, Robert J. Carson, Nicholas E. Bader, Tsolmon Adiya, Erdenebat Bolor, et al. 2010. « Late Pleistocene Slip Rate of the Höh Serh-Tsagaan Salaa Fault System, Mongolian Altai and Intracontinental Deformation in Central Asia: Mongolian Altai Late Pleistocene Slip Rate ». *Geophysical Journal International* 183 (3):1134‑50. https://doi.org/10.1111/j.1365-246X.2010.04826.x.

Frechen, Manfred, Martin Kehl, Christian Rolf, Reza Sarvati, et Armin Skowronek. 2009. « Loess chronology of the Caspian lowland in northern Iran ». *Quaternary International* 198 (1):220–233.

Freed, Andrew M. 2007. « Afterslip (and Only Afterslip) Following the 2004 Parkfield, California, Earthquake ». *Geophysical Research Letters* 34 (6):L06312. https://doi.org/10.1029/2006GL029155.

Gavin, Daniel G. 2001. « Estimation of inbuilt age in radiocarbon ages of soil charcoal for fire history studies ». *Radiocarbon* 43 (1):27–44.

Gold, Peter O., Michael E. Oskin, Austin J. Elliott, Alejandro Hinojosa-Corona, Michael H. Taylor, Oliver Kreylos, et Eric Cowgill. 2013. « Coseismic Slip Variation Assessed from Terrestrial Lidar Scans of the El Mayor–Cucapah Surface Rupture ». *Earth and Planetary Science Letters* 366 (mars):151‑62. https://doi.org/10.1016/j.epsl.2013.01.040.

Gold, Ryan D., Eric Cowgill, J Ramón Arrowsmith, John Gosse, Xuanhua Chen, et Xiao-Feng Wang. 2009. « Riser Diachroneity, Lateral Erosion, and Uncertainty in Rates of Strike-Slip Faulting: A Case Study from Tuzidun along the Altyn Tagh Fault, NW China ». *Journal of Geophysical Research: Solid Earth* 114 (B4):B04401. https://doi.org/10.1029/2008JB005913.

Gold, Ryan D., Nadine G. Reitman, Richard W. Briggs, William D. Barnhart, Gavin P. Hayes, et Earl Wilson. 2015. « On- and off-Fault Deformation Associated with the September 2013 Mw 7.7 Balochistan Earthquake: Implications for Geologic Slip Rate Measurements ». *Tectonophysics* 660 (octobre):65‑78. https://doi.org/10.1016/j.tecto.2015.08.019.

Goldfinger, Chris, C. Hans Nelson, Joel E. Johnson, et Shipboard Scientific Party. 2003. « Holocene earthquake records from the Cascadia subduction zone and northern San Andreas fault based on precise dating of offshore turbidites ». *Annual Review of Earth and Planetary Sciences* 31 (1):555–577.

Gosse, John C., et Fred M. Phillips. 2001. « Terrestrial in situ cosmogenic nuclides: theory and application ». *Quaternary Science Reviews* 20 (14):1475‑1560. https://doi.org/10.1016/S0277-3791(00)00171-2.

Graham, S. A., M. S. Hendrix, C. L. Johnson, D. Badamgarav, G. Badarch, J. Amory, M. Porter, R. Barsbold, L. E. Webb, et B. R. Hacker. 2001. « Sedimentary Record and Tectonic Implications of Mesozoic Rifting in Southeast Mongolia ».

*Geological Society of America Bulletin* 113 (12):1560‑79. https://doi.org/10.1130/0016-7606(2001)113<1560:SRATIO>2.0.CO;2.

Gregory, L.C., A.L. Thomas, R.T. Walker, R. Garland, C. Mac Niocaill, C.R. Fenton, A. Bayasgalan, et al. 2014. « Combined Uranium Series and 10Be Cosmogenic Exposure Dating of Surface Abandonment: A Case Study from the Ölgiy Strike-Slip Fault in Western Mongolia ». *Quaternary Geochronology* 24 (décembre):27‑43. https://doi.org/10.1016/j.quageo.2014.07.005.

Gurrola, Larry D., et Thomas K. Rockwell. 1996. « Timing and slip for prehistoric earthquakes on the Superstition Mountain fault, Imperial Valley, southern California ». *Journal of Geophysical Research: Solid Earth* 101 (B3):5977–5985.

Guy, Alexandra, Karel Schulmann, Norbert Clauer, Pavlina Hasalová, Reimar Seltmann, Robin Armstrong, Ondrej Lexa, et Antonio Benedicto. 2014. « Late Paleozoic–Mesozoic Tectonic Evolution of the Trans-Altai and South Gobi Zones in Southern Mongolia Based on Structural and Geochronological Data ». *Gondwana Research* 25 (1):309‑37. https://doi.org/10.1016/j.gr.2013.03.014.

Haeussler, Peter J., David P. Schwartz, Timothy E. Dawson, Heidi D. Stenner, James J. Lienkaemper, Brian Sherrod, Francesca R. Cinti, et al. 2004. « Surface Rupture and Slip Distribution of the Denali and Totschunda Faults in the 3 November 2002 M 7.9 Earthquake, Alaska ». *Bulletin of the Seismological Society of America* 94 (6B):S23‑52. https://doi.org/10.1785/0120040626.

Hamling, Ian J., Sigrún Hreinsdóttir, Kate Clark, John Elliott, Cunren Liang, Eric Fielding, Nicola Litchfield, et al. 2017. « Complex Multifault Rupture during the 2016 $M_w$ 7.8 Kaikōura Earthquake, New Zealand ». *Science* 356 (6334):eaam7194. https://doi.org/10.1126/science.aam7194.

Hanks, Thomas C., et Hiroo Kanamori. 1979. « A Moment Magnitude Scale ». *Journal of Geophysical Research: Solid Earth* 84 (B5):2348‑50. https://doi.org/10.1029/JB084iB05p02348.

Hanžl, Pavel, Zuzana Krejčí, Battushig Altanbaatar, Ondrej Lexa, David Buriánek, Vojtěch Janoušek, Karel Schulmann, Yingde Jiang, et Kristýna Hrdličková. 2017. « Geology of the Gobi Altai and Tseel Terranes in the Central Part of the Sagsai River Watershed, SE Mongolian Altai ». *Journal of Maps* 13 (2):270‑75. https://doi.org/10.1080/17445647.2017.1297260.

Heumann, Matthew J., Cari L. Johnson, Laura E. Webb, Joshua P. Taylor, Undarya Jalbaa, et Chuluun Minjin. 2014. « Total and Incremental Left-Lateral Displacement across the East Gobi Fault Zone, Southern Mongolia: Implications for Timing and Modes of Polyphase Intracontinental Deformation ». *Earth and Planetary Science Letters* 392 (avril):1‑15. https://doi.org/10.1016/j.epsl.2014.01.016.

Hidy, Alan J., John C. Gosse, Joel L. Pederson, Jann Paul Mattern, et Robert C. Finkel. 2010. « A Geologically Constrained Monte Carlo Approach to Modeling Exposure Ages from Profiles of Cosmogenic Nuclides: An Example from Lees Ferry, Arizona ». *Geochemistry Geophysics Geosystems* 11 (septembre). https://doi.org/10.1029/2010GC003084.

Hinsbergen, Douwe J.J. van, Dickson Cunningham, Gijsbert B. Straathof, Morgan Ganerød, Bart W.H. Hendriks, et Arjan H. Dijkstra. 2015. « Triassic to Cenozoic Multi-Stage Intra-Plate Deformation Focused near the Bogd Fault System, Gobi Altai, Mongolia ». *Geoscience Frontiers* 6 (5):723‑40. https://doi.org/10.1016/j.gsf.2014.12.002.

Hossler, T., L. Bollinger, S.N. Sapkota, J. Lavé, R.M. Gupta, et T.P. Kandel. 2016. « Surface Ruptures of Large Himalayan Earthquakes in Western Nepal: Evidence along a Reactivated Strand of the Main Boundary Thrust ». *Earth and Planetary Science Letters* 434 (janvier):187‑96. https://doi.org/10.1016/j.epsl.2015.11.042.

Huang, Jie, et Wang-Ping Chen. 1986. « Source mechanisms of the Mogod earthquake sequence of 1967 and the event of 1974 July 4 in Mongolia ». *Geophysical Journal International* 84 (2):361‑79. https://doi.org/10.1111/j.1365-246X.1986.tb04360.x.

Huntley, D. J., D. I. Godfrey-Smith, et M. L. W. Thewalt. 1985. « Optical Dating of Sediments ». *Nature* 313 (5998):105‑7. https://doi.org/10.1038/313105a0.

Ionov, Dmitri. 2002. « Mantle structure and rifting processes in the Baikal–Mongolia region: geophysical data and evidence from xenoliths in volcanic rocks ». *Tectonophysics* 351 (1):41–60.

Ionov, Dmitri A., Suzanne Y. O'Reilly, et William L. Griffin. 1998. « A Geotherm and Lithospheric Section for Central Mongolia (Tariat Region) ». In *Mantle Dynamics and Plate Interactions in East Asia*, édité par rtin F. J. Flower, Sun-Lin Chung, Ching-Hua Lo, et Tung-Yi Lee, 127‑53. American Geophysical Union. https://doi.org/10.1029/GD027p0127.

Isenburg, M. 2012. « LAStools-efficient tools for LiDAR processing ». *Available at: http: http://www. cs. unc. edu/∼ isenburg/lastools/[Accessed October 9, 2012]*.

Jain, Mayank, A. S. Murray, et Lars Botter-Jensen. 2004. « Optically stimulated luminescence dating: how significant is incomplete light exposure in fluvial environments? [ Datation par luminescence stimulée optiquement : quelle signification en cas de blanchiment incomplet des sédiments fluviatiles ?] ». *Quaternaire* 15 (1):143‑57. https://doi.org/10.3406/quate.2004.1762.

James, Mike R., et Stuart Robson. 2014. « Mitigating Systematic Error in Topographic Models Derived from UAV and Ground-Based Image Networks: MITIGATING SYSTEMATIC ERROR IN TOPOGRAPHIC MODELS ». *Earth Surface Processes and Landforms* 39 (10):1413‑20. https://doi.org/10.1002/esp.3609.

Johnson, Cari L. 2004. « Polyphase Evolution of the East Gobi Basin: Sedimentary and Structural Records of Mesozoic–Cenozoic Intraplate Deformation in Mongolia ». *Basin Research* 16 (1):79‑99. https://doi.org/10.1111/j.1365-2117.2004.00221.x.

Jolivet, Marc, Jean-François Ritz, Riccardo Vassallo, Christophe Larroque, Régis Braucher, Munkhjargal Todbileg, Alain Chauvet, et al. 2007. « Mongolian summits: an uplifted, flat, old but still preserved erosion surface ». *Geology* 35 (10):871–874.

Kanamori, Hiroo, et Don L. Anderson. 1975. « Theoretical Basis of Some Empirical Relations in Seismology ». *Bulletin of the Seismological Society of America* 65 (5):1073‑95.

Khilko, S. D., R. A. Kurushin, V. M. Kotchetkov, L. A. Misharina, V. I. Melnikova, N. A. Gileva, S. V. Lastochkin, I. Baljinnyam, et D. Monhoo. 1985. « Strong earthquakes, paleoseismogeological and macroseismic data ». *Earthquakes and the Base for Seismic Zoning of Mongolia*, 19–83.

Kim, Young-Seog, David C.P Peacock, et David J Sanderson. 2004. « Fault Damage Zones ». *Journal of Structural Geology* 26 (3):503‑17. https://doi.org/10.1016/j.jsg.2003.08.002.

Kim, Young-Seog, et David J. Sanderson. 2005. « The Relationship between Displacement and Length of Faults: A Review ». *Earth-Science Reviews* 68 (3‑4):317‑34. https://doi.org/10.1016/j.earscirev.2004.06.003.

King, G. C. P. 1986. « Speculations on the Geometry of the Initiation and Termination Processes of Earthquake Rupture and Its Relation to Morphology and Geological Structure ». In *Friction and Faulting*, édité par Terry E. Tullis, 567‑85. Birkhäuser Basel. https://doi.org/10.1007/978-3-0348-6601-9_9.

King, Geoffrey, et John Nabelek. 1985. « Role of Fault Bends in the Initiation and Termination of Earthquake Rupture ». *Science* 228 (mai):984‑88.

Klinger, Y. 2005. « High-Resolution Satellite Imagery Mapping of the Surface Rupture and Slip Distribution of the Mw 7.8, 14 November 2001 Kokoxili Earthquake, Kunlun Fault, Northern Tibet, China ». *Bulletin of the Seismological Society of America* 95 (5):1970‑87. https://doi.org/10.1785/0120040233.

Klinger, Y., J. P. Avouac, N. Abou Karaki, Louis Dorbath, D. Bourles, et J. L. Reyss. 2000. « Slip rate on the Dead Sea transform fault in northern Araba valley (Jordan) ». *Geophysical Journal International* 142 (3):755–768.

Klinger, Y., M. Etchebes, P. Tapponnier, et C. Narteau. 2011. « Characteristic slip for five great earthquakes along the Fuyun fault in China ». *Nature Geoscience* 4 (6):389‑92. https://doi.org/10.1038/ngeo1158.

Klinger, Y, R Michel, et G King. 2006. « Evidence for an Earthquake Barrier Model from Mw~7.8 Kokoxili (Tibet) Earthquake Slip-Distribution ». *Earth and Planetary Science Letters* 242 (3‑4):354‑64. https://doi.org/10.1016/j.epsl.2005.12.003.

Klinger, Yann. 2010. « Relation between Continental Strike-Slip Earthquake Segmentation and Thickness of the Crust ». *Journal of Geophysical Research* 115 (B7). https://doi.org/10.1029/2009JB006550.

Koenderink, Jan J., et Andrea J. van Doorn. 1991. « Affine Structure from Motion ». *JOSA A* 8 (2):377‑85. https://doi.org/10.1364/JOSAA.8.000377.

Kozlovsky, Alexander M., Vladimir V. Yarmolyuk, Ekaterina B. Salnikova, Alexey V. Travin, Alexander B. Kotov, Julia V. Plotkina, Ekaterina A. Kudryashova, et Valery M. Savatenkov. 2015. « Late Paleozoic Anorogenic Magmatism of the Gobi Altai (SW Mongolia): Tectonic Position, Geochronology and Correlation with Igneous Activity of the Central Asian Orogenic Belt ». *Journal of Asian Earth Sciences* 113 (décembre):524‑41. https://doi.org/10.1016/j.jseaes.2015.01.013.

Kurushin, R. A., A. Bayasgalan, M. Ölziybat, B. Enhtuvshin, Peter Molnar, Ch. Bayarsayhan, Kenneth W. Hudnut, et Jian Lin. 1998. « The Surface Rupture of the 1957 Gobi-Altay, Mongolia, Earthquake ». In *Special Paper 320: The Surface Rupture of the 1957 Gobi-Altay, Mongolia, Earthquake*, 320:1‑144. Geological Society of America. https://doi.org/10.1130/0-8137-2320-5.1.

Lal, D., et J. R. Arnold. 1985. « Tracing Quartz through the Environment ». *Proceedings of the Indian Academy of Sciences - Earth and Planetary Sciences* 94 (1):1‑5. https://doi.org/10.1007/BF02863403.

Lamb, Melissa A., Gombosuren Badarch, Tiffani Navratil, et Rebeka Poier. 2008. « Structural and Geochronologic Data from the Shin Jinst Area, Eastern Gobi Altai, Mongolia: Implications for Phanerozoic Intracontinental Deformation in Asia ». *Tectonophysics* 451 (1‑4):312‑30. https://doi.org/10.1016/j.tecto.2007.11.061.

Lamb, Melissa A., Andrew D. Hanson, Stephan A. Graham, Gombosuren Badarch, et Laura E. Webb. 1999. « Left-lateral sense offset of upper Proterozoic to Paleozoic features across the Gobi Onon, Tost, and Zuunbayan faults in southern Mongolia and implications for other Central Asian faults ». *Earth and Planetary Science Letters* 173 (3):183–194.

Lapusta, Nadia, et James R. Rice. 2003. « Nucleation and Early Seismic Propagation of Small and Large Events in a Crustal Earthquake Model ». *Journal of Geophysical Research: Solid Earth* 108 (B4):2205. https://doi.org/10.1029/2001JB000793.

Larroque, Christophe, Jean-François Ritz, Jean-François Stéphan, Vladimir San'kov, Anastassia Arjannikova, Éric Calais, Jacques Déverchère, et Lies Loncke. 2001. « Interaction compression–extension à la limite Mongolie–Sibérie: analyse préliminaire des déformations récentes et actuelles dans le bassin de Tunka ». *Comptes Rendus de l'Académie des Sciences-Series IIA-Earth and Planetary Science* 332 (3):177–184.

Leanni et ASTER team. 2013. « Protocole de préparation de cibles en vue de la mesure du 10Be et de l'26Al par Spectrométrie de masse par accélérateur. »

Lehmann, Jérémie, Karel Schulmann, Ondrej Lexa, Michel Corsini, Alfred Kröner, Pavla Štípská, Dondov Tomurhuu, et Dorjsuren Otgonbator. 2010. « Structural constraints on the evolution of the Central Asian Orogenic Belt in SW Mongolia ». *American Journal of Science* 310 (7):575–628.

Lehmkuhl, Frank. 1998. « Quaternary glaciations in central and western Mongolia ». *Journal of Quaternary Science* 13 (6):153–167.

Lehmkuhl, Frank, et Andreas Lang. 2001. « Geomorphological Investigations and Luminescence Dating in the Southern Part of the Khangay and the Valley of the Gobi Lakes (Central Mongolia) ». *Journal of Quaternary Science* 16 (1):69‑87. https://doi.org/10.1002/1099-1417(200101)16:1<69::AID-JQS583>3.0.CO;2-O.

Leloup, Philippe Hervé, Robin Lacassin, Paul Tapponnier, Urs Schärer, Dalai Zhong, Xiaohan Liu, Liangshang Zhang, Shaocheng Ji, et Phan Trong Trinh. 1995. « The Ailao Shan-Red River shear zone (Yunnan, China), Tertiary transform boundary of Indochina ». *Tectonophysics*, Southeast Asia Structure and Tectonics, 251 (1):3‑84. https://doi.org/10.1016/0040-1951(95)00070-4.

Lienkaemper, James J., et Christopher Bronk Ramsey. 2009. « OxCal: Versatile tool for developing paleoearthquake chronologies—A primer ». *Seismological Research Letters* 80 (3):431–434.

Lin, Aiming, et Su-juan Lin. 1998. « Tree Damage and Surface Displacement, The 1931 M 8.0 Fuyun Earthquake ». *The Journal of Geology* 106 (6):751‑58. https://doi.org/10.1086/516058.

Logatchev, N. A., et N. A. Florensov. 1978. « The Baikal system of rift valleys ». *Tectonophysics*, Symposium on the Rift Zones of the Earth, 45 (1):1‑13. https://doi.org/10.1016/0040-1951(78)90218-4.

Logatchev, N. A., et Yu. A. Zorin. 1992. « Baikal rift zone: Structure and geodynamics ». *Tectonophysics*, Geodynamics of rifting, volume 1 Case history studies on rifts: Europe and Asia, 208 (1):273‑86. https://doi.org/10.1016/0040-1951(92)90349-B.

Mackenzie, D., R. T. Walker, K. Abdrakhmatov, G. Campbell, C. Grützner, A. Moldobaev, et A. Mukambayev. 2015. « INQUA Focus Group on Paleoseismology and Active Tectonics ». https://www.researchgate.net/profile/Christoph_Gruetzner/publication/275711936_A_fault_slip-

rate_on_the_northern_front_of_the_High_Tien_Shan_Kazakhstan/links/55449a860cf234bdb21bfe64.pdf.

Madden, Chris, David E. Haddad, J. Barrett Salisbury, Olaf Zielke, J. Ramón Arrowsmith, Ray J. Weldon, et J. Colunga. 2013. « Appendix R—Compilation of slip-in-the-last-event data and analysis of last event, repeated slip, and average displacement for recent and prehistoric ruptures ». *US Geological Survey Open-File Report* 1165:65.

Madsen, A. T., et A. S. Murray. 2009. « Optically stimulated luminescence dating of young sediments: A review ». *Geomorphology*, Luminescence dating in geomorphology, 109 (1):3‑16. https://doi.org/10.1016/j.geomorph.2008.08.020.

Manighetti, I., C. Perrin, S. Dominguez, S. Garambois, Y. Gaudemer, J. Malavieille, L. Matteo, E. Delor, C. Vitard, et S. Beauprêtre. 2015. « Recovering Paleoearthquake Slip Record in a Highly Dynamic Alluvial and Tectonic Region (Hope Fault, New Zealand) from Airborne Lidar: EARTHQUAKE SLIP RECORD IN LIDAR DATA ». *Journal of Geophysical Research: Solid Earth* 120 (6):4484‑4509. https://doi.org/10.1002/2014JB011787.

McCalpin, James, et Steven L. Forman. 1988. *Chronology of paleoearthquakes on the Wasatch fault zone by thermoluminescence (TL) dating*. Utah State University Foundation.

McCalpin, James P. 2009. *Paleoseismology*. Vol. 95. Academic press. https://books.google.fr/books?hl=fr&lr=&id=RxxEfNPU6ksC&oi=fnd&pg=PP1&dq=paleoseismology&ots=T2EA2vDyG5&sig=BnnpdEG47R9Ybx979VhY_0vscH0.

McDannell, Kalin T., Peter K. Zeitler, Leonard D. Ancuta, Bruce D. Idleman, Shayna S. Boulton, et Karl W. Wegmann. 2014. « The Hangay Dome, central Mongolia: A relict Mesozoic landscape ». *Age (Ma)* 300:350.

McGill, Sally F., et Kerry Sieh. 1991. « Surficial Offsets on the Central and Eastern Garlock Fault Associated with Prehistoric Earthquakes ». *Journal of Geophysical Research: Solid Earth* 96 (B13):21597‑621. https://doi.org/10.1029/91JB02030.

McGrath, Annette G., et Ian Davison. 1995. « Damage zone geometry around fault tips ». *Journal of Structural Geology* 17 (7):1011–1024.

Meltzer, A., L. D. Ancuta, R. W. Carlson, J. K. Caves, P. Chamberlain, J. C. Gosse, B. D. Idleman, et al. 2012. « Intracontinental Deformation and Surface Uplift - Geodynamic Evolution of the Hangay Dome, Mongolia Central Asia ». *AGU Fall Meeting Abstracts* 12 (décembre). http://adsabs.harvard.edu/abs/2012AGUFM.T12A..05M.

Métivier, François, et Yves Gaudemer. 1997. « Mass transfer between eastern Tien Shan and adjacent basins (central Asia): constraints on regional tectonics and topography ». *Geophysical Journal International* 128 (1):1‑17. https://doi.org/10.1111/j.1365-246X.1997.tb04068.x.

Milliner, Christopher W. D., James F. Dolan, James Hollingsworth, Sebastien Leprince, Francois Ayoub, et Charles G. Sammis. 2015. « Quantifying Near-Field and off-Fault Deformation Patterns of the 1992 $M_w$ 7.3 Landers Earthquake: Deformation of the Landers Earthquake ». *Geochemistry, Geophysics, Geosystems* 16 (5):1577‑98. https://doi.org/10.1002/2014GC005693.

Moffitt, F. H. 1959. « PHOTOGRAMMETRY ». https://trid.trb.org/view.aspx?id=91359.

Molnar, Peter, et Denq Qidong. 1984. « Faulting associated with large earthquakes and the average rate of deformation in central and eastern Asia ». *Journal of Geophysical Research: Solid Earth* 89 (B7):6203–6227.

Molnar, Peter, et Paul Tapponnier. 1975. « Cenozoic tectonics of Asia: effects of a continental collision ». *science* 189 (4201):419–426.

Molnar, Peter, et Paul Tapponnier.. 1977. « Relation of the Tectonics of Eastern China to the India-Eurasia Collision: Application of Slip-Line Field Theory to Large-Scale Continental Tectonics ». *Geology* 5 (4):212‑16. https://doi.org/10.1130/0091-7613(1977)5<212:ROTTOE>2.0.CO;2.

Murray, A. S., J. M. Olley, et G. G. Caitcheon. 1995. « Measurement of equivalent doses in quartz from contemporary water-lain sediments using optically stimulated luminescence ». *Quaternary Science Reviews* 14 (4):365‑71. https://doi.org/10.1016/0277-3791(95)00030-5.

Murray, Andrew S., et Jon M. Olley. 2002. « Precision and accuracy in the optically stimulated luminescence dating of sedimentary quartz: a status review ». *Geochronometria* 21 (1):1–16.

Mushkin. 2007. « Quaternary Deformation Across the Central Segment of the Gobi-Altay Fault System, Southwestern Mongolia. »

Mushkin, A., D. Javkhlanbold, A. Bayasgalan, et A. Gillespie. 2004. « Large Paleo Landslides Along the Western Part of the Gobi-Altay Fault System in Southwestern Mongolia ». *AGU Fall Meeting Abstracts* 11 (décembre). http://adsabs.harvard.edu/abs/2004AGUFM.T11C1280M.

Nazari, H., J.-F. Ritz, Reza Salamati, A. Shafei, A. Ghassemi, J.-L. Michelot, M. Massault, et M. Ghorashi. 2009. « Morphological and palaeoseismological analysis along the Taleghan fault (Central Alborz, Iran) ». *Geophysical Journal International* 178 (2):1028–1041.

Nelson, Alan R., Stephen F. Personius, Rolly E. Rimando, Raymundo S. Punongbayan, Norman Tuñgol, Hannah Mirabueno, et Ariel Rasdas. 2000. « Multiple large earthquakes in the past 1500 years on a fault in metropolitan Manila, the Philippines ». *Bulletin of the Seismological Society of America* 90 (1):73–85.

Nissen, Edwin, Richard T. Walker, Amgalan Bayasgalan, Andrew Carter, Morteza Fattahi, Erdenebat Molor, Christoph Schnabel, A. Joshua West, et Sheng Xu. 2009. « The late Quaternary slip-rate of the Har-Us-Nuur fault (Mongolian Altai) from cosmogenic 10Be and luminescence dating ». *Earth and Planetary Science Letters* 286 (3–4):467‑78. https://doi.org/10.1016/j.epsl.2009.06.048.

Okal, Emile A. 1976. « A surface-wave investigation of the rupture mechanism of the Gobi-Altai (December 4, 1957) earthquake ». *Physics of the Earth and Planetary Interiors* 12 (4):319–328.

Olley, Jon, Gary Caitcheon, et Andrew Murray. 1998. « The distribution of apparent dose as determined by Optically Stimulated Luminescence in small aliquots of fluvial quartz ». *Quaternary Science Reviews* 17 (11):1033‑40. https://doi.org/10.1016/S0277-3791(97)00090-5.

Owen, Lewis A., Dickson Cunningham, Benedict W. M. Richards, Edward Rhodes, Brian F. Windley, Dorj Dorjnamjaa, et Jalbuugin Badamgarav. 1999. « Timing of Formation of Forebergs in the Northeastern Gobi Altai, Mongolia: Implications for Estimating Mountain Uplift Rates and Earthquake Recurrence Intervals ». *Journal of the Geological Society* 156 (3):457‑64. https://doi.org/10.1144/gsjgs.156.3.0457.

Pace, B., F. Visini, et L. Peruzza. 2016. « *FiSH* : MATLAB Tools to Turn Fault Data into Seismic-Hazard Models ». *Seismological Research Letters* 87 (2A):374‑86. https://doi.org/10.1785/0220150189.

Pacheco, Javier F., et Lynn R. Sykes. 1992. « Seismic Moment Catalog of Large Shallow Earthquakes, 1900 to 1989 ». *Bulletin of the Seismological Society of America* 82 (3):1306‑49.

Patriat, Philippe, et José Achache. 1984. « India–Eurasia Collision Chronology Has Implications for Crustal Shortening and Driving Mechanism of Plates ». *Nature* 311 (5987):615‑21. https://doi.org/10.1038/311615a0.

Patzelt, A., Huamei Li, Junda Wang, et E. Appel. 1996. « Palaeomagnetism of Cretaceous to Tertiary sediments from southern Tibet: evidence for the extent of the northern margin of India prior to the collision with Eurasia ». *Tectonophysics* 259 (4):259–284.

*Peltzer, G., P. Tapponnier, Y. Gaudemer, B. Meyer, S. Guo, K. Yin, Z. Chen, and H. Dai (1988), "Offsets of Late Quaternary morphology, rate of slip, and recurrence of large earthquakes on the Chang Ma Fault (Gansu, China)"", J. Geophys. Res., 93(B7), 7793–7812, doi:10.1029/JB093iB07p07793.*

Perfettini, H., et J.-P. Avouac. 2007. « Modeling Afterslip and Aftershocks Following the 1992 Landers Earthquake ». *Journal of Geophysical Research: Solid Earth* 112 (B7):B07409. https://doi.org/10.1029/2006JB004399.

Pessarakli, Mohammad. 1999. *Handbook of Plant and Crop Stress, Second Edition*. CRC Press.

Petit, Carole, Jacques Déverchère, Eric Calais, Vladimir San'kov, et Derek Fairhead. 2002. « Deep structure and mechanical behavior of the lithosphere in the Hangai–Hövsgöl region, Mongolia: new constraints from gravity modeling ». *Earth and Planetary Science Letters* 197 (3):133–149.

Petit, Carole, Jacques Déverchère, Frédérique Houdry, Vladimir A. Sankov, Valentina I. Melnikova, et Damien Delvaux. 1996. « Present-Day Stress Field Changes along the Baikal Rift and Tectonic Implications ». *Tectonics* 15 (6):1171‑91. https://doi.org/10.1029/96TC00624.

Philip, Hervé, et Jean-François Ritz. 1999. « Gigantic paleolandslide associated with active faulting along the Bogd fault (Gobi-Altay, Mongolia) ». *Geology* 27 (3):211–214.

Pollitz, Fred, Mathilde Vergnolle, et Eric Calais. 2003. « Fault Interaction and Stress Triggering of Twentieth Century Earthquakes in Mongolia: Stress Triggering Of Earthquakes In Mongolia ». *Journal of Geophysical Research: Solid Earth* 108 (B10). https://doi.org/10.1029/2002JB002375.

Prentice, Carol S. 2002. « Prehistoric Ruptures of the Gurvan Bulag Fault, Gobi Altay, Mongolia ». *Journal of Geophysical Research* 107 (B12). https://doi.org/10.1029/2001JB000803.

Radziminovich, N. A., G. Bayar, A. I. Miroshnichenko, S. Demberel, M. Ulziibat, D. Ganzorig, et A. V. Lukhnev. 2016. « Focal Mechanisms Of Earthquakes And Stress Field Of The Crust In Mongolia And Its Surroundings ». *Geodynamics & Tectonophysics* 7 (1):23‑38. https://doi.org/10.5800/GT-2016-7-1-0195.

Reimer, Paula J., Edouard Bard, Alex Bayliss, J. Warren Beck, Paul G. Blackwell, Christopher Bronk Ramsey, David M. Brown, et al. 2013. « Selection and treatment of data for radiocarbon calibration: an update to the International Calibration (IntCal) criteria ». *Radiocarbon* 55 (4):1923–1945.

Rippington, Stephen, Dickson Cunningham, Richard England, et Bart Hendriks. 2013. « The Crustal Assembly of Southern Mongolia: New Structural, Lithological and

Geochronological Data from the Nemegt and Altan Ranges ». *Gondwana Research* 23 (4):1535‑53. https://doi.org/10.1016/j.gr.2012.09.001.

Ritz, J. F., E. T. Brown, D. L. Bourles, H. Philip, A. Schlupp, G. M. Raisbeck, F. Yiou, et B. Enkhtuvshin. 1995. « Slip rates along active faults estimated with cosmic-ray–exposure dates: Application to the Bogd fault, Gobi-Altaï, Mongolia ». *Geology* 23 (11):1019–1022.

Ritz, J., C. S. Prentice, R. Braucher, S. Marco, R. Vassallo, A. Chauvet, M. Rizza, et al. 2007. « Earthquake Geology of the Bogd Fault, Gobi Altay, Mongolia ». *AGU Fall Meeting Abstracts* 43 (décembre). http://adsabs.harvard.edu/abs/2007AGUFM.T43B1362R.

Ritz, Jean-François, Magali Rizza, C. Prentice, et D. Schwartz. 2009. « Détermination de l'aléa sismique: l'approche paléosismologique ». *Géochronique* 110 (Néotectonique):25–26.

Ritz, J.-F. 2003. « Late Pleistocene to Holocene Slip Rates for the Gurvan Bulag Thrust Fault (Gobi-Altay, Mongolia) Estimated with $^{10}$ Be Dates ». *Journal of Geophysical Research* 108 (B3). https://doi.org/10.1029/2001JB000553.

Ritz, J.-F., R. Vassallo, R. Braucher, E.T. Brown, S. Carretier, et D.L. Bourlès. 2006. « Using in Situ–produced 10Be to Quantify Active Tectonics in the Gurvan Bogd Mountain Range (Gobi-Altay, Mongolia) ». In *Special Paper 415: In Situ-Produced Cosmogenic Nuclides and Quantification of Geological Processes*, 415:87‑110. Geological Society of America. http://specialpapers.gsapubs.org/cgi/doi/10.1130/2006.2415(06).

Rizza, M., J.- F. Ritz, C. Prentice, R. Vassallo, R. Braucher, C. Larroque, A. Arzhannikova, et al. 2015. « Earthquake Geology of the Bulnay Fault (Mongolia) ». *Bulletin of the Seismological Society of America* 105 (1):72‑93. https://doi.org/10.1785/0120140119.

Rizza, M., J.-F. Ritz, R. Braucher, R. Vassallo, C. Prentice, S. Mahan, S. McGill, et al. 2011. « Slip Rate and Slip Magnitudes of Past Earthquakes along the Bogd Left-Lateral Strike-Slip Fault (Mongolia): Slip Rate and Slip Value along the Bogd Fault ». *Geophysical Journal International* 186 (3):897‑927. https://doi.org/10.1111/j.1365-246X.2011.05075.x.

Rizza, Magali. 2010a. « Analyses des vitesses et des déplacements cosismiques sur des failles décrochantes en Mongolie et en Iran: approche morphotectonique et paléosismologique ». Thèse de doctorat, Montpellier, France: Géosciences.

Rizza, Magali. 2010b. « Slip rates and coseismic slips analyses along strike-slip faults in Mongolia and Iran - Morphotectonic and paleoseismic approach ». Theses, Université Montpellier II - Sciences et Techniques du Languedoc. https://tel.archives-ouvertes.fr/tel-00591794.

Rockwell, T. K., et Y. Klinger. 2013. « Surface Rupture and Slip Distribution of the 1940 Imperial Valley Earthquake, Imperial Fault, Southern California: Implications for Rupture Segmentation and Dynamics ». *Bulletin of the Seismological Society of America* 103 (2A):629‑40. https://doi.org/10.1785/0120120192.

Rockwell, Thomas K., Scott Lindvall, Tim Dawson, Rob Langridge, William Lettis, et Yann Klinger. 2002. « Lateral offsets on surveyed cultural features resulting from the 1999 Izmit and Düzce earthquakes, Turkey ». *Bulletin of the Seismological Society of America* 92 (1):79–94.

Rukavičková, L., et P. Hanžl. 2012. « Mud Volcanoes in the Khar Argalantyn Nuruu, NW Gobi Altay, Mongolia as Manifestation of Recent Seismic Activity ». *Journal of GEOsciences*, juillet, 181‑91. https://doi.org/10.3190/jgeosci.024.

« Russian Geological 1:200 000 maps of Mongolia ». 1987. Geological maps. Ulaan Bator.

Ruzhentsev, S. V., H. Badarch, et T. A. Voznesenskaya. 1985. « Tectonics of the Trans-Altai zone of Mongolia (the Gurvansaykhan and Dzolen ranges) ». *Geotectonics* 19 (4):276–284.

Saint-Carlier, Dimitri, Julien Charreau, Jérôme Lavé, Pierre-Henri Blard, Stéphane Dominguez, Jean-Philippe Avouac, et Shengli Wang. 2016. « Major Temporal Variations in Shortening Rate Absorbed along a Large Active Fold of the Southeastern Tianshan Piedmont (China) ». *Earth and Planetary Science Letters* 434 (janvier):333‑48. https://doi.org/10.1016/j.epsl.2015.11.041.

Salisbury, J. Barrett, D.E. Haddad, T. Rockwell, J R. Arrowsmith, C. Madugo, O. Zielke, et K. Scharer. 2015. « Validation of Meter-Scale Surface Faulting Offset Measurements from High-Resolution Topographic Data ». *Geosphere*, octobre, GES01197.1. https://doi.org/10.1130/GES01197.1.

Schlupp, Antoine. 1996. « Neotectonic of western Mongolia analysed using field, seismological and remote sensing data ». Theses, Université Louis Pasteur - Strasbourg I. https://tel.archives-ouvertes.fr/tel-00155858.

Schlupp, Antoine, et Armando Cisternas. 2007. « Source History of the 1905 Great Mongolian Earthquakes (Tsetserleg, Bolnay) ». *Geophysical Journal International* 169 (3):1115‑31. https://doi.org/10.1111/j.1365-246X.2007.03323.x.

Schlupp, Westphal, Bayasgalan, Baatar, Enhtuvshin, Ritz, Philip, et Cisternas. 1995. « Deformation in Western Mongolia since the Neogene using paleomagnetic data of basalts from the Hangay Dome. » *TERRA nova*, 1995.

Schwartz, D. P., A. Bayasgalan, T. C. Hanks, K. Hanson, W. Lund, C. S. Prentice, J. F. Ritz, T. K. Rockwell, et K. Rockwell. 2007. « Paleoseismic investigations of the 1957 Gobi-Altay surface ruptures ». In *50th Anniversary Earthquake Conference Commemorating the 1957 Gobi-Altay Earthquake*.

Schwartz, D. P., T. C. Hanks, C. S. Prentice, A. Bayasgalan, J. F. Dolan, T. K. Rockwell, P. Molnar, et R. B. Hermann. 1996. « The 1957 Gobi-Altay earthquake (M= 8.1); complex: long recurrence (?) interval faulting in the middle of a continent ». *Seismol. Res. Lett* 67:54.

Schwartz, David P., et Kevin J. Coppersmith. 1984. « Fault Behavior and Characteristic Earthquakes: Examples from the Wasatch and San Andreas Fault Zones ». *Journal of Geophysical Research: Solid Earth* 89 (B7):5681‑98. https://doi.org/10.1029/JB089iB07p05681.

Seong, Y. B., Kang, H. C., Ree, J.-H., Yi, C. and Yoon, H. (2011), Constant slip rate during the late Quaternary along the Sulu He segment of the Altyn Tagh Fault near Changma, Gansu, China. Island Arc, 20: 94–106. doi:10.1111/j.1440-1738.2010.00743.x

Shimazaki, Kunihiko, et Takashi Nakata. 1980. « Time-predictable recurrence model for large earthquakes ». *Geophysical Research Letters* 7 (4):279–282.

Siame, Lionel, Olivier Bellier, Régis Braucher, Michel Sébrier, Marc Cushing, Didier Bourlès, Bruno Hamelin, et al. 2004. « Local Erosion Rates versus Active Tectonics: Cosmic Ray Exposure Modelling in Provence (South-East France) ».

*Earth and Planetary Science Letters* 220 (3‑4):345‑64. https://doi.org/10.1016/S0012-821X(04)00061-5.

Sieh, Kebby E. 1978. « Slip along the San Andreas Fault Associated with the Great 1857 Earthquake ». *Bulletin of the Seismological Society of America* 68 (5):1421‑48.

Sieh, Kerry. 1996. « The repetition of large-earthquake ruptures ». *Proceedings of the National Academy of Sciences* 93 (9):3764–3771.

Sieh, Kerry, Lucile Jones, Egill Hauksson, Kenneth Hudnut, Donna Eberhart-Phillips, Thomas Heaton, Susan Hough, et al. 1993. « Near-Field Investigations of the Landers Earthquake Sequence, April to July 1992 ». *Science* 260 (5105):171‑76.

Slater, James A., Graham Garvey, Carolyn Johnston, Jeffrey Haase, Barry Heady, George Kroenung, et James Little. 2006. « The SRTM Data “Finishing” Process and Products ». *Photogrammetric Engineering & Remote Sensing* 72 (3):237‑47. https://doi.org/10.14358/PERS.72.3.237.

Sobel, Edward R., Jie Chen, et Richard V. Heermance. 2006. « Late Oligocene–Early Miocene initiation of shortening in the Southwestern Chinese Tian Shan: Implications for Neogene shortening rate variations ». *Earth and Planetary Science Letters* 247 (1–2):70‑81. https://doi.org/10.1016/j.epsl.2006.03.048.

Sobel, Edward R., et Trevor A. Dumitru. 1997. « Thrusting and Exhumation around the Margins of the Western Tarim Basin during the India-Asia Collision ». *Journal of Geophysical Research: Solid Earth* 102 (B3):5043‑63. https://doi.org/10.1029/96JB03267.

Stone, John O. 2000. « Air Pressure and Cosmogenic Isotope Production ». *Journal of Geophysical Research: Solid Earth* 105 (B10):23753‑59. https://doi.org/10.1029/2000JB900181.

Tapponnier, Paul, et Peter Molnar. 1979. « Active faulting and Cenozoic tectonics of the Tien Shan, Mongolia, and Baykal regions ». *Journal of Geophysical Research: Solid Earth (1978–2012)* 84 (B7):3425–3459.

Tapponnier, P., X. Zhiqin, F. Roger, B. Meyer, N. Arnaud, G. Wittlinger, Y. Jingsui. *Science,* 23 Nov 2001 : 1671-1677

Traynor, J. J., et Chris Sladen. 1995. « Tectonic and stratigraphic evolution of the Mongolian People’s Republic and its influence on hydrocarbon geology and potential ». *Marine and Petroleum Geology* 12 (1):35‑52. https://doi.org/10.1016/0264-8172(95)90386-X.

Vallage, A., Y. Klinger, R. Grandin, H. S. Bhat, et M. Pierrot-Deseilligny. 2015. « Inelastic Surface Deformation during the 2013 Mw 7.7 Balochistan, Pakistan, Earthquake ». *Geology* 43 (12):1079‑82. https://doi.org/10.1130/G37290.1.

Vallage, A., Y. Klinger, R. Lacassin, A. Delorme, et M. Pierrot-Deseilligny. 2016. « Geological Structures Control on Earthquake Ruptures: The Mw7.7, 2013, Balochistan Earthquake, Pakistan ». *Geophysical Research Letters* 43 (19):2016GL070418. https://doi.org/10.1002/2016GL070418.

Van der Woerd, J., F. J. Ryerson, P. Tapponnier, A. -S. Meriaux, Y. Gaudemer, B. Meyer, R. C. Finkel, M. W. Caffee, Zhao Guoguang, et Xu Zhiqin. 2000. « Uniform Slip-Rate along the Kunlun Fault: Implications for Seismic Behaviour and Large-Scale Tectonics ». *Geophysical Research Letters* 27 (16):2353‑56. https://doi.org/10.1029/1999GL011292.

Varnes, David J. 1978. « Slope movement types and processes ». *Special report* 176:11–33.

Vassallo, R., M. Jolivet, J.-F. Ritz, R. Braucher, C. Larroque, C. Sue, M. Todbileg, et D. Javkhlanbold. 2007. « Uplift Age and Rates of the Gurvan Bogd System (Gobi-Altay) by Apatite Fission Track Analysis ». *Earth and Planetary Science Letters* 259 (3‑4):333‑46. https://doi.org/10.1016/j.epsl.2007.04.047.

Vassallo, R., J.-F. Ritz, R. Braucher, M. Jolivet, S. Carretier, C. Larroque, A. Chauvet, et al. 2007. « Transpressional Tectonics and Stream Terraces of the Gobi-Altay, Mongolia: FLUVIAL INCISION VS UPLIFT IN GOBI-ALTAY ». *Tectonics* 26 (5):n/a-n/a. https://doi.org/10.1029/2006TC002081.

Vassallo, Riccardo. 2006. « Chronologie et évolution des reliefs dans la région Mongolie-Sibérie: approche morphotectonique et géochronologique ». Thèse de doctorat, France: Université des sciences et techniques de Montpellier 2.

Vassallo, Riccardo, Jean-Francois Ritz, Regis Braucher, et Sebastien Carretier. 2005. « Dating Faulted Alluvial Fans with Cosmogenic 10Be in the Gurvan Bogd Mountain Range (Gobi-Altay, Mongolia): Climatic and Tectonic Implications ». *Terra Nova* 17 (3):278‑85. https://doi.org/10.1111/j.1365-3121.2005.00612.x.

Vergnolle, Mathilde, Fred Pollitz, et Eric Calais. 2003. « Constraints on the Viscosity of the Continental Crust and Mantle from GPS Measurements and Postseismic Deformation Models in Western Mongolia: CRUST AND MANTLE VISCOSITY IN MONGOLIA ». *Journal of Geophysical Research: Solid Earth* 108 (B10). https://doi.org/10.1029/2002JB002374.

Villaseñor, A., M. H. Ritzwoller, A. L. Levshin, M. P. Barmin, E. R. Engdahl, W. Spakman, et J. Trampert. 2001. « Shear velocity structure of central Eurasia from inversion of surface wave velocities ». *Physics of the Earth and Planetary Interiors*, Tomographic Imagining of 3-D Velocity Structure and Accurate Earthquake Location, 123 (2):169‑84. https://doi.org/10.1016/S0031-9201(00)00208-9.

Walker, R. T., A. Bayasgalan, R. Carson, R. Hazlett, L. McCarthy, J. Mischler, E. Molor, et al. 2006. « Geomorphology and structure of the Jid right-lateral strike-slip fault in the Mongolian Altay mountains ». *Journal of Structural Geology* 28 (9):1607‑22. https://doi.org/10.1016/j.jsg.2006.04.007.

Walker, R. T., E. Nissen, E. Molor, et A. Bayasgalan. 2007. « Reinterpretation of the active faulting in central Mongolia ». *Geology* 35 (8):759–762.

Wallace, Robert E. 1946. « A Portion of the San Andreas Rift in Southern California ». *Eos, Transactions American Geophysical Union* 27 (4):552‑552. https://doi.org/10.1029/TR027i004p00552.

Wallace, Robert E. 1968. « Notes on stream channels offset by the San Andreas fault, southern Coast Ranges, California ». In *Conference on Geologic Problems of the San Andreas Fault System. Stanford University Publication in Geological Sciences*, 11:6–21. http://activetectonics.asu.edu/ActiveFaultingSeminar/Papers/Wallace_1968_Stream_Channels_Offset.pdf.

Wallace, Robert E. 1970. « Earthquake recurrence intervals on the San Andreas fault ». *Geological Society of America Bulletin* 81 (10):2875–2890.

Wallinga, Jakob. 2002. « ON THE DETECTION OF OSL AGE OVERESTIMATION USING SINGLE-ALIQUOT TECHNIQUES. » *Geochronometria: Journal on Methods & Applications of Absolute Chronology* 21. http://www.geochronometria.pl/pdf/geo_21/geo21_02.pdf.

Wei, Shengji, Eric Fielding, Sebastien Leprince, Anthony Sladen, Jean-Philippe Avouac, Don Helmberger, Egill Hauksson, et al. 2011. « Superficial Simplicity of the 2010 El Mayor-Cucapah Earthquake of Baja California in Mexico ». *Nature Geoscience* 4 (9):615‑18. https://doi.org/10.1038/ngeo1213.

Weldon, R. J., T. E. Fumal, T. J. Powers, S. K. Pezzopane, K. M. Scharer, et J. C. Hamilton. 2002. « Structure and earthquake offsets on the San Andreas fault at the Wrightwood, California, paleoseismic site ». *Bulletin of the Seismological Society of America* 92 (7):2704–2725.

Wells, Donald L., et Kevin J. Coppersmith. 1994. « New empirical relationships among magnitude, rupture length, rupture width, rupture area, and surface displacement ». *Bulletin of the seismological Society of America* 84 (4):974–1002.

Went, F. W. 1953. « The Effect of Temperature on Plant Growth ». *Annual Review of Plant Physiology* 4 (1):347‑62. https://doi.org/10.1146/annurev.pp.04.060153.002023.

Wesnousky, S. G. 2008. « Displacement and Geometrical Characteristics of Earthquake Surface Ruptures: Issues and Implications for Seismic-Hazard Analysis and the Process of Earthquake Rupture ». *Bulletin of the Seismological Society of America* 98 (4):1609‑32. https://doi.org/10.1785/0120070111.

Wesnousky, Steven G. 2006. « Predicting the Endpoints of Earthquake Ruptures ». *Nature* 444 (7117):358‑60. https://doi.org/10.1038/nature05275.

Windley, B. F., M. B. Allen, C. Zhang, Z.-Y. Zhao, et G.-R. Wang. 1990. « Paleozoic Accretion and Cenozoic Redeformation of the Chinese Tien Shan Range, Central Asia ». *Geology* 18 (2):128‑31. https://doi.org/10.1130/0091-7613(1990)018<0128:PAACRO>2.3.CO;2.

Wintle, A. G., et A. S. Murray. 2006. « A review of quartz optically stimulated luminescence characteristics and their relevance in single-aliquot regeneration dating protocols ». *Radiation Measurements* 41 (4):369‑91. https://doi.org/10.1016/j.radmeas.2005.11.001.

Xiao, W., B. F. Windley, G. Badarch, S. Sun, J. Li, K. Qin, et Z. Wang. 2004. « Palaeozoic Accretionary and Convergent Tectonics of the Southern Altaids: Implications for the Growth of Central Asia ». *Journal of the Geological Society* 161 (3):339‑42. https://doi.org/10.1144/0016-764903-165.

Yeats, Robert S., Kerry E. Sieh, Clarence R. Allen, et E. L. Geist. 1997. *The geology of earthquakes*. Vol. 568. Oxford university press New York. http://www.ulb.tu-darmstadt.de/tocs/54361400.pdf.

Zielke, O., J. R. Arrowsmith, L. Grant Ludwig, et S. O. Akciz. 2012. « High-Resolution Topography-Derived Offsets along the 1857 Fort Tejon Earthquake Rupture Trace, San Andreas Fault ». *Bulletin of the Seismological Society of America* 102 (3):1135‑54. https://doi.org/10.1785/0120110230.

Zielke, O., J R. Arrowsmith, L. G. Ludwig, et S. O. Akciz. 2010. « Slip in the 1857 and Earlier Large Earthquakes Along the Carrizo Plain, San Andreas Fault ». *Science* 327 (5969):1119‑22. https://doi.org/10.1126/science.1182781.

Zielke, Olaf, et J. Ramon Arrowsmith. 2012. « LaDiCaoz and LiDARimager—MATLAB GUIs for LiDAR data handling and lateral displacement measurement ». *Geosphere* 8 (1):206–221.

Zielke, Olaf, Yann Klinger, et J. Ramon Arrowsmith. 2015. « Fault Slip and Earthquake Recurrence along Strike-Slip Faults — Contributions of High-Resolution Geomorphic Data ». *Tectonophysics* 638 (janvier):43‑62. https://doi.org/10.1016/j.tecto.2014.11.004.

Zorin, Yu A. 1999. « Geodynamics of the western part of the Mongolia–Okhotsk collisional belt, Trans-Baikal region (Russia) and Mongolia ». *Tectonophysics* 306 (1):33–56.

# Annexes

## I. *Supplementary materials*, Chapitre 3 (papier à Tectonophysics)

### *Aerial photographs dataset*

In order to figure out fault surface ruptures and deformations registered by geomorphic markers, an original historical dataset of aerial photographs has been used. These photographs were taken by a Russian mission, a few months after the 1957 Gobi-Altai earthquake, during the first part of 1958 (Florensov and Solonenko, 1965). Only little information about these photographs is available: date and hour of each photographs, the relative horizontality (bubble level, not actually significant in a flying plane), and an approximate value of the focus length of 100.0 ± 0.1 mm. Pictures are printed version, square shaped, 17.9 cm wide, and have been developed a long time ago (at least 40 years). Orientations of the photographs are not known, and checking the bubble level it is assumed that all pictures are near-nadir. Aerial photographs are all referenced, and split in two series. In the first one, named S10000 regarding to the approximate scale of 1:10000, we find low altitude aerial photographs following the main scarps. Ground configuration is therefore linear, and their scales could be quite variable, due to the reliefs of Bogd mountain ranges. The coverage of the surface rupture by S10000 is incomplete, especially along the Baga Bogd Mountain (Eastern third of the Eastern Bogd fault) where the fault rupture is distributed. Almost two thirds of the whole main surface rupture are imaged by these photographs. The second series, named S25000, which covers the integrality of the Bogd mountain ranges, has been taken at variable flight altitudes. These are higher altitude aerial photographs than S10000, with scales ranging from 1:20000 to 1:25000. S25000 photos are used in this study whenever S10000 are not available, or at places where the fault is highly distributed, with part of the surface rupture out of the S10000 coverage. All the useful photographs selected for their interest in studying surface rupture have been scanned at 1600dpi with a professional flatbed scanner. Considering the scale, the picture size and the scanning resolution, resulting orthophotographs resolutions are comprised between 15 to 20 cm (theoretically 18 cm) for orthophotographs generated from S10000, and from 40 to 60 cm for orthophotographs produced from S25000. These document are used together with freely available high-resolution satellite images (e.g. Google Earth, Bing Maps), and SRTM30 DEM dataset (Slater et al., 2006) for further analysis of the Eastern Bogd fault.

### *Orthophotographs generation*

- Parametrization

Due to unknown internal and external parameters of the pictures, it is not possible to process the data using a classical photogrammetric process. Thereafter we use a structure from motion approach (Koenderink and Doorn, 1991), allowing to reconstruct internal parameters (camera locations and orientation). The orthophotographs generation follows a standard structure from motion process using the professionnal *Agisoft® Photoscan Pro* software. Due to the linear disposition of the S10000 photographs and in order to avoid distortion propagation in the photogrammetric treatment, photogrammetric computing projects are composed of 4 to 10 aerial photographs. The spatial coverage of these projects must be located within the same high resolution satellite image, in order to avoid georeferencing disconnection. The 1600 dpi scanned pictures are then loaded with the fiducial marks as well as complementary information (picture reference, level, and clock) manually masked in order to preserve a maximum of the visible surface. The camera calibration is parametrized with a frame camera type and a 100 mm focal length, according to meta-information relative to the photographs. GCPs are mainly natural features, such as isolated rocks, trees and sharp topographic heights, but could also be anthropic like unchanged livestock paddock walls, or archeological features. The GCPs have to be widely distributed on each picture both in planimetry and in altitude to constrain in 3D the correlation model. Because GCP positions within one project are all extracted from a unique satellite image, even if the georeferencing of that image is incorrect, relative distances within the image are preserved. All aerial photographs are of the same dimension in pixel, allowing the focal length approximation by the structure from motion process (James and Robson, 2014). Absolute georeferencing errors are preserved without affecting the orthorectification process regarding the satellite image. Altitude data are specified from the SRTM30 DEM, with expectedly high uncertainties resulting in a low accuracy in altitude of our own 3D models. A minimum of 5 GCPs per picture are specified in UTM coordinates (UTM 47N) with 0.3 m precision and 1 m relative uncertainty.

These values have been used both to maintain the georeferencing accuracy in spite of large uncertainties in altitude inherent to the SRTM DEM, and to allow a certain amount of liberty for the computation in order to avoid incoherencies (e.g. GCPs out of the point cloud or important noise in the point cloud) which might lead to artifacts.

- Processing

The first step in the photogrammetric processing is to align aerial photographs. This step generates a sparse point cloud by computing Tie Points (TPs) between photographs. Next step is to build the geometry (relative position of cameras) from that sparse point cloud. Basically, sparse point cloud average spatial density from the S10000 1958 aerial photography is 2000 to 9000 TP per photograph, not evenly distributed. A first alignment and geometry-building computing allows efficient selection of the GCPs and give estimation of their accuracy. This marker/model error has to be minimized both in pixels (relative to the on-picture position) and in meters (relative to GCPs' coordinates). This error improvement could be done by optimizing the photographs alignment, by adding GCPs, correcting inaccurate GCPs, or by changing the size of photogrammetric projects (the addition of more pictures might foster correlation, or instead discarding some low-neatness picture might optimize the correlation). Once the GCPs location errors optimized and the geometry built, a dense point cloud may be computed. Obtained dense-point clouds are 1 to 10 pts.m$^{-2}$, depending on the accuracy requested for the computing. Based on a trade-off in point density and correlation errors, there are four levels of quality for the TPs detection in *Agisoft® Photoscan* (low, medium, high and very high), generating different TPs density and distribution regarding to the images. In order to optimize orthophotographs quality and due to the age of aerial photographs, several qualities have been computed for each computing project. The last computation steps consist of building a 3D mesh from the dense cloud, and to generate texture elements for each facet. Finally, DEM and orthophotographs are exported in GeoTIFF format. DEMs resolutions are 40 to 50cm for S10000 series, and 1 to 2 m for S25000. Produced DEM exhibit two limitations: i) computational noise due to the poor quality of original photographs; ii) vertical offsets between photogrammetric projects, due to inaccuracy of the GCPs coordinates.

Overall, our DEM are adequate to perform ortho-rectification but do not allow high-quality infra-metric measurements across the fault scarps. Orthophotographs are exported at resolution of 15 cm to 20 cm for the orthophotographs generated from S10000 and 50cm for the orthophotographs produced from S25000. Figure 2.a. illustrates the S10000 orthophotographs rendering compared to Bing image, and their geomorphic interpretations.

- Coverage

The coverage of the fault surface rupture by S10000 is not exhaustive. The linear configuration offers a 1 to 2 km wide band, following the main scarp along the western 2/3 of its total length. However, some images are missing and two projects have been

done from S25000 in order to complete the coverage. Locally, where 1958 data were not available to cover the full surface rupture, modern high resolution optical satellite images have been used. The easternmost 80 km of the Gobi-Altai earthquake surface rupture, corresponding to the Baga Bogd area, present a highly distributed fault pattern, and only a few S10000 pictures display identifiable faulting. These images have been computed to produce orthophotographs, but their coverage is very weak compared to the distributed surface rupture area. Total budget of fault covered by 1958 aerial photos is 150km of localized deformation along the Eastern part of the Bogd fault (Bhaar Uul, Noyon Uul, Ikh Bogd and Dullan Bogd), with 120km covered by S10000 and 30km by S25000.

- Orthophotographs dataset

The orthophotographs have been published in the *figshare* platform, in *kml* format in order to minimize their weight. Titles of the orthophotographs correspond to the names of the site they cover. Associated DOI is 10.6084, and the data can be found at the following URL: https://doi.org/10.6084/m9.figshare.5773134.v1.

- Limits

Such photogrammetric modeling from historical aerial photographs has its limits. As previously exposed, the aim is to be as accurate as possible, staying aware of unavoidable inaccuracies. Main identified limits of this approach are: georeferencing, orthorectification, accuracy and partial coverage. Main limiting factors are low resolution altitude data from SRTM, unknown camera position and orientation, lens distortion, photographs preservation, uncertainties of GCPs locations, and S10000 linear configuration. Actually, linear distribution pattern is not favorable for structure from motion photogrammetric process (James and Robson, 2014).

Due to the old age of the original aerial photographs, some of them could present some defects. For instance all of the original photographs have bug-holes (sometime in the center-part of the pictures); some of them are fuzzy from inadequate printing, others are folded, torn, or have stains and pen strokes. These defects will partially figurate in the final orthophotographs, reducing their readability and accuracy. Moreover, the previously cited inaccuracies in the georeferencing data and some missing information like the camera lens distortion parameters or the camera locations could generate other artefacts during the photogrammetric process. Such artefacts might be miss-georeferencing,

texture artefact, or ghosting within orthophotographs. Artefacts presence will further be integrated in the evaluation of each measurement done on the orthophotographs.

- Validation

In order to validate this orthorectification approach, a validation test has been performed, comparing 100 length measurements done on 5 different satellite images used for the georeferencing process, and the generated orthophotographs. The dataset is divided into 4 classes: [0 - 5 m[, [5 – 15 m[, [15 - 50 m[ and [50 – 150 m].

| Class | Nb. meas. | Err av. (m) | Err av. (%) | 1σ (m) |
|---|---|---|---|---|
| [0-5m] | 25 | 0,15 | 4,16 | 0,17 |
| ]5-15m] | 25 | 0,31 | 3,11 | 0,38 |
| ]15-50m] | 25 | 0,86 | 2,66 | 1,09 |
| ]50-150m] | 25 | 0,87 | 1,23 | 1,17 |

Table: Ortho-rectification validation test results. Nb. meas: number of measurement; Err av.: average absolute error in meters (m) and in percent (%); 1σ: one standard deviation of the error distribution.

Results in table show less than 5 % error for all measurements, and accounting for the average error of about 30 cm for measurement below 15 m and about 90 cm for measurements above 15 m, we conclude that this test validates the accuracy of produced orthophotographs for offset measurements.

### *Mapping*

Detailed mapping is given in 4 kml files. Three are the main strike slip surface rupture: mains scarp, cracks and secondary faults as detailed in the text. One more file is for secondary fault rupture south and south-east from Baga Bogd.

### *Offset measurements dataset*

Annexe VII is a table listing offset measurements. Seg.: segment or relay reference; Lon.: longitude UTM, Lat.: latitude UTM, Marker res.: resolution of the marker (/2), encompassing both sinuosity (/1) and straightness (/1); Nb of splay: number of fault splay affecting the marker; Scarp 2$^{nd}$: number of secondary scarp out of the measurement area; Offset Pref: preferred offset value (in m); Offset min/max:

minimum/maximum offset value (in m); Δ+/-: absolute difference between preferred and maximum/minimum offset values (in m); Image type: type of image used for the measurement (mostly orthophotographs from 1958 aerial photographs, something Bing on Google Map images); Image res.: image resolution (in m).

## II. Radiocarbon ages

| Site | Référence échantillon | Nature | Prof. (cm) | Masse C (mg) | Age (a BP) | Err âge (a BP) | Age (aCalBP) | Err âge (aCalBP) | 68% range (aCalBP) | |
|---|---|---|---|---|---|---|---|---|---|---|
| **Western Bogd Fault** | | | | | | | | | | |
| Rain Creek Riser | M15-RC-CO1 | charbon | 50 | 0,65 | 1965 | 30 | 1925 | 33 | 1891 | 1958 |
| Rain Creek T2 | M15-RC-54 | bulk | 170 | 1,07 | 7135 | 35 | 7970 | 23 | 7947 | 7993 |
| Rain Creek T3 | M15-RCT3-C01 | Charbon | 40 | 1,58 | 9435 | 50 | 10668 | 61 | 10607 | 10729 |
| Rain Creek T3 | M15-RCT3-C02 | MO | 110 | 1,78 | 9160 | 45 | 10330 | 64 | 10266 | 10394 |
| Rain Creek T3 | M15-RCT3-C05 | Charbon | 48 | 1,67 | 9445 | 45 | 10675 | 59 | 10615 | 10734 |
| Rain Creek T3 | M15-RCT3-C06 | Charbon | 40 | 1,03 | 8785 | 45 | 9809 | 89 | 9718 | 9897 |
| Ice Creek Tension Gash | M15-IC-C01 | MO | 45 | 0,94 | 1855 | 30 | 1793 | 46 | 1747 | 1839 |
| Ice Creek Tension Gash | M15-IC-C04 | Tourbe | 45 | 1,50 | 2240 | 30 | 2254 | 64 | 2190 | 2318 |
| Ice Creek Tension Gash | M15-IC-C06 | Charbon + séd | 42 | 1,15 | 2835 | 30 | 2942 | 44 | 2898 | 2986 |
| Ice Creek Tension Gash | M15-IC-C08 | Charbon | 45 | 1,77 | 2965 | 30 | 3146 | 55 | 3091 | 3201 |
| Ice Creek Tension Gash | M15-IC-C09 | MO + Charcoal | 53 | 1,07 | 2445 | 30 | 2534 | 128 | 2406 | 2662 |
| Ice Creek Tension Gash | M15-IC-C10 | Charcoal | 91 | 1,52 | 3485 | 30 | 3769 | 48 | 3721 | 3817 |
| Ice Creek Tension Gash | M15-IC-C11 | Charcoal + séd | 77 | 1,28 | 3090 | 35 | 3314 | 42 | 3272 | 3356 |
| Ice Creek Tension Gash | M15-IC-C12 | bulk | 130 | 1,46 | 5135 | 30 | 5858 | 65 | 5792 | 5923 |
| Chandmani Tension Gash | M15-TG-5 | bulk | 90 | 1,41 | 815 | 30 | 730 | 26 | 703 | 756 |
| Chandmani Tension Gash | M15-TG-6 | bulk | 100 | 1,20 | 1440 | 30 | 1340 | 23 | 1316 | 1363 |
| Swan Lake Trench | MO16_SLT_C01 | Bulk paleosol | 65 | 0,65 | 5645 | 30 | 6435 | 29 | 6406 | 6464 |
| Swan Lake Trench | MO16_SLT_C02 | Bulk paleosol | | 1,14 | 2075 | 30 | 2055 | 45 | 2010 | 2100 |
| Swan Lake Trench | MO16_SLT_C03 | Bulk | 40 | 1,11 | 2305 | 30 | 2332 | 16 | 2316 | 2348 |

| Site | Référence échantillon | Nature | Prof. (cm) | Masse C (mg) | Age (a BP) | Err âge (a BP) | Age (aCalBP) | Err âge (aCalBP) | 68% range (aCalBP) | |
|---|---|---|---|---|---|---|---|---|---|---|
| Moskito Trench | MO16_MT_C02 | Paleosol | 100 | 0,92 | 3355 | 30 | 3601 | 37 | 3564 | 3622 |
| Moskito Trench | MO16_MT_C03 | Sediment | 60 | 0,69 | 2510 | 30 | 2614 | 87 | 2527 | 2701 |
| Moskito Trench | MO16_MT_C04 | Bulk | 75 | 0,84 | 5495 | 30 | 6299 | 13 | 6286 | 6312 |
| Moskito Trench | MO16_MT_C06 | Bulk | 110 | 1,03 | 4510 | 30 | 5179 | 88 | 5091 | 5267 |
| Moskito Trench | MO16_MT_C07 | Charcoal | 125 | 1,04 | 7420 | 45 | 8260 | 54 | 8206 | 8314 |
| Moskito Trench | MO16_MT_C08 | Sediment | 215 | 0,46 | 4350 | 30 | 4917 | 42 | 4875 | 4959 |
| Moskito Trench | MO16_MT_C09 | Bulk | 90 | 0,98 | 3470 | 30 | 3760 | 52 | 3708 | 3812 |
| Moskito Trench | MO16_MT_C12 | Charcoal | 125 | 0,95 | 4310 | 30 | 4892 | 37 | 4855 | 4929 |
| Moskito Trench | MO16_MT_C13 | Charcoal | 300 | 0,46 | 4000 | 30 | 4476 | 35 | 4441 | 4511 |
| | | | | **Tsogt Fault** | | | | | | |
| Fox Creek | TSO_FOX_B2 | Bulk | | 0,83 | 2350 | 30 | 2386 | 38 | 2348 | 2424 |
| Fox Creek | TSO_FOX_C4 | Ecorce | | 0,95 | 660 | 30 | 619 | 42 | 577 | 661 |
| Fox Creek | TSO_FOX16_C3 | Excement | | 1,02 | -1015 | 30 | 941 | 16 | 925 | 957 |

# III. OSL ages along the Western Bogd Fault



## Luminescence analyses Western Bogd Fault, Mongolia

Four sediment samples were dated using infrared stimulated luminescence (IRSL). This method allows determining the last exposure of sediments to sunlight and thus, the last event of transport and deposition. Two parameters have to be determined to derive an IRSL age. These are the equivalent dose ($D_e$, in Gy) and the dose rate ($\dot{D}$, in Gy/ka).

The $D_e$ was determined using the feldspar coarse grain fraction (FS CG, 90-200 µm). The quartz coarse grain fraction (Q CG, 90-200 µm) was also tested for measurements, but suffered from severe feldspar contamination. For this reason, no ages were calculated from coarse grains of quartz. Feldspar measurements are based on the SAR post-IR-IRSL-225 protocol (Buylaert et al., 2009). Further details on measurement settings can be found in Section 3. Radionuclide concentrations of U and Th were determined via alpha counting and K concentrations using ICP-OES. These analyses were carried out at the University of Bayreuth (Department of Geography). The determination of the dose rate is based on conversion factors of Guerin et al. (2011), and consideration of the cosmic dose following Prescott and Hutton (1994). The calculation of dose rates was performed using the program DRAC (Durcan et al., 2015).

### 1. Sample numbers and assignment

*Tab. 1: Overview on dated samples and assignment to field numbers*

| Field number | Lab number | Sampling depth (m) |
|---|---|---|
| Trench 2 OSL1 | Gi304 | *0.30* |
| Trench 2 OSL2 | Gi305 | *0.45* |
| Riser | Gi324 | *0.40* |
| Trench 3 OSL3 | Gi325 | *0.60* |

### 2. Test on feldspar contamination

As mentioned above, the quartz coarse grain fraction suffered from feldspar contamination, evidenced by a strong response to infrared stimulation. Measurements of the quartz coarse grains were not pursued. Fig. 1 shows IRSL signals of the quartz coarse grain fraction of sample GI304.

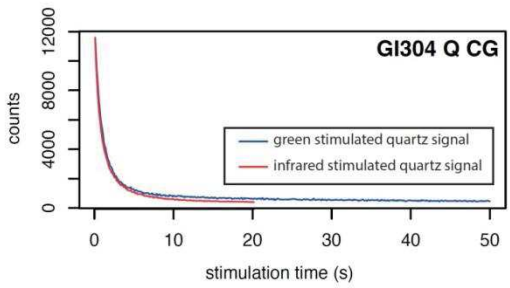


*Fig. 1: Response of test dose to IRSL stimulation (red curve) and to green stimulation (blue curve) using the same test dose, measured on the quartz coarse grain fraction.*

## 3. Standard $D_e$ determination

The following overview lists all relevant settings of the standard post-IR-IRSL-225 measurements:

- Luminescence reader: Lexsyg "Humboldt" (see Lomax et al., 2014)
- Integrals: Initial: 0-1.0 s; Background 240-300 s
- Instrumental error: 0.3 %
- Rejection criteria: > 10% recycling ratio, > 7% test dose error, >20% total error
- Material: K-feldspar coarse grain, 90-200 µm
- Aliquot size: 2 mm aliquots
- Preheat temperature: 250°C
- Stimulation: IR laser diodes (830 ± 3 nm), 300 s @ at 50°C and 225°C, power density 300 mW/cm²
- Mean $D_e$ calculation: Central Age Model (Galbraith et al., 1999)

## 4. Luminescence properties

Feldspars were measured with the post-IR-IRSL-225 protocol (Buylaert et al., 2009). This protocol measures an IRSL signal stimulated at 50°C first (IR50), followed by an IRSL stimulation at 225°C (pIRIR225). It is believed that the 50°C signal is prone to fading and potentially yields underestimated $D_e$ values, whereas the 225°C signal measures a more stable signal.

In order to check if fading is a problem in the analysed samples, basic fading tests were carried out. The samples were irradiated with a known dose (close to the expected natural dose) and then stored for one week. Afterwards, the remaining dose was measured using the standard post-IR-IRSL-225 protocol. Results are shown in Table 2. From these measurements it seems that fading slightly affects the IR50 signals of two older samples, but not the two younger samples.

*Tab. 2: Results of basic fading tests*

| Sample | given dose (Gy) | measured dose IR50 (Gy) | measured dose pIRIR225 (Gy) |
|---|---|---|---|
| *GI304* | 1.3 | 1.3 ± 0.1 (0%) | 1.5 ± 0.1 (+15%) |
| *GI305* | 32.2 | 30.1 ± 0.4 (-7%) | 31.0 ± 0.1 (-4%) |
| *GI324* | 5.8 | 5.6 ± 0.2 (-3%) | 5.8± 0.2 (0%) |
| *GI325* | 38.6 | 36.4 ± 0.3 (-6%) | 38.7 ± 0.4 (0%) |

Furthermore, tests on a potential unbleachable residual were performed for each sample by exposing the samples to sunlight for two days and measuring the residual dose. Residual doses for the IR50 signal varied between 0.4 and 1.1 Gy, and for the pIRIR225 signal between 0.8 and 7.5 Gy. It has however been shown in the past that in nature, samples are usually bleached to a higher degree than in laboratory tests. Therefore, the residuals measured here were not subtracted from the doses derived in the standard measurements (see Section 5). It needs to be kept in mind though that the resulting ages might suffer from slight overestimation due to an unbleachable residual (which is possibly outweighed by slight underestimation due to fading).

## 5. Resulting $D_e$ values and $D_e$ distributions of the standard measurements

Standard measurements yield two $D_e$ values within one measurement protocol. One is the value based on the IR50 signal, and the other one based on the pIRIRSL225 signal. The latter may be less prone to fading, but also more affected by unbleachable residuals and/or incomplete bleaching. Table 3 shows both values. It is observed that for GI324, the two $D_e$ values agree within errors. However, this sample showed problematic behaviour with respect to recycling ratios within the pIRIR225 signals. The resulting age is therefore based on the IR50 signals. This problematic behaviour was even more evident in sample GI304 and led to an exclusion of most of the individual $D_e$ values based on the pIRIRSL signals. For this sample too, the resulting age is based on the IR50 signals.

The two older samples show lower IR50 than pIRIR225 $D_e$ values. Interestingly, these two samples did not show the problematic recycling behaviour like the two younger samples. Due to the tight and symmetric $D_e$ distributions, incomplete bleaching is ruled out as factor for the differing $D_e$ values, and fading seems the most likely explanation. Ages for these two samples are thus based on the pIRIR225 signals.

*Tab. 3: Comparison of IR50 $D_e$ values and pIRIR225, both obtained in the same post-IR-IRSL protocol.*

| Sample | $D_e$ (Gy) IR50 | $D_e$ (Gy) pIRIR225 |
|---|---|---|
| *GI304* | 0.91 ± 0.04 | - |
| *GI305* | 31.9 ± 1.70 | 37.7 ± 1.5 |
| *GI324* | 5.8 ± 0.20 | 5.5 ± 0.3 |
| *GI325* | 29.4 ± 1.10 | 35.3 ± 1.1 |

Fig. 2 shows $D_e$ distributions of the four samples. Except for one or two outlying values, the distributions are narrow and non-skewed. Mean $D_e$ values were calculated using the Central Age Model (Galbraith et al., 1999) without considering outlying values.

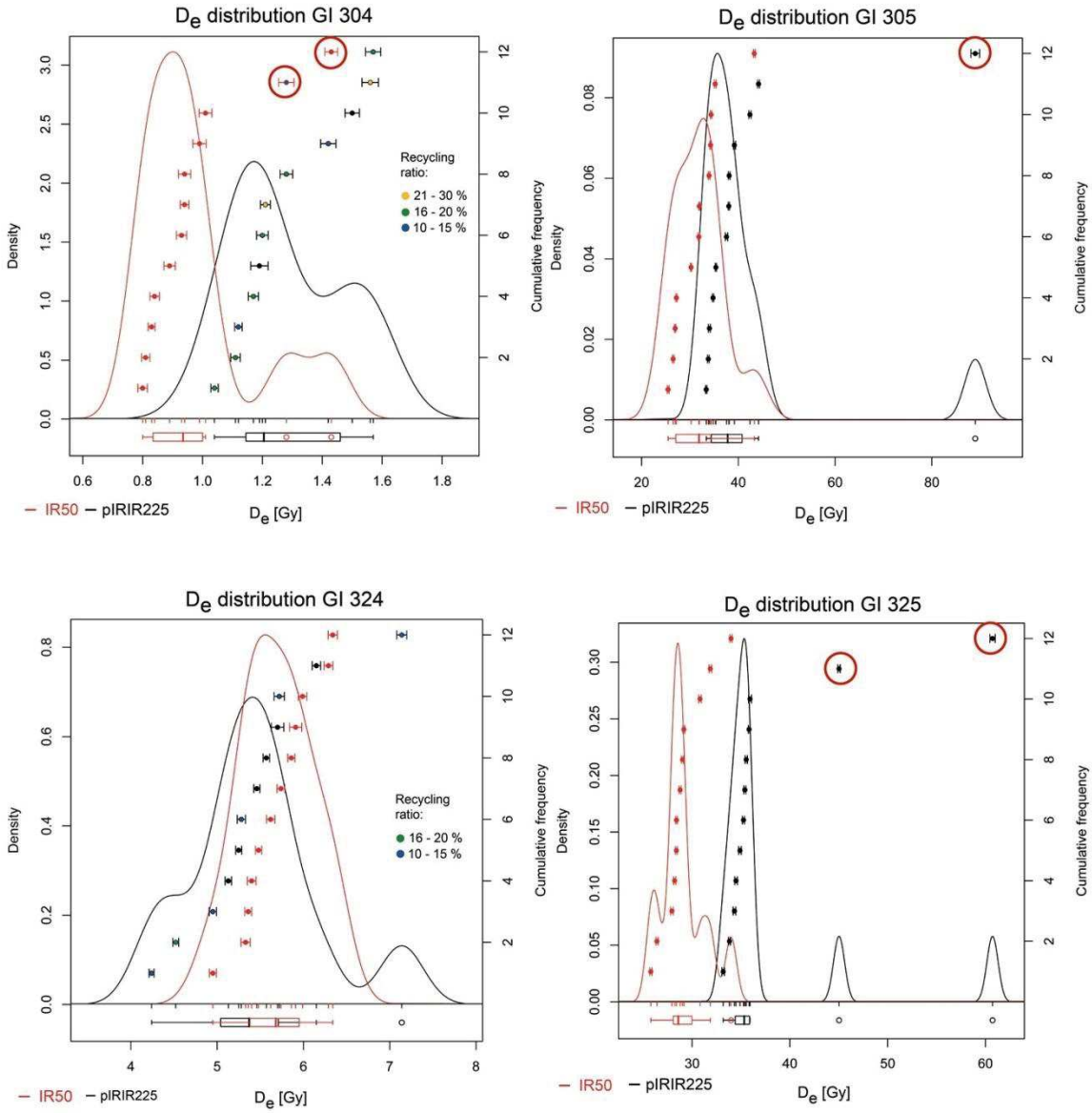


*Fig. 2: $D_e$ distributions of samples GI304, GI305, GI324 and GI325. $D_e$ values based on IR50 signals are shown in red, $D_e$ values based on pIRIR225 signals in black. Outliers which were excluded from mean $D_e$ calculation are marked with red circles. Aliquots which showed recycling ratios above a 10 %-threshold from unity are also shown and marked in yellow, green and blue. This only affected the pIRIR225 measurements of samples GI304 and GI324.*

## 6. Palaeodoses, dose rates and resulting luminescence ages

The following tables list radionuclide concentrations, dose rates (Table 4), palaeodoses, standard deviations, overdispersions and resulting luminescence ages (Table 5).

*Tab. 4: Analytical results of dose rate determination*

| Sample | U (ppm) | Th (ppm) | K (%) | $\dot{D}$ (Gy/ka) Feldspar CG |
|---|---|---|---|---|
| *GI304* | 3.2 ± 0.3 | 7.1 ± 0.8 | 1.7 ± 0.1 | 3.7 ± 0.2 |
| *GI305* | 3.4 ± 0.3 | 8.0 ± 0.9 | 2.2 ± 0.1 | 4.2 ± 0.3 |
| *GI324* | 2.5 ± 0.2 | 6.0 ± 0.7 | 1.5 ± 0.1 | 3.2 ± 0.2 |
| *GI325* | 3.5 ± 0.3 | 7.1 ± 0.8 | 1.8 ± 0.1 | 3.8 ± 0.3 |

*Dose rates were calculated with a-values of 0.08 ± 0.02, internal K-concentrations of 12.5 ± 0.5 % and water contents of 10 ± 5 %.*

*Tab. 5: Analytical results of palaeodose determination and resulting luminescence ages*

| Sample | Signal | $D_e$ (Gy) | n (measured/accepted) | RSD (%) | **Age (ka)** |
|---|---|---|---|---|---|
| *GI304* | IR50 | 0.91 ± 0.04 | ( 12 / 10 ) | (8.8) | **0.25 ± 0.02** |
| *GI305* | pIRIR225 | 37.7 ± 1.50 | ( 12 / 11 ) | (9.6) | **9.0 ± 0.7** |
| *GI324* | IR50 | 5.8 ± 0.20 | ( 12 / 12 ) | (7.3) | **1.8 ± 0.1** |
| *GI325* | pIRIR225 | 35.3 ± 1.10 | ( 12 / 10 ) | (2.6) | **9.2 ± 0.7** |

*RSD = relative standard deviation of accepted $D_e$ values*

## 7. Estimation of reliability of luminescence ages

The ages are in agreement with the stratigraphy and match existing radiocarbon ages within errors. However, all samples maybe affected by fading and/or unbleachable residual, which needs to be considered in the interpretation of the ages.

**References:**

Buylaert, J.P., Murray, A.S., Thomsen, K.J., Jain, M., (2009. Testing the potential of an elevated temperature IRSL signal from K-feldspar. Radiation Measurements 44 (5/6), 560-565.

Durcan, J.A., King, G.E., Duller, G.A.T. (2015). DRAC: Dose Rate and Age Calculator for trapped charge dating. Quaternary Geochronology 28, 54-61.

Galbraith, R.F., Roberts, R.G., Laslett, G.M., Yoshida, H., Olley, J.M. (1999). Optical dating of single and multiple grains of quartz from Jinmium rock shelter, northern Australia: Part I, experimental design and statistical models. Archaeometry 41, 339-364.

Guérin, G., Mercier, N., Adamiec, G. (2011). Dose-rate conversion factors: update. Ancient TL 29(1), 5-8.

Lomax, J., Kreutzer, S., Fuchs, M. (2014): Performance tests using the Lexsyg luminescence reader. Geochronometria 41(4), 327-333.

Murray, A.S., Wintle, A.G. (2000). Luminescence dating of quartz using an improved single-aliquot regenerative-dose protocol. Radiation Measurements, 32, 57-73.

Murray, A.S., Wintle, A.G. (2003). The single aliquot regenerative dose protocol: potential for improvements in reliability. Radiation Measurements 37, 377-381.

Prescott, J.R., Hutton, J.T. (1994). Cosmic ray contributions to dose rates for luminescence and ESR dating: large depth and long-term time variations. Radiation Measurements 23, 497-500.

# IV. OSL ages along the Valley of Lakes Fault

TABLE 1: Quartz OSLand Feldspar IRSL Data and Dates for Valley of Lakes Trench, Mongolia

| Sample information | % Water content[a] | K (%)[b] | U (ppm)[b] | Th (ppm)[b] | Total Dose (Gy/ka)[c] | Equivalent Dose (Gy) | n[d] | Scatter[e] | Age (yrs)[f] |
|---|---|---|---|---|---|---|---|---|---|
| **MO14-OSL1** | 5 (47) | 2.12 ± 0.05 | 3.20 ± 0.28 | 10.5 ± 0.58 | 3.66 ± 0.13 | 12.4 ± 0.24 | 29 (48) | 34% | 3,400 ± 140 |
| **MO14-OSL2** | 2 (28) | 1.92 ± 0.04 | 2.68 ± 0.26 | 8.06 ± 0.37 | 3.30 ± 0.10 | 21.0 ± 0.55 | 9 (48) | 57% | 6,350 ± 260 |
| **MO14-OSL3** | 2 (23) | 1.91 ± 0.04 | 2.71 ± 0.31 | 7.39 ± 0.51 | 3.23 ± 0.14 | 27.1 ± 0.57 | 16 (48) | 33% | 8,390 ± 400 |
| | | | | | 4.63 ± 0.20[g] | 68.2 ± 8.18[g] | 4 (5) | - | 14,740 ± 1,870[g] |

[a]Field moisture, with figures in parentheses indicating the complete sample saturation %. Ages calculated using 25% of the saturated moisture (i.e. 5 (47) = 47 * 0.25 = 12).

[b]Analyses obtained using high-resolution gamma spectrometry (high purity Ge detector).

[c]Includes cosmic doses and attenuation with depth calculated using the methods of Prescott and Hutton (1994). Cosmic doses at 0.39 (top) to 0.27 (bottom) in Gy/ka.

[d]Number of replicated equivalent dose ($D_E$) estimates used to calculate the equivalent dose. Figures in parentheses indicate total number of measurements included in calculating the represented $D_E$ and age using the lowest peak distributions as reported by the radial plot (Peak 1); analyzed via single aliquot regeneration on quartz grains.

[e]Defined as "over-dispersion" of the $D_E$ values. Obtained by the "R" factor program. Values >35% are considered to be poorly bleached sediments.

[f]Dose rate and age for fine-grained 180-90 micron sized quartz. Exponential + linear fit used on equivalent dose, errors to one sigma.

[f]Dose rate and age for fine-grained 180-90 micron feldspar using the 230C post IR peak. Exponential + linear fit used on equivalent dose, errors to one sigma. No fading correction.

**Valley of Lakes Fault, Mongolia-Robin Kurtz and Carol Prentice**

**Dose Rates for sand-grain HF etched, quartz samples**

| Sample ID | K (%) | U (ppm) | Th (ppm) | Elevation (m) | Depth (cm) | H2O (%) | $Dose_R$ | $D_R$ for K | $D_R$ for U | $D_R$ for Th | $D_R$ for Rb | $D_R$ for cosmic ray |
|---|---|---|---|---|---|---|---|---|---|---|---|---|
| MO14-OSL1 | 2.12 | 3.20 | 10.5 | 2150 | 10 | 5 | 3.908 | 1.9718 | 0.7406 | 0.7646 | 0.0399 | 0.3914 |
| | 2.12 | 3.20 | 10.5 | 2150 | 10 | **12** | **3.657** | 1.8295 | 0.6880 | 0.7112 | 0.0370 | 0.3914 |
| | 2.12 | 3.20 | 10.5 | 2150 | 10 | 47 | 2.770 | 1.3289 | 0.5021 | 0.5213 | 0.0267 | 0.3914 |
| | | | | | | | | | | | | |
| MO14-OSL2 | 1.92 | 2.68 | 8.06 | 2150 | 25 | 2 | 3.477 | 1.8498 | 0.6420 | 0.6071 | 0.0375 | 0.3409 |
| | 1.92 | 2.68 | 8.06 | 2150 | 25 | **7** | **3.302** | 1.7456 | 0.6065 | 0.5741 | 0.0353 | 0.3409 |
| | 1.92 | 2.68 | 8.06 | 2150 | 25 | 28 | 2.741 | 1.4117 | 0.4922 | 0.4674 | 0.0284 | 0.3409 |
| | | | | | | | | | | | | |
| MO14-OSL3 | 1.91 | 2.71 | 7.39 | 2150 | 100 | 2 | 3.359 | 1.8402 | 0.6492 | 0.5567 | 0.0373 | 0.2761 |
| | 1.91 | 2.71 | 7.39 | 2150 | 100 | **6** | **3.229** | 1.7613 | 0.6219 | 0.5337 | 0.0356 | 0.2761 |
| | 1.91 | 2.71 | 7.39 | 2150 | 100 | 23 | 2.747 | 1.4713 | 0.5211 | 0.4484 | 0.0297 | 0.2761 |
| | | | | | | | | | | | | |
| MO14-OSL3 | 1.91 | 2.71 | 7.39 | 2150 | 100 | 2 | 4.836 | 1.9948 | 1.4195 | 1.1078 | 0.0373 | 0.27614 |
| IRSL | 1.91 | 2.71 | 7.39 | 2150 | 100 | **6** | **4.630** | 1.9092 | 1.3526 | 1.0564 | 0.0356 | 0.27614 |
| | 1.91 | 2.71 | 7.39 | 2150 | 100 | 23 | 3.884 | 1.5945 | 1.1122 | 0.8711 | 0.0297 | 0.27614 |
| | | | | | | | | | | | | |

I made the moisture at about 25%

## MO14-OSL1: Age of deposition for OSL on 180-90 µ quartz grains using single aliquot analyses

***OSL Analysis at 220°C / 10 seconds***

| | | |
|---|---|---|
| Number of n: 29 (48) | | |
| Dose Rate ($D_R$) | $D_R$ | 1s% |
| with $H_2O$ 5% | 3,91 | 3,5 |
| with $H_2O$ 12% | 3,66 | 3,6 |
| with $H_2O$ 47% | 2,77 | 4,0 |
| | $D_E$ | 1s% |
| Average $D_E$ | 11,73 | 4,06 |

*Riso Equipment, medium grained $SiO_2$*

*Blue LED's*

***Exponential + Linear fit***

***Valley Of Lakes trench, Mongolia***
***Top, Unit 10 (Silty-sand capping unit)***
***post-MRE (Block sample)***

| | |
|---|---|
| with H2O 5% | |
| Age =$D_E/D_R$ | 3,00 ka |
| ± 1s(%) | 5,36 |
| ± 1s(absolute) | 0,16 ka |
| **with H2O 12%** | |
| **Age =$D_E/D_R$** | **3,20 ka** |
| **± 1s(%)** | **5,43** |
| **± 1s(absolute)** | **0,17 ka** |
| with H2O 47% | |
| Age =$D_E/D_R$ | 4,23 ka |
| ± 1s(%) | 5,70 |
| ± 1s(absolute) | 0,24 ka |
| Difference in $H_2O$ corrected values | |
| | 34,13 % |

***Age shown is the weighted mean***

| Disc | De | Error |
|---|---|---|
| 1 | 7,20 | 0,91 |
| 18 | 8,65 | 0,94 |
| 14 | 9,18 | 0,69 |
| 47 | 9,56 | 1,77 |
| 45 | 9,76 | 0,82 |
| 28 | 10,22 | 1,30 |
| 4 | 10,90 | 2,04 |
| 7 | 11,01 | 2,07 |
| 17 | 11,27 | 1,25 |
| 13 | 11,33 | 1,08 |
| 21 | 11,83 | 1,09 |
| 41 | 11,84 | 0,74 |
| 26 | 12,53 | 1,22 |
| 29 | 12,80 | 1,37 |
| 12 | 13,83 | 2,48 |
| 20 | 13,88 | 1,31 |
| 19 | 14,28 | 1,45 |
| 24 | 14,67 | 1,51 |
| 16 | 14,73 | 1,34 |
| 22 | 14,73 | 1,11 |
| 5 | 15,13 | 8,18 |
| 23 | 15,30 | 1,21 |
| 10 | 16,61 | 2,05 |
| 27 | 17,17 | 1,71 |
| 30 | 17,81 | 2,16 |
| 9 | 17,89 | 3,20 |
| 15 | 20,43 | 1,86 |
| 42 | 32,44 | 11,27 |
| 6 | 36,93 | 13,06 |

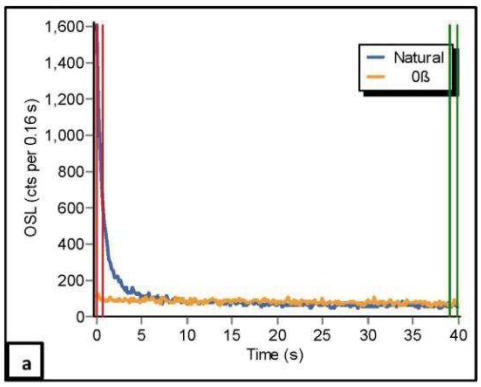


**Disc #41 Decay curve (a) and Growth curve (b)**

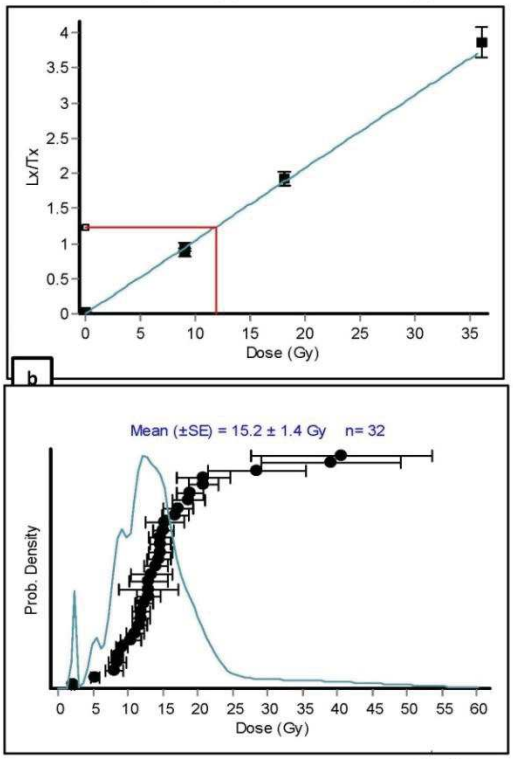


This sample came as a block. Although it was well wrapped and contained when it got to us, I cannot rule out that some exposed grains made it into the final OSL sample. For this reason, I have taken out the very lowest equivalent doses, especially if the measurements were not particuarly robust.

*ALL EQUIVALENT DOSE AND ASSOCIATED DATA*

| Disc # | DE | DE error | N. sig | BG sig | Test Sig | BG T sig | TD error | test dose | residual | test signal | RR1 | RR error | recup 1 |
|---|---|---|---|---|---|---|---|---|---|---|---|---|---|
| 44 | 2,19 | 0,17 | 1388 | 303 | 2513 | 337 | 2,43 | 50 | 481 | 1,04 | 1,02 | 0,09 | 4,00 |
| 3 | 5,13 | 0,51 | 986 | 256 | 950 | 261 | 4,96 | 50 | 300 | 2,50 | 1,02 | 0,11 | 0,13 |
| 1 | 7,20 | 0,91 | 786 | 254 | 603 | 286 | 9,14 | 50 | 337 | 1,46 | 0,86 | 0,14 | 2,91 |
| 18 | 8,65 | 0,94 | 750 | 267 | 1098 | 257 | 4,31 | 200 | 234 | 1,01 | 0,96 | 0,11 | 2,30 |
| 14 | 9,18 | 0,69 | 2333 | 444 | 1441 | 414 | 4,12 | 50 | 460 | 1,53 | 1,23 | 0,12 | 0,77 |
| 47 | 9,56 | 1,77 | 895 | 358 | 666 | 345 | 9,62 | 50 | 377 | 1,32 | 0,83 | 0,24 | 4,49 |
| 45 | 9,76 | 0,82 | 2433 | 499 | 1428 | 403 | 4,10 | 50 | 470 | 0,98 | 0,96 | 0,11 | 3,66 |
| 28 | 10,22 | 1,30 | 486 | 121 | 740 | 132 | 4,79 | 200 | 339 | 2,61 | 1,16 | 0,11 | 17,00 |
| 4 | 10,90 | 2,04 | 774 | 355 | 541 | 383 | 18,50 | 50 | 378 | 1,24 | 1,11 | 0,28 | 5,57 |
| 7 | 11,01 | 2,07 | 728 | 303 | 495 | 310 | 14,84 | 50 | 473 | 1,42 | 0,76 | 0,19 | 15,16 |
| 17 | 11,27 | 1,25 | 653 | 164 | 870 | 154 | 4,41 | 200 | 398 | 1,79 | 0,99 | 0,11 | 24,58 |
| 13 | 11,33 | 1,08 | 1314 | 276 | 728 | 294 | 7,19 | 50 | 342 | 1,82 | 1,15 | 0,15 | 0,09 |
| 21 | 11,83 | 1,09 | 1159 | 135 | 1739 | 156 | 2,73 | 200 | 932 | 2,95 | 1,10 | 0,09 | 22,10 |
| 41 | 11,84 | 0,74 | 5140 | 304 | 4237 | 291 | 1,70 | 100 | 534 | 1,83 | 1,09 | 0,09 | 1,80 |
| 26 | 12,53 | 1,22 | 1221 | 249 | 1573 | 232 | 3,13 | 200 | 934 | 2,39 | 1,03 | 0,09 | 25,12 |
| 29 | 12,80 | 1,37 | 820 | 143 | 1032 | 160 | 3,91 | 200 | 559 | 2,29 | 1,13 | 0,10 | 22,27 |
| 12 | 13,83 | 2,48 | 1115 | 409 | 667 | 398 | 11,72 | 50 | 449 | 1,14 | 0,95 | 0,19 | 6,05 |
| 20 | 13,88 | 1,31 | 1887 | 170 | 2310 | 186 | 2,34 | 200 | 952 | 3,35 | 1,17 | 0,10 | 10,62 |
| 19 | 14,28 | 1,45 | 1041 | 160 | 1211 | 176 | 3,56 | 200 | 686 | 2,96 | 1,12 | 0,10 | 17,81 |
| 24 | 14,67 | 1,51 | 3004 | 172 | 3493 | 195 | 1,83 | 200 | 1983 | 2,32 | 1,05 | 0,08 | 27,00 |
| 16 | 14,73 | 1,34 | 2331 | 230 | 2778 | 219 | 2,13 | 200 | 1323 | 3,41 | 1,18 | 0,10 | 12,75 |
| 22 | 14,73 | 1,11 | 2735 | 207 | 3197 | 203 | 1,94 | 200 | 1403 | 2,57 | 1,04 | 0,08 | 14,95 |
| 5 | 15,13 | 8,18 | 525 | 315 | 372 | 295 | 32,28 | 50 | 343 | 1,20 | 0,88 | 0,54 | 6,95 |
| 23 | 15,30 | 1,21 | 3088 | 258 | 3513 | 244 | 1,86 | 200 | 1222 | 2,39 | 1,12 | 0,09 | 11,27 |
| 10 | 16,61 | 2,05 | 1801 | 308 | 865 | 348 | 6,58 | 50 | 493 | 1,42 | 0,85 | 0,11 | 4,46 |
| 27 | 17,17 | 1,71 | 1020 | 172 | 1014 | 161 | 3,97 | 200 | 432 | 1,72 | 1,08 | 0,10 | 15,41 |
| 30 | 17,81 | 2,16 | 509 | 117 | 503 | 103 | 6,07 | 200 | 202 | 1,93 | 1,15 | 0,12 | 6,80 |
| 9 | 17,89 | 3,20 | 855 | 268 | 454 | 267 | 13,88 | 50 | 317 | 1,40 | 0,83 | 0,22 | 0,32 |
| 15 | 20,43 | 1,86 | 2699 | 463 | 1002 | 408 | 6,16 | 50 | 544 | 1,03 | 1,14 | 0,19 | 5,12 |
| 42 | 32,44 | 11,27 | 388 | 194 | 259 | 213 | 45,73 | 100 | 215 | 1,28 | 0,69 | 0,61 | 1,25 |
| 6 | 36,93 | 13,06 | 1267 | 476 | 620 | 478 | 22,39 | 50 | 541 | 1,16 | 1,22 | 0,33 | 2,62 |
| 11 | 62,48 | 30* | 1053 | 280 | 435 | 279 | 16,58 | 50 | 335 | 1,32 | 1,21 | 0,32 | 1,20 |
| 2 | 85,08 | 50* | 1193 | 452 | 552 | 428 | 24,21 | 50 | 421 | 1,19 | 1,11 | 0,37 | -0,44 |

*blue font indicates those measurements that were originally obtained for other tests (preheat, dose recovery, or thermal transfer)

** red font indicates those samples that have only been partially bleached and therefore are not true representations of the depositonal age of the sediment.

*actual result was infinity

**MAM = Minimum Age Model**
**CAM = Central Age Model**
**Equivalent Dose Models**
**MAM:** 6.79 ± 0.73 Gy
**CAM:** 13.3 ± 0.89 Gy
**Weighted Mean:** 11.7 ± 0.48 Gy

Galbraith, R.F., 2010, On plotting OSL equivalent doses. Ancient TL, V. 29, n1.
Graph generated from RadialPlotter-2015.jar
http://radialplotter.london-geochron.com

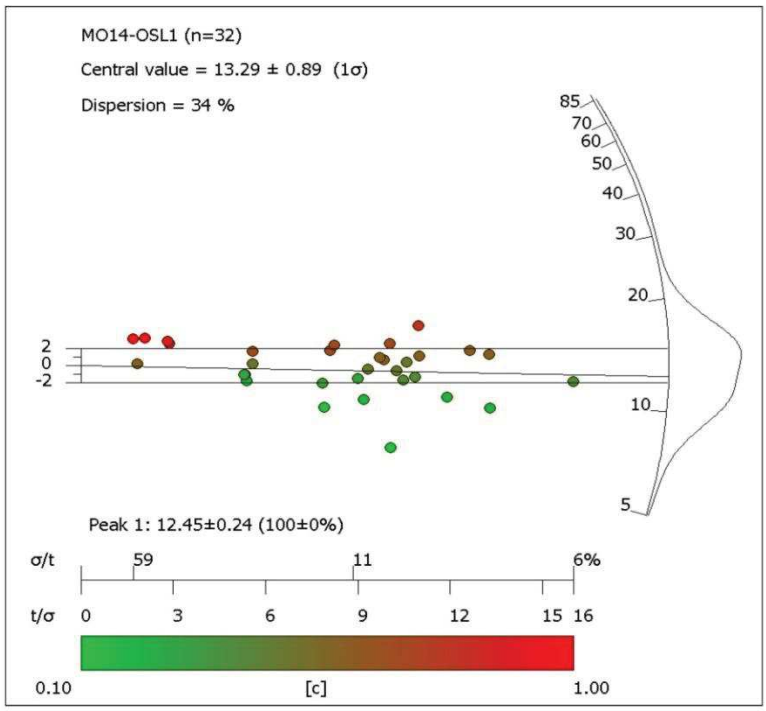

| Disc # | recup error | sig1 | sig2 | BG1 | BG2 | ln/tn | fit | options | r chi squared | radial plot |
|---|---|---|---|---|---|---|---|---|---|---|
| 44 | 2,75 | 1 | 5 | 245 | 250 | 0,49 | 5 | 23 | 2,69 | 0,1 |
| 3 | 1,22 | 1 | 5 | 245 | 250 | 1,05 | 4 | 23 | 0,68 | 0,1 |
| 1 | 3,03 | 1 | 5 | 245 | 250 | 1,52 | 4 | 23 | 1,06 | 0,1 |
| 18 | 4,11 | 1 | 5 | 245 | 250 | 0,58 | 5 | 23 | 2,04 | 0,2 |
| 14 | 0,83 | 1 | 5 | 245 | 250 | 1,89 | 5 | 23 | 5,45 | 0,2 |
| 47 | 2,94 | 1 | 5 | 245 | 250 | 1,74 | 4 | 23 | 1,65 | 0,2 |
| 45 | 1,41 | 1 | 5 | 245 | 250 | 2,08 | 4 | 23 | 3,57 | 0,2 |
| 28 | 2,96 | 1 | 5 | 245 | 250 | 0,59 | 5 | 23 | 49,99 | 0,3 |
| 4 | 4,76 | 1 | 5 | 245 | 250 | 2,25 | 4 | 23 | 1,73 | 0,3 |
| 7 | 5,00 | 1 | 5 | 245 | 250 | 2,22 | 4 | 23 | 8,01 | 0,3 |
| 17 | 3,67 | 1 | 5 | 245 | 250 | 0,69 | 5 | 23 | 71,08 | 0,3 |
| 13 | 1,15 | 1 | 5 | 245 | 250 | 2,30 | 5 | 23 | 1,61 | 0,4 |
| 21 | 2,27 | 1 | 5 | 245 | 250 | 0,64 | 5 | 23 | 173,42 | 0,4 |
| 41 | 0,36 | 1 | 5 | 245 | 250 | 1,23 | 5 | 23 | 28,91 | 0,4 |
| 26 | 2,79 | 1 | 5 | 245 | 250 | 0,73 | 5 | 23 | 141,55 | 0,5 |
| 29 | 2,90 | 1 | 5 | 245 | 250 | 0,76 | 5 | 23 | 95,39 | 0,5 |
| 12 | 3,05 | 1 | 5 | 245 | 250 | 2,74 | 4 | 23 | 2,93 | 0,5 |
| 20 | 1,09 | 1 | 5 | 245 | 250 | 0,80 | 5 | 23 | 155,97 | 0,5 |
| 19 | 2,00 | 1 | 5 | 245 | 250 | 0,84 | 5 | 23 | 142,09 | 0,6 |
| 24 | 2,29 | 1 | 5 | 245 | 250 | 0,85 | 5 | 23 | 268,21 | 0,6 |
| 16 | 1,19 | 1 | 5 | 245 | 250 | 0,82 | 5 | 23 | 209,74 | 0,6 |
| 22 | 1,38 | 1 | 5 | 245 | 250 | 0,85 | 5 | 23 | 204,69 | 0,6 |
| 5 | 7,29 | 1 | 5 | 245 | 250 | 3,68 | 4 | 23 | 0,98 | 0,6 |
| 23 | 1,08 | 1 | 5 | 245 | 250 | 0,87 | 5 | 23 | 180,11 | 0,6 |
| 10 | 1,41 | 1 | 5 | 245 | 250 | 2,68 | 4 | 23 | 8,82 | 0,7 |
| 27 | 2,29 | 1 | 5 | 245 | 250 | 1,01 | 5 | 23 | 62,96 | 0,7 |
| 30 | 2,33 | 1 | 5 | 245 | 250 | 1,02 | 5 | 23 | 11,57 | 0,7 |
| 9 | 2,71 | 1 | 5 | 245 | 250 | 3,15 | 4 | 23 | 0,26 | 0,7 |
| 15 | 1,44 | 1 | 5 | 245 | 250 | 4,15 | 5 | 23 | 15,19 | 0,8 |
| 42 | 5,91 | 1 | 5 | 245 | 250 | 2,99 | 5 | 23 | 0,75 | 0,9 |
| 6 | 2,73 | 1 | 5 | 245 | 250 | 5,49 | 4 | 23 | 0,97 | 0,9 |
| 11 | 1,88 | 1 | 5 | 245 | 250 | 4,99 | 4 | 23 | 2,22 | 1,0 |
| 2 | -2,55 | 1 | 5 | 245 | 250 | 7,39 | 4 | 23 | 0,3 | 1,0 |

## MO14-OSL2: Age of deposition for OSL on 180-90 µ quartz grains using single aliquot analyses

***OSL Analysis at 220°C / 10 seconds***

| | | |
|---|---|---|
| Number of n: 9 (48) | | |
| Dose Rate ($D_R$) | $D_R$ | 1s% |
| with $H_2O$ 2% | 3,48 | 3,1 |
| with $H_2O$ 7% | 3,30 | 3,1 |
| with $H_2O$ 28% | 2,74 | 3,3 |
| | $D_E$ | 1s% |
| Average $D_E$ | 23,05 | 4,43 |

*Riso Equipment, medium grained $SiO_2$*
*Blue LED's*
***Exponential + Linear fit***

***Valley Of Lakes trench, Mongolia***
***Unit 21 (Silt unit) Block sample***
***pre-MRE***

| | |
|---|---|
| with H2O 2% | |
| Age =$D_E/D_R$ | 6,62 ka |
| ± 1s(%) | 5,41 |
| ± 1s(absolute) | 0,36 ka |
| **with H2O 7%** | |
| **Age =$D_E/D_R$** | **6,99 ka** |
| **± 1s(%)** | **5,41** |
| **± 1s(absolute)** | **0,38 ka** |
| with H2O 28% | |
| Age =$D_E/D_R$ | 8,41 ka |
| ± 1s(%) | 5,52 |
| ± 1s(absolute) | 0,46 ka |
| Difference in $H_2O$ corrected values | |
| | 23,79 % |

***Age shown is the weighted mean***

| Disc | De | Error |
|---|---|---|
| **36** | 16,56 | 1,54 |
| **20** | 18,26 | 1,42 |
| **22** | 19,15 | 1,58 |
| **29** | 19,72 | 1,82 |
| **25** | 20,28 | 1,40 |
| **12** | 22,00 | 1,65 |
| **13** | 22,39 | 1,72 |
| **11** | 22,98 | 1,67 |
| **15** | 24,81 | 1,76 |
| **37** | 30,03 | 5,96 |
| **16** | 30,40 | 7,27 |
| **27** | 38,65 | 4,60 |
| **32** | 40,46 | 5,78 |
| **39** | 44,74 | 8,27 |
| **28** | 52,04 | 6,61 |
| **29** | 56,27 | 8,61 |
| **26** | 56,43 | 7,37 |
| **24** | 59,32 | 7,15 |
| **22** | 64,95 | 8,83 |
| **33** | 65,28 | 9,02 |
| **23** | 66,43 | 8,45 |
| **20** | 67,95 | 12,38 |
| **35** | 68,71 | 14,64 |
| **21** | 69,97 | 5,42 |
| **17** | 71,36 | 11,72 |
| **19** | 77,82 | 14,16 |
| **34** | 82,79 | 13,93 |
| **40** | 83,12 | 21,74 |

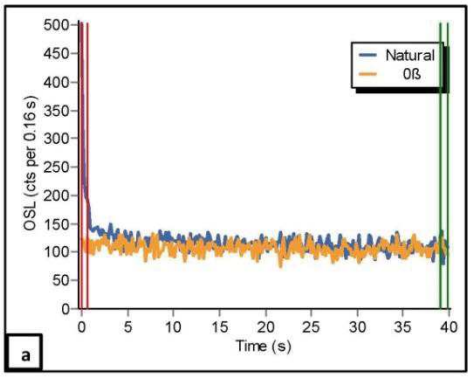


**Disc #39 Decay curve (a) and Growth curve (b)**

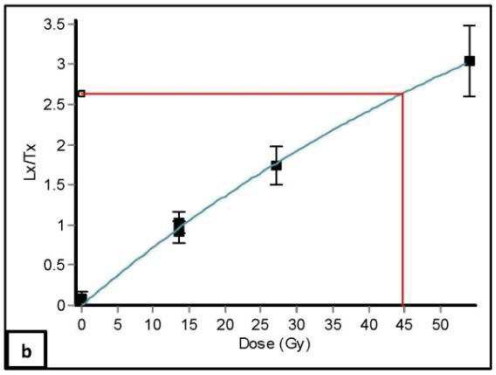


There are TWO distinct populations in this sample (once I threw out a precise outlier). I have chosen to report the 21 Gy population as the most probable fully bleached depositional event.
Maybe there are THREE populations (see radial plots) but only the lowest population is what we care about.

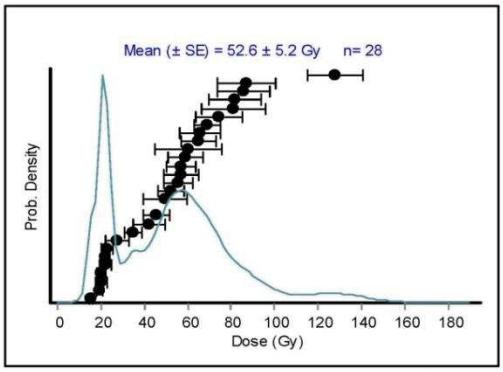

*ALL EQUIVALENT DOSE AND ASSOCIATED DATA*

| Disc # | DE | DE error | N. sig | BG sig | Test Sig | BG T sig | TD error | test dose | residual | test signal | RR1 | RR error | recup |
|---|---|---|---|---|---|---|---|---|---|---|---|---|---|
| 36 | 16,56 | 1,54 | 1579 | 559 | 1406 | 491 | 4,66 | 150 | 568 | 1,01 | 1,09 | 0,13 | 6,44 |
| 30 | 18,26 | 1,42 | 5390 | 161 | 709 | 143 | 5,09 | 20 | 202 | 1,02 | 1,01 | 0,13 | 1,26 |
| 18 | 19,15 | 1,58 | 5012 | 182 | 4440 | 223 | 1,61 | 200 | 702 | 1,46 | 1,07 | 0,08 | 5,89 |
| 14 | 19,72 | 1,82 | 1177 | 150 | 1016 | 171 | 4,03 | 200 | 283 | 1,48 | 1,03 | 0,10 | 7,75 |
| 25 | 20,28 | 1,40 | 9601 | 868 | 3043 | 701 | 2,57 | 50 | 670 | 0,92 | 0,92 | 0,08 | 1,68 |
| 12 | 22,00 | 1,65 | 23675 | 182 | 19435 | 210 | 0,73 | 200 | 561 | 1,56 | 1,06 | 0,08 | 0,96 |
| 13 | 22,39 | 1,72 | 16463 | 220 | 13161 | 204 | 0,89 | 200 | 345 | 1,53 | 1,06 | 0,08 | 0,27 |
| 11 | 22,98 | 1,67 | 16951 | 233 | 13197 | 254 | 0,89 | 200 | 609 | 1,47 | 1,02 | 0,08 | 1,58 |
| 15 | 24,81 | 1,76 | 5860 | 118 | 4363 | 126 | 1,58 | 200 | 230 | 1,76 | 1,05 | 0,08 | 0,95 |
| 37 | 30,03 | 5,96 | 924 | 499 | 717 | 481 | 14,15 | 150 | 546 | 1,21 | 1,03 | 0,25 | 6,05 |
| 16 | 30,40 | 7,27 | 1925 | 640 | 800 | 522 | 12,63 | 50 | 430 | 0,73 | 0,51 | 0,20 | -2,53 |
| 27 | 38,65 | 4,60 | 3909 | 733 | 1174 | 668 | 8,23 | 50 | 507 | 0,88 | 0,92 | 0,15 | 0,34 |
| 32 | 40,46 | 5,78 | 1143 | 429 | 699 | 473 | 14,65 | 150 | 466 | 1,01 | 0,76 | 0,25 | 2,67 |
| 39 | 44,74 | 8,27 | 1413 | 574 | 892 | 507 | 9,41 | 150 | 579 | 1,01 | 0,89 | 0,18 | 3,23 |
| 28 | 52,04 | 6,61 | 5220 | 667 | 1196 | 621 | 7,20 | 50 | 496 | 0,81 | 0,94 | 0,16 | 0,98 |
| 29 | 56,27 | 8,61 | 2987 | 446 | 674 | 406 | 11,86 | 50 | 328 | 0,76 | 1,19 | 0,31 | 0,61 |
| 26 | 56,43 | 7,37 | 3818 | 594 | 979 | 562 | 9,12 | 50 | 470 | 0,87 | 0,91 | 0,18 | 0,51 |
| 24 | 59,32 | 7,15 | 5042 | 723 | 1110 | 672 | 9,32 | 50 | 555 | 0,80 | 0,79 | 0,16 | 2,19 |
| 22 | 64,95 | 8,83 | 5181 | 654 | 967 | 565 | 9,43 | 50 | 458 | 0,78 | 1,00 | 0,20 | 0,84 |
| 33 | 65,28 | 9,02 | 1633 | 513 | 829 | 503 | 10,82 | 150 | 454 | 0,96 | 1,01 | 0,24 | -0,77 |
| 23 | 66,43 | 8,45 | 4898 | 501 | 806 | 429 | 9,05 | 50 | 402 | 0,76 | 0,98 | 0,23 | 0,91 |
| 20 | 67,95 | 12,38 | 3941 | 685 | 907 | 594 | 11,97 | 50 | 503 | 0,80 | 1,33 | 0,55 | 0,72 |
| 35 | 68,71 | 14,64 | 1047 | 418 | 572 | 356 | 13,63 | 150 | 374 | 1,01 | 1,10 | 0,37 | 0,19 |
| 21 | 69,97 | 5,42 | 12389 | 627 | 1410 | 498 | 4,68 | 50 | 421 | 0,72 | 1,02 | 0,14 | 0,18 |
| 17 | 71,36 | 11,72 | 5817 | 568 | 1033 | 495 | 7,07 | 50 | 393 | 0,76 | 1,02 | 0,18 | 0,28 |
| 19 | 77,82 | 14,16 | 4520 | 687 | 909 | 578 | 11,28 | 50 | 530 | 0,84 | 1,44 | 0,31 | 1,56 |
| 34 | 82,79 | 13,93 | 1791 | 463 | 672 | 395 | 11,42 | 150 | 393 | 1,06 | 0,71 | 0,19 | -2,85 |
| 40 | 83,12 | 21,74 | 2654 | 641 | 1206 | 620 | 7,08 | 150 | 610 | 1,07 | 1,01 | 0,15 | 0,95 |
| 38 | 108,68 | 44,29 | 2267 | 504 | 990 | 491 | 7,49 | 150 | 509 | 1,09 | 0,97 | 0,15 | 0,11 |
| 31 | 139,88 | 12,92 | 5991 | 808 | 1510 | 690 | 5,57 | 150 | 727 | 0,88 | 0,92 | 0,14 | 1,94 |

*blue font indicates those measurements that were originally obtained for other tests (preheat, dose recovery, or thermal transfer)

** red font indicates those samples that have only been partially bleached and therefore are not true representations of the depositonal age of the sediment.

**MAM = Minimum Age Model**
**CAM = Central Age Model**
**Equivalent Dose Models**
**MAM:** 18.8 ± 1.7 Gy
**CAM:** 41.4 ± 4.3 Gy
**Weighted Mean:** 23.1 ± 1.03 Gy

Galbraith, R.F., 2010, On plotting OSL equivalent doses. Ancient TL, V. 29, n1.
Graph generated from RadialPlotter-2015.ja
http://radialplotter.london-geochron.com

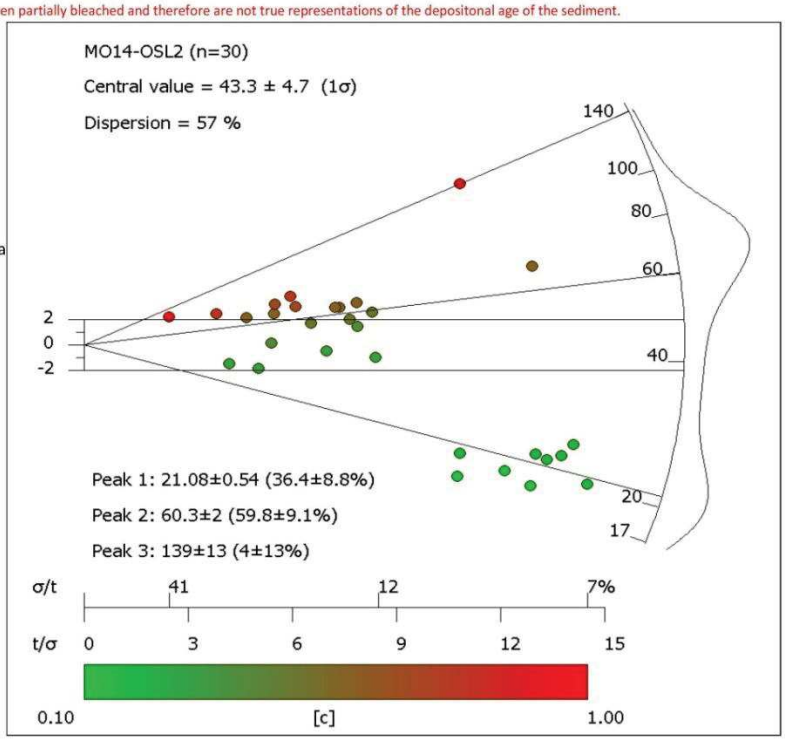


I did not feel that the two largest equivalent doses consistuted a true population so I took then out of the graph and had the program re-draw it. Actually I took the most precise outlier (139.9 ± 12.92 Gy) out of the graph and that changed the population substantially.

| Disc # | recup error | sig1 | sig2 | BG1 | BG2 | ln/tn | fit | options | r chi squared | radial plot |
|---|---|---|---|---|---|---|---|---|---|---|
| 36 | 2,95 | 1 | 5 | 245 | 250 | 1,20 | 4 | 23 | 2,90 | 0,1 |
| 30 | 0,37 | 1 | 5 | 245 | 250 | 9,54 | 5 | 23 | 12,26 | 0,1 |
| 18 | 0,62 | 1 | 5 | 245 | 250 | 1,13 | 5 | 23 | 125,90 | 0,1 |
| 14 | 1,48 | 1 | 5 | 245 | 250 | 1,19 | 5 | 23 | 32,34 | 0,2 |
| 25 | 0,41 | 1 | 5 | 245 | 250 | 4,01 | 5 | 23 | 18,39 | 0,2 |
| 12 | 0,10 | 1 | 5 | 245 | 250 | 1,22 | 5 | 23 | 114,02 | 0,2 |
| 13 | 0,10 | 1 | 5 | 245 | 250 | 1,26 | 5 | 23 | 8,54 | 0,2 |
| 11 | 0,16 | 1 | 5 | 245 | 250 | 1,29 | 5 | 23 | 124,67 | 0,2 |
| 15 | 0,21 | 1 | 5 | 245 | 250 | 1,35 | 5 | 23 | 22,66 | 0,2 |
| 37 | 5,17 | 1 | 5 | 245 | 250 | 1,95 | 4 | 23 | 0,73 | 0,3 |
| 16 | -2,03 | 1 | 5 | 245 | 250 | 8,03 | 5 | 23 | 4,95 | 0,3 |
| 27 | 0,87 | 1 | 5 | 245 | 250 | 7,19 | 5 | 23 | 0,40 | 0,3 |
| 32 | 3,72 | 1 | 5 | 245 | 250 | 2,65 | 5 | 23 | 1,26 | 0,3 |
| 39 | 3,26 | 1 | 5 | 245 | 250 | 2,64 | 4 | 23 | 0,67 | 0,4 |
| 28 | 0,71 | 1 | 5 | 245 | 250 | 8,60 | 4 | 23 | 1,64 | 0,4 |
| 29 | 0,96 | 1 | 5 | 245 | 250 | 11,14 | 1 | 23 | 1,23 | 0,5 |
| 26 | 0,78 | 1 | 5 | 245 | 250 | 8,38 | 5 | 23 | 0,67 | 0,5 |
| 24 | 0,73 | 1 | 5 | 245 | 250 | 11,15 | 1 | 23 | 4,54 | 0,5 |
| 22 | 0,55 | 1 | 5 | 245 | 250 | 14,47 | 1 | 23 | 1,09 | 0,6 |
| 33 | -2,04 | 1 | 5 | 245 | 250 | 3,54 | 1 | 23 | 4,70 | 0,6 |
| 23 | 0,72 | 1 | 5 | 245 | 250 | 14,41 | 1 | 23 | 1,14 | 0,6 |
| 20 | 0,75 | 1 | 5 | 245 | 250 | 14,67 | 1 | 23 | 0,68 | 0,6 |
| 35 | 3,29 | 1 | 5 | 245 | 250 | 4,09 | 1 | 23 | 0,16 | 0,6 |
| 21 | 0,30 | 1 | 5 | 245 | 250 | 15,02 | 1 | 23 | 1,14 | 0,6 |
| 17 | 0,62 | 1 | 5 | 245 | 250 | 11,29 | 4 | 23 | 0,16 | 0,7 |
| 19 | 0,68 | 1 | 5 | 245 | 250 | 17,24 | 1 | 23 | 3,21 | 0,7 |
| 34 | -2,01 | 1 | 5 | 245 | 250 | 6,34 | 1 | 23 | 1,39 | 0,8 |
| 40 | 1,30 | 1 | 5 | 245 | 250 | 3,56 | 4 | 23 | 0,32 | 0,8 |
| 38 | 1,45 | 1 | 5 | 245 | 250 | 3,63 | 4 | 23 | 0,11 | 1,0 |
| 31 | 0,69 | 1 | 5 | 245 | 250 | 7,38 | 5 | 23 | 8,80 | 1,0 |

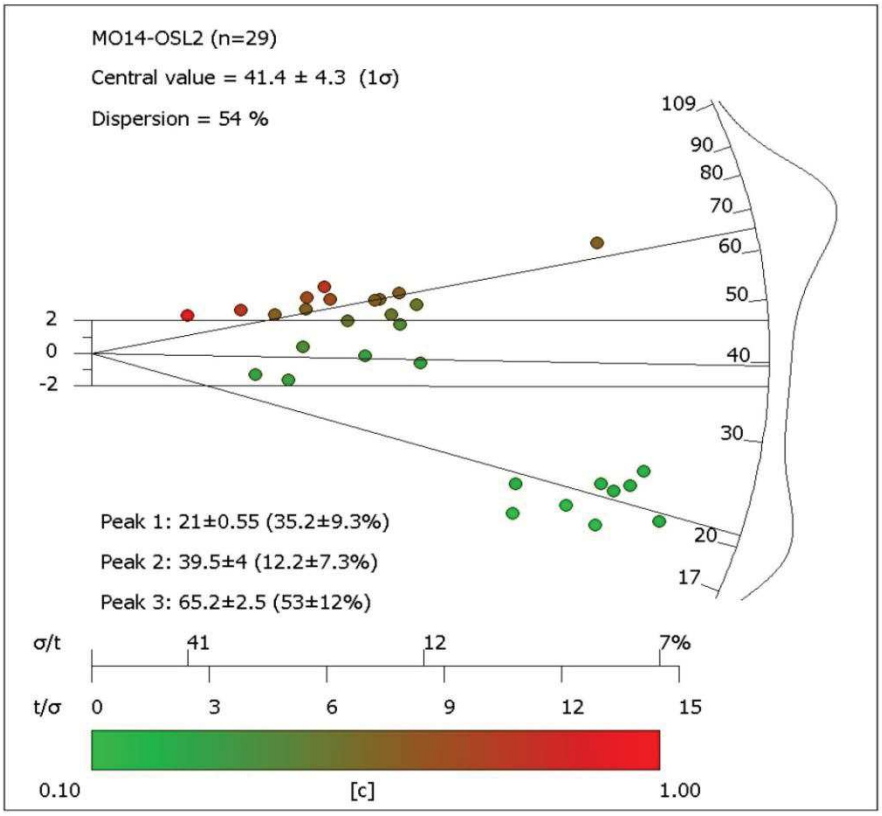

## MO14-OSL3: Age of deposition for OSL on 180-90 µ quartz grains using single aliquot analyses

***OSL Analysis at 220°C / 10 seconds***

| | | |
|---|---|---|
| Number of n: 29 (48) | | |
| | | |
| Dose Rate ($D_R$) | $D_R$ | 1s% |
| with $H_2O$ 2% | 3,36 | 4,3 |
| with $H_2O$ 6% | 3,23 | 4,3 |
| with $H_2O$ 23% | 2,74 | 4,5 |
| | $D_E$ | 1s% |
| Average $D_E$ | 29,19 | 3,47 |

*Riso Equipment, medium grained $SiO_2$*
*Blue LED's*
***Exponential + Linear fit***

***Valley Of Lakes trench, Mongolia***
***Bottom, Unit 40 pre-MRE or pre-PE***
***Block Sample***

| | | |
|---|---|---|
| with H2O 2% | | |
| Age =$D_E/D_R$ | 8,69 | ka |
| ± 1s(%) | 5,53 | |
| ± 1s(absolute) | 0,48 | ka |
| | | |
| **with H2O 6%** | | |
| **Age =$D_E/D_R$** | **9,04** | **ka** |
| **± 1s(%)** | **5,53** | |
| **± 1s(absolute)** | **0,50** | **ka** |
| | | |
| with H2O 23% | | |
| Age =$D_E/D_R$ | 10,65 | ka |
| ± 1s(%) | 5,69 | |
| ± 1s(absolute) | 0,61 | ka |
| | | |
| Difference in $H_2O$ corrected values | | |
| | 20,33 | % |

***Age shown is the weighted mean***

| Disc | De | Error |
|---|---|---|
| **38** | 18,98 | 1,40 |
| **26** | 19,00 | 2,21 |
| **19** | 25,21 | 1,97 |
| **32** | 25,53 | 1,77 |
| **20** | 26,47 | 2,29 |
| **39** | 27,52 | 1,63 |
| **48** | 27,91 | 2,37 |
| **44** | 28,32 | 1,85 |
| **45** | 28,42 | 2,29 |
| **33** | 28,54 | 2,74 |
| **18** | 30,56 | 3,41 |
| **16** | 30,76 | 2,54 |
| **17** | 31,10 | 2,74 |
| **15** | 31,91 | 2,96 |
| **47** | 32,39 | 3,66 |
| **27** | 32,61 | 4,25 |
| **30** | 39,95 | 4,82 |
| **28** | 42,47 | 2,42 |
| **25** | 42,70 | 4,94 |
| **40** | 43,73 | 3,24 |
| **24** | 43,96 | 4,69 |
| **41** | 44,69 | 5,90 |
| **21** | 48,26 | 5,26 |
| **22** | 48,29 | 5,19 |
| **42** | 48,40 | 4,48 |
| **43** | 51,76 | 11,65 |
| **37** | 56,03 | 8,21 |
| **46** | 56,50 | 5,65 |
| **23** | 59,98 | 8,26 |

| | |
|---|---|
| 0,510 | 9,684 |
| 0,205 | 3,890 |
| 0,258 | 6,496 |
| 0,319 | 8,149 |
| 0,191 | 5,048 |
| 0,376 | 10,358 |
| 0,178 | 4,969 |

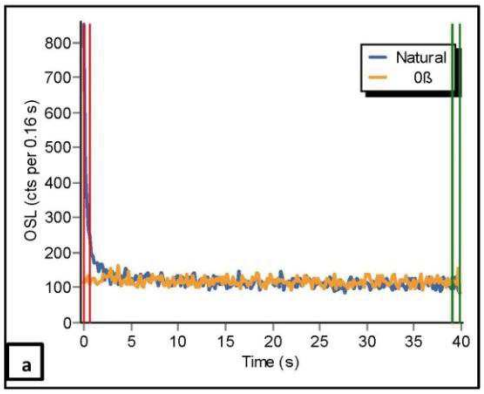


**Disc #24 Decay curve (a) and Growth curve (b)**

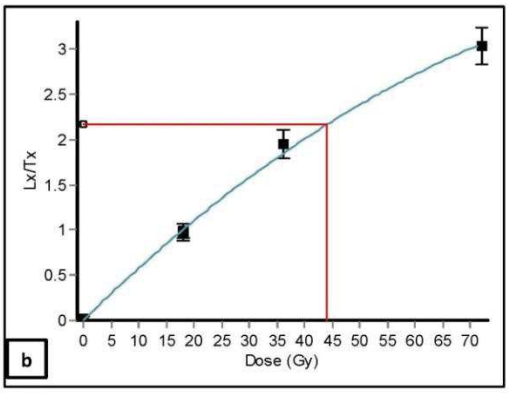


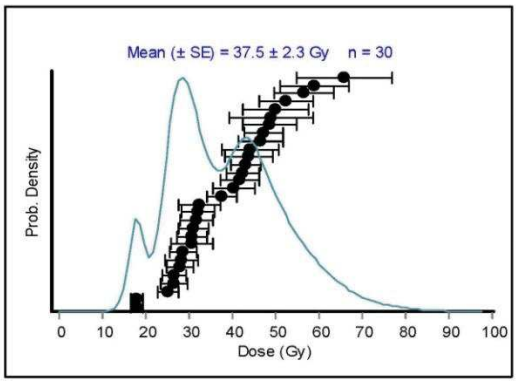

*ALL EQUIVALENT DOSE AND ASSOCIATED DATA*

| Disc # | DE | DE error | N. sig | BG sig | Test Sig | BG T sig | TD error | test dose | residual | test signal | RR1 | RR error | recup 1 |
|---|---|---|---|---|---|---|---|---|---|---|---|---|---|
| 38 | 18,98 | 1,40 | 8489 | 814 | 2868 | 743 | 2,78 | 50 | 758 | 0,90 | 0,93 | 0,09 | 1,65 |
| 26 | 19,00 | 2,21 | 1153 | 475 | 1137 | 435 | 5,52 | 200 | 529 | 1,32 | 1,21 | 0,15 | 1,02 |
| 19 | 25,21 | 1,97 | 15474 | 260 | 11595 | 243 | 0,96 | 200 | 1376 | 1,77 | 1,03 | 0,08 | 3,89 |
| 32 | 25,53 | 1,77 | 2620 | 582 | 928 | 526 | 9,19 | 50 | 674 | 0,94 | 0,86 | 0,20 | 7,30 |
| 20 | 26,47 | 2,29 | 12277 | 261 | 9144 | 256 | 1,09 | 200 | 526 | 1,54 | 1,02 | 0,08 | 1,39 |
| 39 | 27,52 | 1,63 | 3148 | 366 | 782 | 343 | 7,45 | 50 | 391 | 1,07 | 0,97 | 0,17 | 1,94 |
| 48 | 27,91 | 2,37 | 36883 | 387 | 25700 | 394 | 0,64 | 200 | 1135 | 1,42 | 1,02 | 0,08 | 1,44 |
| 44 | 28,32 | 1,85 | 9700 | 687 | 2312 | 583 | 3,06 | 50 | 641 | 0,96 | 1,02 | 0,10 | 1,07 |
| 45 | 28,42 | 2,29 | 92058 | 608 | 62720 | 648 | 0,41 | 200 | 3001 | 1,55 | 1,04 | 0,08 | 1,63 |
| 33 | 28,54 | 2,74 | 3632 | 514 | 1004 | 479 | 7,14 | 50 | 544 | 0,95 | 1,11 | 0,18 | 4,36 |
| 18 | 30,56 | 3,41 | 188129 | 808 | 131202 | 828 | 0,28 | 200 | 6368 | 1,21 | 1,04 | 0,08 | 2,36 |
| 16 | 30,76 | 2,54 | 92305 | 718 | 61037 | 730 | 0,41 | 200 | 3418 | 1,73 | 1,06 | 0,08 | 1,51 |
| 17 | 31,10 | 2,74 | 156712 | 843 | 103280 | 932 | 0,32 | 200 | 4843 | 1,64 | 1,05 | 0,08 | 1,42 |
| 15 | 31,91 | 2,96 | 35364 | 200 | 23363 | 234 | 0,66 | 200 | 1083 | 1,69 | 1,06 | 0,08 | 1,36 |
| 47 | 32,39 | 3,66 | 14650 | 163 | 9910 | 173 | 1,03 | 200 | 339 | 1,36 | 1,01 | 0,08 | 0,81 |
| 27 | 32,61 | 4,25 | 1188 | 508 | 933 | 454 | 7,56 | 200 | 499 | 1,22 | 0,88 | 0,14 | -3,27 |
| 30 | 39,95 | 4,82 | 2037 | 543 | 1351 | 530 | 5,16 | 200 | 679 | 1,31 | 0,99 | 0,12 | 0,63 |
| 28 | 42,47 | 2,42 | 49234 | 997 | 22324 | 943 | 0,71 | 200 | 2431 | 1,45 | 0,98 | 0,07 | 1,82 |
| 25 | 42,70 | 4,94 | 1630 | 570 | 1126 | 583 | 7,40 | 200 | 677 | 1,45 | 1,10 | 0,15 | 2,39 |
| 40 | 43,73 | 3,24 | 9175 | 687 | 1619 | 640 | 4,74 | 50 | 661 | 1,04 | 1,12 | 0,13 | 1,03 |
| 24 | 43,96 | 4,69 | 2167 | 543 | 1293 | 511 | 5,30 | 200 | 601 | 1,30 | 1,01 | 0,12 | 0,37 |
| 41 | 44,69 | 5,90 | 3879 | 638 | 961 | 557 | 9,34 | 50 | 617 | 0,99 | 1,06 | 0,20 | 2,69 |
| 21 | 48,26 | 5,26 | 1457 | 334 | 887 | 349 | 6,38 | 200 | 457 | 1,71 | 1,11 | 0,13 | 2,04 |
| 22 | 48,29 | 5,19 | 1411 | 408 | 855 | 464 | 9,02 | 200 | 508 | 1,36 | 1,09 | 0,20 | 1,05 |
| 42 | 48,40 | 4,48 | 6431 | 678 | 1245 | 603 | 6,51 | 50 | 553 | 0,98 | 0,78 | 0,12 | -0,02 |
| 43 | 51,76 | 11,65 | 2208 | 546 | 703 | 518 | 18,16 | 50 | 457 | 0,86 | 1,01 | 0,34 | 1,22 |
| 37 | 56,03 | 8,21 | 3561 | 548 | 812 | 485 | 10,66 | 50 | 456 | 0,96 | 0,93 | 0,21 | 0,42 |
| 46 | 56,50 | 5,65 | 4020 | 293 | 1772 | 214 | 2,84 | 200 | 216 | 1,27 | 1,04 | 0,09 | 0,85 |
| 23 | 59,98 | 8,26 | 1552 | 432 | 900 | 464 | 8,23 | 200 | 551 | 1,41 | 1,29 | 0,20 | 2,89 |
| 36 | 85,77 | 9,88 | 7425 | 724 | 2104 | 570 | 3,31 | 50 | 1048 | 0,90 | 1,00 | 0,10 | 9,11 |

*blue font indicates those measurements that were originally obtained for other tests (preheat, dose recovery, or thermal transfer)

** red font indicates those samples that have only been partially bleached and therefore are not true representations of the depositonal age of the sediment.

**MAM = Minimum Age Model**
**CAM = Central Age Model**
**Equivalent Dose Models**
**MAM:** 19.0 ± 1.8 Gy
**CAM:** ± Gy
**Weighted Mean:** ± Gy

Galbraith, R.F., 2010, On plotting OSL equivalent doses. Ancient TL, V. 29, n1.
Graph generated from RadialPlotter-2015.ja
http://radialplotter.london-geochron.com

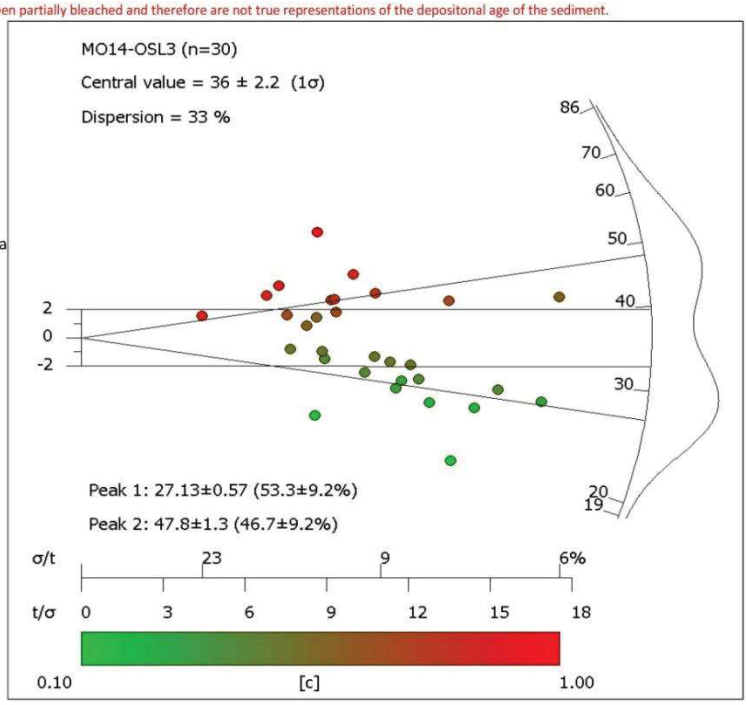

| Disc # | recup error | sig1 | sig2 | BG1 | BG2 | ln/tn | fit | options | r chi squared | radial plot |
|---|---|---|---|---|---|---|---|---|---|---|
| 38 | 0,51 | 1 | 5 | 245 | 250 | 3,74 | 5 | 23 | 11,28 | 0,1 |
| 26 | 2,97 | 1 | 5 | 245 | 250 | 1,02 | 5 | 23 | 2,4 | 0,1 |
| 19 | 0,33 | 1 | 5 | 245 | 250 | 1,34 | 5 | 23 | 227,52 | 0,2 |
| 32 | 1,87 | 1 | 5 | 245 | 250 | 5,89 | 3 | 23 | 20,18 | 0,2 |
| 20 | 0,19 | 1 | 5 | 245 | 250 | 1,35 | 5 | 23 | 67,6 | 0,3 |
| 39 | 0,88 | 1 | 5 | 245 | 250 | 6,68 | 3 | 23 | 5,08 | 0,3 |
| 48 | 0,13 | 1 | 5 | 245 | 250 | 1,44 | 4 | 23 | 90,88 | 0,3 |
| 44 | 0,36 | 1 | 5 | 245 | 250 | 5,55 | 1 | 23 | 7,32 | 0,4 |
| 45 | 0,13 | 1 | 5 | 245 | 250 | 1,47 | 5 | 23 | 290,67 | 0,4 |
| 33 | 1,14 | 1 | 5 | 245 | 250 | 6,37 | 5 | 23 | 17,77 | 0,4 |
| 18 | 0,18 | 1 | 5 | 245 | 250 | 1,44 | 5 | 23 | 333,9 | 0,4 |
| 16 | 0,12 | 1 | 5 | 245 | 250 | 1,52 | 5 | 23 | 283,56 | 0,5 |
| 17 | 0,11 | 1 | 5 | 245 | 250 | 1,52 | 5 | 23 | 313,22 | 0,5 |
| 15 | 0,12 | 1 | 5 | 245 | 250 | 1,52 | 5 | 23 | 206,8 | 0,5 |
| 47 | 0,13 | 1 | 5 | 245 | 250 | 1,49 | 4 | 23 | 23,51 | 0,5 |
| 27 | -3,64 | 1 | 5 | 245 | 250 | 1,6 | 4 | 23 | 0,89 | 0,5 |
| 30 | 1,68 | 1 | 5 | 245 | 250 | 1,85 | 4 | 23 | 0,22 | 0,6 |
| 28 | 0,16 | 1 | 5 | 245 | 250 | 2,26 | 4 | 23 | 101,22 | 0,6 |
| 25 | 1,92 | 1 | 5 | 245 | 250 | 1,91 | 5 | 23 | 2,03 | 0,6 |
| 40 | 0,34 | 1 | 5 | 245 | 250 | 9,1 | 1 | 23 | 5,23 | 0,7 |
| 24 | 1,45 | 1 | 5 | 245 | 250 | 2,17 | 5 | 23 | 0,67 | 0,7 |
| 41 | 0,73 | 1 | 5 | 245 | 250 | 10,02 | 1 | 23 | 5,97 | 0,7 |
| 21 | 1,37 | 1 | 5 | 245 | 250 | 2,03 | 5 | 23 | 3,04 | 0,8 |
| 22 | 2,31 | 1 | 5 | 245 | 250 | 2,24 | 5 | 23 | 3,86 | 0,8 |
| 42 | -0,52 | 1 | 5 | 245 | 250 | 10,14 | 1 | 23 | 0,79 | 0,8 |
| 43 | 1,29 | 1 | 5 | 245 | 250 | 10,57 | 1 | 23 | 1,06 | 0,9 |
| 37 | 0,84 | 1 | 5 | 245 | 250 | 11,42 | 5 | 23 | 0,7 | 0,9 |
| 46 | 0,36 | 1 | 5 | 245 | 250 | 2,52 | 4 | 23 | 3,03 | 0,9 |
| 23 | 1,77 | 1 | 5 | 245 | 250 | 2,39 | 5 | 23 | 5,6 | 0,9 |
| 36 | 1,00 | 1 | 5 | 245 | 250 | 4,86 | 5 | 23 | 129,01 | 1,0 |

## V. Horizontal offset measurements along the Western Bogd Fault

| WBF Reference | Longitude (UTM) | Preferred left-lateral offset (m) | Maximum left-Lateral offset (m) | Minimum left-lateral offset (m) | Obliquity /2 | Marker quality /2 | Image quality /1 | Fault distribution /1 | Measurement qualtity /3 | Scoring /10 |
|---|---|---|---|---|---|---|---|---|---|---|
| 1 | 409530 | 2,1 | 2,8 | 1,5 | 2 | 1 | 1 | 1 | 3 | 8 |
| 2 | 409530 | 11,0 | 12,5 | 8,0 | 2 | 1 | 1 | 1 | 2 | 7 |
| 3 | 409600 | 11,9 | 14,5 | 8,8 | 1 | 2 | 1 | 1 | 2 | 7 |
| 4 | 409590 | 2,8 | 4,2 | 1,7 | 1 | 1 | 1 | 1 | 2 | 6 |
| 5 | 409650 | 3,8 | 5,1 | 2,8 | 1 | 2 | 1 | 1 | 2 | 7 |
| 6 | 409685 | 2,3 | 3,1 | 1,6 | 2 | 1 | 1 | 1 | 2 | 7 |
| 7 | 409710 | 2,3 | 3,0 | 1,7 | 1 | 2 | 1 | 0 | 2 | 6 |
| 8 | 409710 | 4,6 | 6,2 | 3,5 | 0 | 2 | 1 | 0 | 2 | 5 |
| 9 | 409710 | 14,6 | 16,5 | 12,0 | 2 | 1 | 1 | 0 | 1 | 5 |
| 10 | 409735 | 1,5 | 2,3 | 0,9 | 1 | 1 | 1 | 0 | 2 | 5 |
| 11 | 409735 | 4,3 | 6,3 | 3,2 | 2 | 2 | 1 | 0 | 2 | 7 |
| 12 | 409790 | 2,5 | 3,3 | 1,5 | 1 | 2 | 1 | 0 | 3 | 7 |
| 13 | 409795 | 8,8 | 10,2 | 7,0 | 2 | 1 | 1 | 0 | 2 | 6 |
| 14 | 409840 | 8,0 | 9,9 | 6,3 | 1 | 1 | 1 | 0 | 1 | 4 |
| 15 | 409895 | 2,0 | 2,5 | 1,3 | 2 | 2 | 1 | 0 | 3 | 8 |
| 16 | 409895 | 1,8 | 2,7 | 1,3 | 1 | 2 | 1 | 0 | 1 | 5 |
| 17 | 409905 | 6,6 | 7,6 | 5,7 | 2 | 2 | 1 | 0 | 3 | 8 |
| 18 | 409915 | 11,0 | 12,7 | 9,9 | 2 | 1 | 1 | 0 | 2 | 6 |
| 19 | 409928 | 2,0 | 2,8 | 1,4 | 2 | 1 | 1 | 0 | 2 | 6 |
| 20 | 409935 | 3,7 | 4,3 | 2,7 | 2 | 1 | 1 | 0 | 2 | 6 |
| 21 | 409990 | 2,2 | 2,9 | 1,5 | 2 | 2 | 1 | 0 | 2 | 7 |
| 22 | 410030 | 3,6 | 4,6 | 1,8 | 2 | 2 | 1 | 0 | 2 | 7 |
| 23 | 410040 | 1,5 | 2,9 | 0,7 | 2 | 1 | 1 | 0 | 1 | 5 |
| 24 | 410065 | 5,3 | 7,2 | 4,0 | 2 | 1 | 1 | 1 | 2 | 7 |
| 25 | 410080 | 2,3 | 3,5 | 1,3 | 2 | 1 | 1 | 1 | 2 | 7 |
| 26 | 410150 | 25,0 | 32,0 | 18,0 | 0 | 1 | 1 | 1 | 1 | 4 |
| 27 | 410250 | 2,4 | 3,8 | 1,6 | 2 | 1 | 1 | 1 | 2 | 7 |
| 28 | 410275 | 4,6 | 5,9 | 3,4 | 2 | 2 | 1 | 1 | 3 | 9 |
| 29 | 410340 | 2,1 | 3,4 | 1,5 | 1 | 2 | 1 | 1 | 3 | 8 |
| 30 | 410345 | 3,2 | 4,7 | 1,9 | 1 | 2 | 1 | 1 | 2 | 7 |
| 31 | 410400 | 2,7 | 4,3 | 1,3 | 2 | 1 | 1 | 1 | 1 | 6 |
| 32 | 410400 | 9,1 | 13,8 | 5,3 | 2 | 1 | 1 | 1 | 1 | 6 |
| 33 | 410490 | 2,5 | 3,3 | 1,8 | 2 | 2 | 1 | 1 | 3 | 9 |
| 34 | 410510 | 5,7 | 7,0 | 4,2 | 0 | 2 | 1 | 1 | 2 | 6 |
| 35 | 410555 | 4,5 | 6,5 | 2,5 | 2 | 1 | 1 | 1 | 2 | 7 |
| 36 | 410590 | 5,8 | 8,6 | 4,2 | 1 | 1 | 1 | 1 | 1 | 5 |
| 37 | 410600 | 6,1 | 8,3 | 3,6 | 2 | 1 | 1 | 1 | 1 | 6 |
| 38 | 410650 | 18,5 | 22,5 | 13,1 | 2 | 1 | 1 | 1 | 2 | 7 |
| 39 | 410700 | 11,2 | 16,8 | 6,2 | 2 | 1 | 1 | 1 | 2 | 7 |
| 40 | 410725 | 10,3 | 13,4 | 6,8 | 2 | 2 | 1 | 1 | 1 | 7 |
| 41 | 410735 | 2,7 | 4,2 | 1,8 | 2 | 2 | 1 | 1 | 3 | 9 |
| 42 | 411030 | 14,6 | 17,1 | 10,6 | 0 | 1 | 1 | 1 | 1 | 4 |
| 43 | 411030 | 4,0 | 5,8 | 2,2 | 0 | 1 | 1 | 1 | 2 | 5 |
| 44 | 411730 | 10,5 | 14,0 | 8,6 | 0 | 1 | 1 | 1 | 1 | 4 |
| 45 | 412820 | 4,8 | 6,6 | 3,4 | 2 | 2 | 1 | 1 | 2 | 8 |
| 46 | 412870 | 3,2 | 4,8 | 2,6 | 2 | 2 | 1 | 1 | 3 | 9 |
| 47 | 413110 | 3,5 | 4,9 | 2,7 | 1 | 2 | 1 | 1 | 3 | 8 |

## VI. Horizontal offset measurements along the Valley of Lakes Fault

| VOLF Reference | Longitude (UTM) | Preferred left-lateral offset (m) | Maximum left-lateral offset (m) | Minimum left-lateral offset (m) | Sinuosity /2 | Obliquity /3 | Measurement quality /3 | Fault distrubution /2 | Scoring /10 |
|---|---|---|---|---|---|---|---|---|---|
| 1 | 348140 | 16,3 | 20 | 11,6 | 1 | 2 | 1 | 2 | 6 |
| 2 | 349080 | 20,5 | 26,4 | 12,3 | 2 | 2 | 2 | 2 | 8 |
| 3 | 349385 | 4,2 | 5,2 | 3 | 0 | 3 | 3 | 2 | 8 |
| 4 | 349715 | 24,5 | 27,8 | 19,8 | 1 | 2 | 2 | 2 | 7 |
| 5 | 349800 | 16,5 | 21,5 | 13,3 | 1 | 3 | 2 | 2 | 8 |
| 6 | 349850 | 11,3 | 13,7 | 9,6 | 2 | 3 | 3 | 2 | 10 |
| 7 | 350350 | 10,4 | 15,4 | 5,5 | 1 | 3 | 2 | 2 | 8 |
| 8 | 350570 | 3 | 4,7 | 1,6 | 1 | 2 | 2 | 2 | 7 |
| 9 | 351390 | 3,5 | 5,9 | 2,4 | 1 | 2 | 2 | 1 | 6 |
| 10 | 351750 | 30,2 | 38,6 | 23,3 | 1 | 2 | 2 | 2 | 7 |
| 11 | 351980 | 3,7 | 6,3 | 2,7 | 0 | 3 | 3 | 2 | 8 |
| 12 | 352080 | 14,3 | 18,2 | 12,1 | 1 | 2 | 3 | 2 | 8 |
| 13 | 352300 | 32,7 | 36 | 28,7 | 0 | 2 | 3 | 1 | 6 |
| 14 | 352420 | 2,9 | 3,5 | 2,6 | 2 | 3 | 3 | 0 | 8 |
| 15 | 352560 | 15,6 | 21,4 | 11,3 | 2 | 2 | 3 | 0 | 7 |
| 16 | 352650 | 2,4 | 3,6 | 1,2 | 1 | 2 | 2 | 0 | 5 |
| 17 | 352780 | 12,4 | 14,6 | 10,5 | 2 | 3 | 2 | 0 | 7 |
| 18 | 353030 | 8,9 | 11,8 | 6,5 | 1 | 2 | 2 | 1 | 6 |
| 19 | 353300 | 8,9 | 11,5 | 7 | 1 | 1 | 2 | 1 | 5 |
| 20 | 353500 | 4,5 | 7,6 | 2,2 | 2 | 3 | 2 | 1 | 8 |
| 21 | 353600 | 44,8 | 49,8 | 30,1 | 2 | 3 | 2 | 2 | 9 |
| 22 | 353660 | 13,8 | 15,6 | 11,8 | 1 | 3 | 2 | 2 | 8 |
| 23 | 353800 | 2,1 | 3,2 | 1,3 | 1 | 3 | 2 | 1 | 7 |
| 24 | 354380 | 61 | 71 | 52 | 1 | 3 | 3 | 2 | 9 |
| 25 | 354500 | 3 | 4,6 | 1,8 | 2 | 3 | 3 | 2 | 10 |
| 26 | 355390 | 2,7 | 4 | 1,9 | 2 | 2 | 3 | 1 | 8 |
| 27 | 355400 | 9,5 | 13 | 7,2 | 0 | 2 | 1 | 1 | 4 |
| 28 | 355460 | 21,8 | 23,6 | 20,9 | 1 | 2 | 2 | 1 | 6 |
| 29 | 355530 | 2,3 | 2,8 | 1,4 | 1 | 3 | 3 | 2 | 9 |
| 30 | 355640 | 6,9 | 8,4 | 5,2 | 0 | 3 | 2 | 2 | 7 |
| 31 | 355730 | 3,2 | 5,9 | 1,4 | 0 | 3 | 1 | 2 | 6 |
| 32 | 355730 | 9,2 | 12 | 7,3 | 1 | 2 | 2 | 2 | 7 |
| 33 | 355800 | 3,5 | 4,9 | 2,6 | 2 | 3 | 3 | 2 | 10 |
| 34 | 355840 | 2,9 | 5,3 | 1,7 | 1 | 2 | 2 | 1 | 6 |
| 35 | 355960 | 2,1 | 3,1 | 1,1 | 1 | 3 | 2 | 1 | 7 |
| 36 | 356150 | 2,3 | 3,1 | 1 | 1 | 3 | 2 | 1 | 7 |
| 37 | 356260 | 5 | 6 | 2,8 | 0 | 3 | 2 | 1 | 6 |
| 38 | 356530 | 18,2 | 23,5 | 15,4 | 2 | 3 | 3 | 1 | 9 |
| 39 | 356680 | 12,3 | 17,5 | 9 | 1 | 3 | 2 | 0 | 6 |
| 40 | 356750 | 15,2 | 17 | 13,5 | 1 | 3 | 2 | 1 | 7 |
| 41 | 356940 | 9,5 | 11,9 | 6,9 | 2 | 3 | 2 | 2 | 9 |
| 42 | 357200 | 10,1 | 14,5 | 6,6 | 2 | 3 | 2 | 2 | 9 |
| 43 | 357370 | 10,5 | 12,8 | 7,2 | 1 | 3 | 1 | 2 | 7 |
| 44 | 357400 | 5,2 | 6,2 | 4,1 | 1 | 3 | 2 | 2 | 8 |
| 45 | 357500 | 10,4 | 12,4 | 8,8 | 2 | 3 | 3 | 2 | 10 |
| 46 | 357700 | 3,6 | 4,3 | 2,7 | 1 | 3 | 2 | 2 | 8 |
| 47 | 357780 | 3,8 | 4,5 | 3,1 | 1 | 3 | 1 | 2 | 7 |
| 48 | 357860 | 3,3 | 4,3 | 2,7 | 1 | 3 | 2 | 2 | 8 |
| 49 | 358780 | 9,6 | 13,9 | 5,9 | 1 | 2 | 1 | 2 | 6 |
| 50 | 359770 | 1,8 | 3,3 | 0,6 | 0 | 3 | 1 | 2 | 6 |
| 51 | 359910 | 4,6 | 6,6 | 3,8 | 1 | 3 | 1 | 2 | 7 |
| 52 | 359940 | 5 | 6 | 3,9 | 1 | 3 | 3 | 2 | 9 |
| 53 | 359990 | 2,5 | 3,6 | 1,6 | 1 | 2 | 2 | 2 | 7 |

# VII. Horizontal offset measurements along the Eastern Bogd Fault

| Seg. | Lon. (UTM) | Lat. (UTM) | Marker Type | Mark. Obl. | Mark. res. (/2) | Nb. of splay | Scarp 2nd | Offset Pref. (m) | Offset max (m) | Offset min (m) | Δ+ (m) | Δ- (m) | Image type | Image Res. (m) | Image quality (/2) | Total Score (/10) |
|---|---|---|---|---|---|---|---|---|---|---|---|---|---|---|---|---|
| S1 | 507009 | 5003660 | Gully | 3 | 2 | 1 | 0 | 1,8 | 2,3 | 1,2 | 0,5 | 0,7 | Ortho 58 | 0,2 | 2 | 10 |
| S1 | 507600 | 5003400 | Gully | 3 | 2 | 1 | 1 | 3,1 | 3,4 | 3,0 | 0,3 | 0,3 | Ortho 58 | 0,2 | 2 | 9 |
| S1 | 507600 | 5003400 | Abandoned Riser | 2 | 0 | 1 | 1 | 14,3 | 17,9 | 10,1 | 3,6 | 4,2 | Ortho 58 | 0,2 | 2 | 5 |
| S1 | 507642 | 5003382 | Riser | 2 | 0 | 1 | 1 | 1,8 | 2,6 | 1,1 | 0,8 | 0,7 | Ortho 58 | 0,2 | 2 | 5 |
| S1 | 507730 | 5003336 | Riser | 3 | 2 | 1 | 1 | 1,8 | 2,9 | 1,1 | 1,2 | 0,7 | Ortho 58 | 0,2 | 2 | 9 |
| S1 | 507934 | 5003250 | Gully | 2 | 1 | 2 | 1 | 3,9 | 5,3 | 2,8 | 1,3 | 1,1 | Ortho 58 | 0,2 | 2 | 5 |
| S1 | 508006 | 5003219 | Gully | 3 | 1 | 2 | 1 | 1,3 | 1,8 | 1,1 | 0,6 | 0,3 | Ortho 58 | 0,2 | 2 | 7 |
| S1 | 508206 | 5003160 | Talweg | 3 | 0 | 1 | 1 | 2,6 | 4,8 | 1,4 | 2,2 | 1,2 | Ortho 58 | 0,2 | 2 | 7 |
| S1 | 508234 | 5003155 | Gully | 3 | 1 | 2 | 1 | 1,3 | 1,6 | 0,8 | 0,3 | 0,5 | Ortho 58 | 0,2 | 2 | 7 |
| S1 | 508254 | 5003150 | Gully | 3 | 1 | 2 | 1 | 0,7 | 1,0 | 0,5 | 0,3 | 0,3 | Ortho 58 | 0,2 | 2 | 7 |
| S1 | 508456 | 5003112 | Talweg | 3 | 1 | 1 | 1 | 1,3 | 1,6 | 1,1 | 0,3 | 0,3 | Ortho 58 | 0,2 | 2 | 8 |
| S1 | 508690 | 5003092 | Gully | 3 | 1 | 1 | 1 | 3,9 | 4,3 | 3,0 | 0,4 | 0,9 | Ortho 58 | 0,2 | 2 | 8 |
| S1 | 509660 | 5003117 | Fan border | 3 | 1 | 1 | 1 | 2,3 | 3,3 | 1,9 | 1,0 | 0,4 | Ortho 58 | 0,2 | 2 | 8 |
| S1 | 509920 | 5003102 | Gully | 3 | 2 | 1 | 1 | 1,3 | 2,0 | 0,7 | 0,7 | 0,7 | Ortho 58 | 0,2 | 2 | 9 |
| S1 | 509920 | 5003102 | Gully | 3 | 2 | 1 | 1 | 18,4 | 19,0 | 16,9 | 0,9 | 1,5 | Ortho 58 | 0,2 | 2 | 9 |
| S1 | 510090 | 5003067 | Fan apex | 3 | 1 | 1 | 1 | 1,8 | 2,1 | 1,2 | 0,4 | 0,5 | Ortho 58 | 0,2 | 2 | 8 |
| S1 | 510290 | 5003003 | Gully | 3 | 2 | 1 | 1 | 2,0 | 2,5 | 1,6 | 0,5 | 0,4 | Ortho 58 | 0,2 | 2 | 9 |
| S1 | 510470 | 5002948 | Gully | 3 | 1 | 2 | 0 | 2,4 | 2,6 | 2,0 | 0,3 | 0,4 | Ortho 58 | 0,2 | 2 | 8 |
| S1 | 510470 | 5002948 | Gully | 3 | 2 | 2 | 0 | 11,7 | 12,6 | 10,8 | 0,9 | 0,9 | Ortho 58 | 0,2 | 2 | 9 |
| S1 | 510985 | 5002750 | Gully | 3 | 0 | 2 | 1 | 1,5 | 2,2 | 1,3 | 0,7 | 0,3 | Ortho 58 | 0,2 | 2 | 6 |
| S1 | 511300 | 5002770 | Abandoned Riser | 3 | 1 | 2 | 1 | 4,0 | 5,3 | 3,2 | 1,3 | 0,7 | Ortho 58 | 0,2 | 2 | 7 |
| S1 | 511410 | 5002749 | Gully | 3 | 1 | 2 | 1 | 2,1 | 3,1 | 1,4 | 1,0 | 0,7 | Ortho 58 | 0,2 | 2 | 7 |
| S1 | 513130 | 5002885 | Riser | 2 | 0 | 1 | 0 | 2,3 | 3,4 | 1,9 | 1,1 | 0,4 | Ortho 58 | 0,2 | 2 | 6 |
| S1 | 513836 | 5002802 | Gully | 3 | 1 | 1 | 0 | 3,5 | 4,3 | 2,3 | 0,9 | 1,2 | Ortho 58 | 0,2 | 1 | 8 |
| S1 | 514525 | 5002702 | Gully | 3 | 2 | 2 | 0 | 4,5 | 5,0 | 4,0 | 0,6 | 0,5 | Ortho 58 | 0,2 | 2 | 9 |
| S1 | 514675 | 5002688 | Gully | 3 | 2 | 2 | 0 | 3,3 | 3,7 | 2,8 | 0,4 | 0,4 | Ortho 58 | 0,2 | 2 | 9 |
| S1 | 514685 | 5002688 | Gully | 3 | 2 | 2 | 0 | 3,6 | 4,2 | 3,1 | 0,6 | 0,4 | Ortho 58 | 0,2 | 2 | 9 |
| S1 | 514840 | 5002676 | Talweg | 2 | 2 | 1 | 0 | 2,0 | 2,7 | 1,6 | 0,6 | 0,4 | Ortho 58 | 0,2 | 2 | 8 |
| S1 | 514840 | 5002676 | Abandoned | 2 | 1 | 1 | 0 | 14,3 | 16,2 | 13,1 | 1,9 | 1,2 | Ortho 58 | 0,2 | 2 | 7 |

| Seg. | Lon. (UTM) | Lat. (UTM) | Marker Type | Mark. Obl. | Mark. res. (/2) | Nb. of splay | Scarp 2nd | Offset Pref. (m) | Offset max (m) | Offset min (m) | Δ+ (m) | Δ- (m) | Image type | Image Res. (m) | Image quality (/2) | Total Score (/10) |
|---|---|---|---|---|---|---|---|---|---|---|---|---|---|---|---|---|
| S1 | 514986 | 5002664 | Chanel Talweg | 3 | 1 | 1 | 0 | 2,3 | 2,8 | 1,5 | 0,5 | 0,8 | Ortho 58 | 0,2 | 2 | 9 |
| S1 | 514986 | 5002664 | Talweg | 3 | 2 | 1 | 0 | 4,9 | 5,4 | 4,6 | 0,5 | 0,4 | Ortho 58 | 0,2 | 2 | 10 |
| S1 | 514986 | 5002664 | Talweg | 3 | 2 | 1 | 0 | 7,6 | 8,1 | 6,9 | 0,5 | 0,7 | Ortho 58 | 0,2 | 2 | 10 |
| S1 | 514986 | 5002664 | Talweg | 3 | 1 | 1 | 0 | 29,9 | 32,9 | 28,3 | 3,0 | 1,6 | Ortho 58 | 0,2 | 2 | 9 |
| S1 | 514986 | 5002664 | Talweg | 3 | 1 | 1 | 0 | 38,9 | 42,8 | 37,1 | 3,9 | 1,8 | Ortho 58 | 0,2 | 2 | 9 |
| S1 | 515291 | 5002652 | Road | 2 | 2 | 2 | 0 | 4,9 | 5,8 | 4,3 | 0,9 | 0,6 | Ortho 58 | 0,2 | 2 | 7 |
| S1 | 515501 | 5002629 | Riser | 2 | 0 | 2 | 1 | 3,1 | 4,1 | 2,1 | 1,0 | 0,9 | Ortho 58 | 0,2 | 2 | 4 |
| S1 | 515501 | 5002629 | Riser | 2 | 1 | 2 | 1 | 14,7 | 16,0 | 12,5 | 1,4 | 2,1 | Ortho 58 | 0,2 | 2 | 5 |
| S1 | 515560 | 5002620 | Meandre | 1 | 0 | 2 | 1 | 5,4 | 6,7 | 4,0 | 1,3 | 1,4 | Ortho 58 | 0,2 | 2 | 3 |
| S1 | 515560 | 5002620 | Meandre | 2 | 0 | 2 | 1 | 12,1 | 14,7 | 10,3 | 2,5 | 1,8 | Ortho 58 | 0,2 | 2 | 4 |
| S1 | 515711 | 5002584 | Riser | 2 | 2 | 1 | 1 | 2,5 | 3,4 | 2,1 | 0,8 | 0,5 | Ortho 58 | 0,2 | 2 | 7 |
| S1 | 515746 | 5002572 | Gully | 3 | 1 | 4 | 1 | 1,7 | 3,4 | 1,0 | 1,7 | 0,7 | Ortho 58 | 0,2 | 2 | 6 |
| S1 | 516735 | 5002442 | Talweg | 3 | 2 | 2 | 1 | 2,8 | 3,3 | 2,3 | 0,5 | 0,5 | Ortho 58 | 0,2 | 2 | 8 |
| S1 | 516735 | 5002442 | Talweg | 3 | 2 | 2 | 1 | 6,1 | 7,6 | 4,8 | 1,5 | 1,3 | Ortho 58 | 0,2 | 2 | 8 |
| S1 | 516911 | 5002410 | Gully | 3 | 1 | 2 | 1 | 3,3 | 4,9 | 2,2 | 1,5 | 1,1 | Ortho 58 | 0,2 | 2 | 7 |
| S1 | 517290 | 5002343 | Gully | 3 | 1 | 1 | 1 | 2,5 | 4,5 | 1,2 | 2,0 | 1,3 | Ortho 58 | 0,2 | 2 | 8 |
| S1 | 517482 | 5002317 | Gully | 2 | 2 | 3 | 1 | 2,3 | 2,8 | 1,9 | 0,5 | 0,5 | Ortho 58 | 0,2 | 2 | 5 |
| S1 | 517513 | 5002317 | Gully | 2 | 1 | 4 | 1 | 2,5 | 2,7 | 2,0 | 0,3 | 0,4 | Ortho 58 | 0,2 | 2 | 4 |
| S1 | 517540 | 5002317 | Gully | 3 | 1 | 4 | 1 | 2,5 | 3,1 | 1,7 | 0,6 | 0,8 | Ortho 58 | 0,2 | 2 | 6 |
| S1 | 517590 | 5002313 | Gully | 3 | 2 | 1 | 1 | 3,9 | 4,9 | 2,8 | 0,9 | 1,2 | Ortho 58 | 0,2 | 2 | 9 |
| S1 | 517640 | 5002306 | Gully | 3 | 2 | 1 | 1 | 4,4 | 6,2 | 3,2 | 1,8 | 1,2 | Ortho 58 | 0,2 | 2 | 9 |
| S1 | 517651 | 5002306 | Gully | 2 | 1 | 2 | 1 | 4,7 | 5,3 | 3,9 | 0,7 | 0,8 | Ortho 58 | 0,2 | 2 | 5 |
| S1 | 517675 | 5002306 | Gully | 3 | 2 | 1 | 1 | 4,1 | 5,6 | 3,9 | 1,5 | 0,3 | Ortho 58 | 0,2 | 2 | 9 |
| S1 | 517745 | 5002306 | Gully | 3 | 1 | 1 | 1 | 2,8 | 3,2 | 2,3 | 0,4 | 0,5 | Ortho 58 | 0,2 | 2 | 8 |
| S1 | 517765 | 5002311 | Gully | 3 | 2 | 1 | 1 | 3,6 | 4,1 | 3,2 | 0,5 | 0,4 | Ortho 58 | 0,2 | 2 | 9 |
| S1 | 517778 | 5002307 | Gully | 2 | 1 | 1 | 1 | 2,7 | 3,7 | 2,1 | 1,0 | 0,7 | Ortho 58 | 0,2 | 2 | 6 |
| S1 | 517892 | 5002295 | Gully | 2 | 2 | 2 | 1 | 2,3 | 2,9 | 1,8 | 0,6 | 0,5 | Ortho 58 | 0,2 | 2 | 6 |
| S1 | 517955 | 5002295 | Gully | 3 | 2 | 3 | 1 | 2,7 | 2,9 | 1,9 | 0,3 | 0,7 | Ortho 58 | 0,2 | 2 | 7 |
| S1 | 518065 | 5002282 | Riser | 3 | 2 | 2 | 1 | 5,9 | 7,0 | 5,1 | 1,1 | 0,8 | Ortho 58 | 0,2 | 2 | 8 |
| S1 | 518105 | 5002282 | Gully | 1 | 2 | 1 | 1 | 6,8 | 9,9 | 5,9 | 3,1 | 0,8 | Ortho 58 | 0,2 | 2 | 6 |
| S1 | 518140 | 5002282 | Gully | 3 | 2 | 1 | 1 | 3,3 | 4,8 | 2,2 | 1,4 | 1,1 | Ortho 58 | 0,2 | 2 | 9 |
| S1 | 518204 | 5002272 | Riser | 3 | 0 | 1 | 1 | 2,4 | 2,7 | 1,9 | 0,3 | 0,4 | Ortho 58 | 0,2 | 2 | 7 |
| S1 | 51834 | 500225 | Riser | 2 | 1 | 1 | 1 | 2,8 | 4,2 | 2,3 | 1,4 | 0,5 | Ortho | 0,2 | 2 | 6 |

| Seg. | Lon. (UTM) | Lat. (UTM) | Marker Type | Mark. Obl. | Mark. res. (/2) | Nb. of splay | Scarp 2nd | Offset Pref. (m) | Offset max (m) | Offset min (m) | Δ+ (m) | Δ- (m) | Image type | Image Res. (m) | Image quality (/2) | Total Score (/10) |
|---|---|---|---|---|---|---|---|---|---|---|---|---|---|---|---|---|
| | 8 | 7 | | | | | | | | | | | 58 | | | |
| S1 | 518348 | 5002257 | Riser | 3 | 1 | 1 | 1 | 6,1 | 7,3 | 5,3 | 1,1 | 0,9 | Ortho 58 | 0,2 | 2 | 8 |
| S1 | 518756 | 5002171 | Gully | 2 | 1 | 2 | 1 | 2,6 | 4,2 | 1,8 | 1,7 | 0,8 | Ortho 58 | 0,2 | 2 | 5 |
| S1 | 518857 | 5002166 | Gully | 2 | 0 | 3 | 1 | 3,3 | 4,0 | 2,5 | 0,7 | 0,8 | Ortho 58 | 0,2 | 2 | 3 |
| S1 | 518873 | 5002166 | Gully | 2 | 2 | 3 | 1 | 2,9 | 3,5 | 2,7 | 0,6 | 0,3 | Ortho 58 | 0,2 | 2 | 5 |
| S1 | 519134 | 5002174 | Gully | 2 | 0 | 4 | 1 | 1,3 | 1,7 | 1,0 | 0,4 | 0,3 | Ortho 58 | 0,2 | 2 | 3 |
| S1 | 519521 | 5002153 | Gully | 2 | 2 | 1 | 1 | 2,9 | 3,8 | 2,1 | 0,9 | 0,8 | Ortho 58 | 0,2 | 2 | 7 |
| S1 | 519625 | 5002132 | Gully | 3 | 2 | 1 | 1 | 4,0 | 4,5 | 3,6 | 0,5 | 0,4 | Ortho 58 | 0,2 | 2 | 9 |
| S1 | 519660 | 5002132 | Interfluve | 3 | 1 | 1 | 1 | 3,7 | 4,1 | 2,7 | 0,5 | 1,0 | Ortho 58 | 0,2 | 2 | 8 |
| S1 | 519915 | 5002116 | Gully | 2 | 2 | 2 | 1 | 2,1 | 3,0 | 1,5 | 0,9 | 0,7 | Ortho 58 | 0,2 | 2 | 6 |
| S1 | 519870 | 5002092 | Gully | 2 | 0 | 5 | 1 | 5,1 | 7,4 | 3,2 | 2,4 | 1,9 | Ortho 58 | 0,2 | 2 | 3 |
| S1 | 520195 | 5002067 | Riser | 3 | 2 | 1 | 1 | 4,1 | 4,9 | 3,1 | 0,9 | 1,0 | Ortho 58 | 0,2 | 2 | 9 |
| S1 | 520256 | 5002060 | Gully | 2 | 2 | 1 | 1 | 4,0 | 4,5 | 3,3 | 0,5 | 0,7 | Ortho 58 | 0,2 | 2 | 7 |
| S1 | 520268 | 5002060 | Gully | 2 | 2 | 1 | 1 | 3,8 | 4,6 | 3,3 | 0,8 | 0,5 | Ortho 58 | 0,2 | 2 | 7 |
| S1 | 520309 | 5002054 | Gully | 2 | 1 | 2 | 1 | 4,6 | 6,2 | 3,3 | 1,6 | 1,3 | Ortho 58 | 0,2 | 2 | 5 |
| S1 | 520361 | 5002053 | Gully | 2 | 1 | 3 | 1 | 4,5 | 5,2 | 4,3 | 0,7 | 0,3 | Ortho 58 | 0,2 | 2 | 4 |
| S1 | 520388 | 5002052 | Gully | 3 | 2 | 1 | 1 | 4,1 | 4,6 | 3,5 | 0,4 | 0,6 | Ortho 58 | 0,2 | 2 | 9 |
| S1 | 520683 | 5002058 | Gully | 3 | 2 | 2 | 2 | 3,9 | 4,1 | 3,1 | 0,3 | 0,8 | Ortho 58 | 0,2 | 2 | 7 |
| S1 | 520867 | 5002069 | Gully | 3 | 2 | 2 | 2 | 3,7 | 4,4 | 2,8 | 0,7 | 0,9 | Ortho 58 | 0,2 | 2 | 7 |
| S1 | 520943 | 5002059 | Abandoned Chanel | 3 | 1 | 1 | 2 | 4,0 | 4,2 | 3,4 | 0,3 | 0,5 | Ortho 58 | 0,2 | 2 | 7 |
| S1 | 520955 | 5002058 | Gully | 2 | 1 | 1 | 2 | 2,7 | 2,9 | 2,4 | 0,3 | 0,3 | Ortho 58 | 0,2 | 2 | 5 |
| S1 | 520980 | 5002052 | Abandoned Chanel | 2 | 1 | 1 | 2 | 4,1 | 5,7 | 3,6 | 1,7 | 0,5 | Ortho 58 | 0,2 | 2 | 5 |
| S1 | 521010 | 5002050 | River | 1 | 1 | 1 | 2 | 2,6 | 3,1 | 1,2 | 0,5 | 1,5 | Ortho 58 | 0,2 | 2 | 4 |
| S1 | 521092 | 5002030 | Gully | 3 | 2 | 2 | 2 | 4,3 | 6,4 | 3,2 | 2,1 | 1,1 | Ortho 58 | 0,2 | 2 | 7 |
| S1 | 521182 | 5002009 | Gully | 3 | 2 | 1 | 0 | 3,4 | 4,1 | 2,9 | 0,8 | 0,5 | Ortho 58 | 0,2 | 2 | 10 |
| S1 | 521212 | 5002000 | Gully | 3 | 2 | 1 | 0 | 3,6 | 4,2 | 2,8 | 0,6 | 0,8 | Ortho 58 | 0,2 | 2 | 10 |
| S1 | 521272 | 5001986 | River | 3 | 2 | 1 | 0 | 4,5 | 5,2 | 3,8 | 0,8 | 0,7 | Ortho 58 | 0,2 | 2 | 10 |
| S1 | 521272 | 5001972 | River | 3 | 1 | 3 | 0 | 11,3 | 14,0 | 8,8 | 2,7 | 2,5 | Ortho 58 | 0,2 | 2 | 7 |
| S1 | 521479 | 5001940 | Gully | 3 | 1 | 2 | 0 | 3,8 | 4,6 | 2,8 | 0,8 | 1,0 | Ortho 58 | 0,2 | 2 | 8 |
| S1 | 521523 | 5001937 | Gully | 3 | 2 | 1 | 0 | 2,2 | 2,9 | 1,5 | 0,7 | 0,7 | Ortho 58 | 0,2 | 2 | 10 |
| S1 | 521550 | 5001935 | Gully | 3 | 0 | 1 | 0 | 4,2 | 5,3 | 2,9 | 1,1 | 1,3 | Ortho 58 | 0,2 | 2 | 8 |
| S1 | 521590 | 5001928 | Riser | 2 | 1 | 1 | 0 | 3,2 | 4,4 | 2,1 | 1,2 | 1,2 | Ortho 58 | 0,2 | 2 | 7 |
| S1 | 52162 | 500192 | Gully | 3 | 2 | 2 | 0 | 3,2 | 3,6 | 2,7 | 0,4 | 0,5 | Ortho | 0,2 | 2 | 9 |

| Seg. | Lon. (UTM) | Lat. (UTM) | Marker Type | Mark. Obl. | Mark. res. (/2) | Nb. of splay | Scarp 2nd | Offset Pref. (m) | Offset max (m) | Offset min (m) | Δ+ (m) | Δ- (m) | Image type | Image Res. (m) | Image quality (/2) | Total Score (/10) |
|---|---|---|---|---|---|---|---|---|---|---|---|---|---|---|---|---|
| | 7 | 8 | | | | | | | | | | | 58 | | | |
| S1 | 521670 | 5001923 | Gully | 3 | 1 | 1 | 0 | 4,8 | 6,7 | 4,3 | 1,9 | 0,5 | Ortho 58 | 0,2 | 2 | 9 |
| S1 | 521714 | 5001920 | Gully | 3 | 1 | 1 | 0 | 4,7 | 7,0 | 1,9 | 2,3 | 2,8 | Ortho 58 | 0,2 | 2 | 9 |
| S1 | 521828 | 5001904 | Riser | 1 | 1 | 1 | 0 | 5,1 | 6,0 | 3,5 | 0,9 | 1,6 | Ortho 58 | 0,2 | 2 | 6 |
| S1 | 521860 | 5001900 | Riser | 2 | 1 | 1 | 0 | 3,7 | 4,2 | 2,5 | 0,5 | 1,2 | Ortho 58 | 0,2 | 2 | 7 |
| S1 | 521870 | 5001898 | Gully | 2 | 2 | 1 | 0 | 3,0 | 3,6 | 2,0 | 0,7 | 0,9 | Ortho 58 | 0,2 | 2 | 8 |
| S1 | 521885 | 5001897 | Riser | 3 | 2 | 1 | 1 | 3,4 | 4,1 | 3,2 | 0,7 | 0,3 | Ortho 58 | 0,2 | 2 | 9 |
| S1 | 521904 | 5001894 | Riser | 3 | 1 | 1 | 1 | 5,6 | 6,2 | 4,5 | 0,6 | 1,1 | Ortho 58 | 0,2 | 2 | 8 |
| S1 | 521970 | 5001887 | Gully | 3 | 2 | 2 | 1 | 3,7 | 4,4 | 3,4 | 0,7 | 0,4 | Ortho 58 | 0,2 | 2 | 8 |
| S1 | 522002 | 5001883 | Gully | 2 | 1 | 2 | 1 | 2,7 | 4,0 | 2,3 | 1,2 | 0,4 | Ortho 58 | 0,2 | 2 | 5 |
| S1 | 522026 | 5001878 | Gully | 3 | 2 | 3 | 1 | 2,1 | 2,6 | 1,6 | 0,5 | 0,5 | Ortho 58 | 0,2 | 2 | 7 |
| S1 | 522026 | 5001878 | Gully | 3 | 2 | 3 | 1 | 11,3 | 12,6 | 10,2 | 1,3 | 1,1 | Ortho 58 | 0,2 | 2 | 7 |
| S1 | 522222 | 5001843 | Gully | 3 | 2 | 3 | 2 | 2,3 | 2,6 | 1,7 | 0,3 | 0,7 | Ortho 58 | 0,2 | 2 | 6 |
| S1 | 522259 | 5001839 | Gully | 3 | 2 | 2 | 2 | 1,9 | 2,3 | 1,5 | 0,4 | 0,4 | Ortho 58 | 0,2 | 2 | 7 |
| S1 | 522307 | 5001832 | Gully | 3 | 1 | 2 | 1 | 3,2 | 3,7 | 2,4 | 0,5 | 0,8 | Ortho 58 | 0,2 | 2 | 7 |
| S1 | 522334 | 5001824 | Gully | 2 | 1 | 4 | 0 | 4,1 | 6,2 | 3,0 | 2,1 | 1,1 | Ortho 58 | 0,2 | 2 | 5 |
| S1 | 522427 | 5001812 | Gully | 2 | 1 | 4 | 0 | 3,7 | 4,3 | 3,3 | 0,6 | 0,3 | Ortho 58 | 0,2 | 2 | 5 |
| S1 | 522478 | 5001804 | Gully | 2 | 1 | 5 | 0 | 4,5 | 6,1 | 3,2 | 1,7 | 1,3 | Ortho 58 | 0,2 | 2 | 5 |
| S1 | 522573 | 5002050 | Gully | 3 | 1 | 2 | 1 | 2,4 | 4,3 | 1,9 | 2,0 | 0,4 | Ortho 58 | 0,2 | 2 | 7 |
| S1 | 522655 | 5002060 | Riser | 3 | 2 | 2 | 1 | 1,7 | 2,7 | 1,2 | 0,9 | 0,6 | Ortho 58 | 0,2 | 2 | 8 |
| S1 | 522706 | 5002060 | Riser | 3 | 1 | 2 | 1 | 2,8 | 3,9 | 2,4 | 1,1 | 0,4 | Ortho 58 | 0,2 | 2 | 7 |
| S1 | 522773 | 5002053 | Gully | 2 | 1 | 3 | 1 | 2,6 | 3,7 | 2,0 | 1,1 | 0,6 | Ortho 58 | 0,2 | 2 | 4 |
| S1 | 523106 | 5001941 | Riser | 3 | 2 | 1 | 1 | 2,8 | 3,2 | 2,0 | 0,4 | 0,8 | Ortho 58 | 0,2 | 2 | 9 |
| S1 | 523600 | 5001802 | Riser | 3 | 2 | 2 | 1 | 2,5 | 3,0 | 2,2 | 0,4 | 0,3 | Ortho 58 | 0,2 | 2 | 8 |
| S1 | 523631 | 5001797 | Gully | 2 | 1 | 4 | 0 | 2,0 | 2,4 | 1,6 | 0,4 | 0,4 | Ortho 58 | 0,2 | 2 | 5 |
| S1 | 523891 | 5001742 | Gully | 3 | 1 | 1 | 1 | 1,6 | 2,7 | 1,2 | 1,1 | 0,5 | Ortho 58 | 0,2 | 2 | 8 |
| S1 | 523950 | 5001729 | Gully | 2 | 1 | 1 | 1 | 9,7 | 10,4 | 8,6 | 0,6 | 1,2 | Ortho 58 | 0,2 | 2 | 6 |
| S1 | 523950 | 5001729 | Gully | 1 | 1 | 1 | 1 | 16,0 | 17,7 | 15,5 | 1,6 | 0,9 | Ortho 58 | 0,2 | 2 | 5 |
| S1 | 524040 | 5001714 | Gully | 2 | 0 | 2 | 1 | 1,9 | 3,2 | 1,6 | 1,2 | 0,3 | Ortho 58 | 0,2 | 2 | 4 |
| S1 | 524040 | 5001714 | Gully | 3 | 2 | 1 | 1 | 18,7 | 19,4 | 16,9 | 0,9 | 1,8 | Ortho 58 | 0,2 | 2 | 9 |
| S1 | 524100 | 5001712 | Gully | 3 | 1 | 2 | 1 | 1,9 | 2,8 | 1,3 | 0,9 | 0,6 | Ortho 58 | 0,2 | 2 | 7 |
| S1 | 524118 | 5001708 | Gully | 2 | 1 | 2 | 1 | 3,4 | 4,4 | 1,7 | 1,0 | 1,7 | Ortho 58 | 0,2 | 2 | 5 |
| S1 | 524264 | 5001471 | Gully | 3 | 1 | 1 | 1 | 4,2 | 5,8 | 2,6 | 1,6 | 1,6 | Ortho 58 | 0,2 | 2 | 8 |
| S1 | 52432 | 500146 | Riser | 3 | 1 | 1 | 1 | 4,3 | 5,5 | 3,5 | 1,2 | 0,8 | Ortho | 0,2 | 2 | 8 |

| Seg. | Lon. (UTM) | Lat. (UTM) | Marker Type | Mark. Obl. | Mark. res. (/2) | Nb. of splay | Scarp 2nd | Offset Pref. (m) | Offset max (m) | Offset min (m) | Δ+ (m) | Δ- (m) | Image type | Image Res. (m) | Image quality (/2) | Total Score (/10) |
|---|---|---|---|---|---|---|---|---|---|---|---|---|---|---|---|---|
| | 2 | 0 | | | | | | | | | | | 58 | | | |
| S1 | 524322 | 5001460 | Riser | 3 | 2 | 1 | 1 | 13,5 | 16,3 | 10,3 | 2,8 | 3,2 | Ortho 58 | 0,2 | 2 | 9 |
| S1 | 524375 | 5001447 | Gully | 3 | 2 | 1 | 0 | 5,4 | 5,7 | 4,6 | 0,4 | 0,8 | Ortho 58 | 0,2 | 2 | 10 |
| S1 | 524483 | 5001419 | Gully | 3 | 2 | 1 | 1 | 4,2 | 5,0 | 3,5 | 0,8 | 0,8 | Ortho 58 | 0,2 | 2 | 9 |
| S1 | 524513 | 5001419 | Gully | 3 | 1 | 1 | 1 | 4,2 | 5,9 | 3,4 | 1,7 | 0,8 | Ortho 58 | 0,2 | 2 | 8 |
| S1 | 524630 | 5001390 | Gully | 2 | 0 | 4 | 2 | 3,2 | 4,6 | 1,9 | 1,5 | 1,3 | Ortho 58 | 0,2 | 2 | 2 |
| S1 | 524828 | 5001368 | Gully | 2 | 1 | 3 | 1 | 4,6 | 6,2 | 3,5 | 1,6 | 1,1 | Ortho 58 | 0,2 | 2 | 4 |
| S1 | 524858 | 5001368 | Gully | 2 | 1 | 5 | 1 | 3,4 | 4,0 | 2,3 | 0,6 | 1,1 | Ortho 58 | 0,2 | 2 | 4 |
| S1 | 524898 | 5001367 | Riser | 2 | 0 | 4 | 1 | 2,5 | 3,8 | 2,1 | 1,3 | 0,4 | Ortho 58 | 0,2 | 2 | 3 |
| S1 | 524940 | 5001366 | Gully | 2 | 0 | 5 | 1 | 6,4 | 7,7 | 3,8 | 1,4 | 2,6 | Ortho 58 | 0,2 | 2 | 3 |
| S1 | 524960 | 5001363 | Riser | 2 | 2 | 2 | 1 | 8,3 | 9,2 | 6,2 | 0,9 | 2,1 | Ortho 58 | 0,2 | 2 | 6 |
| S1 | 525015 | 5001361 | Gully | 2 | 1 | 3 | 1 | 4,2 | 5,9 | 2,5 | 1,7 | 1,7 | Ortho 58 | 0,2 | 2 | 4 |
| S1 | 526151 | 5001594 | Gully | 2 | 2 | 2 | 1 | 2,4 | 2,9 | 1,8 | 0,5 | 0,6 | Ortho 58 | 0,2 | 2 | 6 |
| S1 | 526418 | 5001609 | Gully | 3 | 1 | 1 | 0 | 2,4 | 3,0 | 1,8 | 0,7 | 0,6 | Ortho 58 | 0,2 | 2 | 9 |
| S1 | 526520 | 5001611 | Riser | 2 | 2 | 1 | 0 | 3,3 | 3,6 | 2,7 | 0,4 | 0,6 | Ortho 58 | 0,2 | 2 | 8 |
| S1 | 526595 | 5001607 | Gully | 3 | 1 | 1 | 0 | 3,9 | 4,5 | 3,5 | 0,6 | 0,4 | Ortho 58 | 0,2 | 2 | 9 |
| S1 | 526655 | 5001602 | Riser | 2 | 2 | 1 | 1 | 4,9 | 5,3 | 4,3 | 0,4 | 0,6 | Ortho 58 | 0,2 | 2 | 7 |
| S1 | 527000 | 5001588 | Gully | 3 | 2 | 1 | 0 | 5,1 | 5,6 | 4,0 | 0,5 | 1,1 | Ortho 58 | 0,2 | 2 | 10 |
| S1 | 527170 | 5001580 | Gully | 1 | 1 | 1 | 0 | 6,5 | 7,9 | 4,5 | 1,4 | 2,0 | Ortho 58 | 0,2 | 2 | 6 |
| S1 | 527352 | 5001578 | Gully | 2 | 2 | 1 | 1 | 3,0 | 3,8 | 2,4 | 0,8 | 0,6 | Ortho 58 | 0,2 | 2 | 7 |
| S1 | 527662 | 5001570 | Gully | 2 | 1 | 2 | 1 | 5,2 | 6,5 | 3,8 | 1,3 | 1,4 | Ortho 58 | 0,2 | 2 | 5 |
| S1 | 528030 | 5001533 | Gully | 2 | 0 | 1 | 1 | 2,1 | 3,6 | 1,3 | 1,6 | 0,8 | Ortho 58 | 0,2 | 2 | 5 |
| S1 | 528090 | 5001475 | Gully | 2 | 0 | 2 | 1 | 1,6 | 1,9 | 1,2 | 0,3 | 0,4 | Ortho 58 | 0,2 | 2 | 4 |
| S1 | 528384 | 5001526 | River | 2 | 2 | 1 | 1 | 5,8 | 6,3 | 5,3 | 0,5 | 0,5 | Ortho 58 | 0,2 | 2 | 7 |
| S1 | 528430 | 5001470 | Gully | 3 | 1 | 2 | 1 | 3,6 | 4,4 | 2,6 | 0,9 | 0,9 | Ortho 58 | 0,2 | 2 | 7 |
| S1 | 528800 | 5001410 | Gully | 1 | 2 | 1 | 1 | 11,6 | 13,4 | 10,7 | 1,7 | 0,9 | Ortho 58 | 0,2 | 2 | 6 |
| S1 | 529740 | 5001342 | Gully | 3 | 2 | 1 | 1 | 3,5 | 4,2 | 2,5 | 0,7 | 1,0 | Ortho 58 | 0,2 | 2 | 9 |
| S1 | 530432 | 5001311 | Riser | 2 | 2 | 1 | 1 | 3,6 | 4,1 | 2,8 | 0,5 | 0,7 | Ortho 58 | 0,2 | 2 | 7 |
| S1 | 530482 | 5001305 | Riser | 1 | 1 | 1 | 1 | 3,0 | 3,9 | 1,8 | 0,9 | 1,1 | Ortho 58 | 0,2 | 2 | 5 |
| S1 | 530563 | 5001297 | Riser | 1 | 1 | 1 | 1 | 4,3 | 4,8 | 2,5 | 0,5 | 1,8 | Ortho 58 | 0,2 | 2 | 5 |
| S1 | 530616 | 5001289 | Riser | 2 | 2 | 1 | 1 | 3,8 | 4,7 | 2,4 | 0,9 | 1,4 | Ortho 58 | 0,2 | 2 | 7 |
| S1 | 530700 | 5001278 | Riser | 2 | 2 | 1 | 1 | 4,6 | 5,7 | 3,7 | 1,1 | 0,9 | Ortho 58 | 0,2 | 2 | 7 |
| S1 | 530712 | 5001277 | Gully | 1 | 1 | 1 | 1 | 2,5 | 3,1 | 1,9 | 0,6 | 0,6 | Ortho 58 | 0,2 | 2 | 5 |
| S1 | 53082 | 500111 | Gully | 2 | 1 | 1 | 0 | 4,4 | 5,8 | 4,1 | 1,4 | 0,3 | Ortho | 0,2 | 2 | 7 |

| Seg. | Lon. (UTM) | Lat. (UTM) | Marker Type | Mark. Obl. | Mark. res. (/2) | Nb. of splay | Scarp 2nd | Offset Pref. (m) | Offset max (m) | Offset min (m) | Δ+ (m) | Δ- (m) | Image type | Image Res. (m) | Image quality (/2) | Total Score (/10) |
|---|---|---|---|---|---|---|---|---|---|---|---|---|---|---|---|---|
| | 4 | 0 | | | | | | | | | | | 58 | | | |
| S1 | 530977 | 5001101 | Gully | 3 | 1 | 1 | 1 | 1,7 | 2,7 | 1,3 | 1,0 | 0,4 | Ortho 58 | 0,2 | 2 | 8 |
| S1 | 531005 | 5001092 | Gully | 3 | 1 | 5 | 1 | 4,4 | 5,1 | 4,1 | 0,8 | 0,3 | Ortho 58 | 0,2 | 2 | 6 |
| S1 | 531131 | 5001220 | Gully | 2 | 1 | 4 | 0 | 5,3 | 6,6 | 3,5 | 1,3 | 1,8 | Ortho 58 | 0,2 | 2 | 5 |
| S1 | 531271 | 5001191 | Gully | 2 | 2 | 5 | 2 | 5,0 | 5,6 | 4,5 | 0,7 | 0,5 | Ortho 58 | 0,2 | 2 | 4 |
| S1 | 531373 | 5001176 | Gully | 2 | 1 | 2 | 1 | 1,3 | 1,5 | 1,1 | 0,3 | 0,3 | Ortho 58 | 0,2 | 2 | 5 |
| S1 | 531591 | 5001166 | Gully | 2 | 1 | 1 | 0 | 3,5 | 4,6 | 2,9 | 1,0 | 0,6 | Ortho 58 | 0,2 | 2 | 7 |
| S1 | 531990 | 5001155 | Gully | 3 | 2 | 1 | 1 | 4,4 | 5,1 | 3,8 | 0,7 | 0,7 | Ortho 58 | 0,2 | 2 | 9 |
| S1 | 532054 | 5001151 | Gully | 3 | 1 | 1 | 1 | 3,1 | 3,9 | 1,4 | 0,7 | 1,7 | Ortho 58 | 0,2 | 2 | 8 |
| S1 | 532365 | 5001126 | Gully | 3 | 2 | 1 | 1 | 2,7 | 3,0 | 2,5 | 0,3 | 0,3 | Ortho 58 | 0,2 | 2 | 9 |
| S1 | 532812 | 5001082 | Gully | 2 | 2 | 2 | 1 | 3,8 | 5,0 | 2,8 | 1,2 | 1,0 | Ortho 58 | 0,2 | 2 | 6 |
| S1 | 532845 | 5001083 | Gully | 2 | 1 | 1 | 1 | 2,8 | 3,3 | 1,7 | 0,5 | 1,0 | Ortho 58 | 0,2 | 2 | 6 |
| S1 | 532890 | 5001070 | Gully | 2 | 0 | 1 | 1 | 2,1 | 2,4 | 1,6 | 0,3 | 0,5 | Ortho 58 | 0,2 | 2 | 5 |
| S1 | 533303 | 5000897 | Gully | 2 | 1 | 4 | 1 | 3,5 | 4,4 | 2,8 | 0,9 | 0,7 | Ortho 58 | 0,2 | 2 | 4 |
| S1 | 533303 | 5000897 | Gully | 2 | 1 | 4 | 1 | 7,0 | 8,2 | 6,4 | 1,2 | 0,7 | Ortho 58 | 0,2 | 2 | 4 |
| S1 | 533675 | 5000963 | Gully | 2 | 1 | 8 | 0 | 4,1 | 5,1 | 3,6 | 1,0 | 0,5 | Ortho 58 | 0,2 | 2 | 5 |
| S1 | 534170 | 5000875 | Talweg | 2 | 1 | 3 | 0 | 3,1 | 3,7 | 2,7 | 0,6 | 0,5 | Ortho 58 | 0,3 | 2 | 5 |
| S1 | 534216 | 5000853 | Talweg | 2 | 1 | 1 | 0 | 2,3 | 3,0 | 1,8 | 0,7 | 0,5 | Ortho 58 | 0,3 | 2 | 7 |
| S1 | 534248 | 5000841 | Talweg | 2 | 1 | 1 | 0 | 3,1 | 4,2 | 2,2 | 1,1 | 0,8 | Ortho 58 | 0,3 | 2 | 7 |
| S1 | 534268 | 5000832 | Talweg | 3 | 1 | 1 | 0 | 2,5 | 3,2 | 1,7 | 0,6 | 0,8 | Ortho 58 | 0,3 | 2 | 9 |
| S1 | 534297 | 5000818 | Talweg | 3 | 2 | 2 | 0 | 6,3 | 7,7 | 5,5 | 1,4 | 0,8 | Ortho 58 | 0,3 | 2 | 9 |
| S1 | 534311 | 5000814 | Talweg | 3 | 2 | 2 | 0 | 3,6 | 4,1 | 3,1 | 0,5 | 0,5 | Ortho 58 | 0,3 | 2 | 9 |
| S1 | 534316 | 5000811 | Talweg | 3 | 2 | 4 | 0 | 7,2 | 8,8 | 6,4 | 1,5 | 0,8 | Ortho 58 | 0,3 | 2 | 8 |
| R1 | 534424 | 5000812 | Talweg | 3 | 1 | 1 | 0 | 4,7 | 6,2 | 3,5 | 1,5 | 1,2 | Ortho 58 | 0,3 | 2 | 9 |
| R1 | 534450 | 5000809 | Talweg | 3 | 2 | 4 | 0 | 5,6 | 6,3 | 4,7 | 0,7 | 0,9 | Ortho 58 | 0,3 | 2 | 8 |
| R1 | 534505 | 5000808 | Talweg | 2 | 0 | 2 | 0 | 2,1 | 2,8 | 1,6 | 0,7 | 0,5 | Ortho 58 | 0,3 | 2 | 5 |
| R1 | 534520 | 5000806 | Talweg | 2 | 1 | 1 | 0 | 3,6 | 4,5 | 3,2 | 0,9 | 0,4 | Ortho 58 | 0,3 | 2 | 7 |
| R1 | 534551 | 5000803 | Talweg | 3 | 1 | 1 | 0 | 2,4 | 2,7 | 2,0 | 0,3 | 0,5 | Ortho 58 | 0,3 | 2 | 9 |
| R1 | 534551 | 5000803 | Talweg | 3 | 2 | 1 | 0 | 4,6 | 5,6 | 3,8 | 1,0 | 0,7 | Ortho 58 | 0,3 | 2 | 10 |
| R1 | 534562 | 5000800 | Talweg | 2 | 1 | 1 | 0 | 3,9 | 5,0 | 3,4 | 1,1 | 0,5 | Ortho 58 | 0,3 | 2 | 7 |
| R1 | 534580 | 5000800 | Talweg | 3 | 2 | 1 | 0 | 3,3 | 4,2 | 3,0 | 0,8 | 0,3 | Ortho 58 | 0,3 | 2 | 10 |
| R1 | 534600 | 5000800 | Talweg | 3 | 2 | 1 | 0 | 2,9 | 3,5 | 1,9 | 0,5 | 1,0 | Ortho 58 | 0,3 | 2 | 10 |
| R1 | 534600 | 5000800 | Riser | 3 | 1 | 1 | 0 | 5,2 | 6,2 | 4,6 | 1,0 | 0,6 | Ortho 58 | 0,3 | 2 | 9 |
| R1 | 53462 | 500080 | Talweg | 3 | 2 | 3 | 0 | 2,4 | 3,7 | 2,0 | 1,2 | 0,4 | Ortho | 0,3 | 2 | 8 |

| Seg. | Lon. (UTM) | Lat. (UTM) | Marker Type | Mark. Obl. | Mark. res. (/2) | Nb. of splay | Scarp 2nd | Offset Pref. (m) | Offset max (m) | Offset min (m) | Δ+ (m) | Δ- (m) | Image type | Image Res. (m) | Image quality (/2) | Total Score (/10) |
|---|---|---|---|---|---|---|---|---|---|---|---|---|---|---|---|---|
| | 6 | 0 | | | | | | | | | | | 58 | | | |
| R1 | 534626 | 5000800 | Talweg | 3 | 1 | 1 | 0 | 9,6 | 10,9 | 7,8 | 1,3 | 1,8 | Ortho 58 | 0,3 | 2 | 9 |
| R1 | 534640 | 5000799 | Talweg | 2 | 2 | 2 | 1 | 1,6 | 1,8 | 1,3 | 0,3 | 0,4 | Ortho 58 | 0,3 | 2 | 6 |
| R1 | 534640 | 5000799 | Talweg | 3 | 2 | 2 | 1 | 3,6 | 4,2 | 3,1 | 0,6 | 0,4 | Ortho 58 | 0,3 | 2 | 8 |
| R1 | 534660 | 5000800 | Talweg | 3 | 2 | 2 | 1 | 2,1 | 2,4 | 1,6 | 0,3 | 0,4 | Ortho 58 | 0,3 | 2 | 8 |
| R1 | 534690 | 5000801 | Talweg | 3 | 1 | 3 | 1 | 3,2 | 4,1 | 2,7 | 0,9 | 0,5 | Ortho 58 | 0,3 | 2 | 6 |
| R1 | 534770 | 5000802 | Ridge | 2 | 0 | 3 | 1 | 2,8 | 3,5 | 2,1 | 0,7 | 0,6 | Ortho 58 | 0,3 | 2 | 3 |
| R1 | 534770 | 5000802 | Talweg | 2 | 1 | 2 | 1 | 5,6 | 6,6 | 4,3 | 0,9 | 1,3 | Ortho 58 | 0,3 | 2 | 5 |
| R1 | 534780 | 5000802 | Riser | 2 | 1 | 1 | 0 | 43,7 | 45,6 | 42,1 | 1,9 | 1,7 | Ortho 58 | 0,3 | 2 | 7 |
| R1 | 534813 | 5000799 | Talweg | 3 | 2 | 1 | 1 | 2,5 | 3,6 | 2,0 | 1,1 | 0,5 | Ortho 58 | 0,3 | 2 | 9 |
| R1 | 534813 | 5000799 | River | 2 | 1 | 1 | 0 | 32,2 | 35,7 | 27,3 | 3,5 | 4,8 | Ortho 58 | 0,3 | 2 | 7 |
| R1 | 534860 | 5000797 | Talweg | 3 | 2 | 2 | 0 | 4,2 | 5,1 | 3,5 | 0,9 | 0,7 | Ortho 58 | 0,3 | 2 | 9 |
| R1 | 534880 | 5000797 | Talweg | 3 | 2 | 1 | 0 | 6,4 | 7,1 | 4,4 | 0,8 | 2,0 | Ortho 58 | 0,3 | 2 | 10 |
| R1 | 534888 | 5000799 | Talweg | 3 | 2 | 1 | 2 | 2,6 | 3,3 | 2,2 | 0,6 | 0,4 | Ortho 58 | 0,3 | 2 | 8 |
| R1 | 534937 | 5000804 | Talweg | 3 | 2 | 1 | 1 | 3,0 | 3,5 | 2,7 | 0,5 | 0,4 | Ortho 58 | 0,3 | 2 | 9 |
| R1 | 534960 | 5000811 | Talweg | 3 | 2 | 1 | 1 | 3,4 | 4,1 | 2,2 | 0,7 | 1,2 | Ortho 58 | 0,3 | 2 | 9 |
| R1 | 535412 | 5000833 | Talweg | 3 | 2 | 1 | 2 | 3,9 | 5,0 | 2,9 | 1,1 | 1,1 | Ortho 58 | 0,3 | 2 | 8 |
| R1 | 535451 | 5000825 | River | 2 | 2 | 1 | 2 | 16,7 | 18,6 | 12,1 | 2,0 | 4,5 | Ortho 58 | 0,3 | 2 | 6 |
| R1 | 535525 | 5000812 | Talweg | 2 | 1 | 3 | 1 | 5,6 | 6,0 | 5,0 | 0,4 | 0,7 | Ortho 58 | 0,3 | 2 | 4 |
| R1 | 535547 | 5000809 | Talweg | 2 | 2 | 4 | 1 | 10,5 | 14,9 | 9,0 | 4,4 | 1,4 | Ortho 58 | 0,3 | 2 | 5 |
| R1 | 535576 | 5000805 | Talweg | 3 | 2 | 3 | 1 | 2,8 | 4,2 | 2,3 | 1,3 | 0,5 | Ortho 58 | 0,3 | 2 | 7 |
| R1 | 535627 | 5000800 | Talweg | 3 | 1 | 2 | 1 | 2,0 | 2,9 | 1,7 | 0,9 | 0,3 | Ortho 58 | 0,3 | 2 | 7 |
| R1 | 535690 | 5000788 | Talweg | 2 | 1 | 1 | 1 | 2,6 | 3,4 | 1,5 | 0,7 | 1,1 | Ortho 58 | 0,3 | 2 | 6 |
| R1 | 535690 | 5000788 | Riser | 2 | 1 | 1 | 1 | 24,3 | 28,5 | 21,9 | 4,2 | 2,5 | Ortho 58 | 0,3 | 2 | 6 |
| R1 | 535690 | 5000788 | Riser | 2 | 1 | 1 | 1 | 55,2 | 59,2 | 50,8 | 4,1 | 4,4 | Ortho 58 | 0,3 | 2 | 6 |
| R1 | 535730 | 5000773 | Talweg | 2 | 2 | 2 | 1 | 10,0 | 11,1 | 8,4 | 1,1 | 1,6 | Ortho 58 | 0,3 | 2 | 6 |
| R1 | 535717 | 5000727 | Talweg | 2 | 1 | 2 | 1 | 3,6 | 5,2 | 1,7 | 1,5 | 1,9 | Ortho 58 | 0,3 | 2 | 5 |
| R1 | 535845 | 5000712 | Talweg | 3 | 2 | 1 | 1 | 3,2 | 3,8 | 2,3 | 0,6 | 1,0 | Ortho 58 | 0,3 | 2 | 9 |
| R1 | 535865 | 5000706 | Talweg | 2 | 2 | 1 | 1 | 3,5 | 4,3 | 3,1 | 0,8 | 0,5 | Ortho 58 | 0,3 | 2 | 7 |
| R1 | 535865 | 5000706 | Talweg | 2 | 1 | 1 | 1 | 9,3 | 10,1 | 8,0 | 0,8 | 1,3 | Ortho 58 | 0,3 | 2 | 6 |
| R1 | 535900 | 5000700 | Ridge | 2 | 1 | 1 | 1 | 4,0 | 4,4 | 2,7 | 0,3 | 1,3 | Ortho 58 | 0,3 | 2 | 6 |
| R1 | 535950 | 5000675 | Talweg | 3 | 2 | 1 | 0 | 2,3 | 3,2 | 1,8 | 0,9 | 0,5 | Ortho 58 | 0,3 | 2 | 10 |
| S2 | 536008 | 5000634 | Talweg | 3 | 0 | 1 | 0 | 4,6 | 4,9 | 4,0 | 0,4 | 0,6 | Ortho 58 | 0,3 | 2 | 8 |
| S2 | 53603 | 500067 | Talweg | 3 | 2 | 1 | 0 | 3,7 | 4,1 | 3,2 | 0,4 | 0,5 | Ortho | 0,3 | 2 | 10 |

| Seg. | Lon. (UTM) | Lat. (UTM) | Marker Type | Mark. Obl. | Mark. res. (/2) | Nb. of splay | Scarp 2nd | Offset Pref. (m) | Offset max (m) | Offset min (m) | Δ+ (m) | Δ- (m) | Image type | Image Res. (m) | Image quality (/2) | Total Score (/10) |
|---|---|---|---|---|---|---|---|---|---|---|---|---|---|---|---|---|
| | 4 | 5 | | | | | | | | | | | 58 | | | |
| S2 | 536067 | 5000611 | Talweg | 3 | 2 | 1 | 0 | 3,5 | 3,9 | 2,7 | 0,4 | 0,7 | Ortho 58 | 0,3 | 2 | 10 |
| S2 | 536100 | 5000600 | Talweg | 3 | 2 | 1 | 0 | 6,1 | 6,7 | 5,7 | 0,6 | 0,4 | Ortho 58 | 0,3 | 2 | 10 |
| S2 | 536110 | 5000599 | Talweg | 3 | 1 | 1 | 0 | 8,1 | 8,8 | 7,7 | 0,7 | 0,4 | Ortho 58 | 0,3 | 2 | 9 |
| S2 | 536119 | 5000597 | Talweg | 2 | 1 | 1 | 0 | 5,9 | 6,4 | 4,3 | 0,5 | 1,5 | Ortho 58 | 0,3 | 2 | 7 |
| S2 | 536131 | 5000595 | Ridge | 3 | 1 | 1 | 0 | 13,6 | 15,2 | 10,9 | 1,6 | 2,7 | Ortho 58 | 0,3 | 2 | 9 |
| S2 | 536155 | 5000584 | Gully | 2 | 1 | 1 | 0 | 2,6 | 3,3 | 2,1 | 0,7 | 0,5 | Ortho 58 | 0,3 | 2 | 7 |
| S2 | 536200 | 5000565 | Talweg | 3 | 2 | 1 | 0 | 2,4 | 2,8 | 2,2 | 0,4 | 0,3 | Ortho 58 | 0,3 | 2 | 10 |
| S2 | 536237 | 5000549 | Gully | 2 | 1 | 1 | 0 | 1,5 | 2,0 | 1,3 | 0,5 | 0,3 | Ortho 58 | 0,3 | 2 | 7 |
| S2 | 536263 | 5000536 | Gully | 3 | 1 | 1 | 0 | 4,2 | 5,0 | 3,7 | 0,8 | 0,5 | Ortho 58 | 0,3 | 2 | 9 |
| S2 | 536300 | 5000523 | Ridge | 3 | 0 | 1 | 0 | 4,5 | 5,2 | 3,8 | 0,7 | 0,6 | Ortho 58 | 0,3 | 2 | 8 |
| S2 | 536361 | 5000491 | Gully | 2 | 1 | 1 | 0 | 5,1 | 5,7 | 4,7 | 0,5 | 0,5 | Ortho 58 | 0,3 | 2 | 7 |
| S2 | 536430 | 5000461 | Gully | 3 | 0 | 1 | 0 | 3,8 | 4,6 | 2,3 | 0,8 | 1,5 | Ortho 58 | 0,3 | 2 | 8 |
| S2 | 536450 | 5000451 | Gully | 1 | 2 | 1 | 0 | 3,7 | 4,9 | 2,5 | 1,1 | 1,2 | Ortho 58 | 0,3 | 2 | 7 |
| S2 | 536520 | 5000425 | Gully | 3 | 2 | 1 | 0 | 5,4 | 6,0 | 4,0 | 0,6 | 1,3 | Ortho 58 | 0,3 | 2 | 10 |
| S2 | 536586 | 5000403 | Gully | 1 | 1 | 1 | 0 | 6,5 | 8,2 | 4,3 | 1,7 | 2,2 | Ortho 58 | 0,3 | 2 | 6 |
| S2 | 536668 | 5000378 | River | 3 | 2 | 1 | 1 | 6,9 | 7,9 | 6,5 | 1,0 | 0,4 | Ortho 58 | 0,3 | 2 | 9 |
| S2 | 536718 | 5000366 | Riser | 3 | 2 | 1 | 1 | 4,2 | 4,7 | 3,9 | 0,5 | 0,3 | Ortho 58 | 0,3 | 2 | 9 |
| S2 | 536718 | 5000366 | Riser | 3 | 2 | 1 | 0 | 7,7 | 8,6 | 7,1 | 0,9 | 0,7 | Ortho 58 | 0,3 | 2 | 10 |
| S2 | 536668 | 5000378 | Riser | 3 | 2 | 1 | 1 | 3,1 | 3,5 | 2,7 | 0,4 | 0,4 | Ortho 58 | 0,3 | 2 | 9 |
| S2 | 536765 | 5000320 | Riser | 3 | 1 | 1 | 0 | 4,5 | 5,2 | 3,4 | 0,8 | 1,1 | Ortho 58 | 0,3 | 2 | 9 |
| S2 | 536798 | 5000314 | Gully | 3 | 1 | 1 | 0 | 5,9 | 8,1 | 3,4 | 2,2 | 2,6 | Ortho 58 | 0,3 | 2 | 9 |
| S2 | 536845 | 5000318 | Gully | 3 | 1 | 1 | 0 | 4,4 | 5,1 | 3,4 | 0,7 | 1,0 | Ortho 58 | 0,3 | 2 | 9 |
| S2 | 536888 | 5000306 | Gully | 2 | 1 | 2 | 0 | 3,5 | 4,3 | 3,1 | 0,8 | 0,4 | Ortho 58 | 0,3 | 2 | 6 |
| S2 | 536888 | 5000306 | Gully | 2 | 1 | 2 | 0 | 7,1 | 8,8 | 6,4 | 1,7 | 0,7 | Ortho 58 | 0,3 | 2 | 6 |
| S2 | 536940 | 5000295 | Gully | 3 | 1 | 1 | 0 | 3,5 | 4,2 | 2,7 | 0,7 | 0,8 | Ortho 58 | 0,3 | 2 | 9 |
| S2 | 536940 | 5000295 | Gully | 2 | 2 | 2 | 0 | 14,0 | 15,3 | 12,3 | 1,3 | 1,7 | Ortho 58 | 0,3 | 2 | 7 |
| S2 | 536940 | 5000295 | Gully | 3 | 1 | 2 | 0 | 21,6 | 22,9 | 19,6 | 1,3 | 2,0 | Ortho 58 | 0,3 | 2 | 8 |
| S2 | 537695 | 5000192 | Riser | 3 | 1 | 2 | 1 | 2,1 | 2,5 | 1,3 | 0,4 | 0,8 | Ortho 58 | 0,3 | 2 | 7 |
| S2 | 537695 | 5000192 | Riser | 3 | 1 | 2 | 1 | 6,2 | 7,5 | 5,3 | 1,3 | 0,9 | Ortho 58 | 0,3 | 2 | 7 |
| S2 | 537695 | 5000192 | Riser | 3 | 1 | 1 | 1 | 11,2 | 13,2 | 9,8 | 2,0 | 1,4 | Ortho 58 | 0,3 | 2 | 8 |
| S2 | 538040 | 5000135 | Gully | 3 | 2 | 1 | 0 | 3,8 | 4,2 | 2,5 | 0,4 | 1,3 | Ortho 58 | 0,3 | 2 | 10 |
| S2 | 538040 | 5000135 | Gully | 3 | 2 | 1 | 0 | 9,6 | 10,3 | 9,3 | 0,7 | 0,3 | Ortho 58 | 0,3 | 2 | 10 |
| S2 | 53814 | 500012 | Riser | 3 | 2 | 2 | 0 | 7,6 | 8,5 | 6,6 | 0,9 | 1,0 | Ortho | 0,3 | 2 | 9 |

| Seg. | Lon. (UTM) | Lat. (UTM) | Marker Type | Mark. Obl. | Mark. res. (/2) | Nb. of splay | Scarp 2nd | Offset Pref. (m) | Offset max (m) | Offset min (m) | Δ+ (m) | Δ- (m) | Image type | Image Res. (m) | Image quality (/2) | Total Score (/10) |
|---|---|---|---|---|---|---|---|---|---|---|---|---|---|---|---|---|
| | 5 | 1 | | | | | | | | | | | 58 | | | |
| S2 | 538145 | 5000121 | Riser | 3 | 1 | 2 | 0 | 13,5 | 15,6 | 12,5 | 2,1 | 1,0 | Ortho 58 | 0,3 | 2 | 8 |
| S2 | 538700 | 5000097 | Gully | 2 | 1 | 1 | 1 | 3,7 | 5,3 | 2,8 | 1,6 | 0,8 | Ortho 58 | 0,3 | 1 | 5 |
| S2 | 538800 | 5000093 | Gully | 1 | 1 | 1 | 1 | 6,6 | 8,9 | 4,9 | 2,3 | 1,7 | Ortho 58 | 0,3 | 2 | 5 |
| S2 | 538800 | 5000093 | Riser | 2 | 0 | 1 | 1 | 18,5 | 19,8 | 17,3 | 1,3 | 1,2 | Ortho 58 | 0,3 | 2 | 5 |
| S2 | 539000 | 5000083 | Riser | 2 | 1 | 1 | 0 | 39,8 | 41,8 | 38,2 | 2,0 | 1,6 | Ortho 58 | 0,2 | 2 | 7 |
| S2 | 539000 | 5000083 | Gully | 2 | 1 | 1 | 0 | 30,1 | 35,3 | 29,4 | 5,3 | 0,9 | Ortho 58 | 0,2 | 2 | 7 |
| S2 | 539079 | 5000080 | Gully | 2 | 2 | 1 | 0 | 12,0 | 13,0 | 9,9 | 1,0 | 2,1 | Ortho 58 | 0,2 | 2 | 8 |
| S2 | 539090 | 5000073 | Gully | 2 | 2 | 1 | 0 | 2,8 | 3,8 | 2,4 | 1,0 | 0,4 | Ortho 58 | 0,2 | 2 | 8 |
| S2 | 539132 | 5000069 | Gully | 2 | 2 | 1 | 0 | 5,3 | 5,9 | 4,0 | 0,6 | 1,3 | Ortho 58 | 0,2 | 2 | 8 |
| S2 | 539150 | 5000067 | Fan | 2 | 1 | 1 | 0 | 5,6 | 8,5 | 3,8 | 2,8 | 1,8 | Ortho 58 | 0,2 | 2 | 7 |
| S2 | 539187 | 5000060 | Riser | 3 | 1 | 1 | 0 | 10,2 | 11,6 | 9,3 | 1,3 | 1,0 | Ortho 58 | 0,2 | 2 | 9 |
| S2 | 539201 | 5000058 | Riser | 3 | 1 | 1 | 0 | 5,6 | 6,9 | 4,0 | 1,4 | 1,6 | Ortho 58 | 0,2 | 2 | 9 |
| S2 | 539262 | 5000048 | Gully | 3 | 0 | 2 | 0 | 1,6 | 2,1 | 1,1 | 0,5 | 0,5 | Ortho 58 | 0,2 | 1 | 6 |
| S2 | 539350 | 5000036 | Gully | 3 | 1 | 2 | 0 | 2,6 | 4,0 | 1,3 | 1,4 | 1,3 | Ortho 58 | 0,2 | 2 | 8 |
| S2 | 539384 | 5000032 | Gully | 3 | 2 | 2 | 0 | 1,8 | 2,0 | 0,9 | 0,3 | 0,9 | Ortho 58 | 0,2 | 2 | 9 |
| S2 | 539460 | 5000022 | Gully | 2 | 2 | 2 | 0 | 2,2 | 3,4 | 1,5 | 1,3 | 0,7 | Ortho 58 | 0,2 | 2 | 7 |
| S2 | 539495 | 5000015 | Gully | 3 | 2 | 1 | 0 | 4,7 | 5,6 | 4,3 | 0,8 | 0,4 | Ortho 58 | 0,2 | 2 | 10 |
| S2 | 539495 | 5000015 | Gully | 3 | 2 | 1 | 0 | 8,4 | 9,3 | 7,4 | 0,9 | 1,0 | Ortho 58 | 0,2 | 2 | 10 |
| S2 | 539520 | 5000008 | Gully | 3 | 2 | 1 | 0 | 2,2 | 2,8 | 1,5 | 0,6 | 0,7 | Ortho 58 | 0,2 | 2 | 10 |
| S2 | 539520 | 5000008 | Gully | 3 | 2 | 1 | 0 | 5,0 | 5,4 | 4,5 | 0,3 | 0,5 | Ortho 58 | 0,2 | 2 | 10 |
| S2 | 539547 | 5000000 | Talweg | 1 | 1 | 1 | 0 | 8,3 | 10,4 | 7,1 | 2,1 | 1,2 | Ortho 58 | 0,2 | 2 | 6 |
| S2 | 539567 | 4999993 | Talweg | 2 | 2 | 1 | 0 | 7,0 | 7,9 | 6,0 | 0,9 | 1,0 | Ortho 58 | 0,2 | 2 | 8 |
| S2 | 539630 | 4999978 | Talweg | 3 | 2 | 1 | 0 | 6,1 | 7,3 | 5,2 | 1,2 | 0,9 | Ortho 58 | 0,2 | 2 | 10 |
| S2 | 539630 | 4999978 | Talweg | 3 | 1 | 1 | 0 | 14,0 | 15,5 | 13,4 | 1,5 | 0,6 | Ortho 58 | 0,2 | 2 | 9 |
| S2 | 539630 | 4999978 | Talweg | 3 | 2 | 1 | 0 | 35,8 | 36,7 | 34,4 | 0,9 | 1,4 | Ortho 58 | 0,2 | 2 | 10 |
| S2 | 539688 | 4999968 | Talweg | 3 | 2 | 1 | 0 | 4,5 | 5,4 | 4,3 | 1,0 | 0,3 | Ortho 58 | 0,2 | 2 | 10 |
| S2 | 539665 | 4999964 | Talweg | 3 | 1 | 1 | 0 | 3,2 | 4,0 | 2,6 | 0,8 | 0,7 | Ortho 58 | 0,2 | 2 | 9 |
| S2 | 539525 | 4999960 | Talweg | 2 | 1 | 1 | 0 | 3,0 | 4,8 | 2,1 | 1,9 | 0,9 | Ortho 58 | 0,2 | 2 | 7 |
| S2 | 539525 | 4999960 | Riser | 2 | 2 | 1 | 0 | 9,0 | 9,9 | 8,4 | 0,9 | 0,6 | Ortho 58 | 0,2 | 2 | 8 |
| S2 | 539750 | 4999955 | Talweg | 2 | 1 | 1 | 0 | 6,2 | 6,8 | 5,5 | 0,6 | 0,7 | Ortho 58 | 0,2 | 2 | 7 |
| S2 | 539770 | 4999950 | Talweg | 3 | 1 | 1 | 0 | 5,6 | 6,3 | 5,2 | 0,7 | 0,4 | Ortho 58 | 0,2 | 2 | 9 |
| S2 | 539778 | 4999948 | Talweg | 3 | 1 | 1 | 0 | 4,7 | 5,1 | 4,4 | 0,4 | 0,3 | Ortho 58 | 0,2 | 2 | 9 |
| S2 | 53979 | 499994 | Talweg | 2 | 0 | 1 | 0 | 6,7 | 7,1 | 5,5 | 0,5 | 1,1 | Ortho | 0,2 | 2 | 6 |

| Seg. | Lon. (UTM) | Lat. (UTM) | Marker Type | Mark. Obl. | Mark. res. (/2) | Nb. of splay | Scarp 2nd | Offset Pref. (m) | Offset max (m) | Offset min (m) | Δ+ (m) | Δ- (m) | Image type | Image Res. (m) | Image quality (/2) | Total Score (/10) |
|---|---|---|---|---|---|---|---|---|---|---|---|---|---|---|---|---|
| | 0 | 5 | | | | | | | | | | | 58 | | | |
| S2 | 539800 | 4999943 | Riser | 3 | 1 | 1 | 0 | 5,8 | 6,3 | 5,4 | 0,5 | 0,4 | Ortho 58 | 0,2 | 2 | 9 |
| S2 | 539812 | 4999940 | Talweg | 3 | 1 | 1 | 0 | 5,6 | 6,5 | 5,2 | 0,9 | 0,4 | Ortho 58 | 0,2 | 2 | 9 |
| S2 | 539844 | 4999934 | Talweg | 2 | 1 | 1 | 0 | 3,2 | 3,7 | 2,5 | 0,5 | 0,7 | Ortho 58 | 0,2 | 2 | 7 |
| S2 | 539863 | 4999930 | Riser | 3 | 1 | 1 | 0 | 3,7 | 4,6 | 3,3 | 0,9 | 0,4 | Ortho 58 | 0,2 | 2 | 9 |
| S2 | 539878 | 4999928 | Talweg | 1 | 1 | 1 | 0 | 2,2 | 2,8 | 1,9 | 0,6 | 0,3 | Ortho 58 | 0,2 | 1 | 5 |
| S2 | 539910 | 4999918 | Talweg | 2 | 1 | 1 | 0 | 2,1 | 2,4 | 1,5 | 0,3 | 0,6 | Ortho 58 | 0,2 | 1 | 6 |
| S2 | 539940 | 4999912 | Talweg | 2 | 2 | 1 | 0 | 8,6 | 10,0 | 7,7 | 1,3 | 1,0 | Ortho 58 | 0,2 | 1 | 7 |
| S2 | 539978 | 4999900 | Talweg | 2 | 2 | 1 | 0 | 3,7 | 4,6 | 3,5 | 0,9 | 0,3 | Ortho 58 | 0,2 | 1 | 7 |
| S2 | 540077 | 4999877 | Talweg | 2 | 0 | 1 | 0 | 7,1 | 7,9 | 6,5 | 0,8 | 0,6 | Ortho 58 | 0,2 | 2 | 6 |
| S2 | 540100 | 4999869 | Talweg | 2 | 1 | 1 | 0 | 6,8 | 7,4 | 6,2 | 0,6 | 0,6 | Ortho 58 | 0,2 | 2 | 7 |
| S2 | 540133 | 4999863 | Talweg | 1 | 2 | 1 | 0 | 6,1 | 7,4 | 5,1 | 1,4 | 1,0 | Ortho 58 | 0,2 | 2 | 7 |
| S2 | 540133 | 4999863 | Talweg | 2 | 2 | 1 | 0 | 13,4 | 13,9 | 12,9 | 0,5 | 0,5 | Ortho 58 | 0,2 | 2 | 8 |
| S2 | 540187 | 4999851 | Riser | 2 | 1 | 1 | 0 | 6,6 | 8,0 | 5,1 | 1,4 | 1,5 | Ortho 58 | 0,2 | 2 | 7 |
| S2 | 540187 | 4999851 | Riser | 3 | 2 | 1 | 0 | 2,7 | 3,6 | 1,7 | 0,9 | 0,9 | Ortho 58 | 0,2 | 2 | 10 |
| S2 | 540187 | 4999851 | Riser | 3 | 1 | 1 | 1 | 2,3 | 2,5 | 0,9 | 0,3 | 1,4 | Ortho 58 | 0,2 | 2 | 8 |
| S2 | 540344 | 4999831 | Riser | 2 | 0 | 2 | 0 | 2,5 | 3,3 | 1,7 | 0,8 | 0,7 | Ortho 58 | 0,2 | 2 | 5 |
| S2 | 540370 | 4999824 | Riser | 2 | 1 | 2 | 0 | 2,8 | 4,4 | 2,0 | 1,6 | 0,8 | Ortho 58 | 0,2 | 2 | 6 |
| S2 | 540490 | 4999809 | Gully | 2 | 1 | 2 | 0 | 14,6 | 20,2 | 10,8 | 5,6 | 3,8 | Ortho 58 | 0,2 | 2 | 6 |
| S2 | 540610 | 4999796 | Gully | 2 | 0 | 2 | 0 | 2,7 | 3,9 | 2,0 | 1,2 | 0,6 | Ortho 58 | 0,2 | 2 | 5 |
| S2 | 540792 | 4999770 | Gully | 2 | 2 | 2 | 0 | 3,6 | 4,7 | 3,2 | 1,1 | 0,4 | Ortho 58 | 0,2 | 2 | 7 |
| S2 | 540850 | 4999759 | Gully | 2 | 1 | 2 | 0 | 1,5 | 2,3 | 1,1 | 0,8 | 0,4 | Ortho 58 | 0,2 | 2 | 6 |
| S2 | 540904 | 4999750 | Gully | 3 | 1 | 1 | 0 | 4,1 | 4,5 | 3,5 | 0,4 | 0,6 | Ortho 58 | 0,2 | 2 | 9 |
| S2 | 540927 | 4999745 | Talweg | 3 | 1 | 1 | 0 | 2,9 | 3,6 | 2,3 | 0,6 | 0,7 | Ortho 58 | 0,2 | 2 | 9 |
| S2 | 540953 | 4999741 | Talweg | 3 | 2 | 1 | 0 | 2,5 | 3,1 | 1,4 | 0,6 | 1,1 | Ortho 58 | 0,2 | 2 | 10 |
| S2 | 540978 | 4999737 | Gully | 3 | 1 | 1 | 0 | 3,3 | 3,6 | 3,1 | 0,3 | 0,3 | Ortho 58 | 0,2 | 2 | 9 |
| S2 | 540993 | 4999735 | Talweg | 2 | 1 | 1 | 0 | 3,9 | 4,4 | 3,7 | 0,4 | 0,3 | Ortho 58 | 0,2 | 2 | 7 |
| S2 | 541012 | 4999730 | Talweg | 3 | 1 | 1 | 0 | 5,3 | 5,7 | 5,1 | 0,3 | 0,3 | Ortho 58 | 0,2 | 2 | 9 |
| S2 | 541035 | 4999725 | Gully | 2 | 2 | 1 | 0 | 4,9 | 6,1 | 2,4 | 1,1 | 2,6 | Ortho 58 | 0,2 | 2 | 8 |
| S2 | 541058 | 4999720 | Talweg | 3 | 2 | 1 | 0 | 3,2 | 3,6 | 2,8 | 0,5 | 0,4 | Ortho 58 | 0,2 | 2 | 10 |
| S2 | 541090 | 4999715 | Talweg | 2 | 1 | 1 | 0 | 4,4 | 5,1 | 3,8 | 0,7 | 0,6 | Ortho 58 | 0,2 | 2 | 7 |
| S2 | 541137 | 4999710 | Talweg | 2 | 1 | 1 | 0 | 4,4 | 4,9 | 4,1 | 0,5 | 0,3 | Ortho 58 | 0,2 | 2 | 7 |
| S2 | 541152 | 4999705 | Talweg | 2 | 1 | 2 | 0 | 3,1 | 3,6 | 2,8 | 0,5 | 0,4 | Ortho 58 | 0,2 | 2 | 6 |
| S2 | 54119 | 499970 | Gully | 3 | 2 | 1 | 0 | 6,4 | 7,9 | 5,2 | 1,5 | 1,2 | Ortho | 0,2 | 2 | 10 |

| Seg. | Lon. (UTM) | Lat. (UTM) | Marker Type | Mark. Obl. | Mark. res. (/2) | Nb. of splay | Scarp 2nd | Offset Pref. (m) | Offset max (m) | Offset min (m) | Δ+ (m) | Δ- (m) | Image type | Image Res. (m) | Image quality (/2) | Total Score (/10) |
|---|---|---|---|---|---|---|---|---|---|---|---|---|---|---|---|---|
| | 0 | 0 | | | | | | | | | | | 58 | | | |
| S2 | 541210 | 4999698 | Gully | 3 | 1 | 1 | 0 | 4,0 | 4,5 | 3,7 | 0,5 | 0,3 | Ortho 58 | 0,2 | 2 | 9 |
| S2 | 541233 | 4999696 | Gully | 3 | 0 | 1 | 0 | 2,1 | 2,7 | 1,6 | 0,5 | 0,5 | Ortho 58 | 0,2 | 2 | 8 |
| S2 | 541263 | 4999688 | Gully | 2 | 1 | 1 | 0 | 2,3 | 2,6 | 1,4 | 0,3 | 0,9 | Ortho 58 | 0,2 | 2 | 7 |
| S2 | 541287 | 4999682 | Talweg | 3 | 2 | 1 | 0 | 5,9 | 6,3 | 5,7 | 0,5 | 0,3 | Ortho 58 | 0,2 | 2 | 10 |
| S2 | 541297 | 4999679 | Talweg | 3 | 1 | 1 | 0 | 5,1 | 5,4 | 4,5 | 0,3 | 0,5 | Ortho 58 | 0,2 | 2 | 9 |
| S2 | 541312 | 4999676 | Talweg | 3 | 2 | 1 | 0 | 4,8 | 5,5 | 4,3 | 0,7 | 0,5 | Ortho 58 | 0,2 | 2 | 10 |
| S2 | 541346 | 4999668 | Talweg | 3 | 1 | 1 | 0 | 2,9 | 4,1 | 1,8 | 1,2 | 1,1 | Ortho 58 | 0,2 | 2 | 9 |
| S2 | 541346 | 4999668 | Talweg | 1 | 1 | 1 | 0 | 22,3 | 28,0 | 19,3 | 5,7 | 3,0 | Ortho 58 | 0,2 | 2 | 6 |
| S2 | 541375 | 4999664 | Talweg | 3 | 1 | 1 | 0 | 4,5 | 5,0 | 3,8 | 0,5 | 0,7 | Ortho 58 | 0,2 | 2 | 9 |
| S2 | 541385 | 4999662 | Talweg | 2 | 2 | 1 | 0 | 4,8 | 5,4 | 4,4 | 0,6 | 0,4 | Ortho 58 | 0,2 | 2 | 8 |
| S2 | 541406 | 4999655 | Talweg | 1 | 2 | 1 | 0 | 2,4 | 3,2 | 1,4 | 0,8 | 1,0 | Ortho 58 | 0,2 | 2 | 7 |
| S2 | 541421 | 4999650 | Talweg | 2 | 2 | 1 | 0 | 3,4 | 3,8 | 3,0 | 0,4 | 0,4 | Ortho 58 | 0,2 | 2 | 8 |
| S2 | 541486 | 4999630 | Talweg | 2 | 1 | 1 | 1 | 4,0 | 5,2 | 3,2 | 1,2 | 0,8 | Ortho 58 | 0,2 | 2 | 6 |
| S2 | 541500 | 4999629 | Talweg | 2 | 1 | 1 | 1 | 4,4 | 4,8 | 3,9 | 0,4 | 0,5 | Ortho 58 | 0,2 | 2 | 6 |
| S2 | 541530 | 4999623 | Talweg | 2 | 2 | 1 | 1 | 4,1 | 4,4 | 4,0 | 0,3 | 0,3 | Ortho 58 | 0,2 | 2 | 7 |
| S2 | 541530 | 4999623 | Talweg | 2 | 2 | 1 | 1 | 5,8 | 6,2 | 5,4 | 0,4 | 0,4 | Ortho 58 | 0,2 | 2 | 7 |
| S2 | 541593 | 4999621 | Talweg | 2 | 1 | 1 | 1 | 4,2 | 4,6 | 3,0 | 0,3 | 1,2 | Ortho 58 | 0,2 | 2 | 6 |
| S2 | 541667 | 4999614 | Riser | 2 | 1 | 1 | 1 | 3,6 | 4,2 | 3,3 | 0,6 | 0,3 | Ortho 58 | 0,2 | 2 | 6 |
| S2 | 541712 | 4999615 | Riser | 2 | 2 | 1 | 1 | 3,1 | 4,1 | 2,6 | 1,0 | 0,5 | Ortho 58 | 0,2 | 2 | 7 |
| S2 | 541712 | 4999615 | Riser | 3 | 2 | 1 | 1 | 8,9 | 9,2 | 8,6 | 0,3 | 0,3 | Ortho 58 | 0,2 | 2 | 9 |
| S2 | 541756 | 4999622 | Ridge | 2 | 1 | 1 | 1 | 23,9 | 27,0 | 20,3 | 3,1 | 3,6 | Ortho 58 | 0,2 | 2 | 6 |
| S2 | 542050 | 4999663 | Gully | 2 | 1 | 4 | 0 | 4,9 | 5,2 | 4,1 | 0,3 | 0,8 | Ortho 58 | 0,2 | 2 | 5 |
| S2 | 542162 | 4999670 | Gully | 2 | 1 | 1 | 1 | 3,5 | 4,1 | 3,4 | 0,6 | 0,3 | Ortho 58 | 0,2 | 2 | 6 |
| S2 | 542183 | 4999671 | Gully | 2 | 1 | 1 | 1 | 3,5 | 3,8 | 3,3 | 0,3 | 0,3 | Ortho 58 | 0,2 | 2 | 6 |
| S2 | 542200 | 4999671 | Gully | 2 | 1 | 1 | 0 | 6,2 | 7,7 | 5,8 | 1,5 | 0,4 | Ortho 58 | 0,2 | 2 | 7 |
| S2 | 542200 | 4999671 | Gully | 2 | 1 | 1 | 0 | 9,1 | 10,1 | 8,1 | 1,0 | 1,0 | Ortho 58 | 0,2 | 2 | 7 |
| S2 | 542250 | 4999671 | Riser | 3 | 1 | 1 | 0 | 4,5 | 6,1 | 4,0 | 1,6 | 0,5 | Ortho 58 | 0,2 | 2 | 9 |
| S2 | 542300 | 4999672 | Riser | 3 | 2 | 1 | 0 | 19,1 | 21,1 | 16,2 | 2,0 | 2,9 | Ortho 58 | 0,2 | 2 | 10 |
| S2 | 542300 | 4999672 | Riser | 3 | 2 | 1 | 0 | 65,5 | 68,1 | 61,3 | 2,6 | 4,1 | Ortho 58 | 0,2 | 2 | 10 |
| S2 | 542310 | 4999671 | Talweg | 3 | 1 | 1 | 0 | 4,3 | 5,0 | 3,4 | 0,7 | 0,9 | Ortho 58 | 0,2 | 2 | 9 |
| S2 | 542332 | 4999668 | Talweg | 3 | 1 | 1 | 0 | 5,4 | 6,7 | 5,1 | 1,3 | 0,3 | Ortho 58 | 0,2 | 2 | 9 |
| S2 | 542364 | 4999664 | Talweg | 3 | 1 | 1 | 0 | 5,3 | 7,3 | 4,3 | 2,0 | 1,0 | Ortho 58 | 0,2 | 2 | 9 |
| S2 | 54239 | 499966 | Talweg | 3 | 1 | 1 | 0 | 5,0 | 5,7 | 4,5 | 0,8 | 0,4 | Ortho | 0,2 | 2 | 9 |

| Seg. | Lon. (UTM) | Lat. (UTM) | Marker Type | Mark. Obl. | Mark. res. (/2) | Nb. of splay | Scarp 2nd | Offset Pref. (m) | Offset max (m) | Offset min (m) | Δ+ (m) | Δ- (m) | Image type | Image Res. (m) | Image quality (/2) | Total Score (/10) |
|---|---|---|---|---|---|---|---|---|---|---|---|---|---|---|---|---|
| | 6 | 3 | | | | | | | | | | | 58 | | | |
| S2 | 542420 | 4999663 | Talweg | 3 | 2 | 1 | 0 | 7,7 | 8,3 | 6,8 | 0,7 | 0,9 | Ortho 58 | 0,2 | 2 | 10 |
| S2 | 542450 | 4999664 | Talweg | 3 | 1 | 1 | 0 | 6,8 | 7,9 | 5,5 | 1,2 | 1,3 | Ortho 58 | 0,2 | 2 | 9 |
| S2 | 542513 | 4999661 | Talweg | 3 | 2 | 1 | 0 | 2,5 | 3,0 | 1,8 | 0,6 | 0,6 | Ortho 58 | 0,2 | 2 | 10 |
| S2 | 542533 | 4999658 | Talweg | 2 | 2 | 1 | 1 | 7,5 | 8,3 | 6,5 | 0,8 | 1,0 | Ortho 58 | 0,2 | 2 | 7 |
| S2 | 542533 | 4999658 | Talweg | 3 | 2 | 1 | 0 | 57,9 | 60,6 | 55,2 | 2,7 | 2,8 | Ortho 58 | 0,2 | 2 | 10 |
| S2 | 542543 | 4999657 | Riser | 3 | 1 | 1 | 1 | 9,3 | 10,6 | 8,4 | 1,3 | 0,9 | Ortho 58 | 0,2 | 2 | 8 |
| S2 | 542551 | 4999655 | Gully | 3 | 0 | 1 | 0 | 4,8 | 6,2 | 3,7 | 1,4 | 1,1 | Ortho 58 | 0,2 | 2 | 8 |
| S2 | 542605 | 4999645 | Talweg | 3 | 2 | 1 | 0 | 3,2 | 3,7 | 2,6 | 0,5 | 0,6 | Ortho 58 | 0,2 | 2 | 10 |
| S2 | 542655 | 4999635 | Talweg | 2 | 2 | 1 | 0 | 2,4 | 3,2 | 1,7 | 0,9 | 0,7 | Ortho 58 | 0,2 | 2 | 8 |
| S2 | 542655 | 4999635 | Talweg | 3 | 2 | 1 | 0 | 5,9 | 7,9 | 5,3 | 2,0 | 0,6 | Ortho 58 | 0,2 | 2 | 10 |
| S2 | 542711 | 4999619 | Riser | 2 | 1 | 2 | 0 | 3,1 | 3,9 | 2,7 | 0,8 | 0,5 | Ortho 58 | 0,2 | 2 | 6 |
| S2 | 542749 | 4999610 | Riser | 2 | 1 | 2 | 0 | 6,2 | 7,0 | 5,7 | 0,8 | 0,5 | Ortho 58 | 0,2 | 2 | 6 |
| S2 | 542749 | 4999610 | Riser | 2 | 1 | 2 | 0 | 9,5 | 10,7 | 9,0 | 1,1 | 0,6 | Ortho 58 | 0,2 | 2 | 6 |
| S2 | 542780 | 4999603 | Riser | 2 | 2 | 1 | 0 | 6,5 | 7,3 | 6,0 | 0,8 | 0,5 | Ortho 58 | 0,2 | 2 | 8 |
| S2 | 542800 | 4999601 | Riser | 2 | 1 | 1 | 0 | 2,8 | 4,0 | 2,1 | 1,2 | 0,7 | Ortho 58 | 0,2 | 2 | 7 |
| S2 | 542800 | 4999601 | Riser | 2 | 1 | 1 | 0 | 10,5 | 11,2 | 10,1 | 0,7 | 0,4 | Ortho 58 | 0,2 | 2 | 7 |
| S2 | 542812 | 4999598 | Gully | 3 | 0 | 2 | 0 | 4,4 | 4,8 | 3,8 | 0,5 | 0,5 | Ortho 58 | 0,2 | 2 | 7 |
| S2 | 542868 | 4999582 | Talweg | 2 | 1 | 1 | 0 | 7,4 | 8,5 | 6,0 | 1,0 | 1,4 | Ortho 58 | 0,2 | 2 | 7 |
| S2 | 542887 | 4999577 | Talweg | 2 | 1 | 1 | 0 | 3,2 | 3,9 | 2,4 | 0,7 | 0,8 | Ortho 58 | 0,2 | 2 | 7 |
| S2 | 542904 | 4999572 | Talweg | 2 | 1 | 1 | 0 | 3,4 | 4,4 | 2,7 | 1,0 | 0,7 | Ortho 58 | 0,2 | 2 | 7 |
| S2 | 542951 | 4999556 | Gully | 2 | 1 | 2 | 0 | 2,1 | 3,5 | 1,5 | 1,4 | 0,7 | Ortho 58 | 0,2 | 2 | 6 |
| S2 | 542966 | 4999551 | Talweg | 3 | 2 | 1 | 0 | 8,7 | 9,6 | 7,9 | 0,9 | 0,7 | Ortho 58 | 0,2 | 2 | 10 |
| S2 | 543060 | 4999526 | Riser | 3 | 1 | 1 | 0 | 5,4 | 6,2 | 4,6 | 0,8 | 0,8 | Ortho 58 | 0,2 | 2 | 9 |
| S2 | 543060 | 4999526 | Riser | 3 | 0 | 1 | 0 | 11,9 | 13,3 | 10,6 | 1,4 | 1,3 | Ortho 58 | 0,2 | 2 | 8 |
| S2 | 543106 | 4999520 | Gully | 2 | 1 | 1 | 0 | 5,3 | 6,7 | 4,5 | 1,4 | 0,9 | Ortho 58 | 0,2 | 2 | 7 |
| S2 | 543157 | 4999505 | Talweg | 3 | 2 | 1 | 0 | 6,4 | 7,3 | 5,8 | 0,8 | 0,7 | Ortho 58 | 0,2 | 2 | 10 |
| S2 | 543255 | 4999480 | Talweg | 3 | 1 | 1 | 0 | 5,6 | 6,8 | 5,2 | 1,2 | 0,4 | Ortho 58 | 0,2 | 2 | 9 |
| S2 | 543255 | 4999480 | Talweg | 3 | 1 | 1 | 0 | 35,7 | 36,5 | 34,5 | 0,9 | 1,2 | Ortho 58 | 0,2 | 2 | 9 |
| S2 | 543330 | 4999464 | Talweg | 3 | 2 | 1 | 0 | 8,3 | 8,7 | 8,0 | 0,4 | 0,3 | Ortho 58 | 0,2 | 2 | 10 |
| S2 | 543366 | 4999457 | Talweg | 2 | 2 | 1 | 0 | 3,6 | 4,9 | 2,6 | 1,3 | 1,0 | Ortho 58 | 0,2 | 2 | 8 |
| S2 | 543400 | 4999451 | Talweg | 3 | 1 | 2 | 0 | 4,2 | 5,0 | 3,1 | 0,8 | 1,1 | Ortho 58 | 0,2 | 2 | 8 |
| S2 | 543438 | 4999445 | Talweg | 2 | 1 | 1 | 0 | 7,0 | 8,1 | 6,1 | 1,1 | 0,9 | Ortho 58 | 0,2 | 1 | 6 |
| S2 | 54343 | 499944 | Talweg | 2 | 1 | 1 | 0 | 20,3 | 22,0 | 19,0 | 1,8 | 1,3 | Ortho | 0,2 | 1 | 6 |

| Seg. | Lon. (UTM) | Lat. (UTM) | Marker Type | Mark. Obl. | Mark. res. (/2) | Nb. of splay | Scarp 2nd | Offset Pref. (m) | Offset max (m) | Offset min (m) | Δ+ (m) | Δ- (m) | Image type | Image Res. (m) | Image quality (/2) | Total Score (/10) |
|---|---|---|---|---|---|---|---|---|---|---|---|---|---|---|---|---|
| | 8 | 5 | | | | | | | | | | | 58 | | | |
| S2 | 543600 | 4999429 | Talweg | 2 | 2 | 1 | 0 | 6,1 | 6,8 | 5,0 | 0,7 | 1,1 | Ortho 58 | 0,2 | 2 | 8 |
| S2 | 543600 | 4999429 | Talweg | 2 | 2 | 1 | 0 | 8,7 | 10,0 | 8,5 | 1,2 | 0,3 | Ortho 58 | 0,2 | 2 | 8 |
| S2 | 543624 | 4999428 | Riser | 3 | 2 | 1 | 0 | 4,8 | 5,4 | 3,6 | 0,6 | 1,2 | Ortho 58 | 0,2 | 2 | 10 |
| S2 | 543656 | 4999426 | Riser | 2 | 1 | 1 | 0 | 5,2 | 5,8 | 4,4 | 0,6 | 0,8 | Ortho 58 | 0,2 | 2 | 7 |
| S2 | 543700 | 4999421 | Talweg | 3 | 1 | 1 | 0 | 4,6 | 5,6 | 4,1 | 1,1 | 0,5 | Ortho 58 | 0,2 | 2 | 9 |
| S2 | 543721 | 4999419 | Abandoned Chanel | 3 | 1 | 1 | 0 | 2,7 | 3,4 | 2,4 | 0,7 | 0,3 | Ortho 58 | 0,2 | 2 | 9 |
| S2 | 543735 | 4999417 | Talweg | 2 | 1 | 1 | 0 | 4,5 | 4,9 | 4,2 | 0,4 | 0,3 | Ortho 58 | 0,2 | 2 | 7 |
| S2 | 543760 | 4999415 | Talweg | 2 | 1 | 1 | 0 | 2,7 | 3,1 | 2,0 | 0,3 | 0,8 | Ortho 58 | 0,2 | 2 | 7 |
| S2 | 543780 | 4999412 | Talweg | 3 | 1 | 1 | 0 | 6,4 | 6,9 | 5,4 | 0,4 | 1,0 | Ortho 58 | 0,2 | 2 | 9 |
| S2 | 543793 | 4999409 | Talweg | 3 | 1 | 1 | 0 | 4,9 | 5,5 | 4,1 | 0,6 | 0,8 | Ortho 58 | 0,2 | 2 | 9 |
| S2 | 543867 | 4999400 | Riser | 2 | 2 | 1 | 0 | 7,2 | 8,2 | 6,0 | 1,0 | 1,2 | Ortho 58 | 0,2 | 2 | 8 |
| S2 | 543874 | 4999397 | River | 3 | 1 | 1 | 0 | 6,9 | 7,8 | 6,3 | 0,9 | 0,7 | Ortho 58 | 0,2 | 2 | 9 |
| S2 | 543883 | 4999393 | Riser | 2 | 1 | 1 | 0 | 8,8 | 9,3 | 8,3 | 0,5 | 0,5 | Ortho 58 | 0,2 | 2 | 7 |
| S2 | 543920 | 4999387 | Riser | 2 | 1 | 1 | 0 | 6,0 | 6,8 | 5,6 | 0,8 | 0,4 | Ortho 58 | 0,2 | 2 | 7 |
| S2 | 543940 | 4999382 | Riser | 2 | 1 | 4 | 0 | 2,8 | 3,0 | 2,4 | 0,3 | 0,3 | Ortho 58 | 0,2 | 2 | 5 |
| S2 | 543977 | 4999387 | Riser | 3 | 1 | 3 | 0 | 7,2 | 7,9 | 6,6 | 0,7 | 0,6 | Ortho 58 | 0,2 | 2 | 7 |
| S2 | 544008 | 4999373 | Riser | 2 | 1 | 1 | 0 | 3,3 | 4,1 | 2,4 | 0,8 | 0,9 | Ortho 58 | 0,2 | 2 | 7 |
| S2 | 544060 | 4999462 | Gully | 2 | 2 | 2 | 0 | 3,9 | 4,7 | 3,0 | 0,8 | 0,8 | Ortho 58 | 0,2 | 2 | 7 |
| S2 | 544060 | 4999462 | Gully | 2 | 1 | 2 | 0 | 11,4 | 12,8 | 10,6 | 1,4 | 0,8 | Ortho 58 | 0,2 | 2 | 6 |
| S2 | 544141 | 4999346 | Talweg | 3 | 1 | 2 | 0 | 3,7 | 4,8 | 2,4 | 1,1 | 1,3 | Ortho 58 | 0,2 | 2 | 8 |
| S2 | 544191 | 4999339 | Riser | 3 | 2 | 1 | 0 | 9,4 | 10,5 | 8,6 | 1,1 | 0,8 | Ortho 58 | 0,2 | 2 | 10 |
| S2 | 544248 | 4999325 | Gully | 2 | 1 | 2 | 0 | 10,4 | 12,4 | 8,7 | 2,0 | 1,7 | Ortho 58 | 0,2 | 2 | 6 |
| S2 | 544348 | 4999315 | Gully | 3 | 2 | 1 | 0 | 7,3 | 8,6 | 6,5 | 1,2 | 0,8 | Ortho 58 | 0,2 | 2 | 10 |
| S2 | 544410 | 4999310 | Ridge | 2 | 1 | 2 | 0 | 9,8 | 11,1 | 9,0 | 1,3 | 0,8 | Ortho 58 | 0,2 | 2 | 6 |
| S2 | 544545 | 4999285 | Gully | 2 | 2 | 1 | 0 | 3,8 | 4,7 | 3,3 | 0,9 | 0,5 | Ortho 58 | 0,2 | 2 | 8 |
| S2 | 544545 | 4999285 | Gully | 2 | 2 | 1 | 0 | 30,7 | 36,4 | 28,3 | 5,8 | 2,4 | Ortho 58 | 0,2 | 2 | 8 |
| S2 | 544600 | 4999278 | Abandoned Chanel | 2 | 1 | 2 | 0 | 9,9 | 12,6 | 8,5 | 2,7 | 1,4 | Ortho 58 | 0,2 | 2 | 6 |
| S2 | 544643 | 4999274 | Gully | 2 | 1 | 4 | 0 | 6,9 | 8,5 | 5,6 | 1,6 | 1,3 | Ortho 58 | 0,2 | 2 | 5 |
| S2 | 544676 | 4999271 | Gully | 2 | 2 | 4 | 0 | 28,9 | 30,4 | 27,1 | 1,4 | 1,8 | Ortho 58 | 0,2 | 2 | 6 |
| S2 | 544708 | 4999269 | Gully | 2 | 1 | 4 | 0 | 11,8 | 13,4 | 10,6 | 1,6 | 1,1 | Ortho 58 | 0,2 | 2 | 5 |
| S2 | 544708 | 4999269 | Gully | 2 | 1 | 2 | 0 | 33,4 | 36,5 | 31,9 | 3,1 | 1,6 | Ortho 58 | 0,2 | 2 | 6 |
| S2 | 54482 | 499926 | Gully | 2 | 1 | 2 | 0 | 5,2 | 6,6 | 4,7 | 1,4 | 0,5 | Ortho | 0,2 | 2 | 6 |

| Seg. | Lon. (UTM) | Lat. (UTM) | Marker Type | Mark. Obl. | Mark. res. (/2) | Nb. of splay | Scarp 2nd | Offset Pref. (m) | Offset max (m) | Offset min (m) | Δ+ (m) | Δ- (m) | Image type | Image Res. (m) | Image quality (/2) | Total Score (/10) |
|---|---|---|---|---|---|---|---|---|---|---|---|---|---|---|---|---|
| | 4 | 0 | | | | | | | | | | | 58 | | | |
| S2 | 544894 | 4999255 | Riser | 3 | 2 | 2 | 0 | 4,0 | 5,5 | 2,4 | 1,6 | 1,6 | Ortho 58 | 0,2 | 2 | 9 |
| S2 | 545029 | 4999242 | Talweg | 1 | 1 | 2 | 0 | 7,1 | 9,0 | 5,4 | 1,9 | 1,7 | Ortho 58 | 0,2 | 2 | 5 |
| S2 | 545029 | 4999242 | Riser | 3 | 2 | 2 | 0 | 64,5 | 67,4 | 62,7 | 2,9 | 1,8 | Ortho 58 | 0,2 | 2 | 9 |
| S2 | 545110 | 4999233 | Riser | 3 | 1 | 1 | 0 | 83,1 | 88,9 | 74,6 | 5,7 | 8,5 | Ortho 58 | 0,2 | 2 | 9 |
| S2 | 545163 | 4999226 | Talweg | 3 | 1 | 1 | 0 | 5,3 | 6,2 | 4,1 | 0,9 | 1,1 | Ortho 58 | 0,2 | 2 | 9 |
| S2 | 545192 | 4999222 | Talweg | 2 | 1 | 1 | 0 | 3,8 | 5,3 | 1,3 | 1,5 | 2,5 | Ortho 58 | 0,2 | 2 | 7 |
| S2 | 545293 | 4999207 | Talweg | 3 | 1 | 1 | 0 | 5,4 | 6,0 | 4,5 | 0,7 | 0,8 | Ortho 58 | 0,2 | 2 | 9 |
| S2 | 545340 | 4999201 | Gully | 2 | 2 | 1 | 0 | 7,8 | 9,2 | 7,2 | 1,4 | 0,6 | Ortho 58 | 0,2 | 2 | 8 |
| S2 | 545477 | 4999184 | Talweg | 3 | 2 | 1 | 0 | 9,3 | 11,0 | 7,8 | 1,7 | 1,5 | Ortho 58 | 0,2 | 2 | 10 |
| S2 | 545539 | 4999174 | Riser | 2 | 1 | 2 | 0 | 11,7 | 18,0 | 7,0 | 6,2 | 4,7 | Ortho 58 | 0,2 | 2 | 6 |
| S2 | 545594 | 4999163 | Riser | 3 | 2 | 1 | 0 | 13,0 | 14,7 | 10,3 | 1,7 | 2,7 | Ortho 58 | 0,2 | 2 | 10 |
| S2 | 545650 | 4999163 | Ridge | 3 | 2 | 1 | 0 | 6,7 | 9,1 | 3,7 | 2,4 | 3,0 | Ortho 58 | 0,2 | 2 | 10 |
| S2 | 545770 | 4999131 | Gully | 2 | 2 | 2 | 0 | 6,4 | 7,1 | 5,9 | 0,7 | 0,5 | Ortho 58 | 0,2 | 2 | 7 |
| S2 | 545830 | 4999125 | Gully | 3 | 2 | 2 | 0 | 3,8 | 4,5 | 2,7 | 0,7 | 1,1 | Ortho 58 | 0,2 | 2 | 9 |
| S2 | 545890 | 4999120 | Talweg | 3 | 1 | 2 | 0 | 4,4 | 8,0 | 2,9 | 3,5 | 1,5 | Ortho 58 | 0,2 | 2 | 8 |
| S2 | 545940 | 4999128 | Talweg | 1 | 2 | 8 | 0 | 2,9 | 3,6 | 2,1 | 0,7 | 0,8 | Ortho 58 | 0,2 | 2 | 5 |
| S2 | 546244 | 4999100 | Gully | 2 | 2 | 2 | 0 | 2,6 | 3,0 | 1,9 | 0,4 | 0,7 | Ortho 58 | 0,2 | 2 | 7 |
| S2 | 546244 | 4999100 | Gully | 2 | 2 | 2 | 1 | 6,2 | 6,4 | 5,7 | 0,3 | 0,4 | Ortho 58 | 0,2 | 2 | 6 |
| S2 | 546280 | 4999096 | River | 3 | 2 | 1 | 1 | 2,7 | 3,9 | 2,1 | 1,2 | 0,6 | Ortho 58 | 0,2 | 2 | 9 |
| S2 | 546343 | 4999084 | Riser | 3 | 1 | 2 | 1 | 8,4 | 8,9 | 7,8 | 0,5 | 0,6 | Ortho 58 | 0,2 | 2 | 7 |
| S2 | 546486 | 4999050 | Talweg | 2 | 1 | 1 | 0 | 6,4 | 8,0 | 4,4 | 1,6 | 2,0 | Ortho 58 | 0,2 | 2 | 7 |
| S2 | 546770 | 4999056 | Gully | 2 | 2 | 1 | 1 | 2,5 | 3,1 | 2,0 | 0,7 | 0,4 | Ortho 58 | 0,2 | 2 | 7 |
| S2 | 546823 | 4999058 | Gully | 3 | 2 | 2 | 1 | 3,1 | 3,6 | 2,6 | 0,5 | 0,5 | Ortho 58 | 0,2 | 2 | 8 |
| S2 | 546860 | 4999060 | Talweg | 3 | 2 | 1 | 1 | 4,0 | 4,5 | 3,6 | 0,5 | 0,4 | Ortho 58 | 0,2 | 2 | 9 |
| S2 | 546910 | 4999063 | Talweg | 3 | 1 | 2 | 1 | 1,8 | 2,7 | 0,9 | 0,9 | 0,9 | Ortho 58 | 0,2 | 2 | 7 |
| S2 | 547015 | 4999068 | Talweg | 3 | 2 | 2 | 0 | 2,3 | 3,6 | 1,7 | 1,3 | 0,6 | Ortho 60 | 0,2 | 2 | 9 |
| S2 | 547132 | 4999049 | Talweg | 3 | 2 | 1 | 0 | 1,4 | 2,4 | 1,0 | 1,0 | 0,4 | Ortho 61 | 0,2 | 2 | 10 |
| S2 | 547200 | 4999041 | Talweg | 3 | 2 | 1 | 1 | 4,0 | 5,0 | 2,4 | 1,0 | 1,6 | Ortho 58 | 0,2 | 2 | 9 |
| S2 | 547250 | 4999035 | Talweg | 3 | 2 | 1 | 1 | 6,7 | 7,5 | 5,4 | 0,8 | 1,2 | Ortho 58 | 0,2 | 2 | 9 |
| S2 | 547250 | 4999068 | Talweg | 2 | 1 | 1 | 1 | 12,8 | 15,0 | 12,1 | 2,3 | 0,7 | Ortho 58 | 0,2 | 2 | 6 |
| S2 | 547275 | 4999030 | Talweg | 2 | 1 | 1 | 1 | 7,6 | 10,3 | 6,0 | 2,6 | 1,7 | Ortho 58 | 0,2 | 2 | 6 |
| S2 | 547322 | 4999023 | Riser | 3 | 2 | 1 | 1 | 13,6 | 17,4 | 12,2 | 3,8 | 1,4 | Ortho 58 | 0,2 | 2 | 9 |
| S2 | 54745 | 499901 | Ridge | 2 | 0 | 1 | 0 | 7,7 | 10,5 | 6,3 | 2,8 | 1,5 | Ortho | 0,2 | 2 | 6 |

| Seg. | Lon. (UTM) | Lat. (UTM) | Marker Type | Mark. Obl. | Mark. res. (/2) | Nb. of splay | Scarp 2nd | Offset Pref. (m) | Offset max (m) | Offset min (m) | Δ+ (m) | Δ- (m) | Image type | Image Res. (m) | Image quality (/2) | Total Score (/10) |
|---|---|---|---|---|---|---|---|---|---|---|---|---|---|---|---|---|
| | 2 | 0 | | | | | | | | | | | 58 | | | |
| S2 | 547662 | 4998964 | Talweg | 2 | 2 | 1 | 0 | 4,7 | 5,3 | 4,2 | 0,6 | 0,5 | Ortho 58 | 0,2 | 2 | 8 |
| S2 | 547718 | 4998955 | Gully | 2 | 1 | 1 | 0 | 2,8 | 3,5 | 2,3 | 0,7 | 0,5 | Ortho 58 | 0,2 | 2 | 7 |
| S2 | 547718 | 4998955 | Gully | 2 | 1 | 1 | 0 | 5,0 | 6,0 | 4,5 | 1,0 | 0,6 | Ortho 58 | 0,2 | 2 | 7 |
| S2 | 547780 | 4998940 | Riser | 2 | 1 | 1 | 0 | 3,8 | 4,7 | 2,7 | 0,9 | 1,1 | Ortho 58 | 0,2 | 2 | 7 |
| S2 | 547780 | 4998940 | Riser | 2 | 1 | 1 | 0 | 8,9 | 10,1 | 8,3 | 1,3 | 0,5 | Ortho 58 | 0,2 | 2 | 7 |
| S2 | 547820 | 4998935 | Gully | 3 | 1 | 1 | 0 | 2,6 | 3,2 | 2,2 | 0,6 | 0,4 | Ortho 58 | 0,2 | 2 | 9 |
| S2 | 547820 | 4998935 | Talweg | 3 | 2 | 1 | 0 | 6,8 | 7,8 | 6,4 | 1,0 | 0,4 | Ortho 58 | 0,2 | 2 | 10 |
| S2 | 547843 | 4998932 | Talweg | 2 | 2 | 1 | 0 | 4,7 | 5,9 | 4,1 | 1,2 | 0,5 | Ortho 58 | 0,2 | 2 | 8 |
| S2 | 547867 | 4998930 | Talweg | 2 | 1 | 1 | 0 | 5,5 | 5,8 | 5,0 | 0,3 | 0,5 | Ortho 58 | 0,2 | 2 | 7 |
| S2 | 547880 | 4998928 | Talweg | 3 | 1 | 1 | 0 | 2,7 | 3,8 | 2,1 | 1,1 | 0,6 | Ortho 58 | 0,2 | 2 | 9 |
| S2 | 547900 | 4998924 | Talweg | 3 | 1 | 1 | 0 | 5,5 | 6,5 | 5,1 | 1,0 | 0,4 | Ortho 58 | 0,2 | 2 | 9 |
| S2 | 547950 | 4998919 | Talweg | 3 | 2 | 1 | 0 | 5,9 | 6,4 | 5,6 | 0,5 | 0,3 | Ortho 58 | 0,2 | 2 | 10 |
| S2 | 547993 | 4998914 | Gully | 3 | 1 | 1 | 0 | 6,5 | 6,7 | 6,0 | 0,3 | 0,4 | Ortho 58 | 0,2 | 2 | 9 |
| S2 | 548020 | 4998912 | Gully | 3 | 2 | 1 | 0 | 5,5 | 5,9 | 5,2 | 0,4 | 0,3 | Ortho 58 | 0,2 | 2 | 10 |
| S2 | 548055 | 4998909 | Talweg | 3 | 1 | 1 | 0 | 3,2 | 4,0 | 2,4 | 0,9 | 0,8 | Ortho 58 | 0,2 | 2 | 9 |
| S2 | 548055 | 4998909 | Talweg | 3 | 2 | 1 | 0 | 7,0 | 8,1 | 6,3 | 1,0 | 0,7 | Ortho 58 | 0,2 | 2 | 10 |
| S2 | 548126 | 4998908 | Talweg | 3 | 2 | 1 | 0 | 6,7 | 7,0 | 5,5 | 0,3 | 1,2 | Ortho 58 | 0,2 | 2 | 10 |
| S2 | 548150 | 4998907 | Talweg | 3 | 2 | 2 | 0 | 4,7 | 5,7 | 3,7 | 1,0 | 1,0 | Ortho 58 | 0,2 | 2 | 9 |
| S2 | 548150 | 4998907 | Talweg | 3 | 2 | 2 | 0 | 9,0 | 10,0 | 8,0 | 1,0 | 1,0 | Ortho 58 | 0,2 | 2 | 9 |
| S2 | 548200 | 4998910 | Fan apex | 2 | 1 | 2 | 0 | 6,3 | 8,4 | 4,0 | 2,1 | 2,3 | Ortho 58 | 0,2 | 2 | 6 |
| S2 | 548223 | 4998912 | Talweg | 3 | 1 | 1 | 0 | 3,4 | 4,1 | 2,7 | 0,6 | 0,7 | Ortho 58 | 0,2 | 2 | 9 |
| S2 | 548250 | 4998915 | Gully | 3 | 1 | 1 | 0 | 3,2 | 3,6 | 2,2 | 0,4 | 1,0 | Ortho 58 | 0,2 | 2 | 9 |
| S2 | 548250 | 4998915 | Gully | 3 | 1 | 1 | 0 | 11,8 | 12,2 | 11,6 | 0,4 | 0,3 | Ortho 58 | 0,2 | 2 | 9 |
| S2 | 548250 | 4998915 | Gully | 3 | 1 | 1 | 0 | 33,0 | 36,3 | 29,7 | 3,3 | 3,3 | Ortho 58 | 0,2 | 2 | 9 |
| S2 | 548345 | 4998922 | Talweg | 3 | 1 | 1 | 0 | 4,9 | 6,3 | 3,4 | 1,3 | 1,6 | Ortho 58 | 0,2 | 2 | 9 |
| S2 | 548385 | 4998924 | Gully | 3 | 1 | 1 | 0 | 4,9 | 6,1 | 4,3 | 1,1 | 0,6 | Ortho 58 | 0,2 | 2 | 9 |
| S2 | 548455 | 4998931 | Riser | 2 | 2 | 4 | 0 | 1,8 | 2,7 | 1,4 | 0,9 | 0,4 | Ortho 58 | 0,2 | 2 | 6 |
| S2 | 548477 | 4998934 | Riser | 3 | 1 | 2 | 0 | 19,1 | 20,8 | 14,8 | 1,7 | 4,3 | Ortho 58 | 0,2 | 2 | 8 |
| S2 | 548500 | 4998935 | Riser | 3 | 2 | 2 | 0 | 3,1 | 3,6 | 2,6 | 0,5 | 0,5 | Ortho 58 | 0,2 | 2 | 9 |
| S2 | 548565 | 4998944 | Riser | 3 | 2 | 2 | 0 | 5,7 | 8,4 | 4,3 | 2,7 | 1,4 | Ortho 58 | 0,2 | 2 | 9 |
| S2 | 548565 | 4998944 | Riser | 3 | 1 | 2 | 0 | 16,8 | 21,4 | 14,3 | 4,7 | 2,4 | Ortho 58 | 0,2 | 2 | 8 |
| S2 | 548420 | 4999008 | River | 2 | 1 | 2 | 1 | 4,6 | 6,7 | 3,5 | 2,1 | 1,0 | Ortho 58 | 0,2 | 2 | 5 |
| S2 | 54878 | 499901 | Aband | 3 | 1 | 1 | 1 | 16,9 | 18,7 | 14,3 | 1,8 | 2,6 | Ortho | 0,2 | 2 | 8 |

| Seg. | Lon. (UTM) | Lat. (UTM) | Marker Type | Mark. Obl. | Mark. res. (/2) | Nb. of splay | Scarp 2nd | Offset Pref. (m) | Offset max (m) | Offset min (m) | Δ+ (m) | Δ- (m) | Image type | Image Res. (m) | Image quality (/2) | Total Score (/10) |
|---|---|---|---|---|---|---|---|---|---|---|---|---|---|---|---|---|
| | 5 | 3 | oned Chanel | | | | | | | | | | 58 | | | |
| S2 | 548970 | 4999070 | Riser | 3 | 2 | 2 | 1 | 2,1 | 3,3 | 1,1 | 1,2 | 1,0 | Ortho 58 | 0,2 | 2 | 8 |
| S2 | 548996 | 4999076 | Riser | 2 | 2 | 2 | 1 | 4,6 | 8,3 | 2,3 | 3,7 | 2,3 | Ortho 58 | 0,2 | 2 | 6 |
| S2 | 549518 | 4999110 | Gully | 2 | 1 | 4 | 0 | 5,9 | 7,6 | 4,1 | 1,7 | 1,8 | Ortho 58 | 0,2 | 2 | 5 |
| S2 | 549557 | 4999107 | Gully | 2 | 1 | 4 | 0 | 16,5 | 18,5 | 15,4 | 2,0 | 1,2 | Ortho 58 | 0,2 | 2 | 5 |
| S2 | 549572 | 4999107 | Riser | 3 | 1 | 3 | 0 | 15,6 | 18,6 | 13,6 | 3,1 | 2,0 | Ortho 58 | 0,2 | 2 | 7 |
| S2 | 549650 | 4999108 | Gully | 3 | 2 | 2 | 0 | 6,0 | 7,3 | 5,4 | 1,2 | 0,7 | Ortho 58 | 0,2 | 2 | 9 |
| S2 | 549650 | 4999108 | Gully | 3 | 2 | 2 | 0 | 20,7 | 22,5 | 19,0 | 1,8 | 1,7 | Ortho 58 | 0,2 | 2 | 9 |
| S2 | 549720 | 4999104 | Gully | 3 | 2 | 2 | 0 | 13,6 | 15,5 | 11,0 | 1,8 | 2,6 | Ortho 58 | 0,2 | 2 | 9 |
| S2 | 549800 | 4999101 | Talweg | 3 | 1 | 2 | 0 | 3,0 | 3,8 | 2,0 | 0,8 | 1,0 | Ortho 58 | 0,2 | 2 | 8 |
| S2 | 550050 | 4999087 | Gully | 2 | 1 | 3 | 1 | 44,1 | 45,9 | 42,4 | 1,8 | 1,7 | Ortho 58 | 0,2 | 2 | 4 |
| S2 | 550515 | 4998980 | Gully | 3 | 1 | 1 | 1 | 4,5 | 5,2 | 4,1 | 0,7 | 0,4 | Ortho 58 | 0,3 | 2 | 8 |
| S2 | 550685 | 4998934 | Gully | 2 | 1 | 1 | 1 | 6,6 | 8,4 | 4,5 | 1,8 | 2,1 | Ortho 58 | 0,3 | 2 | 6 |
| S2 | 551030 | 4998834 | Gully | 3 | 1 | 2 | 0 | 5,0 | 5,9 | 4,8 | 0,9 | 0,3 | Ortho 58 | 0,3 | 2 | 8 |
| S2 | 551130 | 4998807 | Gully | 3 | 2 | 1 | 0 | 6,3 | 7,1 | 5,0 | 0,8 | 1,2 | Ortho 58 | 0,3 | 2 | 10 |
| S2 | 551195 | 4998792 | Ridge | 3 | 1 | 1 | 0 | 8,8 | 11,0 | 6,9 | 2,2 | 1,9 | Ortho 58 | 0,3 | 2 | 9 |
| S2 | 551222 | 4998782 | Gully | 3 | 1 | 1 | 0 | 4,4 | 5,4 | 2,9 | 1,0 | 1,5 | Ortho 58 | 0,3 | 2 | 9 |
| S2 | 551295 | 4998765 | Gully | 3 | 2 | 1 | 0 | 9,9 | 10,9 | 8,2 | 1,0 | 1,7 | Ortho 58 | 0,3 | 2 | 10 |
| S2 | 551295 | 4998765 | Talweg | 3 | 1 | 1 | 0 | 19,5 | 22,1 | 17,7 | 2,6 | 1,8 | Ortho 58 | 0,3 | 2 | 9 |
| S2 | 551407 | 4998737 | Riser | 3 | 1 | 1 | 0 | 4,2 | 5,6 | 3,5 | 1,4 | 0,7 | Ortho 58 | 0,3 | 2 | 9 |
| S2 | 551455 | 4998726 | Gully | 3 | 2 | 2 | 0 | 3,5 | 5,3 | 2,1 | 1,8 | 1,4 | Ortho 58 | 0,3 | 2 | 9 |
| S2 | 551533 | 4998710 | Gully | 3 | 1 | 1 | 0 | 3,7 | 4,4 | 2,8 | 0,6 | 0,9 | Ortho 58 | 0,3 | 2 | 9 |
| S2 | 551590 | 4998700 | Riser | 2 | 2 | 2 | 0 | 6,2 | 7,4 | 5,0 | 1,1 | 1,2 | Ortho 58 | 0,3 | 2 | 7 |
| S2 | 551590 | 4998700 | Riser | 2 | 1 | 2 | 0 | 2,0 | 4,0 | 1,2 | 2,0 | 0,8 | Ortho 58 | 0,3 | 2 | 6 |
| S2 | 551713 | 4998671 | Riser | 2 | 1 | 1 | 0 | 2,8 | 3,3 | 2,3 | 0,5 | 0,5 | Ortho 58 | 0,3 | 2 | 7 |
| S2 | 551713 | 4998671 | Riser | 2 | 1 | 1 | 0 | 6,0 | 8,5 | 3,7 | 2,5 | 2,3 | Ortho 58 | 0,3 | 2 | 7 |
| S2 | 551852 | 4998637 | Gully | 3 | 2 | 1 | 0 | 3,3 | 4,0 | 2,5 | 0,7 | 0,8 | Ortho 58 | 0,3 | 2 | 10 |
| S2 | 551852 | 4998637 | Gully | 3 | 2 | 1 | 0 | 13,4 | 14,7 | 12,4 | 1,3 | 1,0 | Ortho 58 | 0,3 | 2 | 10 |
| S2 | 551868 | 4998634 | Gully | 3 | 1 | 1 | 0 | 5,5 | 6,7 | 4,8 | 1,2 | 0,7 | Ortho 58 | 0,3 | 2 | 9 |
| S2 | 551888 | 4998630 | Gully | 3 | 1 | 1 | 0 | 2,7 | 3,7 | 1,9 | 1,0 | 0,8 | Ortho 58 | 0,3 | 2 | 9 |
| S2 | 551922 | 4998622 | Gully | 3 | 1 | 1 | 0 | 2,8 | 3,5 | 1,8 | 0,7 | 1,0 | Ortho 58 | 0,3 | 2 | 9 |
| S2 | 551953 | 4998613 | River | 3 | 2 | 1 | 0 | 3,9 | 5,3 | 2,9 | 1,4 | 1,0 | Ortho 58 | 0,3 | 2 | 10 |
| S2 | 552330 | 4998503 | Gully | 3 | 1 | 1 | 2 | 3,9 | 4,4 | 3,3 | 0,5 | 0,5 | Ortho 58 | 0,3 | 2 | 7 |

| Seg. | Lon. (UTM) | Lat. (UTM) | Marker Type | Mark. Obl. | Mark. res. (/2) | Nb. of splay | Scarp 2nd | Offset Pref. (m) | Offset max (m) | Offset min (m) | Δ+ (m) | Δ- (m) | Image type | Image Res. (m) | Image quality (/2) | Total Score (/10) |
|---|---|---|---|---|---|---|---|---|---|---|---|---|---|---|---|---|
| S2 | 552353 | 4998495 | Gully | 3 | 1 | 1 | 2 | 3,0 | 3,3 | 2,6 | 0,3 | 0,4 | Ortho 58 | 0,3 | 2 | 7 |
| S2 | 552420 | 4998474 | Riser | 2 | 2 | 2 | 2 | 3,4 | 4,5 | 2,4 | 1,1 | 1,0 | Ortho 58 | 0,3 | 2 | 5 |
| S2 | 552453 | 4998462 | Gully | 3 | 2 | 1 | 1 | 2,0 | 2,6 | 1,6 | 0,6 | 0,5 | Ortho 58 | 0,3 | 2 | 9 |
| S2 | 552472 | 4998446 | Gully | 2 | 1 | 2 | 1 | 2,3 | 3,1 | 1,6 | 0,8 | 0,7 | Ortho 58 | 0,3 | 2 | 5 |
| S2 | 552498 | 4998440 | Gully | 3 | 0 | 2 | 1 | 1,5 | 1,9 | 1,2 | 0,4 | 0,3 | Ortho 58 | 0,3 | 2 | 6 |
| S2 | 552554 | 4998424 | Gully | 3 | 1 | 2 | 1 | 4,4 | 6,1 | 3,7 | 1,7 | 0,7 | Ortho 58 | 0,3 | 2 | 7 |
| S2 | 552554 | 4998424 | Riser | 3 | 1 | 1 | 1 | 2,8 | 3,7 | 2,4 | 0,9 | 0,4 | Ortho 58 | 0,3 | 2 | 8 |
| S2 | 552608 | 4998403 | Gully | 2 | 1 | 1 | 1 | 8,1 | 9,1 | 7,1 | 1,0 | 1,0 | Ortho 58 | 0,3 | 2 | 6 |
| S2 | 552731 | 4998382 | Gully | 3 | 1 | 3 | 0 | 3,5 | 4,3 | 2,8 | 0,8 | 0,7 | Ortho 58 | 0,3 | 2 | 7 |
| S2 | 552731 | 4998382 | Gully | 2 | 2 | 2 | 0 | 18,6 | 20,3 | 17,7 | 1,8 | 0,9 | Ortho 58 | 0,3 | 2 | 7 |
| S2 | 552886 | 4998344 | Gully | 3 | 2 | 1 | 1 | 2,9 | 3,5 | 2,0 | 0,6 | 0,9 | Ortho 58 | 0,3 | 2 | 9 |
| S2 | 552937 | 4998331 | Gully | 3 | 1 | 1 | 1 | 2,3 | 2,8 | 1,6 | 0,5 | 0,6 | Ortho 58 | 0,3 | 2 | 8 |
| S2 | 552967 | 4998323 | Gully | 3 | 2 | 2 | 1 | 2,0 | 2,4 | 1,3 | 0,3 | 0,7 | Ortho 58 | 0,3 | 2 | 8 |
| S2 | 552983 | 4998318 | Gully | 3 | 2 | 3 | 0 | 3,0 | 4,1 | 2,7 | 1,1 | 0,3 | Ortho 58 | 0,3 | 2 | 8 |
| S2 | 553015 | 4998314 | Gully | 3 | 2 | 2 | 0 | 2,5 | 4,0 | 1,9 | 1,6 | 0,6 | Ortho 58 | 0,3 | 2 | 9 |
| S2 | 553141 | 4998294 | Gully | 2 | 2 | 3 | 0 | 5,4 | 6,0 | 4,6 | 0,6 | 0,8 | Ortho 58 | 0,2 | 2 | 6 |
| S2 | 553159 | 4998293 | Gully | 2 | 2 | 3 | 0 | 2,3 | 3,8 | 1,5 | 1,6 | 0,8 | Ortho 58 | 0,2 | 2 | 6 |
| S2 | 553159 | 4998293 | Talweg | 2 | 1 | 3 | 0 | 27,3 | 29,6 | 25,2 | 2,3 | 2,1 | Ortho 58 | 0,2 | 2 | 5 |
| S2 | 553268 | 4998279 | Gully | 2 | 2 | 2 | 1 | 2,8 | 3,7 | 2,0 | 0,8 | 0,9 | Ortho 58 | 0,2 | 2 | 6 |
| S2 | 553268 | 4998279 | Gully | 2 | 2 | 2 | 1 | 32,6 | 33,6 | 31,5 | 1,0 | 1,1 | Ortho 58 | 0,2 | 2 | 6 |
| S2 | 553725 | 4998211 | Riser | 2 | 2 | 1 | 1 | 4,4 | 6,0 | 3,3 | 1,6 | 1,2 | Ortho 58 | 0,2 | 2 | 7 |
| S2 | 553725 | 4998211 | Riser | 2 | 2 | 1 | 1 | 15,3 | 18,4 | 13,6 | 3,1 | 1,7 | Ortho 58 | 0,2 | 2 | 7 |
| S2 | 553882 | 4998209 | River | 3 | 2 | 3 | 1 | 3,4 | 4,8 | 1,3 | 1,4 | 2,1 | Ortho 58 | 0,2 | 2 | 7 |
| S2 | 553922 | 4998200 | Talweg | 3 | 1 | 2 | 1 | 5,3 | 6,4 | 4,1 | 1,1 | 1,2 | Ortho 58 | 0,2 | 2 | 7 |
| S2 | 554045 | 4998189 | Talweg | 3 | 1 | 1 | 1 | 2,6 | 4,7 | 1,5 | 2,0 | 1,1 | Ortho 58 | 0,2 | 2 | 8 |
| S2 | 554100 | 4998183 | Talweg | 3 | 1 | 2 | 1 | 3,1 | 4,7 | 2,0 | 1,6 | 1,1 | Ortho 58 | 0,2 | 2 | 7 |
| S2 | 554100 | 4998183 | Talweg | 2 | 1 | 2 | 1 | 18,7 | 21,7 | 16,6 | 3,1 | 2,0 | Ortho 58 | 0,2 | 2 | 5 |
| S2 | 554270 | 4998190 | Riser | 3 | 1 | 2 | 1 | 1,6 | 2,5 | 1,2 | 0,9 | 0,5 | Ortho 58 | 0,2 | 2 | 7 |
| S2 | 554305 | 4998185 | Ridge | 3 | 1 | 1 | 1 | 6,9 | 7,4 | 5,4 | 0,5 | 1,5 | Ortho 58 | 0,2 | 2 | 8 |
| S2 | 554342 | 4998165 | Talweg | 3 | 2 | 1 | 1 | 5,4 | 6,8 | 4,4 | 1,4 | 1,0 | Ortho 58 | 0,2 | 2 | 9 |
| S2 | 554372 | 4998158 | Ridge | 3 | 1 | 2 | 1 | 4,7 | 5,3 | 3,7 | 0,6 | 1,0 | Ortho 58 | 0,2 | 1 | 6 |
| S2 | 554410 | 4998148 | Talweg | 3 | 1 | 2 | 1 | 2,6 | 3,4 | 2,0 | 0,8 | 0,6 | Ortho 58 | 0,2 | 1 | 6 |
| S2 | 554500 | 4998127 | River | 3 | 2 | 2 | 1 | 4,4 | 5,9 | 3,8 | 1,5 | 0,6 | Ortho 58 | 0,2 | 1 | 7 |

| Seg. | Lon. (UTM) | Lat. (UTM) | Marker Type | Mark. Obl. | Mark. res. (/2) | Nb. of splay | Scarp 2nd | Offset Pref. (m) | Offset max (m) | Offset min (m) | Δ+ (m) | Δ- (m) | Image type | Image Res. (m) | Image quality (/2) | Total Score (/10) |
|---|---|---|---|---|---|---|---|---|---|---|---|---|---|---|---|---|
| S2 | 554530 | 4998125 | Riser | 2 | 1 | 1 | 1 | 2,8 | 3,0 | 2,5 | 0,3 | 0,3 | Ortho 58 | 0,2 | 2 | 6 |
| S2 | 554530 | 4998125 | Riser | 2 | 0 | 1 | 1 | 8,0 | 8,5 | 7,7 | 0,5 | 0,3 | Ortho 58 | 0,2 | 2 | 5 |
| S2 | 554650 | 4998109 | Gully | 3 | 1 | 1 | 1 | 1,9 | 2,6 | 1,4 | 0,7 | 0,5 | Ortho 58 | 0,2 | 2 | 8 |
| S2 | 554700 | 4998104 | Gully | 3 | 2 | 1 | 1 | 3,6 | 4,6 | 3,2 | 1,1 | 0,3 | Ortho 58 | 0,2 | 2 | 9 |
| S2 | 554725 | 4998102 | Riser | 3 | 1 | 1 | 1 | 23,1 | 27,5 | 21,5 | 4,4 | 1,6 | Ortho 58 | 0,2 | 2 | 8 |
| S2 | 554725 | 4998102 | Riser | 3 | 1 | 1 | 1 | 33,0 | 35,9 | 29,9 | 2,9 | 3,1 | Ortho 58 | 0,2 | 2 | 8 |
| S2 | 554830 | 4998084 | Riser | 3 | 1 | 1 | 1 | 26,3 | 28,8 | 23,5 | 2,5 | 2,8 | Ortho 58 | 0,2 | 2 | 8 |
| S2 | 554875 | 4998080 | Riser | 3 | 2 | 1 | 1 | 12,6 | 14,2 | 11,2 | 1,5 | 1,4 | Ortho 58 | 0,2 | 2 | 9 |
| S2 | 555020 | 4998054 | Riser | 3 | 2 | 1 | 1 | 4,0 | 6,3 | 3,4 | 2,3 | 0,6 | Ortho 58 | 0,2 | 2 | 9 |
| S2 | 555070 | 4998062 | Talweg | 3 | 2 | 2 | 2 | 2,3 | 3,4 | 1,0 | 1,1 | 1,2 | Ortho 58 | 0,2 | 2 | 7 |
| S2 | 555120 | 4998062 | Talweg | 3 | 1 | 1 | 2 | 1,8 | 2,8 | 0,5 | 1,0 | 1,3 | Ortho 58 | 0,2 | 2 | 7 |
| S2 | 555120 | 4998062 | Talweg | 3 | 1 | 1 | 2 | 9,1 | 9,9 | 7,2 | 0,9 | 1,9 | Ortho 58 | 0,2 | 2 | 7 |
| S2 | 555340 | 4998023 | Talweg | 2 | 2 | 2 | 2 | 2,9 | 4,4 | 1,8 | 1,6 | 1,1 | Ortho 58 | 0,2 | 2 | 5 |
| S2 | 555340 | 4998023 | Talweg | 2 | 2 | 2 | 2 | 13,7 | 15,1 | 12,3 | 1,4 | 1,4 | Ortho 58 | 0,2 | 2 | 5 |
| S2 | 555666 | 4998046 | River | 3 | 2 | 2 | 1 | 1,9 | 2,9 | 1,7 | 1,0 | 0,3 | Ortho 58 | 0,2 | 2 | 8 |
| S2 | 555666 | 4998046 | River | 3 | 2 | 2 | 1 | 8,5 | 10,6 | 7,5 | 2,1 | 1,0 | Ortho 58 | 0,2 | 2 | 8 |
| S2 | 555745 | 4998056 | Gully | 3 | 2 | 4 | 1 | 4,5 | 5,4 | 3,4 | 0,9 | 1,1 | Ortho 58 | 0,2 | 2 | 7 |
| S2 | 555800 | 4998062 | Gully | 3 | 2 | 4 | 1 | 4,6 | 5,6 | 3,5 | 1,0 | 1,1 | Ortho 58 | 0,2 | 2 | 7 |
| S2 | 555855 | 4998071 | Gully | 3 | 2 | 3 | 1 | 6,0 | 7,7 | 5,8 | 1,7 | 0,3 | Ortho 58 | 0,2 | 2 | 7 |
| S2 | 555890 | 4998077 | Gully | 2 | 1 | 2 | 1 | 3,0 | 4,1 | 1,0 | 1,1 | 2,0 | Ortho 58 | 0,2 | 2 | 5 |
| S2 | 555935 | 4998084 | Gully | 3 | 2 | 2 | 2 | 5,0 | 7,4 | 4,4 | 2,4 | 0,6 | Ortho 58 | 0,2 | 2 | 7 |
| S2 | 555999 | 4998104 | Gully | 3 | 2 | 4 | 2 | 3,0 | 4,4 | 1,7 | 1,3 | 1,4 | Ortho 58 | 0,2 | 2 | 6 |
| S2 | 556045 | 4998119 | Gully | 3 | 2 | 3 | 2 | 2,2 | 2,7 | 1,6 | 0,5 | 0,6 | Ortho 58 | 0,2 | 2 | 6 |
| S2 | 556107 | 4998125 | Gully | 3 | 2 | 3 | 2 | 4,1 | 6,4 | 3,5 | 2,3 | 0,6 | Ortho 58 | 0,2 | 2 | 6 |
| S2 | 556107 | 4998125 | Gully | 2 | 1 | 3 | 2 | 10,7 | 14,1 | 8,1 | 3,5 | 2,6 | Ortho 58 | 0,2 | 2 | 3 |
| S2 | 556185 | 4998112 | Talweg | 3 | 2 | 2 | 0 | 10,0 | 10,3 | 9,1 | 0,3 | 0,9 | Ortho 58 | 0,2 | 2 | 9 |
| S2 | 556270 | 4998092 | Riser | 3 | 2 | 2 | 0 | 13,9 | 17,0 | 11,8 | 3,1 | 2,1 | Ortho 58 | 0,2 | 2 | 9 |
| S2 | 556455 | 4998076 | Talweg | 2 | 2 | 2 | 0 | 5,2 | 6,0 | 3,6 | 0,8 | 1,6 | Ortho 58 | 0,2 | 1 | 6 |
| S2 | 556500 | 4998070 | Gully | 3 | 1 | 1 | 0 | 2,2 | 2,5 | 1,5 | 0,3 | 0,7 | Ortho 58 | 0,2 | 1 | 8 |
| S2 | 556610 | 4998068 | River | 3 | 2 | 1 | 0 | 2,2 | 3,5 | 0,9 | 1,3 | 1,2 | Ortho 58 | 0,2 | 1 | 9 |
| S2 | 556650 | 4998073 | Riser | 2 | 2 | 1 | 0 | 2,6 | 5,0 | 2,1 | 2,4 | 0,6 | Ortho 58 | 0,2 | 1 | 7 |
| S2 | 556755 | 4998102 | Talweg | 3 | 2 | 1 | 1 | 4,7 | 5,4 | 3,5 | 0,7 | 1,1 | Ortho 58 | 0,2 | 2 | 9 |
| S2 | 556860 | 4998122 | Talweg | 3 | 2 | 2 | 1 | 2,9 | 3,7 | 2,0 | 0,8 | 1,0 | Ortho 58 | 0,2 | 2 | 8 |

| Seg. | Lon. (UTM) | Lat. (UTM) | Marker Type | Mark. Obl. | Mark. res. (/2) | Nb. of splay | Scarp 2nd | Offset Pref. (m) | Offset max (m) | Offset min (m) | Δ+ (m) | Δ- (m) | Image type | Image Res. (m) | Image quality (/2) | Total Score (/10) |
|---|---|---|---|---|---|---|---|---|---|---|---|---|---|---|---|---|
| S2 | 556935 | 4998036 | Riser | 3 | 1 | 2 | 0 | 7,3 | 9,3 | 3,9 | 2,1 | 3,4 | Ortho 58 | 0,2 | 1 | 7 |
| S2 | 556969 | 4998150 | Riser | 3 | 2 | 2 | 0 | 2,8 | 4,8 | 2,6 | 2,0 | 0,3 | Ortho 58 | 0,2 | 1 | 8 |
| S2 | 557025 | 4998120 | Riser | 2 | 2 | 2 | 0 | 3,4 | 6,8 | 2,5 | 3,3 | 0,9 | Ortho 58 | 0,2 | 1 | 6 |
| S2 | 557025 | 4998120 | Riser | 2 | 2 | 2 | 0 | 43,4 | 49,8 | 39,3 | 6,4 | 4,1 | Ortho 58 | 0,2 | 1 | 6 |
| S2 | 557090 | 4998107 | Talweg | 3 | 1 | 3 | 1 | 4,0 | 5,5 | 2,7 | 1,5 | 1,3 | Ortho 58 | 0,2 | 1 | 5 |
| S2 | 557170 | 4998121 | Talweg | 3 | 1 | 2 | 1 | 4,3 | 5,9 | 3,5 | 1,6 | 0,8 | Ortho 58 | 0,2 | 1 | 6 |
| R2 | 557500 | 4998156 | Talweg | 2 | 1 | 5 | 1 | 4,9 | 5,9 | 3,8 | 1,0 | 1,0 | Ortho 58 | 0,2 | 2 | 4 |
| R2 | 557575 | 4998151 | Talweg | 2 | 2 | 2 | 0 | 8,0 | 8,8 | 6,8 | 0,8 | 1,2 | Ortho 58 | 0,2 | 2 | 7 |
| R2 | 557575 | 4998151 | Talweg | 2 | 2 | 2 | 0 | 18,3 | 20,2 | 16,4 | 1,9 | 1,9 | Ortho 58 | 0,2 | 2 | 7 |
| R2 | 557700 | 4998149 | River | 3 | 2 | 2 | 0 | 3,6 | 4,2 | 2,2 | 0,6 | 1,4 | Ortho 58 | 0,2 | 2 | 9 |
| R2 | 557700 | 4998149 | Riser | 3 | 2 | 2 | 0 | 5,8 | 6,7 | 5,0 | 1,0 | 0,7 | Ortho 58 | 0,2 | 2 | 9 |
| R2 | 557795 | 4998144 | Ridge | 3 | 1 | 2 | 1 | 8,1 | 9,7 | 5,8 | 1,6 | 2,3 | Ortho 58 | 0,2 | 2 | 7 |
| R2 | 557815 | 4998142 | Talweg | 2 | 1 | 3 | 1 | 3,3 | 4,3 | 2,6 | 1,1 | 0,7 | Ortho 58 | 0,2 | 2 | 4 |
| R2 | 557815 | 4998142 | Talweg | 2 | 1 | 3 | 1 | 5,0 | 5,6 | 4,4 | 0,5 | 0,6 | Ortho 58 | 0,2 | 2 | 4 |
| R2 | 557885 | 4998132 | Talweg | 2 | 1 | 2 | 1 | 4,0 | 5,1 | 2,7 | 1,2 | 1,3 | Ortho 58 | 0,2 | 2 | 5 |
| R2 | 557885 | 4998132 | Talweg | 2 | 1 | 2 | 1 | 8,9 | 10,7 | 7,3 | 1,8 | 1,7 | Ortho 58 | 0,2 | 2 | 5 |
| R2 | 557935 | 4998129 | Talweg | 3 | 1 | 4 | 1 | 2,7 | 3,8 | 1,8 | 1,2 | 0,9 | Ortho 58 | 0,2 | 2 | 6 |
| R2 | 557935 | 4998129 | Talweg | 3 | 1 | 4 | 1 | 15,1 | 16,9 | 12,9 | 1,8 | 2,2 | Ortho 58 | 0,2 | 2 | 6 |
| R2 | 559393 | 4997522 | Riser | 2 | 1 | 2 | 3 | 2,2 | 3,5 | 0,7 | 1,2 | 1,5 | Bing | 0,5 | 2 | 2 |
| R2 | 561000 | 4998126 | Talweg | 3 | 1 | 3 | 2 | 6,0 | 6,2 | 4,4 | 0,3 | 1,5 | Ortho 58 | 0,2 | 2 | 5 |
| R2 | 561092 | 4998137 | Talweg | 3 | 1 | 3 | 2 | 6,2 | 7,2 | 5,2 | 1,0 | 1,0 | Ortho 58 | 0,2 | 2 | 5 |
| R2 | 561230 | 4998260 | Riser | 3 | 2 | 1 | 2 | 4,3 | 5,3 | 2,9 | 1,0 | 1,4 | Ortho 58 | 0,2 | 2 | 8 |
| R2 | 561290 | 4998268 | Riser | 3 | 2 | 1 | 2 | 1,9 | 2,4 | 1,0 | 0,6 | 0,9 | Ortho 58 | 0,2 | 2 | 8 |
| R2 | 561305 | 4998270 | Riser | 2 | 2 | 1 | 2 | 2,6 | 3,9 | 2,3 | 1,3 | 0,3 | Ortho 58 | 0,2 | 2 | 6 |
| R2 | 561305 | 4998270 | Riser | 2 | 1 | 1 | 2 | 7,4 | 9,9 | 4,8 | 2,5 | 2,6 | Ortho 58 | 0,2 | 2 | 5 |
| R2 | 561336 | 4998278 | Gully | 3 | 2 | 1 | 2 | 3,4 | 4,2 | 2,6 | 0,8 | 0,8 | Ortho 58 | 0,2 | 2 | 8 |
| R2 | 561372 | 4998285 | Talweg | 3 | 2 | 2 | 2 | 3,2 | 3,9 | 2,5 | 0,7 | 0,7 | Ortho 58 | 0,2 | 2 | 7 |
| R2 | 561395 | 4998291 | Talweg | 2 | 1 | 2 | 2 | 2,1 | 3,1 | 1,0 | 1,0 | 1,1 | Ortho 58 | 0,2 | 2 | 4 |
| R2 | 561502 | 4998316 | Talweg | 2 | 1 | 2 | 2 | 1,8 | 2,9 | 1,3 | 1,1 | 0,5 | Ortho 58 | 0,2 | 1 | 3 |
| R2 | 561560 | 4998344 | Talweg | 3 | 2 | 2 | 2 | 3,5 | 4,5 | 1,7 | 1,0 | 1,8 | Ortho 58 | 0,2 | 2 | 7 |
| R2 | 561590 | 4998354 | Talweg | 3 | 2 | 1 | 2 | 2,1 | 3,3 | 1,2 | 1,2 | 0,9 | Ortho 58 | 0,2 | 2 | 8 |
| R2 | 561800 | 4998490 | Gully | 3 | 2 | 4 | 2 | 9,8 | 10,7 | 9,1 | 1,0 | 0,6 | Ortho 58 | 0,2 | 2 | 6 |
| R2 | 561895 | 4998440 | Gully | 3 | 2 | 4 | 2 | 4,5 | 7,0 | 3,8 | 2,5 | 0,6 | Ortho 58 | 0,2 | 2 | 6 |

| Seg. | Lon. (UTM) | Lat. (UTM) | Marker Type | Mark. Obl. | Mark. res. (/2) | Nb. of splay | Scarp 2nd | Offset Pref. (m) | Offset max (m) | Offset min (m) | Δ+ (m) | Δ- (m) | Image type | Image Res. (m) | Image quality (/2) | Total Score (/10) |
|---|---|---|---|---|---|---|---|---|---|---|---|---|---|---|---|---|
| R2 | 561990 | 4998430 | Riser | 3 | 2 | 4 | 2 | 4,4 | 7,2 | 3,3 | 2,8 | 1,2 | Ortho 58 | 0,2 | 2 | 6 |
| R2 | 562235 | 4998395 | Gully | 2 | 2 | 1 | 2 | 2,9 | 4,6 | 2,1 | 1,6 | 0,8 | Ortho 58 | 0,2 | 2 | 6 |
| R2 | 562290 | 4998403 | Gully | 3 | 1 | 1 | 2 | 4,6 | 5,4 | 3,6 | 0,9 | 1,0 | Ortho 58 | 0,2 | 2 | 7 |
| R2 | 562345 | 4998411 | Gully | 3 | 2 | 1 | 2 | 2,8 | 3,5 | 1,9 | 0,7 | 0,9 | Ortho 58 | 0,2 | 2 | 8 |
| R2 | 562372 | 4998413 | Gully | 3 | 2 | 1 | 2 | 2,6 | 3,4 | 2,3 | 0,9 | 0,3 | Ortho 58 | 0,2 | 2 | 8 |
| R2 | 562400 | 4998415 | Ridge | 3 | 1 | 2 | 2 | 3,5 | 4,3 | 2,8 | 0,8 | 0,7 | Ortho 58 | 0,2 | 2 | 6 |
| R2 | 562482 | 4998421 | Gully | 3 | 1 | 3 | 1 | 3,7 | 4,7 | 2,9 | 1,0 | 0,7 | Ortho 58 | 0,2 | 2 | 6 |
| R2 | 562655 | 4998402 | Talweg | 3 | 2 | 3 | 1 | 12,9 | 16,1 | 11,1 | 3,2 | 1,8 | Ortho 58 | 0,2 | 2 | 7 |
| R2 | 563100 | 4998320 | Talweg | 3 | 2 | 2 | 1 | 1,4 | 1,8 | 1,2 | 0,5 | 0,3 | Ortho 58 | 0,2 | 2 | 8 |
| R2 | 563100 | 4998320 | Riser | 3 | 2 | 1 | 1 | 3,5 | 4,8 | 2,5 | 1,3 | 1,0 | Ortho 58 | 0,2 | 2 | 9 |
| R2 | 563100 | 4998320 | Riser | 3 | 1 | 1 | 1 | 22,9 | 24,9 | 20,4 | 2,0 | 2,5 | Ortho 58 | 0,2 | 2 | 8 |
| R2 | 563175 | 4998306 | Riser | 3 | 2 | 1 | 1 | 3,0 | 4,0 | 1,8 | 1,0 | 1,2 | Ortho 58 | 0,2 | 2 | 9 |
| R2 | 563175 | 4998306 | Riser | 3 | 2 | 1 | 1 | 9,0 | 10,1 | 7,3 | 1,1 | 1,7 | Ortho 58 | 0,2 | 2 | 9 |
| R2 | 563415 | 4998235 | Talweg | 3 | 2 | 6 | 0 | 7,0 | 8,5 | 5,4 | 1,5 | 1,6 | Ortho 58 | 0,2 | 2 | 8 |
| S3 | 563660 | 4998175 | Riser | 3 | 2 | 2 | 1 | 5,9 | 7,9 | 4,7 | 2,0 | 1,1 | Ortho 58 | 0,2 | 2 | 8 |
| S3 | 563720 | 4998165 | Riser | 3 | 2 | 4 | 0 | 7,9 | 8,7 | 6,9 | 0,8 | 0,9 | Ortho 58 | 0,2 | 2 | 8 |
| S3 | 563757 | 4998159 | Ridge | 3 | 1 | 2 | 0 | 17,7 | 19,5 | 16,0 | 1,8 | 1,7 | Ortho 58 | 0,2 | 2 | 8 |
| S3 | 563790 | 4998151 | Talweg | 3 | 1 | 3 | 0 | 10,2 | 11,3 | 9,2 | 1,1 | 1,1 | Ortho 58 | 0,2 | 2 | 7 |
| S3 | 563790 | 4998151 | Talweg | 3 | 1 | 3 | 0 | 7,2 | 9,8 | 5,3 | 2,6 | 1,8 | Ortho 58 | 0,2 | 2 | 7 |
| S3 | 563790 | 4998151 | Talweg | 3 | 1 | 3 | 0 | 30,0 | 31,0 | 28,7 | 1,0 | 1,4 | Ortho 58 | 0,2 | 2 | 7 |
| S3 | 563830 | 4998145 | Talweg | 2 | 1 | 4 | 0 | 4,4 | 5,0 | 3,5 | 0,6 | 0,9 | Ortho 58 | 0,2 | 2 | 5 |
| S3 | 563890 | 4998141 | Gully | 3 | 2 | 1 | 0 | 2,5 | 3,7 | 2,0 | 1,3 | 0,4 | Ortho 58 | 0,2 | 2 | 10 |
| S3 | 563930 | 4998134 | Riser | 3 | 2 | 2 | 0 | 3,2 | 4,5 | 2,5 | 1,3 | 0,7 | Ortho 58 | 0,2 | 2 | 9 |
| S3 | 563990 | 4998130 | Riser | 2 | 1 | 7 | 0 | 2,5 | 5,6 | 1,8 | 3,1 | 0,7 | Ortho 58 | 0,2 | 2 | 5 |
| S3 | 564040 | 4998129 | Riser | 3 | 1 | 2 | 0 | 7,6 | 8,4 | 5,6 | 0,8 | 2,0 | Ortho 58 | 0,2 | 2 | 8 |
| S3 | 564080 | 4998138 | Gully | 3 | 2 | 3 | 0 | 2,5 | 2,9 | 2,2 | 0,4 | 0,4 | Ortho 58 | 0,2 | 2 | 8 |
| S3 | 564115 | 4998150 | Gully | 3 | 2 | 4 | 0 | 1,1 | 2,3 | 0,7 | 1,2 | 0,4 | Ortho 58 | 0,2 | 2 | 8 |
| S3 | 564245 | 4998145 | Abandoned Chanel | 3 | 1 | 4 | 1 | 9,2 | 11,0 | 8,1 | 1,7 | 1,1 | Ortho 58 | 0,2 | 2 | 6 |
| S3 | 564260 | 4998151 | Riser | 3 | 2 | 4 | 1 | 10,8 | 15,1 | 7,2 | 4,2 | 3,7 | Ortho 58 | 0,2 | 2 | 7 |
| S3 | 564410 | 4998116 | Gully | 3 | 1 | 2 | 0 | 2,7 | 3,4 | 2,1 | 0,7 | 0,6 | Ortho 58 | 0,2 | 2 | 8 |
| S3 | 564498 | 4998102 | Talweg | 3 | 1 | 2 | 0 | 4,7 | 5,6 | 4,1 | 0,9 | 0,6 | Ortho 58 | 0,2 | 2 | 8 |
| S3 | 564525 | 4998103 | Talweg | 3 | 2 | 1 | 0 | 2,3 | 2,8 | 2,1 | 0,5 | 0,3 | Ortho 58 | 0,2 | 2 | 10 |
| S3 | 56454 | 499810 | Gully | 3 | 2 | 2 | 0 | 3,8 | 4,4 | 3,1 | 0,5 | 0,7 | Ortho | 0,2 | 2 | 9 |

| Seg. | Lon. (UTM) | Lat. (UTM) | Marker Type | Mark. Obl. | Mark. res. (/2) | Nb. of splay | Scarp 2nd | Offset Pref. (m) | Offset max (m) | Offset min (m) | Δ+ (m) | Δ- (m) | Image type | Image Res. (m) | Image quality (/2) | Total Score (/10) |
|---|---|---|---|---|---|---|---|---|---|---|---|---|---|---|---|---|
| | 1 | 6 | | | | | | | | | | | 58 | | | |
| S3 | 564567 | 4998102 | Talweg | 3 | 1 | 3 | 0 | 2,9 | 3,9 | 1,9 | 1,0 | 1,0 | Ortho 58 | 0,2 | 2 | 7 |
| S3 | 564590 | 4998100 | Gully | 3 | 1 | 3 | 0 | 1,8 | 2,4 | 1,2 | 0,6 | 0,6 | Ortho 58 | 0,2 | 2 | 7 |
| S3 | 564713 | 4998078 | Riser | 3 | 2 | 3 | 0 | 2,8 | 3,6 | 2,2 | 0,9 | 0,6 | Ortho 58 | 0,2 | 2 | 8 |
| S3 | 564812 | 4998066 | Riser | 3 | 2 | 1 | 0 | 14,3 | 15,7 | 12,7 | 1,4 | 1,6 | Ortho 58 | 0,2 | 2 | 10 |
| S3 | 565075 | 4998002 | Talweg | 3 | 2 | 3 | 0 | 1,0 | 1,5 | 0,5 | 0,5 | 0,5 | Ortho 58 | 0,2 | 2 | 8 |
| S3 | 565133 | 4998003 | Talweg | 3 | 2 | 3 | 0 | 1,8 | 2,2 | 1,3 | 0,4 | 0,5 | Ortho 58 | 0,2 | 2 | 8 |
| S3 | 565160 | 4998002 | Gully | 3 | 1 | 3 | 0 | 7,1 | 8,8 | 5,9 | 1,7 | 1,2 | Ortho 58 | 0,2 | 2 | 7 |
| S3 | 565310 | 4997971 | Talweg | 3 | 1 | 4 | 0 | 3,5 | 5,1 | 2,6 | 1,5 | 1,0 | Ortho 58 | 0,2 | 2 | 7 |
| S3 | 565358 | 4997974 | Gully | 3 | 1 | 2 | 0 | 1,6 | 1,9 | 0,9 | 0,3 | 0,7 | Ortho 58 | 0,2 | 2 | 8 |
| S3 | 565382 | 4997973 | Gully | 3 | 1 | 2 | 0 | 12,1 | 13,4 | 11,3 | 1,3 | 0,8 | Ortho 58 | 0,2 | 2 | 8 |
| S3 | 565382 | 4997973 | Gully | 3 | 1 | 2 | 0 | 4,6 | 5,6 | 3,8 | 1,0 | 0,8 | Ortho 58 | 0,2 | 2 | 8 |
| S3 | 565450 | 4997979 | Gully | 3 | 1 | 3 | 0 | 1,4 | 2,1 | 0,6 | 0,7 | 0,9 | Ortho 58 | 0,2 | 2 | 7 |
| S3 | 565528 | 4997967 | Talweg | 2 | 2 | 1 | 0 | 3,7 | 5,0 | 2,6 | 1,3 | 1,1 | Ortho 58 | 0,2 | 2 | 8 |
| S3 | 565583 | 4997974 | Talweg | 3 | 2 | 2 | 0 | 4,7 | 6,7 | 3,7 | 2,0 | 1,0 | Ortho 58 | 0,2 | 2 | 9 |
| S3 | 565675 | 4997984 | Talweg | 3 | 2 | 2 | 0 | 2,8 | 3,5 | 1,6 | 0,7 | 1,2 | Ortho 58 | 0,2 | 2 | 9 |
| S3 | 565675 | 4997984 | Talweg | 3 | 2 | 2 | 0 | 8,8 | 10,4 | 7,8 | 1,6 | 1,0 | Ortho 58 | 0,2 | 2 | 9 |
| S3 | 565800 | 4998013 | Talweg | 3 | 1 | 1 | 0 | 1,5 | 2,1 | 0,9 | 0,6 | 0,6 | Ortho 58 | 0,2 | 2 | 9 |
| S3 | 565855 | 4998005 | Gully | 2 | 1 | 1 | 0 | 1,5 | 2,2 | 1,1 | 0,7 | 0,4 | Ortho 58 | 0,2 | 2 | 7 |
| S3 | 565955 | 4997982 | Gully | 2 | 2 | 2 | 1 | 3,5 | 4,9 | 2,5 | 1,4 | 1,0 | Ortho 58 | 0,2 | 2 | 6 |
| S3 | 566050 | 4997765 | Gully | 2 | 1 | 2 | 1 | 1,3 | 2,1 | 1,1 | 0,8 | 0,3 | Ortho 58 | 0,2 | 2 | 5 |
| S3 | 566130 | 4997767 | Talweg | 3 | 2 | 3 | 0 | 6,5 | 7,1 | 6,1 | 0,7 | 0,3 | Ortho 58 | 0,2 | 2 | 8 |
| S3 | 566185 | 4997754 | River | 3 | 2 | 1 | 0 | 7,3 | 8,6 | 6,1 | 1,3 | 1,2 | Ortho 58 | 0,2 | 2 | 10 |
| S3 | 566404 | 4997740 | Talweg | 3 | 2 | 2 | 0 | 3,4 | 5,2 | 2,9 | 1,7 | 0,5 | Ortho 58 | 0,2 | 2 | 9 |
| S3 | 566430 | 4997746 | Gully | 3 | 1 | 2 | 0 | 1,7 | 2,3 | 1,4 | 0,6 | 0,3 | Ortho 58 | 0,2 | 2 | 8 |
| S3 | 566770 | 4997645 | Gully | 3 | 2 | 2 | 0 | 3,7 | 4,0 | 3,5 | 0,3 | 0,3 | Ortho 58 | 0,2 | 2 | 9 |
| S3 | 567110 | 4997566 | Talweg | 3 | 2 | 3 | 0 | 3,2 | 3,8 | 2,7 | 0,6 | 0,5 | Ortho 58 | 0,2 | 2 | 8 |
| S3 | 567110 | 4997566 | Talweg | 3 | 2 | 3 | 0 | 4,9 | 6,1 | 3,5 | 1,2 | 1,4 | Ortho 58 | 0,2 | 2 | 8 |
| S3 | 567140 | 4997564 | Talweg | 3 | 1 | 3 | 1 | 1,9 | 2,8 | 1,4 | 0,9 | 0,5 | Ortho 58 | 0,2 | 2 | 6 |
| S3 | 567163 | 4997560 | Talweg | 3 | 2 | 3 | 0 | 4,2 | 4,8 | 3,5 | 0,6 | 0,7 | Ortho 58 | 0,2 | 2 | 8 |
| S3 | 567163 | 4997560 | Talweg | 3 | 1 | 3 | 0 | 6,0 | 7,1 | 4,2 | 1,2 | 1,7 | Ortho 58 | 0,2 | 2 | 7 |
| S3 | 567215 | 4997544 | Talweg | 2 | 2 | 2 | 0 | 2,2 | 3,1 | 1,2 | 0,9 | 1,0 | Ortho 58 | 0,2 | 2 | 7 |
| S3 | 567215 | 4997544 | Talweg | 3 | 1 | 2 | 0 | 14,0 | 15,6 | 13,0 | 1,6 | 1,0 | Ortho 58 | 0,2 | 2 | 8 |
| S3 | 56721 | 499754 | Talweg | 3 | 1 | 2 | 0 | 25,5 | 27,0 | 23,7 | 1,5 | 1,8 | Ortho | 0,2 | 2 | 8 |

| Seg. | Lon. (UTM) | Lat. (UTM) | Marker Type | Mark. Obl. | Mark. res. (/2) | Nb. of splay | Scarp 2nd | Offset Pref. (m) | Offset max (m) | Offset min (m) | Δ+ (m) | Δ- (m) | Image type | Image Res. (m) | Image quality (/2) | Total Score (/10) |
|---|---|---|---|---|---|---|---|---|---|---|---|---|---|---|---|---|
| | 5 | 4 | | | | | | | | | | | 58 | | | |
| S3 | 567240 | 4997539 | Talweg | 2 | 1 | 2 | 0 | 1,8 | 2,6 | 1,4 | 0,8 | 0,4 | Ortho 58 | 0,2 | 2 | 6 |
| S3 | 567275 | 4997529 | River | 3 | 2 | 2 | 0 | 1,8 | 2,1 | 0,7 | 0,3 | 1,1 | Ortho 58 | 0,2 | 2 | 9 |
| S3 | 567295 | 4997521 | Talweg | 2 | 2 | 2 | 0 | 4,7 | 5,8 | 4,0 | 1,1 | 0,7 | Ortho 58 | 0,2 | 2 | 7 |
| S3 | 567311 | 4997518 | Talweg | 2 | 2 | 3 | 0 | 6,8 | 8,4 | 5,1 | 1,6 | 1,7 | Ortho 58 | 0,2 | 2 | 6 |
| S3 | 567340 | 4997507 | Talweg | 3 | 2 | 3 | 0 | 1,7 | 2,5 | 1,1 | 0,8 | 0,6 | Ortho 58 | 0,2 | 2 | 8 |
| S3 | 567370 | 4997500 | Talweg | 3 | 2 | 1 | 0 | 3,5 | 4,4 | 2,5 | 0,9 | 0,9 | Ortho 58 | 0,2 | 2 | 10 |
| S3 | 567525 | 4997471 | Gully | 3 | 2 | 1 | 0 | 4,4 | 5,3 | 3,9 | 0,8 | 0,6 | Ortho 58 | 0,2 | 2 | 10 |
| S3 | 567580 | 4997465 | Talweg | 3 | 1 | 3 | 0 | 2,0 | 2,6 | 1,8 | 0,6 | 0,3 | Ortho 58 | 0,2 | 2 | 7 |
| S3 | 567610 | 4997447 | Talweg | 2 | 1 | 3 | 0 | 2,4 | 3,4 | 1,4 | 1,0 | 1,0 | Ortho 58 | 0,2 | 2 | 5 |
| S3 | 567640 | 4997450 | Talweg | 3 | 1 | 3 | 0 | 1,7 | 2,6 | 1,1 | 0,9 | 0,6 | Ortho 58 | 0,2 | 2 | 7 |
| S3 | 567655 | 4997410 | Gully | 3 | 1 | 1 | 1 | 1,9 | 3,1 | 1,3 | 1,2 | 0,6 | Ortho 58 | 0,2 | 2 | 8 |
| S3 | 567675 | 4997404 | Riser | 3 | 2 | 1 | 1 | 2,5 | 3,0 | 2,2 | 0,5 | 0,4 | Ortho 58 | 0,2 | 2 | 9 |
| S3 | 567770 | 4997382 | Talweg | 3 | 1 | 2 | 0 | 4,3 | 5,0 | 3,2 | 0,7 | 1,0 | Ortho 58 | 0,2 | 1 | 7 |
| S3 | 567800 | 4997375 | Talweg | 3 | 2 | 2 | 0 | 5,0 | 6,6 | 3,4 | 1,6 | 1,7 | Ortho 58 | 0,2 | 2 | 9 |
| S3 | 567835 | 4997360 | Talweg | 3 | 2 | 2 | 0 | 3,4 | 4,9 | 2,7 | 1,5 | 0,7 | Ortho 58 | 0,2 | 2 | 9 |
| S3 | 567835 | 4997360 | Talweg | 3 | 2 | 2 | 0 | 11,5 | 12,6 | 8,9 | 1,1 | 2,6 | Ortho 58 | 0,2 | 2 | 9 |
| S3 | 567900 | 4997340 | Talweg | 3 | 2 | 2 | 0 | 3,5 | 5,1 | 2,4 | 1,6 | 1,1 | Ortho 58 | 0,2 | 2 | 9 |
| S3 | 567900 | 4997340 | Talweg | 3 | 2 | 2 | 0 | 6,4 | 7,2 | 5,6 | 0,9 | 0,7 | Ortho 58 | 0,2 | 2 | 9 |
| S3 | 567900 | 4997340 | Talweg | 3 | 2 | 2 | 0 | 22,8 | 23,4 | 21,6 | 0,9 | 1,2 | Ortho 58 | 0,2 | 2 | 9 |
| S3 | 567920 | 4997332 | Talweg | 2 | 2 | 3 | 0 | 2,6 | 4,0 | 1,8 | 1,4 | 0,8 | Ortho 58 | 0,2 | 2 | 6 |
| S3 | 567940 | 4997327 | Riser | 3 | 1 | 2 | 0 | 4,4 | 5,2 | 3,6 | 0,8 | 0,8 | Ortho 58 | 0,2 | 2 | 8 |
| S3 | 568075 | 4997300 | Gully | 3 | 2 | 2 | 0 | 2,8 | 3,3 | 2,0 | 0,5 | 0,7 | Ortho 58 | 0,2 | 2 | 9 |
| S3 | 568095 | 4997291 | Gully | 3 | 1 | 2 | 0 | 6,1 | 7,0 | 5,4 | 0,9 | 0,7 | Ortho 58 | 0,2 | 2 | 8 |
| S3 | 568121 | 4997283 | Talweg | 2 | 2 | 2 | 0 | 4,2 | 5,1 | 2,8 | 0,9 | 1,4 | Ortho 58 | 0,2 | 2 | 7 |
| S3 | 568175 | 4997273 | Talweg | 2 | 1 | 3 | 0 | 7,9 | 9,6 | 7,5 | 1,6 | 0,4 | Ortho 58 | 0,2 | 2 | 5 |
| S3 | 568225 | 4997263 | Ridge | 3 | 1 | 3 | 0 | 7,5 | 8,4 | 6,7 | 1,0 | 0,7 | Ortho 58 | 0,2 | 2 | 7 |
| S3 | 568235 | 4997262 | Talweg | 3 | 2 | 2 | 0 | 10,3 | 11,0 | 9,5 | 0,7 | 0,8 | Ortho 58 | 0,2 | 2 | 9 |
| S3 | 568260 | 4997260 | Riser | 2 | 1 | 3 | 0 | 7,7 | 8,8 | 7,1 | 1,1 | 0,6 | Ortho 58 | 0,2 | 2 | 5 |
| S3 | 568260 | 4997260 | Riser | 3 | 2 | 3 | 0 | 10,1 | 11,5 | 9,1 | 1,4 | 1,0 | Ortho 58 | 0,2 | 2 | 8 |
| S3 | 568280 | 4997257 | Talweg | 3 | 2 | 2 | 0 | 4,0 | 5,2 | 3,3 | 1,1 | 0,7 | Ortho 58 | 0,2 | 2 | 9 |
| S3 | 568307 | 4997252 | Riser | 2 | 2 | 3 | 0 | 9,5 | 10,5 | 8,3 | 1,0 | 1,2 | Ortho 58 | 0,2 | 2 | 6 |
| S3 | 568344 | 4997250 | Talweg | 3 | 2 | 3 | 0 | 20,3 | 23,4 | 18,8 | 3,1 | 1,5 | Bing | 0,4 | 2 | 7 |
| S3 | 56834 | 499725 | Talweg | 3 | 2 | 3 | 0 | 33,2 | 35,3 | 31,5 | 2,0 | 1,8 | Bing | 0,4 | 2 | 7 |

| Seg. | Lon. (UTM) | Lat. (UTM) | Marker Type | Mark. Obl. | Mark. res. (/2) | Nb. of splay | Scarp 2nd | Offset Pref. (m) | Offset max (m) | Offset min (m) | Δ+ (m) | Δ- (m) | Image type | Image Res. (m) | Image quality (/2) | Total Score (/10) |
|---|---|---|---|---|---|---|---|---|---|---|---|---|---|---|---|---|
| S3 | 568364 | 4990240 | Talweg | 3 | 2 | 2 | 0 | 3,5 | 4,3 | 2,7 | 0,8 | 0,8 | Ortho 58 | 0,2 | 1 | 8 |
| S3 | 568370 | 4997239 | Talweg | 3 | 2 | 2 | 0 | 9,7 | 11,0 | 8,3 | 1,3 | 1,4 | Bing | 0,4 | 2 | 8 |
| S3 | 568390 | 4997233 | Talweg | 3 | 2 | 2 | 0 | 3,5 | 4,5 | 2,5 | 1,0 | 1,0 | Ortho 58 | 0,2 | 1 | 8 |
| S3 | 568412 | 4997227 | Abandoned Chanel | 3 | 1 | 3 | 0 | 7,4 | 8,6 | 7,0 | 1,2 | 0,3 | Ortho 58 | 0,2 | 2 | 7 |
| S3 | 568424 | 4997223 | Talweg | 2 | 2 | 4 | 0 | 3,4 | 3,7 | 2,8 | 0,3 | 0,5 | Ortho 58 | 0,2 | 2 | 6 |
| S3 | 568435 | 4997219 | Talweg | 2 | 2 | 5 | 0 | 5,3 | 6,4 | 3,4 | 1,0 | 2,0 | Ortho 58 | 0,2 | 2 | 6 |
| S3 | 568452 | 4997216 | Talweg | 3 | 2 | 6 | 0 | 2,9 | 3,7 | 1,9 | 0,8 | 1,1 | Ortho 58 | 0,2 | 2 | 8 |
| S3 | 568470 | 4997211 | talweg | 3 | 2 | 3 | 0 | 3,7 | 5,3 | 2,3 | 1,6 | 1,5 | Ortho 58 | 0,2 | 2 | 8 |
| S3 | 568486 | 4997207 | Abandoned Chanel | 3 | 2 | 3 | 0 | 11,4 | 12,6 | 10,3 | 1,2 | 1,0 | Ortho 58 | 0,2 | 2 | 8 |
| S3 | 568522 | 4997195 | Talweg | 3 | 2 | 3 | 0 | 5,1 | 6,6 | 3,7 | 1,5 | 1,4 | Ortho 58 | 0,2 | 2 | 8 |
| S3 | 568535 | 4997188 | Talweg | 3 | 1 | 2 | 0 | 3,4 | 6,1 | 2,1 | 2,7 | 1,3 | Ortho 58 | 0,2 | 2 | 8 |
| S3 | 568570 | 4997180 | Talweg | 2 | 2 | 2 | 0 | 20,1 | 22,2 | 17,7 | 2,1 | 2,4 | Ortho 58 | 0,2 | 2 | 7 |
| S3 | 568577 | 4997175 | Talweg | 2 | 2 | 2 | 0 | 2,5 | 4,2 | 1,6 | 1,7 | 0,8 | Ortho 58 | 0,2 | 2 | 7 |
| S3 | 568610 | 4997160 | Talweg | 3 | 2 | 2 | 0 | 7,7 | 9,2 | 6,5 | 1,5 | 1,2 | Ortho 58 | 0,2 | 2 | 9 |
| S3 | 568640 | 4997146 | Talweg | 2 | 1 | 3 | 0 | 7,9 | 9,1 | 6,6 | 1,2 | 1,3 | Ortho 58 | 0,2 | 2 | 5 |
| S3 | 568670 | 4997137 | Riser | 3 | 2 | 3 | 0 | 2,6 | 5,7 | 1,8 | 3,1 | 0,9 | Ortho 58 | 0,2 | 2 | 8 |
| S3 | 568670 | 4997137 | Riser | 3 | 2 | 3 | 0 | 15,2 | 16,1 | 13,3 | 0,9 | 1,9 | Ortho 58 | 0,2 | 2 | 8 |
| S3 | 568705 | 4997130 | Gully | 3 | 2 | 1 | 0 | 3,6 | 4,9 | 2,4 | 1,3 | 1,2 | Ortho 58 | 0,2 | 2 | 10 |
| S3 | 568785 | 4997114 | Gully | 3 | 2 | 1 | 0 | 2,8 | 3,8 | 2,2 | 1,0 | 0,6 | Ortho 58 | 0,2 | 2 | 10 |
| S3 | 568865 | 4997110 | Gully | 2 | 2 | 3 | 0 | 4,7 | 5,9 | 3,9 | 1,1 | 0,9 | Ortho 58 | 0,2 | 2 | 6 |
| S3 | 568965 | 4997109 | Gully | 3 | 2 | 5 | 0 | 2,9 | 3,9 | 2,2 | 1,0 | 0,7 | Ortho 58 | 0,2 | 2 | 8 |
| S3 | 568986 | 4997108 | Gully | 3 | 1 | 5 | 0 | 5,0 | 5,8 | 3,9 | 0,9 | 1,0 | Ortho 58 | 0,2 | 2 | 7 |
| S3 | 569000 | 4997106 | Gully | 3 | 1 | 3 | 0 | 4,5 | 5,7 | 3,6 | 1,1 | 0,9 | Ortho 58 | 0,2 | 2 | 7 |
| S3 | 569020 | 4997100 | Gully | 3 | 1 | 4 | 0 | 5,4 | 6,1 | 4,8 | 0,7 | 0,6 | Ortho 58 | 0,2 | 2 | 7 |
| S3 | 569055 | 4997091 | Gully | 3 | 2 | 2 | 0 | 7,5 | 9,1 | 6,5 | 1,6 | 1,0 | Ortho 58 | 0,2 | 2 | 9 |
| S3 | 569082 | 4997080 | Gully | 3 | 2 | 2 | 0 | 3,1 | 4,5 | 2,3 | 1,5 | 0,8 | Ortho 58 | 0,2 | 2 | 9 |
| S3 | 569100 | 4997073 | Gully | 3 | 2 | 1 | 0 | 3,4 | 3,6 | 2,5 | 0,3 | 0,9 | Ortho 58 | 0,2 | 2 | 10 |
| S3 | 569100 | 4997073 | Gully | 3 | 2 | 1 | 0 | 11,1 | 12,1 | 10,3 | 0,9 | 0,8 | Ortho 58 | 0,2 | 2 | 10 |
| S3 | 569115 | 4997070 | Gully | 3 | 2 | 2 | 0 | 12,3 | 13,3 | 11,6 | 1,0 | 0,7 | Ortho 58 | 0,2 | 2 | 9 |
| S3 | 569140 | 4997062 | Gully | 3 | 2 | 2 | 0 | 2,7 | 3,0 | 1,7 | 0,3 | 0,9 | Ortho 58 | 0,2 | 2 | 9 |
| S3 | 569172 | 4997056 | Gully | 3 | 2 | 1 | 0 | 4,5 | 6,5 | 3,3 | 2,0 | 1,2 | Ortho 58 | 0,2 | 2 | 10 |
| S3 | 56925 | 499703 | Gully | 3 | 2 | 2 | 0 | 9,0 | 10,6 | 7,3 | 1,6 | 1,6 | Ortho | 0,2 | 2 | 9 |

| Seg. | Lon. (UTM) | Lat. (UTM) | Marker Type | Mark. Obl. | Mark. res. (/2) | Nb. of splay | Scarp 2nd | Offset Pref. (m) | Offset max (m) | Offset min (m) | Δ+ (m) | Δ- (m) | Image type | Image Res. (m) | Image quality (/2) | Total Score (/10) |
|---|---|---|---|---|---|---|---|---|---|---|---|---|---|---|---|---|
| | 0 | 2 | | | | | | | | | | | 58 | | | |
| S3 | 569340 | 4997004 | Gully | 3 | 2 | 1 | 1 | 3,9 | 6,2 | 3,1 | 2,3 | 0,7 | Ortho 58 | 0,2 | 2 | 9 |
| S3 | 569415 | 4996985 | Talweg | 3 | 2 | 2 | 0 | 3,9 | 5,5 | 2,9 | 1,7 | 1,0 | Ortho 58 | 0,2 | 2 | 9 |
| S3 | 569415 | 4996985 | Talweg | 3 | 2 | 2 | 0 | 6,8 | 7,7 | 5,3 | 1,0 | 1,5 | Ortho 58 | 0,2 | 2 | 9 |
| S3 | 569475 | 4996965 | Gully | 3 | 2 | 2 | 0 | 8,1 | 9,6 | 7,3 | 1,5 | 0,8 | Ortho 58 | 0,2 | 2 | 9 |
| S3 | 569495 | 4996956 | Gully | 3 | 2 | 2 | 0 | 10,2 | 11,4 | 9,2 | 1,2 | 1,0 | Ortho 58 | 0,2 | 2 | 9 |
| S3 | 569512 | 4996945 | Gully | 3 | 2 | 1 | 0 | 7,3 | 8,8 | 6,8 | 1,5 | 0,5 | Ortho 58 | 0,2 | 2 | 10 |
| S3 | 569542 | 4996940 | Gully | 3 | 2 | 2 | 0 | 7,0 | 7,8 | 6,2 | 0,8 | 0,7 | Ortho 58 | 0,2 | 2 | 9 |
| S3 | 569575 | 4996938 | Gully | 3 | 2 | 2 | 0 | 6,7 | 8,9 | 5,5 | 2,2 | 1,2 | Ortho 58 | 0,2 | 2 | 9 |
| S3 | 569595 | 4996940 | Gully | 3 | 2 | 2 | 0 | 2,6 | 3,0 | 2,1 | 0,5 | 0,5 | Ortho 58 | 0,2 | 2 | 9 |
| S3 | 569650 | 4996930 | Gully | 3 | 1 | 5 | 0 | 6,6 | 7,9 | 5,6 | 1,3 | 1,0 | Ortho 58 | 0,2 | 2 | 7 |
| S3 | 569875 | 4996875 | Riser | 3 | 2 | 2 | 0 | 5,6 | 7,7 | 3,8 | 2,1 | 1,8 | Ortho 58 | 0,2 | 2 | 9 |
| S3 | 569875 | 4996875 | Riser | 3 | 2 | 2 | 0 | 82,7 | 87,2 | 74,1 | 4,5 | 8,6 | Ortho 58 | 0,2 | 2 | 9 |
| S3 | 570030 | 4996840 | Talweg | 3 | 2 | 2 | 0 | 3,4 | 6,1 | 2,4 | 2,7 | 1,0 | Ortho 58 | 0,2 | 2 | 9 |
| S3 | 570030 | 4996840 | Talweg | 3 | 2 | 2 | 0 | 8,7 | 11,1 | 7,7 | 2,4 | 1,0 | Ortho 58 | 0,2 | 2 | 9 |
| S3 | 570308 | 4996770 | Riser | 3 | 1 | 2 | 1 | 2,0 | 3,7 | 0,9 | 1,7 | 1,1 | Ortho 58 | 0,2 | 2 | 7 |
| S3 | 570411 | 4996760 | Talweg | 3 | 1 | 2 | 2 | 5,3 | 6,7 | 4,1 | 1,4 | 1,2 | Ortho 58 | 0,2 | 2 | 6 |
| S3 | 570452 | 4996747 | Ridge | 3 | 2 | 2 | 1 | 5,3 | 5,8 | 4,7 | 0,5 | 0,5 | Ortho 58 | 0,2 | 2 | 8 |
| S3 | 570470 | 4996690 | Talweg | 3 | 1 | 2 | 1 | 6,3 | 9,3 | 5,2 | 3,0 | 1,1 | Ortho 58 | 0,2 | 2 | 7 |
| S4 | 571940 | 4996400 | Talweg | 2 | 1 | 1 | 0 | 7,9 | 9,7 | 6,7 | 1,9 | 1,1 | Ortho 58 | 0,2 | 1 | 6 |
| S4 | 572025 | 4996340 | Talweg | 3 | 2 | 1 | 0 | 3,9 | 5,1 | 2,6 | 1,2 | 1,3 | Ortho 58 | 0,2 | 1 | 9 |
| S4 | 572240 | 4996285 | Talweg | 3 | 2 | 1 | 1 | 17,8 | 19,2 | 16,9 | 1,3 | 0,9 | Ortho 58 | 0,2 | 1 | 8 |
| S4 | 572350 | 4996262 | River | 3 | 2 | 1 | 0 | 3,8 | 5,2 | 2,4 | 1,4 | 1,4 | Ortho 58 | 0,2 | 1 | 9 |
| S4 | 572350 | 4996262 | River | 3 | 1 | 1 | 1 | 35,0 | 37,7 | 31,9 | 2,7 | 3,1 | Ortho 58 | 0,2 | 2 | 8 |
| S4 | 572507 | 4996213 | Talweg | 2 | 1 | 2 | 1 | 2,3 | 3,7 | 1,5 | 1,4 | 0,8 | Ortho 58 | 0,2 | 2 | 5 |
| S4 | 572555 | 4996185 | Talweg | 2 | 1 | 2 | 1 | 5,5 | 7,1 | 4,1 | 1,6 | 1,4 | Ortho 58 | 0,2 | 2 | 5 |
| S4 | 572730 | 4996130 | Riser | 3 | 2 | 1 | 1 | 3,2 | 3,5 | 2,4 | 0,3 | 0,8 | Ortho 58 | 0,2 | 2 | 9 |
| S4 | 572730 | 4996130 | Riser | 3 | 2 | 1 | 1 | 7,3 | 10,5 | 4,5 | 3,1 | 2,8 | Ortho 58 | 0,2 | 2 | 9 |
| S4 | 572835 | 4996101 | Gully | 3 | 2 | 1 | 1 | 3,1 | 4,1 | 2,0 | 1,0 | 1,1 | Ortho 58 | 0,2 | 2 | 9 |
| S4 | 572950 | 4996050 | River | 3 | 2 | 1 | 1 | 4,7 | 5,5 | 3,6 | 0,9 | 1,1 | Ortho 58 | 0,2 | 2 | 9 |
| S4 | 572950 | 4996050 | River | 3 | 2 | 1 | 1 | 12,2 | 16,9 | 9,0 | 4,7 | 3,2 | Ortho 58 | 0,2 | 2 | 9 |
| S4 | 573025 | 4996035 | Talweg | 3 | 2 | 1 | 1 | 2,1 | 3,0 | 1,6 | 0,9 | 0,5 | Ortho 58 | 0,2 | 2 | 9 |
| S4 | 573050 | 4996025 | Talweg | 3 | 2 | 1 | 1 | 5,0 | 5,7 | 4,2 | 0,7 | 0,8 | Ortho 58 | 0,2 | 2 | 9 |
| S4 | 57315 | 499598 | Talweg | 3 | 1 | 0 | 2 | 4,6 | 7,6 | 3,6 | 3,0 | 0,9 | Ortho | 0,2 | 1 | 4 |

| Seg. | Lon. (UTM) | Lat. (UTM) | Marker Type | Mark. Obl. | Mark. res. (/2) | Nb. of splay | Scarp 2nd | Offset Pref. (m) | Offset max (m) | Offset min (m) | Δ+ (m) | Δ- (m) | Image type | Image Res. (m) | Image quality (/2) | Total Score (/10) |
|---|---|---|---|---|---|---|---|---|---|---|---|---|---|---|---|---|
| | 5 | 0 | | | | | | | | | | | 58 | | | |
| S4 | 573185 | 4995970 | Talweg | 2 | 1 | 0 | 2 | 8,9 | 9,9 | 7,9 | 1,0 | 1,0 | Ortho 58 | 0,2 | 1 | 2 |
| S4 | 573455 | 4995870 | Riser | 3 | 2 | 2 | 1 | 6,3 | 8,5 | 4,2 | 2,2 | 2,1 | Ortho 58 | 0,2 | 1 | 7 |
| S4 | 573525 | 4995850 | Gully | 2 | 1 | 1 | 1 | 5,8 | 7,2 | 5,0 | 1,3 | 0,9 | Ortho 58 | 0,2 | 2 | 6 |
| S4 | 573610 | 4995830 | Riser | 3 | 2 | 2 | 1 | 18,1 | 19,2 | 16,5 | 1,1 | 1,5 | Ortho 58 | 0,2 | 1 | 7 |
| S4 | 574200 | 4995582 | Talweg | 2 | 1 | 1 | 1 | 3,2 | 3,6 | 2,6 | 0,3 | 0,6 | Ortho 58 | 0,2 | 2 | 6 |
| S4 | 574250 | 4995562 | Talweg | 2 | 1 | 3 | 1 | 2,2 | 3,1 | 1,7 | 0,8 | 0,5 | Ortho 58 | 0,2 | 2 | 4 |
| S4 | 574250 | 4995562 | Talweg | 2 | 2 | 3 | 1 | 7,3 | 9,1 | 5,8 | 1,8 | 1,5 | Ortho 58 | 0,2 | 2 | 5 |
| S4 | 574285 | 4995542 | Talweg | 3 | 1 | 2 | 1 | 6,2 | 7,1 | 5,4 | 0,9 | 0,9 | Ortho 58 | 0,2 | 2 | 7 |
| S4 | 574305 | 4995530 | Talweg | 3 | 2 | 2 | 1 | 9,9 | 11,1 | 8,7 | 1,2 | 1,1 | Ortho 58 | 0,2 | 2 | 8 |
| S4 | 574340 | 4995500 | Talweg | 3 | 1 | 2 | 1 | 2,1 | 3,0 | 1,5 | 0,9 | 0,6 | Ortho 58 | 0,2 | 2 | 7 |
| S4 | 574600 | 4995420 | Talweg | 3 | 1 | 1 | 1 | 3,6 | 5,2 | 2,6 | 1,7 | 1,0 | Ortho 58 | 0,2 | 2 | 8 |
| S4 | 574720 | 4995380 | Gully | 3 | 1 | 2 | 1 | 4,1 | 5,1 | 3,2 | 1,0 | 0,9 | Ortho 58 | 0,2 | 2 | 7 |
| S4 | 574770 | 4995362 | Gully | 3 | 1 | 1 | 1 | 3,4 | 4,0 | 3,1 | 0,6 | 0,3 | Ortho 58 | 0,2 | 2 | 8 |
| S4 | 574825 | 4995353 | Talweg | 3 | 2 | 1 | 1 | 3,0 | 3,7 | 1,1 | 0,7 | 1,9 | Ortho 58 | 0,2 | 1 | 8 |
| S4 | 574825 | 4995353 | Abandoned Talweg | 3 | 2 | 1 | 1 | 66,8 | 69,8 | 59,1 | 3,0 | 7,7 | Ortho 58 | 0,2 | 2 | 9 |
| S4 | 574900 | 4995335 | Gully | 3 | 1 | 1 | 1 | 6,4 | 7,5 | 6,0 | 1,1 | 0,4 | Ortho 58 | 0,2 | 2 | 8 |
| S4 | 574940 | 4995320 | Talweg | 3 | 2 | 1 | 1 | 7,9 | 8,8 | 7,2 | 0,9 | 0,7 | Ortho 58 | 0,2 | 2 | 9 |
| S4 | 575000 | 4995310 | Gully | 3 | 1 | 2 | 1 | 4,6 | 5,3 | 3,9 | 0,7 | 0,7 | Ortho 58 | 0,2 | 2 | 7 |
| S4 | 575050 | 4995290 | Talweg | 3 | 2 | 1 | 1 | 5,3 | 6,9 | 4,4 | 1,6 | 0,9 | Ortho 58 | 0,2 | 2 | 9 |
| S4 | 575050 | 4995290 | Talweg | 3 | 2 | 1 | 1 | 20,6 | 22,5 | 19,1 | 1,8 | 1,6 | Ortho 58 | 0,2 | 2 | 9 |
| S4 | 575100 | 4995270 | Talweg | 2 | 2 | 1 | 1 | 3,5 | 4,7 | 2,7 | 1,3 | 0,8 | Ortho 58 | 0,2 | 2 | 7 |
| S4 | 575150 | 4995250 | Talweg | 1 | 2 | 1 | 1 | 9,2 | 12,2 | 7,8 | 3,0 | 1,5 | Ortho 58 | 0,2 | 2 | 6 |
| S4 | 575180 | 4995240 | Talweg | 3 | 2 | 1 | 1 | 4,1 | 5,4 | 3,0 | 1,3 | 1,1 | Ortho 58 | 0,2 | 2 | 9 |
| S4 | 575240 | 4995230 | Talweg | 3 | 2 | 1 | 1 | 5,4 | 7,3 | 4,7 | 1,9 | 0,7 | Ortho 58 | 0,2 | 2 | 9 |
| S4 | 575385 | 4995181 | Riser | 3 | 2 | 1 | 1 | 3,3 | 3,8 | 2,3 | 0,5 | 0,9 | Ortho 58 | 0,2 | 2 | 9 |
| S4 | 575416 | 4995175 | Riser | 3 | 2 | 1 | 1 | 3,7 | 4,7 | 3,5 | 1,0 | 0,3 | Ortho 58 | 0,2 | 2 | 9 |
| S4 | 575416 | 4995175 | Talweg | 3 | 2 | 1 | 1 | 17,1 | 19,4 | 15,6 | 2,3 | 1,4 | Ortho 58 | 0,2 | 2 | 9 |
| S4 | 575445 | 4995165 | Riser | 2 | 0 | 1 | 1 | 17,0 | 19,3 | 15,3 | 2,3 | 1,7 | Ortho 58 | 0,2 | 2 | 5 |
| S4 | 575500 | 4995140 | Riser | 3 | 2 | 1 | 1 | 10,4 | 11,8 | 9,2 | 1,4 | 1,3 | Ortho 58 | 0,2 | 2 | 9 |
| S4 | 575815 | 4995005 | Talweg | 3 | 2 | 1 | 1 | 6,1 | 7,1 | 5,2 | 1,0 | 0,9 | Ortho 58 | 0,2 | 2 | 9 |
| S4 | 575815 | 4995005 | Talweg | 3 | 2 | 1 | 1 | 14,2 | 15,0 | 13,3 | 0,8 | 0,8 | Ortho 58 | 0,2 | 2 | 9 |
| S4 | 575885 | 4994990 | Talweg | 3 | 2 | 1 | 1 | 2,4 | 3,2 | 1,8 | 0,8 | 0,6 | Ortho 58 | 0,2 | 2 | 9 |

| Seg. | Lon. (UTM) | Lat. (UTM) | Marker Type | Mark. Obl. | Mark. res. (/2) | Nb. of splay | Scarp 2nd | Offset Pref. (m) | Offset max (m) | Offset min (m) | Δ+ (m) | Δ- (m) | Image type | Image Res. (m) | Image quality (/2) | Total Score (/10) |
|---|---|---|---|---|---|---|---|---|---|---|---|---|---|---|---|---|
| S4 | 576000 | 4994950 | Gully | 3 | 2 | 2 | 1 | 5,6 | 7,3 | 4,9 | 1,7 | 0,7 | Ortho 58 | 0,2 | 2 | 8 |
| S4 | 576080 | 4994925 | Riser | 3 | 2 | 1 | 1 | 6,0 | 7,4 | 5,2 | 1,3 | 0,8 | Ortho 58 | 0,2 | 2 | 9 |
| S4 | 576140 | 4994905 | Riser | 3 | 2 | 1 | 1 | 7,9 | 8,8 | 6,8 | 0,9 | 1,1 | Ortho 58 | 0,2 | 2 | 9 |
| S4 | 576225 | 4994875 | Gully | 3 | 2 | 1 | 1 | 4,3 | 4,8 | 3,5 | 0,5 | 0,8 | Ortho 58 | 0,2 | 2 | 9 |
| S4 | 576345 | 4994860 | Talweg | 3 | 1 | 3 | 1 | 3,7 | 4,7 | 3,6 | 0,9 | 0,3 | Ortho 58 | 0,2 | 2 | 6 |
| S4 | 576600 | 4994900 | Talweg | 3 | 2 | 4 | 2 | 3,7 | 6,7 | 2,7 | 3,0 | 1,0 | Ortho 58 | 0,2 | 2 | 6 |
| S4 | 576600 | 4994900 | Talweg | 3 | 2 | 4 | 2 | 25,6 | 26,5 | 21,1 | 0,9 | 4,5 | Ortho 58 | 0,2 | 2 | 6 |
| S4 | 576600 | 4994900 | Talweg | 3 | 2 | 4 | 2 | 36,9 | 40,0 | 33,7 | 3,1 | 3,2 | Ortho 58 | 0,2 | 2 | 6 |
| S4 | 576600 | 4994900 | Talweg | 3 | 2 | 4 | 2 | 66,8 | 69,8 | 62,4 | 3,0 | 4,4 | Ortho 58 | 0,2 | 2 | 6 |
| S4 | 576720 | 4994920 | Talweg | 2 | 1 | 2 | 2 | 9,7 | 11,7 | 8,9 | 2,0 | 0,9 | Ortho 58 | 0,2 | 2 | 4 |
| S4 | 576720 | 4994920 | Talweg | 2 | 1 | 2 | 2 | 29,1 | 31,6 | 27,0 | 2,5 | 2,0 | Ortho 58 | 0,2 | 2 | 4 |
| S4 | 576790 | 4994930 | Gully | 2 | 1 | 5 | 3 | 5,5 | 6,2 | 4,3 | 0,7 | 1,2 | Ortho 58 | 0,2 | 2 | 2 |
| S4 | 576870 | 4994940 | Talweg | 3 | 2 | 2 | 2 | 5,1 | 6,5 | 4,2 | 1,3 | 0,9 | Ortho 58 | 0,2 | 2 | 7 |
| S4 | 576870 | 4994940 | Riser | 3 | 1 | 2 | 2 | 47,4 | 50,8 | 44,7 | 3,4 | 2,8 | Ortho 58 | 0,2 | 2 | 6 |
| S4 | 576957 | 4994950 | Gully | 3 | 2 | 2 | 2 | 4,3 | 5,8 | 2,3 | 1,5 | 2,0 | Ortho 58 | 0,2 | 2 | 7 |
| S4 | 577020 | 4994965 | Talweg | 3 | 2 | 2 | 2 | 4,2 | 4,8 | 3,6 | 0,6 | 0,7 | Ortho 58 | 0,2 | 2 | 7 |
| S4 | 577020 | 4994965 | Riser | 3 | 1 | 2 | 2 | 14,7 | 15,6 | 13,1 | 0,9 | 1,6 | Ortho 58 | 0,2 | 2 | 6 |
| S4 | 577020 | 4994965 | Riser | 3 | 1 | 2 | 2 | 24,9 | 27,1 | 22,2 | 2,3 | 2,6 | Ortho 58 | 0,2 | 2 | 6 |
| S4 | 577100 | 4994975 | Riser | 3 | 1 | 2 | 1 | 18,4 | 21,7 | 15,8 | 3,3 | 2,6 | Ortho 58 | 0,2 | 2 | 7 |
| S4 | 577150 | 4994980 | Chanel | 3 | 2 | 1 | 1 | 6,6 | 7,7 | 5,6 | 1,1 | 1,1 | Ortho 58 | 0,2 | 2 | 9 |
| S4 | 577260 | 4995015 | Riser | 2 | 2 | 1 | 1 | 4,6 | 5,6 | 3,6 | 1,0 | 1,0 | Ortho 58 | 0,2 | 2 | 7 |
| S4 | 577420 | 4995020 | Gully | 3 | 2 | 3 | 0 | 4,4 | 6,1 | 3,3 | 1,7 | 1,1 | Ortho 58 | 0,2 | 2 | 8 |
| S4 | 577470 | 4995020 | Talweg | 3 | 1 | 2 | 0 | 2,5 | 3,6 | 1,4 | 1,1 | 1,1 | Ortho 58 | 0,2 | 2 | 8 |
| S4 | 577500 | 4995017 | Gully | 3 | 2 | 3 | 0 | 3,1 | 4,3 | 2,0 | 1,2 | 1,1 | Ortho 58 | 0,2 | 2 | 8 |
| S4 | 577555 | 4995010 | Gully | 3 | 1 | 3 | 0 | 2,1 | 2,8 | 1,3 | 0,7 | 0,8 | Ortho 58 | 0,2 | 2 | 7 |
| S4 | 577670 | 4995008 | Talweg | 2 | 2 | 2 | 1 | 4,6 | 5,8 | 3,0 | 1,2 | 1,6 | Ortho 58 | 0,2 | 2 | 6 |
| S4 | 577720 | 4995005 | Gully | 3 | 2 | 2 | 1 | 4,9 | 5,9 | 2,6 | 1,0 | 2,3 | Ortho 58 | 0,2 | 2 | 8 |
| S4 | 577790 | 4995000 | Talweg | 3 | 1 | 3 | 1 | 8,3 | 11,1 | 6,4 | 2,7 | 1,9 | Ortho 58 | 0,2 | 2 | 6 |
| S4 | 577790 | 4995000 | Talweg | 3 | 1 | 3 | 1 | 12,9 | 14,8 | 10,9 | 2,0 | 2,0 | Ortho 58 | 0,2 | 2 | 6 |
| S4 | 577840 | 4994990 | River | 3 | 2 | 1 | 1 | 6,2 | 7,7 | 3,2 | 1,5 | 3,0 | Ortho 58 | 0,2 | 2 | 9 |
| S4 | 577925 | 4994965 | Talweg | 3 | 1 | 2 | 1 | 5,2 | 6,4 | 3,8 | 1,2 | 1,4 | Ortho 58 | 0,2 | 2 | 7 |
| S4 | 577970 | 4994970 | Talweg | 3 | 2 | 2 | 0 | 13,4 | 15,8 | 12,3 | 2,3 | 1,2 | Ortho 58 | 0,2 | 2 | 9 |
| S4 | 578010 | 4994960 | Riser | 3 | 1 | 2 | 0 | 18,2 | 18,8 | 16,4 | 0,9 | 1,8 | Ortho 58 | 0,2 | 2 | 8 |

| Seg. | Lon. (UTM) | Lat. (UTM) | Marker Type | Mark. Obl. | Mark. res. (/2) | Nb. of splay | Scarp 2nd | Offset Pref. (m) | Offset max (m) | Offset min (m) | Δ+ (m) | Δ- (m) | Image type | Image Res. (m) | Image quality (/2) | Total Score (/10) |
|---|---|---|---|---|---|---|---|---|---|---|---|---|---|---|---|---|
| S4 | 578115 | 4994940 | Riser | 2 | 2 | 1 | 1 | 13,3 | 18,3 | 12,0 | 5,0 | 1,4 | Ortho 58 | 0,2 | 2 | 7 |
| S4 | 578190 | 4994910 | Talweg | 2 | 2 | 1 | 1 | 3,9 | 6,2 | 2,0 | 2,3 | 1,9 | Ortho 58 | 0,2 | 2 | 7 |
| S4 | 578300 | 4994875 | Talweg | 3 | 2 | 1 | 1 | 5,3 | 6,3 | 3,3 | 1,1 | 2,0 | Ortho 58 | 0,2 | 2 | 9 |
| S4 | 578375 | 4994840 | Gully | 3 | 2 | 1 | 1 | 5,0 | 6,5 | 3,9 | 1,5 | 1,1 | Ortho 58 | 0,2 | 2 | 9 |
| S4 | 578475 | 4994840 | Talweg | 3 | 1 | 1 | 1 | 5,9 | 7,3 | 4,8 | 1,4 | 1,2 | Ortho 58 | 0,2 | 2 | 8 |
| S4 | 578560 | 4994850 | Talweg | 3 | 2 | 1 | 1 | 4,8 | 5,8 | 3,5 | 1,0 | 1,3 | Ortho 58 | 0,2 | 2 | 9 |
| S4 | 578635 | 4994855 | Talweg | 3 | 2 | 1 | 1 | 4,4 | 5,0 | 3,7 | 0,6 | 0,6 | Ortho 58 | 0,2 | 2 | 9 |
| S4 | 578655 | 4994860 | Gully | 3 | 1 | 1 | 1 | 5,1 | 6,3 | 4,4 | 1,2 | 0,7 | Ortho 58 | 0,2 | 2 | 8 |
| S4 | 578705 | 4994870 | Talweg | 3 | 2 | 1 | 1 | 6,7 | 7,2 | 5,6 | 0,5 | 1,1 | Ortho 58 | 0,2 | 2 | 9 |
| S4 | 578840 | 4994865 | Gully | 3 | 2 | 1 | 1 | 4,7 | 5,9 | 4,2 | 1,2 | 0,5 | Ortho 58 | 0,2 | 2 | 9 |
| S4 | 579320 | 4995115 | Talweg | 3 | 2 | 2 | 2 | 3,7 | 4,1 | 2,8 | 0,4 | 0,9 | Ortho 58 | 0,2 | 1 | 6 |
| S4 | 579350 | 4995125 | Talweg | 3 | 2 | 2 | 2 | 9,1 | 10,6 | 8,4 | 1,5 | 0,7 | Ortho 58 | 0,2 | 2 | 7 |
| S4 | 579395 | 4995135 | Talweg | 3 | 1 | 2 | 2 | 3,0 | 4,2 | 1,5 | 1,2 | 1,5 | Ortho 58 | 0,2 | 2 | 6 |
| S4 | 579430 | 4995140 | Gully | 3 | 1 | 2 | 2 | 2,2 | 3,5 | 1,6 | 1,3 | 0,6 | Ortho 58 | 0,2 | 2 | 6 |
| S4 | 579480 | 4995140 | Gully | 3 | 2 | 1 | 2 | 6,5 | 7,8 | 6,1 | 1,2 | 0,5 | Ortho 58 | 0,2 | 2 | 8 |
| S4 | 579500 | 4995140 | Riser | 3 | 2 | 1 | 2 | 5,1 | 7,1 | 4,5 | 2,0 | 0,6 | Ortho 58 | 0,2 | 2 | 8 |
| S4 | 579655 | 4995105 | Talweg | 3 | 2 | 2 | 1 | 2,6 | 3,2 | 1,7 | 0,6 | 0,9 | Ortho 58 | 0,2 | 2 | 8 |
| S4 | 579700 | 4995095 | Talweg | 3 | 2 | 2 | 1 | 4,8 | 6,1 | 3,6 | 1,2 | 1,2 | Ortho 58 | 0,2 | 2 | 8 |
| S4 | 579700 | 4995095 | Talweg | 3 | 2 | 1 | 1 | 8,5 | 10,8 | 6,0 | 2,2 | 2,5 | Ortho 58 | 0,2 | 2 | 9 |
| S4 | 579700 | 4995095 | Talweg | 3 | 2 | 1 | 1 | 10,0 | 12,0 | 7,2 | 2,0 | 2,8 | Ortho 58 | 0,2 | 2 | 9 |
| S4 | 579700 | 4995095 | Talweg | 3 | 2 | 1 | 1 | 16,6 | 18,1 | 14,1 | 1,5 | 2,5 | Ortho 58 | 0,2 | 2 | 9 |
| S4 | 579700 | 4995095 | Talweg | 3 | 2 | 1 | 1 | 24,9 | 27,9 | 23,1 | 3,0 | 1,8 | Ortho 58 | 0,2 | 2 | 9 |
| S4 | 579700 | 4995095 | Talweg | 3 | 2 | 1 | 1 | 28,1 | 30,6 | 26,4 | 2,6 | 1,7 | Ortho 58 | 0,2 | 2 | 9 |
| S4 | 579700 | 4995095 | Talweg | 3 | 2 | 1 | 1 | 30,7 | 33,5 | 26,4 | 2,8 | 4,3 | Ortho 58 | 0,2 | 2 | 9 |
| S4 | 579700 | 4995095 | Talweg | 3 | 2 | 1 | 1 | 32,0 | 34,4 | 28,4 | 2,3 | 3,6 | Ortho 58 | 0,2 | 2 | 9 |
| S4 | 579700 | 4995095 | Talweg | 3 | 2 | 1 | 1 | 36,3 | 40,3 | 33,9 | 4,1 | 2,4 | Ortho 58 | 0,2 | 2 | 9 |
| S4 | 579700 | 4995095 | Talweg | 3 | 2 | 1 | 1 | 49,9 | 51,6 | 48,2 | 1,7 | 1,7 | Ortho 58 | 0,2 | 2 | 9 |
| S4 | 579700 | 4995095 | Talweg | 3 | 2 | 1 | 1 | 53,5 | 57,8 | 50,8 | 4,2 | 2,7 | Ortho 58 | 0,2 | 2 | 9 |
| S4 | 579750 | 4995090 | Talweg | 3 | 2 | 2 | 1 | 5,5 | 6,5 | 3,7 | 1,1 | 1,8 | Ortho 58 | 0,2 | 2 | 8 |
| S4 | 579820 | 4995080 | Talweg | 3 | 2 | 2 | 1 | 4,1 | 4,9 | 3,4 | 0,8 | 0,8 | Ortho 58 | 0,2 | 2 | 8 |
| S4 | 579870 | 4995070 | Talweg | 3 | 2 | 1 | 1 | 4,7 | 5,1 | 3,2 | 0,4 | 1,6 | Ortho 58 | 0,2 | 2 | 9 |
| S4 | 579930 | 4995057 | Talweg | 3 | 2 | 1 | 1 | 5,3 | 6,3 | 3,3 | 1,1 | 1,9 | Ortho 58 | 0,2 | 2 | 9 |
| S4 | 580390 | 4994915 | Riser | 3 | 1 | 2 | 2 | 2,7 | 3,7 | 1,9 | 1,1 | 0,8 | Bing | 0,4 | 2 | 5 |

| Seg. | Lon. (UTM) | Lat. (UTM) | Marker Type | Mark. Obl. | Mark. res. (/2) | Nb. of splay | Scarp 2nd | Offset Pref. (m) | Offset max (m) | Offset min (m) | Δ+ (m) | Δ- (m) | Image type | Image Res. (m) | Image quality (/2) | Total Score (/10) |
|---|---|---|---|---|---|---|---|---|---|---|---|---|---|---|---|---|
| S4 | 580480 | 4994935 | Talweg | 3 | 2 | 2 | 2 | 4,7 | 5,4 | 3,5 | 0,7 | 1,2 | Bing | 0,4 | 2 | 6 |
| S4 | 580520 | 4994925 | Gully | 3 | 1 | 2 | 2 | 3,4 | 4,4 | 2,5 | 1,0 | 0,9 | Bing | 0,4 | 2 | 5 |
| S4 | 580660 | 4994906 | Riser | 2 | 2 | 1 | 2 | 7,2 | 9,8 | 6,4 | 2,6 | 0,8 | Bing | 0,4 | 2 | 5 |
| S4 | 580730 | 4994880 | Talweg | 3 | 2 | 2 | 2 | 3,1 | 5,1 | 2,5 | 2,0 | 0,6 | Bing | 0,4 | 2 | 6 |
| S4 | 580730 | 4994880 | Talweg | 3 | 1 | 1 | 2 | 6,0 | 7,6 | 4,8 | 1,6 | 1,2 | Bing | 0,4 | 2 | 6 |
| S4 | 580730 | 4994880 | Talweg | 3 | 2 | 1 | 2 | 13,9 | 16,0 | 12,2 | 2,1 | 1,7 | Bing | 0,4 | 2 | 7 |
| S4 | 580795 | 4994875 | Talweg | 3 | 2 | 2 | 1 | 13,3 | 14,6 | 12,1 | 1,3 | 1,2 | Bing | 0,4 | 2 | 7 |
| S4 | 580795 | 4994875 | Talweg | 3 | 2 | 2 | 1 | 6,8 | 8,3 | 5,8 | 1,5 | 1,0 | Bing | 0,4 | 2 | 7 |
| S4 | 580820 | 4994870 | Talweg | 3 | 2 | 2 | 1 | 4,1 | 4,7 | 3,3 | 0,7 | 0,7 | Bing | 0,4 | 2 | 7 |
| S4 | 580820 | 4994870 | Talweg | 3 | 2 | 2 | 1 | 4,2 | 5,4 | 3,7 | 1,1 | 0,5 | Bing | 0,4 | 2 | 7 |
| S4 | 580890 | 4994868 | River | 3 | 1 | 3 | 1 | 2,9 | 3,4 | 2,2 | 0,4 | 0,7 | Bing | 0,4 | 2 | 5 |
| S4 | 581090 | 4994875 | Riser | 2 | 2 | 1 | 1 | 4,2 | 5,4 | 3,7 | 1,2 | 0,5 | Bing | 0,4 | 2 | 6 |
| S4 | 581150 | 4994890 | Talweg | 3 | 2 | 1 | 1 | 5,5 | 6,5 | 4,9 | 1,0 | 0,6 | Bing | 0,4 | 2 | 8 |
| S4 | 581180 | 4994883 | Talweg | 3 | 2 | 1 | 1 | 3,1 | 3,7 | 2,1 | 0,6 | 1,0 | Bing | 0,4 | 2 | 8 |
| S4 | 581180 | 4994883 | Talweg | 3 | 2 | 1 | 1 | 8,5 | 9,2 | 8,1 | 0,7 | 0,4 | Bing | 0,4 | 2 | 8 |
| S4 | 581240 | 4994886 | Talweg | 3 | 2 | 1 | 1 | 10,2 | 10,6 | 9,6 | 0,4 | 0,6 | Bing | 0,4 | 2 | 8 |
| S4 | 581240 | 4994886 | Talweg | 3 | 2 | 1 | 1 | 14,4 | 15,9 | 13,9 | 1,5 | 0,5 | Bing | 0,4 | 2 | 8 |
| S4 | 581240 | 4994886 | Talweg | 3 | 2 | 1 | 1 | 17,0 | 19,9 | 16,3 | 2,9 | 0,9 | Bing | 0,4 | 2 | 8 |
| S4 | 581330 | 4994895 | Riser | 3 | 2 | 1 | 1 | 7,0 | 9,1 | 5,1 | 2,1 | 1,9 | Bing | 0,4 | 2 | 8 |
| S4 | 581610 | 4994915 | Gully | 3 | 2 | 2 | 1 | 4,2 | 5,5 | 2,1 | 1,3 | 2,1 | Bing | 0,4 | 2 | 7 |
| S4 | 582000 | 4995075 | River | 3 | 2 | 2 | 1 | 11,9 | 15,7 | 9,1 | 3,8 | 2,9 | Bing | 0,4 | 2 | 7 |
| S4 | 582320 | 4995050 | River | 3 | 2 | 4 | 1 | 23,9 | 26,7 | 20,6 | 2,8 | 3,3 | Bing | 0,4 | 2 | 6 |
| S4 | 582320 | 4995050 | River | 3 | 2 | 4 | 1 | 50,7 | 53,7 | 46,7 | 3,0 | 4,1 | Bing | 0,4 | 2 | 6 |
| S5 | 582420 | 4995050 | Riser | 3 | 2 | 4 | 1 | 49,3 | 53,9 | 45,3 | 4,5 | 4,0 | Bing | 0,4 | 2 | 6 |
| S5 | 582500 | 4995100 | Riser | 3 | 1 | 5 | 2 | 3,7 | 4,3 | 3,2 | 0,6 | 0,5 | Bing | 0,4 | 2 | 4 |
| S5 | 582530 | 4995100 | Riser | 3 | 2 | 5 | 3 | 4,0 | 5,3 | 3,2 | 1,2 | 0,8 | Bing | 0,4 | 2 | 4 |
| S5 | 582560 | 4995100 | Riser | 3 | 2 | 5 | 3 | 13,2 | 16,1 | 10,7 | 2,9 | 2,5 | Bing | 0,4 | 2 | 4 |
| S5 | 583210 | 4994985 | Talweg | 2 | 1 | 3 | 0 | 4,9 | 7,1 | 3,1 | 2,1 | 1,8 | Bing | 0,4 | 2 | 4 |
| S5 | 583210 | 4994985 | Talweg | 2 | 1 | 3 | 0 | 22,6 | 26,2 | 21,2 | 3,6 | 1,4 | Bing | 0,4 | 2 | 4 |
| S5 | 583340 | 4994970 | Gully | 3 | 1 | 4 | 0 | 3,2 | 3,6 | 1,9 | 0,4 | 1,2 | Bing | 0,4 | 2 | 6 |
| S5 | 583340 | 4994970 | Gully | 3 | 1 | 4 | 0 | 22,6 | 25,1 | 21,8 | 2,5 | 0,9 | Bing | 0,4 | 2 | 6 |
| S5 | 583500 | 4994950 | Riser | 3 | 2 | 3 | 0 | 2,2 | 2,7 | 1,0 | 0,5 | 1,2 | Bing | 0,4 | 2 | 7 |
| S5 | 583725 | 4994885 | Gully | 3 | 2 | 3 | 0 | 9,5 | 13,0 | 6,7 | 3,6 | 2,8 | Bing | 0,4 | 2 | 7 |

| Seg. | Lon. (UTM) | Lat. (UTM) | Marker Type | Mark. Obl. | Mark. res. (/2) | Nb. of splay | Scarp 2nd | Offset Pref. (m) | Offset max (m) | Offset min (m) | Δ+ (m) | Δ- (m) | Image type | Image Res. (m) | Image quality (/2) | Total Score (/10) |
|---|---|---|---|---|---|---|---|---|---|---|---|---|---|---|---|---|
| S5 | 583800 | 4994870 | Talweg | 2 | 2 | 2 | 0 | 3,6 | 4,8 | 2,4 | 1,2 | 1,3 | Bing | 0,4 | 2 | 6 |
| S5 | 583800 | 4994870 | Talweg | 3 | 2 | 2 | 0 | 15,7 | 17,9 | 12,6 | 2,2 | 3,1 | Bing | 0,4 | 2 | 8 |
| S5 | 583835 | 4994850 | Talweg | 3 | 2 | 2 | 0 | 7,9 | 9,4 | 6,1 | 1,5 | 1,8 | Bing | 0,4 | 2 | 8 |
| S5 | 583835 | 4994850 | Talweg | 3 | 2 | 2 | 0 | 16,5 | 18,3 | 14,7 | 1,8 | 1,8 | Bing | 0,4 | 2 | 8 |
| S5 | 584000 | 4994830 | River | 3 | 2 | 3 | 0 | 3,5 | 4,9 | 2,7 | 1,4 | 0,7 | Bing | 0,4 | 2 | 7 |
| S5 | 584000 | 4994830 | River | 3 | 2 | 3 | 0 | 6,4 | 7,2 | 5,3 | 0,9 | 1,1 | Bing | 0,4 | 2 | 7 |
| S5 | 584165 | 4994800 | Talweg | 3 | 1 | 2 | 0 | 9,4 | 10,2 | 8,7 | 0,8 | 0,7 | Bing | 0,4 | 2 | 7 |
| S5 | 584215 | 4994795 | Talweg | 3 | 1 | 2 | 0 | 13,8 | 15,2 | 12,1 | 1,4 | 1,7 | Bing | 0,4 | 2 | 7 |
| S5 | 584270 | 4994790 | Talweg | 3 | 1 | 2 | 0 | 8,6 | 10,6 | 7,6 | 2,1 | 1,0 | Bing | 0,4 | 2 | 7 |
| S5 | 584305 | 4994785 | Riser | 3 | 2 | 2 | 0 | 8,9 | 10,5 | 7,7 | 1,6 | 1,3 | Bing | 0,4 | 2 | 8 |
| S5 | 584400 | 4994765 | River | 3 | 2 | 2 | 0 | 7,6 | 8,4 | 6,5 | 0,8 | 1,1 | Bing | 0,4 | 1 | 7,5 |
| S5 | 584500 | 4994760 | Talweg | 3 | 1 | 2 | 0 | 8,1 | 10,8 | 6,7 | 2,7 | 1,4 | Bing | 0,4 | 1 | 6,5 |
| S5 | 584545 | 4994755 | Talweg | 2 | 2 | 2 | 0 | 6,0 | 7,1 | 4,8 | 1,1 | 1,2 | Bing | 0,4 | 1 | 5,5 |
| S5 | 584545 | 4994755 | Talweg | 3 | 1 | 2 | 0 | 22,1 | 24,2 | 20,6 | 2,1 | 1,5 | Bing | 0,4 | 1 | 6,5 |
| S5 | 584700 | 4994740 | Talweg | 3 | 2 | 2 | 0 | 5,9 | 7,4 | 5,1 | 1,5 | 0,8 | Bing | 0,4 | 1 | 7,5 |
| S5 | 584700 | 4994740 | Talweg | 3 | 2 | 2 | 0 | 22,6 | 24,2 | 20,2 | 1,6 | 2,4 | Bing | 0,4 | 1 | 7,5 |
| S5 | 584760 | 4994725 | Riser | 3 | 2 | 2 | 0 | 3,9 | 5,1 | 2,8 | 1,3 | 1,1 | Bing | 0,4 | 2 | 8 |
| S5 | 584922 | 4994720 | Talweg | 3 | 1 | 2 | 0 | 3,0 | 3,8 | 2,2 | 0,9 | 0,7 | Bing | 0,4 | 2 | 7 |
| S5 | 584980 | 4994688 | Talweg | 2 | 1 | 3 | 0 | 4,2 | 4,9 | 3,0 | 0,6 | 1,2 | Bing | 0,4 | 2 | 4 |
| S5 | 585060 | 4994678 | Riser | 3 | 1 | 2 | 0 | 2,2 | 2,9 | 1,6 | 0,7 | 0,5 | Bing | 0,4 | 2 | 7 |
| S5 | 585120 | 4994675 | Talweg | 3 | 1 | 2 | 0 | 4,9 | 5,8 | 4,2 | 0,9 | 0,8 | Bing | 0,4 | 2 | 7 |
| S5 | 585350 | 4994675 | Riser | 3 | 1 | 1 | 0 | 4,2 | 5,1 | 3,4 | 0,8 | 0,8 | Bing | 0,4 | 2 | 8 |
| S5 | 585610 | 4994610 | Talweg | 3 | 1 | 3 | 0 | 2,3 | 3,1 | 1,5 | 0,8 | 0,8 | Bing | 0,4 | 2 | 6 |
| S5 | 585660 | 4994614 | Talweg | 3 | 2 | 2 | 0 | 3,1 | 4,0 | 2,1 | 0,9 | 1,0 | Bing | 0,4 | 2 | 8 |
| S5 | 585690 | 4994612 | Ridge | 3 | 1 | 2 | 0 | 3,8 | 4,4 | 3,0 | 0,6 | 0,7 | Bing | 0,4 | 2 | 7 |
| S5 | 585880 | 4994532 | Talweg | 3 | 1 | 1 | 1 | 3,7 | 4,6 | 3,2 | 0,9 | 0,6 | Bing | 0,4 | 2 | 7 |
| S5 | 585930 | 4994545 | Talweg | 3 | 1 | 1 | 1 | 3,4 | 5,2 | 1,9 | 1,8 | 1,5 | Bing | 0,4 | 2 | 7 |
| S5 | 585990 | 4994510 | Talweg | 3 | 1 | 1 | 2 | 2,8 | 4,0 | 2,2 | 1,2 | 0,6 | Bing | 0,4 | 3 | 6,5 |
| S5 | 586035 | 4994460 | Talweg | 3 | 2 | 1 | 2 | 3,9 | 5,6 | 2,7 | 1,7 | 1,2 | Bing | 0,4 | 2 | 7 |
| S5 | 586060 | 4994458 | Gully | 3 | 2 | 1 | 1 | 3,2 | 5,1 | 2,3 | 1,9 | 0,9 | Bing | 0,4 | 2 | 8 |
| S5 | 586080 | 4994460 | Gully | 3 | 1 | 1 | 1 | 3,7 | 4,6 | 3,0 | 0,9 | 0,6 | Bing | 0,4 | 2 | 7 |
| S5 | 586880 | 4994230 | Talweg | 3 | 1 | 2 | 1 | 5,9 | 7,1 | 4,5 | 1,2 | 1,4 | Bing | 0,4 | 2 | 6 |
| S5 | 588590 | 4994020 | Riser | 3 | 2 | 3 | 1 | 6,3 | 9,1 | 5,0 | 2,8 | 1,3 | Ortho 58 | 0,6 | 2 | 6 |

| Seg. | Lon. (UTM) | Lat. (UTM) | Marker Type | Mark. Obl. | Mark. res. (/2) | Nb. of splay | Scarp 2nd | Offset Pref. (m) | Offset max (m) | Offset min (m) | Δ+ (m) | Δ- (m) | Image type | Image Res. (m) | Image quality (/2) | Total Score (/10) |
|---|---|---|---|---|---|---|---|---|---|---|---|---|---|---|---|---|
| S5 | 588630 | 4993990 | Riser | 3 | 2 | 3 | 1 | 4,1 | 5,1 | 3,6 | 1,0 | 0,5 | Bing | 0,4 | 2 | 6 |
| S5 | 588630 | 4993990 | Riser | 3 | 2 | 3 | 1 | 9,2 | 11,0 | 8,2 | 1,8 | 1,0 | Ortho 58 | 0,6 | 2 | 6 |
| S5 | 588710 | 4993956 | Riser | 3 | 2 | 1 | 1 | 4,8 | 5,7 | 3,7 | 0,9 | 1,1 | Bing | 0,4 | 2 | 8 |
| S5 | 588925 | 4993930 | Riser | 3 | 1 | 3 | 1 | 18,7 | 21,7 | 15,2 | 3,0 | 3,5 | Ortho 58 | 0,6 | 2 | 5 |
| S5 | 588955 | 4993890 | Riser | 3 | 1 | 3 | 1 | 3,9 | 5,0 | 2,9 | 1,1 | 1,0 | Bing | 0,4 | 2 | 5 |
| S5 | 589010 | 4993900 | Riser | 3 | 1 | 1 | 1 | 3,2 | 4,6 | 2,3 | 1,4 | 0,9 | Bing | 0,4 | 2 | 7 |
| S5 | 589060 | 4993850 | Talweg | 3 | 1 | 1 | 1 | 3,3 | 4,1 | 2,6 | 0,8 | 0,7 | Bing | 0,4 | 2 | 7 |
| S5 | 589060 | 4993850 | Talweg | 3 | 1 | 1 | 1 | 8,5 | 9,7 | 7,1 | 1,2 | 1,4 | Ortho 58 | 0,6 | 2 | 7 |
| S5 | 589140 | 4993810 | Talweg | 3 | 2 | 2 | 1 | 2,4 | 3,2 | 1,6 | 0,7 | 0,8 | Bing | 0,4 | 2 | 7 |
| S5 | 589170 | 4993795 | Gully | 3 | 2 | 2 | 1 | 3,1 | 4,0 | 2,6 | 0,9 | 0,6 | Bing | 0,4 | 2 | 7 |
| S5 | 589170 | 4993795 | Gully | 3 | 2 | 2 | 1 | 35,6 | 40,7 | 32,3 | 5,1 | 3,3 | Ortho 58 | 0,6 | 2 | 7 |
| S5 | 589200 | 4993785 | Talweg | 3 | 2 | 2 | 1 | 6,5 | 7,5 | 4,3 | 1,0 | 2,2 | Bing | 0,4 | 2 | 7 |
| S5 | 589370 | 4993750 | Riser | 3 | 2 | 2 | 2 | 4,0 | 4,6 | 3,8 | 0,7 | 0,3 | Bing | 0,4 | 2 | 6 |
| S5 | 589470 | 4993730 | Riser | 3 | 1 | 2 | 2 | 5,2 | 6,1 | 3,9 | 0,9 | 1,2 | Bing | 0,4 | 2 | 5 |
| S5 | 589470 | 4993730 | Riser | 3 | 1 | 2 | 2 | 9,8 | 12,0 | 9,0 | 2,2 | 0,8 | Bing | 0,4 | 2 | 5 |
| S5 | 589470 | 4993730 | Riser | 3 | 1 | 2 | 2 | 51,9 | 55,4 | 50,0 | 3,6 | 1,9 | Ortho 58 | 0,6 | 2 | 5 |
| S5 | 589625 | 4993730 | Talweg | 3 | 1 | 2 | 0 | 6,1 | 7,3 | 4,7 | 1,2 | 1,4 | Bing | 0,4 | 2 | 7 |
| S5 | 589625 | 4993730 | Talweg | 3 | 1 | 2 | 0 | 11,9 | 13,1 | 9,7 | 1,2 | 2,1 | Ortho 58 | 0,6 | 2 | 7 |
| S5 | 589780 | 4993725 | Talweg | 3 | 2 | 2 | 0 | 5,8 | 6,3 | 5,4 | 0,5 | 0,4 | Bing | 0,4 | 2 | 8 |
| S5 | 589780 | 4993725 | Talweg | 3 | 2 | 2 | 0 | 11,9 | 14,2 | 9,8 | 2,2 | 2,1 | Ortho 58 | 0,6 | 2 | 8 |
| S5 | 589860 | 4993720 | Talweg | 3 | 2 | 2 | 0 | 3,2 | 3,7 | 2,7 | 0,5 | 0,4 | Bing | 0,4 | 2 | 8 |
| S5 | 589885 | 4993715 | Talweg | 3 | 1 | 2 | 0 | 2,3 | 2,5 | 1,7 | 0,3 | 0,5 | Bing | 0,4 | 2 | 7 |
| S5 | 589925 | 4993680 | Talweg | 3 | 1 | 4 | 0 | 3,6 | 4,8 | 2,7 | 1,2 | 0,9 | Ortho 58 | 0,6 | 2 | 6 |
| S5 | 590150 | 4993620 | Talweg | 3 | 2 | 4 | 0 | 37,5 | 41,5 | 33,5 | 4,0 | 4,0 | Ortho 58 | 0,6 | 2 | 7 |
| S5 | 590170 | 4993640 | Talweg | 3 | 2 | 4 | 0 | 5,3 | 5,9 | 3,9 | 0,6 | 1,4 | Bing | 0,4 | 2 | 7 |
| S5 | 590250 | 4993575 | Talweg | 3 | 1 | 4 | 0 | 5,1 | 7,4 | 3,2 | 2,3 | 2,0 | Ortho 58 | 0,6 | 2 | 6 |
| S5 | 590300 | 4993570 | Riser | 3 | 1 | 1 | 0 | 8,4 | 9,7 | 6,1 | 1,3 | 2,3 | Bing | 0,4 | 2 | 8 |
| S5 | 590300 | 4993570 | Riser | 3 | 1 | 1 | 0 | 29,2 | 33,4 | 27,4 | 4,2 | 1,8 | Ortho 58 | 0,6 | 2 | 8 |
| S5 | 590780 | 4993450 | Talweg | 3 | 1 | 2 | 0 | 8,4 | 9,6 | 7,4 | 1,2 | 1,0 | Bing | 0,4 | 2 | 7 |
| S5 | 590780 | 4993450 | Talweg | 3 | 1 | 2 | 0 | 18,7 | 20,0 | 17,9 | 1,3 | 0,9 | Bing | 0,4 | 2 | 7 |
| S5 | 590810 | 4993445 | Talweg | 3 | 1 | 2 | 0 | 7,3 | 8,9 | 6,4 | 1,6 | 1,0 | Bing | 0,4 | 2 | 7 |
| S5 | 590870 | 4993430 | Talweg | 3 | 1 | 2 | 0 | 4,5 | 5,4 | 3,1 | 0,8 | 1,4 | Bing | 0,4 | 2 | 7 |
| S5 | 590905 | 4993425 | Talweg | 3 | 1 | 2 | 0 | 3,6 | 4,3 | 2,7 | 0,8 | 0,9 | Bing | 0,4 | 2 | 7 |

| Seg. | Lon. (UTM) | Lat. (UTM) | Marker Type | Mark. Obl. | Mark. res. (/2) | Nb. of splay | Scarp 2nd | Offset Pref. (m) | Offset max (m) | Offset min (m) | Δ+ (m) | Δ- (m) | Image type | Image Res. (m) | Image quality (/2) | Total Score (/10) |
|---|---|---|---|---|---|---|---|---|---|---|---|---|---|---|---|---|
| S5 | 590945 | 4993415 | Gully | 3 | 2 | 2 | 0 | 5,0 | 5,9 | 4,3 | 0,9 | 0,7 | Bing | 0,4 | 2 | 8 |
| S5 | 591000 | 4993415 | Talweg | 3 | 2 | 2 | 0 | 3,7 | 4,5 | 3,0 | 0,7 | 0,8 | Bing | 0,4 | 2 | 8 |
| S6 | 591030 | 4993420 | Talweg | 3 | 1 | 4 | 0 | 15,3 | 17,8 | 14,0 | 2,6 | 1,3 | Bing | 0,4 | 2 | 6 |
| S6 | 591070 | 4993425 | Talweg | 3 | 2 | 8 | 0 | 10,6 | 11,7 | 8,5 | 1,0 | 2,1 | Bing | 0,4 | 2 | 7 |
| S6 | 591200 | 4993450 | Riser | 3 | 2 | 4 | 0 | 61,6 | 66,1 | 57,5 | 4,5 | 4,1 | Bing | 0,4 | 2 | 7 |
| S6 | 591200 | 4993450 | Riser | 3 | 2 | 4 | 0 | 151,0 | 158,1 | 146,3 | 7,1 | 4,8 | Bing | 0,4 | 2 | 7 |
| S6 | 591340 | 4993440 | Riser | 3 | 2 | 1 | 0 | 9,4 | 11,8 | 6,0 | 2,4 | 3,4 | Bing | 0,4 | 2 | 9 |
| S6 | 593445 | 4993095 | Talweg | 3 | 1 | 2 | 1 | 12,6 | 18,7 | 10,9 | 6,1 | 1,8 | Ortho 58 | 0,5 | 1 | 5,5 |
| S6 | 593545 | 4993060 | Talweg | 3 | 2 | 2 | 1 | 45,1 | 47,9 | 42,1 | 2,8 | 3,0 | Ortho 58 | 0,5 | 1 | 6,5 |
| S6 | 593622 | 4993020 | Talweg | 3 | 2 | 2 | 1 | 4,8 | 6,1 | 3,4 | 1,3 | 1,4 | Ortho 58 | 0,5 | 1 | 6,5 |
| S6 | 594200 | 4992870 | Talweg | 3 | 1 | 2 | 2 | 10,9 | 14,4 | 8,6 | 3,5 | 2,3 | Ortho 58 | 0,5 | 1 | 4,5 |
| S6 | 594420 | 4992850 | Gully | 3 | 2 | 3 | 1 | 4,8 | 6,5 | 4,3 | 1,6 | 0,5 | Ortho 58 | 0,5 | 1 | 5,5 |
| S6 | 594445 | 4992845 | Gully | 3 | 1 | 3 | 1 | 2,8 | 3,7 | 1,8 | 0,9 | 1,0 | Ortho 58 | 0,5 | 1 | 4,5 |
| S6 | 594520 | 4992830 | Gully | 3 | 2 | 2 | 1 | 6,6 | 8,0 | 5,9 | 1,4 | 0,7 | Ortho 58 | 0,5 | 1 | 6,5 |
| S6 | 594560 | 4992815 | Gully | 3 | 2 | 3 | 1 | 5,0 | 6,0 | 4,2 | 1,1 | 0,8 | Ortho 58 | 0,5 | 1 | 5,5 |
| S6 | 594580 | 4992810 | Riser | 3 | 2 | 2 | 1 | 6,8 | 8,9 | 5,2 | 2,1 | 1,6 | Ortho 58 | 0,5 | 1 | 6,5 |
| S6 | 594705 | 4992780 | Riser | 3 | 2 | 3 | 1 | 9,1 | 10,5 | 6,2 | 1,4 | 2,9 | Ortho 58 | 0,5 | 1 | 5,5 |
| S6 | 594865 | 4992775 | Talweg | 2 | 1 | 3 | 1 | 16,5 | 18,7 | 14,7 | 2,2 | 1,8 | Ortho 58 | 0,5 | 1 | 2,5 |
| S6 | 594900 | 4992770 | Talweg | 3 | 1 | 3 | 1 | 32,8 | 35,4 | 29,6 | 2,6 | 3,2 | Ortho 58 | 0,5 | 1 | 4,5 |
| S6 | 595080 | 4992735 | Talweg | 3 | 1 | 1 | 1 | 7,1 | 9,6 | 4,0 | 2,6 | 3,0 | Ortho 58 | 0,5 | 1 | 6,5 |
| S6 | 595175 | 4992710 | Talweg | 3 | 2 | 1 | 1 | 3,0 | 4,6 | 1,1 | 1,6 | 1,9 | Ortho 58 | 0,5 | 1 | 7,5 |
| S6 | 595270 | 4992680 | Talweg | 3 | 1 | 1 | 1 | 21,9 | 24,7 | 20,1 | 2,8 | 1,8 | Ortho 58 | 0,5 | 1 | 6,5 |
| S6 | 595650 | 4992665 | Talweg | 3 | 2 | 1 | 1 | 3,0 | 4,8 | 1,2 | 1,8 | 1,8 | Ortho 58 | 0,5 | 1 | 7,5 |
| S6 | 595700 | 4992330 | Talweg | 3 | 1 | 1 | 2 | 8,5 | 10,5 | 6,8 | 1,9 | 1,7 | Ortho 58 | 0,5 | 1 | 5,5 |
| S6 | 595805 | 4992355 | Talweg | 3 | 2 | 1 | 2 | 10,4 | 12,6 | 8,0 | 2,1 | 2,4 | Ortho 58 | 0,5 | 1 | 6,5 |
| S6 | 595840 | 4992340 | Talweg | 3 | 2 | 1 | 2 | 4,2 | 5,7 | 2,0 | 1,6 | 2,2 | Ortho 58 | 0,5 | 1 | 6,5 |
| S6 | 596050 | 4992260 | Talweg | 3 | 1 | 1 | 2 | 4,8 | 6,7 | 2,5 | 1,9 | 2,3 | Ortho 58 | 0,5 | 1 | 5,5 |
| S6 | 597400 | 4991250 | River | 3 | 1 | 2 | 2 | 25,0 | 32,5 | 22,4 | 7,5 | 2,6 | Ortho 58 | 0,5 | 1 | 4,5 |
| S6 | 597400 | 4991250 | River | 3 | 1 | 2 | 2 | 104,7 | 111,1 | 99,2 | 6,4 | 5,5 | Ortho 58 | 0,5 | 1 | 4,5 |
| S6 | 598600 | 4991040 | Gully | 3 | 2 | 1 | 1 | 5,6 | 7,6 | 4,3 | 2,0 | 1,3 | Ortho 58 | 0,5 | 1 | 7,5 |
| S6 | 598660 | 4991055 | Gully | 3 | 1 | 1 | 1 | 4,6 | 5,9 | 3,5 | 1,3 | 1,1 | Ortho 58 | 0,5 | 1 | 6,5 |
| S6 | 598785 | 4991085 | Talweg | 3 | 1 | 1 | 1 | 10,4 | 12,8 | 7,7 | 2,4 | 2,6 | Ortho 58 | 0,5 | 1 | 6,5 |
| S6 | 598850 | 4991100 | Gully | 2 | 1 | 1 | 1 | 26,7 | 28,9 | 24,6 | 2,2 | 2,1 | Ortho 58 | 0,5 | 1 | 4,5 |

| Seg. | Lon. (UTM) | Lat. (UTM) | Marker Type | Mark. Obl. | Mark. res. (/2) | Nb. of splay | Scarp 2nd | Offset Pref. (m) | Offset max (m) | Offset min (m) | Δ+ (m) | Δ- (m) | Image type | Image Res. (m) | Image quality (/2) | Total Score (/10) |
|---|---|---|---|---|---|---|---|---|---|---|---|---|---|---|---|---|
| S6 | 598950 | 4991130 | Gully | 2 | 2 | 1 | 1 | 9,8 | 12,9 | 6,4 | 3,1 | 3,4 | Ortho 58 | 0,5 | 1 | 5,5 |
| S6 | 599085 | 4991163 | Gully | 2 | 1 | 1 | 1 | 10,7 | 14,4 | 5,1 | 3,7 | 5,6 | Ortho 58 | 0,5 | 1 | 4,5 |
| S6 | 599150 | 4991170 | Gully | 2 | 1 | 1 | 1 | 7,7 | 10,8 | 5,4 | 3,1 | 2,3 | Ortho 58 | 0,5 | 1 | 4,5 |
| S6 | 599900 | 4991000 | Gully | 2 | 1 | 3 | 1 | 10,2 | 12,7 | 7,5 | 2,5 | 2,7 | Ortho 58 | 0,5 | 1 | 2,5 |
| S6 | 599980 | 4991000 | Gully | 3 | 2 | 2 | 1 | 9,4 | 15,7 | 7,5 | 6,2 | 1,9 | Ortho 58 | 0,5 | 1 | 6,5 |
| S6 | 600140 | 4990985 | Gully | 3 | 1 | 2 | 1 | 60,0 | 67,8 | 55,3 | 7,8 | 4,8 | Ortho 58 | 0,5 | 1 | 5,5 |
| S6 | 600450 | 4990850 | Gully | 3 | 1 | 2 | 1 | 17,1 | 23,2 | 11,2 | 6,1 | 5,9 | Ortho 58 | 0,5 | 1 | 5,5 |
| S6 | 601000 | 4990400 | Ridge | 3 | 1 | 2 | 2 | 5,6 | 8,2 | 3,4 | 2,6 | 2,2 | Ortho 58 | 0,5 | 1 | 4,5 |
| S6 | 601080 | 4990365 | Talweg | 3 | 2 | 2 | 2 | 10,9 | 14,2 | 8,7 | 3,3 | 2,2 | Ortho 58 | 0,5 | 1 | 5,5 |
| S6 | 601080 | 4990365 | Talweg | 3 | 2 | 1 | 2 | 23,7 | 28,3 | 21,4 | 4,6 | 2,3 | Ortho 58 | 0,5 | 1 | 6,5 |
| S6 | 601120 | 4990355 | Gully | 3 | 1 | 1 | 2 | 10,7 | 13,1 | 9,8 | 2,4 | 0,9 | Ortho 58 | 0,5 | 1 | 5,5 |
| S6 | 601155 | 4990340 | Gully | 3 | 0 | 1 | 2 | 6,3 | 7,6 | 4,8 | 1,3 | 1,5 | Ortho 58 | 0,5 | 1 | 4,5 |
| S6 | 601190 | 4990330 | Talweg | 3 | 2 | 1 | 2 | 12,8 | 14,9 | 11,3 | 2,1 | 1,5 | Ortho 58 | 0,5 | 1 | 6,5 |
| S6 | 601250 | 4990280 | Talweg | 3 | 1 | 1 | 2 | 8,7 | 11,8 | 7,2 | 3,1 | 1,5 | Ortho 58 | 0,5 | 1 | 5,5 |
| S6 | 601310 | 4990200 | Talweg | 3 | 1 | 2 | 2 | 6,2 | 7,8 | 4,9 | 1,6 | 1,3 | Ortho 58 | 0,5 | 1 | 4,5 |
| S6 | 601740 | 4990010 | Riser | 3 | 1 | 1 | 1 | 11,1 | 13,6 | 9,5 | 2,5 | 1,6 | Ortho 58 | 0,5 | 1 | 6,5 |
| S6 | 601825 | 4990005 | Gully | 3 | 1 | 2 | 2 | 3,5 | 4,9 | 2,3 | 1,4 | 1,3 | Ortho 58 | 0,5 | 1 | 4,5 |
| S6 | 601910 | 4990005 | Riser | 3 | 2 | 3 | 2 | 17,0 | 18,4 | 14,9 | 1,4 | 2,1 | Ortho 58 | 0,5 | 1 | 4,5 |
| S6 | 602000 | 4989980 | Gully | 3 | 1 | 2 | 2 | 6,8 | 9,1 | 5,8 | 2,3 | 1,0 | Ortho 58 | 0,5 | 1 | 4,5 |
| S6 | 602300 | 4990025 | Gully | 2 | 1 | 1 | 2 | 12,7 | 14,9 | 10,2 | 2,2 | 2,5 | Ortho 58 | 0,5 | 1 | 3,5 |
| S6 | 602500 | 4989925 | Gully | 3 | 1 | 1 | 2 | 4,1 | 4,8 | 3,1 | 0,7 | 1,0 | Ortho 58 | 0,5 | 1 | 5,5 |
| S6 | 602615 | 4989680 | Talweg | 3 | 2 | 2 | 1 | 5,7 | 8,0 | 3,8 | 2,2 | 1,9 | Ortho 58 | 0,5 | 1 | 6,5 |
| S6 | 602670 | 4989680 | Gully | 3 | 1 | 2 | 1 | 5,3 | 6,7 | 4,1 | 1,4 | 1,2 | Ortho 58 | 0,5 | 1 | 5,5 |
| S6 | 602690 | 4989675 | Riser | 3 | 2 | 2 | 1 | 4,6 | 5,4 | 4,0 | 0,9 | 0,6 | Ortho 58 | 0,5 | 1 | 6,5 |
| S6 | 602715 | 4989670 | Riser | 3 | 2 | 2 | 1 | 3,5 | 4,2 | 2,3 | 0,7 | 1,2 | Ortho 58 | 0,5 | 1 | 6,5 |
| S6 | 603300 | 4989640 | Gully | 3 | 1 | 1 | 2 | 3,8 | 6,3 | 2,1 | 2,5 | 1,6 | Ortho 58 | 0,5 | 1 | 5,5 |
| S6 | 604210 | 4989025 | Talweg | 3 | 1 | 1 | 1 | 4,7 | 5,5 | 3,0 | 0,8 | 1,7 | Ortho 58 | 0,5 | 1 | 6,5 |
| S6 | 604355 | 4989045 | Talweg | 3 | 2 | 1 | 1 | 10,8 | 16,1 | 7,5 | 5,3 | 3,3 | Ortho 58 | 0,5 | 1 | 7,5 |
| S6 | 604450 | 4989045 | Gully | 3 | 2 | 1 | 1 | 14,2 | 16,4 | 13,6 | 2,2 | 0,6 | Ortho 58 | 0,5 | 1 | 7,5 |
| S6 | 604490 | 4989042 | Talweg | 3 | 2 | 1 | 1 | 12,1 | 15,6 | 9,6 | 3,6 | 2,5 | Ortho 58 | 0,5 | 1 | 7,5 |
| S6 | 604545 | 4989045 | Talweg | 3 | 2 | 1 | 1 | 10,0 | 11,9 | 7,6 | 2,0 | 2,3 | Ortho 58 | 0,5 | 1 | 7,5 |
| S6 | 604750 | 4989090 | Talweg | 3 | 2 | 1 | 1 | 5,6 | 7,7 | 3,9 | 2,0 | 1,8 | Ortho 58 | 0,5 | 1 | 7,5 |
| S6 | 604770 | 4988410 | Gully | 3 | 2 | 2 | 1 | 9,2 | 11,6 | 5,4 | 2,4 | 3,8 | Ortho 58 | 0,5 | 1 | 6,5 |

| Seg. | Lon. (UTM) | Lat. (UTM) | Marker Type | Mark. Obl. | Mark. res. (/2) | Nb. of splay | Scarp 2nd | Offset Pref. (m) | Offset max (m) | Offset min (m) | Δ+ (m) | Δ- (m) | Image type | Image Res. (m) | Image quality (/2) | Total Score (/10) |
|---|---|---|---|---|---|---|---|---|---|---|---|---|---|---|---|---|
| S6 | 604850 | 4988390 | Riser | 3 | 1 | 2 | 1 | 12,0 | 17,6 | 8,8 | 5,6 | 3,2 | Ortho 58 | 0,5 | 1 | 5,5 |
| S6 | 605000 | 4988380 | Riser | 3 | 1 | 2 | 1 | 10,6 | 13,5 | 8,5 | 2,8 | 2,1 | Ortho 58 | 0,5 | 1 | 5,5 |
| S6 | 605060 | 4988400 | Riser | 3 | 1 | 2 | 1 | 8,7 | 12,3 | 4,1 | 3,6 | 4,6 | Ortho 58 | 0,5 | 1 | 5,5 |
| S6 | 605300 | 4988370 | Talweg | 2 | 1 | 1 | 1 | 13,9 | 20,1 | 10,9 | 6,2 | 3,0 | Ortho 58 | 0,5 | 1 | 4,5 |
| S6 | 605300 | 4988370 | Talweg | 2 | 1 | 1 | 1 | 16,9 | 20,9 | 10,0 | 4,0 | 6,9 | Ortho 58 | 0,5 | 1 | 4,5 |
| S6 | 605300 | 4988370 | Talweg | 2 | 1 | 1 | 1 | 52,4 | 57,9 | 47,2 | 5,5 | 5,2 | Ortho 58 | 0,5 | 1 | 4,5 |
| S6 | 605680 | 4988350 | Talweg | 3 | 1 | 1 | 1 | 17,3 | 21,6 | 12,1 | 4,3 | 5,2 | Ortho 58 | 0,5 | 1 | 6,5 |
| S6 | 606200 | 4988600 | Talweg | 2 | 1 | 2 | 2 | 3,5 | 4,9 | 1,3 | 1,4 | 2,2 | Ortho 58 | 0,4 | 2 | 3 |
| S6 | 606320 | 4988572 | Gully | 3 | 2 | 1 | 2 | 7,0 | 8,1 | 5,9 | 1,1 | 1,1 | Ortho 58 | 0,4 | 2 | 7 |
| S6 | 606335 | 4988566 | Ridge | 3 | 1 | 1 | 2 | 6,3 | 8,0 | 5,5 | 1,7 | 0,8 | Ortho 58 | 0,4 | 2 | 6 |
| S6 | 606350 | 4988560 | Talweg | 3 | 1 | 1 | 2 | 20,5 | 22,8 | 19,0 | 2,3 | 1,5 | Ortho 58 | 0,4 | 2 | 6 |
| S6 | 606365 | 4988555 | Ridge | 3 | 2 | 1 | 2 | 24,6 | 26,1 | 22,5 | 1,5 | 2,1 | Ortho 58 | 0,4 | 2 | 7 |
| S6 | 606390 | 4988545 | Talweg | 3 | 2 | 1 | 2 | 18,9 | 22,6 | 17,0 | 3,7 | 1,9 | Ortho 58 | 0,4 | 2 | 7 |
| S6 | 606390 | 4988545 | Talweg | 3 | 1 | 1 | 2 | 40,3 | 41,7 | 36,8 | 1,4 | 3,6 | Ortho 58 | 0,4 | 2 | 6 |
| S6 | 606435 | 4988535 | Ridge | 3 | 1 | 1 | 2 | 32,9 | 35,4 | 30,3 | 2,5 | 2,5 | Ortho 58 | 0,4 | 2 | 6 |
| S6 | 606455 | 4988530 | Talweg | 3 | 1 | 1 | 2 | 22,5 | 24,7 | 20,6 | 2,3 | 1,8 | Ortho 58 | 0,4 | 2 | 6 |
| S6 | 606475 | 4988530 | Ridge | 3 | 1 | 1 | 2 | 3,9 | 5,6 | 2,2 | 1,7 | 1,7 | Ortho 58 | 0,4 | 2 | 6 |
| S6 | 606490 | 4988528 | Talweg | 3 | 1 | 1 | 2 | 26,2 | 27,8 | 24,3 | 1,6 | 1,9 | Ortho 58 | 0,4 | 2 | 6 |
| S6 | 606500 | 4988528 | Talweg | 2 | 2 | 1 | 2 | 4,3 | 8,1 | 2,0 | 3,9 | 2,3 | Ortho 58 | 0,4 | 2 | 5 |
| S6 | 606570 | 4988525 | Talweg | 3 | 2 | 1 | 2 | 4,1 | 5,2 | 2,0 | 1,1 | 2,0 | Ortho 58 | 0,4 | 2 | 7 |
| S6 | 606630 | 4988520 | Talweg | 3 | 2 | 1 | 2 | 3,2 | 5,0 | 2,7 | 1,8 | 0,5 | Ortho 58 | 0,4 | 2 | 7 |
| S6 | 606730 | 4988500 | Talweg | 3 | 1 | 1 | 2 | 27,8 | 31,7 | 25,0 | 3,8 | 2,9 | Ortho 58 | 0,4 | 2 | 6 |
| S6 | 606770 | 4988495 | Ridge | 3 | 0 | 1 | 2 | 26,8 | 30,0 | 24,3 | 3,2 | 2,5 | Ortho 58 | 0,4 | 2 | 5 |
| S6 | 606790 | 4988490 | Abandoned chanel | 3 | 1 | 1 | 2 | 19,9 | 21,9 | 16,1 | 2,0 | 3,8 | Ortho 58 | 0,4 | 2 | 6 |
| S6 | 607225 | 4988425 | River | 3 | 2 | 1 | 2 | 3,1 | 4,2 | 2,1 | 1,1 | 1,0 | Ortho 58 | 0,4 | 2 | 7 |
| S6 | 607225 | 4988425 | River | 3 | 2 | 1 | 2 | 8,6 | 10,1 | 6,5 | 1,5 | 2,1 | Ortho 58 | 0,4 | 2 | 7 |
| R5 | 607245 | 4988420 | Gully | 3 | 1 | 1 | 2 | 1,9 | 2,7 | 1,1 | 0,8 | 0,8 | Ortho 58 | 0,4 | 2 | 6 |
| R5 | 607285 | 4988420 | Gully | 3 | 2 | 1 | 2 | 3,0 | 3,9 | 2,0 | 0,9 | 1,0 | Ortho 58 | 0,4 | 2 | 7 |
| R5 | 607310 | 4988420 | Talweg | 3 | 1 | 1 | 2 | 9,6 | 11,2 | 7,4 | 1,6 | 2,2 | Ortho 58 | 0,4 | 2 | 6 |
| R5 | 607430 | 4988425 | Riser | 3 | 1 | 1 | 2 | 18,1 | 20,8 | 16,3 | 2,7 | 1,8 | Ortho 58 | 0,4 | 2 | 6 |
| R5 | 607490 | 4988430 | River | 3 | 2 | 1 | 2 | 3,8 | 5,5 | 2,5 | 1,7 | 1,3 | Ortho 58 | 0,4 | 2 | 7 |
| R5 | 607510 | 4988430 | Riser | 3 | 2 | 1 | 2 | 7,8 | 9,9 | 6,9 | 2,1 | 0,9 | Ortho 58 | 0,4 | 2 | 7 |
| R5 | 60772 | 498845 | Talweg | 3 | 2 | 1 | 2 | 3,8 | 5,8 | 2,8 | 2,0 | 1,0 | Ortho | 0,4 | 2 | 7 |

| Seg. | Lon. (UTM) | Lat. (UTM) | Marker Type | Mark. Obl. | Mark. res. (/2) | Nb. of splay | Scarp 2nd | Offset Pref. (m) | Offset max (m) | Offset min (m) | Δ+ (m) | Δ- (m) | Image type | Image Res. (m) | Image quality (/2) | Total Score (/10) |
|---|---|---|---|---|---|---|---|---|---|---|---|---|---|---|---|---|
| | 5 | 0 | | | | | | | | | | | 58 | | | |
| R5 | 607840 | 4988490 | Talweg | 3 | 1 | 1 | 1 | 2,0 | 3,2 | 1,1 | 1,2 | 0,8 | Ortho 58 | 0,4 | 2 | 7 |
| R5 | 608300 | 4988600 | Riser | 3 | 1 | 1 | 2 | 50,9 | 57,0 | 47,0 | 6,1 | 3,9 | Ortho 58 | 0,4 | 2 | 6 |
| R5 | 608400 | 4988650 | Riser | 3 | 1 | 1 | 2 | 44,6 | 48,0 | 40,5 | 3,4 | 4,1 | Ortho 58 | 0,4 | 2 | 6 |
| R5 | 608470 | 4988690 | Gully | 3 | 2 | 1 | 1 | 5,5 | 6,5 | 4,6 | 1,0 | 0,9 | Ortho 58 | 0,4 | 2 | 8 |
| R5 | 608540 | 4988715 | RIver | 3 | 2 | 1 | 1 | 5,2 | 6,1 | 4,4 | 0,9 | 0,8 | Ortho 58 | 0,4 | 2 | 8 |
| R5 | 608530 | 4988745 | Riser | 3 | 2 | 1 | 1 | 9,0 | 10,5 | 7,0 | 1,5 | 2,0 | Ortho 58 | 0,4 | 2 | 8 |
| R5 | 608650 | 4988750 | Bar | 3 | 1 | 1 | 1 | 3,1 | 3,9 | 2,1 | 0,8 | 1,0 | Ortho 58 | 0,4 | 2 | 7 |
| R5 | 608700 | 4988770 | Bar | 3 | 1 | 1 | 1 | 3,2 | 4,3 | 2,3 | 1,1 | 0,9 | Ortho 58 | 0,4 | 2 | 7 |
| R5 | 608740 | 4988780 | Bar | 3 | 1 | 1 | 1 | 6,3 | 7,7 | 5,8 | 1,5 | 0,4 | Ortho 58 | 0,4 | 2 | 7 |
| R5 | 608800 | 4988800 | Riser | 3 | 1 | 1 | 1 | 9,8 | 12,3 | 6,1 | 2,6 | 3,7 | Ortho 58 | 0,4 | 2 | 7 |
| R6 | 622100 | 4984740 | Gully | 3 | 2 | 1 | 1 | 10,1 | 11,1 | 9,4 | 0,9 | 0,8 | Ortho 58 | 0,2 | 2 | 9 |
| R6 | 622440 | 4984830 | Riser | 3 | 2 | 1 | 2 | 7,7 | 9,2 | 6,3 | 1,6 | 1,3 | Ortho 58 | 0,2 | 2 | 8 |
| R6 | 622760 | 4984736 | Gully | 3 | 1 | 1 | 3 | 3,1 | 4,1 | 2,4 | 1,0 | 0,6 | Ortho 58 | 0,2 | 2 | 6 |
| R6 | 622815 | 4984680 | Riser | 3 | 2 | 1 | 1 | 2,8 | 3,5 | 1,7 | 0,7 | 1,1 | Ortho 58 | 0,2 | 2 | 9 |
| R6 | 622815 | 4984680 | Riser | 3 | 2 | 1 | 1 | 5,1 | 6,6 | 4,0 | 1,5 | 1,2 | Ortho 58 | 0,2 | 2 | 9 |
| R6 | 622880 | 4984636 | Talweg | 3 | 1 | 1 | 1 | 7,7 | 9,8 | 6,8 | 2,1 | 0,9 | Ortho 58 | 0,2 | 2 | 8 |
| R6 | 623035 | 4984480 | Riser | 3 | 1 | 1 | 0 | 3,1 | 4,2 | 2,0 | 1,0 | 1,1 | Ortho 58 | 0,2 | 2 | 9 |
| R6 | 623050 | 4984470 | Chanel | 3 | 0 | 1 | 0 | 1,5 | 1,9 | 0,7 | 0,3 | 0,8 | Ortho 58 | 0,2 | 2 | 8 |
| R6 | 623050 | 4984470 | Riser | 3 | 1 | 1 | 0 | 4,6 | 5,1 | 3,9 | 0,5 | 0,7 | Ortho 58 | 0,2 | 2 | 9 |
| R6 | 623100 | 4984455 | Talweg | 3 | 1 | 2 | 0 | 9,3 | 10,1 | 8,1 | 0,7 | 1,2 | Ortho 58 | 0,2 | 2 | 8 |
| R6 | 623200 | 4984375 | Riser | 3 | 2 | 1 | 0 | 2,7 | 3,6 | 2,0 | 0,8 | 0,7 | Ortho 58 | 0,2 | 2 | 10 |
| S8 | 623285 | 4983870 | Talweg | 3 | 1 | 1 | 0 | 1,1 | 1,8 | 0,8 | 0,6 | 0,3 | Ortho 58 | 0,2 | 2 | 9 |
| S8 | 623300 | 4983870 | Talweg | 3 | 1 | 1 | 0 | 1,6 | 2,5 | 1,2 | 0,9 | 0,4 | Ortho 58 | 0,2 | 2 | 9 |
| S8 | 623320 | 4983870 | Talweg | 3 | 1 | 1 | 0 | 2,1 | 2,8 | 1,5 | 0,7 | 0,6 | Ortho 58 | 0,2 | 2 | 9 |
| S8 | 623335 | 4983870 | Talweg | 3 | 2 | 1 | 0 | 3,8 | 4,2 | 3,3 | 0,3 | 0,5 | Ortho 58 | 0,2 | 2 | 10 |
| S8 | 623425 | 4983865 | River | 3 | 2 | 1 | 0 | 2,8 | 3,1 | 2,3 | 0,3 | 0,5 | Ortho 58 | 0,2 | 2 | 10 |
| S8 | 623520 | 4983865 | Gully | 3 | 1 | 3 | 0 | 2,1 | 2,6 | 1,6 | 0,5 | 0,5 | Ortho 58 | 0,2 | 2 | 7 |
| S8 | 623575 | 4983850 | Riser | 3 | 2 | 1 | 0 | 1,4 | 1,8 | 0,9 | 0,4 | 0,5 | Ortho 58 | 0,2 | 2 | 10 |
| S8 | 623610 | 4983845 | Talweg | 3 | 2 | 2 | 1 | 3,1 | 3,3 | 2,8 | 0,3 | 0,3 | Ortho 58 | 0,2 | 2 | 8 |
| S8 | 623666 | 4983845 | Talweg | 3 | 2 | 2 | 1 | 2,6 | 2,9 | 2,4 | 0,3 | 0,3 | Ortho 58 | 0,2 | 2 | 8 |
| S8 | 623700 | 4983845 | Talweg | 3 | 1 | 3 | 1 | 2,8 | 3,5 | 2,1 | 0,7 | 0,7 | Ortho 58 | 0,2 | 2 | 6 |
| S8 | 623700 | 4983845 | Talweg | 3 | 1 | 3 | 1 | 13,9 | 16,8 | 12,9 | 2,9 | 1,0 | Ortho 58 | 0,2 | 2 | 6 |
| S8 | 62380 | 498388 | Riser | 3 | 2 | 1 | 0 | 5,5 | 7,0 | 4,0 | 1,5 | 1,5 | Ortho | 0,2 | 2 | 10 |

| Seg. | Lon. (UTM) | Lat. (UTM) | Marker Type | Mark. Obl. | Mark. res. (/2) | Nb. of splay | Scarp 2nd | Offset Pref. (m) | Offset max (m) | Offset min (m) | Δ+ (m) | Δ- (m) | Image type | Image Res. (m) | Image quality (/2) | Total Score (/10) |
|---|---|---|---|---|---|---|---|---|---|---|---|---|---|---|---|---|
| | 0 | 0 | | | | | | | | | | | 58 | | | |
| S8 | 623815 | 4983880 | Chanel | 3 | 2 | 1 | 0 | 7,3 | 8,8 | 5,8 | 1,4 | 1,5 | Ortho 58 | 0,2 | 2 | 10 |
| S8 | 623840 | 4983885 | Chanel | 3 | 2 | 1 | 0 | 5,4 | 6,8 | 4,4 | 1,3 | 1,0 | Ortho 58 | 0,2 | 2 | 10 |
| S8 | 623925 | 4983910 | Riser | 3 | 2 | 1 | 1 | 2,6 | 3,3 | 1,7 | 0,7 | 0,9 | Ortho 58 | 0,2 | 2 | 9 |
| S8 | 624090 | 4983910 | Riser | 3 | 2 | 1 | 2 | 5,9 | 7,9 | 4,3 | 2,0 | 1,5 | Ortho 58 | 0,2 | 2 | 8 |
| S8 | 624200 | 4983770 | Talweg | 3 | 1 | 2 | 3 | 2,3 | 3,7 | 1,5 | 1,4 | 0,8 | Ortho 58 | 0,2 | 2 | 5 |
| S8 | 624400 | 4983660 | Talweg | 3 | 1 | 2 | 3 | 3,0 | 4,5 | 1,7 | 1,4 | 1,4 | Ortho 58 | 0,2 | 2 | 5 |
| S8 | 624470 | 4983685 | Talweg | 3 | 1 | 2 | 2 | 4,9 | 6,0 | 1,4 | 1,0 | 3,5 | Ortho 58 | 0,2 | 2 | 6 |
| S8 | 624730 | 4983750 | Talweg | 3 | 1 | 2 | 3 | 7,1 | 7,8 | 4,7 | 0,7 | 2,3 | Ortho 58 | 0,2 | 2 | 5 |
| S8 | 626130 | 4983388 | Talweg | 3 | 2 | 2 | 0 | 3,6 | 4,1 | 3,1 | 0,4 | 0,6 | Ortho 58 | 0,2 | 2 | 9 |
| S8 | 626130 | 4983388 | Talweg | 3 | 2 | 2 | 0 | 18,8 | 22,1 | 16,9 | 3,2 | 1,9 | Ortho 58 | 0,2 | 2 | 9 |
| S8 | 626200 | 4983388 | Riser | 3 | 1 | 1 | 0 | 21,8 | 23,1 | 20,1 | 1,3 | 1,6 | Ortho 58 | 0,2 | 2 | 9 |
| S8 | 626230 | 4983376 | Gully | 3 | 2 | 1 | 0 | 2,0 | 2,7 | 1,3 | 0,7 | 0,7 | Ortho 58 | 0,2 | 2 | 10 |
| S8 | 626255 | 4983376 | Abandoned chanel | 3 | 1 | 2 | 0 | 2,3 | 3,4 | 1,6 | 1,1 | 0,7 | Ortho 58 | 0,2 | 2 | 8 |
| S8 | 626270 | 4983376 | Gully | 3 | 1 | 2 | 0 | 2,7 | 3,6 | 1,9 | 0,9 | 0,8 | Ortho 58 | 0,2 | 2 | 8 |
| S8 | 626300 | 4983370 | Gully | 3 | 2 | 2 | 0 | 3,7 | 4,9 | 3,0 | 1,2 | 0,7 | Ortho 58 | 0,2 | 2 | 9 |
| S8 | 626360 | 4983365 | Gully | 2 | 2 | 2 | 0 | 4,9 | 8,6 | 2,9 | 3,7 | 2,0 | Ortho 58 | 0,2 | 2 | 7 |
| S8 | 626450 | 4983350 | Gully | 3 | 2 | 1 | 0 | 4,8 | 6,4 | 3,7 | 1,6 | 1,0 | Ortho 58 | 0,2 | 2 | 10 |
| S8 | 626450 | 4983350 | Riser | 3 | 2 | 1 | 0 | 18,1 | 20,3 | 17,1 | 2,2 | 1,1 | Ortho 58 | 0,2 | 2 | 10 |
| S8 | 626470 | 4983350 | Gully | 3 | 2 | 1 | 0 | 2,4 | 3,2 | 1,8 | 0,8 | 0,6 | Ortho 58 | 0,2 | 2 | 10 |
| S8 | 626490 | 4983350 | Gully | 3 | 2 | 1 | 0 | 2,7 | 3,6 | 2,1 | 0,8 | 0,6 | Ortho 58 | 0,2 | 2 | 10 |
| S8 | 626515 | 4983350 | Gully | 3 | 1 | 3 | 0 | 4,9 | 5,7 | 4,4 | 0,9 | 0,5 | Ortho 58 | 0,2 | 2 | 7 |
| S8 | 626535 | 4983350 | Gully | 3 | 2 | 1 | 0 | 4,1 | 4,7 | 3,0 | 0,6 | 1,1 | Ortho 58 | 0,2 | 2 | 10 |
| S8 | 626550 | 4983350 | Gully | 3 | 2 | 1 | 0 | 4,3 | 5,0 | 3,7 | 0,7 | 0,6 | Ortho 58 | 0,2 | 2 | 10 |
| S8 | 626640 | 4983350 | Talweg | 3 | 2 | 1 | 0 | 2,1 | 3,7 | 1,7 | 1,6 | 0,5 | Ortho 58 | 0,2 | 2 | 10 |
| S8 | 626700 | 4983340 | Talweg | 2 | 1 | 2 | 0 | 4,2 | 4,8 | 2,9 | 0,6 | 1,2 | Ortho 58 | 0,2 | 2 | 6 |
| S8 | 626730 | 4983344 | Gully | 3 | 2 | 2 | 0 | 3,6 | 4,6 | 2,9 | 1,0 | 0,7 | Ortho 58 | 0,2 | 2 | 9 |
| S8 | 626730 | 4983344 | Gully | 3 | 2 | 2 | 0 | 11,6 | 12,8 | 11,1 | 1,2 | 0,5 | Ortho 58 | 0,2 | 2 | 9 |
| S8 | 626750 | 4983350 | Riser | 3 | 2 | 2 | 0 | 6,1 | 6,9 | 5,1 | 0,8 | 1,1 | Ortho 58 | 0,2 | 2 | 9 |
| S8 | 626780 | 4983350 | River | 3 | 2 | 2 | 0 | 1,7 | 2,0 | 1,1 | 0,3 | 0,6 | Ortho 58 | 0,2 | 2 | 9 |
| S8 | 626815 | 4983350 | Talweg | 3 | 2 | 2 | 0 | 9,6 | 11,1 | 8,1 | 1,4 | 1,6 | Ortho 58 | 0,2 | 2 | 9 |
| S8 | 626880 | 4983350 | River | 3 | 2 | 1 | 0 | 2,6 | 4,7 | 1,6 | 2,0 | 1,0 | Ortho 58 | 0,2 | 2 | 10 |
| S8 | 627035 | 4983350 | Talweg | 3 | 2 | 2 | 0 | 3,9 | 5,3 | 3,1 | 1,4 | 0,8 | Ortho 58 | 0,2 | 2 | 9 |

| Seg. | Lon. (UTM) | Lat. (UTM) | Marker Type | Mark. Obl. | Mark. res. (/2) | Nb. of splay | Scarp 2nd | Offset Pref. (m) | Offset max (m) | Offset min (m) | Δ+ (m) | Δ- (m) | Image type | Image Res. (m) | Image quality (/2) | Total Score (/10) |
|---|---|---|---|---|---|---|---|---|---|---|---|---|---|---|---|---|
| S8 | 627035 | 4983350 | Talweg | 3 | 2 | 2 | 0 | 15,4 | 17,4 | 13,7 | 2,0 | 1,7 | Ortho 58 | 0,2 | 2 | 9 |
| S8 | 627065 | 4983350 | Gully | 3 | 1 | 2 | 0 | 6,1 | 6,9 | 5,5 | 0,9 | 0,6 | Ortho 58 | 0,2 | 2 | 8 |
| S8 | 627125 | 4983345 | River | 3 | 2 | 3 | 0 | 3,2 | 3,5 | 2,1 | 0,4 | 1,1 | Ortho 58 | 0,2 | 2 | 8 |
| S8 | 627180 | 4983345 | Talweg | 3 | 2 | 3 | 0 | 2,5 | 3,6 | 1,3 | 1,1 | 1,2 | Ortho 58 | 0,2 | 2 | 8 |
| S8 | 627310 | 4983340 | Talweg | 3 | 2 | 2 | 0 | 3,0 | 4,0 | 2,4 | 1,0 | 0,6 | Ortho 58 | 0,2 | 2 | 9 |
| S8 | 627380 | 4983330 | Talweg | 3 | 2 | 2 | 0 | 9,6 | 10,4 | 8,7 | 0,8 | 0,9 | Ortho 58 | 0,2 | 2 | 9 |
| S8 | 627425 | 4983325 | Talweg | 3 | 1 | 2 | 0 | 4,6 | 5,6 | 3,3 | 1,0 | 1,3 | Ortho 58 | 0,2 | 2 | 8 |
| S8 | 627470 | 4983310 | Talweg | 3 | 2 | 1 | 0 | 3,8 | 4,6 | 3,0 | 0,8 | 0,8 | Ortho 58 | 0,2 | 2 | 10 |
| S8 | 627570 | 4983290 | Riser | 3 | 2 | 1 | 1 | 4,0 | 4,4 | 3,0 | 0,4 | 1,0 | Ortho 58 | 0,2 | 2 | 9 |
| S8 | 627640 | 4983270 | Gully | 2 | 2 | 1 | 2 | 4,6 | 5,2 | 3,0 | 0,6 | 1,6 | Ortho 58 | 0,2 | 2 | 6 |
| S8 | 627777 | 4983255 | Gully | 3 | 1 | 1 | 0 | 2,4 | 2,8 | 1,9 | 0,4 | 0,5 | Ortho 58 | 0,2 | 2 | 9 |
| S8 | 627790 | 4983250 | Riser | 3 | 2 | 1 | 0 | 3,5 | 4,1 | 2,4 | 0,6 | 1,0 | Ortho 58 | 0,2 | 2 | 10 |
| S8 | 627815 | 4983245 | Riser | 3 | 2 | 1 | 0 | 2,6 | 3,8 | 1,8 | 1,2 | 0,9 | Ortho 58 | 0,2 | 2 | 10 |
| S8 | 627980 | 4983270 | Riser | 3 | 2 | 4 | 0 | 2,4 | 2,8 | 1,8 | 0,4 | 0,6 | Ortho 58 | 0,2 | 2 | 8 |
| S8 | 627980 | 4983270 | Fan apex | 3 | 2 | 4 | 0 | 12,6 | 16,6 | 10,9 | 4,0 | 1,7 | Ortho 58 | 0,2 | 2 | 8 |
| S8 | 628060 | 4983270 | Riser | 3 | 2 | 3 | 0 | 4,1 | 4,8 | 3,3 | 0,8 | 0,8 | Ortho 58 | 0,2 | 2 | 8 |
| S8 | 628060 | 4983270 | Fan apex | 3 | 2 | 3 | 0 | 12,7 | 15,8 | 10,0 | 3,2 | 2,7 | Ortho 58 | 0,2 | 2 | 8 |
| S8 | 628100 | 4983270 | Gully | 2 | 1 | 2 | 0 | 8,6 | 9,6 | 7,7 | 0,9 | 0,9 | Ortho 58 | 0,2 | 2 | 6 |
| S8 | 628130 | 4983262 | Gully | 3 | 2 | 1 | 0 | 3,2 | 3,8 | 2,4 | 0,6 | 0,8 | Ortho 58 | 0,2 | 2 | 10 |
| S8 | 628145 | 4983260 | Gully | 3 | 1 | 1 | 0 | 1,9 | 2,7 | 1,1 | 0,8 | 0,8 | Ortho 58 | 0,2 | 2 | 9 |
| S8 | 628185 | 4983250 | Talweg | 3 | 1 | 1 | 0 | 2,7 | 3,6 | 1,6 | 0,9 | 1,1 | Ortho 58 | 0,2 | 2 | 9 |
| S8 | 628285 | 4983210 | Talweg | 2 | 2 | 1 | 0 | 2,7 | 3,7 | 2,3 | 1,0 | 0,4 | Ortho 58 | 0,2 | 2 | 8 |
| S8 | 628285 | 4983210 | Talweg | 3 | 2 | 1 | 0 | 15,9 | 18,8 | 12,4 | 2,9 | 3,5 | Ortho 58 | 0,2 | 2 | 10 |
| S8 | 628320 | 4983200 | Gully | 3 | 1 | 1 | 1 | 1,2 | 1,9 | 0,9 | 0,7 | 0,3 | Ortho 58 | 0,2 | 1 | 7 |
| S8 | 628360 | 4983180 | Talweg | 3 | 1 | 2 | 0 | 3,7 | 4,8 | 2,9 | 1,0 | 0,9 | Ortho 58 | 0,2 | 2 | 8 |
| S8 | 628405 | 4983200 | Gully | 3 | 2 | 2 | 0 | 2,8 | 3,0 | 2,4 | 0,3 | 0,4 | Ortho 58 | 0,2 | 2 | 9 |
| S8 | 628450 | 4983195 | Talweg | 3 | 2 | 1 | 0 | 6,5 | 7,2 | 5,9 | 0,7 | 0,6 | Ortho 58 | 0,2 | 2 | 10 |
| S8 | 628450 | 4983195 | Riser | 2 | 2 | 1 | 0 | 12,4 | 14,6 | 11,6 | 2,2 | 0,8 | Ortho 58 | 0,2 | 2 | 8 |
| S8 | 628487 | 4983187 | Riser | 3 | 1 | 1 | 0 | 7,7 | 9,1 | 5,9 | 1,5 | 1,8 | Ortho 58 | 0,2 | 2 | 9 |
| S8 | 628510 | 4983177 | Gully | 3 | 2 | 1 | 0 | 5,8 | 6,5 | 5,3 | 0,7 | 0,5 | Ortho 58 | 0,2 | 2 | 10 |
| S8 | 628540 | 4983166 | Riser | 3 | 1 | 1 | 0 | 7,9 | 8,9 | 7,4 | 1,1 | 0,5 | Ortho 58 | 0,2 | 2 | 9 |
| S8 | 628600 | 4983150 | Gully | 3 | 2 | 1 | 0 | 8,1 | 8,8 | 7,4 | 0,6 | 0,7 | Ortho 58 | 0,2 | 2 | 10 |
| S8 | 628640 | 4983130 | Riser | 3 | 1 | 1 | 0 | 6,5 | 7,2 | 5,8 | 0,7 | 0,7 | Ortho 58 | 0,2 | 2 | 9 |

| Seg. | Lon. (UTM) | Lat. (UTM) | Marker Type | Mark. Obl. | Mark. res. (/2) | Nb. of splay | Scarp 2nd | Offset Pref. (m) | Offset max (m) | Offset min (m) | Δ+ (m) | Δ- (m) | Image type | Image Res. (m) | Image quality (/2) | Total Score (/10) |
|---|---|---|---|---|---|---|---|---|---|---|---|---|---|---|---|---|
| S8 | 628750 | 4983115 | Talweg | 3 | 1 | 2 | 0 | 4,8 | 5,4 | 4,1 | 0,7 | 0,6 | Ortho 58 | 0,2 | 2 | 8 |
| S8 | 628800 | 4983105 | Talweg | 3 | 2 | 2 | 0 | 4,3 | 5,1 | 3,4 | 0,9 | 0,9 | Ortho 58 | 0,2 | 2 | 9 |
| S8 | 628840 | 4983095 | Gully | 3 | 2 | 2 | 0 | 3,9 | 4,7 | 3,1 | 0,9 | 0,8 | Ortho 58 | 0,2 | 2 | 9 |
| S8 | 628890 | 4983080 | Talweg | 3 | 1 | 2 | 0 | 2,4 | 3,2 | 1,6 | 0,8 | 0,8 | Ortho 58 | 0,2 | 2 | 8 |
| S8 | 628890 | 4983080 | Talweg | 3 | 1 | 2 | 0 | 15,7 | 16,7 | 14,9 | 1,1 | 0,9 | Ortho 58 | 0,2 | 2 | 8 |
| S8 | 628920 | 4983075 | Talweg | 3 | 1 | 1 | 0 | 2,3 | 2,8 | 1,4 | 0,5 | 0,9 | Ortho 58 | 0,2 | 2 | 9 |
| S8 | 628960 | 4983070 | Gully | 3 | 1 | 2 | 0 | 2,2 | 3,5 | 1,4 | 1,3 | 0,9 | Ortho 58 | 0,2 | 2 | 8 |
| S8 | 628995 | 4983065 | Talweg | 3 | 1 | 2 | 0 | 2,6 | 3,7 | 1,9 | 1,1 | 0,7 | Ortho 58 | 0,2 | 2 | 8 |
| S8 | 628995 | 4983065 | Talweg | 3 | 2 | 2 | 0 | 8,0 | 8,5 | 7,4 | 0,5 | 0,6 | Ortho 58 | 0,2 | 2 | 9 |
| S8 | 629025 | 4983055 | Talweg | 3 | 2 | 2 | 0 | 2,4 | 3,0 | 1,9 | 0,5 | 0,5 | Ortho 58 | 0,2 | 2 | 9 |
| S8 | 629025 | 4983055 | Talweg | 3 | 1 | 2 | 0 | 6,8 | 7,6 | 6,3 | 0,8 | 0,5 | Ortho 58 | 0,2 | 2 | 8 |
| S8 | 629025 | 4983055 | Talweg | 3 | 1 | 2 | 0 | 10,7 | 11,1 | 10,3 | 0,5 | 0,3 | Ortho 58 | 0,2 | 2 | 8 |
| S8 | 629060 | 4983045 | Talweg | 3 | 2 | 1 | 0 | 3,3 | 3,7 | 2,8 | 0,4 | 0,5 | Ortho 58 | 0,2 | 2 | 10 |
| S8 | 629060 | 4983045 | Talweg | 3 | 2 | 1 | 0 | 9,1 | 9,7 | 8,3 | 0,7 | 0,8 | Ortho 58 | 0,2 | 2 | 10 |
| S8 | 629090 | 4983035 | Gully | 3 | 2 | 1 | 0 | 4,3 | 4,6 | 3,9 | 0,3 | 0,3 | Ortho 58 | 0,2 | 2 | 10 |
| S8 | 629090 | 4983035 | Gully | 3 | 1 | 1 | 0 | 9,1 | 9,7 | 8,4 | 0,6 | 0,8 | Ortho 58 | 0,2 | 2 | 9 |
| S8 | 629170 | 4983015 | Riser | 2 | 1 | 1 | 0 | 23,2 | 24,7 | 22,3 | 1,6 | 0,9 | Ortho 58 | 0,2 | 2 | 7 |
| S8 | 629260 | 4982995 | Talweg | 2 | 1 | 1 | 0 | 5,8 | 6,6 | 4,9 | 0,9 | 0,9 | Ortho 58 | 0,2 | 2 | 7 |
| S8 | 629295 | 4982990 | Talweg | 2 | 2 | 1 | 0 | 6,5 | 7,4 | 5,1 | 0,9 | 1,3 | Ortho 58 | 0,2 | 2 | 8 |
| S8 | 629335 | 4982985 | Riser | 3 | 2 | 1 | 0 | 2,8 | 3,2 | 2,2 | 0,4 | 0,6 | Ortho 58 | 0,2 | 2 | 10 |
| S8 | 629335 | 4982985 | Riser | 3 | 2 | 1 | 0 | 5,5 | 6,4 | 4,9 | 0,9 | 0,6 | Ortho 58 | 0,2 | 2 | 10 |
| S8 | 629360 | 4982980 | Talweg | 3 | 1 | 1 | 0 | 4,4 | 5,1 | 3,5 | 0,7 | 0,9 | Ortho 58 | 0,2 | 2 | 9 |
| S8 | 629390 | 4982975 | Talweg | 3 | 2 | 2 | 0 | 12,9 | 13,6 | 11,8 | 0,7 | 1,0 | Ortho 58 | 0,2 | 2 | 9 |
| S8 | 629410 | 4982965 | Talweg | 3 | 2 | 1 | 0 | 3,3 | 4,7 | 2,0 | 1,4 | 1,2 | Ortho 58 | 0,2 | 2 | 10 |
| S8 | 629410 | 4982965 | Talweg | 3 | 1 | 1 | 0 | 11,1 | 13,0 | 8,8 | 2,0 | 2,3 | Ortho 58 | 0,2 | 2 | 9 |
| S8 | 629430 | 4982965 | Talweg | 3 | 2 | 2 | 0 | 2,3 | 3,1 | 1,7 | 0,8 | 0,6 | Ortho 58 | 0,2 | 2 | 9 |
| S8 | 629460 | 4982960 | Talweg | 3 | 2 | 2 | 0 | 4,6 | 6,0 | 3,2 | 1,4 | 1,4 | Ortho 58 | 0,2 | 2 | 9 |
| S8 | 629500 | 4982945 | Talweg | 3 | 2 | 1 | 0 | 3,1 | 4,3 | 1,9 | 1,2 | 1,2 | Ortho 58 | 0,2 | 2 | 10 |
| S8 | 629530 | 4982935 | Talweg | 2 | 1 | 2 | 0 | 2,9 | 3,7 | 2,2 | 0,8 | 0,7 | Ortho 58 | 0,2 | 2 | 6 |
| S8 | 629530 | 4982935 | Talweg | 3 | 1 | 2 | 0 | 7,1 | 8,3 | 6,4 | 1,2 | 0,7 | Ortho 58 | 0,2 | 2 | 8 |
| S8 | 629545 | 4982933 | Talweg | 3 | 1 | 1 | 0 | 2,2 | 2,5 | 1,3 | 0,4 | 0,9 | Ortho 58 | 0,2 | 2 | 9 |
| S8 | 629570 | 4982930 | Talweg | 2 | 2 | 1 | 0 | 3,4 | 4,0 | 3,0 | 0,6 | 0,4 | Ortho 58 | 0,2 | 1 | 7 |
| S8 | 629570 | 4982930 | Talweg | 3 | 2 | 1 | 0 | 3,9 | 4,5 | 3,4 | 0,6 | 0,5 | Ortho 58 | 0,2 | 2 | 10 |

| Seg. | Lon. (UTM) | Lat. (UTM) | Marker Type | Mark. Obl. | Mark. res. (/2) | Nb. of splay | Scarp 2nd | Offset Pref. (m) | Offset max (m) | Offset min (m) | Δ+ (m) | Δ- (m) | Image type | Image Res. (m) | Image quality (/2) | Total Score (/10) |
|---|---|---|---|---|---|---|---|---|---|---|---|---|---|---|---|---|
| S8 | 629570 | 4982930 | Talweg | 2 | 2 | 1 | 0 | 7,9 | 8,9 | 5,3 | 0,9 | 2,6 | Ortho 58 | 0,2 | 2 | 8 |
| S8 | 629605 | 4982920 | Talweg | 3 | 1 | 1 | 0 | 4,3 | 4,8 | 3,7 | 0,5 | 0,6 | Ortho 58 | 0,2 | 2 | 9 |
| S8 | 629640 | 4982910 | Talweg | 3 | 2 | 2 | 0 | 5,3 | 5,9 | 4,6 | 0,6 | 0,7 | Ortho 58 | 0,2 | 2 | 9 |
| S8 | 629640 | 4982910 | Talweg | 3 | 1 | 2 | 0 | 10,3 | 11,2 | 9,5 | 0,9 | 0,8 | Ortho 58 | 0,2 | 2 | 8 |
| S8 | 629700 | 4982900 | Talweg | 3 | 1 | 2 | 0 | 24,7 | 27,9 | 21,2 | 3,2 | 3,5 | Ortho 58 | 0,2 | 2 | 8 |
| S8 | 629880 | 4982850 | Talweg | 3 | 2 | 3 | 0 | 7,0 | 8,6 | 4,4 | 1,6 | 2,7 | Ortho 58 | 0,2 | 2 | 8 |
| S8 | 630040 | 4982800 | Talweg | 3 | 1 | 3 | 1 | 2,9 | 3,7 | 2,5 | 0,8 | 0,4 | Ortho 58 | 0,2 | 2 | 6 |
| S8 | 630130 | 4982780 | Gully | 3 | 1 | 1 | 2 | 6,8 | 7,7 | 6,3 | 0,9 | 0,4 | Ortho 58 | 0,2 | 2 | 7 |
| S8 | 630230 | 4982720 | Riser | 3 | 2 | 1 | 1 | 3,5 | 4,3 | 2,8 | 0,8 | 0,8 | Ortho 58 | 0,2 | 2 | 9 |
| S8 | 630270 | 4982705 | Riser | 3 | 2 | 3 | 1 | 7,8 | 9,3 | 6,5 | 1,6 | 1,3 | Ortho 58 | 0,2 | 2 | 7 |
| S8 | 630515 | 4982615 | Gully | 3 | 1 | 1 | 1 | 3,8 | 4,6 | 3,0 | 0,8 | 0,8 | Ortho 58 | 0,2 | 2 | 8 |
| S8 | 630530 | 4982613 | Talweg | 3 | 1 | 2 | 1 | 3,6 | 4,6 | 2,7 | 1,0 | 0,9 | Ortho 58 | 0,2 | 2 | 7 |
| S8 | 630590 | 4982585 | Talweg | 3 | 2 | 2 | 1 | 3,5 | 4,4 | 2,8 | 0,9 | 0,6 | Ortho 58 | 0,2 | 2 | 8 |
| S8 | 630640 | 4982555 | Talweg | 3 | 2 | 1 | 1 | 3,5 | 4,1 | 2,9 | 0,6 | 0,7 | Ortho 58 | 0,2 | 2 | 9 |
| S8 | 630640 | 4982555 | Talweg | 3 | 2 | 1 | 1 | 10,7 | 11,5 | 10,1 | 0,8 | 0,6 | Ortho 58 | 0,2 | 2 | 9 |
| S8 | 630665 | 4982545 | Talweg | 3 | 2 | 1 | 1 | 4,6 | 6,0 | 4,1 | 1,4 | 0,6 | Ortho 58 | 0,2 | 2 | 9 |
| S8 | 630715 | 4982550 | Talweg | 3 | 2 | 1 | 2 | 3,4 | 4,0 | 2,8 | 0,6 | 0,6 | Ortho 58 | 0,2 | 2 | 8 |
| S8 | 630780 | 4982525 | Talweg | 3 | 2 | 2 | 1 | 1,6 | 2,6 | 1,3 | 1,0 | 0,3 | Ortho 58 | 0,2 | 2 | 8 |
| S8 | 630820 | 4982510 | Talweg | 2 | 2 | 1 | 1 | 2,9 | 4,0 | 2,1 | 1,0 | 0,8 | Ortho 58 | 0,2 | 2 | 7 |
| S8 | 630860 | 4982500 | Talweg | 3 | 1 | 1 | 0 | 3,6 | 5,2 | 3,1 | 1,6 | 0,4 | Ortho 58 | 0,2 | 2 | 9 |
| S8 | 630890 | 4982490 | Talweg | 3 | 2 | 1 | 0 | 3,2 | 3,8 | 2,8 | 0,7 | 0,3 | Ortho 58 | 0,2 | 2 | 10 |
| S8 | 630930 | 4982475 | Talweg | 3 | 1 | 1 | 0 | 2,4 | 3,4 | 1,5 | 1,0 | 0,8 | Ortho 58 | 0,2 | 2 | 9 |
| S8 | 630945 | 4982470 | Gully | 3 | 2 | 1 | 0 | 3,1 | 3,9 | 2,7 | 0,8 | 0,3 | Ortho 58 | 0,2 | 2 | 10 |
| S8 | 631000 | 4982455 | Talweg | 3 | 1 | 2 | 0 | 3,0 | 3,8 | 2,4 | 0,7 | 0,6 | Ortho 58 | 0,2 | 2 | 8 |
| S8 | 631000 | 4982455 | Talweg | 3 | 1 | 2 | 0 | 5,9 | 6,9 | 5,4 | 1,0 | 0,5 | Ortho 58 | 0,2 | 1 | 7 |
| S8 | 631020 | 4982450 | Talweg | 3 | 2 | 1 | 0 | 3,4 | 4,2 | 2,5 | 0,8 | 1,0 | Ortho 58 | 0,2 | 2 | 10 |
| S8 | 631020 | 4982450 | Talweg | 3 | 2 | 1 | 0 | 9,6 | 10,3 | 9,0 | 0,7 | 0,6 | Ortho 58 | 0,2 | 2 | 10 |
| S8 | 631050 | 4982448 | Ridge | 3 | 1 | 1 | 0 | 6,0 | 7,8 | 5,1 | 1,8 | 0,9 | Ortho 58 | 0,2 | 2 | 9 |
| S8 | 631100 | 4982433 | Talweg | 3 | 2 | 2 | 1 | 3,2 | 4,7 | 2,2 | 1,6 | 0,9 | Ortho 58 | 0,2 | 2 | 8 |
| S8 | 631140 | 4982425 | Gully | 3 | 2 | 3 | 1 | 3,6 | 5,1 | 2,7 | 1,5 | 0,9 | Ortho 58 | 0,2 | 2 | 7 |
| S8 | 631290 | 4982410 | Talweg | 3 | 1 | 2 | 0 | 7,9 | 9,7 | 6,0 | 1,8 | 1,9 | Ortho 58 | 0,2 | 2 | 8 |
| S8 | 631320 | 4982415 | Talweg | 2 | 1 | 3 | 0 | 20,6 | 22,3 | 19,7 | 1,8 | 0,9 | Ortho 58 | 0,2 | 2 | 5 |
| S8 | 631395 | 4982390 | Gully | 3 | 1 | 3 | 0 | 3,5 | 4,6 | 2,8 | 1,1 | 0,8 | Ortho 58 | 0,2 | 2 | 7 |

| Seg. | Lon. (UTM) | Lat. (UTM) | Marker Type | Mark. Obl. | Mark. res. (/2) | Nb. of splay | Scarp 2nd | Offset Pref. (m) | Offset max (m) | Offset min (m) | Δ+ (m) | Δ- (m) | Image type | Image Res. (m) | Image quality (/2) | Total Score (/10) |
|---|---|---|---|---|---|---|---|---|---|---|---|---|---|---|---|---|
| S8 | 631425 | 4982390 | Talweg | 3 | 1 | 2 | 0 | 9,0 | 10,5 | 6,8 | 1,5 | 2,2 | Ortho 58 | 0,2 | 2 | 8 |
| S8 | 631425 | 4982390 | Talweg | 3 | 2 | 2 | 0 | 19,2 | 21,2 | 16,4 | 1,9 | 2,8 | Ortho 58 | 0,2 | 2 | 9 |
| S8 | 631425 | 4982390 | Talweg | 3 | 2 | 3 | 0 | 38,9 | 44,4 | 34,8 | 5,5 | 4,1 | Ortho 58 | 0,2 | 2 | 8 |
| S8 | 631470 | 4982385 | Talweg | 3 | 2 | 3 | 0 | 6,4 | 8,4 | 4,8 | 1,9 | 1,6 | Ortho 58 | 0,2 | 2 | 8 |
| S8 | 631490 | 4982392 | Gully | 3 | 1 | 4 | 0 | 2,3 | 3,3 | 1,9 | 1,0 | 0,4 | Ortho 58 | 0,2 | 2 | 7 |
| S8 | 631500 | 4982390 | Gully | 3 | 2 | 4 | 0 | 25,7 | 27,1 | 24,1 | 1,5 | 1,6 | Ortho 58 | 0,2 | 2 | 8 |
| S8 | 631550 | 4982390 | River | 3 | 2 | 4 | 0 | 16,6 | 22,4 | 13,3 | 5,8 | 3,3 | Ortho 58 | 0,2 | 2 | 8 |
| S8 | 631575 | 4982385 | Gully | 3 | 2 | 3 | 1 | 3,9 | 5,5 | 3,0 | 1,5 | 0,9 | Ortho 58 | 0,2 | 2 | 7 |
| S8 | 631600 | 4982385 | Gully | 3 | 2 | 3 | 1 | 10,2 | 12,0 | 9,1 | 1,8 | 1,1 | Ortho 58 | 0,2 | 2 | 7 |
| S8 | 631670 | 4982375 | Talweg | 3 | 1 | 1 | 0 | 10,4 | 12,6 | 7,3 | 2,2 | 3,1 | Ortho 58 | 0,2 | 2 | 9 |
| S8 | 631730 | 4982370 | Gully | 3 | 2 | 2 | 0 | 11,8 | 13,6 | 10,7 | 1,8 | 1,1 | Ortho 58 | 0,2 | 2 | 9 |
| S8 | 631755 | 4982365 | Talweg | 3 | 1 | 2 | 0 | 3,2 | 4,5 | 2,5 | 1,3 | 0,7 | Ortho 58 | 0,2 | 2 | 8 |
| S8 | 631755 | 4982365 | Talweg | 3 | 1 | 2 | 0 | 26,8 | 28,8 | 23,2 | 2,0 | 3,6 | Ortho 58 | 0,2 | 2 | 8 |
| S8 | 631800 | 4982360 | Gully | 3 | 2 | 3 | 1 | 11,0 | 12,2 | 9,1 | 1,2 | 1,9 | Ortho 58 | 0,2 | 2 | 7 |
| S8 | 631850 | 4982345 | Talweg | 3 | 1 | 2 | 1 | 6,9 | 10,1 | 5,6 | 3,1 | 1,3 | Ortho 58 | 0,2 | 2 | 7 |
| S8 | 631945 | 4982335 | Talweg | 3 | 2 | 1 | 1 | 6,8 | 7,7 | 4,5 | 0,9 | 2,3 | Ortho 58 | 0,2 | 2 | 9 |
| S8 | 632000 | 4982335 | Talweg | 3 | 1 | 1 | 1 | 127,7 | 136,8 | 116,7 | 9,2 | 11,0 | Ortho 58 | 0,2 | 2 | 8 |
| S8 | 632735 | 4982205 | Riser | 3 | 2 | 1 | 1 | 2,0 | 2,4 | 1,4 | 0,5 | 0,5 | Ortho 58 | 0,2 | 2 | 9 |
| S8 | 632760 | 4982200 | Riser | 3 | 2 | 1 | 1 | 10,4 | 11,6 | 9,0 | 1,2 | 1,4 | Ortho 58 | 0,2 | 2 | 9 |
| S8 | 632810 | 4982195 | Talweg | 3 | 2 | 4 | 1 | 2,5 | 3,4 | 2,3 | 0,8 | 0,3 | Ortho 58 | 0,2 | 2 | 7 |
| S8 | 632810 | 4982195 | Talweg | 3 | 2 | 4 | 1 | 5,4 | 6,7 | 4,7 | 1,3 | 0,8 | Ortho 58 | 0,2 | 2 | 7 |
| S8 | 632900 | 4982190 | Talweg | 2 | 2 | 2 | 1 | 25,7 | 29,5 | 21,2 | 3,7 | 4,5 | Ortho 58 | 0,2 | 2 | 6 |
| S8 | 633015 | 4982175 | Riser | 3 | 2 | 2 | 0 | 5,6 | 6,3 | 4,4 | 0,7 | 1,2 | Ortho 58 | 0,2 | 2 | 9 |
| S8 | 633050 | 4982165 | River | 3 | 2 | 1 | 0 | 3,4 | 4,4 | 2,9 | 1,0 | 0,5 | Ortho 58 | 0,2 | 2 | 10 |
| S8 | 633050 | 4982165 | River | 3 | 2 | 1 | 0 | 12,5 | 13,3 | 11,3 | 0,8 | 1,1 | Ortho 58 | 0,2 | 2 | 10 |
| S8 | 633155 | 4982145 | Gully | 3 | 1 | 1 | 0 | 2,9 | 3,6 | 2,3 | 0,7 | 0,6 | Ortho 58 | 0,2 | 2 | 9 |
| S8 | 633175 | 4982135 | Gully | 3 | 2 | 1 | 0 | 5,2 | 5,9 | 4,7 | 0,7 | 0,5 | Ortho 58 | 0,2 | 2 | 10 |
| S8 | 633260 | 4982100 | Talweg | 3 | 2 | 2 | 0 | 3,2 | 3,6 | 2,9 | 0,4 | 0,3 | Ortho 58 | 0,2 | 2 | 9 |
| S8 | 633260 | 4982100 | Talweg | 3 | 1 | 2 | 0 | 4,2 | 5,2 | 3,0 | 1,0 | 1,1 | Ortho 58 | 0,2 | 2 | 8 |
| S8 | 633350 | 4982070 | Talweg | 3 | 1 | 1 | 0 | 3,2 | 4,3 | 1,4 | 1,1 | 1,8 | Ortho 58 | 0,2 | 2 | 9 |
| S8 | 633390 | 4982065 | Gully | 3 | 1 | 1 | 0 | 6,5 | 7,1 | 5,8 | 0,6 | 0,7 | Ortho 58 | 0,2 | 2 | 9 |
| S8 | 633420 | 4982058 | Gully | 3 | 1 | 2 | 0 | 2,3 | 2,7 | 1,8 | 0,4 | 0,5 | Ortho 58 | 0,2 | 1 | 7 |
| S8 | 633435 | 4982055 | Talweg | 2 | 1 | 3 | 0 | 3,1 | 3,8 | 2,2 | 0,7 | 0,9 | Ortho 58 | 0,2 | 1 | 4 |

| Seg. | Lon. (UTM) | Lat. (UTM) | Marker Type | Mark. Obl. | Mark. res. (/2) | Nb. of splay | Scarp 2nd | Offset Pref. (m) | Offset max (m) | Offset min (m) | Δ+ (m) | Δ- (m) | Image type | Image Res. (m) | Image quality (/2) | Total Score (/10) |
|---|---|---|---|---|---|---|---|---|---|---|---|---|---|---|---|---|
| S8 | 633553 | 4982042 | Gully | 3 | 1 | 1 | 0 | 7,0 | 8,5 | 6,5 | 1,5 | 0,5 | Ortho 58 | 0,2 | 2 | 9 |
| S8 | 633680 | 4982012 | Talweg | 3 | 1 | 1 | 0 | 4,2 | 5,2 | 3,2 | 1,0 | 0,9 | Ortho 58 | 0,2 | 2 | 9 |
| S8 | 633730 | 4981995 | Ridge | 3 | 2 | 1 | 0 | 12,1 | 14,0 | 10,3 | 1,9 | 1,9 | Ortho 58 | 0,2 | 2 | 10 |
| S8 | 633730 | 4981995 | Ridge | 3 | 1 | 1 | 0 | 2,1 | 2,9 | 1,8 | 0,9 | 0,3 | Ortho 58 | 0,2 | 2 | 9 |
| S8 | 633770 | 4981980 | Talweg | 3 | 1 | 1 | 0 | 13,2 | 14,1 | 11,0 | 1,0 | 2,2 | Ortho 58 | 0,2 | 2 | 9 |
| S8 | 633770 | 4981980 | Talweg | 3 | 1 | 1 | 0 | 3,9 | 4,3 | 2,4 | 0,4 | 1,6 | Ortho 58 | 0,2 | 2 | 9 |
| S8 | 633337 | 4981970 | Talweg | 3 | 1 | 1 | 0 | 6,5 | 7,3 | 4,1 | 0,8 | 2,4 | Ortho 58 | 0,2 | 2 | 9 |
| S8 | 633907 | 4981955 | Ridge | 3 | 1 | 1 | 0 | 2,0 | 2,4 | 1,3 | 0,4 | 0,7 | Ortho 58 | 0,2 | 2 | 9 |
| S8 | 633930 | 4981953 | Riser | 3 | 2 | 1 | 0 | 3,3 | 5,4 | 1,2 | 2,1 | 2,1 | Ortho 58 | 0,2 | 2 | 10 |
| S8 | 633950 | 4981950 | Gully | 3 | 1 | 1 | 0 | 3,5 | 4,9 | 2,5 | 1,4 | 1,0 | Ortho 58 | 0,2 | 2 | 9 |
| S8 | 634050 | 4981935 | Gully | 3 | 1 | 1 | 0 | 1,7 | 3,4 | 0,8 | 1,7 | 0,9 | Ortho 58 | 0,2 | 2 | 9 |
| S8 | 634515 | 4981915 | Riser | 3 | 1 | 1 | 2 | 4,9 | 5,5 | 3,6 | 0,6 | 1,2 | Ortho 58 | 0,2 | 2 | 7 |
| S8 | 634600 | 4981900 | River | 3 | 2 | 1 | 2 | 3,2 | 4,2 | 2,7 | 1,0 | 0,5 | Ortho 58 | 0,2 | 2 | 8 |
| S8 | 634665 | 4981874 | Talweg | 3 | 2 | 1 | 2 | 6,9 | 8,7 | 4,6 | 1,9 | 2,2 | Ortho 58 | 0,2 | 2 | 8 |
| S8 | 634770 | 4981836 | Talweg | 2 | 1 | 1 | 2 | 7,3 | 8,4 | 5,5 | 1,1 | 1,8 | Ortho 58 | 0,2 | 2 | 5 |
| S8 | 634860 | 4981820 | Talweg | 3 | 1 | 1 | 2 | 7,1 | 8,8 | 4,5 | 1,7 | 2,6 | Ortho 58 | 0,2 | 2 | 7 |
| S8 | 634887 | 4981815 | Talweg | 3 | 1 | 1 | 2 | 3,4 | 4,2 | 2,8 | 0,8 | 0,6 | Ortho 58 | 0,2 | 2 | 7 |
| S8 | 634910 | 4981812 | Talweg | 3 | 1 | 1 | 2 | 4,4 | 5,6 | 3,4 | 1,2 | 1,0 | Ortho 58 | 0,2 | 1 | 6 |
| S8 | 634970 | 4981804 | Talweg | 3 | 1 | 1 | 2 | 3,1 | 3,9 | 2,6 | 0,8 | 0,4 | Ortho 58 | 0,2 | 2 | 7 |
| S8 | 635005 | 4981806 | Talweg | 3 | 1 | 1 | 2 | 5,9 | 7,3 | 5,5 | 1,4 | 0,4 | Ortho 58 | 0,2 | 2 | 7 |
| S8 | 635050 | 4981800 | Talweg | 3 | 2 | 1 | 2 | 6,9 | 8,3 | 5,9 | 1,4 | 1,0 | Ortho 58 | 0,2 | 2 | 8 |
| S8 | 635050 | 4981800 | Talweg | 3 | 2 | 1 | 1 | 10,9 | 12,4 | 10,1 | 1,6 | 0,8 | Ortho 58 | 0,2 | 2 | 9 |
| S8 | 635230 | 4981775 | Talweg | 3 | 1 | 1 | 1 | 4,9 | 6,5 | 3,9 | 1,6 | 1,0 | Ortho 58 | 0,2 | 2 | 8 |
| S8 | 635530 | 4981577 | Riser | 3 | 2 | 1 | 1 | 4,4 | 5,5 | 3,5 | 1,2 | 0,8 | Ortho 58 | 0,2 | 2 | 9 |
| R7 | 635850 | 4981500 | Talweg | 2 | 1 | 1 | 1 | 4,9 | 6,9 | 4,4 | 2,0 | 0,6 | Ortho 58 | 0,2 | 2 | 6 |
| R7 | 635910 | 4981485 | Riser | 3 | 1 | 1 | 1 | 4,6 | 5,4 | 4,1 | 0,8 | 0,6 | Ortho 58 | 0,2 | 2 | 8 |
| R7 | 635966 | 4981470 | Talweg | 3 | 1 | 1 | 1 | 4,8 | 5,6 | 4,0 | 0,8 | 0,9 | Ortho 58 | 0,2 | 2 | 8 |
| R7 | 635966 | 4981470 | Talweg | 3 | 1 | 1 | 1 | 12,1 | 13,6 | 11,0 | 1,5 | 1,1 | Ortho 58 | 0,2 | 2 | 8 |
| R7 | 635995 | 4981450 | Talweg | 3 | 2 | 1 | 1 | 3,6 | 4,4 | 3,1 | 0,8 | 0,5 | Ortho 58 | 0,2 | 2 | 9 |
| R7 | 636035 | 4981438 | Talweg | 3 | 1 | 1 | 1 | 3,0 | 4,4 | 2,2 | 1,4 | 0,8 | Ortho 58 | 0,2 | 2 | 8 |
| R7 | 636060 | 4981420 | Talweg | 3 | 2 | 1 | 1 | 6,7 | 7,8 | 5,8 | 1,2 | 0,9 | Ortho 58 | 0,2 | 2 | 9 |
| R7 | 636110 | 4981400 | Talweg | 3 | 1 | 1 | 1 | 7,1 | 7,8 | 6,3 | 0,7 | 0,8 | Ortho 58 | 0,2 | 2 | 8 |
| R7 | 636170 | 4981360 | Talweg | 3 | 1 | 1 | 1 | 10,4 | 12,4 | 7,5 | 2,0 | 2,9 | Ortho 58 | 0,2 | 2 | 8 |

| Seg. | Lon. (UTM) | Lat. (UTM) | Marker Type | Mark. Obl. | Mark. res. (/2) | Nb. of splay | Scarp 2nd | Offset Pref. (m) | Offset max (m) | Offset min (m) | Δ+ (m) | Δ- (m) | Image type | Image Res. (m) | Image quality (/2) | Total Score (/10) |
|---|---|---|---|---|---|---|---|---|---|---|---|---|---|---|---|---|
| R7 | 636265 | 4981330 | Talweg | 3 | 2 | 1 | 1 | 3,0 | 3,6 | 2,1 | 0,6 | 0,9 | Ortho 58 | 0,2 | 2 | 9 |
| R7 | 636315 | 4981310 | Talweg | 3 | 2 | 1 | 1 | 2,3 | 3,1 | 1,5 | 0,7 | 0,9 | Ortho 58 | 0,2 | 2 | 9 |
| R7 | 636340 | 4981300 | Riser | 3 | 1 | 1 | 1 | 2,3 | 3,0 | 1,3 | 0,7 | 1,0 | Ortho 58 | 0,2 | 2 | 8 |
| R7 | 636473 | 4981230 | Talweg | 3 | 2 | 1 | 1 | 2,6 | 3,6 | 2,0 | 1,0 | 0,6 | Ortho 58 | 0,2 | 2 | 9 |
| R7 | 636645 | 4982100 | Gully | 3 | 1 | 1 | 1 | 4,7 | 6,9 | 2,8 | 2,2 | 2,0 | Bing | 0,6 | 2 | 7 |
| R7 | 636900 | 4982100 | Gully | 3 | 1 | 1 | 1 | 10,3 | 13,1 | 8,7 | 2,8 | 1,7 | Bing | 0,6 | 2 | 7 |
| R7 | 637250 | 4981977 | Riser | 3 | 2 | 1 | 1 | 9,3 | 11,0 | 7,5 | 1,7 | 1,8 | Bing | 0,6 | 2 | 8 |
| R7 | 637330 | 4981968 | Bare | 2 | 1 | 1 | 1 | 21,0 | 24,4 | 18,3 | 3,4 | 2,7 | Bing | 0,6 | 2 | 5 |
| R7 | 637560 | 4981950 | Ridge | 3 | 1 | 1 | 1 | 50,2 | 57,2 | 42,8 | 7,0 | 7,4 | Bing | 0,6 | 2 | 7 |
| R7 | 638820 | 4981744 | Gully | 3 | 1 | 2 | 0 | 2,0 | 2,5 | 1,6 | 0,5 | 0,4 | Ortho 58 | 0,2 | 2 | 8 |
| R7 | 638875 | 4981750 | Gully | 3 | 2 | 2 | 0 | 3,3 | 3,8 | 2,8 | 0,4 | 0,5 | Ortho 58 | 0,2 | 2 | 9 |
| R7 | 638875 | 4981750 | Gully | 2 | 1 | 2 | 0 | 13,7 | 14,1 | 12,9 | 0,4 | 0,9 | Ortho 58 | 0,2 | 2 | 6 |
| R7 | 638985 | 4981735 | Gully | 2 | 2 | 2 | 0 | 4,2 | 4,8 | 3,7 | 0,6 | 0,5 | Ortho 58 | 0,2 | 2 | 7 |
| R7 | 638985 | 4981735 | Riser | 3 | 1 | 2 | 0 | 27,1 | 28,5 | 26,6 | 1,4 | 0,9 | Ortho 58 | 0,2 | 2 | 8 |
| R7 | 639105 | 4981730 | Riser | 3 | 2 | 1 | 0 | 2,2 | 2,6 | 1,9 | 0,4 | 0,3 | Ortho 58 | 0,2 | 2 | 10 |
| R7 | 640970 | 4981555 | Swale | 3 | 1 | 1 | 1 | 1,9 | 2,3 | 1,3 | 0,4 | 0,6 | Ortho 58 | 0,2 | 2 | 8 |
| R7 | 641100 | 4981530 | Riser | 3 | 2 | 2 | 1 | 4,2 | 5,2 | 3,2 | 1,0 | 1,0 | Ortho 58 | 0,2 | 2 | 8 |
| R7 | 641115 | 4981465 | Talweg | 3 | 1 | 1 | 1 | 4,2 | 4,6 | 3,6 | 0,4 | 0,6 | Ortho 58 | 0,2 | 2 | 8 |
| R7 | 641170 | 4981525 | Talweg | 3 | 2 | 1 | 1 | 4,2 | 4,7 | 2,1 | 0,6 | 2,1 | Ortho 58 | 0,2 | 2 | 9 |
| R7 | 641275 | 4981470 | Talweg | 3 | 2 | 1 | 1 | 4,0 | 4,9 | 2,9 | 0,8 | 1,1 | Ortho 58 | 0,2 | 2 | 9 |
| R7 | 641465 | 4981440 | Talweg | 3 | 1 | 1 | 1 | 2,2 | 3,3 | 1,6 | 1,1 | 0,6 | Ortho 58 | 0,2 | 2 | 8 |
| R7 | 641500 | 4981440 | Talweg | 3 | 2 | 1 | 1 | 3,4 | 4,7 | 2,7 | 1,3 | 0,7 | Ortho 58 | 0,2 | 2 | 9 |
| R7 | 641520 | 4981440 | Talweg | 3 | 1 | 1 | 1 | 12,5 | 14,6 | 10,9 | 2,0 | 1,6 | Ortho 58 | 0,2 | 2 | 8 |
| R7 | 641560 | 4981435 | Talweg | 3 | 2 | 1 | 1 | 21,0 | 24,7 | 16,6 | 3,7 | 4,4 | Ortho 58 | 0,2 | 2 | 9 |
| S9 | 641750 | 4981414 | Talweg | 3 | 2 | 2 | 0 | 2,9 | 3,8 | 2,4 | 0,9 | 0,5 | Ortho 58 | 0,2 | 2 | 9 |
| S9 | 641840 | 4981425 | Talweg | 3 | 1 | 2 | 0 | 3,3 | 4,1 | 2,6 | 0,8 | 0,7 | Ortho 58 | 0,2 | 2 | 8 |
| S9 | 641850 | 4981426 | Talweg | 3 | 2 | 2 | 0 | 2,6 | 3,4 | 2,3 | 0,8 | 0,3 | Ortho 58 | 0,2 | 2 | 9 |
| S9 | 641925 | 4981432 | Talweg | 3 | 2 | 2 | 0 | 4,6 | 6,4 | 4,2 | 1,7 | 0,5 | Ortho 58 | 0,2 | 2 | 9 |
| S9 | 641960 | 4981434 | Talweg | 3 | 2 | 2 | 0 | 4,3 | 5,3 | 3,8 | 1,0 | 0,5 | Ortho 58 | 0,2 | 2 | 9 |
| S9 | 641990 | 4981436 | Talweg | 3 | 1 | 2 | 0 | 4,7 | 5,3 | 4,0 | 0,6 | 0,6 | Ortho 58 | 0,2 | 2 | 8 |
| S9 | 642025 | 4981436 | Gully | 3 | 1 | 2 | 0 | 2,6 | 3,3 | 2,0 | 0,6 | 0,6 | Ortho 58 | 0,2 | 2 | 8 |
| S9 | 642040 | 4981439 | Gully | 3 | 1 | 2 | 0 | 2,9 | 3,7 | 2,5 | 0,8 | 0,4 | Ortho 58 | 0,2 | 2 | 8 |
| S9 | 642060 | 4981440 | Talweg | 3 | 1 | 2 | 0 | 1,9 | 3,1 | 1,4 | 1,1 | 0,6 | Ortho 58 | 0,2 | 2 | 8 |

| Seg. | Lon. (UTM) | Lat. (UTM) | Marker Type | Mark. Obl. | Mark. res. (/2) | Nb. of splay | Scarp 2nd | Offset Pref. (m) | Offset max (m) | Offset min (m) | Δ+ (m) | Δ- (m) | Image type | Image Res. (m) | Image quality (/2) | Total Score (/10) |
|---|---|---|---|---|---|---|---|---|---|---|---|---|---|---|---|---|
| S9 | 642190 | 4981450 | Gully | 3 | 1 | 1 | 0 | 4,1 | 5,4 | 2,6 | 1,3 | 1,5 | Ortho 58 | 0,2 | 2 | 9 |
| S9 | 642225 | 4981450 | Gully | 3 | 1 | 1 | 0 | 9,7 | 10,6 | 8,2 | 0,9 | 1,4 | Ortho 58 | 0,2 | 2 | 9 |
| S9 | 642240 | 4981450 | Talweg | 3 | 1 | 1 | 0 | 1,9 | 2,4 | 1,2 | 0,4 | 0,8 | Ortho 58 | 0,2 | 2 | 9 |
| S9 | 642310 | 4981433 | Riser | 3 | 1 | 1 | 0 | 2,6 | 3,3 | 1,9 | 0,7 | 0,7 | Ortho 58 | 0,2 | 2 | 9 |
| S9 | 642360 | 4981430 | Gully | 3 | 1 | 2 | 0 | 10,8 | 11,7 | 9,5 | 1,0 | 1,3 | Ortho 58 | 0,2 | 2 | 8 |
| S9 | 642500 | 4981410 | Gully | 3 | 1 | 1 | 0 | 2,0 | 2,2 | 1,5 | 0,3 | 0,4 | Ortho 58 | 0,2 | 2 | 9 |
| S9 | 642620 | 4981395 | Riser | 2 | 1 | 2 | 0 | 5,1 | 6,1 | 4,1 | 1,0 | 1,0 | Ortho 58 | 0,2 | 2 | 6 |
| S9 | 642720 | 4981387 | Gully | 3 | 2 | 1 | 0 | 4,1 | 5,0 | 3,1 | 0,9 | 1,0 | Ortho 58 | 0,2 | 2 | 10 |
| S9 | 642770 | 4981380 | Talweg | 3 | 1 | 2 | 0 | 2,6 | 3,2 | 2,4 | 0,6 | 0,3 | Ortho 58 | 0,2 | 2 | 8 |
| S9 | 642770 | 4981380 | Talweg | 3 | 1 | 2 | 0 | 25,9 | 26,4 | 25,3 | 0,9 | 0,9 | Ortho 58 | 0,2 | 2 | 8 |
| S9 | 642850 | 4981355 | Talweg | 3 | 1 | 1 | 0 | 5,1 | 5,9 | 4,1 | 0,9 | 1,0 | Ortho 58 | 0,2 | 2 | 9 |
| S9 | 642850 | 4981355 | Talweg | 1 | 1 | 1 | 0 | 57,4 | 63,3 | 53,7 | 5,8 | 3,8 | Ortho 58 | 0,2 | 2 | 6 |
| S9 | 642980 | 4981330 | Talweg | 3 | 2 | 1 | 0 | 2,5 | 3,1 | 2,0 | 0,6 | 0,4 | Ortho 58 | 0,2 | 2 | 10 |
| S9 | 643000 | 4981325 | Talweg | 3 | 2 | 1 | 0 | 2,5 | 3,8 | 1,8 | 1,3 | 0,7 | Ortho 58 | 0,2 | 2 | 10 |
| S9 | 643150 | 4981300 | Ridge | 3 | 1 | 2 | 0 | 3,4 | 4,7 | 2,3 | 1,3 | 1,1 | Ortho 58 | 0,2 | 2 | 8 |
| S9 | 643350 | 4981290 | Riser | 3 | 2 | 2 | 0 | 5,0 | 7,1 | 4,1 | 2,1 | 0,9 | Ortho 58 | 0,2 | 2 | 9 |
| S9 | 643250 | 4981280 | Riser | 3 | 1 | 1 | 0 | 3,2 | 4,3 | 2,6 | 1,1 | 0,6 | Ortho 58 | 0,2 | 2 | 9 |
| S9 | 643340 | 4981255 | Gully | 3 | 1 | 1 | 0 | 3,4 | 4,2 | 2,6 | 0,8 | 0,8 | Ortho 58 | 0,2 | 2 | 9 |
| S9 | 643373 | 4981247 | Gully | 3 | 2 | 1 | 0 | 2,7 | 3,1 | 2,2 | 0,5 | 0,4 | Ortho 58 | 0,2 | 2 | 10 |
| S9 | 643440 | 4981230 | Riser | 3 | 1 | 1 | 0 | 1,7 | 2,4 | 1,1 | 0,7 | 0,6 | Ortho 58 | 0,2 | 2 | 9 |
| S9 | 643550 | 4981200 | Gully | 3 | 1 | 1 | 0 | 3,2 | 4,7 | 1,8 | 1,5 | 1,4 | Ortho 58 | 0,2 | 2 | 9 |
| S9 | 643640 | 4981175 | Talweg | 3 | 2 | 1 | 0 | 7,4 | 8,3 | 6,6 | 0,9 | 0,7 | Ortho 58 | 0,2 | 2 | 10 |
| S9 | 643667 | 4981165 | Talweg | 3 | 2 | 1 | 0 | 2,4 | 3,2 | 1,9 | 0,8 | 0,4 | Ortho 58 | 0,2 | 2 | 10 |
| S9 | 643687 | 4981158 | Talweg | 2 | 2 | 1 | 0 | 2,6 | 3,2 | 2,1 | 0,7 | 0,5 | Ortho 58 | 0,2 | 2 | 8 |
| S9 | 643720 | 4981147 | Talweg | 3 | 1 | 1 | 0 | 2,9 | 3,9 | 1,9 | 0,9 | 1,1 | Ortho 58 | 0,2 | 2 | 9 |
| S9 | 643760 | 4981132 | Fan apex | 3 | 2 | 1 | 0 | 9,9 | 11,2 | 8,3 | 1,3 | 1,6 | Ortho 58 | 0,2 | 2 | 10 |
| S9 | 643780 | 4981125 | Talweg | 3 | 1 | 1 | 0 | 2,3 | 3,3 | 1,8 | 0,9 | 0,6 | Ortho 58 | 0,2 | 2 | 9 |
| S9 | 643880 | 4981080 | Talweg | 3 | 1 | 1 | 0 | 5,1 | 6,7 | 3,6 | 1,5 | 1,5 | Ortho 58 | 0,2 | 2 | 9 |
| S9 | 643925 | 4981062 | Talweg | 3 | 1 | 1 | 0 | 4,8 | 5,6 | 3,9 | 0,8 | 0,9 | Ortho 58 | 0,2 | 2 | 9 |
| S9 | 643970 | 4981042 | Talweg | 3 | 1 | 1 | 0 | 20,5 | 21,8 | 17,7 | 1,3 | 2,8 | Ortho 58 | 0,2 | 2 | 9 |
| S9 | 644000 | 4981031 | Gully | 3 | 1 | 1 | 0 | 2,5 | 3,0 | 1,9 | 0,5 | 0,6 | Ortho 58 | 0,2 | 2 | 9 |
| S9 | 644000 | 4981031 | Talweg | 3 | 1 | 1 | 0 | 17,8 | 19,2 | 17,0 | 1,4 | 0,9 | Ortho 58 | 0,2 | 2 | 9 |
| S9 | 644035 | 4981010 | Talweg | 3 | 1 | 1 | 0 | 2,9 | 3,9 | 2,0 | 1,0 | 0,9 | Ortho 58 | 0,2 | 2 | 9 |

| Seg. | Lon. (UTM) | Lat. (UTM) | Marker Type | Mark. Obl. | Mark. res. (/2) | Nb. of splay | Scarp 2nd | Offset Pref. (m) | Offset max (m) | Offset min (m) | Δ+ (m) | Δ- (m) | Image type | Image Res. (m) | Image quality (/2) | Total Score (/10) |
|---|---|---|---|---|---|---|---|---|---|---|---|---|---|---|---|---|
| S9 | 644060 | 4980997 | Talweg | 3 | 1 | 1 | 0 | 6,7 | 8,3 | 6,0 | 1,7 | 0,7 | Ortho 58 | 0,2 | 2 | 9 |
| S9 | 644115 | 4980973 | Talweg | 3 | 2 | 1 | 0 | 3,6 | 4,5 | 3,2 | 0,9 | 0,4 | Ortho 58 | 0,2 | 2 | 10 |
| S9 | 644075 | 4980940 | Talweg | 3 | 2 | 1 | 0 | 2,7 | 3,3 | 1,9 | 0,6 | 0,7 | Ortho 58 | 0,2 | 2 | 10 |
| S9 | 644075 | 4980940 | Talweg | 3 | 2 | 1 | 0 | 13,2 | 14,2 | 12,2 | 1,0 | 1,0 | Ortho 58 | 0,2 | 2 | 10 |
| S9 | 644380 | 4980825 | Talweg | 3 | 1 | 1 | 0 | 4,7 | 5,1 | 3,3 | 0,4 | 1,3 | Ortho 58 | 0,2 | 2 | 9 |
| S9 | 644440 | 4980795 | Talweg | 1 | 1 | 2 | 0 | 3,9 | 5,2 | 2,7 | 1,3 | 1,2 | Ortho 58 | 0,2 | 2 | 5 |
| S9 | 644915 | 4980505 | Talweg | 3 | 1 | 1 | 0 | 1,4 | 2,1 | 0,9 | 0,7 | 0,5 | Ortho 58 | 0,2 | 2 | 9 |
| S9 | 644915 | 4980505 | Talweg | 3 | 1 | 1 | 0 | 12,6 | 13,8 | 12,0 | 1,1 | 0,6 | Ortho 58 | 0,2 | 2 | 9 |
| S9 | 644915 | 4980505 | Talweg | 3 | 1 | 1 | 0 | 30,0 | 31,2 | 28,4 | 1,1 | 1,7 | Ortho 58 | 0,2 | 2 | 9 |
| S9 | 644930 | 4980500 | Talweg | 3 | 1 | 1 | 0 | 2,1 | 2,4 | 1,6 | 0,3 | 0,5 | Ortho 58 | 0,2 | 2 | 9 |
| S9 | 644930 | 4980500 | Talweg | 3 | 1 | 1 | 0 | 5,0 | 5,6 | 3,6 | 0,6 | 1,3 | Ortho 58 | 0,2 | 2 | 9 |
| S9 | 644945 | 4980490 | Talweg | 3 | 1 | 1 | 0 | 1,6 | 2,4 | 0,9 | 0,8 | 0,7 | Ortho 58 | 0,2 | 2 | 9 |
| S9 | 644975 | 4980467 | Talweg | 3 | 1 | 1 | 0 | 1,3 | 2,3 | 0,9 | 0,9 | 0,5 | Ortho 58 | 0,2 | 2 | 9 |
| S9 | 645000 | 4980445 | Talweg | 3 | 2 | 1 | 0 | 1,3 | 2,6 | 1,1 | 1,3 | 0,3 | Ortho 58 | 0,2 | 2 | 10 |
| S9 | 645030 | 4980420 | Talweg | 3 | 2 | 1 | 0 | 2,2 | 2,7 | 1,9 | 0,5 | 0,3 | Ortho 58 | 0,2 | 2 | 10 |
| S9 | 645030 | 4980420 | Talweg | 3 | 2 | 1 | 0 | 33,0 | 33,8 | 31,5 | 0,9 | 1,6 | Ortho 58 | 0,2 | 2 | 10 |
| S9 | 645030 | 4980420 | Talweg | 3 | 2 | 1 | 0 | 66,7 | 70,1 | 62,2 | 3,4 | 4,5 | Ortho 58 | 0,2 | 2 | 10 |
| S9 | 645105 | 4980366 | Talweg | 2 | 2 | 1 | 0 | 2,7 | 3,3 | 2,2 | 0,6 | 0,5 | Ortho 58 | 0,2 | 2 | 8 |
| S9 | 645130 | 4980350 | Talweg | 3 | 2 | 1 | 0 | 3,0 | 3,4 | 2,8 | 0,5 | 0,3 | Ortho 58 | 0,2 | 2 | 10 |
| S9 | 645130 | 4980350 | Talweg | 3 | 2 | 1 | 0 | 4,6 | 5,0 | 3,6 | 0,4 | 1,1 | Ortho 58 | 0,2 | 2 | 10 |
| S9 | 645130 | 4980350 | Talweg | 3 | 1 | 1 | 0 | 29,8 | 30,8 | 28,7 | 0,9 | 1,1 | Ortho 58 | 0,2 | 2 | 9 |
| S9 | 645150 | 4980340 | Talweg | 3 | 2 | 1 | 0 | 3,6 | 4,2 | 3,1 | 0,6 | 0,6 | Ortho 58 | 0,2 | 2 | 10 |
| S9 | 645150 | 4980340 | Talweg | 3 | 2 | 1 | 0 | 7,2 | 7,6 | 6,5 | 0,3 | 0,7 | Ortho 58 | 0,2 | 2 | 10 |
| S9 | 645235 | 4980280 | Talweg | 3 | 1 | 1 | 0 | 3,4 | 4,0 | 2,6 | 0,7 | 0,7 | Ortho 58 | 0,2 | 2 | 9 |
| S9 | 645270 | 4980260 | Talweg | 3 | 2 | 1 | 0 | 4,5 | 5,1 | 3,9 | 0,6 | 0,6 | Ortho 58 | 0,2 | 2 | 10 |
| S9 | 645325 | 4980230 | Talweg | 3 | 2 | 1 | 0 | 3,8 | 4,6 | 2,8 | 0,8 | 0,9 | Ortho 58 | 0,2 | 2 | 10 |
| S9 | 645355 | 4980217 | Talweg | 3 | 2 | 1 | 0 | 10,0 | 12,3 | 9,8 | 2,3 | 0,3 | Ortho 58 | 0,2 | 2 | 10 |
| S9 | 645355 | 4980217 | Talweg | 3 | 2 | 1 | 0 | 3,0 | 4,0 | 1,9 | 1,0 | 1,1 | Ortho 58 | 0,2 | 2 | 10 |
| S9 | 645390 | 4980200 | Talweg | 3 | 1 | 1 | 0 | 3,3 | 4,5 | 2,2 | 1,1 | 1,1 | Ortho 58 | 0,2 | 2 | 9 |
| S9 | 645390 | 4980200 | Talweg | 3 | 1 | 1 | 0 | 9,8 | 11,6 | 8,0 | 1,8 | 1,8 | Ortho 58 | 0,2 | 2 | 9 |
| S9 | 645405 | 4980193 | Talweg | 3 | 2 | 1 | 0 | 4,4 | 5,4 | 3,0 | 1,0 | 1,5 | Ortho 58 | 0,2 | 2 | 10 |
| S9 | 645405 | 4980193 | Talweg | 3 | 1 | 1 | 0 | 9,0 | 10,2 | 7,9 | 1,2 | 1,0 | Ortho 58 | 0,2 | 2 | 9 |
| S9 | 645433 | 4980185 | Talweg | 3 | 1 | 1 | 0 | 4,6 | 6,1 | 3,2 | 1,5 | 1,3 | Ortho 58 | 0,2 | 2 | 9 |

| Seg. | Lon. (UTM) | Lat. (UTM) | Marker Type | Mark. Obl. | Mark. res. (/2) | Nb. of splay | Scarp 2nd | Offset Pref. (m) | Offset max (m) | Offset min (m) | Δ+ (m) | Δ- (m) | Image type | Image Res. (m) | Image quality (/2) | Total Score (/10) |
|---|---|---|---|---|---|---|---|---|---|---|---|---|---|---|---|---|
| S9 | 645460 | 4980168 | Talweg | 3 | 2 | 1 | 0 | 4,7 | 5,9 | 3,9 | 1,2 | 0,8 | Ortho 58 | 0,2 | 2 | 10 |
| S9 | 645485 | 4980156 | Talweg | 2 | 2 | 1 | 0 | 4,2 | 5,6 | 3,6 | 1,4 | 0,6 | Ortho 58 | 0,2 | 2 | 8 |
| S9 | 645520 | 4980141 | Talweg | 3 | 0 | 1 | 0 | 3,6 | 4,4 | 2,5 | 0,8 | 1,1 | Ortho 58 | 0,2 | 2 | 8 |
| S9 | 645640 | 4980092 | Talweg | 3 | 1 | 1 | 1 | 7,8 | 11,8 | 5,5 | 4,0 | 2,3 | Ortho 58 | 0,2 | 2 | 8 |
| S10 | 648725 | 4979600 | Gully | 3 | 2 | 1 | 1 | 7,3 | 8,5 | 6,1 | 1,2 | 1,2 | Ortho 58 | 0,5 | 1 | 7,5 |
| S10 | 648770 | 4979590 | Gully | 3 | 2 | 1 | 1 | 8,7 | 11,6 | 7,5 | 2,9 | 1,3 | Ortho 58 | 0,5 | 1 | 7,5 |
| S10 | 648770 | 4979590 | Gully | 3 | 2 | 1 | 1 | 17,0 | 18,8 | 14,9 | 1,8 | 2,1 | Ortho 58 | 0,5 | 1 | 7,5 |
| S10 | 648840 | 4979565 | Gully | 3 | 2 | 1 | 1 | 7,8 | 11,1 | 5,6 | 3,3 | 2,2 | Ortho 58 | 0,5 | 1 | 7,5 |
| S10 | 648860 | 4979562 | Gully | 3 | 2 | 1 | 1 | 8,9 | 11,5 | 6,7 | 2,5 | 2,3 | Ortho 58 | 0,5 | 1 | 7,5 |
| S10 | 648900 | 4979555 | Gully | 3 | 1 | 1 | 1 | 4,1 | 6,6 | 3,0 | 2,5 | 1,1 | Ortho 58 | 0,5 | 1 | 6,5 |
| S10 | 648945 | 4979547 | Gully | 3 | 1 | 1 | 1 | 6,0 | 8,9 | 3,4 | 3,0 | 2,5 | Ortho 58 | 0,5 | 1 | 6,5 |
| S10 | 648975 | 4979537 | Talweg | 2 | 2 | 1 | 1 | 7,1 | 9,6 | 4,1 | 2,6 | 2,9 | Ortho 58 | 0,5 | 1 | 5,5 |
| S10 | 648975 | 4979537 | Talweg | 2 | 2 | 1 | 1 | 16,4 | 18,9 | 14,2 | 2,5 | 2,2 | Ortho 58 | 0,5 | 1 | 5,5 |
| S10 | 648915 | 4979530 | Talweg | 3 | 1 | 1 | 1 | 7,8 | 10,8 | 5,4 | 3,0 | 2,5 | Ortho 58 | 0,5 | 1 | 6,5 |
| S10 | 649100 | 4979508 | Talweg | 2 | 2 | 1 | 1 | 6,4 | 13,7 | 3,9 | 7,3 | 2,5 | Ortho 58 | 0,5 | 1 | 5,5 |
| S10 | 649100 | 4979508 | Talweg | 2 | 2 | 1 | 1 | 11,6 | 16,8 | 8,6 | 5,1 | 3,1 | Ortho 58 | 0,5 | 1 | 5,5 |
| S10 | 649135 | 4979500 | Talweg | 3 | 1 | 1 | 1 | 4,6 | 6,1 | 3,2 | 1,5 | 1,4 | Ortho 58 | 0,5 | 1 | 6,5 |
| S10 | 649135 | 4979500 | Talweg | 2 | 1 | 1 | 1 | 16,2 | 21,4 | 13,7 | 5,2 | 2,6 | Ortho 58 | 0,5 | 1 | 4,5 |
| S10 | 649155 | 4979493 | Talweg | 3 | 2 | 1 | 1 | 7,5 | 11,1 | 6,3 | 3,6 | 1,2 | Ortho 58 | 0,5 | 1 | 7,5 |
| S10 | 649170 | 4979487 | Talweg | 3 | 2 | 1 | 1 | 6,4 | 8,2 | 4,9 | 1,8 | 1,5 | Ortho 58 | 0,5 | 1 | 7,5 |
| S10 | 649210 | 4979478 | Talweg | 3 | 1 | 1 | 1 | 9,3 | 12,1 | 6,7 | 2,8 | 2,6 | Ortho 58 | 0,5 | 1 | 6,5 |
| S10 | 649210 | 4979478 | Talweg | 3 | 1 | 1 | 1 | 18,9 | 20,0 | 17,5 | 1,1 | 1,3 | Ortho 58 | 0,5 | 1 | 6,5 |
| S10 | 649210 | 4979478 | Talweg | 3 | 1 | 1 | 1 | 34,7 | 37,2 | 33,4 | 2,4 | 1,4 | Ortho 58 | 0,5 | 1 | 6,5 |
| S10 | 649240 | 4979470 | Talweg | 3 | 2 | 1 | 1 | 5,7 | 7,2 | 4,7 | 1,4 | 1,1 | Ortho 58 | 0,5 | 1 | 7,5 |
| S10 | 649280 | 4979455 | Talweg | 3 | 1 | 1 | 1 | 9,8 | 13,1 | 7,5 | 3,3 | 2,3 | Ortho 58 | 0,5 | 1 | 6,5 |
| S10 | 649280 | 4979455 | Talweg | 3 | 1 | 1 | 1 | 20,4 | 22,2 | 18,1 | 1,8 | 2,3 | Ortho 58 | 0,5 | 1 | 6,5 |
| S10 | 649225 | 4979440 | Talweg | 3 | 2 | 1 | 1 | 13,5 | 17,9 | 9,3 | 4,4 | 4,2 | Ortho 58 | 0,5 | 1 | 7,5 |
| S10 | 649385 | 4979420 | Talweg | 3 | 1 | 1 | 1 | 8,3 | 10,1 | 7,2 | 1,8 | 1,1 | Ortho 58 | 0,5 | 1 | 6,5 |
| S10 | 649385 | 4979420 | Talweg | 3 | 1 | 1 | 1 | 38,9 | 41,8 | 37,1 | 2,9 | 1,8 | Ortho 58 | 0,5 | 1 | 6,5 |
| S10 | 649455 | 4979395 | Talweg | 3 | 1 | 1 | 1 | 11,3 | 18,1 | 7,5 | 6,7 | 3,8 | Ortho 58 | 0,5 | 1 | 6,5 |
| S10 | 649530 | 4979367 | Talweg | 3 | 2 | 1 | 1 | 11,9 | 15,6 | 7,5 | 3,6 | 4,5 | Ortho 58 | 0,5 | 1 | 7,5 |
| S10 | 649530 | 4979367 | Talweg | 3 | 2 | 1 | 1 | 5,9 | 8,4 | 4,6 | 2,5 | 1,4 | Ortho 58 | 0,5 | 1 | 7,5 |
| S10 | 649775 | 4979272 | Gully | 3 | 2 | 1 | 1 | 5,8 | 6,8 | 4,6 | 1,1 | 1,2 | Ortho 58 | 0,5 | 1 | 7,5 |

| Seg. | Lon. (UTM) | Lat. (UTM) | Marker Type | Mark. Obl. | Mark. res. (/2) | Nb. of splay | Scarp 2nd | Offset Pref. (m) | Offset max (m) | Offset min (m) | Δ+ (m) | Δ- (m) | Image type | Image Res. (m) | Image quality (/2) | Total Score (/10) |
|---|---|---|---|---|---|---|---|---|---|---|---|---|---|---|---|---|
| S10 | 649810 | 4979267 | Gully | 3 | 2 | 1 | 1 | 5,1 | 6,8 | 3,5 | 1,7 | 1,6 | Ortho 58 | 0,5 | 1 | 7,5 |
| S10 | 650040 | 4979175 | Talweg | 3 | 1 | 1 | 1 | 3,6 | 4,5 | 2,4 | 0,9 | 1,2 | Ortho 58 | 0,5 | 1 | 6,5 |
| S10 | 650075 | 4979160 | Talweg | 3 | 2 | 1 | 1 | 7,7 | 10,2 | 4,8 | 2,5 | 2,9 | Ortho 58 | 0,5 | 1 | 7,5 |
| S10 | 650100 | 4979150 | Talweg | 3 | 1 | 1 | 1 | 8,4 | 12,2 | 6,9 | 3,8 | 1,5 | Ortho 58 | 0,5 | 1 | 6,5 |
| S10 | 650100 | 4979150 | Talweg | 3 | 2 | 1 | 1 | 17,1 | 18,3 | 14,7 | 1,2 | 2,3 | Ortho 58 | 0,5 | 1 | 7,5 |
| S10 | 650130 | 4979138 | Talweg | 3 | 2 | 1 | 1 | 33,5 | 37,1 | 30,5 | 3,6 | 3,0 | Ortho 58 | 0,5 | 1 | 7,5 |
| S10 | 650300 | 4979076 | Ridge | 3 | 1 | 1 | 1 | 12,8 | 18,5 | 7,8 | 5,7 | 5,0 | Ortho 58 | 0,5 | 1 | 6,5 |
| S10 | 650400 | 4979040 | River | 3 | 2 | 1 | 1 | 5,5 | 7,9 | 2,3 | 2,4 | 3,2 | Ortho 58 | 0,5 | 1 | 7,5 |
| S10 | 650400 | 4979040 | River | 3 | 2 | 1 | 1 | 20,2 | 23,7 | 18,2 | 3,4 | 2,1 | Ortho 58 | 0,5 | 1 | 7,5 |
| S10 | 650530 | 4979010 | Talweg | 3 | 2 | 1 | 1 | 30,3 | 33,6 | 27,3 | 3,3 | 3,0 | Ortho 58 | 0,5 | 1 | 7,5 |
| S10 | 650677 | 4978975 | Talweg | 2 | 1 | 1 | 1 | 3,1 | 4,7 | 2,3 | 1,6 | 0,8 | Ortho 58 | 0,2 | 1 | 5 |
| S10 | 650677 | 4978975 | Talweg | 3 | 1 | 1 | 1 | 12,4 | 15,4 | 9,7 | 3,0 | 2,7 | Ortho 58 | 0,2 | 1 | 7 |
| S10 | 650780 | 4978950 | Talweg | 1 | 1 | 1 | 1 | 20,8 | 27,2 | 15,5 | 6,5 | 5,2 | Ortho 58 | 0,2 | 1 | 4 |
| S10 | 650885 | 4978915 | Ridge | 3 | 2 | 1 | 1 | 3,0 | 5,0 | 1,8 | 2,0 | 1,3 | Ortho 58 | 0,2 | 1 | 8 |
| S10 | 650975 | 4978885 | Talweg | 3 | 1 | 1 | 1 | 2,6 | 4,3 | 1,6 | 1,7 | 1,0 | Ortho 58 | 0,2 | 1 | 7 |
| S10 | 650975 | 4978885 | Talweg | 3 | 1 | 1 | 1 | 5,3 | 6,0 | 2,4 | 0,7 | 2,9 | Ortho 58 | 0,2 | 1 | 7 |
| S10 | 651000 | 4978880 | | 2 | | | | 8,5 | 12,4 | 5,8 | 3,9 | 2,8 | Ortho 58 | 0,2 | 1 | 2 |
| S10 | 651055 | 4978858 | Talweg | 3 | 1 | 1 | 1 | 3,6 | 4,6 | 3,0 | 1,0 | 0,6 | Ortho 58 | 0,2 | 1 | 7 |
| S10 | 651055 | 4978858 | Talweg | 3 | 1 | 1 | 1 | 4,9 | 6,7 | 4,2 | 1,8 | 0,8 | Ortho 58 | 0,2 | 1 | 7 |
| S10 | 651090 | 4978850 | Talweg | 3 | 2 | 1 | 1 | 4,1 | 5,8 | 3,7 | 1,6 | 0,4 | Ortho 58 | 0,2 | 1 | 8 |
| S10 | 651110 | 4978845 | Talweg | 3 | 1 | 1 | 1 | 3,2 | 4,6 | 2,5 | 1,4 | 0,7 | Ortho 58 | 0,2 | 1 | 7 |
| S10 | 651150 | 4978830 | Talweg | 2 | 1 | 2 | 1 | 3,9 | 5,5 | 2,3 | 1,6 | 1,6 | Ortho 58 | 0,2 | 1 | 4 |
| S10 | 651190 | 4978815 | Talweg | 3 | 2 | 1 | 1 | 3,2 | 5,6 | 2,4 | 2,4 | 0,8 | Ortho 58 | 0,2 | 1 | 8 |
| S10 | 651190 | 4978815 | Talweg | 3 | 2 | 1 | 1 | 9,4 | 10,2 | 8,4 | 0,8 | 0,9 | Ortho 58 | 0,2 | 1 | 8 |
| S10 | 651280 | 4978780 | Riser | 3 | 1 | 1 | 1 | 7,5 | 9,6 | 7,0 | 2,1 | 0,5 | Ortho 58 | 0,2 | 1 | 7 |
| S10 | 651280 | 4978780 | Riser | 3 | 2 | 1 | 1 | 19,4 | 21,5 | 16,1 | 2,1 | 3,3 | Ortho 58 | 0,2 | 1 | 8 |
| S10 | 651315 | 4978775 | Talweg | 3 | 2 | 1 | 1 | 11,9 | 14,6 | 9,4 | 2,7 | 2,6 | Ortho 58 | 0,2 | 1 | 8 |
| S10 | 651380 | 4978756 | Talweg | 2 | 2 | 1 | 1 | 2,9 | 6,1 | 1,8 | 3,2 | 1,0 | Ortho 58 | 0,2 | 1 | 6 |
| S10 | 651445 | 4978740 | Gully | 3 | 2 | 2 | 1 | 3,5 | 6,1 | 2,6 | 2,6 | 0,9 | Ortho 58 | 0,2 | 1 | 7 |
| S10 | 651505 | 4978730 | Gully | 3 | 2 | 1 | 1 | 3,5 | 5,4 | 2,1 | 1,9 | 1,3 | Ortho 58 | 0,2 | 1 | 8 |
| S10 | 651505 | 4978730 | Gully | 3 | 2 | 1 | 1 | 6,2 | 8,4 | 3,1 | 2,2 | 3,0 | Ortho 58 | 0,2 | 1 | 8 |
| S10 | 651565 | 4978715 | Talweg | 3 | 2 | 1 | 1 | 6,1 | 9,3 | 3,4 | 3,2 | 2,7 | Ortho 58 | 0,2 | 1 | 8 |
| S10 | 651600 | 4978710 | Talweg | 3 | 1 | 1 | 1 | 5,8 | 6,9 | 3,7 | 1,1 | 2,2 | Ortho 58 | 0,2 | 1 | 7 |

| Seg. | Lon. (UTM) | Lat. (UTM) | Marker Type | Mark. Obl. | Mark. res. (/2) | Nb. of splay | Scarp 2nd | Offset Pref. (m) | Offset max (m) | Offset min (m) | Δ+ (m) | Δ- (m) | Image type | Image Res. (m) | Image quality (/2) | Total Score (/10) |
|---|---|---|---|---|---|---|---|---|---|---|---|---|---|---|---|---|
| S10 | 651695 | 4978700 | Gully | 2 | 1 | 1 | 1 | 22,2 | 25,5 | 18,9 | 3,3 | 3,3 | Ortho 58 | 0,5 | 1 | 4,5 |
| S10 | 651755 | 4978690 | Talweg | 2 | 2 | 1 | 1 | 7,8 | 10,7 | 5,7 | 2,9 | 2,1 | Ortho 58 | 0,5 | 1 | 5,5 |
| S10 | 651920 | 4978650 | River | 2 | 2 | 1 | 1 | 20,4 | 23,9 | 16,3 | 3,5 | 4,1 | Ortho 58 | 0,5 | 1 | 5,5 |
| S10 | 652130 | 4978630 | Talweg | 3 | 2 | 1 | 1 | 4,9 | 5,9 | 3,7 | 1,0 | 1,2 | Ortho 58 | 0,5 | 1 | 7,5 |
| S10 | 652240 | 4978620 | River | 3 | 2 | 1 | 2 | 8,9 | 12,8 | 5,8 | 3,9 | 3,1 | Ortho 58 | 0,5 | 1 | 6,5 |
| S10 | 652240 | 4978620 | River | 3 | 2 | 1 | 2 | 11,8 | 17,2 | 8,9 | 5,3 | 2,9 | Ortho 58 | 0,5 | 1 | 6,5 |
| S10 | 652315 | 4978620 | Gully | 3 | 1 | 1 | 2 | 4,4 | 7,1 | 2,8 | 2,8 | 1,5 | Ortho 58 | 0,5 | 1 | 5,5 |
| S10 | 652420 | 4978610 | Gully | 3 | 2 | 1 | 2 | 4,6 | 6,4 | 3,1 | 1,8 | 1,5 | Ortho 58 | 0,5 | 1 | 6,5 |
| S10 | 652540 | 4978600 | Gully | 2 | 2 | 1 | 2 | 4,3 | 5,5 | 3,5 | 1,2 | 0,8 | Ortho 58 | 0,5 | 1 | 4,5 |
| S10 | 652540 | 4978600 | Gully | 2 | 2 | 1 | 2 | 24,1 | 28,3 | 22,4 | 4,2 | 1,7 | Ortho 58 | 0,5 | 1 | 4,5 |
| S10 | 652745 | 4978605 | Talweg | 2 | 2 | 1 | 2 | 6,4 | 8,9 | 3,4 | 2,6 | 2,9 | Ortho 58 | 0,5 | 1 | 4,5 |
| S10 | 652810 | 4978620 | Talweg | 2 | 2 | 1 | 2 | 6,9 | 10,4 | 2,9 | 3,6 | 4,0 | Ortho 58 | 0,5 | 1 | 4,5 |
| S10 | 652900 | 4978630 | River | 3 | 2 | 1 | 2 | 4,1 | 7,9 | 2,1 | 3,8 | 2,0 | Ortho 58 | 0,5 | 1 | 6,5 |
| S10 | 653120 | 4978620 | Gully | 2 | 2 | 1 | 1 | 6,4 | 9,2 | 3,9 | 2,9 | 2,5 | Ortho 58 | 0,5 | 1 | 5,5 |
| S10 | 653310 | 4978600 | Talweg | 2 | 2 | 1 | 1 | 6,4 | 7,1 | 3,5 | 0,7 | 2,8 | Ortho 58 | 0,5 | 1 | 5,5 |
| S10 | 653355 | 4978590 | Gully | 3 | 1 | 1 | 1 | 3,9 | 5,9 | 2,1 | 2,0 | 1,8 | Ortho 58 | 0,5 | 1 | 6,5 |
| S10 | 653430 | 4978570 | Talweg | 3 | 2 | 1 | 1 | 4,9 | 7,1 | 4,1 | 2,1 | 0,8 | Ortho 58 | 0,5 | 1 | 7,5 |
| S10 | 653485 | 4978555 | Talweg | 3 | 2 | 1 | 0 | 3,2 | 7,9 | 2,4 | 4,7 | 0,8 | Ortho 58 | 0,5 | 1 | 8,5 |
| S10 | 653450 | 4978540 | Talweg | 3 | 1 | 1 | 0 | 4,4 | 6,4 | 2,4 | 1,9 | 2,0 | Ortho 58 | 0,5 | 1 | 7,5 |
| S10 | 653645 | 4978520 | Talweg | 3 | 2 | 1 | 0 | 11,5 | 15,1 | 8,8 | 3,6 | 2,7 | Ortho 58 | 0,5 | 1 | 8,5 |
| S10 | 653720 | 4978515 | Gully | 3 | 2 | 1 | 1 | 2,7 | 4,3 | 2,0 | 1,6 | 0,8 | Ortho 58 | 0,5 | 1 | 7,5 |
| S10 | 654055 | 4978513 | Gully | 3 | 2 | 1 | 1 | 6,7 | 10,7 | 4,2 | 4,0 | 2,5 | Ortho 58 | 0,5 | 1 | 7,5 |
| S10 | 654090 | 4978512 | River | 3 | 1 | 1 | 1 | 4,7 | 7,1 | 3,1 | 2,3 | 1,7 | Ortho 58 | 0,5 | 1 | 6,5 |
| S10 | 654090 | 4978512 | River | 3 | 1 | 1 | 1 | 78,7 | 90,5 | 61,1 | 11,8 | 17,6 | Ortho 58 | 0,5 | 1 | 6,5 |
| S10 | 654090 | 4978512 | River | 3 | 1 | 1 | 1 | 4,0 | 6,7 | 1,7 | 2,7 | 2,3 | Ortho 58 | 0,5 | 1 | 6,5 |
| S10 | 654230 | 4978510 | Talweg | 3 | 2 | 1 | 1 | 26,3 | 32,1 | 21,3 | 5,8 | 5,0 | Ortho 58 | 0,5 | 1 | 7,5 |
| S10 | 654230 | 4978510 | Talweg | 3 | 1 | 1 | 1 | 54,4 | 59,6 | 49,6 | 5,2 | 4,8 | Ortho 58 | 0,5 | 1 | 6,5 |
| S10 | 654230 | 4978510 | Talweg | 3 | 1 | 1 | 1 | 123,1 | 138,5 | 112,3 | 15,4 | 10,9 | Ortho 58 | 0,5 | 1 | 6,5 |
| S10 | 654230 | 4978510 | Talweg | 3 | 1 | 1 | 1 | 4,7 | 6,5 | 3,5 | 1,8 | 1,2 | Ortho 58 | 0,5 | 1 | 6,5 |
| S10 | 654400 | 4978500 | Ridge | 3 | 1 | 1 | 1 | 6,3 | 10,0 | 3,1 | 3,7 | 3,2 | Ortho 58 | 0,5 | 1 | 6,5 |
| S10 | 654470 | 4978490 | Talweg | 3 | 1 | 1 | 1 | 3,5 | 5,2 | 2,0 | 1,8 | 1,5 | Ortho 58 | 0,5 | 1 | 6,5 |
| S10 | 654525 | 4978490 | Riser | 3 | 2 | 1 | 1 | 7,7 | 9,7 | 5,4 | 2,0 | 2,4 | Ortho 58 | 0,5 | 1 | 7,5 |
| S10 | 654580 | 4978480 | Talweg | 3 | 2 | 1 | 1 | 5,8 | 6,9 | 3,8 | 1,1 | 2,0 | Ortho 58 | 0,5 | 1 | 7,5 |

| Seg. | Lon. (UTM) | Lat. (UTM) | Marker Type | Mark. Obl. | Mark. res. (/2) | Nb. of splay | Scarp 2nd | Offset Pref. (m) | Offset max (m) | Offset min (m) | Δ+ (m) | Δ- (m) | Image type | Image Res. (m) | Image quality (/2) | Total Score (/10) |
|---|---|---|---|---|---|---|---|---|---|---|---|---|---|---|---|---|
| S10 | 654680 | 4978466 | Talweg | 3 | 2 | 1 | 0 | 6,5 | 8,7 | 4,7 | 2,1 | 1,8 | Ortho 58 | 0,5 | 1 | 8,5 |
| S10 | 654770 | 4978458 | Talweg | 3 | 2 | 1 | 0 | 19,1 | 21,9 | 16,8 | 2,8 | 2,3 | Ortho 58 | 0,5 | 1 | 8,5 |
| S10 | 654770 | 4978458 | Talweg | 3 | 1 | 1 | 0 | 74,9 | 98,9 | 63,3 | 24,0 | 11,6 | Ortho 58 | 0,5 | 1 | 7,5 |
| S10 | 654830 | 4978440 | Talweg | 2 | 2 | 1 | 0 | 10,9 | 16,0 | 6,4 | 5,1 | 4,5 | Ortho 58 | 0,5 | 1 | 6,5 |
| S10 | 655160 | 4978413 | RIver | 3 | 2 | 1 | 0 | 3,4 | 4,4 | 1,7 | 1,0 | 1,8 | Ortho 58 | 0,5 | 1 | 8,5 |
| S10 | 655160 | 4978413 | RIver | 3 | 2 | 1 | 0 | 10,2 | 11,3 | 9,6 | 1,1 | 0,6 | Ortho 58 | 0,5 | 1 | 8,5 |
| S10 | 655239 | 4978409 | Talweg | 3 | 1 | 1 | 0 | 8,3 | 10,3 | 7,2 | 1,9 | 1,1 | Ortho 58 | 0,5 | 1 | 7,5 |
| S10 | 655239 | 4978409 | Talweg | 3 | 1 | 1 | 0 | 21,3 | 23,0 | 19,6 | 1,7 | 1,7 | Ortho 58 | 0,5 | 1 | 7,5 |
| S10 | 655270 | 4978404 | Talweg | 3 | 2 | 1 | 0 | 2,8 | 3,6 | 2,0 | 0,8 | 0,8 | Ortho 58 | 0,5 | 1 | 8,5 |
| S10 | 655270 | 4978404 | Talweg | 3 | 1 | 1 | 0 | 6,2 | 7,6 | 5,5 | 1,4 | 0,7 | Ortho 58 | 0,5 | 1 | 7,5 |
| S10 | 655455 | 4978380 | Talweg | 3 | 2 | 1 | 0 | 3,0 | 3,6 | 2,5 | 0,6 | 0,6 | Ortho 58 | 0,5 | 1 | 8,5 |
| S10 | 655455 | 4978380 | Talweg | 3 | 2 | 1 | 0 | 9,3 | 10,4 | 8,1 | 1,2 | 1,2 | Ortho 58 | 0,5 | 1 | 8,5 |
| S10 | 655570 | 4978375 | Talweg | 3 | 2 | 1 | 0 | 4,6 | 5,3 | 3,5 | 0,7 | 1,1 | Ortho 58 | 0,5 | 1 | 8,5 |
| S10 | 655640 | 4978370 | River | 3 | 2 | 1 | 0 | 3,5 | 4,0 | 2,9 | 0,6 | 0,6 | Ortho 58 | 0,5 | 1 | 8,5 |
| S10 | 655640 | 4978370 | River | 3 | 2 | 1 | 0 | 7,0 | 8,6 | 5,2 | 1,6 | 1,8 | Ortho 58 | 0,5 | 1 | 8,5 |
| S10 | 655820 | 4978360 | Riser | 3 | 1 | 1 | 0 | 6,5 | 8,8 | 3,7 | 2,2 | 2,8 | Ortho 58 | 0,5 | 1 | 7,5 |
| S10 | 655870 | 4978355 | Talweg | 3 | 2 | 1 | 0 | 4,6 | 6,0 | 3,8 | 1,4 | 0,8 | Ortho 58 | 0,5 | 1 | 8,5 |
| S10 | 655870 | 4978355 | Talweg | 3 | 2 | 1 | 0 | 9,4 | 11,0 | 7,2 | 1,6 | 2,2 | Ortho 58 | 0,5 | 1 | 8,5 |
| S10 | 655990 | 4978356 | Riser | 3 | 1 | 1 | 0 | 4,1 | 5,9 | 3,5 | 1,7 | 0,6 | Ortho 58 | 0,2 | 2 | 9 |
| S10 | 655990 | 4978356 | Riser | 3 | 2 | 1 | 0 | 13,6 | 15,3 | 12,0 | 1,8 | 1,6 | Ortho 58 | 0,2 | 2 | 10 |
| S10 | 656050 | 4978360 | River | 3 | 2 | 2 | 0 | 2,9 | 3,6 | 2,0 | 0,6 | 0,9 | Ortho 58 | 0,2 | 2 | 9 |
| S10 | 656050 | 4978360 | River | 3 | 2 | 1 | 0 | 9,2 | 10,9 | 7,4 | 1,7 | 1,8 | Ortho 58 | 0,2 | 2 | 10 |
| S10 | 656280 | 4978360 | Talweg | 3 | 2 | 1 | 0 | 7,2 | 8,1 | 6,6 | 0,9 | 0,6 | Ortho 58 | 0,2 | 2 | 10 |
| S10 | 656320 | 4978360 | Talweg | 3 | 2 | 2 | 0 | 2,7 | 3,4 | 1,7 | 0,8 | 0,9 | Ortho 58 | 0,2 | 2 | 9 |
| S10 | 656320 | 4978367 | Talweg | 3 | 2 | 2 | 0 | 4,1 | 5,8 | 3,2 | 1,7 | 0,9 | Ortho 58 | 0,2 | 2 | 9 |
| S10 | 656360 | 4978376 | Gully | 3 | 2 | 1 | 0 | 2,5 | 3,5 | 2,0 | 1,0 | 0,5 | Ortho 58 | 0,2 | 2 | 10 |
| S10 | 656380 | 4978376 | Talweg | 3 | 2 | 1 | 0 | 5,0 | 6,1 | 4,4 | 1,1 | 0,6 | Ortho 58 | 0,2 | 2 | 10 |
| S10 | 656380 | 4978376 | Talweg | 3 | 2 | 1 | 0 | 7,4 | 9,0 | 6,6 | 1,6 | 0,8 | Ortho 58 | 0,2 | 2 | 10 |
| S10 | 656430 | 4978370 | Talweg | 3 | 1 | 1 | 0 | 5,1 | 6,1 | 3,7 | 1,0 | 1,4 | Ortho 58 | 0,2 | 2 | 9 |
| S10 | 656470 | 4978370 | Talweg | 3 | 2 | 1 | 0 | 3,4 | 5,5 | 2,3 | 2,1 | 1,1 | Ortho 58 | 0,2 | 2 | 10 |
| S10 | 656550 | 4978365 | Talweg | 3 | 2 | 1 | 0 | 5,8 | 7,3 | 5,0 | 1,5 | 0,8 | Ortho 58 | 0,2 | 1 | 9 |
| S10 | 656550 | 4978365 | Talweg | 3 | 2 | 1 | 0 | 11,4 | 12,5 | 9,7 | 1,1 | 1,7 | Ortho 58 | 0,2 | 1 | 9 |
| S10 | 656620 | 4978360 | Talweg | 3 | 2 | 1 | 0 | 3,1 | 4,1 | 2,0 | 1,0 | 1,1 | Ortho 58 | 0,2 | 1 | 9 |

| Seg. | Lon. (UTM) | Lat. (UTM) | Marker Type | Mark. Obl. | Mark. res. (/2) | Nb. of splay | Scarp 2nd | Offset Pref. (m) | Offset max (m) | Offset min (m) | Δ+ (m) | Δ- (m) | Image type | Image Res. (m) | Image quality (/2) | Total Score (/10) |
|---|---|---|---|---|---|---|---|---|---|---|---|---|---|---|---|---|
| S10 | 656665 | 4978360 | Gully | 3 | 2 | 1 | 0 | 2,0 | 3,0 | 1,2 | 1,0 | 0,8 | Ortho 58 | 0,2 | 1 | 9 |
| S10 | 656675 | 4978360 | Gully | 3 | 2 | 1 | 0 | 5,9 | 7,0 | 5,3 | 1,1 | 0,6 | Ortho 58 | 0,2 | 1 | 9 |
| S10 | 656715 | 4978355 | River | 3 | 2 | 1 | 0 | 3,7 | 4,9 | 2,0 | 1,2 | 1,7 | Ortho 58 | 0,2 | 2 | 10 |
| S10 | 656715 | 4978355 | River | 3 | 2 | 1 | 0 | 6,2 | 8,6 | 5,3 | 2,4 | 0,9 | Ortho 58 | 0,2 | 2 | 10 |
| S10 | 656740 | 4978355 | Talweg | 3 | 2 | 2 | 0 | 3,4 | 4,4 | 3,0 | 1,0 | 0,3 | Ortho 58 | 0,2 | 2 | 9 |
| S10 | 656755 | 4978355 | Talweg | 3 | 2 | 2 | 0 | 2,3 | 2,9 | 1,4 | 0,6 | 1,0 | Ortho 58 | 0,2 | 2 | 9 |
| S10 | 656755 | 4978355 | Talweg | 3 | 1 | 2 | 0 | 4,8 | 5,8 | 4,1 | 1,0 | 0,7 | Ortho 58 | 0,2 | 2 | 8 |
| S10 | 656770 | 4978360 | Talweg | 3 | 2 | 2 | 0 | 1,9 | 2,6 | 1,3 | 0,6 | 0,6 | Ortho 58 | 0,2 | 2 | 9 |
| S10 | 656770 | 4978360 | Talweg | 3 | 2 | 2 | 0 | 3,2 | 3,8 | 2,0 | 0,6 | 1,1 | Ortho 58 | 0,2 | 2 | 9 |
| S10 | 656785 | 4978360 | Talweg | 3 | 2 | 2 | 0 | 1,9 | 2,8 | 1,4 | 0,9 | 0,5 | Ortho 58 | 0,2 | 2 | 9 |
| S10 | 656785 | 4978360 | Talweg | 3 | 2 | 2 | 0 | 3,3 | 4,2 | 2,8 | 0,9 | 0,5 | Ortho 58 | 0,2 | 2 | 9 |
| S10 | 656785 | 4978360 | Talweg | 3 | 2 | 2 | 0 | 4,1 | 4,6 | 3,4 | 0,5 | 0,6 | Ortho 58 | 0,2 | 2 | 9 |
| S10 | 656800 | 4978360 | Talweg | 3 | 2 | 2 | 0 | 5,1 | 7,0 | 4,3 | 1,9 | 0,8 | Ortho 58 | 0,2 | 2 | 9 |
| S10 | 656820 | 4978355 | Talweg | 3 | 1 | 2 | 0 | 3,7 | 4,5 | 3,0 | 0,7 | 0,7 | Ortho 58 | 0,2 | 2 | 8 |
| S10 | 656850 | 4978350 | Talweg | 3 | 2 | 1 | 0 | 3,7 | 4,5 | 3,0 | 0,9 | 0,7 | Ortho 58 | 0,2 | 2 | 10 |
| S10 | 656850 | 4978350 | Talweg | 3 | 1 | 1 | 0 | 5,2 | 7,6 | 4,2 | 2,5 | 1,0 | Ortho 58 | 0,2 | 2 | 9 |
| S10 | 656870 | 4978350 | Talweg | 3 | 2 | 1 | 0 | 3,6 | 5,1 | 2,9 | 1,4 | 0,8 | Ortho 58 | 0,2 | 2 | 10 |
| S10 | 656870 | 4978350 | Talweg | 3 | 1 | 1 | 0 | 8,1 | 9,7 | 6,6 | 1,6 | 1,6 | Ortho 58 | 0,2 | 2 | 9 |
| S10 | 656900 | 4978340 | Talweg | 3 | 1 | 1 | 0 | 4,7 | 6,2 | 3,7 | 1,5 | 1,0 | Ortho 58 | 0,2 | 2 | 9 |
| S10 | 656930 | 4978333 | Talweg | 3 | 2 | 1 | 0 | 2,4 | 3,4 | 1,2 | 1,1 | 1,1 | Ortho 58 | 0,2 | 2 | 10 |
| S10 | 656930 | 4978333 | Talweg | 3 | 2 | 1 | 0 | 3,7 | 5,1 | 2,7 | 1,4 | 0,9 | Ortho 58 | 0,2 | 2 | 10 |
| S10 | 656980 | 4978342 | Talweg | 3 | 2 | 1 | 0 | 2,9 | 3,9 | 2,0 | 1,0 | 0,9 | Ortho 58 | 0,2 | 2 | 10 |
| S10 | 657015 | 4978342 | Talweg | 3 | 1 | 2 | 0 | 2,4 | 3,4 | 1,3 | 1,0 | 1,1 | Ortho 58 | 0,2 | 2 | 8 |
| S10 | 657060 | 4978335 | Gully | 3 | 2 | 3 | 0 | 3,0 | 5,0 | 1,8 | 2,0 | 1,2 | Ortho 58 | 0,2 | 2 | 8 |
| S10 | 657180 | 4978315 | River | 3 | 2 | 2 | 0 | 5,4 | 6,6 | 4,6 | 1,2 | 0,8 | Ortho 58 | 0,2 | 2 | 9 |
| S10 | 657180 | 4978315 | River | 3 | 1 | 2 | 0 | 22,4 | 26,9 | 8,8 | 4,5 | 13,6 | Ortho 58 | 0,2 | 2 | 8 |
| S10 | 657290 | 4978300 | Talweg | 3 | 2 | 1 | 0 | 8,8 | 11,1 | 5,9 | 2,2 | 2,9 | Ortho 58 | 0,2 | 1 | 9 |
| S10 | 657360 | 4978300 | Talweg | 3 | 2 | 1 | 0 | 8,4 | 9,5 | 6,2 | 1,1 | 2,2 | Ortho 58 | 0,2 | 1 | 9 |
| S10 | 657400 | 4978300 | Talweg | 3 | 2 | 1 | 0 | 6,8 | 8,5 | 5,3 | 1,6 | 1,5 | Ortho 58 | 0,2 | 1 | 9 |
| S10 | 657400 | 4978300 | Talweg | 3 | 2 | 1 | 0 | 17,2 | 19,0 | 15,1 | 1,8 | 2,1 | Ortho 58 | 0,2 | 1 | 9 |
| S10 | 657490 | 4978300 | Talweg | 3 | 1 | 1 | 1 | 4,2 | 5,6 | 2,8 | 1,3 | 1,4 | Ortho 58 | 0,2 | 2 | 8 |
| S10 | 657570 | 4978290 | Talweg | 3 | 2 | 1 | 1 | 1,7 | 3,2 | 1,1 | 1,4 | 0,7 | Ortho 58 | 0,2 | 2 | 9 |
| S10 | 657590 | 4978295 | Talweg | 3 | 2 | 1 | 1 | 2,9 | 3,3 | 2,5 | 0,5 | 0,3 | Ortho 58 | 0,2 | 2 | 9 |

| Seg. | Lon. (UTM) | Lat. (UTM) | Marker Type | Mark. Obl. | Mark. res. (/2) | Nb. of splay | Scarp 2nd | Offset Pref. (m) | Offset max (m) | Offset min (m) | Δ+ (m) | Δ- (m) | Image type | Image Res. (m) | Image quality (/2) | Total Score (/10) |
|---|---|---|---|---|---|---|---|---|---|---|---|---|---|---|---|---|
| S10 | 657590 | 4978295 | Talweg | 3 | 2 | 1 | 1 | 8,9 | 9,7 | 7,8 | 0,8 | 1,1 | Ortho 58 | 0,2 | 2 | 9 |
| S10 | 657620 | 4978295 | Talweg | 3 | 1 | 3 | 1 | 1,8 | 2,7 | 1,2 | 0,9 | 0,7 | Ortho 58 | 0,2 | 2 | 6 |
| S10 | 657640 | 4978295 | Talweg | 3 | 2 | 2 | 1 | 5,6 | 6,8 | 4,9 | 1,1 | 0,7 | Ortho 58 | 0,2 | 2 | 8 |
| S10 | 657660 | 4978295 | Talweg | 3 | 2 | 2 | 1 | 7,6 | 7,9 | 6,6 | 0,4 | 0,9 | Ortho 58 | 0,2 | 2 | 8 |
| S10 | 657680 | 4978290 | talweg | 3 | 2 | 2 | 1 | 4,1 | 4,7 | 3,5 | 0,6 | 0,5 | Ortho 58 | 0,2 | 2 | 8 |
| S10 | 657680 | 4978290 | Talweg | 3 | 2 | 1 | 1 | 9,9 | 11,3 | 9,4 | 1,4 | 0,6 | Ortho 58 | 0,2 | 2 | 9 |
| S10 | 657700 | 4978285 | Talweg | 3 | 1 | 1 | 1 | 4,0 | 5,8 | 2,7 | 1,7 | 1,3 | Ortho 58 | 0,2 | 2 | 8 |
| S10 | 657700 | 4978285 | Talweg | 3 | 1 | 1 | 1 | 5,9 | 7,1 | 5,4 | 1,2 | 0,5 | Ortho 58 | 0,2 | 2 | 8 |
| S10 | 657745 | 4978270 | Talweg | 3 | 2 | 1 | 1 | 5,1 | 6,3 | 4,4 | 1,2 | 0,7 | Ortho 58 | 0,2 | 2 | 9 |
| S10 | 657810 | 4978260 | Talweg | 3 | 2 | 1 | 1 | 3,0 | 4,4 | 2,2 | 1,3 | 0,9 | Ortho 58 | 0,2 | 1 | 8 |
| S10 | 657810 | 4978260 | Talweg | 3 | 2 | 1 | 1 | 4,7 | 5,9 | 4,2 | 1,2 | 0,4 | Ortho 58 | 0,2 | 1 | 8 |
| S10 | 657810 | 4978260 | Talweg | 3 | 2 | 1 | 1 | 28,0 | 29,3 | 27,0 | 1,3 | 0,9 | Ortho 58 | 0,2 | 1 | 8 |
| S10 | 657875 | 4978250 | Talweg | 3 | 1 | 3 | 1 | 2,7 | 4,0 | 1,7 | 1,3 | 1,0 | Ortho 58 | 0,2 | 2 | 6 |
| S10 | 657875 | 4978250 | Talweg | 3 | 2 | 3 | 1 | 8,9 | 10,0 | 8,0 | 1,1 | 0,9 | Ortho 58 | 0,2 | 2 | 7 |
| S10 | 657875 | 4978250 | Talweg | 3 | 1 | 3 | 1 | 17,1 | 17,9 | 16,0 | 0,9 | 1,1 | Ortho 58 | 0,2 | 2 | 6 |
| S10 | 657875 | 4978250 | Talweg | 3 | 1 | 3 | 1 | 32,0 | 36,4 | 29,3 | 4,4 | 2,7 | Ortho 58 | 0,2 | 2 | 6 |
| S10 | 657950 | 4978250 | Talweg | 3 | 1 | 1 | 1 | 3,8 | 5,4 | 2,4 | 1,6 | 1,3 | Ortho 58 | 0,2 | 2 | 8 |
| S10 | 658020 | 4978245 | Talweg | 3 | 2 | 1 | 1 | 6,2 | 8,2 | 5,3 | 2,0 | 0,9 | Ortho 58 | 0,2 | 1 | 8 |
| S10 | 658020 | 4978245 | Talweg | 3 | 2 | 1 | 1 | 11,2 | 13,2 | 8,7 | 2,0 | 2,5 | Ortho 58 | 0,2 | 1 | 8 |
| S10 | 658070 | 4978240 | Talweg | 3 | 2 | 1 | 1 | 1,9 | 2,2 | 0,9 | 0,3 | 0,9 | Ortho 58 | 0,2 | 1 | 8 |
| S10 | 658120 | 4978240 | Talweg | 3 | 1 | 3 | 1 | 5,5 | 6,9 | 4,4 | 1,4 | 1,1 | Ortho 58 | 0,2 | 1 | 5 |
| S10 | 658180 | 4978235 | Riser | 3 | 2 | 2 | 1 | 3,3 | 4,8 | 2,0 | 1,5 | 1,3 | Ortho 58 | 0,2 | 2 | 8 |
| S10 | 658210 | 4978235 | Gully | 3 | 2 | 2 | 1 | 2,5 | 3,2 | 2,0 | 0,7 | 0,5 | Ortho 58 | 0,2 | 2 | 8 |
| S10 | 658235 | 4978235 | Talweg | 3 | 2 | 2 | 1 | 2,8 | 3,3 | 2,4 | 0,4 | 0,4 | Ortho 58 | 0,2 | 2 | 8 |
| S10 | 658245 | 4978235 | Talweg | 3 | 2 | 2 | 1 | 2,0 | 2,3 | 1,4 | 0,3 | 0,6 | Ortho 58 | 0,2 | 2 | 8 |
| S10 | 658245 | 4978235 | Talweg | 3 | 2 | 2 | 1 | 12,1 | 13,0 | 11,6 | 0,9 | 0,5 | Ortho 58 | 0,2 | 2 | 8 |
| S10 | 658255 | 4978235 | Talweg | 3 | 1 | 3 | 1 | 7,2 | 7,9 | 6,2 | 0,7 | 1,0 | Ortho 58 | 0,2 | 2 | 6 |
| S10 | 658255 | 4978235 | Talweg | 3 | 1 | 3 | 1 | 9,1 | 12,3 | 7,2 | 3,2 | 1,9 | Ortho 58 | 0,2 | 2 | 6 |
| S10 | 658235 | 4978237 | Talweg | 3 | 1 | 2 | 1 | 3,5 | 4,1 | 3,0 | 0,6 | 0,5 | Ortho 58 | 0,2 | 2 | 7 |
| S10 | 658245 | 4978237 | Talweg | 3 | 2 | 2 | 1 | 6,6 | 7,5 | 5,9 | 0,9 | 0,7 | Ortho 58 | 0,2 | 2 | 8 |
| S10 | 658280 | 4978240 | Talweg | 3 | 2 | 2 | 1 | 3,7 | 4,4 | 3,2 | 0,8 | 0,4 | Ortho 58 | 0,2 | 2 | 8 |
| S10 | 658300 | 4978240 | Talweg | 2 | 1 | 2 | 1 | 3,4 | 4,9 | 2,7 | 1,5 | 0,7 | Ortho 58 | 0,2 | 2 | 5 |
| S10 | 658300 | 4978240 | Talweg | 2 | 2 | 2 | 1 | 8,2 | 10,0 | 7,0 | 1,8 | 1,2 | Ortho 58 | 0,2 | 2 | 6 |

| Seg. | Lon. (UTM) | Lat. (UTM) | Marker Type | Mark. Obl. | Mark. res. (/2) | Nb. of splay | Scarp 2nd | Offset Pref. (m) | Offset max (m) | Offset min (m) | Δ+ (m) | Δ- (m) | Image type | Image Res. (m) | Image quality (/2) | Total Score (/10) |
|---|---|---|---|---|---|---|---|---|---|---|---|---|---|---|---|---|
| S10 | 658316 | 4978240 | Talweg | 3 | 2 | 1 | 1 | 8,8 | 10,5 | 7,3 | 1,7 | 1,5 | Ortho 58 | 0,2 | 2 | 9 |
| S10 | 658340 | 4978235 | Talweg | 3 | 1 | 1 | 1 | 10,6 | 11,7 | 9,4 | 1,1 | 1,2 | Ortho 58 | 0,2 | 2 | 8 |
| S10 | 658360 | 4978230 | Talweg | 3 | 2 | 1 | 1 | 10,7 | 11,2 | 10,2 | 0,5 | 0,5 | Ortho 58 | 0,2 | 2 | 9 |
| S10 | 658375 | 4978230 | Talweg | 3 | 1 | 1 | 1 | 8,6 | 9,7 | 8,3 | 1,1 | 0,3 | Ortho 58 | 0,2 | 2 | 8 |
| S10 | 658405 | 4978218 | Talweg | 3 | 1 | 1 | 1 | 13,0 | 13,9 | 11,9 | 0,9 | 1,1 | Ortho 58 | 0,2 | 2 | 8 |
| S10 | 658440 | 4978215 | Talweg | 3 | 2 | 2 | 1 | 3,2 | 5,9 | 2,1 | 2,7 | 1,1 | Ortho 58 | 0,2 | 2 | 8 |
| S10 | 658470 | 4978215 | Riser | 3 | 2 | 2 | 2 | 14,6 | 16,5 | 13,5 | 1,9 | 1,1 | Ortho 58 | 0,2 | 2 | 7 |
| S10 | 658490 | 4978215 | Riser | 3 | 2 | 1 | 2 | 5,1 | 6,4 | 3,5 | 1,3 | 1,6 | Ortho 58 | 0,2 | 2 | 8 |
| S10 | 658510 | 4978220 | River | 3 | 1 | 1 | 2 | 5,6 | 6,9 | 4,1 | 1,3 | 1,4 | Ortho 58 | 0,2 | 2 | 7 |
| S10 | 658525 | 4978220 | Riser | 3 | 2 | 1 | 2 | 5,6 | 7,1 | 4,8 | 1,6 | 0,8 | Ortho 58 | 0,2 | 2 | 8 |
| S10 | 658550 | 4978220 | Fan | 3 | 1 | 2 | 2 | 5,9 | 7,3 | 3,2 | 1,4 | 2,7 | Ortho 58 | 0,2 | 2 | 6 |
| S10 | 658585 | 4978225 | Talweg | 3 | 1 | 2 | 2 | 5,9 | 8,6 | 4,6 | 2,7 | 1,3 | Ortho 58 | 0,2 | 2 | 6 |
| S10 | 658600 | 4978230 | Talweg | 3 | 1 | 2 | 2 | 10,8 | 12,9 | 8,8 | 2,0 | 2,0 | Ortho 58 | 0,2 | 2 | 6 |
| S10 | 658620 | 4978230 | Ridge | 3 | 1 | 2 | 2 | 8,3 | 10,5 | 6,8 | 2,2 | 1,4 | Ortho 58 | 0,2 | 2 | 6 |
| S10 | 658650 | 4978230 | Talweg | 3 | 2 | 1 | 2 | 9,2 | 10,6 | 8,1 | 1,3 | 1,1 | Ortho 58 | 0,2 | 2 | 8 |
| S10 | 658660 | 4978235 | Riser | 3 | 2 | 1 | 1 | 11,2 | 13,9 | 8,9 | 2,7 | 2,2 | Ortho 58 | 0,2 | 1 | 8 |
| S10 | 658680 | 4978235 | Talweg | 3 | 1 | 1 | 1 | 3,8 | 5,0 | 2,7 | 1,2 | 1,1 | Ortho 58 | 0,2 | 1 | 7 |
| S10 | 658700 | 4978235 | Talweg | 3 | 1 | 1 | 1 | 4,5 | 6,4 | 2,4 | 2,0 | 2,1 | Ortho 58 | 0,2 | 1 | 7 |
| S10 | 658715 | 4978235 | Talweg | 3 | 1 | 1 | 1 | 12,5 | 15,0 | 11,4 | 2,4 | 1,1 | Ortho 58 | 0,2 | 1 | 7 |
| S10 | 658760 | 4978235 | Talweg | 3 | 2 | 2 | 1 | 3,4 | 4,0 | 1,3 | 0,6 | 2,1 | Ortho 58 | 0,2 | 2 | 8 |
| S10 | 658800 | 4978235 | Talweg | 3 | 2 | 2 | 1 | 4,6 | 6,5 | 1,9 | 1,9 | 2,7 | Ortho 58 | 0,2 | 2 | 8 |
| S10 | 658860 | 4978225 | talweg | 3 | 2 | 1 | 0 | 43,0 | 44,7 | 41,8 | 1,7 | 1,2 | Ortho 58 | 0,2 | 2 | 10 |
| S10 | 658880 | 4978220 | Talweg | 3 | 1 | 1 | 0 | 15,8 | 17,6 | 13,1 | 1,8 | 2,7 | Ortho 58 | 0,2 | 2 | 9 |
| S10 | 658920 | 4978215 | Talweg | 3 | 2 | 1 | 0 | 5,8 | 8,7 | 5,1 | 2,9 | 0,7 | Ortho 58 | 0,2 | 1 | 9 |
| S10 | 658960 | 4978210 | Talweg | 3 | 1 | 1 | 0 | 3,0 | 5,9 | 2,1 | 2,9 | 0,9 | Ortho 58 | 0,2 | 1 | 8 |
| S10 | 659010 | 4978200 | Talweg | 3 | 2 | 1 | 0 | 19,2 | 21,2 | 17,4 | 2,0 | 1,8 | Ortho 58 | 0,2 | 0 | 8 |
| S10 | 659050 | 4978200 | Talweg | 3 | 0 | 2 | 0 | 9,7 | 12,1 | 8,2 | 2,4 | 1,4 | Ortho 58 | 0,2 | 0 | 5 |
| S10 | 659080 | 4978200 | Talweg | 3 | 1 | 2 | 0 | 2,7 | 4,1 | 1,5 | 1,4 | 1,3 | Ortho 58 | 0,2 | 1 | 7 |
| S10 | 659080 | 4978200 | Talweg | 3 | 1 | 2 | 0 | 8,3 | 10,7 | 7,2 | 2,3 | 1,1 | Ortho 58 | 0,2 | 1 | 7 |
| S10 | 659080 | 4978200 | Talweg | 3 | 2 | 2 | 0 | 6,8 | 7,6 | 5,4 | 0,8 | 1,4 | Ortho 58 | 0,2 | 1 | 8 |
| S10 | 659200 | 4978195 | Talweg | 3 | 2 | 2 | 0 | 6,3 | 7,1 | 5,4 | 0,8 | 0,9 | Ortho 58 | 0,2 | 2 | 9 |
| S10 | 659200 | 4978195 | Talweg | 3 | 2 | 2 | 0 | 27,9 | 30,7 | 20,0 | 2,8 | 7,9 | Ortho 58 | 0,2 | 2 | 9 |
| S10 | 659200 | 4978195 | Talweg | 3 | 2 | 2 | 0 | 36,5 | 37,7 | 35,6 | 1,2 | 0,9 | Ortho 58 | 0,2 | 2 | 9 |

| Seg. | Lon. (UTM) | Lat. (UTM) | Marker Type | Mark. Obl. | Mark. res. (/2) | Nb. of splay | Scarp 2nd | Offset Pref. (m) | Offset max (m) | Offset min (m) | Δ+ (m) | Δ- (m) | Image type | Image Res. (m) | Image quality (/2) | Total Score (/10) |
|---|---|---|---|---|---|---|---|---|---|---|---|---|---|---|---|---|
| S10 | 659200 | 4978195 | Talweg | 3 | 2 | 2 | 0 | 61,6 | 63,0 | 60,2 | 1,4 | 1,4 | Ortho 58 | 0,2 | 2 | 9 |
| S10 | 659250 | 4978190 | Riser | 3 | 2 | 2 | 0 | 3,9 | 5,7 | 2,2 | 1,8 | 1,7 | Ortho 58 | 0,2 | 2 | 9 |
| S10 | 659250 | 4978190 | Riser | 3 | 1 | 2 | 0 | 16,1 | 18,3 | 14,6 | 2,2 | 1,5 | Ortho 58 | 0,2 | 2 | 8 |
| S10 | 659320 | 4978190 | Talweg | 3 | 1 | 1 | 0 | 7,3 | 8,5 | 5,7 | 1,2 | 1,6 | Ortho 58 | 0,2 | 2 | 9 |
| S10 | 659340 | 4978190 | Riser | 3 | 1 | 1 | 0 | 4,4 | 5,4 | 3,9 | 1,0 | 0,5 | Ortho 58 | 0,2 | 2 | 9 |
| S10 | 659380 | 4978190 | Riser | 3 | 2 | 2 | 0 | 6,6 | 8,0 | 4,4 | 1,4 | 2,2 | Ortho 58 | 0,2 | 2 | 9 |
| S10 | 659380 | 4978190 | Riser | 3 | 1 | 2 | 0 | 14,3 | 16,0 | 12,9 | 1,7 | 1,4 | Ortho 58 | 0,2 | 2 | 8 |
| S10 | 659400 | 4978185 | Riser | 3 | 2 | 2 | 0 | 3,9 | 5,1 | 3,0 | 1,2 | 0,9 | Ortho 58 | 0,2 | 2 | 9 |
| S10 | 659440 | 4978185 | Talweg | 3 | 1 | 2 | 1 | 6,4 | 8,6 | 3,9 | 2,2 | 2,4 | Ortho 58 | 0,2 | 2 | 7 |
| S10 | 659490 | 4978185 | Talweg | 3 | 1 | 2 | 1 | 5,8 | 8,5 | 4,5 | 2,7 | 1,3 | Ortho 58 | 0,2 | 2 | 7 |
| S10 | 659490 | 4978185 | Talweg | 3 | 1 | 2 | 1 | 14,4 | 19,6 | 10,6 | 5,2 | 3,8 | Ortho 58 | 0,2 | 2 | 7 |
| S10 | 659640 | 4978200 | talweg | 2 | 2 | 2 | 1 | 10,1 | 11,0 | 9,0 | 0,9 | 1,0 | Ortho 58 | 0,2 | 2 | 6 |
| S10 | 659660 | 4978205 | talweg | 3 | 2 | 2 | 1 | 8,3 | 9,7 | 7,0 | 1,4 | 1,3 | Ortho 58 | 0,2 | 2 | 8 |
| S10 | 659660 | 4978205 | Talweg | 3 | 2 | 2 | 1 | 13,3 | 15,3 | 10,1 | 2,0 | 3,1 | Ortho 58 | 0,2 | 2 | 8 |
| S10 | 659680 | 4978205 | Talweg | 3 | 2 | 3 | 1 | 4,3 | 5,4 | 3,3 | 1,1 | 1,0 | Ortho 58 | 0,2 | 2 | 7 |
| S10 | 659680 | 4978205 | Talweg | 3 | 2 | 3 | 1 | 10,4 | 12,5 | 8,1 | 2,2 | 2,2 | Ortho 58 | 0,2 | 2 | 7 |
| S10 | 659690 | 4978205 | Talweg | 3 | 2 | 2 | 1 | 4,9 | 5,8 | 3,0 | 0,9 | 1,9 | Ortho 58 | 0,2 | 2 | 8 |
| S10 | 659705 | 4978205 | Talweg | 3 | 2 | 2 | 1 | 8,0 | 11,1 | 5,5 | 3,1 | 2,5 | Ortho 58 | 0,2 | 2 | 8 |
| S10 | 659705 | 4978205 | Talweg | 3 | 2 | 2 | 1 | 12,7 | 13,7 | 11,0 | 1,0 | 1,6 | Ortho 58 | 0,2 | 2 | 8 |
| S10 | 659715 | 4978205 | Talweg | 3 | 2 | 2 | 1 | 8,6 | 9,0 | 5,5 | 0,4 | 3,2 | Ortho 58 | 0,2 | 2 | 8 |
| S10 | 659765 | 4978205 | Talweg | 3 | 1 | 2 | 1 | 3,8 | 4,7 | 3,2 | 0,9 | 0,6 | Ortho 58 | 0,2 | 2 | 7 |
| S10 | 659785 | 4978205 | Talweg | 3 | 1 | 2 | 1 | 4,4 | 5,4 | 2,7 | 1,0 | 1,7 | Ortho 58 | 0,2 | 2 | 7 |
| S10 | 659800 | 4978205 | Talweg | 3 | 1 | 2 | 1 | 3,9 | 5,3 | 2,7 | 1,4 | 1,2 | Ortho 58 | 0,2 | 2 | 7 |
| S10 | 659820 | 4978205 | Ridge | 3 | 2 | 2 | 1 | 9,3 | 12,0 | 7,8 | 2,7 | 1,5 | Ortho 58 | 0,2 | 2 | 8 |
| S10 | 659840 | 4978205 | Talweg | 3 | 2 | 2 | 1 | 4,7 | 5,8 | 3,2 | 1,1 | 1,4 | Ortho 58 | 0,2 | 2 | 8 |
| S10 | 659840 | 4978205 | Talweg | 3 | 2 | 2 | 1 | 9,7 | 12,5 | 7,0 | 2,8 | 2,7 | Ortho 58 | 0,2 | 2 | 8 |
| S10 | 659870 | 4978205 | Talweg | 3 | 2 | 2 | 1 | 5,6 | 7,4 | 4,7 | 1,8 | 0,9 | Ortho 58 | 0,2 | 2 | 8 |
| S10 | 659870 | 4978205 | Talweg | 3 | 2 | 2 | 1 | 20,0 | 22,7 | 18,4 | 2,7 | 1,6 | Ortho 58 | 0,2 | 2 | 8 |
| S10 | 659900 | 4978205 | River | 3 | 2 | 2 | 1 | 6,5 | 9,1 | 5,2 | 2,7 | 1,3 | Ortho 58 | 0,2 | 1 | 7 |
| S10 | 659900 | 4978205 | River | 3 | 2 | 2 | 1 | 14,3 | 18,8 | 12,4 | 4,5 | 1,8 | Ortho 58 | 0,2 | 1 | 7 |
| S10 | 659925 | 4978205 | Talweg | 3 | 2 | 2 | 1 | 4,2 | 5,5 | 1,6 | 1,2 | 2,7 | Ortho 58 | 0,2 | 1 | 7 |
| S10 | 659925 | 4978205 | Talweg | 3 | 2 | 2 | 1 | 14,5 | 16,9 | 12,5 | 2,5 | 2,0 | Ortho 58 | 0,2 | 2 | 8 |
| S10 | 659925 | 4978205 | Talweg | 3 | 2 | 2 | 1 | 11,1 | 13,1 | 9,5 | 2,0 | 1,6 | Bing | 0,2 | 2 | 8 |

| Seg. | Lon. (UTM) | Lat. (UTM) | Marker Type | Mark. Obl. | Mark. res. (/2) | Nb. of splay | Scarp 2nd | Offset Pref. (m) | Offset max (m) | Offset min (m) | Δ+ (m) | Δ- (m) | Image type | Image Res. (m) | Image quality (/2) | Total Score (/10) |
|---|---|---|---|---|---|---|---|---|---|---|---|---|---|---|---|---|
| S10 | 659970 | 4978205 | Talweg | 3 | 1 | 2 | 1 | 12,0 | 13,8 | 10,3 | 1,8 | 1,7 | Bing | 0,2 | 2 | 7 |
| S10 | 659970 | 4978205 | Talweg | 3 | 1 | 2 | 1 | 13,7 | 15,9 | 11,3 | 2,2 | 2,4 | Bing | 0,2 | 2 | 7 |
| S10 | 659970 | 4978205 | Talweg | 3 | 1 | 2 | 1 | 3,6 | 5,3 | 2,7 | 1,7 | 0,9 | Bing | 0,2 | 2 | 7 |
| S10 | 660000 | 4978205 | River | 3 | 1 | 2 | 1 | 5,1 | 7,5 | 4,3 | 2,4 | 0,8 | Ortho 58 | 0,2 | 1 | 6 |
| S10 | 660000 | 4978205 | River | 3 | 1 | 2 | 1 | 11,1 | 13,4 | 8,4 | 2,3 | 2,7 | Ortho 58 | 0,2 | 1 | 6 |
| S10 | 660060 | 4978210 | Talweg | 3 | 2 | 2 | 1 | 6,9 | 8,2 | 5,9 | 1,3 | 1,0 | Ortho 58 | 0,2 | 2 | 8 |
| S10 | 660060 | 4978210 | Talweg | 3 | 2 | 2 | 1 | 11,2 | 14,6 | 9,2 | 3,3 | 2,0 | Ortho 58 | 0,2 | 2 | 8 |
| S10 | 660100 | 4978215 | Talweg | 3 | 1 | 2 | 1 | 6,5 | 8,7 | 4,0 | 2,2 | 2,5 | Ortho 58 | 0,2 | 2 | 7 |
| S10 | 660100 | 4978215 | Talweg | 3 | 1 | 2 | 1 | 10,0 | 12,2 | 7,9 | 2,2 | 2,1 | Ortho 58 | 0,2 | 2 | 7 |
| S10 | 660130 | 4978225 | River | 3 | 2 | 2 | 1 | 4,7 | 5,8 | 3,6 | 1,1 | 1,1 | Ortho 58 | 0,2 | 2 | 8 |
| S10 | 660130 | 4978225 | River | 3 | 2 | 2 | 1 | 8,3 | 9,8 | 7,0 | 1,5 | 1,3 | Ortho 58 | 0,2 | 2 | 8 |
| S10 | 660220 | 4978245 | River | 3 | 2 | 2 | 1 | 9,5 | 13,1 | 9,1 | 3,6 | 0,4 | Ortho 58 | 0,2 | 2 | 8 |
| S10 | 660250 | 4978245 | Talweg | 3 | 1 | 1 | 1 | 7,3 | 9,7 | 5,3 | 2,4 | 2,0 | Ortho 58 | 0,2 | 2 | 8 |
| S10 | 660350 | 4978245 | Talweg | 3 | 2 | 1 | 1 | 9,8 | 12,0 | 6,6 | 2,2 | 3,3 | Ortho 58 | 0,2 | 2 | 9 |
| S10 | 660420 | 4978245 | River | 3 | 2 | 1 | 0 | 5,7 | 7,7 | 4,8 | 2,0 | 0,9 | Ortho 58 | 0,2 | 2 | 10 |
| S10 | 660420 | 4978245 | River | 3 | 2 | 1 | 0 | 9,0 | 10,1 | 7,6 | 1,1 | 1,4 | Ortho 58 | 0,2 | 2 | 10 |
| S10 | 660420 | 4978245 | Talweg | 3 | 2 | 1 | 0 | 34,3 | 36,5 | 32,6 | 2,2 | 1,8 | Ortho 58 | 0,2 | 2 | 10 |
| S10 | 660490 | 4978250 | Talweg | 3 | 2 | 1 | 0 | 3,8 | 4,6 | 3,0 | 0,8 | 0,8 | Ortho 58 | 0,2 | 2 | 10 |
| S10 | 660542 | 4978255 | Gully | 2 | 1 | 1 | 0 | 3,1 | 4,8 | 2,1 | 1,7 | 0,9 | Ortho 58 | 0,2 | 2 | 7 |
| S10 | 660595 | 4978250 | Gully | 3 | 2 | 1 | 0 | 2,8 | 3,9 | 2,3 | 1,1 | 0,6 | Ortho 58 | 0,2 | 2 | 10 |
| S10 | 660625 | 4978250 | Riser | 3 | 1 | 1 | 0 | 3,8 | 4,8 | 2,9 | 1,0 | 0,9 | Ortho 58 | 0,2 | 2 | 9 |
| S10 | 660640 | 4978250 | Talweg | 3 | 1 | 1 | 0 | 5,2 | 6,9 | 3,3 | 1,6 | 2,0 | Ortho 58 | 0,2 | 2 | 9 |
| S10 | 660680 | 4978250 | Talweg | 3 | 1 | 1 | 0 | 5,1 | 6,9 | 3,7 | 1,8 | 1,4 | Ortho 58 | 0,2 | 2 | 9 |
| S10 | 660750 | 4978260 | Talweg | 3 | 2 | 1 | 0 | 3,1 | 5,6 | 2,3 | 2,5 | 0,8 | Ortho 58 | 0,2 | 1 | 9 |
| S10 | 660790 | 4978262 | Talweg | 3 | 2 | 1 | 0 | 5,1 | 6,5 | 4,5 | 1,5 | 0,5 | Ortho 58 | 0,2 | 2 | 10 |
| S10 | 660820 | 4978262 | Talweg | 3 | 1 | 1 | 0 | 11,0 | 12,7 | 10,2 | 1,7 | 0,8 | Ortho 58 | 0,2 | 2 | 9 |
| S10 | 660970 | 4978230 | Gully | 3 | 2 | 1 | 1 | 5,6 | 7,2 | 4,7 | 1,5 | 0,9 | Ortho 58 | 0,2 | 2 | 9 |
| S10 | 661185 | 4978215 | Talweg | 3 | 2 | 2 | 1 | 2,9 | 4,1 | 1,4 | 1,1 | 1,5 | Ortho 58 | 0,2 | 2 | 8 |
| S10 | 661220 | 4978215 | Talweg | 3 | 2 | 2 | 1 | 27,6 | 28,9 | 26,5 | 1,4 | 1,1 | Ortho 58 | 0,2 | 2 | 8 |
| S10 | 662230 | 4978015 | Riser | 2 | 1 | 2 | 0 | 3,4 | 4,8 | 2,4 | 1,4 | 0,9 | Ortho 58 | 0,2 | 2 | 6 |
| S10 | 662420 | 4977965 | Talweg | 3 | 1 | 1 | 1 | 3,0 | 3,9 | 1,6 | 0,9 | 1,3 | Ortho 58 | 0,2 | 2 | 8 |
| S10 | 662450 | 4977960 | Talweg | 3 | 2 | 1 | 1 | 4,3 | 5,7 | 3,3 | 1,3 | 1,0 | Ortho 58 | 0,2 | 2 | 9 |
| S10 | 662450 | 4977960 | Talweg | 3 | 2 | 1 | 1 | 10,5 | 11,6 | 9,2 | 1,1 | 1,3 | Ortho 58 | 0,2 | 2 | 9 |

| Seg. | Lon. (UTM) | Lat. (UTM) | Marker Type | Mark. Obl. | Mark. res. (/2) | Nb. of splay | Scarp 2nd | Offset Pref. (m) | Offset max (m) | Offset min (m) | Δ+ (m) | Δ- (m) | Image type | Image Res. (m) | Image quality (/2) | Total Score (/10) |
|---|---|---|---|---|---|---|---|---|---|---|---|---|---|---|---|---|
| S10 | 662465 | 4977960 | Talweg | 3 | 1 | 1 | 1 | 5,0 | 6,4 | 4,2 | 1,4 | 0,8 | Ortho 58 | 0,2 | 2 | 8 |
| S10 | 662490 | 4977955 | Talweg | 3 | 2 | 1 | 1 | 13,5 | 14,9 | 12,2 | 1,4 | 1,3 | Ortho 58 | 0,2 | 2 | 9 |
| S10 | 662505 | 4977950 | Talweg | 3 | 2 | 1 | 1 | 5,1 | 5,4 | 4,2 | 0,3 | 0,9 | Ortho 58 | 0,2 | 2 | 9 |
| S10 | 662520 | 4977947 | Talweg | 3 | 2 | 1 | 1 | 4,2 | 4,9 | 3,7 | 0,7 | 0,6 | Ortho 58 | 0,2 | 2 | 9 |
| S10 | 662550 | 4977943 | Talweg | 3 | 2 | 1 | 1 | 6,0 | 6,6 | 5,4 | 0,6 | 0,6 | Ortho 58 | 0,2 | 2 | 9 |
| S10 | 662600 | 4977935 | Talweg | 3 | 2 | 1 | 1 | 5,4 | 6,0 | 4,8 | 0,6 | 0,6 | Ortho 58 | 0,2 | 2 | 9 |
| S10 | 662600 | 4977935 | Talweg | 3 | 2 | 1 | 1 | 9,1 | 10,7 | 8,5 | 1,6 | 0,6 | Ortho 58 | 0,2 | 2 | 9 |
| S10 | 662600 | 4977935 | Talweg | 3 | 1 | 1 | 1 | 19,8 | 22,6 | 18,0 | 2,8 | 1,8 | Ortho 58 | 0,2 | 2 | 8 |
| S10 | 662640 | 4977930 | Talweg | 2 | 2 | 1 | 1 | 5,0 | 5,6 | 4,0 | 0,7 | 1,0 | Ortho 58 | 0,2 | 2 | 7 |
| S10 | 662655 | 4977925 | Talweg | 3 | 2 | 1 | 1 | 4,9 | 6,0 | 4,1 | 1,1 | 0,8 | Ortho 58 | 0,2 | 2 | 9 |
| S10 | 662670 | 4977925 | Talweg | 3 | 2 | 1 | 1 | 4,2 | 5,5 | 3,3 | 1,3 | 0,9 | Ortho 58 | 0,2 | 2 | 9 |
| S10 | 662685 | 4977920 | Talweg | 3 | 2 | 1 | 1 | 4,2 | 5,0 | 3,6 | 0,8 | 0,6 | Ortho 58 | 0,2 | 2 | 9 |
| S10 | 662685 | 4977920 | Talweg | 3 | 2 | 1 | 1 | 12,5 | 13,3 | 11,2 | 0,8 | 1,3 | Ortho 58 | 0,2 | 2 | 9 |
| S10 | 662685 | 4977920 | Talweg | 2 | 1 | 1 | 1 | 32,4 | 35,6 | 28,0 | 3,3 | 4,4 | Ortho 58 | 0,2 | 2 | 6 |
| S10 | 662740 | 4977911 | Gully | 3 | 1 | 1 | 1 | 2,8 | 3,3 | 2,3 | 0,6 | 0,5 | Ortho 58 | 0,2 | 2 | 8 |
| S10 | 662760 | 4977907 | Talweg | 3 | 2 | 1 | 1 | 5,8 | 6,7 | 5,3 | 0,9 | 0,5 | Ortho 58 | 0,2 | 2 | 9 |
| S10 | 662800 | 4977905 | Talweg | 3 | 1 | 1 | 1 | 5,3 | 6,5 | 4,4 | 1,1 | 0,9 | Ortho 58 | 0,2 | 2 | 8 |
| S10 | 662800 | 4977905 | Talweg | 3 | 1 | 1 | 1 | 9,9 | 14,1 | 7,4 | 4,3 | 2,5 | Ortho 58 | 0,2 | 2 | 8 |
| S10 | 662840 | 4977900 | Talweg | 3 | 2 | 1 | 1 | 5,5 | 6,8 | 4,5 | 1,3 | 1,0 | Ortho 58 | 0,2 | 2 | 9 |
| S10 | 662855 | 4977895 | Talweg | 3 | 2 | 1 | 1 | 3,7 | 5,4 | 2,5 | 1,7 | 1,2 | Ortho 58 | 0,2 | 2 | 9 |
| S10 | 662930 | 4977890 | Talweg | 3 | 2 | 1 | 0 | 3,9 | 4,7 | 2,9 | 0,8 | 1,0 | Ortho 58 | 0,2 | 2 | 10 |
| S10 | 662955 | 4977895 | Talweg | 3 | 2 | 1 | 0 | 3,5 | 5,1 | 2,5 | 1,7 | 0,9 | Ortho 58 | 0,2 | 2 | 10 |
| S10 | 662955 | 4977895 | Talweg | 3 | 2 | 1 | 0 | 6,2 | 7,4 | 5,4 | 1,3 | 0,8 | Ortho 58 | 0,2 | 2 | 10 |
| S10 | 662955 | 4977895 | Talweg | 3 | 2 | 1 | 0 | 24,4 | 27,2 | 21,7 | 2,9 | 2,6 | Ortho 58 | 0,2 | 2 | 10 |
| S10 | 663000 | 4977880 | Talweg | 3 | 2 | 1 | 0 | 5,3 | 6,4 | 4,4 | 1,1 | 0,9 | Ortho 58 | 0,2 | 2 | 10 |
| S10 | 663000 | 4977880 | Talweg | 3 | 2 | 1 | 0 | 12,6 | 15,0 | 10,3 | 2,4 | 2,2 | Ortho 58 | 0,2 | 2 | 10 |
| S10 | 663000 | 4977880 | Talweg | 3 | 1 | 1 | 0 | 53,5 | 56,4 | 50,6 | 2,9 | 2,8 | Ortho 58 | 0,2 | 2 | 9 |
| S10 | 663000 | 4977880 | Talweg | 3 | 1 | 1 | 0 | 70,2 | 75,4 | 68,5 | 5,3 | 1,7 | Ortho 58 | 0,2 | 2 | 9 |
| S10 | 663060 | 4977873 | Talweg | 3 | 2 | 1 | 0 | 4,4 | 5,7 | 2,7 | 1,3 | 1,8 | Ortho 58 | 0,2 | 2 | 10 |
| S10 | 663060 | 4977873 | Talweg | 3 | 1 | 1 | 0 | 25,5 | 28,6 | 21,3 | 3,1 | 4,2 | Ortho 58 | 0,2 | 2 | 9 |
| S10 | 663080 | 4977873 | Talweg | 3 | 2 | 1 | 0 | 4,1 | 6,2 | 2,6 | 2,0 | 1,5 | Ortho 58 | 0,2 | 2 | 10 |
| S10 | 663120 | 4977864 | Talweg | 3 | 1 | 1 | 0 | 14,0 | 16,6 | 10,1 | 2,6 | 3,9 | Ortho 58 | 0,2 | 2 | 9 |
| S10 | 663180 | 4977860 | Talweg | 3 | 1 | 1 | 0 | 8,3 | 10,3 | 5,1 | 2,0 | 3,2 | Ortho 58 | 0,2 | 2 | 9 |

| Seg. | Lon. (UTM) | Lat. (UTM) | Marker Type | Mark. Obl. | Mark. res. (/2) | Nb. of splay | Scarp 2nd | Offset Pref. (m) | Offset max (m) | Offset min (m) | Δ+ (m) | Δ- (m) | Image type | Image Res. (m) | Image quality (/2) | Total Score (/10) |
|---|---|---|---|---|---|---|---|---|---|---|---|---|---|---|---|---|
| S10 | 663450 | 4977820 | Talweg | 2 | 1 | 1 | 0 | 11,6 | 14,0 | 9,6 | 2,4 | 1,9 | Ortho 58 | 0,2 | 2 | 7 |
| S10 | 663450 | 4977820 | Talweg | 2 | 1 | 1 | 0 | 25,4 | 27,2 | 23,7 | 1,8 | 1,6 | Ortho 58 | 0,2 | 2 | 7 |
| S10 | 663480 | 4977820 | Gully | 3 | 2 | 1 | 0 | 4,4 | 5,4 | 3,5 | 1,0 | 0,8 | Ortho 58 | 0,2 | 2 | 10 |
| S10 | 663540 | 4977808 | Talweg | 3 | 1 | 1 | 0 | 4,1 | 4,9 | 3,3 | 0,8 | 0,8 | Ortho 58 | 0,2 | 2 | 9 |
| S10 | 663540 | 4977808 | Talweg | 3 | 1 | 1 | 0 | 21,5 | 22,8 | 21,1 | 1,3 | 0,9 | Ortho 58 | 0,2 | 2 | 9 |
| S10 | 663758 | 4977795 | Gully | 3 | 2 | 1 | 0 | 2,7 | 3,5 | 2,4 | 0,7 | 0,3 | Ortho 58 | 0,2 | 2 | 10 |
| S10 | 663835 | 4977790 | Talweg | 3 | 1 | 1 | 0 | 3,9 | 4,3 | 1,8 | 0,4 | 2,1 | Ortho 58 | 0,2 | 2 | 9 |
| S10 | 663867 | 4977790 | Talweg | 3 | 1 | 1 | 0 | 3,6 | 4,8 | 3,1 | 1,2 | 0,5 | Ortho 58 | 0,2 | 2 | 9 |
| S10 | 663867 | 4977790 | Talweg | 3 | 2 | 1 | 0 | 9,1 | 10,1 | 7,7 | 1,0 | 1,3 | Ortho 58 | 0,2 | 2 | 10 |
| S10 | 663867 | 4977790 | Talweg | 3 | 2 | 1 | 0 | 11,5 | 12,2 | 10,3 | 0,7 | 1,3 | Ortho 58 | 0,2 | 2 | 10 |
| S10 | 663927 | 4977780 | Talweg | 3 | 1 | 1 | 0 | 3,6 | 5,3 | 2,9 | 1,7 | 0,6 | Ortho 58 | 0,2 | 2 | 9 |
| S10 | 663927 | 4977780 | Talweg | 3 | 1 | 1 | 0 | 6,4 | 8,1 | 5,3 | 1,6 | 1,1 | Ortho 58 | 0,2 | 2 | 9 |
| S10 | 663980 | 4977775 | Talweg | 1 | 1 | 1 | 0 | 5,4 | 7,4 | 4,2 | 2,0 | 1,2 | Ortho 58 | 0,2 | 2 | 6 |
| S10 | 664026 | 4977770 | Talweg | 3 | 1 | 1 | 0 | 3,0 | 4,9 | 2,3 | 1,9 | 0,7 | Ortho 58 | 0,2 | 2 | 9 |
| S10 | 664080 | 4977765 | Riser | 2 | 1 | 1 | 0 | 3,5 | 4,9 | 2,4 | 1,4 | 1,1 | Ortho 58 | 0,2 | 2 | 7 |
| S10 | 664115 | 4977750 | Talweg | 2 | 1 | 1 | 0 | 4,2 | 5,4 | 3,2 | 1,2 | 1,0 | Ortho 58 | 0,2 | 2 | 7 |
| S10 | 664175 | 4977740 | Talweg | 3 | 2 | 1 | 0 | 3,6 | 4,6 | 2,6 | 1,0 | 1,0 | Ortho 58 | 0,2 | 2 | 10 |
| S10 | 664200 | 4977740 | Talweg | 2 | 2 | 1 | 0 | 6,8 | 8,7 | 5,1 | 1,9 | 1,7 | Ortho 58 | 0,2 | 2 | 8 |
| S10 | 664230 | 4977730 | Talweg | 3 | 2 | 1 | 0 | 3,6 | 5,0 | 2,9 | 1,3 | 0,7 | Ortho 58 | 0,2 | 2 | 10 |
| S10 | 664230 | 4977730 | Talweg | 3 | 2 | 1 | 0 | 6,3 | 9,4 | 2,8 | 3,1 | 3,4 | Ortho 58 | 0,2 | 2 | 10 |
| S10 | 664250 | 4977727 | Talweg | 3 | 2 | 1 | 0 | 2,9 | 5,2 | 1,6 | 2,2 | 1,4 | Ortho 58 | 0,2 | 2 | 10 |
| S10 | 664270 | 4977724 | Talweg | 3 | 1 | 1 | 0 | 3,3 | 4,3 | 2,0 | 1,0 | 1,3 | Ortho 58 | 0,2 | 2 | 9 |
| S10 | 664300 | 4977720 | Talweg | 3 | 2 | 1 | 0 | 2,4 | 3,6 | 1,9 | 1,2 | 0,4 | Ortho 58 | 0,2 | 2 | 10 |
| S10 | 664330 | 4977715 | Gully | 3 | 1 | 1 | 0 | 3,0 | 4,3 | 2,3 | 1,3 | 0,7 | Ortho 58 | 0,2 | 2 | 9 |
| S10 | 664360 | 4977710 | Gully | 3 | 2 | 1 | 0 | 4,4 | 6,2 | 2,9 | 1,8 | 1,6 | Ortho 58 | 0,2 | 2 | 10 |
| S10 | 664360 | 4977710 | Gully | 3 | 2 | 1 | 0 | 23,4 | 25,4 | 20,5 | 2,0 | 2,9 | Ortho 58 | 0,2 | 2 | 10 |
| S10 | 664400 | 4977700 | Gully | 3 | 1 | 1 | 0 | 4,6 | 5,9 | 3,8 | 1,3 | 0,8 | Ortho 58 | 0,3 | 2 | 9 |
| S10 | 664425 | 4977700 | Gully | 3 | 1 | 1 | 0 | 9,3 | 12,0 | 7,6 | 2,6 | 1,7 | Ortho 58 | 0,3 | 2 | 9 |
| S10 | 664550 | 4977695 | Talweg | 3 | 1 | 1 | 0 | 2,9 | 4,4 | 1,6 | 1,5 | 1,3 | Ortho 58 | 0,3 | 2 | 9 |
| S10 | 664590 | 4977690 | Talweg | 3 | 2 | 1 | 0 | 8,9 | 10,0 | 7,7 | 1,1 | 1,1 | Ortho 58 | 0,3 | 2 | 10 |
| S10 | 664625 | 4977690 | Talweg | 3 | 2 | 1 | 0 | 2,2 | 3,1 | 1,5 | 0,9 | 0,7 | Ortho 58 | 0,3 | 2 | 10 |
| S10 | 664660 | 4977685 | Talweg | 3 | 2 | 1 | 0 | 3,8 | 5,2 | 2,9 | 1,4 | 1,0 | Ortho 58 | 0,3 | 2 | 10 |
| S10 | 664700 | 4977680 | Gully | 3 | 1 | 1 | 1 | 5,0 | 5,9 | 3,4 | 1,0 | 1,6 | Ortho 58 | 0,3 | 2 | 8 |

| Seg. | Lon. (UTM) | Lat. (UTM) | Marker Type | Mark. Obl. | Mark. res. (/2) | Nb. of splay | Scarp 2nd | Offset Pref. (m) | Offset max (m) | Offset min (m) | Δ+ (m) | Δ- (m) | Image type | Image Res. (m) | Image quality (/2) | Total Score (/10) |
|---|---|---|---|---|---|---|---|---|---|---|---|---|---|---|---|---|
| S10 | 664700 | 4977680 | Gully | 3 | 1 | 1 | 1 | 15,4 | 17,2 | 13,8 | 1,8 | 1,6 | Ortho 58 | 0,3 | 2 | 8 |
| S10 | 664750 | 4977680 | Gully | 2 | 2 | 2 | 1 | 4,3 | 8,1 | 3,1 | 3,7 | 1,2 | Ortho 58 | 0,3 | 2 | 6 |
| S10 | 664750 | 4977680 | Gully | 2 | 2 | 2 | 1 | 15,4 | 19,4 | 13,5 | 4,0 | 1,9 | Ortho 58 | 0,3 | 2 | 6 |
| S11 | 664790 | 4977680 | Talweg | 3 | 2 | 2 | 1 | 3,0 | 4,3 | 2,3 | 1,3 | 0,8 | Ortho 58 | 0,3 | 2 | 8 |
| S11 | 664820 | 4977680 | Gully | 3 | 2 | 2 | 1 | 3,8 | 5,5 | 1,1 | 1,6 | 2,8 | Ortho 58 | 0,3 | 2 | 8 |
| S11 | 664830 | 4977680 | Gully | 3 | 2 | 2 | 2 | 4,1 | 6,1 | 2,7 | 2,0 | 1,4 | Ortho 58 | 0,3 | 2 | 7 |
| S11 | 664860 | 4977677 | Gully | 3 | 1 | 2 | 2 | 3,0 | 4,1 | 1,4 | 1,0 | 1,6 | Ortho 58 | 0,3 | 2 | 6 |
| S11 | 664900 | 4977677 | Gully | 3 | 1 | 2 | 2 | 3,4 | 4,9 | 2,1 | 1,5 | 1,3 | Ortho 58 | 0,3 | 2 | 6 |
| S11 | 664900 | 4977677 | Gully | 3 | 1 | 2 | 2 | 7,7 | 10,7 | 6,9 | 3,0 | 0,8 | Ortho 58 | 0,3 | 2 | 6 |
| S11 | 665010 | 4977677 | Gully | 2 | 1 | 2 | 1 | 5,4 | 9,5 | 2,1 | 4,1 | 3,3 | Ortho 58 | 0,3 | 2 | 5 |
| S11 | 665060 | 4977672 | Gully | 3 | 1 | 2 | 1 | 7,1 | 8,3 | 6,5 | 1,2 | 0,5 | Ortho 58 | 0,3 | 2 | 7 |
| S11 | 665150 | 4977665 | Gully | 3 | 2 | 2 | 1 | 8,3 | 9,6 | 6,7 | 1,3 | 1,6 | Ortho 58 | 0,3 | 2 | 8 |
| S11 | 665170 | 4977660 | Gully | 3 | 2 | 2 | 1 | 23,0 | 25,8 | 21,2 | 2,9 | 1,8 | Ortho 58 | 0,3 | 2 | 8 |
| S11 | 665230 | 4977700 | Gully | 3 | 1 | 1 | 2 | 2,3 | 2,9 | 1,3 | 0,6 | 1,0 | Ortho 58 | 0,2 | 2 | 7 |
| S11 | 665320 | 4977700 | Gully | 3 | 1 | 1 | 2 | 1,7 | 3,1 | 0,6 | 1,4 | 1,1 | Ortho 58 | 0,2 | 2 | 7 |
| S11 | 665320 | 4977700 | Gully | 3 | 1 | 1 | 2 | 22,4 | 24,9 | 21,1 | 2,5 | 1,3 | Ortho 58 | 0,2 | 2 | 7 |
| S11 | 665475 | 4977685 | Gully | 3 | 2 | 2 | 1 | 4,2 | 5,5 | 3,0 | 1,3 | 1,2 | Ortho 58 | 0,2 | 2 | 8 |
| S11 | 665540 | 4977685 | Gully | 3 | 2 | 2 | 1 | 3,9 | 5,3 | 2,2 | 1,4 | 1,7 | Ortho 58 | 0,2 | 2 | 8 |
| S11 | 665600 | 4977680 | Gully | 3 | 2 | 2 | 1 | 4,8 | 6,6 | 2,4 | 1,8 | 2,4 | Ortho 58 | 0,2 | 2 | 8 |
| S11 | 665600 | 4977680 | Gully | 3 | 2 | 2 | 1 | 12,1 | 16,0 | 9,0 | 3,9 | 3,1 | Ortho 58 | 0,2 | 2 | 8 |
| S11 | 665710 | 4977590 | Gully | 3 | 1 | 1 | 2 | 2,4 | 3,7 | 1,9 | 1,3 | 0,5 | Ortho 58 | 0,2 | 2 | 7 |
| S11 | 665760 | 4977590 | Gully | 3 | 2 | 1 | 2 | 2,5 | 3,2 | 1,5 | 0,7 | 1,0 | Ortho 58 | 0,2 | 2 | 8 |
| S11 | 665760 | 4977590 | Gully | 3 | 2 | 1 | 2 | 2,9 | 8,0 | 2,5 | 5,1 | 0,5 | Ortho 58 | 0,2 | 2 | 8 |
| S11 | 665760 | 4977590 | Gully | 3 | 2 | 1 | 2 | 2,6 | 3,8 | 1,4 | 1,1 | 1,3 | Ortho 58 | 0,2 | 2 | 8 |
| S11 | 666210 | 4977480 | Gully | 3 | 1 | 1 | 2 | 3,9 | 5,6 | 2,5 | 1,7 | 1,5 | Ortho 58 | 0,2 | 2 | 7 |
| S11 | 666500 | 4977390 | Gully | 3 | 2 | 1 | 2 | 1,9 | 2,5 | 1,0 | 0,5 | 1,0 | Ortho 58 | 0,2 | 2 | 8 |
| S11 | 666600 | 4977450 | Gully | 3 | 2 | 1 | 2 | 9,4 | 12,4 | 7,9 | 3,0 | 1,5 | Ortho 58 | 0,2 | 2 | 8 |
| S11 | 666650 | 4977333 | Gully | 2 | 1 | 1 | 2 | 4,6 | 6,7 | 2,9 | 2,1 | 1,7 | Ortho 58 | 0,2 | 1 | 4 |

## Abstract

Western Mongolia experienced an exceptional intracontinental seismic activity during the first part of the XX$^{th}$ century, with four seismic events with Mw > 7.9, located on large strike-slip faults with a transpressive left-lateral motion. This historical seismicity has been qualified as a cluster, and paleoseismological studies indicate that this phenomenon might have occurred 3 to 4 ka ago. Although the eastern part of the Gobi-Altai mountain range broke during the eponymous earthquake in 1957 (Mw8) along the Eastern Bogd Fault (EBF), several fault traces affecting Holocene formations and presenting continuous fault length > 100 km have been documented on the western part of the range, while not been the purpose of quantitative studies. This thesis first gives an inventory of the seismic activity within the Gobi-Altai, through detailed mapping of the fault scarps which show activity during the late-Pleistocene, also with an analyze of the fault segmentation regarding to geometric and kinematic criteria. Secondly, some morphotectonical and paleoseismological surveys have been carried on, along with dating techniques as $^{10}$Be *in situ*, OSL and radiocarbon, which allow quantifying the faults slip-rates since late-Pleistocene, and paleo-ruptures ages during the Holocene period on the two main strike slip faults analyzed : the Valley of Lakes Fault (VOLF), and the Western Bogd Fault (WBF). Preliminary data also allow quantifying the slip rates and the age of the most recent event along the Tsogt Fault (TF) and the Tsagaan Gol fault (TGF), respectively located in the westward continuation of the WBF and the VOLF. Moreover, systematic lateral offset measurements have been carried on along the faults traces, and especially along the 1957 surface rupture, where a statistical approach based on probability density has been applied in order to assess the average lateral offsets successively recorded by the landforms, and reveals that the slip distribution along the EBF on 3 seismic cycles. This suggests first that the slip distributions rather even along the rupture, and secondly that the slip related to the 1957 earthquake is of the same amount than previous major ruptures on that fault, for half of the main 1957 surface rupture. This approach of average coseismic slip assessment on several seismic cycles is promising, but still presents some inconsistencies, and we propose developments and validation perspectives. Morphotectonic parameters and ages of paleo-earthquakes reported in this thesis present a strong consistency with former studies along the EBF, with slow slip-rates (0,7 ± 0,2 mm.yr$^{-1}$ on the WBF and 0,5 ± 0,1 mm.yr$^{-1}$ on the VOLF), and significant left lateral coseismic offsets of 1.5 to 4.0 m for most recent events. Our measurements of slip rates indicate furthermore a distribution of the on-fault deformation from the EBF to the WBF and the VOLF, splitting the deformation in two branches, the north one reaching the TGF and the southern one visibly branches on the TF. Assessments of the paleoearthquakes ages show three possible clusters between the studied faults during the Holocene time, and one of them may break the three faults (WBF, EBF and VOLF), and seems as well to correspond to the cluster possibly identified 3-4 kyr ago. The fault parameters presented in this thesis allow computing the paleomagnitudes related to last seismic events along the WBF and the VOLF, ranging from Mw7.6 and Mw8, depending of parameters and empirical relations considered.

Finally, those fundamental data may serve as basic pattern for current seismic hazard assessments in Mongolia

## Résumé

La Mongolie occidentale a connu une sismicité intracontinentale exceptionnelle au cours de la première moitié du XX$^{e}$ siècle, avec 4 évènements sismiques d'une magnitude supérieure à 7.9, localisés sur des grandes structures décrochantes en régime transpressif senestre. Cette sismicité historique a été qualifiée d'essaim sismique, et des études paléosismologiques indiquent que ce phénomène a déjà pu se produire par le passé (3 à 4 ka). Mais si la partie Est de la chaine du Gobi-Altaï a rompu lors du séisme du même nom en 1957 (Mw8) le long de la faille de Bogd orientale (EBF), plusieurs traces de failles affectant des formations Holocènes et présentant des longueurs > 100 km ont été documentées dans la partie ouest du massif, sans pour autant faire l'objet d'études quantitatives. Cette thèse apporte un état des lieux de l'activité sismique dans le Gobi-Altaï, au travers d'une cartographie détaillée des escarpements de failles actives au cours du pléistocène supérieur, associée à une analyse de la segmentation au regard de critères géométriques et cinématiques. Parallèlement, des investigations morphotectoniques et paléosismologiques, couplées à des méthodes de datations au 10Be *in situ*, OSL et $^{14}$C, ont permis de quantifier les vitesses de glissement depuis le Pléistocène supérieur, et les âges des paléo-ruptures au cours de l'Holocène sur les deux principaux décrochements analysés : les failles de la Vallée des Lacs (VOLF), et de Bogd occidentale (WBF) ; des données préliminaires permettent également de contraindre l'âge de la dernière rupture et la vitesse de glissement sur les failles de Tsogt (TF) et de Tsagaan Gol (TGF), situées respectivement dans le prolongement occidental de la WBF et de la VOLF. De plus, des mesures systématiques des décalages cosismiques horizontaux enregistrés par la morphologie, notamment le long de la rupture de surface du séisme de 1957, couplés à l'utilisation et le développement d'une approche statistique de détermination des glissements cosismiques moyens au regard de la segmentation, a permis de déterminer la fonction de distribution du glissement le long de l'EBF sur 3 cycles sismiques. Ces résultats suggèrent d'une part une distribution du glissement assez homogène le long de la rupture, et d'autre part que le glissement du séisme généré en 1957 est d'une amplitude comparable de celle des précédents séismes, pour au moins 50 % de la rupture principale. Cette approche de détermination statistique des glissements moyens sur plusieurs cycles sismiques est prometteuse mais présente néanmoins certaines incohérences, et des voies de développement et de validations sont proposées. Les paramètres morphotectoniques et les âges des paléoséismes documentés dans cette thèse présentent une grande cohérence avec les données précédemment acquises sur l'EBF, avec des vitesses de faille lentes (0,7 ± 0,2 mm.a$^{-1}$ sur la WBF et 0,5 ± 0,2 mm.a$^{-1}$ sur la VOLF), des périodes de retour longues (4,0 ± 1,2 ka pour la WBF), et des décalages cosismiques de 1,5 à 4,0 m pour les derniers évènements. Nos mesures de vitesses de faille indiquent par ailleurs une distribution de la déformation depuis la EBF vers les WBF et VOLF, séparant la déformation en deux faisceaux de failles, l'un se branchant au nord depuis la VOLF sur la TGF, et le second se branchant sur la TF au sud. Les déterminations des âges de paléoséismes indiquent une possibilité de cluster entre les différentes failles étudiées, avec trois ruptures potentiellement synchrones au cours de l'Holocène, dont une, rompant l'intégralité des décrochements analysés (WBF, EBF et VOLF), s'avère être temporellement corrélée au précédent cluster potentiellement identifié à 3 – 4 ka. Les paramètres présentés dans cette thèse permettent finalement de calculer des paléomagnitudes associées aux deniers évènements sur les WBF et VOLF, comprises entre Mw7,6 et Mw8 selon les paramètres et les lois considérés. Ces données fondamentales pourront servir de canevas de base pour les actuelles études d'aléas sismique en Mongolie.